

Jaroslav Šesták
Miroslav Holeček
Jiří Málek

Institute of Physics, Academy of Sciences of ČR, v. v. i.,
Division of Solid State Physics, Prague
University of West Bohemia,
Research Centre – New Technologies, Pilsen
University of Pardubice,
Faculty of Chemical Technology, Pardubice

Some Thermodynamic, Structural and Behavioral Aspects of Materials Accentuating Non-crystalline States

AMORPHOUS SEDIMENTARY OPAL

Edited by
Jaroslav Šesták
Miroslav Holeček
Jiří Málek

Some Thermodynamic, Structural and Behavioral Aspects
of Materials Accentuating Non-crystalline States

Pilsen 2009

ISBN 978-80-87269-06-0



Some Thermodynamic, Structural and Behavioral Aspects of Materials
Accentuating Non-crystalline States

2009

Published under the financial support
of following institutions and projects:

Grant Agency of the Academy of Sciences of the Czech Republic, N° A100100639
and N° 1001007123, as well as by
Scientific Foundation of the Czech Republic, N° P204/10/13121,
Ministry of Education, Youth and Sport, NPV II 2E08042,
Czech industrial grant, N° FR-TI 1/335,
Institutional Research Plan of Institute of Physics ASCR, v.v.i., N° AV0Z10100521
and
the Foundation “Precioza” Opletalova 17, CZ-46667 Jablonec n/N

Some Thermodynamic, Structural and Behavioral Aspects of Materials Accentuating Non-crystalline States



Picturesque world of webs, arrangements, structures, disarrays and fractals

Welcome

Institute of Physics of the Academy of Sciences of the Czech Republic, v.v.i.,
Division of Solid State Physics, Cukrovarnická str. 10, CZ-16200 Praha;

University of West Bohemia, Univerzitní str. 8, CZ-30614 Plzeň,
Research Centre - New Technologies in Westbohemian Region;

University of Pardubice,
Faculty of Chemical Technology, Studentská str. 573, CZ-53210 Pardubice.

Some Thermodynamic, Structural and Behavioral Aspects of Materials Accentuating Non-crystalline States

Edited by

Jaroslav Šesták

Miroslav Holeček

Jiří Málek



Institute
of Physics



NEW TECHNOLOGIES
RESEARCH CENTRE
UNIVERSITY
OF WEST BOHEMIA



Univerzita
Pardubice

OPS Plzeň 2009



SOME THERMODYNAMIC, STRUCTURAL AND BEHAVIORAL
ASPECTS OF MATERIALS ACCENTUATING
NON-CRYSTALLINE STATES

University internal booklet – not for commercial distribution
Edited by Jaroslav Šesták, Miroslav Holeček and Jiří Málek
Assemblage and technical editorial by Jaroslav Šesták
Cover design by Jan Dienstbier, Jaroslav Šesták and Paul S. Thomas
Art photos by Pavel Šesták and Jaroslav Šesták
University reviewer Jaroslav Fiala
Text were not revised and English not corrected
Published by OPS Pilsen 2009
640 pp; Printed and bound by Typos, Pilsen
Manufactured in the Czech Republic

ISBN 978-80-87269-06-0

CONTENTS

PREFACE 2-6

INTRODUCING NON-CRYSTALLINE, DISORDERED, AMORPHOUS,
VITREOUS AND GLASSY CONCEPTS 8-28

C.A. Queiroz (Portugal), J. Šesták (Czechia)

1. Introduction: from continuum mechanics to a thermodynamic based perspective
2. Transformation Temperature, Fictive Temperature and Kauzmann Temperature
3. Dynamics of the glassy state: noncrystallinity, vitroids and Deborah number
4. Structural features of the glassy state: nano-scale or micro-scale heterogeneities
5. Specificity of noncrystalline chalcogenide materials
6. Pressure and temperature-induced amorphization
7. Vitrification versus crystallization: reduced T_g and the Hrubý parameter
8. Conclusion: distinction between amorphous and glassy materials
References (116 citations)

1. SOME HISTORICAL FEATURES FOCUSED BACK TO THE PROCESS
OF EUROPEAN EDUCATION REVEALING SOME IMPORTANT
SCIENTISTS, ROOTS OF THERMAL ANALYSIS AND THE ORIGIN OF
GLASS RESEARCH 30-58

J. Šesták (Czechia)

- 1.1. Model classification and their development in historical applications
- 1.2. Historical Prague, its famous Charles University and some medieval alchemists
- 1.3. Renaissance of Prague physics and noteworthy personalities
- 1.4. History of thermal analysis
- 1.5. Some introductory aspects of glass and its historical features
- 1.6. Following lines of glass investigation
References (166 citations)

2. PHENOMENOLOGICAL MEANING OF TEMPERATURE 60-78

J. J. Mareš (Czechia)

- 2.1. Introduction
- 2.2. Phenomenological conjugate variables
- 2.3. Diathermic partition, thermal equilibrium
- 2.4. Thermoscope
- 2.5. Thermoscopic states
- 2.6. The use of fixed points for calibration of thermoscopes

- 2.7. Mach's postulates-
 - 2.8. Mathematical structure of hotness manifold
 - 2.9. Definition of temperature
 - 2.10. Ideal (perfect) gas temperature scale
 - 2.11. Absolute temperature
 - 2.12. Carnot's theorem
 - 2.13. Kelvin's proposition
- References (33 citations)

3. FROM CARNOT TO NONEQUILIBRIUM AND ABSTRACT THERMODYNAMICS AND SOME CONSEQUENCES FOR THERMAL ANALYSIS

80-96

M. Holeček (Czechia)

- 3. 1. A lucky discovery of the second law of thermodynamics
 - 3. 2. Clausius' fundamental contribution: the birth of entropy
 - 3. 3. Irreversible processes and nonequilibrium thermodynamics
 - 3. 4. Abstract thermodynamics – from a system to its surrounding
 - 3. 5. Abstract formulation of the Carnot's theorem and the Second Law
 - 3. 6. Material sample in a varying temperature field
 - 3. 7. Conclusions
- References (21 citations)

4. NEW THERMODYNAMIC POTENTIALS AND CLAPEYRON EQUATIONS FOR CONDENSED PARTLY OPEN SYSTEMS APPLICABLE TO NONSTOICHIOMETRIC PHASES

98-116

P. Holba (Czechia)

- 4.1. Introduction - biographical context
 - 4.2. Category of partly open systems
 - 4.3. Hyperfree energy constructed by Legendre transformation
 - 4.4. Quasimolar fractions, quasimolar quantities and common tangent in quasibinary systems
 - 4.5. Clapeyron equations for quasiunary partly open systems
 - 4.6 Applications and illustrations
- References (38 citations)

5. THE PHASES BETWEEN SOLID AND LIQUID, CHARACTERIZED BY THERMAL ANALYSIS

118-138

B. Wunderlich (USA)

- 5.1. Introduction: solids, liquids and their transitions
- 5. 2. Phases
- 5. 3. Measurements of thermal properties
- 5. 4. Interpretation of the heat capacity of solids
- 5. 5. Large amplitude motion

- 5. 6. First order phase transition
- 5. 7. Glass transition
- 5. 8. Conclusions
- References (70 citations)

6. PHASE SEPARATION IN POLYMER SYSTEMS

140-156

I. Krakovský (Czechia), Y. Ikeda (Japan)

- 6. 1. Polymers
- 6. 2. Polymer solutions and blends
- 6. 3. Block copolymers
- 6. 4. Nanophase separation in polymer networks
- 6.5. Nanophase separation (crystallization) in polymer networks induced by strain
- References (24 citations)

7. SOME IMPORTANT FEATURES OF GLASSINESS AND THE NATURE OF AMORPHOUS SOLIDS

158-174

H. Suga (Japan)

- 7. 1. Nature of the amorphous solids
- 7. 2. Characterizations of Amorphous Solids
- 7. 3. Glassy transitions in crystals: glassy crystals
- 7. 4. Other aspects of glassy solids
- References (27 citations)

8. BIOLOGICAL GLASSES AND THEIR FORMATION DURING OVERWINTERING AND CRYOPRESERVATION OF PLANTS

176-198

J. Zámečník, J. Šesták (all Czechia)

- 8. 1. Life with anomalous behavior of water
- 8.2. Need for a man-made safeguarding of biological systems
- 8. 3. Man's strategy how to generate glassy state for plants' survival at ultra-low temperature
- 8. 4. Glass transition temperature, freezing point depression temperature and supercooling temperature
- 8.5. Specificity of biological samples
- 8. 6. Stability of biological glass: an important condition for reaching its long-term storage
- 8. 7. Peculiarities of the thermal analysis when applied to cryogenic samples
- References (77 citations)

9. PROPERTIES OF SOME NATURAL GLASSES: AUSTRALIAN OPALS AND CZECH TEKTITE MOLDAVITES

200-218

P.S. Thomas (Australia), K. Heide (Germany), J. Šesták (Czechia), E. Füglein (Germany), P. Šimon (Slovakia)

- 9.1. Origin of natural inorganic non-crystalline solids

- 9.2. Australian Opal
- 9.3. Tektites – Moldavites
- 9.4. Rare natural non-crystalline game stones
References (62 citations)

10. CHALCOGENIDE GLASSES AS MODEL SYSTEMS FOR STUDYING THERMAL PROPERTIES

220-246

Z. Černošek, J. Holubová, E. Černošková (all Czechia)

- 10. 1. Differential Scanning Calorimetry – DSC
- 10 .2. Glass transition
- 10.2. Enthalpic relaxation - the model
- 10.2 Ideal glass – Kauzmann temperature and the glass transition
- 10. 3. Crystallization – kinetic analysis
- 10. 4. Crystallization of selenium supercooled liquid:
isothermal and non-isothermal kinetics by DSC experiments
References (72 citations)

11. APPLICATION OF ISOCONVERSIONAL METHODS FOR THE PROCESSES OCCURRING IN GLASSY AND AMORPHOUS MATERIALS

248-264

P. Šimon (Slovakia), P.S. Thomas (Australia)

- 11. 1. Introduction
- 11.2. Single-step approximation
- 11.3. Isoconversional methods at linear heating
- 11.4. Kissinger method
- 11.5. Ozawa methods
- 11.6. Description of the kinetics of nucleation by the induction period of crystallization
- 11.7. Other isoconversional methods
- 11. 8. Isoconversional description of the kinetics of glass transition
Reference (63 citations)

12. CRYSTALLIZATION KINETICS IN AMORPHOUS AND GLASSY MATERIALS

266-284

D. Švadlák, P. Honcová, J. Málek (all Czechia)

- 15. 1. Introduction
- 12. 2. Theoretical part - growth rates
- 12.3. Experimental – calorimetry and optical measurements
- 12. 4. Results and discussion - . Comparison of crystal growth and DSC data
Reference (61 citations)

13. ON THE APPLICATION OF DTA/DSC METHODS FOR THE STUDY OF GLASS CRYSTALLIZATION KINETICS

286-306

**V.M. Fokin (Russia), A. Cabral Jr., M. L.F. Nascimento, E. D. Zanotto (all Brazil),
J. Šesták (Czechia)**

- 13.1. Traditional determination of overall crystallization kinetics by thermal analysis
- 13.2. Determination of crystal nucleation rates from TA methods and optical measurements
Reference (70 citations)

**14. CRYSTALLIZATION OF METALLIC MICRO- AND NANO-
CRYSTALLINE GLASSES** **308-326**

E. Illeková (Slovakia), J. Šesták (Czechia)

- 14. 1. Introduction to metallic glasses
- 14. 2. General reviewing of crystallization kinetics
- 14. 3. Crystallization kinetics of metallic glasses
- 14. 4. Two types of the crystallization kinetics in rapidly quenched ribbons
Reference (40 citations)

**15. TRANSPORT AND RELAXATION MECHANISMS IN IONIC
PHOSPHATE GLASSES** **328-342**

P. Bury, P. Hockicko (all Slovakia)

- 15. 1. Introduction
- 15.2 Transport and relaxation properties of ion conductive glasses
- 15.3. Electrical characterization of ion transport and relaxations
- 15.4. Mechanical and acoustic characterization of ion relaxations
- 15. 5. Transport and relaxation study of ionic phosphate glasses
Reference (33 citations)

**16. STUDYING STRUCTURE AND THERMAL PROPERTIES OF
OXIDE GLASSES** **344-362**

M. Liška (Slovakia)

- 16. 1. Introduction
- 16.2. Thermodynamics of glass formation [1, 2]
- 16. 3. Glass structure
- 16. 4. Deducing the structure from stoichiometry
- 16. 5. Thermodynamic models of glass
- 16. 6. Quantitative Raman spectroscopy and Thermodynamic modeling
Reference (49 citations)

**17. NON-BRIDGING OXYGEN IN SILICA BIO-COMPATIBLE GLASS-
CERAMICS AND MAGNETIC PROPERTIES OF Fe_2O_3 ADDED BORATE
GLASSES** **364-386**

J. Šesták (Czechia), N. Koga (Japan), Z. Strnad (Czechia)

17. 1. Introduction to bridging and non-bridging oxygen
17. 2. Some volume considerations about of ionic sites in silicate glasses
17. 3. Simple calculation concept for non-bridging oxygen in silica bio-glasses
17. 4. Property and application of bio-active glass-ceramic materials
17. 5. Borate glasses containing Fe_2O_3 and their structural and magnetic properties
17. 6. Magnetic properties of the $(\text{Fe,Mn})_2\text{O}_3\text{-B}_2\text{O}_3$ splat-quenched system of variously doped melted mixtures
- 17.7. Specific case of speromagnetic behavior of rapidly quenched and laser melted $(\text{Fe,Mn})_2\text{O}_3\text{-(B,Bi)}_2\text{O}_3$ glasses
Reference (85 citations)

18. STRUCTURAL CHANGES IN LIQUIDS, CREATION OF VOIDS, MICRO-MOVEMENT OF VIBRATION CENTERS AND BUILT-IN BLOKS TOWARD THE GLASS TRANSITION TEMPERATURE 388-412

B. Hlaváček, J. Šesták (all Czechia)

18. 1. Model structure of liquids
18. 2. Amplitudes of vibration movements below the critical temperature
18. 3. First experimental justification of the structural heterogeneity of liquids
18. 4. Linear cooperative phenomena in the built-in blocks
18. 5. Source of diffusional movements on account of non-deterministic elements
18. 6. Energy associated with the bottom uplift of a potential well participating in viscoelastic structures
18. 7. Structure of liquid state at higher temperatures when depicting the growing number of voids
18. 8. Alpha process and beta slow processes
- 18.9. Boson peaks and the „Angel’s fragility“ – a correlation between two of vastly separated temperature-judicious areas
References (117 citations)

19. VISCOSITY, DIFFUSION AND ENTROPY: A NOVEL CORRELATION FOR GLASSES 414-426

I. Avramov (Bulgaria)

19. 1. Introduction
19. 2. Mean stay time and mean jump frequency
19. 3. Diffusion of fast moving ions
19. 4. Percolation and nucleation
19. 5. Viscosity
References (25 citations)

20. TRANSDICIPLINARITY OF DIFFUSION INCLUDING ASPECTS OF QUASIPARTICLES, QUANTUM DIFFUSION AND SELF-ORGANIZED REACTION PERIODICITY 428-454

Z. Kalva, J. Šesták, J.J. Mareš, J. Stávek (all Czechia)

- 20.1. Historical introduction: Fourier 's heat transfer and the Laws of Fick and Ohm
 - 20.2. Non-stationary heat diffusion and the generalized Schrödinger equation
 - 20.3. Heat as quasiparticles and further concept of diffusion transdisciplinary
 - 20. 4. Magnetocaloric effect
 - 20.5. Quantum criteria and diffusion
 - 20.6. Oscillatory regimes in some inorganic systems
 - 20.7. Belousov–Zhabotinsky periodic reactions
 - 20.7. Speed of diffusion
 - 20.9. Transmission of information – the photon codes
- References (105 citations)

21. LOW-TEMPERATURE MEASUREMENTS OF DISORDER-INDUCED EFFECTS IN LOW-DIMENSIONAL SYSTEMS 456-484

P. Hubík, J. J. Mareš (all Czechia)

- 21.1. Introduction
 - 21.2. Electron transport in 3D and 2D disordered metals - basic concepts
 - 21.3. Weak localization in 2D and 2D-like systems
 - 21.4. Quantum Hall effect in disordered 2DEG
 - 21.5. Grain boundaries in superconductive nanodiamond
- References (76 citations)

22. DIFFUSION STRUCTURAL DIAGNOSTICS OF SELF-IRRADIATED AMORPHOUS MINERALS 486-496

V. Balek (Czechia), I. von Beckman (Russia)

- 22.1. Diffusion structural diagnostics of solids
 - 22.2. The ETA application in the diffusion structural diagnostics of materials
- References (19 citations)

23. BASALT FILAMENTS – PROPERTIES AND APPLICATIONS 498-520

J. Militký, V. Kovačič, D. Křemenáková (all Czechia)

- 23. 2. Basalt fibres
 - 23. 3. Materials
 - 23. 4. Statistical Analysis of Fibres Strength
 - 23. 5. Basalt fibres properties after the thermal exposition
 - 23. 6. Thermomechanical analysis
 - 23. 7. Degradation in liquids
 - 23 . 8. Analysis of emitted particles during basalt handling
- References (25 citations)

24. NUCLEAR WASTE GLASSES: BEAUTIFUL SIMPLICITY OF COMPLEX SYSTEMS 522-536

P.R. Hrma (USA)

- 24. 2. HLW Glass Formulation
- 24.3. Settling of Solids in HLW Glass Melter
- 24. 4. Foaming
- 25. 5. Salt Segregation
- 24. 7. Feed-to-Glass Conversion
- 24. 8. Crystallization [33]
- 24. 9. Chemical Durability
- References (35 citations)

25. PHYSICO-CHEMICAL SURFACE PROPERTIES, THEIR MODIFICATIONS AND HEALING CAPACITY OF INORGANIC ENDOSTEAL BIOMATERIALS USED FOR MIMETIC BONE SUBSTITUTION IN IMPLANTOLOGY

538-554

J. Strnad, Z. Strnad (all Czechia)

- 25.1. Healing and new bone formation
- 25.2. Main types of bone-implant interface
- 25.3. Surface characteristics of titanium implants and their effect on osseointegration
- 25.4. Bioactivation of titanium
- References (57 citations):

26. GEOPOLYMERS – AMORPHOUS CERAMICS VIA SOLUTION

556-584

F. Šoukal, T. Opravil, P. Ptáček, B. Foller, J. Brandštetr, P. Roubíček (all Czechia)

- 26.1. Geopolymers – introduction and history
- 26.2. Geopolymerization – alkali dissolution and polycondensation
- 26.3. Raw materials
- 26.4. Alkaline activators
- 26.5. Constituents mixing order
- 26.6. Hydration of alkali-activated slag
- 26.7. Physical and mechanical properties of geopolymers
- 26.8. Geopolymers durability
- 26.9. Some examples of utilization of geopolymers
- 26.10. Conclusion and Shortcuts and symbols index
- References (72 citation)

27. APPLICATION OF SCANNING TRANSITIOMETRY IN PETROLEUM INDUSTRY AND IN POLYMER AND FOOD SCIENCES

586-602

J.-P. E. Grolier (France)

- 27.1. Introduction
- 27.2. Scanning transitiometry
- 27.3. Selected results (petroleum industry, polymers, foos science)
- 27.4. Concluding remarks
- References (39 citations)

AUTHORS

Avramov Isak, Prof., Ph.D., D.Sc., Department of Amorphous Materials, Institute of Physical Chemistry, G. Bonchev Str., Block 11, BG-1113 Sofia, Bulgaria;
Email: avramov@ipc.bas.bg

Balek Vladimír, Doc., M.Sc., Ph.D., D.Sc., Nuclear Research Institute Řež, CZ- 25068 Řež, Czech Republic; *Email:* bal@ujv.cz

Beckman von N. Igor, Prof., Ph.D., D.Sc., Chemical Fakulty, Moscow State University, Moscow, RU-199234 Russia; *Email:* beckman@radio.chem.msu.ru ,

Brandštetr Jiří, Prof., M.Eng., Ph.D., D.Sc., Institute of Materials Chemistry, Dept. of Chemistry, Brno University of Technology, Pukyňova 118, CZ-61200 Brno, Czech Republic;
E-mail : brandstetr@fch.vutbr.cz.

Bury Peter, Prof., Ph.D., Department of Physics, Faculty of Electrical Engineering, Žilina University, Univerzitná 8215/1, SK-01026 Žilina, Slovakia; *Email:* bury@fel.uniza.sk

Cabral A. Aluisio, Jr., Dr., Ph.D., Federal Institute of Maranhao, Department of Exact Sciences, Av. Getulio Vargas, n. 4, Monte Castelo, B-65030-000, Sao Luis, MA, Brazil;
Email: aluisio_cab@yahoo.com.br

Černošek Zdeněk, Prof., M.Eng., Ph.D., University of Pardubice, Department of General and Inorganic Chemistry, Studentská 573, CZ-532 10 Pardubice, Czech Republic;
Email: zdenek.cernosek@upce.cz

Černošková Eva, Doc., M.Eng., Ph.D., Joint Laboratory of Solid State Chemistry of the Institute of Macromolecular Chemistry (Academy of sciences CR) and the University of Pardubice, Studentská 84, CZ-532 10 Pardubice, Czech Republic;
Email: eva.cernoskova@upce.cz

Fiala Jaroslav (reviewer) Prof. RNDr., Ph.D., D.Sc., University of West Bohemia, Research Centre - New Technologies, Department of Structural Analysis, Univerzitní 8, CZ- 30614, Plzeň, Czech Republic; *Email:* fiala@ntc.zcu.cz

Fokin M. Vladimír, Dr., Ph.D., S.I.Vavilov's State Optical Institute, 36-1 Babushkina str., RU- 193171, St. Petersburg, Russia; *Email:* vfokin@pisem.net

Foller Bronislav, Dr., Ph.D., University of West Bohemia, Research Centre New Technologies, Department of Polymer Composites Technology, Univerzitní 8, CZ- 30614, Plzeň, Czech Republic; *Email:* foller@ntc.zcu.cz;

Füglein Ekkehard, Dr.rer.nat., Dipl.-Chem., NETZSCH-Gerätebau GmbH, Wittelsbacherstraße 42, D-95100, Germany;
Email: ekkehard.fueglein@netsch.com

Grolier E. Jean-Pierre, Prof., Ph.D., D.Sc., IACT President and Fulbright Professor, Laboratoire de Thermodynamique des Solutions et des Polymères, Université Blaise Pascal de Clermont-Ferrand, F-63177 Aubière, France; *Email*: j-pierre.grolier@univ-bpclermont.fr

Heide Klaus, Prof, Dr., Ph.D., Institut für Geowissenschaften, Friedrich Schiller-Universität Jena, Burgweg 11, D-07749 Jena, Germany; *Email*: ckh@uni-jena.de

Hlaváček Bořivoj, Doc., M.Eng., Ph.D., University of Pardubice, Department of Polymers, Studentská 84, CZ-532 10 Pardubice, Czech Republic; *Email*: borivoj.hlavacek@upce.cz

Hockicko Peter, Dr., Ph.D., Department of Physics, Faculty of Electrical Engineering, University of Žilina, Univerzitná 8215/1, SK-01026 Žilina, Slovakia; *Email*: hockicko@fyzika.uniza.sk

Honcová Pavla, M.Eng., Ph.D., University of Pardubice, Faculty of Chemical Technology, Studentská 573, CZ-53210 Pardubice, Czech Republic; *Email*: pavla.honcova@upce.cz

Holba Pavel, M.Eng., Ph.D., Thermal Analysis Group of the Czech Chemical Society, CZ - 190 00 Prague 9, K Lipám 293, Czech Republic; *Email*: holbap@gmail.com

Holeček Miroslav, Doc. Dr., RNDr., Research Centre - New Technologies in Westbohemian Region, University of West Bohemia, Univerzitní 8, CZ- 30614, Plzeň, Czech Republic; *Email*: holecek@ntc.zcu.cz

Holubová Jana, Doc., RNDr., Ph.D., University of Pardubice, Department of General and Inorganic Chemistry, Studentská 573, CZ-532 10 Pardubice, Czech Republic; *Email*: jana.holubova@upce.cz;

Hrma R. Pavel, M.Eng., Ph.D., Pacific Northwest National Laboratory, K6-24, PO Box 999, Richland, WA 99354, USA; *Email*: pavel.hrma@pnl.gov

Hubík Pavel, RNDr., Ph.D., Division of Solid-State Physics, Institute of Physics of the Academy of Sciences, ČR, v.v.i., Cukrovarnická 10, CZ-16200 Praha 6, Czech Republic; *Email*: hubik@fzu.cz

Ikeda Yuko, Doc., Ph.D., M.Eng., Graduate School of Science and Technology, Kyoto Institute of Technology, Matsugasaki, Kyoto 606-8585, Japan; *Email*: yuko@kit.ac.jp;

Illeková Emilie, Dr.rer.nat., Ph.D., D.Sc. Institute of Physics,, Slovak Academy of Sciences, Dúbravská cesta 9, SK-845 11 Bratislava, Slovakia; *Email*: fyziille@savba.sk

Kalva Zdeněk, Ph.D., RNDr., formerly with Centrum of Theoretical Studies of the Academy of Sciences and of Charles University, Davídkova 2102/93, CZ-18000 Prague 8, Czech Republic; *Email*: kalvaz@centrum.cz

Koga Nabuyoshi, Prof., Dr., Ph.D., Chemistry Laboratory, Department of Science Education, Graduate School of Education, Hiroshima University, 1-1-1 Kagamiyama, Higashi-Hiroshima 739-8524, Japan; *Email*: nkoga@hiroshima-u.ac.jp

Kovačič Vladimír, M.Eng., Eur.Eng., Textile Faculty, Technical University of Libverec, Studentska 2, CZ-46117 Liberec, Czech Republic; *Email*: vladimir.kovacic@tul.cz

Krakovský Ivan, , Doc., Dr.rer.nat., Ph.D., Department of Macromolecular Physics, Faculty of Mathematics and Physics, Charles University, V Holešovičkách 2, CZ-180 00 Praha 8, Czech Republic; *Email: ivank@kmf.troja.mff.cuni.cz*

Křemenáková Dana, Doc., Ph.D., M.Eng., Dept. of Textile Technology, Textile Faculty of the Technical University of Liberec, Studentská 1, CZ-460 17 Liberec, Czech Republic; *Email: dana.kremenakova@tul.cz*

Liška Marek, Prof., M.Eng., Ph.D., D.Sc., Vitrum Laugaricio, Joint Glass Center of Institute of Inorganic Chemistry (Slovak Academy of Sciences) and Alexander Dubček University of Trenčín and RONA, j.s.c. glassfactory, Studentska 2, Trenčín, SK-911 50, Slovak Republic; *Email: liska@tnuni.sk*

Málek Jiří, Prof., M.Eng., Ph.D., Dr.Sc., University of Pardubice, Faculty of Chemical Technology, Studentská 573, CZ-53210 Pardubice, Czech Republic; *Email: jiri.malek@upce.cz*

Mareš J. Jiří, RNDr., Ph.D., Division of Solid-State Physics, Institute of Physics of the Academy of Sciences, ČR, v.v.i., Cukrovarnická 10, CZ-16200 Praha 6, Czech Republic; *Email: semicon@fzu.cz*

Militký Jiří, Prof., M.Eng., Ph.D., Eur.Eng., Textile Faculty, Technical University of Liberec, Studentská 2 CZ - 461 17 Liberec, Czech Republic; *Email: jiri.militky @tul.cz*

Nascimento L.F. Marcio, Dr., Vitreous Materials Lab., Materials Engineering Department, Federal University of São Carlos, Rod. Washington Luis, Km. 235, 13.565-905, São Carlos, SP, Brazil; *Email: mlfn@ufb.br*

Opravil Tomáš, M.Eng., Brno University of Technology, Faculty of Chemistry, Institute of Material Chemistry, Purkyňova 464/118, CZ-61200, Brno, Czech Republic; *Email: opravil@fch.vutbr.cz;*

Ptáček Petr, Ph.D., Brno University of Technology, Faculty of Chemistry, Institute of Material Chemistry, Purkyňova 464/118, CZ-61200, Brno, Czech Republic; *Email: ptacek@fch.vutbr.cz;*

Queiroz A. Carlos, Dr, Ph.D., VICARTE - Glass and Ceramics Research Unit, Faculty of Sciences and Technology, New University of Lisbon, P - 2829 - 516 Caparica, Portugal; *Email: c.queiroz@fct.unl.pt*

Roubíček Pavel, M.Eng., CLUZ - České lupkové závody, a.s., Nové Strašecí 1171, CZ-27111, Nové Strašecí, Czech Republic; *Email: roubicek@cluz.cz;*

Stávek Jiří, M.Eng., Ph.D., Laboratory of Diffusion Processes, Bazovského 1228, CZ-16300 Prague, Czech Republic; *Email: stavek@volny.cz*

Strnad Jakub M.Eng., Dr., Ph.D., LASAK, Ltd., Laboratory for Glass and Ceramics, Papírenská 25, CZ-16000 Prague 6, Czech Republic; *Email: strnadj@lasak.cz*

Strnad Zdeněk, Doc., M.Eng., Ph.D., LASAK, Ltd., Laboratory for Glass and Ceramics, Papírenská 25, CZ-16000 Prague 6, Czech Republic; *Email: strnadz@lasak.cz*

Suga Hiroshi, Prof., Ph.D., D.Sc., Prof. Emeritus of the Osaka University, Faculty of Science, Toyonaka, Osaka 560-0043, Japan; *Email*: suga-hiroshi777@hcn.zaq.ne.jp

Šesták Jaroslav, Prof., M.Eng., Ph.D., D.Sc., Division of Solid-State Physics, Institute of Physics, *v.v.i.*, the Academy of Sciences of ČR, Cukrovarnická 10, CZ-16200 Praha 6, Czech Republic; *Email*: sestak@fzu.cz and New Technology - Research Center in the Westbohemian Region, University of West Bohemia, Univerzitní 8, CZ- 30614, Plzeň; *Email*: jarda.sestak@gmail.com,

Šimon Peter, Prof., M.Eng., Ph.D., D.Sc., Institute of Physical Chemistry and Chemical Physics, Faculty of Chemical and Food Technology, Slovak University of Technology, Radlinského 9, SK-812 37 Bratislava, Slovakia; *Email*: peter.simon@stuba.sk

Šoukal František, M.Sc., Ph.D., Brno University of Technology, Faculty of Chemistry, Institute of Material Chemistry, Purkyňova 464/118, CZ-61200, Brno, Czech Republic; *Email*: soukal@fch.vutbr.cz;

Švedlák Daniel, M.Eng., Ph.D., University of Pardubice, Faculty of Chemical Technology, Studentská 573, CZ-53210 Pardubice, Czech Republic; *Email*: daniel.svadlak@paramo.cz

Thomas S. Paul, Prof., Ph.D., DIC, CChem, FRACI, Department of Chemistry, Materials and Forensic Sciences, Faculty of Science, University of Technology, PO Box 123, Broadway, Sydney, NSW 2007, Australia; *Email*: Paul.Thomas@uts.edu.au

Wunderlich Bernhard, Prof., Dr., Ph.D. Professor Emeritus of the University of Tennessee, Knoxville and Rensselaer Polytechnic Institute, 200 Baltusrol Road, Knoxville, TN 37934-3707, USA; *Email*: Wunderlich@CharterTN.net

Zámečník Jiří, Doc., M.Eng, Ph.D., Crop Research Institute, Molecular Biology Department, Plant Physiology and Cryobiology Laboratory, Drnovska 507, CZ- 161 06 Prague 6, Czech Republic; *Email*: zamecnik@vurv.cz

Zanotto D. Edgar, Prof., Dr., Ph.D., Materials Science & Engineering, Federal University of São Carlos, Department of Materials Engineering, Vitreous Materials Lab. Rod. Washington Luiz, Km.235, B-13565-905, Sao Carlos, SP, Brazil; *Email*: dedz@ufscar.br

*The above academic degrees and grades shown behind the names comply with the following abbreviations: **Prof.** represents the Full Professor (in the Czech Republic is granted by the President); **Doc.** means the Habilitated Docent (granted after defending the habilitation dissertation, which rank lays somewhere between the US levels of associate and full professors); **Dr.Sc.** or D.Sc. (doctor of science, is honoring the life-gen-work, which is the highest degree granted after defending the achievement thesis – common, e.g., in England, Russia and also Czechia); **Ph.D.** (has an equivalent in the former grade ‘CSc’ used in the past socialistic countries); **M.Eng.** often abridge Dipl.Ing. (engineer/master degree received after five years technical studies and graduation); **RNDr.** = Dr. rer. nat. (doctor degree received after five years university studies and graduation in natural sciences).*



Preface

„The ability to represent time and space and number is a precondition for having any experience whatsoever“

PREFACE

It is clear that vast amount of speedily expanding data on glass-formation as a result of melt suitable cooling and its re-crystallization upon glass consequent heating has required certain taxonomy leading to the early foundation of specific journals and symposia. Associated theoretical studies on nucleation, crystallization and crystal growth have also escalated being viewed from both limiting sides: on one hand it was the solidification upon a slow self-cooling of melts and on the other hand the determinedly suppressed crystallization of quickly quenched (freeze-in) melts. The best efforts, however, was made in the field of oxide glasses where the traditional symposia on advances in nucleation and crystal growth were originally held every ten years resulting in the valuable proceedings, beginning at early seventies by "*Advances in nucleation and crystallization of glasses*" edited by L.L. Hench and S.W. Freiman and published by American Ceramic Society (Columbus, Ohio 1972) and followed by "*Nucleation and crystallization of glasses*" edited by J.H. Simmons, D.R. Uhlmann and G.H. Beall and published in "*Advances of Ceramics*" (Amer. Cer. Soc., Columbus, Ohio 1982); "*Nucleation and crystallization in liquids and glasses*" edited by M.C. Weinberg and published in "*Ceramic Transactions*" (Amer. Cer. Soc., Westerville, Ohio 1993) and finally "*Crystallization in glasses and liquids*" (the symposium in Vaduz, Liechtenstein 2000), edited by W. Höland, M. Schweiger and V. Rheinberger and published in *Glastech. Ber. Glass. Sci. Tech.* 73 C, 2000 (with 425 pp.).

In this respect, the book should present (with a hopefully enough coherent content), the continuation of such a traditional publication activity particularly mentioning our previous monograph, which received abundant citation responses. Namely, it was a special issue of the journal *Thermochimica Acta*, Vol. 280/281 (Elsevier, Amsterdam 1996 with 533 pp. and edited by J. Šesták) entitled "*Vitrification, transformation and crystallization of glasses*". Its arrangement was initiated upon the cooperation with D.R. Uhlmann, N.J. Kreidl and M.C. Weinberg during the Šesták's 1994 visiting professorship at the University of Arizona in Tucson. Final book assembly was made possible by help of the most renowned US glass scientist such as C.A. Angel, D.E. Day, L.L. Hench, P.M. Mehl, C.T. Moynihan, C.S. Ray or M.C. Weinberg who also contributed the compendium. The multiple authorship was completed by other recognized scientists such as Argentinean C.J.R. Gonzales-Oliver, O.F. Martinez; Brazilian E.D. Zanotto; Czech Z. Kožíšek, Z. Chvoj; British P.F. James, M.J. Richardson; Bulgarian I.B. Gugov, I. Gutzov; French M. Poulain; German R. Müller; Hungarian I. Granasy; Indian K.S. Dubey, P. Ramachandrarao; Italian A. Buri, F. Branda; Liechtenstein W. Höland, V. Rheinberger; Japanese T. Kokubo, T. Komatsu, M. Matusita, M. Tatsumisago; Russian V. Filipovich, G. Moiseev, A. Kalinina, I. Tomilin or Spanish J.M. Barandiarán, I. Tellería. The resulted book contained as many as 40 contributions, which covered material oriented chapters on oxide, chalcogenide, metallic, polymeric and food glasses eloquent with their specific kinetic, thermodynamic, glass-forming, or even, bioactive behavior.

Another analogous collection, entitled "*Thermal studies beyond 2000*", is also worth mentioning as published as a special issue of the *Journal of Thermal Analysis and Calorimetry*, Vol. 60 (Kiadó, Budapest and Kluwer, Dordrecht 2000, 402 pp., edited by M.E. Brown, J. Málek, J. Mimkes and N. Koga and dedicated to J. Šesták's sixties. The most recent monograph "*Glass: the challenge for the 21st century*" was published by Trans Tech Publications (Switzerland 2008, 692 pp., edited by M. Liška, D. Galusek, R. Klement) as the proceedings of IX. ESG/ICG conference (held in Trenčín, Slovakia 2008).

The idea of collecting broader viewpoints toward the formation and devitrification of glasses, particularly aimed at the confrontation of various aspects of descriptive theories, evaluative treatments and applied technologies useful to all sorts of inorganic and organic materials, was repetitively the entire subject during the series of renowned Kreidl's memorial conferences. The one on "*Advances of glasses*" was held in Liechtenstein 1994 (proceedings edited D.R. Uhlmann and W. Hölland). The subsequent (last) meeting "*Building the bridges between glass science and glass technology*" was held in Trenčín 2004 (proceedings published in *Glass. Ber. Glass. Sci. Tech. 77C*, 2004, and edited by J. Šesták and M. Liška).

The tremendous potentiality of various impacts of a general area of vitrification provides almost inestimable properties of intrigued glassy state together with delicacy of associated processes inherent in nucleation and crystal growth. The longest tradition of a theoretical approach occurs in the field of oxide glasses with its own congresses originating in the 1930s, already putting emphasis on the formation and crystallization of vitreous media (e.g., J. Frenkel or W.T. Richards). In the 1950s this was followed by the extended theory of crystal growth in undercooled liquids (e.g., W.D. Hillig and J. Frankel), measurements of devitrification characteristics (e.g., A.J. Milue), use of DTA (e.g., the Indian school of T.S. Das, H.H. Gupta and R.L. Thakur in the 1960s) and the detailed analysis of nucleation-growth processes in glasses (amongst others, C.A. Angell, J.D. Mackenzie, P.W. McMillan, P.F. James or D.R. Uhlmann). The other types of inorganic glasses have created their own history, in the first period, typically not interacting with the other fields creating their own crystallization systematic. Namely it is the field of chalcogenides (e.g., D.W. Henderson) which followed the boom of amorphous semiconductors starting their symposia in the 1960s. Even more effectively, the field of metallic glasses has appeared starting their symposia in the 1970s and presenting valuable contributions to crystal-growth theories (for example, F. Spaepen, H.A. Davies, F.E. Luborsky, A.L. Greer or U. Koester). Glassy (melt quenched) or amorphous (disintegrated) states have become essential precursors for the preparation of many advanced materials such as magnetics, solid electrolytes, oxide superconductors or generally low-dimensional systems (e.g., quasiparticles, semiconductor quantum wells and dots). Moreover, the sol-gel method has successfully competed to become one of the most progressive techniques in preparing the various inorganic, organic and mutually mixed glasses not attainable by other techniques. Certainly we should not forget the traditional field of organic glasses, having their important past in polymer science (e.g., B. Wunderlich) and recently in cryogenics (e.g., P. Bourton). Progress in various aspects of solidification should also be noted as carried out in the areas of nucleation (e.g., B. Mutaftschiev), stability (e.g., J.J. Favier) and growth (e.g., A.A. Chernov).

The theory development has proceeded in various stages using different means in order to study general processes of formation of solids upon cooling or other methods of crystal network disintegration; recently based even on the extended capabilities of large computers. It can be roughly ranked into two general groups:

(i) Molecular dynamics and Monte Carlo methods involving the determination of coordinate impulses in the so-called mechanical approach. It deals with equations of motion or potential interactions and evaluation is controlled by kinetic equations based on single and/or multiple particle behavior characterized by three-dimensional distribution functions. The hastily increasing capacity of computers enables solution of the empirical quasi- and multi-particle potentials toward quantum-chemical methods (DFT– density functional theory).

(ii) Phenomenological methods covering the typically hydrodynamic approaches, which use equations of heat and mass transfers and fluid convection, as well as the kinetics of phase transitions through phenomenological and statistical physics including thermodynamics.

Particularly thermodynamic and structural thoughts are vastly useful for elucidation of some aspects of glassiness. Let us first remind that even all crystals (exhibiting so called ‘long-range order’) comprise at a finite temperature some imperfections (non-stoichiometric sites, defects or vacancies), which density do not continue to diminish with decreasing temperature perpetually toward the zero temperature but freezes-in near a temperature at which the imperfection healing (by diffusing or some other lattice rebuilding) ceases. At rising temperature, however, the imperfection density and their size amplify until a critical stage leading eventually to a phase transition. Under particular circumstances the imperfections can act as sources of specific properties; such as photo-sensitivity in the case of chalcogenides, where the valence alternative pairs can provide, for example, the form of exalted defectiveness (defect density of about 10^{17} cm^{-3}) creating a positively charged over-coordinated atom and a negative under-coordinated counter-partner without changing the total number of bonds but yielding thus photo-sensitive centers.

By the same argument we can treat glasses (exhibiting so called ‘short-range order’), which encompass also intrinsic defects (interconnected blocs/islands, voids, etc.) defined as a deviation from the lowest energy bonding arrangement. Throughout freezing of such defects complex processes can subsist, which stages we attend to associate with certain assortment of temperatures characterized all the way down from the state of liquid still down to undercooled liquid (e.g. T_g) and finally to glass. A needed definition of short-range order imposed that each constituent species (e.g. atoms) fulfils its chemical valence requirement (so called 8-N rule), however, the stronger heteropolar bonds (e.g. As-S) are favored over the homopolar bonds (S-S, As-As). It is worth noting that the constrained bond length survives within $\sim 1\%$ equivalency of the bonds existing in the long-range ordered in a corresponding crystal. We can distinguish a topological short-range order, in which the structural defects are subject to relaxation and annihilation at annealing temperatures close to T_g and which is usually associated by collective movements of constitutional species related to both the atomic or the whole cluster hauling. On the other hand, there is common a compositional short-range ordering, in which chemically similar species (such as Ni, Fe or Co in metallic glasses) can mutually exchange their atomic positions often resulting in re-arrangement of the nearest neighbors ensuing magnetic anisotropy, etc. Finally there can happen a diffusion ordering connected with mutual survival and disappearance of various structural defects, which are shaped due to the samples inflict to great temperature gradients (e.g. quenching), which subsequently yields various adjustment due to relaxation of mechanical stresses and deformations.

Another element of randomness is the variation of bond angles sometime assumed to be crucial in further distinguishing constrained states of glassy and amorphous materials. The flexibility of covalent bond is largest for the two-fold coordination groups of VI-elements and is lowest for the tetrahedrally coordinated groups of IV-elements. For instance, in the SiO_2 glasses the oxygen atoms are bridging the Si-tetrahedral providing the essential flexibility, which is considered necessary to form a random covalent network (without exhibiting excess of strain). However, if such a covalent random network is formed without the flexing bridges of the group VI-elements the structure becomes amorphous (as the deposited strain-confined films of, e.g., As_2S_3), which can exist in many various forms of non-crystalline configurations (often experimentally irreproducible). The highly constrained nature of variously obtained amorphous films suggests that defects might not be randomly distributed but could be predominantly located as internal blocks, voids and strain-relief interfaces between low-strain regions. In contrast to glasses, the amorphous films can thus exist in many non-crystalline configurationally states the thermal annealing of which can lower its tense energy, however, cannot transform the over-constrained amorphous configuration from one ranking to another. A drastic atomic rearrangement would be enforced as to accomplish such an ‘unstructured’

reconstruction, which would, instead, materialize overlapping by more pertinent as well as unprompted crystallization.

However, a possible interference of so called ‘medium-range order’ (or ‘modulated structures’) becomes particularly common in resolving various non-crystalline materials, pertinent typically semiconductors, where the concept of homogeneously random network and its heterogeneity was most extensively studied. It is closely connected with the fashionable use of adjective ‘nano’ (*nano-technology or nano-materials*) touching the limits where the ordered and disordered states transpire factually a guaranteed delimitability. The standard observations, based on measuring crystallographic characteristics and the amount of crystalline phases, such as typical XRD, are capable to detect the crystalline phase down to about 2 % within the glassy matrix (certainly under certain crystal-size detectability). If not assuming here the capability to distinguish a minimum of yet-crystal-magnitude (by traditional XRD peak broadening), nor we account for a specialized diffraction measurement at low diffraction angles (radial distribution function); we can concentrate toward the critical amount of crystalline phase in the glassy sample. This issue is yet befitting the crucial question how to relevantly define the limit of yet ‘true glassiness’ and already ‘nano-crystallinity’. There became known a few proposals but the generally accepted figure is, for long, the value of 10^{-6} vol. % (less common 10^{-3} %), of crystallites to exist within glass matrix not yet disturbing its non-crystalline characterization and consequent definition of glassiness. The appropriateness of this value, however, is difficult to authorize persisting in its maintenance on basis of acute convenience and reiteration.

There are many other features and aspects of glassiness, which are hopefully dealt with in appropriate details within the individual book chapters. For a limited number of enclosed printed book pages it, therefore, was impossible to cover all subjects of variously deviating interests being thus forced to restrict the chapters’ subject matter and focused them to a chosen but narrowed attitude. Nevertheless, some emerging areas of research were daringly introduced such as non-stoichiometry, in-between existence of various phases and their separation in macromolecular systems, polymers, bio-polymers and geo-polymers, natural biological and native geological glasses, assorted kinetic assessments and methods of evaluation, chalcogenide, oxide and metallic glasses, preparation of amorphous ceramics via solutions, interdisciplinary aspects of variously comprehended diffusion, disordered and metamic materials, nuclear waste and basaltic fibrous glasses. We allowed novel questioning of temperature measurements and innovative phenomenology of heat, low temperature and magnetic measurements as well as the special mode of emanation-diagnostic measurements or transiometry. The editors are optimistic that such a widespread book concoction will find a positive reader’s responses helpful to an augmentation of their inventive comprehension.

The philosophy of this book is specifically distinctive being sourced on and related to the long-lasting Czech-Slovak national cooperation between their various national universities and institutions. The content was completed by invited contributions offered by some matching, vastly renowned scientists from abroad. Sensitively decided invitations and carefully selected authors assured a desirable diversity of views and ideas including mixture of various themes and subjects treatment from a choice of regions. Worth mention is an assortment of subjects accessible within the recent Czech-Slovak glass research and engineering among others, mentioning mathematical modeling of glass melting and formation (TU Liberec, Glass Service Vsetín, VŠChT Praha); molecular dynamics (VŠChT Praha, U. Trencin); relaxation processes in Tg region (UK Praha, U. Pardubice, U. Trencin, U. Nitra, UMCh AcSc Praha); theory of glass nucleation and crystallization (U. Pardubice, FZU AcSc Praha, U. Pardubice, STU Bratislava); specificity of chalcogenide (U. Pardubice), metallic (FU SAV Bratislava) and phosphate glasses (U. Pardubice, U. Nitra) not forgetting other

various research and technological aspects (TC ZČU Plzeň, LASAK Praha, VŠChT Praha, TU Brno, U. Zlin, U. Nitra, TU Liberec), etc..

We should like to thank very much, indeed, all contributors who spared their valuable time submitting their manuscripts for this book. The 28 herewith published scripts were peer reviewed (and selected out of 33 contributions) and arranged as the resulting chapters grouped as follows: *theory and thermodynamics, macromolecules and polymers, vitreous states, crystallization kinetics, structural and transport properties, diffusion and low-dimensional systems and technological applications*. We intentionally included even such contributions, which are not from the main stream of current trends in order to show the fascinating state-of-art of the field of chemistry and physics of solids (including the liquid hinterland), which, in quite a few aspects, still keep indubitable character of certain 'hot' issues, particularly when drawing the reader's attention to the metastable states inherent in glassy, amorphous and otherwise disordered materials.

Praha-Plzeň-Pardubice 2009, The editors:



Jaroslav Šesták senior scientist of the Academy of Science, ČR;
Professor of New York University in Prague and the Emeritus Professor of
Kyoto University in Japan



Miroslav Holeček, Director of the New Technologies – Research
Centre in the West Bohemian Region, Associated professor of
thermomechanics of the Faculty of Applied Science, West Bohemian
University in Pilsen



Jiří Málek, Rector of the Pardubice University and
Professor of physical chemistry of the Faculty of Chemical Technology



Introduction
Glassy and amorphous

INTRODUCING NON-CRYSTALLINE, DISORDERED, AMORPHOUS, VITREOUS AND GLASSY CONCEPTS

Carlos A. Queiroz, Jaroslav Šesták

1. Introduction: from continuum mechanics to a thermodynamic based perspective

Dealing with pure substances we can easily distinguish and define perfect gases from real gases, while within liquids we may distinguish adequately among distinct classes of liquids, as electrolyte solutions, organic solutions, liquid metals, molten salts or ionic melts. Considering the solid state we can make a distinction between perfect and defective crystals, metals and ceramics and, certainly, we can recognize amorphous and glassy materials having, by the same arguments, intrinsic defects too, defined as deviations from the lowest energy bonding arrangements [1]. However, we still lack a widely accepted conceptual borderline to distinguish states of matter thought to be intermediate between the classic concepts of solid and liquid. It is particularly noticeable that the concepts of glassy and amorphous solids appear often confused, having no adjusted convention for their exploitation in the published literature, while still lacking more widely accepted associated definitions.

In 1968, a special commission nominated by the *National Research Council* of the U.S.A., proposed to define glass as an «*X-ray amorphous solid which exhibits the glass transition, the latter being defined as that phenomenon in which a solid amorphous phase exhibits with changing temperature a more or less sudden change in the derivative thermodynamic properties, such as heat capacity and expansion coefficient, from crystal-like to liquid-like values*» [2]. As it can be appreciated, this definition suggests implicitly that all glasses are to be considered amorphous while the opposite is not necessarily true.

There are two basic approaches when trying to describe a material substance in a scientifically sounding way. One can look into the substance as a static entity and try to examine it from a microscopic structural perspective; or we can examine the behaviour of the entire substance as it follows some kind of a course of action. Such a process can be of several kinds. It can subsist of a chemical-physical procedure [3], such as an ordinary thermal treatment (showing how the substance responds to heat fluxes) or a precipitation from various solutions (displaying chemically induced formation of non-crystalline precipitants typically by sol-gel). It can also be a less acknowledged process of whichever origin, for example, mechanical (how the substance responds to external forces applied as pressure and stresses), electromagnetic (when interacting with the electromagnetic fields), depository (how it responds to the physical beam epitaxy or to chemical vapour deposition). It may even result from particle bombardment (interacting with such relevant particles), from mechanical disintegration (responding to intensive milling) or can be a consequence

from interactive biological processes (conveying with living organisms [4]).

Herewith we can specifically recognize various manners of disordering a regular network, which thus ensues *disordered states* of various cause and portrayal, often in low-dimensional systems (as thin layers), and including the particularity of quantum dots or wells, which, however, falls beyond the framework of this brief introduction. These processes are principally of macroscopic origin, bearing dynamic perspectives, although they can be related with the microscopic structure of matter owing to adequate theoretical models.

Macroscopically, and from a continuum mechanics perception, which deals with a material body response to external contact forces, a solid is a physical system which resists quasi-statically to external stresses applied at the surface, although some kind of motion is generally expected. Such stresses are specified by the stress tensor and the extent of body motion can be theoretically related with the stress tensor by constitutive equations. A number of ideal materials may be defined as representing particular relations between the stress motion and the intact motion. These are theoretical models used to represent and approach the behaviour of real materials.

A liquid does not responses to contact forces as a solid does, as it easily flows away, without resisting noticeably to the applied external stresses. In either case the volume of the substance is expected to change only slightly due to the applied external forces, while the substance responds elastically, and we may often approximately assume that it does change at all. A crystalline solid never accommodates its natural macroscopic flow as glass does, even if extremely slowly. Although continuum mechanics allow us to theoretically treat solids and liquids under a unifying perspective, comprising intermediate cases as well, and under an experimental perspective, the rheological approach may be considered as pretty accomplishing the same; however, we still lack a comparable satisfactory unifying thermodynamic treatment.

Of course, much of the apparent success of the continuum mechanics approach is actually elusive, as the whole collection of such idealized models may still be unable to perfectly translate the behaviour of some real materials, and intermediate cases may be particularly difficult to encompass within the continuum mechanics theoretical framework. On the other hand, thermodynamics tries to adopt a unifying perspective, has a general method that it tries to apply to all substances, which is less dependent on particular modelling hypothesis concerning idealized substances.

From a classical thermodynamic perspective a single homogeneous substance in some definite state of matter is treated as a *phase* (a homogeneous region of matter, not necessarily continuous, which is part of the thermodynamic system) and we are mostly concerned with the evolution of the system's macroscopic properties as a response to heat flow (heating or cooling). This may be also a convenient perspective to distinguish and characterize different materials. Statistical thermodynamics, also named statistical mechanics, bridges classical thermodynamics, as a phenomenological global approach, to a particles' based approach relying in quantum mechanics. It is concerned with the interpretation and prediction of the macroscopic properties of matter in terms of properties of the microscopic elementary subsystems that compose it, such as molecules, atoms, ions, electrons, etc. Here we are mainly concerned with *equilibrium* properties (e.g. temperature, pressure, specific heat, viscosity, etc.) and the macroscopic system should comprise a large number of subsystems, typically of about the order of the magnitude of the Avogadro

number, so that the statistical averages can provide a reliable description of the macroscopic system at its most probable state (thus in *equilibrium*, in the sense that it remains unchanged with time). The statistical thermodynamics approach has been quite successful working with gases (including real gases) and solids, but rigorous predictions of the thermophysical properties of dense fluids are currently difficult to obtain.

Still another way to possibly classify material substances relies on stressing their natural or artificial nature, the raw-materials involved on their preparation, or the main features of their preparation method, as for instance, we distinguish between natural and artificial polymers; or from melted, metallic, and sol-gel glasses. Such approach treats differently substances that can actually be quite similar, either from a thermodynamic or from a structural perspective, and doesn't transmit any insight on the structural nature, or on the main thermodynamic properties of the substance considered.

For a general material outlook there subsists a widespread acquaintance with the measurable reality that near the melting temperature, T_m , the melts of most ready-to-crystallize solids possess viscosities less than 1 poise (while, for comparison, the anomalous water has that of mere 0.1 poise) [1]. It is worth to remark that metallic glasses do not show this characteristic reduction on viscosity; their melts remain very fluid, which requests the application of extremely high quenching rates ($>10^6$ °C s⁻¹ in order to ever produce a noncrystalline solid). However, the moderate melt quenching of alloy compositions in the neighbourhood of deep eutectics, such as 80% of metals (Fe, Ni, Co, Mo, Cu, Cr) combined with 20% of glass-forming metalloids (B, Si, P, C, Ge) produce technologically beneficial glasses (magnetic) in which, however, the glass transition is seldom observed.

Most melts can undercool by perhaps 10-20°C below T_m , but the presence of impurities, slight disturbances, or even the mere contact with the container, will lead to a prompt crystallization. Low viscosity facilitates the diffusion of constituent species, which is unavoidable to make possible the necessary reconstruction of the fluid liquid web to that of rigid solid. The pre-nucleus (embryonic) sites, often existing in the melt, may enhance straight-forwarded crystallization [3], which is also favoured by their crystallographic orientation (e.g., lower symmetry, like monoclinic, which can bestow easier configuration and growth of such nuclei). Semiconductors are recognized materials to possess a large portion of pre-nuclei clusters in their melts, the extent of which can be handled by suitable annealing. Due to its atypical constitution, water, which exhibits an unusual pentagonal symmetry for the liquid containing clusters needs to transform to the hexagonal ice symmetry at a deeper undercooling (providing thus more time for the key symmetry reconstruction), being this one of extreme cases [4].

The melt viscosity (η) tends to increase rapidly along with decreasing temperature and reaches the traditionally expected value near T_m in order of 10^7 poise [1]. Diffusion dies down speedily and, for that reason, crystal formation turns out to be more and more intricate, but enabling, on the other hand, certain 'stability' improvement toward the 'metastability' of a supercooled liquid until the development of viscosity near $\eta \cong 10^{14}$ poise permits the headway of a freeze-in state of a metastably-rigid and radically-constrained glass.

2. Transformation Temperature, Fictive Temperature and Kauzmann Temperature

The supercooled liquid constitutes a metastable phase in a state of constrained internal equilibrium, while its free *Gibbs* energy is higher than that at the state of stable equilibrium. The free energy of the metastable liquid is thus kept at a local minimum, but not at an absolute minimum (that would imply the crystallization of the glass).

In the transformation region, hereafter assumed to lie below the melting temperature (T_m) but above the *Kauzmann* temperature¹ (T_K), the specific volume depends on the thermal history of the material (e.g., annealing time). This dependency cannot be fully understood within the framework of classic thermodynamics, were the specific volume is treated as a function of state, thus depending only on temperature and pressure. *Tool* [5] contoured this difficulty introducing the concept of fictive temperature, T_f [5-7], which corresponds to the extrapolated temperature of the *supercooled liquid*. The concept of fictive temperature associates itself to the assumption that the glass structure corresponds approximately to that of a frozen liquid, overcooled to T_f .

Considering a molar volume *versus* temperature plot (Figure 1; the upper plot), and herewith the prolongation of the line of the *supercooled liquid* towards the equilibrium crystal line below T_g , which, according to the thermodynamic theory proposed by *Gibbs* and *DiMarzio* [8-11] can well be considered as an equilibrium line between the *supercooled liquid* and the *glass*, it seems acceptable that over the extrapolated segment the fictive temperature equals the real temperature. As a melted glass under cooling enters the transformation region, a specific cooling rate may actually be selected so that a certain fictive temperature, T_f , located over the extrapolated segment range, can be reached by the *supercooled liquid*. T_f tends to decrease as the cooling rate decreases. Extrapolation for infinitely slow cooling carries out the fictitious temperature towards the line of solid state and that would conduct T_f down to a specific temperature, known as the *Kauzmann* temperature [12], T_K . It is supposed that the glass transition would then present itself as a sharp elbow, thus without any curvature at all [13]. This implies that T_K represents a lower

¹ There are some important points related to the glassy region revealing the allied characteristic temperatures. Most common is the *Kauzmann* temperature, T_K , which is given as the intersection of extrapolated line for the equilibrium liquid with that of equilibrium solid. The so called *Vogel* temperature, T_v , is decisive for the moment where the shear modulus terminates its increase and the viscosity becomes infinite according to the *Vogel-Fulcher-Tammann* model. This implies a discontinuity where viscous flow ceases (on cooling), at a certain finite temperature (the *Vogel* temperature, T_v). For polymers it customarily lays 52 °C below T_g but for inorganic glasses is about 100°C lower. The *Kauzmann* temperature, T_K , may get coincidental with T_v if derived from the entropy plot. The temperature when the shear elasticity disappears is often located as the crossover temperature, T_{cr} , were the residue is only shear viscosity (or elongation viscosity), which, for an undercooled liquid, is independent of the extent of deformation (but correlated with the speed of deformation).

limit of the glass transition². The glass transition would then lose his dynamic character (its time dependency), thus presenting itself as a static structural transition [13,14].

Slower cooling rates led to glasses of lower enthalpy contents, and providing that crystallization does not occur, the isobaric heat capacity (C_p) is expected to present a step-like non-linear variation with some hysteresis, within a temperature range centred at the calorimetric T_g , decreasing from values close to that of the equilibrium liquid to values close to that of the equilibrium crystal, although a positive but relatively small gap is still expected (Figure 1; the bottom plot). Excess values for entropy, enthalpy, and C_p , are expected for glasses below T_g , as compared to the corresponding crystallized substance, and such excess are even expected to be retained below T_K , although the observed gaps can somehow decrease as the temperature drops until they eventually vanish by absolute zero, as long as we assume that Nernst's theorem is obeyed, what is still a question of debate for glasses in general [e.g. 15]. As *Kauzmann* first pointed out [12], such gaps are expected to be smaller and smaller for lower cooling rates, and eventually, for a sufficiently slow cooling rate, they are actually expected to vanish at a positive finite temperature (T_K).

Below T_K the concept of fictive temperature loses its significance and any configurationally rearrangements typical of the glass transition are not expected to occur. It seems thus reasonable to consider that a glass kept below T_K stays stable in a state of non-equilibrium, without change on its specific volume, and of course, no crystallization is anticipatable. Above T_K , the glass is unstable with regards to the liquid *supercooled liquid* [16]. In this sense, it seems possible to consider T_K as the temperature that corresponds to the transition between 'glass' (unstable) and 'amorphous solid' (stable).

Taking in consideration the theoretical model proposed by *Adam* and *Gibbs* [17], T_K may stand as the transition temperature of the *supercooled liquid* for the hypothetical case of a idealized "glass" with null (zero) configurationally entropy, and this transition would correspond to infinite relaxation time [18,19]. It may be admitted that, in these idealized conditions, the glass transition would correspond to a discontinuity in the first derivative of the molar volume (transition of second order) while true crystallization occurs with discontinuity of the specific volume (transition of the first order). Since one cannot carry out experiments under such a limiting condition (while taking into account a theoretical point of view), and the glass transition is, in reality, still not fully understood [20,21], we must face extrapolations with some reservation.

It is worth noticing that at T_K only librational motion frequencies are expected to freeze-in. These can be associated to the liquid's configurational heat capacity. The higher frequencies are still expected to hold at lower temperatures, as they are associated with the vibrational frequency modes of the amorphous solid. However, the structural relaxation of the supercooled liquid is expected to be completed at T_K . Below T_K the 'glass' still shows higher specific volume and entropy than the corresponding crystalline solid, but in either case the contributions for the specific heat are mainly vibrational.

² Actually the entropy *versus* temperature plot should be preferred for obtaining a T_K estimate by extrapolation, but since the lines present some curvature in such a graph, the extrapolation procedure cannot rely on the straightforward linear extrapolation procedures being therefore more prone to error.

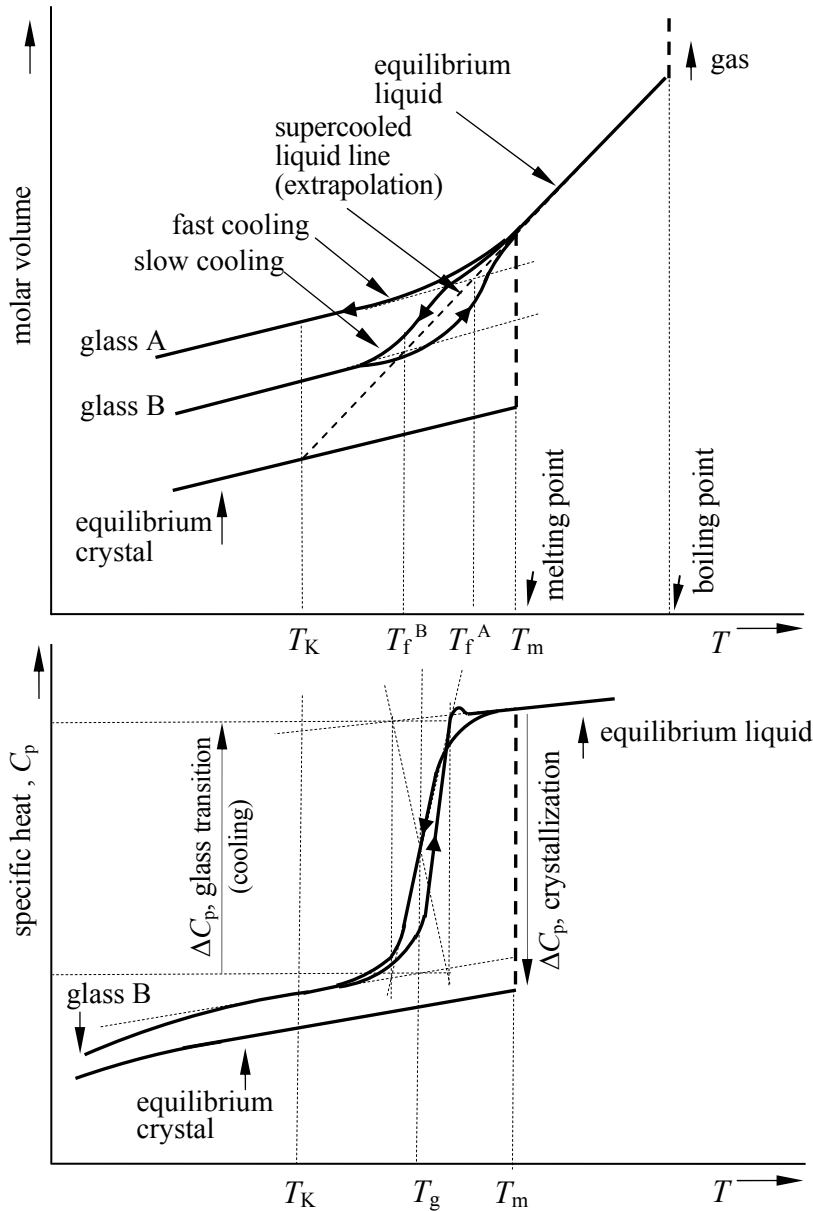


Fig. 1. Schematic typical plots for glass transition.

Upper: molar volume versus temperature; glasses, A and B, with decreasing fictive temperature (T_f^A and T_f^B) can be derived by decreasing the cooling rate; a T_K estimate may be obtained as the extrapolation limit at null cooling rate; hysteresis effect is shown for glass B, only. Bottom: isobaric heat capacity (C_p) showing a step-like non-linear variation with some hysteresis at the calorimetric T_g (depicted for glass B, on cooling).

An ‘ideal’ glass transition can be interpreted as, more or less, resembling a second order phase transition, according to the *Ehrenfest* classification [22-24]³. The corresponding theory assures that the two coexisting phases (a gluey *supercooled liquid* and

³ According to the *Ehrenfest* classification, if thermodynamic equilibrium may be assumed for the phases, it may be stated that for a first order transition, the first derivatives of the *Gibbs* free energy with regards to the temperature and pressure present a discontinuity at the phase transition temperature. If the first derivatives are continuous but the second ones are discontinuous, the phase transition is said of second order. For low cooling rates, and considering glasses cooled from melts, the glass transition may be seen approximately as a second order phase transition since in thermodynamic equilibrium the molar volume may be expressed as partial derivative of the *Gibbs* free energy with regards to the pressure: $V = [\partial G / \partial P]_T$.

an extremely viscous *glass*) should then possess matching entropy, possessing, however, distinct specific heat [e.g. 24]. This implies that the two phases should then become structurally isentropic. Besides, the molar volume of these two phases must also tend to reach a common value. The jump verified in the specific heat suggests a certain *congealment* of some kind of structural movements at the *Kauzmann* temperature, which are expected to cease their contribution toward the specific heat. One may interpret the rise in the glass transition temperature (T_g) above T_K for a ‘real’ glass transition as related with the period of time available for the observation of such freezing movements during typical laboratory experimentation.

It is worth noting that a number of authors took into account that the inspired existence of some higher (presumably second order) transition should be regarded as somewhat speculative. Accordingly, bearing in mind that at the matching conditions of internal equilibrium, the heat capacity of the undercooled liquid is indistinguishable to that of the congruous stable crystal, it comes to pass defensible, instead, that the glass transition may be best thought as a first-order-like transition, although of a disordered type [25-27]. The thermodynamic properties of such an undercooled highly vitreous melt possesses novel properties of an ideal glass structure, becoming therefore very similar to those of the crystalline state, as first noticed by *Cohen* and *Turnbull* [28]. The meaning of *Kauzmann* temperature for chalcogenide glasses was studied in more details by *Černošek et al.* [29] and other statistical, structural and frequential details of *Kauzmann* (and other temperatures) are given by *Hlaváček et al.* [30].

Studies based on *mode coupling theory* (MCT), developed by *Götze* and collaborators [31-42], and considering the percolation concept, showed that the temperature T_v of *Vogel-Fulcher-Tammann-Hesse* (VFTH) equation [43-45] (known as the above mentioned *Vogel* temperature) may be capable for an identification with T_K [46-47], at least approximately. This conclusion also was corroborated by the fluctuation theory proposed by *Donth* [48-49] and by a thermodynamic approach developed for the model of *spin-glasses* [50-51], and also by means of a stochastic model suggested by *Odagaki et al.* [52]. Experimental results obtained by the technique of *specific heat spectroscopy* seem to support this identification as well [53]. Taking $T_v > 0K$, B and η_0 (a pre-exponential factor) as fitting parameters, the equation of VFTH expresses the glass viscosity as:

$$\eta(T) = \eta_0 \exp\left(\frac{B}{T - T_v}\right) \quad (1)$$

In the limiting case of $T_v \rightarrow 0K$, the VFTH equation reduces to a familiar dependence of the *Arrhenius* type, where T_0 is habitually determined from adjusted experimental viscosity data reported for $T > T_g > T_v$. For this reason, the attributions of physical meaning to the parameter of adjusting T_v can be questioned outside the range where the experimental data can be obtained. For a common window glass a typical value would be $T_v \sim 249$ °C [54], while for the *Pyrex*[®] glass one could obtain $T_v \sim 282$ °C [55]. A study reported by *Mohanty* [56] based on fourteen distinct glasses suggests that we will be able to obtain a rough estimate of T_K considering that, as a rule of thumb, $T_K \sim 0.78T_g$ ($\pm 5.8\%$ for the reported glasses).

3. Dynamics of the glassy state: noncrystallinity, vitroids and Deborah number

Eckstein [57] classified non-crystalline solids as *vitroids*, referring to organic and inorganic materials in the vitreous state, including inorganic glasses and organic plastics. Vitroid structures are interpreted as paracrystalline networks, thought as intermediary arrangements between melts and the corresponding crystals. Such structures can be quantitatively characterized by temperature-like parameters, named “configurational temperatures”. Interesting is the use of a terminology that combines the term “solids” with the term “vitroids”, seen within the framework of rheology. This is because such a *vitroid* changes with time, thus being dependent on the existent observation time involved in detecting the extent of the change (as with viscous flow).

Reiner [58] introduced the so-called *Deborah number* expressing the ratio between the time of the material’s relaxation and that of its actual observation time, i.e., the experimental time scale ($De = \tau / \theta$). The name comes from the bible, where the prophetess Deborah’s song after the victory over Philistines includes: “*the mountains flowed before the Lord*”. For gases it reaches $\sim 10^{-12}$; for crystals we have $De \sim 10^{10}$; and for glasses it lays in an order of units. For an ordinary, as-quenched glass, the experimental relaxation time of a given frozen structure, represented by T_g , is said to be proportional to the shear stress relaxation time related to a shear viscosity expediently laying in order of 10^{13} P s. The Deborah number may be used as a criterion to distinguish solid from liquid-like behaviour [59]. At the glass transition temperature we expect $De \sim 1$.

Suga and *Seki* [60] stressed out that the glassy state is thermodynamically unstable and can be assumed to subsist as an undercooled metastable state obtained at a certain instant of continuous cooling through the glass transformation process, which is considered to be a general property of all such metastable phases. They also recommended a further classification for the generality of glasses into *glassy liquids*, *glassy liquid crystals* and *glassy crystals*; formed by glass transformation from their respective metastable states, either from liquids (traditional melts), or from liquid and solid crystalline phases, which can freeze-in a certain molecular motion (often rotation).

As *Wong* and *Angell* [61] pointed the distinction between *supercooled liquid* and *glass*, assumes that experimental essays are carried out in a time scale of seconds or minutes, that is, in the usual range of the *Maxwell* relaxation time [62] for a glass within the T_g region. This is the relaxation time for tensions when a constant shear is applied, and can be obtained as the ratio between the viscosity (η) and the shear modulus at infinite frequency (G_∞):

$$\eta = G_\infty \tau \quad (2)$$

Remarkably enough is that the shear modulus remains fairly insensitive to the variation of temperature [18, 63-65].

The glass transition occurs when the time of structural relaxation considered reaches the order of magnitude of a reasonable time period needed for the observation of the phenomena with the available laboratory equipment (usually $\sim 1-10^3$ s), and, as a consequence, for subsequent cooling experimenters cease to observe structural rearrangements in the glass network [66]. Pointing in the same direction, *Nieuwenhuizen* [67-68] refers that “a system is glassy when the observation time is much smaller than the

equilibration time". As a glassy system cools through the transformation region, the relaxation time of slow dissipative phenomena (named 'α-process') becomes much larger than the time of observation; while the fast processes ('β-process') are still observable at equilibrium. The distinction between relaxation processes α and β (classification after *Johari-Goldstein* [69-71]) is following: the leading relaxation process (α) is characterized by a time constant that increases from $\sim 10^{-12}$ s ($\sim 10^{12}$ Hz) to ~ 100 s ($\sim 10^{-2}$ Hz) in the glass transition region, accompanying (in an approximately proportional form) the increase of the viscosity, and deviating from *Arrhenius* law. Moreover, one may be able to observe a secondary process of relaxation (β), in the kHz region ($\sim 10^{-3}$ s), which obeys the *Arrhenius* law and is not significantly altered within the glass transition region. One may thus consider this last process as fast in the transition region with respect to the alternative α process [50]. The β process can be attributed to reorientation movements in the glass network [72]. At higher temperatures (above $\sim 1.2T_g$) the process α and β combine themselves in a unique process [32, 73-75]. A deeper connection between α and β relaxation processes seems to exist, as it was recently discussed by *Prevosto et al.* [76].

4. Structural features of the glassy state: nano-scale or micro-scale heterogeneities

The assumption of heterogeneity in liquid phase goes back to the assumption of a semi-crystalline phase by *Kauzmann* [12], as well as to the assumptions of coexistence of gas-liquid (semi-evaporated) structural units related to numerous works, e.g., *Cohen* and *Thurnbull* [28, 30]. The non-linear oscillators contribute also to an abnormal coefficient of thermal expansion and the amorphous-like liquid is thus structurally different from the amorphous-like solids, which casts some light into the explanations regarding the *Kauzmann paradox* [12, 77]. Below T_g thermodynamic properties as the specific heat and the coefficient of expansion decrease noticeably and simple extrapolations towards lower temperatures lead to the expectancy that the supercooled liquid would ultimately decrease to lower energy, entropy, and molar volume, as compared to the crystal, which seems unreasonable, hence the paradox. The *Kauzmann* paradox is based on extrapolation and does not take into account the fact that the liquid is a mechanically heterogeneous substance in which the heterogeneity is partially removed as the temperature goes down below T_g , and the highly non-linear oscillators disappear. The liquid phase is structurally different from the solid in mechanical sense, viz. by the appearance and disappearance of highly mobile, diffusive, non-linear oscillators.

The blocks, and their inter-blocks [30] bonding structure, form the main contributing factor responsible for dynamical parameters, such as the viscosity or bulk elasticity of the liquid phase. The blocks are also responsible for complex relaxation effects, because the interconnected linear oscillators forming their structures interact. On the other hand, the 'semi-evaporated' particles acting as the non-linear oscillators can perform their oscillations on several different amplitudes [78], and their motions carry with them elements of uncertainty, that can be described, in most cases by the non-linear, non-deterministic theories of chaos. Because the initial positional coordinates of such non-linear oscillator for its subsequent position and momentum cannot be determined in advance, the differential changes in initial conditions will bring completely different trajectories. The general rule for the nondeterministic chaos theories is thus consequently reflected into the

structure of the amorphous body in glassy state [30, 78-79], which depends on the way of cooling and will have this irregular character.

Micro-scale in-homogeneities linked to the glass transition process were also found in frozen aqueous solutions of organic solutes. *Sikora et al.* [80] found that as a result of a phase separation processes accompanying the freezing process of aqueous solutions of sucrose from -120°C to 30°C , at least two crystalline phases and two amorphous glasses could generally be clearly identified, while solutions of composition close to the eutectic were usually found to freeze directly into glass.

A feasible intervention of heterogeneity within the range of a so called ‘medium-range order’ (or ‘modulated structures’) becomes particularly common in resolving the liquid and glassy states of various non-crystalline semiconductors, where the concept of inhomogeneous random network was most extensively studied [1]. This is also connected with the limits where the ordered and disordered states transpire its factual distinguishing (‘delimitability’). The standard way for such observations, based on measuring the crystallographic characteristics and the amount of crystalline phases (typically by XRD), is able to detect the amount of crystalline phase down to about 2% within the glassy matrix (certainly under the restrain of a minimum crystal-size ‘detectability’) [3, 81].

Since we are not concerned here with the capability to distinguish a minimum of crystallite magnitude (which can be accessed by traditional XRD peak broadening), neither we account for a specialized diffraction measurement at low diffraction angles (to obtain the radial distribution function), we can direct our attention towards the critical amount of crystalline phase that subsists in the glassy sample. This issue is yet befitting the crucial question how relevant is to define the limit of yet ‘true glassiness’ and already ‘nanocrystallinity’. There are a few proposals but the generally accepted figure is, for long, the value of 10^{-6} vol. % (or a less common 10^{-3} %), of crystallites existing within glass matrix [3] as not yet disturbing its non-crystalline categorization and consequent definition of glassiness. The appropriateness of this value is difficult to authorize but, however, keeps its continuance on basis of severe convenience.

5. Specificity of noncrystalline chalcogenide materials

Another dimension is offered by the structure modelling of chalcogenide glasses, which is difficult or better too-all-embracing due to the great flexibility in the range of the structural units forming the random web. The concept of homogeneous random (covalent) network has been examined [82]. It is difficult, however, to encompass the differences flanked by various characters of non-crystalline chalcogenides, which incongruity is due to the bonding constrains and the number of degree of freedom allowed by their three-dimensional network, arranged towards the flexibility required accommodating the given random mismatch [83]. For a binary A_xB_{x-1} exhibiting only a short range order, the average coordination number is $m = x N_{\text{cn}}(\text{A}) + (1-x) N_{\text{cn}}(\text{B})$ where the number of constrains (N_{co}) per atom (A and B) is given by $N_{\text{co}}(m) = m/2 + m(m-1)/2 \cong m^2/2$. When equating the number of constrains to the ideal three spatial degrees of freedom, *Phillips* [83] showed that a most favourable average coordination is $m_c = \sqrt{6} = 2.45$ corresponding to an optimal connectivity. As a consequence, the glass-forming tendency occurs greatest when the short-range order imposed by bond stretching and bending forces is just sufficient to exhaust the local degrees of freedom. The internal strain increases with m while the entropy follows the

opposite trend because the non-crystalline state becomes *insufficiently interconnected* ('cross-linked'). Therefore, the conventional state of chalcogenide glasses is typically restricted to lie in the region $\sim 3.3 > m > 2$; while with $m > 3.3$ becomes *over-constrained* amorphous; yet higher, with $m > 4.3$, associates with unusual non-crystalline metals. On the other hand, those having the lower connectivity ($m < 2$) are assumed to be under-cross-linked amorphous materials, such as thin films of inert gases or halides. As any other possible criteria, this one suffers from uncertainty around the borderlines ($m \cong 2$ or $m \cong 3,3$), since the long-range interactions, ionicity, size effects, etc., have been neglected, as well as its applicability to the class of quenched tetrahedral glasses (e.g., $A^{II}B_2^V$ like $CdAs_2$ and their derivatives with admixtures of Ge, P, etc.). Even glasses with the average coordination $m = m_c$ contain a considerable strain, which magnitude can be accessed from the difference in heats of solution, such as, that for vitreous silica ($m=2.67$) 2.16 Kcal/mol, while for crystalline α -cristobalite one obtains 1.52 Kcal/mol. The flexibility of covalent bond is largest for the two-fold coordination groups of VI-elements and is lowest for the tetrahedrally coordinated groups of IV-elements. For instance, in the SiO_2 glasses the oxygen atoms are bridging the Si-tetrahedral providing the essential flexibility, which is considered necessary to form a random covalent network. However, if such a covalent random network is formed without the flexing bridges the structure tends to become amorphous (as the deposited strain-confined films of, e.g., As_2S_3), which can exist in many various forms of non-crystalline configurations (often experimentally irreproducible). Structural ordering associated with a medium-range order (i.e., sizable heterogeneity) is known to exist in many deposited-like structures, such as hydrogen-rich interconnecting tissue of a thin film deposited by glow-charge over a-Si:H alloys [84], or domains of $\sim 600\text{\AA}$ found at evaporated thick films of As_2Se_3 , or smaller domains existing at most amorphous structures based on As_2S_3 or $GaSe_2$.

6. Pressure and temperature-induced amorphization

Transformation of a crystalline phase into an amorphous phase can be achieved without going through the conventional steps of bulk-liquid melting-and-quenching envisaging micro-processes where, e.g., powdered particles could in their neighbourhood melt thanks to high temperatures locally achieved due to the plastic deformation, which is hauling a lot of energy, and moreover, including many other processes of interstitial incorporation and segregation into nonstoichiometric sites, defective links, etc. Such an *amorphization* can result from chemical, irradiative, thermal or pressure-induced disruption of the crystalline order, when the free energy of the crystal obviously exceeds that of an allied amorphous phase [85-87]. Compressive amorphization was first discovered already 25 years ago when ice-crystals were observed to amorphize at 77K and 1GPa [85, 88]. There are numerous examples of amorphization of originally genuine well-crystallized materials, which is inducible by a variety of processes, ranging from bombardment with high energy particles, spray- and freeze-drying, dehydration of hydrates (common in pharmaceuticals [89]), to continuous grinding and milling, cold-rolling (common with metals' tryout [87, 90-92]), and applicable to an inquisitive assortment of materials [e.g. 93].

The different routes to amorphization can be best monitored in the ring statistics of silica recovered after amorphization. In these cases amorphization will involve the breaking and reforming of bonds and is reconstructive. Usually, pressure induced amorphization signifies the existence of a metastable amorphous phase with a lower free energy compared to the parent crystal and that transformation into a more stable high-pressure crystalline phase is kinetically hindered. This metastable amorphous phase may correspond to high-pressure thermodynamic melting of the parent crystal phase at a significantly low temperature, where the *Clapeyron* slope for the melting transition (dP/dT) is negative. For instance, the metastable extension of the melting curve of SiO_2 to higher pressures [94] yields reasonable estimates of the amorphization pressure of quartz, which occurs around 30GPa at ambient temperature [86]. Some correlations indicate that the denser the starting ambient for the crystalline phase, the higher the mechanical work needed to complete the route to obtain a denser glass.

Worth of attention is the model of *Ponyatovsky* and *Barkolov* [95], where crystalline instability under thermobaric stress (shown by perturbation of P and/or T) is attributed to the coexistence of a *low-density amorphous* phase (= LDA) and a *high-density amorphous* phase (= HDA). The LDA and the HAD phases represent polymorphs with the same composition as the crystal but different density. Thermobaric amorphization was experimentally studied in zeolites [86, 96-97], which readily convert to amorphous alumina-silicates under heating and/or at modest pressures. In the case of a zeolite collapse, order-disorder transitions are found dependent on the rate at which the thermobaric stress is applied [86]. Whether amorphization is thermally induced isobarically or pressure-induced isothermally, the low-density crystalline structure should convert to a final high-density HDA phase via a low density LDA phase. The zeolite–LDA transition is expected to be of the displacive type, while the LDA-HDA transition is reconstructive.

Another fascinating finding is the noticeable fact that the temperature of isobaric amorphization, T_A , shows a significant depression as the heating rate is reduced. This type of kinetic behaviour seems reminiscent of the comparable trend followed by the glass transition temperature, T_g , on varying the cooling rate. The relatively large scale of the changes in T_A , is thought to suggest that this effect might be controlled by the viscosity of a very strong liquid. The idea of a perfect glass, with zero configurational entropy, S_c , was first discussed by *Kauzmann* [12], in the context of melt-quenching, and coincides in *Adam-Gibbs* theory [17] and with the discontinuity at T_v in the VFTH relation. An interesting outcome of the comparisons between the dynamics of zeolite collapse, and that of structural relaxation in conventional melts, is that below T_g , i.e., for very slow heating or for low pressure-increase rates, respectively for the isobaric and for the isothermal amorphization processes, zeolites are expected to collapse more rapidly than the final HDA phase can respond. In either case, highly ordered glasses with very low configurational entropy, S_c , might be obtained if the LDA phase could be isolated [86]. Indeed, *Angell* and co-workers [98] have speculated that the ideal glass state might be better approached via such a phase transition involving a kind of ‘superstrong’ liquid. If the LDA phase is chemically ordered, then the network will comprise only even membered rings, and this compares with the chemically disordered HDA phase where odd membered rings are required topologically to accommodate bonding contacts (as Al-Al or Si-Si). Zeolites and glasses amorphized from them show a clear relationship between the size of secondary building units and features in the Boson peak, i.e., the Boson peak, accessed in the low-

-frequency range of vibrational spectroscopy, is hugely enhanced in low-density networks [97]. If amorphization can ever bestow a practical route to the state of an “ideal” glass accomplished directly from the crystalline state, rather than via freeze-in from the liquid state, then the idea of *Kauzmann* glass [12] might be better realized.

7. Vitrification versus crystallization: reduced T_g and the Hrubý parameter

For a quenched glass, the energy radial distribution function (investigated by XRD) depends on a general configurational coordination, showing a minimum, which bottom lies higher than that of the minimum of a corresponding crystalline state because of the inherent strain energies. The barrier between the two main minima represents the kinetic hindrance preventing crystallization of the glass below T_g , which surmounting is only possible by a substantial atomic rearrangement. The amorphous deposited solids, in contrast, can exist in many crystalline configurationally coordination exhibiting thus multiple (but smaller) energy distribution minima, which over-constrained state can be lowered by a suitable thermal treatment (e.g. common annealing, which helps compacting the structure thus lowering and/or overlapping the minima; while, in some cases, the mere temperature increase may yield a catalyst-like pseudo-crystallization to occur yet below T_g [99].

Šesták [99] showed that quenched glasses reveal upon heating a clear glass transformation, T_g , as a noticeable step-wise deviation from the base line measured by differential thermal analysis (DTA), followed by the base-line (crystallization) peak. On the other hand, in amorphous materials the T_g effect is often overlapped by a too early crystallization, the last being revealed by non-matching onset and outset of the DTA peak base lines. Worth repeating is that rapidly quenched metallic glasses does not regularly reveal distinguishable thermal changes, which can be noticeably associable with the glass transition.

The quality of the glassy state is possible to classify by examining the reduced quantities [81] such as typically glass transition temperature (T_{gr}) given by the ratio T_g/T_m ; a lower ratio reveals a higher difference of T_g and T_m thus showing a greater stability of the glassy state. Referring to a large set of available experimental data obtained for nucleation of several silicate glasses, *Zanotto* [100-103] concluded that glasses having T_{gr} higher than $\sim 0.58-0.60$ display only surface (mostly heterogeneous) crystallization, while glasses showing volume (homogeneous) nucleation have $T_{gr} < 0.58-0.60$. The reduced glass transition temperature [81] was examined in more details by *Sakka* and *Mackenzie* [104] and for metallic glasses by *Davis* [105]. Determination of theoretical values of reduced temperatures were approached by *Angell* [106] based on extension and extrapolation by means of application of the *Vogel-Tamman-Fulcher* equation for viscosity. Even a more sensitive interrelation to the glass formation peculiarities can be found on basis of *Hrubý* coefficient [107-109], which, however, is typically available only upon physical preparation of a given type of glass: $K_H = (T_{cr}-T_g)/(T_m-T_{cr})$, where T_{cr} is the crystallization temperature and T_m is the melting temperature. Various connotations and alternative forms of various reduced quantities were analysed in detail by Šesták [3, 81]. Various models and limitations towards clarification of various features of vitrification were extensively described by *Parthasarathy et al.* [110], who presented glass transition as a transition from ergodic to nonergodic behaviour and discussed the meaning of residual entropy. Glass is considered as nonergodic because the laboratory time scale on which we observe glass is

usually much shorter than its structural relaxation time.

Example of microstructures associated with amorphous and crystalline structures examined in a phase separated silicate-phosphate glass are given in Figure 2.

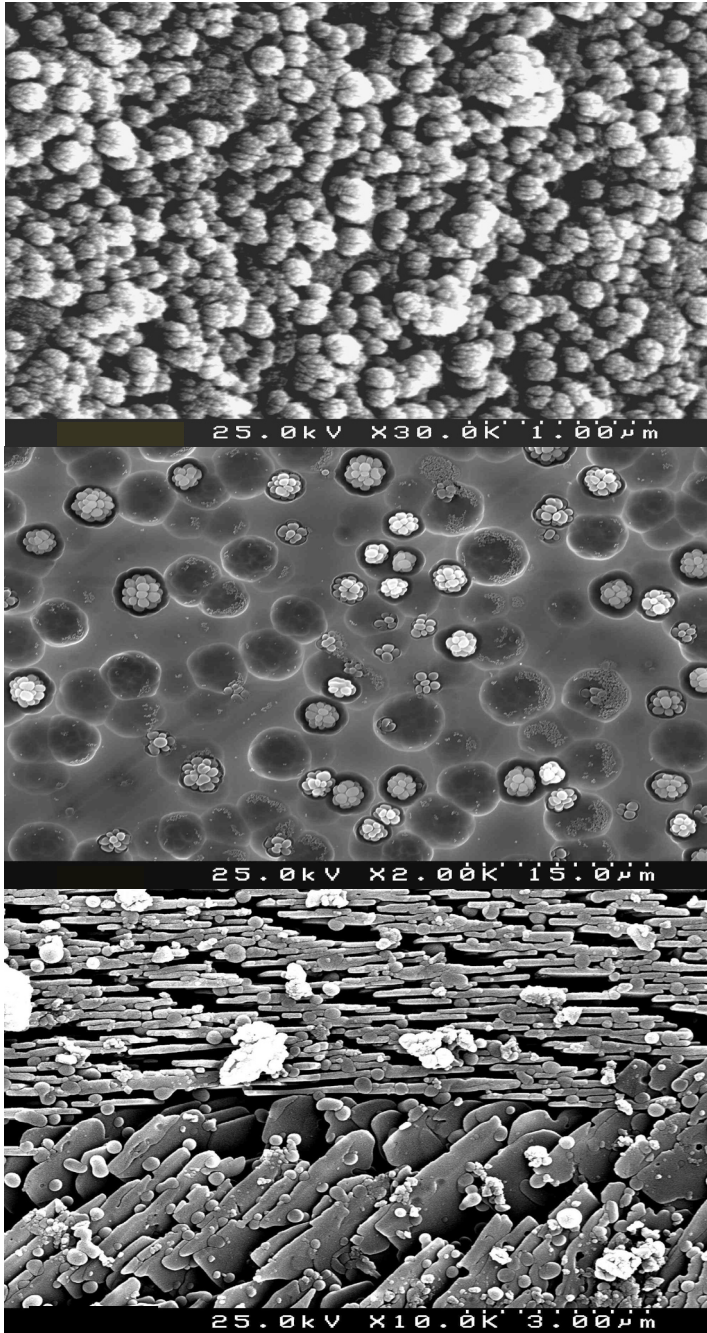


Fig. 2. Examples of different amorphous and crystalline microstructures examined by SEM in a phase separated glass of molar composition

$0.45\text{SiO}_2 - 0.405\text{MgO} - 0.045\text{K}_2\text{O} - 0.1(3\text{CaOP}_2\text{O}_5)$ [111].

Upper: morphology of large grains of frit (2–4 mm), showing clusters of poorly delimited grains, attributed to variation of composition in the nanometric scale; the silica-enriched regions were preferably leached-out by HF etching (5%, 5s), as compared to phosphate-enriched regions, hence revealing fractal-like microstructural features, possibly related with a spinodal type of phase separation.

Middle: The structure of a bulk sample annealed at 650°C (1h), showing globular aggregates identified as amorphous SiO_2 by EDS under TEM examination; these are surrounded by phosphate-enriched regions seemingly resultant of diffusional processes (leached out by HNO_3 etching: 20%, ~8s).

Bottom: Microstructure observed in a grain of glass frit (sized 0.5–1mm) heated at 10°C/min to 980°C, revealing piles of plate-like whitlockite crystals, arranged in patterned stair-like domains, corresponding to $\text{Ca}_7\text{Mg}_2\text{P}_6\text{O}_{24}$ and/or $\text{Ca}_{18}\text{Mg}_2\text{H}_2(\text{P}_4)_{14}$ (etchant: HF: ~8s).

8. Conclusion: distinction between amorphous and glassy materials

According to Roy [112,113] the concept of noncrystallinity (meaning structurally disordered) should be considered as hierarchically superior to the glassy and amorphous

concepts, the latter being more popular to describe certain types of semiconductors and metals. These are, however, two related but misleading controversial concepts as it was noticed by *Gupta* [114], as he demonstrated that non-crystalline solids could be divided into two distinct classes, *amorphous* and *glassy solids*, because they behave differently upon heating, and he proposed a structure-based definition for distinctions. Accordingly *Gupta*, a non-crystalline solid is a glass if the short range order of the freeze-in solid below glass transition and that of the delivering melt are the same.

Glasses are also distinctive on exhibiting a glass transition upon cooling and/or heating. These two conditions are always satisfied for any non-crystalline solids, which is obtained by way of melt cooling because the liquid must undergo a glass transition to vitrify (if earlier crystallization is prevented). On the other hand, a non-crystalline solid is of an amorphous structural disposition if the short range order is not equal for the melt and its solid non-crystalline counter-partner, which is exhibited, for instance, by some amorphous semiconductors like Si or Ge (showing, e.g., different coordination number; see §.5). Such amorphous solids may be produced by special techniques such as sol-gel, precipitation from solutions, sputtering, mechanical alloying, impact at high pressures (explosion), milling, bombardment of high energy particles or by other modes of crystal disintegration (generally termed as *amorphisation*).

On the other hand, it would be also possible to distinguish the glassy state from the amorphous one, from a purely thermodynamic perspective, considering the *Kauzmann* temperature as a borderline, since it allows for a clear-cut distinction independent of cooling rate effects or of the thermal story of the substance. However we would have to accept the inconvenience of its intricate but not well précised experimental estimate. If such a distinction is to be accepted the glassy state should clearly be defined as an above T_K state, while the amorphous state would be fine-tuned to lie below.

Pointing in this direction, it is possible to propose that, in a restricted sense, the concepts of glass and that of an amorphous solid could well be distinguished from each other, if we define glass as «*a substance experiencing a time-dependent change of thermodynamic state, between its Kauzmann and liquidus temperatures, slowly changing from the amorphous solid to the supercooled liquid state, or vice-versa*», thus restraining the concept of the glass to the temperature range $[T_K, T_L]$, while the companion concept of amorphous solid was defined as corresponding to a disordered solid kept below its Kauzmann temperature. Here, the designation ‘state’ actually refers to a dynamic non-equilibrium thermodynamic state, which depends on the characteristic time associated with the structural relaxation associated with the glass transition.

Because this restrictive glass definition is not fully compatible with the current concept of (solid) glass as a material substance, and with several previous currently accepted glass definitions [115,116], a better compatibility could be found if we accept to abandon the quest for a universal definition, and instead accept a distinction to be traced among three categories of glass. In this way, the given concept of glass would actually correspond to the special case of a “*transforming glass*”, which allows for extension of the previous concept, either to the melt region ($> T_L$), corresponding to “*melted glass*”, and to the amorphous solid region ($< T_K$), corresponding to “*amorphous glass*”. Here the concept of glass is used in a more general sense, to stress that the substance involved can in fact change its state to a ‘transforming glass’. Of course, the proposed designations of “*melted glass*” and “*amorphous glass*” should be restricted to such substances that can, in fact,

evolve through the so-called transformation region.

Acknowledgement: *This study was supported by the Portuguese Foundation for Science and Technology (FCT, by the Czech Science Foundation No. P 204/10/1312 and the Czech industrial grant FR-TI 1/335.*

References

1. H. Fritzche, *What are Non-Crystalline Semiconductors*, Vol. 25 of: *Fundamental physics of amorphous semiconductors* (F. Yonezawa, ed.), Springer-Verlag, Heidelberg, 1981.
2. National Res. Council Ad Hoc Committee on Infrared Transmitting Materials, National Academy Sci. Res. Council, Mater. Advisory Board, 1968, p 243.
3. J. Šesták, *Glasses: phenomenology of non-isothermal glass formation and crystallization*, in book: *Kinetic Phase Diagrams: non-equilibrium phase transitions* (Z. Chvoj and J. Šesták, eds.), Elsevier, Amsterdam, 1991, pp. 164-277.
4. J. Šesták and J. Zámečník, *Can clustering of liquid water and thermal analysis be of assistance for better understanding of biological germplasm exposed to ultra-low temperatures*, J. Thermal Anal. Calor. 88 (2007) 411-416.
5. A.Q. Tool, *Viscosity and the extraordinary heat effects in glass*, J. Res. Nat. Bur. Stand. 37 (1946) 73-90.
6. A.Q. Tool, *Relation between inelastic deformability and thermal expansion of glass in its annealing range*, J. Am. Ceram. Soc. 29 (1946) 240-253.
7. A.Q. Tool, *Effect of heat-treatment on density and constitution of high-silica glasses of the borosilicate type*, J. Am. Ceram. Soc. 31 (1948) 177-86
8. J.H Gibbs and E.A. DiMarzio, *Nature of the glass transition and the glassy state*, J. Chemical Phys. 28 (1958) 373-383.
9. E.A. DiMarzio, *Equilibrium theory of glasses – an equilibrium theory of glasses is absolutely necessary*, Annals New York Acad. Sci. 371 (1981) 1-1.
10. E.A. Di Marzio, *The entropy theory of glass formation after 40 years*, Computational Mater. Sci. 4 (1995) 317-324.
11. E.A. Di Marzio and A.J.M. Yang, *Configuration entropy approach to the kinetics of glasses*, J. Res National Inst. Standards Tech. 102 (1997) 135-157.
12. W. Kauzmann, *The nature of the glassy state and the behaviour of liquids at low temperatures*, Chemical Reviews 43 (1948) 219-256.
13. Th.M. Nieuwenhuizen, *Ehrenfest relations at the glass transition: solution to an old paradox*, Physical Review Letters, Vol. 79 1997, 1317-1320.
14. Th.M. Nieuwenhuizen, *Thermodynamic description of a dynamical glassy transition*, J. of Physics A 31 (1998) L201-L207.
15. L. Wondracze and R. Conradt, *“Preface – Glass and entropy”*, J. Non-Cryst. Solids, 355 (2009) pp. vii-viii.
16. A.K. Varshneya, *Fundamentals of Inorganic Glasses*, Academic Press Inc. – Harcourt Brace & Co. Publishers, Boston, 1994, pp. 242-243.
17. G. Adam and J.H. Gibbs, *On the temperature dependence of cooperative relaxation properties in glass-forming liquids*, J. Chemical Phys. 43 (1965) 139-146.

18. Y. Bottinga and P. Richet, *Silicate melt structural relaxation: rheology, kinetics, and Adam-Gibbs theory*, Chemical Geology 128 (1996) 129-141.
19. S. Franz and G. Parisi, *Effective potential in glassy systems: theory and simulations*, Physica A: Statistical Theoretical Phys. 261 (1998) 317-339.
20. R.W. Rendell, K.L. Ngai and D.J. Plazek, *Volume-dependent rate processes predicted by the coupling model*, J. Non-Cryst. Solids 131/133 (1991) 442-450.
21. I. Campbell, P.-O. Mari, A. Alegría and J. Colmenero, *A random walk in search of the glass transition*, Europhysics News 29 (1998) 46-50.
22. P. Ehrenfest, *Phasenumwandlungen im ueblichen und erweiterten sinn, classifiziert nach dem entsprechenden singularitaeten des thermodynamischen potentiales*, Proc. Koninklijke Nederlandse Akademie van Wetenschappen (Amsterdam) 36 (1933) 153-157.
23. G. Jaeger, *The Ehrenfest classification of phase transitions: introduction and evolution*, Archive for History of Exact Sciences 53 (1998) 51-81.
24. A.B. Pippard, *Higher-order transitions*, Chap. 9 in: *Elements of Classical Thermodynamics - for Advanced Students of Physics*, Cambridge University Press, Cambridge, 1981, 136-159.
25. T.R. Kirkpatrick, D. Thirumalai and P.G. Wolynes, *Scaling concepts for the dynamics of viscous liquids near an ideal glassy state*, Physical Review A 40 (1989), 1045-1054.
26. P.G. Wolynes, *Entropy Crises in Glasses and Random Heteropolymers*, J. Res. National Inst. Standards Tech. 102 (1997) 187-194.
27. X. Xia and P.G. Wolynes, *Fragilities of liquids predicted from the random first order transition theory of glasses*, Proc. Natl. Acad. Sci. USA 97 (2000) 2990-2994.
28. M. Cohen and D. Turnbull, *Molecular transport in liquids and glasses*, J. Chem. Phys., 31 (1959) 1164-1169.
29. Z. Černošek, J. Holubová and E. Černošková, *Kauzmann temperature and the glass transition*, J. Optoelectr. Mater., 7 2005, 2941-2944.
30. B. Hlaváček, J. Šesták, L. Koudelka, P. Mošner and J. J. Mareš, *Forms of vibrations and structural changes in liquid state*, J. Thermal Anal. Calor. 80 (2005) 271-283.
31. H. De Raedt and W. Gotze, *Scaling properties of correlation functions at the liquid-glass transition*, J. Phys. C: Solid State Phys. 9 (1986) 2607-2612.
32. W. Gotze and L. Sjogren, *α -relaxation near the liquid-glass transition*, J. Phys. C: Solid State Phys. 20 (1987) 879-894.
33. W. Götze and L. Sjögren, *Relaxation processes in supercooled liquids*, Reports Progress Phys. 55 (1992) 241-376.
34. W. Götze and L. Sjögren, *The mode coupling theory of structural relaxations*, Transport Theory and Statistical Phys. 24 (1995) 801-853.
35. W. Gotze, in: E. Luscher, G. Fritsch and G. Jacucci (Eds.), *Amorphous and Liquid Materials*, NATO ASI Series E, Vol. 118, Nijho Publishers, Dordrecht, 1987, pp. 34-81.
36. W. Götze, *Aspects of structural glass transitions*, in: J.P. Hansen, D. Levesque and J. Zinn-Justin (eds.), *Liquids, Freezing and Glass Transition*, (Les Houches, 1989), North-Holland 1990, pp. 287-503.
37. W. Götze, *The mode-coupling theory of liquid-to-glass transitions*, J. Phys.: Condens. Matter, 2 (1990), pp. SA201-SA205.

38. W. Götze, *The scaling functions for the β -relaxation process of supercooled liquids and glasses*, J. Phys.: Condens. Matter 2 (1990) 8485-8498.
39. W. Götze, *Recent tests of the mode-coupling theory for glassy dynamics*, J. Phys.: Condens. Matter A 11 (1999), pp. A1-A45.
40. M. Fuchs, W. Götze, S. Hildebrand and A. Latz, *A theory for the beta-relaxation process near the liquid-to-glass crossover*, J. Phys.: Condens. Matter 4 (1992) 7709-7744.
41. T. Franosch and W. Gotze, *A theory for a certain crossover in relaxation phenomena in glasses*, J. Phys.: Condens. Matter 6 (1994) 4807-4822.
42. H.Z. Cummins, G.Li, Y.H. Hwang, G.Q. Shen, W.M. Du, J. Hernandez and N.J. Tao, *Dynamics of supercooled liquids and glasses: comparison of experiments with theoretical predictions*, Zeitschrift für Physik B: Condensed Matter 103 (1997) 501-519.
43. D.H. Vogel, *Das temperatur-abhängigkeitsgesetz der viskosität von flüssigkeiten*, Physikalische Zeitschrift 22 (1921) 645-646.
44. G.S. Fulcher, *Analysis of recent measurements of the viscosity of glasses*, J. Am. Ceram. Soc. 8 (1925) 339-355.
45. G. Tammann and W. Hesse, *Die abhängigkeit der viskosität von der temperatur bei unterkühlten flüssigkeiten*, Zeitschrift für Anorganische und Allgemeine Chemie 156 (1926) 245-257.
46. F. Mezei, *Scaling behaviour of structural relaxation near glass transition: a critical analysis*, J. Non-Cryst. Solids 131/133 (1991) 317-326.
47. V.N. Novikov, E. Rössler, V.K. Malinovsky and N.V. Surovtsev, *Strong and fragile liquids in percolation approach to the glass transition*, Europhysics Letters 35 (1996) 289-294.
48. E. Donth, *Characteristic length of glass transition*, J. Non-Cryst. Solids 131/133 (1991) 204-206.
49. E. Donth, *The Glass Transition, Relaxation Dynamics in Liquids and Disordered Materials*, Springer Verlag, Berlin/Heidelberg, 2001.
50. L. Leuzzi and T.M. Nieuwenhuizen, *Effective temperatures in an exactly solvable model for a fragile glass*, Physical Review E 64 (2001), pp. 011508-1/011508-24.
51. L. Leuzzi and T.M. Nieuwenhuizen, *Inherent structures in models for fragile and strong glass*, Physical Review E 64 (2001), pp. 066125-1/066125-15.
52. T. Odagaki, J. Matsui and Y. Hiwatari, *On the glass transition singularities and slow dynamics*, Physica A, 224 (1996) 74-83.
53. C.A. Angell, *Structural instability and relaxation in liquid and glassy phases near the fragile liquid limit*, J. Non-Cryst. Solids 102 (1988) 205-221.
54. E.A. Marí, *Los Vidrios: Propriedades, Tecnologías de Fabricación y Aplicaciones*, Editorial América Lee, Buenos Aires (Argentina) 1982, p. 54.
55. M.J. Pascual, L. Pascual and A. Durán, *Determination of the viscosity-temperature curve for glasses on the basis of fixed viscosity points determined by hot stage microscopy*, Phys. Chem. Glasses 42 (2001) 61-66.
56. U. Mohanty, *On the nature of supercooled and glassy states of matter*, Physica A: Statistical and Theoretical Physics 177 (1991) 345-355.
57. B. Eckstein, *Vitreous states*, Materials Research Bulletin 3 (1968) 199-207.
58. M. Reiner, *The Deborah Number*, Physics Today 17 (1964) 62.

59. M. Giordano, M. Russo, P. Capoluongo, A. Cusano and L. Nicolais, *The effect of cooling rate on the glass transition of an amorphous polymer*, J. Non-Cryst. Solids 351 (2005) 515-522.
60. H. Suga and S. Seki, *Frozen-in states of orientational and positional disorder in molecular solids*, Faraday Discuss. Chem. Soc. 69 (1980) 221-240.
61. J. Wong and C.A. Angell, *Glass Structure by Spectroscopy*, Marcell Dekker Inc., Nova Iorque (EUA) 1976, pp. 2-3.
62. J.C. Maxwell, *On the dynamical theory of gases*, Philosophical Magazine 35 (4th Series; 1868) 129-145 and 185-217.
63. D.B. Dingwell and S.L. Webb, *Relaxation in silicate melts*, Eur. J. Mineralogy 2 (1990) 427-449.
64. Y. Bottinga, P. Richet and A. Sipp, *Viscosity regimes of homogeneous silicate melts*, American Mineralogist 80 (1995) 305-318.
65. S. Webb and R. Knoche, *The glass-transition, structural relaxation and shear viscosity of silicate melts*, Chemical Geology 128 (1996) 165-183.
66. L. Sjögren and W. Götze, *α -relaxation near the glass transition*, J. Non-Cryst. Solids, 131/133 (1991) 153-160.
67. Th.M. Nieuwenhuizen, *Thermodynamics of the glassy state: effective temperature as an additional system parameter*, Physical Review Letters 80 (1998) 5580-5583.
68. Th.M. Nieuwenhuizen, *Thermodynamic picture of the glassy state gained from exactly solvable models*, Physical Review E 61 (2000) 267-292.
69. G.P. Johari and M. Goldstein, *Viscous Liquids and the Glass Transition. II. Secondary Relaxations in Glasses of Rigid Molecules*, J. Chem. Phys. 53 (1970) 2372-2388.
70. G.P. Johari, *Intrinsic mobility of molecular glasses*, J. Chem. Phys. 58 (1973) 1766-1770.
71. G.P. Johari, in: *The Glass Transition and the Nature of the Glassy State*, (M. Goldstein and R. Simha, eds.), Ann. New York Acad. Sci. 279 (1976) 117-140.
72. G.P. Johari, *Localized molecular motions of α -relaxation and its energy landscape*, J. Non-Cryst. Solids, 307/310 (2002) 317-325.
73. E. Rössler, *Experimental results revealing a change of diffusion mechanism above T_g* , J. Non-Cryst. Solids, 131/133 (1991) 242-247.
74. A. Kudlik, C. Tschirwitz, S. Benkhof, T. Blochowicz and E. Rössler, *Slow secondary relaxation process in supercooled liquids*, Europhysics Letters 40 (1997) 649.
75. R. Richert and C. A. Angell, *Dynamics of glass-forming liquids. V. On the link between molecular dynamics and configurational entropy*, J. Chemical Phys. 108 (1998) 9016-9026.
76. D. Prevosto, S. Capaccioli, M. Lucchesi, P.A. Rolla and K.L. Ngai, *Does the entropy and volume dependence of the structural α -relaxation originate from the Johari–Goldstein β -relaxation?*, J. Non-Cryst. Solids 355 (2009) 705-711.
77. C.A. Angell, *Thermodynamic aspects of the glass transition in liquids and plastic crystals*, Pure Appl. Chem. 63 (1991) 1387-1392.
78. B. Hlaváček, J. Šesták and J. Mareš, *Mutual interdependence of partitions functions in the vicinity of glass T_g - transition*, J. Therm. Anal. Cal. 67 (2002) 239-248.
79. J. Šesták, *Thermal dynamics and non-equilibrium phenomena*, in book: *Heat, Thermal Analysis and Society*, NUCLEUS publ. house, Hradec Králové 2004, p. 222.

80. A. Sikora, V.O. Dupanov, J. Kratochvíl and J. Zámečník, *Transitions in aqueous solutions of sucrose at subzero temperatures*, J. Macromolecular Science: Part B 46 (2007) 71-85.
81. J. Šesták, *Some thermodynamic aspects of glassy state*, Thermochim. Acta 95 (1985) 459-471.
82. G.N. Greaves and E.A. Davis, *A continuous random network model with three-fold coordination*, Phil. Mag. 29 (1974) 1201-1206.
83. J.C. Phillips, *Topology of covalent non-crystalline solids I: Short-range order in chalcogenide alloys*, J. Non-Cryst. Solids 34 (1979) 153-181.
84. J.A. Reimert, R.W. Vaughan, J. Knights, *Proton Magnetic Resonance Spectra of Plasma-Deposited Amorphous Si: H Films*, Phys. Rev. Lett. 44 (1980) 193-196.
85. G. N. Greaves and S. Sen, *Inorganic glasses, glass-forming liquids and amorphizing solids*, Advances in Physics 56 (2007) 1-166.
86. G.N. Greaves, F. Meneau, A. Sapelkin, L.M. Colyer, I. Gwynn, S. Wade and G. Sankar, *The rheology of collapsing zeolites amorphized by temperature and pressure*, Nature Mater. 2 (2003) 622-629.
87. H. Sieber, G. Wilde and J. H. Perepezko, *Solid State Amorphization by Cold-Rolling*, in: *Materials Development and Processing - Bulk Amorphous Materials, Undercooling and Powder Metallurgy* (J.V. Wood, L. Schultz and D. M. Herlach: editors); Series Euromat 99 – Vol. 8, WILEY-VCH 2000, pp. 3-9.
88. W. Zheng, D. Jewitt and R.I. Kaiser, *Amorphization of crystalline water ice*, arXiv:0801.2805v1 [astro-ph], internet site: <http://arxiv.org/>, 2008.
89. J. F. Willart and M. Descamps, *Solid State Amorphization of Pharmaceuticals*, Mol. Pharmaceutics, 5 (2008) 905-920.
90. J.H. Perepezko, J. Hamann, R.J. Hebert, H. Rösner and G. Wilde, *Amorphization and devitrification reactions in metallic glassy alloys*, Materials Sci. Eng.: A 449/451 (2007) 84-89.
91. C. Suryanarayana, *Solid-State Amorphization*, Chap. 12 in: C. Suryanarayana, *Mechanical Alloying and Milling*, Marcel Dekker, New York 2004, pp. 269-362.
92. T. Nagase, T. Hosokawa and Y. Umakoshi, *Solid state amorphization and crystallization in $Zr_{66.7}Pd_{33.3}$ metallic glass*, Intermetallics 14 (2006) 1027-1032.
93. C.N.R. Rao, A. Govindaraj, H.N. Aiyer, R. Seshadri, *Polymerization and Pressure-Induced Amorphization of C_{60} and C_{70}* , J. Phys. Chem. 99 (1995) 16814-16816.
94. P. Richet and P. Gillet, *Pressure-induced amorphization of minerals; a review*, Eur. J. Mineral. 9 (1997) 907-933
95. E.G. Ponyatovsky and O.I. Barkolov, *Pressure induced amorphous phases*, Mater. Sci. Rep. 8 (1992) 147-191.
96. N. N. Ovsiuk and S.V. Goryainov, *Amorphous-to-amorphous phase transition in zeolites*, JETP Letters, 83 (2006) 109–112; translated from Russian: Zhur. Éksperiment. i Teoret. Fiziki, 83 (2006) 138–142.
97. G.N. Greaves, F. Meneau, O. Majérus, D.G. Jones and J. Taylor, *Identifying vibrations that destabilize crystals and characterize the glassy state*, Science 308 (2005) 1299-1302.
98. C.A. Angell, C.T. Moynihan and M. Hemmati, *'Strong' and 'superstrong' liquids, and an approach to the perfect glass state via phase transition*, J. Non-Cryst. Solids 274 (2000) 319-331.

99. J. Šesták, *Use of phenomenological enthalpy versus temperature diagram (and its derivative – DSC) for a better understanding of transition processes in glasses*; in monograph: *Vitrification, transformation and crystallization of glasses* (J. Šesták, ed.), special issue of *Thermochim. Acta*, Vol. 280/281, Elsevier, Amsterdam 1996, 175-191.
100. E.D. Zanutto, *Isothermal and adiabatic nucleation in glass*, *J. Non-Cryst. Solids* 89 (1987) 361-370.
101. E.D. Zanutto and M.C. Weinberg, *Trends in homogeneous crystal nucleation in oxide glasses*, *Phys. Chem. Glasses* 30 (1989) 186-192.
102. V.M. Fokin, E.D. Zanutto and J.W.P. Schmelzer, *Homogeneous nucleation versus glass transition temperature of silicate glasses*, *J. Non-Cryst. Solids* 321 (2003) 52-65.
103. V.M. Fokin, E.D. Zanutto and J.W.P. Schmelzer, *Homogeneous crystal nucleation in silicate glasses: a 40 years perspective*, *J. Non-Cryst. Solids* 352 (2006) 2681-2714.
104. S. Sakka and J.D. Mackenzie, *Relation between apparent glass transition temperature and liquids temperature for inorganic glasses*, *J. Non-Cryst. Solids* 6 (1971) 145-162.
105. H.A. Davies, *The kinetics of formation of a Au–Ge–Si metallic glass*, *J. Non-Cryst. Solids* 17 (1975) 266-272.
106. C.A. Angell, *Oxide Glasses in Light of the "Ideal Glass" Concept: I, Ideal and Nonideal Transitions, and Departures from Ideality*, *J. Amer. Cer. Soc.* 51 (1968) 117-124.
107. A. Hrubý, *Evaluation of glass forming tendency by means of DTA*, *Czech. J. Phys.* B22 (1972) 1187-1193.
108. A. Hrubý, *Glass-forming tendency in the GeS_x system*, *Czech. J. Phys B*, 53 (1973) 1263-1272.
109. A.A. Cabral Jr, C. Fredericci and E.D. Zanutto, *A test of the Hrubý parameter to estimate glass-forming ability*, *J. Non-Cryst. Solids* 219 (1997) 182-186.
110. R. Parthasarathy, K.J. Rao, and C.N.R. Rao, *The Glass Transition: Salient Facts and Models*, *Chem. Soc. Rev.* 12 (1983) 361-385.
111. C.M.G.A. Queiroz, *Cristalização de Biomateriais Vitrocerâmicos e Mineralização em Meio Fisiológico Simulado* (Ph.D. Thesis), University of Aveiro, 2005, pp. 114, 117, 131 [<http://dited.bn.pt/30532/1521/1947.pdf>; <http://biblioteca.sinbad.ua.pt/Teses/2007000254>].
112. R. Roy, *Gel Route to Homogeneous Glass Preparation*, *J. Amer. Cer. Soc.* 52 (1969) 344-344.
113. R. Roy, *Classification of non-crystalline solids*, *J. Non-Cryst. Solids* 3 (1970) 33-40.
114. P.K. Gupta, *Non-crystalline solids: glasses and amorphous solids*, *J. Non-Cryst. Solids* 195 (1996) 158-164.
115. C.A. Queiroz, *What is glass? A journey across glass definitions*, submitted to *Phys. Chem. Glasses* (2009).
116. C.A. Queiroz and J. Šesták, *Modern Aspects of Non-crystalline States*, submitted to *Int. J. Appl. Glass Sci.* (Wiley-Blackwell, US, 2009).



Chapter 1

History, education and research

1. SOME HISTORICAL FEATURES FOCUSED BACK TO THE PROCESS OF EUROPEAN EDUCATION REVEALING SOME IMPORTANT SCIENTISTS, ROOTS OF THERMAL ANALYSIS AND THE ORIGIN OF GLASS RESEARCH

Jaroslav Šesták

1.1. Model Classification and their Development in Historical Applications

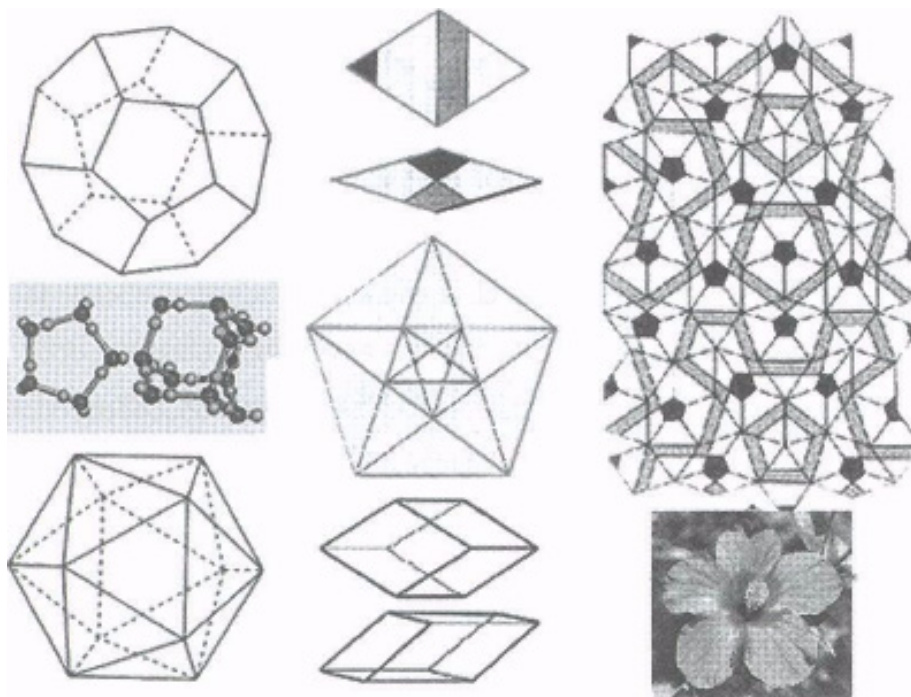
According to early Greek belief (e.g. *Aristotle*, 384-322 BC), the four basic elements were *fire*, *air*, *earth* and *water*. These elements were firstly introduced by *Empedocles* (492-432 BC) and used in various models and metaphors to signify the substantiality of which all subsistence is composed (i.e., quantities as well as interconnecting qualities like warmth, dryness, coldness and humidity). They were thought to possess the integrative and structural essence *ether* or *form* (in the sense of an imperishable firmament) [1,2]. The Greek philosophy was derived from the notion *philia* (~ love), which explains the attraction of different forms of matter and which is complementary to the opposing force called *neikos* (~ strife) which accounts for separation. Today however, mathematical modeling ensues differently not only from a further approved physical existence but also from an existence that is assigned by our more cultured mental perceptions. It is not just the precision but also the subtle sophistication and mathematical beauty of successful models that is profoundly mysterious. Mathematics is crucially concerned about *truth* and philosophers would agree that there are some other fundamental (almost absolute) concerns, namely that of *beauty* and of *good*, which exist since the Platonic geometrical world of mathematical forms [3,4].

The early elements were first depicted by the metaphors of simple, equilateral triangles either pointing up, in order to escape like air or fire, or down, in order to rest like water or earth. Later *Plato* (427-347 BC) used more explicit geometrical models spatially arranging multiple triangles, i.e., three triangles formed *tetrahedron* (~ fire), eight triangles — *octahedron* (~ air), six squares or twelve triangles — *cube* (~ earth). Water, however, was represented by a more complex geometrical body called *icosahedra* (twenty triangles, see following text and Fig. 1). In Greek culture the term symmetry was interpreted as the harmony of different parts of an object. *Symmetria* (~ common measure) is composed of the prefix *syn* (~ common) and *metres* (~ measure). The Greek *Gaius Plinius Secundus* (23-79) provided the fundament for crystallography (derived from Greek *crystallos* ~ piece of ice) as he gave primary rules for the plan-metric faces of crystals and their visually imagery shaping.

In the first attempt to ever categorize well-ordered earth stones as geological specimens, which form variously shaped natural crystals, Bohemian metallurgist *Georg Bauer Agricola* from Jáchymov (1494-1555) developed a visual classification including color, transparency, weight, shape, etc. [5]. This classification somehow resembled Platonian geometries. However, the most impressive historical treatise on crystallography was written by *Johann Kepler* (1571-1612, while resident in Prague within the years 1600-1612) and was devoted to the description of snowflakes. In analyzing their numerous forms bearing a steady hexagonal symmetry, Kepler suggested a certain generalization model for the densest arrangement of rigid balls. Factually, he introduced the coordination-like number for a ball environment and declared the consistency of angles between analogical crystal planes and edges. It can be assumed that some implication of Platonian geometry was also inherent in Kepler's applications [6]. Though *Auguste Bravais* (1811-1863) was not sure that crystals are internally arranged in a repeatable manner, he mathematically modeled the fourteen

geometrical figures that can be spatially arranged in a periodic mode [7]. They can be characterized by a combination of one or more rotations and inversions in a lattice that is understood as a regular array of discrete points representing individual structural units (atoms, molecules), which thus appear exactly the same viewed from any point of the array [8]. This discovery allows us to classify crystal shapes nowadays in the seven geometrically-basic schemes: area and/or space can be filled completely and symmetrically with tiles of *three, four and six sides*. This is close to the Platonian conceptions of geometrical bodies but excludes, however, any *pentagonal* arrangement (involved in Platonic bodies) because it is not possible to fill any area completely with its 5-fold symmetry. In the early 1970ies, however, *Roger Penrose* (1931-) discovered that a surface can be wholly tiled in an asymmetrical but non-repeating manner [7] providing some constructions similar to the cluster structure of liquid water [9] or non-crystalline state of glasses, which has been for a long run in the core of attention [10], see fig 1.

Fig. 1: Some constructions associable with the cluster structure of liquid water. The object (in the upper left column) shows a dodecahedron, which Plato associated with a firmament. It can model, in a special case, certain water clusters in the surface contact with plants. Below you see the ball-like model of a cyclic pentamer and a tricyclodecamer, representing relatively stable but small clusters of water, which can mutually interconnect to ease the formation of large clusters of a icosahedron (shown below), often containing as many as 250 molecules of water.9 Plato associated this geometry already with water. The Middle column portrays the diamond tiles (sometimes called



Penrose Basic) with a specific shape called «rhombus». The upper thick rhomb has a longer diagonal equal to the «Golden ratio» phi ($\Phi = 1.618034\dots$, which is related to the number 5 by the formula $(1-\sqrt{5})/2$, playing a crucial role in various aspects of natural and art constructions) while the thinner rhomb has its shorter diagonal equal to $1/\Phi$. Both rhombs can be derived from a pentagon (below). Its five diagonals match to the Golden ratio Φ and its 5-side structure leaves inevitable gaps when used to be continuously repeated in space.7 On the other hand, the rhombs can fill the surface in an asymmetrical and non-repeating manner, which is known as "continuous but non-repeating structure*" (sometimes called «quasi-crystals» when discovered to appear in quenched glassy alloys after annealing)2. On expanded tiling to cover greater areas, the ratio of the quantity of thick rhombs to thin ones approaches Φ again - if the rhombs are marked by shadow strips they form the unbroken structure (right) and we can localize both chains (like polymeric water) and pentagons (like water clusters). Such a structure can also be applied to a spatial distribution if the two kinds of rhombohedra are assembled (bottom of the middle column) to form icosahedrons.

These relations can be followed far back to history when the geometry of pentagon (and the pentagram inscribed within it) bore its high metaphysical association as explored by the

Pythagoreans (after *Pythagoras* 586-506 BC): they considered it as an emblem of perfection. It was a doctrine that all things proceed from numbers and the number five, as being formed by the union of the odd and the first event was deemed of a peculiar value. In China the central number five, similarly, represented the fifth element — earth as the allied symbol of the great China [2]. In astrology, geometrical figures kept engendering mystical and occult connotations [1,2] such as with the supposed magical powers of pentagons and pentagrams. This effect lasted until recently as various occult guilds are often symbolized by five leave rose (see bottom figure of the right column) [1].

In the middle of the 18th century, the technical revolution brought the novel steam engine, which actually interconnected three early elements in another metaphor: heating *water* by *fire* to get thick *air* (steam) being then capable to provide useful work by moving a piston and turning a wheel, the latter symbolizing the forth element, *earth*. This element, however, is bearing a functional *form* by know-how, today information (*in-form-ation*) [2]. In contemporary physics, the four elements can be understood as a metaphor for *solids* (= earth), *liquids* (~ water) and *gases* (~ air), *fire* being associated with the forth state of matter (= plasma). Their further association can be extended to describe the state of society [2,11], as *hierarchy* (~ solid monarchy), *democracy* (~ liquid equality) and *anarchy* (~ gaseous disorder) simply depending on the degree of mutual interactions (~ *fight of opposing forces*), which in a mixture (~ *society*) of components (~ *people*) can be integrative (~ *love*) or hostile (~ *strife, hate*) with a transitional indifference (~ *apathy*) replacing the thermodynamic requirement (~ *nature*) for a state of minimum of energy (~ *law*) by a societal need (~ *culture*) of maximum happiness, health or satisfaction (~ *best feelings*).

Such an unusual physical-chemical model assumes, however, people as unvarying «thermodynamic» particles without taking their own «human» self-determination into account [12]. The interactions of such «sedentary» particles are given by their inherent nature (internal state, charge), properties of the host matrices (neighboring energetic makeup, structure) and can be reinforced by their collaborative incorporation (collective execution, stimulated amplification) in the set-up vicinity. Certainly, this model can be incorporated in the so called “*game models*” if we focus on the plausible cooperation between people as somehow unrelated individuals when aiming to show their reciprocal strategies of behavior that are merging spontaneously as a result of the same “sightless” (i.e., a driving force, which is trying to assure survival [13]). More advanced models anticipate that economic straddles share out science and humanities [14]. Yet another model hits ecosystems that tend to increase energy by reaching a maximum of steadiness. They are introducing a further model of the so called “*forth law of thermodynamics*”, which is based on the useful part of energy sometime identified as “*exergy*” [15,16]. These examples show that limits of mathematical models and the chronological usage of scientific metaphors in perception are boundless [17].

1.2. Historical Prague, its famous Charles University and some medieval alchemists

One of the most important moments in the cultural history of a focal Middle European territory - Bohemia [18-20] was the year 1232 when the Dominican Order (“*domini canes*” meaning the “Dogs of the Lord”) first seated in Prague near the old Judith’s bridge (the predecessor of the famous Charles bridge build afterward in 1357). This Dominican monastery was called ‘*Clementinum*’ and represented not only a clerical institution but also an important place of social and learning activities (even within the years 1278-1348 the Land Council was held there). One of mentioned historical personality was *Kolda from Koldic*, the author of “*Passional of Princess Kunhuta*” a top work of the Czech Gothic book arts, published in 1318. The Dominican Latin School, brought there from Paris in 1347, was

factually the ancestor of the 1348 foundation of the famous *Charles University* in Prague, cf. Fig. 2., as the first European university north of the Alps (by the Emperor Charles the IV).

One of the new university first achievements was the introduction of medieval kinematics, which was brought to Prague by *Johannes de Holandria*, an Oxfordian from Merton College, who in the year 1368 provided the so called Merton' theorem of uniform acceleration to public and detailed this approach during his stay in Prague. Later Czech astronomer *Jan Šindel* (1375-1456) was studying the planetary motion and his astronomical tables were greatly appreciated by *Tycho de Brahe* while staying in Prague at the end of the 16th century. Šindel had also a share in designing the advanced astrolabe in the famous Prague's astronomical clock. We cannot forget practical impacts of improved learning such as the early foundation of a brewery in *Domažlice* 1378 or a glasswork in *Chřibská* 1414 not forgetting the first print out of the Czech written bible in *Plzeň* 1468.

Little renown but important medieval personality [21,22] was *Ioannes Marcus Marci* (*Jan Marek Marků*, 1595-1667) who most likely helped to reveal the fundamental properties of the spectral colors that emerge when light passes through glass prism. He was already aware of the light monochromatic properties, i.e., any succeeding refraction or reflection did not change colors and he provided studies how color changes in rays when spectral colors are mixed and entered the field of spectral dispersion of light being thus a factual predecessor of *Isac Newton* (1642-1726). Marci wrote for that time very advanced books [22], which possibly foreshadowed some important laws. Besides the refraction of light he conducted the first-ever systematic study of the reciprocated impact of bodies, he discovered the difference between elastic and inelastic impacts intuitively moving his thoughts within the reach of the conservation laws. Marci, however, was strongly convinced that white light was the simplest element (*'quinta essentia'*), which, interestingly, was close to the subsequent concept of 'elementary waves' propounded about fifty years later by *Christian Huyghens* (1629-1695) in the wave theory of light. There, however, is incomplete information concerning Marci's educational activities as a rector of Charles University.



Fig. 2: From left: *Charles University in Prague* (founded by Emperor Charles IV. 1348 and some of their exceptional members and associates, astronomer: *Kepler Johannes* (1571-1639), rector and mathematician *Marcus Marci Ioannes* (from Kronland, 1595-1667) and famous professor of mathematics and practical geometry *Doppler Christian* (1803-1853).

When *Rudolph the II.* (1552-1612) became the Emperor of the Holy Roman Empire and the King of Bohemia, he provided in Prague court a vital support to alchemists, astronomers and physicists and granted *Clementinum* a university status developing thus the worldwide growth of arts and learning. Among the most outstanding scientists were *Tycho de Brahe* (1546-1601) and *Johannes Kepler* (1571 - 1630) whose astronomical observations and

calculations were published in the well-known Rudolphine tables. After the death of Tycho de Brahe, Johannes Kepler replaced his position of a royal mathematician in Prague in the year 1601. Using Tycho de Brahe's data, Kepler determined elliptic orbit of Venus. In his 1609 treatise "*Astronomia Nova*" Kepler published his two first laws, controlling the motion of planets and according to which the orbit of a planet/comet about the Sun is an ellipse with the Sun's center of mass at one focus

Foremost Czech physician and astronomer, Chief Medical Supervisor of the Kingdom of Bohemia at the court of Rudolph the II, was *Thaddaeus Hagecius ab Hagek* (Tadeáš Hájek z Hájků, 1525-1600), see Fig. 3., known as an author of several astronomical tractates and books on geodesy, botanic and medicine particularly acknowledged for the first concise book on the beer-making, '*De cerevisia*' (1585). Hájek essentially helped the flourishing period of alchemy and played a significant role in persuading Rudolph the II to invite Tycho de Brahe to come to Prague. Moreover a Jewish scholar, *David Gans* (1541-1613) detailed in that time the observations of Tycho de Brahe published in his astronomical work "*Nehmad ve-naim*" ('Delightful and Pleasant').

In the year 1618, the Czech Estates rose up against the ruling Habsburgs and the Jesuits were driven out of Prague. After their shortly return, the dominating Protestantism was prohibited in the Czech lands and the Charles University, the protestant one, was struck with persecution until it merged with the parallel Jesuits University in 1622. Famous Spanish visiting professor from that time was *Roderigo Arriga* (1592-1667) who authored "*Cursus Philosophicus*" (The course of philosophy). Later the Thirty Year's War badly influenced the life (mentioning just the 1648 legendary battle of Clementinum students on the Charles Bridge protecting the Old Town from pillaging by the Swedish army).



Fig. 3: From left: Hájek Tadeáš (from Hájků, 1526-1600), Komenský Jan Amos (Comenius, 1592-1670), Prokop Diviš (1696-1765) and Bolzano Bernard (1781-1848)

Special attention should be paid to the Czech thinker and Bohemian educator [20], latter refugee *Jan Amos Comenius* (Jan Amos Komenský, 1592-1670). In his "*Physicae Synopsis*", which he finished in 1629 and published first in Leipzig in 1633, he showed the importance of hotness and coldness in all natural processes. Heat (or better fire) is considered as the cause of all motions of things. The expansion of substances and the increasing the space they occupy is caused by their dilution with heat. By the influence of cold the substance gains in density and shrinks: the condensation of vapor to liquid water is given as an example. *Comenius* also determined, though very inaccurately, the volume increase in the gas phase caused by the evaporation of a unit volume of liquid water. In Amsterdam in 1659 he published a focal but rather unfamiliar treatise on the principles of heat and cold [23], which was probably inspired by the works of the Italian philosopher *Bernardino Telesius*. The third chapter of this

Comenius' book was devoted to the description of the influence of temperature changes on the properties of substances. The aim and principles of thermal analysis were literally given in the first paragraph of this chapter: citing the English translation [2,24] " *In order to observe clearly the effects of heat and cold, we must take a visible object and observe its changes occurring during its heating and subsequent cooling so that the effects of heat and cold become apparent to our senses.*" In the following 19 paragraphs of this chapter Comenius gave a rather systematic description (and also a partially correct interpretation) of the effects of continuous heating and cooling of water and air, and also stressed the reversibility of processes such as, for example, evaporation and condensation, etc., anticipating somehow the concept of latent heat. Comenius concludes this chapter as follows: "*All shows therefore that both heat and cold are a motion, which had to be proved.*". In the following chapter Comenius described and almost correctly explained the function of a thermoscope ('*vitrum caldarium*') and introduced his own qualitative scale with three degrees of heat above and three degrees of cold below the ambient temperature.

Other active famous alchemists of that time worth noting are a dilettante mathematician and astronomer *Bavor Radovský z Huntířova* (1526-1592) who wrote several books on alchemy, philosophy and even on culinary arts. However, a most important personality was *Daniel Stolcius* (1600-1660), who even maintained correspondence with Comenius and who wrote a significant book "*Virodarium chemicum*" (1624) and was seemingly cofounder of a mystical alchemical society: "*Fraternitas Rosae Cruis*". He, perhaps, introduced a world first specialization called „*chimiatrie*“, which was conceivably taught as a rather unusual subject with regards the traditional university disciplines: major '*artes liberales*' and minor '*artes mechanicae*' (i.e., learning common crafts such as warfare, navigation, business, agriculture, hunting, medicine or veterinary) but not in '*artes incertae*' (that was a part of the habitually rejected '*equivocal arts*' associated with occultism, which traditionally involved alchemy).

It, however, is difficult to trace [20] and thus hard to say if it was possible (though likely) to disseminate the idea of caloric from Amsterdam (when Comenius mostly lived and also died) to Scotland where a century later a new substance, or better a matter of fire, likewise called *caloric* (or caloricum), was thoroughly introduced by *Joseph Black* (1728-1799, and his student *Irvine*. It was assumed, e.g., that caloric creeps between the constituent parts of a substance causing its expansion. Although caloric differed from foregoing concept of *phlogiston* (because it could be later measured with an apparatus called a *calorimeter*) it is not clear who was the first using such an instrument. If we follow the studies of *Mackenzie* and *Brush* [24,25] and *Thenard* [26] they assigned it to *Wilcke*. It, however, contradicts to the opinion presented in the study by *McKie* and *Heathcode* [27] who consider it just a legend and assume that the priority of familiarity of ice calorimeter belongs to *Laplace* who was most likely the acknowledged inventor and first true user of this instrument (likely as early as in 1782). In fact, *Lavoisier* and *Laplace* entitled the first chapter of their famous "*Mémoire sur la Chaleur*" (Paris 1783) as "*Presentation of a new means for measuring heat*" (without referring Black because of his poor on paper evidence). Whilst the report of calorimetric employment done by *Black* seemed to first appear almost a century later in the *Jamin's Course of Physics* (Mallet-Bachelier, Paris 1868).

Caloric was seen as an imponderable element with its own properties. Unfortunately, the great propagator Black published almost nothing in his own lifetime [28] and his attitude was mostly reconstructed from contemporary comments and essays published after his death. Black supposed that heat was absorbed by a body during melting or vaporization, simply because at the melting- or boiling- points sudden changes took place in the ability of the body to accumulate heat (~1761). Irvine accounted that the relative quantities of heat contained in equal weights of different substances at any given temperature (i.e., their '*absolute heats*')

were proportional to their ‘*capacities*’ at that temperature and it is worth noting that the term ‘*capacity*’ was used by both Black and later also Irvine to indicate specific heats [2,28]. Black also introduced the term ‘*latent heat*’ which meant the absorption of heat as the consequence of the change of state.

Black’s elegant explanation of latent heat to the young *James Watts* (1736-1819) became the source of the invention of the businesslike steam engine as well as the inspiration for the first research in theory related to the novel domain of thermochemistry, which searched for general laws that linked heat, with changes of state. *Thompson Benjamin (Count Rumford)*, 1753-1814) presented qualitative arguments for such a fluid theory of heat with which he succeeded to evaluate the mechanical equivalent of heat. This theory, however, was not accepted until the later approval by *Julius Robert Mayer* (1814-1878) and, in particular, by *James Prescott Joule* (1818-1889), who also applied Rumford’s theory to the transformation of electrical work. The use of customary units called ‘*calories*’ was coined by *Clément*, who was giving in the year 1824 the following definitions: a “*small calorie*” allowed to increase by one degree the temperature of 1 g of water, whereas a “*large calorie*” allowed to melt 1 g of ice. The word “*calorie*” was then introduced into the vocabulary of academic physicists and chemists by *Favre* and *Silbermann* [29] in 1845. The characterization of one kilocalorie as 427 kilogram-meters was launched by Mayer in the year 1845. Captivatingly, the caloric-like description of heat as a fluid has survived, until today being, nevertheless, a convenient tool for easy mathematical description of simplified heat flows [30, 31-34]. Worth noting is the work by *Calander* [35] who proposed an alternative unit called ‘*carnot*’ (“Cr” or “Cn”) representing one unit of caloric, which provides the work of one joule during a reversible process under the gradient of one Kelvin.

Let us return to historical Prague, where professor of mathematics, *Karel Slaviček* (1678-1745), was a disciple of *Jakub Kresta* (1648-1715) whose works of trigonometry and theory of functions remained as a significant part of the mathematical history (he was often called „Euclid of the West“). Slaviček was sent as a Jesuits missionary to Chinese Empire and his letters were an ample source of focal observations of the life, customs and science in China particularly explaining Chinese astronomy.

Worth noting is the theory of *Prokop Diviš* (Procopius Divisch, 1696–1765), which belongs to early pioneering times. Accordingly, “*Light of the First Day of Creation*” (האור של יום אהד) is regarded to be identical with electricity, which is an inherent quality of all things, permeating the whole Universe and manifesting itself by electric and thermal phenomena [36]. Such an idea is, surprisingly, in an apparent agreement with the modern idea of electromagnetic zero-point background radiation [37]. The last often mentioned yet-chemist was *Kryštof Berger* (1721-1793) who in the year 1760 founded first chemical-technological laboratory and defined that mercury and sulfur react in the ration 1:1. He wrote a book on coal and important textbook “*Chemische Versuche und Erfahrungsungen*” (1792) and even constructed the first functional stove.

Important role played the Prague Jesuit College of Clementinum and its famous library and observatory (opened in the 1720s) where about 1780 *Antonin Strnad* (1747-1799) laid the foundation to the oldest known series of systematic metrological observations. Worth noting are physicists and mathematicians *Josef Stepling* (1716-1778) who transposed Aristotelian logic into formulas becoming thus and early forerunners of modern logic and *Jan Tesánek* (1728-1788) who published many original studies and initiated publishing of Prague edition of Newton’s ‘*Principia*’ supplemented with his own commentaries, in that time best edition reasoned with better mathematical background.

Worth noting is the formation of Clementinum famous library, which is associated with the name of his first director *Karel R. Unger* (1743-1807) who introduced not only the

first library reference system but also established a specific department of books written in Czech – the National Gallery. By the turn of 19th Century the Clementinum library was exhibiting as many as 140 000 volumes. In 1783, ten years after the dissolution of the Jesuits Order, the Clementinum became the seat of education (General Seminary) and by 1784 was there created the Czech Society of Sciences (in the Czech language: *Česká společnost nauk*), which was closely connected with the origins and formation of the ancestor organization to the today's *Academy of Sciences*.

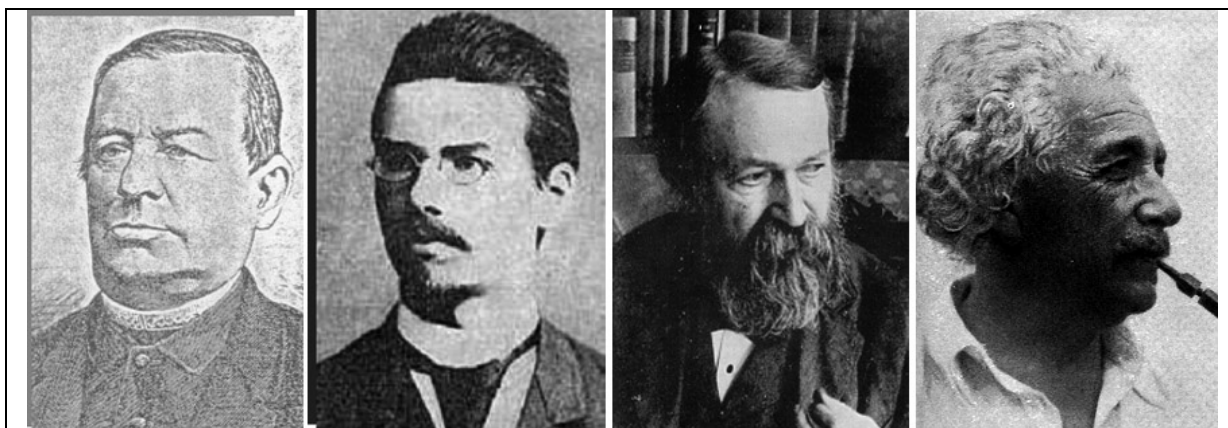


Fig.4: From left: *Václav Šimerka* (1819 – 1887), *Friedrich Reinitzer* (1857 – 1927), *Ernest Mach* (1838 – 1916) and *Albert Einstein* (1879 – 1955)

1.3. Renaissance of Prague physics and noteworthy personalities

The first half of the 19th Century mathematical and physical studies in Prague became again on a par with the world science [18-20]. Important role paid some scientists such as *František J. Gestner* (1756-1832) who is also known as a pioneer of the railway transport in Europe. Excellent achievements are duly associated with the name of *Bernard Bolzano* (1781-1848) particularly in mathematical logic and analysis and with his friend *Christian Doppler* (1803-1853) who came to Prague from Vienna in 1829. His famous paper was inspired by astronomical phenomenon: the components of many binary stars differ from each other in color. Though, according to present knowledge, the observed color difference is due to the difference of surface temperatures and not to the difference in radial velocities, the principle itself is correct, being verified, e.g., in acoustics and optics.

In 1867 arrived to Prague *Ernest Mach* (1838-1916) and spent there nearly 30 years. He is known for his discussion of Newton's *Principia* and critique of conceptual monstrosity of absolute space in his book '*The Science of Mechanics*' (1883). Mach encouraged and inspired one of his students (later professor of theoretical physics) *Jan Kolářek* (1851-1913) to study some of his hypothesis later approving that the Mach's theory correctly describes the dispersion of light, dichroism and circular birefringence. The Mach successor at Prague German University was *Ernst Lecher* (1856-1926) who is well known for his research on electromagnetic waves (i.e. '*Lecher wires*'). Mach also analyzed conceptual basis of calorimetry from more general, almost philosophical, point of views [38]. His influence on the further development of physics was tremendous and he established a mathematically specialized school - a great deal of his attention devoted to optics and acoustics. One of his personal scientific contacts was Czech famous *Jan E. Purkyně* (1787-1869) internationally known for discoveries in physiology. Another young assistant of Mach was *Čeněk Strouhal* (1850-1922), later first Czech professor appointed for experimental physics. His studies in

acoustic are well known and the *Strouhal's number* concerning friction tones (oscillations) is named after him. He wrote an exceptional book on the science of heat [39].

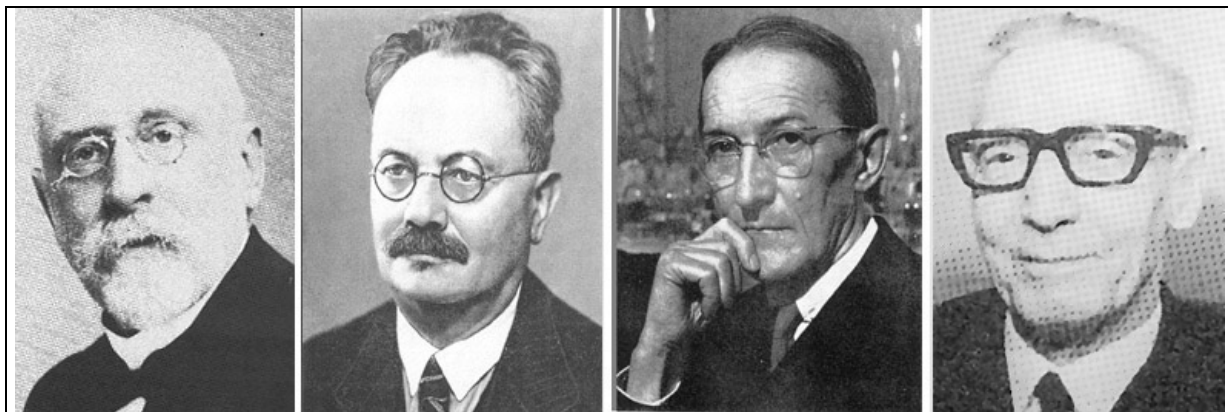


Fig. 5: From left: Čeněk Strouhal (1850 – 1922) František Závěška (1879 – 1945), Jaroslav Heyrovský (1890-1967) and Stanislav Škramovský (1901 – 1983)

Czech priest and, unfortunately, rather unknown dilettante mathematician *Václav Šimerka* (1819–1887), cf. Fig. 4, introduced quantitative evaluation in psychology (particularly mentioning his logarithmic connotation of feelings) providing thus early basis for the theory of information [40]. Czech-born *Friedrich Reinitzer* (1857–1927) is famous as the discoverer of cholesterol (including its metamorphosis and stoichiometry formulae $C_{27}H_{46}O$) and is also known for his pioneering work in the field of liquid crystals (latter widespread by *Lehmann*). *Bohumil Kučera* (1874-1921) examined effect of electrical polarization on surface tension in the interface of two liquids prompting the idea of a new technique latter know as the drop-weight method, which provided physical basis for a new, today widely utilized, analytical method called *polarography* [41] as introduced by *Jaroslav Heyrovský* (1890-1967), which was awarded by Nobel prize in 1959 [41]. We cannot present a more detailed historical foreword, for more details see, e.g., [42, 43].

A most prominent personality, which spent fruitful time in Prague was *Albert Einstein* (1879-1955) [44], a German physicist, originator of theories of relativity, laws of motion and rest, simultaneity and interrelation of mass and energy, quantum theory of photoelectric effect, theory of specific heats, Brownian motion, etc. (see the book '*Builders of the Universe*' 1932). In 1911 he obtained his first professorship at theoretical physics at the German University of Prague where he closely cooperated with his friend professor of mathematics, *Georg Pick* (1859-1942). While in Prague Einstein published 11 papers, most extensive being the survey of the theory of specific heats and very important were studies related with his favorite problem – the interaction of radiation with matter and effort to construct a relativistic theory of gravitation [45].

Worth noting is the so called Planck-Einstein transformation formula for temperature, which reads $T = T_0 \sqrt{[1 - (v/c)^2]}$ [45] and which is possibly related to the previous dissertation work by *K. von Mosengeil*, posthumously published in ref. [46]. It means that the temperature of a body observed from the system moving with a relative velocity, v , is lower than the temperature in rest system. Basing on this idea in the article published in *Ann. Physik* 26(1908)1, *Planck* assumed that the First and Second Law of thermodynamics keep their form in all inertial frames. In the year 1953, however, Einstein wrote a letter to *M. von Laue* in which he doubted the correctness of this formula and rather speculated about a formula used in the inverse form (temperature as observed in moving system is higher). This statement,

which was later proved by *H. Ott* [47], thus reads as $T = T_0 / \sqrt{1 - (v/c)^2}$, see ref. [48]. In both these cases information about the temperature is regarded to be mediated by the coherent electromagnetic radiation. Interestingly, in the case, where temperature is considered to be essentially a local property and the thermometer reading is transferred to a moving system, e.g., by means of digital coding, the temperature, in the contrast to both above formulae, must be seemingly considered as *relativistically invariant* as all other intensive properties of fields (pressure, etc.). Therefore, we need to look for an alternative relativistic transformation aimed towards the habitually adjusted meaning of certain physical constant [48], such as the traditional thermal constant viewed as a substitute, $k \cong k_0 \sqrt{1 - (v/c)^2}$, etc., [48].

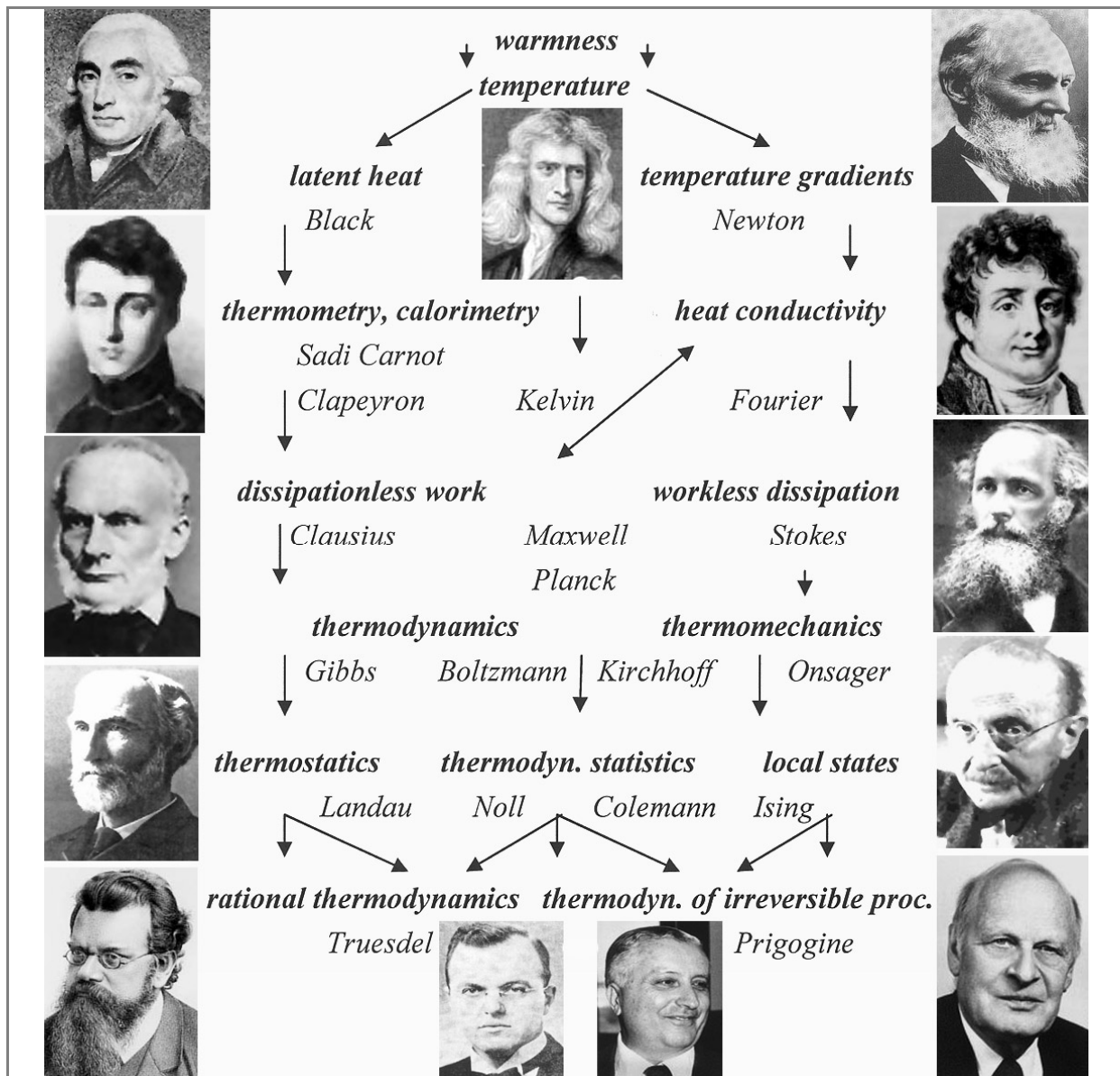


Fig. 6. Approximate sketch of the parallel growth of thermodynamic conceptions with the portraits of some famous pioneers, left column from above: Joseph Black (1728-1799), Sadi Nicholas Carnot (1796-1832), Rudolf Julius Clausius (1822-1888), Josiah Willand Gibbs (1839-1903), Ludwig Eduard Boltzmann (1844-1906), right: Kelvin, Baron of Larges, Lord Williams Thompson (1824-1907), Jean Baptiste Fourier (1768-1830), James Clark Maxwell (1831-1879), Max Carl Planck (1858-1947), Lars Onsager (1903-1976), middle: Sir Issak Newton (1642-1726), Clifford Ambrose Truesdell (1921-) and Ilya Prigogine (1917-2003).

Another distinguished, but unjustly not very appreciated, savant born in Prague was *Reinhold Fürth* (1893–1979) who devoted his scientific life to the research into the fundamentals of statistical physics [49]. Besides an extensive work concerning Brownian motion and noise phenomena he is also author of stochastic interpretation of quantum mechanics [50]. Accordingly to this theory, the Schrödinger equation is nothing but the classical diffusion equation with *complex diffusion constant* $\sim j/2m$ [51]. This statement became later a corner-stone of so called stochastic electrodynamics, which provides an alternative to quantum mechanics [47,48] and initiated our further studies in applied quantum physics [52–54]. Another target of our extended studies has been focused toward alternative thermodynamics based on the historical caloric in the meaning of entropy [12,55–57]. In this framework of the caloric theory the elementary derivation of the *efficiency of real heat engines*, $\eta_K = 1 - \sqrt{(T_2/T_1)}$, was approved showing that it is a direct consequence of the linearity of Fourier’s law of heat transfer [57].

One of the outstanding Czech teachers, who earned great merit for introducing modern theoretical physics and thermodynamics to the curriculum of Charles University, was *Frantisek Závíska* (1879–1945), cf Fig. 5. One of his textbooks was the first monograph on relativity published in Czech and he is an author of excellent books on thermodynamics [58]. He also concerned waveguides and independently deduced relevant theory early before the microwave technique became important. Other notable physicist was *Augustin Žáček* (1886–1961) who studied damped electromagnetic oscillations in vacuum electronic systems. His extended studies culminated at 1924 in the discovery of the principle of magnetron, later becoming the basis for development of radar systems.

1.4. History of thermal analysis

Roots of thermal analysis extended back to the 19s Century where temperature became a monitorable parameter [43,58–60] associated with underpinning the field of thermodynamics, see Fig. 6. Most important was the development of ‘thermocouple’ [61] as a more accurate temperature measuring device, which rapidly gets wider use as followed by *Osmond* [62] who investigated the heating and cooling behaviour of iron with a view to elucidating the effects of carbon so that he factually introduced thermal analysis to then most important field: metallurgy. However, in 1891, *Roberts-Austen* [63] was known to construct a device to give a continuous record of the output from thermocouple and he termed it as ‘*Thermoelectric Pyrometer*’. Such an innovative system of measuring the temperature difference between the sample and a suitable reference material placed side-by-side in the same thermal environment, factually initiated the development of DTA instruments.

The term *thermal analysis* was introduced by *Tammann* [64] within the years 1903–1905 who demonstrated theoretically the value of cooling curves in phase-equilibrium studies of binary systems. It was helped by this new approach that enabled the determination of composition of the matter without any mechanical separation of crystals just on basis of monitoring its thermal state by means of its cooling curves – the only method capable of a rectifiable examination of hard-to-melt crystal conglomerates.

The first automatic control was published by *Friedrich* in 1912 [43], which used a resistance box with a specially shaped, clock-driven stepped cam-plate on top. As the cam rotated it displaced a pawl outwards at each step and this in turn caused the brush to move on to the next contact, thus reducing the resistance of furnace winding. Suitable choice of resistance and profiling of the cam achieved the desired heating profile. There came also the reduction of sample size from 25 g down to 2.5 g, which reduced the ambiguity in melting

point determination from about >2 C down to ~ 0.5 C. Rates of about 20 K/min were fairly common during the early period later decreased to about quarter. Early in 1908, it was *Burgess* who considered the significance of various experimental curves in detail concluding that the area of the inverse-rate curve is proportional to the quantity of heat generated divided by the rate of cooling.

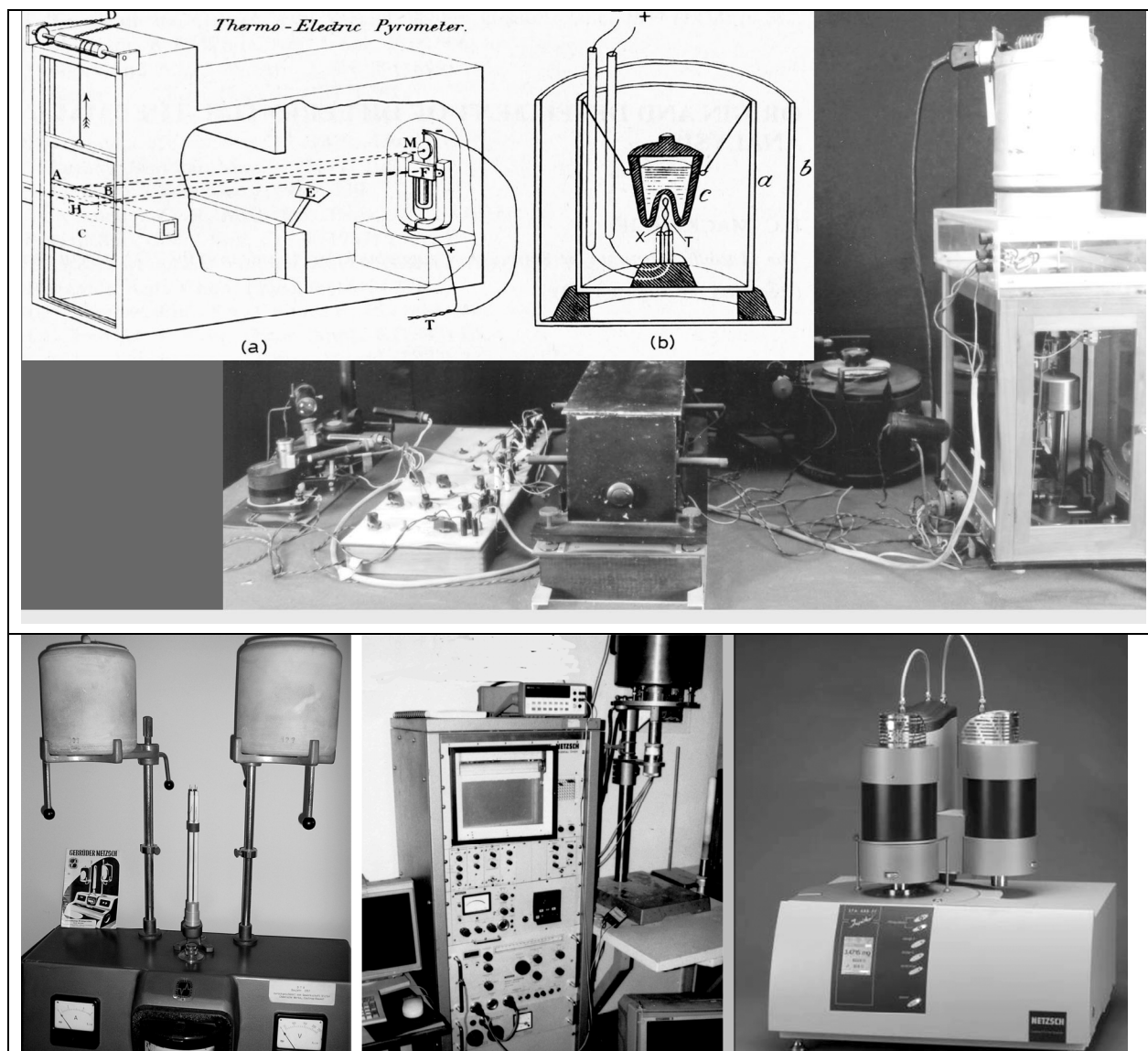


Fig. 7. Upper: Thermo-Electric Pyrometer of Roberts-Austen (1881) showing the instrument (left) and its cooling arrangement (right) with particularity of the sample holder. Middle: Historical photo of the early set-up of Hungarian “Derivatograph” (designed by brothers Paulik), which was one of the most frequent instruments in the former Eastern bloc. Below the photo of one time very popular and widespread instruments for high -temperature DTA produced by the Netzsch Gerätebau GmbH (Selb, Germany) from its early version (left) presented to the market on fifties up to the latest third-generation rendering new STA 449 F1 Jupiter (right). The middle type (yet based on then fashionable analogous temperature control) was notably sold during seventies and survived in many laboratories for a long period (being gradually subjected to enduring computerization and digital data processing) [43].

The few papers published in the period up to 1920 gave, however, little experimental details [43] so that *White* was first to show theoretically the desirability of smaller samples providing a more exhaustive study of the effect of experimental variables on the shape of

heating curves as well as the influence of temperature gradients and heat fluxes taking place within both the furnace and the sample. It is obvious that DTA was initially more an empirical technique, though the experimentalists were generally aware of its quantitative potentialities.

Final theoretical analysis of DTA was based on the calculation of heat flux balances introduced by *Factor* and *Hanks* [66], detailed in 1975 by *Grey* [67], which premises were completed in 1982 by the consistent theory made up by *Holba* and *Šesták* [68]. It was embedded within a ‘caloric-like’ framework centred on macroscopic heat flows encountered between large bodies (DTA cells, thermostats) co-developed for a generalised calorimetric classification by *Velíšek* [69]. Present DTA/DSC instruments marched to high sophistication, computerization and miniaturization, see Fig. 7.

Another modification was found necessary for high-resolution temperature derivatives to match to the ‘noise’ in the heat flow signal. Instead of the standard way of eliminating such ‘noise/fluctuations’ by a more appropriate tuning of an instrument, or by intermediary measurements of the signal in distinct windows, the fluctuations were incorporated in a controlled and regulated way. The temperature oscillation (often sinusoidal) were superimposed on the heating curve and thus incorporated in the entire experimentation – the method known as *temperature-modulated DTA/DSC* (*Reading* 1993 [70]). This was preceded by the method of so-called *periodic thermal analysis* introduced by *Proks* as early as in 1969 [71], which was aimed at removing the kinetic problem of ‘undercooling’ by cycling temperature. Practically the temperature was alternated over its narrow range and the ample investigated was placed directly onto a thermocouple junction) until the equilibrium temperature for the coexistence of two phases was attained.

Most DTA instruments can be described in terms of a double non-stationary calorimeter [2,12,69,72] in which the thermal behavior of the sample is compared with that of an inert reference material. The resulting effects (temperature difference ΔT) can be analyzed at four different but gradually escalating levels: fingerprinting (identity), quality, quantity (peak areas) and kinetics (peak shape). Consequential DSC traces are of a different nature evaluating instead temperature difference ($\Delta T \Rightarrow 0$) compensating heat fluxes introduced to equalized temperatures of the sample and the reference. Both DTA/DSC were extensively applied to study behavior of glasses [2,9,12,43] because of its easy accessibility. Most useful demonstration of inherent processes is viewed as a diagram of temperature (T) versus enthalpy (H) [73], which derivative resembles the entire DTA/DSC curve, see below Fig. 8.

The historical development and practical use of DTA in the territory of former Czechoslovakia [73] was linked with the names *Josef Burian* (1873-1942), see Fig 9., *Otto Kallauner* (1886-1972) and *Joseph Matějka* (1892-1960) who introduced thermal analysis as the novel technique during the period of the so called “*rational analysis*” of ceramic raw materials [74]. Much credit for further development of modern thermal analysis was attributed with *Rudolph Barta* (1897-1985) who stimulated thermal analysis activity at his coworkers (*Vladimír Šatava*, *Svante Procházka* or *Ivo Proks*) and his students (*Jaroslav Šesták*) at the Institute of Chemical Technology (abbreviated as VŠChT) in Prague.

In this aspect a special notice should be paid to the lengthy efforts, long journey and fruitful service of *International Confederation of Thermal Analysis and (later) Calorimetry* (ICTA/ICTAC) as an important forerunner and developer in the field of thermal analysis, cf. Fig. 10. It has an important preceding history [43] connected with the former Czechoslovakia and thermoanalytical meetings organized by Prof. R. Barta just mentioning earliest” the 1st Conference on DTA, Prague 1956, the 2nd (Prague 1958) and the 3rd Conference on Thermography, Prague 1961 and the 4th Conference on DTA in Bratislava 1966. *Robert C. Mackenzie* (1920-2000) from Scotland was an invited guest at the 1961 meeting and upon the previous communication with Russian *L.G. Berg*, US *P.D. Garn* and *C.B. Murphy* as well as

Hungarian *L. Erdey* an idea for the creation an international society was cultivated aiming to enable easier contacts between national sciences, particularly across the separating ‘iron face’, which in that time divided the East and West Europe [43]. The first international conference on thermal analysis was then held in the Northern Polytechnic in London, April 1965 and was organized by British scientists namely *B.R. Currell, D.A. Smith, J.P. Redfern, W. Gerrard, C.J. Keattch* and *D. Dollimore* with a help of *R.C. Mackenzie* and US professors *P.D. Garn* and *W.W. Wendlant*, Canadian *H.G. McAdie*, French *M. Harmelin*, Hungarian *L. Erdey*, Swedish *G. Berggren* and Italian *G. Lombardi*. Some invited speakers from

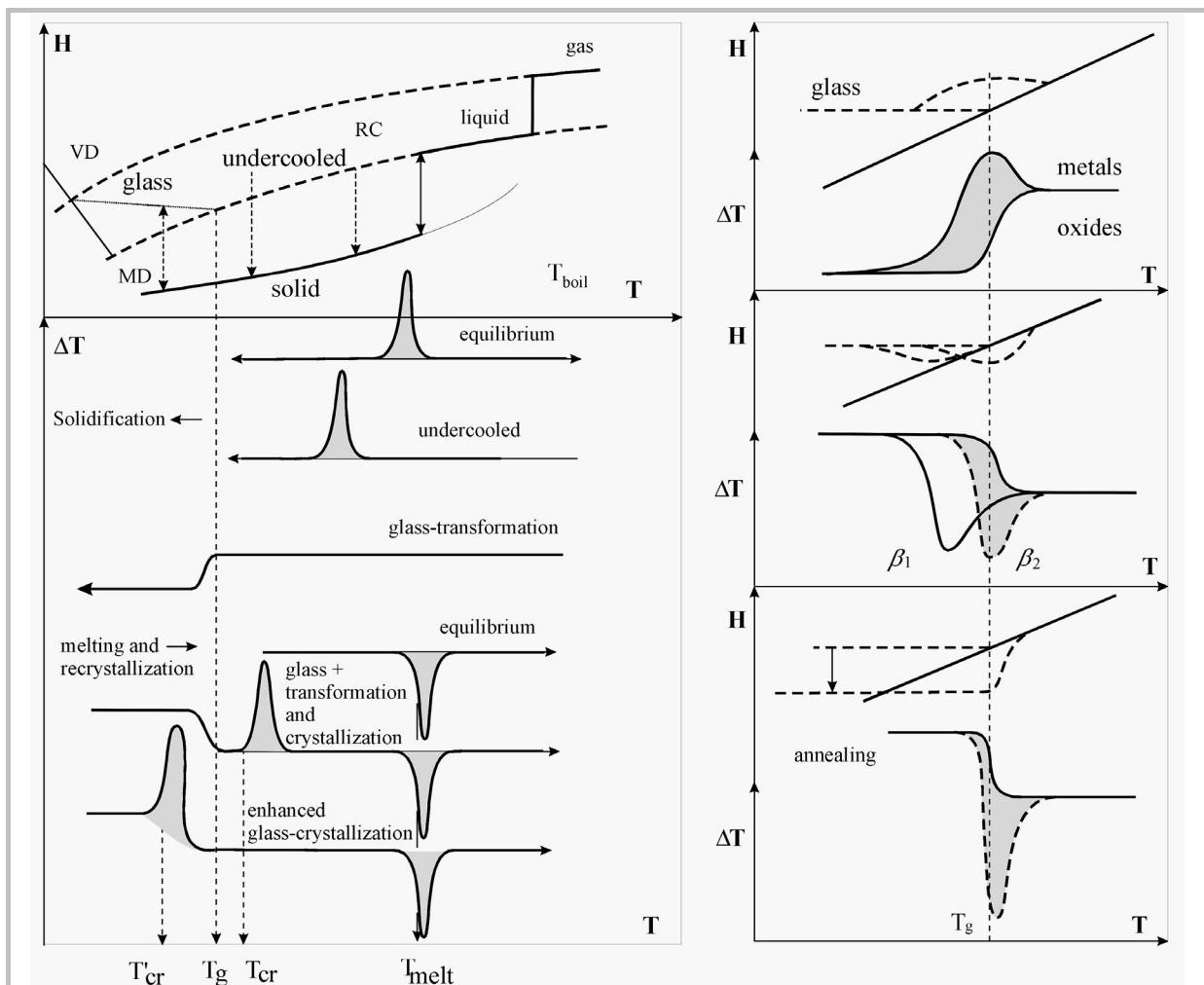


Fig. 8. Left column: solid line indicates regions of stable gaseous, liquid and solid phases while dashed lines designate regions of metastability (undercooling) and thin line unstable territory of glass. Normal or rapid liquid cooling (RC) can result to either equilibrium or retarded crystallization (exo-peak, T_{cr}) or non-equilibrium vitrification trough the step-wise glass transition (T_g). Under consequent reheating DTA/DSC shows exothermic crystallization (T_{cr}) commencing below temperature of melting (T_m). Distinctive amorphous phase (obtained, e.g., by vapor deposition – VD) can habitually behave differently because its more reactive state can enhance early crystallization overlapping thus with glass transition (such effect thus often neglected or misinterpreted). Certain points are conveniently employed for material characterization, such as the reduced temperatures (T_g/T_m) [153], Hruby coefficient of glass-formation $(T_c - T_g)/(T_m - T_g)$ [2, 12, 163]. In the right column are shown some typical experimental traces of thermal characterization of glass transformation region (T_g), which are found distinctive for dissimilar materials and/or different heating rates (β) or when involving additional temperature annealing [2]. It well illustrates a wide spectrum of possible non-equilibrium portraying of T_g transition strongly related to the experimental conditions applied [72].

the East Europe were particularly asked to come over to bridge then existing tough political control on physical, freedom and civil frontiers then strongly restricting the human rights of the Easterners (dominated by Soviet Union until the late 80s), such as *F. Paulik* (Hungary) and *J. Šesták* (Czechoslovakia). The consequent ICTA foundation in Aberdeen, September 1965, was thus established by these great progenitors of thermal analysis, besides above mentioned Barta and Mackenzie, particularly pointing out Russian *Lev G. Berg* (1896-1985) and US *Cornelius B. Murphy* (1918-1994), the first ICTA presidents. Consequentially the Czech group on thermal analysis (CWGTA) working at the Czech Chemical Society started to function in the year 1972, their chairmen gradually being *Karel Habersberger*, *Vladimír Balek*, *Jaroslav Šesták* and recently *Petra Šulcová*.

More details about the history and state-of-art of thermal science and the associated field of thermal analysis were published elsewhere [12,20,42,43,59, 60,73].

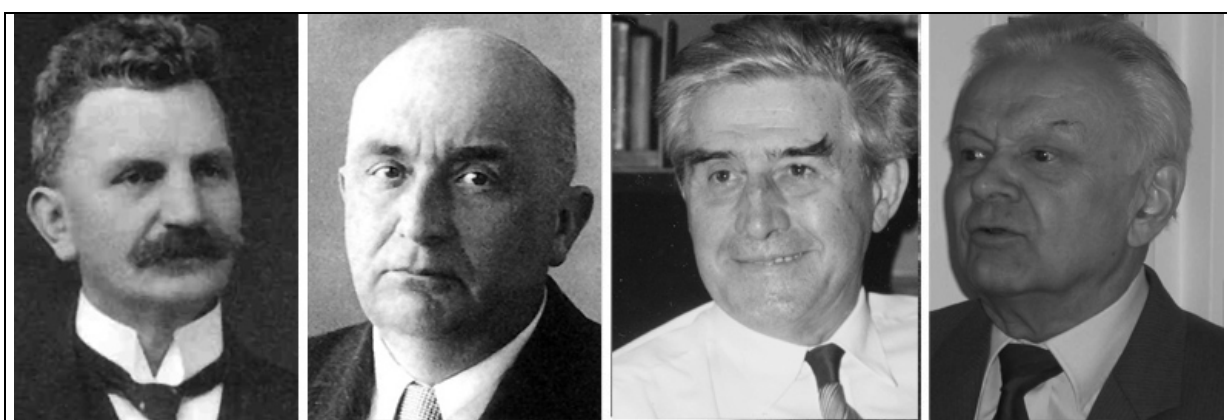


Fig. 9. Leading personalities in the early age of pioneering field of thermal analysis in the former Czechoslovakia, among others *Josef Burian* (1873-1942), *Rudolf Barta* (1897-1985)- ICTA confounder in the year 1965, *Vladimír Šatava* (*1922) and *Ivo Proks* (*1926)

Worth a special attention is an original development of weight measurements that is connected with the name *Stanislav Škramovský* (1901-1983), who, at the Charles University, investigated thermal decomposition of complex oxalates which led him in 1932 to his own construction of an apparatus named “*stathmograph*” (from Greek “*stathmos*” = mass, weight) [75] that made it possible to measure mass changes. Independently, in the same time *Duval* used for his way of weight measurements the Latin-based term “*thermogravimetry*” that later became generally accepted in thermal analysis [12,43]. As the principle scheme of the stathmograph instrument is not generally known, it is perhaps worth mentioning to describe the arrangement. Škramovský placed a weighted sample into the drying oven on a dish suspended on a long filament passing through a hole in its upper wall (forming the balance case) and hooked to the left arm of an analytical balance. A mirror attached to the beam was reflecting the image of a light slit into a slowly rotating drum lined with photosensitive paper. The unwanted vibration was reduced by an attached glass rod immersed into paraffin oil and temperature was registered automatically by means of a mercury thermometer provided by platinum contacts distributed along the whole length of capillary.

Some other original principles and unique techniques were developed and applied by the Czech-Slovak scientists, such as a periodic thermal analysis by *Proks* [71], permeability thermal analysis by *Komrska* [76], dielectric thermal analysis by *Bergstein* [77], photometric thermal analysis by *Chromý* [78], hydrothermal thermal analysis by *Šatava* [79] and emanation thermal analysis by *Balek* [80]. The development of the determination of heat

capacities at high-and-low temperature ranges was also significant such as a high-temperature calorimeter, which was designed by the *Roubal* [81] allowing determination of heat capacities in the range of 900-1900 K. Furthermore *Pekárek* initiated the construction of a isoperibolic calorimeter for the determination of hydrogenation heats in catalytic studies [73,82] and *Tydlidát* designed a calorimeter for investigating the hydration of cement pastes at increased temperatures [83]. It was preceded by the development of one of the first commercially produced thermogravimetric instrument named “TEGRA” and constructed by *Blažek* [84].



1.5. Some introductory aspects of glass and its historical features

Glass is often viewed as a remarkable non-crystalline substance regarded to have magical origin though usually made from the simplest raw materials upon the effect of firing. Mimicking evolution, however, became responsible for the creation of further families of a wide variety of glassy materials, which have gradually appeared through human creativity particularly during last hundred years. Properly chosen procedure of rapid extraction of heat (= *quenching*) turned up to be in charge for a successful glass-formation (= *vitrification*) of almost all substances in general (thus assistant for physicists to prepare glassy state from different sorts of various inorganic materials even metals) in contrast to the previously mentioned, traditional chemical approach seeking just for an appropriate composition to vitrify under a customary self-cooling.

The first natural glasses were formed as the Earth cooled and therefore predate creation of living organisms by about 1.5 billion years. Such primordial glasses were limited in composition and versatility as were the first primitive unicellular organisms (bacteria), however, some compositions (in an unstable state of glass) have survived unchanged enormously long (similarly to certain strains of bacteria). A still open intellectual terrain ahead is apparent in each of the material class associated with real bodies either advanced naturally or created synthetically - particularly interested in *glasses* when assuming rather curious but apparent degree of similarity with *biopolymers* (genes) [85]. Both are in a reinforced (unstable thermodynamic) state formed due to kinetic reasons, which are existing until glasses transform into a stable structure (melt of the lowest free energy) or biopolymers (occurring as parts of living organisms) stops its biological activity (life). Both glasses and biopolymers adapt to their environment and previous history and there is an almost limitless range of compositions of glasses and countless numbers of different living species, each family having particular molecular building blocks and severe structural rules although some compositional restrictions of glasses were gradually overcome. Although the origin of glass is nevertheless lost in prehistorically obscurity all imaginable glasses can be synthesized making thus the natural and manmade glasses indistinguishable. Another intriguing parallel can be drawn in their spontaneously apparent emergence of new phyla or groups of species involving both the disordered state of glasses and highly ordered situation of biopolymers as well as their often highly non-equilibrated status.

The structure and properties of these materials are understood and subjected to monitor in ways that were unheard of decades ago (although materials have been central to the growth, prosperity, security and quality of life of humans since the beginning of history [86-93]). Despite all the similarities one difference is fundamental: life forms are self-replicable and living organisms cannot be created in the laboratory yet; any attempt did not even produce a simple protein macromolecule. All cells contain proteins and, on the other hand, proteins synthesis requires enzymes. So how biosynthesis could begin without enzymes is the question to be resolved. This dilemma may involve our better understanding of possible convergence of glass and genes assuming known bioactivity of certain inorganic glasses, particularly their “-OH” active surface capable of binding to living tissues under their specific compositions, porosity (‘self-similarity’ and ‘fractality’ [2,3,12]) and pre-treatments [2,85].

The diversification of glasses has been known since humans learned how to control fire - roughly few hundred thousand years ago. The first manmade glasses were synthesized unintentionally by the fortuitous smelting of sand and alkaline plant flux by fire about ten thousand years ago. Glass-working was mentioned with connotation “*just to take plentiful sand and plant ashes and, by submitting them to the transmuting agencies of fire to produce melt which whilst cooling could be shaped into a an infinite variety of forms, which would solidify into a transparent material with appearance of solid water and which is smooth and cool to the touch, was and still is a magic of the glass workers art*”. Some glasses were created naturally [86] by accidental melting due to the charge of lightning (‘*lechatelierite*’) and worth of noting are ‘*obsidians*’ (glassy volcanic rocks consisting of natural acidic silicate glasses exhibiting a high melting point) and ‘*pumice*’ (famed volcanic glass), which were formed by terrestrial upshot of volcanism and have attracted the men’s attention since prehistoric times (used as cutting instruments, amulets or cult objects). A special attention deserves tektite-strewn fields famous for deeply sculptured pieces of olive greenish, usually rapidly frozen, droplets of a meteoritic impact origin (in the Southern Bohemia are known as *Moldavites* since their proper description in 1787 when they were listed among precious stones used in jewelry). It is also worth noting that the extent of natural glass on earth is in the range of a tenth of a percent with the ratio of about 4000 minerals versus mere 5 types of natural glass while on the moon (and

possibly also other planets) it is possible to identify only ~60 minerals against 35 glasses- the frequency of glass deposits being at least one order of magnitude higher than that on the Earth.

An important role in the medieval development of glass making was played by North Bohemia [90,91]. Surrounded by mountains the most remarkable factor was the creation of the oldest glassworks in the continent, some of them were operating without interruption from its foundation (such as in little town *Chřibská* since 1414). Contrary to the greater part of preserved German medieval glass, usually of a rich green color due to the admixture of iron, the glass of *Bohemian firings* [92,93] is as a rule lighter, almost transparent, and only a little tinged with yellow, brown or light green. Glass cups and goblets of various shapes were decorated on their surface with large or small stuck-on bead adornments. Hollow glass of the 14th Century manifested a long-standing production tradition with its refined shapes and difficult and complicated hand-executed decorations. The most typical glass of the Czech environment were flute shaped glass beakers, tall slender goblets called the "*Bohemian type*", Bohemian glass, however, was never so fine and flexible as so called "*Venetian glass*" [90], which was more suitable for forming fantastically shaped vessels (because rich in soda from sea plants it was less viscous). On the other hand, beech (and both less frequent and suitable oak) wood used for firing, the refined ash, rich in lime and potash, and the country's quality siliceous sand contributed to the greater purity of the Bohemian glass which was composed of potassium calcium silicate. Hard, clear glass which resembled natural rock crystal, generally called Bohemian mountain glass, was suitable for engraving and foreign producers considered themselves privileged when given the right to make glass marked "*ad uso de Bohemia*".

Several notable milestones of more modern science depended on the availability of onwards glass as a preeminent choice of alchemist for their apparatuses. Relatively unstable and fragile glass was always essential for many chemical operations in early times. Dissatisfied with the chemical durability of glass, glass properties were modified by adjusting composition; however, this could not yet have been done properly because chemistry was still on a mystical basis, and the techniques of analysis needed did not exist. An important cornerstone was *Galileo's* work on the motion of planets based on glass lenses in astronomical telescopes as well as *Newton's* pioneering work in optics (1666) requiring in addition prisms and mirrors. Other basic investigations required specific glass apparatuses to describe the properties of gases, introduce thermometry, barometry and develop microscopy. The first reasonably documented description of glass-making procedures is associated with the invention of lead glass around 1676. The most influential books appeared to be *Neril's "L'Arte Vetraria"* (1612) and *Kuncel's "Ars Vitraria Experimentalis"* (1679) which were translated into other languages (as well as many others such as the *Encyclopedia* published in the year 1765, etc.) all of them remained, however, not more than recipe manual. In the middle of the seventeenth century a proper understanding of heat was yet lacking so that melting, solidification and glass formation could not be understood well enough so that the only important glass properties were those easily measurable were, such as density and refractive index.

The other problem was associated with furnaces, first, the material to build them from, secondly, how to attain a high enough temperature together with a way to measure and control it. The net caloric value of wood decreased with moisture content, falling almost to zero at about 70% of moisture. Even well dried wood still contained around 20% of moisture so that the maximum temperature attainable did not exceed 1200 °C. A typical (Bohemian) furnace was above ground level, vaulted and oval in shape, in which glass was obviously also pre-melted, melted and blown, with a lower part for annealing of glass on the opposite side to the orifice for product insertion. The exhausted gases passed over the pots and out of the working holes where a space was reserved for oak wood drying. An extraordinary good level of medieval glassmaking is exhibited by the quality of mosaic still retained on the Golden Gate of Prague's St. Vitus Cathedral ("*The Last Court*" from 1370-1376).

Since medieval times manual skill allowed the making of window glass by the crown process (forming a shallow bowl and, after reheating, spinning to make it open into almost a flat circular disc) and by the cylinder process (blowing a cylinder, cutting off the ends and cracking it longitudinally) often mentioned as "*procede de Boheme*". Chemically resistant boron-containing glass was produced as early as in 1830 by *Kavalier* and later continued by high silica glass (80% SiO₂) called "*unexcelled*". The nineteenth century showed an enormous progress in optical glasses through effective stirring and later by fruitful investigation of the property versus composition relationships. The tank furnace made possible continuous large scale production, and machines for automated production of containers were most innovative in the glass industry. By the turn of the century *Owens* produced a successful six arm rotary machine which differed from most others in the way it was supplied with glass, and it remained almost unchanged until the 1960s when it was supplanted by gob feeders. Patents for sheet glass production date back to the 1850s but with little success. The invention of mechanical drawing of sheet glass was made by the Belgian *Fourcault* in 1914 but not finalized due to the war. The actual production took place in 1919 in a newly built glassworks in North Bohemian *Hostomice*. The original serial pulling was there later improved by the system called "*Bohemian cross*", but the most important large scale production took place in the 1950s by a rather expensive redundant plate process (laying melt to cool on the surface of liquid tin). The production of foam glass and fused basalts is also worth mentioning in the same period. The large scale production of glass fibers for insulation and for textiles was another important twentieth century development as well as less known advances in high quality, dimensionally accurate pressing or optical fibers, gradient index glasses, etc. As a curiosity we can mention that the first British TV employed a screen in which bulbs were handmade by precise blowing from a single piece of lead glass and then were imported from the former Czechoslovakia in the late 1930's. Since that the sphere of glass developed to unimaginable diversities, see next Fig. 11.



Fig 11. Various images of glass and glassy state, from left: cut lead-containing oxide glass, magnetic metallic glassy ribbons, hydrophilic gelled lenses and micro-photos of either the biological glass emerging in undercooled plants and the non-crystalline portrayal of natural sedimentary opal.

As a matter of interest, Czech scientists have become world famous in macromolecular chemistry of polymers especially when introducing '*hydro gels*' as a widely used material for the fabrication of contact lenses for eyes. Such an idea for correcting eye astigmatism was first mentioned in the year 1827 by the British physicist *Herschel* but was realized in practice as late as 1887 by the eye glass craftsman *Müller* who used very well cut and polished glass pieces. The Czech physician *Teissler* succeeded in replacing rigid oxide glass by a rubbery material based on celluloid foil as early as 1935. The major '*mismatching*' disadvantage (the difference between the mechanical properties of lenses and the cornea) was not defeated until the 1952 invention by *O. Wichterle* and *D. Lim* who proposed the use of hydrophilic gels to match not only the

mechanical properties of the cornea but also to enable a free exchange of biological liquids and oxygen. It was first prepared by radical polymerization of methacrylesters of ethylene glycol obtaining poly(2-hydroxyethyl methacrylate), abbreviated as poly(HEMA). It becomes easily water-swollen but still remaining mechanically applicable. The problem of preparation of optically well-defined lenses' geometry was overcome by rotatory casting (legendary realized on bases of a toy brick-box) and since it has become a Czech patent widely applied in various countries (particularly USA). Nowadays this type of material is used not only for intraocular lenses but also for bio-imitation of other organs such as blood vessels, etc. It is clear that a special world of glassiness may naturally include constitution of almost all organic macromolecules, including polymers and overall plastics, which we herewith incorporated into our account of amorphous materials.

1.6. Following lines of glass investigation

The sort of non-crystalline materials, which are called glasses are special resources that are formed merely under favorable thermally non-equilibrium conditions; which are either provided by nature or created by man. We should note that the previously used term “*non-crystalline*” comprise two expressions where “*amorphous*” is a more general, generic term (often associated with methods of disordering such as intensive polycrystalline milling) in comparison with the term “*glass*” (linked with the melt cooling technique called ‘*vitrification*’); glasses subsists also a rather universal engineering material. Most glass products manufactured on a commercial scale are made by suitable cooling a mixture from their state of melt/liquid. For some particular applications, glasses are also made by other technologies, for example by chemical vapor deposition to achieve extreme purity, as required in optical fibers for communication, or by roller shilling in the case of amorphous metals, which need extremely high cooling rates (‘*quenching*’). Variation of the composition results in a huge variety of glass types, families, or groups, and a corresponding variety of properties. In large compositional areas of oxides, the properties depend continuously on composition, thus allowing one to design a set of properties to fit a specific application. In narrow ranges, the properties depend linearly on composition; in wide ranges, nonlinearity and step-function behavior have to be considered. The most important historical and subsequently engineering glasses are mixtures of various oxide compounds. For some special requirements, e.g., a particular optical transmission window or coloration, fluorides, chalcogenides, and colloidal (metal or semiconductor) components are also used. A very special glass is single-component silica, which is a technological material with extraordinary properties and many important applications. On a quasi-macroscopic scale (> 100 nm), glasses seem to be homogeneous and isotropic; this means that all structural effects are, by definition, seen only as average properties. This is a consequence of the manufacturing process associated with various cooling rates and undercooling states. A structure with a well-defined short-range order (on a scale of $< 0,5$ nm, to fulfill the energy-driven bonding requirements of structural elements made up of specific atoms) and a highly disturbed long-range order (on a scale > 3 nm, disturbed by misconnecting lattice defects and admixture of different structural elements). When on cooling the crystallization is bypassed, we speak of a frozen-in, super-cooled or better undercooled, liquid-like structure. This type of quasistatic solid structure is not controlled by traditional thermodynamics only but is greatly depending on kinetics and thus is not in a completely stable state, which tends to relax and slowly approach an associated equilibrium structure of melt (whatever this may be in a complex multicomponent composition representing a minimum of the Gibbs free energy). This also means that all properties change with time and temperature, but in most cases at an extremely low rate, which cannot be observed under the conditions of classical applications (in the range of ppm,

ppb, or ppt per year at room temperature). However, if the material is exposed to a higher temperature during its practical dispensing or in the final application, the resulting relaxation may outcome in an objectionable deformation or internal stresses that then limit its consequent use.

The melt-cooling processes responsible for the formation of vitreous states are not the only methods which generate glassiness. Low temperature diagenetic and biotic processes also result in amorphous solids such as hyalites and opals (when the ‘opaline’ state is a status containing curiously a low degree of short range order while attaining a high degree of order at long range). Other non-crystalline materials are various alumina-silicates (based on the mixture of meta-kaolin with an alkaline activator producing thus hardening pastes), which are frequently termed as alkaline inorganic polymers, geo-polymers or hydro-ceramics exhibiting, among other interesting properties, amalgamated qualities peculiar to cements with those of glass-ceramics and zeolites. They need a special attention targeted in the consequent chapters.

There are thousands worth noting researches, scientists and engineers who contributed better understanding of glass science and technology mentioning just few. Among the mostly significant scientific achievements was the *Griffith's* theory [94] of the strength of brittle materials published in 1920s. X-ray diffraction analysis was a particularly exciting field having enormous impact on glass science in the first quarter of the 20's Century. It led *Zachariesen* (1932) to consider his principles on how bonding requirements were met and nearest neighbor coordination maintained without imposing an exact long range order [95] common for crystalline materials. Other important notional impacts were done by *Tammann* [96], *Vogel* [97], *Fulcher* [98], *Kauzmann* [99], *Tool* [100], *DiMarzio* [102], *Turnbull* [102], *Frenkel* [106] (and many others such as *Davis*, *Gibbs*, *Cohen*, *Angel*, *Fisher*, etc.) not forgetting *Kreidl* [115], see Fig. 12., which were mostly aimed toward the theory of glass formation and glass transition. In particular *Davies'* and *Jones* published early treaties on thermodynamics of glass formation [104] and from that time there have appeared countless studies, which were trying to clarify the disequilibrium state of glasses, the status of which, however, still remains in the focal point of better understanding of glassiness [105], see more details in this book introductory chapter. There is available a wide range of various books on inorganic [e.g. 106-140] as well as organic [141- 149] glasses and many thousands of papers laying outside of any real reach of citing and reviewing them (just mentioning our survey publications completed in the framework of the Institute of Physics [150-163]).

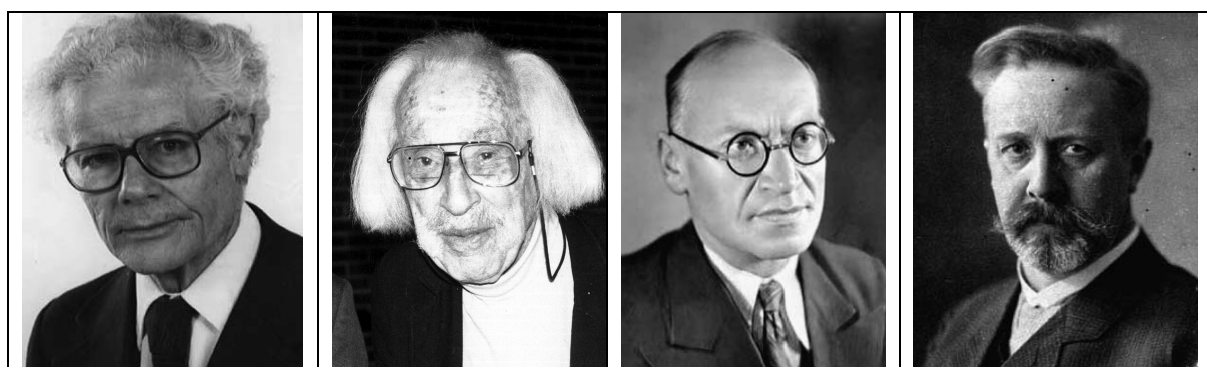


Fig. 12. Some famous personalities in the glass research, from left: D. Turnbull, N.J. Kreidl, J. Frenkel and G. Tammann

It is worth noting that the theoretical progress is still ongoing particularly pointing out, for example, novel frontierey means of a geometrical modelling based on an abnormal pentagonal assemblage (notoriously known to be incapable to fill any area completely with its

irregular 5-fold symmetry) but yet providing possibility to arrange a surface and/or space tiling in an asymmetrical but repeating manner [7]. These yet avant-garde constructions have already found applicability in portraying the cluster structure of liquid water [9] and may become useful in describing the randomness state of non-crystallites and glasses [2], see the first paragraph. Worth of a further accentuating is also the long-lasting promotion on glass carried out by the *International Commission on Glass* (ICG), outstandingly achieved by its Committee on glass nucleation and crystallization (abbreviated ‘CT 7’, see the next Fig. 13.) toward the progress of glass science and technology of mostly inorganic systems based on oxide.



Fig. 13. The 2001 composition of TC7 committee (of ICG) working in the configuration (from right) G. Völksch (Germany), V.M. Fokin (Russia), M. Davis (USA), R. Müller (Germany), late P. James (UK), kneeling E. Zanotto (present chairman, Brazil), late M. Weinberg (USA), W. Hölland (past chairman, Liechtenstein), T. Kokubo (Japan), I. Szabo (Hungary), I. Donald (UK), L. Pinckney (USA), W. Panhorst (former chairman, Germany), J. Šesták (Czech Republic).

Since the thirties the conferences on oxide glasses started and their regular series were later followed by conferences on non-conventional glasses (chalcogenides in 50s, metals in 70s and halides in 80s). An extensive search for novel glass with properties not previously known or studied was launched within which prevailed chemical-like studies trying to find (for a given method of a technologically convenient cooling) a relevant composition with advantageous properties. It was located in contrary to an avant-garde physical approach enduring to find a fast enough method of quenching for every-individual (given) material [among others: 109,126,132,150,154]. It resulted in the introduction of novel families of unconventional glasses; first varieties, worth mentioning, are the non-oxide glasses of chalcogenides [109], metals [110-113,119] or fluorides [120], which exhibited many general features shared with oxide glasses. Serial interdisciplinary conferences were started in the fifties and most wide-spreading came later with the challenging development of xerography, electro-photography, lithography, etc.. Afterward, there appeared quite unexpected inorganic systems of which halide, oxynitride and metallic glasses are most notable. Since the sixties those motivation unlocked the regular meetings scattered to multiple specializations and applications. Halide glasses, for example, have a potential for exploitation as ultra low-loss

optical fibers (operating in the mid IR and nonlinear optics), while "*metglasses*" and nowadays a more sophisticated nano-crystalline "*finemetals*" have already found their place in various magnetic materials (exhibiting parallel spins in crystalline 'ferro-magnetic' and disparate spins in glassy 'spero-magnetic' states [119]). Worth noting is also the underpinning of glassy-like carbon in the 1960s, which is achieved by solid carbonization of thermosetting resins (once used for inert implants) that appearing in the same year as the first metallic glass by splat cooling of Au-Si alloys [110-113]. There, however, was an almost parallel progress of the particularized description of vitrification and crystallization in different material's branches all based on the divergent but consequently unified theories of nucleation and crystal growth, which was also true for another, previously somehow separate, makeup of organic and polymeric glasses of various macromolecular systems?

Nowadays the formerly variant theories have marched to amalgamation [e.g., 122-138,147-149,158-161]. Among many others let us just mention that well before the development of any generalized nucleation theory for condensed systems, *Tammann* [96] already called earlier attention to a tendency revealing that the higher the melt viscosity at the melting temperature, the lower is its crystallizability. Qualitatively, this tendency can be explained by an increased inhibition of motion or molecular rearrangement of the basic units of any melt with increasing viscosity. Later, for chalcogenide systems, *Hruby* [163] defined a phenomenological glass-formation tendency more rigorously as the ratio between the differences of temperatures of the crystallization T_c , melting T_m and glass transition T_g , (i.e. $(T_g - T_c)/(T_m - T_g)$) [72, 163,164] – cf. previous Fig. 8). Regarding the reduced glass transition temperature, T_{gr} , [153] *Zanotto* concluded [165] that glasses having T_{gr} ($= T_g/T_m$) higher than ~ 0.59 display only surface (mostly heterogeneous) crystallization, while glasses showing volume (homogeneous) nucleation possess $T_{gr} < 0.59$ [165] (as supported by experimental nucleation data for abundant silicate glasses). He also assisted creation of a rather consistent theoretical basis summarised in ref. [166], which alternatives are also the subjects of the book.

Literature 1

- [1] H. Gebelein, „*Alchemie, die Magie des Stofflichen*“ Diderichs, Munich 1991
- [2] J. Šesták, „*Heat, Thermal Analysis and Society*” Nucleus, Hradec Kralove 2004
- [3] J. Šesták, „*Some model classification of geometrical bodies and their development in historical applications*” in book „*Approaching scientific knowledge*” (A.Wittwer, E. Knut, V. Pliska, G. Folker, eds.) Collegium Helveticum, Zurich 2008, pp.87
- [4] R. Penrose, „*The Road to Reality: a complete guide to the laws of the Universe*” Vintage, London: 2004
- [5] G. Agricola, „*De re metallica libri XII*”, 1556
- [6] J. Kepler, . „*Strena seu nive sexangula* » 1611
- [7] A. Bravais, „*Etudes cristallographiques* » 1861
- [8] R. Penrose, „*The Emperor's New Mind: concerning computers, minds and the laws of physics*” Oxford University Press, Oxford 1989
- [9] J. Šesták, J. Zámečník, „*Can clustering of liquid water be of assistance for better understanding of biological germplasm exposed to cryopreservation*” J. Thermal Anal. Calor. 8 (2007) 411.
- [10] D. Eisenberg, W. Kauzmann, „*The structure and properties of water*” Oxford University, London 1969
- [11] J. Mimkes, „*Society as a Many Particle System*” J. Thermal Anal. Calor. 60 (2000) 1055.

- [12] J. Šesták, “*Science of Heat and Thermophysical Studies: a generalized approach to thermal analysis*” Elsevier, Amsterdam 2005.
- [13] J.W. Weibull, „*Evolutionary Game Theory*” MIT Press, Cambridge 1995
- [14] R.N. Montenegro, H.F. Stanley, “*Introduction to Econophysics: correlation and complexity in finance*” Cambridge University, Cambridge 2000.
- [15] S.E. Jorgensen, Y.M. Svireshev, “*Towards a Thermodynamic Theory for Ecological Systems*”. Amsterdam, Elsevier 2004
- [16] S.A. Kauffman, “*Investigations*” Oxford Press, New York 2000.
- [17] D.J. Barrow, “*Impossibility: limits of science and science of limits*” Vintage, New York 1999
- [18] J. Janta, J. Niederle (eds) „*Physics and Prague*“ Academie, Prague 2005
- [19] I. Kraus “*Dějiny technických věd a vynálezů v českých zemích*“ (The history of technical science in the territory of Czechia and Moravia) Academia, Praha 2004
- [20] J. Šesták, J.J. Mareš „*From cloric to statmograph and polarography*“, J. Thermal Anal. Calor. 88 (2007) 763
- [21] I. Štoll „*Jan Marek Marci*“ Prométheus, Praha 1996
- [22] J.M. Marci: „*De proportione motu*“, Prague 1639
- [23] J.A. Comenius: „*Disquisitiones de Caloris et Frigoris Natura*“, Amsterdam 1659
- [24] R.C. Mackenzie „*History of Thermal Analysis*“, special issue of Thermochim. Acta, Vol. 73, Elsevier, Amsterdam 1984
- [25] S. G. Brush “*The Kind of Motion we call Heat*”. Vol. I & II , North Holand, Amsterdam 1976
- [26] L. Thenard “*Treatise of Chemistry*” 6th edition, Crochard, Paris 1836
- [27] D. McKie and N.H.V. Heathcote “*The Discovery of Specific and Latent Heats*”; Arnold, London, 1935
- [28] R. Fox “*The Caloric Theory of Gases: from Lavoasier to Regnault*”, Claredon Press, Oxford 1971
- [29] P. Favre and J. Silbermann, C.R.Acad.Sci. 20(1845)1567
- [30] R. Clausius “*Mechanische Wärmetheorie*” Vieweg u. Sohn, Braunschweig 1876
- [31] J.M. Socquet “*Essai sur le calorique*”, Paris 1801
- [32] P. Kelland “*Theory of Heat*”, Cambridge 1837
- [33] R.B. Lindsay “*Energy: historical development of the concept*” Dowden, Stroudsburg 1975
- [34] J.J. Mareš “*On the Development of Temperature Concept*” J. Thermal Anal. Calor., 60 (2000) 1081
- [35] J. H.L. Callendar, Proc. Phys. Soc. of London 23 (1911) 153.
- [36] P. Divisch „*Längst verlangte Theorie von der meteorologischen Electricite, Magiam Naturalem benahmet*“ J.H.P. Schramm, Tübingen 1765
- [37] M. Sparnaay “*Historical Background of the Casimir Effect*” in “*Physics in the Making*” (A. Sarlemijn, M. Sparnaay, eds.), Elsevier, Amsterdam 1989
- [38] E. Mach „*Die Principien der Wärmelehre*“ Leipzig 1896
- [39] Č. Strouhal “*Thermika*” (Thermics), JČMF, Praha 1908
- [40] P.V. Šimerka, “*Síla přesvědčení: pokus v duchovní mechanice*” (Strength of conviction as an attempt to mental mechanics), Časopis pro pěstování matemat. fyziky, 11 (1882) 75
- [41] J. Heyrovsky “*Poralographie*” Springer, Vienna 1941
- [42] B. Bensande-Vincent, I. Stenger “*History of Chemistry*” Harvard Press, London 1996

- [43] J. Šesták “Some historical aspects of thermal analysis: origins of Termanal, CalCon and ICTA” in the proceedings of Int. Conf. on Thermal Analysis “TERMANAL” (eds. E.Klein, E. Smrčková, P. Šimon), Bratislava 2005, p.3; or on private websites: www.fzu.cz/~sestak
- [44] J. Bičák: “Einstein’s route to the general theory of relativity” Čes.čas.fyz. A29(1979)222
- [45] A. Einstein, Jhb. Radioact. Electron 4 (1907) 411
- [46] K. von Mosengeil, Ann. Physik 22 (1907) 867
- [47] H. Ott, Z. Phys. 175 (1963) 70.
- [48] J.J. Mareš, J. Šesták, V. Špička, P. Hubík, key lect. “Temperature relativistic transform. and Mosengeil-Ott’s antinomy”, at Proc. 3rd Int. Conf. Frontiers of Quantum and Mesoscopic Thermodyn., Prague 2008, p.81; Physica E, in print 2009 (doi: 10.1016/j.physe.2009.06.038)
- [49] R. Fürth, Z. f. Phys. 81 (1933) 143
- [50] G. Holton “Thematic Origins of Scientific Thoughts: from Kepler to Einstein” Harvard University, Cambridge 1973 (reedited 1988);
- [51] A. Einstein “Investigation on the theory of Brownian motion” (R. Furth, ed.), reedition Dower Publ., New York 1956
- [52] Z. Kalva, J. Šesták “Transdisciplinary aspects of diffusion” J. Thermal Anal. Calor. 76 (2004) 67
- [53] J.J. Mareš, J. Stávek, J. Šesták “Quantum aspects of self-organized periodical chemical reactions” J. Chem. Phys. 121 (2004) 1499; J. J. Mareš, J. Šesták, J. Stávek, H. Ševčíková, J. Křištofik and P. Hubík, “Do periodic chemical reactions reveal Furth’s quantum limit” Physica E 29 (2005) 145
- [54] J.J. Mareš, J. Šesták “An attempt at quantum thermal physics“ J. Thermal Anal. Calor. 82 (2005) 681
- [55] B. Hlaváček, J.J. Mareš, book: “Fyzika struktur amorfních a krystalických materiálů“ (Physics of Structures of Amorphous and Crystalline Materials; J. Šesták, ed.), Publ.House Pardubice University, Pardubice 2008 (in Czech)
- [56] J. J. Mareš, P. Hubík, J. Šesták, V. Špička, J. Křištofik and J. Stávek “Phenomenological Approach to the Caloric Theory of Heat” Thermochim. Acta 474 (2008) 16
- [57] J. Šesták, J.J. Mareš, P. Hubík and I. Proks „Contribution by Lazare and Sadi Carnot to the Caloric Theory of Heat and its inspiration role in thermodynamics“ J Thermal Anal Calor., in print 2009 (doi: 10.1007/s10973-008-9710-y)
- [58] F. Závíška „Termodynamika“ (Thermodynamics), JČMF, Praha 1943 (in Czech)
- [59] I. Proks “Evaluation of the Knowledge of Phase Equilibria” in book “Kinetic Phase Diagrams” (Z. Chvoj, J. Šesták, A. Třiska, eds.), Elsevier, Amsterdam 1991, p.1; and book “Chapters from the history of exact sciences: The whole is simpler than its parts), Slovak Academy of Sciences, Bratislava, in print 2010 (in Slovak)
- [60] P. Cardillo “A history of thermochemistry through the tribulations of its development” J. Thermal Anal. Calor. 72 (2002) 7
- [61] H. LeChatelier, C.R.Acad.Sci. Paris, 102 (1886) 819
- [62] F. Osmon, C.R.Acad.Sci. Paris 106 (1888) 1156
- [63] W.C. Roberts-Austen Proc. Inst.. Mech. Eng. 1891, 543
- [64] G. Tammann, “Über die Anwendung der Thermische Analysen in abnormen Fällen”. Anorg. Chem. 45 (1905) 701
- [65] W.P. White, J.Am.Chem.Soc. 36 (1914) 2292
- [66] M.M. Factor, R. Hanks, Trans. Farad. Soc., 63 (1959) 1129

- [67] A.P. Grey in proc. 4th ICTA, "Thermal Analysis", Akademia Kiado, Budapest 1974
- [68] P. Holba, J. Šesták "Theory and practice of DTA/DSC" Silikáty (Prague) 29 (1976) 83 and J. Šesták, P. Holba, G. Lombardi, "Quantitative evaluation of thermal effects: theoretical basis of DTA/DSC" Annali di Chimica (Roma) 67 (1977) 73
- [69] J. Velíšek, Chem. listy (Prague) 72 (1978) 801
- [70] M. Reading, Trends Polym. Sci., 1993, p.248
- [71] I. Proks, J. Zlatkovský, Chem. Zvesti (Bratislava) 23 (1969) 620
- [72] J. Šesták "Use of phenomenological enthalpy versus temperature diagram (and its derivative - DTA) for a better understanding of transition phenomena in glasses" Thermochem. Acta 280/281 (1996) 175
- [73] J. Šesták "History of thermal analysis on the territory of former Czechoslovakia" Thermochem. Acta 100 (1986) 255 and "The history and future of thermal analysis; thermochemical and thermodynamic background" J. Mining Metallurgy 35 (1999) 367
- [74] C. Kallauner, J. Matějka, Sprechsaal 47 (1914) 423
- [75] S. Škramovský, Chemické listy (Prague) 26 (1932) 521
- [76] J. Komrská, Silikáty (Prague) 11 (1967) 51
- [77] A. Bergstein, Collect. Czech. Chem. Com. 20 (1955) 1058
- [78] J. Chromý, Amer. Mineral. 54 (1969) 549
- [79] V. Šatava, O. Vepřek, Silikáty (Prague) 15(1971) 1 and J. Amer. Cer. Soc. 58 (1975) 357
- [80] V. Balek, Silikáty (Prague) 13 (1969) 39 and J. Mater. Sci. 4 (1969) 919
- [81] M. Roubal, V. Landa, Strojírnoství (Prague) 25 (1975) 559
- [82] M. Abbrent, V. Pekárek, Chemické Listy (Prague) 63 (1969) 1042 and Chemické Zvesti (Bratislava) 30 (1976) 621
- [83] V. Tydlidát, Czech. J. Phys. B 21 (1971) 817
- [84] A. Blažek, Silikáty (Prague) 1 (1957) 177
- [85] L.L. Hench "Glasses and genes: a forecast for the future" Glastechn. Ber. Glass. Sci. Technol. 70C (1997) 439; "Life and death: the ultimate phase transformation" Thermochem. Acta, Vol. 280/281 (1996)1
- [86] V. Bouška "Natural Glasses" Academia, Praha 1993
- [87] G. Tammann "Die Aggregatzustände" Yoss Verlag, Leipzig 1922; States of Aggregation, Nostrand, New York 1925 and „Der Glaszustand, Leopold Voss, Leipzig 1933
- [88] E. Barrington-Haynes "Glass through the Ages", Penguin, Harmondsworth 1948
- [89] C.J. Phillips "Glass the Miracle Maker", Pitman & sons, London 1948
- [90] V. Vondruška, A. Langhamer "Bohemian Glass: history, tradition and present" Grafitisk, Děčín (Czechia) 1991
- [91] O. Drahotová (ed.) „Historie sklářské výroby v českých zemích" (History of glasswork in the Czech countries), Vol. I. & II. Academia, Praha 2005
- [92] V. Hulínský V., O. Gedeon, E. Černá „Microanalysis of early-medieval glass gems found in the Bohemian and Moravian region" in „Microbeam Analysis 2000" (by D.B. Williams and R. Shimizu, eds.), Inst. Physics, Bristol 2000 and V. Hulinsky, Z. Cilova "Medieval glassworks and the glass production in the North-Western Bohemia" Glastechn. Ber. Glass. Sci. Technol. 77C (2004) 359
- [93] J. Šesták, L. Kadečka, R. Kobr "North Bohemian Rocailles: technology and art of glass beads" Glastechn. Ber. Glass Sci. Tech. 67C (1994) 596
- [94] A.A. Griffith „The phenomena of rupture and flow in solids" Phil.Trans.Roy.Soc.

London_A221 (1920) 163.

[95] W.H. Zacharisen „*Atomic arrangement in glass*“ J. Am. Cer. Soc. 54 (1932) 3841

[96] G. Tammann “*Über die Grenzen des festen Zustandes*” Wied. Ann. 16 (1897) 280-299; “*Über die natur der flüssegem crystalle*” Ann Physik 19 (1906) 421-425 *Über die wirkung von Silicium MetatitanÄuhedrat*”; Z. Elektrochemie 10 (1904) 532; “*Die abhängigkeit der viskosität von der temperatur bei unterkühlten flüssigkeiten*“ Zeit. Anorg. Allgem. Chemie 156 (1926) 245-257.

[97] D.H. Vogel, “*Das temperatur-abhängigkeitsgesetz der viskosität von flüssigkeiten*“ Phys. Zeitschrift 22 (1921) 645.

[98] G.S. Fulcher, *Analysis of recent measurements of the viscosity of glasses*, J. Am. Ceram. Soc. 8(6) (1925) 339-355.

[99] W. Kauzmann: „*Nature of the glassy state and the behavior of liquids at lower temperatures*“ Chem. Reviews 43 (1948) 1_

[100] A.Q. Tool, “*Viscosity and the extraordinary heat effects in glass*” J. Res. Nat. Bur. Stand. 37 (1946) 73-90; “*Relation between inelastic deformability and thermal expansion of glass in its annealing range*” J. Am. Ceram. Soc. 29 (1946) 240-253.

[101] J.H Gibbs and E.A. DiMarzio, *Nature of the glass transition and the glassy state*, J. Chem. Phys. 28 (1958) 373-383; E.A. DiMarzio, *Equilibrium theory of glasses ~ an equilibrium theory of glasses is absolutely necessary*, Annals New York Acad. Sci. 371 (1981) 1.

[102] D. Turnbull, J.C. Fisher “*Rate of Nucleation in Condensed Systems*” J. Chem. Phys. 17 (1949) 71 and 18 (1950) 769.

[103] M. Cohen and D. Turnbull, *Molecular transport in liquids and glasses*, J. Chem. Phys., 31 (1959) 1164-1169 and D. Turnbull and M.H. Cohen in ref. [107], p. 111 (1960)

[104] R.O. Davies, G.O. Jones, “*The Irreversible Approach to Equilibrium in Glasses*” Proc. Roy. Soc. 26 (1953) 217

[105] C.A. Angell, *Oxide Glasses in Light of the "Ideal Glass" Concept: Ideal and Non-ideal Transitions and Departures from Ideality*, J. Amer. Ceram. Soc. 51 (1968) 117-124; and *Structural instability and relaxation in liquid and glassy phases near the fragile liquid limit*, J. Non-Cryst. Sol. 102 (1988) 205-221; and “*Thermodynamic aspects of the glass transition in liquids and plastic crystals*”, Pure Appl. Chem. 63 (1991) 1387-1392.

[106] J. Frenkel, „*Kinetic Theory of Liquids*“ University Press, Oxford 1946; and Dower, New York 1955

[107] J.D. Mackenzie (ed) “*Modern Aspects of Vitreous State*” Butterworth, London 1960

[108] H. Rawson “*Inorganic Glass-forming Systems*” Academic Press, London 1967

[109] J. Tauc, „*Amorphous and Liquid Semiconductors*“ Springer, Berlin 1974

[110] P. Duhaj, P. Mrafko (edts) „*Amorphous Metallic Materials*“ Veda, Bratislava (Slovakia) 1980

[111] W.A. Philips (ed.), “*Amorphous Solids: low temperature properties*” Springer, Berlin 1981

[112] F.E. Luborsky (ed) “*Amorphous Metallic Alloys*” Butterworth, London 1983

[113] S.R. Elliot “*Physics of Amorphous Metallic Alloys*” Butterworth, New York 1983; “*Progress of Amorphous Materials*” Longman, London 1984; and “*Physics of Amorphous Materials*” Wiley, New York 1990

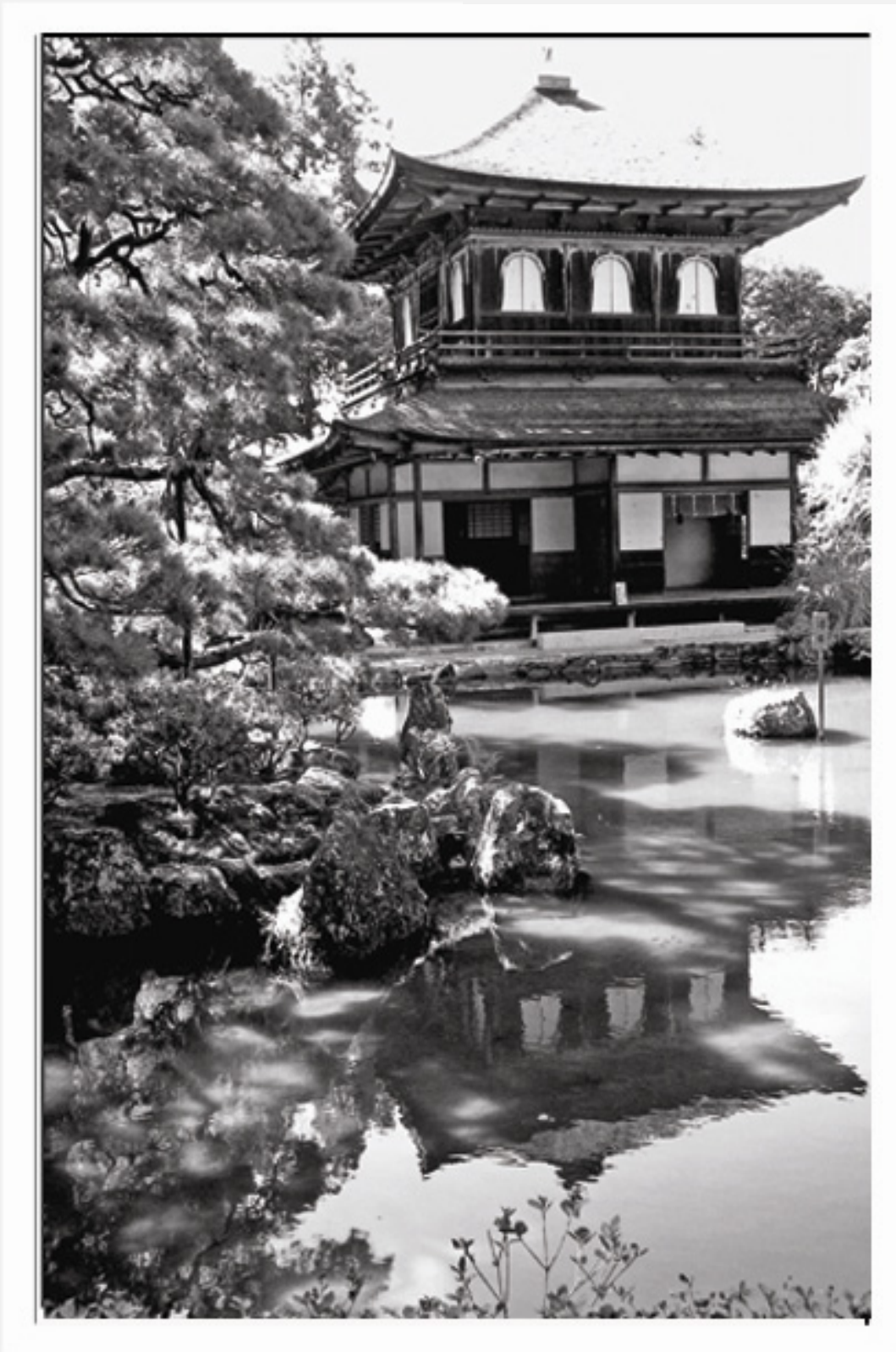
[114] J. Voldán, V. Dušánek „*Electrical Properties of Glasses*“ SNTL, Praha 1983

[115] D.R. Uhlmann, N.J. Kreidl (edts) “*Glass: science and technology*” Academic, New York 1983; “*Advances in Structural Analysis*” and “*Structure, Microstructure and Properties*”, both by Tokyo Academic, Boston 1990

- [116] A. Feltz „*Amorphe und Glasartige Anorganische Festkörper*“ Akademie, Berlin 1983; and “*Amorphous Inorganic Materials and Glasses*” VCH Weinheim 1993
- [117] M.B. Volf „*Chemical Approach to Glass*“, Elsevier, Amsterdam 1984 and „*Technical Approach to Glass*” Elsevier, Amsterdam 1990
- [118] P. Balta, E. Balta „*Introduction to Physical Chemistry of Vitreous State*“ Abacus Press, Tunbridge 1984
- [119] K. Moorjani, J.M.D. Coey “*Magnetic Glasses*” Elsevier, Amsterdam 1984
- [120] A. E. Comyns (ed) “*Fluoride Glasses*” Wiley, New York 1989
- [121] Z. Strnad “*Glass-ceramic Materials: liquid separation, nucleation and crystallization*” Elsevier, Amsterdam 1986
- [122] R. Zallen „*Physics of Amorphous Solids*“ Wiley, New York 1988
- [123] B.O. Mysen: *Structure and Properties of Silicate Melts*. Elsevier, Amsterdam 1988 and *Silicate Glasses and Melts - Properties and Structure*. Developments in Geochemistry, Vol. 10. Elsevier, Amsterdam 2005
- [124] I. Fanderlik “*Silica Glass and Its Application*” Elsevier, Amsterdam 1991
- [124] J. Zarzycki “*Glasses and the Vitreous State*” Cambridge University Press, 1991
- [126] H.H. Liebermann (ed) “*Rapidly Solidified Alloys: processes, structure and properties*” Marcel Dekker, New York 1993
- [127] R.H. Doremus „*Glass Science*“, Wiley, New York 1994
- [128] A.K. Varshneya, “*Fundamentals of Inorganic Glasses*” Academic Press, Harcourt Brace Publishers, Boston, 1994
- [129] I. Gutzow, J. Schmelzer, „*The Vitreous State: thermodynamics, structure, rheology and crystallization*“ Springer, Berlin 1995
- [130] S. Nemilov “*Thermodynamic and Kinetic Aspects of the Vitreous State*” Boca Raton CRC Press 1995
- [131] Yohiro Abe “*Superconducting Glass-Ceramics*” World Scientific, 1997
- [132] C. Suryanarayana (ed) „*Non-equilibrium Processing of Materials*“ Pergamon, New York 1999.
- [133] E.J. Donth “*Relaxation and Thermodynamics in Polymers*” Akademie, Berlin 1992; “*Glass Transition, Relaxation and Disordered States*” Springer, Berlin 2001
- [134] W. Höland, G. Beall, “*Glass-ceramic Technology*”, Amer. Cer.Society 2002.
- [135] K.J. Rao “*Structural Chemistry of Glasses*” Wiley, New York 2002
- [136] J. Sheby “*Glass Science and Technology*”, Royal Sci. Chem., Cambridge 2005
- [137] D. Jürn, W.P. Schmelzer (eds) „*Nucleation Theory and Application*“ Wiley, New York 2005
- [138] L. Leuzzi, Th. M. Nieuwenhuizen, „*Thermodynamics of the Glassy State*“ Taylor and Francis, New York 2008
- [139] T.J. Sluckin, D.A. Danmur, H. Stegemeyer “*Crystals that Flow*” Taylors & Francis
- [140] L. Wondraczek, R. Conradt (eds) “*Glass and Entropy*” special issue of J. Non-Crystal. Solids, Vol. 355, 2009
- [141] A.V. Tobolsky, “*Properties and Structure of Polymers*” Wiley, New York 1960
- [142] F. Bueche “*Physical Properties of Polymers*” Interscience, New York 1962
- [143] J. Schultz, “*Polymer Material Science*”, Prentice Hall, New Jersey 1974
- [144] L.R.G. Treloar, “*Physics of Rubber Elasticity*”, Clarendon Press, Oxford 1975
- [145] J.D. Ferry, “*Viscoelastic Properties of Polymers*” Wiley, New York 1980
- [146] J.E. Mark, “*Physical Properties of Polymers*”, United Book, Baltimore 1993

- [147] E.A. Turi (ed), “*Thermal Characterization of Polymers*” Academic, New York, 1997
- [148] G.R. Strobl, “*Physics of Polymers*” Springer, Berlin/Heidelberg 1996
- [148] H. Bauer “*Thermophysics of polymers*” Springer, Berlin/Heidelberg 1999
- [149] B. Wunderlich “*Thermal Analysis of Polymeric Materials*” Springer, Berlin 2005
- [150] J. Šesták “*Phenomenology of glass-formation and crystallization of glasses*” chapter in book “*Kinetic Phase Diagrams; non-equilibrium transformations*” (Z. Chvoj, J. Šesták, A. Tríska, eds), Elsevier, Amsterdam 1991, p. 169
- [151] J. Šesták „*Oxide melt fast solidification and glass crystallization as a route for preparation of high-Tc superconductors*“ chapter in book: „*High Temperature Superconductors*“ (J. Narliken, ed), Nova Publ. Inc., New York 1991, p. 44
- [152] A. Varschavski, J. Šesták „*Applications of DSC for the study of transformation processes in quenched glassy alloys*“ chapter in book: „*Characterization Techniques of Glasses and Ceramics*“ (J.M. Rincon, M. Romero, eds.), Springer, Berlin 1999, p. 144
- [153] J. Šesták “*Some thermodynamic aspects of glassy state*” *Thermochim. Acta* 95 (1985) 459 and „*The role of thermal annealing during processing of metallic glasses and resulting magnetic properties*“ *Thermochim. Acta* 116 (1988) 427
- [154] J. Šesták “*Art and horizon of non-equilibrated and disordered states and the new phase formation and growth*” *Glasstech. Berichte Glass. Sci. Tech.* 70C (1997) 153 and „*Miracle of reinforced states of matter: glasses - old and new structures for the third millennium*“ *J. Thermal Anal. Calor.* 61 (2000) 305
- [155] N. Koga, Z. Strnad and J. Šesták “*Thermodynamics of non-bridging oxygen in silica bio-compatible glass-ceramics*” *J. Thermal Anal. Calor.* 71 (2003) 927-937.
- [156] N. Koga and J. Šesták “*Crystal nucleation and growth in lithium diborate glass studied by thermal analysis*” *J. Am. Ceram. Soc.* 83 (2005) 1753-1760.
- [157] Z. Chvoj, J. Šesták, Z. Kožíšek, monograph: „*Non-equilibrium processes of melt solidification, consequent nucleation, crystallization and metastable phase formation by freeze-in procedures*” special issue of *Thermochim. Acta*, Vol. 153, Elsevier, Amsterdam 1989
- [158] J. Šesták (ed) : “*Reaction kinetics by thermal analysis*”, special issue of *Thermochim. Acta*, Vol. 203, Elsevier, Amsterdam 1992
- [159] J. Šesták, Z. Strnad (eds.) “*Special technologies and materials*” Academia, Praha 1993
- [160] M. Sorai, J. Šesták (eds.) „*Transition phenomena in condensed matter*“ Special issue of *Thermochim. Acta*, Vol. 266, Elsevier Amsterdam 1995
- [161] J. Šesták (ed.) “*Vitrification, transformation and crystallization of glasses*” special issue of *Thermochim. Acta*, Vol. 280/281 Elsevier, Amsterdam 1996
- [162] J. Šesták, M. Liška (eds.) „*Building the bridges between glass science and glass technology*” Special issue of *Glass. Ber. Glass. Sci. Tech.*, Vol. 77C, 2004
- [163] A. Hrubý, “*Evaluation of glass forming tendency by means of DTA*” *Czech J. Phys.* B22 (1972) 1187 and “*Glass-forming tendency in the GeS_x*” B23 (1973) 1623;
- [164] A.A. Cabral Jr, C. Fredericci and E.D. Zanotto “*A test of the Hrubý parameter to estimate glass-forming ability*” *J. Non-Cryst. Solids* 219 (1997) 182-186.
- [165] E.D. Zanotto “*Isothermal and adiabatic nucleation in glass*” *J. Non-Cryst. Sol.* 89 (1987) 361; and E.D. Zanotto and M.C. Weinberg, “*Trends in homogeneous crystal nucleation in oxide glasses*” *Phys. Chem. Glasses* 30 (1989) 186
- [166] V.M. Fokin, E.D. Zanotto, J.W.P. Schmelzer „*Homogeneous nucleation versus glass transition temperature of silicate glasses*” *J. Non-Cryst. Sol.* 321 (2003) 52; and “*Crystal homogeneous nucleation: a 40 years perspective*” *J. Non-Cryst. Sol.* 352 (2006) 2681

Ginkakuji (Silver Temple), Kyoto, Japan



Chapter 2

Temperature and heat

2. PHENOMENOLOGICAL MEANING OF TEMPERATURE

Jiří J. Mareš

Dolus latet in universalibus

2.1. Introduction

It is difficult to imagine the immense effort which was necessary for the transformation of ancient theory of thermal phenomena based on the peripatetic concepts of *Antiperistasis* and *Doctrine of Four Elements* (coldness, hotness, dryness, humidity) [1,2] into the modern system based on measurable quantities having definite magnitudes and physical dimensions, which would be convenient for effective mathematical processing. Path-breaking statement “*Coldness is nothing but the absence of hotness*” which can be found in the Galileo’s correspondence with his pupils [3] and denying the very fundamentals of Aristotelian physics, was probably even more heretical than his famous statement concerning the rotation of Earth. It should be noticed here that the research into the thermal phenomena is enormously difficult in comparison with e.g. the research into the mechanics because the concepts involved are of very abstract nature. For example, it took an appreciable time, more than ~150 years, till the “intensive” and “extensive” aspects of heat were in a pregnant way introduced into the thermal physics by J. Black [4], where they substituted a vague term of “heat” closely related to our sensations. Another serious obstacle in the development of thermal physics is its universality. Considering namely any process in the nature, one immediately recognizes that it is controlled or at least influenced by the “thermal” conditions in which it takes place. Therefore the theory of thermal phenomena has to be inevitably quite universal and consequently very prone to misinterpretations and far reaching persistent errors (according to our motto in the heading, “*Deception is concealed in the universality*”). Keeping thus in mind just this last important circumstance, we have made an attempt to outline anew the logical structure of the phenomenological thermal physics which is, as we are convinced, far from being well established. In this short review we have focused our attention mainly on one crucial concept of the thermal physics, namely on the temperature.

What does the temperature actually mean? It is a classically simple question astonishingly lacking an appropriate answer. The answers, namely, which can be found in the textbooks on thermodynamics, are only hardly acceptable without serious objections. For illustration, let us give a few typical examples here and the reader himself can easily find others in the current literature. To the most hand-waving belong the statements such as that “the temperature is known from the basic courses of physics” or even “temperature is known intuitively”. More frankly sounds the practical formulation that “the temperature is reading on the scale of thermometer” throwing doubt, perhaps without awareness, upon the very existence of temperature if the thermometer is not at our disposal. In contrast to it, rather philosophical is the statement that “temperature is a physical property of a system that underlies the common notions of hot and cold” which, nevertheless, rather specifies what the temperature should be, giving no idea of what it actually is. To a high scientific standard pretends the definition telling us that “on the macroscopic scale the temperature is the unique physical property that determines the direction of heat flow between two objects placed in thermal contact” being in fact an explanation *obscurum per obscurius* which transforms the temperature problem to the problem of flow of something even more uncertain. In order not to

fall, however, into an unfruitful and non-constructive criticism we stop now with examples the purpose of which was only to illustrate the state of affairs and turn our attention to the other aspects of the problem.

Of course, there is no doubt that the temperature is a central concept of thermal physics and therefore a lot of researchers feeling the lack of a good definition were trying, in different ways, to bring the temperature concept on the safer grounds. For example, the authors preferring the axiomatic approach are, as a rule, inclined to assume that the temperature is a primitive concept which need not be, in principle, derived from other presumable more primitive ideas. Unfortunately, the experimental determination of temperature in any particular case requires performing a lot of non-trivial operations which should be substantiated by its definition. Thus such a shift from the operative physical definition to the metaphysical one, very comfortable for theoreticians, makes an inexplicable obscure ritual any actual temperature measurement performed by experimentalists.

For researchers who consider the thermal physics being nothing but an outgrowth of statistical mechanics, the equilibrium temperature of a system can be (up to an arbitrary factor) defined as an inverse of the derivative of natural logarithm of the statistical weight of its actual macroscopic state with respect to the energy of the system. Nevertheless, practically no actual measurement of temperature is directly linked with the evaluation of statistical data related to a certain ensemble of particles and excitations but it is as a rule performed by means of various forms of thermometers converting the temperature to another measurable physical quantity. It is thus evident that prior to the identification of the temperature defined in the frame of statistical theory with the phenomenological temperature, the latter has to be satisfactorily defined first.

The purpose of this contribution is thus to re-examine a fundamental concept of thermal physics, *temperature*, partly from the historical and partly from a logical point of view. In order to avoid very general abstract considerations the exposition is confined practically only to fluids, i.e. mechanical systems for which are the constitutive relations simple and well known. The mathematical structure of the precursor of temperature, *hotness manifold*, is, as far as we know, for the first time discussed in terms of *elementary set theory*. In the exposition of the subject the emphasis is put on experiment and on the generalization of empiric data while mathematical proofs of some statements has reader confer with special references already given.

2.2. Phenomenological conjugate variables

The very task of any mathematical theory of material systems is to establish general rules for the further treatment of *empirical constitutive relations* describing the state of a body in terms of suitably chosen parameters. We do not mean here the parameters specific for the description of thermal effects but just the parameters already introduced in other branches of physics and generally known as the *phenomenological variables* [5]. The existence of such variables, playing the roles of macroscopic conditions which are compatible with a huge number of parameters describing each microscopic component of the body, is clearly a matter of experience. Usually, there is an appreciable number of various phenomenological variables determining the state of the body but fixing a chosen one by external means, this number can ever be diminished by one. Continuing such a procedure the number of significant phenomenological variables can be finally reduced to two. It is a fact worth to noticing that the two-parameter system is the simplest model of a real system because it enables one to construct a meaningful constitutive relation and, simultaneously, it is apt for straightforward generalization, e.g. by adding another pair of independent variables. In order to ensure easy perceptibility of mathematical description of two-parameter systems a special form of

phenomenological variables was found to be desirable. It is a well known fact that the terms entering the energy balance equations in mechanics and electrodynamics have a canonical form which may be characterized by means of the following dimensional relation

$$[\text{Energy}] = [X] \times [Y], \quad (1)$$

where square brackets mean the physical dimension of the quantities enclosed. As the energy is an extensive quantity, it is favourable for first phenomenological variable to choose also an extensive quantity, say X. In such a case, however, the second parameter has to be inevitably an intensive quantity, Y [6]. Such a couple of quantities obeying relation (1) is then called a couple of *conjugate variables*. (For example, the list of the most frequently used conjugate parameters is given in Table 1.) The existence of the intensive and extensive “aspects” of heat which was already recognized by J. Black [4] is thus in this context the discovery of primary importance for the formalization of theory of heat and its compatibility with other branches of physics. His “intensity of heat” and “matter of heat” can be, namely, quite naturally assigned to a certain couple of conjugate variables, which may be tentatively called „temperature „ and „heat“. Formal compatibility of these two quantities with the system of quantities already introduced in other branches of physics is thus only a matter of proper choice of suitable operative definitions and units.

Table 1. Selected conjugate variables

Extensive quantity	X	Intensive quantity	Y	Energy term E
Volume	V	pressure	p	pV
Momentum	G	velocity	v	vG
Charge	Q	el. potential	φ	φQ
Mass	M	grav. pot.	γ	γM

2.3. Diathermic partition, thermal equilibrium

The idea to treat real system in terms of conjugate variables enable one to introduce some fundamental concepts of thermal physics in a quite systematic way and, somewhat astonishingly, without a priori reference to the thermal phenomena *per se*, particularly to the quantities of temperature and heat [7]. The important role plays here the so called *correlation test*. It is the procedure frequently used in the practical thermometry which enables one to check whether the thermometer is in proper thermal contact with the measured body. Simultaneously, it provides the basis for the following operational definition of diathermic and adiabatic partitions (walls), viz: Let us have two systems characterized by couples of conjugate variables (X,Y) and (X',Y'), respectively, and separated by a macroscopically firm material partition (wall) defining their common boundary. Such a partition is called *diathermic* if the changes of the variables (X,Y) induce the changes of the variables (X', Y') and vice versa (“diathermic“ originates from Greek *διά* = through, *θερμός* = warm). A concept complementary to that of diathermic partition is the *adiabatic* partition (from Greek *α-* = negation, *διά* = through, *βαίνειν* = to go) which prevents the thermal contact of neighbouring bodies, i.e. ensures their thermal insulation. Obviously this concept is a limiting one, depending to an appreciable extent on the accuracy of the correlation test. The adiabatic

partition is, namely, any diathermic partition for which the experimental proof of its ability to realize the thermal contact by the said test failed.

Using then the language of two-parameter description, the general definition of the equilibrium state as known from other branches of physics can be extrapolated also to the region of thermal phenomena. Let us recall first what the equilibrium state means e.g. in mechanics. Standard formulation for the two-parameter system reads: Any state of a body in which the conjugate coordinates X and Y remain constant so long as the external conditions are unchanged is called *equilibrium state*. Combining then this definition with that of the diathermic partition we can immediately define the concept of thermal equilibrium, which already belongs to the scope of thermal physics, namely:

If two bodies being in diathermic contact are both in equilibrium state, they are in *thermal equilibrium*.

2.4. Thermoscope

The first devices known as thermoscopes have appeared during the later Renaissance in connection with the first edition of Latin translation of Hero's "*Pneumatica*" by F. Commandino Urbinate (1575) [8]. The influence of this book dealing with various unexplained natural phenomena and curious contrivances worked by air, water or steam was

so general that it is almost impossible to tell, whether a particular device was directly derived from Hero's descriptions or whether it is an original invention. Therefore, one can find in the literature a long series of "inventors of thermometer", e.g. Cardano, Galileo, Sanctorius, Besson, de la Porta, Drebbel, Fludd, Leurechon, Ens, Harsdoerfer, Kirchner etc. [9], but to decide about the priority of any one of them is a very difficult task. Quite early it was recognized that these devices, having various forms of fluid or air dilatometers, enable the objectification of the subjective feelings of hot and cold. Almost simultaneously appeared an idea that the thermal states of bodies, which are in common terms described by means of ordered series of terms cold, cool, tepid, warm, hot, could be characterized by the ordered series of thermoscope readings as well. The substitution of *thermoscope* for human *sensations* in experiments leads finally to the conviction that the thermal state of bodies or of environment can be characterized by thermoscope readings incomparably better than by means of sensation in itself.

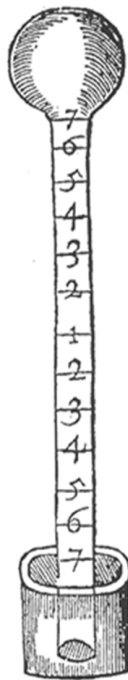


Fig. 1. A typical early thermoscope provided with an arbitrary scale. Glass tube and bottom vessel were filled with wine, bulb thus contained a mixture of air with water and alcohol vapours. (According to [10].)

The thermoscope was thus promoted to the device apt to indicate with "absolute exactness" the thermal state of vicinal bodies. Such a (of course, very optimistic!) belief reflects also famous Fludd's quotation [10] "Weather-glass (i.e. thermoscope) became a mighty weapon in the Herculean fight between Truth and Falsehood" (see Fig. 1).

2.5. Thermoscopic states

In order to continue this story in a more contemporary and systematic way we will call *thermoscope* any two-parameter system in which one of the conjugate parameters, say Y , can be fixed, $Y = Y_0$. It is further assumed that thermoscope can be brought into a diathermic contact with other bodies and that it is sufficiently “small” in comparison with these bodies in order to not appreciably disturb their thermal equilibrium. The second conjugate real parameter X , which is called in this connection *thermoscopic variable*, is generally of quite a diverse physical nature and dimension. It may be length, volume, resistance, voltage, frequency and many others. In order to distinguish formally among various thermoscopic variables, differently constructed thermoscopes and physical conditions under which they operate, a small Latin index is used. Applying this convention, reading $X_k(P)$ of the k -th thermoscope which is in diathermic contact with a body under investigation defines the *thermoscopic state* P of the body. The corresponding set of the thermoscopic states which can be observed in this way is then marked as \mathbf{H}_k . Notice that the readings X_k are related to the thermoscope while the indicated thermoscopic state as e.g. $P \in \mathbf{H}_k$, already relates to the body. It is a matter of fact that the phenomenological parameters were introduced into classical mechanics and electrodynamics as continuous quantities covering certain closed intervals of real axis. Therefore, according to our definitions, such a property is transferred also to the thermoscopic variables X_k . We will thus assume that the numerical values of quantity X_k also continuously cover a certain closed interval \mathbf{I}_k , operation range of the k -th thermoscope, which is a proper part of the set of real numbers, \mathbf{E}_1 . In usual symbols we can thus write¹:

$$X_k \in \mathbf{I}_k \subset \mathbf{E}_1. \quad (2)$$

If it is further for every couple $P, Q \in \mathbf{H}_k$,

$$P \neq Q, \Leftrightarrow X_k(P) \neq X_k(Q), \quad (3)$$

the set \mathbf{H}_k can be ordered in accordance with the intrinsic order already existing in real interval $\mathbf{I}_k \subset \mathbf{E}_1$. Simultaneously, condition (3) ensures the existence of one-to-one mapping between the sets \mathbf{I}_k and \mathbf{H}_k and we can thus define order (\prec, \succ) in \mathbf{H}_k by the following equivalences:

$$\begin{aligned} P \prec Q &\Leftrightarrow X_k(P) < X_k(Q) \\ P \succ Q &\Leftrightarrow X_k(P) > X_k(Q) \\ P = Q &\Leftrightarrow X_k(P) = X_k(Q) \end{aligned} \quad (4a-c)$$

Moreover, we have a liberty of choosing the “arrow” indicating the order because the symbols $<, >$ on the right side of relations (4a,b) can be changed, according to our need, into $>, <$.

It is apparent that conditions (4a-c) provide basis for the construction of a primitive temperature scale. Indeed, unambiguous assignment of a certain value $X_k(P)$ to every state $P \in \mathbf{H}_k$ is nothing but realisation of a local *empirical temperature scale* in terms of thermoscopic variable X_k . It is, however, an important fact belonging rather to the scope of epistemology, that although the empirical scales enable one to characterize the thermal states

¹ We do not distinguish here the physical quantity and its corresponding numerical value. See also [6].

of bodies, for the revealing of the very nature of physical quantity called temperature are almost useless and further development of more involved concepts is thus necessary.

There is another requirement ensuring the objectivity of the above conception. It is so called *Principle of indifference* according to which different thermoscopes k, j operating in the common range of thermoscopic states should distinguish any two different states $P \neq Q$,

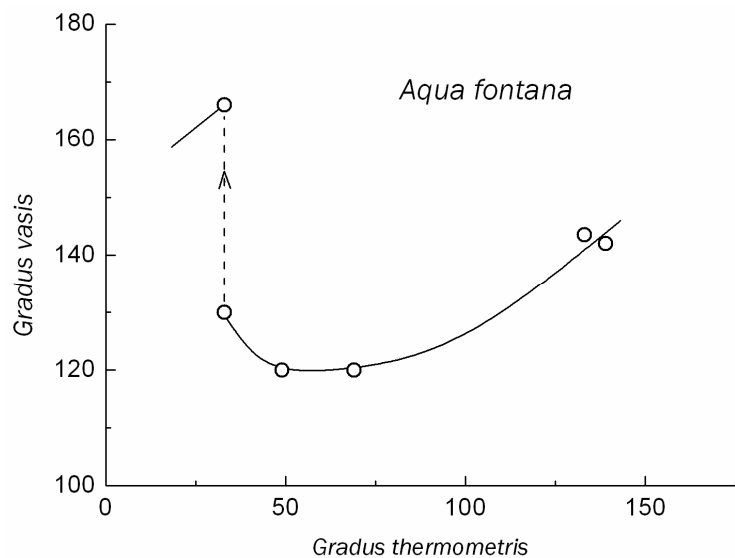


Fig. 2. Dulong-Petit plot of an alcohol-filled thermometer (*Gradus thermometris*) vs. readings on dilatometer (*Gradus vasis*) filled with fresh water showing the so called water anomaly. Data were obtained by *Accademia del Cimento* about 1660. [2,12]

monotonic. Interestingly, very similar method was used much earlier by savants of *Accademia del Cimento* who discovered in this way, just above the freezing point of water its anomaly (i.e. non-monotonic Dulong-Petit plot with respect to the other at that time known thermoscopes, see Fig. 2) [12], which excludes the water from being in this range a suitable thermometric substance.

2.6. The use of fixed points for calibration of thermoscopes

An appreciable irreproducibility of early thermoscopes was a serious obstacle for development of non-peripatetic thermal physics. There were attempts to improve the situation by making exact copies of a standard instrument and by sending them to the various laboratories where they were intended to serve as secondary standards [12]. This, theoretically correct approach had nevertheless lot of practical limitations. It required a really high reproducibility of glass-blowing and preparation of glass and thermometric substances. Consequently, standard “thermometers” were very expensive and the transport of such delicate instruments over the long distances was quite risky. Therefore an important qualitative step toward the scientific thermometry was done when the so called *fixed thermometric points* were discovered and became in general use. The fixed point is called a body prepared by a definite prescription revealing by some observable qualitative property its physical state (e.g. boiling point of helium, melting point of water, melting point of platinum – all at normal atmospheric pressure) and which being in thermal equilibrium with other bodies defines unambiguously their thermoscopic state. Fixed points thus may serve as a mean for realization of fiducial points on empirical temperature scales corresponding to the

$P, Q \in (\mathbf{H}_k \cap \mathbf{H}_j)$, regardless of their construction, thermometric substances, variables X and other physical conditions used. A procedure worked out by Dulong and Petit [11] is used in practical thermometry for the comparison of different empirical temperature scales. So called Dulong-Petit plot is a locus of readings X_k of one thermometer versus readings X_j of another thermometer both being in thermal contact with the same body (thermal bath). Evidently, in terms of such a plot the Principle of indifference may be formulated simply as follows: Two empirical temperature scales agree with the Principle of indifference just if their Dulong-Petit plot is

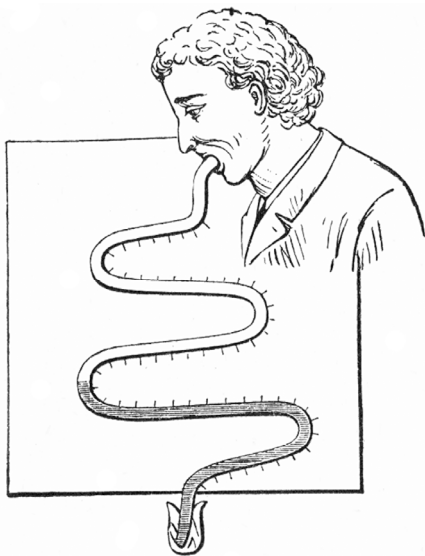


Fig 3. Thermoscope invented by Professor Santorius, serving for determination of “*temperatura*” of human body, about 1612. Instrument was made of glass and filled with wine. The bulb having diameter of golf ball was during the measurement inserted into patient’s mouth.

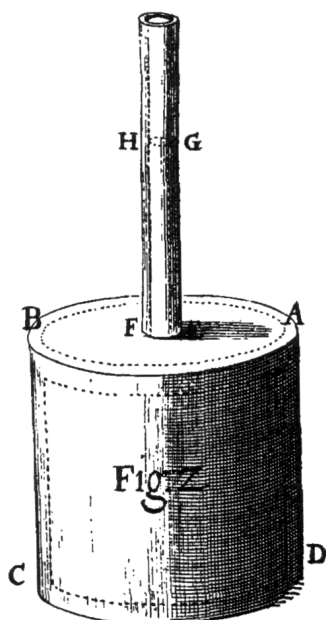


Fig. 4. Dilatometer designed by R. Hooke for realization of standard temperature scale based on single fixed point [13].

thermoscopes of different construction and different physical nature of thermoscopic variable. Probably the first who recognized the existence of a fixed point was Santorius, professor of medicine in Venetia (see Fig. 3). Studying by means of a simple thermoscope the “*temperatura*” of many patients he recognized that the reading of thermoscope was practically the same in all cases where the patient was healthy.

Very soon a lot of other fixed points, sometimes quite curious, were discovered and introduced into the practical thermometry. At this place it is interesting to mention that very likely the first savant who suggested the use the freezing and boiling points of water as fiducial points of temperature scale was Ch. Huygens. In his letter from January 2, 1665 addressed to the first president of Royal Society of London, R. Moray, he wrote: “*Je vous remercie du thermomètre...Il seriot bon de songer à une mesure universelle et déterminée du froid et du chaud,... et puis prenant pour commencement le degré de froid par le quel l’eau commence à geler, ou bien le degré de chaud de l’eau bouillante, a fin que sans envoyer de thermomètres l’on peut se communiquer les degrez du chaud et du froid, qu’on auriot trouvé dans les experiences, et les consigner a la posterité.*” From the last sentence of this quotation it is quite apparent that the aim of his suggestion was to substitute the unpractical sending of the thermometers for comparison of their scales by much more versatile calibration method.

Historically, there are essentially two methods used for the graduation (calibration) of thermoscopes by means of fixed points. These methods exploit either single or at least two fixed points. The first one is likely due to R. Hooke [13]. His specially designed dilatometer consisted of a cylindrical vessel with the cylindrical tube projecting out of its top (see Fig. 4). The tube had an inner diameter equal to one-tenth of the large vessel and was marked in intervals equal to one-tenth of its depth. One division („degree“) on the tube thus represented an expansion (contraction) of one-thousands above (below) the volume of the fluid at a chosen fixed point, e.g. freezing point of water, giving thus an objective (i.e. reproducible in different places and times) measure of thermal state. Belief in the universality of this method is

based on a tacit assumption that a dilatometer and thermometric substance used can reveal all in the nature accessible thermal states.

The first significant attempt at application of two-point calibration of thermometers belongs to members of *Accademia del Cimento* (1657-1667) [14]. They divided into three hundred degrees the interval between two marks indicating somewhat vague “fixed points”, namely, the greatest summer heat and the most severe winter cold. Two-point calibration

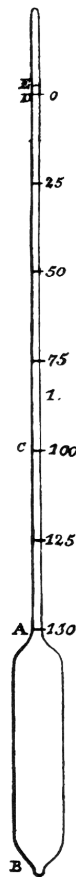


Fig. 5. An example of graduation of a thermometer by means of two-fixed point's method. Figure depicts a thermometer provided with the original “reverted” centigrade scale (Celsius, 1742). It is also shown the uncertainty of boiling point of water (=zero) which is due to fluctuations of barometric pressure [15].

technique but based on more reliable fixed points, melting point of ice and boiling point of water (incidentally the fiducial points which were proposed much earlier by Huygens!) were used also by C. Rinaldini (1693) for realization a his 12-degree thermometric scale. This well-done temperature scale was never in general use, however, a half century later, in hands of Celsius [15], became essentially the same scale the basis of our centigrade thermometric system. On the problem of graduation of thermometers worked independently Danish astronomer O. Rømer, and especially his immediate follower, German instrument maker G. D. Fahrenheit, who had used large deal of Rømer's know-how [16]. Accordingly, Fahrenheit accepted as a lower fixed point mixture of salt and ice (0°F) and normal body temperature (96°F) as the upper one. The freezing point of water (32°F) was retained as a subsidiary calibration point [17]. Enormous care was devoted to the purification of thermometric substance, mercury, improvements of glass-blowing procedure and exact specification of conditions for realization of fixed points. As a result, Fahrenheit's thermometers were much admired throughout the scientific community for their accuracy and extraordinary reproducibility and became thus for a long time a thermometric standard. In 1742 Swedish astronomer A. Celsius created a two-fixed point's temperature scale whereby zero represented the boiling point of water and one hundred represented the freezing point of water (see Fig. 5). In his lectures announced the observations showing that melting point of ice was effectively unaffected by pressure. He also determined with remarkable precision how boiling point of water varied as a function of atmospheric pressure and proposed that zero on his temperature scale (= boiling point of water) would be calibrated at the mean barometric pressure at mean sea level (standard atmosphere). As his scale was intended for meteorological observations where the temperatures are always below the temperature of boiling point of water, the scale was, in order to avoid the changes of the sign, reverted in comparison with the contemporary centigrade scale. Two years later, however, the famous Swedish botanist C. Linnaeus changed the Celsius's scale in order to be more convenient for the use in his greenhouse, constructing the thermometric scale where zero represented the melting point of ice and 100 represented boiling point of water. As the “centigrade” system was compatible with the philosophy of

metric centesimal system the Celsius's scale became later to the scale almost exclusively used on the Continent [15].

2.7. Mach's postulates

Importance of fixed points for thermometry is, however, not confined only to the calibration of thermoscopes but as was recognized not before the end of 19th century their theoretical significance is much more general. Quite interestingly, it has been originally taken for a self-evident empirical fact that it is always possible to find in an operation range of any thermoscope a sufficient number of fixed points enabling calibration of a local empirical scale, sewing it up with other overlapping empirical scales and to check, by means of the Dulong-Petit plots, the validity of Principle of indifference. The choice of fixed points for such purposes was quite pragmatic, respecting especially their easy realization, suitable distribution and stability (see e.g. Table 2). The very fact that such a liberty of choice can only be a consequence of the existence of enormous (if not infinite) number of fixed points falling into any interval of thermoscopic states remained for a long time quite unnoticed. Similar fate, i.e., being effectively undiscovered, has also the fact that the fixed points can be always found out of any interval of thermoscopic states.

Table 2. Selection of fixed points of the ITS-90

Substance	State	T ₉₀ /K
Cd	S	0.5190
Zn	S	0.8510
Al	S	1.1796
In	S	3.4145
Pb	S	7.1996
e-H	T	13.8033
Ne	T	24.5561
O ₂	T	54.3584
Ar	T	83.8058
Hg	T	234.3156
H ₂ O	T	273.1600
Ga	M	302.9146
In	F	429.7485
Sn	F	505.0780
Zn	F	692.6770
Al	F	933.4730
Ag	F	1234.9300
Au	F	1337.3300
Cu	F	1357.7700

S – superconductivity transition
T – triple point
M – melting point
F – freezing point
(both at a pressure of 101325 Pa)

These and other experimentally observed properties of fixed points have been generalized by means of method of incomplete induction, the reasoning according to which the conclusion related even to the infinite number of cases is drawn from the knowledge of a finite number of cases provided that they, without exception, imply the same conclusion. Such a type of generalization of experience resulting into certain verities or postulates is quite analogous to that made e.g. prior the axiomatic construction of Euclidean geometry.

First of all, as every fixed point defines unambiguously a certain thermoscopic state and because the set of thermoscopic states \mathbf{H}_k is ordered by means of relation (\prec, \succ) , it can be assumed that the *set of fixed points* ($\mathbf{F} = \cup \mathbf{F}_k$, where \mathbf{F}_k are related to \mathbf{H}_k) can be also ordered just according to this relation. Giving to such an idea a physical meaning, we can say that calibration of empirical scales by means of fixed points is nothing but an ordering of fixed points. We can thus postulate:

1) *The set of fixed points \mathbf{F} is ordered by means of relation (\prec, \succ) .*

The generalizations of experience with experimental establishment of new fixed points and of making their inventory list lead then to the following three postulates:

2) *To every fixed point $P \in \mathbf{F}$ exists at least one fixed point Q such that $Q \succ P$.*

3) *To every fixed point $R \in \mathbf{F}$ exists at least one fixed point S such that $S \prec R$.*

4) *For every couple of fixed points $P \prec R$ there exists at least one interlaying point Q such that the relations $P \prec Q$ and $Q \prec R$ are simultaneously valid.*

There is another remarkable empirical property of the set of thermoscopic states closely related to that of fixed points which can be generalized as follows (see Fig. 6).

5) *If a body changes its thermoscopic state from the state corresponding to a fixed point A to the point represented by a fixed point E , it must inevitably pass all the interlaying states*

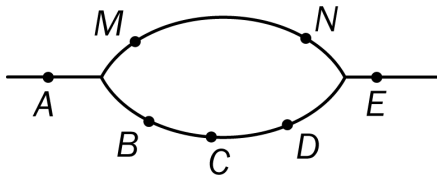


Fig.6. *Illustration to 5th Mach's postulate. If there is a thermal process connecting thermoscopic states A and E via states B, C, D , the alternative path $AMNE$ is then excluded [11].*

*corresponding to say fixed points B, C and D . The alternative path e.g. through the points M and N disjunctive with the path involving the points B, C and D is excluded. As these propositions received their first explicit formulation in the hands of E. Mach [11], we suggest calling them tacitly *Mach's postulates*. The formulation of these postulates enabled Mach to introduce intuitively the concept of *hotness manifold* (*Mannigfaltigkeit der Wärmestände*) which is the ultimate experimentally accessible concept representing the thermal states of bodies.*

2.8. Mathematical structure of hotness manifold

It is a matter of historical fact that formulation of Mach' postulates (1896) and establishment of Cantor's set theory (1895) were practically contemporaneous events. That is probably why the mathematical structure of hotness manifold has not been fully appreciated and, as far as we know, has never been systematically analyzed from the point of view of the set theory. In terms of this theory (e.g. [18]) Mach's postulates may be interpreted in the following way. Taking first into account the fact that the realizations of fixed points are real bodies, their number must be either finite or equivalent to the set of natural numbers, i.e. \mathbf{F} must be countable. In the 4th Mach's postulate one can easily recognize the definition of dense sets belonging to Cantor's theory; from this we can immediately conclude that \mathbf{F} is also dense.

Postulates 2 and 3 then mean that the set \mathbf{F} has no upper or lower bound. Any ordered countable dense set is, however, called rational series or set of rational numbers. We can thus summarize, the set of fixed points \mathbf{F} is equivalent to an unbounded set of rational numbers.

The mathematical structure of *hotness manifold* \mathbf{H} , which is a union of all sets of thermoscopic states \mathbf{H}_k , $\mathbf{H} = \cup \mathbf{H}_k$, is not as simple as the structure of \mathbf{F} . It is necessary first to make clear the operational method (i.e. a method related to the experimental procedures which can be really performed) enabling sewing-up the overlapping sets of thermal states and matching of corresponding empirical temperature scales. Let us assume that two sets of thermal states, \mathbf{H}_k , \mathbf{H}_{k+1} , overlap, i.e. that $\mathbf{H}_k \cap \mathbf{H}_{k+1} \neq \emptyset$. In order to realize this fact in experiment one has to find a fixed point $R \in \mathbf{F}$ belonging to both these sets, i.e. $R \in \mathbf{H}_k$, $R \in \mathbf{H}_{k+1}$. Theoretically the possibility of such an operation is ensured by 4th Mach's postulate. For the sake of definiteness and without loss of generality we can further construct the subsets $\mathbf{H}'_k \subset \mathbf{H}_k$, and $\mathbf{H}'_{k+1} \subset \mathbf{H}_{k+1}$ in such a way that $Q \prec R$ for every $Q \in \mathbf{H}'_k$ and $P \succ R$ for every $P \in \mathbf{H}'_{k+1}$. Evidently, the empirical temperature scale for thermal states from $\mathbf{H}_k \cup \mathbf{H}_{k+1} = \mathbf{H}'_k \cup \mathbf{H}'_{k+1}$ corresponds below R to empirical scale in \mathbf{H}_k and above R to that in \mathbf{H}_{k+1} . Moreover, in order to assign the same value of empirical temperature to the common point R , it is necessary to make formal changes at least in one of empirical scales. Applying the procedure just described and simultaneously looking for new fixed points and for new physical effects enabling the construction of new kinds of thermoscopes, we can build a chain of \mathbf{H}_k 's more and more extending the region of accessible thermal states. We are obliged to Professor Mach for belief that such a procedure is limited only by our skills². Taking now into account the fact that every \mathbf{H}_k is equivalent to a real interval $\mathbf{I}_k \subset \mathbf{E}_1$ it is obvious that \mathbf{H}_k is a continuous set. Furthermore, fixed points, e.g. such as R , are then nothing but rational cuts in sets \mathbf{H}_k and \mathbf{H}_{k+1} [Hu]. Analyzing these circumstances we can conclude that the properties of the hotness manifold $\mathbf{H} = \cup \mathbf{H}_k$ discussed above can be put in the form of two axioms already well-known from the set theory, namely

Dedekind's axiom: If \mathbf{H}_1 and \mathbf{H}_2 are any two non-empty parts of \mathbf{H} , such that every element of \mathbf{H} belongs either to \mathbf{H}_1 or to \mathbf{H}_2 and every element of \mathbf{H}_1 precedes every element of \mathbf{H}_2 , then there is at least one element $R \in \mathbf{H}$ such that:

- i) any element that precedes R belongs to \mathbf{H}_1 ,
- ii) any element that follows R belongs to \mathbf{H}_2 .

Axiom of linearity: The hotness manifold \mathbf{H} contains countable subset $\mathbf{F} \subset \mathbf{H}$ in such a way that between any two points $P \prec Q \in \mathbf{H}$ there is a point $R \in \mathbf{F}$ such as $P \prec R$ and $Q \succ R$.

As the second axiom ensures that the requirements of 5th Mach's postulate are automatically satisfied, the couple of Dedekind's axiom and axiom of linearity may be regarded as a concise reformulation of Mach's postulates. The simultaneous validity of both these axioms, however, defines in set theory the class of sets which are equivalent to the set of

² Speaking in terms of temperature, the temperatures observed range from $\sim 10^{-10}$ K (Low Temperature Lab, Helsinki University of Technology) up to $\sim 10^9$ K (supernova explosion) without any traces that the ultimate limits were actually reached. Speculative upper limit provides only the so called Planck temperature $T_p = \sqrt{(\hbar c/G)} \times (c^2/k) \approx 1.417 \times 10^{32}$ K, hypothetically corresponding to the first instant of Big Bang and depending on the assumption that the constants involved are really universal. Therefore the conjecture referred to as Mach's postulates 2 and 3, i.e. that the hotness manifold has no upper or lower bound, is obviously operating at least for all phenomena already known.

real numbers \mathbf{E}_1 . The mathematical structure of hotness manifold may thus be summarized as follows:

Hotness manifold (a set of all accessible thermoscopic states) \mathbf{H} is a set topologically equivalent to the set of all real numbers (real axis) \mathbf{E}_1 . It contains a countable, dense and unbounded subset of all fixed points $\mathbf{F} \subset \mathbf{H}$, realizing the skeleton of \mathbf{H} .

As we have seen above, the construction of this manifold is based on well-defined operational methods specifying conditions and procedures necessary for determination or reestablishment of a particular thermoscopic state. Manifold \mathbf{H} is just the experimentally accessible entity enabling one to judge how hot or cold the bodies are³. Therefore, it is this entity which is right to be regarded as an entity objectively existing in the Nature and representing the universal Platonic idea behind the usual concept of temperature, in philosophical jargon, the “temperature *an sich*”. Of course, as the set \mathbf{H} has no intrinsic *metric properties* it yields directly no physical quantity. Introduction of corresponding physical quantity, tacitly called temperature, thus requires special definitions which obviously have to take into account all the properties of hotness manifold.

2.9. Definition of temperature

As has been shown in previous paragraphs, the temperature and even the hotness manifold cannot be taken for primary concepts of thermal physics but are in fact the subjects of somewhat convoluted constructions. In the hierarchy of conceptual basis of thermal physics, however, the concept of temperature plays the role subordinate to that of hotness manifold \mathbf{H} , which is characterized just only by its topological properties. On the other hand it is quite clear that hotness manifold alone is not sufficient for the development of quantitative theory of thermal effects. For such a purpose, namely, a regular physical quantity [6] is necessary. The introduction of such a quantity called temperature into the thermal physics, which would simultaneously preserve all essentials of hotness manifold, may be based on the following definition:

Temperature is any continuous one-to-one order-preserving mapping of hotness manifold on a simply connected open subset of real numbers.

From this definition it is evident that we are at enormous liberty of choosing a particular temperature scale which thus rests entirely upon a convention. It is further quite clear that the rationality or irrationality of the choice of the temperature scale (i.e. of the said continuous one-to-one order-preserving mapping) will be decisive for further performance and intelligibility of theory of thermal effects. Obviously, in order to be able to continue with the development of the theory we have to make a decision concerning the temperature scale being simultaneously aware that such a decision has a character of provisional working hypothesis which may have in the future unexpected consequences. Traditionally the safest guide for introduction of new concepts into the science is the so called *anthropomorphic principle*. This principle taking into regard previous experience, commonly accepted patterns of thinking, human feeling of reality and other practical or cultural aspects usually generates

³ Interestingly enough, admitting the scheme above we are in fact transferring the mathematical structure of continuous quantities X_k introduced in other branches of physics into the thermal physics; e.g. without such a step the hotness manifold would not be continuous. Shortly in Hilbert's terminology, just through this gate enter thermal quantities to Cantor's Paradise governed by actual infinity and continuum [19].

intelligible, almost self-evident theories, which can be further developed and easily applied. On the other hand, a theory not respecting the anthropomorphic principle is, as a rule, very abstract, incomprehensible, and full of antinomies and with vague relation to reality. Its further development requires enormous effort and makes it thus an esoteric doctrine accessible only for limited audience.

As an example of successful application of anthropomorphic principle in thermal physics, may serve just the choice of universal thermometric scale. On the more-or-less historical and practical grounds, in other words, on the basis of arbitrary anthropomorphic criteria, a special mapping of the hotness manifold on the set of positive real numbers known as the International Kelvin Temperature Scale (T) was established. There are two alternative ways how to approach this scale, both based on a certain idealization procedure. The first one uses an idealization of a real substance (*perfect gas*), while the second one results from the idealization of a real physical process (*Carnot's reversible cycle*).

2.10. Ideal (perfect) gas temperature scale

The first approach mentioned above is based on the idealization of the most salient common features of constitutive relations of real gases. The behavior of majority of real gases is, namely, almost the same in cases where the gases have sufficiently low density. This fact was used for the definition of the perfect gas and later for the construction of the *ideal (perfect) gas temperature scale* T. The equation controlling the behavior of the ideal gas, which is a hypothetical substance or concept rather than a real thing, reads:

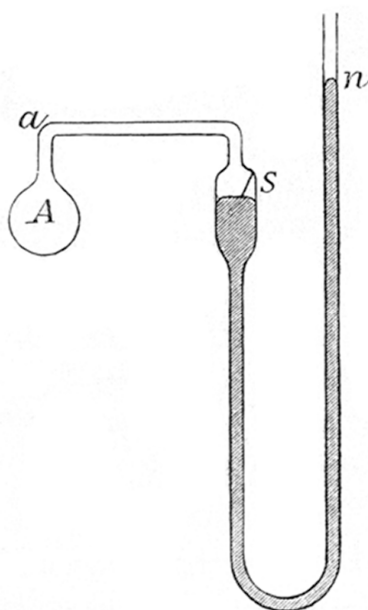


Fig. 7. A schematic view of a simple constant volume gas thermometer which simultaneously represents an operational device for realization of ideal gas temperature scale [21].

$$T = pV / nR, \quad (5)$$

where p and V are respectively the pressure and the volume of the ideal gas which may both alternatively play the role of thermoscopic variables. As the hypothetical thermoscope a conventional gas thermometer [21] filled with n moles, $n > 0$, of ideal gas is considered (see Fig. 7). The constant R on the right side of equation (5), has then a form of product $R = k N$ where k and N are Boltzmann's and Avogadro's constants, respectively (in SI system of units $k = 1.38 \times 10^{-23}$ J/K, $N = 6.02 \times 10^{23}$ mol⁻¹). Formula (5) defining the temperature T by means of constitutive properties of non-existing substance, perfect gas, reveals remarkable symmetry with respect to quantities p and V . We can thus exploit anyone of

these two quantities as a thermoscopic variable keeping the other constant. Comparing these two cases it must be inevitably:

$$T_p = T_v = T \quad (6)$$

where T_p and T_v are temperatures of a body (e.g. corresponding to temperature of a certain fixed point) determined by means of constant pressure and constant volume method,

respectively. The exact realization of condition (6) in experiments with real gases and with prescribed high accuracy (typically of order of 0.1%) is very difficult if not impossible. However, Berthelot [22] devised a simple mathematical method based on plausible assumptions which enables to extrapolate experimental data obtained on real gases at finite pressures to the case corresponding to the ideal gas and finally determine also the value of T satisfying conditions (6). From these facts it is thus apparent that the ideal gas temperature scale can be experimentally realized in the range where the gaseous phase of real gases exists.

2.11. Absolute temperature

The ideal gas temperature scale T defined by means of equation (5) has some other remarkable properties. For example, as both quantities p and V have a natural lower bound equal to zero, the temperature T has also this lower bound. In this connection it is interesting to mention considerations of French savant G. Amontons (1703) [23,24] who made extensive experiments with constant volume gas thermometer filled with dry air. By means of extrapolation of a regular “centigrade” temperature scale, constructed between boiling and freezing points of water, down to the zero pressure he obtained a value of -240°C (contemporary measurements would provide the value near -273°C). As for him it was absolutely inconceivable that the temperature of any body in the Universe could decrease below the point in which the activity of such a “vivacious” substance as the air disappears, he started to call this hypothetical temperature *l’extrêm froid*. Interestingly, quite independently but on the basis of similar experiments, introduced *absolute zero of temperature* (*zéro absolu de la chaleur*) also Clément and Désormes [25]. Nevertheless, not diminishing huge merits of these distinguished men of science, their considerations were not correct in principle. Indeed, as was already mentioned, every thermoscope enables to order the thermoscopic states only locally, within a certain well-defined range. The extrapolations out of this range are not permissible. Moreover, technical collapse of a particular type of thermoscope (e.g. due to the freezing of air in its bulb) cannot serve as a proof for non-existence of other types of thermoscopes possibly working at lower temperatures. On the other hand the definition of temperature gives us a sufficient freedom to introduce the scale with absolute zero not on the basis of some recognized “Law of Nature” but simply on the basis of our decision. Such a scale, namely, may have besides compatibility with equation (5) some advantages, e.g. numerous problems with sign can be avoided, the evaluation of integrals depending on temperature is simplified etc. The definition of absolute temperature⁴ scale then reads [20]:

Any temperature scale which is chosen in such a way that their functional values have highest lower bound equal to zero (i.e. T is always positive), is called absolute temperature scale and the corresponding temperatures are called absolute temperatures.

Notice that the possible value $T = 0$ (equal to highest lower bound) is already excluded by our definition of temperature, because due to the absence of the lowest hotness level in the hotness manifold any continuous one-to-one order-preserving transformation on the set with lower bound = 0, has inevitably to map its improper point (i.e. $-\infty$) just on the point corresponding to absolute zero. *Nernst’s law* of unattainability of absolute zero of temperature (“Third Law of Thermodynamics”) [26] is thus together with its consequences intrinsically

⁴ Notice that this definition of absolute temperature scale differs from that due to Lord Kelvin who related the adjective “absolute” rather to the independence of temperature scale of thermometric substance than to the existence of lower bound of temperature values.

involved in this definition of temperature and, consequently, needs no additional, sometimes very curious, justifications or “proofs” [27].

2.12. Carnot’s theorem

Reasonably chosen temperature function which maps the hotness manifold on a subset of real numbers should be, as was already mentioned in paragraph 2.2., conformal with other terms entering the energy balance equation. In such a case will temperature (intensive quantity, T) and heat (extensive quantity, ζ) make up a couple of conjugate variables obeying dimensional equation (1) i.e.

$$[\text{Energy}] = [T] \times [\zeta].$$

The principal possibility to write down the thermal energy term just in this form was confirmed by early experiments on the development of mechanical work by means of heat engines. In spite of the fact that these experiments were backed by a rather primitive technique (e.g. temperatures were measured by roughly calibrated mercury thermometers and heat by the weight of burned coal) being thus of doubtful accuracy, their analysis enabled S. Carnot to introduce some new theoretical concepts and draw out definite conclusions. In the present context play among new Carnot’s concepts the most important roles two idealizations of real thermal process taking place in the heat engine, namely, the *cyclic process* and *reversible process*. By cyclic process (*cycle*) is meant any thermal process in which initial and final physical state of the heat engine are the same. The reversible process is then a thermal process in which heat engine works without wastes of heat. For heat engines utilizing the cyclic reversible process (so called *ideal heat engines*) was Carnot able to formulate a theorem which in its archaic version reads⁵ [28]

“The motive power of heat is independent of the agents set at work to realize it; its quantity is fixed solely by the temperatures of the bodies between which, in the final result, the transfer of caloric is done.” (S. Carnot, 1824)

Of course, from the modern point of view is Carnot’s theorem rather a desideratum than piece of scientific knowledge. (Remarkable is also a somewhat inconsistent use of heat and caloric as synonyms!) On the other hand, it has a form of the energy balance postulate we are searching for. Indeed, if we, namely, transform the theorem into mathematical symbols we can write it in terms of finite differences [29]

$$\Delta L = \zeta F'(t) \Delta t, \quad (8)$$

where ζ means the quantity of heat regardless of the method of its measurement, ΔL is the motive power (i.e. useful work done by heat engine) and Δt is the difference between empirical temperatures of heater and cooler. The unknown dimensionless function $F'(t)$ called *Carnot’s function* should be for concrete empirical scale determined by experiment. As the

⁵ It should be stressed here that there can be found in the literature a lot of various arbitrarily changed forms of “Carnot’s theorem” or “principle” which are not equivalent one to each other and which essentially differs in their very content from the original formulation. As was thus quite correctly pointed out by distinguished researcher into the vapour turbines and president of Royal Society, H. L. Callendar [29], the original oldest Carnot’s formulation of his principle is at the same time the best one.

gained work ΔL has a dimension of energy and as this energy must be for reversible cycle equal per definition to the thermal energy of heat ζ supplied to the ideal heat engine, we can conclude that the terms suitable for insertion into the energy balance equation have to have a form of products $\zeta \Delta t$ properly modified by Carnot's function.

2.13. Kelvin's proposition

A revolutionary step toward the definition of temperature scale independent of particular type of thermometer and thermometric substance was made at 1848 by Lord Kelvin [30]. He proposed to treat Carnot's theorem not as a heuristic statement deduced from experiments of rather a limited accuracy but as a fundamental postulate of absolute validity. He further pointed out that the very purpose of Carnot's function is to modify or correct the difference of temperatures measured in a particular empirical temperature scale in such a way that it could serve as a exact proportionality factor between work, ΔL , and heat, ζ . As this factor has to be according to Carnot's postulate the same for all substances, Kelvin, inverting the logics of reasoning, suggested to define a universal (in his terminology "absolute", see footnote ⁴) temperature scale just by *prescribing* a proper analytical form of Carnot's function. For example, giving to Carnot's function the simplest permissible analytical form, namely, $F'(*T) = 1$ (so called caloric gauge⁶) we are in fact defining a new temperature scale $*T$ in terms of which equation (7) reads:

$$\Delta L = \zeta (*T_2 - *T_1). \quad (9)$$

It is immediately seen that using such a definition of temperature scale the energy terms have the desired form of a product of two conjugate variables ζ and $*T$. Interestingly enough, equation (10) is simultaneously a fundamental relation of caloric theory of heat (cf. [31]). Accordingly, the heat is from phenomenological point of view a kind of substance or fluid, caloric (*calorique*, *Wärmestoff*, *теплородъ*, *teplík*), which being dissolved in all bodies is responsible for their thermal state. It is treated as an indestructible fluid (recall that the only method how to get rid of heat is to convey it away), which is created in every irreversible processes such as rubbing, chemical reactions, burning, absorption of radiation and eating during which "something" simultaneously disappears for ever. The properties of so defined quantity are thus very near to the concept of heat in a common sense [32,33]. Taking further into account the structure of equation (9) we can also conclude that the development of moving force in an ideal heat engine is not connected with some actual consumption of heat as is claimed in thermodynamics but rather with its transfer from hotter body to a colder one (water-mill analogy [28]). At the same time equation (9) defines an entropy-like unit of heat fully compatible with the SI system which may be, according to *Callendar's* suggestion, appropriately called "Carnot" (Abbreviation "Ct") [29]. 1 Ct is then that quantity of heat which is in a reversible process capable of producing 1 J of work per 1 K temperature fall.

In the present context is, nevertheless, far more important another aspect of equation (9). Accordingly, namely, the temperature difference $*T_2 - *T_1$ between two bodies used e.g. as "heater" and "cooler" of an ideal heat engine, is identical with the ratio $\Delta L/\zeta$ where both of

⁶ Due to the later general acceptance of Joule-Mayer's postulate claiming the equivalence of work and heat it was no more possible to choose freely Carnot's function which had inevitably the form J/T (thermodynamics' gauge), where J is so called mechanical equivalent of heat [31]. Fortunately, this fact does not influence our further considerations but rather gives an opportunity to the exercise in elementary algebra interpreted in textbooks as a "proof" of mechanical origin of the Kelvin temperature scale.

these quantities are measurable in principle; ΔL by means of standard methods well-known from mechanics and ζ e.g. by amount of fuel consumed by heating the heater or, if the cooler is kept at 0 °C, by amount of ice melted during the cycle. It is quite obvious that such a technique of temperature measurement, although possible in principle, is rather a curiosity which would be very difficult to realize with sufficiently high accuracy in practice. The idea of this method is, however, of primary importance for theory. Obviously, due to Carnot's postulate equation (9) has to be valid for any ideal heat engine regardless of its construction and working substance used. Analyzing thus one representative case of ideal heat engine general conclusions can be made. For example, if we imagine an ideal heat engine driven by perfect gas and working in cycles which consist of two isothermal and two isochoric reversible processes, the useful work can be easily computed, provided that the temperatures are measured in terms of perfect gas scale. The result of such a computation reads

$$\Delta L = nR \ln(V_2/V_1) (T_2 - T_1), \quad (10)$$

where V_1 and V_2 are limits of volume between which the engine operates. It is apparent at first glance that this last equation is fully congruent with equation (9) with the proviso that the heat (measured in entropy units, e.g. Ct) transferred from heater to cooler per cycle is given by $\zeta = nR \ln(V_2/V_1)$. The congruence of these equations means that the system of units can be always chosen in such a way that scales $*T$ and T will be identical [6]. Expressing this fact more physically we can say:

Measurement of temperatures by means of ideal gas thermometer is equivalent to the measurement of temperatures by means of ideal heat engine.

The theoretical significance of this theorem is enormous because it enables one to relate without ambiguity the ideal gas (Kelvin) temperature scale to the temperatures defined by other types of ideal heat engines e.g. “*gedanken*” reversible cycles in systems controlled by electric, magnetic or electrochemical forces. Besides, it should be stressed that this theorem, although it is based on arbitrary assumptions, is by no means accidental. The idealization of constitutive relation of real gases and idealisation involved in Carnot's postulate have the same anthropomorphic roots, namely, the feeling that the thermal dilatation of bodies must be linearly dependent on their thermal state. Incidentally, in the range between 0°C and 100°C are the air scale and the mercury temperature scale, prevailingly used in experiments related to establishment of Carnot's theorem, almost identical.

2.14. Scholion

The concept of fundamental quantity of thermal physics, *temperature*, is defined as an arbitrary one-to-one order preserving continuous mapping of so-called *hotness manifold* on a certain simple connected open subset of real numbers. The hotness manifold \mathbf{H} representing all in the Nature existing thermoscopic (thermal) states is the only entity accessible to direct physical observation. The set \mathbf{H} , which was proved to be topologically equivalent to the set of all real numbers (real axis), contains a countable, dense and unbounded subset of all *fixed points* $\mathbf{F} \subset \mathbf{H}$. Any fixed point is realized by means of a specially prepared body which defines just one thermal state. The properties of set \mathbf{F} and its relation to the manifold \mathbf{H} are specified by means of Mach's postulates. As has been finally shown, the special mapping of \mathbf{H} on the set of all positive real numbers known as the *International Kelvin Temperature Scale* T was chosen on the grounds of two anthropomorphic idealizations providing a concordant result, namely, ideal substance, *perfect gas* and ideal process in heat engine, *reversible cycle*.

Acknowledgement

The present work was supported by Institutional Research Plan of Institute of Physics ASCR v.v.i. No AV0Z10100521.

References

- [1] Giua M.: *Storia della chimica*. Union Tipografico, Torino (1962), Russian transl. Dzhuha M.: *Istoriya Khimii*. Izdatel'stvo Mir, Moscow (1975)
- [2] Meyer-Bjerrum K.: *Die Entwicklung des Temperaturbegriffs im Laufe der Zeiten*. Vieweg und Sohn, Braunschweig (1913)
- [3] Burckhardt F.: *Die Erfindung des Thermometers und seine Gestaltung im XVII Jahrhundert*. Basel (1867)
- [4] Black J.: *Lectures on the Elements of Chemistry*. W. Creech, Edinburgh (1803), Germ. transl.: *Vorlesungen über Chemie*. Crell, Hamburg (1804)
- [5] Fürth R.: *Algemeine Grundlagen der Physik, Prinzipien der Statistik*. In: *Handbuch der Physik Bd. IV*. Springer, Berlin (1929)
- [6] Palacios J.: *Dimensional Analysis*. Macmillan & Co. Ltd., London (1964)
- [7] Balamuth L., Wolfe H. C., Zemansky M. W.: *The Temperature Concept from the Macroscopic Point of View*. Am. J. Phys. **9**, 199 (1941)
- [8] Boas M.: *Hero's Pneumatica, A Study of its Transmission and Influence*. Isis **40**, 38 (1949)
- [9] Hoppe E.: *Geschichte der Physik*. F. Vieweg und Sohn, a.G., Braunschweig (1926)
- [10] Fludd R.: *Mosaical Philosophy*. H. Moseley, London (1659)
- [11] Mach E.: *Die Principien der Wärmelehre*. Verlag von J. A. Barth, Leipzig (1896)
- [12] *Saggi di naturali sperienze fatte nel'Accademia del Cimento*, Firenze (1667)
- [13] R. Hooke R.: *Micrographia*. Roy. Soc. of London, Brouncker imprimatur, London (1665), Reprint: Dover Publications, Inc., Mineola (2003)
- [14] Boyer C. B.: *Early Principles in the Calibration of Thermometers*. Am. J. Phys. **10**, 176 (1942)
- [15] A. J. von Oettingen A. J.: *Abhandlungen über Thermometrie von Fahrenheit, Réaumur, Celsius*. Ostwald's Klassiker No.57, W. Engelmann, Leipzig (1894)
- [16] Barnett M. K.: *The Development of Thermometry and the Temperature Concept*. Osiris **12**, 269 (1956)
- [17] Fahrenheit D. G.: *Experiments and observations on the Freezing of Water in Vacuo*. Phil. Trans. Abridged **33**, 22 (1724)
- [18] Huntington E. V.: *The Continuum and Other Types of Serial Order*. Harvard University Press, New York (1917), Reprint: Dover Phoenix Editions, New York (2003)
- [19] Hilbert D.: *Über das Unendliche*. Math. Ann. **95**, 161 (1926)
- [20] Truesdell C., Bharatha S.: *Concepts and Logic of Classical Thermodynamics as a Theory of Heat Engines*. Springer, New York (1977)
- [21] Nieto A., Paul F.: *Mesure des Températures*. Éditions Radio, Paris (1958)
- [22] Wensel H. T.: *Temperature and Temperature Scales*. J. Appl. Phys. **11**, 373 (1940)
- [23] Brush S. G.: *The Kind of Motion We Call Heat*. North-Holland, Amsterdam (1976)
- [24] Amontons G.: *Le Thermomètre*. Mémoires de l'Académie Royale des Sciences **6**, 64 (1703)

- [25] Clément C. B., Désormes N.: *Détermination expérimentale du zéro absolu de la chaleur et du calorique spécifique des gaz*. Journal de physique **89**, 321,428 (1819)
- [26] Nernst W.: *The New Heat Theorem*. (1926) Reprint: Dover Publications, Inc., New York (1969)
- [27] Boas M. L.: *A Point of Logic*. Am. J. Phys. **28**, 675 (1960)
- [28] Carnot S.: *Réflexions sur la puissance motrice du feu et sur les machines propres à développer cette puissance*. Bachelier, Paris (1824), Germ. transl.: Ostwald's Klassiker, Nr. **37**, Egelmann, Leipzig (1909)
- [29] Callendar H. L.: *The Caloric Theory of Heat and Carnot's Principle*. Proc. Phys. Soc. London **23**, 153 (1911)
- [30] Thomson W. (Lord Kelvin of Largs): *On the Absolute Thermometric Scale founded on Carnot's Theory of the Motive Power of Heat*. Phil. Mag. **33**, 313 (1848)
- [31] Mareš J. J., Hubík P., Šesták J., Špička V., Křištofik J., Stávek J.: *Phenomenological approach to the caloric theory of heat*. Thermochemica Acta **474**, 16 (2008)
- [32] Job G.: *Neudarstellung der Wärmelehre – Die Entropie als Wärme*. Akad. Verlagsges., Frankfurt am Main (1972)
- [33] Falk G., Herrmann F., Schmid G. B.: *Energy Forms or Energy Carriers?* Am. J. Phys. **51**, 1074 (1983)

Caucasus, (Užbinské plateau - 4100 m), Russia



Chapter 3

Abstract thermodynamics

3. FROM CARNOT TO NONEQUILIBRIUM AND ABSTRACT THERMODYNAMICS AND SOME CONSEQUENCES FOR THERMAL ANALYSIS

Miroslav Holeček

3. 1. A lucky discovery of the second law of thermodynamics

As well known, the fundamental work of Sadi Carnot, *Réflexions sur la puissance motrice du feu* [1], initiated the birth of an essentially new physical discipline – the thermodynamics. Though Carnot's insight was fundamental his contribution to principles of physics is very often misunderstood and incorrectly interpreted. The crucial discovery of Sadi Carnot does not concern an explanation of the way in which heat is transformed onto work. His ideas concerning heat are even false – he supposes that heat goes through the working medium unchanged during the cycle. To be concrete, Carnot supposes that the medium borrows heat from a body A – the furnace – and the same quantity of heat is transmitted into a body B – the refrigerator. Precisely speaking, Carnot uses the term 'caloric' (*calorique*) instead of heat in this statement. Nevertheless, the word 'heat' (*chaleur*) is also used, for example the crucial consideration about exchange of caloric between body A and B begins as follows [1] (p. 10).

If we wish to produce motive power by carrying a certain quantity of heat from the body A to the body B we shall proceed as follows: (1) To borrow caloric from the body A to make steam with it-that is, to make this body fulfill the function of a furnace, or rather of the metal composing the boiler in ordinary engines-we here assume that the steam is produced at the same temperature as the body A.

The use of two different terms might tempt us into the interpretation that 'caloric' could be something akin to the entropy in the current terminology (see e.g. [2], p. 32) – then Carnot's considerations would be true. Nevertheless, the only passage when Carnot explicitly speaks about this question is the note at page 20 where the word 'heat' is used:

We tacitly assume in our demonstration, that when a body has experienced any changes, and when after a certain number of transformations it returns to precisely its original state, that is, to that state considered in respect to density, to temperature, to mode of aggregation-let us suppose, I say, that this body is found to contain the same quantity of heat that it contained at first, or else that the quantities of heat absorbed or set free in these different transformations are exactly compensated. This fact has never been called in question. It was first admitted without reflection, and verified afterwards in many cases by experiments with the calorimeter. To deny it would be to overthrow the whole theory of heat to which it serves as a basis. For the rest, we may say in passing, the main principles on which the theory of heat rests require the most careful examination. Many experimental facts appear almost inexplicable in the present state of this theory.

Many authors assert, however, that Carnot never uses this assumption for proving any of his conclusions. In our opinion, however, the idea of heat transferring without a change of its quantity through the system played the crucial role in the discovery of the second law of thermodynamics. It was mistaken, nevertheless, this mistake was lucky because it allowed Carnot to discover the second law as a very convincing statement.

How did Carnot discover this fundamental law? The crucial point of his considerations is the possibility of performing a special process in which heat performs an amount of work in an *inverse direction*. During this reverse action the *same amount of work*, W , has to be supplied and the same amount of heat is taken from the refrigerator and the same amount of heat is returned to the furnace. Carnot assumed (tacitly) that the heat (caloric) taken from the refrigerator is the same as that returned to the furnace. (We know that it would disturb the first law of thermodynamics and hence these heats have to be different. Nevertheless, no point in Carnot's thinking is false due to this assumption because it is never explicitly used.) Carnot's ingenious (and indeed revolutionary) idea consists in imagining a cycle realized partially by a more sophisticated arrangement of the engine that is more *efficient* than the reversible one. Such an engine would perform *more* work in the forward running, say $W' > W$, by withdrawing the same amount of heat from the furnace. The reverse operation of the reversible engine, however, could be performed by using only a part of the work W' , namely W , and a positive amount of work, $W' - W$, would be obtained. Carnot argues that it is inadmissible because we could restore the initial conditions and repeat this cycle again and again to gain more and more work [1] (p. 12):

Now if there existed any means of using heat preferable to those which we have employed, that is, if it were possible by any method whatever to make the caloric produce a quantity of motive power greater than we have made it produce by our first series of operations, it would suffice to divert a portion of this power in order by the method just indicated to make the caloric of the body B return to the body A from the refrigerator to the furnace, to restore the initial conditions, and thus to be ready to commence again an operation precisely similar to the former, and so on: this would be not only perpetual motion, but an unlimited creation of motive power without consumption either of caloric or of any other agent whatever. Such a creation is entirely contrary to ideas now accepted, to the laws of mechanics and of sound physics. It is inadmissible.

Carnot is entirely right, it is inadmissible. This inadmissibility expresses nothing but the second law of thermodynamics. Nevertheless, its reasoning is supported by the fact that it is "an unlimited creation of motive power without *consumption either of caloric or of any agent whatever*". But it is not true. The more efficient run of the engine would transmit *less* heat to the refrigerator than the heat *taken* from the refrigerator during the reverse run. Hence the whole fictitious cycle would only *consume* heat from refrigerator. The inadmissibility of *that* is the core of the second law. Nevertheless, it is *not* an obvious statement. If Carnot were aware of the fact that the heat transmitted to the refrigerator is less than that obtained from the furnace he could hardly conclude so convincingly that the fictitious cycle is inadmissible.

These considerations led Carnot to the quite fundamental conclusion. Namely, if there is no possibility of constructing a more efficient engine than the reversible one, reversible transformations present limit cases maximizing a possible gain of work from heat. Moreover, Carnot introduced his famous cycle and by using it he supported his important concluding result [1] (p. 20):

The motive power of heat is independent of the agents employed to realize it; its quantity is fixed solely by the temperatures of the bodies between which is effected, finally, the transfer of the caloric.

It is clear that by "motive power of heat" Carnot thinks the mechanical work that can be gained from an amount of heat, i.e., its maximal value. This statement became the entirely new principle in physics. It is called the Carnot's theorem. Its modern formulation may be as follows (see [2], p. 33):

The efficiency of reversible Carnot cycles is independent of the modes of operation and the material used, and is maximum. It depends only on the temperatures of the heat reservoirs.

This theorem is equivalent to the second law of thermodynamics [2] (p. 36).

3. 2. Clausius' fundamental contribution: the birth of entropy

A Carnot's work from 1824 was beyond recall for ten years until Clapeyron published its clearer version in 1834. It was a starting point of further investigations in thermodynamics concerning the second law. Probably the most important was the work by Rudolf Clausius. His contributions were published in a series of papers started at 1850 (the collection of these fundamental papers is published in the book [3]). At that times, the equivalence of work and heat and their mutual transformability started to be well understood and experimentally confirmed (the most important contributions came from Julius Robert von Mayer, James Prescott Joule and Hermann von Helmholtz [4,5]). Clausius formulated this transformability by the following maxim [3] (p. 18)

In all cases where work is produced by heat, a quantity of heat proportional to the work done is consumed; and inversely, by the expenditure of a like quantity of work, the same amount of heat may be produced.

This statement is an evident contradiction with the Carnot's reasons justifying the inadmissibility of a more efficient engine than the reversible one. Namely, when an amount of heat is consumed during the run of the machine (since the work is done) it cannot be transmitted to the refrigerator without any loss. The main protagonists of the story thus found themselves in a delicate situation. The question was whether Carnot's conclusions should have been refused. The dilemma was resolved by attaching to Carnot's conclusions. Clausius wrote [3] (p. 17):

It is not even requisite to cast the theory of Carnot overboard; a thing difficult to be resolved upon, inasmuch as experience to a certain extent has shown a surprising coincidence therewith. On a nearer view of the case, we find that the new theory is opposed, not to the real fundamental principle of Carnot, but to the addition "no heat is lost", for it is quite possible that in the production of work both may take place at the same time; a certain portion of heat may be consumed, and a further portion transmitted from a warm body to a cold one; and both portions may stand in a certain definite relation to the quantity of work produced. This will be made plainer as we proceed; and it will be moreover shown, that the inference to be drawn from both assumptions may not only exist together, but that they mutually support each other.

He noticed that the Carnot's principle [3] (p. 116) "...expresses a relation between two kinds of transformations, the transformation of heat into work, and the passage of heat from a warmer to colder body, which may be regarded as the transformation of heat at a higher, into heat at a lower temperature." To emphasize that he reformulated it as follows:

In all cases where a quantity of heat is converted into work, and where the body effecting this transformation ultimately returns to its original condition, another quantity of heat must necessarily be transferred from a warmer to a colder body; and the magnitude of the last quantity of heat, in relation to the first, depends only upon the temperatures of the bodies between which heat passes, and not upon the nature of the body effecting the transformation.

Since both transformations are linked together, Clausius realized that the Carnot's principle might be modified by the principle concerning the passage of heat itself. He formulated the principle [3] (p. 117)

Heat can never pass from colder to a warmer body without some other change, connected therewith, occurring at the same time.

This principle seemed to him more obvious since (p. 118) “...*heat everywhere manifests a tendency to equalize existing differences of temperature, and therefore to pass in a contrary direction, i.e. from warmer to colder bodies.*” Nevertheless, he was well aware of an impossibility of simplifying this principle to the fact that “heat cannot pass from a colder to a warmer body” because it would be false. We may imagine many various arrangements in which heat passes from colder to warmer bodies. But each of them is connected with another change of something else. Heat cannot pass from colder to hotter body *by itself*. By this completion, however, the modified Carnot’s principle is not so obvious. Both the Carnot’s principle and its modified version are the formulations of the second law of thermodynamics. We stress again that it is *not* an obvious statement, regardless which formulation is chosen.

Thus Clausius elucidated the essence of the Carnot’s theorem – the inadmissibility of a more efficient device (obtaining a more amount of work from a given quantity of heat) has nothing in common with the impossibility of “*an unlimited creation of motive power without consumption either of caloric or of any other agent whatever*“ [1] (p. 12). Rather, it is connected with an impossibility of obtaining work only by transforming it from heat (without other changes connected therewith). This transformation *must* be accompanied by another transformation, namely that in which an amount of heat passes from a hotter body to a colder one. The exclusiveness of reversible processes consists in the fact that when realizing a reversible change these transformations are mutually *compensated*. Clausius concludes that “...*these transformations may be regarded as phenomena of the same nature*” and finds “...*the law according to which the transformations must be expressed as mathematical magnitudes, in order that the equivalence of two transformations may be evident from the equality of their values.*” [3] (p. 122). He calls the searched “*value of a transformation*” its *equivalence-value*. This “*equivalence-value*” is an ancestor of the concept of entropy.

The passage in which Clausius searches for these mathematical magnitudes [3] (pp. 123-127) looks rather strange. He postulates that “...*the equivalence-value of the transformation of work into the quantity of heat Q , of the temperature t , may be represented generally by*

$$Q \cdot f(t),$$

wherein $f(t)$ is a function of temperature, which is the same for all cases.” Similarly, the value of the passage of the quantity of heat Q , from the temperature t_1 to the temperature t_2 may be expressed by

$$Q \cdot F(t_1, t_2).$$

However, there is no physical explanation of these formulas. The quantity $Q \cdot f(t)$, for example, does not mean something assigned to work - it is only related to the transformation of work into heat. Clausius calls the transformation to be *positive* if it is either the change of work into heat or the passage of heat from warmer to colder bodies. That is, positive transformations occur naturally (spontaneously) in Nature – heat is produced by friction as well as it passes from warmer to colder bodies.

Though Clausius speaks only about *reversible* transformations he lately applies the results also to *irreversible* ones. We comment this important point in next paragraph. For now, however, it is an indication that the equivalence value is not related only to reversible changes (it concerns for instance a spontaneous heat conduction between two bodies of

different temperatures). The only property assigned to the transformations is the symmetry of the heat exchange expressed by the formula

$$F(t_1, t_2) = -F(t_2, t_1).$$

The main point of the Clausius consideration is following: he assumes that the sum of equivalence-values of all transformations during a *reversible cyclic* process is *zero*. Since the equivalence-value is a universal function it may be applied to various cycles and their combinations. By doing that it may be easily revealed that

$$F(t_1, t_2) = f(t_1) - f(t_2).$$

Then the universal function of temperature, $f(t)$, may be denoted as $1/T$ and we obtain the most important result of the whole thermodynamics, namely that *the generation of quantity of heat Q of the temperature t from work, has the equivalence-value*

$$\frac{Q}{T},$$

and the passage of the quantity of heat Q from the temperature t_1 to the temperature t_2 , has the equivalence value

$$Q \left(\frac{1}{T_1} - \frac{1}{T_2} \right),$$

wherein T is a function of the temperature, independent of the nature of the process by which the transformation is effected” [3] (p. 126).

Afterwards he discusses a process when the several bodies K_1, K_2, K_3, \dots , serving as reservoirs of heat at the temperatures t_1, t_2, t_3, \dots , have received during the process the quantities of heat Q_1, Q_2, Q_3, \dots , respectively, so that the total value N of all transformations is

$$N = \frac{Q_1}{T_1} + \frac{Q_2}{T_2} + \frac{Q_3}{T_3} + \dots \quad (1)$$

This formula assumes the constant value of the temperature of individual bodies during the process. Nevertheless a generalization to the case when the bodies may change its temperatures is easy: we simply sum small pieces of heat, dQ , divided by the temperature at which they are exchanged. Moreover, we may imagine all bodies as a one, unevenly heated, and interpret dQ as a global heat exchanged of all parts of this large body at a concrete temperature¹. As a result, we get the well-known expression, namely

$$N = \int \frac{dQ}{T}. \quad (2)$$

The crucial result is that $N = 0$ during a *reversible cyclic* process (though the proof is not so easy [3], pp. 127-129), i.e.

$$\oint_{rev} \frac{dQ}{T} = 0. \quad (3)$$

Up to now, the temperature $T(t)$ means the temperature of heat reservoirs (bodies surrounding the system) with which (or among which) the heat is exchanged. Therefore the essential step is done when Clausius identifies T with the temperature of the body itself [3] (p. 130):

¹ It is the essence of the “heat measure” introduced for example by Šilhavý [6] (p. 112).

“...let us assume that all parts of the body have the same temperature; then in order that the process may be reversible, the changing body when imparting or receiving heat can only be placed in communication with such bodies as have the same temperature as itself, for only in this case can the heat pass in an opposite direction. [...] In this case it is of course of no importance whether t [...] represents the temperature of the reservoir of heat just employed, or the momentary temperature of the changing body, inasmuch as both are equal.”

It is worth stressing that this identification is possible *only* if the process is reversible.

By understanding T as the temperature of the studied system and $-dQ$ its exchange of heat (the minus sign means that heat is understood with respect to the system and not to the surrounded reservoirs), the fact that a cyclic integral vanishes independently of which cyclic reversible process is done allows us to define a *state* variable

$$S = S_0 - \int_{rev} \frac{dQ}{T} \quad (4)$$

where 0 is an (arbitrarily chosen) “referential” state and 1 represents an arbitrary state to which the value S is assigned. Clausius called lately (in 1865) the quantity S the *entropy* from the Greek word meaning the transformation [3] (p. 357).

3. 3. Irreversible processes and nonequilibrium thermodynamics

Thermodynamics is based on fundamental Carnot’s idealization – the reversible process. Namely, the (theoretical) possibility of realizing a transition between two states in a reversible way is crucial for all considerations. Only by using it we can actually use the second law and obtain important results concerning *arbitrary* processes. The crucial step is nothing but the Carnot’s mental procedure consisting in a reversible return into a demanded (e.g. initial) state. That is exactly the way in which Clausius studies *irreversible processes*. Since temperatures T in the formula (2) are the temperatures of surrounding reservoirs (e.g. the environment) the quantity N may be defined for an arbitrary process (supposing that these temperatures are defined at each time moment) because dQ may be determined at any time moment as a heat supplied or absorbed by some of the reservoirs². Clausius proves (by using such reversible returns) that the quantity N cannot be negative, i.e.

$$N = \oint \frac{dQ}{T} \geq 0. \quad (5)$$

He calls N the *uncompensated heat*, because in irreversible processes some positive processes (in which Q/T is positive, e.g. friction or spontaneous heat conduction) are not compensated by a production of work (e.g. in a form of rising a weight in gravitational field) that may be used afterwards in a reverse run for a return of the heat into reservoirs.

The uncompensated heat may be determined in an arbitrary (non-cyclical) process. It is shown by Clausius by using a reversible return again. Namely let the system change its state, denoted by 0, into an arbitrary state, denoted by 1, by an irreversible process. Suppose that there is a reverse return from this state to the state 0. Then the uncompensated heat during the whole cycle equals

² In beginning of Clausius considerations, the heat is not exchanged primarily with the system – it may be produced by the reservoirs or absorbed by them or even exchanged between them (the role of the system is only auxiliary because it may assist to this exchange).

$$N = \int_0^1 \frac{dQ}{T} + \int_{1(rev)}^0 \frac{dQ}{T}. \quad (6)$$

The second term calculated along the reversible path, however, equals the difference of entropies due to the formula (4), i.e.

$$\int_{1(rev)}^0 \frac{dQ}{T} = S - S_0, \quad (7)$$

where S denotes the entropy of the state 1. The uncompensated heat occurs only along the irreversible run, i.e. N corresponds to the process from the state 0 into the state 1, $N = N_{0 \rightarrow 1}$. Its value thus equals

$$N_{0 \rightarrow 1} = \int_0^1 \frac{dQ}{T} + S - S_0. \quad (8)$$

Notice that the fact that $N = N_{0 \rightarrow 1}$ implies that $N_{0 \rightarrow 1} \geq 0$ too. It implies that

$$S - S_0 \geq - \int_0^1 \frac{dQ}{T}. \quad (9)$$

It is called the *Clausius-Duhem inequality*. If now the irreversible process from 0 to 1 is *adiabatic*, i.e. there is no exchange of heat, $dQ = 0$, then the Clausius-Duhem inequality implies that

$$S \geq S_0, \quad (10)$$

i.e. the entropy cannot decrease during an irreversible, adiabatic process. Notice that this relation may be formulated only thanks to the fact that some reversible path connecting the initial and final state of the irreversible process exists.

Since the time of Clausius' epochal discoveries no essentially new ideas concerning the description of irreversible processes have appeared. All approaches are, in a way, only various modifications or precise mathematical formulations of original Clausius' ideas. There exist only various approaches attacking the problem of description of irreversible processes by different approximations. They differ by the way in which the irreversible processes are related into the reversible ones. In *classical irreversible thermodynamics*, for example, an arbitrary state is understood as a composition of infinitely many "infinitesimally small" cells in equilibrium. It allows assuming the existence of entropy assigned to any state (as an infinite sum of entropies of individual cells).

The so-called *rational thermodynamics* stems from the Clausius inequality, especially its special form, the Clausius-Duhem inequality. An interesting novelty is the idea of Noll and Coleman consisting in using the Clausius-Duhem inequality as a "sorting" principle choosing from an arbitrarily conceivable material responses only those that fulfill the inequality in an arbitrary admissible process [8] (see also [6], p.153). The relation of the description of rational thermodynamics into equilibrium is hidden in using the concept of temperature that is the crucial quantity for formulating the Clausius inequality (because it realizes the passage from heat into a state variable – the entropy). In Clausius derivations, the understanding of T as the (equilibrium) temperature of some bodies (heat reservoirs) in thermal equilibrium is crucial. Namely these derivations insist on the Clausius' formulation of the second law that claims the strict impossibility of a spontaneous (i.e. realized by itself) heat transfer from colder to warmer bodies. The rational thermodynamics uses the temperature as a primitive

concept occurring in the Clausius-Duhem inequality [6] (p. 109). May it mean something else than the *equilibrium temperature*? Imagine that two bodies are in thermal nonequilibrium and we assign to them a quantity, say T_{neq} , called the nonequilibrium temperature (there are many methods of doing that – we know for instance the contact temperature, the kinetic temperature etc.). Nevertheless, any relation of these temperatures, for example $T_{neq} < T'_{neq}$, does not guarantee that the heat cannot spontaneously flow from the body with the temperature T_{neq} into the second one. It indicates that the temperature used in the Clausius-Duhem inequality may be hardly interpreted as a nonequilibrium one.

In *extended irreversible thermodynamics* [9] the second law is formulated formally as an impossibility of negative production of entropy. The starting point is the assumption that there is a state function called the nonequilibrium entropy that may be assigned to nonequilibrium states. The nonequilibrium entropy is used for the definition of the so-called nonequilibrium temperature θ by the relation

$$\theta^{-1} = \frac{\partial s}{\partial u}. \quad (11)$$

These assumptions, however, are highly problematic. Namely, the concept of entropy as well as temperature is closely related to the second law. There is no relation of the definition (11) to the second law if the system is not in equilibrium [10]. Also other approaches use some equilibrium thermodynamic quantities defined at nonequilibrium states (like entropy or temperature), nevertheless a careful operational relation into some ‘near’ or ‘accompanying’ equilibrium states is ever supposed, e.g. in *thermodynamics with internal variables* [11].

A rather radical approach is presented in the work by B.C. Eu [2] who interprets the uncompensated heat N in the relation (2) as a quantity being *independent* on the circular integral at the right-hand side of this relation. That is, (2) is understood not as a definition of N but as a genuine physical equality. It implies that by supposing the uncompensated heat in the form $N = \oint dN$ we obtain from (2) that exists a *state variable* ψ defined by $d\psi = dN - T^{-1}dQ$ (since the circle integral of $d\psi$ is always zero). The crucial problem of Eu’s approach is the assumption of existence of the uncompensated heat as an independent physical quantity. Without a deep physical explanation of this fact, however, all obtained results look rather formally and problematic.

3. 4. Abstract thermodynamics – from a system to its surrounding

In comparison with Newtonian physics, the Carnot’s epochal discovery looks very strange. There is no evident point of concurrence of these theories as seen at the first glance by striking difference of their languages. Since Newtonian mechanics had become an excellent description of physical reality, the oncoming history of thermodynamics was stigmatized by an intensive effort to include thermodynamics into the framework of Newtonian physics. It is not incidental that the collection of Clausius’ works [3] was named the ‘‘Mechanical theory of heat’’. Understanding heat as a form of motion makes feeling that thermodynamics is nothing but a part of mechanics. However, the differences are principal and cannot be so easily bridged over.

Look for instance the problem of explanation the ‘heat’ from the viewpoint of Newtonian physics. Namely it cannot be identified with a kind of molecular motion. It is rather an ‘‘energy transfer to the hidden molecular modes’’ as observed by H. B. Callen [12] (p.8). The essence of heat is thus an energetic ‘‘communication’’ between macroscopic and microscopic scales. However, the concept of macroscopic scale is difficult to be defined as

well as the form of this “communication”. Nevertheless, we can avoid the problem by defining the heat via the familiar thermodynamic relation (the first law),

$$dE = -\delta W + \delta Q, \tag{12}$$

where dE is an infinitesimal change of the energy of the system and δW the performed work. These quantities have an evident relation to Newtonian physics – the energy as well as the work is defined in mechanics. In thermodynamics, however, the concept of work is not so simple because its mechanical definition as a “force times distance” is insufficient. The question is *which* forces and *which* distances. Namely, if we calculated the sum of “forces times distances” for all molecules of the system the work would always equal the change of the whole energy of the system and no heat would appear in (12).

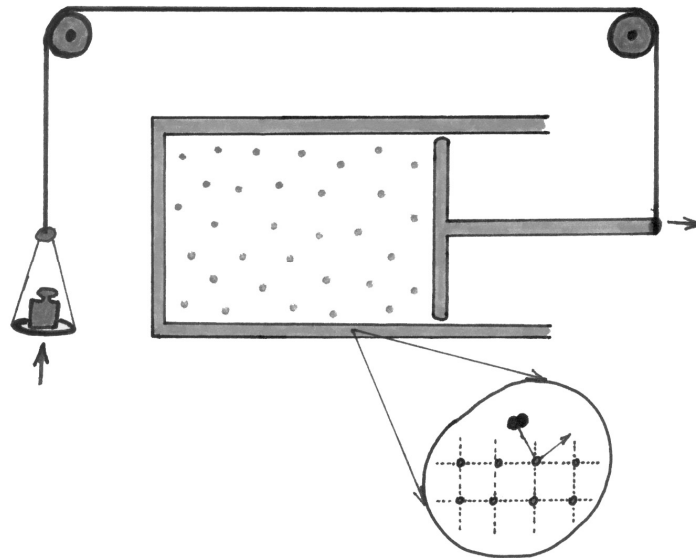


Fig. 1. What is work? If we calculated a sum of all “forces times distance” including interatomic forces we would obtain a full energy exchange of the system with its surrounding. The work, however, is the “force times distance” concerning only the movement of the piston.

Let us illustrate this on the familiar thermodynamic system consisting of a gas in a box that includes a movable piston. The piston is connected through a rope with a weight in gravitational field as illustrated in Fig 1. The work is defined by the displacement of the piston. However, if this physical system is understood as a conglomerate of molecules of the gas and molecules of the box and piston, then the “displacement of the piston” is only a special molecular movement (among many others). Why *this* movement has a fundamental meaning to define the decomposition of the energy into work and heat? And how it could be generally defined? It is difficult to answer such questions from the point of view of the *system itself* in a different way than speaking about some “macroscopic modes” of the movement (see e.g. [12], Section 1.2) and their eminent relevance for thermodynamics. Thereby we again face the problem with an explanation of the word “macroscopic”.

Let us try to look at the system from the point of view of the other physical system in its surrounding -- the weight that interacts with the system through a connecting rope (see

Fig.1). When displacing the weight, the piston begins to move. The weight thus *defines* what is meant by that special "mode" of the motion. It is enabled by a special arrangement that allows *manipulation* with the system by another system. The thermodynamic work then may be defined as a form of energy communication between the system and its surrounding which arises in special manipulations with the system³. In the pioneering work by R. Giles [14], that is attempting to formulate an axiomatic foundation of thermodynamics, the author introduces a class of "mechanical systems" that serve as suitable surroundings allowing to define the *adiabatic process* ([14], Chapter 5), i.e., the process when the only energy transfer is realized by the work. Recently, the Giles' work has been successfully crowned by proposing a perfect axiomatic system of equilibrium thermodynamics by E. H. Lieb and J. Yngvason [15]. Though the authors are getting near the Giles' work at many points, they avoid any attempts to define adiabatic processes (and work) in this way. Instead, they introduce the concept of adiabatic accessibility (in the spirit of Planck's formulation of the second law) by using only a very special "mechanical system" in the surrounding of studied thermodynamic system – a weight in gravitational field⁴.

Thermodynamics thus seems as not being able to avoid the presence of something (a mechanical device, the weight in a gravitational field, etc.) in the *surrounding* of the studied system. If the system were only alone, the concept of heat, work or adiabatic accessibility would become superfluous or even nonsensical. In the Newtonian physics the term "alone" means to be the only one in space (so that the influence of other bodies may be neglected). The (hypothetical) possibility for any system to be studied as "being alone" is hence the leading idea of the Newton's program: it allows simplifying considerable external interactions and studying inner dynamics of the system⁵. Thus thermodynamics presents a small but remarkable conceptual controversy with the Newtonian scheme because its basic concepts cannot be principally defined when using only systems in empty space.

Keeping that in mind we go back into the Carnot's and Clausius' considerations and try to pinpoint their "non-Newtonian" features. The first striking fact is that we, in fact, do not do physical considerations about the "studied" system (like a gas in a box) but about various heat reservoirs in its surrounding. Namely the cyclic processes that have the crucial role in those considerations mean that the system goes back into its initial state. That is when comparing the initial and final states of the "world" the system remains in the same state and hence does not play a role. The system is rather an auxiliary "device" allowing to compensate heat flow by an amount of work. The gas in a box with piston that may be adiabatically closed and ingeniously put into contact with heat reservoirs enables us to realize even the most efficient, reversible transfer of heat into work. The core of Carnot's statement does not consist in that what happens with the system but in that what does with the reservoirs. To show it let us repeat the Carnot's proof of maximal efficiency of a reversible cycle in detail.

Let there be a device D' producing much work during a working cycle than the reversible device D. The both device withdraw the same amount of heat from the heat reservoir, say Q. The heat transmitted to the second reservoir (e.g. the environment) by individual device, however, must be different (we do not follow Carnot in this point and use the first law), namely the reversible device returns $Q' = Q - W$, the more efficient one does

³ S. Kauffman [13], a biologist, (when realizing in the discussion with a physician P. W. Anderson that the concept of work is far to be clear, p. 96) specifies work as "constrained release of energy" whereas by "constrains" means external organization of energy transfer by various pistons, wheels, paddles and so on.

⁴ The other place where the concept of work is used is the passage when the authors define simple systems. The "work" is represented there only by a sort of special coordinates without a detail explanation ([14], p. 38).

⁵ For example, when deriving the Kepler's laws of motion of planets around the Sun, we imagine one planet (e.g. the Earth) and the Sun as a physical system which is alone in empty space.

$Q'' = Q - W' < Q'$. Now we consider the two device putting side by side and construct a new cycle consisting of two subsequent operations: first the more efficient device does a cycle withdrawing Q from the hot reservoir while the second does nothing. Then the reversible device does the reverse run and returns this heat Q to the hot reservoir (and the more efficient one does nothing). The reverse run needs the work W that means that the amount of work

$$\Delta W = W' - W > 0$$

is obtained from this double cycle at the expense of the heat $Q' - Q''$ that is taken from the second reservoir. Otherwise nothing is changed ``in the world'' because the first reservoir is in the same state as at the beginning – the heat Q has been returned to it – and both device are in their initial states. This contradicts the second law because the work ΔW is obtained only from the heat pumped from the second reservoir.

It is worth noting that the role of both reservoirs is not symmetric. In the previous consideration, the first one returns into its initial state because the heat Q is given back to it. From this viewpoint this reservoir is understood as a physical system whose initial state may be reconstructed if necessary (the role of reversibility in Carnot's considerations is just the possibility of this reconstruction). The second reservoir plays rather the role of an uncontrolled environment – the merit of the proof consists in impossibility of pumping the heat from it (without compensation). Second, the role of a system (e.g. a box with gas) is only auxiliary to allow realizing a reverse run – we never use its other properties during the consideration. Taking into account these facts we may try to formulate the Carnot's theorem and the second law in a very abstract form.

3. 5. Abstract formulation of the Carnot's theorem and the second law

The main step in our new formulation consists in assigning a totally different role to the both reservoirs. The first reservoir together with the auxiliary system (e.g. a box with gas) will be understood as the *system* in a common physical meaning of this word. In Newtonian physics, any physical system may be understood as being alone in empty space that cannot be influenced by the system in a way (as a result, the law of conservation of energy may be assumed because the system cannot exchange energy with the space). Here, we introduce the crucial deflection: the ``space'' is not empty and it may interact with the system. Namely the second reservoir may be understood as an infinite ``sea'' that is homogeneous and isotropic. This ``sea'' may exchange energy with the system. Nevertheless, the ``sea'' may be supposed to be unchangeable (not changing its state during interactions with the system) because it may be understood to be extremely large in comparison with the system. In other words, any ``material'' interpretation of the ``sea'' is superfluous – we may simply imagine something like an empty space but such that the energy of the system in this space is not conserved.

Moreover we need a physical definition of performed work. The problem with work is that it is a special energy transfer to the exterior of the system (we cannot avoid this fact!). Following [15] we define the work by a weight in gravitational field somewhere else – its displacement defines the performed or gained work. Therefore the work may be quantified by one length parameter, say l . If l is positive, the weight has risen up, if l is negative, it has fallen down. Our description thus looks as follows. The state of surrounding is parameterized by a length parameter l and the energy of the system may not be conserved. This ``violation'' of the law of energy conservation, however, may not be related to the change of the parameter l . The exact relation is expressed via the second law. It may be formulated as follows.

Second law. *During an arbitrary process in which the system returns into its initial state, the parameter l may only decrease its value or remain constant.*

The system is understood as being alone in our generalized space. The crucial fact is that there is *no restriction* on what is understood under the system. For example, the system may not be macroscopic⁶. Similarly, its initial state may be also arbitrary. Notice for instance that the system may be in nonequilibrium state. It may look surprisingly when we remember that the system here includes also the first reservoir (the furnace) in Carnot's work. Nevertheless, the only property of this reservoir that is really used is a possibility of returning the borrowing heat during a reverse run⁷. It is worth stressing that the equilibrium of the second reservoir, by contrast, is a necessary condition. Here this reservoir is represented by a homogenous, isotropic "sea".

The crucial concept in our abstract approach is the concept of *process*. Its precise definition in a very abstract, general form not using the idea of a spatiotemporal background is given at [16] (Chapter 2). It is based on the concept of 'change' that is introduced as an ordered couple $[s, s']$ where s and s' are two states of the system⁸. The *reversible process* means such a change $[s, s']$ that there exists another change, $[s', s]$, so that the parameter l' of this change equals $-l$, where l is the parameter of the change $[s, s']$. The generalized Carnot's theorem then may be formulated as follows.

Carnot's theorem. *Let p be a reversible process connecting the state s with another state s' of the system. Then the parameter $l = l_{rev}(s, s')$ does not depend on a concrete realization of the process (i.e. is the same for all reversible processes). If p' is an arbitrary process connecting s with s' then the parameter l of this process cannot exceed $l_{rev}(s, s')$.*

The proof is completely the same as that concerning only the hot reservoir whose state is changed by withdrawing an amount of heat – here s' corresponds to the state of the reservoir (plus the auxiliary system) after losing a part of thermal energy (while the auxiliary system getting into the same state). Namely an arbitrary process connecting s with s' is connected with a subsequent reversible process in the reverse run.

3. 6. A material sample in a varying temperature field

After a very general discussion of the foundations of thermodynamics we will study a simple illustrative example. Let us imagine a small material sample that is in an environment that is heated or cooled by an externally controlled way. This is a typical situation in thermal analysis where special measurements of material responses to temperature changes are done. When the heating or cooling is very slow and no thermal gradients exist in the environment, a permanent thermal equilibrium within the sample may be supposed and the temperature of the sample equals the current temperature of the environment. This situation is that mentioned by Clausius when he identified the temperature of heat reservoirs with that of the studied body, which enabled him to introduce a new state variable of the body – the entropy.

Nevertheless, the formulation of the second law does not insist on such an assumption. As clearly seen in the abstract formulation of thermodynamics, the role of the "studied body"

⁶ If the system is microscopic, say a molecule, the surrounding "sea" corresponding to a 'space' cannot be a matter consisting of atomic particles – namely then it would not be a homogeneous and isotropic background (since the matter looks highly heterogeneous at molecular scales). These questions are deeply related to possible violations of the second law at small spatial scales [17]. In our formulation, however, the second law is perfectly valid at all spatial scales – only the surrounding thermodynamic space (the "sea") has to be chosen appropriately to the studied system.

⁷ In Carnot's engine the equilibrium of both reservoirs is necessary only for an explicit constructing the reverse run of the engine.

⁸ The change is however always connected with an external manipulation with the system.

is only auxiliary and no assumption about its thermal equilibrium is necessary. Keeping that in mind let us go back to the typical situation in thermal analysis – a studied sample of material is *not* in thermal equilibrium with the environment. Moreover, same thermal gradients may even occur in this environment (see Fig. 2).

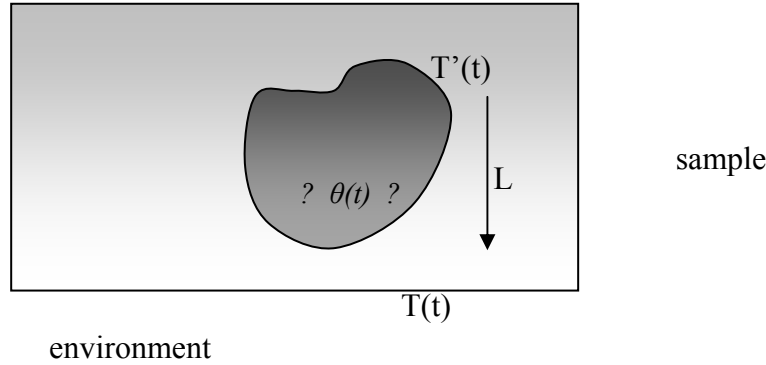


Fig 2. A typical situation in thermal analysis: a sample is located in an environment that is heated or cooled by an externally controlled way. There may or may not be some thermal gradients in the environment, say $\text{grad}(T) \sim (T' - T)/L$. The question is, however, what is an effective current temperature, say $\theta(t)$, of the sample during the process that is responsible for triggering various processes within the sample (like melting, evaporation, glass transition and so on). It is worth stressing that this temperature cannot be identified with the environment temperature $T(t)$ even if there is no thermal gradient within the environment (i.e. $T(t)$ corresponds to the temperature of the environment that is in perfect thermal equilibrium at each time instant). Namely if the heating or cooling process is not infinitely slow the current sample temperature does not equal $T(t)$.

We will suppose that the current distribution of the environment temperature (or simply the current environment temperature) may be determined at each time instant⁹. In other words, we assume that the temperature at the border of the sample is known at each time instant. The formula (2) may be then written in the form

$$N = \iint_A \frac{q \cdot n}{T} dA, \quad (13)$$

where q is the vector of heat flux at a point of a body surface A , n is the vector of external normal of the body surface and T is the temperature of the environment at a point near the body surface; whereas the first integral represents the sum (1), i.e., it may be interpreted as a time integral representing the varying heat fluxes during the process.

The crucial assumption concerning the temperature inside the sample is that there is a smooth continuation of the environment temperature distribution over the whole sample. The temperature field within the sample may be therefore denoted as that in the environment, i.e. $T(x,t)$. Nevertheless, it is important to stress again that the thermal distribution (or thermal gradients) within the sample cannot be measured (ref. [18], p. 6) or otherwise determined (e.g. by some indirect methods or calculations). A partial fixation of the thermal field within the sample may be done by using the divergence theorem and writing (13)

⁹ For example, when measuring the temperature at two points around the sample we may approximate the distribution of the temperature by a linear function approximating the measured gradient (see Fig. 2).

$$N = \int_A \frac{q \cdot n}{T} dA = \int_V \nabla \cdot \frac{q}{T} dV . \quad (14)$$

The integral on the right-hand is taken across the body, which means that the smooth continuation of the field $T(x,t)$ has to fulfill this identity. Nevertheless, it is quite insufficient – the temperature field within the sample may be defined by infinite manners that fulfill the identity.

Though the temperature within the sample is not homogeneous we detect anyway only “global” physical effects of this temperature, such as a change of the sample weight or its overall phase transitions. In other words, no detail temperature distribution within the sample but an averaged value of its, say θ , is important for physical evaluation of a thermal analysis procedure. A possible way of defining such an averaged value is for instance the arithmetic mean, namely

$$\theta(t) \equiv V^{-1} \int_V T(x,t) dV , \quad (15)$$

where V is the volume of the sample. The relation of this value to the current environment temperature is of the crucial importance. Let us suppose for simplicity that the (heated or cooled) body is spherical in shape. Then we can use a very general mathematical lemma derived recently [19]. Namely whenever the smooth field T at the center of the body fulfills the inequality

$$\frac{\partial T}{\partial t} \Delta T > 0 , \quad (16)$$

there is a nonzero distance l so that the arithmetic mean of the temperature over the sphere with the radius l or smaller, $\langle T \rangle_l$, equals the averaged temperature over the surface of this sphere,

$$\langle T \rangle_l^A(t) \equiv A^{-1} \int_A T(x,t) dA , \quad (17)$$

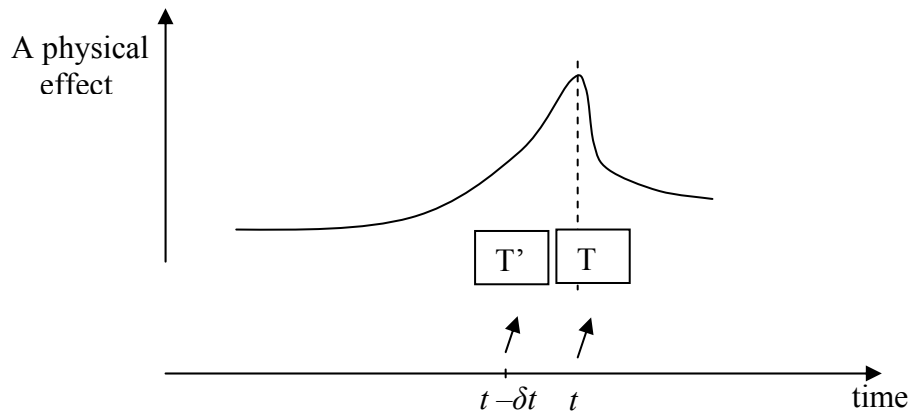


Fig. 3. At the moment when we observe a physical effect the measured temperature is T . But the temperature of the sample at this moment is not T but T' that corresponds to the measured temperature at the previous moment $t - \delta t$.

but at a delayed time instant, namely

$$\langle T \rangle_l(t + \delta t) = \langle T \rangle_l^A(t). \quad (18)$$

It implies that if the sample is sufficiently small so that its radius R is smaller than l , we may use the formula (18) directly for the sample, i.e. with $l = R$ when $\langle T \rangle_R = \theta$. Then its interpretation is straightforward: the averaged current temperature of the sample, $\theta(t)$, does not equal precisely the measured temperature corresponding to a (mean) temperature of the environment at the same time moment. If the typical time scale of the heating (or cooling) process is comparable with the time delay δt , the averaged temperature of the sample at time t corresponds to the measured temperature at time $t' = t - \delta t$ (see Fig. 3). The time delay δt depends on the size of the sample and the dynamics of heat conduction process in the sample. For example, if the heat conduction is governed by the diffusion equation,

$$\frac{\partial T}{\partial t} = D\Delta T, \quad (17)$$

the time delay may be expressed as [19]

$$\delta t_{diff} \approx \frac{1}{15} D^{-1} R^2 \quad (18)$$

where R is the radius of the sample. It is worth noticing that the condition (15) is automatically satisfied if (17) is valid since D is always positive. Nevertheless, if the process of heat conduction is governed by other law, the formula (18) may not be valid and we get another time delay. For example, if the heat conduction process is governed by the hyperbolic heat conduction,

$$\frac{\partial T}{\partial t} + \tau \frac{\partial^2 T}{\partial t^2} = D\Delta T, \quad (19)$$

we get the time delay that depends on the time derivatives of T at the center of the sample

$$\delta t_{hc} \approx \frac{1}{15} \left(1 + \tau \frac{\partial^2 T}{\partial t^2} \cdot \left(\frac{\partial T}{\partial t} \right)^{-1} \right) D^{-1} R^2. \quad (20)$$

A determination of the time delay thus may be important for understanding the heat process in the sample. It may be determined by finding a shift on the time axis when comparing the time when a typical physical process occurs in a very slow realization of the experiment and the fast one.

3. 7. Conclusions

The book [16] presents an attempt of formulating a physical description without using a given spatiotemporal background (which is necessary in Newtonian physics). Instead of an external 'flow of time' there is only an abstract 'change' defined as a couple of states. Similarly, an indifferent spatial background is not used and the concept of 'surrounding' as a genuine physical system is used instead. The source of changes are manipulations coming externally into the system from its surrounding. The main interest concerns the concept of *adiabatic accessibility* that is crucial in Lieb's and Yngvason's axiomatic scheme. Nevertheless, the considerations are very general and no many comparisons with the classical thermodynamic description are presented. That is why this contribution deals more with these questions. We have tried to summarize main ideas of S. Carnot and R. Clausius who laid the

foundations of thermodynamics [1,3,5,12,16,20,21]. The crucial noticing is the fact that the main role in their thinking and logical considerations (especially those concerning the formulation of the second law) plays rather the surrounding reservoirs than the system itself. The system (like a box with a gas) plays an auxiliary role as a "device" enabling us to minimize the uncompensated heat by a sophisticated use of flows of heat energy into performing an amount of work. This work then may be used to perform a reverse run.

The development of nonequilibrium thermodynamics battles with several mental barriers. Namely the possibility of realizing a reverse path connecting two states of the world is crucial in studying nonequilibrium processes. The problem is, however, that the reverse path is historically connected with an equilibrium process (such as the ingenious Carnot's realization of a concrete reverse run). The other critical point in the history of thermodynamics is Clausius' identifying the temperature of reservoirs with the temperature of the system itself. Then the thermal equilibrium of the system with its surrounding is a necessary condition. As we have seen, however, Clausius' considerations about equivalence-values of transformations do not concern the system itself but the surrounding reservoirs. Hence *their* temperatures appear in famous formulas like (1) or (2) (see also [10]). Nevertheless without a connection of these temperatures with a state of the system the concept of (Clausius') entropy can be hardly defined as a state variable assigned to the system. The problem of defining the temperature of the system in various processes thus seems as crucial in formulating a consistent theory of nonequilibrium processes. The definition of any physical quantity is deeply related to methods of its measurement. That is why "pure experimental" questions concerning measurement of temperatures in extreme conditions as well as the generalized approach to thermal analysis [20] could play the crucial role in further development of nonequilibrium thermodynamics [7,9].

Acknowledgement: *This work is supported by the Czech Ministry of Education, Youth and Sports, the project MSM 4977751303.*

References 3

- [1] S. Carnot "Réflexions sur la puissance motrice du feu" Bachelier, Paris 1824 (cited passages are taken from the translation by R.H. Thurston (ed.) "Reflections on the Motive Power of Heat and on Machines Fitted to Develop That Power" John Wiley & Sons, New York 1890)
- [2] B.C. Eu "Generalized Thermodynamics" Kluwer Academic Publishers, Dordrecht / Boston / London 2002
- [3] R. Clausius "The Mechanical Theory of Heat" with the Applications to the Steam-Engine and to the Physical Properties of Bodies" Tyler and Francis, London 1867
- [4] D. Kondepudi, I. Prigogine "Modern Thermodynamics" John Wiley & Sons, Chister / New York / Weinheim / Brisbane / Toronto / Singapore 1999
- [5] I. Muller "A History of Thermodynamics" Springer, Verlag / Berlin / Heidelberg 2007
- [6] M. Šilhavý, "The Mechanics and Thermodynamics of Continuous Media" Springer Verlag, Berlin / Heidelberg 1997
- [7] S.R. deGroot, P. Mazur "Non-Equilibrium Thermodynamics" North Holland, Amsterdam 1969
- [8] B.D. Coleman, W. Noll, Arch. Rational Mech. Anal. 13 (1963) 167-178

- [9] D. Jou, J. Casas-Vazquez & G. Lebon ``*Extended Irreversible thermodynamics*'' Springer-Verlag, New York / Berlin 1996
- [10] B.C. Eu, Phys. Rev. E, Vol. 54, No. 3 (1996) 2501-2511
- [11] G.A. Maugin ``*The Thermomechanics of Nonlinear Irreversible Behavior*'', World Scientific, Singapore / New Jersey / London / Hong Kong 1999
- [12] H.B. Callen ``*Thermodynamics and an Introduction to Thermostatistics*'', Wiley, New York 1985
- [13] S. Kauffman ``*Investigations*'' Pergamon Press 2000
- [14] R. Giles ``*Mathematical foundations of thermodynamics*'' Pergamon, Oxford 1964
- [15] E.H. Lieb, J. Yngvason, Phys. Rep. 310 (1999) 1-96
- [16] M. Holeček ``*Abstract Thermodynamics*'' O.P.S., Plzeň / Nymburk 2006
- [17] G. M. Wang, E. M. Sevick, E. Mittag, D. J. Searles & D. J. Evans, Phys. Rev. Lett., Vol. 89, No. 5 (2002) 050601/1-4
- [18] T. Hatakeyama, L. Zhenhai (Eds.) ``*Handbook of Thermal Analysis*'', Wiley, Chichester 1998
- [19] M. Holeček, Appl. Comput. Mechanics (2009), to appear
- [20] J. Šesták ``*Science of Heat and Thermophysical Studies: a generalized approach to thermal analysis*'' Elsevier, the Netherlands 2005
- [21] J. Šesták, J.J. Mareš, P. Hubík and I. Proks „*Contribution by Lazare and Sadi Carnot to the Caloric Theory of Heat and its inspiration role in thermodynamics*“ J Thermal Anal Calor, in print 2009 (doi: 10.1007/s10973-008-9710-y)

Vysoké Tatry (High Tatras Mt.), Slovakia



Chapter 4

Thermodynamic potentials

4. NEW THERMODYNAMIC POTENTIALS AND CLAPEYRON EQUATIONS FOR CONDENSED PARTLY OPEN SYSTEMS APPLICABLE TO NONSTOICHIOMETRIC PHASES

Pavel Holba

4.1. Introduction

4.1.1. *Biographical context*

At the end of 1960s I was inspired by the Callen's textbook (1960 [1]) adapting Gibbs free energy to be a more adequate tool for describing the equilibria of solid oxides with gaseous surroundings. The corresponding thermodynamic potential was used in my first dissertation (submitted in 1971 [2]), however, it was never accepted to an oral defense because I was branded as „politically unreliable dissident“ due to my activities during the so called “1968 Prague Spring”. Subsequently, I lost my position at the Czechoslovak Academy of Sciences, however, at the times of Gorbachev's „perestroika“ the Czech political situation was loosening consequently easing the submission of my new dissertation [3], which was defended in 1986.

After the Czechoslovak „Velvet Revolution“ in the year 1990, I accepted the offer to return from my enforced dissenting employment back to scientific work at the Physical Institute of Academy of Sciences where I had worked in the past. At the beginning of the 1990's I prepared thermodynamic chapter for the book edited by A. Koller (published in 1994 [4]) and an article on thermodynamics of partially open systems [5].

At the end of 1990 I was elected a member of Council of the Prague City and consequently in the year 1993 I became the Deputy Mayor. In this position I helped to introduce information and communication technology (ICT) systems into the City Hall and subsequently in 1995 I was appointed the Director of Institute of Municipal Informatics (IMIP) dealing with digital maps of Prague [6] easing the city administration.

At the end of 2006 my mission in the public administration was finished and I was able to return back to science as a free private explorer in a new era of “Information Age”.

It is worth noting that on browsing on the Internet I found information on studies dealing with the problem of partly open systems far before my first attempts back in the year in 1970. Therefore, my present article is a continuous attempt to introduce the ideas and methods for exploitation of the partly open system in more generalized thermodynamics.

4.1.2. *Roots of the idea of partly open system*

Inauguration of most assessments in chemical thermodynamics was established on theoretical bases by Josiah Willard Gibbs (1876-1878) who introduced an important concept of „component“, „chemical potential“, „phase“ and ingeniously declared the „phase rule“ [7]. It was necessary to wait another thirty years for the Lewis' concept of „activity“ (1907) [8] as a more practical form of chemical strength of component and for a yet more practical depiction of „negative decadal logarithm of H^+ activity“ suggested by Sorensen two years later (1909) [9] today's known as pH quantity. All these concepts had formed a basis for studies of real material systems in chemistry, geochemistry, metallurgy, hydrochemistry and material science.

The choice of an adequate type of thermodynamic system is one of the tools for analyses and predictions of the equilibrium behavior of all material systems. However, the supply of categories of thermodynamic systems in textbooks on physical chemistry, as they were limited to the isolated and closed systems only, were not sufficient for problems to be solved by science in 20th century.

Efforts to better understanding of the genesis of rocks led Koržinskij [10] in 1936 to distinguish two classes of components in geochemical systems: „inert components“ whose amounts (masses or numbers of moles) are independent on amounts of any other component and on processes inside the system, and „perfectly mobile components“¹, whose chemical potentials (or other intensive parameters) are independent factors of equilibrium.

In 1944, another attempt to overcome the traditional limits of „closed systems“ was accomplished by Ellingham [11]), when he showed the relations between decomposition temperatures of various metal oxides in ΔG vs T plot. In 1948, Richardson & Jeffes [12] improved Ellingham diagrams by adding a monographic scale, which allowed to read the decomposition temperature of metal oxide under various types of atmosphere formed by gaseous mixtures (such as O_2 + inert gas, CO + CO_2 and/or H_2 + H_2O). It seems that the so called „Richardson diagrams“ appeared three years after the foremost publication by Darken & Gurry [13] dealing with equilibria of condensed Fe-O phases under the controlled gaseous atmosphere (captivatingly prepared by using a new gas-mixing technique).

Quite different application, which was overcoming „closed systems“ was started through the work published in 1946 by Pourbaix [14], who suggested the diagrams consisting of the plot of redox potential (E) versus acidobasic potential (pH) to portray equilibria of dilute aqueous solution at room temperature. Associated applications became widely known in hydrochemistry probably due to books by Garrels [15] and Garrels & Christ [16].

Data by Darken and Gurry [13] on equilibrium non-stoichiometry of wüstite and magnetite supported the efforts of other scientists to determine phase relations in the systems containing several metal oxides for various composition of atmosphere. A notable result in this direction was the significant book by Muan & Osborn [17], which presented phase diagrams obtained under conditions of partly open systems, e.g., under air atmosphere or in the contact with liquid iron.

Apart from the Publishing Houses of the above mentioned English-written papers and books, Koržinskij (one of the famous Russian geologists) helped to develop the „physicochemical basis for analysis of mineral parageneses“ and revealed its for publication in 1957 [18]. According to this book, translated into English in 1959 [18], Koržinskij analyzed „relations between mineralogical composition and values of chemical potentials of components“ as early as in 1944 [19] later supplying the concept of thermodynamic potentials for „systems with perfectly mobile components“ (1949 [20]). The applications of his new potentials were rejected by geologist Nikolajev [21] but publications of Verhoogen [22] and Thompson [23] and also paper by Palatnik & Landau [24] supported Koržinskij in his ideas. In 1956 Koržinskij published „derivation of thermodynamic potentials for systems with mobile components“ in a more internationally available Russian journal [25].

In 1950s the study of equilibria of oxides with atmosphere was also stimulated by the industry's interest in order to produce new ceramic materials (e.g., ferrites) of required properties using an adequate high-temperature preparation procedure. In connection with this challenge a detailed research focused on ferrites [26] and non-stoichiometric oxides [27] proceeded in 1960's and successively continued in the field of oxide superconductors [28]

¹ in Russian: „вполне подвижные компоненты“

ongoing from the end of 1980's. However, in spite of so much work, which have been concentrated on these systems of variable composition, no application towards the partly open system was used in thermodynamic studies.

It seems be obvious that no information on Koržinkij's „systems with mobile components“ penetrated from the world of geologists into the world of chemists during the last half of century. As a positive example, the Czech textbook „Phase equilibria for geologists“ (1997 [29]) can be mentioned including the chapter „Phase diagrams for open systems“ where publications by Koržinskij are mentioned and commented on².

4.2. Category of partly open systems

One of the important tasks of thermodynamics is to predict the equilibrium behavior (i.e., the equilibrium state) that will be achieved by system with a known initial state and under the exposition to certain contacts with the surroundings, whose state is known being invariant. Such a prediction task can be expressed by the following scheme:

initial state of system	+	invariable state of surroundings	+	character of contact between system and surroundings	→	resulting equilibrium state of system
----------------------------	---	-------------------------------------	---	--	---	---

Thermodynamic courses starts usually with the definition of thermodynamic systems and classification of the systems with respect to character of contact between a given system and its surroundings (which are considered as inexhaustible and unsaturated reservoirs). The systems are named, characterized and connected with certain functions serving as criteria for their thermodynamic equilibrium as follows:

Isolated	- adiabatic & isochoric -	$S(U)$
Thermally insulated	- adiabatic & isobaric -	$S(H)$
Closed (isochoric)	- isothermal & isochoric -	F
Closed (isobaric)	- isothermal & isobaric -	G
Open	- exchanging matter with surroundings	Ω ,

where S, U, H, F, G, Ω mean entropy, internal energy, enthalpy, Helmholtz free energy, Gibbs free energy and grand potential³, respectively.

Matter (substance) in thermodynamics is represented by sub-substances called components. The closed thermodynamic system contains amounts of several components, each of them is constant. Number of (independent) components of system means the lowest number of substances which are necessary to express composition of any homogeneous volume part of the system, which can occur as a coexisting part of equilibrium state.

In reality we can observe not only the closed systems whose every component is isolated from the surroundings but also such systems whose one component (e.g., water) is exchanged with (i.e., can escape into) the surroundings but other components (as sugar or

² In a very approximate translation: „... theory of inert and mobile components is not easy nor sufficiently investigated from the theoretical point of view. This field had been exclusively in the center of Russian school, whose main trends, conceptions and results was summarized by Bulach (1968 [30]).“

³ In physically oriented thermodynamics the open structures are defined as isothermal, isochoric and isodynamic systems with a grand potential $\Omega = U - TS - \mu N = -PV$ (see [31] or [32] as an example).

salt) remains in our system un changed (e.g., during drying or baking). Let us call as *partly open systems* such systems, which contain both the *free components* (capable of exchanging between the system and its surroundings) and *conservative components*, (whose amounts are remaining constant).

Table 1. Classification of N-component thermodynamic systems

System	Specification	Predictors =		Crite- rion function	Resulting (equilibrium) parameters
		Initial parameters of			
		system	surroundings		
Isolated N = C	adiabatic isochoric isoplectic for all N components <i>i</i>	$U, V, \{N_i\}$	-	S	$T, P, \{a_i\}$
Thermally insulated N = C	adiabatic isobaric isoplectic for all N components <i>i</i>	$H, \{N_i\}$	P	S	$T, V, \{a_i\}$
Closed isochoric N = C	isothermal isochoric isoplectic for all N components <i>i</i>	$V, \{N_i\}$	T	F	$S, P, \{a_i\}$
Closed isobaric N = C	isothermal isobaric isoplectic for all N components <i>i</i>	$\{N_i\}$	T, P	G	$S, V, \{a_i\}$
Partly open isobaric ⁴ N = C + F	isothermal isobaric isoplectic for C conservative components <i>c</i> isodynamic for F free components <i>f</i>	$\{N_c\}$	$T, P, \{a_f\}$	Z	$S, V, \{a_c\}, \{N_f\}$
Open N = F	isothermal isochoric isodynamic for all N components <i>i</i>	V	$T, \{a_i\}$	Ω	$S, P, \{N_i\}$

Now it is useful to call conditions necessary of the systems' isolation from its surroundings with respect to the exchanging components in analogy to pairs

adiabatic – isothermal and isochoric – isobaric.

The suggested pair would be

isoplectic – isodynamic

(when plethos ($\pi\lambda\eta\theta\omicron\varsigma$) denotes Greek amount and dynamis ($\delta\upsilon\nu\alpha\mu\epsilon\iota\varsigma$) means power, strength or ability).

⁴ Besides isobaric partly open systems the **isochoric partly open systems** can be used for example in earth science.

Using the last mentioned terms we can introduce the classification of N-component systems, where two different types of components, i.e., *C conservative components* and *F free components* ($C + F = N$), can be comprehended. The N-component system with F free components and C equal to (N - F) conservative components can be labeled as „N-component system with C conservative components“ or “N-component but effectively C-component system”, e.g., the system of three components consisting one free component can be called „ternary but quasibinary system“.

The above mentioned classification is given in Table 1 where N_i ($i \in 1, N$), N_f ($f \in 1, F$), N_c ($c \in 1, C$) are mole numbers, and a_i ($i \in 1, N$), a_f ($f \in 1, F$), a_c ($c \in 1, C$) are activities of components i, f and c , respectively; Symbols T, P, V are standard denomination for temperature, pressure and volume, respectively and Z stands for a new measure – a criterion function, which we may identify with an innovative thermodynamic potential for *partly open system* and which we may conventionally call *hyperfree energy*.

4.3. Hyperfree energy constructed by Legendre transformation

Criterion (or better characteristic) of thermodynamic functions H, F, G were formed using the Legendre transformation of the internal energy U . Legendre transformations generally permit the replacement of an original function g of variables $\{x_i\}$ by different (transformed) function h , in which some of the original variables x_i are replaced by their partial derivatives $\partial g / \partial x_i = d_i$, customarily subtracting the product $d_i x_i$ from its original function.

For example, for a function of two variables:

$$\begin{aligned} g &= g(x_1, x_2) & d_1 &= (\partial g / \partial x_1)_{x_2} & d_2 &= (\partial g / \partial x_2)_{x_1} \\ h_1 &= g - d_1 x_1 & h_1 &= h_1(d_1, x_2) & h_2 &= g - d_2 x_2 & h_2 &= h_2(x_1, d_2) \end{aligned} \quad (1)$$

The partial derivatives of the internal energy U as a function of variables $S, V, \{N_i\}$ are the resulting variables T, P , and chemical potentials $\{\mu_i\}$:

$$T = (\partial U / \partial S)_{V, n_i}; \quad P = - (\partial U / \partial V)_{S, n_i}; \quad \mu_i = (\partial U / \partial N_i)_{S, V, n_j \neq i} \quad (2),$$

The chemical potential of i -th component is depending on its chemical activity a_i (R means molar gas constant and μ_i^0 is the chemical potential at the standard state of i -th component which is equal to the standard Gibbs free energy G_i^0 of a pure component i :

$$\mu_i(T, P) = \mu_i^0(T, P) + RT \ln a_i = G_i^0(T, P) + RT \ln a_i \quad (3).$$

Function	Definition equation	Fundamental equation (4)
Internal energy	U	$U = U(S, V, \{N_{ij}\})$
Enthalpy:	$H = U + PV;$	$H = H(S, P, \{N_{ij}\})$
Helmholtz free energy:	$F = U - TS;$	$F = F(T, V, \{N_{ij}\})$
Gibbs free energy:	$G = H - TS;$	$G = G(T, P, \{N_{ij}\})$

If the mole quantity of components $\{N_i\}$ play the role of predictors then (in addition to the internal energy further three „energy functions“ can be predictably formed using the above shown Legendre transformation:

Differentiating the definition equations (see the left sides of eq. 4 in the last table) and by substituting basic relation for the total differential of internal energy dU

$$dU = T dS - P dV + \mu_1 dN_1 + \dots + \mu_i dN_i + \dots + \mu_N dN_N \quad (5)$$

following total differentials for the enthalpy and the free energies are located, i.e.,

$$dH = T dS + V dP + \sum_i \mu_i dN_i \quad (6)$$

$$dF = - S dT - p dV + \sum_i \mu_i dN_i \quad (7)$$

$$dG = - S dT + V dP + \sum_i \mu_i dN_i \quad (8),$$

Consequently the following relations for partial derivatives are easy to derive:

$$(\partial H/\partial N_i)_{S,P,N_{j \neq i}} = (\partial F/\partial N_i)_{T,V,N_{j \neq i}} = (\partial G/\partial N_i)_{T,P,N_{j \neq i}} = \mu_i \quad (9)$$

$$(\partial H/\partial S)_{P,N_i} = T; \quad (\partial F/\partial V)_{T,N_i} = - P \quad (10), (11)$$

$$(\partial H/\partial P)_{S,N_i} = (\partial G/\partial P)_{T,N_i} = V; \quad (\partial F/\partial T)_{V,N_i} = (\partial G/\partial T)_{P,N_i} = - S \quad (12), (13)$$

$$[\partial(H/P)/\partial(1/P)]_{S,N_i} = [\partial(F/T)/\partial(G/T)]_{P,N_i} = - S \quad (14)$$

$$[\partial(G/P)/\partial(1/P)]_{T,N_i} = F; \quad [\partial(G/T)/\partial(1/T)]_{P,N_i} = H \quad (15), (16).$$

Assuming that the internal energy U is a homogeneous (first order) function with respect to the other extensive thermodynamic quantities the Euler equation for internal energy is found in the form:

$$U = T S - P V + \mu_1 N_1 + \dots + \mu_i N_i + \dots + \mu_N N_N \quad (17),$$

and upon the differentiating of (17) and comparing it with (5) the Gibbs-Duhem equation is straight forwarded:

$$S dT - V dP + N_1 d\mu_1 + \dots + N_i d\mu_i + \dots + N_N d\mu_N = 0 \quad (18).$$

Similarly the Euler equation for the enthalpy H and free energies F and G undertake the forms:

$$H = T S + \sum_i \mu_i N_i \quad (19)$$

$$F = - P V + \sum_i \mu_i N_i \quad (20)$$

$$G = \sum_i \mu_i N_i \quad (21),$$

Upon the differentiating of any of these forms and by comparing them with (17) the corresponding relations of (6-8) is obtained bearing the transparent similarity with the Gibbs-Duhem equation (18).

In the case when mole amounts of only C components (with amounts $N_{c1}, \dots, N_c, \dots, N_C$) from all N components play the role of predictors and amounts of other F (= N - C) components are adjusted by their activities ($a_{f1}, \dots, a_f, \dots, a_F$) and/or their chemical potentials ($\mu_{f1}, \dots, \mu_f, \dots, \mu_F$) in surroundings the new function (a thermodynamic potential) can be formed by the standard Legendre transformation as previously guarded within the new term of *hyperfree energy*:

$$Z = G - \sum_f \mu_f dN_f; \quad Z = Z(T, P, \{N_c\}, \{\mu_f\}) \quad (22)$$

with its total differential

$$dZ = -S dT + V dp + \sum_c \mu_c dN_c - \sum_f N_f d\mu_f \quad (23).$$

The following equations are then found for partial derivatives of this hyperfree energy:

$$(\partial Z / \partial n_c)_{T,P,N_{j \neq c}, \mu_f} = \mu_c; \quad (\partial Z / \partial \mu_f)_{T,P,N_c, \mu_{g \neq f}} = -n_f \quad (24), (25).$$

Hyperfree energy Z possesses its Euler equation in the form:

$$Z = \sum_c \mu_c N_c \quad (26)$$

and the matching Gibbs-Duhem equation (18) follows by the differentiating (26) and by comparing it with (23).

It was proved (see Appendix B in ref. [5]) that the criterion function for equilibrium in partly open system is just the above derived hyperfree energy Z so that the condition of equilibrium in partly open system is represented by the minimum of hyperfree energy Z.

4.4. Quasimolar fractions, quasimolar quantities and common tangent in quasibinary systems

One of problems connected with partly open systems is the fact that their mass or molar amount of *all* components is not constant. Magnitude of system cannot be characterized by total mass or total number of moles of all components, so that usual molar fractions or molar thermodynamic quantities are not adequate for a satisfactory description of partly open systems.

Magnitude of closed N-component system is usually characterized by the sum of mole numbers (molar amounts) of all N components N_m

$$N_m = \sum_i N_i \quad (27)$$

Using this quantity (N_m) the mole fractions X_i and molar quantities (as molar volume V_m , molar entropy S_m , molar enthalpy H_m , molar free energies F_m , and G_m) are determined:

$$X_i = N_i / N_m; \quad V_m = V / N_m; \quad S_m = S / N_m; \quad H_m = H / N_m; \quad F_m = F / N_m; \quad G_m = G / N_m \quad (28)$$

The Euler equation for G_m gives then a form

$$G_m = \sum_{i=1} \mu_i X_i \quad (29)$$

and due to the fact (resulting from (27))

$$\sum_{i=1} X_i = \sum_{i=1} (N_i/N_m) = \sum_{i=1} (N_i/(\sum_{i=1} N_i)) = 1; \quad X_1 = 1 - \sum_{i=2} X_i \quad (30)$$

the equation (29) is equivalent to

$$G_m = \mu_1 + \sum_{i=2} (\mu_i - \mu_1) X_i \quad (31)$$

Considering a two-phase field ($\alpha + \beta$) in phase diagram of closed (isothermal-isobaric) binary system of components A and B (system A-B) the boundaries of this two-phase field can be calculated using the rule of common tangent. Explicitly, the points limiting boundaries of two-phase region are the points where common tangent touches the two curves expressing molar Gibbs energies as functions of molar fraction X_B (at given temperature T) for phases α ($G_m^\alpha = f(X_B)$) and β ($G_m^\beta = f(X_B)$) as it is shown in Fig. 1.

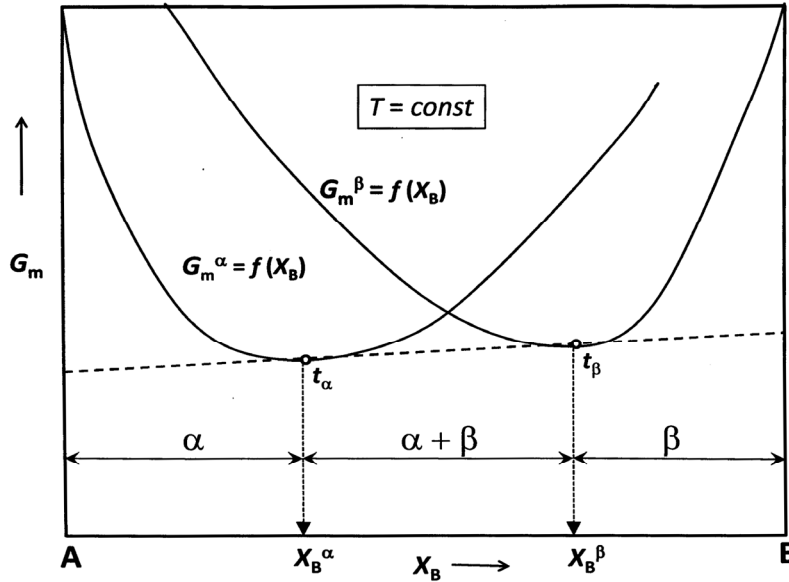


Fig. 1. Common tangent in binary system A-B. Common tangent passed through tangent points t_α and t_β whose X_B coordinates (molar fractions X_B^α and X_B^β) determined the boundaries of two-phase ($\alpha + \beta$) region.

The rule of common tangent for two-phase region of binary closed system A-B is derived from two conditions of equilibrium coexistence of phase α and phase β :

$$\mu_A^\alpha = \mu_A^\beta (\equiv \mu_A^*); \quad \mu_B^\alpha = \mu_B^\beta (\equiv \mu_B^*) \quad (32),$$

where μ_A^α , μ_A^β are chemical potentials of component A and μ_B^α , μ_B^β chemical potentials of component B in phases α and β . If molar Gibbs energies of the phases are denoted by G_m^α and G_m^β , and molar fractions by X_B^α , X_A^α , X_B^β , X_A^β and the relation (30) is applicable when applying (31). The following equations and their difference are obtained

$$G_m^\alpha = \mu_A^* + X_B^\alpha (\mu_B^* - \mu_A^*) \quad (33)$$

$$G_m^\beta = \mu_A^* + X_B^\beta (\mu_B^* - \mu_A^*) \quad (34)$$

$$(G_m^\beta - G_m^\alpha) = (X_B^\beta - X_B^\alpha) (\mu_B^* - \mu_A^*) \quad (35)$$

and upon the partial differentiating (33), (34) and by modification of (35) the equations expressing the rule of common tangent are achieved:

$$(\partial G_m^\alpha / \partial X_B^\alpha) = (\partial G_m^\beta / \partial X_B^\beta) = (G_m^\beta - G_m^\alpha) / (X_B^\beta - X_B^\alpha) [= (\mu_B^* - \mu_A^*)] \quad (36).$$

For partly open system the sum of amount of all components (N_m) is changed and only sum of all conservative components N_q is constant, i.e.:

$$N_q = \sum_c N_c \quad (37)$$

Instead of molar quantities the quasimolar fractions Y_i and quasimolar volume V_q , entropy S_q , enthalpy H_q , Gibbs free energy G_q (as well as quasimolar hyperfree energy Z_q) are accessible:

$$Y_i = N_i / N_q; \quad V_q = V / N_q; \quad S_q = S / N_q; \quad H_q = H / N_q; \quad G_q = G / N_q; \quad Z_q = Z / N_q \quad (38).$$

The Euler equation for Z_q gives then a form

$$Z_q = \sum_{c=1} \mu_c Y_c \quad (39)$$

and due to the fact (resulting from (37))

$$\sum_{c=1} Y_c = \sum_{c=1} (N_c / N_q) = \sum_{c=1} (N_c / (\sum_{c=1} N_c)) = 1; \quad Y_{c1} = 1 - \sum_{c=2} Y_c \quad (40)$$

the equation (39) is equivalent to

$$Z_q = \mu_{c1} + \sum_{c=2} (\mu_c - \mu_{c1}) Y_c \quad (41).$$

The boundary of two-phase field ($\alpha + \beta$) in phase diagram of partly open ternary but quasibinary system of two conservative components A and B and one free component C (system A-B-(C)) is calculated per analogism using the rule of common tangent to curves of quasimolar hyperfree energies expressed as functions of the quasimolar fraction Y_B (at given temperature T and at given activity of free component C (a_C) for phases α ($Z_q^\alpha = f(Y_B)$) and β ($Z_q^\beta = f(Y_B)$) as it is shown in Fig. 2. The rule of common tangent for two phase region of the ternary but quasibinary partly open system A-B-(C) is derived from two conditions of equilibrium coexistence of phase α and phase β :

$$\mu_A^\alpha = \mu_A^\beta (\equiv \mu_A^*); \quad \mu_B^\alpha = \mu_B^\beta (\equiv \mu_B^*) \quad (42),$$

and equations expressing the conditions of common tangent could be derived by procedure analogical to (53)-(56) in the form:

$$(\partial Z_q^\alpha / \partial Y_B^\alpha) = (\partial Z_q^\beta / \partial Y_B^\beta) = (Z_q^\beta - Z_q^\alpha) / (Y_B^\beta - Y_B^\alpha) [= (\mu_B^* - \mu_A^*)] \quad (43).$$

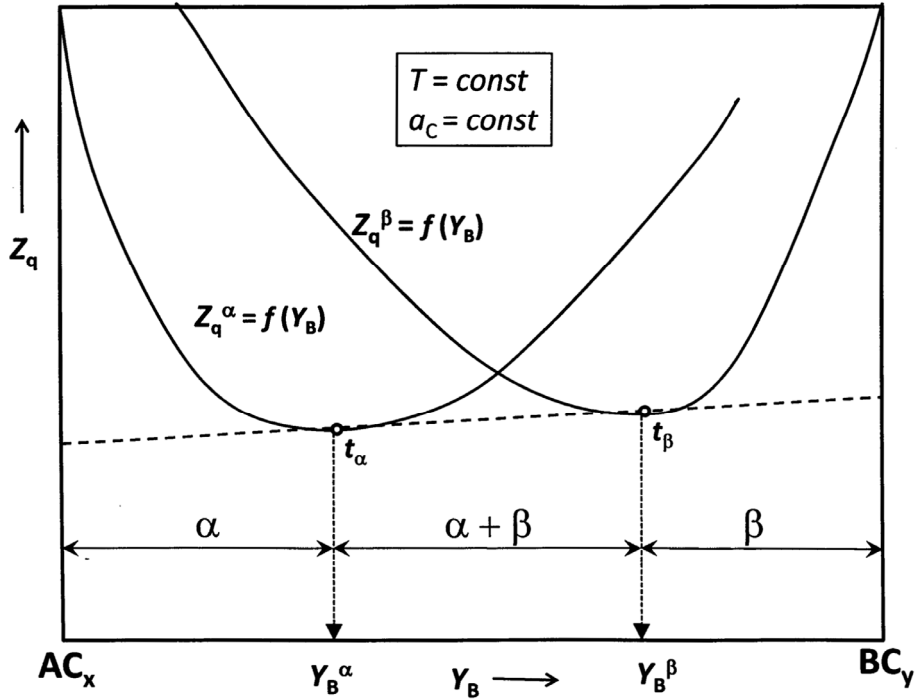


Fig. 2. Common tangent in quasibinary system A-B-(C). Common tangent passed through tangent points t_α and t_β whose Y_B coordinates (molar fractions Y_B^α and Y_B^β) determined the boundaries of two-phase ($\alpha + \beta$) region.

Application is shown in the part 4.6. of this article (see Fig. 3).

4.5. Clapeyron equations for quasiunary partly open systems

The Clapeyron equation can be derived from one of rules for partial derivations valid for implicit function $F = F(x, y, z) = \text{const}$

$$(\partial y / \partial x)_{F,z} = - (\partial F / \partial x)_{y,z} / (\partial F / \partial y)_{x,z} \quad (44).$$

Classical form of Clapeyron equation could be derived from (44) using $\Delta_t G$ (integral change of Gibbs energy at transition) instead of F , and T, P (temperature, pressure) instead of x, y .

The free energy G of a closed system at the equilibrium corresponding to coexistence of an initial phase α with an adequate final phase β during a first-order transition could be constructed from the free energies G_α, G_β of both phases weighted by the degree of phase conversion ξ

$$G = (1 - \xi) G_\alpha + \xi G_\beta \quad (45).$$

Condition of equilibrium at phase transition (index t) in a closed system requires

$$\partial G / \partial \xi \equiv \Delta_t G = G_\beta - G_\alpha = 0 \quad (46)$$

where $\Delta_t G(T, P) = \text{const}$ means the integral change of free energy at the transition $\alpha \rightarrow \beta$, whose relation to temperature T and pressure P is given by

$$\Delta_t G = \Delta_t U + P \Delta_t V - T \Delta_t S \quad (47),$$

$$\Delta_t G = \Delta_t H - T \Delta_t S = 0 \quad \Rightarrow \quad \Delta_t S = \Delta_t H / T_t \quad (48)$$

where $\Delta_t H$, $\Delta_t S$, $\Delta_t U$, $\Delta_t V$ are the integral change of enthalpy, entropy, internal energy and volume (corresponding the transition), respectively.

Applying (44) to $\Delta_t G(T, P)$ as $F(x, y, z)$ and T, P as x, y the following equation is found

$$(\partial P / \partial T)_{\Delta_t G} = - (\partial \Delta_t G / \partial T)_P / (\partial \Delta_t G / \partial P)_T \quad (49)$$

and using (47) and (48) the Clapeyron equation is recovered:

$$(\partial P / \partial T)_{\Delta_t G} = \Delta_t S / \Delta_t V = (\Delta_t H / T_t) / \Delta_t V = \Delta_t H_m / (T_t \Delta_t V_m) \quad (50),$$

where $\Delta_t H_m = \Delta_t H / N_m$ and $\Delta_t V_m = \Delta_t V / N_m$ are molar integral change of enthalpy and volume, respectively.

Similar procedure can be used for a transition in a partly open system with one conservative (c -th) and two free (f -th and g -th) components and its hyperfree energy Z is then constructed from the fractional hyperfree energies Z_α (of initial phase α) and Z_β (of final phase β) at advancement (degree of conversion) ξ

$$Z = (1 - \xi) Z_\alpha + \xi Z_\beta \quad (51)$$

From equilibrium condition the integral hyperfree energy change $\Delta_t Z$ can be found to equal zero, i.e.,

$$\partial Z / \partial \xi \equiv \Delta_t Z = Z_\beta - Z_\alpha = 0 \quad (52),$$

where $\Delta_t Z(T, P, \mu_f, \mu_g) = \text{const}$ means integral change of hyperfree energy at the transition $\alpha \rightarrow \beta$, which the relation to temperature T , pressure P and chemical potentials μ_f, μ_g is given by

$$\Delta_t Z = \Delta_t G - \Delta_t N_f \mu_f - \Delta_t N_g \mu_g = 0 \quad (53).$$

It should be noted, then for system of one conservative component the total molar amount of all conservative components N_q is identical to the molar amount of the c -th component N_c .

At this point some problem arises because we are usually unable to adjust chemical potentials but we can do tuning for activities of free components. Thus we have to substitute (3) with the standard Gibbs free energy of free components G_i^0

$$\Delta_t Z = [\Delta_t G - \Delta_t N_f G_f^0 - \Delta_t N_g G_g^0] - RT_t (\Delta_t N_f \ln a_f + \Delta_t N_g \ln a_g) = 0 \quad (54).$$

Three member of the right side (in squared brackets) have the meaning of an integral change of Gibbs free energy of the decomposition (d) under study

$$\alpha \rightarrow \beta + \Delta_t N_f f(G) + \Delta_t N_g g(G),$$

where $f(G)$ and $g(G)$ denotes free components f and g in gaseous state (G). The integral change of Gibbs energy at the mentioned decomposition (index d) can be introduced as a new quantity $\Delta_d G$

$$\Delta_d G \equiv \Delta_t G - \Delta_t N_f G_f^0 - \Delta_t N_g G_g^0 \quad (55),$$

and its dependences on temperature and pressure are expressed by relations

$$\Delta_d G = \Delta_d H - T \Delta_d S = \Delta_d U + P \Delta_d V - T \Delta_d S \quad (56),$$

where integral quantities $\Delta_d H$, $\Delta_d S$, $\Delta_d V$ are defined as

$$\Delta_d H = \Delta_t H - \Delta_t N_f \cdot H_f^0 - \Delta_t N_g \cdot H_g^0 \quad (57)$$

$$\Delta_d S = \Delta_t S - \Delta_t N_f \cdot S_f^0 - \Delta_t N_g \cdot S_g^0 \quad (58)$$

$$\Delta_d V = \Delta_t V - \Delta_t N_f \cdot V_f^0 - \Delta_t N_g \cdot V_g^0 \quad (59).$$

The equation (54) can be then written as

$$\Delta_t Z = \Delta_d G - RT_t (\Delta_t N_f \ln a_f + \Delta_t N_g \ln a_g) = \Delta_d H - T_t (\Delta_d S + \Delta_t N_f \ln a_f + \Delta_t N_g \ln a_g) = 0$$

so that

$$\Delta_d H / T_t = \Delta_d S + \Delta_t N_f \ln a_f + \Delta_t N_g \ln a_g \quad (60).$$

Using these quantities the partial derivatives of Z_{tr} can be written in the following form

$$(\partial \Delta_t Z / \partial T) = - \Delta_d S - R(\Delta_t N_f \ln a_f + \Delta_t N_g \ln a_g) = - \Delta_d H / T_t \quad (61),$$

$$(\partial \Delta_t Z / \partial P) = \Delta_d V - RT_t (\Delta_t N_f \partial \ln a_f / \partial P + \Delta_t N_g \partial \ln a_g / \partial P) \quad (62),$$

$$(\partial \Delta_t Z / \partial \ln a_f) = - RT_t \Delta_t N_f \quad (63),$$

$$(\partial \Delta_t Z / \partial \ln a_g) = - RT_t \Delta_t N_g \quad (64),$$

and the ensuing Clapeyron equation is furnished by

$$(\partial P / \partial T) = (\Delta_d H / T_t) / (\Delta_d V + RT_t (\Delta_t N_f (\partial \ln a_f / \partial P) + \Delta_t N_g (\partial \ln a_g / \partial P))) \quad (65).$$

If the surrounding atmosphere is considered to be an ideal mixture of ideal gases (containing free components as gases f and g in a mixture with molar fractions X_f^G , X_g^G) then partial pressures p_f and p_g of the gases in atmosphere with pressure P are given by:

$$p_f = X_f^G P \quad ; \quad p_g = X_g^G P \quad (66),$$

and if the standard molar volume of the gaseous free components is expressed by relation (with P^0 as reference pressure)

$$V_f^0 = V_g^0 = RT / P^0 \quad (67),$$

then for activities of free components we can write

$$a_i = X_i^G(P/P^0) \Rightarrow \ln a_i = \ln X_i^G + \ln (P/P^0) \Rightarrow \quad \partial \ln a_i / \partial P = 1/P_t \quad (68)$$

and the Clapeyron equation for dP/dT undertake the following form (using (57) and (59))

$$\partial P / \partial T = (\Delta_d H / T_i) / (\Delta_d V - RT_t (1/P^0 - 1/P_t)) (\Delta_t N_f + \Delta_t N_g) \quad (69).$$

A more simple form can be found for the Clapeyron equation ($d \ln a_f / d \ln a_g$) as follows:

$$(\partial \ln a_f / \partial \ln a_g)_{\Delta t Z, T, P} = -(-RT_t \Delta N_g^{lr}) / (-RT_t \Delta N_f^{lr}) = -\Delta_t N_g / \Delta_t N_f = -\Delta_t Y_g / \Delta_t Y_f \quad (70).$$

and the entire form for the alternative ($d \ln a_f / dT$) is then

$$(\partial \ln a_f / \partial T)_{\Delta t Z, P, a_g} = -(\Delta_d H / T_i) / (RT_t \Delta_t N_f) \quad (71).$$

If new quantities $\bar{\mathcal{E}}$ and $\Delta_t \bar{\mathcal{E}}$ are introduced by formulas

$$\bar{\mathcal{E}} \equiv Z/T \quad \text{and} \quad \Delta_t \bar{\mathcal{E}} \equiv \Delta_t Z/T \quad (72)$$

a more simple relation between the activity of free component and temperature can be obtained from the relation

$$(\partial \Delta_t \bar{\mathcal{E}} / \partial (1/T)) = (\partial (\Delta_d G / T) / \partial (1/T)) = \Delta_d H \quad (73)$$

together with

$$(\partial \Delta_t \bar{\mathcal{E}} / \partial \ln a_f) = -R \Delta_t N_f \quad (74).$$

The resulting Clapeyron equation comprise the form

$$(\partial \ln a_f / \partial (1/T)) = (\Delta_d H / R) / \Delta_t N_f \quad (75)$$

and/or

$$(\partial \ln a_f / \partial (1/T)) = (\Delta_d H_q / R) / \Delta_t Y_f \quad (76)$$

where

$$\Delta_d H_q = \Delta_d H / N_q = \Delta_d H / N_c \quad \text{and} \quad \Delta_t Y_f = \Delta_t N_f / N_q = \Delta_t N_f / N_c \quad (77).$$

4.6. Applications and illustrations

In the recent lecture [33] were introduced some applications of the thermodynamic potentials and Clapeyron equations derived above. Three examples of such applications are used for illustration in the following paragraphs.

4.6.1 The equation of common tangent (43) could be applied to $T - y_{Mn}$ (y_{Mn} is weight fraction of Mn_3O_4 in initial mixture of Mn_3O_4 and Fe_3O_4) diagram of the ternary but quasibinary system Fe-Mn-(O) or FeO_x - MnO_z in air ($a_{O_2} = 0,21$) published in [17].

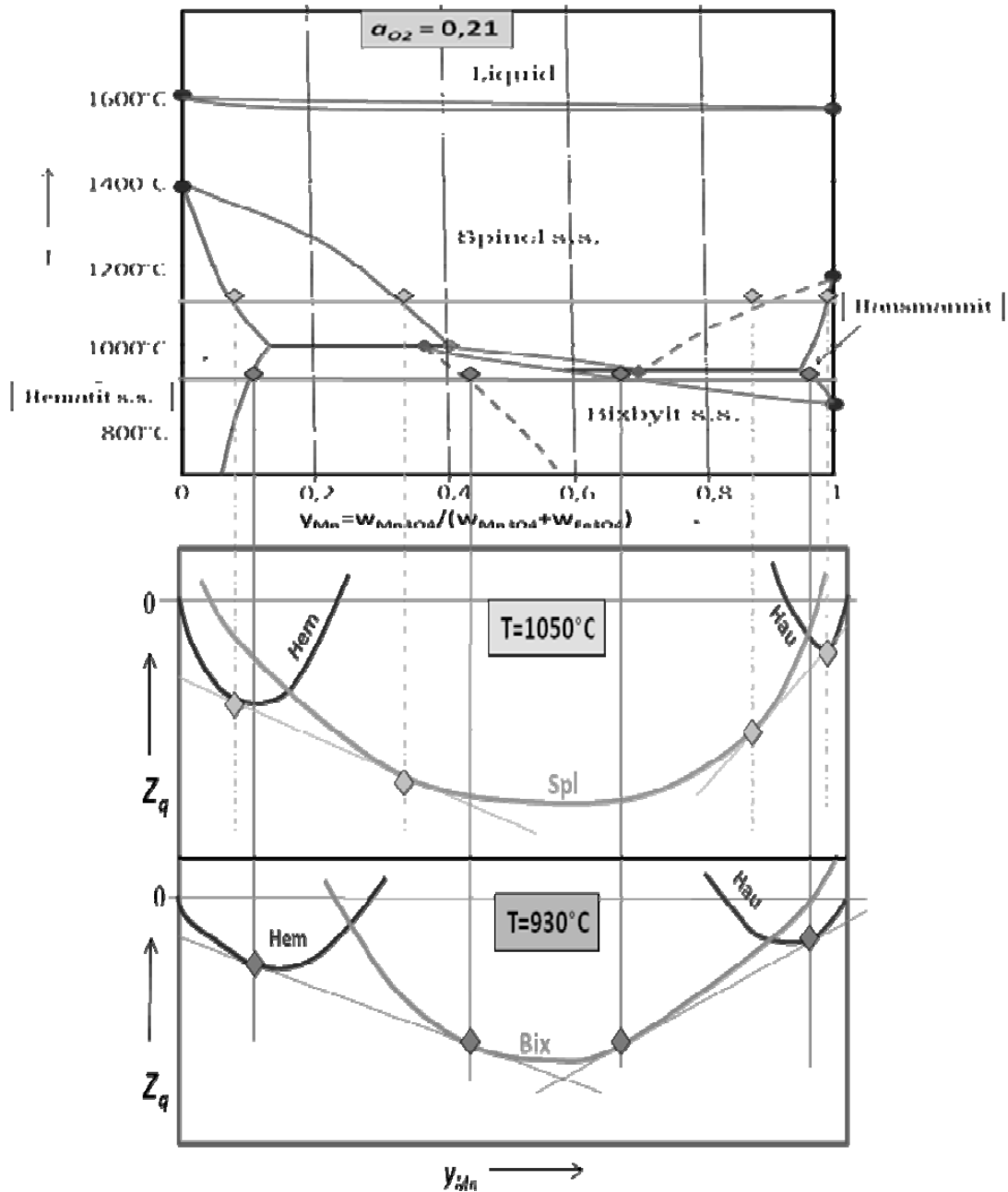


Fig. 3: Diagram of quasibinary system FeO_x - MnO_2 or Fe - Mn -(O) in air atmosphere and its correspondence to quasimolar hyperfree energy dependences on quasimolar fraction $Z_q = Z_q(y_{Mn})$. The symbols Hem, Spl, Hau, Bix mean mixed phases of Hematite ($Fe_{2-x}Mn_xO_3$), Spinel ($Mn_xFe_{3-x}O_{4+\square}$), Hausmannite ($Mn_{3-x}Fe_xO_4$) and Bixbyite ($Mn_{2-x}Fe_xO_3$) phases.

4.6.2 The Clapeyron equation (76) could be applied to the $1/T$ vs $\log a_{O_2}$ plot (Fig. 5) corresponding to the T - X_O phase diagram of Fe - O system (Fig. 4) published by Darken Gurry [13]

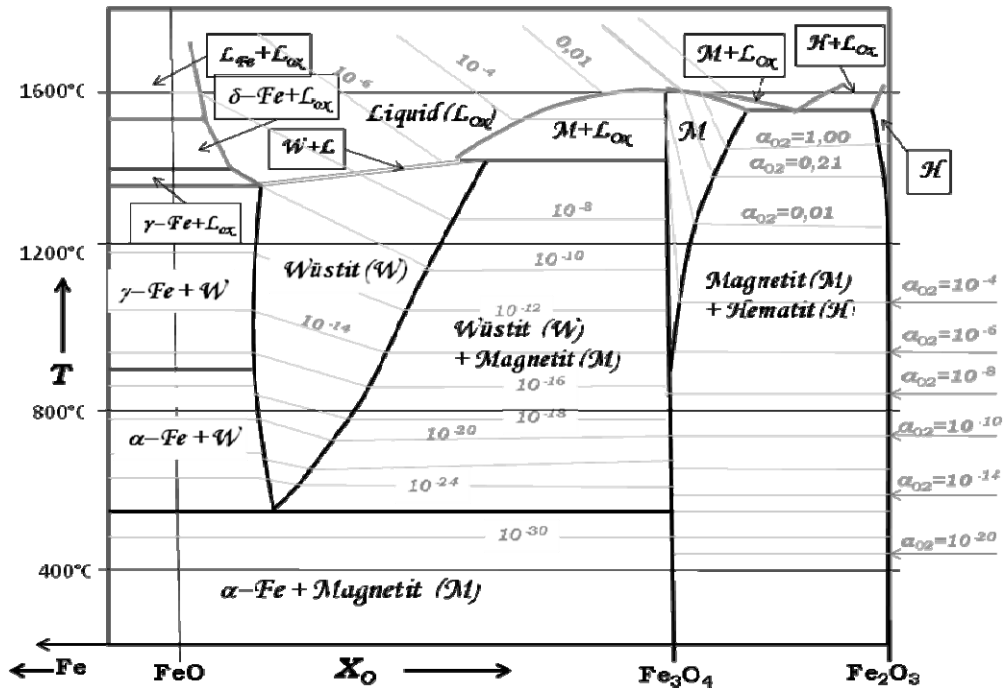


Fig. 4. Phase relations in binary system Fe-O found by Darken & Gurry [17] plotted in $T-X_{O_2}$ diagram

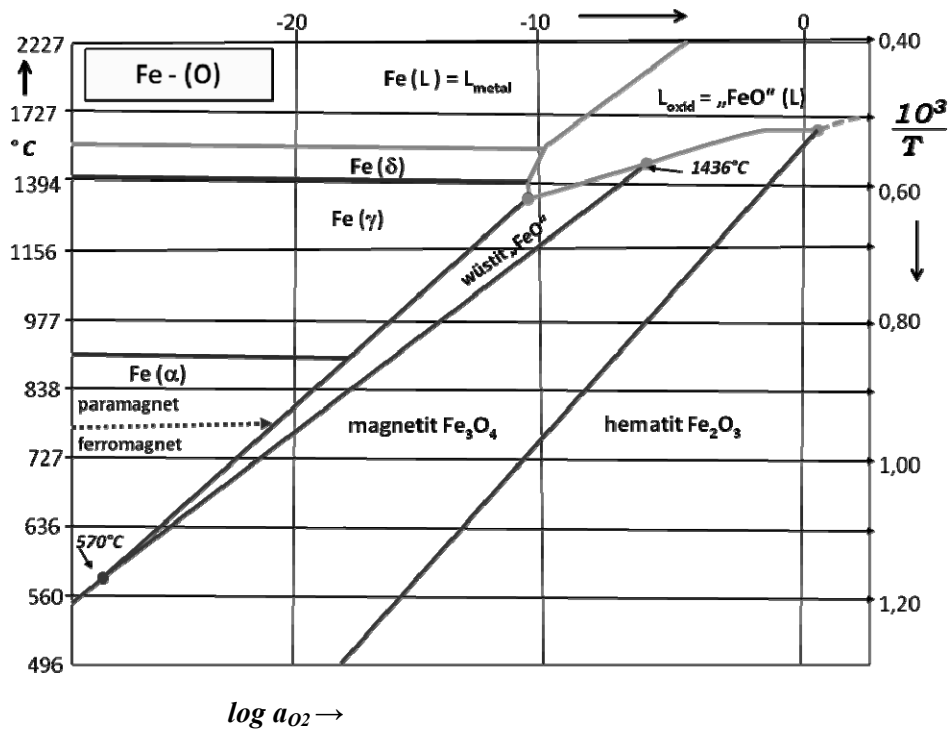


Fig. 5. Phase relations in binary system Fe-O found by Darken & Gurry [17] plotted in $1/T - \log a_{O_2}$ diagram (as quasiunary system Fe - (O))

4.6.3 The Clapeyron equation (70) could be illustrated by phase relations in ternary system Fe-S-O plotted in $\log a_S - \log a_{O_2}$ diagram (as quasiunary system Fe-(O-S)) according to book of Koržinskij [18] as shown in Figure 6.

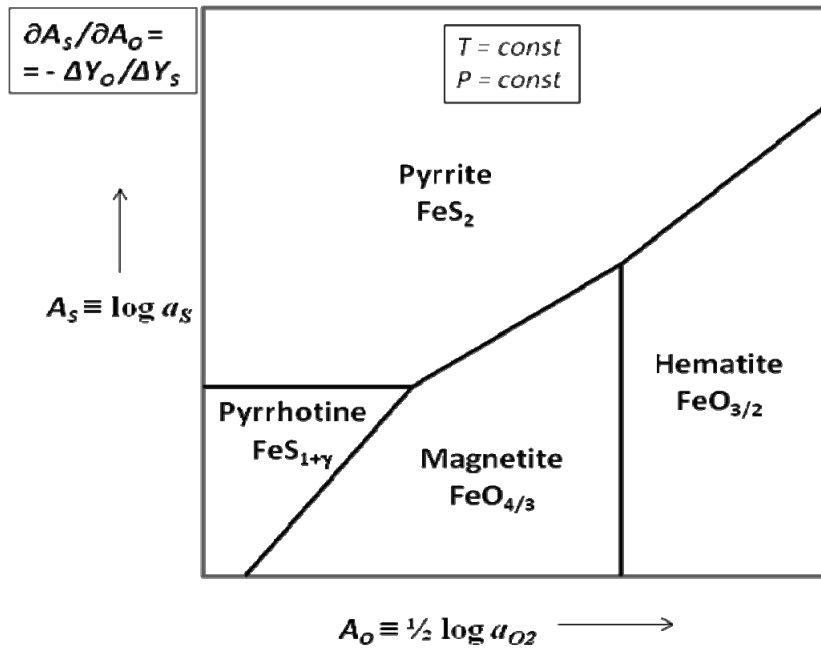


Fig. 6: Phase relations in ternary system Fe-S-O plotted in $\log a_S - \log a_O$ diagram (as quasiunary Fe-(S-O) system) according to Koržinskij [18].

4.6.4 Applications on Systems of Oxide Superconductors

Thermodynamics of partly open system can be applied to oxide systems exhibiting high temperature superconductivity [34-38] e.g. Y-Ba-Cu-O [35,36], Bi-Sr-Ca-Cu-O, Tl-Ba-Ca-Cu-O and Hg-Ba-Ca-Cu-O [34,38] as it is shown in the following figures.

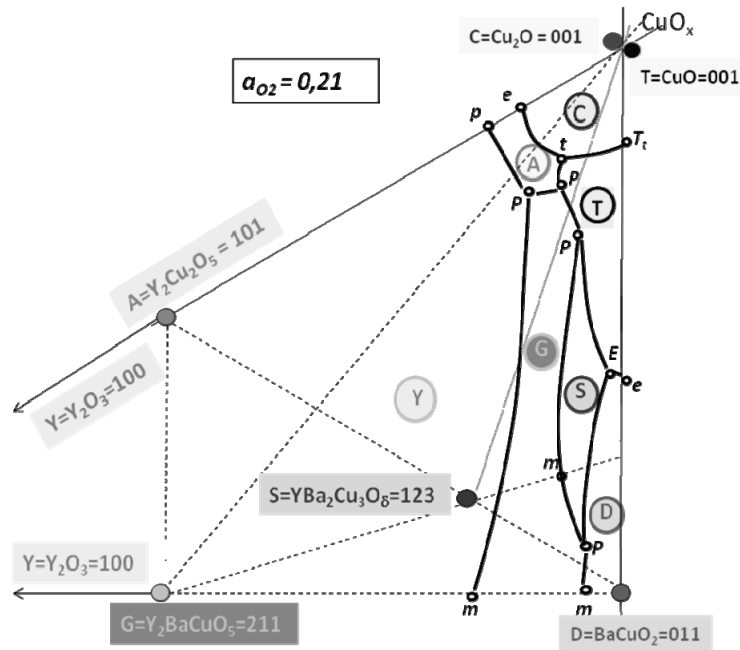


Fig. 7: Primary crystallization fields (PCF) in system Y-Ba-Cu-O under air atmosphere according to [35]

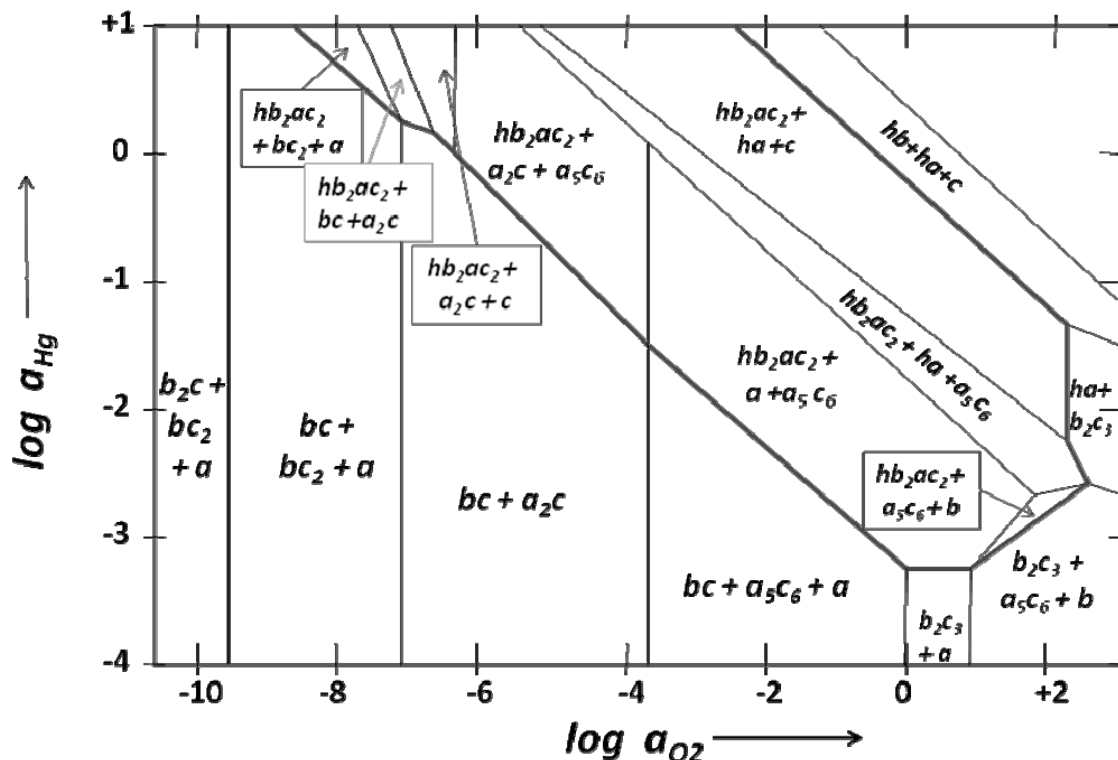


Fig. 8: Phase relations in system Hg-Ba-Ca-Cu-O for section Ba:Ca:Cu = 2:2:3 at 500°C plotted in diagram $\log a(\text{Hg})$ vs. $\log a(\text{O}_2)$ according to [34]:

$hb_2ac_2 = \text{HgBa}_2\text{CaCu}_2\text{O}_6$ (superconductive phase), $b_2c = \text{Ba}_2\text{CuO}_{3.1}$, $bc_2 = \text{BaCu}_2\text{O}_2$, $a = \text{CaO}$, $bc = \text{BaCuO}_2$, $a_2c = \text{Ca}_2\text{CuO}_3$, $c = \text{CuO}$, $a_5c_6 = \text{Ca}_{0.83}\text{CuO}_{1.83}$, $ha = \text{HgCaO}_2$, $hb = \text{HgBaO}_2$, $b_2c_3 = \text{Ba}_2\text{Cu}_3\text{O}_{6-x}$, $b = \text{BaO}_2$

References 4

1. Callen H. B.: *Thermodynamics*; 394 pp., John Wiley, New York, 1960.
2. Holba P.: Rovnováhy spinelů $\text{Mn}_x\text{Fe}_{3-x}\text{O}_{4+\gamma}$ s plynným kyslíkem a jejich interpretace (*Equilibria of Mn-Fe-O Spinel with Gaseous Oxygen and Their Interpretation*), Praha, září 1970, 110 pp. - Thesis in Czech submitted to VŠChT (Tech. Univ. Chem. & Technol.), Prague, in February 1971.
3. Holba P.: Modely rozpořádání ve fyzikálně-chemické analýze rovnovážného chování krystalických látek (*Disorder models in physicochemical analysis of equilibrium behavior of crystalline phases*), Praha, prosinec 1985, 222 p. - Thesis in Czech defended at VŠChT (Techn. Univ. Chem. and Technol.), Prague, in September 1986
4. Holba P.: *Thermodynamics and Ceramic Systems, in Structure and Properties of Ceramic Materials* (A. Koller, Editor), Elsevier, Amsterdam – London – New York – Tokyo 1994, pp.17-113.
5. Holba P.: *Thermodynamics of Partially Open Systems*, Czech J. Phys. **B42**, No.6, 549-575 (1992)
6. PRAHA, *atlas ortofotomap*; Kartografie - IMIP – Geodis, Praha (2004), 394 p.

7. Gibbs J.W.: *On the Equilibrium of Heterogeneous Substances*, Trans. Connecticut Acad. **3**, 108-248 (1876), 343-524 (1878)
8. Lewis G.N.: *Outline of a New System of Thermodynamic Chemistry*, Proc. Am. Acad. **43** 259-93 (1907); Z. physikal. Chem. **61** 129 (1908)
9. Sørensen, S.P.L.: Enzymstudier II. Om Maalingen og Betydningen af Brintion-koncentrationen ved enzymatiske Processer. Meddelelser fra Carlsberg Laboratoriet, (Enzym Studies II. *On Measurement and Importance of Hydrogen-Ion Concentration at Enzymatic Processes*); **8**, 1-153 + 373-7 (1909); (German version in Biochemische Zeitschrift **21**, 131-140 (1909))
10. Koržinskij, D.S.: Podvižnost i inertnost komponentov pri metasomaze (*Mobility and inertness of components at metamorphosis*); Izv. Akad. nauk SSSR, ser. geol., (1936) No.1
11. Ellingham H. J. T., *The physical chemistry of process metallurgy*. J. Soc. Chem. Ind. (London) **63** 125 (1944)
12. Richardson F.D. & Jeffes J.H.E.: "Free energies of formation of metal oxides as a function of temperature" J. Iron Steel Inst., vol. 160., pp. 261-73 (1948).
13. Darken L.S & Gurry R.W.: *The system iron – oxygen I. + II.*; J. Am. Chem. Soc., **67**. [8]. 1398-1412 (1945) + J. Am. Chem. Soc. **68**, 798-816 (1946).
14. Pourbaix M.J.N.: *Thermodynamics of Dilute Aqueous Solutions*, 136 pp. E.Arnold & Co., London (1949) (French original: „Thermodynamique des Solutions Aqueuses Diluées“ from 1946)
15. Garrels R. M.: *Mineral Equilibria*, New York (1960)
16. Garrels R. M. & Christ C. L. *Solutions, minerals, and equilibria*. New York: Harper & Row, (1965) 450 p.
17. Muan, A. & E. F. Osborn, *Phase Equilibria Among Oxides in Steelmaking*, 236 pp., Addison- Wesley, Reading, MA, (1965).
18. Koržinskij D.S.: Fizikochimičeskie osnovy analiza paragenesisov mineralov; Izd. Akad. nauk SSSR, Moskva (1957), 184 pp.; English translation: *Physicochemical basis of the analysis of the paragenesis of minerals*, Consultants Bureau, New York (1959)
19. Koržinskij D.S.: Sootnošenje meždu mineralogičeskim sastavom i veličinoj chimičeskich potencialov komponentov (*Relations between mineralogical composition and values of chemical potential of components*); Zap. Vseross. min. obšč., (1944), č.73, No.1
20. Koržinskij D.S.: Termodinamičeskiye potencialy otkrytych sistem i primer ich primenenija v geochimii (*Thermodynamic Potentials of Open Systems and Example of their Application in Geochemistry*); Izv. Sektora fiz.-chim. analiza Akad. nauk SSSR (1949), **19**
21. Nikolajev V.A.: Ob odnom iz osnovnych uravnenij termodinamiky i ego primeněni k otkrytym sistemam (*On one of the Fundamental Equations of Thermodynamics and on its Application to Open Systems*); Zap. Vses. min. obšč., (1954), č.83, No.4
22. Verhoogen J.: *Thermodynamics of a magmatic gas phase*; Univ of California publ., Bull. Depart. Geol. Sci., (1949), **28**, No.5

23. Thompson J.B.: *The thermodynamic basis for the mineral facies concept.*, Am. Journ. Sci. (1955), **253**, No.2, 65-103
24. Palatnik L.S. & Landau A.I.: K teorii ravnovesia geterogennych mnogokomponentnykh system (*On Theory of Equilibrium of Heterogeneous Multicomponent Systems*); Dokl. Akad. nauk SSSR, (1955) **102** No.1, 125 + Fazovyje ravnovesia mnogokomponentnykh sistemach (*Phase Equilibria of Multicomponent Systems*); 406 pp., Izd. Charkov. univ., Charkov (1961)
25. Koržinskij D.S.: Vyvod termodinamičeskich potencialov sistem s podvižnymi komponentami (*Derivation of Thermodynamic Potentials of Systems with Mobile Components*); Dokl. Akad. nauk SSSR, (1956) **106** No.2
26. Tretjakov, Ju D.: Termodinamika ferritov (*Thermodynamics of Ferrites*); 304 pp., Izd. Chimija, Leningrad (1967)
27. Tretjakov, Ju. D.: Chimija nestechimetričeskych okislov (*Chemistry of Nonstoichiometric Oxides*); 364 pp., Izd. Mosk.Univ., Moskva (1974)
28. Whittler J.D, Vanderah T.A., Roth R.S, McMurdie H.F.: *Phase Diagrams for High T_c Superconductors*, National Institute of Standards and Technology, published by The American Ceramic Society, Westerville, Ohio, (1991) + *Phase Diagrams for High T_c Superconductors II.*, ACerS & NIST, Westerville, Ohio, (1997)
29. Rieder M. & Povondra P.: Fázové rovnováhy pro geology (*Phase Equilibria for Geologists*); Karolinum, Praha (1997), 252 + 66 pp. [1st Edition: SPN Praha (1979)]
30. Bulach, A.G.: Metody termodinamiky v mineralogii (*Methods of Thermodynamics in Mineralogy*); Izd Něždra, Leningrad (1968), 175 pp.
31. Kvasnica, J.: Termodinamika (*Thermodynamics*); 394 pp., SNTL Praha (1965)
32. Greiner W., Neise L., Stöcker H.: *Thermodynamics and Statistical Mechanics*, Springer (1995)
33. Holba P.: Částečně otevřené soustavy a termická analýza (*Partly Open Systems and Thermal Analysis*), L6; In Proc. OSTA09 (Ostravský seminář termické analýzy), Ostrava, 2009 January, 21-23.; ISBN 978-80-86238-63-0; <http://katedry.osu.cz/kch/osta09/l6.pdf>
34. Šesták J.: *Heat, Thermal Analysis and Society*, p.314-315; (372 +28 pp.), Nucleus Hradec Králové (2004); <http://www.fzu.cz/~sestak>
35. Nevřiva M., Holba P., Durčok S., Zemanová D., Pollert E., Tříska A.: *On melt equilibria in the Y-Ba-Cu-(O) system*; Physica C **157**, 334 (1989)
36. Šesták J.: „Phase diagrams of CuO-based high temperature superconductors“ Pure Appl. Chem. **64**, 125 (1992)
37. Moiseev G.K., Šesták J.: „Some calculations methods for estimation of thermodynamical properties of inorganic compounds - a review“ Prog. Crystal Growth and Charact. **30**, 23 (1995)
38. Šesták J., Sedmidubský D., Moiseev G.K.: „Some thermodynamic aspects of oxide high temperature superconductors“ J. Therm. Anal. **48**, 1105 (1997)



Chapter 5

Between solid and liquid

5. THE PHASES BETWEEN SOLID AND LIQUID, CHARACTERIZED BY THERMAL ANALYSIS

Bernhard Wunderlich

5.1. Introduction: solids, liquids and their transitions

The dictionary definitions of the words ‘solid’ and ‘liquid’ are long established. Meriam-Webster’s Collegiate Dictionary (1) traces the meaning of the noun “solid” to the 15th century and suggests that a solid is “a substance that does not flow perceptibly under moderate stress, has a definite capacity for resisting forces (as compression or tension) which tend to deform it, and under ordinary conditions retains a definite size and shape.” A liquid, in turn, “is a fluid (as water) that has no independent shape but has a definite volume and does not expand indefinitely and that is only slightly compressible.” For common use, these definitions are sufficient, but phrases in the definition of the solid such as ‘does not flow perceptibly,’ ‘moderate stress,’ ‘definite capacity,’ and ‘ordinary conditions,’ and, of the liquid such as ‘indefinitely’ and ‘slightly’ are imprecise as long as one does not set specific limits. To improve on these definitions, one might want to use operational definitions, as suggested by Bridgman (2), i.e., look for quantitative experiments (operations) which can answer the question whether a given substance is a solid or a liquid. The chosen experiment should provide a simple yes or no result.

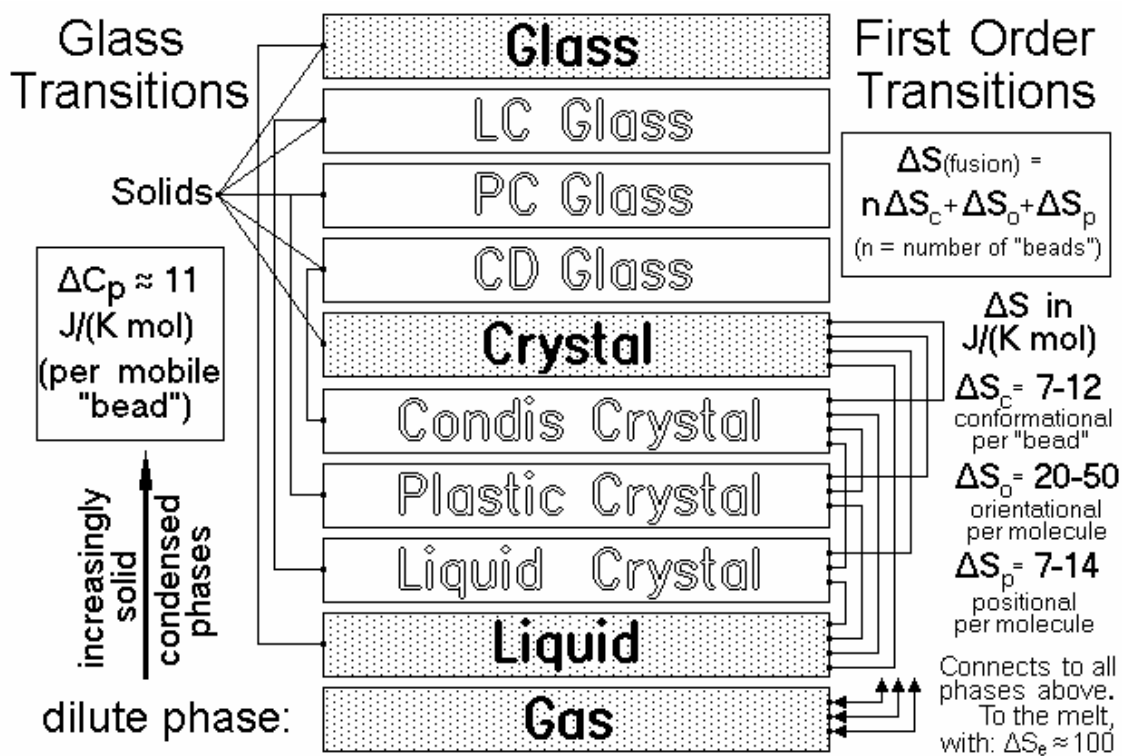


Fig. 1: Today’s ten phases of matter, their states and transitions, characteristics by their transitions and molecular motion (3). First suggested in (4) and detailed in (5) and (6).

In antiquity, Empedocles (490–430 BC) suggested a well-known cosmogenic theory based on two pairs of qualities ‘hot and cold’ and ‘wet and dry.’ These qualities were thought to be able to combine with a ‘primeval matter’ to account for the four basic ‘roots’ of all structures of the world: ‘Solids’ (earth = dry & cold), ‘Liquids’ (water = wet & cold), and ‘Gaseous’ (air = wet & hot). These three roots or elements represent the three classical phases. ‘Fire’ (= hot & dry) was proposed to be a fourth root. Today we know that the nature of fire is different from the three phases. It is not linked to matter alone, but characterized by molecular motion described by temperature and energy (3). For the three classical phases, not much has changed in the last 2,500 years. Their number, however, has been expanded to 10, as shown in Figure 1 (4–6) to account for discoveries made in the last 200 years.

The dictionary meaning of the word transition is a “passage from one state, stage, subject, or place to another” (1). In the present Chapter, the two transitions listed in Figure 1 will be discussed, namely, the glass and first order transitions. Going from the bottom phase in Figure 1 upward to the crystal, the phases are listed as “increasingly solid,” and the transitions governing the changes to solids are the glass transitions. *This makes it reasonable to choose the measurement of the glass transition temperature, T_g , as the operation to define a solid.* Below its glass transition temperature, a phase is a solid (one of the upper five phases), above, it is the fluid phase (one of the five lower phases). The nature of the phases, its glass transitions and additional details about gases, crystals, and the ‘first-order transitions’ are to be given in this Chapter with reference to Figure 1.

5. 2. Phases

First, the term ‘phase,’ already mentioned in the Introduction, needs some clarification. For this, one does not have to go back to the dictionary definition [“a homogeneous, physically distinct, and mechanically separable portion of matter present in a nonhomogeneous physicochemical system” (1)]. The International Union of Pure and Applied Chemistry, IUPAC, has provided a binding scientific definition (7). A phase is to be “an entity of a material system which is uniform in chemical composition and physical state.” A phase defined such, must be sufficiently large so that the inhomogeneity due to the size of its constituent atoms is insignificant. Since atoms are smaller in diameter than one nanometer and the smallest phase that can be seen with the unaided eye is bigger than 0.01 mm (= 10 μm = 10,000 nm), the homogeneity is not endangered by the molecular structure when working with ‘visible phases.’ To distinguish these from smaller phases, to be discussed next, they will be called ‘macrophases.’ The thermal properties of the macrophases are to be represented by the well-established thermodynamics, developed more than 100 years ago (8).

It already was recognized by early thermodynamicists that small phases have different properties than larger ones. It was proposed in Gibbs’ “theory of capillarity (8)” that the “influence of surfaces of discontinuity upon the equilibrium of heterogeneous masses” must be considered. Two observations can be clarified by considering the effect of surfaces. One is the existence of ‘colloidal particles’ with typical sizes of less than one micrometer. Today, phases of this size are called ‘microphases.’ Colloidal particles or droplets are kept in metastable dispersion by their surface charge, which prohibits coagulation to a more stable, larger phase. The other observation is a change in the overall thermodynamic quantities due to the surface free energy. One can use the Gibbs-Thomson equation (9–11) to calculate, for example, the lowering of the melting temperature, ΔT_m , for known, small volumes, V , or in turn, to calculate the surface free energy from the measured ΔT_m .

$$\Delta T_m = (\sigma T_m^{\circ} A) / (\Delta h_f \rho V), \quad (1)$$

where σ is the specific surface free energy; T_m° , the bulk equilibrium melting temperature; A , the surface area; Δh_f , the specific heat of fusion (per gram); and ρ , the mass density of the crystal. Equation (1) can easily be expanded for the case of more than one specific surface free energy.

The lowering of the melting temperature due to microphase formation is of particular importance for the understanding of semicrystalline macromolecules (3). For a 10 nm thick, laterally large, chain-folded lamella of a polyethylene crystal, for example, ΔT_m is 26 K (4). In this case, only the two fold surfaces of the lamella contribute significantly to the surface free energy. Clearly, when increasing the lamellar thickness ($= V/A$) beyond that of the microphase dimension, let us say to 10 μm , the lowering of the melting temperature, ΔT_m , decreases to a negligible 0.026 K. Such phase is then a ‘macrophase,’ practically unaffected in its thermal properties by the presence of the surface.

In the last 20 years, it became customary to use the term ‘nanophase’ (12,13) for phases which approach a nanometer scale. For a long time, the development of this terminology was not given an operational definition (14). Feynman when he speculated about ‘very small phases,’ suggested in 1959 already that “on a small scale we will get an enormously greater range of possible properties that substances can have” (15). This suggestion will be used next for an operational definition.

In the field of flexible macromolecules (polymers), it is obvious that rather small, disordered entities existed which are larger than typical crystal defects and smaller than microphases. These defects were initially called ‘amorphous defects’ (4). Ultimately, it became clear, that these amorphous defects behave like very small phases with different properties than the bulk-amorphous microphases. On hand of many literature examples on phase separation of small and large molecules, an operational definition was suggested which can distinguish nanophases from microphases on the basis of its properties (16): “In nanophases, the opposing surfaces of a phase area are sufficiently close to interact.” While the microphase is described as a phase with a sufficiently large surface area to cause changes in the overall properties, it is still a bulk phase, enveloped by a distinct surface layer. Only the surface has different properties from the bulk it encloses, such as mass density, order, force-field, etc. The nanophase, in contrast, with its contacting surfaces, has *no* remaining bulk phase. In addition, the differences of the surface properties from the bulk are known to change gradually with distance from the surface. In nanophases, thus, one expects a continuous change of the properties from the outside to the center without reaching the plateau of the macrophase. The operation to distinguish a nanophase from a microphase, thus, must involve the detection of the bulk phase in its center. An experiment most suited, is the measurement of the glass transition, since the glass transition of a phase is characterized by the properties of a ‘hole’ of only about 1–2 nm in diameter, including its defining layers of matter.

Nanometer-sized structures were suggested in 1963 to account for certain defects in semicrystalline fibers (17). This structure was similar to the amorphous defect proposed at the same time (4,18) and was later shown to be a nanophase, as mentioned above. In such nanophases the macromolecules can cross the phase boundary multiple times. The crystalline phases in semicrystalline polymers are usually sufficiently large to be classified as microphases, resulting in a globally metastable aggregate of two or more types of the phases depicted in Figure 1. Similarly amphiphilic crystals, of small, flexible molecules, are synthesized out of two incompatible, chemically different segments can be considered as being nanophases,. A crystal structure of alternating aliphatic and aromatic layers, for example, was found for 4-n-octyloxybenzoic acid (19).

A number of such amphiphilic crystals undergo separate solid-liquid phase transitions at different temperatures in the different layers (5,6).

To characterize a material one must know which of the phases listed in Figure 1 are present and then specify their sizes and interconnection. In addition, the ‘class of the molecules’ must be given. After the last class of molecules, the flexible, linear macromolecules, had been recognized by Staudinger (20), it became obvious, that there are three distinct classes of molecules, ‘small molecules,’ ‘flexible macromolecules,’ and ‘rigid macromolecules’ (4, Vol. 3 pgs. 4–5). This new classification scheme is closely connected to the phase properties (21). Rigid macromolecules can only exist as solids. On liquefaction or evaporation, the strong bonds defining the molecules are broken, destroying the integrity of the molecule. Flexible macromolecules can be disordered without losing their integrity, so that for many, liquid as well as solid states are possible (but not the gaseous state). Small molecules under proper conditions may exist in all three states, solid, liquid, and gaseous. Examples of the three classes of molecules are found in the historically defined inorganic, organic, and biological molecules which show no unique characteristics and do not make a good classification.

For an overall description of samples, one can then identify three classes of molecules, three phase sizes, and ten phase types. Gases, however, must be of small molecules, and because of the lack of self-sustaining surfaces cannot be microphases or nanophases. Rigid macromolecules may not become liquids or mesophases. Finally, mesophases may be coupled to specific molecule types. This leaves 57 different possible condensed states in addition to the gas (16).

5. 3. Measurements of thermal properties

With the description and classification of the molecule and phases, one can return to Figure 1 and consider the measurements that lead to the properties listed on the sides of the schematic. On the left, the changes are indicated when going from the dilute and mobile gas at the bottom, through increasingly more solid condensed phases, to the solids. The thermal property of interest is the change in heat capacity when becoming a solid at T_g , ΔC_p (at constant pressure, p , and composition, n). The heat capacity C_p is equal to $(\partial H/\partial T)_{p,n}$, where H is the enthalpy ($= U + pV$, the internal energy, U , plus the product of pressure and volume, V). Its change is equal to the ‘heat’ gained or lost by the system (7).

On the right of Figure 1, the various thermal transitions are indicated which have a more abrupt change in molecular order. These changes are usually related to thermodynamic first-order transitions. The change in order is assessed by the change in entropy, $\Delta S (= L/T)$, to be calculated for equilibrium transitions from the heat of transition or latent heat, L (7).

To understand the experimental basis of Figure 1, calorimetry, as the tool to measure heat will be considered in this Section and an interpretation in terms of molecular structure and motion will be given thereafter. Today it is well known, that ‘heat’ is a form of energy exchanged between systems (7) and has its microscopic origin in molecular motion (3). The measurement of unknown heat effects always involves its comparison to known effects. The SI unit for energy, work, and heat is the joule ($\text{kg m}^2 \text{s}^{-2}$) (22). The most common calorimeters are the adiabatic calorimeter, differential scanning calorimeter (DSC), the temperature-modulated differential scanning calorimeter (TMDSC) and the quasi-isothermal, non-scanning version of TMDSC, the TMDC. Classical, adiabatic calorimetry was developed in the early 20th century to sufficient precision. It allows to

start measurements at temperatures close to 0 K (23). The total H is accessible by measuring heat exchanges over the whole temperature range. Increasingly more automated calorimeters have been developed over the years (24–26) [see also (3)].

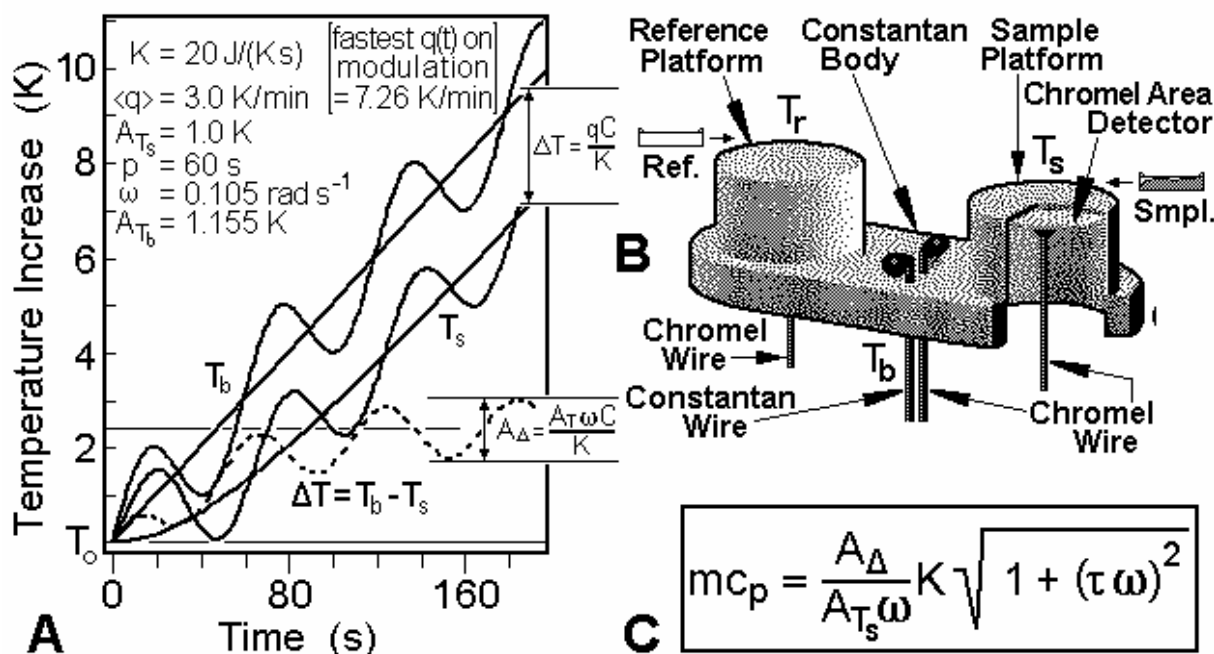


Fig. 2: Differential calorimeter of type TA Instruments Q1000. (A) Graph of the change of sample and body temperatures, T_s and T_b , during a heating scan. (B) The measuring principle. The calorimeter assembly is placed in a temperature-controlled enclosure, filled with slow-flowing N_2 gas free of turbulence, also kept at T_b . (C) The TMDSC equation, for C_p (expressed by sample mass, m , in g, and specific heat capacity, c_p , in $\text{J K}^{-1} \text{g}^{-1}$) from the measured amplitudes (A in K) of T_s and Δ ($= T_r - T_s$), the angular modulation frequency (ω in rad s^{-1}), and the two calibration constants (K and τ).

Quantitative DSC and modulated calorimetry developed only in the second half of the 20th century. In the meantime, these more convenient techniques also have reached considerable precision. An example of a calorimeter capable to perform standard DSC as well as TMDSC and TMDC is shown in Figure 2. The roots of DSC are the qualitative cooling and heating curves of the 18th century (3). When inserting a sample into a bath of constant temperature, T_0 , Newton's law allows to describe its measured temperature $T(t)$, as a function of time, t . The value of $T(t)$ exponentially approaches T_0 :

$$dT/dt = K(T_0 - T). \quad (2)$$

Over small temperature ranges, K is constant and accounts for the nature, geometry, heat capacities, and thermal conductivities of sample and container.

The calorimeter in Figure 2B can perform the modern version of such 'Newton's Law' measurement and then permits the extraction of the changes in H as a function of temperature. The key to quantitative DSC is proper calibration and comparison to a standard of known C_p , often

sapphire (single-crystalline Al_2O_3). The function of the constant-temperature bath is taken over by the constantan body of temperature T_b , changing linearly with temperature at the rate $q = dT_b/dt$. Figure 2A illustrates that about 60 s into the measurement, steady state is reached, i.e., thereafter ΔT changes only slowly as C_p changes with temperature. The thin cylindrical walls leading to the sample platform cause the major temperature lag of the sample temperature, T_s . As indicated in the figure, the sample (of typically 1–20 mg) is enclosed in a sample pan (of high thermal conductivity, usually Al or Au). This configuration is to keep the temperature gradient within the sample pan small (perhaps <0.5 K) to stay within the error limit. The asymmetry of the platforms must be established by calibration. Experience has taught that extra time spent on calibrations and checking the constancy of the calorimeter, repays with increased precision. The heat capacity of sample *and* pan, C (at T_s or time t) can then be extracted from the top equation in Figure 2A. By performing DSC, i.e., also measuring the reference temperature, T_r , the sample $C_p (= mc_p)$ can be obtained:

$$\Delta T = T_r - T_s = q m c_p / K, \quad (3)$$

where m is the sample mass and c_p the specific heat capacity of the sample in $\text{J}/(\text{K g})$.

The Newton's law constant K needs a second calibration, namely the conversion of the measured quantities ($\Delta T/q$, in s) into C_p in units J/K . This is done by performing a third run on a reference material of known C_p . This should be done under identical conditions and with a similar magnitude of ΔT as the sample run. Careful handling of the calorimeter and samples, carrying out the measurement and two calibrations, equalizing the pan weights, etc., are the main issues for a quantitative DSC (3). Unfortunately, qualitative runs, of value only for preliminary information, still find their way into the literature. Under optimum conditions, accuracies should be $\pm 1.0\%$ or better. Data can easily be obtained from 100 K using liquid N_2 as a coolant to temperatures above 1,000 K.

Standard DSC has been expanded in the last 15 years by temperature modulation to TMDSC. Figure 2B shows that no new hardware is needed. The linear increase of T_b is now modulated with a periodic change (commonly between 0.1–5.0 K) and a fixed period (usually between 10 and 500 s). The heating rate becomes an 'underlying heating rate,' $\langle q \rangle$. In case the response of the calorimeter to the modulation is strictly linear, a sliding average over the time of one modulation period yields the underlying quantities, indicated by the angular brackets, $\langle \rangle$. The TMDSC values of $\langle q \rangle$, $\langle T_r \rangle$, and $\langle T_s \rangle$ correspond to the standard DSC values of q , T_r , and T_s . The dotted curve in Figure 2A indicates that the steady state of TMDSC is reached after two minutes, later than for standard DSC.

By subtraction of $\langle T \rangle$ from the instantaneous, modulated value of T , one can extract the effect of modulation as a function of temperature (or time), usually being called the 'reversing temperature.' Its analysis is done using a pseudo-iso-thermal method since the underlying changes have been removed (27,28). The result is the reversing heat capacity C indicated by the bottom equation of Figure 2A. Changing, as before, to a differential measurement with $\Delta T = T_r - T_s$, the TMDSC equation results:

$$mc_p = [A_\Delta / (A_{T_s} \omega)] K, \quad (4)$$

where ω is the angular modulation frequency (in rad s^{-1}). If steady state and linearity are preserved and the heat capacities computed from eqs. (3) and (4) are identical, C_p is reversible. Complications arise in the transition regions, to be discussed below. In the latter cases, the response is often

nonlinear. As long as reversibility is not proven, the heat capacity by TMDSC must be called reversing. The basic calibrations of TMDSC remain similar to that of the standard DSC, but gets more involved since the amplitude responses are identical for positive and negative deviations, an effect which can be assessed by considering the phase shift of the response (3,29).

In order to correct for the frequency-dependence of K , an additional calibration constant τ is introduced in Figure 2C (28,30). Figure 3 illustrates its evaluation.

$mc_p = \frac{K\Delta T}{q} \quad (1)$	$mc_p = \frac{A_{HF}}{A_{TS}\omega} K \quad (2)$	$K = K' \sqrt{1 + \tau(m)^2 \omega^2} \quad (3)$
--	--	--

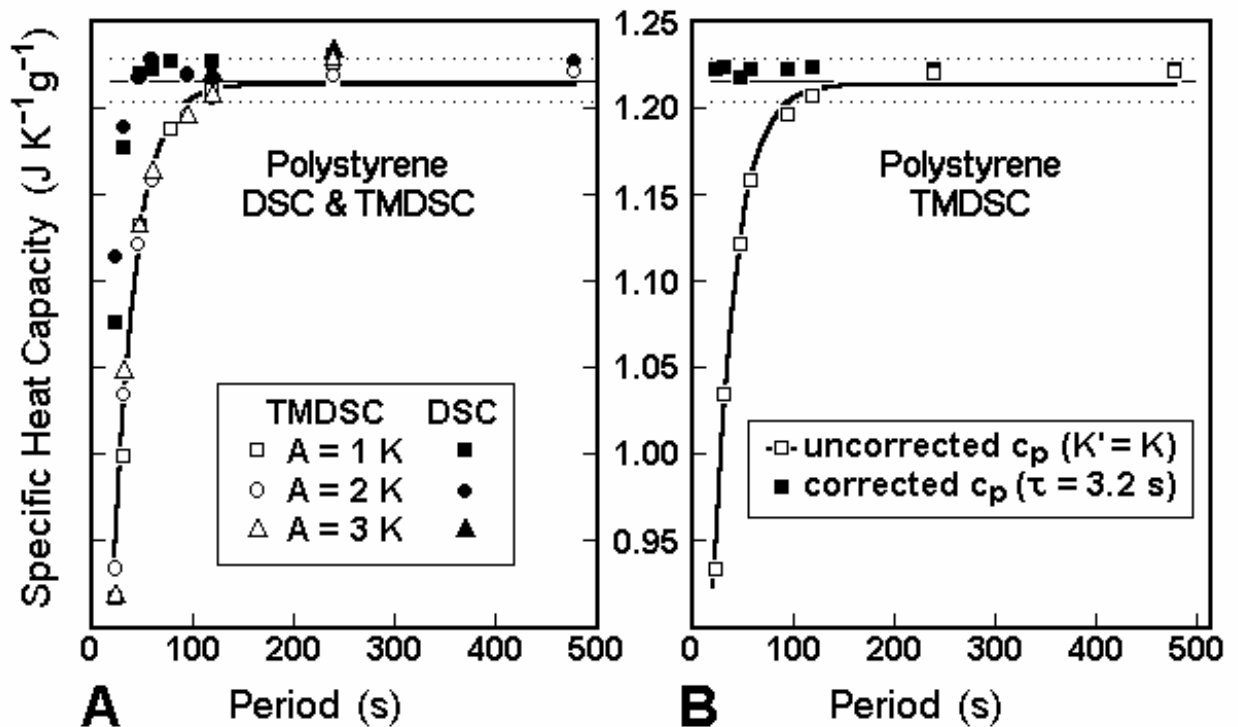


Fig. 3: Comparison of DSC and TMDSC data (39). The equations at the top correspond (1) to the standard DSC analysis, (2) to the TMDSC analysis with $K = K'$, and (3) fitted to a constant τ , as suggested in Figure 2C. For periods less than 10 s, τ changes with frequency and mass, can, however, still be calibrated by evaluating its change with ω (31).

In Figure 3A, a comparison of heat capacity by DSC and TMDSC is shown. In DSC, the measurement was made at constant q at the end of the indicated time period and c_p calculated with eq. (1) of Figure 3. The reversing c_p by TMDSC at the indicated amplitudes of modulation was calculated with eq. (2) of Figure 3. As expected from Figure 2A, the standard DSC reaches steady state faster than the TMDSC. In Figure 3B, the TMDSC data for a 2.0 K modulation are plotted, as in Figure 3A. In addition, the correction as given by eq. (3) in Figure 3 is marked by the filled squares. Periods as short as 10 s can generate acceptable data when properly corrected. But even at

much shorter periods, quantitative information can be gained by calibration of τ as a function of not only sample mass, but also frequency (31). It is important, that all three runs must be independently corrected for frequency.

The TMDSC can further be varied by coupling different underlying heating rates with the modulation, or by modulating simultaneously with multiple, superimposed frequencies and amplitudes. Of importance are the modes that never go beyond prior reached maximum or minimum temperatures. This avoids reversals of phase changes. The quasi-isothermal mode, TMDC, is carried out at an underlying constant temperature, i.e., the measurement is performed by modulation only ($\langle q \rangle = 0$) without scanning. The TMDC results are derived by similar procedures, as derived in Figures 2 and 3 (28) and can be extended to very long times to analyze the kinetics of slow changes. In TMDSC with multiple frequencies, the response can be separated by Fourier analysis. Methods have involved superimposed sinusoidal frequencies, as well as simple wave functions with multiple components, such as saw-tooth modulation, or various step functions (3,29).

5. 4. Interpretation of the heat capacity of solids

In this Section, an attempt will be made to link the macroscopically measured heat capacity with its microscopic, molecular origin. The first success in this endeavor was Einstein's discussion of the possible vibrations in crystalline metals and salts (32). It was shown that the vibrations of each atom or ion are determined by the force field of its 6–12 symmetrically placed neighbors. It was proposed then to approximate the force field with spherical symmetry, giving each vibration in the solid the same frequency, the Einstein frequency. Calorimetry revealed that this approximation was valid only at intermediate temperatures and even then only for solids of the highest symmetry. The problem was resolved by replacing the single Einstein function (33) by a three-dimensional Debye distribution (34,35), derived from a macroscopic description of acoustic vibrations, extended to higher frequencies until the maximum number of degrees of freedom of an atomic assembly (7) was accounted for. This treatment described the heat capacities of many metals and salts over wide temperature ranges by specifying only the end-frequency of the spectrum, $\nu_{(\text{Debye})}$, the Debye temperature $\Theta_3 [= h\nu_{(\text{Debye})}/k$, in kelvin ($h = \text{Planck's constant}$, $k = \text{Boltzmann's constant}$, $1\text{Hz} _ 4.8 \cdot 10^{-11} \text{K}$)]. An extensive discussion with data comparisons is available in (36).

Solid linear macromolecules, however, do not fit such an analysis. Strong deviations occur, starting at rather low temperatures. For polyethylene, for example, only the crystalline solids yield the expected increase of heat capacity at low temperature with T^3 , and even this, only up to about 10 K! Figure 4 illustrates a frequency spectrum for polyethylene, suitable to understand IR and Raman spectra (37). This spectrum fits C_p at higher temperatures, but not at low temperatures.

Empirical equations for the approximation of low-temperature heat capacities for linear and two-dimensional macromolecules were suggested by Tarasov (38) and are shown in Figure 5A. They were based on a three-dimensional Debye function for the lowest-frequencies (35), starting with the acoustical vibrations. This is followed by a two-dimensional and/or a one-dimensional Debye function to average the rest of the so-called skeletal vibrations (39,40). The remaining vibrations are group vibrations, known to change only insignificantly for the same chemical grouping in different molecules. Their contribution to the heat capacity can be computed from spectroscopic analysis of the molecule in question, or even of model compounds. Because of the rather limited coupling between the group vibrations, they are narrow local modes of vibration and can be either treated as single Einstein modes (33) or approximated by a box distribution fitted at the upper and

lower frequency limit with a one-dimensional Debye function (41–43).

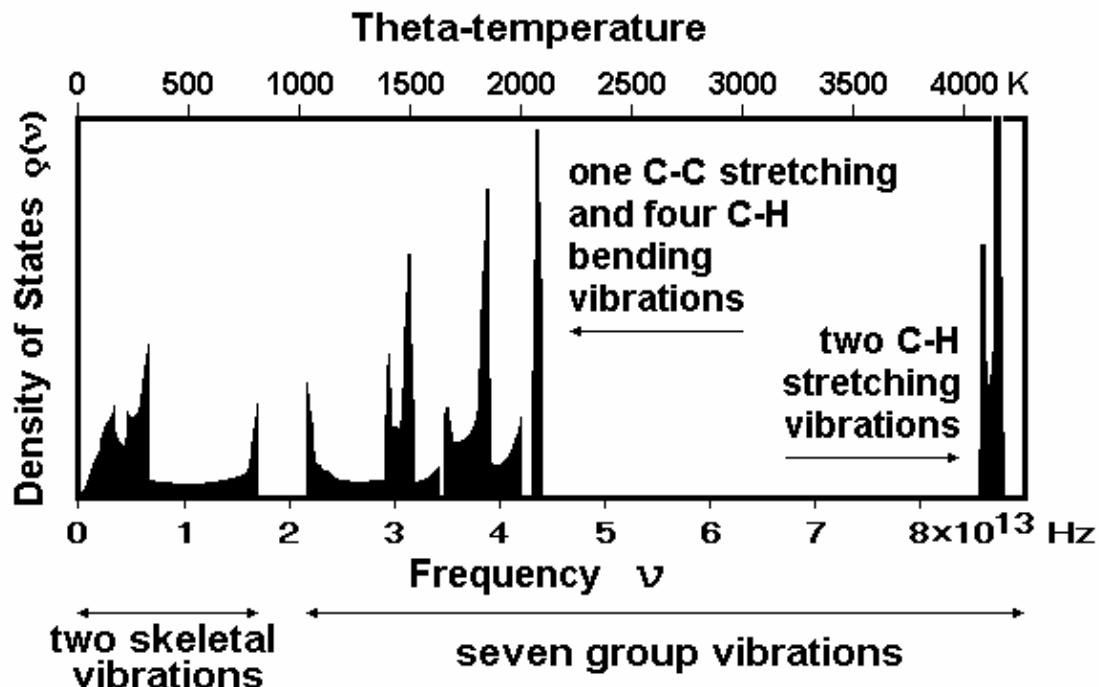


Fig. 4: Vibrational spectrum of crystalline polyethylene, derived from normal-mode calculations based on a fit to the measured infrared and Raman frequencies (37).

Figures 5A–C illustrate such a fitting for crystalline polyethylene in the different frequency ranges. In Figure 5A, the general Tarasov treatment for the two skeletal modes with three Θ -temperatures is shown (43). The remaining seven group vibrations are approximated as five box distributions (B), and eight Einstein vibrations (C). A comparison with the spectrum in Figure 4 allows to judge the simplifications.

Figure 6A illustrates $C_p(\text{solid})$ and $C_p(\text{liquid})$, and Figure 6B the contributions from the skeletal and group vibrations for crystalline polyethylene. The difference between C_p and C_v can be computed from information on compressibility and expansivity (44,45). Below 200 K this difference is negligible. Up to 150 K the C_v ($\approx C_p$) is almost fully accounted for by the skeletal vibrations and calorimetry permits an easy fit to the approximate frequency spectrum in Figure 5A. At the melting temperature (414.6 K), the heat capacity of the crystal and liquid are almost the same. The agreement between measured and calculated data from the approximate frequency spectrum of Figure 5 is $\pm 3\%$. When sufficient data on heat capacities of linear macromolecules were measured (46) and their link to the vibrational motion established, it was possible to generate a reliable Advanced Thermal Analysis Scheme (ATHAS) to evaluate the approximations of the skeletal vibrations (3,47): After conversion of C_p to C_v (44,45), the group vibration contributions to C_v are subtracted, and the remaining skeletal contributions are fitted to the proper Tarasov equation (42,43).

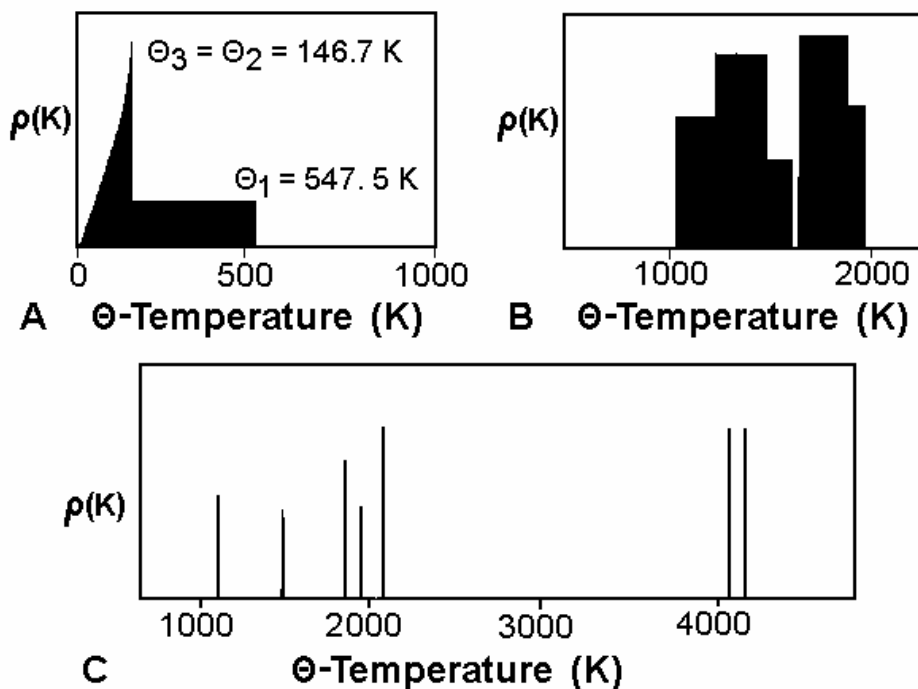


Fig. 5: Various approximations of the vibrations of crystalline polyethylene (CH_2)_x (43). The repeating unit has nine normal modes of vibration. (A) The two skeletal vibrations (overall chain torsion and bending in addition to the inter-chain acoustic vibrations) approximated by the three Θ -parameters of the Tarasov treatment (38). (B) Five partial, coupled modes approximated by box-distributions (mainly consisting of CH_2 wagging, twisting, and rocking modes, total modes 2.4). (C) The remaining eight partial and full modes of the group vibrations. (The three highest frequencies are the complete CH_2 stretching and bending modes, total modes 4.6).

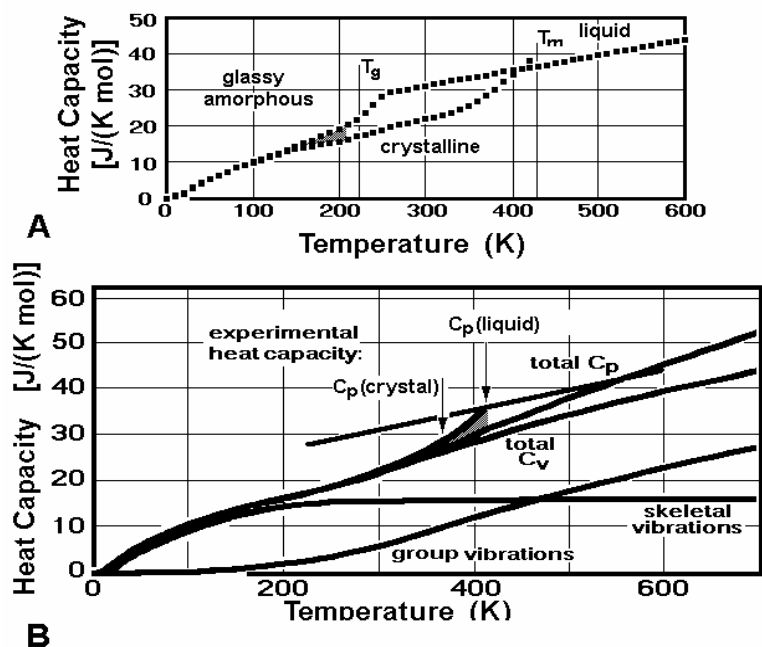


Fig. 6: Measured and calculated heat capacities of glassy, liquid, and crystalline polyethylene. (A) Measured data, extrapolated to 100% amorphous and 100% crystalline content, based on about 100 publications reviewed for the ATHAS Data Bank (46). (B) Comparison with the vibrational heat capacity (total C_v) calculated from an approximate frequency spectrum.

At the minimum:
 $\Theta_1 = 631 \text{ K}$
 $\Theta_3 = 79 \text{ K}$
 error: $0.5 \pm 3.2\%$

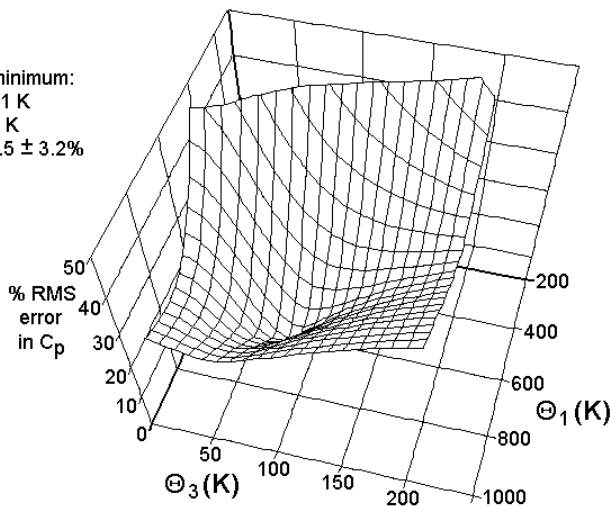


Fig. 7: Fit of the skeletal heat capacity of α -chymotrypsinogen with the ATHAS data using a minimization algorithm (49).

Figure 7 illustrates the quality of one of the most complicated fits yet attempted, that for bovine α -chymotrypsinogen type II protein (48). This molecule consists of 245 amino acid repeating units with a total molar mass of 25,646 Da and 3005 skeletal vibrations. The minimization of the error in the figure shows a unique solution and allows

a reproduction of the experimental data. Such data are now available for more than 100 linear macromolecules in their solid states. A number of small molecules, as well as rigid macromolecules have also been analyzed. Overall, these frequency spectra reveal that the vibrations below 10^{12} Hz with a time scale larger than one picosecond (10^{-12} s), which ultimately end below $\approx 2 \times 10^4$ Hz in the acoustic vibrations, are negligible with respect to their contributions to the integrated thermodynamic functions H , S , and G . This means that in calorimetry, the heat capacity of solids is describable by vibrations which react instantaneously to the changes in temperature. Any lags are due to heat conduction delays and slow transitions.

Because of the great similarity of the weak intermolecular forces in polymers and their strong C, N, O intramolecular backbone-bonding, the ATHAS Data Base can also be used to estimate the C_p of samples which have not been measured yet. The overall error is usually less than $\pm 5\%$. This scheme is valuable to assess the unlimited numbers of proteins and synthetic copolymers (3). All solid phases of the same polymer have a closely similar C_p down to about 50 K. Below 50 K, C_p for glasses yields a lower Θ_3 -temperature. For glassy polyethylene, Θ_3 is 80 K, compared to 147 K for the crystals (see Figure 5A, Θ_1 is identical for both, crystal and glass).

Liquid, flexible macromolecules have a long temperature-range of linearly changing C_p (46). In addition, they are additive with respect to their structure units. To develop a more precise theoretical description, however, has proven difficult because of problems to assess the large-amplitude motion in liquids with a wide variety of intermolecular barriers to translation and rotation (49,50).

5. 5. Large amplitude motion

Besides the small-amplitude vibrational molecular motion about an equilibrium position, there are a number of large-amplitude motions. Easiest is the description of the three translational degrees of freedom known from the ideal gas theory via:

$$M \overline{v^2} = 1/2 RT = U, \quad (5)$$

where M is the molar mass of the particle in question, $\overline{v^2}$ the mean square translational velocity, so

that the left third of the equation represents the kinetic energy, linked to the internal energy of the gas U on the right, and R , in the center, is the gas constant. The heat capacity at constant volume is then simply: $C_v = (\partial U/\partial T)_v = 1/2 R$. A similar expression can be derived for the rotational degrees of motion. Both, translational and rotational energies refer to the molecule as a whole and one does not expect either in the ideal form (without additional potential energy contributions) in the solid state.

The intramolecular conformational rotation is the basic large-amplitude motion of flexible molecules. It represents a hindered rotation between parts of a molecule about a covalent bond. The different conformational isomers reached by this internal rotation have well-defined potential-energy minima. The process can be simulated in crystals by using large-scale molecular-dynamics calculations (51). In simulations of polyethylene-like solids the main motion involves three backbone bonds (a 2g 1 defect. At room temperature such isolated defects have a lifetime of the order of magnitude of 10^{-12} s and a concentration of 0.5%. The calculations substantiated that the deviations of C_p from the vibration-only value seen in Figure 6 start for the amorphous glass at about 150 K, while for the crystal at about 300 K (52). A comparison of the calculated concentrations of gauche conformations with measurements by IR spectroscopy on paraffin of similar length (53) was shown in (54).

The contribution to C_p of an isolated, internal rotation at low temperature is similar to a torsional vibration. At higher temperature, when the potential energy barrier to rotation into the next minimum can be overcome, it reaches a maximum, and finally it drops to that of a free rotator reaching half the vibrational C_p (55). The internal rotations involving cooperative motion of neighboring molecules are sufficiently slow to be measurable by DSC and TMDSC. Model calculations made use of the hole model of Eyring (56). It describes the configuration involved in the cooperative, large-amplitude conformational as motion of a 'hole' with a one-nanometer or smaller radius.

5. 6. First order phase transition

The integral calorimetric data, H , S , and G , will be the basis for the description of the transitions. Figure 8 summarizes the data for polyethylene as they are available from the ATHAS Data Bank (46). Both information on the fully crystalline and amorphous sample is given, normalized for the enthalpy of the crystalline state at 0 K, H_c^0 , to be zero. The enthalpy change is represented not only by C_p , but there are also contributions from latent heats, $L [= (\partial H/\partial n)_{p,T}]$ at constant pressure and temperature:

$$dH = (\partial H/\partial T)_{p,n} dT + (\partial H/\partial n)_{p,T} dn . \quad (6)$$

In standard DSC experiments, one has to separate the two contributions from the measured, apparent heat capacity, $C_p^{\#} (= dH/dT)$. The second contributions in eq. (6) depends on dn/dT , the amount of phase transformations during the change of temperature. This can be assessed by TMDSC with a proper choice of frequency and heating or cooling rate. It can be written as $(dn/dt)/(dT/dt)$ and introduces the time, t , in form of the ratio of rate of transformation and the rate of temperature change $q = dT/dt$ (see Figs. 2 and 3), if continuous equilibrium is dn/dT , time and frequency independent.

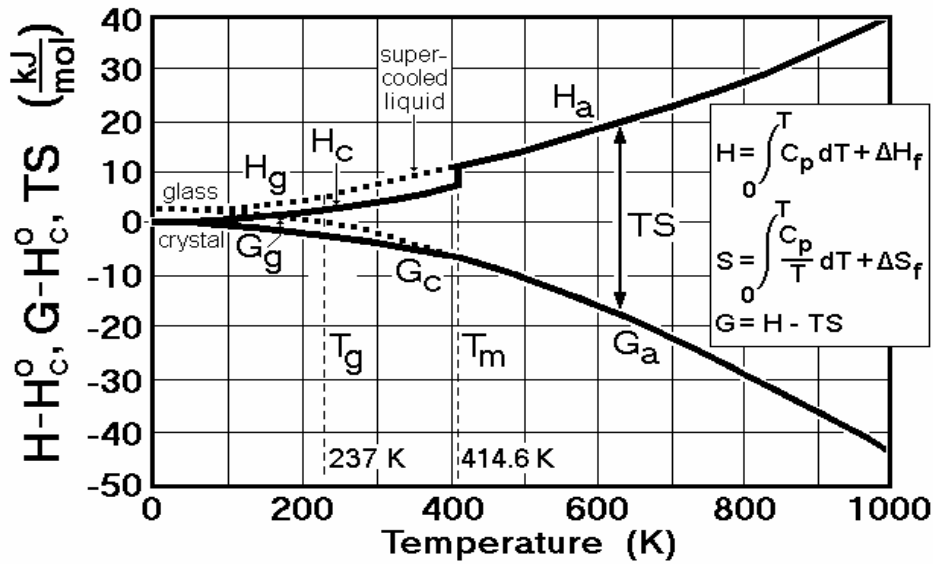


Fig. 8: The integral thermodynamic functions of amorphous (a), crystalline (c), and glassy (g) polyethylene, based on calorimetric measurements

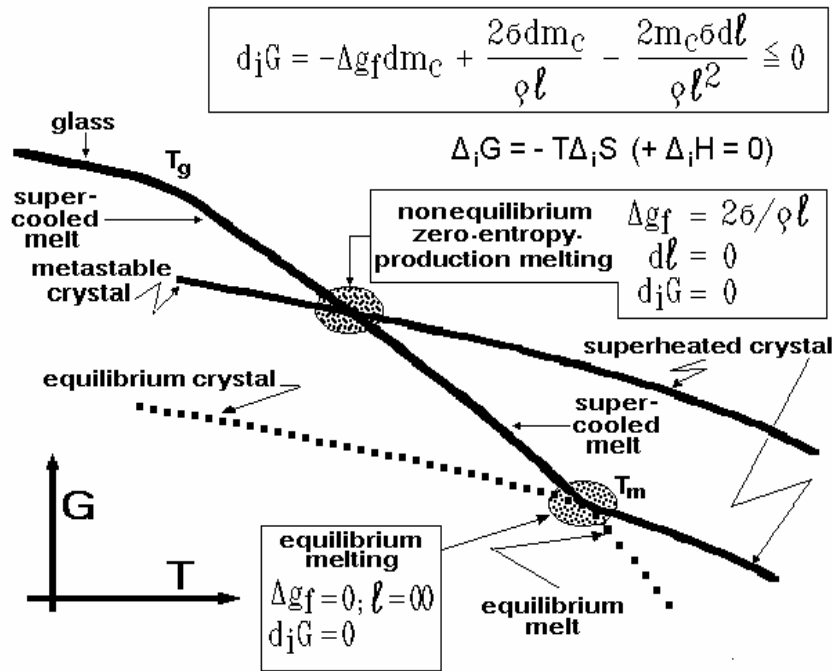


Fig. 9: Schematic of the free enthalpy of a system capable to display equilibrium and nonequilibrium states. The equations are derived from the Gibbs-Thomson eq. (1) expressed for lamellar crystals with negligible side-surface effects and thickness l . The latent heat effect on fusion $\Delta h_f = \Delta g_f + T \Delta s_f$. The lower case letters signify specific quantities, subscript c refers to crystals, the prefix i indicates the “production” quantities (deviation from equilibrium). The glass transition temperature is marked as T_g . The first law of thermodynamics forbids enthalpy production ($\Delta_i H = 0$), the second law upward motion in the diagram to reach a different phase line ($\Delta_i G \leq 0$, or $\Delta_i S \geq 0$).

A schematic of the free enthalpy as a function of temperature is drawn in Figure 9, allowing the discussion of equilibrium states (dotted lines), as well as metastable or unstable states of higher free enthalpy (continuous lines). The equilibrium melting temperature, T_m , is easily recognized in Figures 8 and 9 at the point where $G_a = G_c$, and $H_a - H_c$ produces an entropy of fusion which can be connected to the increase in disorder. The entropy contribution introduced during the transition has predictable limits, as shown on the right-hand side of Figure 1.

The various values have been established over the years (4, Volume 3, pages 5–23), ΔS_c is Trouton's rule, ΔS_p is Richards' rule, ΔS_o is Walden's rule, and ΔS_c was established based on the ATHAS Data Bank. Also shown on the right-hand side of Figure 1, are the possible connections between the various phases via (largely) first-order transitions. Besides the melting and crystallization transitions one can note partial ordering and disordering involving mesophases (at T_o and T_d), isotropization of mesophases (at T_i) and naturally, the boiling and sublimation, involving the gas phase at a fixed pressure (T_b and T_s).

The transitions characterized by an entropy of transition have a discontinuity in the slope of G , $\partial G/\partial T = -\Delta S$, when progressing along the curve of Figures 8 and 9, but not in G itself. Such transitions were called by Ehrenfest 'first order transitions' (57). A first order transition was to be distinguished from a 'second order transition' which has a discontinuity in curvature, $\partial^2 G/\partial T^2 (= -\Delta C_p/T)$, but not in slope. These definitions are to apply for systems which stay in equilibrium throughout the transitions, a condition which can be approximated for systems of simple structure, but is difficult to achieve for flexible, linear macromolecules. All transitions marked on the right side of Figure 1 have, at least approximately, been analyzed by assuming a first-order transition formalism.

Only one metastable crystal is marked in Figure 9, naturally many more might exist. A series of lamellar crystals, for example, distinguished by different lamellar thicknesses would lead to parallel states with increasing metastability, fixed in metastability by the decreasing lamellar thickness and calculated with eq. (1). In case the degree of order of the metastable crystal is different from the equilibrium crystals, as in a mesophase, the slope of $G (= -S)$ would vary in addition to the level of G at constant temperature. Under proper conditions, the metastable state may then cross G of the crystal, as well as of the melt and reach equilibrium at a limited range of intermediate temperatures (3).

Following G of the metastable crystal in Figure 9 and inspecting the point of nonequilibrium zero-entropy-production melting, one notes that formally this point is similar to equilibrium melting. The degree of metastability is set by the fold length, identical to the metastability of the supercooled melt. The main issue in using nonequilibrium thermodynamics is to avoid the ever-present possibility that the metastable states becomes unstable and change during measurement (58). For analysis, unstable systems must be followed as a function of time. Useful calorimetric techniques are then to follow the process with TMDC until a new metastable state is reached for analysis based on the observed changes (29). The second technique is to speed up the analysis such, that the change during the analysis is negligible, a technique which by now has reached thermal analyses of up to 10^6 K s^{-1} with superfast chip calorimetry (59). While the lamellar crystals of linear, flexible macromolecules are frequently metastable and melt quickly at the zero-entropy-production T_m , the superheated crystals are usually unstable and their kinetics must be followed (60).

5. 7. Glass transition

The glass transitions are marked on the left side of Figure 1, producing a jump in heat capacity, ΔC_p , as can also be seen in Figure 6A for glassy polyethylene. At T_g , the function of G shows a change in curvature, but no change in its slope, as can be seen in Figures 8 and 9, i.e., there is a change in C_p , but no change in entropy, S . Both of these observations are the requirements of a second order transition (57), but the glass transition is not an equilibrium transition, rather a kinetic transition. The glass transition temperature, T_g , is located best at the mid-point of the change in C_p , at half-completion of the transition in the given heating or cooling rate, q . It also depends on the thermal history of the sample (3). An empirical analysis of many glasses of flexible molecules suggests, that ΔC_p depends on the number of 'beads' that gain mobility at T_g , being linked to the number of internal rotators.

Besides with calorimetry, the glass transition can also be identified by its jump in thermal expansivity at T_g . Furthermore, the glass transition can be recognized by the change it causes in response to simple mechanical tests. Based on these, the glass transition has also been called the 'brittle point,' the 'softening point,' the 'thread-pull temperature,' the 'maximum in the loss tangent,' etc. All these point to the glass transition as being an easy operation to distinguish solids from liquids, as suggested in the Introduction. Of special interest is the observation, that the viscosity of a liquid (which increases on cooling), reaches commonly a value of about 10^{12} P s at the glass transition temperature. Viscosity of such magnitude is also observed in ice crystals close to their melting temperature. Based on these experiments, a glass can be identified as a solid that changes at T_g to a more mobile phases which may be a liquid or mesophase. The solidity of many crystals must be questioned. Often, ordering of a phase increases the glass transition. Ultimately, this may move the glass transition to the melting temperature and melting and devitrification or crystallization and vitrification occur simultaneously. In these cases a crystal should be a solid. There are, however, many highly symmetric crystals which possess deformation mechanisms involving travel of successively generated one-dimensional dislocation defects along two-dimensional slip planes. For example, many metals are ductile or malleable. The presence of the same types of dislocations was inferred from the increase in heat capacity beyond the vibrational limit in Figure 6, but for macromolecules dislocations are usually sessile (immobile) in directions different from the chain direction (3,4).

The glass transition of amorphous polystyrene, PS, was one of the earliest analyzed in detail by calorimetry (61). In order to achieve high precision for T_g , a thermocouple was directly embedded into the sample. Figure 10 illustrates the results and also shows the reasonable agreement of the data when fitting with the hole model of Hirai and Eyring, mentioned above (56). The exponential curve suggests that infinitely slow cooling may retain C_p of the liquid, to absolute zero. Such slow experiments, however, are impossible to extend far below T_g and it is also erroneous to extrapolate the experimental, linear C_p of the liquid to temperatures below T_g to assess the thermodynamic functions of a hypothetical, supercooled liquid below T_g . Such extrapolation would keep the higher C_p of the liquid and result ultimately in a lower entropy than that of the crystal, the so-called Kauzman paradox (62). With better estimates of C_p of the liquid, it could be shown for polyethylene that this paradox does not seem to exist (63). Even avoiding the glass transition, C_p of the liquid drops on cooling sufficiently quickly so that the amorphous solid and supercooled liquid have similar C_p s and the liquid retains a positive entropy at 0 K, in addition to the substantial positive G_a .

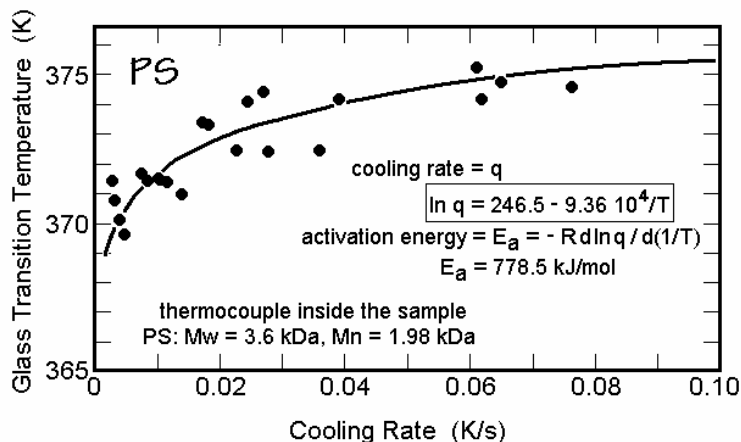


Fig. 10: Glass transition of polystyrene, PS, as a function of the cooling rate, q , measured by finding the half-change of heat capacity on going from the liquid to the glass.

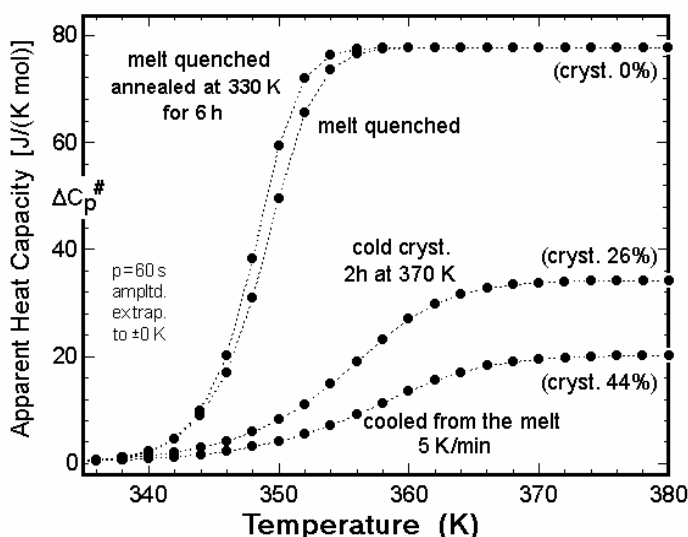


Fig. 11: Change of heat capacity of amorphous and semicrystalline poly(ethylene terephthalate), PET, in the glass transition region, as measured by TMDC (67). The thermal pre-treatments are listed next to the data points.

Looking to the onset of the glass transition, one notes a similarity of glass and crystal. For polyethylene, one can see in Figure 6 that up to 150 K below T_g and T_m there are only vibrational contributions. As the transitions are approached, defect-based, large-amplitude motion is noted. For the glass transition, close to T_g , it gradually turns into the characteristic cooperative motion. For the crystals melting intervenes before a glass transition is reached. It was found,

however, that for crystals of some nylons (64) and poly(oxymethylene) (65) the full glass transition can be reached before disordering of the crystals occurs, i.e. these polymers have a separate T_g and T_m (66), while for polyethylene, crystals show the final increase in C_p to that of the liquid only at T_m .

An analysis of the kinetics of the glass transition of amorphous and various semicrystalline poly(ethylene terephthalate)s is reproduced in Figure 11 (67). The TMDC data were taken during the last 10 min of a 20 min run ($p = 60$ s). The time before data collection was long enough to reach repeatability and cause the overall drift of the sample toward equilibrium to be negligible (see Figures 2 and 3). The modulation was properly chosen so that the Lissajous ellipse of a plot of sample temperature versus heat-flow rate did not change and was symmetric over the last 10 modulation cycles. The sequence of measured runs of temperatures, T_o , could be performed on cooling and heating with identical results. The frequency data of different amplitude were extrapolated to zero amplitude.

Analyzing the different samples with a simple, first-order kinetics, based on the hole theory yields different relaxation times for the different samples, accounting for the broadening of the transition when going from amorphous, annealed glasses to slowly cooled, semicrystalline samples (68,69). In addition to the broadening of the glass transition, the change in heat capacity through the glass transition was not linear with crystallinity measured from the latent heat of fusion, rather it

suggested a sizable amorphous fraction that does not participate in the measured glass transition. This fraction remains rigid on heating and shows a separate glass transition at higher temperature. It was identified as a ‘rigid-amorphous fraction,’ RAF of nanophase dimension (29,70). Both crystallinity and RAF, thus, must be known to judge the mechanical properties of semicrystalline polymers. Several different responses can be understood from the chosen simplified ‘hole model.’ 1.) A small, constant contribution to C_p . 2.) A second-harmonic contribution to C_p besides the main, first-harmonic response. 3.) A frequency-shift of the main, first-harmonic response. All these effects make the calorimetric response at T_g non-linear, so that an analysis is only possible with proper model calculations (3).

Above the glass transition, semicrystalline macromolecules, being metastable, may become unstable with increasing temperature. On approach of the melting temperature, for example, a multitude of reorganization, irreversible melting, and recrystallization may occur. These effects cause changes in $C_p^\#$ of eq. (6) with a much longer time scale than the fast vibrations with frequencies in the THz region (10^{12} Hz), shown in Figures 4 for polyethylene. For the interpretation of the measured data, they must be compared to the thermodynamic functions caused by vibrations only, which represent a hypothetical, solid equilibrium crystal. A larger number of experimental data have been collected and discussed in (29). With the modern modulated calorimetry and the ultrafast calorimetry of small sample mass, much progress is expected in not only by understanding the thermal behavior, but also by the link of mechanical properties, and molecular motion to thermal properties.

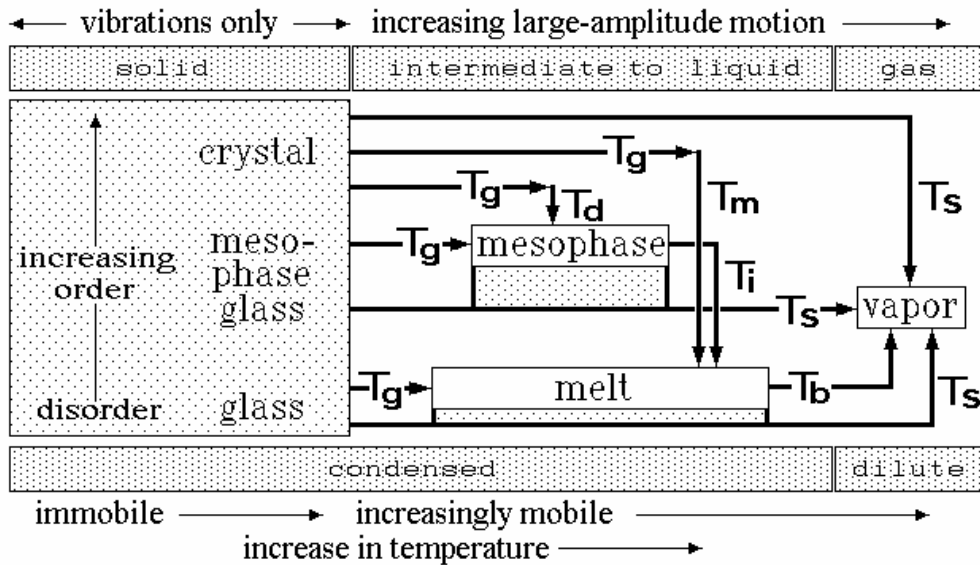


Fig. 12: Schematic of the changes in molecular motion and structural order on going through the various phase transitions indicated in Figure 1.

5. 8. Conclusions

The characterization of the phases between solid and liquid using thermal analysis was begun with a review of the definitions and classifications. Of particular importance were changes suggested for the definition of the solid state, types of molecules, and of small phases. A phase to be analyzed by thermal analysis is suggested to be identified in terms of one of 58 types [based on three molecule

classes (small molecules, flexible macromolecules, and rigid macromolecules), the 10 phase types of Figure 1, and three phase sizes (macrophase, microphase, and nanophase)]. In case the sample is heterogeneous, the global fitting of the different phases must be identified by their shapes and possibly molecular interconnections across the interfaces, which calls for a rather extensive analysis program (3,29).

Next, the new experimental tools of calorimetry which permit the measurements of heat capacity and latent heat, have been summarized with Figures 2 and 3. Modern developments were detailed, and methods available to not only measure equilibrium properties, but also to handle non-equilibrium and kinetic processes were displayed. The conclusion is that the success of quality data in differential calorimetry lies in the quality of the calibration.

Molecular motion, then, was linked to C_p . The vibrational motion in the solid state with a time scale shorter than one picosecond accounts for most of the enthalpy of the solid state, as illustrated with Figures 4–6 and 8. The large-amplitude conformational motion evolves at higher temperature out of torsional oscillations. Depending on the molecular structure, it may begin with the creation of isolated, intramolecular, conformational defects. At this stage the large-amplitude motion may also have a timescale in the picosecond range. The larger potential energy needed for the defect creation is detectable by a gradual deviation of C_p beyond the vibrational level as shown in Figure 6. At higher temperatures, the large-amplitude motion expands into intermolecular, cooperative, liquid-like motion, starting when approaching T_g with a high activation energy (Figure 10). In case the molecules are sufficiently small to undergo rotation and translation, these additional large-amplitude motions also begin when reaching the glass transition. The molecular motion, thus, is intimately connected to the glass transition (Figures 1, 6A, 8–11) and the transition involving a change in entropy, the first-order transitions (Figures 1, 6B, 8 and 9).

These conclusions are combined in Figure 12. Starting from a disordered glass (bottom) and going to increasingly ordered mesophase glasses and the crystal (top), the transition behavior changes. The transformation of the glass to the liquid (melt) occurs at T_g . Subsequent boiling, at T_b , produces the dilute gas phase (vapor). Mesophase glasses as detailed in Figure 1, show an analogous T_g to the mobile mesophase, which then can disorder to the melt (liquid) at the isotropization temperature, T_i . In rare cases the crystal may also undergo a glass transition of its own, but in many cases, it is so densely packed that large amplitude motion becomes only possible on disordering to a mesophase, combining T_g and T_d , or on melting, combining T_g and T_m . Crystals, particularly those of high symmetry are, however, often ductile by defect motion along glide planes, so that a crystal cannot always be identified as a solid. Finally, all condensed phases are directly linked to the vapor or gas phase by sublimation.

References 5

1. *Merriam Webster's Collegiate Dictionary*, 11th Edition, Merriam-Webster, Inc., Springfield, MA, 2003, see also: <http://www.m-w.com/>.
2. P.W. Bridgeman, *The Logic of Modern Physics*, MacMillan, New York, 1927.
3. See, for example, B. Wunderlich, *Thermal Analysis of Polymeric Materials*, Springer-Verlag, Berlin, 2005. ISBN 978-3-540-23629-0 (Print) 978-3-540-26360-9 (Online). See also the Computer Course: *Thermal Analysis of Materials*, <http://athas.prz.rzeszow.pl>, www.scite.eu, or <http://www.evitherm.org/index.asp>.

4. B. Wunderlich, *Macromolecular Physics*, Volumes 1–3, Academic press, New York, 1973–1980 (A pdf reprint with a new Preface and electronically searchable index republished in 2005, available from web-site of the European Virtual Institute for Thermal Metrology: <http://www.evitherm.org/index.asp>).
5. B. Wunderlich and J. Grebowicz, *Adv. Polymer Sci.*, 1984, 60/61, 1–59.
6. B. Wunderlich, M. Möller, J. Grebowicz, H. Baur, *Conformational Motion and Disorder in Low and High Molecular Mass Crystals*. Springer Verlag, Berlin (*Adv. Polymer Sci.*, Volume 87), 1988.
7. IUPAC. *Compendium of Chemical Terminology* (the “Gold Book”) Oxford (1997). Originally Compiled by A. D. McNaught and A. Wilkinson. Blackwell. XML on-line corrected version: <http://goldbook.iupac.org> (2006-), created by M. Nic, J. Jirat, B. Kosata; updates compiled by A. Jenkins. ISBN 0-9678550-9-8. doi: 10.1351/goldbook.
8. J. W. Gibbs, *Trans. Conn. Acad.* III, 1875/76, 108–248, and 1877/78, 343–524; an extended abstract was published in: *Am. J. Science, Ser. 3*, 1878, 16, 441–458; both are reprinted in H. A. Bumstead, R. Gibbs van Name, *The Scientific Papers of J. Willard Gibbs*, Volume 1, *Thermodynamics*, Dover Publ. New York, 1961.
9. T.L. Hill, *J. Chem. Phys.*, 1962, 36, 3182–3197, see also: *Thermodynamics of Small Systems, Parts I and II*, Benjamin, New York, 1963, 1964; reprinted: Dover, New York, 1994.
10. For an early discussion see: G. Tammann, *Z. anorg. allg. Chemie*, 1920, 111, 166–168; and R. C. Tolman, *J. Chem. Phys.*, 1948, 16, 758–774.
11. For early experiments see F. Meissner, *Z. anorg. allg. Chemie*, 1920, 111, 169–186.
12. H.-F. Eicke, *Surfactant Science Series*, 1987, 21, 41–92.
13. R. W. Siegel, S. Ramasamy, H. Hahn, Z. Li, T. Lu, R. Gronsky, *Journal of Materials Research*, 1988, 3, 1367–1372.
14. For a recent description of nanophases see: B. Wunderlich, *Thermochim. Acta*, in press, 2009.
15. Quoted from a lecture of <http://www.its.caltech.edu/~feynman/plenty.html>.
16. W. Chen, B. Wunderlich, *Macromol. Chem. Phys.*, 1999, 200, 283–311.
17. R. Hosemann, *J. Appl. Phys.*, 1963, 34, 25–41.
18. B. Wunderlich, D. Poland, *J. Polymer Sci., Part A*, 1963, 1, 357–372.
19. R. F. Bryan, P. Hartley, R. W. Miller, M.-S. Shen, *Mol. Cryst. Liq. Cryst.*, 1980, 62, 281–309.
20. The term “macromolecule” was first used by H. Staudinger, J. Fritschi, *Helv. Chim. Acta*, 1922, 5, 785–806. In his Nobel Lecture of 1953 Staudinger sets the limit of small molecules at 1,000 atoms (H. Staudinger, *Arbeitserinnerungen*, Hüthig, Heidelberg, Germany, 1961, pg 317).
21. Summary of these classifications see B. Wunderlich, *Thermochim. Acta*, 1999, 340/41, 37–52.
22. Green Book: *IUPAC Quantities, Units and Symbols in Physical Chemistry*. Second Edition, Blackwell Scientific Publications, Oxford, 1993.
23. W. H. Nernst, *Ann. Physik*, 1911, 36, 395–439.
24. A. E. Worthington, P. C. Marx, M. Dole, *Rev. Sci. Instr.*, 1955, 26, 698–702.

25. E. Gmelin, P. Rödhammer. *J. Phys. E. Sci. Inst.*, 1981, 14, 223–228.
26. Z.-C. Tan, Q. Shi, B.-P. Liu, H.-T. Zhang, *J. Thermal Anal. Calorim.*, 2008, 92, 367–374.
27. A. Boller, Y. Jin, B. Wunderlich, *J. Thermal Analysis*, 1994, 42, 307–330.
28. B. Wunderlich, Y. Jin, A. Boller, *Thermochim. Acta*, 1994, 238, 277–293.
29. B. Wunderlich, *Progress in Polymer Science*, 2003, 28/3, 383–450.
30. R. Androsch, I. Moon, S. Kreitmeier, B. Wunderlich, *Thermochim. Acta*, 2000, 357/358, 267–278.
31. R. Androsch, B. Wunderlich, *Thermochim. Acta*, 1999, 333, 27–32.
32. A. Einstein, *Ann. Physik*, 1907, 22, 180–190 and 800.
33. Einstein function tables, see: J. Sherman, R. B. Ewell, *J. Phys. Chem.*, 1942, 46, 641–62.
34. P. Debye, *Ann. Physik*, 1912, 39, 789–839.
35. Tables of three dimensional Debye functions: J. A. Beattie. *J. Math. Phys. (MIT)*, 1926, 6, 1–32.
36. E. Schrödinger in H. Geiger, K. Scheel, F. Henning, eds.: *Handbuch der Physik*, Springer, Berlin, 1926, Volume 10, *Thermische Eigenschaften der Stoffe*, p. 275.
37. J. Barnes, B. Fanconi. *J. Phys. Chem. Ref. Data* 7, 1309–1321 (1978).
38. V. V. Tarasov, *Zh. Fiz. Khim.*, 1950, 24, 111–128; 1953, 27, 1430–1435; V. V. Tarasov, G. A. Yunitskii, *Zh. Fiz. Khim.*, 1965, 39, 2077–2080.
39. Crystals with planar molecules and tables for the two dimensional Debye functions are given in: U. Gaur, G. Pultz, H. Wiedemeier, B. Wunderlich. *J. Thermal Analysis*, 1981, 21, 309–326.
40. A first analysis of the heat capacity of crystalline polyethylene and tables of one dimensional Debye functions are available in: B. Wunderlich. *J. Chem. Phys.*, 1962, 37, 1207–1216.
41. For initial computer programs and discussions of the fitting of C_p of linear macromolecules, see: Yu. Y. Cheban, S. F. Lau, B. Wunderlich. *Colloid Polymer Sci.*, 1982, 260, 9–19.
42. G. Zhang, B. Wunderlich, *J. Thermal Analysis*, 1996, 47, 899–911.
43. Using 3-, 2-, and 1-dimensional Debye functions is described in: M. Pyda, M. Bartkowiak, B. Wunderlich, *J. Thermal Analysis and Calorimetry*, 1998, 52, 631–656.
44. J. Grebowicz, B. Wunderlich, *J. Thermal Anal.*, 1985, 30, 229–236.
45. R. Pan, M. Varma, B. Wunderlich, *J. Thermal Anal.*, 1989, 35, 955–966.

46. U. Gaur, H.-C. Shu, A. Mehta, S.-F. Lau, B. B. Wunderlich, M. Varma-Nair, B. Wunderlich, *J. Phys. Chem., Ref. Data*, 1981, 10, 89 119 1001 1051; 1982, 11, 313 1065; 1983, 12, 29, 65, 91; 1991, 20, 349 (1991); an internet version is available through: <http://athas.prz.rzeszow.pl>.
47. B. Wunderlich, *Pure Appl. Chem.* 1995, 67, 1019–1026; see also, *Shin Netsu Sokuteino Shinpo*, 1990, 1, 71–100.
48. G. Zhang, S. Gerdes, B. Wunderlich, *Macromolecular Chem. Phys.*, 1996, 197, 3791–3806.
49. M. Pyda, B. Wunderlich, *Macromolecules*, 1999, 32, 2044–2050.
50. K. Loufakis, B. Wunderlich, *J. Phys. Chem.*, 1988, 92, 4205–4209.
51. B. G. Sumpter, D. W. Noid, G. L. Liang, B. Wunderlich, *Adv. Polymer Sci.*, 1994, 116, 27–72.
52. B. Wunderlich, *J. Chem. Phys.*, 1962, 37, 2429–2432; *J. Polymer Sci., Part C*, 1963, 1, 41–64.
53. Y. Kim, H. L. Strauss, R. G. Snyder, *J. Phys. Chem.*, 1989, 93, 7520–7526.
54. B. Wunderlich, M. Pyda, J. Pak, R. Androsch, *Thermochim. Acta.*, 2001, 377, 9–33.
55. G. Herzberg, *Infrared and Raman Spectra of Polyatomic Molecules*. Van Nostrand, New York, 1945.
56. H. Eyring, *J. Chem. Phys.*, 1936, 4, 283–291; see also N. Hirai, H. Eyring. *J. Appl. Phys.*, 1958, 29, 810–816.
57. P. Ehrenfest, “Phase Changes in the Ordinary and Extended Sense Classified According to the Corresponding Singularities of the Thermodynamic Potential.” *Proc Acad Sci, Amsterdam*, 1933, 36, 153–157. Suppl. 75b, Mitt Kammerlingh Onnes Inst, Leiden.
58. B. Wunderlich, *Polymer*, 1964, 5, 125–134 and 611–624.
59. M. Pyda, E. Nowak-Pyda, J. Heeg, H. Huth, A. A. Minakov, M. L. Di Lorenzo, C. Schick, and B. Wunderlich, *J. Polymer Sci., Part B: Polymer Phys.*, 2006, 44, 1364–1377.
60. E. Hellmuth, B. Wunderlich, *J. Appl. Phys.*, 1965, 36, 3039–3044.
61. B. Wunderlich, D. M. Bodily, M. H. Kaplan, *J. Appl. Phys.* 1964, 35, 95–102.
62. W. Kauzmann, *Chem. Rev.*, 1948, 43, 219–256.
63. M. Pyda, and B. Wunderlich, *J. Polymer Sci., Part B: Polymer Phys.*, 2002, 40, 1245–1253.
64. B. Wunderlich, *Journal Thermal Analysis and Calorimetry*, 2008, 93, 7–17.
65. W. Qiu, M. Pyda, E. Nowak-Pyda, A. Habenschuss, and B. Wunderlich, *Macromolecules*, 2005, 38, 8454–8567.
66. B. Wunderlich, *Thermochim. Acta*, 2006, 446, 128–134.
67. I. Okazaki, B. Wunderlich. *J. Polymer Sci., Part B: Polymer Phys.*, 1996, 34, 2941–2952.
68. B. Wunderlich, A. Boller, I Okazaki, S. Kreitmeier, *J. Thermal Analysis*, 1996, 47, 1013–1026.
69. B. Wunderlich, I. Okazaki., *J. Thermal Analysis*, 1997, 49, 57–70.
70. H. Suzuki, J. Grebowicz, B. Wunderlich, *British Polymer Journal*, 1985, 17,



Chapter 6
Phase separation

6. PHASE SEPARATION IN MACROMOLECULAR SYSTEMS

Ivan Krakovský, Yuko Ikeda

6. 1. Polymers

Methods of thermal analysis, such as, e.g., differential scanning calorimetry (DSC) and dynamic mechanical analysis (DMA) in combination with other methods (optical microscopy, small-angle X-ray and neutron scattering (SAXS, SANS), etc.) are very helpful in investigation of phase behaviour and physical properties of heterogeneous systems. Advantage of DSC relative to other methods consists in small amount of material necessary for the measurement, simple sample preparation and short measuring time.

Polymers are one of the most important materials in nature as well as modern technology. Polysaccharides such as cellulose represent main constituents of wood and paper. Other natural polymeric materials, e.g., caoutchouc have been exploited for centuries. Proteins and nucleic acids are biopolymers which play a crucial role in life processes. Today list of synthetic polymers is amazing and includes polyethylene, polypropylene, polystyrene to mention just a few.

It will be useful to remind what is common for all polymeric materials mentioned above despite a great difference in their properties. Polymers are distinguished from other materials by the structure of their molecules – the prevailing motif is represented by a long linear sequence of atoms or groups of atoms referred to as polymer chain or macromolecule [1]. Therefore, polymers are materials which are built of molecules with highest molecular weight. Polymer chains may be also linked together into one giant molecule of macroscopic dimensions – polymer network - as it takes place in rubbers or resins. Though majority of synthetic as well natural polymers is composed of a few kinds of elements, only, they exhibit an extremely rich variety of chemical compositions, spatial forms and topologies.

Unlike details of their structure there is something universal for all polymer chains: despite of different degrees of flexibility any *sufficiently long* polymer chain obtains a form of complicated interwoven coil resembling a trail of an object flying randomly in 3D space. Many properties of polymers can be explained exploiting the resemblance between polymer chain and random walk [2], see Fig. 1.

For example, the size of polymer coil can be estimated from the mean-square root of the distance between the origin and end of the random walk, $\sqrt{\langle R^2 \rangle}$:

$$\sqrt{\langle R^2 \rangle} = b\sqrt{N} \quad (1)$$

where the number of steps, N , and their length, b , correspond to the number of (statistical) segments and persistent length of the polymer chain, respectively [2]. Obviously, polymer coil, typically formed by a linear chain composed of hundreds of

statistical segments of the length of few nanometers has a characteristic size of a few nanometers which explains why polymers are very attractive for nanotechnology¹.

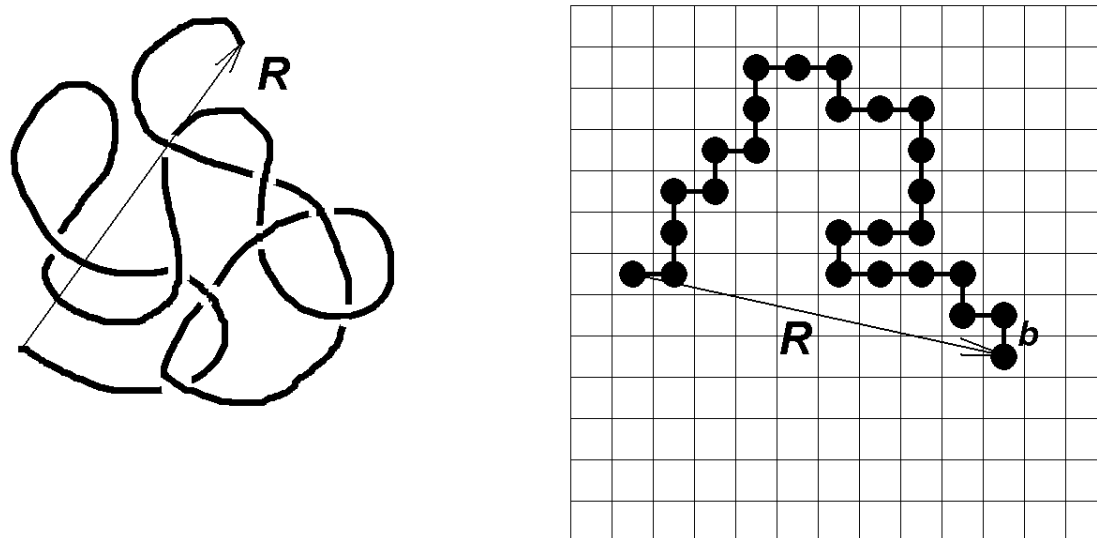


Fig. 1. Illustration of the analogy between the space form of polymer chain (polymer coil in 3D) and random walk (in 2D).

Many characteristic properties of polymers originate from the chain structure of macromolecules, e.g.:

- Polymers are poor in (configurational) entropy,
- Large part of elasticity of polymers at temperatures above glass transition temperature is of entropic origin,
- In polymers there is a wide spectrum of processes with very broad characteristic time – from very slow translational and rotational dynamics of whole chains realized by means of torsional movements of their segments of large amplitude to very fast vibrations of bond length and angles of small amplitude.

Thermal properties of an amorphous polymer (i.e., polymer unable of crystallization) are similar to that of any glass-forming substance. If the temperature of the substance is decreased a big increase in viscosity and response time to external perturbations is observed. Below the glass transition temperature, T_g , the material is not able to attain its equilibrium state and falls out of equilibrium (see Fig. 2). This state is referred to as glassy state. Due to non-equilibrium character of the glassy state, the glass transition temperature is not well-defined parameter since its value depends on the cooling rate.

Despite a great effort, the exact nature of the glass transition has not yet been fully clarified. As regards to polymers, the reduction in configurational entropy of the system seems to play an important role [3,4]. If a polymer is cooled down at a constant rate to a temperature below the glass temperature and the system is annealed for a time, a slow relaxation to an “equilibrium” state occurs which is reflected in a

¹ At the same time, the length of the same chain in fully stretched state, L , is: $L = bN \gg b\sqrt{N}$ for $N \gg 1$.

decrease of the enthalpy, H . If the system is heated again at a rate used typically in DSC, its enthalpy can evolve in two ways shown in Fig. 2. A recovery peak is found in heating DSC curves which represent temperature dependences of specific heat at constant pressure, $c_p = (\partial H / \partial T)_p$. The peak can occur either before glass transition (a) or (more often) it is superimposed on it (b).

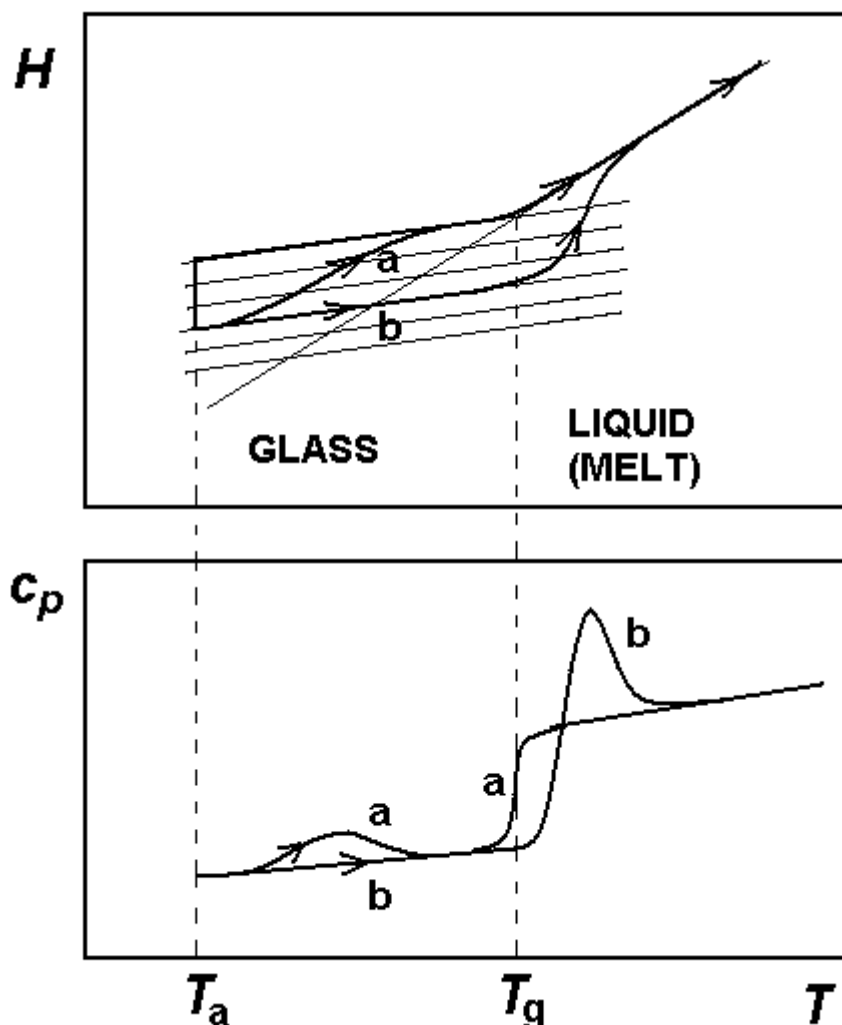


Fig. 2. Two possible ways of enthalpy relaxation during heating of a polymer annealed for a time in the glassy state. Adapted from [5].

6. 2. Polymer solutions and blends

Polymer solutions and blends represent multicomponent systems. Similar to low-molecular-weight systems, they exhibit a rich variety of phase behaviour, which can be described by the methods of general thermodynamics. Fig. 3a shows one special example of the phase diagram for a binary mixture exhibiting upper critical solution temperature (UCST).

At temperatures higher than the critical temperature, T_c , the one-phase state of the binary mixture is stable for all compositions, described by, e.g., molar fraction of the component 2, x_2 . Cooling of the mixture with certain composition can bring it into region where it is metastable. It starts to demix and droplets of new phase appear after some delay because an energy barrier against diffusion of the components into two

new phases has to be overcome. The curve allocating the onset of phase separation in the phase diagram is referred to as cloud point curve or binodal line (Fig. 3). If viscosity of the system is low enough as it is the case in polymer solutions, the droplets coalesce and the two phases can be isolated and analysed. However, in polymer blends the viscosity of phases is usually much higher and full demixing would require unrealistic time. Eventually, heterogeneous material with a particulate morphology which is in non-equilibrium state is obtained.

Sufficiently deep and fast cooling can bring the mixture into unstable state which is marked out by spinodal line in the phase diagram (Fig. 3). In unstable state, the energy barrier against diffusion vanishes and the system spontaneously separates into two phases by a mechanism known as a spinodal decomposition. As in the above case, in polymer blends the process is again hindered by high viscosity of the system. Fixation of the system in this state by freezing or a chemical reaction provides a way of preparation of the heterogeneous materials with bicontinuous morphology.

Spinodals and binodals touch each other in the critical point where they have also common tangent (Fig. 3).

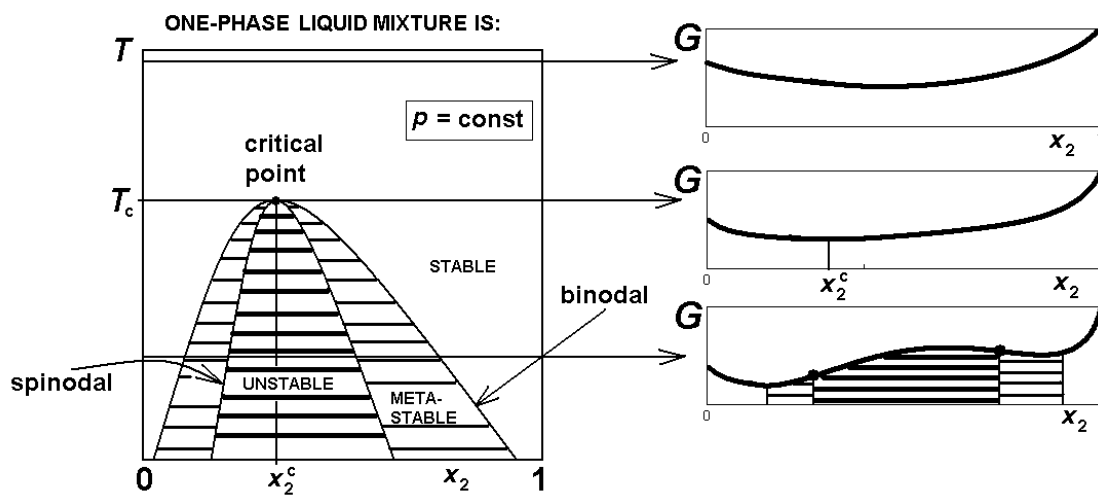


Fig. 3. Phase diagram of a binary mixture exhibiting upper critical solution temperature (UCST).

For a binary mixture the location of binodal, spinodal lines and critical point in the phase diagram can be determined by virtue of the derivatives of the Gibbs free energy, G , as

$$\begin{aligned} \mu_1^I &= \mu_1^{II} \\ \mu_2^I &= \mu_2^{II} \end{aligned} \quad \text{binodal (equality of chemical potentials in individual phases) (2)}$$

$$\frac{\partial^2 G}{\partial x_2^2} = 0 \quad \text{spinodal} \quad (3)$$

$$\frac{\partial^2 G}{\partial x_2^2} = 0 \quad \text{and} \quad \frac{\partial^3 G}{\partial x_2^3} = 0 \quad \text{critical points} \quad (4)$$

Therefore, if an expression for the Gibbs energy of a binary mixture as a function of temperature and composition can be derived on base of a microphysical model its phase diagram as well as its thermodynamic properties can be calculated. First model of this kind for polymer solutions was developed by Flory, Huggins, Miller and others almost 60 years ago [6-8], see also [1]. It is a lattice model: polymer chains and solvent molecules are “inweaved” into 3D simple cubic lattice such as in Fig. 1 and the sum over states of the system is calculated in the mean-field approximation. Final expression for the Gibbs energy of the polymer solution derived by Flory is:

$$G = N_1\mu_1^0 + N_2\mu_2^0 + k_B T \left[(N_1 + rN_2)\chi v_1 v_2 + N_1 \ln v_1 + N_2 \ln v_2 \right] \quad (5)$$

where N_1 , N_2 are numbers of solvent and polymer molecules, μ_1^0 , μ_2^0 their chemical potentials in pure form, and v_1 , v_2 their volume fractions. In discussion of the phase behaviour of mixtures involving polymers volume fractions are preferred to molar fractions due to high molecular weight of polymers.

In the derivation of eq. 5 it is assumed that polymer chains consist of equal number of segments, r , which are linked into a flexible array. The segment is supposed to occupy the same volume as a solvent molecule. Interaction parameter, χ , represents a measure of readiness of individual polymer segments to mutual mixing with solvent molecules.

Similar expression can be also derived for binary mixture of two polymers with the numbers of segments r_1 and r_2 , respectively:

$$G = N_1\mu_1^0 + N_2\mu_2^0 + k_B T \left[(r_1 N_1 + r_2 N_2)\chi v_1 v_2 + N_1 \ln v_1 + N_2 \ln v_2 \right] \quad (6)$$

Polymers are generally polydisperse, which leads to the generalization of eq.5 for polydisperse polymer solutions:

$$G = N_1\mu_1^0 + \sum_k N_{2k}\mu_{2k}^0 + k_B T \left[\left(N_1 + \sum_k r_k N_{2k} \right) \chi v_1 v_2 + N_1 \ln v_1 + \sum_k N_{2k} \ln v_{2k} \right] \quad (7)$$

where N_{2k} are numbers of k -mers consisting of r_k segments, μ_{1k}^0 their chemical potentials in pure form, and v_{2k} their volume fractions ($\sum_k v_{2k} = v_2$). Binodal line is defined by generalization of eq.2, i.e., equality of chemical potentials of the components for all the phases coexisting in the system. On spinodal line, the equation

$$\det \frac{\partial^2 G}{\partial v_{2k} \partial v_{2l}} = 0 \quad (8)$$

has to be satisfied. Binodal and spinodal lines have again a common tangent in the critical point. However, as a result of the polydispersity, they do not have a common extremum, and critical point is shifted appreciably towards higher polymer concentration even for polymers of low polydispersity (see Fig. 4).

ONE-PHASE LIQUID MIXTURE IS:

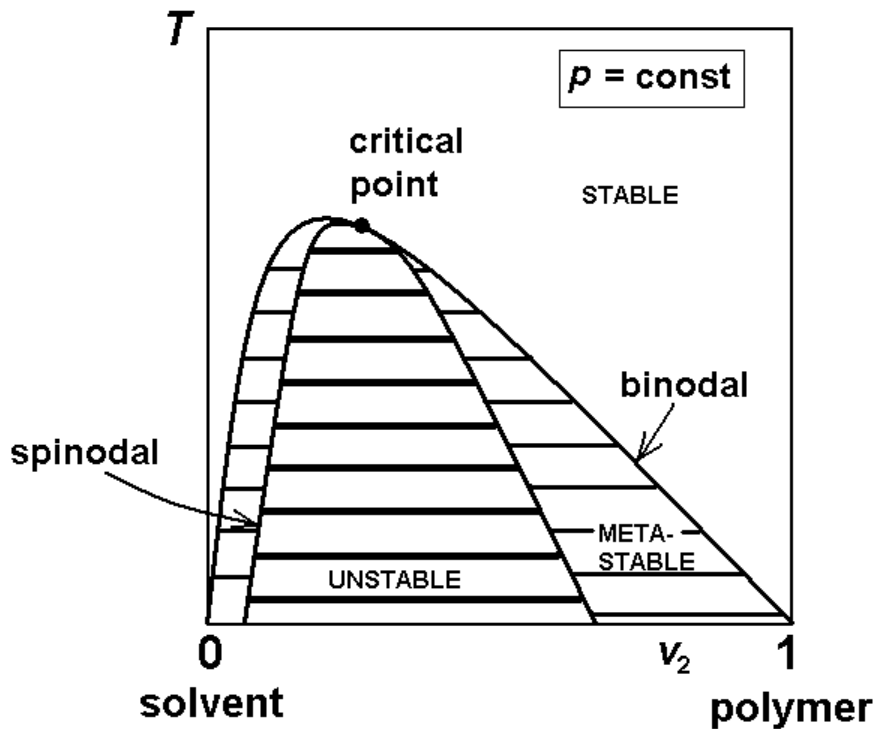


Fig. 4. Phase diagram of a solution of polydisperse polymer with UCST.

The lower value of the interaction parameter the higher readiness of polymer segments to mutual mixing. In the original treatment by Flory and Huggins, χ is assumed to be a function of temperature, only:

$$\chi(T) = \chi_s + \frac{\chi_H}{T} \quad (9)$$

where χ_s and χ_H are entropic and enthalpic part of the interaction parameter.

A large variety of phase diagrams found for polymer solutions and blends can be described formally assuming empirical form for the interaction parameter [9]:

$$\chi(T) = A + \frac{B}{T} + \frac{C}{T^2} \quad (10)$$

with three constants A , B and C .

However, in practice it turns out that χ also depends on the composition of mixtures. For example, Šolc et al. [10] showed that assuming the form:

$$\chi(T, v_2) = \left(\chi_s + \frac{\chi_H}{T} \right) + av_2 + bv_2^2 \quad (11)$$

where a , b are constants, allows explanation of double critical points observed in some systems, such as, e.g., aqueous solution of poly(vinylmethylether) (PVME).

In polymer solutions, binodals can be determined by observation of cloud points. For experimental location of spinodals methods like pulse-induced critical scattering has to be used [11]. Calorimetry can be also exploited for determination of

binodal lines. The method is based on the measurement of the change of enthalpy that occurs during demixing process induced by heating or cooling as illustrated in Fig. 5.

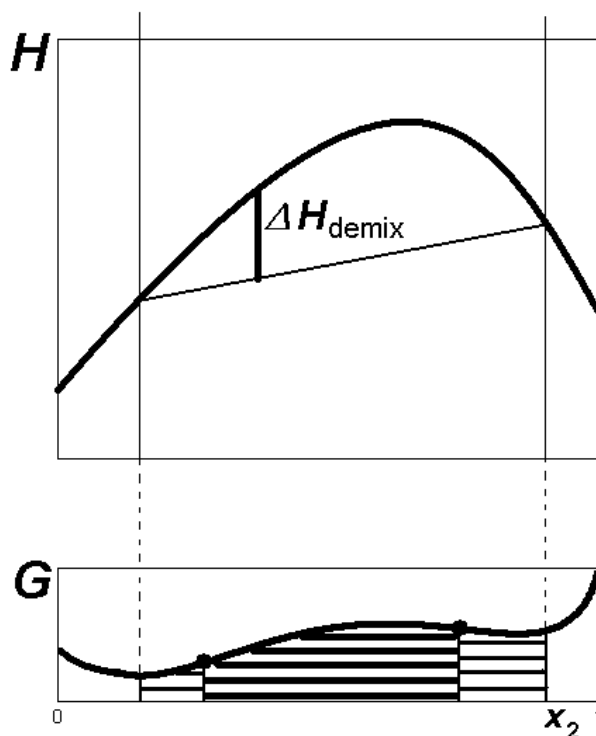


Fig. 5. Compositional dependence of the enthalpy and Gibbs free energy of a binary mixture at a temperature where the system is partially miscible.

In metastable or unstable one-phase state the enthalpy of the mixture is larger (thick curve in Fig. 5) than the enthalpy in two-phase state (thin line in Fig. 5). Demixing is therefore accompanied by an enthalpy jump, ΔH_{demix} , which can be measured by a calorimetric method if the jump is sufficiently large. This is the case for the aqueous solution of PVME as is illustrated in Fig. 6 where DSC traces obtained in heating and cooling are shown. Demixing in heating and remixing in cooling of the system is clearly visible. Note that this system has lower critical solution temperature (LCST) unlike the phase diagram with UCST shown in Fig. 3.

Enthalpy of demixing for a polymer solution or blend can be also calculated from the Flory-Huggins formulas (eqs. 5., 6 or 7) by virtue of the Gibbs-Helmholtz relation.

So far we dealt with phase behaviour of liquid binary systems – polymer solutions or blends in liquid state. What will happen if these systems are cooled to lower temperatures? In the case of the system with UCST, the components in individual phases pass into glassy state eventually. The glass transition can be preceded by crystallization if some components have a suitable regular molecular structure.

Systems with LCST which are one-phase liquids below the critical temperature exhibit phase diagrams similar to those found for low-molecular-weight mixtures, as illustrated in Fig. 6 by the phase diagram of the aqueous solution of Jeffamine ED2003. This polymer is basically poly(oxyethylene)) and crystallization (melting) of water and polymer, glass transition of polymer and formation of the eutectic mixture are found on DSC scans as shown in Fig. 7.

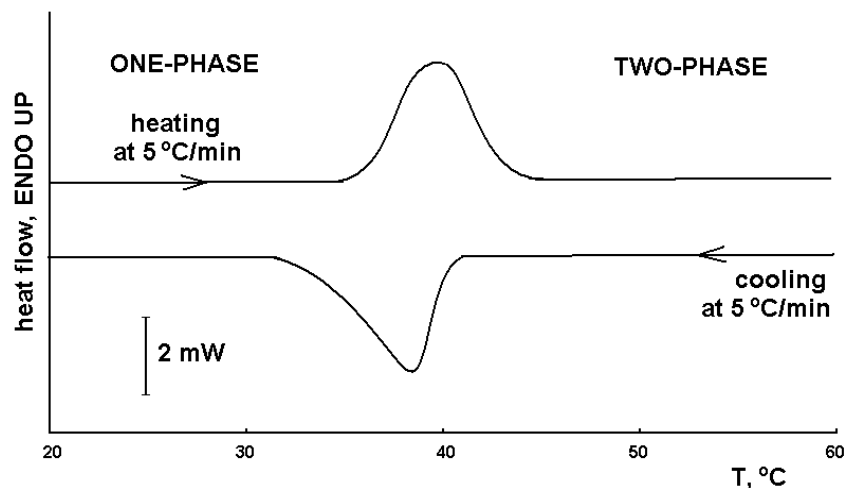


Fig. 6. DSC scans of poly(vinylmethylether) aqueous solution (volume fraction of polymer, $v_2 \approx 0.07$). Adapted from [12].

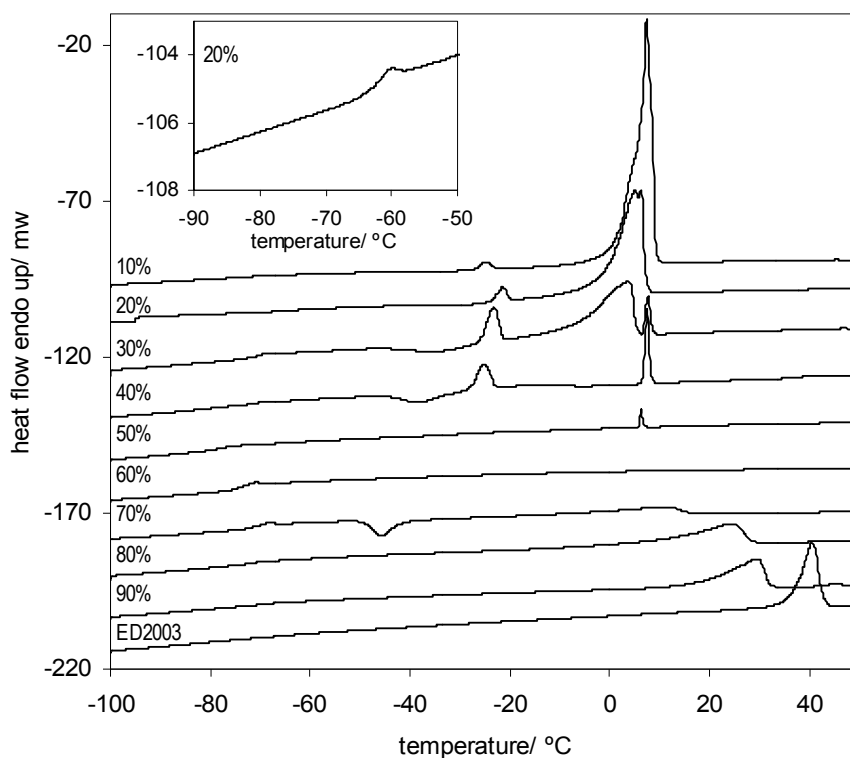


Fig. 7. DSC thermograms at a heating rate of $10^\circ\text{C}/\text{min}$ for the Jeffamine ED2003 aqueous solutions. The number on each curve represents the weight percentage of polymer in the solution. The insert shows a detail of the glass transition region for one of the solutions with high water content. Reproduced from [13] with the permission of Elsevier.

Actually, reheating of a system from its glassy state and determination of the glass temperatures of phases is the simplest and most often way used for investigation of phase behaviour and miscibility of polymer blends. An accepted unambiguous indication of one-phase state, i.e., that the components are miscible, is a single T_g which is close to a value calculated from T_g 's of the components by means of additivity rules [14,15]. Detection of multiple transitions, coincident with or shifted

from those determined for the neat components, proves that the system is in the multi-phase state.

Implementation of this procedure requires that glass transitions of phases are separated by a sufficiently large gap, at least 10 – 20 °C. The domains of individual phases should also have a size bigger than a critical size to manifest a unique glass transition. The critical size was estimated to be about 10 – 15 nm [16].

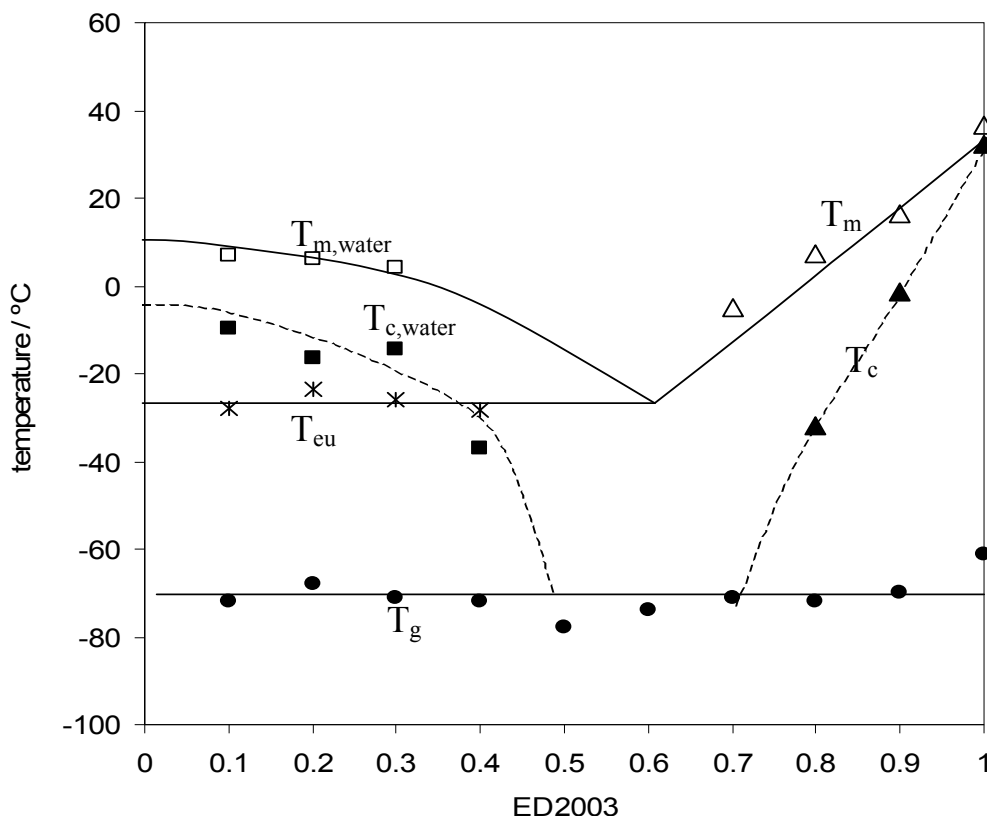


Fig. 8. Experimental phase diagram for the Jeffamine ED2003 aqueous solutions; (●) glass transition, (□) water melting, (■) water crystallization, (Δ) polymer melting, (▲) polymer crystallization, (*) eutectic. Lines are a guide to eye. Reproduced from [13] with the permission of Elsevier.

This is illustrated in Fig. 9 by thermal behaviour of poly(methylmetacrylate) (PMMA)/polyvinylacetate (PVAc) 50/50 blend cast from chloroform [17]. This blend is transparent at room temperature and a single glass transition is observed during first heating scan (curve A). This temperature lies between glass transition temperatures of neat PVAc and PMMA (curve C). Enthalpy relaxation peak is also present which is the result of the sample annealing in glassy state. This peak is erased by the first heating scan (curve B). However, heating of the blend to higher temperatures causes phase separation of the system as indicated by two glass transition temperatures in DSC trace obtained during heating scan of the blend annealed to 227 °C before the heating scan (curve C).

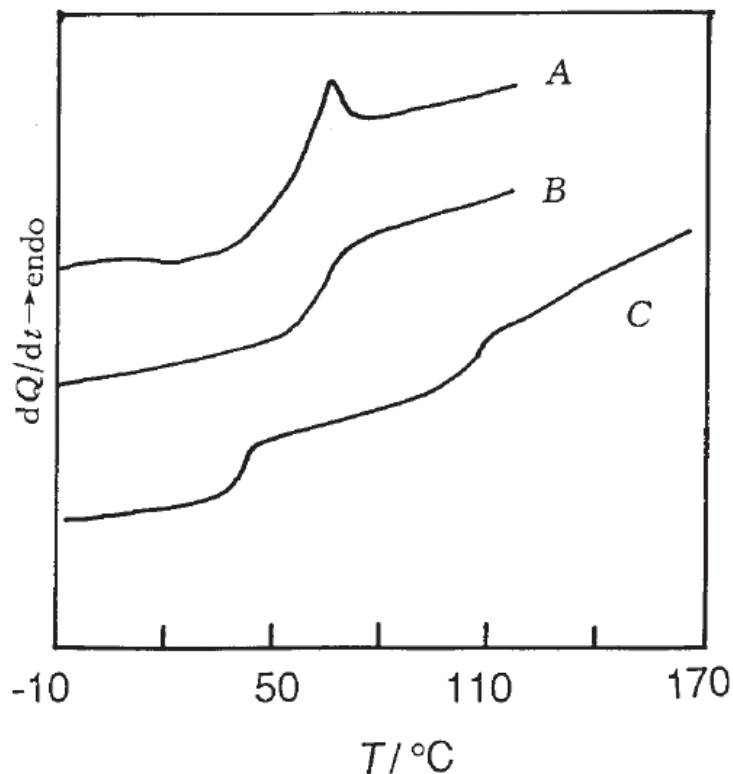


Fig. 9. DSC traces for 50/50 (mass ratio) PMMA/PVAc blend cast from chloroform. (A) first scan; (B) second scan (after heating to 117 °C); (C) after heating to 227 °C. The weight-average molecular weights of PMMA and PVAc are 60 000 and 453 000, respectively. Reproduced from [17] with the permission of Kluwer Academic Publishers.

Enthalpy relaxation, which is illustrated in Fig. 2., can be exploited in identification of multiphase structure in cases when glass transition temperatures of the components are close each other. The method is attractive due to its simplicity as illustrated in Fig. 9 where thermal behaviour of the polystyrene (PS), poly(methylmetacrylate) (PMMA) and their blend (67/33 % by weight) is shown [18]. The samples were first heated to temperature 150 °C which is higher than glass transition temperature of both polymers (106 °C and 126 °C for PS and PMMA, respectively). Before heating (scans shown in Fig. 10.), the samples were subject to three different thermal histories: annealing at 92 °C for 24 hrs (Fig. 10a), annealing at 98 °C for 320 hrs (Fig. 10b) and annealing at 112 °C for 24 hrs (Fig. 10c).

In the case of short annealing time (Fig. 10a), distinct enthalpy relaxation peak is observed for PS during heating scan. The peak for PMMA is much smaller because of higher T_g of PMMA and correspondingly much slower relaxation time at the annealing temperature. This is also reflected in the heating scan of PS/PMMA blend which has to be phase separated at 150 °C. Longer annealing at somewhat higher temperature makes the enthalpy relaxation peak of PMMA more distinct (Fig. 10b). Annealing at a temperature between the glass transitions of PS and PMMA for 24 hrs suppresses (Fig. 10c) enthalpy relaxation peak of PS and further sharpens the peak of PMMA.

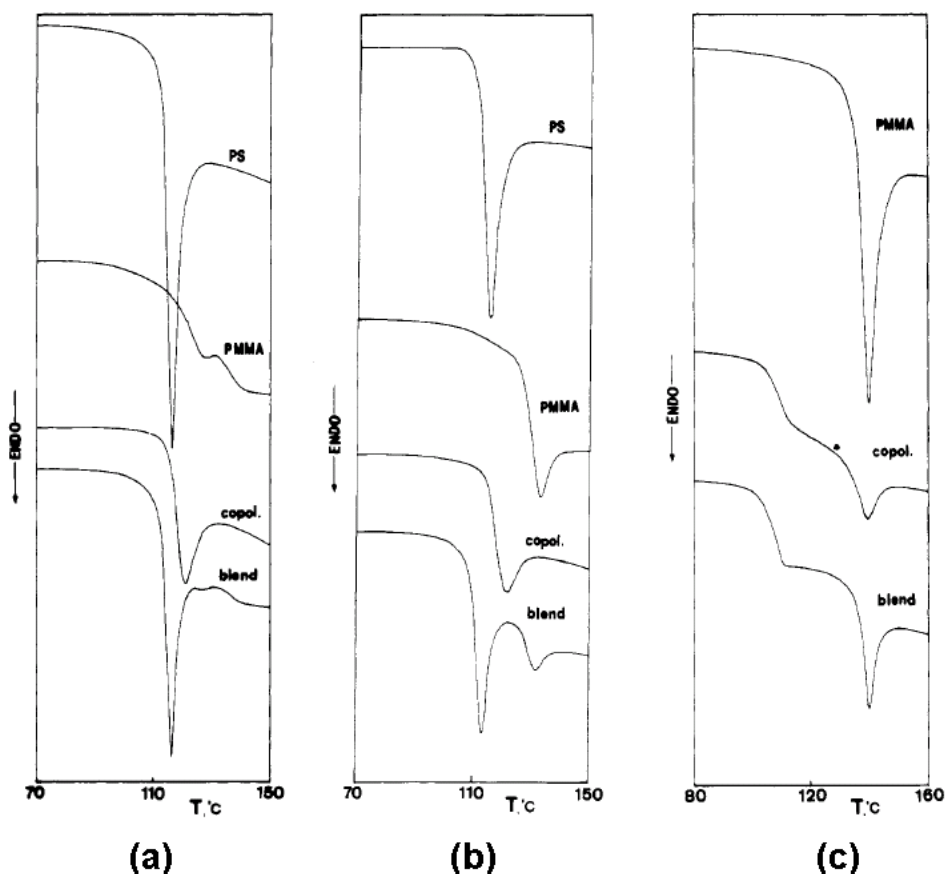


Fig. 10. DSC traces from polystyrene, polymethylmetacrylate, their blend (67/33 by weight) and block copolymer: a) annealed at 92 °C for 24 h, b) annealed at 98 °C for 320 h, c) annealed at 112 °C for 24 hrs. Note that in this figure endotherms are oriented down. Reproduced from Ref. [18] with the permission of The American Chemical Society.

6. 3. Block copolymers

A two-phase blend prepared by mixing of two different homopolymers is usually heterogeneous on micrometer scale. If the pairs of different homopolymer chains are linked covalently at their terminals giving rise to block copolymer chains, the phase separation of the resulting material on micrometer scale would require splitting of the copolymer chains into original parts which is not allowed due to strength of covalent bonds. Instead of that, the material separates into domains of the size commensurable with a characteristic length of the chain blocks. The magnitude of this length can be estimated using the mean root square of the end-to-end distance of chain blocks, $\sqrt{\langle R^2 \rangle}$. As it was mentioned above, for common polymers, the values of this parameter are in nanometer range and the domains can be therefore referred to as nanodomains. The nanodomains obtain various geometrical forms as shown in Fig. 10. Equilibrium morphology of the system is that which corresponds to the minimum of the Gibbs free energy at given temperature and composition expressed, e.g., by molar fraction of one of the blocks in the copolymer chain, X_B . There are three important phenomena which must be taken into account in the calculation of the Gibbs free energy of the system: a) interaction and mixing of the blocks analogical to that in polymer blend, b) stretching of the copolymer chains and c) formation of the new surface between (nano)phases, see, e.g. [19].

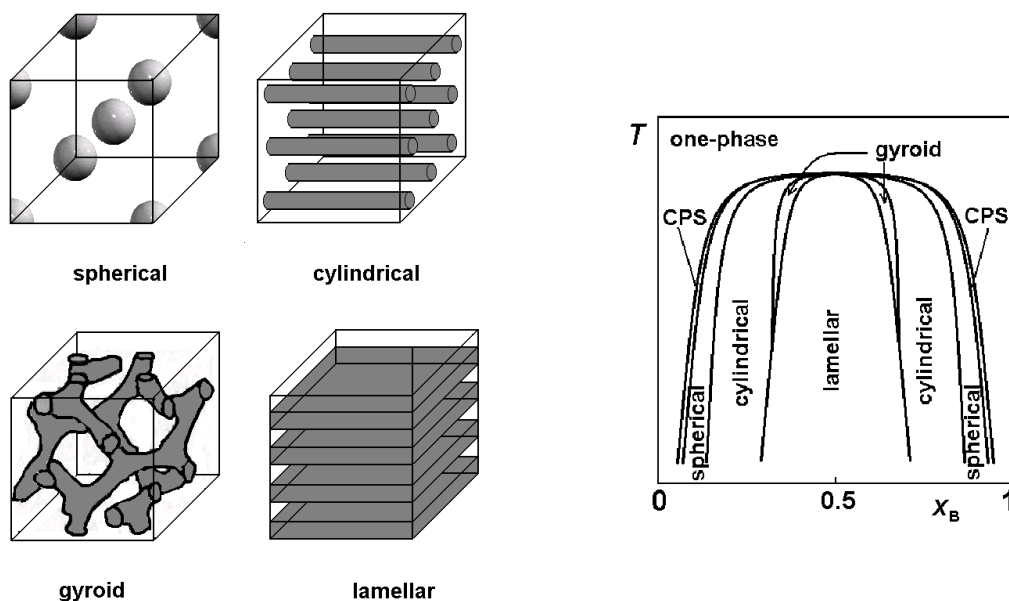


Fig. 11. Morphologies and schematic phase diagram for linear AB diblock copolymer. CPS = closest packed spheres. Adapted from [19].

Both, glass transitions and enthalpy relaxations of individual blocks can be used to reveal nanophase separation in block copolymers as illustrated in Fig. 12 and 10, respectively. Of course, morphology of the copolymer has to be identified by other method, such as X-ray scattering or transmission electron microscopy.

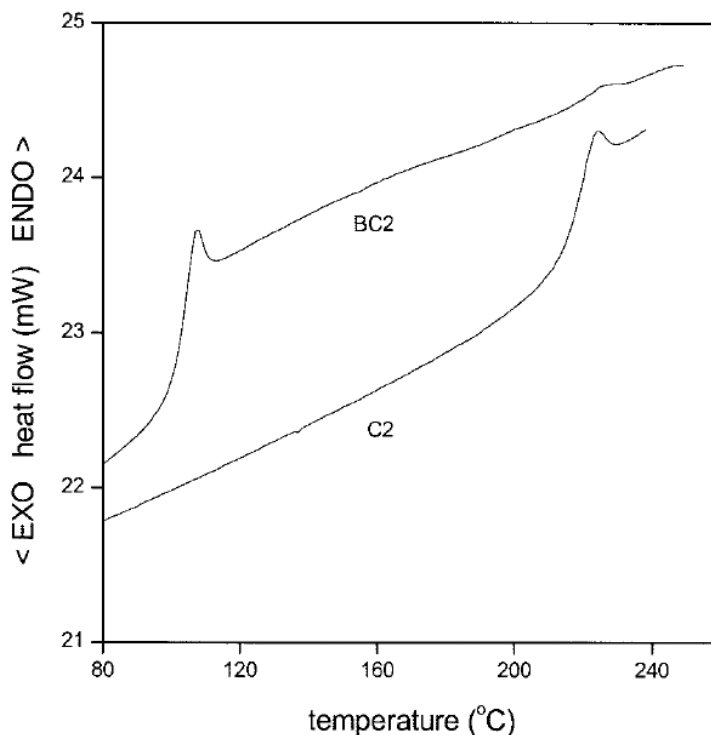


Fig. 12. DSC curves (the second heating scans) of the alternating styrene-maleimide copolymer (C2) and poly(styrene-co-maleimide)-block-polystyrene diblock copolymer (BC2). Reproduced from [20] with the permission of John Wiley & Sons, Inc.

6. 4. Nanophase separation in polymer networks

Polymer networks represent a system in which polymer chains are linked into one molecule of macroscopic dimensions (therefore, “infinite” on the molecular length scale). There are two main ways in which polymer network can be formed from polymer chains: a) random crosslinking (the links are distributed randomly along the chain) or b) end-linking (the chains are linked at their ends).

Cross- or endlinking of one of the components of the (multicomponent) reaction mixture is accompanied by change of the phase diagram of the system as illustrated in Fig. 13. With increasing molecular weight the binodals are shifted to higher temperature and initially homogeneous mixture can become unstable in the course of the reaction. The structure of the mixture can be SAXS as it is illustrated in Fig. 14 by endlinking of the mixture of poly(butadiene) diol (PBD) and poly(oxypropylene) triol (POPT) by diphenylmethane diisocyanate (MDI) [21]. Analogous to block copolymers, the phase separation cannot evolve into micrometer range because of the formation of covalent polymer network. As a result, nanophase separated polyurethane network is formed. The phases can be again identified using DSC by glass transitions of the components as shown in Fig. 15 for a series of nanophase separated polyurethane networks.

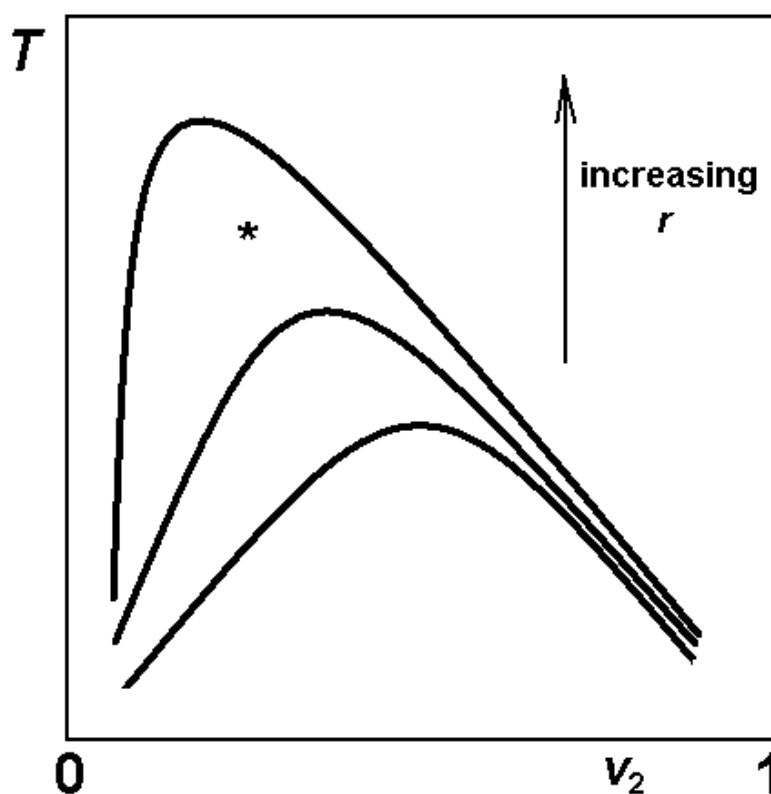


Fig. 13. Change of the phase diagram (shift of binodal line) with increasing molecular weight of polymer formed by cross- or endlinking (r denotes number of chain segments in the Flory-Huggins model). The asterisk denotes the state of the reaction mixture at the beginning of the reaction.

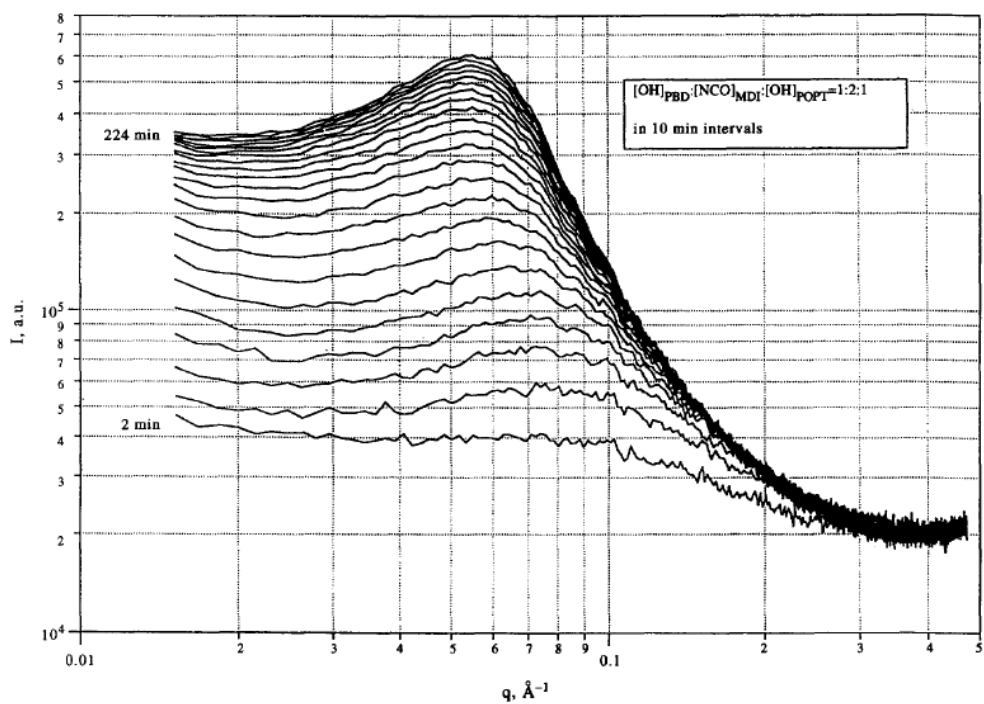


Fig. 14. Time-resolved SAXS patterns from the formation of nanophase separated polyurethane network by endlinking reaction of PBD and POPT with MDI. Reproduced from [21] with the permission of Elsevier.

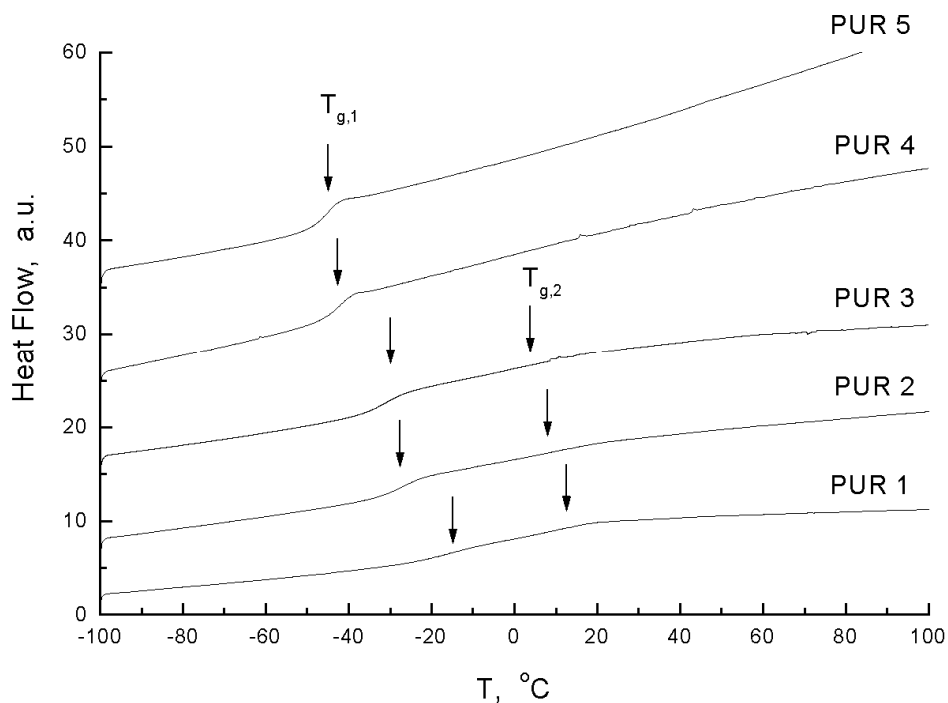


Fig. 15. DSC traces (second heating scans) from the series of nanophase separated polyurethane networks formed by endlinking reaction of PBD and POPT with MDI. The networks differ in molecular weight of PBD which is increasing from PUR1 to PUR5. The arrows indicate phase transitions of soft and hard segment nanophases. Reproduced from [22] with the permission of Elsevier.

6.5. Nanophase separation (crystallization) in polymer networks induced by strain

Conformations of polymer chains with longer end-to-end distance are less probable because they have lower number of realizations. Consequently, stretching of polymer chains is accompanied by a decrease of entropy of the system. If the polymer chains are cross- or endlinked into polymer network and the polymer network is stretched, the process is accompanied by decrease of the entropy (increase of the Gibbs free energy) and a change of the phase diagram. However, if the polymer chains in the network have suitable regular structure owing to stretching force the chain segments can orient themselves and form a new (crystalline) phase of lower internal energy. As the result, the Gibbs free energy of the stretched network with crystalline domains may be lower than its energy in fully amorphous state. The presence of covalent polymer network restricts the extent of the phase separation to nanometer scale as illustrated by WAXS patterns obtained from crosslinked natural rubber (NR) shown in Fig. 16 [23]. The phenomenon is referred to as strain-induced crystallization.

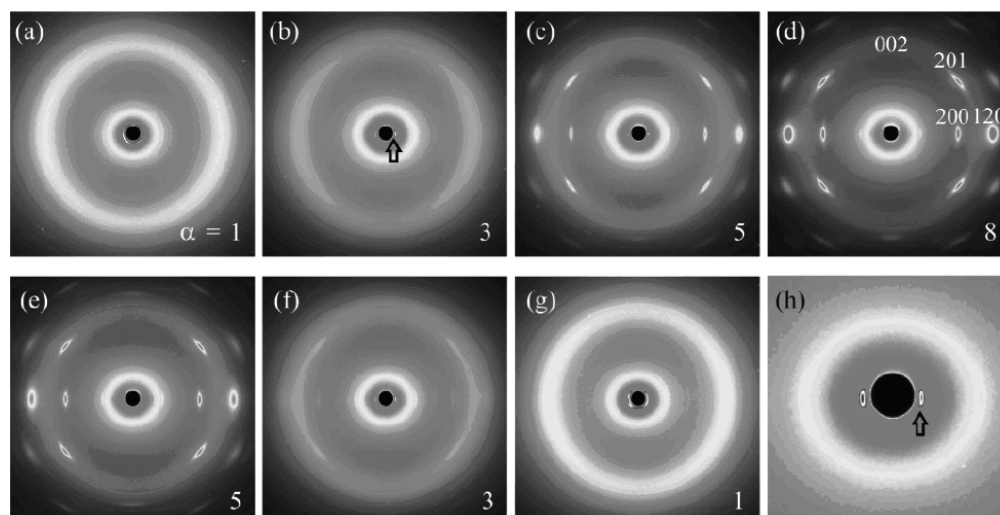


Fig. 16. Sequential change of WAXD patterns from NR-4. Stretching direction is vertical. Corresponding strain values are indicated at the right bottom in parts a-g of the figure. Indices of crystalline reflections of NR are indicated in part d. Part h shows the enlarged image of the center of part b. Reproduced from [23] with the permission American Chemical Society.

Strain-induced crystallization may be also observed by DSC. To realize DSC measurements on stretched samples in usual DSC apparatus, Lyon et al. [24] developed an ingenious way consisting in winding of a stretched fiber of the material on a spool-like sample holder. The results obtained from heating scans on the samples of segmented polyurethane stretched to different extension ratios, λ ($\lambda = L/L_0$ where L and L_0 are lengths of the fiber in stretched and unstretched state, respectively) are illustrated in Fig. 17. In the unstretched state ($\lambda=1$), only glass transition of soft segments (poly(oxytetramethylene), PTMO) at ca 220 K and thermally induced formation of crystalline domains of folded chains (ca 260 K) are

observed. The broad endotherm near room temperature is an indication of the formation of a mixed morphology at intermediate extensions. The growth of the strain-induced endotherm at 330 K at higher extension ratios is attributed to the formation of extended-chain crystalline domains. Change of the form of the glass transition of PTMO with extension ratio can be also noted.

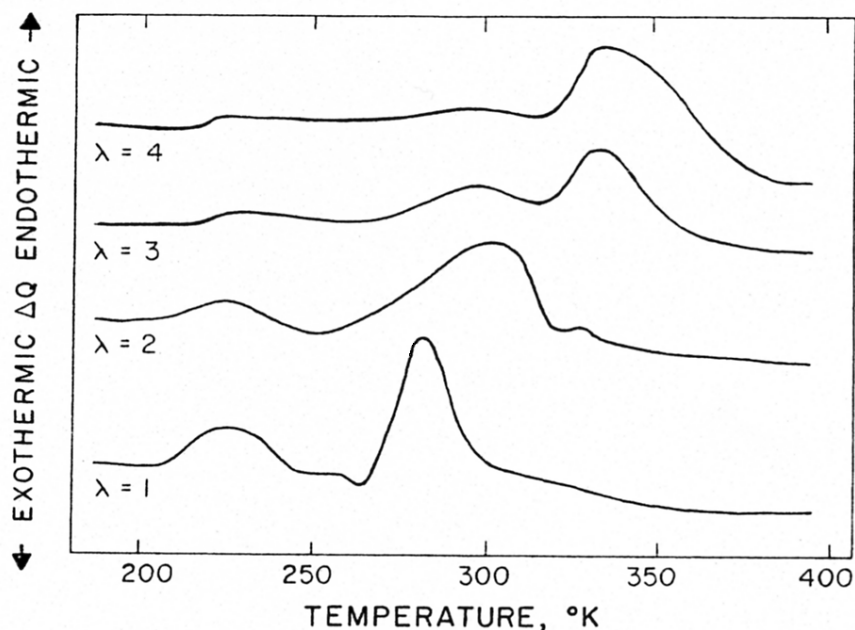


Fig. 17. DSC traces (heating scans) from a segmented PTMO elastomeric fiber at various fixed extension ratios, λ . Reproduced from [24] with the permission of the John Wiley & Sons, Inc.

Acknowledgement: Financial support from the Ministry of Education of the Czech Republic (project MSM 0021620835) is gratefully acknowledged.

References 6

1. Flory, P.J.: *Spatial Configuration of Macromolecular Chains*. In: Forsen, S. (ed.) Nobel Lecture. Chemistry 1971-1980, pp. 147 - 178, World Scientific Publishing Co., Singapore (1993)
2. Kawakatsu, T.: *Statistical Physics of Polymers*, Springer, Berlin (2004)
3. Gibbs, J.H, Di Marzio, E.A.: *Nature of the glass transition and the glassy state*. J. Chem. Phys. 28, 373-383 (1958)
4. Di Marzio, E.A., Gibbs, J.H.: *Chain stiffness and the lattice theory of polymer phases*. J. Chem. Phys. 28, 807-813 (1958)
5. ten Brinke, G., Oudhuis, L., Ellis, T.S.: *The thermal characterization of multicomponent systems by enthalpy relaxation*. Thermochim. Acta 238, 75-98 (1994)
6. Flory, P.J.: *Thermodynamics of high polymer solutions*. J. Chem. Phys. 9, 660 (1941); *Thermodynamics of high polymer solutions*. J. Chem. Phys. 10, 51-61 (1942)
7. Huggins, M.L.: *Solutions of long chain compounds*. J. Chem. Phys. 9, 440 (1941); *Some properties of solutions of long-chain compounds*. J. Phys. Chem. 46, 151-158 (1942)
8. Miller, A.R.: *The Theory of Solutions of High Polymers*, Clarendon Press, Oxford (1948)

9. Eitoni, H.B., Balsara N.P.: *Thermodynamics of Polymer Blends*. In: Mark, J.E. (ed.): *Physical Properties of Polymers Handbook*, pp. 359-356, Springer, N.Y. (2007)
10. Šolc, K., Dušek, K., Koningsveld, R., Berghmans, H.: "Zero" and "off-zero" critical concentrations in solutions of polydisperse polymers with very high molar masses. *Collect. Czech. Chem. Commun.* 60, 1661 - 1688 (1995)
11. Kiepen F., Borchard W.: *Light scattering as tool for the determination of adiabatically performed temperature changes*. *Makromol. Chem.* 189, 1543-1550 (1988)
12. Arnauts, J., De Cooman, R., Vandeweerd, P., Koningsveld, R., Berghmans, H.: *Calorimetric analysis of liquid-liquid phase-separation*. *Thermochim. Acta* 238, 1-16 (1994)
13. Gómez Ribelles J.L., Salmerón-Sánchez M., Torres de la Osa, L., Krakovský I.: *Thermal transitions in a,w-diamino terminated poly(oxypropylene)-block-poly(oxyethylene)-block-poly(oxypropylene) aqueous solutions and their epoxy networks*. *J.Non-Cryst.Solids*, 351, 1254-1260 (2005)
14. Utracki, L.: *Polymer Blends Handbook*, Springer, NewYork (2002)
15. Olabisi, O., Robeson, L.M., Shaw, M.T.: *Polymer-Polymer Miscibility*, Academic Press, NewYork (1979)
16. Utracki, L.: *Polymer Blends and Alloys*, Hanser Gardner Publ., NewYork (1990)
17. Qipeng, G., Zhenhai, L.: *Phase behavior of polymer blends*. *J. Therm. Anal. Cal.*, 59, 101-120 (2000)
18. Tsitsilianis, C., Staikos, G.: *Phase Behavior in PS-b-PMMA Block Copolymer by Enthalpy Relaxation*. *Macromolecules* 25, 910-916 (1992)
19. Bates, F.S., Fredrickson G.H.: *Block Copolymers - Designer Soft Materials*. *Physics Today*, February 1999, 32-38 (1999)
20. Krakovský I., Lokaj J., Sedláková Z., Ikeda Y., Nishida K.: *Hydrogen Bonding Interactions of Styrene-Maleimide Copolymers with Diaminotriazine Derivatives*. *J. Appl. Polym. Sci.* 101, 2338-2346 (2006)
21. Krakovský I., Urakawa H., Kajiwara K.: *Inhomogeneous structure of polyurethane networks based on poly(butadiene)diol. 2. Time-resolved SAXS study of the microphase separation*. *Polymer* 38, 3645-3653 (1997)
22. Krakovský I., Pleštil J., Baldrian J., Wübbenhorst M.: *Structure of inhomogeneous polymer networks prepared from telechelic polybutadiene* *Polymer* 43, 4989-4996 (2002)
23. Tosaka, M., Murakami, S., Poompradub, S., Kohjiya, S., Ikeda Y., Toki Y., Sics, Y., Hsiao, B.S.: *Orientation and crystallization of natural rubber network as revealed by WAXD using synchrotron radiation*. *Macromolecules* 37, 3299-3309 (2004)
24. Lyon, R.E., Farris, R.J., MacKnight, W.J.: *A differential scanning calorimetry method for determination strain-induced crystallization in elastomeric fibers*. *J.Polym.Sci. Polym. Lett. Ed.* 21, 323-328 (1983)



Chapter 7

Features of glassiness

7. SOME IMPORTANT FEATURES OF GLASSINESS AND THE NATURE OF AMORPHOUS SOLIDS

Hiroshi Suga

If you should understand the nature of a substance, but are allowed only one type of measurement to understand it, choose the heat capacity (A. Einstein)

The deepest and most important unsolved problem in condensed matter science is the nature of glass and the glass transition (P. W. Anderson)

7. 1. Nature of the amorphous solids

Glass products have long been used from ancient times not only in our daily life but also in some laboratory experiments such as the U tube for the measurement of volume of a gas as a function of pressure. Liquefaction of “the last permanent gas helium” was done successfully with an apparatus entirely made of glass. Formerly the glasses have been produced by cooling the melts of silicate minerals without crystallization until they become hard and brittle solids. Later the glasses were found to exhibit halo diffraction patterns similar to those of the liquids against an incident X-ray beam. Some important concepts are involved in this description. The first is the method of preparation. The melt-cooling was used in some of the modern definitions of glasses. The second is the starting materials of inorganic origin. Organic substances such as glycerol and synthetic polymers were found to behave similarly. Thus the term glasses can be extended to a wide range of substances that easily undercool to form amorphous solids. The third is the metastability of the undercooled liquids and glasses compared to the corresponding crystalline solids. If the cooling rate is adequately slow to induce nucleation, the melt becomes crystalline solid possessing regular lattice with lower Gibbs energy. Thus the formation of glass is a problem of bypassing or avoiding the crystallization. Although the main subjects of this book are the structures and properties of ordinary network glasses of inorganic origin, it will be instructive to start with the description of the general features of glassiness exhibited by various kinds of condensed matters in which the constituents are held together by the interaction forces, irrespectively of the van der Waals, hydrogen bonding, ionic or covalent types.

In spite of the long history of practical usage of the ordinary glasses, the scientific research of the glassy state began in the 20th century. It is surprising to realize that the first measurement of glass transition is more recent event than the discovery of the radioactivity. Pioneering work of the calorimetric measurement by *Simon and Lange* [1] has shown that glycerol glass exhibited a sudden increase in the heat capacity C_p over a narrow temperature region, and possessed residual entropy S_0 at 0 K. The temperature region is called the glass transition temperature T_g , and is an important keyword for the glass science and technology. Other thermodynamic quantities such as the volume V and thermal expansivity α also undergo some changes at T_g . This experiment gave the first paramount example of the solid that deviated from the third law of thermodynamics. In Simon’s word [2], the law is expressed as “The contribution to the entropy of a system by each aspect which is in internal equilibrium tends to zero at 0 K”. The realization of the internal equilibrium in some systems becomes quite serious for a human being with a short life span. In this way, the glasses are the frozen-in non-equilibrium states with respect to some degrees of freedom in a metastable phase of the system. In modern terminology, the glasses or glassy states are designated as

non-ergodic. Thus any liquid that satisfies the ergodicity hypothesis in statistical mechanics becomes out of equilibrium with some aspects of the system during a continuous cooling. The breaking of the ergodicity occurs at a small temperature interval T_g , which depends naturally on the experimental time-scale. In this way, the glass transition temperature, the residual entropy, the metastability, and the crystallization are the important keywords for the thermodynamic characterizations of the glassy systems.

Over the past 50 years, many amorphous solids have been prepared by various methods other than the traditional liquid-cooling. Amorphous semiconductor used for the solar cells is one example. Much of the intense research interest in amorphous solids is driven by the technological importance of these amorphous solids. Intellectual fascination with the amorphous solids arises from the basic understanding of the state of aggregation of the constituent entities in the solids. These amorphous solids combine liquid-like disordered structure and crystal-like rigidity, and display unique features that are generally absent in their counterparts in the crystalline solids. The exotic formation of amorphous solids can be done by either physical or chemical methods. Some methods do not pass at all their liquid state during the formation of amorphous solids. Glasses are just one example of the amorphous solids formed from the liquid states. What is the relation between glasses and amorphous solids? The question was raised by *Secrist* and *Mackenzie* [3]. The two terms had been used for some times without any clear distinction.

Molecular assembly is traditionally divided into four states of aggregation of the constituent molecules. The division of assembly into gas, liquid, and solid is based on the mechanical properties of the assembly, such as density and fluidity. Further division of the solid into crystalline and non-crystalline solids is obviously based on the structural point of view. The division of metastable liquids below their melting points into glassy and undercooled liquids is based on the non-equilibrium and the equilibrium nature of both states based on the thermodynamic reasoning. Thus criteria of the classification are multifarious in nature. The glasses are just one example of the amorphous solids with frozen-in disordered structure of liquids, but the reverse is not true necessarily without some experimental verification. One method to answer this question is to detect in amorphous solids possible existence of either the glass transition or the residual entropy that have been observed to occur concomitantly in many glass-forming liquids. This problem is discussed first in the following section.

It is worthy to note here another metastable nature of the polymeric materials. Most of the synthetic polymers consist of the crystalline and amorphous parts. The ratio of both parts can be changed arbitrarily by keeping them at particular temperature range. This nature produces a wide variety of properties in one and the same polymer, and enhances the usefulness in the applications of the polymeric materials. According to the phase rule, however, only a single phase should appear generally in any single-component system at a particular T and p other than the melting line. The coexistence of two parts will be a consequence of a distribution of masses in the constituent molecules of the system. Any synthetic polymers, even composed of one kind of pure monomer, cannot be regarded as the “single-component system”, for which the phase rule holds rigorously. One intriguing exception would be atactic polymers in which a trace of crystalline part cannot be observed to exist. It is not easy to imagine any conformation of the molecules in the atactic polymer that guarantees the translational invariance in the spatial arrangement of molecules placed on any regular lattice points. Strictly speaking, there exist no single-component system in pure substances if we take into consideration the existence of isotopes. The effect of isotope on the phase behavior appears, however, only at very low temperatures. In fact, liquid helium, being a mixture of He^3 and He^4 , exhibits a phase separation at a cryogenic temperature that depends on the composition. The phase separation is a kind of ordering process that reduces the

entropy of the system. Most of the substances are believed to be in frozen-in disordered states with respect to their isotopic species.

7.2. Characterizations of Amorphous Solids

A wide variety of amorphous solids can be prepared by physical and/or chemical methods. The former is

- (1) rapid cooling of liquid;
- (2) deposition of vapor onto a cold substrate;
- (3) mechanical milling of crystal;
- (4) particle bombardment onto crystal;
- (5) compression or depression of crystal, and so on.

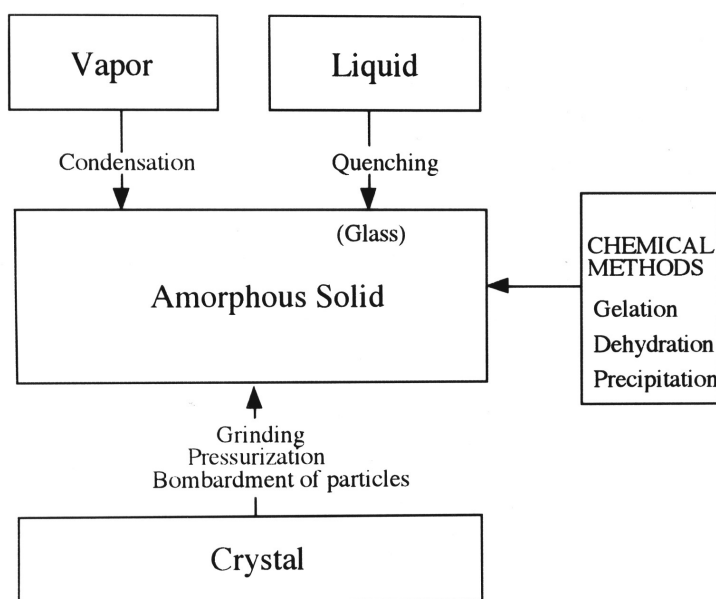
While the latter is

- (6) gelatination;
- (7) precipitation by chemical reaction;
- (8) dehydration of hydrate crystal, and so on.

In the former processes, the composition of substance does not change during the formation of amorphous solids [4]. The first is the most familiar one. A hyper-quenching method, with a cooling rate of nearly 10^6 K s^{-1} , was developed and applied to water or metallic liquids that had strong crystallization tendency. The other physical methods do not pass in principle their liquid state. Vapor deposition is one of the powerful methods in forming amorphous solids. The kinetic energies of vapor molecules are extracted efficiently during the condensation on to a substrate kept at a temperature far below the hypothetical T_g , so as to arrest the deposited molecules in a frozen disordered state. Crystals are used in the remaining physical methods. High energy in the form of compression, shear stress, or radiation is supplied to the crystal to destroy the neatly ordered arrangements of the constituents. Amorphization of ice, SiO_2 and others were done by this way. Mechanical milling was another energizing method and applied first to a metallic mixture forming an amorphous alloy. These non-equilibrium processes can be done without passing their liquids. Amorphization by any low-temperature routs is useful particularly for substances that are unstable at high temperatures. Thermal decomposition can be observed in some of the molecular crystals, as in the case of sugars. Sucrose as a disaccharide is known to decompose on melting, giving rise to a mixture of monosaccharides. Various methods for production of the amorphous solids are depicted schematically in Fig. 1.

Mechanical alloying is a non-equilibrium amorphization process and has been used in the development of new metallic systems. This can be done by milling of a mixture composed of two or more metals at room temperature. In contrast to the metallic systems, milling of molecular crystals produces amorphous solids even in a single system. For example, salicin, deoxycholic acid (DCA), trehalose, tri-*O*-methyl- β -cyclodextrin (TMCD) etc have been amorphized easily even in single system. Supply of mechanical energy to a crystalline substance beyond a critical level induces lattice instability of the crystal and freezes it in an energized state that has lost the original periodicity. Obviously the process must be carried out at temperatures below the “crystallization-dangerous” region of the resulting amorphous solids. Nature of the formed amorphous solid depends on the milling conditions. Both the T_g -value and the enthalpy of crystallization of the obtained solid are found to increase asymptotically with the milling time.

For some binary molecular crystals, milling of a mixture results in the molecular alloys with a single T_g varying with the composition. This indicates that the component molecules mix uniformly in a molecular level to exhibit a single relaxation process over the



whole composition range. Formation of solid solutions in the crystalline state is highly limited by many factors such as the shared crystal symmetry, the similar sizes of the unit cells, the similar molecular shapes, and so on. Alloying of otherwise immiscible substances in the solid state is possible only under non-equilibrium condition.

Fig. 1. Methods of preparation of amorphous solids.

The chemical methods accompany necessarily some changes in chemical potentials of the system. In method (6), the sample in a sol is brought into a gel state and then removal of extra components forms the corresponding amorphous solid. Some oxides were amorphized by this way in the form of fibers or lumps. The method (7) utilizes the fact that some chemical reactions in solution produce amorphous precipitates. Students in the course of analytical chemistry experience fine precipitates in the exercise when H_2S gas is passed into an aqueous solution including As^{3+} or Sb^{3+} ions. The yellow precipitates are fine particles and are known to be amorphous from powder X-ray diffraction experiment. Some hydroxides are also amorphous when they are precipitated rapidly in solutions. Water molecules are important ingredients in hydrate crystals. If the molecules are extracted by rapid evacuation, the resulting anhydride cannot keep anymore the crystalline lattice in some hydrate crystals. Magnesium acetate tetrahydrate, $\text{Mg}(\text{CH}_3\text{COOH})_2 \cdot 4\text{H}_2\text{O}$, belongs to this category. By evacuation, the hydrate crystal changes into amorphous anhydride solid. In this way, there exist many methods for the formation of amorphous solids other than the traditional liquid cooling.

The chemical precipitates $\text{As}_2\text{S}_3(\text{am})$ was examined by thermal analysis, and found to exhibit a glass transition T_g at about 477 K. The temperature was essentially the same as that of $\text{As}_2\text{S}_3(\text{am})$ prepared by the liquid-cooling of orpiment, being crystalline mineral $\text{As}_2\text{S}_3(\text{cr})$ occurring in nature. While, $\text{Sb}_2\text{S}_3(\text{am})$ can be prepared either by the chemical precipitation or by vapor deposition. Both the samples showed T_g at essentially the same temperature of 489 K. These results [5] are summarized in Table 1.

The C_p values of amorphous tri-*O*-methyl- β -cyclodextrin TMCD were essentially the same at temperatures below and above T_g for both samples prepared by the mechanical milling and the liquid-quenching. Thus it turned out that the terms amorphous solids and glasses are synonymous. Obviously the extent of frozen-in disorder of any amorphous solids depends on the condition by which the amorphous solids were formed. In the vapor deposition experiments, it was revealed that the lower the substrate temperature, the larger the amount of residual entropy S_0 . This indicates that the faster removing of the kinetic energy of vapor molecules results in larger extent of frozen-in disorder in the solid.

The extent of frozen-in disorder in amorphous solid can be described also by the concept of fictive temperature T_{fic} , that was introduced by Tool as an extra variable necessary for the description of glass and was defined as the temperature at which a glass with a given enthalpy would be at equilibrium if it followed the iso-structural change as the temperature was changed [6].

Table 1. Glass transition temperature T_g of various amorphous solids

Substance	T_g /K	Method	Substance	T_g /K	Method
propane	46	VC	methanol	103	VC
(propane) _x (propene) _{1-x}	46~55	VC	vinyl acetate	123	LQ
propene	55	VC	isopropylbenzene	126	LQ
	55	LQ	H ₂ O	135	VC
(propene) _x (1-butene) _{1-x}	55~60	VC	ethylene glycol	153	LQ
1-butene	60	VC	1,3-propanediol	166	LQ
	60	LQ	<i>m</i> -cresol	200	LQ
(propene) _x (1-pentene) _{1-x}	55~72	VC	resorcinol	250	LQ
(butane) _x (1-butene) _{1-x}	60~62	VC	salicin	333	MM
(1-butene) _x (1-pentene) _{1-x}	60~72	VC	sucrose	342	MM
1-pentene	72	VC	tri- <i>O</i> -methyl- β - cyclodextrin (TMCD)	352	LQ
CCl ₄	60	VC		352	MM
isopentane	65	LQ	phenolphthalene	362	MM
CHCl ₃	79	VC	TMCD+benzoic acid	337	LQ
3-methylpentane (0.1 MPa)	77	LQ		337	MM
	(108 MPa) 85	LQ	brucine	359	MM
	(198 MPa) 92	LQ	deoxycholic acid (DCA)	363	MM
ethanol	90	LQ	trehalose	384	MM
cyclohexene	92	LQ	magnesium acetate	469	DH
dichloromethane	93	LQ	As ₂ S ₃	477	CR
1-propanol (0.1 MPa)	97	LQ		477	LQ
	(108 MPa) 104	LQ	Sb ₂ S ₃	489	VC
	(198 MPa) 109	LQ	polytetrahydrofuran	185	LQ
butyronitrile	97	VC	polyoxacyclobutane	193	LQ
	97	LQ	polyoctamethyleneoxide	255	LQ

LQ : Liquid quenching; VC : Vapor condensation; CR : Chemical reaction;
MM : Mechanical milling of crystal; DH : Dehydration of hydrate crystal

The thermal motions in high-temperature liquids permit rapid and effective exploration of alternative molecular packing. But such structural change becomes increasingly sluggish as the temperature is lowered, and it largely ceases if further cooling passes through T_g . If a liquid is cooled at a constant rate, the equilibrium enthalpy deviates from the equilibrium curve at a particular temperature T_{fic} . The value becomes lower as the cooling rate is lowered. The value T_{fic} will change with time in the glassy state, depending on the annealing conditions at temperatures below the initial T_{fic} . Thus the determination of T_{fic} of a sample at the measurement stage requires the determinations of enthalpy of the actual glass and of the equilibrium liquid. In this way, calorimetric measurements give the quantitative data of C_p , isopropylbenzene [5] plotted against temperature. The figure shows common features of the amorphous solids prepared by the liquid-cooling of liquid.

The heat capacity of a liquid is generally larger than its crystal, primarily because the configurational degrees of freedom are excited in the liquid but no

t in the crystal. In addition to the primary or α glass transition $T_{g,\alpha}$, a secondary or β glass transition $T_{g,\beta}$ can be found by the measurement. The heat capacity jump associated with the β transition is so small that very careful and precise measurements are required for the detection. The quantity T_K is designated as the Kauzmann temperature and is described later.

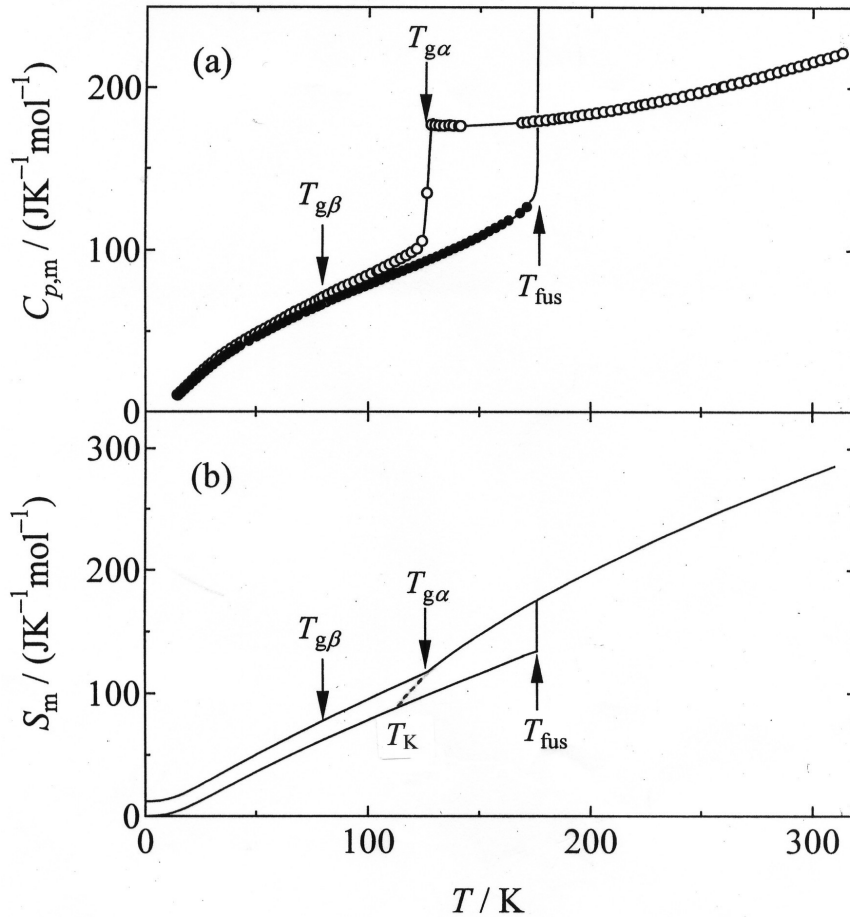


Fig. 2.
Heat capacity and entropy of isopropylbenzene

Many physical properties, say the enthalpy, of glass tend to relax toward the equilibrium values of the liquid at a constant temperature with a characteristic time. The relaxation process for the configurational enthalpy is well described by the *Kohlrausch-Williams-Watts'* (KWW) equation [7],

$$\Delta H_c(t) = \Delta H_c(0) \exp[-(t/\tau)^\beta], \quad (1)$$

where H_c is the part of enthalpy related to the structure or configuration of the liquid, τ is the average relaxation time, β ($0 \leq \beta \leq 1$) is the non-exponential parameter, $\Delta H_c(t)$ and $\Delta H_c(0)$ are the configurational enthalpy to be relaxed at the time $t = t$ and $t = 0$, respectively.

The non-exponential relaxation is one of the characteristic phenomena observed in many glasses. The smaller is the β value, the larger is the distribution of relaxation times. The remaining part of the enthalpy, called the vibrational enthalpy H_{vib} , responds always quickly to the temperature variation. Since the total enthalpy of a sample, $H_{\text{total}} = H_{\text{vib}} + H_c$, can be kept constant under the adiabatic condition, it follows

$$d\Delta H_c(t)/dt = - [d\Delta H_{\text{vib}}(t)/dT][dT/dt] = - C_{\text{vib}}[dT/dt]. \quad (2)$$

Obviously the temperature T means the vibrational temperature. The structural relaxation is, therefore, a process by which T and T_{fic} equalize. This is essentially a problem of heat conduction between two thermal reservoirs with T and T_{fic} , respectively. Thus the enthalpy

relaxation causes a spontaneous temperature change of sample under an adiabatic condition. The following equation is derived for the sample temperature in an adiabatic calorimeter as a function of time [8].

$$T(t) = a + bt + c \exp[(-t/\tau)^\beta]. \quad (3)$$

The second term bt is the temperature change arising from residual heat leakage, and is of the order of several mK h^{-1} in most of the experimental temperature range. Analysis of the $T \sim t$ curve of the calorimeter enables us to determine experimentally the kinetic parameters governing the structural relaxation through the enthalpy. It should be reminded that a constant temperature of a sample with time is a prerequisite for the thermal equilibrium (The zeroth law of thermodynamics). Any spontaneous temperature change with time under an adiabatic condition indicates that the sample is in a non-equilibrium state and is relaxing toward the equilibrium state. The time domain covered by this method is $0.1 \text{ ks} \sim 1 \text{ Ms}$ and can be extended by patience of experimentalist. The T_g value determined by the calorimetry corresponds to the temperature at which τ becomes 10^3 s or 1 ks , being the time necessary for a single heat-capacity determination. It is interesting to note that for 1-pentene prepared by vapor-deposition, $T_{\text{fic}} = 85 \text{ K}$ and $\beta = 0.45$, is quite different from those for the liquid-cooled sample, $T_{\text{fic}} = 72 \text{ K}$ and $\beta = 0.92$. This indicates the effectiveness of the formation of glass with high extent of disorder along with wider distribution of the relaxation times by the vapor-condensation process compared to an ordinary cooling process. In this way, the adiabatic calorimeter does work as an ultra-low frequency spectrometer in addition to the conventional tool.

The viscosity of liquid is one measure of the structural relaxation time for the undercooled fluid, and is an important quantity from a practical point of view. The viscosity η can be measured routinely and it becomes a convenient kinetic parameter for the glass relaxation. Over a small temperature interval, the viscosity changes by several orders of magnitude from typically 10^{-1} Pa s in the liquid state to about 10^{12} Pa s in the glassy state. Since a value of η in the order of 10^{12} Pa s is associated with the solid state, one can define T_g newly as the temperature at which the viscosity reaches this value as the temperature is lowered. According to the Maxwell theory of viscoelasticity, the viscosity η can be related to the relaxation time τ through the following equation [9].

$$\tau = G_\infty^{-1} \eta, \quad (4)$$

where G_∞ is the instantaneous shear modulus. Numerical evaluation of this equation shows that the new definition, $\eta(T_g) = 10^{12} \text{ Pa s}$, corresponds to the relaxation time of several hundred seconds at T_g , being again the time scale for a single heat-capacity determination. For some network-forming glasses, such as ordinary silicate glasses, the viscosity changes with temperature T in the Arrhenius fashion, $\eta = \eta_0 \exp[A/T]$. Many molecular liquids, on the other hand, show pronounced deviation from the Arrhenius behavior and can generally be better described by the *Vogel-Tammann-Fulcher* (VTF) equation.

$$\eta = \eta_0 \exp[A/(T - T_0)], \quad (5)$$

where η_0 , A , and T_0 are the constants depending on the nature of the liquid. In this way the viscosity η , hence the relaxation time α , tends to diverge towards the temperature T_0 .

Experiments of the enthalpy relaxation at a temperature below T_g showed that the relaxation rate depends not only the amount of ΔH_c but also the initial sign of departure.

The rate depends on whether the relaxation is structure-breaking or structure-forming process. The data for τ plotted against $1/T$ exhibit generally non-Arrhenius behavior, and the relaxation time diverges towards a temperature T_0 as the temperature is lowered, as already mentioned in the case of viscosity. Experimental data showed that this temperature is quite near to the Kauzmann temperature T_K , at which the extrapolated entropy of liquid crosses that of crystal [10]. Since any liquid that possesses entropy less than that of crystal is hard to imagine, the extrapolated entropy of the liquid should bend at T_K , and follows that of the crystal in the temperature range below T_K . The seemingly second-order transition that the actual liquid exhibits at T_g is considered to be a kinetic manifestation of the underlying equilibrium phase transition arising from the variation of the entropy at the Kauzmann temperature T_K . There exist other scenario that avoids the entropy crisis at T_K . Experimental verification of the validity of any models that should occur at T_K in an equilibrium liquid is not possible owing to our short life span.

The deviation from the Arrhenius behavior of τ is correlated phenomenologically with a fragility parameter m as follows [11].

$$m = d \log \tau / d(T_g/T) |_{T=T_g}. \quad (6)$$

For the Arrhenius behavior, for which m is assigned to be 17, the liquid is designated as strong liquid. The structure does not change much with temperature and the heat capacity jump ΔC_p at T_g is rather small. The larger the m value is, the structure becomes fragile with change in temperature. These are designated as fragile liquids, and exhibit rather large jump ΔC_p at T_g .

Adam and Gibbs [12] proposed a model for explaining the non-Arrhenius behavior of the relaxation time. They expressed the relaxation time τ by the following equation.

$$\tau = A \exp [z^* \Delta \mu / kT] = A \exp [N_A \Delta \mu s_c^* / kT Sc(T)]. \quad (7)$$

Here $Sc(T)$ is the macroscopic configurational entropy of liquid, $\Delta \mu$ the chemical potential per molecule hindering the cooperative rearrangement of a group of molecules, z^* the number of molecules constituting the group (or cluster), s_c^* the configurational entropy of the smallest group that can undergo the rearrangement, and N_A is Avogadro's constant. The configurational entropy is determined by subtracting the vibrational entropy from the experimentally determined entropy. The vibrational heat capacity of the glass expressed in terms of a combination of the Debye and the Einstein heat-capacity functions should be determined first by the least-square's fitting of the experimental data in the low-temperature range. The value $Sc(T)$ becomes zero at T_K for the ideally equilibrated liquid, and this situation results in the divergence of τ towards T_K as the temperature is lowered. The non-Arrhenius behavior can be considered to be due to the fact that τ is a function of T as well as of Sc . Likely the number z^* will not be constant but change with temperature. This entropy theory is supported by experiment [13], showing good correlation between $TSc(T)$ and $\log \tau$ for some glasses prepared under different conditions. In spite of the large differences in T_g among the samples, the glass transition takes place at essentially the same TSc value.

The number of molecules z^* in a cooperatively rearranging unit, or a cluster, can be estimated by considering the following relation that can be derived from Eq. (7).

$$z^*(T_1) / z^*(T_2) = Sc(T_2) / Sc(T_1) \quad (8)$$

If the value z^* is assumed to be 1 for the liquid at high temperatures where the unimolecular

process is dominant, the equation makes possible to estimate the number of molecules z^* in the undercooled and glassy states. This has been done for some systems [14]. One difficult problem in this analysis is to determine accurately the configurational entropy in the liquid at high temperatures. Contrary to other spectroscopic experiments, the data obtained by the heat capacity spectroscopy are not limited by any “selection rules”. Every degree of freedom can contribute to the total entropy of the liquid. Especially the contribution from the anharmonicity involved in the vibrational degrees of freedom to the entropy will increase as the temperature is raised.

Davies and Jones [15] have discussed the glass from quasi-thermodynamical point of view, and considered necessary number of internal parameter for the thermodynamic description of the glassy state as a frozen-in disordered system. This required the experimental determination of the Prigogine-Defay ratio Π , defined as

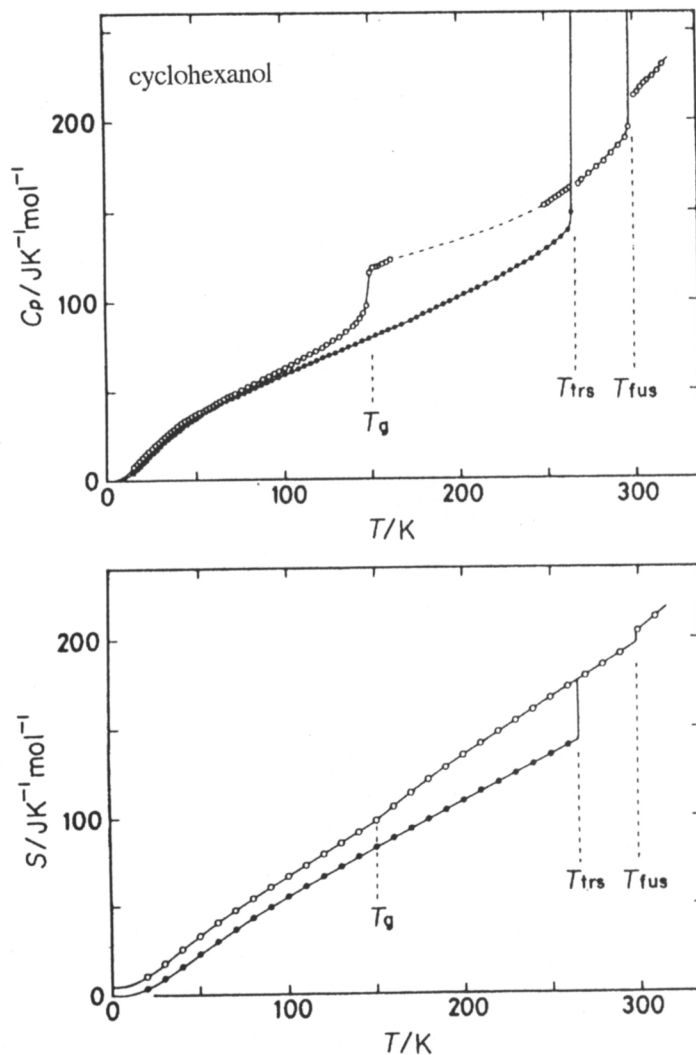
$$\Pi = VT(\Delta\alpha)^2/[\Delta\kappa \Delta C_p], \quad (9)$$

where ΔC_p , $\Delta\alpha$, and $\Delta\kappa$ are the jump of the heat capacity, thermal expansivity, and isothermal compressibility at T_g , respectively. If $\Pi = 1$, only a single parameter, say T_{fic} , is sufficient enough for the description of glass. If $\Pi > 1$, two parameters are necessary. A very precise calorimeter for the simultaneous measurements of volume V and enthalpy H workable over a wide range of temperature and pressure was developed in our laboratory, and applied to the determination of Π for two systems. The data clearly showed that $\Pi > 1$ [16]. Gupta proposed a concept of fictive pressure p_{fic} as the second parameter [17]. This kind of discussion requires further experimental tests.

7.3. Glassy transitions in crystals: glassy crystals

Most of the molecular crystals fuse directly into isotropic liquids. Some crystals fuse in two steps, either through the liquid crystal phases or the orientationally disordered crystal phases. These mesophases have the entropy values close to those of the isotropic liquids, indicating a great deal of disorder in these mesophases. Most of the orientationally disordered crystals have face-centered cubic (fcc) or body-centered cubic (bcc) lattice with molecules possessing a great deal of orientational disorder. If such a phase is cooled rapidly by avoiding the transformation into an ordered crystal, the undercooled disordered phase undergoes freezing-in process at a temperature at which the relevant relaxation time τ crosses the experimental time, as in the case of ordinary glasses. Particularly the glassy states of crystals designated as “glassy crystals” are interesting. This is because glasses and crystals are two extremes in our concept of structural regularity in solids, and the seemingly contradicting concepts must be combined in this new state of aggregation of molecules [5].

Analogy between the dielectric and enthalpy relaxations will be helpful in understanding the concept of frozen-in disordered crystals. Dipolar liquids generally show the dielectric relaxation in the equilibrium or undercooled liquid phases depending on the frequency f of an external electric field. The dielectric permittivity drops at a temperature at which the dielectric relaxation time τ_d becomes $(2\pi f)^{-1}$, indicating a freezing-in of the orientation polarization. The actual T_g value of the liquid corresponds to the temperature at which the value τ_d becomes ~ 1 ks. The same thing can happen in some orientationally disordered crystals in which the centers-of-mass of the molecules form three-dimensional lattice but their orientations are random among several equi-energetical directions, say eight $|111|$ directions of their fcc or bcc lattices. These crystals exhibit, therefore, the dielectric relaxation likely if the crystal is composed of polar molecules. The reorientational motion is dynamic at high temperatures but becomes quiet as the temperature is lowered until the



motion becomes dormant. The heat capacity drops suddenly more or less in a narrow temperature range just in a way similar to the liquids. In spite of the paradoxical nature of the concepts involved in the nomenclature “glassy crystals”, time is now giving it proof as an intriguing new state of aggregation of molecules.

Fig. 3. Heat capacity and entropy of cyclohexanol.

Cyclohexanol forms an fcc lattice below T_{fus} . The high crystallographic symmetry arises entirely from a great deal of orientational disorder of the molecule that has only mirror symmetry. When the fcc phase is cooled by avoiding the transformation into an ordered low-temperature phase, the undercooled orientational

disordered phase exhibits T_g at about 150 K and has a definite amount of residual entropy. The behavior of enthalpy relaxation is unable to discriminate in all aspects from those of ordinary glasses only except for the existence of a long-range positional order in cyclohexanol crystal. The heat-capacity tail below T_g is noticeable. The long heat-capacity tail below T_g causes the S_c to decrease over a wide range of temperature. This phenomenon has been observed more or less in many glassy liquids and the effect on the residual entropy of cyclohexanol crystal was discussed in details [5,18]. The heat capacity along with the entropy of cyclohexanol crystal is shown in Fig 3.

In the case of ethanol, two kinds of glass transitions were observed for its liquid and the orientational disordered phases, respectively. Some textbooks described that ethanol was a good glass-forming liquid based on the observation of T_g . The old observation of T_g by calorimetric measurements turned out to be for its orientational disordered phase and not for the liquid. Glassy liquid of ethanol turned out to be realized only by a rapid cooling of the liquid with a rate faster than 50 K min^{-1} . The glass transition for the liquid takes place at essentially the same temperature of 97 K. Two glass transitions can occur for different phases of one and the same substance of $\text{C}_2\text{H}_5\text{OH}$. This observation strongly suggests that the kinetic feature of the molecular reorientation in condensed phases is primarily responsible for the freezing process and that the re-orientational motion governs the translation-rotation-coupled rearrangement of molecules in the liquid. Figure 4 shows the heat capacity and entropy of ethanol around their glass transitions, [5].

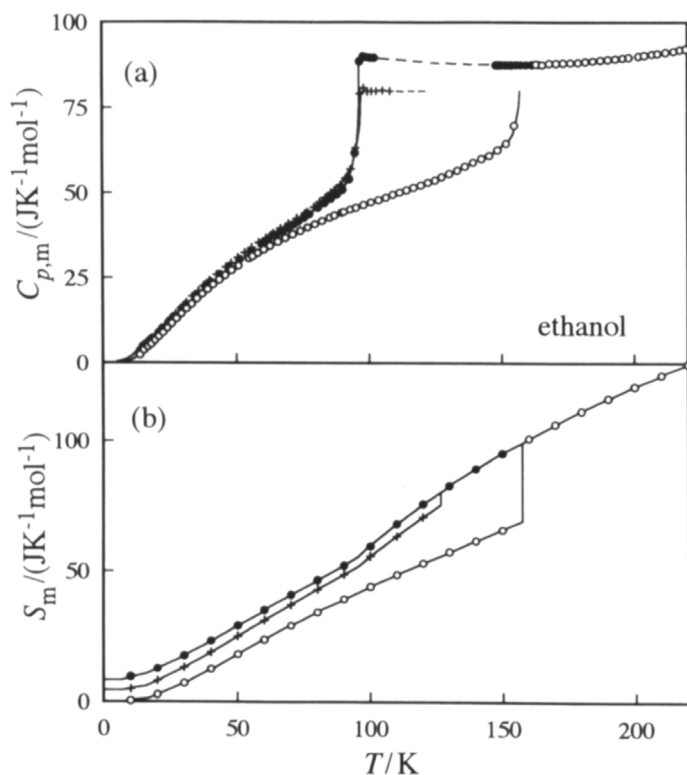


Table 2 lists some examples of the glassy crystals along with their T_g values. Likely, glassy state of undercooled liquid crystal can be realized by avoiding the transformation of the liquid crystalline phase into an ordered crystal [5]. In a liquid crystalline phase, molecules of an elongated shape have almost parallel orientational order, but positional disorder. Another name “anisotropic liquids” given to the liquid crystals comes from this fact.

Fig. 4. Heat capacity and entropy of ethanol.

The substance
N-p-n-hexyloxybenzylidene-*p*
'-n-butylaniline,

$C_6H_{13}O-C_6H_4-CH=N-C_6H_4-C_4H_9$ provides one example of the liquid crystals. This substance shows the following phase sequence: Crystal – Smectic G – Smectic B – Smectic A – Nematic – Isotropic liquid (IL).

The highly disordered nature of the Smectic G phase is quantified by the large entropy change $\Delta_{\text{trs}}S$ (Cr - S_G) amounting $75.98 \text{ J K}^{-1} \text{ mol}^{-1}$ that exceeds far the sum of the remaining entropies of transition: $2.53 (S_G - S_B) + 10.14 (S_B - S_A) + 9.37 (S_A - N) + 5.37 (N - IL)$. The smectic G phase possessing a great deal of disorder readily undercools and exhibits two-step glass transitions at temperatures around 200 K. The nature of double glass transitions is not clear at the moment, but one of them will be associated with the freezing of molecular modes characteristic of layered structure, either the undulation mode of a layer or anisotropic translational diffusions parallel and perpendicular to a smectic layer.

It turned out that the glass transitions are not characteristic property of liquids but of wide occurrence in a wide variety of substances irrespective of their translational invariance with respect to their center-of-masses. The glassy crystals can be a model substance for elucidating the complex nature of disordered solids, as the degrees of freedom associated with the freezing in the glassy crystals are almost pure orientational ones, weakly coupled with lattice vibrations [5, 18]. The situation will greatly simplify the character of frozen disorder.

The situation of frozen-in disorder is not limited to the metastable undercooled phase of crystal. Another category of glassy crystals can be found in the stable crystals, such as CO and H₂O crystals. Both of the substances provide good examples of crystals that do not obey the third law of thermodynamics. Structural and dynamic studies of CO crystals disclose the presence of a head-to-tail motion of the weakly polar molecules. The motion is active at high temperatures but cannot overcome a potential barrier hindering the motion at low temperatures before the crystal reaches a hypothetical ordering temperature. While the name “crystal” derives from the Greek “Krustallos” which meant ice. Ice has long been considered as a typical crystalline substance surrounding us. Thus the deviation of ice from the third law

of thermodynamics embarrassed many scientists since 1936 when the residual entropy of ice was found experimentally. Each water molecule in ice I_h has six equi-energetical orientations in the hydrogen-bonded network, but their reorientational motions must be done in a highly cooperative way under the constraints of the “ice rules”. The relaxation time for the cooperative motion becomes longer and longer as the temperature is lowered until the disorder becomes immobilized below a certain temperature. Whether the disorder should be described as static or dynamic depends *inter alia* on the height of the potential barrier, along with the temperature and the time-scale of the observation. The half-hydrogen model proposed by Pauling cannot be an equilibrium structure of ice crystal at 0 K, but absence of any anomalous heat capacity ascribable to an ordering transition has puzzled many scientists for a long time [19].

Table 1. Glass transition temperature T_g of various glassy crystals

Metastable phase	T_g /K	Stable phase	T_g /K
<i>thiophene</i>	37	<i>thiophene</i>	42
<i>2,3-dimethylbutane</i>	76	<i>buckminsterfullerene C₆₀</i>	87
<i>isocyanocyclohexanol</i>	55	\square - <i>cyclodextrin</i> ·11H ₂ O	150
	130	<i>ethylene oxide</i> ·6.86H ₂ O	85
	160	<i>tetrahydrofuran</i> ·17H ₂ O	85
<i>CFCl₂-CFCl₂</i>	60	<i>acetone</i> ·17H ₂ O	90
	90	<i>CO</i>	18
	130	<i>RbCN</i>	30
<i>ethanol</i>	90	<i>CsNO₂</i>	42
<i>cyclohexene</i>	92	<i>TlNO₂</i>	60
	93	<i>SnCl₂·2H₂O</i>	150
<i>cycloheptane</i>	100	<i>SnCl₂·2D₂O</i>	155
	100	<i>H₂O (hexagonal)</i>	105
	93	<i>H₂O (cubic)</i>	140
<i>cycloheptatriene</i>	106	<i>D₂O (hexagonal)</i>	115
<i>cycloheptanol</i>	135	<i>pinacol</i> ·6H ₂ O	155
<i>cyclohexanol</i>	150	<i>H₃BO₃</i>	290
<i>Cs_{0.7}Tl_{0.3}NO₂</i>	48	<i>D₃BO₃</i>	298
		<i>lysozyme</i>	ca 150
<i>C₂Cl₆ in thiourea adduct</i>	59	<i>myoglobin</i>	ca 170

T_g value of protein crystal depends strongly on water content.

In fact, a glass transition was found to occur at about 15 K for CO and 110 K for ice I_h . Thus the freezing process is believed to occur during cooling before a hypothetical ordering temperature is reached for each crystal [5, 18]. The dielectric and enthalpy relaxation times of ice, τ_d and τ , turned out to lie on the same straight line in an Arrhenius plot. Extrapolation of these data to 60 K, a hypothetical ordering temperature of ice I_h proposed by *Pitzer* and *Polissar* [20], gave a value of 10^{13} s for τ . It must be this geological time that hindered the crystal from realizing an ordered phase of ice I_h in our laboratory time. *Onsager* [21] has suggested using some impure ice samples for inducing the expected ordered phase. The impurity might hopefully relax the severe constraints “ice rules” imposed to the cooperative motion of water molecules in the lattice and enhance the orientational mobility.

A minute amount of KOH doped into the ice lattice was found to accelerate dramatically the reorientational motion of water dipoles [22]. The hydroxide ion OH⁻ creates necessarily a hydrogen bond without proton in the neighborhood, and the creation of this L

(leer in Germany) defect in the network will surely relax the severe constraints for the cooperative water motion. Thus, an ice sample doped with KOH in the mole fraction of 2×10^{-5} and kept at 65 K for 2 days induced a first-order phase transition at 72 K. The transition removed a substantial fraction of the residual entropy and changed the lattice symmetry from $P6_3/mmc$ of I_h to $Cmc2_1$ of the low temperature phase. The proton-ordered phase was designated as ice XI. Examination of the experimental data showed that the relaxation time of the doped ice was shortened by a factor of 10^8 at 90 K. This is the reason why the suggested ordering transition has escaped notice since 1936 when the residual entropy was first observed, and now appeared by the catalytic action of the minute amount of dopant that relaxes greatly the severe constraints imposed to the rearrangements of the water molecules in ice I_h . The Kauzmann paradox does not occur in ice crystal because I_h is the most stable modification of ice under atmospheric pressure. This experiment shows the wide validity of the third law of thermodynamics in one hand, and reveals a facet of a possible ordering process for the otherwise frozen-in disordered systems in other hand.

Essentially the same things were observed for the clathrate hydrates of the type II structure. The host lattice composed of water molecules forms two kinds of cages that accommodate some guest molecules of suitable size and shape. Two kinds of molecular disorder exist in the crystal; the first is the orientational disorder of the host water molecules similar to that of ice, and the second is the reorientational motion of the guest molecules inside the cages. This can be clearly indicated by the observation of two kinds of the dielectric relaxations, if the guest is dipolar molecule. The one that appear at higher temperature is for the water dipole, and the other occurring at cryogenic temperature is for the guest dipole. The latter exhibits a great deal of orientational disorder inside the cavity with almost spherical symmetry. The calorimetric measurement of the clathrate hydrate enclathrating tetrahydrofuran showed a tiny heat capacity anomaly with relaxational nature that is similar in the ice crystal. When the crystals are doped with a minute amount of KOH, a first-order phase transition appeared at 61.9 K. The transition temperature depended on the nature of the guest molecules: 46.6 K for acetone hydrate, and 34.5 K for trimethylene oxide hydrate. Dielectric measurements showed that both of the host and guest molecules in the tetrahydrofuran hydrate were ordered at temperatures below T_{trs} . Most probably, the ordering of the host water dipoles produced a strong electric field that forced the guest molecules to align along a preferred orientation.

Our experiments are always governed by the *Deborah* number D [23], which is defined as the ratio of the relaxation time τ and observation time t ; $D = \tau/t$. As far as $D \ll 1$, we can observe the whole shape of heat capacity anomaly associated with the possible ordering transition that is determined by intermolecular interaction and cooperative nature of the interaction. For a system $D \gg 1$, we will miss a part or full of the relevant thermodynamic quantity owing to our limited experimental time. The relaxation time is determined by the disordered structure and barrier height hindering the rearrangement of the structure. A particular impurity doped into the system will modify the cooperative nature of the rearrangement and shorten the relaxation time as a whole. Only this process makes possible to observe a transition that has been concealed for a kinetic reason. Modification of chemical potential of a system by a particular impurity can hopefully result in a drastic change of dynamical situation in the system. We may call this new field “doping chemistry”.

A particular kind of dopant acted on frozen-in disordered system as catalyst for releasing the immobilized state and recovering the equilibrium state in our observation time. In relation to this fact, one might raise an inquiry “What kind of physical or chemical impurity will release the frozen-in state of the liquid?” If a particular dopant were discovered luckily for this purpose, we will be blessed to observe in reality what will happen at the Kauzmann temperature of a liquid? As a matter of fact, it is not easy for us to imagine some disordered

solids without any configurational entropy, designated as an “ideal glass”.

7. 4. Other aspects of glassy solids

In spite of its simple molecular structure, a wide variety of states of aggregation of water molecules have been observed hitherto. At least thirteen crystalline forms of ice designated as I_h , I_c , II, III, IV, \dots , XI, as well as vapor-deposited amorphous ice have been found to exist under atmospheric and high pressures as of 1982. Amorphous ice is, galactically speaking, a very abundant material in space. The Comet’ tail is strongly connected to the formation of amorphous ice. The idea that there is an amorphous solid form of water was first put forward in 1935 when water vapor was deposited onto a cold substrate [19]. A calorimetric measurement showed that the amorphous ice exhibited a glass transition at 135 K [24] and had a strong crystallization tendency. The crystallization starts to occur progressively at temperatures even below T_g , so that the heat capacity jump is masked to some extent by an exothermic effect arising from the crystallization. Hyper-quenching of the liquid water can also produce the amorphous ice and its T_g value was determined to be 136 K by a DSC measurement [25]. These values are consistent with that obtained by extrapolation of unambiguous T_g data from glass-forming binary solutions up to pure water. On the other hand, Angell has proposed that the T_g of amorphous ice must be higher than 150 K. The discussion is mainly based on the fact that if the heat capacity of the undercooled liquid follows the extrapolated line of the equilibrium liquid, the entropy of the amorphous ice becomes smaller than that of hexagonal ice below about 150 K. Heated discussions are still continued [26].

Pressurization of I_h at low temperatures above 1.3 GPa turned out to be a new way for preparation of amorphous ice with high density (HDA) [27]. The HDA ice transforms to a low-density amorphous (LDA) ice by warming the HDA ice under atmospheric pressure. Both the amorphous ices change each other by an apparent first-order transition. The phenomenon designated as “polyamorphism” has opened a new realm in amorphous solids. In the case of ice crystal, the amorphization by pressurization turned out to be due to negative Grüneisen parameter that induces softening of some vibrational modes, leading to instability of the crystalline lattice beyond some critical pressure [28].

Particularly interesting is the properties of LDA ice. It is becoming increasingly clear that LDA ice is of extraordinary character among amorphous solids. What is unexpected is that the thermal conductivity increases sharply when the HDA ice transforms to LDA ice. Usually the denser forms of substances are the better thermal conductors. Even more unexpected is that the thermal conductivity of the LDA ice increases with decreasing temperature, the opposite behavior to that of the HDA ice and of all other amorphous solids [29]. The LDA behavior is like that of crystals in which the scattering of phonons by other phonons decreases with decreasing temperature. This anomalous behavior implies the existence of a special kind of order in the LDA ice. This conclusion is consistent with the observation that LDA ice does not show boson peaks that are widely observed in glass-forming liquids. An X-ray scattering experiment showed that the dispersion relation of LDA ice for vibrational modes is similar to that of cubic ice I_c , the metastable form of ice at atmospheric pressure. It seems likely that in LDA ice we closely approaching an ideal glassy state [30]. It is an embarrassment, however, that it is not certain that a characteristic T_g can be assigned to this almost ideal glass. Recent discovery of very high-density amorphous (VHDA) ice makes the situation more complex [31]. Further works with novel idea is highly encouraged for an improved understanding of this intriguing and important substance.

Another interest is concerning with cryo-preservation of biological substances: cryogenic storage by amorphization of the water solution system within the biologically active cell.

When the biological cell is kept at low temperature without formation of ice, the biological activity is preserved, independently of the storage period. The solution system is in a glassy state at low temperatures, with all the molecules and ions being in a frozen state. For successful vitrification, diverse treatments of the cell or tissues are required to protect from ice formation. The optimum conditions for the successful preservation depend on the particular cells/tissues and added glass-forming substances.

It is interesting to describe here some analogies between proteins and glasses. Proteins are known to have a free-energy landscape possessing a large number of energy valleys, separated by potential barriers. This arises from the conformational degrees of freedom of the polypeptide chains. The energy valleys are called the conformational substates and correspond to slightly different higher-order structures in a protein molecule. At physiological temperatures, protein molecule fluctuates among many substates, as if they were liquid. This fluctuation is believed to play an important role in the biological activity such as the enzyme-substrate reactions. With lowering temperature, they are expected to freeze in a substate. In fact, protein crystals undergo the glass transition at low temperatures, depending strongly on the amount of water in the crystal. Water molecules are important ingredient of the protein crystal [32]. Lowering of the water content in the crystal causes a decrease in the mobility of the component molecules, resulting in an increase of T_g . Below a certain amount of water, the glass transition takes place at temperatures above 300 K. This means that conformational and orientational degrees of freedom of both molecules are in a frozen-in disordered state at our physiological temperatures. Any biological function cannot be expected to appear in such a frozen-in state.

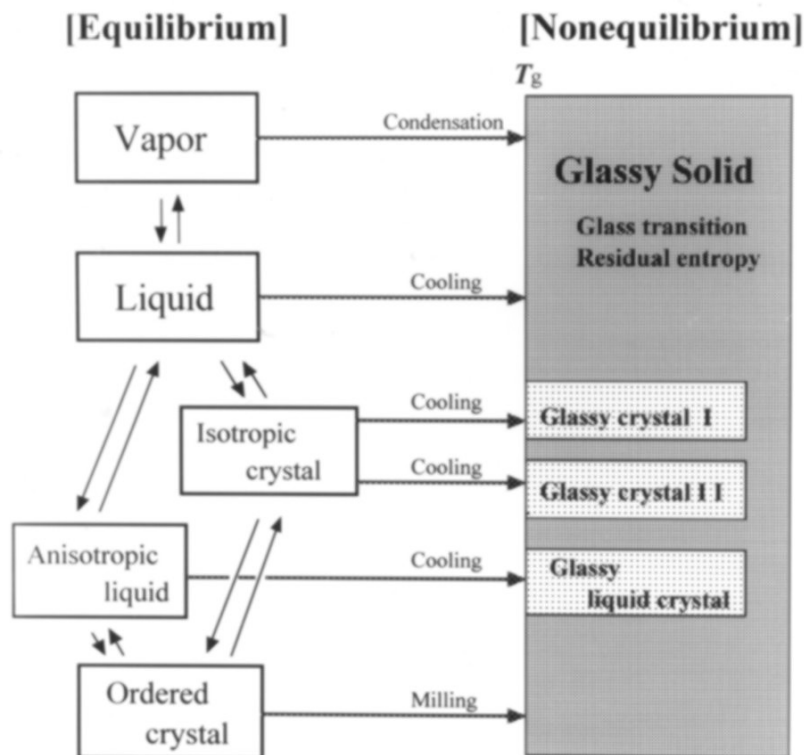


Fig. 5. States of aggregation of molecules in the equilibrium and non-equilibrium states.

Above shown Fig. 5. summarizes all the observed states of aggregation of molecules in the equilibrium and non-equilibrium states of molecular assembly, as revealed by calorimetric measurements. It can be concluded that the glass transitions observed exclusively in liquids so far are just one example of “transitions” that must be of wide occurrence in solids in relation to the freezing of some degrees of freedom, irrespectively of the translational invariance in the system. Molecular assembly can produce various states of aggregation that are much richer than our anticipation. The subdivision of the glassy states will deepen our basic understanding of the substance and require a renewal of the concept of the glass transition. Freezing processes in seemingly dissimilar substances could be analyzed on the same thermodynamic basis, indicating the universality of the underlying thermodynamic principles. A new realm of amorphous solid-state science with many unsolved problems is confronting us and must be challenged.

Acknowledgement: *The author would like to express his sincere thanks to the late Professor I. Nitta and Professor Emeritus S. Seki for the continued encouragements throughout the present works. Thanks are extended to many collaborators for their hard works and useful discussions.*

References 7

- 1 Gibson, G. E., Giauque, W. F.: *The Third Law of Thermodynamics: Evidence from the Specific Heats of Glycerol That the Entropy of a Glass Exceeds That of a Crystal at Absolute Zero.* J. Am. Chem. Soc. **45**, 93-104 (1923)
- 2 Wilks, J.: *The Third Law of Thermodynamics.* Oxford University Press, Oxford (1961)
- 3 Mackenzie, J. D. Ed.: *Modern Aspects of the Vitreous State.* Vol. 3, Chapter 6, Butterworth, London (1964)
- 4 Oguni, M., Suga, H.: *Amorphous Materials and Their Elucidation by Adiabatic Calorimetry, in Chemical Thermodynamics,* ed. Letcher, T. M. IUPAC Monograph, Blackwell Science, 227-237 (1999)
- 5 Suga, H., Seki, S: *J. Non-cryst. Solids: Thermodynamic Investigation on Glassy States of Pure Simple Compounds.* **16**, 171-194 (1974); Suga, H., Seki, S: *Frozen-in States of Orientational and Positional Disorder in Molecular Solids.* Faraday Discussion **No 69**, 221-240 (1980)
- 6 Suga, H: *Frozen-in Disorder and Slow Relaxation in Crystals.* J. Chem. Thermodyn. **25**, 463-484 (1993); Suga, H: *Prospects of Material Science; From Crystalline to Amorphous Solids.* J. Thermal Anal. Calor. **60**, 957-969 (2000)
- 7 Brawer, S.: *Relaxation in Viscous Liquids and Glasses. Review of Phenomenology, Molecular Dynamics Simulations, and Theoretical Treatment.* The Amer. Ceram. Soc. Inc, Columbus Ohio (1985)
- 8 Suga, H., Matsuo, T.: *Adiabatic Calorimeter as an Ultra-low Frequency Spectrometer.* Pure Appl. Chem., **61**, 1123-1132 (1989)
- 9 Kauzmann, W.: *The Nature of the Glassy States and the Behavior of Liquids at Low Temperature.* Chem. Rev. **43**, 219-287 (1948)
- 10 Angell, C. A.: *Relaxation in Liquids, Polymers and Plastic Crystals.* J. Non-cryst. Solids **13**, 131-133 (1991)
- 11 Adam, G., Gibbs, J. H.: *On the Temperature Dependence of Cooperative Relaxation Properties in Glass-forming Liquids.* J. Chem. Phys. **43**, 139-165 (1965)
- 12 Takahara, S., Yamamuro, O., Suga, H.: *Heat Capacities and Glass Transitions of 1-Propanol and 3-Methylpentane under High Pressure. New Evidence for the Entropy*

- Theory*. J. Non-cryst. Solids **171**, 259-270 (1994)
- 13 Yamamuro, O., Tsukushi, I., Lindqvist, A., Takahara, S., Ishikawa, M., Matsuo, T.: *Calorimetric Study of Toluene and Ethylbenzene: Thermodynamic Approach to Spatial Heterogeneity in Glass-forming Liquids*. J. Phys. Chem. **B102**, 1605-1609 (1998)
 - 14 Suga, H.: *Calorimetric Study of Frozen-in Disordered Solids*. J. Phys. Condens Matter **15**, S775-S789 (2003); Suga, H.: *Frozen-in Disorder in Condensed Phases*. Russian J. Phys. Chem. **77**, S7-S16 (2003); Suga, H.: *Study of Transition Phenomena in Molecular Solids*. J. Thermal. Anal. Calor. **80**, 49-55 (2005)
 - 15 Eisenberg, D., Kauzmann, W.: *The Structure and Properties of Water*, Clarendon Press, Oxford (1969); Petrenko, V. F., Whitworth, R. W.: *Physics of Ice*. Oxford University Press, Oxford (1999)
 - 16 Onsager, L.: *Ferroelectricity of Ice?* in *Ferroelectricity*, ed. Weller, E. Elsevier, Amsterdam, 16-19 (1967)
 - 17 Tajima, Y., Matsuo, T., Suga, H.: *Phase Transition in KOH-doped Ice*. Nature **299**, 810-812 (1982); Suga, H., Matsuo, T., Yamamuro, O.: *Thermodynamic Study of Ice and Clathrate Hydrates*. Pure Appl. Chem. **64**, 17-26 (1992); Suga, H.: *Ultra-slow Relaxation in Ice and Related Substances*. Proc. Japan Acad. **B81**, 349-362 (2005)
 - 18 Reiner, M.: *The Deborah Number*. Physics Today **17**, 62 (1964)
 - 19 Sugisaki, M., Suga, H., Seki, S.: *Calorimetric Study of Glassy State V. Heat Capacities of Glassy Water and Cubic Ice*. Bull. Chem. Soc. Jpn. **41**, 2591-2599 (1968)
 - 20 Johari, G. P., Hallbrucker, A., Mayer, E.: *The Glass-Liquid Transition of Hyperquenched Water*. Nature **330**, 552-553 (1987)
 - 21 Yue, Y., Angell, C. A.: *Clarifying the Glass Transition Behaviour of Water by Comparison with Hyperquenched Inorganic Glasses*. Nature **427**, 717-720 (2004)
 - 22 Mishima, O., Calvert, L. D., Whalley, E.: *Melting of Ice I at 77 K and 10 kbar*. Nature **310**, 393-395 (1984)
 - 23 Andersson, O., Suga, H.: *Thermal Conductivity of Amorphous Ices*. Phys. Rev. **B65**, 140201-140204 (2002)
 - 24 Angell, C. A.: *Amorphous Water*. Annu. Rev. Phys. Chem. **55**, 559-583 (2004)
 - 24 Loerting, T., Schustereder, W., Winkel, K., Salzmann, C. G., Kohl, I., Mayer, E.: *Amorphous Ice: Stepwise Formation of Very High Density Amorphous Ice from Low Density Amorphous Ice*. Phys. Rev. Lett. **96**, 025702-1~4 (2006)
 - 25 Miyazaki, Y., Matsuo, T., Suga, H.: *Low Temperature Heat Capacity and Glassy Behavior of Lysozyme Crystal*. J. Phys. Chem. **B104**, 8044-8052 (2000)
 - 26 Šesták J. and Zámečník J., *Can clustering of liquid water and thermal analysis be of assistance for better understanding of biological germplasm exposed to ultra-low temperatures*, J. Thermal Anal. Calor. **88** 411-416 (2007)



Chapter 8

Biological glasses in nature

8. BIOLOGICAL GLASSES AND THEIR FORMATION DURING OVERWINTERING AND CRYOPRESERVATION OF PLANTS

Jiří Zámečník, Jaroslav Šesták

8. 1. Life with anomalous behaviour of water

We are dwellers in a perceptibly lucky but also sensitive world where our Mother Earth keeps viable environment providing, e.g., mean temperature of ~ 17 °C due to the atmosphere outward (albedo: $A \sim 35\%$) and inward (green house effect: $G \sim 45\%$) reflection [1]. If both A and G equalled zero, the mean Earth temperature would drop to a mere 5° C and local freezing, based on the transformation of liquid water to solid ice with subsequent influence on viability, would be more comprehensive in its effect on inhabitants.

Nevertheless, the freezing temperatures well below 0 °C (or 32 F) are common and there are many mechanisms for both plants and animals to survive such exposures. Some plants involve the production of proteins and/or carbohydrates that act as anti-freezes. Others actually induce freezing of extracellular water before the water can breach the cell membrane. Other mechanisms include slowing, but not necessarily preventing the freezing of water, because the sudden freezing of water is far more destructive than its slow course of action, and others engage warming via heat provided by external crystallization yet.

Processes associated with water freezing (particularly in conjunction with its supercooling) have been intensively studied [2-4] for many years due to their significance both in nature plants [5] and in human activity (food storage) [6,7]. In the Earth environment, these phenomena are well known to be connected with the formation of snow and hail and freezing of various water flows. In human activity they play an important role in many production processes from plain ice making to the complex foodstuffs freezing. Even more important role they play in the viability of plants.

Water is a compound, which exhibits some extraordinary uncommon and very amazing properties and strange behaviour, differing considerably from those properties of to water related chemical compounds. It concerns a relatively high boiling point, exceptionally large specific heat capacity and surface tension, and anomalous ability to dissolve both ionic and polar compounds. When water is left standing for a longer period, it tends to develop thixotropic properties, which implies a rather fragile but charge-containing (pH-variation) macrostructure (OH^-/H^+ assembling), curiously capable to even store and release amounts of pre-introduced charge [8]. Impurities dissolved in water decrease both its melting and boiling temperatures. Unlike most other compounds, water expands as it freezes. It is believed that the reason for such properties is a great dipole moment in the water molecules and creation of attractions among them. Enlightenment comes from a better understanding that water molecules form an infinite hydrogen-bonded network with confined and structured clustering which becomes more intensive and better localized under decreasing temperatures. Recent studies, done via molecular dynamics, identified experimentally water clusters [2,3,4,9], which grow in size and become more compact as temperature decreases. Their size can be characterized by a fractal dimension consistent with patterns common in natural world, having the correlation length proportional to the configurational entropy [10]. Upon cooling, hexagonal icy crystals are more easily reconstructed from the smaller water clusters $\{(\text{H}_2\text{O})_n$ with n up to 20} even if consisting of an atypical pentagonal symmetry [4] (expectedly existing at temperatures >10 °C). However, the larger pentagonal liquid-containing clusters

($n > 20$) are more reluctantly altered to hexagonal crystals ensuing thus a greater undercooling, which is more readily inaugurating irregular glassy configuration to occur at lower temperatures $\ll 0$ °C. For that reason, we often confront in nature such a curiosity that warmer water transform to crystalline ice more willingly than cool water, which provides a potential danger to nature as to suffer from sharp drops when happening from higher temperatures.

The decrease of the region of glass transition temperature with the increasing cluster size was experimentally observed to be much less operative than the corresponding change of melting temperatures. The mutual order of the melting and glass-transition temperatures were found to be reversed when compared with that observed for bulk water. Glass-formation of water was treated within the concept of polymeric-polymorphic structure [4,11]. Water supercooling and ice formation have been theoretically analysed [12] within traditional nucleation theory and the ice formation can be conventionally described by homogeneous nucleation if no foreign/irrelevant nucleation centres are present. However, this is a very rare case in nature, because microscopic particles of solid phase or biological interfaces (e.g. bacteria) are always present inwards liquids (together with the outer-bordering surfaces) and act as nucleation sites, yielding thus overwhelming heterogeneous nucleation. The man-made induced supercooling, preceding homogeneous nucleation, so far created in laboratory on the fine free droplets (very pure water clouds), ranged between -253 and -233 °C, being dependant (and growing) with the decrease of droplet size and increasing curvature. Measurement of temperature hysteresis, thus occurring between melting and solidification of confined water in cavities, is a standard methodology called thermoporometry [13]. However, the possible interference/overlapping of the temperature hysteresis, caused either by the diminutive porous size or originating from water (independent) supercooling, is not clear yet.

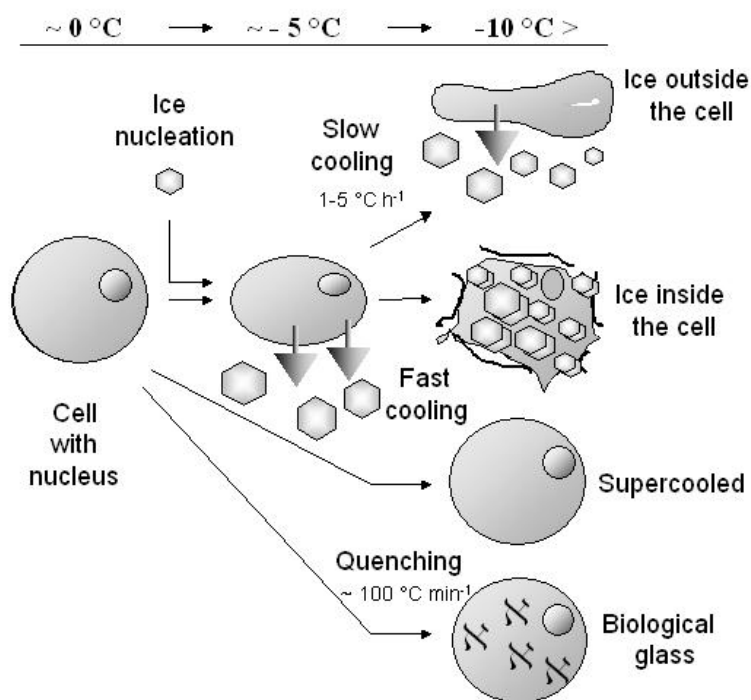


Fig. 8.1. Natural plant behaviour while exposed to cooling explained by diagram of the freezing process in plant tissue. Freezing process is sorted according to the cooling rate and the degree of ice crystal formation. Ice crystals inside the cells are predominantly lethal for plant.

Woody plants, tolerating ice crystals in their tissues have several overall strategies to stay alive during temperatures below zero (Fig. 8.1). The first living strategy is to avoid freezing by supercooling or, by lowering the melting point of

their tissues, and organs. Supercooling (sometimes called more properly *undercooling*) is a known effect in many plants and plant tissues. For example parenchymatic cells [14], whole organs as generative buds of *Ribes* [12], *Malus* [15] or vegetative buds of *Abies* [16]. The level of supercooling may go down to below -40 °C [17]. As the solid hexagonal ice has the structure that is uncanonical, with respect to the pentagonal-like symmetry of a solidifying clusters of liquid water that contains a high number of incommensurable nuclei of icosahedron and dodecahedron. The second living strategy of plants is based on tolerating the

extracellular freezing [13,15,17,18,19]. Survival of such plant cells/tissues is based on their tolerance to excessive dehydration of the protoplast. In the nature, quite a few of plant tissues survive temperatures down to $-41\text{ }^{\circ}\text{C}$, and with the techniques used for preservation of plant genetic material they can survive temperatures even below -150°C . The third strategy towards a better survival during sudden cooling is called an “extraorgan” freezing [16,20]. The whole plant organ (for example bud) is protected by this type of survival strategy against ice nucleation and ice spreading inside the organ. Extraorgan ice formation resulted in bud deep supercooling following frost dehydration [21]. Above survival strategies of plant species while tolerating ice in their tissues can become shared, for example, the woody plants can exhibit extra organ freezing in their buds, extracellular freezing in their bark tissues and supercooling in their parenchymatic cells of xylem rays [22].

A question remains what is the state of water or better the state of protoplasm in the plant cells subjected to subzero and even lower temperatures. The physical rules bear witness that supercooled liquid can eventually change into the form of non-crystalline solid, i.e. glass. The glass formation at the narrow temperature range called glass transition (T_g), which, fortunately, does not possess the volume change as it does during the transformation to ice. The glassy state found, for example, in dormant twig of a poplar tree [2,22,23] offers the explanation, what state of solid water can be found in frozen tissues supposing that this state occurred due to freezing dehydration of tissues.

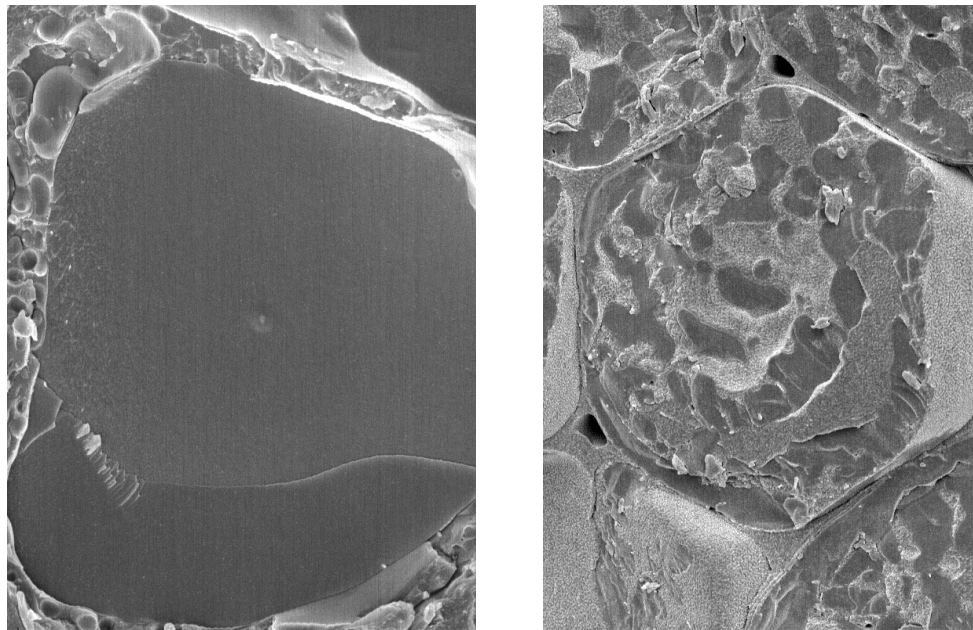


Fig. 8.2. Cells from garlic shoot tip of dormant bulbils. Samples were quenched directly in liquid nitrogen, fractured and etched. Left is a cross fractured vitrified cell after the process of plant vitrification (Plant Vitrification Solution No. 2 - treatment, magnification 10 000x). Right is non-vitrified cell with the visible ice-crystal structure inside the protoplast (magnification 3 000x) [24]

8.2. Need for a man-made safeguarding of biological systems

Detrimental influence of man-affected environment bears, however, an injurious impact on plant growth and endurance. In some cases, the hostile environmental conditions (such as a volcano explosion, catastrophic impact of a meteorite, global atomic war or spread out of deadly infections) may even lead to a serious depression, and in limit, extinction of the

population density of certain plant specimens on our planet. On the other hand, there are also many plant species close to the edge of their disappearance under the current deterioration effect of changing environment or even under a routine fatality of species vanishing. Recently, there has been vast progress in genomics and the ongoing growth of genetically modified organism (GMO) was done. There is a supplementary call for the urgent need to store plants with their entire genetic information, using preferably the cultural varieties, land-races and original wild-plant genetic resources. Fortunately, it is not necessary to store a whole plant but it is enough to have its buds, even just protoplast, because the plant cells are totipotent. Therefore it is possible to store only a small part of plants, mostly a part of meristematic tissues of vegetatively propagated plants [25] or a seed axis of generatively propagated plants. The plant storage at low or even at ultra low temperatures (cryopreservation) is one of the appropriate ways how to keep their viability in a long term prospect.

However, the intracellular ice-crystal formation, which habitually occurs during the lower temperature exposure of plants, is in every case lethal for plant survival due to the inherent volume expansion of newly formed ice in comparison with the original volume of liquid. It grants a consequent destruction of interfacial cell membranes, sometimes happening even on reheating. One way how plants can withstand the low temperatures in the nature is their tolerance to movement of intracellular water to extracellular domains, which, in result, brings a higher tolerance to cell dehydration [4,25-27]. However, the supercooled states frequently possess no dehydration effects or ice-crystal formation, but this state is noticeably unstable, providing somewhat predictable processes of ice recrystallization upon reheating. The exceedingly low viscosity at rapidly cooling conditions of '*freeze-in*' states give often birth to a new non-crystalline state of rigid glasses, and such a process of vitrification is not associated with any volume changes. The *freeze-in* states can nearly hinder any diffusion of molecules, preventing thus biochemical transformations and, accordingly, excluding also any genetic changes. The formation of glassy state is not yet fully understood [28] but it is expedient to a successful storage of plants at a low temperature in liquid nitrogen .

From the view of cryopreservation, the glassy state, which possesses the same volume as liquid, occurs as the most suitable state for a long-term biological storage of germplasm. This strategy of '*being in the glassy state*', is repeatedly exploited by plants in the nature in order to withstand unfavourable freezing conditions of surrounding environment, which can be seen as a sort of miracle. For example, plant pollen flying in the air has a potential to be in glassy state, keeping its viability after stigma pollination. Dormant poplar twigs can survive the low temperatures being in the glassy state in midwinter. It is possible to add other examples of glassy state occurrence in plant species in the nature. However, the conditions at which the glassy state is induced are not fully understood. Though the glass formation in plants can be of help for controlling the '*cryogenic status*' the optimal cooling conditions always achieve a suitable cryopreservation state of plant germplasm.

The process of vitrification [29] is, however, closely associated with the anomalous behaviour of liquid water [30]. Its apparent tendency to pentagonal orderliness within the liquid state toward decreasing temperatures, as well as possible interaction of liquid water with the pentagonal self-similarity of plant cells, the structures of which possess fractal and self-affinity architecture [17]. Incompatible to yield focal points for indispensable nucleation sites inhibiting thus ice formation. Therefore, it seems to be necessary to reiterate some basic data about the structure of liquid water. Mainly its structural quasi-periodicity, which becomes factually important for the formation conditions of quasi-crystalline nuclei and their capability to form the state of either biologically optimal glass or hazardous ice.

An important factor is the rate of freezing, which is crucial for the ice growth and sizing. The ice formation in plants meets a certain temperature stress. At low temperature, the

cooling rate relocate water from intracellular to extracellular space, where ice crystals can form easily. However, the ice crystals outside the plant cells are not harmful. When the rate of freezing becomes too intensive and thus water retains not enough time to move/diffuse outside the cells, the ice crystals start forming inside the cell, which has a lethal effect on the cell.

8. 3. Man's strategy how to generate a glassy state vital for plants' survival at ultra-low temperature

A new approach how to store plant samples at ultra-low temperature is [31,32] so called '*ice free cryogenic storage*', which is based on the instigated formation of biological glasses. The strategy how to reach the glass transition in plant samples for their long-term storage by cryopreservation methods is prospective in the three following ways of an external control of:

- (i) The rate of cooling/warming,
- (ii) Dehydration removing access of water from the tissue, safeguarding enough water volume in the tissue to keep the plants alive. The dehydration can be done by three ways (see below),
- (iii) Infiltration of plant samples with substances shielding the unwanted crystallization, so called '*cryoprotective*' fixatives, which are usually efficacious glass formers.

8.3.1. Rate of cooling and/or warming

By application of a well guarded rate of cooling/warming, the cryopreservation method subsists as the oldest method, which was ever used [33,34]. For the first time, it was demonstrated that the willow twigs collected during very strong winter, additionally prefrozen at -30° C, were successfully cryopreserved in liquid nitrogen for one year with subsequent plant regeneration [33]. The principle of this method is to give it enough time to precede the extracellular freezing of water by slow cooling. In principle, it is like the natural freezing occurring in wildlife.

During a controlled cooling rate, the extracellular nucleus with the highest ice nucleation temperature multiplies being supported by low concentration of extracellular solution, resulting in extracellular ice crystals formation. The driving force for extracellular freezing of water is the difference between the water vapour above supercooled solution inside the cells and those extracellularly occurred crystals of ice. This dehydration, which occurs during slow freezing, was studied intensively throughout eighties of the last Century by scientists dealing with frost resistance of various plants (both herbaceous and non-herbaceous[33]). According to nuclear magnetic resonance measurement, it was found that plants behave at freezing temperatures like an ideal solution according to the van't Hoff law of osmotic pressure for dilute solution. It declares that the reciprocal water volume is a linear function to osmotic pressure. In such complex tissues like roots, shoot meristems, etc., which are concerned in the crown of cereals or buds of trees, the water is frozen while moved out of the cells. The rest of the cell is concentrated as an ideal solution [35].

The volume of water inside the cell is decreasing while the concentration of solutes increases until the equilibrium of water activity outside and inside the cells is reached. A control of glass formation in the tissue during this researching method was invented by authors [34,36] but not proved yet. After freeze dehydration it is speculated that plants can adapt to survival due to inherent glass transition ongoing inside the plant's cells. It is anticipated by means of the following facts. The intracellular matrix occurs highly concentrated owing to extracellular freezing so that the intracellular ice nucleation cannot take place during the slow cooling and, therefore, the plants turn out to be capable to survive even

ultra-low temperatures. When the intracellular ('freezable') water is reduced to that level, which is not dangerous for the plants plunging into liquid nitrogen, its remaining amount is, however, still high enough to keep viable function of cellular compartments inside the cells. Usually, after the dehydration the cells are able to recover and/or repair their full function indispensable for living.

However, the plants cannot get customarily adapted toward such ultra-low temperatures just during their evolutionary growth because such a low temperatures cannot commonly occur during plant evolution or during their lifespan. The lowest temperature measured on the surface of the Earth was $-89.2\text{ }^{\circ}\text{C}$ (at the Russian Vostok Station in Antarctica), still far above the boiling point of nitrogen. The tolerance of plants to the ultra-low temperatures does not arise from their long-term evolution or through acclimation to the lowest temperatures on the Earth but is allowed by the inbuilt physiological state of their membranes being a result of their hardening. Surprisingly, after certain procedures the plants become capable of endurance of ultra-low temperatures artificially provided by immersion in liquid nitrogen [33].

Homogenous and/or heterogeneous ice nucleation in over-wintering plant parts exposed to the low temperature comes to pass at approximately $-40\text{ }^{\circ}\text{C}$ and depends on the sample size. Besides the common effect of crystallization during the cooling, the comparable re-crystallization may possibly occur during re-warming as well, known as a "cold crystallization" which may be equally dangerous for plant cells. Simulated ice nucleation of plant samples is thus used for investigation, and the seeding by ice crystal is the simplest method so far developed. After equilibration (and at a suitable level of freezer capable of providing the high rate of cooling), a sudden decrease of temperature is applied in order to induce ice nucleation and such a freezing protocol is commonly serviceable for uniform samples. This can be done at an exact temperature, which corresponds to the exothermic event taking place after the preliminary first freezing run of control samples. Various producers supplied different companies freezers with various auto-seeding accessories based on the other methods such as conditioning ice nucleation by vibration, ultrasound, etc. Alternatively, for an entrapped ice nucleation certain active bacteria can become applicable to fasten nucleation at a proper temperature [37]. Using a suitable method of the bacterial entrapping ice nuclei, the slower cooling rates could be applied to give enough time for water movement outside the cells [4].

The two-step freezing method was successfully applied to hardy tree buds, which were recovered by grafting [38,39]. Controlled rate of cooling is efficient for storing suspension and callus cultures, embryogenic cultures and in-vitro shoot tips from temperate and subtropical plants. In addition, cryopreservation of cultured cells and meristems was achieved by controlled slow pre-freezing to about $-40\text{ }^{\circ}\text{C}$ in the presence of a relevant cryoprotectant [40] where single chemicals or their combination in various ratios (mixed in a suitable cryoprotective cocktails) can be employed. These cryoprotectants help the plant samples to stabilize their membranes and proteins after deep dehydration, alternatively acting as an energy pool during the recovery of plants. For a common use, dimethylsulfoxide (DMSO) is utilized as a representative cryoprotectant of colligative group capable of penetrating inside the cells. The polysaccharides (mainly sucrose and polyethylene glycols) are representative of non-penetrating cryoprotectants [41].

Warming rates are rather critical for the plant survival when taken from liquid nitrogen. Especially the injury due to inappropriate slow cooling could become restrictive because it may give enough time for extracellular ice formation during crystallization and re-crystallization. The controlled rate of warming is mainly important for the two-step freezing method. In the case of controlled rate of cooling taking place in the presence of cryoprotectant, the consequent higher warming rates are frequently applied. Upon such a

higher rate of warming it is believed that the re-crystallization becomes avoidable. However, immediately after warming, the potentially toxic cryoprotectant must be washed out from the plants. The highest rate of warming can be reached by quench-immersing cryovials into the hot water held at about 40 °C. The high rates of warming minimize cold crystallization often proceeding after the glass transition.

The advantages of controlled rate of cooling include the use of standardized procedures associated with pre-programmed cooling rates, and the use of larger samples. However, the disadvantage of controlled rate of cooling is enslavement toward possessing a freezer capable to maintain low temperatures of -40 °C together with a controlled unit for providing low cooling rates.

In the course of a slow cooling, ice crystals start to grow inside the cells, which is mostly lethal. Extracellular artificially-induced ice nucleation can, however, avoid the random intracellular nucleation. Moreover, slow cooling rate may result in colligative concentration of the solution inside the cell where the ions in the highly concentrated solution can interact with the main components of membranes [42], causing thus non-reversible injury.

When the rate of cooling is too rapid ($>3 \text{ }^\circ\text{C min}^{-1}$), cells will not likely remain in an equilibrium with extracellular ice, and the intracellular solution would become supercooled. Such a supercooled state of the intracellular solution is lacking ice crystal formation and bears alongside a sensitive state of plant called metastable state, which could be dangerous, likewise. When the ice formation occurs in a supercooled state at ultra-low temperatures, it usually leads to intracellular ice formation from either intracellular ice nucleation [43] or through seeding via extracellular ice [29,44]. Mostly, this metastable state becomes noxious for plants. At ultra-high cooling rates (applied down to ultralow temperatures taking place during rapid quenching under $\sim 500 \text{ }^\circ\text{C s}^{-1}$) [34], the supercooled water is often transited into an amorphous/glassy state. Plant cells exploit such a non-extensible glassy state and its diminishable possibility of ice crystal formation.

The survival of seeds exposed to liquid nitrogen temperatures is also influenced by an interaction between cooling rate and moisture content. Rapid cooling of seeds with higher moisture contents (where ‘freezable’ water is clearly displayed) has beneficial effects, while rapid cooling of dry seeds with high lipid contents is detrimental. It is suggested that glass transitions are associated with the two effects of the water and lipid components of the seed [45].

8.3.2. Dehydration

Plant cells and tissues that are supposed to survive impact of liquid nitrogen need to be dehydrated to a certain level ahead of their immersion into liquid nitrogen. The aim of all following dehydration approaches is to increase cell-inner viscosity to the level at which the ice crystallization is inhibited and the intracellular matter becomes present in glassy state.

Three main methods for dehydration of plant tissue used in cryopreservation of plants are the following:

- (i) Evaporative dehydration in the air – the driving force for dehydration is a lower vapour tension than that over the plant sample.
- (ii) Osmotic dehydration – the driving force for dehydration is a lower osmotic potential in solution than that of the plant sample.
- (iii) Freezing dehydration – the driving force for dehydration is a difference in water vapour tension pressure over the supercooled state of water in plants and over the ice in the surrounding space.

During dehydration, the viscosity of plant protoplast increases to a level required for glass formation, avoiding accordingly the dangerous voluminosity crystal formation (Fig. 8.1)

Tab .8. I. *Temperature and dehydration conditions for glass transition involvement as a basis for plant cryopreservation methods.*

Dehydration method	Cryopreservation method	Dehydration driving force	Dehydration at temperature	Glass transition temperature
Air dehydration	Droplet freezing, encapsulation - dehydration	$\Delta p = p_p - p_a$	$T > 0$	$T_g < T$
Osmotic dehydration	Plant vitrification solution (PVSx, MPVS)	$\Delta\Psi = \Psi_{\pi s} - (\Psi_{\pi p} + \Psi_T)$	$T > T_m$	$T_g < T$
Freezing dehydration	Two step freezing, Controlled rate cooling	$\Delta p = p_{sw} - p_i$	$\sim 40 < T < 0$	$T_g < T_m$

Note: Δp - difference in water vapour tension; p_p - water vapour tension in plants; p_a - water vapour tension in air; $\Delta\Psi$ - difference in water potential; $\Psi_{\pi s}$ - osmotic potential of plant vitrification solution; $\Psi_{\pi p}$ - osmotic potential in plants; Ψ_T - turgor potential (turgor potential at plasmolysis is zero); p_{sw} - water vapour tension of supercooled solution in plant cells; p_i - water vapour tension over ice; T - ambient temperature; T_g - glass transition temperature; T_m - temperature of freezing point depression. PVSx Plant Vitrification Solution (PVS2 Sakai [46] PVS3 [47], MPVS [48]).

8.3.3. Desiccation

It is worth reminding the water activity depends on the inherent temperature, water content and on the associated glass transition. If we know them we can assume a certain critical water activity corresponding to the relation $T_g = T$. The relationship between water activity and the state diagram was described by Slade and Levine [49]. Water remains fairly mobile within glassy plant parts and the water activity in glassy state can thus be determined.

The relationship between glass transition temperature, T_g , and the water content can be measured. This relationship is useful for finding at what a low level we need to dry/desiccate the plants to incorporate the glass transition to surface inside plant tissues. The subsequent importance for such a desiccation is the threshold of water content up to which the plant is able to fully regenerate its recovering to original/new plant. Between these two limits of water content the cryopreservation of plants is feasible for enough long time. A high probability of plant liveability and associated plant crucial recovery is reaching after warming them from the conservation state at ultra-low temperatures.

It seems to be very difficult to encompass a standard method for proper measuring T_g as a function of water content. There are, nevertheless, procedures which can be well standardized, particularly regarding the sample preparation methods:

- (i) Anhydrous samples of materials not undergoing thermal reactions (be prepared by melting and quenching).
- (ii) Freeze-dried plant materials consequently stored in vacuum desiccators (packed with a resolute dryer). The vacuum is essential to have a hermetic system, as water transfer will otherwise occur between the vessel and the atmosphere

- (iv) A preferred method for most plant materials is the sample equilibration in vacuum desiccator over saturated salt solutions (this method will also furnish the value of water activity).

In all cases, T_g values must be determined for the number of gradually changed water contents. This must be accomplished in such a way as to become sure that the transition measured is really a glass transition relevant to the water and not, for example, an associated glass transition for lipids and other substances. Since the plant matrix is complex, a phase separation often occurs. The local water content in sub-localities (micro-regions, micro-domains) may become very important. For example, the sugar and amino acid are possible to be phase separated, which means that the reactants are differing both in the water content and in the level of plasticization. Though the water activity in both phases may be the same, the reactant may go through alternative glass transitions because the glass transitions can be at a variance with plasticization in the different amorphous phases. The driving force for desiccation of the plants in the air is related to the difference between water vapour tension in the tissue and the surrounding air (Tab. 8.I). The greater the difference, the greater the strength for removing water from plant tissue.

The decrement of water vapour in surrounding air is possible to decipher in two ways using the so called static and dynamic dehydration.

(i) The static dehydration is the dehydration under a constant relative humidity, which constancy can be reached by equilibration of plant tissues over a saturated salts solution (where the excess of water is dissolved into the oversaturated solution). The salt solutions can be adjusted for an activity of water from $a_w=1$ for distilled water to $a_w=0.086$ for $ZnBr_2 \cdot H_2O$, for example. Advantage of this method is based on the realization of certain equilibrium of the water content as a response to the proper activity of water. Its inherent disadvantage is a relatively long- time when the constant water content is accomplished.

(ii) The dynamic dehydration is carried out when the air with constant air humidity is flow removing water from plant samples to equilibrate within certain time. By moving air, the excess of water vapour is removed from the sample leaving it with a higher humidity than relative humidity in the input. The advantage of these methods is a shorter time for removing the water from plant samples in comparison with the static method but it has some exceptions. The rate of hydration depends on many coupled features, such as the ratio of sample volume to surface, diffusibility of water vapour in the surface to water vapour, sensitivity of plants to the dehydration speed, etc. In the samples dehydrated too quickly, the surface can turn out to be over-dehydrated and even can get covered by a glassy layer, which bestows a diffusion barrier to further dehydration. When lower air humidity is used then a shorter time is needed for dehydration but requires a greater air flow (with a defined constant humidity). The parallel samples must be weighted for the determination of the final amount of water inside the samples. For dehydration, it is usually used a sterilized air flow in laminar flow boxes. Therefore, a rather difficult control of the final dehydration level yields an undesirable disadvantage of this method.

8.3.4. Osmotic and freeze dehydration

Osmotic dehydration is one of the most common ways of how to remove water from plant samples not only providing less water but also featuring a possible incorporation of some osmotic compounds for a direct protection. In principle, during the osmotic dehydration a plant part is factually bathed in solution, which has a higher concentration of solutes than that inside the cells. The driving force for the osmotic dehydration is the difference in water potential between cells and the osmotic potential of surrounding solution.

Fully turgid¹ plant cells have water potential close to zero like a very low concentrated solution. The highly concentrated solution inside the cells (representing low osmotic potential) is compensated by turgor potential with opposite signs. For an involved glass transition, the osmotic dehydration must be very deep, which means that the osmotic potential of dehydrating solution must be low in order to remove water excess from the tissue solution. In the case of an excessive volume of osmotic solution, the changes in osmotic potential of the surrounding solution can be constant, taking in account a rather lower separated volume of water being removed from the tissue. It means the samples are gradually dehydrated by water removal until equilibrium with the surrounding osmotic solution is reached.

The plant samples dehydration at low temperatures during the cryopreservation is connected with a freeze-drying method, which is used for stabilization of rather labile substances such as in pharmaceutical industry for storage of protein-containing drugs and other biotechnology products.

8.3.5. Cryoprotectants

Glass-formation involving the vitrification of special solutions [46,50,51] and the encapsulation by dehydration techniques [52] were developed in the 1990s, and since then the number of cryopreserved species has increased markedly [53].

An ethylene glycol-based solution applied for glass-formation procedure was first presented by *Steponkus* and colleagues [50]. For dehydration of winter rye protoplasts they used a concentrated vitrification solution made of ethylene glycol and sorbitol and bovine serum albumin (BSA) acting at 0°C. In the same year, Sakai and colleagues [46] published another combination of chemicals useful for vitrification. The cells of navel orange were sufficiently dehydrated with a highly concentrated cryoprotective solution (PVS2) prior to direct plunge into liquid nitrogen. The PVS2 contains glycerol (30 % w/v), ethylene glycol (15% w/v) and dimethylsulfoxide (DMSO, 15 %w/v). However, this solution is toxic to plants, which ability to survive is just several minutes using PVS2 solution at room temperature. This disadvantage is overcome by keeping the plant parts in PVS2 solution at lower (0 °C) temperature prolonging its non-toxic time to an hour. Less toxic cryoprotective solution (without DMSO) for plants is a 'Plant Vitrification Solution' (No.3) (PVS3)[47]. Subsequently, cryotubes containing meristems (in 0.5 ml PVS2) are directly plunged into liquid nitrogen at the cooling rate of about 300 °C min⁻¹. Alternatively, meristems are put on the aluminium foil with or without small drop of PVSx. Since the first publication of positive results on cryopreservation when using PVS2, this treatment was applied to more than 200 species and varieties, which exhibited a successful storability in liquid nitrogen through vitrification [53]. Using different types of cryoprotectants, one can manage to distinguish what kind of a cryoprotectant and at what extension the transportation takes place, and to which part of the plant tissue they are delivered.

Naturally occurring cryoprotectants, such as 'Antifreeze Proteins' (AFPs), expectably undertaking a direct interaction with ice, likely modify the freezing process '*in planta*'. In cold-acclimated leaves, AFPs inhibit the propagation of ice from the surface of a leaf so no freezing occurs until the tissue reaches its equilibrium freezing point when ice starts to propagate through the apoplast. After the leaves get frozen, AFPs inhibit the re-crystallization

¹ Turgor pressure or turgidity is the main pressure of the cell contents against the cell wall in plant cells, determined by the water content mainly of the vacuole, resulting from osmotic pressure. Osmotic pressure is a result of solution in an intracellular space separated by a semi permeable plasma membrane. Turgor pressure is regarded as the driving force for cell extension and thus for plant growth. The terms osmotic potential and turgor potential are widely used. The osmotic potential is with negative sign in contrary to positive values of turgor potential in most cases of plant cells.

of extracellular ice. AFPs may become particularly protective by slowing ice propagation in such situations where fluctuating temperatures cause repeated freezing and thawing of tissues. Where an insulating snow cover could stay at ambient temperatures near the melting point of the extracellular ice it may get promoting re-crystallization. Although ice can re-crystallize more slowly at colder sub-zero temperatures, inhibition of ice re-crystallization may be also befitable for those plants that are kept frozen for a prolonged periods [54].

8. 4. Glass transition temperature, freezing point depression temperature and supercooling temperature - important points on temperature scale

Under normal atmospheric pressure, the liquid water can be easily supercooled down to about -25°C , with some further difficulties (purity) down to about -38°C and with an enhanced supercooling (such as in small droplets of $\sim 5\ \mu\text{m}$ diameter) down to minimal -42°C . The lower temperature limit for supercooling of water (also known as the homogeneous freezing point) is for water activity close to 1. The freezing point depression (ΔT_m) with water activity equal one is 0°C . Where salts or hydrophilic solutes are present, the homogeneous freezing point reduces about twice as much as the melting point.

However, some sugars, for example, have very low glass transition temperatures and the time for ice formation (at T_g) becomes almost infinite. Therefore, two separate transitions may appear in the experimental time scales, such as the T_g and T_m , which correspond to the onset of the glass transition and the onset of the ice melting, respectively. The term "*onset*" (lines extrapolated intersection) should be underlined, because merely taking the value of T_g from the curve midpoint is not reasonable. This is because of the following reasons:

- (i) The "*onset*" of T_g and T_m coincide for high molecular weight compounds
- (ii) At low temperatures, the T_m lays around the outset of the glass transition.

As both the molecular weight and T_g increase, the T_m takes place closer to the T_g and no T_g midpoint or outset can be determined. Therefore, the T_g and T_m cannot represent simply the onset and outset of the T_g .

The T_m data can be directly obtained by differential scanning calorimeter (DSC) and the appropriate value of T_m can be measured for a plant by means of melting microscope where T_m is defined when the last ice crystals melt under cryoscope.

8.5. Specificity of biological samples

Different types of methods are commonly used to determine the temperature span of glass transition, preferably based on:

- (i) Thermodynamics, that is, using conventional differential scanning calorimetry (DSC) or differential thermal analysis (DTA) technique,
- (ii) Other dynamic measurements of properties such as mechanical spectroscopy.

Characteristic times can then be associated with enthalpic and mechanical relaxations, which may be different because of certain "decoupling" between dissimilar relaxation modes. It should be considered there are differences induced by the given method of experimental data analysis:

- (i) Definition of T_g on the DSC, DTA curves,
- (ii) Characterization of relaxation times,
- (iii) Mechanical measurements often determined in terms of modulus, such as dielectric measurements in terms of compliance.

One of the main advantages of DSC, DTA is that the measurements can be performed in sealed pans (micro-container cells). The size of plant samples is usually small enough to fit to the hermetic pan. One to three pieces of *Allium* shoot tips weigh 3-5 mg and 3-8 mg equal the weight of 1-3 vegetative apple buds, as an example. For practical purposes, the measuring method should be adjusted according to the required application.

Although DSC is not the most sensitive method to measure T_g , the main advantage of DSC is that it allows repeated and relatively reproducible measurements easy to carry out along a wide temperature range. On the other hand, the shortcomings of DMA are instantaneously recognizable:

- (i) It is almost impossible to prepare samples with exact dimensions just on the basis of plant materials;
- (ii) The measurements can be made more or less for rigid/solid samples;
- (iii) The curves are routinely difficult to analyze exactly enough because of the flatness of the peaks and the higher noise involved (often causing misinterpretation);
- (iv) Evaporation of water from the samples is always a serious problem.

Moreover, some investigators stressed out that DMTA is, nevertheless, more sensitive than DSC.

8.5.1. Particularity of measurements of biological glass

Glassy state and associated phase appraisal during cryopreservation can be best indicated by the help of DSC, which is a sensitive method for the determination of various crossing phenomena occurring towards the vitrification. Second consequent DSC run with the same biological sample could, however, be substantially different from the first run, because the plant samples could be transformed (alternatively phrased as 'injured') or completely destroyed after the first run completion.

Starting temperature. It is very important to retain plant samples in equilibrium allied with the starting temperature. Room temperature as a starting temperature for plant investigation is often for their non-acclimated state. Starting temperature for cold-hardened plants should be at least close to 0 °C and should be accepted after a long-time equilibrium.

Rate of cooling and warming.

At extremely slow cooling rates, degrading biological samples could occur frequently.

Tab. 8.I. Comparisons of the levels of various organic and inorganic solutes in stem tracheal (xylem) sap and fruit tip (phloem) sap of legume *Lupinus albus* [57]

	Xylem sap (tracheal)	Phloem sap (fruit bleeding)
	mg ml ⁻¹	
Sucrose	-	100-160
Amino acids	1.0-2.5	16-30
	µg ml ⁻¹	
Nitrate	10-140	-
Potassium	179	2 256
Sodium	82	140
Magnesium	39	124
Calcium	95	63
Iron	1.5	9.6
Zinc	0.8	5.0
Manganese	2.72	12.4
Copper	0.55	3.8

Maximum warming temperature.

The highest temperature of warming can bring a change of substances causing, e.g., protein denaturation, sugar caramelization.

Autosampler conditions.

The temperature of an autosampler is important for long-running measurement.

A new technique, called *dynamic cooling protocols*, is using a conventional DSC and has been developed to obtain chart of dynamic and quantitative water transport data in cell suspensions during freezing [55]. Optimization of this technique for cryopreservation was connected with the water permeability, which is characteristic during freezing in the presence of extracellular ice and cryoprotective agents (CPAs); for details see ref. [55].

8.5.2. Glass forming substances occurring in plants

a) Elements

From a comparison of the average content of elements [56] which may emerge in plant bodies with those forming easily glasses (cf. Tab. 8.II). It is not clear to derive a strict relationship of glass formability in wider organic nature. A certain exception can be seen in carbohydrates, mainly in the region of high concentration of sucrose.

Tab. 8. II. *Examples of substances that form glasses (those commonly present in plants are in bold letters) - adapted from [56,58,59].*

Type	Limited examples
Elements	P, S, Se
Oxides	SiO₂ , GeO ₂ , B ₂ O ₃ , P₂O₅ , As ₂ O ₃ , Sb ₂ O ₃
Halides	BeF ₂ , ZnCl ₂
Aqueous solutions	H ₂ SO ₄ (aq.), KOH (aq.), (Na,K,Li)Cl (aq.),
Organic compounds	Methanol, ethanol, glycerol, glucose , toluene, o-terphenyl, m-xylene, fructose, sucrose
Polymers	Poly(ethylene), polystyrene, poly(vinyl) chloride, etc.

b) Water

Any commence of a state diagram for water relies, at least, on two sources of data:

- (i) Variation of glass transition temperature (T_g) as a function of water content;
- (ii) Curve-based determination of a freezing point depression (T_m) can be completed up to the intersection (with the T_g curve).
- (iii) Temperature of both curves for homogenous and heterogeneous nucleation depends on water concentration. A state diagram cannot be created without precise knowledge of water content and the corresponding glass transition temperature, thus the glass transition temperature must be defined. Glass transition temperature for hyperquenched water is generally believed to lay at about -133 to -138 °C [60].
- (iv) The highest heat capacity is that of water (Tab.8.III). The same is valid for ice at temperatures below zero in comparison with other substances occurring in plants.

c) Carbohydrates

Sugars are commonly used as cryoprotectants. Their concentrations and the individual types of sugars must be optimized toward developing cryopresevation methods [26]. The

cryobiologists tested various carbohydrates in an attempt to improve the percentage of explants surviving with their regeneration. Unlike sugar alcohols such as sorbitol and manitol, which are not readily metabolised in the cells of many plant species, sucrose is readily metabolized and is thought to have several protective functions during dehydration and subsequent freezing.

Tab.8. III. Heat capacity ($Jg^{-1}K^{-1}$) of water, ice, main organic substances and ash from plants. Data calculated according published equations [61].

Temperature		H ₂ O	Ice	Protein	Fat	Carbohydrate	Fiber	Ash
°C								
40		3.82		2.05	2.04	1.62	1.91	1.16
30		3.91		2.04	2.02	1.60	1.90	1.15
20		4.00		2.03	2.01	1.59	1.88	1.13
10		4.09		2.02	2.00	1.57	1.86	1.11
0		4.18	2.06	2.01	1.98	1.55	1.85	1.09
-10			2.12	2.00	1.97	1.53	1.83	1.07
-20			2.18	1.98	1.95	1.51	1.81	1.05
-30			2.24	1.97	1.94	1.48	1.79	1.03
-40			2.31	1.96	1.92	1.46	1.77	1.01

Most of these sugar alcohols are not as effective cryoprotectants as is sucrose. Sucrose has been found to be the most effective cryoprotectant in other studies [26,62]. Sugar activities are an important intermediary for cryopreservation:

- (i) Can decrease water content by osmotic dehydration;
- (ii) After influx of sugars into the cells, the osmotic potential of plant tissues often gets decreased;

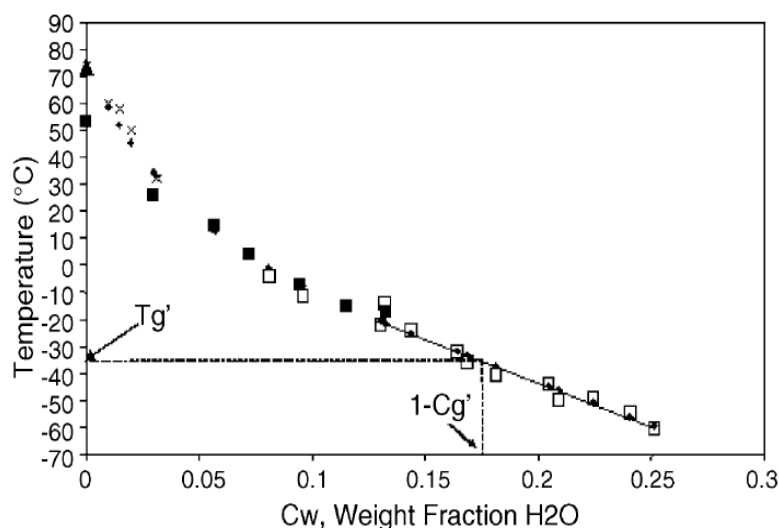


Fig. 8. 3. T_g in aqueous sucrose solution as a function of different water content: literature data ((\times) data from [64]; (\blacksquare) data from [65]; (\square) data from [66]; (\blacktriangle) [67]; (\blacklozenge) calculated T_g from Eq. (1)). Redrawn from [60] the concentration of the solute in the freeze concentrated solution is usually denoted C_g (weight fraction of solut)

- (iii) Osmoprotectants (sugars like sucrose) are thought to contribute maintaining the membrane integrity during the dehydration and freezing processes. It is intermediated by the formation of hydrogen bonds between sugars and the hydrophilic components of cellular embranes [63];
- (iv) Act as a glue sticking the shoot tips to the carrier (e.g. aluminium foil) after dehydration

- (v) Accomplishes the first aid during the energy starvation throughout the plant regeneration after warming.

Sugars are seen as the most usable cryoprotectants involved in plants as a reaction to abiotic stress (mainly in drought and cold conditions). The sucrose is used also the most acceptable cryoprotectant added to the plant during their cryopreservation at ultra-low temperatures. On the sugar as a cryoprotective example, it can be shown how difficult it is to interpret complex behaviour of such a simple substance and how difficult it can be to define its mixtures in the plant tissue (Fig 8.3 and 8.4). No expression derived from theoretical models is found suitable to predict satisfactorily enough.

The glass transition temperature for a binary mixture - the semi-empirical *Couchman* and *Karasz* expression [27] is only partially successful in aqueous solutions.

Although empirical, the *Couchman* and *Karasz* equation seems to be the best model to describe varying T_g with composition. A modified Gordon-Taylor equation (MGT, Eq. (1)) can be used to estimate the T_g values of single-phase sucrose solutions (i.e. no ice present). Glass transition temperature data for sucrose with various water contents were gained from the literature Fig. 8.3 and were fit by Eq. (1)

$$T_g = ((kT_{g2} - C_w(kT_{g2} - T_{g1}))/((C_w(1 - kT_g) + kT_g))) + \alpha_1 C_w(1 - C_w) + \alpha_2 C^2(1 - C_w) \quad (1)$$

where C_w is the concentration of water at T_g (weight fraction), T_{g1} and T_{g2} are the mid-points of the glass transitions for pure water and sucrose, while k , α_1 and α_2 are constants. Here we use 348.2K for T_{g2} , the glass transition temperature of pure sucrose, and T_{g1} for water is taken as 135 K. The “best fit values” for the parameters are $k = 0.092$, $\alpha_1 = 481$ and $\alpha_2 = -1225$ [60].

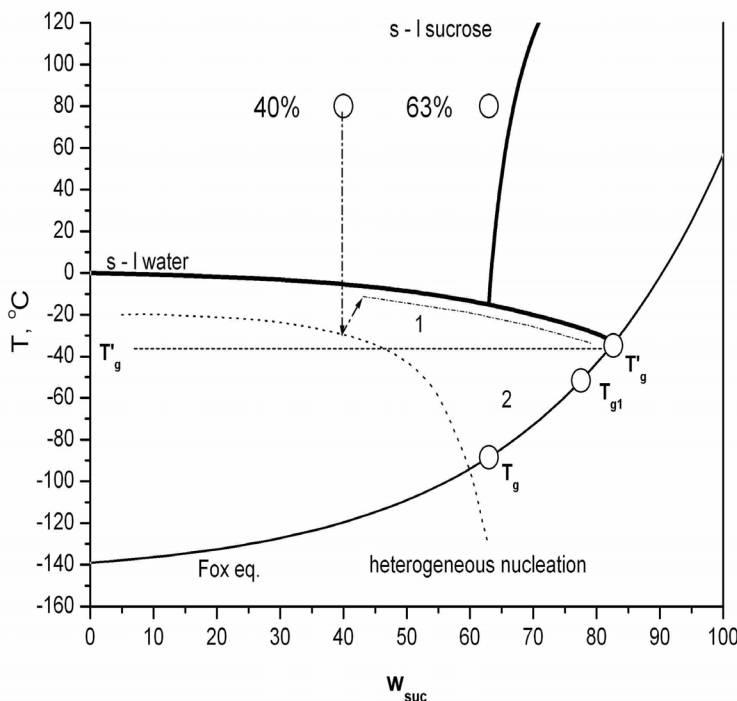


Fig.8.4. Schematic state diagram of aqueous solution of sucrose[69], an example of 40% concentrated sucrose. 1 is for equilibrium freezing, 2 is for thawing of 63 % frozen solution. It shows the glass transitions corresponding to the nominal composition of the initial solution of sucrose T_g , and glass transition of maximum freeze concentrated phase T_{g1} , as well as the glass transition around sucrose crystals T_g' Solid curves are for of water solid- liquid boundary (s-l water) and sucrose solid- liquid boundary (s-l sucrose).

There are no attempts to apply this equation to multi component plant samples, but it could be possible under further credentials. However, the equation allows

considering a mixture of several components as one given component and water as another one providing thus some practical values. The problem still remains because it does not know the definite ΔC_p for even pure water which the Couchman-Karasz equation uses for predicting the T_g data of multi component systems. Nevertheless, both equations were

satisfactorily used for description of water content and glass transition for such multi-component biological material as the fruit powders [68].

From the above mentioned results, it follows that diluted and semi-concentrated aqueous solutions of sucrose (w_{suc} weight fraction of sucrose in Fig 8.4, Tab. 8.IV) freeze under a non-equilibrium state. The system is heterogeneous and contains crystals of ice and sucrose, which exhibit two types of domains of amorphous solids (or better glass), which composition corresponds to that of maximum freeze concentrated phase (MFCP) characterised by glass transition temperature T'_g . The solution inside the domains around sucrose crystals is characterised by glass transition temperature T_{g1} . At very low temperatures, the resulting structure of the solution is heterogeneous containing, in any case, ice, sucrose crystals, and two glasses formed from the freeze-concentrated phase and the solution laying in the neighbourhood of sucrose crystals.

Recently, *Goff and Sahagian* [6] used modulated DSC together with a parallel microscopy to examine the glass transition behaviour of frozen 40% sucrose solutions. They concluded that the high temperature transition complies with a glass transition, T_g , That results from the formation of a concentrated, non-equilibrated sucrose phase in the region of rapidly nucleated ice and/or from the solute inclusions within the crystals themselves. The second annealing process at -35 °C looks as if to result due to the disappearance of the higher temperature transition [6].

Tab.8. IV Glass transitions corresponding to the nominal composition of the initial solution of sucrose T_g , glass transition of maximum freeze concentrated phase T_{g1} , glass transition domains around sucrose crystals T'_g , melting temperatures of ice or sucrose $T_{m,i}$, $T_{m,suc}$ and melting enthalpy per gram of ice or sucrose $\Delta H_{m,i}$, $\Delta H_{m,suc}$ of aqueous solutions of sucrose weigh fraction (w_{suc}). Cooling and heating rate of measurement was 2 °C min^{-1} [69].

w_{suc}	T_g (°C)	T_{g1} (°C)	T'_g (°C)	$T_{m,i}$ (°C)	$\Delta H_{m,i}$ (J/g _i)	$T_{m,suc}$ (°C)	$\Delta H_{m,suc}$ (J/g _{suc})
0.05	–	-50.2	-35.9	1.0	320.1	5.1	–
0.1	–	-48.1	-35.2	0.0	309.2	1.1	4
0.2	–	-48.0	-35.1	-1.3	272.4	0.7	58.7
0.3	–	-46.7	-34.8	-2.7	234.7	0.9	26
0.4	–	-46.3	-35.9	-5.3	208.0	0.4	5
0.53	–	-45.5	-36.2	-9.7	143.8	–	–
0.63	-83.2	-44.9	–	-16.1	134.1	-4.3	0.9
0.76	-56.9	–	–	–	–	–	–

The aqueous sucrose solution behaves differently according to the momentary status of concentration resulting from given cooling and warming. The behaviour does not appear simple as the sucrose concentration (representing four concentration regions) can be subdivided into four parts, each exhibiting its characteristic glass transition. At one moment, the sucrose can show up the three distinctive temperatures of glass transition taking place in different domains of the down-cooled sucrose solution. This depends on various settings of sucrose solution concentration, rates of cooling and warming, annealing temperature and time.

During plant freezing and drying, sucrose works as a definite (natural) protecting agent, but a mere accumulation of sucrose alone is not a sufficient condition for all plant species survival of the ultra-low temperatures.

8. 6. Stability of biological glass: an important condition for reaching its long-term storage

Glassy status as a common solid/rigid state occurring in biological samples habitually results from a suitable circumvention of crystallization. The quality of glassy state is possible to classify simply by ratio (T_g, T_m) - the lower ratio reveals the higher difference of T_g and T_m , thus showing a greater stability of glassy state. A more sensitive interrelation to the glass formation peculiarities can be found on the basis of *Hruby* coefficient K_{gl} :

$$K_{gl} = (T_c - T_g) / (T_m - T_g) \quad (2)$$

where T_c , T_g , T_m are temperatures of crystallization, glass transition and melting temperature, respectively, the values of which, however, can be found only by suitable experiment using the ready-to measure sample (pre-prepared glasses) [17]. It is clear that the greater the value of K_{gl} the better is the glass-forming. The best utilization of K_{gl} is in the comparison of glass-forming ability and glassy state stability of different biological materials under different conditions and thermal treatments. *Hruby* coefficient (K_{gl}) indicates the glass stability against crystallization on heating and could be used to estimate the vitrification ability of glass forming liquids. These both characteristics (T_g, T_m) are easily measured by conventional DTA/DSC during warming samples in glassy state. The correlation between glass stability characterized by *Hruby* parameter and the glass forming tendency characterized by critical rate of cooling for glass formation was confirmed [70].

The kinetic property of biological means in glassy state is yet poorly understood. Dynamic processes including the membrane fusion and solute leakage of frozen and dry liposomes in carbohydrate glasses, and ice formation haemolysis of frozen human red blood cells, were recently studied [71]. The kinetic stability of biological glasses is clearly T_g -dependent. The reaction rate constants deviated notably from the traditional Arrhenius behaviours can be well fitted to the *Williams-Landel-Ferry* (WLF) [72] equation

$$\log a(T) = -C_1 (T - T_g) / \{C_2 + (T - T_g)\} \quad (3)$$

where C_1 and C_2 are universal WLF constants. It was found that different polymers exhibit very similar WLF constants. The universal values of constants in the WLF equation, used for abroad spectrum of amorphous materials ($C_1 = 17.44$, $C_2 = 52.1$) do not match, however, to the dynamic processes of biological material. The derived C_1 and C_2 constants of the WLF equation for seed survival of three species at $T > T_g$ are: for *Glycine* ~ 37.5 and 269.8, for *Pisum sativum* 22.3 and 179.2, and for *Phaseolus vulgaris* 22.1 and 183.1, respectively [73].

Angell [74] defined fragility *via* the diagrams of $\log(\eta)$ vs. T_g/T , where η is viscosity. When the temperature dependency of viscosity is high, such a glass is called fragile. At temperatures higher than a glass transition temperature, a different behaviour of glasses can be commonly distinguished according to the ratio of the crystalline melting point (T_m) and glass transition temperature (T_g). According to *Slade* and *Levine* [49], consequently, it is possible to define three classes of amorphous systems

(i) The ratio $T_m/T_g \approx 1.5$ is characteristic for the first-class. The amorphous system in this class of biologic-like materials is represented by glucose, for example, where the viscosity decrease is moderate. Description is typical to comply with some 'well-behaved' polymers or 'fragile' liquids [27]. The common constants in WLF equation are 17.44 for C_1 and 51.6 for C_2 .

(ii) The ratio $T_m/T_g \gg 1.5$ is often categorized for the second-class. The viscosity decrease is very small. Such glasses are typical products of ‘poorly behaved’ polymers or strong liquids. This ‘typical but not well-behaved’ class is a readily crystallisable matter (e.g., water) and the WLF constants are about 20 and 155 for C_1 and C_2 , respectively.

(iii) The ratio $T_m/T_g \ll 1.5$ (when the temperature of glass transition is close to the temperature of the melting) is distinguished for the third-class. The WLF constants of $C_1 = 12.3$ and $C_2 = 22.3$ apply [7] and the glass-forming systems are described as ‘a typical and poorly behaved’ class represented by, e.g., native starch, gelatine, fructose or galactose and/or other very fragile liquids.

The kinetics of ice formation also deviates from the Arrhenius relationship, following the WLF kinetics. The WLF constants for the process of ice formation were calculated to be 2.1 and 11.2 for C_1 and C_2 , respectively. These values are significantly different from those ones (i - iii). Therefore, the ice formation in frozen cells may be distinguished by WLF constants from glass transition in the above mentioned three classes (i - iii).

For some supercooled liquids, typically water, there exists a fragile-strong transition [75]. The simple model system has been reported by *Angel et al.* [76]. For electrolyte solutions that are very fragile, and become stronger as concentration increases due to the replacement of weaker hydrogen bonding with stronger ion-dipole interaction. In contrast, any sugar solution becomes more fragile as concentration increases. High molecular weight proteins such as gluten are relatively strong.

The prediction of the stability of biological materials preserved in the amorphous matrix is of a very particular interest. From the WLF equation (3), one can easily derive that the stability of biological materials in the amorphous matrix will decrease at a rate proportional to (10^{T-T_g}) if held in the rubbery state at temperatures $T > T_g$ [54].

However, a more accurate estimation is needed in practice. A conceptual illustration has been provided by Slade and Levine, who used the constants of WLF equation to characterize the three classes of amorphous systems (see previous discussion). For the systems of the first class paragraph i) above/, a change by factor 10 for every 3 °C is recognizable. However, for both the second (ii) and the third (iii) class, this stability may show the decrease by a factor of 10 for any increase of every 6 °C [17]. Sun has done a similar calculation using the derived WLF constants knowing that the rate of ice formation in frozen blood cells (prepared during the devitrification) increases approximately by the factor $10^{(T-T_g)/6}$ (this is a 10-fold increase over a 6 °C interval above the T_g). This value matches wonderfully to the second class of amorphous systems, which includes water [7]. However, the stability of frozen and dehydrated biological cells and membranes, as measured by haemolysis and solute leakage, turns up to decrease much slower than expected, roughly at a rate of $10^{(T-T_g)/15}$ at temperatures $T > T_g$, (i.e., a 10-fold decrease over 15 °C above the T_g).

8. 7. Peculiarities of the thermal analysis when applied to cryogenic samples

The entire study was carried out at two experimental conditions:

Soft: (i) plants in containers were grown in the natural conditions assured by our laboratory and the samples were collected in the middle of winter at the outside temperature < -15 °C. The sampled twigs covered in the plastic bags were then placed into the freezing box at $T = -20$ °C. After several days of equilibration, the samples were either further cooled for liquid nitrogen storage or prepared for direct thermal investigations in such a way they were cut from plants and the measurements were performed on either dormant bud or meristematic tissues. The aluminium pans loaded with samples were isothermally transferred into the pre-

cooled DSC measuring head (Fig. 8.5B) at $T = -20\text{ }^{\circ}\text{C}$ helium as a purge gas. Water content in samples was assessed gravimetrically. Control plants in a container were slowly thawed at $T = 4\text{ }^{\circ}\text{C}$ and after the plant was grown in the greenhouse at $T = 24\text{ }^{\circ}\text{C}$, their dormant bud vitality was verified.

In the *intense case*: (ii) the deep supercooling of samples was guaranteed by PC-programmable cryostats, which enabled to achieve temperatures of liquid nitrogen when the samples were moved to a storage space. For easier obtaining a slow rate of dehydration, we often used alginate bead with encapsulated shoot tip during dehydration. The DSC (TA Instruments, TA 2920) measurements were then carried out from the temperature of liquid nitrogen, which necessitated a specially developed procedure of isothermal transferring samples into the DSC measuring head, all kept continuously under liquid nitrogen. The representative sample is sealed into the hermetic pans parallel to the cryopreserved plant samples. The pans with the plant sample are quench freeze. The samples are transferred in liquid nitrogen to the pre-cooled DSC head (Fig. 8.5B) filled with liquid nitrogen. After warming up to -140 to $-130\text{ }^{\circ}\text{C}$, the pans (two pans with samples and empty pan as reference) are moved to the measuring places by forceps pre-cooled in liquid nitrogen (Fig. 8.5B). Then the standard warming rate ($10\text{ }^{\circ}\text{C min}^{-1}$) is applied for heat flow measurement by DSC. By this procedure, it is possible to check the glass transition temperature periodically in parallel stored samples in liquid nitrogen. A typical procedure for DSC measurements is depicted in Fig. 8.5.

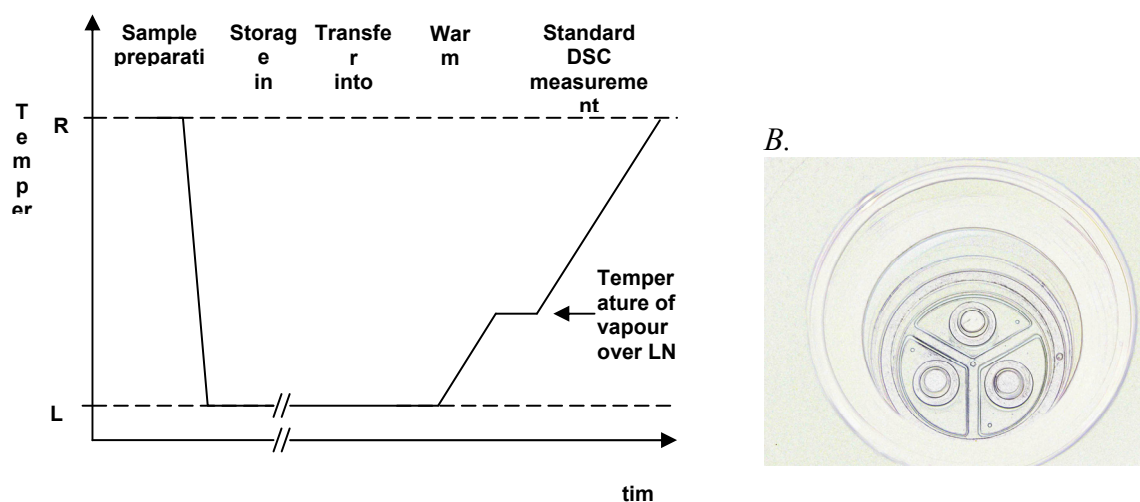


Fig. 8. 5. (A). Procedure of glass checking for plant samples after their certain time of storage in liquid nitrogen. Two main procedures are deopuiscted: * plant samples in hermetic sealed pan were quench-frozen in the same procedure as cryopreserved samples down to liquid nitrogen temperature. **measuring head is warmed up to evaporate excess of liquid nitrogen and pans are fitted to the measuring places (B) by pre-cooled forceps. (B). Detail of measuring head for three measuring places with hermetic pans in their right positions. Standard warming rate ($10^{\circ}\text{C min}^{-1}$) is used. Abbreviations: LN - liquid nitrogen, RT – room temperature (for more details see text).

Literature 8

- [1] Šesták, J., *How it is with the warming our planet Earth and what is the role of green house gases*. Chemické listy 101, 832-, (2007)
- [2] Bartell L.S., *On possible interpretations of the anomalous properties of supercooled water*. J. Phys. Chem. B 101,7573-7583, (1997)
- [3] Nitsch, K., *Thermal analysis study on water freezing and supercooling*. J. Thermal Anal. Calor. 95,11-14,(2009)

- [4] Šesták, J., Zámečník, J., *Can clustering of liquid water and thermal analysis be of assistance for better understanding of biological germplasm exposed to ultra-low temperatures.* J. Thermal Anal. Calor. 88,411-416,(2007)
- [5] Burke, D., Kaufman, P., Mcneil, M., Albershe P., *Structure of Plant-Cell Walls: Survey of Walls of Suspension-Cultured Monocots.* Plant Physiol. 54,109-115,(1974)
- [6] Goff, H. D., Sahagian, M. E., *Glass transitions in aqueous carbohydrate solutions and their relevance to frozen food stability.* Thermochim. Acta 280,449-464,(1996)
- [7] Slade L., Levine H., *A food polymer science approach to structure-property relationships in aqueous food systems: non-equilibrium behavior of carbohydrate-water systems.* Advances in experimental medicine and biology. 302,29-101,(1991)
- [8] Ovchinnikova, K., Pollack, G. H., *Can Water Store Charge?* Langmuir 25, 542, (2009)
- [9] Giovambattista, N., Buldyrev, S. V., Stanley, H. E., Starr, F. W., *Clusters of mobile molecules in supercooled water.* Physical Review 72, 11202-11214, (2005)
- [10] Chvoj Z., Šesták J., Tříska A, *Kinetic Phase Diagrams: non-equilibrium phase transitions.* Elsevier, Amsterdam (1991)
- [11] Minaev, V. S., Timoshenkov, S. P., Chernykh, S. P., *Polymorphous-crystalloid nature of vitreous and liquid H₂O.* J. Optoelectronics Adv. Matter. 6, 103-112, (2004)
- [12] Ashworth E.N., Wisniewski M.E., *Response of Fruit Tree Tissues to Freezing Temperatures.* HortScience 26, 501-504, (1991)
- [13] Nedelec J.-M., Grolier J.-P.E., Baba M. „*Thermoporosimetry: a powerful tool to study the cross-linking in gels networks*“ J. Sol-Gel Sci. Tech. 40, 191-200, (2006);
Beurroies, I., Denoyel, R., Llewellyn, P., Rouquerol, J., *Melting-solidification and capillary condensation hysteresis in mesoporous materials: application to the interpretation of thermoporometry data.* Thermochim. Acta 421, 11-18, (2004)
- [14] Ristic Z., Ashworth E.N., *Response of xylem ray parenchyma cells of red osier dogwood (Cornus sericea L.) to field freezing stress, and to freeze-thaw cycle.* J. Plant Physiol. 149, 735-745, (1996)
- [15] Bilavčík, A., Zámečník, J., *Localization of endogenous ice nuclei in flowering apple shoots.* Biologia 51, 62-, (1996)
- [16] Sakai, A., *Freezing Tolerance of Shoot and Flower Primordia of Coniferous Buds by Extra-Organ Freezing I.* Plant Cell Physiol. 23, 1219-1227, (1982)
- [17] Šesták J., *Heat, thermal analysis and society.* Nucleus, Hradec Kralove, (2004)
- [18] Malone, S. R., Ashworth, E. N., *Freezing Stress Response in Woody Tissues Observed Using Low-Temperature Scanning Electron-Microscopy and Freeze Substitution Techniques.* Plant Physiol. 95, 871-881, (1991)
- [19] Warmund, M. R., George, M. F., Cumbie, B. G., *Supercooling in Darrow Blackberry Buds.* J. Am. Soc. Hort. Sci. 113, 418-422, (1988)
- [20] Sakai, A., *Freezing Avoidance Mechanism of Primordial Shoots of Conifer Buds 1.* Plant Cell Physiol. 20, 1381-1390, (1979)
- [21] Chalkerscott, L., *Disruption of An Ice-Nucleation Barrier in Cold Hardy Azalea Buds by Sublethal Heat-Stress.* Annal. Bot. 70, 409-418, (1992)
- [22] Hirsh, A. G., Williams, R. J., Meryman, H. T., *A Novel Method of Natural Cryoprotection - Intracellular Glass-Formation in Deeply Frozen Populus.* Plant Physiol. 79, 41-56, (1985)

- [23] Šesták J., *Science of Heat and Thermophysical Studies: a generalized approach to thermal analysis*. Elsevier, Amsterdam, Netherlands (2005)
- [24] Bilavčík A., Faltus M., Zámečník J., *Nové teoretické poznatky o vlivu ultranízkých teplot na rostliny* In: Sborník příspěvků a laboratorních postupů z workshopu "Metody kryoprezervace vegetativně množených rostlin", 13. dubna 2005, Prague, 8-15,(2005)
- [25] Zámečník J., Bilavčík A., Faltus M., Šesták J., *Water state in plants at low and ultra-low temperatures*. CryoLett. 24, 412-, (2003)
- [26] Paul, H., Daigny, G., Sangwan-Norreel, B. S., *Cryopreservation of apple (Malus x domestica Borkh.) shoot tips following encapsulation-dehydration or encapsulation-vitrification*. Plant Cell Rep. 19, 768-774, (2000)
- [27] Couchman, P. R., Karasz, F. E., *Classical Thermodynamic Discussion on Composition Effects of Glass-Transition Temperatures*. Macromolecules 11,117-119, (1978)
- [28] Šesták, J., "Art and horizon of non-equilibrated and disordered states and the phase formation" Glasstech. Berichte Glass. Sci. Tech. 70C, 153, (1997)
- [29] Šesták J., *Miracle of reinforced states of matter: glasses as innovative materials for the third millennium*. J. Thermal Anal. Calorim. 61, 305-323, (2000)
- [30] Buitink, J., Leprince, O., *Glass formation in plant anhydrobiotes: survival in the dry state*. Cryobiology 48, 215-228, (2004)
- [31] Sakai A., *Plant cryopreservation*. In: Fuller B, Lane N, Benson EE (eds) *Life in the Frozen State*. CRC Press, London, New York 329-345,(2004)
- [32] Benson, E. E., *Cryopreservation of phytodiversity: A critical appraisal of theory practice*. Critical Rev. Plant Sci. 27, 141-219, (2008)
- [33] Sakai, A., *Survival of the Twig of Woody Plants at -196 Degrees-C*. Nature 185,393-394, (1960)
- [34] Sakai, A., *Survival of Plant Tissue at Super-Low Temperatures .4. Cell Survival with Rapid Cooling and Rewarming*. Plant Physiol. 41, 1050-1054, (1966)
- [35] Burke, M. J., Gusta, L. V., Quamme, H. A., Weiser, C. J., Li, P. H., *Freezing and Injury in Plants*. Ann. Rev. Plant Physiol. Plant Mol. Biol. 27, 507-528, (1976)
- [36] Reed, B. B., Uchendu, E., *Controlled Rate Cooling . Plant Cryopreservation: A Practical Guide* e Editor B M. Reed, Springer 77 -92 ,(2008)
- [37] Zamecnik, J., Skladal, V., Kudela, V., *Ice Nucleation by Immobilized Ice Nucleation Active Bacteria*. Cryo-Lett. 12, 149-154, (1991)
- [38] Forsline, P. L., Towill, L. E., Waddell, J. W., Stushnoff, C., Lamboy, W. F., McFerson, J. R., *Recovery and longevity of cryopreserved dormant apple buds*. J. American Society for Horticultural Science 123, 365-370, (1998)
- [39] Sakai, A., Nishiyama, Y., *Cryopreservation of Winter Vegetative Buds of Hardy Fruit-Trees in Liquid-Nitrogen*. HortScience 13, 225-227, (1978)
- [40] Sugawara, Y., Sakai, A., *Survival of Suspension-Cultured Sycamore Cells Cooled to Temperature of Liquid-Nitrogen*. Plant Physiol. 54, 722-724, (1974)
- [41] Tao, D. L., Li, P. H., *Classification of Plant-Cell Cryoprotectants*. J. Theor. Biol. 123, 305-310, (1986)
- [42] Iljin W.S., *Über den kaeltetod de Pflanzen und seine Ursache*. Protoplasma 20,105-125, (1934)
- [43] Levitt L., *Responses of Plants to Environmental Stresses*. Academic Press, New York. (1980)

- [44] Morris, G. J., Mcgrath, J. J., *Intracellular Ice Nucleation and Gas Bubble Formation in Spirogyra*. *Cryo-Lett.* 2, 341-352, (1981)
- [45] Vertucci, C. W., *Effects of Cooling Rate on Seeds Exposed to Liquid-Nitrogen Temperatures*. *Plant Physiol.* 90, 1478-1485, (1989)
- [46] Sakai, A., Kobayashi S., Oiyama, I., *Cryopreservation of nucellar cells of navel orange (Citrus sinensis Osb. var. brasiliensis Tanaka) by vitrification*. *Plant Cell Rep.*, 9, 30-33, (1990)
- [47] Nishizawa, S., Sakai, A., Amano, Y., Matsuzawa, T., *Cryopreservation of Asparagus (Asparagus-Officinalis L) Embryogenic Suspension Cells and Subsequent Plant-Regeneration by Vitrification*. *Plant Sci.* 91, 67-73, (1993)
- [48] Seufferheld M.J., Fitzpatrickm J., Walsh, T., Stushnoff C., *Cryopreservation of dormant buds from cold tender taxa using a modified vitrification procedure*. *Cryobiol.* 28, 576-, (1991)
- [49] Slade, L., Levine, H., *Beyond Water Activity - Recent Advances Based on An Alternative Approach to the Assessment of Food Quality and Safety*. *Critical Rev. Food Sci.Nutrit.* 30, 115-360, (1991)
- [50] Langis, R., Steponkus, P. L., *Cryopreservation of Rye Protoplasts by Vitrification*. *Plant Physiol.* 92, 666-671, (1990)
- [51] Yamada, T., Sakai, A., Matsumura, T., Higuchi, S., *Cryopreservation of Apical Meristems of White Clover (Trifolium-Repens L)*. *Plant Sci.* 73, 111-116, (1991)
- [52] Fabre, J., Dereuddre, J., *Encapsulation Dehydration - A New Approach to Cryopreservation of Solanum Shoot-Tips*. *Cryo-Lett.* 11, 413-426, (1990)
- [53] Sakai, A., Hirai D., Niino T., *Development of PVS-Based Vitrification and Encapsulation-Vitrification Protocols. : Plant Cryopreservation: A Practical Guide* (Ed. B M. Reed), Springer 33-59, (2008)
- [54] Griffith, M., Lumb, C., Wiseman, S. B., Wisniewski, M., Johnson, R. W., Marangoni, A. G., *Antifreeze proteins modify the freezing process in planta*. *Plant Physiol.* 138, 330-340, (2005)
- [55] Devireddy, R. V., Raha, D., Bischof, J. C., *Measurement of water transport during freezing in cell suspensions using a differential scanning calorimeter*. *Cryobiol.* 36, 124-155, (1998)
- [56] Zanutto E.D., Countinho F.A.B., *How many non-crystalline solids can be made from all the elements of the periodic table*. *J. Non-cryst. Sol.* 347, 285-288, (2004)
- [57] Pate, J. S., Sharkey, P. J., Lewis, O. A. M., *Xylem to Phloem Transfer of Solutes in Fruiting Shoots of Legumes, Studied by A Phloem Bleeding Technique*. *Planta* 122, 11-26, (1975)
- [58] Debenedetti P.G., *Metastable Liquids. Concepts and Principles*. Cambridge University Press, (1996)
- [59] Zarzycki J., *Glasses and the Vitreous State*. Cambridge University Press (1991)
- [60] Chang L., Milton N., Rigsbee D, Mishra D.S., Tang X., Thomas L.C, Pikala M.J., *Using modulated DSC to investigate the origin of multiple thermal transitions in frozen 10% sucrose solutions* . *Thermochim. Acta* 444, 141-147, (2006)
- [61] Choi Y., Okos M.R., *Effects of temperature and composition on the thermal properties of foods*. In: M. Maguer and P. Jelen, Editors, *Engineering and Process Applications*, Elsevier Applied Science, London 93-101,(1986)

- [62] Martinez, D., rroyo-Garcia, R., Revilla, M. A., *Cryopreservation of in vitro grown shoot-tips of Olea europaea L-var. Arbequina*. Cryo-Lett. 20, 29-36, (1999)
- [63] Taylor, M. J., *Physico-chemical principles in low temperature biology*. In Grout BWW, Morris GJ (eds). *The effects of low temperature on biological systems*. Edward Arnold, Publisher 3-70, (1987)
- [64] Salekigerhardt, A., Zografi, G., *Nonisothermal and Isothermal Crystallization of Sucrose from the Amorphous State*. Pharmaceutical Res. 11, 1166-1173, (1994)
- [65] Hatley, R. H. M., Mant, A., *Determination of the Unfrozen Water-Content of Maximally Freeze-Concentrated Carbohydrate Solutions*. Int. J. Biol. Macromol. 15, 227-232, (1993)
- [66] Hatley, R. H. M., Vandenberg, C., Franks, F., *The Unfrozen Water-Content of Maximally Freeze Concentrated Carbohydrate Solutions - Validity of the Methods Used for Its Determination*. Cryo-Lett. 12, 113-124, (1991)
- [67] Shamblin, S. L., Tang, X. L., Chang, L. Q., Hancock, B. C., Pikal, M. J., *Characterization of the time scales of molecular motion in pharmaceutically important glasses*. J. Phys. Chem. B 103, 4113-4121, (1999)
- [68] Khalloufi, S., El-Maslouhi, Y., Ratti, C., *Mathematical model for prediction of glass transition temperature of fruit powders*. J.Food Sci. 65, 842-848, (2000)
- [69] Sikora, A., Dupanov, V. O., Kratochvil, J., Zamecnik, J., *Transitions in aqueous solutions of sucrose at subzero temperatures*. J. Macromol. Sci. Part B-Physics 46, 71-85, (2007)
- [70] Cabral, A. A., Fredericci, C., Zanotto, E. D., *A test of the Hruby parameter to estimate glass-forming ability*. J. Non-Cryst. Solids 219, 182-186, (1997)
- [71] Sun W.Q., *Stability of frozen and dehydrated cells and membranes in the amorphous carbohydrate matrix: The Williams –Lander –Ferry kinetics*. Cryo-Lett. 19, 105-114, (2008)
- [72] Williams M.L., Landel R.F., Ferry J.D., *The temperature dependence of relaxation mechanisms in amorphous polymers and other glass-forming liquids*. J. Am. Chem. Soc. , 77, 3701-3707, (1955)
- [73] Sun, W. Q., *Glassy state and seed storage stability: The WLF kinetics of seed viability loss at $T > T_g$ and the plasticization effect of water on storage stability*. Ann. Bot. 79, 291-297, (1997)
- [74] Angell, C. A., Bressel, R. D., Green, J. L., Kanno, H., Oguni, M., Sare, E. J., *Liquid Fragility and the Glass-Transition in Water and Aqueous-Solutions*. J. Food Eng.g 22, 115-142, (1994)
- [75] Bergman, R., Swenson, J., Borjesson, L., Jacobsson, P., *Dielectric study of supercooled 2D water in a vermiculite clay*. J.Chem.Phys. 113, 357-363, (2000)
- [76] Angell, C. A., Poole, P. H., Shao, J., *Glass-Forming Liquids, Anomalous Liquids, and Polyamorphism in Liquids and Biopolymers*. Nuovo Cimento Della Societa Italiana di Fisica D-Condensed Matter Atomic Molecular and Chemical Physics Fluids Plasmas Biophysics 16, 993-1025, (1994)
- [77] Angell C.A. *Liquid Fragility and the Glass Transition in Water and Aqueous Solutions* Chem. Rev. 102, 2627-2650, (2002)



Chapter 9

Natural inorganic glasses

9. PROPERTIES OF SOME NATURAL GLASSES: AUSTRALIAN OPALS AND CZECH TEKTITE MOLDAVITES

Paul Thomas, Klaus Heide, Jaroslav Šesták, Ekkehard Füglein, Peter Šimon

9.1. Origin of natural inorganic non-crystalline solids

Vitreous and amorphous silicates are commonly found on the Earth and lunar surfaces in a variety of geological environments. As the vitreous (or amorphous) state is a state which contains no structural order, classification of non-crystalline solids is most easily and commonly made by relative comparison of the structural framework at the atomic scale and, as shown by *Trömel* [1] in terms of short and long range order which results in four generalised states schematically shown in Fig. 9.1.

The top left corner has the lowest degree of order in the solid state and is defined as the amorphous state where there is no long or short range order and represents a dynamic condensed liquid-like phase where relatively long scale segmental motion exists. Ductile solids and gel like solids may be placed in this category. The bottom right of the diagram represents the crystalline state which, of course, contains a high degree of structural order both in the short and long range. In between these extremes are degrees of structural order which form at the short range and long range and are the topic of discussion of this chapter.

The glassy state is, in a sense, a specific subset of the non-crystalline state and contains no long range order, but its short range order is increased by the freezing of gross molecular or segmental motion. The freezing of molecular motion results in a characteristic brittleness of the glassy state. A subset of the glassy state is the vitreous state which encompasses materials that are cooled rapidly from the melt at a rate that inhibits crystallisation. Tektites, such as moldavite, are examples of such materials produced naturally

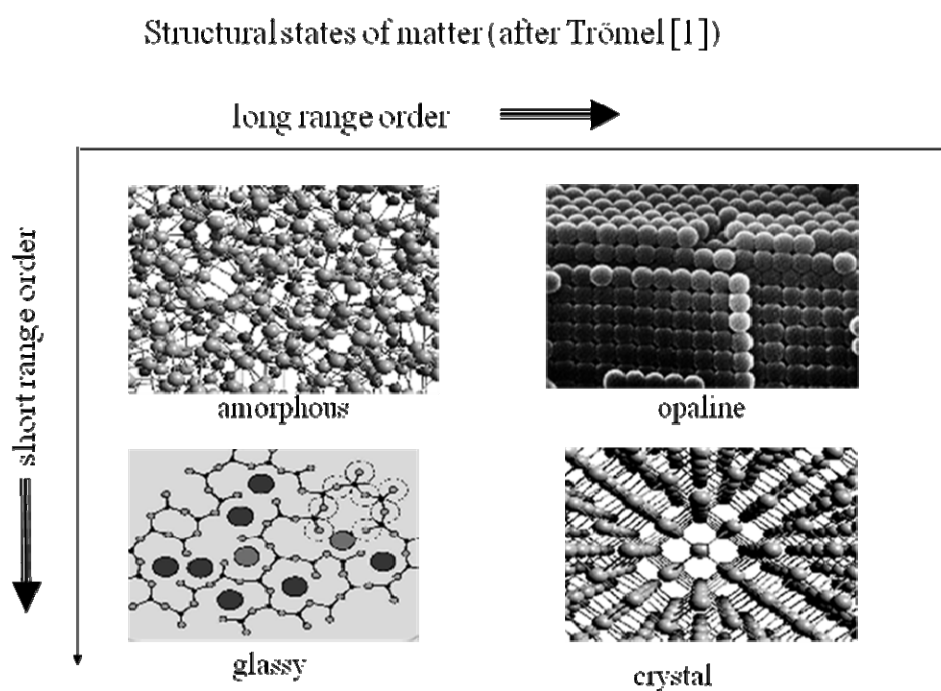


Fig. 9.1. Structural classification of non-crystalline and crystalline solids in terms of long and short range order (taken from Ref. [2]).

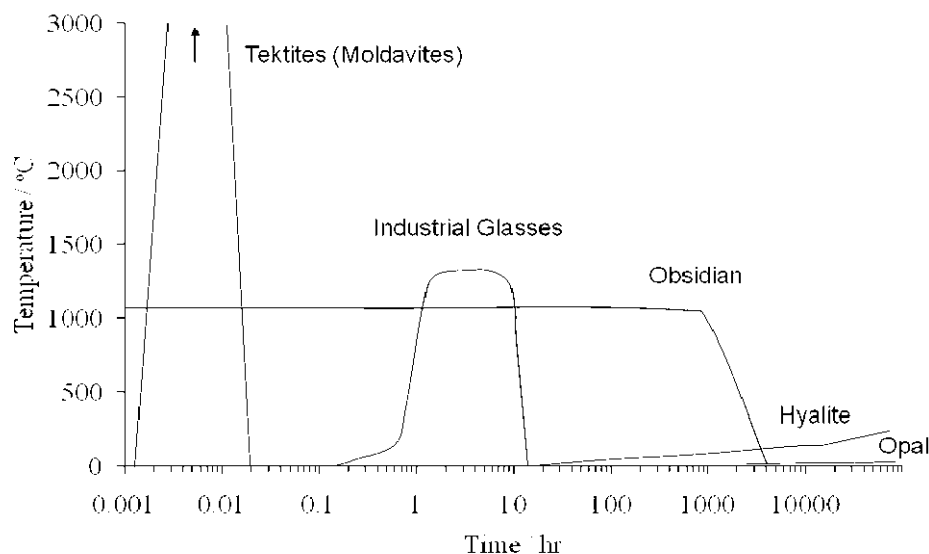


Fig. 9.2. Schematic *T-t*-plot of glass-forming processes in nature and industry (taken from Ref [2]).

through fusion of rocks and rapid quenching of melts during the high energy impact of meteorites with the Earth's surface. Magmatic and metamorphic processes are also important sources of the vitreous state.

The high temperature processes responsible for the formation of the vitreous state are not the only processes which result in amorphous, glassy solids. Low temperature diagenetic and biotic processes also result in amorphous, glassy solids; hyalite and 'potch' opal (opal that is not opaline) are examples. In rare cases, the diagenetic process results in the opaline state. The opaline state is a state containing a low degree of short range order while attaining a high degree of order at long range. The opaline state is so called because of the ability of the ordered long range microstructure to diffract visible light giving the observer the impression of dancing colours or play-of-colour (POC) resulting in opalescence. In principle the second order structure is not influenced by the primary structure at short range and, hence, the short range order at the atomic level may range from the amorphous gel like structures of sedimentary opal to the paracrystalline structures observed in volcanic opal.

Natural inorganic glasses, such as the vitreous glasses or the opaline glasses produced by diagenetic processes may be found widely distributed across the Earth's surface. The quantities of these naturally produced glassy solids is dependent on the formation process and ranges from micrograms up to kilo tonnes and, hence, the occurrence is from microscopic glassy inclusions to "glassy mountains" [3]. Much of the natural glasses are vitreous materials which have been quenched from the melt. The thermal history of glass forming processes in nature varies significantly from the conditions used in the glass industry which are optimised between processing speed and energy conservation (Fig. 2). In the extremes, tektites like moldavites are formed by extremely fast heating and melting at very high temperatures (> 3000 K) with consequent extreme cooling rates ($\geq 10^6$ K/sec). By contrast the formation of amorphous glasses from mineral diagenesis or biotic processes occurs at ambient temperatures; the formation processes are essentially isothermal and take place over long periods of time of the order of months to years or at extremely low cooling rates (K/year) (Fig. 9.2).

In contrast to industrially produced glass, the chemical composition of the majority of natural vitreous glasses is silica rich ($> 70\%$ SiO_2), peraluminous (i.e. $\text{Al}_2\text{O}_3 > \text{Na}_2\text{O} + \text{K}_2\text{O} + \text{CaO}$) and is principally characterized by a rhyolitic composition. The low diagenetic or biotic glasses tend to have even higher silica contents which can approach 99% of the anhydrous

composition and are also peraluminous. The high silica and alumina content of natural glasses results in chemical and physical properties which differ significantly from industrial glass, including glass transformation, nucleation and crystallization, the H₂O content and long time durability. For example, water contents range from 0.01% in tektites to between 3 and 13% (or greater) in opaline “glasses” which compares with approximately 0.2% in industrial glass.

The vitreous or amorphous state is inherently frozen-in thermodynamically as there is a tendency towards crystallisation or devitrification as well as the potential for weathering. Industrial glasses are susceptible to weathering and degradation at relatively short periods of time (<1000 years). Specimens of natural vitreous or amorphous materials, however, are known to have significant durability. For example, in relatively inert environments, such as on the surface of the moon, vitreous solids have existed for more than a billion years. This inherent stability may be ascribed to the high silica and low alkali content of natural glasses.

Given the extremes of formation, durability and property of natural glasses, this chapter focuses on two types of natural vitreous or amorphous solid states which correspond to two of the four structural orders discussed above; Australian opal which has the opaline structure and the tektite moldavite which is a vitreous glassy material. Both of these materials are rare non-crystalline materials and are prized primarily for their aesthetic value and for use in jewellery.

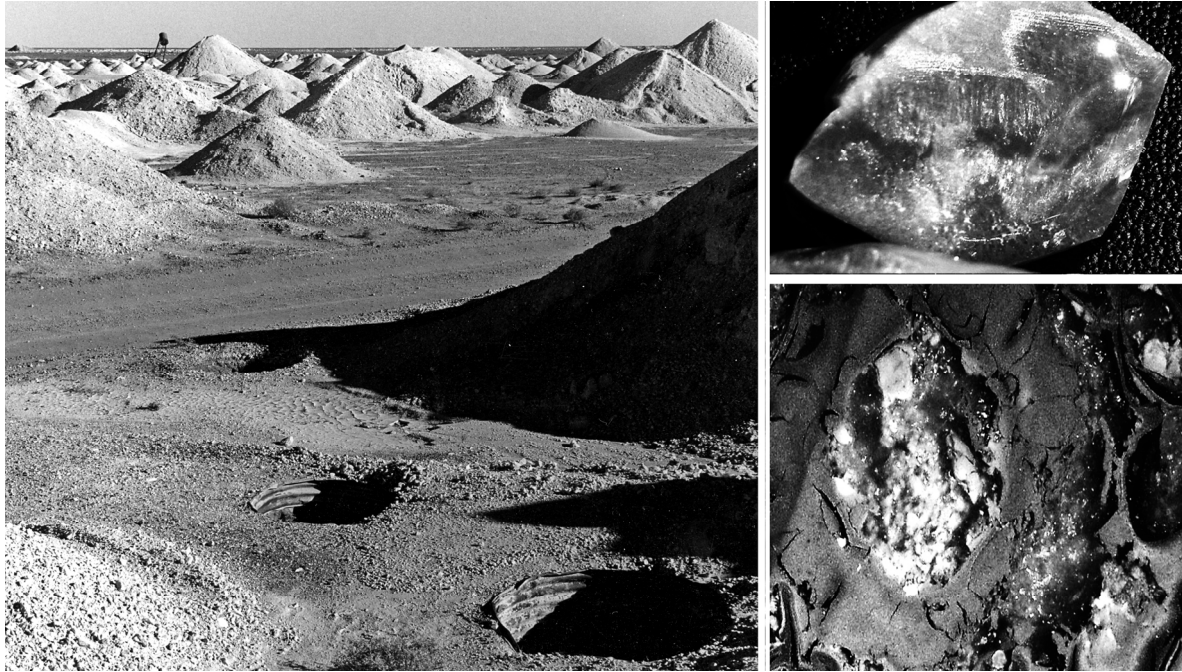
9.2. Australian Opal

The history of opal is a little confused by the current and historical meaning of the word “*opalus*” or its modern Latin derivative opal. Some texts suggest that opal as a gemstone has been mined and valued since Roman times. It is however likely that Roman opal refers to a number of glassy minerals showing brightness [4]. The first recorded systematic mining of opal (in its current meaning) began in the 17 century in north-eastern part of Hungarian Empire which is now Eastern Slovakia. Precious opal, that has the opaline structure and displays opalescence or play-of-colour, became an important and popular gem of the Royals of Europe during the 18th and 19th Centuries when the Slovakian mines were at their most productive. During the 19th and 20th Centuries commercial opal deposits were found in Australia, which has since dominated world opal production, Mexico, Peru, Brazil, Honduras and Indonesia amongst other localities.

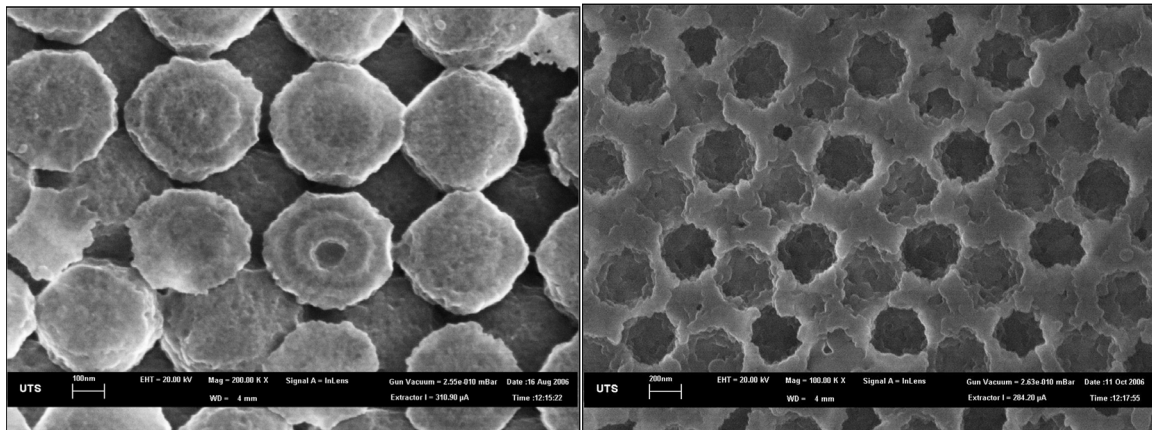
9.2.1. Basic geology of Australian opal

In Australia, the commercial production of precious opal occurs mainly in the sedimentary environments and accounts for as much as 90% of total world precious opal production [5]. The distinction of the sedimentary environment is important as the sedimentary nature is a predominant characteristic of the commercial Australian opal fields. Most of the production from outside Australia is derived from volcanic environments and, hence, volcanic host rocks such as andesite and rhyolitic tuff [6-8].

The Australian sedimentary geological environment is associated with the Great Australian (Artesian) Basin (GAB); the opal forms within the weathered sedimentary profiles that make up the GAB. In Coober Pedy, South Australia, for example, the opal-bearing stratum consists mostly of clay stones that form the Stuart Range, an east facing escarpment along the western margin of the GAB. Opal is found associated with the chemically weathered rocks that comprise the Bulldog Shale which is part of the Marree formation and is of early Cretaceous age. The Bulldog Shale is subdivided into two stratigraphic units; an intensely weathered and bleached claystone (called sandstone by the miners) and an unweathered to partly weathered claystone. Precious opal is most often found at the interface between these two stratigraphic units. Whilst this is a simplified description of geology of opal deposits, a correlation between these layered weathered profiles and the profiles in the



(a)



(b)

(c)

Fig. 9.3. (a) Image of the mullock heaps (mine tailings) around the 3 foot holes in Coober Pedy (left), and examples of rough cut opal specimens from Andamooka, South Australia (top right) and Koroit, Queensland (bottom right). SEM micrographs of hydrofluoric acid vapour etched fracture surfaces of (b) a Coober Pedy white play-of-colour (POC) opal and (c) a Tintenbar crystal opal (taken from Ref [14]).

other South Australian fields as well as in the Lightning Ridge (NSW) and White Cliffs (NSW) opal fields is evident [9].

Similar features are found in the main opal producing volcanic environment in Australia in the Tintenbar district of north eastern NSW. The occurrence of the Tintenbar ‘volcanic’ opal represents, commercially, the largest producing district of volcanic environment precious opal in Australia, although its production is small when compared to the sedimentary environments. In Tintenbar, the opal is associated with the decomposed basalt of the Lismore Basalt and part of the Lamington Volcanics of Miocene age. In this area, the Lismore volcanics consist of three distinct volcanic flows. The precious opal occurs

mainly near the junction of the first and second basalt flows as loose nodules in the soil and as amygdaloids in the decomposed vesicular basalt [10-11].

9.2.2. *Origins of the silica of precious Opal*

Precious or noble opal is prized for its play-of-colour, the origins of which are based on the diffraction of visible light off ordered arrays of monodispersed silica spheres [12-13]. Precious opal is an unusual material as it is composed of amorphous hydrous silica with the general formula $\text{SiO}_2 \cdot n\text{H}_2\text{O}$, but is precipitated as monodispersed colloidal particles from 150 to 400 nm in diameter. The monodispersed colloid is then concentrated by sedimentation, evaporation or by filtration under pressure to form the ordered arrays of the monodispersed silica spheres that are responsible for the diffraction of light observed (Fig. 9.3b).

The monodispersed silica colloid is formed through the dissolution and precipitation of silica. A likely source of the silica is from the weathering of silicates such as feldspars [13, 15]. In the weathering model, the source of the silica is the sandstones associated with the GAB where the chemical weathering of relatively soluble silicates such as the feldspars contained in these sediments results in the formation of an alkaline silica solution. An example of such a mineral is potassium feldspar which weathers through the idealised stoichiometry:



by the permeation of ground water through the sediments resulting in kaolinite, dissolved silica and an increase in pH through the release of potassium hydroxide. Reported trace element distributions in opal from a wide variety of sources are consistent with such a weathering model [16-18]. Once the silica is in solution, the enrichment of the solution by evaporation or filtration can occur. Increasing the concentration of the silica solution coupled with a lowering of the pH through alkali ion exchange with the surrounding clays allows the nucleation of primary silica spheres and, subsequent, sphere growth as more silica is supplied to the system. The supply of silica in the solution also appears to be a cyclic process as generations of growth rings are observed in the silica spheres (Fig. 9.3(b)). Once the monodispersed silica colloid has reached a suitable size, concentration of the silica colloid is then required and in certain cases, ‘crystallisation’ of the monodispersed colloid occurs to form the ordered arrays which results in the prized play-of-colour. The interstices are subsequently in-filled with a silica cement completing the formation of the opal producing a hard material which, despite the gel-like structure, has a Berkovich hardness of 5.7 to 6.2 GPa which is similar to that of soda glass (6.4 GPa), but, as might be expected for a gel like material, is significantly less than that of fused silica (10.8 GPa) [19].

Although the weathering model is important in aiding the understanding of the formation of opal, a number of other models have been proposed to account for specific observations in specimens acquired by the authors of these models. Examples of such models are the “microbial” model where microbes have been observed in Lightning Ridge matrix specimens suggesting that microbial action is responsible for the source of the silica [20], the syntectonic fluid model where high pressure, warm hydraulic silica rich fluids are the silica source [21] and the mound spring model where the silica rich alkaline waters derived from the artesian basin well up through the mound springs supplying the silica rich solutions required for opal formation [22]. Although these models source the silica from different origins, the formation of the monodispersed colloid must occur by homogenous precipitation followed by a concentration mechanism such as evaporation, filtration or sedimentation.

A sedimentation mechanism for the formation of opal does have some support [18, 23]. Elemental distributions in banded opal have suggested that although the bands must be

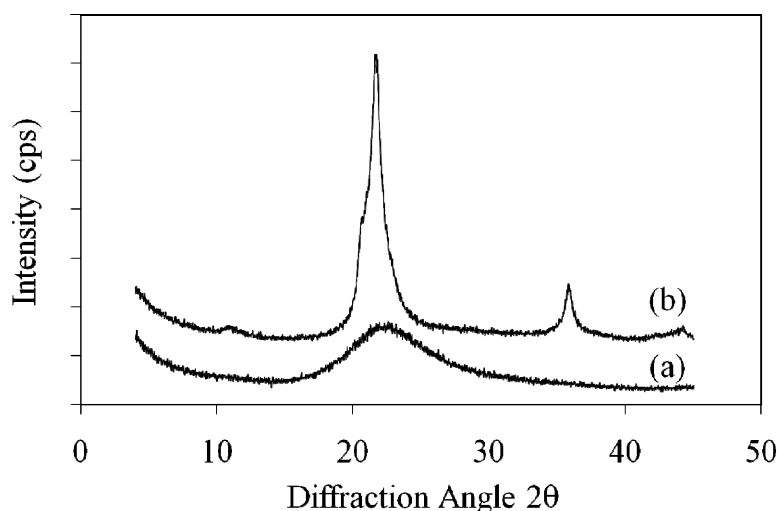


Fig. 9.4. X-ray diffraction patterns for (a) a Coober Pedy white play-of-colour (POC) opal and (b) a Tintenbar crystal opal. The Tintenbar opal show peaks characteristic of opal-CT while the amorphous ‘hump’ of the Coober Pedy opal is characteristic of opal-AG [28].

formed from the same solution (e.g. constant aluminium concentrations across bands), the variation in ion concentration between bands of highly charged metal ions suggests that the bands form by flocculation of the silica colloid. Leisegang type phase separation (repeating colour rings) on precipitation of the silica may also explain the concentration variations of trace elements between bands.

The ‘sol-gel’ nature of the formation of opal is responsible for the hydrous gel-like structure of the silica and as a consequence opal contains a significant proportion of water much of which is reported to be molecular [24-25]. Four types of water have been postulated; molecular water surface adsorbed (e.g. pore), bulk cage molecular water, surface silanol water and bulk silanol water [15]. Quantification of the amount of each species has proven to be difficult; however, Langer and Flörke [25] from their infrared spectroscopic studies suggested that approximately 90% of the water contained in sedimentary opal was present as molecular water which confirmed Segnet et al’s [24] postulation based on the calculation of surface area of the spheres that comprised play-of-colour opal. Further confirmation has been supplied by ^{29}Si NMR measurements where approximately 10% and 26% of the water was estimated to be in the form of silanol groups in Coober Pedy white POC opal and Tintenbar crystal opal, respectively [26-27]. Thermal analysis has also demonstrated the presence of a significant proportion of molecular water in both volcanic and sedimentary opal [28].

9.2.3. Morphology of Opal

The environment in which opal is formed is important as can be discerned from the differences in physical properties of opal derived from the volcanic and sedimentary environments and, in particular, the morphology of the opal [7, 14, 28]. In general, hydrous opaline silica has been found to occur with a range of morphologies which, based on x-ray diffraction (XRD) measurements [29], were originally divided into three categories; crystalline opal predominantly composed of cristobalite, opal-C, partially crystalline opal containing XRD characteristics of cristobalite and tridymite, opal-CT, and amorphous opal, opal-A. Subsequent analysis by Langer and Flörke [25] resulted in a sub-division of opal-A into two further categories, amorphous network silica, opal-AN (e.g. hyalite), and an amorphous gel silica, opal-AG (e.g. precious opal displaying play-of-colour), based on their relative proportions of water and appearance. These forms of silica are related by their relative

Table 1.*Physical properties of sedimentary opal-AG and volcanic opal-CT.*

	Sedimentary Opal	Volcanic Opal	Refs.
X-ray Diffraction (XRD)	Opal-AG	Opal-CT	[25, 29]
Crystallinity	Amorphous	Partially crystalline	[25, 29]
Density	~ 2.15	~ 2.00	[36]
NMR	Less Q ² , Q ³	More Q ² , Q ³	[26-27]
Water content	4% – 9%	9%-18%	[25, 35]
Water Types - Silanol	More silanol - OH	Less Silanol - OH	[25-27]
Water Types - Molecular	Less Molecular – H ₂ O	More Molecular – H ₂ O	[25-27]
Refractive Index	1.42 -1.45	1.40 – 1.42	[35-36]
Photoluminescence	Strong emission @ 2.65eV, excitation @ 5.0eV	Negligible	[36]

solubility in water and their thermodynamic stability resulting in an Ostwald like succession for formation:



which occurs under low temperature solution diagenesis [15, 30-33]. Australian sedimentary opal, opal-AG, may be considered as the first generation of silica formed by these low temperature aqueous processes as it is the first of the ‘pure’ silica phases that are produced from the weathering of basic aluminosilicates. Both sedimentary and volcanic opals typically contain approximately 1% trace element impurities based on the mass of silica present [16,18].

Opal derived from volcanic environments is generally found to have the opal-CT morphology. This significant difference in morphology demonstrates the significance of the environment on the formation of opal as can be seen from the typical XRD patterns shown in Fig. 9.4 [14, 28]. Although volcanic opal may be categorised as opal-CT based on the XRD data, the designation of volcanic opal as a second generation silica polymorph is contentious. As volcanic opal displays play of colour, it contains a monodispersed ordered array of silica spheres (Fig. 9.3c). This fact suggests that a monodispersed colloid is the precursor of the opal which suggests homogeneous precipitation and, hence, a first generation silica [14, 28]. Higher generation opal and silica polymorphs are formed as the equilibrium concentration of silica reduces; the solubility of each phase decreases according to the order represented by Eq. (9.2). The first generation of silica in Eq. (9.2) should, therefore, be extended to include precious play-of-colour volcanic opal-CT in addition to opal-AG as being formed by homogeneous precipitation with later generations formed through a heterogeneous nucleation and growth mechanism.

9.2.4. Physical properties of sedimentary and volcanic Opal

A number of observations and features distinguishing opals from the sedimentary and volcanic environments have been reported and are listed in Table 9.1. The water content of volcanic opals tends to be in the range 10 to 20% by mass while for Australian sedimentary opal the range is lower at circa 6 to 10% [12, 24-25, 34]. In keeping with the higher water content of volcanic opals, the refractive index is also lower for the volcanic opals [35]. Another interesting difference is the relative density [36]. Although the volcanic opals have a

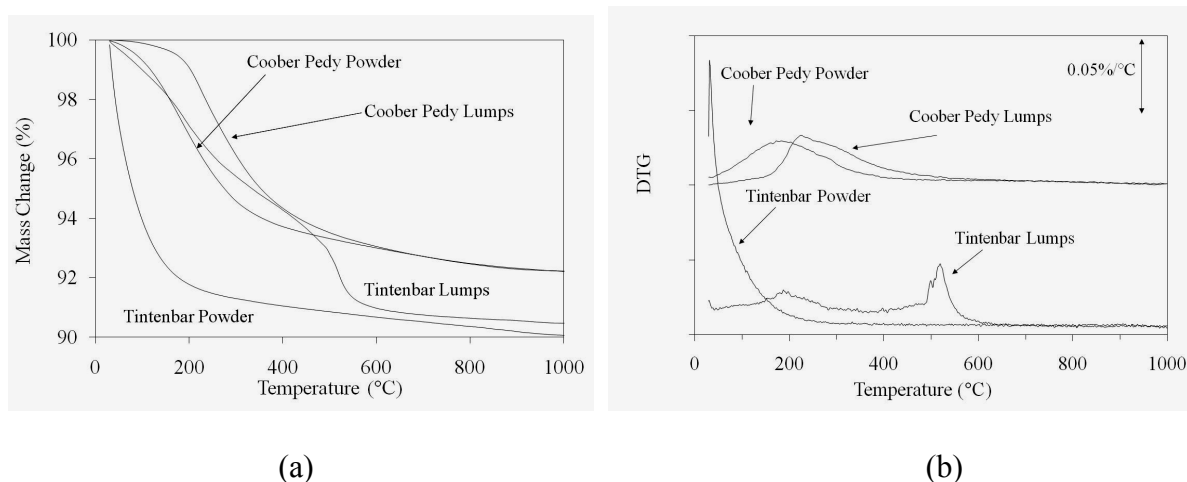


Fig. 9.5. Thermogravimetric analysis data for Coober Pedy (sedimentary origin) and Tintenbar (volcanic origin) opals; (a) mass loss data, (b) differential mass loss (DTG) data, heated to 1000°C at 1K/min in an air atmosphere (taken from Ref [28]).

higher degree of order (i.e. opal-CT), the density of volcanic opal is usually around 2.00 g/cm³ while for the amorphous sedimentary opals the density is higher at 2.15 g/cm³. It is also interesting to note that sedimentary opals tend to be fluorescent while volcanic opals are not [36]. A further significant difference is in the manner in which the opals etch. Hydrofluoric acid (HF) vapour etched fracture surfaces of a Coober Pedy and a Tintenbar opal are shown in Fig. 9.3. Both opals show the distinct ordered array with the significant difference that it is the silica cement that is etched in the sedimentary opal while it is the spheres that are etched in the volcanic opal, a feature that has also been reported for Ethiopian and Mexican volcanic opal [37].

Thermogravimetric analysis has also shown significant differences in the character of the structure of sedimentary and volcanic opals. Coober Pedy white POC opal and Tintenbar crystal opal have been investigated using thermogravimetric analysis (TG). Mass loss data for specimens of each opal are shown in Fig. 9.5a for specimens that have been denoted as lumps and powder. Significant differences are observed both between the opal types and between lump and powder forms. In order to clarify the presentation of the data, differential TG (DTG) curves are shown in Fig. 9.5b. The peak position represents the temperature at which the maximum rate of mass loss, which for the opal is the maximum rate of water loss. For the Coober Pedy specimens, the peak position (measured as the centre of mass) for the lump specimens is at 267°C while for the powder specimens the peak position is at 190°C. This significant shift in the peak position is accounted for by the change in the geometry of the specimens. As the water in opal is predominantly present as molecular water, the shift in the peak to lower temperatures for the powdered specimen may be accounted for by the reduced path length required for the diffusion of the water molecules [38-39].

Further TG and differential scanning calorimetric (DSC) studies have been carried out on the CP white play of colour opal by heating to 1640°C (Fig. 9.6). The measurements were carried out at a heating rate of 20 K/min. The endotherm in the 1st heating run at 303°C corresponds to the maximum water loss and is observed at a higher temperature than in Fig. 9.5 due to the high heating rate (20 K/min as opposed to 1 K/min in Fig. 9.5). The conversion of opal to cristobalite during the heat treatment is observable in the 2nd heating run DSC curve, where a sharp endothermic peak is observed at 217°C corresponding to the α - β cristobalite transition. It is likely that this crystallisation is occurring from 1166°C where exothermic behaviour is observed in the 1st heating run DSC curve. This relatively easy crystallisation along with the amorphous peak centred on the cristobalite peak at 22° 2 θ

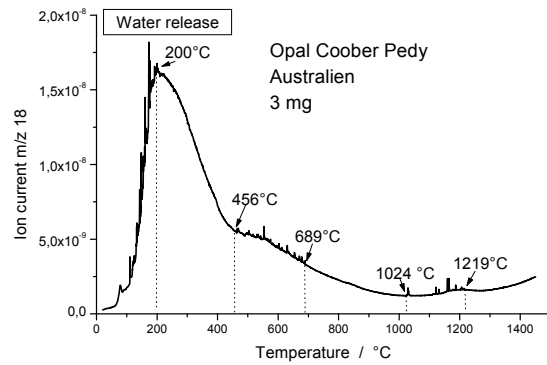
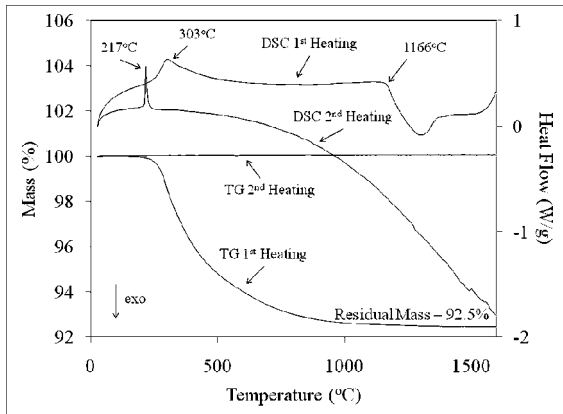


Fig. 9.6 (left) TG and DSC data of the CP white play-of-colour opal heated to 1640°C at 20K/min in an air atmosphere. The 2nd heating run shows the $\square\square$ cristobalite transition at 217°C suggesting crystallisation has occurred corresponding to the exotherm observed above 1166°C in the 1st heating run.

Fig. 9.7 (right) Water release from Coober Pedy white play-of-colour opal under high vacuum between 20°C up to 1000°C at a heating rate of 10 K/min. The water loss corresponds to 99.63 wt% of the total mass loss. The spiky release of water between 456°C and 689°C is 0.29 wt% and between 1024 and 1219 °C is 0.08 wt% and corresponds to sudden releases from enclosed pores or fluid inclusions.

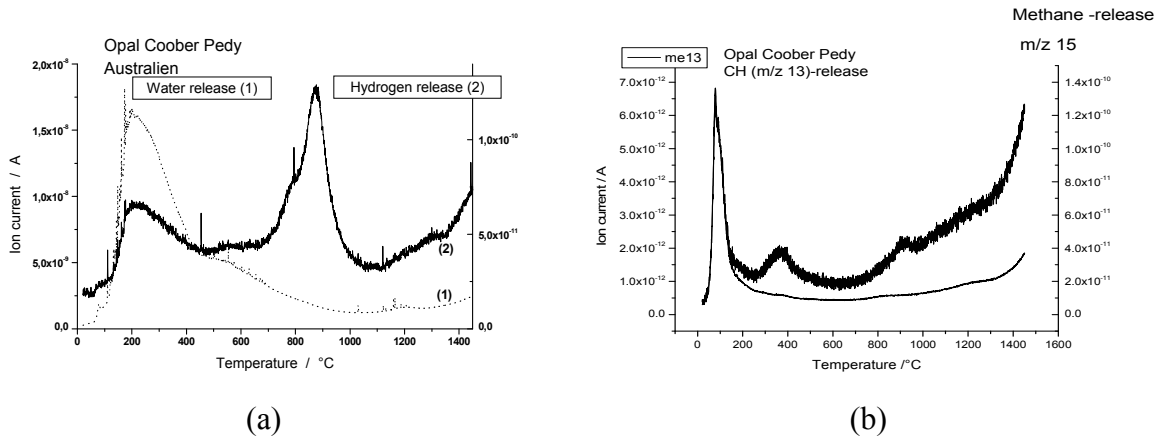


Fig. 9.8. Hydrogen release with a maximum of 877°C and methane release with a maximum at 100°C for the Coober Pedy opal studied in Fig. 9.7.

suggests that the opal-AG (amorphous sedimentary opal) is tending toward the cristobalite structure. It is also indicative of the high silica content and low alumina content of opal (circa 99% and 1%, respectively, of the anhydrous mass). This propensity, however, does give credence to the models that suggest that precious opal-CT of volcanic origin is a second generation opal and conforms to the Ostwald ripening scheme of Eq. (9.2).

Although the water loss in Fig. 9.5 and 9.6 for the Coober Pedy white play-of-colour opal is apparently through a single peak, the desorption is actually more complex as shown by the high vacuum hot extraction DEGAS data displayed in Fig. 9.7 which was carried out at a heating rate of 10 K/min to 1400°C. The main peak of desorption is observed around 200°C which concurs with the TG data. The DEGAS data, however, also shows shoulder peak between 400 and 700°C and continued mass loss up to and beyond 1000°C which also corresponds to water loss although trace concentrations of hydrogen and methane were



Fig. 9.9. Images of typical Moldavites specimens conforming to the aerodynamic shapes expected from the quenching of the molten glass at high velocities.

detected (Fig. 9.8) amounting to less than 0.4% of the total mass loss. The evidence of higher temperature water loss suggests that the structure of the sedimentary opal is not as homogeneous as previously implied. It is also notable that the spikes in the data in Fig. 9.7 correspond to sudden losses which may be ascribed to sudden release from fluid inclusions or entrapped micropores in which the pressure escalated beyond the breaking stress of the opal. The hydrogen released around 880°C is likely to be derived from micellar decomposition of silanols [41], but the methane evolved around 100°C is a little more difficult to explain as the temperatures are too low for the micellar reactions inferred for the evolution of hydrogen. It is possible that very small proportions of molecular methane are trapped in the gel structure as the opal network is formed.

The characterisation of the materials properties of sedimentary opal and the differences in the properties between sedimentary and volcanic opal are important as they aid the further understanding of the processes involved in the formation of the opal. In general terms, the volcanic opal contains more water and is of lower density than the sedimentary opal. This suggests that the volcanic opal has more open structure. The HF etching (which will remove material that is more susceptible and, hence, less dense) removes the sphere silica in the volcanic opal also indicates a less dense silica network. These differences in properties may be associated with the temperature of formation, the concentration of electrolytes or the pH of the precipitating solution. The origins of the difference in property are not currently clear. However, given the differences in the physical properties observed between volcanic and sedimentary opals, the environment must play a clear and important role in the formation of opal.

9.3. Tektites – Moldavites

‘*Moldavites*’ (in Czech terminology “*vltavín*”) are specific forms of tektite which are prized for their unique shape, clarity and distinctive greenish colour resulting in a fascinating and beautiful gemstone [42-43]. It is one of the rarest “minerals” on the Earth, and was first found in a few limited areas in the south of the Czech Republic. Moldavites were described as early as in 1787 when they were listed among precious stones (used in jewellery which continues to the modern day) and are classed, by believers, as among the most powerful gemstone tools for spiritual expansion of consciousness and self-discovery (often associated with the legendary “Stone of the Holy Grail” - fallen from the sky and being a talisman for healing the Earth [44]).

Tektites are centimetre to decimetre-sized bottle green to blackish glassy “bodies”. *Tektite* is derived from the Greek, *tektos* meaning molten and *tekein* to melt. They are found in gravels ranging in age from upper tertiary to alluvial in the Radomilice area, Chlum near

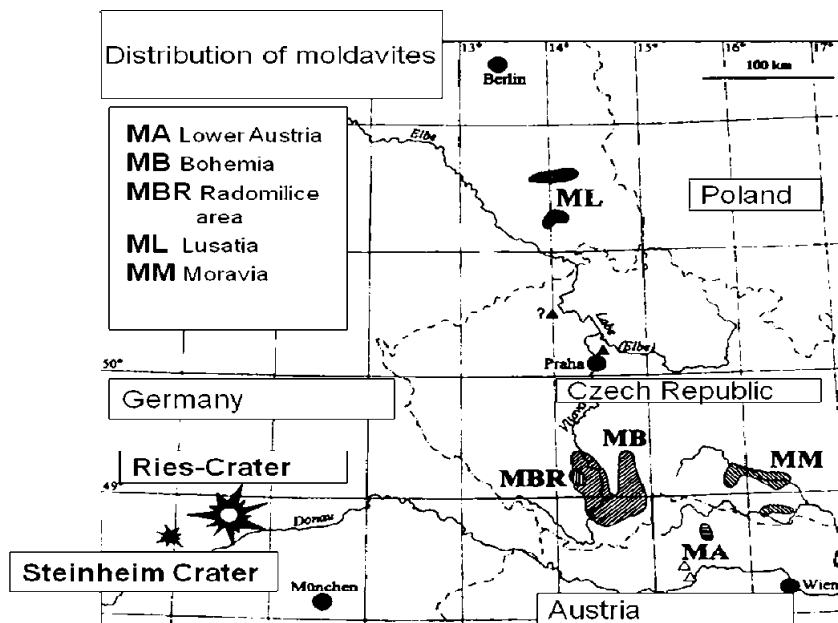


Fig. 9.10. *The Moldavite strewn field showing the asteroid impact sites and regions where moldavites of consistent chemical composition are found (taken from Ref. [49]).*

the Moldau river in Moravia, Bohemia, Czech Republic (Moldavites), in Lusatia, Saxonia Germany, in Indochina, Vietnam, Thailand, Malayan Peninsula, Java, Flores, Billiton, Borneo, Philippines, Australia and Tasmania (Australites), in Zhamnanshin (Irghizites) Kazakhstan, Ouellée on the Ivory Coast in Africa, Texas and Georgia in the United States (Bediasites). Microtektites (vitreous/crystalline spherules < 500µm) have been found in deep-sea deposits in the Gulf of Mexico, Caribbean Sea, north-western Atlantic Ocean and on Barbados. The chemical composition of microtektites is closely associated with the North American tektites. Transparent colourless to pale brown microtektites are also found associated with clinopyroxene spherules in the western Pacific and Indian Ocean in the upper Eocene marine deposits [45].

The origin of tektites was intensively studied and discussed in the last century, particularly in the latter decades, with respect to the mass extinction during the short time event known as the Cretaceous – Tertiary boundary. The discussion was dominated by two alternative origins of tektite material: the Terrestrial Impact Theory (TIT) and the Lunar Volcanic Theory (LVT) [46-47]). As Izokh [46] noted the TIT “won a complete victory over O’Keefe’s [47] Lunar Volcanic Theory” and, currently, the majority of scientific community discusses the origin of tektites and mass extinction event on the basis of TIT as, in particular, the chemical evidence supports the formation of tektites from terrestrial rocks and soils [48].

The terrestrial impact theory is based on the significant transfer of energy from impacting asteroids with the earth’s surface. As asteroids are massive, impact with the earth surface produces high energy collisions and high pressures and temperatures in the impact zone which results in the fusion and vaporisation of the material around the impact zone. The energy of these impacts was such that fused and vaporised material was catapulted out to near space. As this material returned to earth, it rapidly cooled and solidified with an absence of gaseous inclusions (although vacuous inclusions are observed). During the quenching process the solidifying phase was generally shaped aerodynamically and as the molten droplets were spinning, a range of bizarre shapes; plate, spheroid, rod, dumbbell, teardrop, star, curly, winkled and bubble, were produced (Fig. 9.9). As these particles were returned to earth, the particles were distributed by aerodynamic transport over large areas on the Earth-surface in strewn fields. The tektites found in particular strewn fields are postulated to have been derived

Table 9.2.*Typical chemical compositions of Moldavites*

Oxide	Moldavites [49] n= 69	Australites [52] n = 32	Microtektites Australasian [45]	Obsidians Utah, Yellow Stone Park, Island [53 p. 183]
SiO ₂	79.0	73.1	72.0	75.0
TiO ₂	0.3	0.7	0.8	0.11
Al ₂ O ₃	10.3	12.2	13.6	12.5
Fe ₂ O ₃	-	0.6	-	-
FeO	1.7	4.1	4.9	1.0
MgO	2.1	2.0	2.4	0.03
CaO	2.5	3.4	3.6	0.6
Na ₂ O	0.4	1.3	0.6	2.9
K ₂ O	3.4	2.2	1.9	5.1
P ₂ O ₅	0.06*	-	-	0.1
H ₂ O	< 0.02 ⁺	-	-	0.3

*[54], ⁺[55]**Table 9.3***Element ratios of tektite and impactite and for several terrestrial and lunar materials.*

Material	K/Sc	K/Rb	K/Zr	K/Cs	K/Ba	K/U	Ti/Zr	Cr/Ni	Rb/Zr	Ba/Rb	Ba/Zr
Moldavite T8201*	7.180	271	145	2.010	49	12.550	8.60	1.50	0.54	5.86	3.01
Average	6.400	240	135	2.060	45	12.200	8,60	1.40	0.56	5.64	3.10
Earth Average granite	6.000	247	240	10.500	50	14.000	6.85	0.91	0.97	4.94	4.8
Earth Average sandstone	10.700	179	49	-	358	23.800	6.81	17.5	0.27	0.50	0.14
Moon bulk	4.37	296	5,93	6.920	9.43	2.515	129		0.020	31.4	0.63
Apollo 15 Green glass	-	345	7.33	-	11.1				0.0264	31.0	0.82
Apollo 12 fines	-	327	3.88	-	6.7				0.0086		0.58

*[51]

from the same impact event due to the high degree of compositional homogeneity within an individual strewn field (Fig. 9.10. [49]).

The impact-formed or metamorphic glasses have a significant durability. The age of impact-formed glasses at the earth's surface has been determined to be between 700000 years (australites) and 34 million years (bediasites). In a more inert environment such as at the lunar surface, durability of the metamorphic glasses has been demonstrated by glass spherules which have been aged at more than 2 billion years. In general, recovered specimens of tektite have been observed to be resistant to hydration or devitrification of the bulk [50]. Only a characteristic corrosion of the surface is observed at the Bohemian tektites - the moldavites [42].

9.3.1. The chemical composition of Tektites

The content of main elements of tektites is similar to the terrestrial volcanic glasses, in particularly to the obsidians. In terms of the geochemical nomenclature the "tektites" are

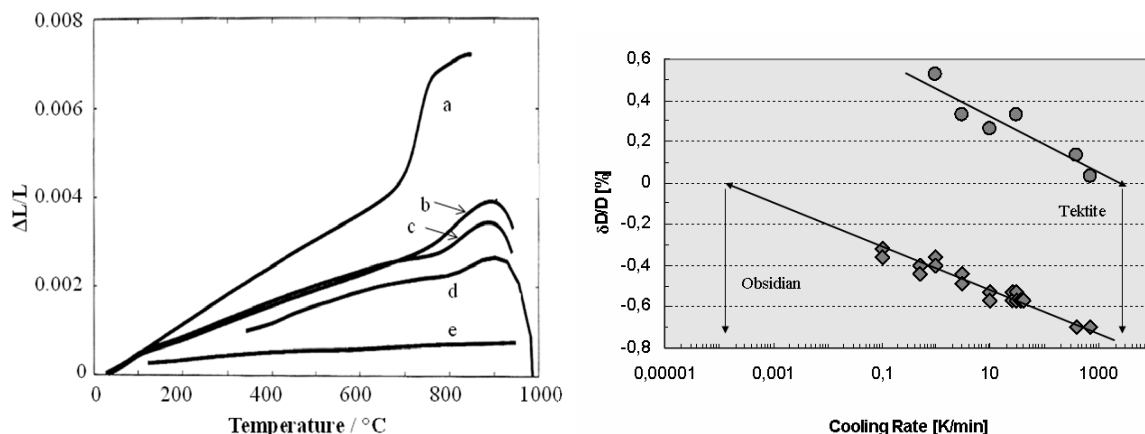


Fig. 9.11. (left) Thermal expansion of (a) obsidian, (b) Bohemian moldavite first heating, (c) Bohemian moldavite second heating, (d) Mahren moldavite and (e) fused silica (heating rate: 5 K/min) (taken from Ref [56]).

Fig. 9.12. (right) Density changes as a function of the cooling rates for known thermal histories are plotted to allow estimation of the cooling rates of the natural glasses during formation (taken from Ref [57, 58]).

peraluminous ($\text{Al}_2\text{O}_3 > \Sigma(\text{Na}_2\text{O} + \text{K}_2\text{O} + \text{CaO})$) rhyolitic glasses ($\text{SiO}_2 > 70 \text{ wt}\%$). The composition of a selection of tektites is given in Table 1. Although tektites have a similar elemental composition to volcanic rhyolitic glasses such as obsidians, a remarkable difference in the water content exists between tektites and obsidians (tektites $< 0.01 \text{ wt}\%$, obsidians $> 0.1 \text{ wt}\%$) and in the redox state (in tektites $\text{Fe}^{2+} \gg \text{Fe}^{3+}$, in obsidians $\text{Fe}^{2+} \geq \text{Fe}^{3+}$).

For the evaluation of the origin of natural materials, the trace element ratios are important tools. Correlation coefficients of geochemical well known pairs show a clear distinction between different bodies of the solar system. By these ratios (e.g. K/Sc; Ba/Zr, La/Yb), the tektites are chemical indistinguishable from terrestrial materials providing evidence that tektites originate from terrestrial materials and are likely to be of sedimentary origin (Tables 2 and 3) [50].

9.3.2. Physical properties of Tektites

The thermal properties of tektites are most easily characterised by the thermal expansion. Fig. 9.11 shows the thermal expansion of a series of natural glasses showing that the thermal expansion coefficient α for the moldavite ($3.7 \times 10^{-6} \text{K}^{-1}$) is significantly greater than fused silica ($0.5 \times 10^{-6} \text{K}^{-1}$), but less than that of obsidian ($6.3 \times 10^{-6} \text{K}^{-1}$) and soda lime glass ($7.5 \times 10^{-6} \text{K}^{-1}$) [2, 50]. The comparison with obsidian is most apt as both minerals have a similar rhyolitic composition (Table 9.2). The difference in the expansion coefficient is most likely due to the relative proportions of sodium and potassium with respect to calcium and magnesium within the silica network. The higher CaO and MgO and lower Na_2O content of moldavites results in a more tightly bound structure resulting in a lower expansion coefficient. The glass transition temperature ($T_g \sim 780^\circ\text{C}$) is also observed to follow this trend and is approximately 100K higher for moldavite than obsidian.

Although expansion coefficients of the moldavites are lower than those of obsidian and commercial glass due to the high alumina, calcium and magnesia content, the fictive temperatures of moldavites tend to be high and are higher than common industrial silica-glasses. The origins of the high fictive temperatures lies in the initial melt temperature and the rate of quenching. The high melting temperature produces a lower density melt which is rapidly cooled and, hence, the low density or high fictive temperature is preserved by the

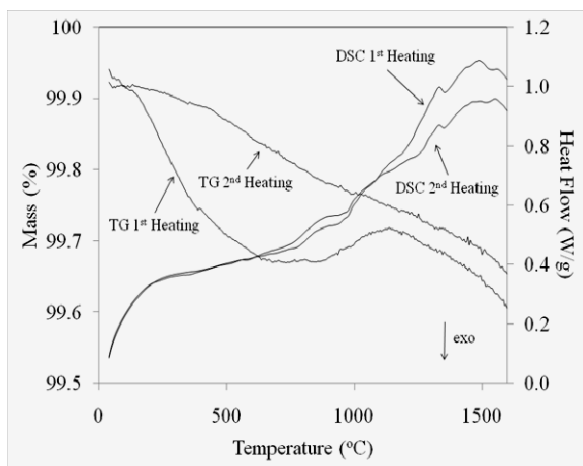


Fig. 9.13. (left) TG and DSC data for a moldavite specimen heated at 20K/min in and air atmosphere up to 1640°C showing little variation in the mass

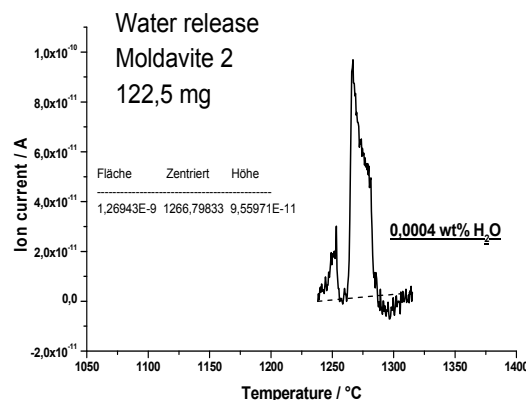


Fig. 9.14. (right) Plot of water evolution from a moldavite specimen showing traces of strong bounded OH-species released from the sample above 1200°C as water.

thermal history and relaxation of the lower density structure at $\sim 600^\circ\text{C}$ occurs as the moldavite is heated (Fig. 9.11).

These origins of the differences in fictive temperature can be confirmed by estimation of the cooling rates in the formation of the moldavites. A method for the estimation of cooling rates during the quenching of glass, known as the geospeedometric double-density technique, was developed by Klöss [58]. The method relies on the difference in density between the quenched and thermally annealed specimens of glass which produces a linear relationship that can be used to extrapolate to an unknown cooling rate based on a measured density. Fig. 9.12 plots the relative density of tektite and obsidian glasses as a function of cooling rate (i.e. model thermal history). By the regression of data in Fig. 9.12 the natural cooling rate q_0 [K/min] may be determined from the experimental cooling rate q [K/min], a geospeedometric coefficient Θ and the determined density change $\Delta D/D$, $q = q_0 e^{-\Theta \cdot (\Delta D/D)}$. In case of a magmatic glass like obsidian the natural cooling rate was determined $\sim < 50\text{K/a}$ and for the tektite glass $> 10\text{K/s}$ (Fig. 9.12).

Further evidence of the high cooling rates from high temperatures may be gleaned from the characteristic intermediate range order which, in glasses, may be defined by the magnitudes of two parameters a and f [56]. The “ a -value” is a measure of the average diameter of typical space-filling polyhedra, which in moldavites are composed of SiO_4 and AlO_4 tetrahedra. This parameter results from the bond length and the ring size; for low-quartz $a = 0.436$ nm and for high-cristobalite $a = 0.497$ nm. Moldavite has a cristobalite-like intermediate structure with $a \sim 0.485$ nm (industrial silica glass $a \sim 0.510$ nm). The “ f -value” characterizes the fluctuations of the intermediate range order. It monitors the “quality” of glass structure and can be calculated from the ratio of the “ a -value” to the “correlation length”. In a homogenous and relaxed silicate glass f is ~ 0.35 . Short fusion processes and fast cooling increase the “ f -value”. For moldavites $f \sim 0.46$ and is greater than that of a relaxed glass. The value of a tending toward that of cristobalite correlates with the quenching of the glass from high temperature. The high value of the “ f -value” correlates with a rapid cooling regime. The values of these parameters for moldavite suggest a short fusion process leading to high degree of structural and chemical disorder. Annealing of moldavites by heating up to 1000°C reduces the fluctuations and especially the mechanical stress.

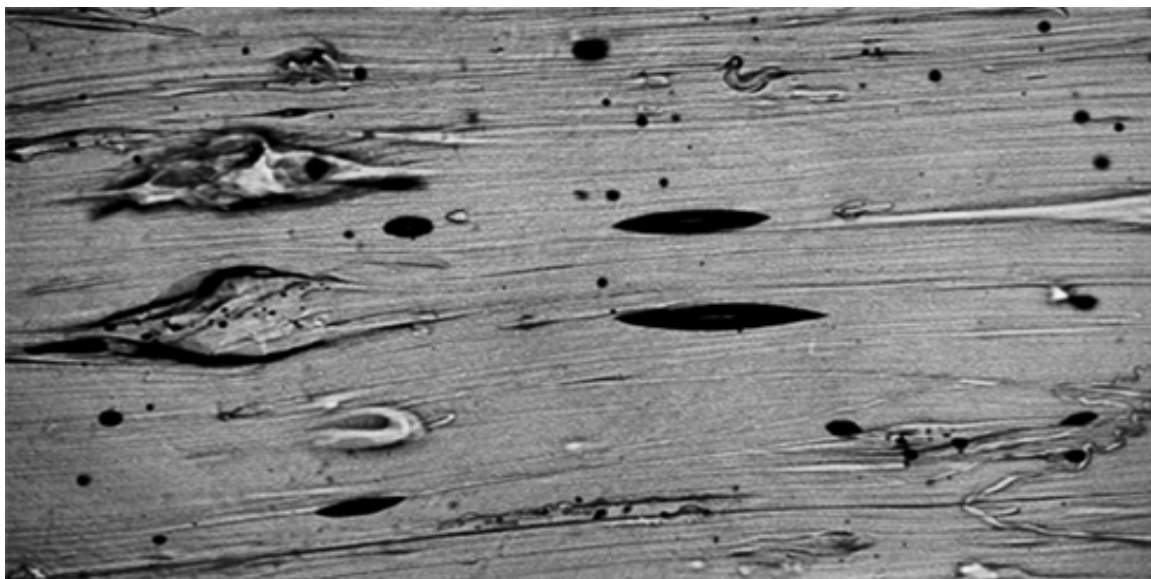


Fig. 9.15. *Micrograph of the surface of a moldavite specimen showing bubbles and strias resulting from rapid gas release.*

The origins of tektites as rapidly quenched glasses from high temperature melts is further supported by the low degree of dissolved gases found in tektites. Mass loss measurements at atmospheric pressure show little mass loss up to 1600°C for Bohemian moldavites (Fig. 9.13). Additionally, due to the high alumina content, the glass is inhibited from devitrifying and, hence, no crystallisation takes place. In the TG experiments some mass loss is observed, but it is apparent that a similar mass loss is observed from both the first and second heating runs suggesting that mass loss is associated with adsorption of atmospheric gases at low temperature. This view is supported by the degassing experiments on these Bohemian moldavites. The degassing under vacuum shows even lower gas content and water content of the order of few ppm (0.0004 wt% (Fig. 9.14). The degassing experiments were carried out using a special high-vacuum-hot-extraction method DEGAS combined with a quadrupole mass spectrometer [57]. Analysis was performed using vacuum conditions (10^{-4} to 10^{-3} Pa), a linear heating rate (10K/min) from room temperature (RT) to 1450°C. The gaseous species were analyzed in multiple ion detection mode (MID) and correlated with the total pressure change in the heating chamber [58-60].

In contrast to degassing experiments using a Knudsen cell or capillary systems, the DEGAS experiments occur under highly non-equilibrium conditions. Under high vacuum, the reversibility of decomposition reactions producing volatile products is inhibited due to the rapid removal of volatile reaction products. Gas phase reactions are also inhibited due to the rapid removal of the gaseous products. The reaction products analysed are therefore more likely to be products of the primary decomposition or degassing process. Quantitative determination of volatiles is possible by calibration with crystalline materials e.g. for H₂O from muscovite or CO₂ from calcite decomposition. A typical resolution limit for water in glasses is approximately 1 ppm H₂O. A gas content of 0.0004% fits within the resolution of the measurement [60]. The low volatile content of the moldavites is further confirmed in the micrograph shown in Fig. 9.15 where a number of bubbles and strias are observed as a consequence of rapid gas release during solidification.

9.4. Rare natural non-crystalline solids

Moldavites and opal are rare natural non crystalline solids, whose primary value is aesthetic. Both material types are important both in their as found shapes, in the case of moldavite – the aerodynamic forms and colour and in the case of opal – the infilling of void seams, cracks and in fossil replacement, and as mineral gems for jewellery. Both of these natural “minerals” have an important part to play in the understanding of geological processes as their formation is a record of change in the natural environment [61,62]. The tektites, based on their models of formation have given an insight into the impact processes that have remodelled the Earth’s fauna and flora. The opal is the first step to understanding the diagenesis of silica and its mobility. Even though both of these non-crystalline solids are formed at the extremes of forming processes, both tektites and opals as forms of silica help to enrich our lives [50, 58].

References 9

- [1] Trömel M.: Kristalle, *Glas und Antiglas*. Z.Krist **183** 15-26 (1988)
- [2] Heide K., Heide G., Kloess G.: *Glass chemistry of tektites*. Planetary and Space Science **49**, 839–844 (2001).
- [3] Heide K.: *Geheimnisse des “gläsernen Bergs”* Die DFG-forschung **3** 24 – 27 (2007)
- [4] Frazier S. and Friazer A.: *The Opal Enigma: Science, History and Lore*. In Ed by Clifford J., Clifford P., Frazier A. Frazier S., Gaber B.P., Gaber C.J., Neumeier G. and Staebler G., “*Opal the Phenomenal Gemstone*”, Lithographie, LLC, East Hampton Connecticut, USA (2007).
- [5] Olliver J.G. and Townsend I.J.: *Gemstones in Australia*. Australian Gemstone Industry Council, Australian Government Publishing Service, Canberra, Australia. pp3-18 (1993).
- [6] Banerjee A. and Wenzel T.: *Black Opal from Honduras*. Eur. J. Mineral., **11**, 401-408 (1999).
- [7] Caucia F., Ghisoli C., Adamo I. and Boiocchi M.: *Opal-C, Opal-CT and Opal-T from Acari, Peru*. Australian Gemmologist **23**(2), 266-271 (2008).
- [8] Rondeau B, Fritsch E., Guiraud M. and Renac C.: *Opals from Slovakia (‘Hungarian’ Opals): a Reassessment of the Conditions of Formation*. Eur. J. Mineral., **16**, 789-799 (2004).
- [9] Barnes L.C., Townsend I. J., Robertson R.S. and Scott D.C.: *Opal South Australia’s Gemstone*. Handbook No. 5 Revised edition. Department of Mines and Energy Geological Survey of South Australia (1992).
- [10] MacNevin A.A. and Holmes G.G.: *Notes on Precious Opal and its Occurrence in NSW*. Geological Survey Report GS 1979/268, Geological Survey of NSW, p64 (1979).
- [11] Mumme I.A., Seibright L. and Ball R.: *On the Origin of Volcanic Opal from Houghlahan’s Creek (near Teven)*. Australian Gemmologist, **12**(8), 235 (1975).
- [12] Jones J.B., Sanders J.V., and Segnit E.R.: *The structure of opal*. Nature **4962**, 991 (1964).
- [13] Darragh P. J., Gaskin A.J. and Sanders J.V.: *Opals*. Scientific American, **234**(4), 84 (1976).
- [14] Smallwood A.G., Thomas P.S. and Ray A.S.: *The Thermophysical Properties of Australian Opal*. Australian Institute of Mining and Mineralogy Publication Series No. 8, 557-560 (2008).
- [15] Iler R.K.: *The Chemistry of Silica, Solubility, Polymerisation, Colloid and Surface Properties, and Biochemistry*. John Wiley and Sons Inc., New York (1979).

- [16] McOrist, G. D., and Smallwood, A.: *Trace elements in precious and common opals using neutron activation analysis*. J. Radioanal. Nucl. Chem., **223**(1-2), 9-15 (1997).
- [17] Erel E., Aubriet F., Finqueneisel G. and Muller J.F.: *Capabilities of Laser Ablation Mass Spectrometry in the Differentiation of Natural and Artificial Opal Gemstones*. Anal. Chem., **75**(23), 6422-6429 (2003).
- [18] Brown L.D., Ray A.S. and Thomas P.S.: *Elemental Analysis of Australian Amorphous Opals by Laser-Ablation ICPMS*. Neues Jahrbuch für Mineralogie Monatshefte, **2004**(9) 411-424 (2004).
- [19] Thomas P.S., Smallwood A.S., Ray A.S., Briscoe B.J. and Parsonage D.: *Nanoindentation Hardness of Banded Australian Sedimentary Opal*. J. Phys. D, **41**(7), 074028 (doi:10.1088/0022-3727/41/7/074028), 6pp (2008).
- [20] Behr H.J., Behr K. and Watkins J.J.: *Cretaceous microbes – producer of black opal at Lightning Ridge, NSW, Australia*. Geological Abstracts No. 59. 15th Australian Geological Convention. Sydney July 2000 (2000).
- [21] Pecover S.R.: *A new Genetic model for the origin of precious opal*. Extended Abstracts No. 43. Mesozoic geology of Eastern Australia plate conference. Geological Society of Australia. pp450-454 (1996).
- [22] Devison B.: *The origin of precious opal – a new model*. Australian Gemmologist **22**(2), 50-58 (2004).
- [23] Brown L.D., Thomas P.S., Ray A.S. and Prince K.: *A SIMS Study of the Transition Metal Element Distribution Between Bands in Banded Australian Sedimentary Opal From the Lightning Ridge Locality*. N. Jb. Miner. Monatshefte, **182**(2), 193-199 (2006).
- [24] Segnit E.R., Stevens T.J. and Jones J.B.: *The Role of Water in Opal*. J. Geol. Soc. Aust., **12**(2), 211-226 (1965).
- [25] Langer K. and Flörke O.W.: *Near Infrared Absorption Spectra (4000-9000cm⁻¹) of Opals and the Role of Water in these SiO₂.nH₂O Minerals*. Fortschritte der Mineralogie, **52**(1), 17-51 (1974).
- [26] Brown L.D.: *Characterisation of Australian Opals*. PhD Thesis, University of Technology Sydney (2005).
- [27] Brown L.D., Ray A.S. and Thomas P.S.: *²⁹Si and ²⁷Al NMR Study of Amorphous and Paracrystalline Opals from Australia*. J. Non-cryst. Solids, **332**, 242-248 (2003).
- [28] Smallwood A.G., Thomas P.S. and Ray A.S.: *Thermal Characterisation of Australian Sedimentary and Volcanic Precious Opal*. J. Therm. Anal. Cal., **92**(1) 91-95 (2008).
- [29] Jones J.B., and Segnit E.R.: *The Nature of Opal. I. Nomenclature and Constituent Phases*. J. Geol. Soc. Australia, **18**(1), 57 (1971).
- [30] Williams L.A. and Crerar D.A.: *Silica diagenesis, I. Solubility controls*. J. Sedimentary Petrology, **55**(3), 301-311 (1985).
- [31] Williams L.A. and Crerar D.A.: *Silica diagenesis, II. General Mechanisms*. J. Sedimentary Petrology, **55**(3), 312-321 (1985).
- [32] Landmesser M.: *Mobility by Metastability in Sedimentary and Agate Petrology: Silica Transport and Accumulation at Low Temperatures*. Chem. Erde, **55**, 149-176 (1995).
- [33] Landmesser M.: *Mobility by Metastability: Applications*. Chem. Erde, **58**, 1-22 (1998).
- [34] Brown L.D., Ray A.S., Thomas P.S. and Guerbois J.P.: *Thermal Characteristics of Australian Sedimentary Opals*. J. Therm. Anal. Cal., **68**, 31-36 (2002).
- [35] Phillips W.R. and Griffin D.T.: *Optical Mineralogy, the Non Opaque Minerals*. W.H Freeman and Company. San Francisco, p326 (1981).

- [36] Smallwood A.G.: *Chemical and Physical Evaluation of Australian Precious Opal*. MSc Thesis, University of Technology Sydney (1999).
- [37] Fritsch E., Ostrooumov M., Rondeau B., Barreau A., Albertini D., Marie A.M., Lasnier B., Wery J.: *Mexican Gem Opals. Nano- and Micro-structure, Origin of Colour, Comparison with Other Common Opals of Gemmological Significance*. Australian Gemmologist, **21**(6), 230 (2002).
- [38] Thomas P.S., Šimon P., Smallwood A. and Ray A.S.: *Estimation of the Diffusion Coefficient of Water Evolved During the Non-isothermal Dehydration of Australian Sedimentary Opal*. J. Therm. Anal. Cal., **88**(1), 231-235 (2007).
- [39] Smallwood A.G., Thomas P.S., Ray A.S. and Šimon P.: *A Fickian Model for the Diffusion of Water in Australian Sedimentary Opal*. J. Therm. Anal. Cal., submitted (2008).
- [40] Arndt J, Rombach N.: *Derivation of the thermal history of tektites and lunar glasses from their thermal expansions characteristics*; Proc.Lunar Sci.Conf. 7th 1123- 1141 (1976).
- [41] Heide K., Woermann E. and Ulmer G.: *Volatiles in pillows of the Mid-Ocean-Ridge-Basalt (MORB) and vitreous basaltic rims*. Chemie der Erde **68**, 353–368 (2008).
- [42] Bouška V.: “*Natural Glasses*”, Academia, Praha 1993
- [43] Konta J. (edt.): *Proceedings of 2nd Int.Conf. on Natural Glasses*, Charles University, Praha (1987)
- [44] R. Simmons.,K. Warner “*Moldavites*” Heaven & Earth, Vermont, USA 1988.
- [45] Glass B.P.: *Tektites*. J. Non-Cryst. Solids **67**, 333 – 344 (1984).
- [46] Izokh E.P.: *Origin of tektites: An alternative to terrestrial impact theory*. Chemie d.Erde **56**, 458 – 474 (1996).
- [47] O’Keefe J.A.: *Tektites and their Origin*. Elsevier, Amsterdam (1976).
- [48] O’Keefe J.A.: *Natural glasses*. J. Non-Cryst. Solids **67**, 1 – 17 (1984).
- [49] Lange J.M.: *Lausitzer Moldavite und ihre Fundschichten*; Schriftenr.f.Geowiss **3** (1995) 7 – 138
- [50] Heide K., Kletti H.: *Resistance of natural glass*. Glass Sci.Technol. **76** 118 – 124 (2003)
- [51] Koeberl C., Kluger F., Kiesel W.: *Trace element correlations as clues to the origin of tektites and impactites*. Chem Erd. **45** 1 -21 (1986) 1
- [52] Schnetzler C.C., Pinson jr. W.H.: *Tektites* ed. J.A.O’Keefe (1963) Chicago Press p. 101
- [53] Hölzle-Vuynovich A.: *Petrographische und geochemische Untersuchungen an Schneeflockenobsidianen und verwandtem Material aus den USA, Island und der Osterinsel*; Heidelberger Geowiss. Abh. **56** (1992) Universität Heidelberg
- [54] Luft E.: *Zur Bildung der Moldavite beim Ries-Impakt aus tertiären Sedimenten*; Enke Verlag p.57 (1983).
- [55] Rost R.: *Vitaviny a tektity*; Czech.Acad.Sci.Publ. Academ.Press Prague, p.241 (1972).
- [56] Heide G., Müller B.: *Zur Struktur von Moldavitglas*. Schr. Staatl.Mus.Mineral.Geol. Dresden **10** 30 – 33 (1999)
- [57] Kloess G., Heide G.: *ρ - ρ_t Geospeedometrie an Tektiten*. Schr. Staatl.Mus.Mineral.Geol. Dresden **10** 52 – 54 (1999)
- [58] Kloess G.: *Dichtfluktuationen natürlicher Gläser*, Habilitation, Jena 2000
- [59] Heide K., Gerth K., Hartmann E.: *The detection of an inorganic hydrocarbon formation in silicate melts by means of a direct-coupled-evolved-gas-analysis-system (DEGAS)*. Thermochim.Acta **354** 165 – 172 (2000)
- [60] Heide K., Schmidt Ch.: *Volatiles in vitreous basaltic rims, HSDP 2, Big Island, Hawaii*. J.Non-cryst. Solids **323** 97 – 103, (2003)

[61] Engelhardt W. v., Luft E., Arndt J., Schock H., Weiskirchner W. *Origin of moldavites*. Geochim.Cosmochim.Acta **51** 1425 – 1443 (1987)

[62] P. Thomas, J. Šesták, K. Heide, E. Füglein and P. Šimon “*Thermal Properties of Australian Sedimentary Opals and Czech Moldavites*” Proc. Mediterian conf on TA, 2009



Chapter 10
Chalcogenide glasses

10. CHALCOGENIDE GLASSES AS MODEL SYSTEMS FOR STUDYING THERMAL PROPERTIES

Zdeněk Černošek, Jana Holubová, Eva Černošková

Introduction

Chalcogenide glasses have been intensively studied from the seventieth of 20th century as the important new class of promising high-tech materials for semiconducting devices and infrared optics. Chalcogenide glasses are formed by chalcogens, stoichiometric chalcogenides, e.g. germanium and/or arsenic sulfides or selenides or by non-stoichiometric alloys which composition (and physicochemical properties) can be modified in broad ranges. They have unique optical properties – low phonon energies as compared with oxide glasses, high refractive index, infrared luminescence and so on. The advantage of many chalcogenide glasses is that they can be obtained using very simple technologies.

Besides applicability in many areas outlined above chalcogenide glasses represent excellent model materials for thermoanalytical studies. Extremely stable glasses and undercooled melts can be prepared, as well as very temperature-sensitive unstable ones. Glass transition temperature can be changed easily from subambient temperatures (glassy sulphur, for example) up to temperatures over 500 °C (germanium disulphide or diselenide). This makes chalcogenide glasses ideal candidates for differential scanning calorimetry (DSC) studies, because these apparatuses operate in mentioned temperature region.

All chalcogenide glasses used in following studies were prepared by direct synthesis from high purity elements (semiconductor purity - 5N elements) in evacuated silica ampoules in a rocking furnace and quenched in air or in cold water. Other glasses (organic polymers, oxide glasses) were commercial products.

10. 1. Differential Scanning Calorimetry - DSC

The development of differential scanning calorimetry (DSC) technique in last two decades was done by introduction of commercially available calorimeters with temperature modulation, MDSC, by TA Instruments. Using conventional heat-flux DSC whose heating block temperature is sinusoidally modulated and so the sample temperature is modulated in the same manner about a constant ramp. The resulting instantaneous heating rate varies sinusoidally about the underlying heating rate (average heating rate). The average heat flow is called total heat flow. This one is the only quantity that is available and hence it is the only quantity that is always measured in conventional DSC experiments. The sample temperature and the amplitude of instantaneous heating flow are measured and finally, using Fourier transformation of the experimentally obtained data, the quantity termed reversing heat flow is obtained. The nonreversing heat flow is the difference between the total heat flow and the reversing heat flow and represents heat flow due to kinetically hindered process. Process is called reversing if the system responds in a reversible way on the timescale of the experiment (or faster) and nonreversing if the system is either too slow to respond reversibly on the timescale of the experiment or if it is irreversible altogether (on any timescale). In case of MDSC it means that reversing process is in-phase with temperature modulation and nonreversing process with some phase lag is out-of-phase.

Reversing isobaric heat capacity can be determined by MDSC using the magnitude of heat flow and heating rate obtained by averaging over one modulation period. As a complex heat capacity has been defined, see [1], the nonreversing heat flow recalculation to the nonreversing

heat capacity has also been used. Detailed information about MDSC one can found in [2-5] and references therein.

More recent and from MDSC essentially different technique, StepScan DSC by Perkin-Elmer, is based on enthalpic method of isobaric heat capacity, C_p , determination adapted to the high sensitive power-compensated apparatus. This method allows equilibration of the system after each step in a series of small step increases (decreases) in temperature. The area under the resulting curve (the total enthalpy change in the step) is evaluated and divided by the temperature step to give the heat capacity at the midpoint of the temperature step. Enthalpic changes connected with possible kinetic effects are recorded in the timescale during equilibration after each one temperature step. StepScan DSC method allows obtaining not only C_p at the midpoint of the temperature step but also enthalpic changes connected with slow processes (compare to the time of temperature change) after temperature step. As a result two curves are obtained. The first of them is the temperature dependence of C_p (reversible part) and the second one is the temperature dependence of slow processes' enthalpy changes (irreversible part); these parts have been termed by Perkin-Elmer as thermodynamic and kinetic ones, respectively.

The result obtained by StepScan DSC seems to be close to this one obtained by MDSC, but two crucial differences should be stressed. Firstly, when TMDS is used, the sample temperature is continually periodically changed, aside from the extent of possible kinetic effects, whereas in the case of StepScan DSC the software-controlled variable isotherm duration allows the sample to achieve the state close to the thermal equilibrium at each temperature step. Secondly, no special mathematical operation, like Fourier transformation, is needed to obtain results by StepScan DSC.

10.2. Glass transition

10.2.1. Capability of conventional DSC, temperature modulated DSC (MDSC) and StepScan DSC for the glass transition phenomenon study

Bulk glass of As_2S_3 was used as the model glass. The power-compensated differential scanning calorimeter Pyris 1 operated with Pyris software (both Perkin-Elmer) capable of working in all three modes under study was used.

DSC mode was used with heating rates successively 1, 10, 20, 50 and 100 K/min. For experimental curves, see Fig. 1.

Dynamic DSC (DDSC) is the Perkin-Elmer version of MDSC. To avoid possible confusion the MDSC will be used as a common mark for temperature modulated DSC, despite of calorimeter manufacturer. Dynamic mode operated with saw-tooth modulation was used with

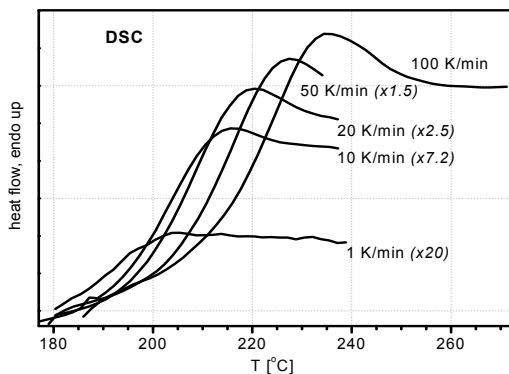


Fig. 1

Conventional DSC results. Number in brackets is magnification factor.

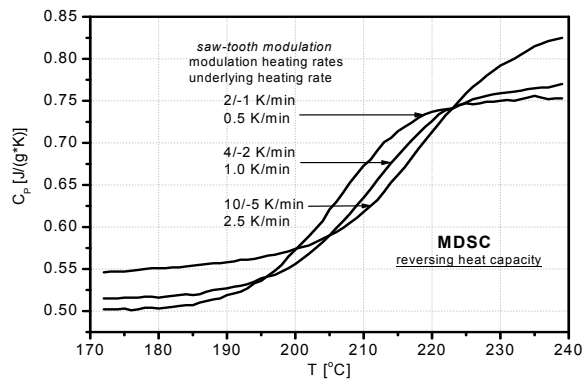


Fig. 2

Reversing C_p dependence on T obtained from MDSC measurements. For details, see text.

period 40 s, temperature amplitude 0.75 K and heating/cooling rates 2/-1, 4/-2 and 10/-5 K/min. These experimental conditions correspond to underlying heating rate 0.5, 1.0 and 2.5 K/min, respectively. For temperature dependence of reversing C_p , see Fig. 2.

StepScan DSC experiments were carried out with temperature step 1 K, heating rates in the temperature step successively 1, 10 and 100 K/min and isotherm duration either 60 sec. or with maximal allowed heat flow difference $\pm 0.1 \mu\text{W}$ per approx. 2 sec. before next step. The experimental set up corresponds to average underlying heating rate 0.50, 0.91 and 0.99 K/min, respectively. For results, see Fig. 3.

In the glass transition temperature range the influence of three available DSC methods on the determination of glass transition temperature, T_g , was studied. T_g was determined as a temperature of half-change of heat flow (DSC) or isobaric heat capacity, ΔC_p , (MDSC, StepScan DSC). Results are collected in Fig. 4.

The T_g dependence on the heating rate obtained by conventional DSC was significant as it is well-known and is discussed elsewhere [6-14].

Results obtained by MDSC show still distinguishable dependence of T_g on heating rate (more correctly on underlying heating rate) even though these rates are slow at all. The T_g values are from 10 °C up to 22 °C higher comparing with conventional DSC results at the comparable heating rates. Furthermore, it must be stressed that with increasing underlying heating rate besides the glass transition temperature also temperature dependence of isobaric heat capacity, C_p , has been shifted up but without changing of isobaric heat capacity change at glass transition, ΔC_p , see Fig. 2.

From above mentioned follows that experimental MDSC dependencies have been moved up in both axis when underlying heating rate increases. It means that MDSC requires both careful calibration and choice of experimental set up. It is well known that both T_g and C_p depend not only on frequency but also on amplitude of temperature modulation (it means on mean rate of temperature change). It seems to be clear that MDSC reversing heat flow is in fact not fully in phase with the temperature change. The permanent periodical change of sample temperature probably causes that sample is not close to thermal equilibrium, especially in the case when reversing process is attended by some slow nonreversing one. The glass transition is one of typical examples.

The values of C_p given by StepScan DSC are independent on the average heating rate and in consequence of that T_g value remains unchanged, see Figs. 3 and 4, and also [15].

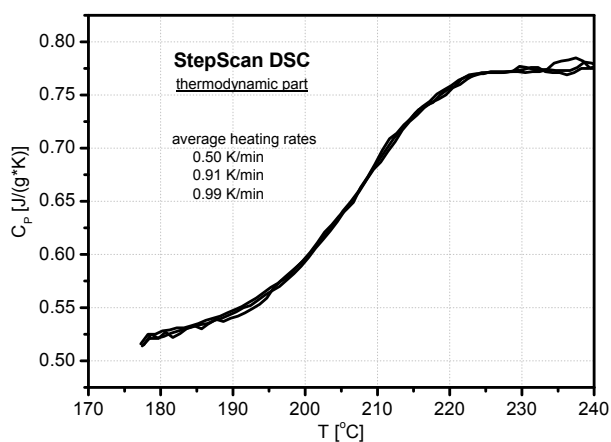


Fig. 3

StepScan DSC thermodynamic (reversing) part at different average heating rates, see text.

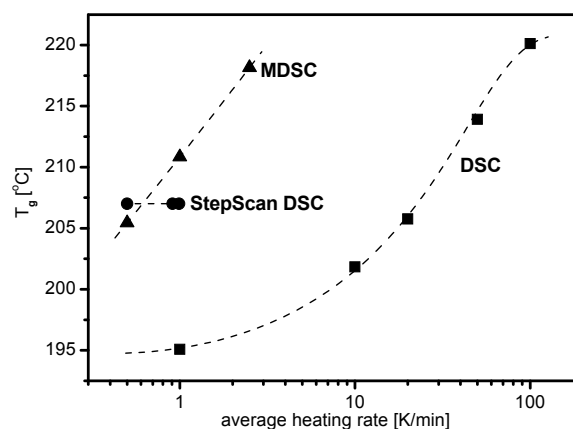


Fig. 4

Heating rate dependencies of T_g , obtained by indicated DSC methods.

Average heating rate is governed both by the temperature step heating rate and duration of following isotherm. The isotherm duration is variable, depending on the amount and average relaxation time of kinetic processes at the given temperature. It means that the average heating rate of the one step can differ more or less from the other one at every heating-isotherm step. It can be simply said that in every step the StepScan DSC method will wait for termination of all processes being slower than experimental time of the temperature step, of course within the instrument sensitivity. As follows, the heat flow of nonreversing (kinetic) process is effectively separated from reversing (thermodynamic) one and so the temperature dependence of isobaric heat capacity, and from it T_g , can be determined without influence of both thermal history of glass and experimental conditions.

10.2.2. Enthalpic relaxation and the glass transition

The glassy state is generally the non-equilibrium one and is characterized by an excess of thermodynamic properties (e.g. enthalpy, entropy, volume). The as-quenched and thus non-equilibrium glass seeks to attain a lower energy metastable equilibrium especially if this one is held at temperature not too far below the glass transition temperature. This time dependent variation in physical properties following glass formation is called structural or enthalpic relaxation if the change of enthalpy is the studied thermodynamic property [16]. While the glass transition has been described as “fast” process associated primarily with the vibrational degrees of freedom, the subsequent slow structural relaxation is connected with a change in the frozen liquid structure [17]. So the relaxation kinetics of glasses is determined not only by the thermodynamic temperature, T , but also by the instantaneous structure of the glass, which is characterized by fictive temperature, T_f , firstly introduced by Tool [18]. The fictive temperature is defined as the temperature at which the observed value of an intensive property would be the equilibrium one. During relaxation T_f approaches relaxation temperature T_r . In the metastable equilibrium $T_f = T_r$ and the departure from equilibrium is measured by $|T_f - T|$. The initial non-equilibrium state of glass is not unique but depends on the conditions of glass formation and the relaxation process is strongly influenced by the complete thermal history of glass.

Besides the great interest of structural relaxation the considerable attention has paid to the glass transition. Historically, the glass transition has been observed in undercooled liquids and, therefore, is regarded as a characteristic property of liquids. Later experiments, however, showed that this phenomenon is quite common for non-crystalline materials prepared by various methods other than traditional liquid cooling, see [19] and references cited in.

The glass transition temperature is “defined” by various inconsistent manners, for example:

i) The glass transition temperature denotes a temperature for which relaxation time in the supercooled liquid become longer than typical observation time. The ratio between these two times, the Deborah number, is approximately unity for $T = T_g$. (Prophetess Deborah declared that what appeared to mortals to be stationary are not necessarily so to an eternal deity.)

ii) The glass transition temperature is the one at which the viscosity of the supercooled liquid reaches 10^{13} Poise. It is important to note that the viscosity is continuous through T_g , exhibiting any of the discontinuities observed in heat capacity [20] and thus this definition has no physical meaning.

iii) The glass transition temperature is the one at which configurational entropy vanishes during melt cooling.

Notwithstanding these “definitions” the glass transition is characterized by a gradual break in slope of extensive thermodynamic variables (enthalpy, entropy and volume). The region over which the changes of slope occur is termed glass transition region. This region is usually characterized by midpoint temperature called glass transition temperature, T_g . Continuous change of extensive thermodynamic variables through the glass transition implies that there must be a discontinuity in derivative variables at T_g , such as a heat capacity or a coefficient of thermal

expansion. Such differences are used to distinguish two classes of glass forming liquids - strong and fragile [21]. For review on supercooled liquids and the glass transition refer to [22] and references cited in.

It is well-known that T_g is not regarded as a material constant because when measured for instance by DSC it depends on many parameters as for instance heating rate, q^+ , [6-8], the cooling rate, q^- , [8,9] and the physical aging [7,10,11]. If the T_g is determined by heating the temperature obtained often differs from the one from cooling measurement. These values of T_g may vary in the range of 10 to 20 % depending on difference of cooling rates and heating rates.

The nature of the glass transition is very complex and poorly understood so far. It is clear that regarding long structural relaxation time relatively to laboratory time scale during measurement the material is out of thermodynamic equilibrium. Elimination of this influence of scanning rate on determining of T_g was the main aim of some models. Expression relating dependence of T_g on the cooling rate was derived by Kovacs [12]. More often the linear dependence of T_g on $\ln(q^+)$ proposed by Lasocka [13] has been used. Extrapolation of the experimental results to $q^\pm = 0$ K/min in order to obtain the "correct" glass transition temperature has been suggested [23]. It must be noted that logarithmic dependence lacks of physical meaning when q^\pm is less then 1 K/min or limited to infinity and thus logarithmic model only hardly can be correct.

10.2.3. Enthalpic relaxation - the model

Enthalpic relaxation (physical aging, structural relaxation) of glassy materials has been studied by a number of techniques, but in particular the differential scanning calorimetry (DSC) has been used extensively to measure the kinetics of enthalpic relaxation of glasses.

According to the Tool's concept of fictive temperature, the specific enthalpy of a glassy sample can be expressed as a function of fictive temperature, T_f , and thermodynamic temperature, T :

$$H(T, T_f) = H(T_o, T_o) + \int_{T_f}^{T_f} C_{pm}(T) dT + \int_{T_f}^T C_{pg}(T) dT, \quad (1)$$

where C_{pm} , C_{pg} are specific isobaric heat capacities of metastable melt and glass, respectively, and T_o is an arbitrary sufficiently high reference temperature at which the sample is in a metastable thermodynamic equilibrium. Narayanaswamy generalized Tool's model [24] by allowing for distribution of relaxation time and obtained the following expression for the fictive temperature that can be calculated for any thermal history:

$$T_f(t) = T(t) - \int_0^t dt' \left(\frac{dT}{dt} \right)_{t'} M_H[\xi(t) - \xi(t')]. \quad (2)$$

T is time, M_H is a Kohlrausch-William-Watts (KWW) relaxation function:

$$M_H(\xi) = \exp(-\xi^\beta), \quad (3)$$

β is the non-exponentiality parameter ($0 < \beta \leq 1$), which is inversely proportional to the width of a distribution of relaxation times of independent relaxation processes. ξ is the dimensionless reduced relaxation time:

$$\xi(t) = \int_0^t \frac{dt'}{\tau(t')}. \quad (4)$$

The contribution to the relaxation time $\tau(T, T_f)$, simply τ , from both the temperature and fictive temperature is controlled by a non-linearity parameter x ($0 \leq x \leq 1$) according to the Tool-Narayanaswamy-Moynihan (TNM) equation [9]:

$$\tau = \tau_0 \exp \left[\frac{x\Delta h^*}{RT} + \frac{(1-x)\Delta h^*}{RT_f} \right], \quad (5)$$

where τ_0 is a constant, Δh^* is an apparent activation energy, R is the universal gas constant.

The time course of the normalized molar heat capacity $C_{p,\text{eff}}(t)$, e.g. the DSC measurement output, may be obtained from the definition:

$$C_{p,\text{eff}}(t) = C_{pg}[T(t)] + \{C_{pm}[T_f(t)] - C_{pg}[T_f(t)]\} \frac{dT_f}{dT}, \quad (6)$$

On the assumption of the temperature independence of C_{pm} and a linear temperature dependence of C_{pg}

$$C_{pg}(t) = C_{pg,0} + C_{pg,1}T \quad (7)$$

and using Eqs.(1)-(6) $C_{p,\text{eff}}(t)$ may be calculated for an arbitrary time-temperature schedule. The unknown parameters of the proposed model may be estimated by using the standard non-linear least-squares model, i.e. minimizing the target function F :

$$F(C_{pg,0}, C_{pg,1}, C_{pm}, \tau_0, x, \Delta h^*, \beta) = \int_0^{t_{\text{max}}} [C_{p,\text{eff}}^{\text{calc}}(t) - C_{p,\text{eff}}^{\text{exp}}(t)]^2 dt, \quad (8)$$

where t_{max} is the time of completion of the DSC experiment.

10.2.4. Enthalpic relaxation

Perkin-Elmer Pyris 1 DSC calorimeter was used for enthalpic relaxation measurements. All experiments were carried out without removing the sample from the instrument. To ensure good thermal contact of glass and aluminium pan and to minimize thermal gradient inside sample thin disks (thickness less than 1 mm) of glassy sample for relaxation study was prepared directly in calorimeter. Encapsulated powder of bulk glass (approx. 10 mg) was melted and equilibrated at 420 °C ($T_m(\text{As}_2\text{Se}_3) = 375$ °C) and subsequently cooled to 50 °C with rate $q^- = -100$ °C/min. Glass prepared by such a way was immediately heated by heating rate $q^+ = +100$ °C/min onto relaxation temperature T_r . After isothermal relaxation the sample was cooled down to the temperature 50 °C by cooling rate $q = -100$ °C/min. After this the DSC curve was recorded up to 420 °C by heating rate $q^+ = +20$ °C/min. This scan was used for computer simulation. Glasses were isothermally relaxed at temperatures 145, 150, 155, 160, 165 and 170 °C with duration between 15 minutes and 35 hours. All in-instrument steps were computer controlled using Pyris 1 software.

Generally the relaxation enthalpy, ΔH , corresponds to area of so called overshoot on the DSC heating scan. The values of ΔH were obtained as a difference between overshoot areas of relaxed glass scan and non-relaxed glass one. The relaxation enthalpy, ΔH , increases with increasing time (or duration) of relaxation, t_r , at every relaxation temperature, T_r , used for isothermal aging. Relaxation enthalpy, ΔH , reaches its limit value, $\Delta H_{\text{eq}}(T_f = T_r)$ after the sufficiently long time, t_r , at each isothermal relaxation. This means that glass achieves a metastable equilibrium at given temperature. The dependence of obtained values of ΔH_{eq} on relaxation temperature is shown in Fig. 5. When relaxation temperature decreases the value of ΔH_{eq} increases, but not linearly. At relaxation temperatures sufficiently below T_g ($T_r \sim T_g - 30$ °C) the enthalpy changes from that one of non-relaxed glass to the enthalpy of metastable equilibrium of glass and achieves its final value $\Delta H_{\text{eq}}^{\text{max}}$. This value does not change with further decreasing of T_r , see Fig. 5. For As_2Se_3 glass the maximal enthalpic change is $\Delta H_{\text{eq}}^{\text{max}}(\text{As}_2\text{Se}_3) \sim 6.4$ kJ/mol.

DSC curves were normalized to pass from zero to unity as the sample goes from glassy state to the equilibrium undercooled liquid state. When above mentioned model of enthalpic relaxation was used and all normalised DSC scans were computer simulated the complete set of parameters

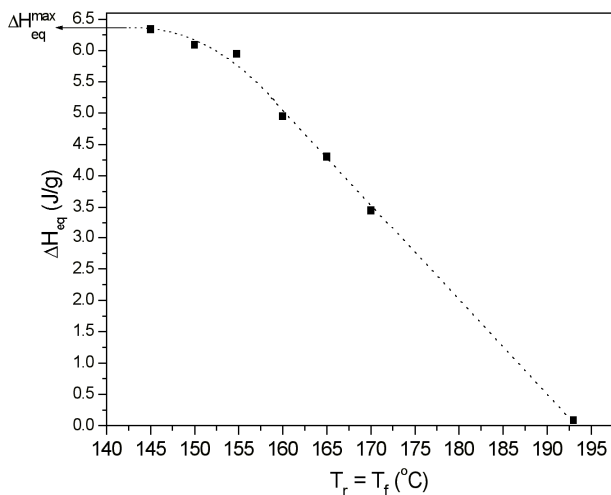


Fig. 5

The dependence of pseudo-equilibrium value ΔH_{eq} on relaxation temperature T_r . The curve is guide for eye.

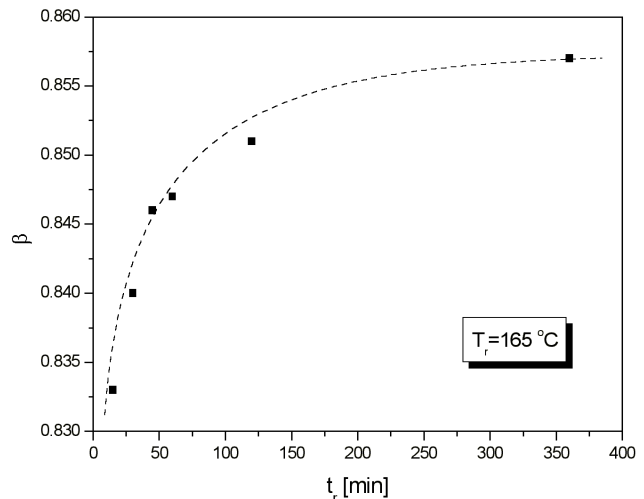


Fig. 6

The time dependence of non-exponentiality parameter β at relax. temperature $165\text{ }^\circ\text{C}$. The curve is guide for eye.

of TNM model were obtained for each of relaxation. This set contains the parameter of non-exponentiality, β , non-linearity, x , fictive temperature, T_f , and apparent activation energy, Δh^* .

Non-exponentiality parameter β was found not to be constant in both the time scale of isothermal relaxation and the temperature scale of the set of T_r . That parameter increases with increasing time of relaxation at every relaxation temperature used. The time dependence of β at relaxation temperature $165\text{ }^\circ\text{C}$ is shown in the Fig. 6. As one can see, after sufficiently long duration of relaxation (when $T_f = T_r$) the parameter β achieves its final value $\beta_{eq}(T_r)$ corresponding to the metastable equilibrium structure of glass at T_r .

Value of β_{eq} increases when the T_r decreases, see Fig. 7. Based on these results one can conclude that the non-exponentiality parameter is both time and temperature dependent, $\beta = f(t_r, T_r)$.

It was found that for given relaxation temperature the value of $\beta_{eq}(T_r)$ is independent on the way in which the glass reached its metastable equilibrium at given temperature, Fig. 8. The as-quenched glass was subsequently completely relaxed at $T_f = T_r = 165\text{ }^\circ\text{C}$ and the value of $\beta_{eq} = 0.86$.

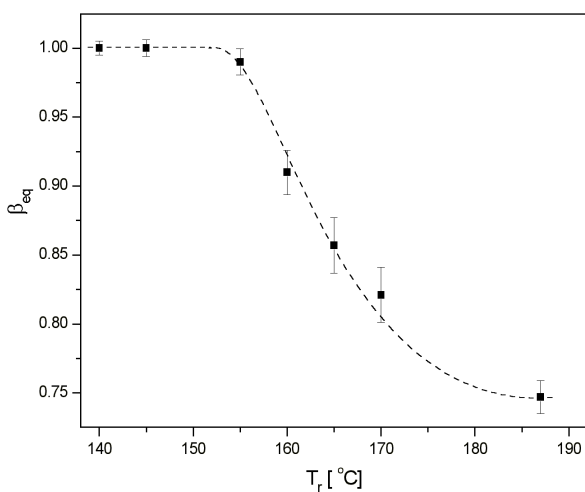


Fig. 7

The dependence of parameter $\beta_{eq}(T_f = T_r)$ on the relaxation temperature T_r . The curve is guide for eye.

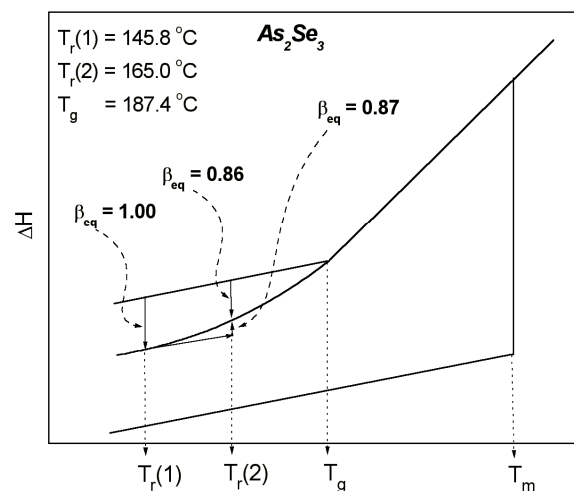


Fig. 8

Qualitative concept of enthalpic relaxation. The values of parameter β_{eq} (for $T_f = T_r$) were obtained experimentally.

Another sample of glass was completely relaxed at $T_f = T_r = 145\text{ }^\circ\text{C}$ ($\beta_{eq} = 1.00$) and after temperature jump it was completely relaxed again at $T_r = 165\text{ }^\circ\text{C}$. The β_{eq} was then found 0.87, within error the same as it was found in previous experiment. It is necessary to emphasize that the first relaxation at $165\text{ }^\circ\text{C}$ is the exothermic process and the second one is the endothermic process, see Fig. 8.

In the case when the change of the relaxation enthalpy reaches its maximal value, ΔH_{eq}^{max} (as it was mentioned above) the value of β_{eq} reached its maximal value $\beta_{eq}^{max} = 1$, see Fig. 9.

Non-linearity parameter, x , increases as T_f is getting near T_r during isothermal relaxation. This parameter was found in range 0.60 - 0.75 and these values reflect relatively small influence of structure to relaxation time. During annealing this influence still decreases.

The apparent activation energy is nearly constant and independent on both temperature and time of relaxation, $\Delta h^*(As_2Se_3) = 263 \pm 15\text{ kJ/mol}$.

It was found that glass reached the metastable equilibrium at each of relaxation temperature used. Corresponding limiting value of the enthalpy change, $\Delta H_{eq}(T_r)$, are indispensable lower than the expected values from linear extrapolation of melt equilibrium enthalpy, see Fig. 10. This figure is based on experimental results. At certain temperature, T_o , sufficiently below the glass transition temperature the enthalpy loss achieves its maximal value ΔH_{eq}^{max} . This one is invariant at temperatures lower than T_o for relaxed glass. For As_2Se_3 glass it was found $T_o \sim 155\text{ }^\circ\text{C}$ and $\Delta H_{eq}^{max} \sim 6.4\text{ kJ/mol}$. The changes of $H(T)$ of fully relaxed glass at temperature lower than T_o bear on the changes of vibrational enthalpy. These changes are the same as for crystal of the same chemical composition because of known fact that heat capacities for both the crystalline and glassy states of most of materials are essentially the same [20,25,26], except at ultra-low temperatures [25], and arise from vibrational contributions. As one can see in the Fig. 9 the curve of metastable equilibrium has the same slope as this one of non-relaxed glass. It corresponds with finding that the specific heat is insensitive on the thermal history of a glass, see below. All these facts confirm assumption that metastable equilibrium is not identical with equilibrium linearly extrapolated of the equilibrium enthalpy above T_g , see Fig. 9. This conclusion agrees with some works, published lately [26-28], that linear extrapolation of equilibrium enthalpy of the liquid state above T_g to this one below T_g is unrealistic.

The obtained dependence of non-exponentiality parameter $\beta = f(t_r, T_r)$ need to be interpreted in two steps. Firstly the attention was focused on $\beta = f(t_r)$, thus on results obtained from isothermal relaxation ($T_r = \text{const.}$).

The relaxation function, which is frequently simplified by KWW stretched exponential Eq. (3), may be expressed by a sum of exponential terms of N individual simultaneous relaxation processes [29]:

$$M_H = \sum_{i=1}^N w_i \exp\left[-\frac{t}{\tau_{oi}}\right] \approx \exp\left[-\left(\frac{t}{\tau_o}\right)^\beta\right], \quad (9)$$

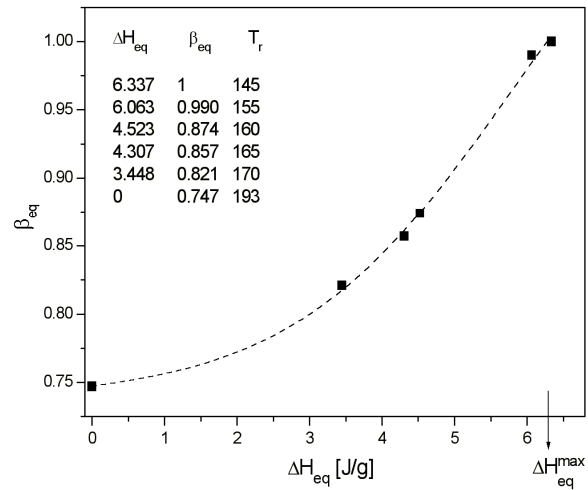


Fig. 9

The dependence of the parameter β_{eq} on the enthalpy change ΔH_{eq} between non-relaxed state of as-quenched glass and metastable equilibrium at the same temperature, see inset.

where w_i are weighting factors, τ_{0i} are independent relaxation times and t is duration of isothermal relaxation. In the right part of Eq. (9) the KWW parameter τ_0 means relaxation time of all relaxation processes at actual time t and β reflects the variation of weighting factors w_i (the distribution of relaxation times) in this time. From the theories describing structural relaxation it follows that the non-exponentiality parameter is inversely proportional to the distribution of structural relaxation times. $\beta = 1$ corresponds to a single relaxation time and as β decreases the distribution broadens. It is reasonable assumption that in the course of relaxation to the metastable equilibrium, $T_f \rightarrow T_r$, the number of independent relaxation processes decreases in consequence of decreasing disorder. Therefore the experimentally found growth of parameter β during the isothermal relaxation, Fig. 6, may be interpreted as a consequence of restriction of relaxation times distribution when structure becomes relaxed.

Dependence of non-exponentiality parameter on relaxation temperature, $\beta = f(T_r)$, is interesting especially in case of its limit value β_{eq} , thus for $T_f = T_r$, Fig. 7. These values, inversely proportional to the distribution of relaxation times of glass in the metastable equilibrium, have shown namely that with decreasing temperature the metastable equilibrium structure approaches the state with only one relaxation time ($\beta_{eq}^{max} = 1$ at the temperature $T_r \leq T_0$). This structure is characterized also by a final relaxation enthalpy, ΔH_{eq}^{max} , Fig. 9, as it was mentioned above. In contrast to results mentioned above some researchers found, especially on organic polymers, that β decreases when temperature decreases [30,31]. These results are only hardly compatible with the idea of structural relaxation. The metastable equilibrium structure becomes denser when temperature goes down and the number of independent relaxation processes goes down, as well. Consequently distribution of relaxation times becomes narrower and thus β rises up. Also it has found that β_{eq} does not depend on fact whether metastable equilibrium was reached by exothermic or by endothermic relaxation, Fig. 8. Therefore non-exponentiality parameter of metastable equilibrium is path independent.

It can be concluded that it would be better to express the parameter β dependent on the structure of glass than on the time of relaxation t_r . While the time increases constantly from the beginning of process irrespective of relaxation extent, the change of the structure of glass is finite. The change of the structure is described by the change of fictive temperature, T_f . Then one may summarize that β depends on thermodynamic temperature and simultaneously on fictive temperature, $\beta(T_r, T_f)$.

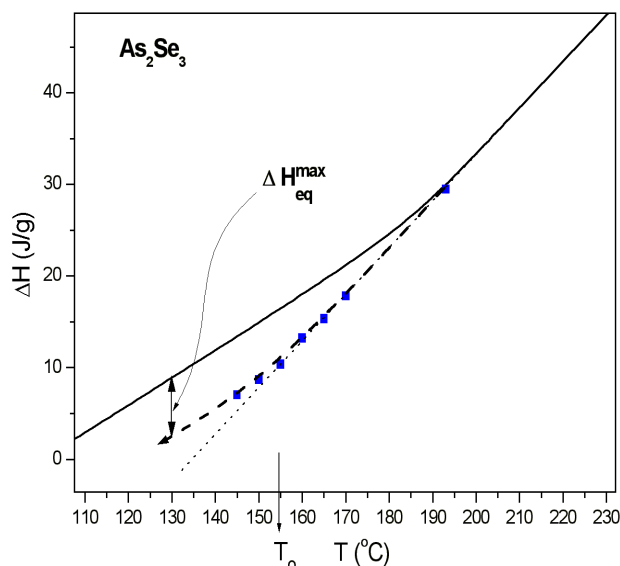


Fig. 10

Real enthalpic temperature dependence observed on glass during isothermal relaxation at annealing temperatures below glass transition. Full lines are calculated from C_p measurement during glass formation and points (ΔH_{eq}) reflect the results of isothermal relaxation. Compare with Fig. 5.

10.2.5. The description of glass transition

Conventional DSC measurements were carried out using of DSC 7 calorimeter and stepwise technique StepScan DSC was carried on the Pyris 1 DSC (both Perkin-Elmer) with special software. Powdered glassy samples (weigh around 4 mg for conventional DSC and 10 mg for StepScan DSC measurements, see below) were encapsulated into sealed aluminium pans.

Conventional DSC scans were done using heating and cooling rates $q^{\pm} = (1 - 20) \text{ }^{\circ}\text{C} / \text{min}$.

To distinguish results of conventional DSC and StepScan DSC, the glass transition temperature, T_g , and ΔC_p measured by StepScan DSC are labeled by superscript "eq", i.e., T_g^{eq} , ΔC_p^{eq} .

Typical StepScan DSC traces of As_2S_3 melt cooling through the glass transition region and trace of As_2S_3 glass heating are shown in Fig. 11. The reversible (thermodynamic) component, C_p , and enthalpic change corresponding to irreversible (kinetic) one are separated.

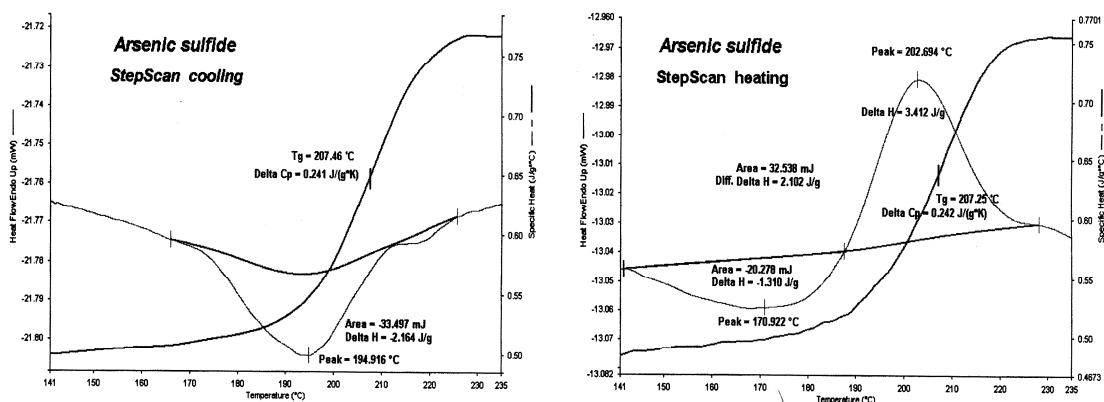


Fig. 11

Typical results of StepScan DSC method. On the irreversible part of cooling scan is seen exothermic peak ($\Delta H = -2.16 \text{ J/g}$). On heating scan both exothermic undershoot ($\Delta H = -1.31 \text{ J/g}$) and endothermic overshoot ($\Delta H = +3.14 \text{ J/g}$) are seen and their difference is within experimental error equal to enthalpic change in course of glass formation. Reversible parts (C_p vs. T) are identical for cooling and heating.

Reversible (thermodynamic) parts are shown in Figs. 12 (including the lead-silicate glass NBS 711 [32]) and 13. When glass is formed the exothermic peak is clearly seen in Fig. 11, as well as both exothermic undershoot and endothermic overshoot when glass is heated and undergoes glass transformation. The temperature of overshoot maximum is always lower than the thermodynamic T_g^{eq} , $T_p < T_g^{\text{eq}}$, Tab. 1 and Fig. 11, contrary to the conventional DSC where $T_p > T_g$ every time. Remind that T_g^{eq} and T_g were determined as the temperature of ΔC_p^{eq} (StepScan DSC) and/or heat flow difference, ΔQ , (conventional DSC) midpoint between glass and undercooled liquid.

When the undercooled liquid was cooled to obtain glass, the exothermic change in the glass transition region was observed on irreversible component, Fig. 11. Its enthalpy is independent on cooling rate within experimental error, contrary to enthalpy of irreversible changes obtained during heating.

Important result shown in Fig. 12 clearly demonstrates that the C_p measurement close to isothermal equilibrium when irreversible component is separated removes completely both well-known hysteresis of thermal capacity and shape difference during heating and cooling. Temperature dependence of C_p obtained by this way is independent on both heating/cooling rate and thermal history. Similar result was found also for organic polymer [33].

It is well known that conventional DSC traces obtained during cooling and heating differ significantly in the shape and thus also in the value of the specific heat capacity change, ΔC_p , e.g.

[34-38]. This is also well known that the value of glass transition temperature, T_g , is dependent on heating and cooling rate, q^+ and q^- , and with increasing rates, q^\pm , the glass transition temperature increases, see e.g. [13,35].

Results of conventional DSC experiments carried out at different heating or cooling rates are in Figs. 13A, B. Part A shows the dependence of T_g on the heating rate. It is pointed out, that dependence of T_g on heating rate, Fig. 13A doesn't need to be logarithmic contrary to Lasocka's proposal [13]. The application of two-phase exponential association equation (also known as pseudo-first order association kinetics eq.), Fig. 13A, allows us to extrapolate the T_g values from zero heating rate even to the infinity. The values of T_g obtained in this manner are more realistic compared to application of logarithmic dependence. Glass transition temperatures obtained by StepScan DSC, T_g^{eq} , are represented by shaded stripe with width of $2 \cdot (\text{std. deviation})$ of T_g^{eq} , Fig. 13A. Very surprising is dependence of ΔC_p on heating and cooling rates obtained by conventional DSC, Fig. 13B, which has not been published and systematically studied, yet. It shows namely that ΔC_p determined either from heating or cooling scans going to be significantly different when rates q^\pm decrease. On the other hand the values of ΔC_p^{eq} are practically constant (Fig. 13B, half-filled circles, and Tab. 1). In other words, the application of new method of measurement eliminates influence of thermal history of glass and also influence of heating or cooling rate on the glass transition temperature, T_g^{eq} , and on the ΔC_p^{eq} . It can be easily shown that the sum of thermodynamic and kinetic components is equivalent to the conventional DSC scan at the same heating rate.

According to the results there is directly proposed conception that in the glass transition region the glass may be viewed as an equilibrium mixture - supercooled liquid \leftrightarrow glass. Starting from the upper temperature end of a glass transition region when temperature decreases this equilibrium moves towards the glass and at the temperature T_0 , see Fig. 10, the supercooled liquid completely disappears and vice versa. Temperature dependence of isobaric specific heat in the glass transition interval also supports this concept. In the case of studied glass this change of the total quantity of ΔC_p is also finished practically at the temperature T_0 . The fact that the overwhelming majority of studies of the relaxation have been done in the glass transition region, e.g. [39], probably due to strongly increasing time-consumption at lower temperatures is worthy of remark.

Conventional DSC measurements of the glass transition temperature showed that the glass transition temperature T_g approaches StepScan DSC T_g^{eq} in the case of sufficiently high heating rates, Fig. 13A. It is clear that the explanation of known heating/cooling rate dependence of the

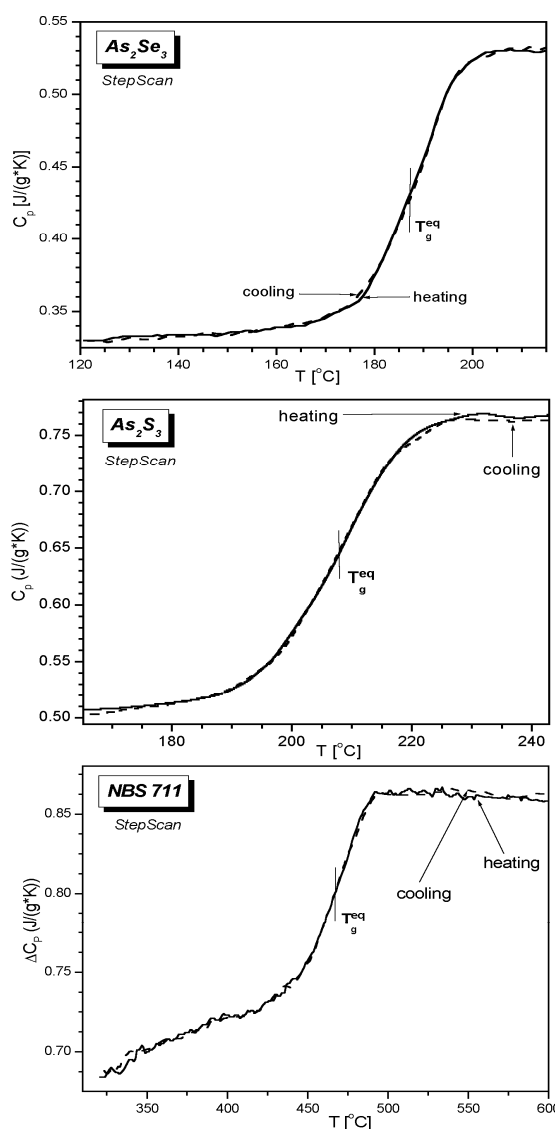


Fig. 12
Reversible (thermodynamic) part of the glass transition. StepScan DSC.

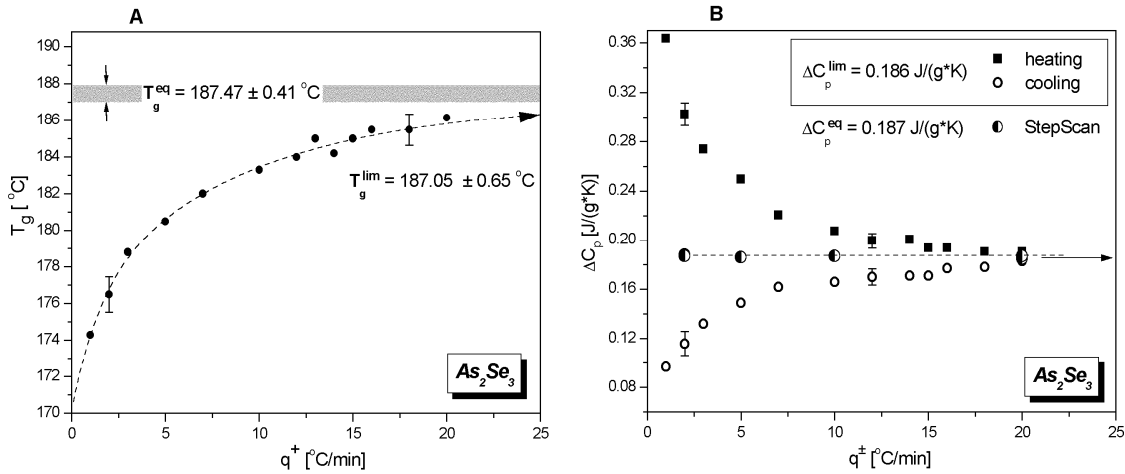


Fig. 13

A) Heating rate dependence of the glass transition temperature, T_g , obtained by conventional DSC (full circles). The T_g^{eq} , obtained by StepScan DSC, is represented by shaded stripe of width $2 \cdot (\text{std. deviation})$ of T_g^{eq} .

B) The heating/cooling rate dependence of both ΔC_p (conventional DSC) and ΔC_p^{eq} (StepScan DSC). The radius of half-filled circles is equal to $2 \cdot (\text{std. deviation})$ of ΔC_p^{eq} .

glass transition temperature should be searched in relaxation times of processes in the glass transition region. The temperature dependence of reversible (thermodynamic) C_p , essentially the change of vibrational amplitudes, is rapid enough in comparison with experimental time of DSC technique and thus this reversible part cannot be influenced by the rate of temperature changes. To elucidate the experimental results it is necessary to focus attention on irreversible (kinetic) component, because of strong temperature and structure dependent relaxation time $\tau(T, T_f)$, simply τ . One can expect that this fact should influence considerably the shape of the non-isothermal DSC scans.

The kinetics of isothermal structural relaxation, $T = T_r = \text{const.}$, can be expressed:

$$\frac{dT_f}{dt} \approx \frac{|T_f - T|}{\tau(T, T_f)} \quad (10)$$

For non-isothermal relaxation kinetics this equation can be rewritten in the form:

$$\frac{dT_f}{dT} \approx \frac{1}{q} \frac{|T_f - T|}{\tau(T, T_f)}, \quad (11)$$

where q is a heating rate, $q = \frac{dT}{dt}$.

For the forthcoming discussion on influence of non-isothermal structural relaxation on the shape of conventional DSC curve, and thus on the T_g and ΔC_p values, refer to Fig. 14.

Heating scan will be discussed at first. Provided that $(T_f > T)_{T < T_g}$, then the glass relaxes exothermally toward the equilibrium structure at T . It manifests itself as so-called undershoot on the non-isothermal DSC scan, see Fig. 11. On the other hand when $(T_f < T)_{T < T_g}$ the relaxation is endothermic and its typical overshoot is found at the temperature above conventional DSC glass transition temperature. In the limit case of $(T_f = T)_{T < T_g}$ the glass is in metastable equilibrium. It is important to point out here that this is the case only when T_f crosses line $T = T_f$. At this moment exothermic relaxation changes to endothermic one, Fig. 14.

Because the relaxation time, τ , increases exponentially with decreasing temperature so at glass formation structural relaxation time is much longer than experimental time, $\tau \gg t$, for the temperatures not much lower than T_g ($T \sim T_g - 10$ °C). As a matter of fact the fictive temperature of non-relaxed glasses is practically always substantially higher than thermodynamic temperature ($T_f \gg T$). It results in well-known fact that during glass heating the exothermic relaxation (undershoot) can be observed in many cases. Its magnitude depends on the difference between the rate of glass formation (the rate of cooling) and the rate of following heating. In case of a low heating rates the equilibrium structure can be reached, $(T_f = T)_{T < T_g}$, and crossed. In such case further increasing of temperature leads to departure from equilibrium and subsequent endothermic process proceeds toward a new equilibrium. Thus an overshoot begins to appear at DSC scan.

Very slow heating of quickly cooled glass, represented by curve 2 in Fig. 14, leads to deep undershoot and very small overshoot when conventional DSC is used. Resulting shape of DSC scan is known as so-called pre-peak, or sub- T_g peak. Origin of this is unclear up to now, see e.g. [40,41]. When non-relaxed or only slightly relaxed glass is heated with sufficiently high rate the exothermic undershoot decreases and at the same the endothermic overshoot shifts up to higher temperature because the equality $(T_f = T)_{T < T_g}$ is reached at higher temperature, Fig. 14.

Relaxation kinetics influences not only determination of the glass transition temperature but it also crucially affects the value of isobaric specific heat capacity change, ΔC_p , in course of glass transition. The dependence of the specific heat capacity change on heating/cooling rate is shown on Fig. 13B. When the rate, q^\pm , rises up the change of specific heat limits to constant equal to StepScan DSC ΔC_p^{eq} , Fig. 13B, in the same manner as a glass transition temperature does, Fig. 13A. The explanation is simple: when a glass is heated the relaxation proceeds and because the quicker heating the lower extend of relaxation and therefore shallower undershoot tends to determination of lower value of ΔC_p , closer to correct value of heat capacity difference. In the case of sufficiently high heating rate the glass almost don't relax exothermally at the temperature below T_g and thus $\Delta C_p \sim \Delta C_p^{eq}$.

With regard to conventional DSC cooling scan the explanation is not prima facie so clear. During cooling of the melt the exothermic process (relaxation) takes place in and below the glass transition region, Fig. 11. Now it should be pointed out that the conventional DSC doesn't measure directly the specific heat but only the heat flow and the later is higher in the glass than in the melt. Therefore when melt is cooled and glass is formed the heat flow of exothermal changes is subtracted from the growth of heat flow during glass transition, Fig. 15. It leads consequently to erroneous lower values of both T_g and ΔC_p obtained from conventional DSC cooling scan, as it is

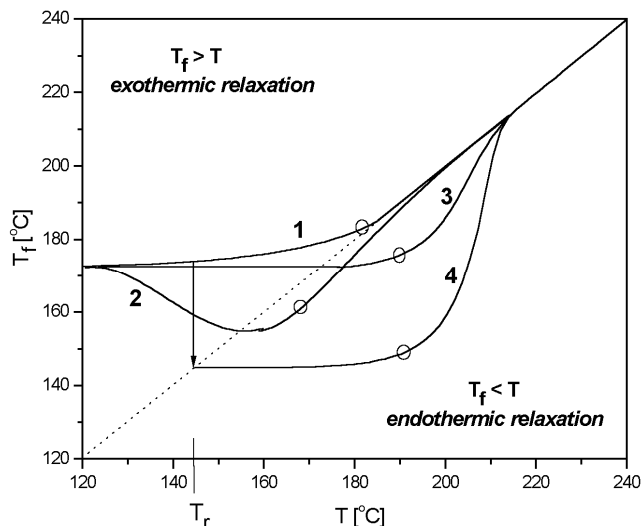


Fig. 14

A schematic drawing of relation between fictive (structural) temperature, T_f , and thermodynamic temperature, T . Circles indicate the points corresponding to conventional DSC glass transition temperatures. Curves: 1 – cooling, 2 – slowly heated non-relaxed glass, 3 – quickly heated non-relaxed glass, 4 – quickly heated glass fully relaxed at T_r . See text for details.

demonstrated on Fig. 15. At increasing cooling rates the extent of relaxation decreases and ΔC_p tends to ΔC_p^{eq} , Fig. 13B.

The opposite sign of heat flow of the glass transition and of the exothermic structural relaxation during cooling and, on the other hand, the same sign of changes of both heat flow components, when the heated glass undergoes the glass transformation, causes the completely different shape of conventional DSC traces. These differences led to erroneous conclusion that when the melt is cooled through the glass transition region there is not exothermal counterpart to endothermic overshoot.

From the aforesaid it is obvious that the value of glass transition temperature obtained by conventional DSC is strongly affected by the facts that i) relaxation kinetic affects significantly shape of DSC scan, and that ii) glass transition temperature is actually determined on an ascending part of irreversible endothermic overshoot added on the reversible $C_p(T)$ dependence.

The heating rate dependence of the overshoot peak shift is widely used for determination the apparent activation energy of relaxation, e.g. [42]. Heating rate dependence of the glass transition temperature has been used to find the activation energy of either the glass transition [42-44] or the activation energy of relaxation [45]. From aforesaid results it is evident that both relaxation peak and T_g shift bear on relaxation and thus it doesn't surprise that the obtained activation energies of relaxation and of glass transition are very close each other. Their difference is caused only by the fact that in the first case the peak shift and in the second one the shift of the ascending part of endothermic overshoot is used, but always it is only more less good estimation of activation energy of relaxation.

It's clear that using conventional DSC it is possible only to approach more or less correctly the values of T_g^{eq} and ΔC_p^{eq} (characteristic values of reversible changes).

From obtained results follows one crucial question whether or not the glass transition is the kinetic effect at all. To test possibility of solving of this problem by StepScan DSC, the heating scan was stopped in the glass transition region and was continued after 30 minutes isotherm (sufficient long time to reach thermal equilibrium, because at this temperature the mean relaxation time is of order of

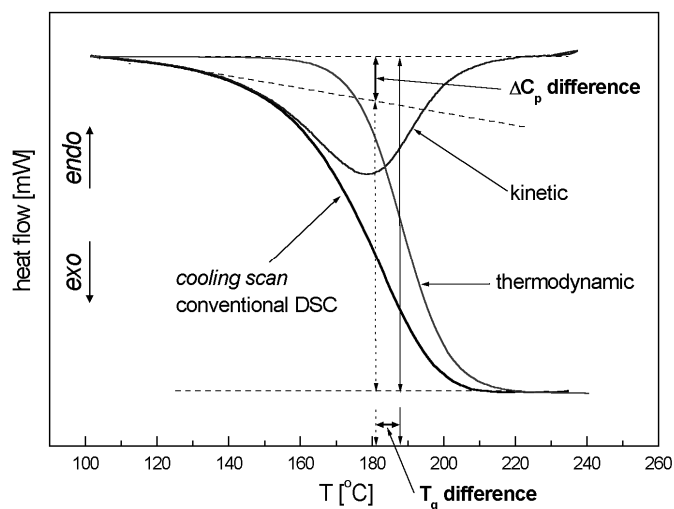


Fig. 15

The influence of exothermic process on the shape of conventional DSC cooling scans in course of glass transformation. Errors of determination of both T_g and ΔC_p are indicated.

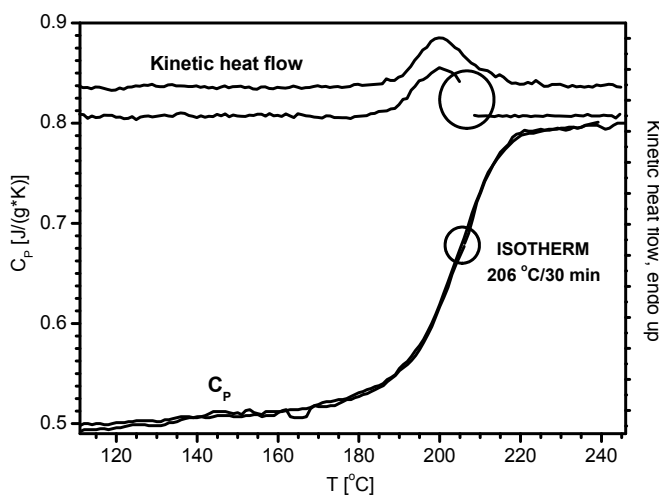


Fig. 16

StepScan DSC measurements in the glass transition range of As_2S_3 bulk glass. Reversing parts are labeled C_p , the nonreversing ones are labeled Kinetic heat flow, see text.

hundred seconds). At this moment it can be decided whether or not the separation of experimentally obtained heat flow into reversing and nonreversing parts could presents only software separation of entirely kinetic processes. In such case both reversing and non-reversing (kinetic) parts should change during the sufficiently long isotherm. Comparison of results obtained without and with inserted isotherm, however, shows clearly that only kinetic overshoot disappeared after isothermal dwell whereas the sigmoidally shaped reversing part remains unchanged, Fig. 16.

This result, along with previous finding that reversible part (and consequently T_g) depends only on the chemical composition of glass [14,15], shows that the commonly used concept that glass transition is entirely kinetic process is probably not fully realistic. It should be stressed at this moment that well known T_g dependence on the thermal history of glass and on the experimental conditions, when conventional DSC is used, can be caused by superimposition of the slow kinetic effects on the sigmoidally shaped glass transition C_p change, for more details, see [14].

10.2.6. Modeling the glass transition

Using StepScan DSC kinetic effects were separated and sigmoidal-shaped curves corresponding to the changes of isobaric heat capacity in the glass transformation region (reversible part) were obtained for wide class of non-crystalline materials, e.g. chalcogenide glasses (As_2Se_3 , As_2S_3 , GeS_2 , $Ge_4As_4S_9$, S and Se bulk glasses), oxide glass LiPbPBO ($40Li_2O:10PbO:10B_2O_3:40P_2O_5$), lead-silica glass NBS 711 [32], poly(styrene-*co*-acrylonitrile), 75/25, PSA, from BASF and poly(ethylen terephtalate), PET.

On basis of above-mentioned experiment it can be further concluded that the temperature T in the glass transition region can be considered to be the equilibrium transformation temperature. It means that the reversible part of the glass transition (C_p vs. T) may be referred to the temperature dependence of glass \leftrightarrow undercooled melt equilibrium. This dependence after normalization represents the temperature dependence of glass \rightarrow undercooled melt conversion $\alpha(T)$.

If temperature dependent transformation occurs randomly in the material and the fraction dx of glass is transformed to undercooled melt, it is possible to write:

$$d\alpha = (1 - \alpha)dx, \quad (12)$$

where α varies from zero to unity (the end of the transformation). Integration of this equation yields to:

$$\alpha = 1 - \exp(-x). \quad (13)$$

In case of the glass transition, the temperature dependence of the conversion α can be expressed by the measurable values as $\alpha = (C_p(T) - C_{pg})/\Delta C_p$. $C_p(T)$ is the actual value of isobaric heat capacity at temperature T , ΔC_p is its total change during the glass transition and C_{pg} is the heat capacity of glass at the lowest temperature of the glass transition region. Substitution of x for $(T/T_g)^n$ yields to the following equation:

$$\alpha = 1 - \exp\left(-\left(\frac{T}{T_g}\right)^n\right) \quad (14)$$

describing well the experimentally obtained data. In this equation T_g is the temperature of inflexion point of α vs. T dependence, and n is a steepness parameter. The α vs. T form is more suitable for computer fitting than C_p vs. T because the use of degree of conversion instead of isobaric heat capacities eliminates their temperature dependencies out of glass transition region.

The applicability of Eq. (14) at the description of reversible part of the glass transition was tested on many non-crystalline materials of a different chemical nature mentioned above. The reversible parts of the glass transformation process were normalized and fitted by Eq. (14). It was found that this equation fits the glass transition region fairly well in all cases. As an example, see Fig. 17.

From the Eq. (14) it arises that in the inflection point ($T = T'_g$) the conversion must always be $\alpha = (1 - 1/e) = 0.632$, where e is the base of natural logarithm. Therefore when reduced temperature, T/T'_g , is used, the conversion curves of all glasses studied must intersect within an experimental error at $\alpha \sim 0.63$. Experimental results are in the excellent agreement with this presumption, see Fig. 18. It is evident that the reversible parts differ in the shape. The steepness of curves is determined by the value of parameter n in Eq. (14). By differentiation of this equation for $T = T'_g$ the parameter n is obtained as $n = e \cdot d\alpha/d(T/T'_g)$ and it is the slope of the glass \leftrightarrow undercooled melt conversion curve in the inflexion point. Values of n calculated for all materials studied are included into Fig. 19. From it follows that n decreases when T'_g increases regardless of the chemical composition of glass. It means that if glasses of different chemical composition have close values of T'_g than the shape of reversible part of glass transition will be very similar.

The physical meaning of parameter n is not still clear, its dependence on T'_g is noticeably close to the same dependency of Angell's fragility index m [21,46]. Straight lines with markedly different slopes crossing at approx. 150 °C divide the n dependency on T'_g into two regions, see Fig. 19. From both n and m dependencies it follows that undercooled melts of glasses with glass transition temperature higher than approx. 150 °C are "strong". It means, that their viscosity obeys arrhenian temperature dependency. However, further experiments are needed for detailed n explanation.

From experimental results it follows that the glass transition can be regarded as a temperature dependence of a glass \leftrightarrow undercooled melt equilibrium. The semi-empirical two-parametric equation was proposed to describe the temperature dependence of glass \leftrightarrow undercooled melt conversion. One of the parameters, T'_g , determines temperature of inflexion point of sigmoidal shaped curve and the second one, n , is the steepness at T'_g . Applicability of proposed equation was tested using various non-crystalline materials with very different chemical composition. All experimentally

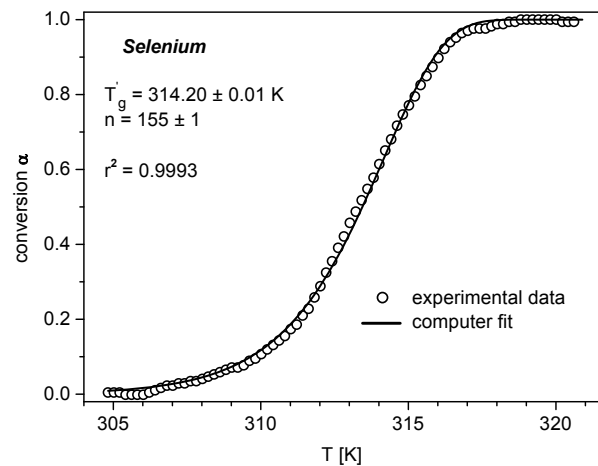


Fig. 17

Normalized reversible part of the glass transition (conversion α) of glassy Se and its computer fit obtained by Eq. (14).

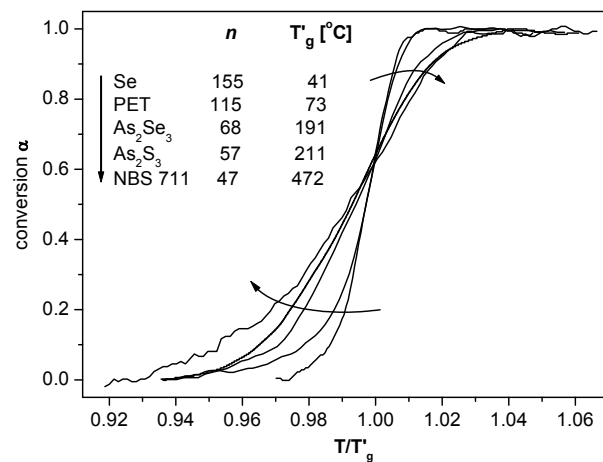


Fig. 18

Normalized reversible parts of the glass transition of some studied samples. All curves intersect close to $\alpha \sim 0.63$ for T/T'_g . Some results have been omitted in order to avoid cluttering in the figure.

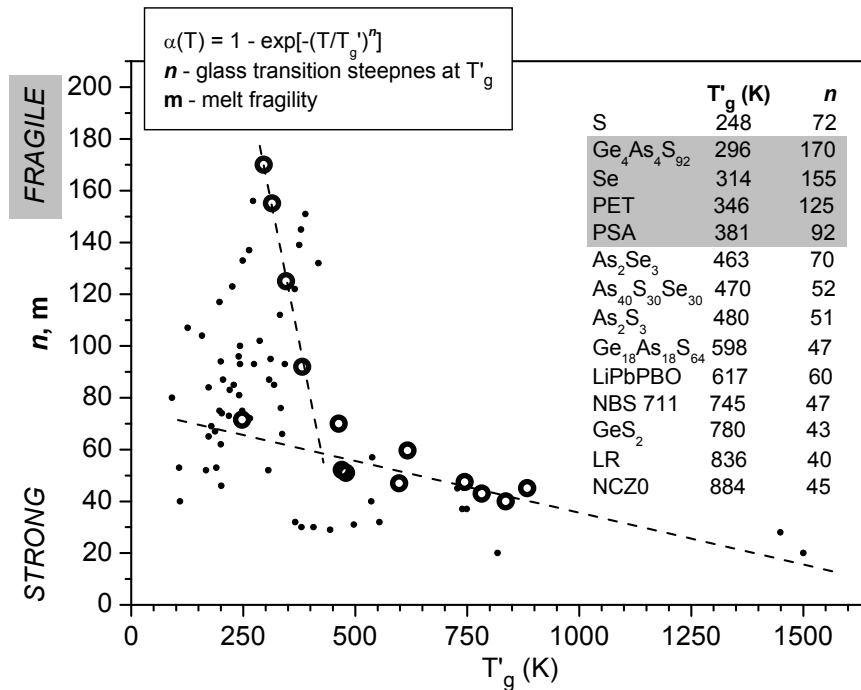


Fig. 19

The dependence of the glass transition steepness parameter n (circles) and the fragility index m (points) [47] on the glass transition temperature T'_g .

obtained reversible parts were fitted fairly well and in agreement with the proposed equation an inflection point at $\alpha \approx 0.63$ was found in all cases. The steepness, n , was found to be inversely proportional to the glass transition temperature. The temperature of inflection point, T'_g , should be used as unambiguously defined glass transition temperature.

10.2.7. Ideal glass – Kauzmann temperature and the glass transition

In 1948 Kauzmann pointed out that the entropy of supercooled liquid decreases rapidly on cooling towards the kinetic glass transition temperature, T_g , and extrapolates to the entropy of the crystal no far below T_g , [48]. Temperature dependence of the entropy of glass intersects this one of crystal at so called Kauzmann temperature, T_K . If the entropy of supercooled liquid become smaller than that of the stable crystal, its entropy would eventually become negative at sufficiently low temperature, violating the Third Law of Thermodynamics. This situation is termed Kauzmann's paradox or entropy crisis, see e.g. [49-51] and references cited therein. One way of avoiding the entropy crisis is, for the liquid, to form an "ideal glass" at T_K . This is the thermodynamic view of the glass transition according to which the observable glass transition (e.g. by viscosity or DSC measurements) is manifestation of a second-order phase transition at Kauzmann temperature, masked by kinetics. According to Kauzmann, spontaneous freezing at kinetic glass transition prevents equilibration of supercooled liquid near T_K . Because kinetic glass transition is higher than Kauzmann temperature, it intervenes before the entropy crisis occurs.

Based on results obtained by novel experimental techniques of DSC the glass transition seems not to be only a kinetic phenomenon, but it is the reversible process in the thermodynamic sense [53,54]. From this perspective on the glass transition it is interesting to test whether Kauzmann temperature can be achieved and "ideal glass" in Kauzmann sense can exist in reality. The As₂Se₃ and As₂S₃ bulk glasses were chosen because of their easy preparation in high purity as well as possibility of slow cooling of its undercooled melt without crystallization. Nucleation

temperature of As_2Se_3 is lower than the crystallization one. On the other hand crystalline As_2Se_3 can be prepared relatively easily [55], contrary to crystalline As_2S_3 [56].

Results obtained by StepScan DSC on the crystalline and glassy arsenic trichalcogenides have been used to calculate temperature dependence of entropy changes. The temperature dependence of the entropy change for both crystalline and non-crystalline samples is given by the sum of the thermodynamic contribution and of the enthalpy change of kinetic process divided by its temperature:

$$\Delta S(T) = \int_{T_1}^{T_2} \frac{C_p}{T} dT + \frac{\Delta H_{\text{kin}}}{T_x} \quad (15)$$

C_p is isobaric heat capacity, ΔH_{kin} is enthalpy changes obtained from irreversible kinetic part, T_x is either the glass transition temperature, T_g , or the crystal melting one, T_m , and $T_1 \ll T_g$ and $T_2 \gg T_m$.

In fact, because the irreversible kinetic processes are spread over indispensable temperature interval the contribution of the kinetic part to the entropy change in course of the glass transformation and/or of the crystal melting was replaced by $\Delta S_{\text{kin}}(T)$ and calculated according equation:

$$\frac{\Delta H_{\text{kin}}}{T_x} \approx \Delta S_{\text{kin}}(T) = \frac{1}{m \cdot \beta} \int_{T_1}^{T_2} \frac{Q_{\text{kin}}(T)}{T} dT, \quad (16)$$

m is the sample mass, β is the underlying heating/cooling rate, $Q_{\text{kin}}(T)$ is the heat flow related to kinetic processes. Using entropy temperature dependence obtained, the Kauzmann temperature of As_2Se_3 was found to be $T_K = 164^\circ\text{C}$, see Fig. 20. This temperature is 23°C below the glass transition temperature, $T_g = 187^\circ\text{C}$.

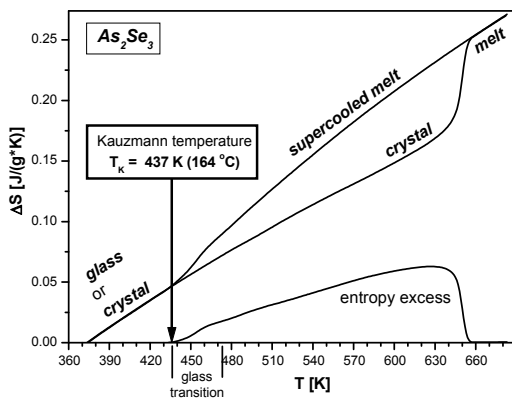


Fig. 20

Entropy, entropy excess and Kauzmann temperature of As_2Se_3 bulk glass.

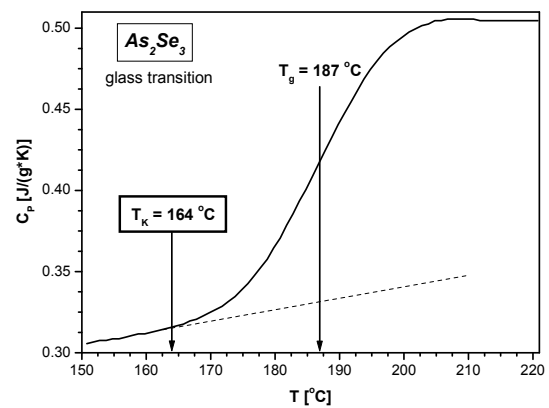


Fig. 21

Kauzmann temperature and glass transition region (reversible part) of As_2Se_3 bulk glass.

Confronting obtained Kauzmann temperature and thermodynamic part of the glass transition of As_2Se_3 , it was found that T_K is identifiable with the low-T onset of the glass transition region, Fig. 21, and very close to the viscosity- T_g at 166°C ($\eta = 10^{12}$ Pa.s) [57]. The temperature of this low-T onset is exactly that one at which supercooled liquid is completely transformed to glass. This result has physical meaning and according to the Kauzmann idea, the glass transition of As_2Se_3 bulk glass is the thermodynamic one and this glass can be termed as an ideal glass.

On the other hand, surprising result was obtained on As_2S_3 bulk glass. As one can find anywhere, this glass has been widely used as an "ideal glass" because of its easy preparation and

extremely low crystallization tendency of its undercooled melt. Kauzmann temperature of As_2S_3 was found at approx. 97 °C, Fig. 22. This temperature is approx. 78 °C below low-T onset (175 °C) of the glass transition region and it is clear, that ideal glass transition (thermodynamic one) is masked by the kinetic effects at significantly higher temperature. Based on the Kauzmann temperature idea, the As_2S_3 glass contains some excess of the entropy of fusion and therefore glass preserves a certain extent of undercooled melt nature.

At the end it must be pointed out that it is not possible to obtain the same results using conventional DSC because cooling scans over the glass transition region is distorted due to the simultaneous endothermic and exothermic events, for details see [14].

It was shown, contrary to the commonly accepted opinion, that undercooled liquid can really (but unfortunately rarely) achieve the Kauzmann temperature and thus avoids the entropy crisis thermodynamically and not only by the kinetic effects.

10.3. Crystallization

Kinetics of the first order phase transformations, e.g. crystallization of undercooled liquids, has often been determined by the various techniques. The calorimetric methods, in particular differential scanning calorimetry (DSC), are widely being used for the study of kinetics of the above-mentioned processes. This method has some advantages, e.g. it is quite sensitive, it is not demanding with regard to sample preparation and is relatively independent of the sample geometry. DSC measures a volume fraction transformed as a function of time (isothermal DSC) or temperature (non-isothermal) by measuring the heat released or absorbed during a phase change. In recent years, especially the non-isothermal DSC measurements became very attractive for the study of phase transformations. The non-isothermal experiments can be performed more rapidly compared with isothermal ones, and they can also be used for extension of a temperature range of the measurement beyond the one accessible to isothermal experiments.

General theory of transformation kinetics was derived for the case of isothermal transformation conditions [58]. Numerous methods have been developed for a treatment of non-isothermal DSC data in order to obtain the kinetic parameters that could reproduce the experimental data and predict a behavior of the system in different conditions [59-61].

In case of the study of phase transformations involving nucleation and growth under isothermal conditions, an analysis of the data obtained has been mostly carried out using the Johnson-Mehl-Avrami (JMA) formalism [62-64]. This method is based on integral expression for the fraction transformed:

$$\alpha(t) = 1 - \exp((-kt)^n), \quad (17)$$

$\alpha(t)$ is a fraction of the transformation completed at the time t , n is parameter reflecting nucleation rate and growth morphology. Rate constant k has an Arrhenius temperature dependence:

$$k = k_0 \exp(-E/k_B T), \quad (18)$$

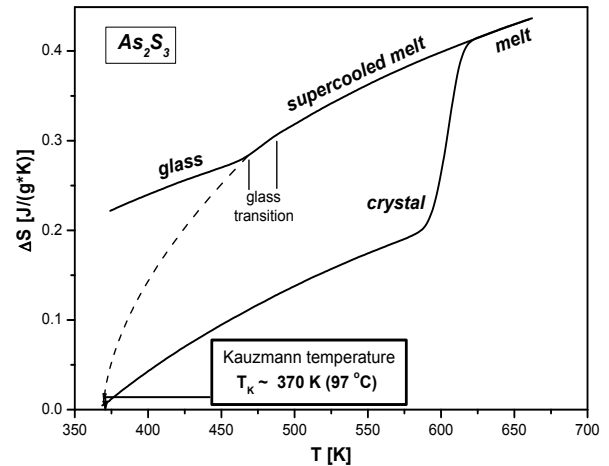


Fig. 22

Temperature dependence of entropy of As_2S_3 system and approximation of the Kauzmann temperature.

where E is the activation energy, k_B is Boltzmann constant.

The validity of applying this model to non-isothermal transformation kinetics has been examined by Henderson [59]. He has shown that JMA formalism can be used under some specific restrictions that limit applicability of this formalism to so-called "site saturation" transformation only. In this case, nucleation takes place at a very start of transformation, and the nucleation rate is then zero. However, it seems that there are still some problems associated with a proper use of this model in analysis of non-isothermal data because in many papers, one can find a great dependence of activation energy on degree of conversion and variation of JMA exponent n on temperature.

In many cases, JMA model is unsatisfactory and the non-isothermal transformation kinetics has to be described by the Šesták-Berggren (SB) model [65,66], which is an empirically found accommodation function:

$$\frac{d\alpha}{dt} = \alpha^m (1-\alpha)^n \quad (19)$$

The SB model is a very flexible function with regard to the DSC data fitting but lacking a physical meaning (especially the exponents m and n have no clear physical consequence but can be related to the JMA exponent [66]).

10.3.1. Isothermal crystallization

Isothermal DSC measurements of As_2Se_3 undercooled melt were used in a wide temperature range (270 - 360 °C) to obtain more detailed information about crystallization kinetics of this material. The enthalpy of crystallization was found to be $\Delta H_{\text{cryst}} = -91.5 \pm 2.7$ J/g. Crystallization peaks were integrated and the time dependence of degree of crystallization α_i was obtained, Fig. 23. Temperature dependence of maximum crystallization rate is shown in Fig. 24. The crystallization rate increases to the temperature 350 °C. Close to the melting temperature the equilibrium between crystal growth and melting occurs significantly, Fig. 23, curve no.10, and crystallization rate falls down rapidly, as one can assume, Fig. 24. All data were analyzed in terms of JMA model, eq. (17), Fig. 25. The values of parameters k and n of JMA equation were obtained. Based on the thermal dependence of the rate constant k the value of apparent energy E was determined. The value of E is 1.58 eV (pre-exponential factor $A = 1.10^6$ s⁻¹) at temperatures below approximately 570 K (297 °C) and above this temperature the E value decreases to 0.99 eV ($A = 7.10^6$ s⁻¹). Because the mechanism of crystallization process can be temperature dependent, two different mechanisms with different value of E can be assumed. Nucleation together with crystal growth are dominating at lower temperature region while entirely crystal growth is crucial at higher temperatures.

Furthermore the kinetic exponent n exhibits a temperature dependence and its value decreases from 3.8 to 1.9 over the whole studied temperature interval. The temperature dependence of the kinetic exponent can clearly be divided into four parts, marked **A-D** in Fig. 26.

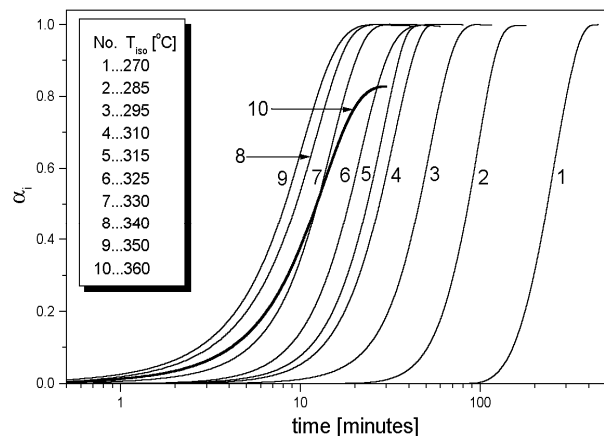


Fig.23

Time dependence of degree of crystallization obtained by integration of experimental data. Curve 10 (360 °C) is pertinent to equilibrium of crystal growth and melting.

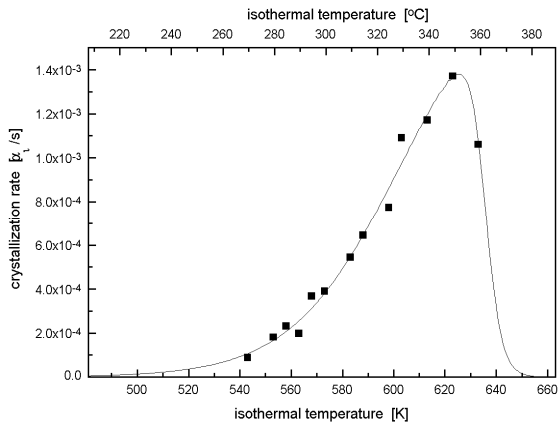


Fig. 24

Temperature dependence of isothermal crystallization rate (points) obtained from computer fit of degree of crystallization time dependence.

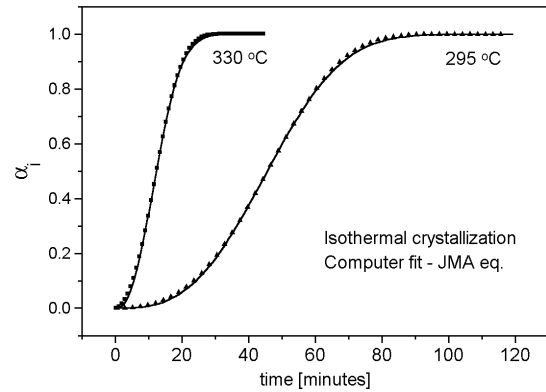


Fig. 25

Experimentally obtained degree of crystallization vs. time (points) and its computer fit (lines), JMA eq. was used.

In the part **A** the kinetic exponent n decreases from the value ~ 3.8 to 2.75. With respect to the higher value of apparent activation energy ($E = 1.58$ eV) one can suppose that the nucleation and the crystal growth take place at same time. This conclusion is in accordance with values with values of n for various crystallization processes predicted by Mora [38].

In the part **B** the n value (~ 2.75) is practically constant. In accordance with experimentally obtained value of n and lower value of apparent activation energy $E = 0.99$ eV only the crystal growth is probably dominating process. Optical microscopy measurement confirmed that consistent with the value of n the crystals growing under these thermal conditions are three-dimensional. This agrees well with [38] again.

In third temperature region (**C**) the kinetic exponent n decreases from 2.75 to 1.9 and the E value remains constant ($E = 0.99$ eV). The crystal growth process is probably the same as in previous case but dimensionality of crystals changes. Two dimensional plate-like crystals come up together with three dimensional ones as confirmed by optical microscopy.

The last region (**D**) approaches at the end the melting point of As_2Se_3 crystals. The plate-like crystal growth morphology predominates, which is in accord with experimentally founded kinetic exponent value ($n \sim 1.9$).

Results obtained differ from results published by Henderson and Ast [67] especially in the magnitude of kinetic exponent values. They found n changed from value 4.5 in the low temperature region to $n = 4$ (at 335 °C) and the value of n was interpreted regardless of the crystallite growth morphology.

Temperature dependence of kinetic exponent n obtained experimentally is in the strong contradiction with assumption of constant n used in numerical analysis of non-isothermal data [68-70]. The result obtained by analysis of non-isothermal data can be incorrect at least at some cases. Especially in those cases when non-isothermal crystallization can be observed over wide thermal interval. It is well known from

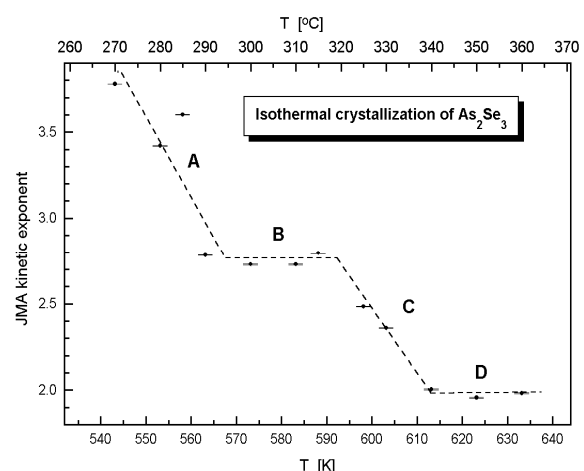


Fig. 26

Temperature dependence of JMA kinetic exponent n obtained from computer fit of experimental data.

many experiments that only Šesták-Bergren accommodation function (without physical meaning, unfortunately), eq. (19), can be used to description of experimental data in these cases.

10.3.2. Non-isothermal crystallization

The problems in the analysis of non-isothermal data originate very probably from the fact that the models used for analysis of non-isothermal DSC data were originally derived for isothermal condition and some simplifications were done for using these models on non-isothermal data. In case of JMA model, the assumption of constant temperature independent kinetic exponent n is one of the most problematic simplifications. As it was mentioned above the temperature dependence of kinetic exponent n was found, its value decreased with an increasing temperature. From this point of view, one can assume that if the kinetic exponent n varies with temperature during non-isothermal crystallization, the frequently used kinetic analysis of non-isothermal data do not develop this fact and erroneous conclusions concerning kinetic model and activation energy could be done.

10.3.3. Kinetic analysis of non-isothermal DSC data – computer aided test of its applicability

To elucidate problem of non-isothermal data analysis the JMA model with various temperature dependence of n and $E = 130$ kJ/mol was used and three series of theoretical DSC curves of non-isothermal crystallization were computer simulated and analyzed in usual way. It means that activation energy and subsequently the kinetic model were determined from theoretical DSC scans and compared with these one used for simulation. It was found:

a) in case that the value of kinetic exponent used for computer simulation was constant ($n = 2$), the kinetic model obtained subsequently by analysis of theoretical DSC scans was of JMA one.

Apparent activation energy was independent on α , see Fig. 27, and its value can be determined correctly ($E = 130 \pm 1$ kJ/mol). Using the analysis based on the JMA model, the correct value of kinetic exponent $n = 2$ was also found.

b) if the value of n used for computer simulation is not constant, the kinetic model obtained by analysis of simulated curves was not found unambiguously JMA but mostly SB, see Fig. 28. The value of apparent activation energy depends significantly on α which results in the impossibility of its correct determination, Fig. 29, see wrong value $E = 118.9 \pm 0.9$ kJ/mol found by kinetic analysis. However, for the low values of heating rate, it is, in some cases, possible to interpret the DSC curves by the JMA model also at a temperature dependent kinetic exponent. The reason for this is a relatively narrow width of the DSC peak at the low values of heating rate when a relatively small change of the value n is occurring in this narrow temperature interval of the phase transformation, see Fig. 28.

By means of computer simulation of the DSC curves, it was shown that extension of originally isothermal transformation kinetic equations to non-isothermal conditions is really the basic problem. It is possible to conclude that if the kinetic analysis of non-isothermal DSC curves of crystallization results into JMA model then a found model is most probably a realistic one. In

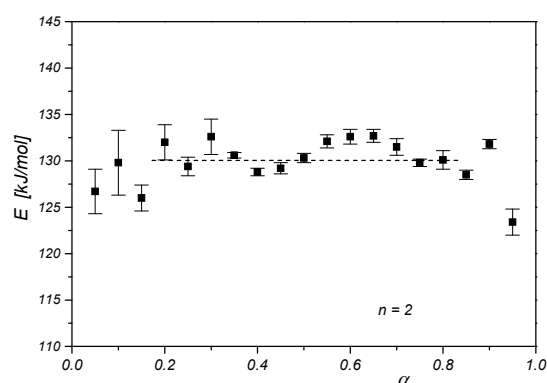


Fig. 27

Activation energy as a function of degree of conversion, α , calculated by the isoconversional method (simulated DSC traces with temperature independent JMA exponent $n=2$). Dashed curve denotes mean value of $E = 130 \pm 1$ kJ/mol.

such case, a value of activation energy is basically not dependent on α and its value, as well as the value of kinetic parameter n , reflects correctly the crystallization kinetics.

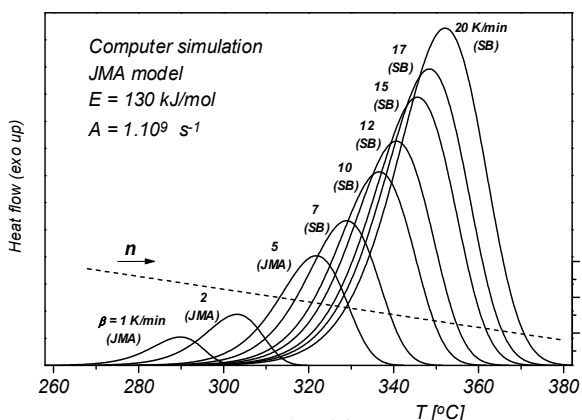


Fig. 28

DSC traces computer simulated with temperature dependent JMA exponent. The found kinetic model (JMA or SB) is introduced beside each curve.

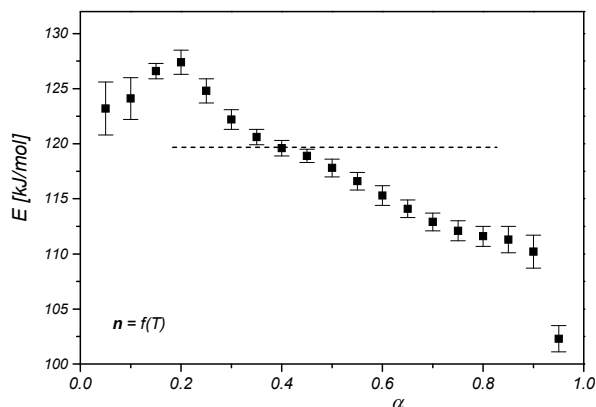


Fig. 29

Activation energy as a function of degree of conversion, α , (simulated DSC traces, linear temperature dependence of JMA exponent n , Fig. 5). Mean value of apparent activation energy is $E=118.9\pm 0,9$ kJ/mol (dashed curve).

However, if the kinetic analysis of non-isothermal DSC curves of crystallization results into SB model then it is not possible to distinguish whether or not it really concerns the kinetics of a process that can be described by SB model or JMA mechanism with a non-constant value of the kinetic parameter n . On basis of analysis of the simulated DSC curves it can be assumed that a seemingly satisfactory use of SB model for a description of crystallization kinetics developing by JMA mechanism, is accompanied by a not negligible dependence of apparent activation energy E on α .

10. 4. Crystallization of selenium supercooled liquid: kinetic analysis of isothermal and non-isothermal DSC experiments

10.4.1. Isothermal crystallization

Isothermal crystallization of selenium was studied in a wide temperature range 90–210 °C. The temperature dependence of crystallization enthalpy was found 65.5 ± 2.9 J/g (110 - 180 °C). Using Raman spectroscopy it was found that this mean value of enthalpy corresponds to crystallization of hexagonal selenium. Crystallization process at temperatures lower than 110 °C brings experimental problems in correct determination of the crystallization enthalpy because of its long duration. From this reason the results obtained at this temperature range were excluded from further study.

The kinetics of isothermal crystallization of selenium was also studied. The maximum rate of crystallization was determined as a slope in the inflexion point of degree of crystallization

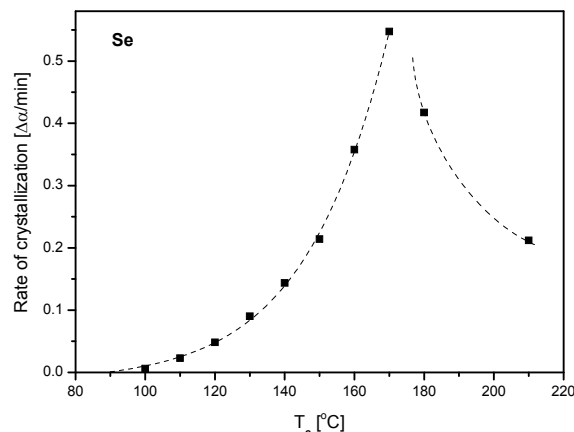


Fig. 30

Temperature dependence of the maximum rate of selenium melt crystallization.

α vs. time curves and its temperature dependence is in Fig. 30. As one can expect maximal crystallization rate increases with increasing temperature, but only up to ~ 180 °C and then it decreases probably due to melt \leftrightarrow crystal equilibrium. The curves in Fig. 30 are only guides for eyes and thus apparent discontinuity is related with the fact that measurements were done with temperature step 10 °C and the highest maximum crystallization rate is somewhere between 170 and 180 °C.

It was found that the Johnson-Mehl-Avrami model (JMA) describes very well experimental DSC data of isothermal crystallization of selenium. The parameters of JMA model (the kinetic exponent n and rate constant k) were determined. The kinetic exponent n is nearly constant ($n \sim 3.5$) in the temperature region 110 – 210 °C. The value of n reflects morphology of the crystal growth [38] and so it is possible to assume 3D crystal growth accompanied by the completion of nucleation. Using Arrhenius plot of the rate constant k the value of the activation energy of selenium crystallization was determined to be $E_a = 83 \pm 2$ kJ/mol.

10.4.2. Non-isothermal crystallization

The crystallization of selenium was also studied under non-isothermal conditions using heating rates 5–20 K/min. Experimental data were treated by frequently used methods of kinetic analysis of non-isothermal data. The activation energy of crystallization, E_a , was determined by means of three commonly used methods. Methods of Kissinger and Ozawa gave $E_a = 64.1 \pm 2.5$ kJ/mol and 68 ± 3.1 kJ/mol, respectively, in agreement with [71]. A little bit lower value of activation energy (58.0 ± 2.1 kJ/mol) was found by the isoconversial method. All values of activation energy found by kinetic analysis of non-isothermal data are lower than this one determined on basis of isothermal crystallization measurements. Determination of activation energy from non-isothermal data is not quite correct because the kinetics of crystallization is studied in the case when the temperature is changed in a wide region. Based on results of isothermal experiments it can be assumed that the crystallization of selenium is accompanied by the termination of nucleation process and just the influence of nucleation could distort the energy calculation.

Using all values of activation energy determined above the appropriate kinetic model of non-isothermal crystallization was found. The non-isothermal data obtained at low heating rates (max. 10 K/min) can be unambiguously described by JMA model but on the other hand Šesták-Berggren SB(m,n) model is the only one convenient for the data obtained at higher heating rates. The explanation of these findings could be following. In case of low heating rates the crystallization realizes in relatively narrow temperature interval and this situation is closer to the isothermal measurement and thus it is possible to find correct kinetic model (JMA). With increasing heating rate the kinetics of crystallization is measured over increasingly wide temperature region and so

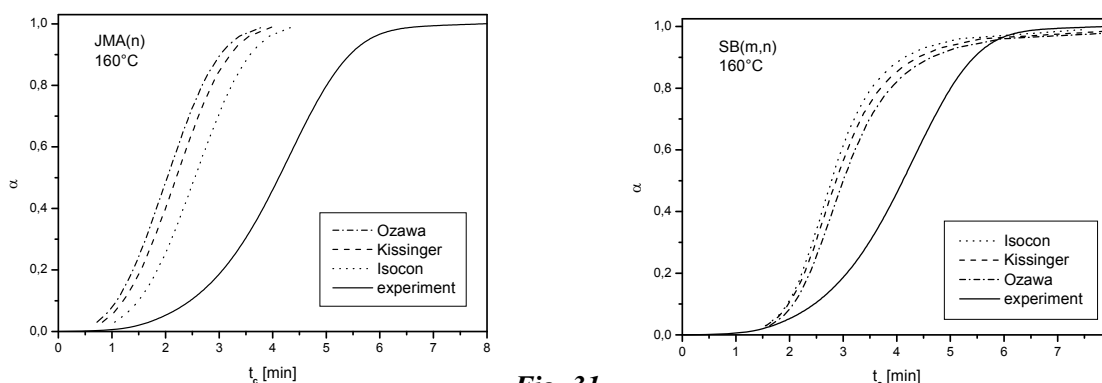


Fig. 31

Isothermal crystallization at 160 °C - experimental data and calculated predictions based on results of kinetic analysis of non-isothermal data for JMA model (left) and SB model (right).

both the temperature dependent nucleation and crystallization rates vary indispensably and one can suppose that this complex process influences the shape of non-isothermal DSC scans markedly. The kinetic model obtained at these conditions is SB one. Unfortunately, the SB function is in fact only very flexible accommodation function rather than model with the physical meaning.

To verify correctness of model determined, the prediction of isothermal crystallization at 160 °C were calculated using non-isothermal parameters of both JMA and SB models. Calculated curve were compared with the curve of isothermal crystallization obtained experimentally, see Fig. 31. As one can clearly see the prediction does not at all agree to the experiment. The both models of non-isothermal crystallization predict significantly shorter time necessary for full crystallization of sample than it follows from experiment. The results obtained are in good agreement with [72] that the prior knowledge of crystallization mechanism is necessary to correct data interpretation when the non-isothermal experiment is used.

Acknowledgements: This work was supported continuously by the project of the Ministry of Education of the Czech Republic MSM 0021627501.

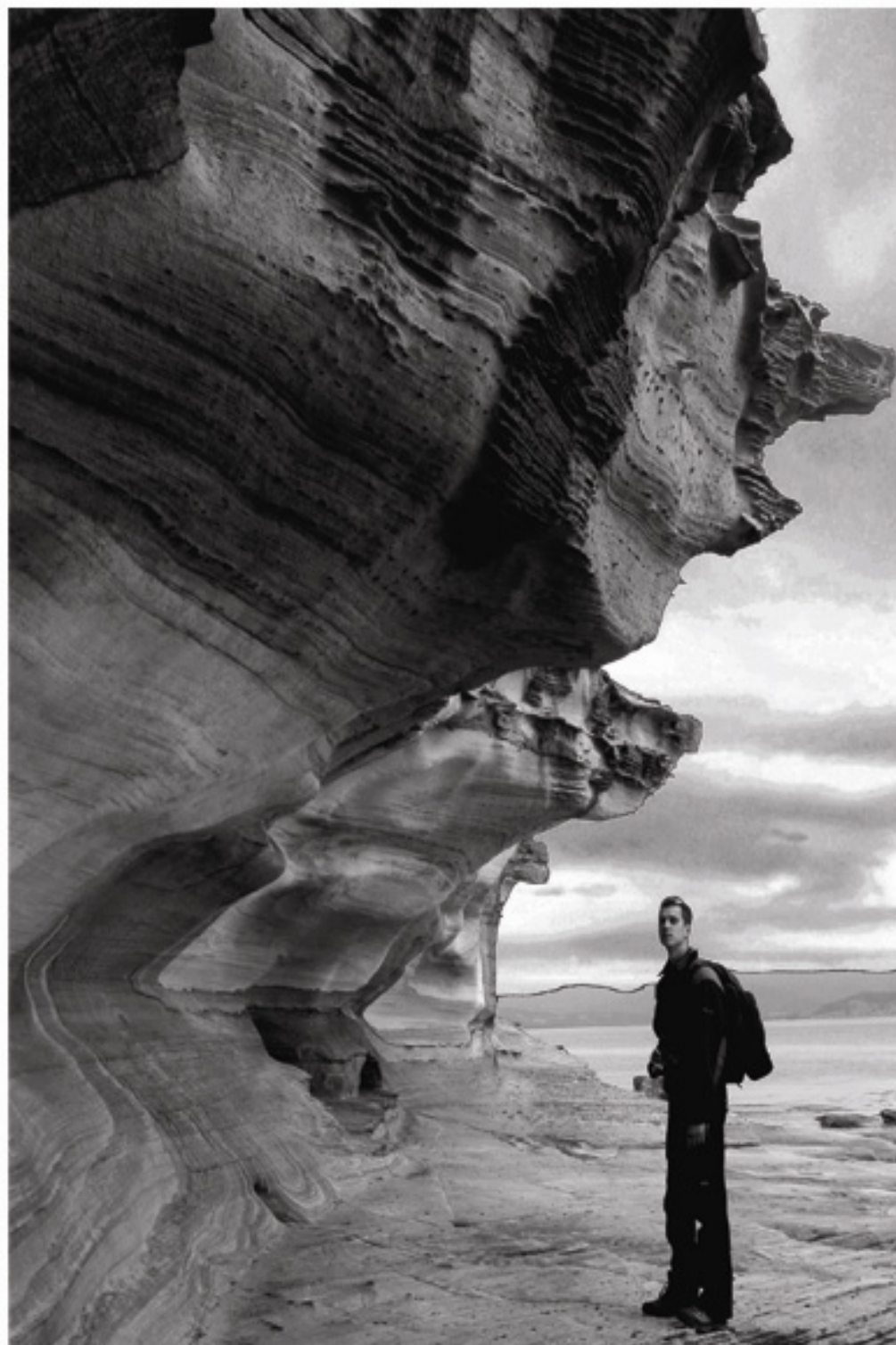
References 10

- [1] J.E.K. Schawe, *Thermochim. Acta*, **261** (1995) 183.
- [2] *Modulated DSC Compendium*, TA Instruments, (1995).
- [3] B. Wunderlich, *Thermochim. Acta* **300** (1997) 43.
- [4] S. L. Simon, *Thermochim. Acta*, **374** (2001) 55.
- [5] M. Merzyakov, C. Schick, *Thermochim. Acta*, **380** (2001) 5.
- [6] I. Avramov, I. Gutzow, *J. Non-Cryst. Solids*, **104** (1988) 148.
- [7] J. Grenet, J.P. Larmagnac, P. Michon, C. Vautier, *Thin Solid Films*, **76** (1981) 53.
- [8] A.J. Kovacs, J.M. Hutchinson, *J. Polym. Sci.*, **17** (1979) 2031.
- [9] C.T. Moynihan, A.J. Easteal, M.A. DeBolt, J. Tucker, *J. Am. Ceram. Soc.*, **59** (1976) 12.
- [10] J. Grenet, J.M. Saiter, C. Vautier, J. Bayard, *J. Thermal Anal.*, **38** (1992) 557.
- [11] T. Derrey, J.M. Saiter, J.P. Larmagnac, C. Vautier, *Mater. Lett.*, **3** (1985) 308.
- [12] A.J. Kovacs, *Adv. Polym. Sci.*, **3** (1963) 394.
- [13] M. Lasocka, *Mater. Sci. Eng.*, **23** (1976) 173.
- [14] Z. Černošek, J. Holubová, E. Černošková, M. Liška, *J. Optoelectron. Adv. Mat.*, **4** (2002) 489.
- [15] J. Holubová, Z. Černošek, E. Černošková, *J. Optoelectron. Adv. Mat.*, **7** (2005) 2671.
- [16] I.M. Hodge, *J. Non-Cryst. Solids*, **169** (1994) 211.
- [17] C.T. Moynihan, in: *Reviews in Mineralogy*, Vol. 32 – *Structure, Dynamics and Properties of Silicate Melts*, J.F. Stebbins, P.F. McMillan, D.B. Dingwell (Eds.), Mineralogical Society of America, 1995, Washington, DC, USA.
- [18] A.Q. Tool, *J. Am. Ceram. Soc.*, **31** (1948) 177.
- [19] H. Suga, *J. Therm. Anal. Cal.*, **60** (2000) 957.
- [20] S. R. Elliott, in: *Physics of amorphous materials*, 2nd edition, Longman Scientific & Technical, Essex, 1990, UK.
- [21] C.A. Angell, *J. Non-Cryst. Solids*, **120** (1988) 205.
- [22] P.G. Debenedetti, F.H. Stillinger, *Nature*, **410** (2001) 259.

- [23] P.D. Garn, in: *Thermoanalytical Methods of Investigations*, Academic Press, New York, 1965, p. 194.
- [24] O.S. Naryanaswamy, *J. Am. Ceram. Soc.* **54** (1971) 191.
- [25] I. Gutzow, J. Schmelzer, *The Vitreous State*, Springer Verlag, Berlin, 1995.
- [26] M.D. Ediger, C.A. Angell, S.R. Nagel, *J. Phys. Chem.*, **100**, No. 31 (1996) 13200.
- [27] A. Brunacci, J.M.G. Cowie, R. Fergusson, I.J. McEwen, *Polymer*, **38** (1997) 865.
- [28] S. Montserrat, J.L. Gomez Ribelles, J.M. Meseguer, *Polymer*, **39** (1998) 3801.
- [29] J.-P. Ducroux, S.M. Rekhson, F.L. Merat, *J. Non-Cryst. Solids*, **172 – 174** (1994) 541.
- [30] C.A. Angell, K.L. Ngai, G.B. McKenna, P.F. McMillan, S.W. Martin, *J. Appl. Phys.*, **88** (2000) 3113.
- [31] J.R. Atkinson, J.N. Hay, M.J. Jenkins, *Polymer*, **43** (2002) 731.
- [32] Certificate of Viscosity Values, Standard Sample No.711 Lead-Silica Glass, U.S. Department of Commerce, National Bureau of Standards, Washington, D.C. 20235.
- [33] N.A. Bailey, J.N. Hay, D.M. Price, *Thermochim. Acta*, **367-368** (2001) 425.
- [34] G.W. Scherer, in: *Materials Science and Technology*, vol. 9 (J. Zarzycki, ed.) VCH, Cambridge, 1991, UK.
- [35] M.J. Richardson, A.G. Savill, *Polymer*, **16** (1975) 753.
- [36] S.M. Rekhson, A.V. Bulaeva, O.V. Mazurin, *Sov. J. Inorg. Mater.*, **7** (1971) 622.
- [37] O.V. Mazurin, *J. Non-Cryst. Solids*, **25** (1977) 130.
- [38] M.T. Mora, in: *Amorphous Insulators and Semiconductors*, (M.F. Thorpe, M.I. Mitkova, eds.) Kluwer Academic Publishers, 1997, London, p. 57.
- [39] J.M. Hutchinson, P. Kumar, *Thermochim. Acta*, in press.
- [40] A.J. Pappin, J.M. Hutchinson, M.D. Ingram, *J. Non-Cryst. Solids*, **172-174** (1994) 584.
- [41] I.M.Hodge, *J. Non-Cryst. Solids*, **169** (1994) 211.
- [42] M.M.A. Imran, D. Bhandari, N.S. Saxena, *Mater. Sci. Eng.*, **A292** (2000) 56.
- [43] J.M. Saiter, J. Ledru, A. Hamou, A. Zumailan, *Mater. Lett.*, **33** (1997) 91.
- [44] S.O. Kassap, S. Yannacopoulos, *Phys. Chem. Glasses*, **31** (1990) 71.
- [45] C.T. Moynihan, S.K. Lee, M. Tatsumisago, T. Minami, *Thermochim. Acta*, **280** (1996) 153.
- [46] C.A. Angell, *J. Phys. Chem. Solids*, **49** (1988) 863.
- [47] R. Böhmer, K.L. Ngai, C.A. Angell, D.J. Plazek, *J. Chem. Phys.*, **99** (1993) 4201.
- [48] W. Kauzmann, *Chem. Rev.*, **43** (1948) 219.
- [49] F.H. Stillinger, *J. Chem. Phys.*, **88** (1988) 7818.
- [50] P.G. Debenedetti, F.H. Stillinger, *Nature*, **410** (2001) 259.
- [51] R.J. Speedy, *Biophys. Chem.*, **105** (2003) 411.
- [52] P. Boolchand, D.G. Georgiev, B. Goodman, *J. Optoelectron. Adv. Mat.*, **3** (2001) 703.
- [53] J. Holubová, Z. Černošek, E. Černošková, *Book of Abstracts, Conf. on Non-Crystalline Inorganic Materials 2003*, Bonn, Germany, 2003, p. 99.
- [54] M. Chromčíková, J. Holubová, M. Liška, Z. Černošek, E. Černošková, *Ceramics*, **49**(2005) 91.
- [55] E. Černošková, J. Holubová, Z. Černošek, *J. Therm. Anal. Cal.* **56** (1999) 423.
- [56] Z. Černošek, E. Černošková, L. Beneš, *Mat. Letters*, **38** (1999) 336.
- [57] J. Málek, J. Šhánělová, *J. Non-Cryst. Solids* **351** (2005) 3458.
- [58] J.W. Christian, *The Theory of Transformation in Metals and Alloys*, 2nd Edition, Pergamon

Press, 1975, London.

- [59] D.W. Henderson, *J. Therm. Anal.*, **15** (1979) 325.
- [60] H. Yinnon, D.R. Uhlmann, *J.Non.-Cryst.Solids*, **54** (1983) 253-275.
- [61] J. Málek, *Thermochim. Acta*, **200** (1992) 257.
- [62] M. Avrami, *J.Phys.Chem.*, **7** (1939) 103-112.
- [63] M. Avrami, *J.Phys.Chem.*, **8** (1939) 212-224.
- [64] W.A. Johnson, R.F.Mehl, *Trans. Am. Inst. Min. (Metal.) Eng.*, **135** (1939) 416.
- [65] J. Šesták, G. Berggren, *Thermochim. Acta*, **3** (1971) 1-7.
- [66] J. Šesták, *Science of heat and thermophysical studies: a generalized approach to thermal analysis*, Elsevier, Amsterdam 2005
- [67] D.W. Henderson, D.G. Ast, *J. Non-Cryst. Solids*, **64** (1984) 43-70.
- [68] J. Málek, *Thermochim. Acta*, **200** (1992) 257.
- [69] J. Málek, *Thermochim. Acta*, **267** (1995) 61.
- [70] C. Wagner, J. Vázquez, M. Domínguez, P. Villares, R. Jiménez-Garay, *Mat. Chem. Phys.*, **43** (1996) 227.
- [71] F. Ye, K. Lu, *Acta Mater.*, **46** (1998) 5965.
- [72] J. Holubová, Z. Černošek, E. Černošková, *J. Therm. Anal. Cal.*, **62** (2000) 715.



Chapter 11

Isoconversional methods

11. APPLICATION OF ISOCONVERSIONAL METHODS FOR THE PROCESSES OCCURRING IN GLASSY AND AMORPHOUS MATERIALS

Peter Šimon, Paul S.Thomas

11. 1. Introduction

An attribute of amorphous/glassy state is that it is a solid state in which the atoms or molecules are not arranged in any long-range regular order. A glass is traditionally understood the product obtained from a melted material which has been cooled at a sufficiently high cooling rate to obtain a rigid material without crystallizing. The term amorphous state is more general; amorphous substances may be prepared also in other ways, not only from melt. Most of solid materials can be prepared in glassy/amorphous state so that many branches of science are touched with the problem of amorphous state properties, such as the glass science, polymer science, metallurgy, biology, pharmaceutical science and further scientific disciplines.

Due to the absence of the long-range order, the glassy/amorphous state is generally a metastable, non-equilibrium state and, therefore, there exists a thermodynamic driving force towards crystallization. The crystallization itself is an exothermic process; hence, thermoanalytical methods, such as differential scanning calorimetry (DSC) and differential thermal analysis (DTA), are convenient and extensively employed in studying the kinetics of phase transformations due to their straightforwardness and ease of use.

Experimental data on the kinetics of crystallization are treated using two different approaches. The first one is the model-fitting approach when the experimental data are mostly interpreted in terms of the nucleation-growth model formulated by *Avrami* [1-3]. This model describes the time dependence of the fractional crystallization in the following form:

$$\alpha = 1 - \exp\left[-(kt)^m\right] \quad (1)$$

where α is the conversion of the crystallization, k and m are constants with respect to time, t . The constant m means the number of crystal growth dimensions. After the differentiation with respect to time, the rate equation called *Johnson-Mehl-Avrami-Kolmogorov* (JMAK) equation is obtained [1-6]:

$$\frac{d\alpha}{dt} = km(1-\alpha)\left[-\ln(1-\alpha)\right]^{1-1/m} \quad (2)$$

The validity of Eq. (2) is based on the assumptions of isothermal crystallization conditions and homogeneous nucleation or heterogeneous nucleation at randomly dispersed preexisting nuclei. Further, it is assumed that the growth rate of crystals is independent of time and is the same in all directions (isotropic crystal growth) [7-9].

The first approach assumes that the mechanism of the process is known and, subsequently, the rate equation based on the mechanism is derived. The kinetic curves of conversion vs. time/temperature are then fitted to the kinetic model. The methods are

summarized in a number of publications, see for example [6,7,10-14] and also in other chapters of this book.

Another equation routinely applied is the *Šesták and Berggren* equation [15]:

$$\frac{d\alpha}{dt} = k\alpha^m (1-\alpha)^n [-\ln(1-\alpha)]^p \quad (3)$$

This equation is a combined form of differential equations suggested for the reactions controlled by the movement of phase boundaries, by simple nucleation, by nucleation followed by nuclei growth and by diffusion. The (often non-integer) exponents m , n and p serve merely for fitting but can be eventually associated with the exponents in JMAK equation. The last logarithmic term in Eq. (3) is often neglected using thus only two parameter ($m + n$) equations [16] bearing a resemblance to a logistic function.

In the alternative, the isoconversional approach, the kinetic analysis is carried out over a set of kinetic runs at a fixed value of conversion. This approach is often labelled “model-free” since the value of conversion function for the fixed value of conversion is implicitly involved in one of the adjustable parameters [10,17-19] and the reaction rate is a function of temperature only.

The isoconversional methods can be crudely divided into two groups, i.e., the isothermal methods and the methods at linear heating. Isothermal crystallization studies are generally quite time-consuming. In addition, there is a transient period with ill-defined temperature when establishing the isothermal regime which may bring about a systematic error in the results obtained. The isothermal isoconversional method is analyzed, e.g., in [18]. On the contrary, a DSC or DTA measurement performed at a constant heating rate is much more rapid and enables several transformations to be identified covering a wide temperature range [20]. Therefore, the experiments with constant heating rate are much more widely applied to study the processes of crystallization and attention will be paid only to them in this chapter. The group of isoconversional methods with linear heating can be further subdivided into differential, integral and incremental methods. The number of papers and textbooks outlining the basic ideas of the isoconversional methods, analysing the advantages and drawbacks and demonstrating their use, is almost countless, see for example [10,17-19] and the references cited therein.

In this chapter, fundamentals of the isoconversional methods are summarised and their use for the processes of crystallization and glass transition are reviewed.

11.2. Single-step approximation

In this section, a purely formal approach to the condensed phase kinetics will be presented. Mechanisms of the processes in condensed phase are very often unknown or too complicated to be characterized by a simple kinetic model. Rate of these processes is generally a function of temperature and conversion:

$$\frac{d\alpha}{dt} = \Phi(T, \alpha) \quad (4)$$

The single-step approximation employs the assumption that the function Φ in Eq. (4) can be expressed as a product of two separable functions independent of each other, the first one, $k(T)$, depending solely on the temperature T and the other one, $f(\alpha)$, depending solely on the conversion of the process, α :

$$\Phi(T, \alpha) = k(T)f(\alpha) \quad (5)$$

Combining Eqs. (4) and (5), the rate of the complex multi-step condensed-state process can be formally described as [16,18,21]

$$\frac{d\alpha}{dt} = k(T)f(\alpha) \quad (6)$$

Eq. (6) is mostly called the general rate equation. Indeed, it resembles a single-step equation, even though it is a representation of the kinetics of a complex condensed-phase process. For a complex process, each step should be described by its own rate equation. The single-step approximation thus resides in substituting a generally complex set of kinetic equations by the sole single-step kinetics equation. Eq. (6) represents a mathematical formulation of the single-step approximation.

The temperature function in Eq. (6) is mostly considered to be the rate constant and the conversion function is believed to reflect the mechanism of the process. It was discussed in [22] that this interpretation of the both functions may not be correct. Since Eq. (6) is a formulation of the single-step approximation, the functions $k(T)$ and $f(\alpha)$ represent, in general, just the temperature and conversion components of the kinetic hypersurface [21,22]. The kinetic hypersurface is a three-dimensional dependence of conversion on temperature and time [22].

Obviously, due to the prevailing interpretation of $k(T)$ as the rate constant, the Arrhenius equation is universally employed as the temperature function in both crystallization and glass transition processes:

$$k(T) = A \exp\left[-\frac{E}{RT}\right] \quad (7)$$

where A is the preexponential factor, E is the activation energy and R stands for the gas constant.

11.3. Isoconversional methods at linear heating

For the linear heating, the sample temperature, T , is expressed as

$$T = T_0 + \beta t \quad (8)$$

where T_0 is the starting temperature of the measurement and β stands for the heating rate. As mentioned above, the kinetic parameters are obtained from a set of kinetic runs where the evaluation is carried out at the fixed conversion α .

11.3.1. Integral methods

Assuming the Arrhenius temperature dependence of the rate constant, combination of Eqs.(6) and (7) gives:

$$\frac{d\alpha}{dt} = A \exp\left[-\frac{E}{RT}\right] f(\alpha) \quad (9)$$

After the separation of variables and integration, the latter equation gives the result:

$$\int_0^\alpha \frac{d\alpha}{f(\alpha)} = A \int_0^{t_\alpha} \exp\left[-\frac{E}{RT}\right] dt \quad (10)$$

where t_α is the time at which the fixed conversion α is reached, i.e. the isoconversional time. After some manipulation, Eq. (10) can be rewritten as:

$$1 = A_{\alpha} \int_0^{t_{\alpha}} \exp\left[-\frac{E_{\alpha}}{RT}\right] dt \quad (11)$$

where the kinetic parameter A_{α} given as:

$$A_{\alpha} = \frac{A}{F(\alpha) - F(0)} \quad (12)$$

The function F is a primitive function of $1/f$ and the subscript “ α ” designates the fixed value of conversion at which the parameters A_{α} and E_{α} are calculated. This designation is introduced since the values of kinetic parameters quite often depend on the conversion α . Eq. (11) should hold for any temperature regime and enables calculation of the time at which the fixed conversion α is reached.

For the linear heating and from the combination of Eqs. (8) and (11), it can be obtained [18]:

$$\beta = A_{\alpha} \int_0^{T_{\alpha}} \exp\left[-\frac{E_{\alpha}}{RT}\right] dT \quad (13)$$

where T_{α} is the temperature at which the fixed conversion α is reached, i.e. the isoconversional temperature. The lower integration limit in Eq. (13) is usually set $T_0 = 0$ K since no process is observed to occur in the sample at the starting temperature of the experiment.

The experiment is arranged in that way that the isoconversional temperature is measured as a function of heating rate. The temperature integral at the right side of Eq. (13) cannot be expressed in a closed form so that Eq. (13) is written in an unnatural form as a function of independent variable on the dependent variable.

A number of methods have been proposed to overcome the problem of applying Eq. (13) in the treatment of experimental data. In the 1950s and 1960s, in particular, when thermoanalytical methods became increasingly popular, a demand for the treatment of experimental data arose; however, the computational facilities were basic relative to the facilities available today and, hence, treatment was aimed at obtaining simple formulas. An example is the *Flynn-Wall-Ozawa* (FWO) method [23,24] which uses the *Doyle* [25] approximation for the temperature integral in Eq. (13):

$$\ln \beta = -5.331 + \ln \frac{A_{\alpha} E_{\alpha}}{R} - 1.052 \frac{E_{\alpha}}{RT_{\alpha}} \quad (14)$$

The dependence of $\ln \beta = f(1/T_{\alpha})$ should be a straight line with the slope equal to $(-1.052E_{\alpha}/R)$ and the intercept $(-5.331 + \ln(A_{\alpha} E_{\alpha}/R))$. Thus, from the slope and intercept the kinetic parameters A_{α} and E_{α} can be obtained.

Application of the *Coats-Redfern* approximation [26] leads to the *Kissinger-Akahira-Sunose* (KAS) method [27]:

$$\ln \left(\frac{\beta}{T_{\alpha}^2} \right) = \ln \frac{A_{\alpha} R}{E_{\alpha}} - \frac{E_{\alpha}}{RT_{\alpha}} \quad (15)$$

For this method, the dependence of $\ln(\beta/T_\alpha^2) = f(1/T_\alpha)$ should be a straight line with the slope equal to $(-E_\alpha/R)$ and the intercept $\ln(A_\alpha R/E_\alpha)$. From the slope and intercept of Eq. (15), the kinetic parameters A_α and E_α can be obtained.

In order to achieve a better precision, an advanced isoconversional method has been developed by *Vyazovkin* [28]. As all other integral isoconversional methods, this method is based on the assumption that the reaction model is independent of the heating program, $T(t)$. By the virtue of this assumption, the right side of Eq. (13) divided by the corresponding value of the heating rate is equal to unity for any given value of β . This equality is equivalent to the condition of a minimum of the following function

$$\sum_{i \neq j}^n \sum_{j=1}^n \frac{I(E_\alpha, T_{\alpha i}) \beta_j}{I(E_\alpha, T_{\alpha j}) \beta_i} = \min \quad (16)$$

where $I(E_\alpha, T_{\alpha i})$ is the integral term on the right side of Eq. (13) corresponding to the i -th heating rate.

The parameters A_α and E_α in Eq. (13) can be obtained by minimizing the sum of squares between experimental and calculated values for various heating rates as proposed in [29-31]:

$$\sum_{i=1}^n (T_{\alpha i, \text{exptl}} - T_{\alpha i, \text{calcd}})^2 = \min \quad (17)$$

where $T_{\alpha i, \text{exptl}}$ is the temperature measured for a specific degree of conversion, α , and the calculated value of $T_\alpha (T_{\alpha i, \text{calcd}})$ for a given heating rate is given by Eq. (13). The integration indicated in Eq. (13) is carried out by the Simpson method. Minimization of the sum of squares given by Eq. (17) is carried out by the simplex method.

11.3.2. Differential method

For the linear temperature program, from Eq. (9) one can obtain

$$\left(\frac{d\alpha}{dt} \right)_\alpha = \left(\beta \frac{d\alpha}{dT} \right)_\alpha = Af(\alpha) \exp \left[-\frac{E_\alpha}{RT_\alpha} \right] = A_\alpha \exp \left[-\frac{E_\alpha}{RT_\alpha} \right] \quad (18)$$

The subscript “ α ” at the reaction rate indicates the rate at the fixed conversion α . In Eq. (18), the parameter A_α is defined as the product $Af(\alpha)$. Eq. (18) is generally used after a logarithmic transformation:

$$\ln \left(\beta \frac{d\alpha}{dT} \right)_\alpha = \ln A_\alpha - \frac{E_\alpha}{RT_\alpha} \quad (19)$$

From Eq. (19) it follows that the dependence of $\ln(\beta d\alpha/dT)_\alpha = f(1/T_\alpha)$ should be linear. The method represented by Eq. (19) is named after *Friedman* [32]. Since the *Friedman* method employs instantaneous rate values, it is very sensitive to experimental noise and tends to be numerically unstable [27,33].

11.3.3. Incremental method

Using incremental methods can obviate the trouble with the instability of the *Friedman* method. An incremental integral isoconversional method has been suggested

recently [6]. For the linear heating program, if Eq. (10) is integrated within the conversion increment α_1 - α_2 , one can arrive at:

$$\beta = \frac{A}{F(\alpha_2) - F(\alpha_1)} \int_{T_1}^{T_2} \exp\left[-\frac{E_\alpha}{RT}\right] dT = A_\alpha \int_{T_1}^{T_2} \exp\left[-\frac{E_\alpha}{RT}\right] dT \quad (20)$$

In this case, the definition of the parameter A_α is obvious from Eq. (20). Due to the integration, the influence of experimental noise is eliminated to a great extent. For an infinitely small increment, Eq. (20) degenerates into Eq. (18) [18]. If it is set $\alpha_1=0$ at $T_1=0$, Eq. (20) degenerates into Eq. (13). From Eq. (20), the incremental isoconversional method to account for variation in the activation energy [33] can be derived.

11.4. Kissinger method

The *Kissinger* method [34] was originally developed for the n-th order decomposition reactions; however, it is very popular in characterizing the transformation kinetics. It is based on the fact that with increasing heating rate the temperature of the peak maximum in DSC records, corresponding to the maximum rate of the process observed, is shifted towards a higher value. After expressing the rate of the process as a product of the Arrhenius temperature function and the n-th order conversion function and finding the temperature of the peak maximum, one can arrive at the formula

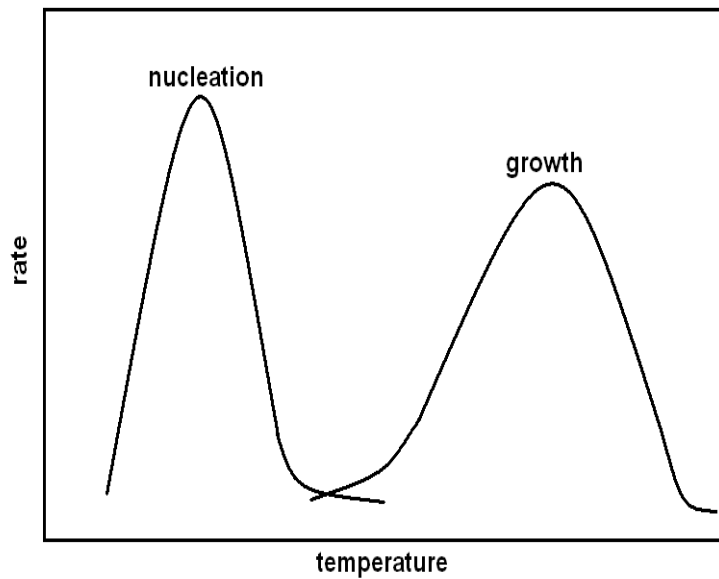
$$\ln\left(\frac{\beta}{T_p^2}\right) = C - \frac{E_a}{RT_p} \quad (21)$$

where C is a constant and T_p is the temperature at the maximum rate of the process, i.e. the peak temperature. Comparing Eqs. (15) and (21), it can be seen that the Kissinger method is just a special case of isoconversional method where the constant conversion corresponds to the maximum rate of the process observed.

Henderson [8] has published a critical analysis of the nonisothermal methods which shows under what conditions the Kissinger method is rigorously justified. In Ref. [35] it has been reasoned that the Kissinger method used for determining the activation enthalpy of the nucleation-and-growth process can be used for a grain-growth process as well. *Matusita* and *Sakka* criticized the arbitrary and unsupported application of the Kissinger plot [36].

5. Ozawa methods

Various modifications of the Avrami theory have been applied to nonisothermal crystallization. *Ozawa* [37] developed an equation to analyze the crystallization of polymers from the melt at constant cooling rate by replacing $t = T/\beta$. Later [38], he derived rigorous equations for the nonisothermal kinetics of crystal growth from pre-existing nuclei with negligible concurrent random nucleation [38]. The equations have been derived for two models. The first model describes crystal growth from impurity or from a nucleating agent where the number of nuclei is independent of the thermal history of the material under study.



The second model describes crystal growth for the case where homogenous nucleation is initiated by cooling the specimen to a temperature below that which crystal growth may occur. The temperature range for random nucleation is much lower than that for the crystal growth, and the two temperature ranges are separated clearly as illustrated in Fig.1

Fig.1: Schematic temperature dependence of the rates of nucleation and growth.

In the second model, the number of the nuclei existing in the beginning of the growth is constant during the growth but dependent on the thermal history in the nucleation temperature range.

For the isoconversional evaluation, for the first model the FWO-like or KAS-like equations have been obtained depending on the approximation used for the evaluation of the temperature integral. For the second model, the following equations have been obtained:

$$\ln \beta = C_1 - 1.052 \frac{m}{m+1} \frac{E_a}{RT_\alpha} \quad (22)$$

$$\ln \frac{\beta^{m+1}}{T_\alpha^{2m}} = C_2 - \frac{E_a}{RT_\alpha} \quad (23)$$

where m is the number of crystal growth dimensions. It has been proven that the conversion at the maximum rate is independent of the heating rate and is equal to $\alpha=0.632$.

In the kinetic analysis of experimental data, it is first necessary to determine whether the process under study corresponds to the first model or to the second one. For this purpose it is useful to observe the effect of thermal history in the nucleation temperature range by changing the cooling and heating rates in a wide range. In the case of the mechanism of the crystal growth from impurity the area of the crystallization peak does not depend on the cooling and heating rates in the nucleation temperature range. In the case of random nucleation, the peak area is inversely proportional to the heating and cooling rates.

The value of m can be obtained from isothermality dependence $\ln(-\ln(1-\alpha))=f(\ln\beta)$. The dependence should be linear with the slope equal to m in the case of the

first model and $m+1$ in the case of the second model [38]. An example of the isotherm analysis can be found in [39].

Kinetic modeling of the crystallization process is further complicated by the origin of nucleation; either bulk or surface. Recently, *Ozawa* presented the kinetic analysis of crystal growth from pre-existing surface nuclei [40]. *Ozawa's* model demonstrates that the thickness of the specimen has a significant influence on the crystallization process and, therefore, nucleation mechanism and sample geometry are further aspects that should also be taken into account in the application of theory to the kinetic analysis. It has been concluded that the *Friedman* plot (plot of logarithm of the rate of the process vs. the reciprocal absolute temperature at a given conversion – Eq.(18)) for results using the specimen of the same thickness is similar to the Arrhenius plot, and the temperature dependence of the growth rate constant can be obtained. When the plot is linear, we can get the activation energy of the process. Furthermore, the *Flynn – Wall - Ozawa* plot (plot of logarithm of the heating rate vs. the reciprocal absolute temperature at a given conversion – Eq.(14)) and the *Kissinger - Sunose - Akahira* plot (plot of logarithm of the heating rate by the square of the absolute temperature vs. the reciprocal absolute temperature at a given conversion – Eq.(15)) can also be applied, but only for results obtained by heating and for the process of Arrhenius type temperature dependence. If the plot is not linear or if the obtained activation energy is dependent on the conversion, the process under observation is not the process in which a single elementary process is involved and the temperature dependence of the rate constant is not of the Arrhenius type.

Identification of internal bulk and surface crystallization can be made by the method of *Ray and Day* [41].

11.6. Description of the kinetics of nucleation by the induction period of crystallization

Nucleation and crystallization processes are of fundamental importance in the control of glass formability in technological applications where the formation of nuclei and the subsequent crystal growth must be avoided. On the other hand, the formation of nuclei and crystal growth by controlled crystallization can give rise to polycrystalline solids containing residual glass phase, e.g. the glass ceramics. Therefore, it is very important to evaluate the thermal stability of glasses against crystallization. In [29], a new criterion for evaluating the thermal stability of glasses based on the induction period of crystallization was suggested.

Processes occurring in the condensed phase often exhibit an induction period. During the induction period, the technique used registers no signal so that the sample seemingly remains unchanged. As a matter of fact, the induction period is a preparatory stage where the species and intermediates necessary for the occurrence of the main stage of the process are formed. The end of induction period is determined as a sudden increase in the rate of the process under study, i.e. it is determined as the onset time for isothermal measurements or the onset temperature for measurement with linear heating [31]. The rate of crystal nucleation in glass reaches the maximum at temperatures somewhat higher than the glass transition temperature and then decreases rapidly with increasing temperature, while the rate of crystal growth reaches the maximum at a temperature much higher than the temperature at which the nucleation rate is highest

[42,43] (see Fig.1). It is discussed in [29] that the end of the induction period of crystallization corresponds to completion of the nucleation stage of crystallization.

The theory of induction periods is based on the single-step approximation [44]. Since Eq. (6) is general, it is assumed that it also describes the kinetics of the processes occurring during the induction period. For the induction periods, Eq. (10) takes the form:

$$\int_0^{\alpha_i} \frac{d\alpha}{f(\alpha)} = \int_0^{t_i} A \exp\left[-\frac{E}{RT}\right] dt \quad (24)$$

The degree of conversion α_i in Eq. (24) represents the completed conversion of the processes occurring during the induction period and corresponds to the end of the induction period, i.e., to the start of the main process detected by the apparatus, and t_i is the length of the induction period. Further it is assumed that the degree of conversion α_i is the same for any temperature. Then, for a constant heating rate, one can get:

$$\beta = \int_0^{T_i} \frac{dT}{A_n \exp\left[\frac{B_n}{T}\right]} \quad (25)$$

where T_i is the temperature of the end of induction period, i.e. the onset temperature of the crystallization peak. The parameter B_n is related to the activation energy of nucleation through the relationship $B_n = E_n/R$. The point of the steep increase of the DTA record due to crystallization is taken as the onset temperature. Since the existence of the processes occurring during induction period is not detected by the apparatus used, the conversion α_i at the measured onset temperature is unknown. This is the main peculiarity of the method. However, as for any isoconversional methods, it is assumed that the conversion α_i has the same value for any heating rate or for any temperature regime. For a chosen constant temperature the length of induction period can be expressed by an Arrhenius-like relationship:

$$t_n = A_n \exp\left[\frac{B_n}{T}\right] \quad (26)$$

where t_n is the nucleation time coincident with the length of induction period, A_n and B_n are kinetic parameters.

The method of study the kinetics of nucleation by induction periods of crystallization has several simplifications. First, it is implicitly assumed that the nucleation is athermal, i.e. it is not observed by DSC or DTA. Second, it is implicitly assumed that the crystal growth begins immediately after the nucleation stage as depicted in Fig.1. There can be a gap between the nucleation and growth stages which is not reflected in the upper integration limit of Eq. (25). The upper integration limit is always the quantity that can be measured, i.e. the onset temperature of crystallization, T_i . Third, after reaching its maximum, the rate of nucleation decreases with increasing temperature (see Fig.1). This is not reflected in the temperature function. The temperature function employed is the Arrhenius equation. This function increases monotonously with increasing temperature.

The validity of the criterion was verified by applying it to $\text{Li}_2\text{O} \cdot 2\text{SiO}_2 \cdot n\text{TiO}_2$ and $\text{Li}_2\text{O} \cdot 2\text{SiO}_2 \cdot n\text{ZrO}_2$ systems [29,31] and for the crystallization of metallic glasses [30]. Despite the oversimplifications mentioned above, the method reliably identifies the

differences in the stability of glasses. No relationship has been found between the values of the activation energies and the order of stabilities.

The peak maximum of DSC/DTA record corresponds to the maximum rate of the crystal growth, i.e. to the moment when the growing crystals start to interconnect. Given that the degree of conversion at the peak in the DTA curve during crystallization does not depend on the heating rate, the kinetic parameters of the crystal growth can be obtained by the incremental isoconversional method Eq. (20) where the integration is carried out between T_i and T_p :

$$\beta = \int_{T_i}^{T_p} \frac{dT}{A_g \exp\left[\frac{B_g}{T}\right]} \quad (27)$$

Duration of the growth under isothermal conditions can be calculated using an equation analogical to Eq. (26):

$$t_g = A_g \exp\left[\frac{B_g}{T}\right] \quad (28)$$

where A_g and B_g are the kinetic parameters describing the crystal growth. From the linear-heating measurements, the parameters A_n and B_n in Eq. (25), or the parameters A_g and B_g in Eq. (27), can be obtained. Application of Eq. (28) was tested for $\text{Li}_2\text{O} \cdot 2\text{SiO}_2 \cdot n\text{TiO}_2$ and $\text{Li}_2\text{O} \cdot 2\text{SiO}_2 \cdot n\text{ZrO}_2$ systems [31]. Again, the differences in the stability of glasses were reliably identified and no relationship was found between the values of the activation energies and the order of stabilities.

11.7. Other isoconversional methods

A method intermittently encountered in the literature is the one by *Matusita et al.* [43]. In a similar manner to *Ozawa* [38], they considered the temperature-dependent growth of crystals. Based on the condition of maximum crystallization rate at the peak temperature, they derived the equation

$$\ln\left(\frac{\beta^n}{T_p^2}\right) = -1.052m \frac{E_a}{RT_p} + \text{constant} \quad (29)$$

where m is the crystal growth dimension, $n = m + 1$ for a quenched glass containing no nuclei and $n = m$ for a glass containing sufficiently large number of nuclei. This method was criticized by *Ozawa* for being too crude [38].

Starink and *Zahra* [45] derived a quantitative model for the progress of a nucleation and growth controlled reaction during heating at a constant rate. The model incorporates nucleation, growth and impingement, takes account of temperature dependent solubility and distinguishes between diffusion controlled growth and linear growth. The model was applied to the DSC data on the precipitation in Al-Si alloys. Despite the fact that different assumptions have been adopted, the equation similar to the Kissinger method was obtained [45].

Michaelsen and *Dahms* [20] applied the JMAK theory for nucleation and growth transformations. They derived a model with three kinetic parameters, i.e. the activation energy, transformation order and frequency factor. The potential of the proposed model was demonstrated on the Ti-Al multilayer thin film. They obtained a Kissinger-type equation for the determination of activation energy.

In the literature, further isoconversional methods describing the kinetics of phase transformation can be encountered, such as [46,47]. The theory of the amorphous state crystallization is under continuous development.

11. 8. Isoconversional description of the kinetics of glass transition

Upon cooling, the material changes from a supercooled liquid to a solid. The transition from the liquid state to the glass, at a temperature below the equilibrium melting point of the material, is called the glass transition and the corresponding temperature is the glass transition temperature, T_g . The glass transition temperature is approximately the temperature at which the viscosity of the liquid exceeds a value about 10^{12} Pa·s. The glass transition is often formally considered to be a second-order phase transition since a jump in the heat capacity or expansion coefficient of the sample at the glass transition temperature is observed.

DSC and DTA are routinely applied to the measurement of the glass transition temperature. The transition appears as a step in the heat capacity - temperature curve [19]. An increase in the heating rate causes this step to shift to higher temperatures suggesting that the process is thermally activated. This shift can be used for determining the activation energy of the process using some of the equations (13)-(16). However, the value of activation energy depends significantly on the method used for the determination of T_g . The glass temperature can be obtained as temperature of an extrapolated onset, inflection point, midpoint in the c_p curve or the position of a peak upon heating [19]. The differently defined values of T_g correspond to different stages of the glass transition. It has been reported [48,49] that the value of activation energy decreases with increase in the T_g value.

To explore this phenomenon more closely, *Vyazovkin* et al. [50] employed an isoconversional method that enabled the assessment of the variations in activation energy throughout the glass transition. The conversion α was defined as

$$\alpha = \frac{c_p - c_{pg}}{c_{pl} - c_{pg}} \quad (30)$$

where c_p is the observed heat capacity, and c_{pg} and c_{pl} are the glassy and liquid heat capacities, respectively. Since the values of c_{pg} and c_{pl} depend on temperature, they are extrapolated to the glass transition region.

The application of the isoconversional method revealed a decreasing dependence of the activation energy on α for maltitol [19]. The variability in E has been found to correlate with the dynamic fragility of the glass-forming systems [19].

11.9. Discussion

11.9.1. Discriminating ability of the isoconversional methods

First of all it will be analyzed whether it is possible to discriminate between various mechanisms of nucleation and growth from the output kinetic parameters of isoconversional methods.

The purely formal approach represented by the single-step approximation lead to the derivation of FWO, KAS, *Vyazovkin* and our method represented by Eqs. (13)-(16). All the methods originate in Eq. (13) so that they are, essentially, equivalent. The

differences in the values of kinetic parameters obtained by various methods are just the consequence of different approximations of the temperature integral and different objective functions used in the computational methods of data treatment. The kinetic parameters should be obtained from the source experimental data since any transformation of the data leads to the deformation of the distribution of errors, heteroskedasticity and a shift in the position of minima of the sum of squares between experimental and calculated values [18]. Thus, the methods using the objective functions with transformed experimental data may lead to biased estimates of activation parameters comparing to the values using directly the source experimental data.

The Kissinger method is based on the model of n-th order reaction. However, the resulting Eq. (21) is a KAS-type equation given by Eq. (15). In Section 5, two models of crystal growth are analyzed and the equations for isoconversional treatment of experimental data are derived. The first model of crystal growth from impurity leads to the FWO-like or KAS-like equations. The second model of random nucleation leads to Eqs. (22) or (23). On the first sight, Eq. (23) is not analogous to Eq. (15). Nonetheless, Eq. (23) can be rewritten into the form

$$\ln \frac{\beta}{T_{\alpha}^2} = \frac{C_2}{m+1} - \frac{1}{m+1} \frac{E_a}{RT_{\alpha}} - \frac{2}{m+1} \ln T_{\alpha} \quad (31)$$

Eq. (31) thus represents a KAS-like dependence with the apparent activation energy

$$E_{\text{app}} = \frac{E_a - 2RT_{\alpha}}{m+1} \quad (32)$$

In the single-step approximation, no meaning is ascribed to the temperature and conversion functions. *Kissinger*, *Ozawa* and *Matusita* methods were derived by imposing a single mechanistic process for the conversion function ($f(\alpha)$) in the generalized rate equation (Eq. (6)). Both approaches lead to the same type of equations. Thus it can be surmised that no mechanistic conclusions can be drawn solely from the results obtained from the isoconversional methods. Additional information is needed from varying heating rates in the nucleation temperature range, from isotherm and model-fitting methods. Furthermore, it is advisable to employ other techniques besides thermal analysis, such as X-ray spectroscopy, FTIR, etc.

11.9.2. Dependence of the activation energy on conversion

Some authors mean that the application of isoconversional methods naturally leads to effective activation parameters dependent on the extent of conversion [33,51,52]. Quite serious conclusions are occasionally drawn from the dependence of activation energy on conversion; for example, the parameters of the Hoffman-Lauritzen equation have been evaluated from the dependence of activation energy of polyethylene terephthalate crystallization on conversion [53].

It is necessary to stress that the temperature and conversion functions in Eqs. (5) and (6) should be separable. The imperative of the function separability is reasoned in detail in [21,54]. For the integral isoconversional methods, assumption of a constant value of activation energy is implicit and inevitable for the separation of the variables in Eq. (10). One can easily prove that, even for the case of the simplest linear dependence of activation energy on α , the variables cannot be separated. Any dependence of the activation energy on conversion invalidates Eq. (10) which means that all the

subsequent formulas are mathematically incorrect. Thus, the conclusions drawn from the dependence of the activation energy on conversion can hardly be considered trustworthy.

Hence, for the sake of function separability the activation energy should be constant throughout the whole range of conversions. Ozawa has also concluded that when the activation energies vary with conversion, the observed process is inconsistent with the model from which the theory and the method are derived and we should abandon the kinetic analysis [38]. The function separability is implicitly involved in the concepts of master plots and reduced time.

11.9.3. Physical meaning and use of the kinetic parameters

The concept of activation energy generally identifies the energy connected with the barrier to the bond redistribution in an elementary reaction [55]. When employing the isoconversional methods, a complex multi-step process is treated as a single-step one. The activation energy obtained is thus apparent and does not have any mechanistic significance so that there is no reason to interpret the apparent activation energy in terms of a free energy barrier. Kinetic studies frequently appear to be motivated in reporting magnitudes of the activation parameters. In some articles, the magnitude of activation energy reported appears to be the principal result, perhaps even the dominant motivation for the investigation. However, compelling reasons for such a preoccupation with the measurements of activation parameters are not usually provided [52]. The value of activation energy cannot be used for far-reaching conclusions frequently encountered in academic environment, such as systematization of the information available, developing theories on the mechanisms of the processes, etc. [18].

For practitioners, the values of the apparent activation parameters enable modeling of processes without the necessity of a deeper insight into their mechanisms. This is the principal merit of the isoconversional methods. For modeling, Eq. (11) can be employed enabling the calculation of the isoconversional temperatures, times, reaction rates, etc. In order to integrate Eq. (11), both parameters A_α and B_α are needed. Temperature can be an arbitrary function of time [18].

11.9.4. Non-Arrhenian character of crystallization and glass transition

As discussed in the paper by Ozawa [56], crystallization is a complicated process, so that sometimes it is not well understood. The following two points are essential to be considered:

1. In general, crystallization proceeds by two elementary processes, i.e., nucleation and growth. The temperature ranges of these processes are different from each other (see Fig.1).

2. Generally, the Arrhenius law does not hold for these processes, except for special cases. For both processes, the temperature dependences are so complicated that the rate constants decrease below the melting temperature with increase of the temperature, and they increase in a lower temperature range with increase of the temperature. Approximated relations for constant rate of heating or cooling hitherto used for non-isothermal kinetics of chemical reactions are based on the Arrhenius law. Therefore, these relations cannot generally be applied for non-isothermal kinetics of crystallization [56].

Hence, neither nucleation nor crystal growth kinetics obey the Arrhenius law. Despite this, in the field of thermal analysis, evaluation of the crystallization data is carried out exclusively on the methods based on the Arrhenius law. For the crystal growth it has been derived in [57] that the apparent activation energy can be expressed as

$$E_g = E_0 + \frac{\Delta H}{1 - \exp\left[\frac{\Delta H(1 - T/T_m)}{RT}\right]} \quad (33)$$

where E_0 is the true activation energy of the crystal growth, T_m is the crystal melting temperature and ΔH is the enthalpy change of the liquid to crystal phase transformation. From Eq. (33) it is obvious that the apparent activation energy depends strongly on temperature. The apparent activation energy of the crystal growth becomes negative for temperatures higher than

$$T = T_m \frac{\Delta H}{RT_m \ln\left(1 + \frac{\Delta H}{E_0}\right) + \Delta H} \quad (34)$$

A similarly complicated relationship could be derived from the paper [57] for the apparent activation energy of nucleation.

It is necessary to emphasize that the apparent activation energies are obtained from the treatment of experimental data based on the Arrhenius equation [16,58]. This treatment implicitly involves the assumption that the kinetic data can be approximated by the Arrhenius equation within the range of temperatures measured. When using the methods based on the Arrhenius equation, the extrapolation of the results outside the temperature range of measurement must not be carried out [31].

Koga and *Šesták* showed that even the kinetic compensation effect mathematically results from the exponential form of the rate constant [16,59-61]. A change of activation energy is thus compensated by the same change in temperature or in the logarithm of the pre-exponential factor [59]. Non-Arrhenian functions in connection with the glass transition are discussed in ref. [62].

References 11

- [1] M. Avrami: *Kinetics of phase change. I. General theory*. J.Chem.Phys. 7 (1939) 1103-1112.
- [2] M. Avrami: *Kinetics of phase change. II. Transformation-time relations for random distribution of nuclei*. J.Chem.Phys. 8 (1940) 212-224.
- [3] M. Avrami: *Kinetics of phase change. III. Granulation, phase change, and microstructure kinetics of phase change*. J.Chem.Phys. 9 (1941) 177-184.
- [4] A.E. Kolmogorov: *On the statistic theory of metal crystallization (in Russian)*. Izv. Akad. Nauk SSSR, Ser.Mat. 1 (1937) 355-359.
- [5] W.A. Johnson and R.F. Mehl: *Reaction kinetics in processes of nucleation and growth*. Trans.Amer.Inst.Mining Metall.Petro.Engrs. 135 (1939) 416-458.
- [6] J.W. Christian: *The Theory of Transformations in Metals and Alloys*, 2nd Edition, Pergamon Press, New York, 1975.

- [7] D.W. Henderson: *Experimental analysis of non-isothermal transformations involving nucleation and growth*. J.Therm.Anal. 15 (1979) 325-331.
- [8] D.W. Henderson: *Thermal analysis of nonisothermal crystallization kinetics in glass forming liquids*. J.Non-Cryst.Solids 30 (1979) 301-315.
- [9] M.P. Shepilov, D.S. Baik: *Computer simulation of crystallization kinetics for the model with simultaneous nucleation of randomly-oriented ellipsoidal crystals*. J.Non-Cryst.Solids 171 (1994) 141-156.
- [10] J. Šesták: *Thermophysical Properties of Solids. Their Measurements and Theoretical Analysis*, Elsevier, Amsterdam, 1984.
- [11] J. Málek: *Kinetic analysis of crystallization processes in amorphous materials*. Thermochim.Acta 355 (2000) 239-253.
- [12] E.D. Zanutto: *Crystallization of liquids and glasses*. Brazil.J.Phys. 22 (1992) 77-84.
- [13] E.D. Zanutto: *The applicability of the general theory of phase transformations to glass crystallization*. Thermochim.Acta 280/281 (1996) 73-82.
- [14] M.C. Weinberg: *Glass-formation and crystalization kinetics*. Thermochim.Acta 280/281 (1996) 63-71.
- [15] J. Šesták and G. Berggren: *Study of kinetics of mechanism of solid state reactions at increasing temperature*. Thermochim.Acta 3 (1971) 1-12.
- [16] J. Šesták: *Science of heat and thermophysical studies*. Elsevier, Amsterdam 2005.
- [17] M.E. Brown, D. Dollimore, A.K.Galwey: *Comprehensive chemical kinetics, Vol. 22*. Elsevier, Amsterdam, 1980.
- [18] P. Šimon: *Isoconversional methods – fundamentals, meaning and application*. J.Therm.Anal.Calorim. 76 (2004) 123-132.
- [19] S. Vyazovkin: *Isoconversional kinetics*. In: *Handbook of Thermal Analysis and Calorimetry, vol.5., chapter 13*. Ed. by M. Brown and P. Gallagher, ELSEVIER 2007, ISBN-13: 978-0-444-53123-0.
- [20] C. Michaelson and C. Dahms: *On the determination of nucleation and growth kinetics by calorimetry*. Thermochim.Acta 288 (1996) 9-27.
- [21] P. Šimon: *Considerations on the single-step kinetics approximation*. J.Therm.Anal.Calorim. 82 (2005) 651-657.
- [22] P. Šimon: *Single-step kinetics approximation employing non-Arrhenius temperature functions*. J.Therm.Anal.Calorim. 79 (2005) 703-708.
- [23] J.H. Flynn and L.A. Wall: *A quick, direct method for the determination of activation energy from thermogravimetric data*. Polym.Lett., 4 (1966) 323-328.
- [24] T. Ozawa: *A new method of analyzing thermogravimetric data*. Bull.Chem.Soc.Jpn. 38 (1965) 1881-1886.
- [25] C.D. Doyle: *Estimating isothermal life from thermogravimetric data*. J.Appl.Polym.Sci. 6 (1962) 639-642.
- [26] A.W. Coats and J.P. Redfern: *Kinetic parameters from thermogravimetric data*. Nature 201 (1964) 68-69.
- [27] N. Sbirrazzuoli, Y. Girault and L. Elégant: *Simulations for evaluation of kinetic methods in differential scanning calorimetry. Part 3 — Peak maximum evolution methods and isoconversional methods*. Thermochim.Acta, 293 (1997) 25-37.

- [28] S. Vyazovkin: *Evaluation of activation energy of thermally stimulated solid-state reactions under arbitrary variation of temperature*. J.Comput.Chem. 18 (1997) 393-402.
- [29] P. Šimon, K. Nemčeková, E. Jóna, A. Plško and D. Ondrušová: *Thermal stability of glass evaluated by the induction period of crystallization*. Thermochim.Acta 428 (2005) 11-14.
- [30] P. Šimon, E. Illeková and S.C. Mojumdar: *Kinetics of crystallization of metallic glasses studied by non-isothermal and isothermal DSC*. J.Therm.Anal.Calorim. 83 (2006) 67-69.
- [31] P. Šimon, E. Jóna and V. Pavlík: *Thermal properties of oxide glasses. Part III. Thermal stability of $\text{Li}_2\text{O}\cdot 2\text{SiO}_2\cdot n\text{MeO}_2$ glasses (Me=Ti, Zr)*. J.Therm.Anal.Calorim. 94 (2008) 421-425.
- [32] H.L. Friedman: *Kinetics of thermal degradation of char-forming plastics from thermogravimetry. Application to a phenol plastic*. J.Polym.Sci. 6C (1963) 183-195.
- [33] S. Vyazovkin: *Modification of the integral isoconversional method to account for variation in the activation energy*. J.Comput.Chem. 22 (2001) 178-183.
- [34] H.E. Kissinger: *Reaction kinetics in differential thermal analysis*. Anal.Chem. 29 (1957) 1702-1706.
- [35] L.C. Chen and F. Spaepen: *Analysis of calorimetric measurements of grain growth*. J.Appl.Phys. 69 (1991) 679-688.
- [36] K. Matusita and S. Sakka: *Kinetic study of the crystallisation of glass by differential scanning calorimetry*. Phys.Chem.Glasses 20 (1979) 81-84.
- [37] T. Ozawa: *Kinetic analysis of derivative curves in thermal analysis*. Polymer 12 (1971) 150-158.
- [38] T. Ozawa: *Nonisothermal kinetics of crystal growth from preexisting nuclei*. Bull.Chem.Soc.Jpn. 57 (1984) 639-643.
- [39] P. Thomas and P. Šimon: *A pseudoisothermal kinetic analysis of the recrystallisation of nickel sulphide measured by non-isothermal DSC*. J.Therm.Anal.Calorim. 80 (2005) 77-80.
- [40] T. Ozawa: *Kinetics of growth from pre-existing surface nuclei*. J.Therm.Anal.Calorim. 82 (2005) 687-690.
- [41] C.S. Ray and D.E. Day: *Identifying internal and surface crystallization by differential thermal analysis for the glass-to-crystal transformations*. Thermochim.Acta 280/281 (1996) 163-174.
- [42] D. Turnbull and M.H. Cohen: *Modern aspects of the vitreous state*. Ed. by J.D.Mackenzie, Butterworth, London 1960, pp. 38-62.
- [43] K. Matusita, T. Komatsu and R. Yokota: *Kinetics of non-isothermal crystallization process and activation energy for crystal growth in amorphous materials*. J.Mater.Sci. 19 (1984) 291-296.
- [44] P. Šimon: *Induction periods – theory and applications*. J.Therm.Anal.Calorim. 84 (2006) 263-270.
- [45] M.J. Starink and A.M. Zahra: *An analysis method for nucleation and growth controlled reactions at constant heating rates*. Thermochim.Acta 292 (1997) 159-168.

- [46] J.A. Augis and J.E. Bennett: *Calculation of the Avrami parameters for heterogeneous solid state reactions using a modification of the Kissinger method.* J.Therm.Anal.Calorim. 13 (1978) 283-292.
- [47] A. Dobrevá, A. Stoyanov and I. Gutzow: *Analysis of differential scanning calorimetry data on the nonisothermal kinetics of crystallization in polymer melts.* J.Appl.Polym.Sci.: Appl.Polym.Symp. 48 (1991) 473-480.
- [48] C.A. Angell, R.C. Stell and W. Sichina: *Viscosity-temperature function for sorbitol from combined viscosity and differential scanning calorimetry studies.* J.Phys.Chem. 86 (1982) 1540-1542.
- [49] D Lacey, G. Nestor and M.J. Richardson: *Structural recovery in isotropic and smectic glasses.* Thermochim.Acta 238 (1994) 99-111.
- [50] S. Vyazovkin, N. Sbirrazzuoli and I. Dranca: *Variation of the Effective Activation Energy Throughout the Glass Transition.* Macromol.Rapid Commun. 25 (2004) 1708-1713.
- [51] S. Vyazovkin and C.A. Wight: *Kinetics in solids.* Ann.Rev.Phys.Chem. 48 (1997) 125-149.
- [52] S. Vyazovkin: *Kinetic concepts of thermally stimulated reactions in solids: a view from a historical perspective.* Int.Revs.Phys.Chem. 19 (2000) 45-60.
- [53] S. Vyazovkin and N. Sbirrazzuoli: *Isoconversional Approach to Evaluating the Hoffman–Lauritzen Parameters (U^* and K_g) from the Overall Rates of Nonisothermal Crystallization.* Macromol. Rapid Commun. 25 (2004) 733–738.
- [54] P. Šimon: *The single-step approximation: Attributes, strong and weak sides.* J.Therm.Anal.Calorim. 88 (2007) 709-715.
- [55] S. Vyazovkin: *Reply to “What is meant by the term ‘variable activation energy’ when applied in the kinetics analyses of solid state decompositions (crystolysis reactions)?”* Thermochim.Acta 397 (2003) 269-271.
- [56] T. Ozawa, *Comments on “The non-isothermal devitrification of glasses in the CaO 4GeO₂–SrO 4GeO₂ composition range” by M. Catauro and A. Marotta (in Thermochimica Acta 371 (2001) 121–126).* Thermochim.Acta 386 (2002) 99–100.
- [57] J.R. Frade, C.M. Queiroz and M.H. Fernandez: *Re-examination of effects of nucleation temperature and time on glass crystallization.* J.Non-Cryst.Solids 333 (2004) 271-277.
- [58] N. Koga and J. Šesták “*Crystal nucleation and growth kinetics of lithium diborate glass by thermal analysis*” J. Am. Ceram. Soc. 83 (2000) 1753-1760.
- [59] N. Koga and J. Šesták: *Kinetic compensation effect as a mathematical consequence of the exponential rate constant.* Thermochim.Acta 182 (1991) 201-208.
- [60] N. Koga and J. Šesták “*Further aspects of the kinetic compensation effect*” J. Therm. Anal. 37 (1991) 1103-108.
- [61] N. Koga, “*Kinetic compensation effect, a review*” Thermochim. Acta 244 (1994) 1 and 258 (1995) 145-149
- [62] L.M. Hodge: *Enthalpy relaxation and recovery in amorphous materials.* J.Non-Cryst.Solids 169 (1994) 211-266.



Chapter 12

Crystallization kinetics

12. CRYSTALLIZATION KINETICS IN AMORPHOUS AND GLASSY MATERIALS

Daniel Švadlák, Pavla Honcová, Jiří Málek

12. 1. Introduction

The crystal growth in non-crystalline materials can be described within two approaches. The first one is direct microscopic observation of the growing crystal. This approach is based on different physical features of the amorphous and crystalline phase. Only methods of optical and electron microscopy (including their modifications) are used in this case. Morphology and isotropy of crystal growth is analyzed. The crystal-liquid interface can be described more closely by means of the standard growth models.

The other often used access is the macroscopic approach which is based on an indirect study of the crystal growth. Such an indirect approach can be based on the specific behavior of the studied system during the crystallization process - thermal behavior of the system, intensities of diffractive lines of partially and fully crystalline samples, electrical conductivity or magnetic features of the crystalline phase. Among the most often used indirect methods belong the thermoanalytical techniques performed under isothermal or non-isothermal conditions. The essential part of the macroscopic approach is the kinetic analysis that provides certain kinetic parameters of the crystallization process (activation energy of the process, certain kinetic model for the process and the parameters of the model).

The main subject of this article is to analyze the combination of microscopic and macroscopic studies of the crystal growth of Sb_2S_3 in highly undercooled melts of the $(\text{GeS}_2)_x(\text{Sb}_2\text{S}_3)_{1-x}$ system. The obtained results will be interpreted using the standard phenomenological models for the crystal-liquid interface. The interconnection and correlations between the microscopic and macroscopic approach can help to find a physical meaning of the kinetic parameters obtained from the DSC analysis.

12. 2. Theoretical part

Three phenomenological models are normally used for the description of the interface controlled crystal growth [1]: *normal growth*, *screw dislocation growth* and *two-dimensional surface nucleated growth*. These models are based on different assumptions concerning the interface and the nature of the sites on the interface where atoms are added and from where are removed.

12.2.1. Normal growth

According to the normal growth model [1-4] the interface must be *rough* on an atomic scale and is characterized by a large fraction of step sites where atoms can preferably be added or removed, which can be done from any other site on the crystal-liquid interface. This model does not require all sites on the interface to be step sites, but merely that the interface is characterized by a sizable fraction of such sites and that this fraction does not change appreciably with undercooling. According to this assumption and if the motion on the scale of a molecular diameter is involved in the interface jump process then the growth rate for normal growth model can be expressed as [5]

$$u = f \cdot \frac{D}{a_0} \cdot [1 - \exp(-\frac{\Delta G}{R \cdot T})] \approx f \cdot \frac{D}{a_0} \cdot [1 - \exp(-\frac{\Delta H_{JM} \cdot \Delta T}{R \cdot T \cdot T_M})] \quad (1)$$

where u is the crystal growth rate, f is the interface site factor (the fraction of preferred growth sites on the interface) which is for this model close to the unity, a_0 is the distance advanced by the interface in a unit kinetic process (in the range of a molecular diameter), D is an effective diffusion coefficient of the molecular species that control the atomic or molecular attachment at the crystal-liquid interface, ΔG is the free energy change upon crystallization, R is the gas constant and T is the absolute temperature of the interface in Kelvin degrees. For small departures from equilibrium, this model predicts a linear relation between the growth rate and undercooling.

The free energy, ΔG , for a single component system can be expressed by

$$\Delta G = \Delta H_{JM} \cdot \frac{T_M - T}{T_M} - \int_T^{T_M} \Delta c_p dT + T \int_T^{T_M} \frac{\Delta c_p}{T} dT \quad (2)$$

where ΔH_{JM} is the heat of fusion per mole, $\Delta T = T_M - T$ is the undercooling where T_M is the melting point, Δc_p is the difference in specific heat between the liquid and crystal measured at T . If Δc_p is constant over the temperature range then Eq. 2. can be rewritten with the Hoffman expression [6]:

$$\Delta G = \Delta H_{JM} \cdot \frac{T_M - T}{T_M} - \Delta c_p \left[(T_M - T) - T \ln \frac{T_M}{T} \right] \quad (3)$$

If Δc_p is unknown or equal to zero then the value of ΔG is calculated according to the Turnbull's [5] approximation ($\Delta G = \Delta H_{JM} \cdot \Delta T / T_M$).

12.2.2. Screw dislocation growth

According to the screw dislocation model [1-4,7] the growth takes place at step sites provided by screw dislocations intersecting the interface. Such dislocations would provide a self-perpetuating ledge as atoms are added to the interface. The proportion of this step sites on the interface is defined by parameter f given by:

$$f = \frac{a_0 \cdot \Delta G}{4\pi \cdot \sigma \cdot V_M} \cong \frac{\Delta T}{2\pi \cdot T_M}$$

where σ is the specific surface energy of the melt and V_M is the molar volume. The crystal growth rate is calculated according Eq. 1. with f defined by Eq. 4. For typical departures from equilibrium the value of f is in the range of 10^{-2} to 10^{-3} ; it increases with increasing undercooling. For small departures from equilibrium this model predicts the growth rate which varies with the square of undercooling. The model provides a useful representation of growth if the interface is smooth on an atomic scale and imperfect, so that the growth takes place only at step sites provided by screw dislocation ramps.

12.2.3. Two-dimensional surface nucleated growth

In the 2-D surface nucleated growth model [1-3,8], the growth occurs by the formation and lateral growth of two-dimensional nuclei on the interface. The surface nucleation model is given by

$$u = B \cdot \frac{D_u}{a_0^2} \cdot \exp(-\frac{\pi \cdot a_0 \cdot V_M \cdot \sigma_E^2}{3 \cdot k_B \cdot T \cdot \Delta G}) \approx B \cdot \frac{D_u}{a_0^2} \cdot \exp(-\frac{C}{T \cdot \Delta T}) \quad (5)$$

$$B = \frac{(\pi \cdot n_s \cdot a_0^5 / 3)^{1/3}}{\Gamma(4/3)} \cdot [1 - \exp(-\frac{\Delta G}{R \cdot T})]^{2/3} \quad (6)$$

$$C = \frac{\pi \cdot a_0 \cdot V_M \cdot T_M \cdot \sigma_E^2}{3 \cdot k_B \cdot \Delta H_{fM}} \quad (7)$$

where k_B is the Boltzmann's constant and σ_e is the specific surface energy of the nucleus, V_M is the molar volume, n_s is the number of growth sites per unit area, and Γ is the gamma function (an extension of the factorial function to real and complex numbers). The growth rate of this model varies exponentially with the undercooling and for small undercooling is negligible. This model is applicable if the interface is smooth on an atomic scale and readily formed (free of intersecting screw dislocations).

12.2.4. Reduced growth rate

The operative growth mechanism can be deduced from a plot of the reduced growth rate U_R versus the undercooling ΔT . The reduced growth rate is given [3,9]

$$U_R = \frac{u \cdot \eta}{[1 - \exp(-\frac{\Delta G}{R \cdot T})]} \approx \frac{u \cdot \eta}{[1 - \exp(-\frac{\Delta H_{fM} \cdot \Delta T}{R \cdot T \cdot T_M})]} \quad (8)$$

where u is the crystal growth rate and η is the shear viscosity. Thus the reduced growth rate indicates the operative growth mechanism via the temperature dependence of the interface site factor. Hence, for normal growth where the interface site factor is essentially independent of temperature, the reduced growth rate versus undercooling plot is expected to be a horizontal line. The relation defined by Eq. 8. should yield a straight line with positive slope passing through the origin for screw dislocation growth, and a curve with increasing positive slope passing through the origin for 2-D surface nucleated growth (Fig. 1.).

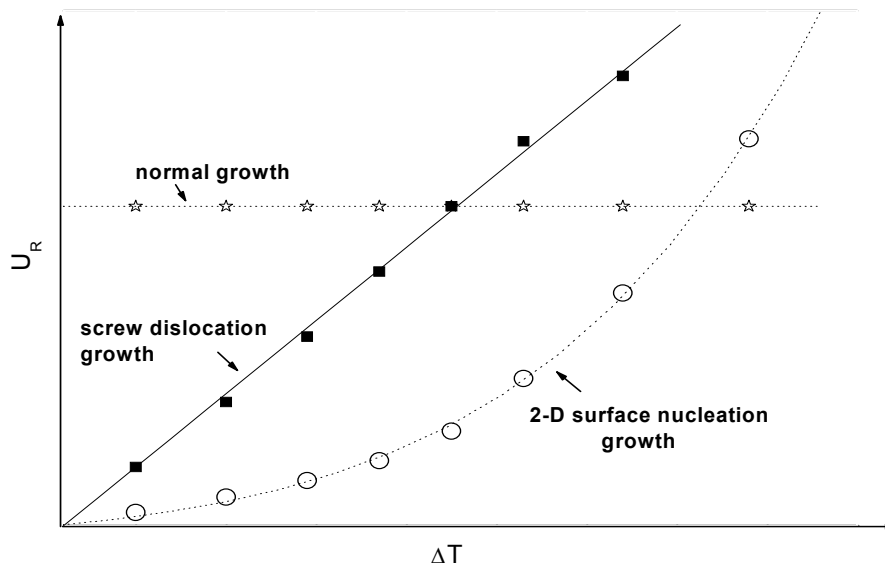


Fig.1.: Variations of the reduced growth rate U_R with ΔT for three limiting growth mechanism of crystal-liquid interface [10].

12.2.5. Entropy of fusion

The growth rate strongly depends on detailed structure of the interface. According to Jackson's treatment of the interface [1-3], the entropy of fusion can be used to classify materials with respect to their crystallization and melting behavior.

For materials characterized by low entropies of fusion ($\Delta S_{fM} < 2R$, where R is the universal gas constant and ΔS_{fM} is the entropy of fusion per atom) is the most closely packed interface plane rough (Fig. 2.A) on an atomic scale for both, the crystallization and the melting. The anisotropy of the growth is small. There should be no barrier to the advance of the interface in either process, defects have no significant influence on growth. The crystal-liquid interfaces are non-faceted for both, the crystallization and melting. The curves of melting rate and crystallization rate versus motive force (overheating or undercooling) continue with the same slope through the melting point. Examples of glassforming materials belonging to this group are SiO_2 , GeO_2 , GeS_2 and other summarized in Table 1. The description of crystal growth for these materials is carried out using the normal growth model.

The materials characterized by large entropies of fusion ($\Delta S_{fM} > 4R$) have the most closely packed interface plane smooth on an atomic scale (Fig. 2B) and the less closely packed interfaces is rough. The anisotropic growth is large. Defects strongly influence the growth so that the growth rate should not be described by the model of normal growth.

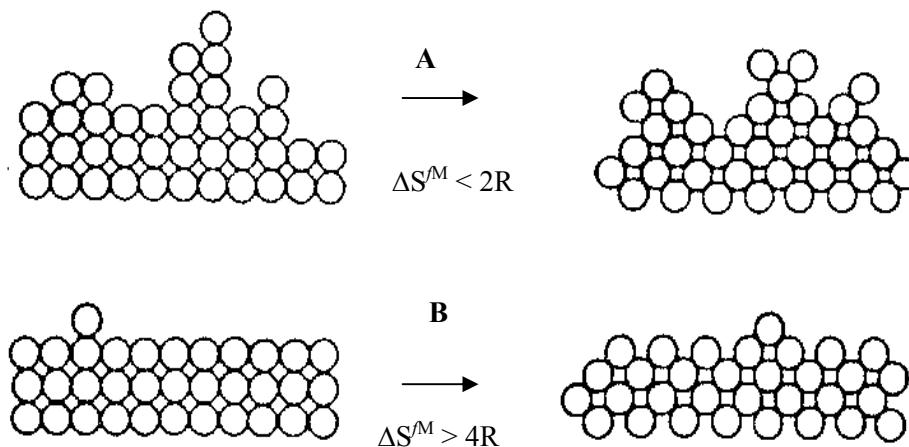


Fig. 2.: A –Crystal-liquid interface for materials characterized by low entropies of fusion ($\Delta S_{fM} < 2R$), B - Crystal-liquid interface for materials characterized by large entropies of fusion ($\Delta S_{fM} > 4R$) [3].

Because of the significant difference in interface site distributions for the crystallization and melting the pronounced asymmetry is observed in the vicinity of the melting point. Consequently, except for the limiting cases the growth rates of these materials are not well described by the standard models for surface nucleation and screw dislocation growth. Examples of glassforming materials belonging to this group are inorganic and chalcogenide glasses and some organic materials summarized in Table X.2.

Table 1.:
Materials with
low entropy of
fusion ($\Delta S_{m} < 2R$)

system	$\Delta S_{m}/R$	system	$\Delta S_{m}/R$	system	$\Delta S_{m}/R$	system	$\Delta S_{m}/R$	system	$\Delta S_{m}/R$
<i>Glass systems</i>		<i>Glass systems</i>		<i>Glass systems</i>		<i>Organic materials</i>		<i>Tellurium substances</i>	
GeO ₂ [11,12]	1.3	PbO·2B ₂ O ₃ [3,27,28]	30;15.1	Cadmium [19]	1.3	Butyl chloride [22]	< 2	Sb ₂ Te ₃ [32]	13.3
GeS ₂ [13-15]	1.2;1.8	K ₂ O·4B ₂ O ₃ [29]	13.4	Zinc [19]	1.2	Butyl bromide [22]	< 2	As ₂ Te ₃ [34,37]	8.3;10.4
SiO ₂ [16-18]	0.4;0.5	LiO ₂ ·2B ₂ O ₃ [8,25]	12.2	Nickel [19]	1.2	Cykllohexane [22]	< 2	PbTe [38]	5.8
<i>Metals and semi-metals</i>		SiO·2B ₂ O ₃ [30]	11.6	Silver [19]	1.1	Cykllohexanol [22]	< 2	SnTe [38]	5.0
Tin [19,20]	1.7	Cs ₂ O·3B ₂ O ₃ [31]	8.6	Cobalt [19]	1.1	Methylalcohol [22]	< 2	GeTe [38]	4.9
Selenium [21]	1.5	<i>Sulfur substances</i>		Gold [19]	1.1	<i>Others</i>			
Aluminium [19]	1.4	P ₄ S ₁₀ [32]	8.8	Copper [19]	1.1	Ammoniumchloride [22]	< 2R		
		Sb ₂ S ₃ [32,33]	5.9; 6.7	Lead [19,20]	1.0	P ₄ [20]	1.0		
		As ₂ S ₃ [32,34]	5.9	Indium [19]	0.9				
		As ₄ S ₄ [35]	5.1						
<i>Silicate glasses</i>		<i>Borate glasses</i>		<i>Selenium substances</i>		<i>Organic materials</i>		<i>Tellurium substances</i>	
MgO·Al ₂ O ₃ :SiO ₂ [23]	13.4	PbO·2B ₂ O ₃ [3,27,28]	30;15.1	S ₈ (monoclinic) [20]	4.2	tri- α -naphthyl benzene [39]	10.7		
CaO·Al ₂ O ₃ :2SiO ₂ [24]	10.9	K ₂ O·4B ₂ O ₃ [29]	13.4			glycerine [1,40]	7.5		
CaO·MgO·2SiO ₂ [9]	10.0	LiO ₂ ·2B ₂ O ₃ [8,25]	12.2			phenylsalicylate [1]	7		
Na ₂ O·2CaO·SiO ₂ [25]	6.6	SiO·2B ₂ O ₃ [30]	11.6			1,2-diphenyl benzene [3,41]	6.8		
LiO ₂ ·2SiO ₂ [25,26]	5.6	Cs ₂ O·3B ₂ O ₃ [31]	8.6						
2Na ₂ O·CaO·3SiO ₂ [25]	5.4								
Na ₂ O·2SiO ₂ [9]	4.0	<i>Sulfur substances</i>							
K ₂ O·2SiO ₂ [24]	4.2	P ₄ S ₁₀ [32]	8.8						
CaO·SiO ₂ [25]	4.2	Sb ₂ S ₃ [32,33]	5.9; 6.7						
		As ₂ S ₃ [32,34]	5.9						
		As ₄ S ₄ [35]	5.1						

Table 2.: Materials with high entropy of fusion $\Delta S_{m} \geq 4R$

12.3. Experimental

The microscopic and macroscopic approaches were applied in the analysis of crystallization kinetics of Sb_2S_3 in $(\text{GeS}_2)_x(\text{Sb}_2\text{S}_3)_{1-x}$ glasses. The compositions where $x = 0.1 - 0.5$ were prepared by the synthesis from pure elements (5N purity). A mixture of these elements (8-12 g of total weight) was placed in a quartz ampoule. The ampoule was then evacuated to a pressure of 10^{-4} Pa for 0.5 h, sealed and then placed in a rocking furnace. After heat treatment and homogenization at 950 °C for 17.5-20 h, the ampoule was rapidly cooled in water with ice. The amorphous nature of the quenched glass was examined by X-ray diffraction analysis and optical microscopy was used to verify the homogeneity of prepared materials. The glass transition temperature, T_g , the maximum of crystallization peak, T_P , and the melting point, T_M , were determined by differential scanning calorimetry at heating rate 10 Kmin^{-1} (Table 3.).

Table 3.: *The values of glass transition temperature, T_g , the maximum of crystallization peak, T_P , and the melting point, T_M , during non-isothermal crystallization of $(\text{GeS}_2)_x(\text{Sb}_2\text{S}_3)_{1-x}$ glass for heating rate 10 K.min^{-1} .*

$(\text{GeS}_2)_x(\text{Sb}_2\text{S}_3)_{1-x}$	T_g °C	T_P °C	T_M °C
0.1	230	289	541
0.2	238	340	520
0.3	245	365	470
0.4	256	395	456
0.5	266	-	410

12.3.1. Optical measurements of crystal growth

Optical measurements of crystal growth were performed by using Olympus BX60 microscope and thin samples of primary materials (glasses about 1.5 mm thick) polished to optical quality. These samples were previously heat-treated in a computer-controlled furnace at selected temperatures for various times (central hot zone temperature was constant within ± 0.5 °C). Temperatures were selected within a proper range (see Table 4.) optimal for each composition. These temperature intervals represent an optimum choice because outside of them the crystal growth rates are either too high or too low to be observed by microscopy. However, because of a sizable difference in reflectivity between the crystalline and amorphous phases it was possible to observe crystal growth kinetics in reflected light for a relatively wide temperature range. Only $(\text{GeS}_2)_{0.5}(\text{Sb}_2\text{S}_3)_{0.5}$ composition was also studied using transmission polarized light. All heat-treated samples were extensively examined and the sizes of the well-developed crystals grown in the bulk material were measured and recorded.

It was found that the crystallization process starts in all cases predominantly within the bulk of the annealed glass and the crystals grow from randomly distributed nuclei. The morphology of growing crystals changes significantly with composition in the $(\text{GeS}_2)_x(\text{Sb}_2\text{S}_3)_{1-x}$ system (Fig. 3.).

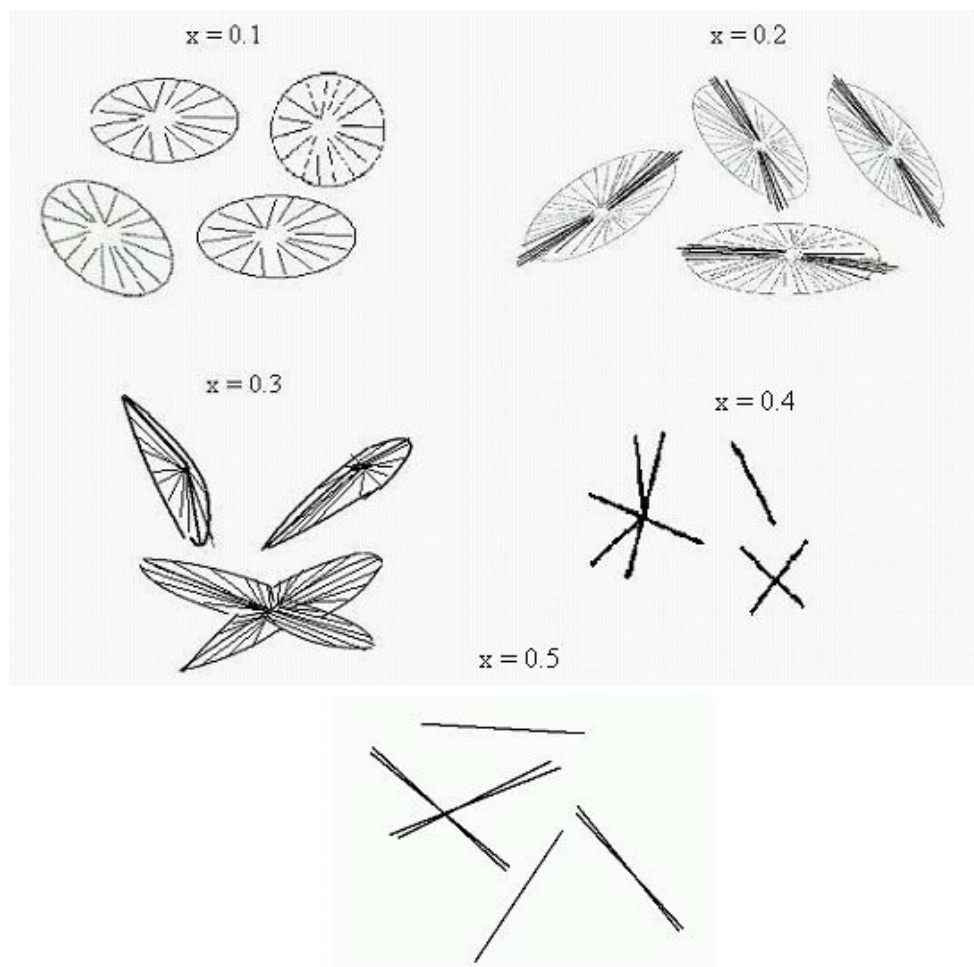


Fig. 3.: The morphology of growing crystals changes with the composition of glass from the oval crystalline aggregates for $(\text{GeS}_2)_{0.1}(\text{Sb}_2\text{S}_3)_{0.9}$ to the needle-shaped crystalline aggregates in the case of $(\text{GeS}_2)_{0.5}(\text{Sb}_2\text{S}_3)_{0.5}$.

Table 4.: Temperature ranges of crystallization studied by optical microscopy and by differential scanning calorimetry during isothermal (iso) and non-isothermal experiments (non-iso) for the $(\text{GeS}_2)_x(\text{Sb}_2\text{S}_3)_{1-x}$ system.

Composition	optical microscopy	DSC iso °C	DSC non-iso (heating rate 10 K.min ⁻¹)
	°C		°C
0.1	218.5-241.5	290-310	280-342
0.2	252.0-282.5	316-328	309-393
0.3	271.0-310.0	320-340	335-425
0.4	293.0-327.5	-	-
0.5	331.5-364.0	-	-

12.3.2. Calorimetric measurement of crystallization kinetics

The calorimetric experiments were performed by a Perkin-Elmer differential scanning calorimeter (DSC) Pyris 1 (calibrated with standards Hg, Ga, In, Sn, Pb and Zn). The bulk samples (about 30 mg) of the studied glass were prepared in the form of thin plates both-side

polished to optical quality. The measurements were performed in the standard aluminum pans under dry nitrogen atmosphere. The crystallization behavior was studied under isothermal and non-isothermal conditions for $x = 0.1; 0.2$ and 0.3 . Heating rates of $150\text{--}200 \text{ Kmin}^{-1}$ were used in the initial step of isothermal measurements, i.e. when heating the samples from laboratory temperature to the selected isotherm temperature.

The crystallization behavior was observed under non-isothermal and isothermal conditions. One glass transition and one exothermal crystallization peak were observed during heating the samples up to $550 \text{ }^\circ\text{C}$. The crystallization peaks were found within the temperature range given in Table 4. for the heating rates $5\text{--}30 \text{ Kmin}^{-1}$. Temperature ranges where the isothermal crystallization occurred are shown in Table 4. too. These intervals represent an optimum condition for isothermal measurement. At higher temperatures the crystallization response is too fast and due to significant time constant of the DSC instrument some part of experimental data may be lost. Lower temperatures bring another difficulty because the signal-to-noise ratio negatively affects the accuracy of the measurement.

12. 4. Results and discussion

12.4.1. Optical measurements of crystal growth

Optical measurements of Sb_2S_3 crystal growth in $(\text{GeS}_2)_x(\text{Sb}_2\text{S}_3)_{1-x}$ glasses ($x = 0.1 - 0.5$) were performed using optical microscope. The lengths of the crystallite long axis or diameters of aggregate crystalline structures were measured as a function of time at selected temperatures for different $(\text{GeS}_2)_x(\text{Sb}_2\text{S}_3)_{1-x}$ compositions (Table 4.). The time dependences of crystal length are linear for all temperatures and compositions. This type of behavior is typical for crystal growth controlled by interface kinetics. The logarithm of crystal growth rate u versus reciprocal temperature $1/T$ is shown in Fig. 4. The full lines correspond to the least-square fit of experimental data. The activation energy of crystal growth E_G was obtained from the slope of this plot (Table 5.), assuming the Arrhenius behavior

$$u(T) = u_0 \cdot e^{-\frac{E_G}{R \cdot T}} \quad (9)$$

where T is the temperature, u is the crystal growth rate, u_0 is the pre-exponential factor.

The operative growth mechanism can be then assessed from the reduced growth rate U_R given by the Eq. 8. For the calculations the value of entropy of fusion $\Delta S_M = 49.39 \text{ Jmol}^{-1}\text{K}^{-1}$ and melting point of Sb_2S_3 $T_M = 550 \text{ }^\circ\text{C}$ were used [33]. Fig. 5. shows the plot of U_R vs. undercooling ΔT calculated using the viscosity data reported for $(\text{GeS}_2)_x(\text{Sb}_2\text{S}_3)_{1-x}$ melts [42]. The positive curvatures of this plot suggest 2D surface nucleated growth for compositions $x = 0.1; 0.2$ and 0.3 . For compositions 0.4 and 0.5 straight lines were detected but the fits of 2D surface nucleated growth were still better. Therefore the kinetics of crystals growth was for all compositions described by the 2D surface nucleated growth. According to Eq. 5. the $\ln(u \cdot \eta)$ versus $(T \cdot \Delta T)^{-1}$ plot should be a straight line with negative slope. This plot is shown in Fig. X.6. for all studied compositions. It is seen that the predicted linear dependence is confirmed for crystal growth of Sb_2S_3 in the whole range of temperatures. The parameters B and $\ln(C)$ (Eq. 5.) corresponding to the slope and intercept of these lines were obtained by using the least-squares fit (Table 6.). The straight lines for all compositions do not have any breakpoints which means that the crystal growth mechanism does not change in the observed temperature range.

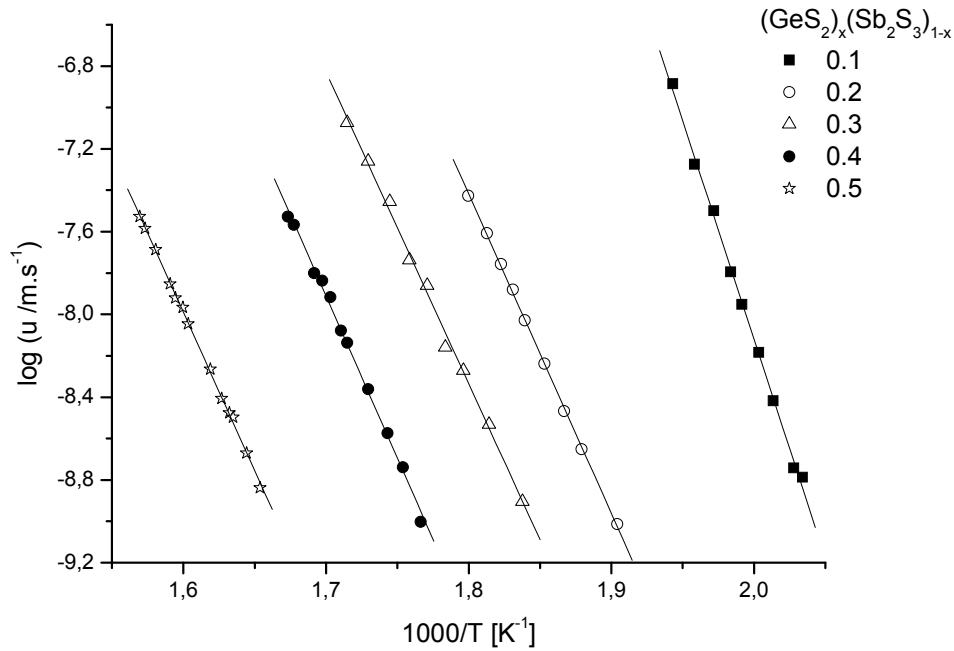


Fig. 4.: Arrhenius plot of the crystal growth rate dependence on temperature measured by optical microscopy for different compositions of $(\text{GeS}_2)_x(\text{Sb}_2\text{S}_3)_{1-x}$ glass. The lines correspond to the least-square fit of these data.

Table 5.: The activation energy of crystal growth E_G , activation energy of viscous flow E_η and activation energy of crystallization E_A (obtained by DSC) in highly undercooled $(\text{GeS}_2)_x(\text{Sb}_2\text{S}_3)_{1-x}$ melts.

$(\text{GeS}_2)_x(\text{Sb}_2\text{S}_3)_{1-x}$	growth data E_G kJ.mol^{-1}	viscosity data E_η kJ.mol^{-1}	E_A (DSC data)	
			non-isothermal (Kissinger) kJ.mol^{-1}	isothermal (isoconversional method) kJ.mol^{-1}
			0.1	405
0.2	296	438	178	268
0.3	288	485	167	242
0.4	274	400	-	-
0.5	293	423	-	-

In Table 7. are the maxima of crystal growth rate and corresponding temperatures estimated using the simplified Eq. 5.

Table 6.: Parameters B and $\ln C$ of 2-D surface nucleated growth model in Eq. 5. describing crystal growth kinetics in highly undercooled $(\text{GeS}_2)_x(\text{Sb}_2\text{S}_3)_{1-x}$ melts.

Composition of glass $(\text{GeS}_2)_x(\text{Sb}_2\text{S}_3)_{1-x}$	$B \times 10^6$ $[\text{K}^2]$	$\ln C$ $[\text{N.m}^{-1}]$
0.1	7.3 ± 0.6	52.0 ± 3.6
0.2	5.3 ± 0.2	34.1 ± 1.2
0.3	5.0 ± 0.2	30.0 ± 2.0
0.4	2.5 ± 0.1	14.7 ± 0.8
0.5	1.5 ± 0.1	5.9 ± 0.3

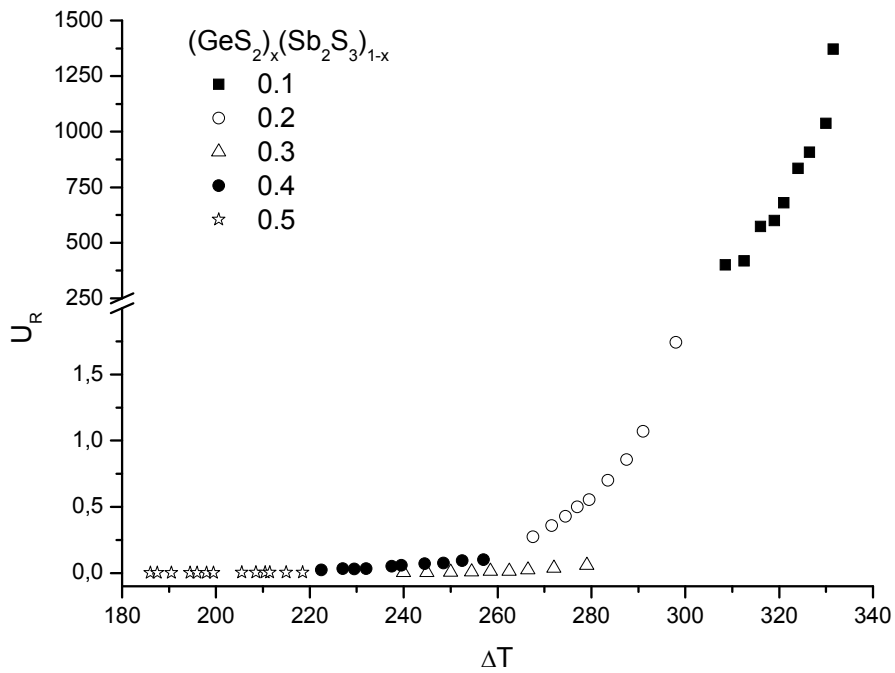


Fig. 5.: Reduced growth rate U_R versus undercooling ΔT for Sb_2S_3 crystal growth in highly undercooled $(\text{GeS}_2)_x(\text{Sb}_2\text{S}_3)_{1-x}$ melts.

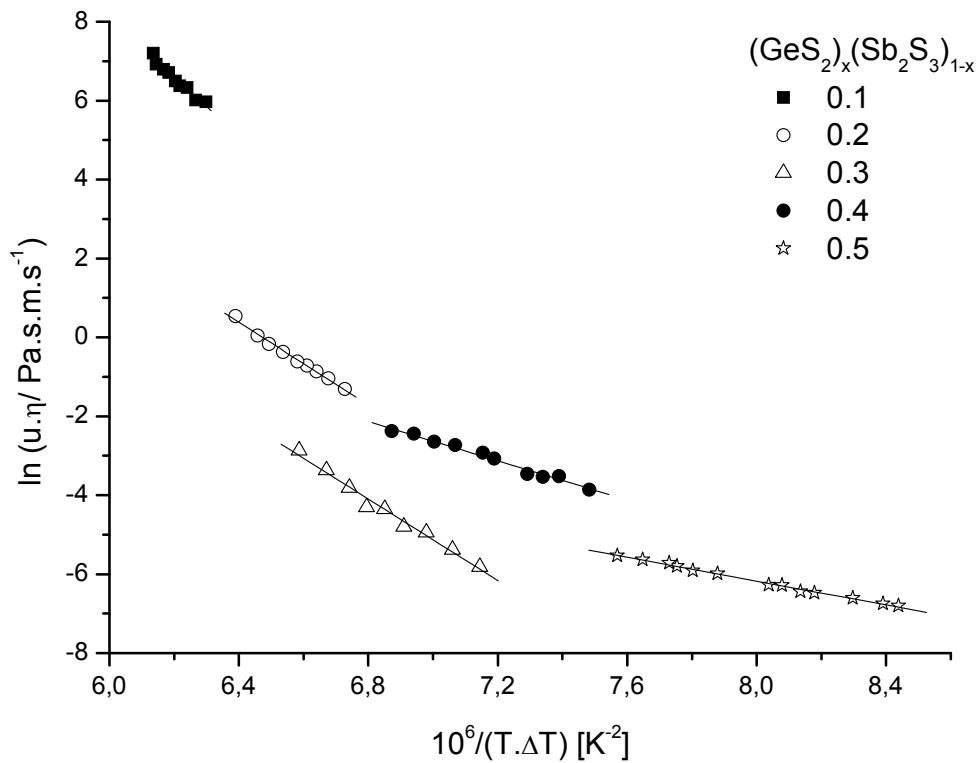


Fig. 6.: Plot of logarithm $\ln(u \cdot \eta)$ vs. $(T \cdot \Delta T)^{-1}$ for Sb_2S_3 crystal growth in $(\text{GeS}_2)_x(\text{Sb}_2\text{S}_3)_{1-x}$ undercooled melts. The lines correspond to the least-square fit of the data.

Table 7.: The calculated values of the maximum of crystal growth rate and the corresponding temperature for undercooled $(\text{GeS}_2)_x(\text{Sb}_2\text{S}_3)_{1-x}$ melts (the model was predicted using Eq. 5. with parameter B and C from Table 6.). The range of viscosity where the crystal growth was observed is shown in the last column.

$(\text{GeS}_2)_x(\text{Sb}_2\text{S}_3)_{1-x}$	T_{\max} °C	u_{\max} $\mu\text{m}\cdot\text{min}^{-1}$	$\log(\eta_{\text{growth}}/\text{Pa}\cdot\text{s})$ -
0.1	334	36886	9.48 – 11.92
0.2	346	69	6.85 – 9.25
0.3	357	44	4.54 – 7.66
0.4	389	28	5.85 – 7.97
0.5	421	20	4.57 – 6.43

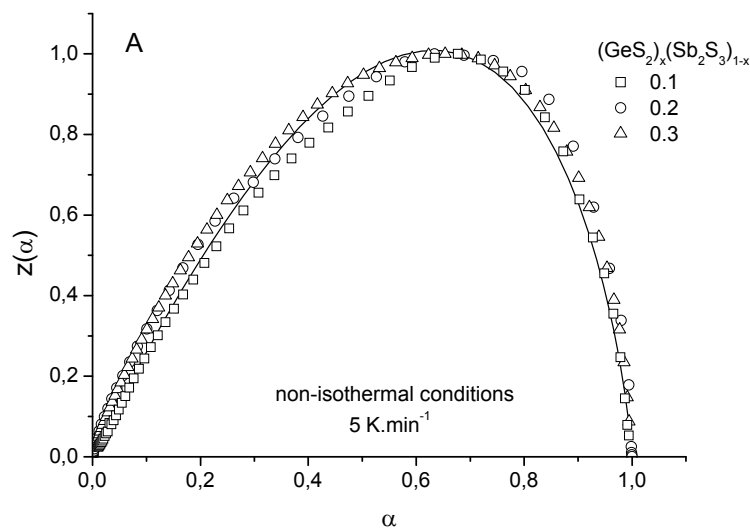
12.4.2. Calorimetric measurement of crystallization kinetics

It is assumed that measured heat flow Φ is proportional to the overall crystallization rate $d\alpha/dt$:

$$\Phi = \Delta H \cdot \frac{d\alpha}{dt} \quad (10)$$

where ΔH is the crystallization enthalpy and α is the conversion ratio. This assumption can be made for small samples and moderate heating rates assuming that temperature and calorimetric calibrations were done properly. As the enthalpy change ΔH is a constant the crystallization rate can easily be calculated from the heat flow versus temperature plot. The fractional conversion α is then obtained by partial integration of these data (as a function of time t or temperature T).

Determination of suitable kinetic model is based on the $z(\alpha)$ function which can be easily obtained by a simple transformation of DSC data. The $z(\alpha)$ function is defined under isothermal conditions as $z(\alpha) = \Phi \cdot t$ and under non-isothermal conditions as $z(\alpha) = \Phi \cdot T^2$ [43]. The $z(\alpha)$ function is normalized within range $\langle 0, 1 \rangle$. The $z(\alpha)$ functions for crystallization measured under non-isothermal and isothermal conditions for $(\text{GeS}_2)_x(\text{Sb}_2\text{S}_3)_{1-x}$ glass where $x = 0.1; 0.2$ and 0.3 are shown in Fig. 7.



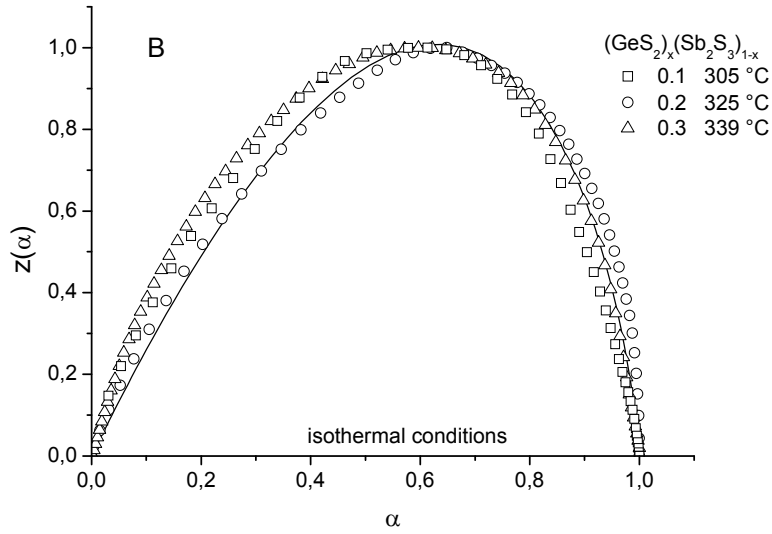


Fig. 7.: Normalized $z(\alpha)$ function for non-isothermal (A) and isothermal (B) crystallization of $(\text{GeS}_2)_x(\text{Sb}_2\text{S}_3)_{1-x}$ glass. Points correspond to DSC data and solid line is a prediction for JMA model.

Characteristic value of maximum of $z(\alpha)$ function for nucleation-growth (JMA) kinetic model is 0.632 [43]. This value is a characteristic ‘fingerprint’ of the JMA model, and it can be used as a simple test of the JMA applicability. The maximum of $z(\alpha)$ dependences found for isothermal and non-isothermal conditions are summarized in Table 8. Taking into account these $\alpha(z)_{\max}$ values the crystallization process of Sb_2S_3 in the $(\text{GeS}_2)_x(\text{Sb}_2\text{S}_3)_{1-x}$ glass where $x = 0.1; 0.2$ and 0.3 can be described by JMA model under non-isothermal and isothermal conditions.

The JMA model can be expressed as [44,45]

$$\alpha = 1 - \exp[-(kt)^n] \quad (11)$$

Here n reflects nucleation rate and growth morphology, and k is a function of temperature that depends on both nucleation rate and growth rate. Usually it is assumed that its temperature dependence can be expressed as

$$k = A \cdot \exp(-E_A / RT) \quad (12)$$

where R is the gas constant, A is the pre-exponential factor and E_A is the effective activation energy that should not depend on temperature and the fraction transformed. The DSC data measured under non-isothermal conditions can be used to calculate the value of activation energy by Kissinger method [46]

$$\ln\left(\frac{\beta}{T_p^2}\right) = -\frac{E_A}{R} \cdot \frac{1}{T_p} + \text{konst.} \quad (13)$$

where β is the heating rate and T_p is the temperature of the maximum of crystallization peak. Dependence of $\ln(\beta/T_p^2)$ on $1/T_p$ is the straight line with slope corresponding to E_A . The obtained effective activation energies of the crystallization process for isothermal and non-isothermal conditions are summarized in Table 5.

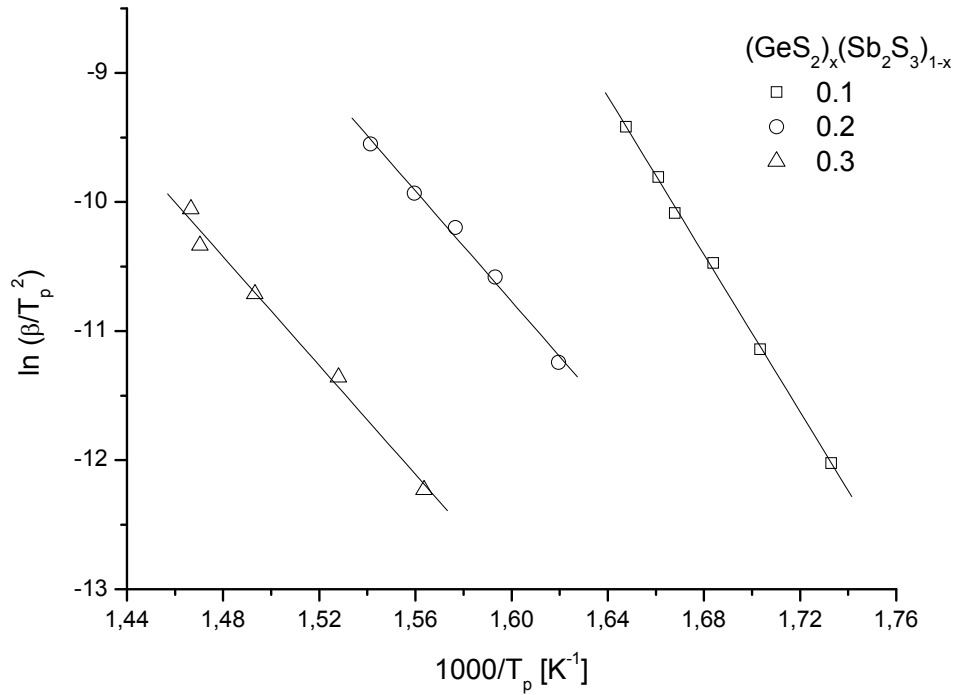


Fig. 8.: Kissinger plot of the $\ln(\beta/T_p^2)$ dependence on $1/T_p$ in $(\text{GeS}_2)_x(\text{Sb}_2\text{S}_3)_{1-x}$ undercooled melts. The lines correspond to the least-square fits of the data.

Another method for determining E_A for non-isothermal and also for isothermal data is the isoconversional method [47]

$$\ln \Phi_\alpha = \ln[\Delta H \cdot A \cdot f(\alpha)] - \frac{E_A}{R} \cdot \frac{1}{T_\alpha} \quad (14)$$

where $f(\alpha)$ is the analytical expression of the kinetic model. The linear plots of $\ln \Phi_\alpha$ versus $1/T_\alpha$ were obtained for different values of α . The values of effective activation energies were calculated from these slopes. These activation energies did not depend on the conversion ratio α in the range $0.3 \leq \alpha \leq 0.7$ and the values are summarized in Table 5.

If nucleation frequency and growth rate vary in an *Arrhenius* way with temperature then the effective activation energy in Eq. 14. can be expressed as [48]

$$E_A \cong \frac{E_N + mE_G}{n} \quad (15)$$

where E_N and E_G are the activation energies for nucleation and crystal growth, m depends on the growth mechanism and dimensionality of crystals. For interface controlled growth m assumes the values, 1, 2 and 3 for one-, two-, and three-dimensional growth, respectively.

The rate equation of crystallization process can be obtained by differentiation of Eq. 11. with respect to time

$$\left(\frac{d\alpha}{dt} \right) = k \cdot n(1-\alpha) [-\ln(1-\alpha)]^{1-1/n} \quad (16)$$

It is very important to emphasize that Eqs. 13. – 16. have been derived strictly under isothermal conditions. Henderson [49] has shown that the validity of these equations can be extended to non-isothermal conditions under two assumptions: (i) the growth rate of a new phase is controlled only by temperature and it is independent of time, i.e. linear growth kinetics proceeds, (ii) homogeneous nucleation or heterogeneous nucleation at randomly dispersed second phase particles takes place (see also [50]).

The value of parameter n can be calculated from equation [43]:

$$n = \frac{1}{1 + \ln(1 - \alpha(y_{\max}))} \quad (17)$$

where $y(\alpha)$ is a characteristic function defined under non-isothermal conditions as $y(\alpha) = \Phi \exp(E_A/RT)$ and under isothermal conditions $y(\alpha) = \Phi$ [43,51]. The value of $\alpha(y_{\max})$ is maximum of $y(\alpha)$ function and for isothermal and non-isothermal conditions are summarized in Table 8. The $y(\alpha)$ function for non-isothermal conditions was calculated for E_A presented in Table 5. (*Kissinger method*). The particular values of JMA parameter n calculated from Eq. 17. for non-isothermal and isothermal crystallization are summarized in Table 9.

Table 8.: Values of maximum of $z(\alpha)$ and $y(\alpha)$ functions for non-isothermal (non-iso) and isothermal (iso) conditions of crystallization for $(\text{GeS}_2)_x(\text{Sb}_2\text{S}_3)_{1-x}$ glasses.

$(\text{GeS}_2)_x(\text{Sb}_2\text{S}_3)_{1-x}$	$\alpha(z)_{\max}$		$\alpha(y)_{\max}$	
	non-iso	iso	non-iso	iso
0.1	0.62 ± 0.04	0.69 ± 0.07 [51]	0.35 ± 0.06	0.22 ± 0.06 [51]
0.2	0.63 ± 0.03	0.63 ± 0.01 [52]	0.43 ± 0.02	0.34 ± 0.02
0.3	0.67 ± 0.03	-	0.48 ± 0.05	-

Table 9.: Values of kinetic parameter n of nucleation-growth model (JMA) describing non-isothermal (non-iso) and isothermal (iso) crystallization data for $(\text{GeS}_2)_x(\text{Sb}_2\text{S}_3)_{1-x}$ glasses.

$(\text{GeS}_2)_x(\text{Sb}_2\text{S}_3)_1$	JMA(n)	
	non-iso	iso
0.1	1.5 ± 0.4	1.7 ± 0.2 [53]
0.2	2.3 ± 0.2	1.7 ± 0.2
0.3	2.3 ± 0.7	-

The crystallization process of Sb_2S_3 in the $(\text{GeS}_2)_x(\text{Sb}_2\text{S}_3)_{1-x}$ glasses where $x = 0.1; 0.2$ and 0.3 can be described by JMA model under non-isothermal and isothermal conditions with parameter $n = 1.5 - 2$.

12.4.3. Comparison of crystal growth and DSC data

It has been found that experimentally observed growth of Sb_2S_3 crystals in $(\text{GeS}_2)_x(\text{Sb}_2\text{S}_3)_{1-x}$ system (where $x = 0.1 - 0.5$) starts from nuclei randomly distributed in the volume of the bulk specimen. The time dependence of crystal growth corresponds to the linear behavior typical for interface controlled kinetics. Under these assumptions the JMA equation should be valid for both isothermal and non-isothermal conditions [49-55].

Microscopic observations suggest that the crystallized sample is being formed by crystalline aggregates, showing no indication for a secondary nucleation. Therefore, one can assume that the nucleation and crystal growth processes are well separated and that the exothermic heat flow corresponds practically to the macroscopic crystal growth kinetics. This makes possible to neglect a complicated temperature dependence of nucleation frequency and then from Eq. 15. follows that $E \cong mE_G/n$. Microscopic observation reveals that spherulite type aggregates are made for $x = 0.1 - 0.3$ and this spherulites are composed from Sb_2S_3 needle crystals that follow one-dimensional growth, i.e. $m = 1$. For compositions 0.4 and 0.5 only separated needle Sb_2S_3 crystals that follow too one-dimensional growth are observed. When is $m/n = 1$ in Eq. 15. then the activation energies of crystals growth should be comparable to activation energies of isoconversional method. This has been confirmed only for $x = 0.2$ and 0.3 (see Table 5.).

When the parameter of JMA model is 1.5-2 and $m = 1$ (one-dimensional growth of needles) the activation energies of crystallization calculated with Eq. 15. are $203 - 270 \text{ kJ.mol}^{-1}$ for $x = 0.1$; $148 - 197 \text{ kJ.mol}^{-1}$ for $x = 0.2$ and $144 - 192 \text{ kJ.mol}^{-1}$ for $x = 0.3$. These values are not so different to activation energies obtained by Kissinger method for non-isothermal conditions.

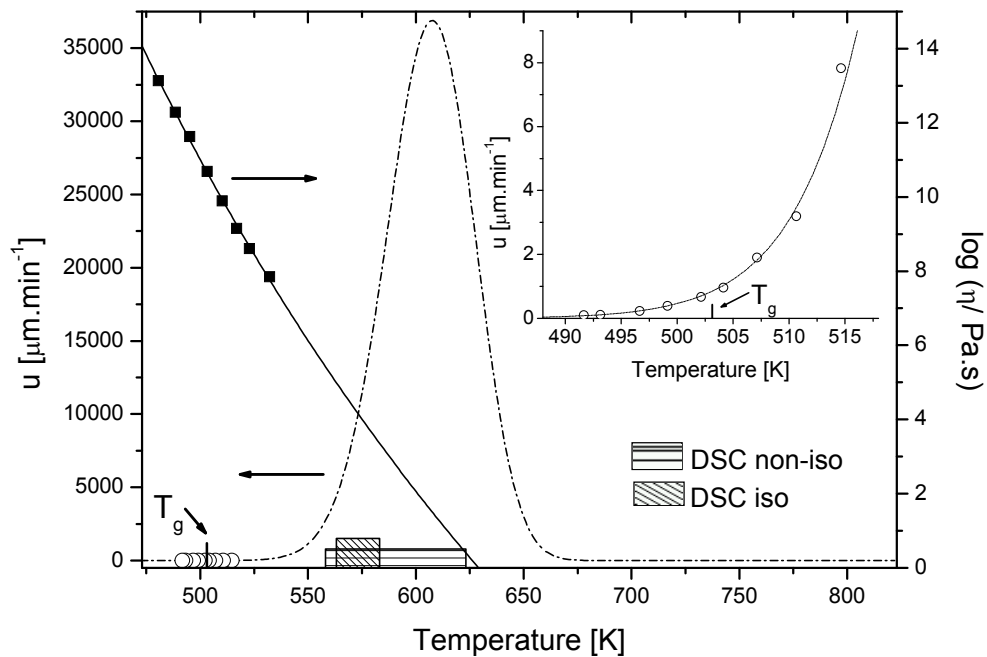


Fig. 9.: Temperature dependence of crystal growth rate and viscosity in $(GeS_2)_{0.1}(Sb_2S_3)_{0.9}$ undercooled melt. The dash dotted line corresponds to calculated data by Eq.X.5. Solid line corresponds to extrapolated viscosity data. [42,59]

Fig. 9. [58,59] combines the experimental growth rate data, the curves calculated by using Eq. 5. for parameters from Table 6., and the viscosity data taken from Ref. [42]. Similar relations were found for other compositions of the $(GeS_2)_x(Sb_2S_3)_{1-x}$ system [59-61]. The growth of Sb_2S_3 crystals in undercooled melt of $(GeS_2)_x(Sb_2S_3)_{1-x}$ glasses observed by optical microscopy takes place at lower temperature than at which the crystallization detected by DSC under isothermal and non-isothermal conditions occurs. The calculated crystal growth rates for temperatures of isothermal and non-isothermal DSC experiments show that the

growth rates are in these temperatures intervals too fast and out of observation limits of optical microscopy method.

The activation energy of crystal growth represents about 60-80 % of the activation energy of viscous flow in $(\text{GeS}_2)_x(\text{Sb}_2\text{S}_3)_{1-x}$ undercooled melt (Table 5.). The value of approximately 60 % has been reported for crystallization of glassy As_2Se_3 [36].

12.5. Conclusions

The crystal growth kinetics of Sb_2S_3 in $(\text{GeS}_2)_x(\text{Sb}_2\text{S}_3)_{1-x}$ glasses where $x = 0.1-0.5$ has been studied by DSC and microscopy. In the temperature range studied by DSC one exothermic peak corresponding to the crystallization of Sb_2S_3 (stibnite) was detected. It was observed that the crystals grow from randomly distributed nuclei in the volume of the studied highly viscous undercooled melts. It has been confirmed that the crystal length increases linearly with time. This is indicative of the interface controlled crystal growth kinetics. The reduced growth rate plot (i.e., the growth rate corrected for mobility) versus undercooling suggests that the most probable mechanism of crystallization is for $x = 0.1$; 0.2 and 0.3 the interface controlled 2-D nucleated growth. For $x = 0.4$ and 0.5 the screw dislocation growth model was detected but the differences between experimental and calculated data for this model lead to the use of the 2D nucleated growth model instead. From the linear dependence of $\ln(u \cdot \eta)$ versus $(T \cdot \Delta T)^{-1}$ the parameters B and C for the 2D nucleated growth were calculated. The straight lines for all compositions do not have any breakpoints which means that the crystal growth mechanism does not change in the observed temperature range. The temperatures and crystal growth rate of maximum of crystal growth was approximately estimated. The crystallization behavior under non-isothermal and isothermal conditions was described by the Johnson–Mehl–Avrami model with parameter $n = 1.5-2$.

References 12

1. Jackson, K.A., Uhlmann, D.R., Hunt, J.D.: *On the nature of crystal growth from the melt*. J. Cryst. Growth **1**, 1-36 (1967)
2. Jackson, K.A.: *Advanced in Growth and Perfection of Crystals*. Wiley, New York (1958)
3. Uhlmann, D.R.: *Advances in Nucleation and Crystallization in Glasses*. Am. Ceram. Soc., Columbus (1972)
4. Burgner, L.L., Weinberg, M.C.: *Crystal growth mechanisms in inorganic glasses*. Phys. Chem. Glasses **42**, 184-190 (2001)
5. Turnbull, D., Cohen, M.H.: *Crystallization Kinetics and Glass Formation, Advanced in Modern Aspects of the Vitreous State*. Butterworth & Co., London (1960)
6. Hoffman, J.D.: *Thermodynamic driving force in nucleation and growth processes*. J. Chem. Phys. **29**, 1192-1193 (1958)
7. Nascimento, M.L.F., Zanotto, E.D.: *Mechanisms and dynamics of crystal growth, viscous flow and self-diffusion in silica glass*. Phys. Rev. B **73**, 024209 (2006)
8. Smith, G.L., Weinberg, M.C.: *Experimental test of surface nucleated crystal growth model in lithium diborate glass*. Phys. Chem. Glasses **35**, 6-9 (1994)
9. Meiling, G.S., Uhlmann, D.R.: *Crystallization and melting kinetics of sodium disilicate*. Phys. Chem. Glasses **8**, 62-68 (1967)
10. Tudokan, E.T.: *Crystal Growth in Undercooled Liquids and Glasses, Advanced in Physico-chemical Properties of Molten Slags and Glasses*. Metals Society, London (1983)

11. Vergano, P.J., Ullmann, D.R.: *Reactivity of Solids*. John Wiley, New York (1969)
12. Vergano, P.J., Ullmann, D.R.: *Crystallization kinetics of germanium dioxide: the effect of stoichiometry on kinetics*. Phys. Chem. Glasses **11**, 30-38 (1970)
13. Málek, J., Klikorka, J.: *Crystallization kinetics of glassy GeS₂*. J. Therm. Anal. **32**, 1883-1893 (1987)
14. Novozhilov, A. F., Zlomanov, V. P.: *Determination of the heats of phase transition in GeSe, GeSe₂, GeS and GeS₂ by thermography*. Inorg. Mater. **13**, 438-439 (1977)
15. Shánělová, J., Málek, J., Alcada, M. D., Criado, J. M.: *Kinetics of crystal growth of germanium disulfide in Ge_{0.38}S_{0.62} chalcogenide glass*. J. Non-Cryst. Solids **351**, 557-567 (2005)
16. Wagstaff, F.E.: *Crystallization and melting kinetics of cristobalite*. J. Am. Ceram. Soc. **52**, 650-654 (1969)
17. Ainslie, N.G., Mackenzie, J.D., Turnbull, D.: *Melting kinetics of quartz and cristobalite*. J. Phys. Chem. **65**, 1718-1724 (1961)
18. Scherer, G., Vergano, P.J., Uhlmann, D.R.: *A study of quartz melting*. Phys. Chem. Glasses **11**, 53-58 (1970)
19. Stolen, S., Gronvold, F.: *Critical assessment of the enthalpy of fusion of metals used as enthalpy standards at moderate to high temperatures*. Thermochim. Acta **327**, 1-32 (1999)
20. Honig, R.E., Kamer, D.A.: *Vapor pressure data for solid and liquid elements*. RCA Review **30**, 285-305 (1969)
21. Tausend, A., Wobig, D.: *Determination of Tl-Se phase-diagram in range of 33.3 to 75 atomic percent selenium by means of differential scanning calorimetry (DSC)*. Z. Phys. Chem. N.F. **96**, 199-214 (1975)
22. Jackson, K.A., Hunt, J.D.: *Transparent compounds that freeze like metals*. Acta. metall. **13**, 1212-1215 (1965)
23. Diaz-Mora, N., Zanotto, E. D., Neryt, R., Muller, R.: *Surface crystallization and texture in cordierite glasses*. J. Non-Cryst. Solids **273**, 81-93 (2000)
24. Neiman, T.S., Yinnon, H., Uhlmann, D.R.: *Crystallization kinetics of lead metasilicate*. J. Non-Cryst. Solids **48**, 393-403 (1982)
25. Granasy, L., James, P. F.: *Nucleation and growth in cluster dynamics: A quantitative test of the classical kinetic approach*. J. Chem. Phys. **113**, 9810-9821 (2000)
26. Burgner, L.L., Weinberg, M.C.: *An assessment of crystal growth behavior in lithium disilicate glass*. J. Non-Cryst. Solids **279**, 28-43 (2001)
27. Eagan, R. J., De Luca, J. P., Bergeron, C. G.: *Crystal growth in the system PbO-B₂O₃*. J. Am. Ceram. Soc **53**, 214-219 (1970)
28. De Luca, J.P., Eagan, R.J., Bergeron, C.G.: *Crystallization of PbO-2B₂O₃ from its supercooled melt*. J. Am. Ceram. Soc. **52**, 322-326 (1969)
29. Leedecke, C.J., Bergeron, C.G.: *The growth of K₂B₈O₁₃ in its stoichiometric melt*. J. Cryst. Growth **32**, 327-331 (1976)
30. Nagel, S. R., Bergeron, C. G.: *Crystallization of SrB₄O₇ from its melt*. Am. Ceram. Soc. Bull. **50**, 414-414 (1971)
31. Marlor, A. J., Kumar, H.S.A., Bergeron, C. G.: *Crystallization of caesium hexaborate from its undercooled melt*. Phys. Chem. Glasses **16**, 108-111 (1975)

32. Linke, D.: *Thermochemical and structural interpretation of reactions occurring in glassforming chalcogenide melts*. Amorphous Semiconductors, Proc. Int. Conf., Meeting date 1976, 499-504 (1977)
33. Johnson, G.K., Papatheodorou, G.N., Johnson, C.E.: *The enthalpies of fusion of $SbF_5(I)$ and $Sb_2S_3(C)$ and the high-temperature thermodynamic functions of $Sb_2S_3(C)$ and $Sb_2S_3(I)$* . J. Chem. Thermodyn. **13**, 745-754 (1981)
34. Myers, M.B., Felty, E.J.: *Heats of fusion of the $A_2^VB_3^{VI}$ compounds, As_2S_3 , As_2Se_3 , As_2Te_3 and Sb_2S_3* . J. Electrochem. Soc. **117**, 818-820 (1970)
35. Street, G.B., Munir, A.: *The structure and thermal properties of synthetic realgar (As_4S_4)*. J. Inorg. Nucl. Chem. **32**, 3769-3776 (1970)
36. Henderson, D.W., Ast, D.G.: *Viscosity and crystallization kinetics of As_2Se_3* . J. Non-Cryst. Solids **64**, 43-70 (1984)
37. Blachnik, R., Schneider, A.: *High-temperature enthalpies of As_2Te_3 , Sb_2Se_3 , Bi_2Se_3 , $GeAs$, $GeAs_2$ and $SnAs$* . J. Chem. Thermodyn. **3**, 227-233 (1971)
38. Blachnik, R., Kluge, W.: *Chemical bonding in melts of $a(IV)b(VI)$ compounds*. Thermochim. Acta **3**, 317-325 (1972)
39. Magill, J.H., Plazek, D.J.: *Physical properties of aromatic hydrocarbons. 2. Solidification behavior of 1,3,5-tri-alpha-naphthylbenzene*. J. Chem. Phys. **46**, 3757-3769 (1967)
40. Volmer, M., Marder, M.: *Theorie der Linearen Kristallisationsgeschwindigkeit Unterkühlter Schmelzen*. Physik. Chem. **154**, 97-112 (1931)
41. Greet, R.J.: *Solidification kinetics of 1,2-diphenylbenzene*. J. Cyst. Growth **1**, 195-203 (1967)
42. Šhánělová, J., Košťál, P., Málek, J.: *Viscosity of $(GeS_2)_x(Sb_2S_3)_{1-x}$ supercooled melts*. J. Non-Cryst. Solids **352**, 3952-3955 (2006)
43. Málek, J.: *Kinetic analysis of crystallization processes in amorphous materials*. Thermochim. Acta **355**, 239-253 (2000)
44. Johnson, W.A., Mehl, R.F.: *Reaction kinetics in processes of nucleation and growth*. Tran. Am. Inst. Miner. Eng. **135**, 416-458 (1939)
45. Avrami, M.: *Kinetics of phase change II*. J. Phys. Chem. **8**, 212-225 (1940)
46. Kissinger, H.E.: *Reaction kinetics in differential thermal analysis*. Anal. Chem. **29**, 1702-1706 (1957)
47. Friedman, H.L.: *Kinetics of thermal degradation of Char-forming plastics from thermogravimetry. Application to a phenolic plastics*. J. Polym. Sci C **6**, 183-195 (1964)
48. Yinnon, H., Uhlmann, D.R.: *Applications of thermoanalytical techniques to the study of crystallization kinetics in glass-forming liquids. 1. Theory*. J. Non-Cryst. Solids **54**, 253-275 (1983)
49. Henderson, D.W.: *Thermal analysis of non-isothermal crystallization kinetics in glass forming liquids*. J. Non-Cryst. Solids **30**, 301-315 (1979)
50. Kemény T. and Šesták J.: *Comparison of crystallization kinetics determined by isothermal and non-isothermal calculation methods*. Thermochim. Acta **110**, 113-121 (1987)
51. Málek J.: *The kinetic analysis of non-isothermal data*. Thermochim. Acta **200**, 257-269 (1992)
52. Šesták J. and Málek J.: *“Diagnostic limits of phenomenological models of heterogeneous reactions and thermal analysis kinetics”*. Solid State Ionics **63/65**, 245-254 (1993)
53. Koga N. and Šesták J.: *“Thermal analysis kinetics and physico-geometry of the monisothermal crystallization of glasses”*. Bull. Soc. España Cer. Vidro **31**, 185 (1992).

54. Koga N. and Šesták J. „Crystal nucleation and growth in lithium diborate glass by thermal analysis“ J. Am. Ceram. Soc. **83**, 1753 (2000)
55. Šesták J., book “Science of heat and thermophysical studies: a generalized approach to thermal analysis” Elsevier, Amsterdam 2005
56. Pustková, P., Zmrhalová, Z., Málek J.: *The particle size influence on crystallization kinetics of $(GeS_2)_{0.1}(Sb_2S_3)_{0.9}$ glass*, Thermochem. Acta **466**, 13-21 (2007)
57. Pustková, P., Švadlák, D., Šhánělová, J., Málek, J.: *The non-isothermal crystallization kinetics of Sb_2S_3 in the $(GeS_2)_{0.2}(Sb_2S_3)_{0.8}$ glass*. Thermochem. Acta **445**, 116-120 (2006)
58. nonpublished results
59. Švadlák, D., Zmrhalová, Z., Pustková, P., Málek, J., Pérez-Maqueda, L.A., Criado, J.M.: *Crystallization behavior of $(GeS_2)_{0.1}(Sb_2S_3)_{0.9}$ glass*. J. Non-Cryst. Solids **354**, 3354-3361 (2008)
60. Švadlák, D., Pustková, P., Košťál, P., Málek, J.: *Crystal growth kinetics in $(GeS_2)_{0.2}(Sb_2S_3)_{0.8}$ glass*. Thermochem. Acta **446**, 121-127 (2006)
61. Málek, J., Švadlák, D., Mitsuhashi, T., Haneda, H.: *Kinetics of crystal growth of Sb_2S_3 in $(GeS_2)_{0.3}(Sb_2S_3)_{0.7}$ glass*. J. Non-Cryst. Solids **352**, 2243-2253 (2006)



Chapter 13

Application of DTA/DSC

13. ON THE APPLICATION OF DTA/DSC METHODS FOR THE STUDY OF GLASS CRYSTALLIZATION KINETICS

Vladimir M. Fokin, Aluisio Cabral Jr., Marcio L.F. Nascimento,
Edgar D. Zanotto, Jaroslav Šesták

13.1. Traditional determination of overall crystallization kinetics by thermal analysis

Thermoanalytical (TA) data, such as those determined by differential thermal analysis (DTA) and differential scanning calorimetry (DSC), are of macroscopic nature since the measured overall (observed) occurrence is commonly averaged over both the whole DTA/DSC peak and the sample assemblage under study [1-3]. Despite this fact, experimentally resolved shapes of TA curves have been widely used as a potential source for kinetic appreciation of solid-state reactions taking place in the sample (either internally or superficial) aiming to discriminate stepwise processes of nucleation and crystallization. The shape of a TA curve is often taken as a characteristic feature of the reaction dynamics and its kinetic interpretation is then mathematically linked with the analytical form of model functions, $f(\alpha)$, representing the overall reaction mechanism, which are a part of the traditional relationship:

$$d\alpha / dt = \alpha' = k(T)f(\alpha), \quad (1)$$

where α is the volume fraction transformed at time t (or, for the case focused here the degree of crystallization) derived from the ratios of instantaneous and total areas encircled by a DTA/DSC crystallization peak.

Determination of the so called kinetic constants, such as the value of activation energy, E (inherent in the Arrhenius equation $k(T) = A \exp(-E/RT)$) is typically carried out in two reasonable ways, either to find directly a linear dependence between the functions involved, or by undertaking further differentiation or integration. A rather popular method of kinetic data analysis is based on expressing the maximum values on the dependence of α' vs. T [1,2], which are often displayed as the Kissinger plot [4] (known since 1959) and which, in various modifications [5], is applicable for a series of peak apexes at different heating rates [4-8] using the following expression:

$$\ln(\phi / T_m^2) = \frac{E}{R} \left(\frac{1}{T_m} \right), \quad (2)$$

where ϕ is the heating rate and T_m is the peak (apex) temperature. Worth noting is the similar determination of activation energy for the structural relaxation [9] and viscous flow in the glass structure region from the heating rate dependence of the glass transition temperature T_g or the cooling rate dependence of the limiting fictive temperature T_f using DTA/DSC traces [10].

Recently the so-called integral methods of evaluation became more widespread. They are based on a modified, integrated form of the function $f(\alpha)$, which is determined as

$$g(\alpha) = \int_{\alpha_0}^{\alpha} d\alpha / f(\alpha) = \int_{T_0}^T k(T) dT / \phi. \quad (3)$$

However, it should be emphasized that such a procedure involves the integration of the Arrhenius function $k(T)$, which needs approximations [11], but which sufficiently precise calculation might be seen as a marginal problem, though it has led to exceptionally intense publication activity. It can be shown that its nature leads to simple solutions, because in most kinetic calculations the effect of the approximations is small and is thus routinely neglected, implying that $k(T)$ is considered to behave as an isothermal constant, again, and instead of a complex integration, is simply put in front of the integral ($\int k(T) dt \approx k(T) \int dt$), which is often hidden behind complicated mathematics [1-3,11]. It is worth noting that the plain passage between integral and differential representation must be reversible under all circumstances, though we may recollect early brainteaser of what is the true meaning of partial derivatives of a time-temperature dependent expression of degree of conversion, $\alpha = \alpha(t, T)$ [1,3], which was even misrepresented in former kinetic analysis of glass crystallization [12,13].

The most intricate process is the resolution of a model function, $f(\alpha)$ [1-3] which is not known *a priori* and which is supposed to be determined in analytical form (simultaneously taking into account its plausible diagnostic potential). The specification of $f(\alpha)$ is thus required by means of substitution by an explicit or approximate analytical function frequently derived on basis of modeling the reaction pathways (mechanism) by means of physical-geometric assumptions [14]. Such models usually incorporate a rather hypothetical description of consequent and/or concurrent processes of the interface chemical reaction, nucleation, crystal growth and diffusion structured within the perception of simplified geometrical bodies being responsible for the built-in particles. Such a derived analytical function, $f(\alpha)$, determinedly depends on these physical-chemical and geometrical relations at the interface between the product and the reactants [3,15,16]. Let us remind that if we are not accounting on these interfaces or other inhomogeneity we deal with an apparently uncomplicated case of concentration-dependent homogeneous reactions and $f(\alpha)$ is associated with the so-called reaction order, $(1 - \alpha)^n$ [1,3]. However, for glass crystallization the heterogeneity effects ought to be included, which is actually accounting the crystallite interfaces as an explicit disturbing 'defect'. The mathematical description becomes thus more complicated due to the fact that not the (rather undeterminable) bulk concentration but the inherent phase interfaces may carry out the most significant function in controlling the reaction progress. The most common models are derived for isothermal conditions and are often associated with the so called shrinking-core mechanism, which maintains a sharp reaction boundary [3,15,16]. Using a simple geometrical representation, the reacting system can be classified as a set of spheres where the reaction interface must be reached by reacting components through diffusion. Any interfacial (separating) layer bears the role of kinetic impedance and the slower of the two principal processes, diffusion and chemical interface reaction, then become the rate-controlling process.

Isothermal crystallization kinetics is traditionally evaluated using the generalized Johnson-Mehl-Avrami-Yerofeeyev-Kolmogorov (JMAVK) equation [17-20], which is accepted as the rate equation for all types of interface-controlled crystallization, as well as for the case of diffusion-controlled crystallization [1-3,21] in the comprehensive form of

$$\ln(1 - \alpha) = -(k(T)t)^r \quad (4)$$

Generally the exponent, r , can be seen as a multipart number as a robust analysis of the basic JMAYK equation reveals that the apparent (overall) values of activation energies, E_{app} (particularly being the center of interest when determined on the basis of DTA/DSC measurements), can be commonly correlated to the partial activation energies of nucleation, E_N , growth, E_G and/or diffusion, E_D . It follows that

$$E_{app} = \frac{aE_N + bdE_G}{a + bd}, \quad (5)$$

where a and b are characteristic multiplying constants providing that the denominator ($a + b d$) equals to the power exponent, r , of the JMAYK equation, and the value b corresponds to 1 or $\frac{1}{2}$ related to the movement of growth front controlled by either chemical reaction (1) or diffusion ($\frac{1}{2}$). Moreover, the coefficients d and b are associated with the nucleation velocity and the growth dimension, respectively; see Table 1 [22].

Table 1. DIMENSIONALITY OF NUCLEATION AND GROWTH

nuclei↓ growth⇒	Growth dimension	Interface reaction $E_{app} =$	Diffusion controlled $E_{app} =$
Instantaneous nucleation from fixed sites	1-D	$r=1, E_G$	$r=0.5, E_D/2$
	2-D	$r=2, 2 E_G$	$r=1, E_D$
	3-D	$r=3, 3 E_G$	$r=1.5, 2 E_D/3$
Constant rate of homogeneous nucleation	1-D	$r=2, E_G + E_N$	$r=1.5, E_D/2 + E_N$
	2-D	$r=3, 2 E_G + E_N$	$r=2, E_D + E_N$
	3-D	$r=4, 3 E_G + E_N$	$r=3, 3 E_D/2 + E_N$

This mathematical treatment can be extended to other thermal regimes (such as a non-isothermal, which is common during DTA/DSC measurements) by incorporating a temperature-dependent integration [23-26]. Such a case was analyzed in detail by Kemeny and Šesták [27] yielding the concealed but anticipated fact that the non-isothermal equivalent of the isothermally derived JMAYK differs only by an integration-dependent, dimensionless multiplying constant [1-3,11]. However, the JMAYK relation bears its analytical integral form, too, i.e.,

$$g(\alpha) = (1 - \alpha)[- \ln(1 - \alpha)]^p, \quad (6)$$

which is sometimes generalized into a two exponent (JMAYK modified) equation,

$$g(\alpha) = (1 - \alpha)^n [- \ln(1 - \alpha)]^p \cong (1 - \alpha)^n \alpha^m, \quad (7)$$

where p is related to the original form of JMAYK through the relation $p = (1 - 1/r)$. In practice, however, the introduction of new exponent n may result that both values of n and p may become numerically non-integral. The JMAYK equations (6) and (7) have been widely applied for the description of overall crystallization kinetics yielding numerous data on “apparent” activation energies and power exponents. When allowing for the existence of fractal exponents, there is almost no restriction to its matching

applicability, however, a simple preliminary test of the JMAYK applicability to a given type of DTA/DSC peak may be useful on basis of its asymmetry [28] and worth of application before actual kinetic analysis. The shape of continuous-heating DSC/DTA peak, which is supposed to be compatible with the JMYAK equation, is routinely asymmetrical (somewhat irrespectively to the power exponents) but the peaks always exhibit shifts of their apexes with increasing heating rate showing slower rise on its low-temperature (onset) side [29, 30]. Such a peak asymmetry is a characteristic feature for the majority of simple interface and/or diffusion controlled crystallizations. Any temperature pre-annealing usually increases its initially transformed fraction, which shifts the peak to lower temperatures and makes it broaden.

Worth mentioning is another relevant alternative to the JMAYK crystallization kinetics, which is the so-called NGG mechanism (normal-grain-growth model) introduced by Atkinson [31], which has been effectively applied by Illekova [32] and at her chapter “Kinetic characteristic of nanocrystal formation in metallic glasses” in [33]. It factually reflects the process of coarsening of the microcrystalline phases, justifiable in most cases of nano-crystalline glass-ceramics (like finemetals) when the mean grain size is below 10 nm. In this instance, the shape of DSC/DTA exothermic peak becomes different with an atypical symmetry (when comparing with JMAYK peaks) with little shifts of the apexes with heating rate. The discrepancy results from rationales arising from the differences in JMAYK and NGG modeling. The process of pre-annealing has also different consequences increasing the initial micro-grain radius, thus shifting the onset of the NGG peak to higher temperatures and leading to a narrower transformation range.

We should mention that the term $[-\ln(1-\alpha)]^p$ can be mathematically converted to another simpler function, α^m , through an expansion in the infinite series, recombined and converted back. The resulting two parameter form, $\alpha^m(1-\alpha)^n$, is identical to the Šesták-Berggren (SB) equation [34], which has been widely used throughout kinetic examinations resulting in abundant literature on transformation kinetics [1-3]. This equation consists of two essential but counteracting parts, the first responsible for mortality, $\cong \alpha^m$ (i.e., reagent disappearance and product formation) and the other for fertility, $\cong (1-\alpha)^n$ (i.e., a kind of product hindrance generally accepted as an ‘autocatalytic’ effect) resembling an extended reaction-order concept $(1-\alpha)^n$ (particularly when completed by the so called “accommodation function” α^m [35]). Such a SB equation has, however, no analytical form for its integral version, but is conventionally exploited in those cases where the standard JMYAK equation (6) fails to provide reasonable values of the power exponents losing thus its desired diagnostic role and providing mere data fitting. Nevertheless this SB equation has become a standard method of kinetic evaluation [36] with a wide applicability [37] and, in some cases, used instead JMAYK equation [38-41].

There have been numerous studies on glass crystallization kinetics [2, 42-44], but their foremost trouble is that most kinetic data are assessed only on the basis of TA measurements, which are, in many cases, rather incompatible with visual observations [45]. We found some matching data between a DTA study and electrical measurements of conductivity [46,47] and did a thorough investigation on bulk and powder crystallization of glasses in the system $\text{SiO}_2\text{-Al}_2\text{O}_3\text{-ZnO}$ doped with ZrO_2 [48,49]. DTA measurements were accomplished on glassy samples casted either directly to the DTA cells (diameter 7mm, height 10mm) or additionally powdered. Separate modes of nucleation and crystal growth were examined by optical observation in a microscope.

Good coincidence was found between the onset of DTA peaks with that calculated from optically determined nucleation and growth data. By application of the JMAK equation, the DTA curve was reconstructed on the basis of the overall degree of crystallization adjusted to the nucleation and growth figures bestowing a rather good coincidence between calculated and measured curves. However, such a type of detailed analysis is often missing in recent studies though it is much needed for reaching a better appreciation of DTA measurements [50,51] and more trustworthy kinetic evaluation. A better elucidation of DTA/DSC measurements is the purpose of our contribution showing some examples in the next paragraphs.

13.2. Determination of crystal nucleation rates from TA methods

About a century ago Gustav Tamman [52] proposed a method to estimate the number density of crystal nuclei in undercooled organic liquids. The technique relies on the development of such nuclei at a relatively high temperature (higher than the previous nucleation temperature) up to a size large enough to be visible with optical or electron microscopy. This method - known as Tamman's or "development" method - has been extensively used to measure crystal nucleation rates in inorganic glasses since 1968 [53, 54]. For a number of silicate glasses, nucleation rates varying from about $10\text{m}^{-3}\text{s}^{-1}$ to $10^{13}\text{m}^{-3}\text{s}^{-1}$ have been estimated by Deubener and Fokin respectively [55]. This method gives correct values of the number of super critical nuclei, needed for estimation of the nucleation rates and the time-lag for nucleation, but is quite laborious and cannot be always employed.

Beginning in 1980s, other methods based on DTA/DSC experiments have been developed [56-61]. These non-isothermal methods are, in principle, faster than the traditional (isothermal) microscopy method and can be divided in two following groups:

i) The first of them the crystal growth rate than on the number of crystals. allows one to determine the temperature dependence of the nucleation rates. To start a study of nucleation kinetics one often needs to know the temperature range covering to the nucleation rate maximum. Such types of non-isothermal methods are based on the reasonable assumption that the inverse temperature of the crystallization peak, $1/T_c$, on a DSC/DTA curve is proportional to the number density of nuclei, since the higher the crystal number the faster is the overall crystallization kinetics and, hence, the release of the heat of crystallization can be detected at a lower temperature. Therefore, a plot of $1/T_c$ versus T_N , the temperature of pre-nucleation heat treatment for a given time may reflect the temperature dependence of the nucleation rate, or more exactly, the crystal number density nucleated in a given period of time. Sometimes, the height of the crystallization peak is used, since, to a first approximation, the peak area is considered constant, but it is noticeable that its width decreases with increasing crystal number. This effect results in an increase of the height of the exothermic peak. It should be noted, however, that the time necessary for full crystallization, which determines the width of the crystallization peak, depends more on

ii) The second method, proposed by Ray and Day [60], is based on a pre-heat treatment of the glass samples to induce partial crystallization and on the estimation of the crystallized volume fraction by the decrease of the crystallization peak area, A , of the residual glass on a DTA/DSC curve. The preliminary nucleation at T_N for time t_N plus growth at $T_G > T_N$ for time t_G lead to a decrease of the fraction of residual glassy matrix. The crystallized volume fraction, α , is given by the above mentioned JMAK

(Jonhson-Mehl-Avrami-Yerofeeyev-Kolmogorov [17-20]) Eq. (4) adjusted for a more detailed description of growth of a given number of crystals with constant rate U :

$$\alpha(t_G) = 1 - \exp\left(-\frac{4\pi}{3}(I(T_N)t_N + N_{at})U(T_G)t_G^3\right) \quad (8)$$

Here $(I(T_N)t_N + N_{at})$ is the total number of nuclei formed by nucleation at T_N with rate I plus athermic nuclei (N_{at}), which include the nuclei formed during cooling of the melt (quenched-in nuclei, N_q) and during the heating run up to the temperature T_G .

The decrease of the residual glass fraction due to preliminary crystallization reduces the crystallization peak area, A , since, in the general case, it is proportional to the mass of transformed material. Varying the growth time, t_G , at fixed nucleation conditions (T_N, t_N) one can change α and hence A . The following equation was proposed by Ray and Day [60] for the ratio of the peak areas corresponding to different t_G

$$\frac{A_1}{A_2} = \frac{M_1 \left[1 - \frac{4\pi}{3}(I t_N + N_{at})(U t_{G1})^3 \right]}{M_2 \left[1 - \frac{4\pi}{3}(I t_N + N_{at})(U t_{G2})^3 \right]}, \quad (9)$$

where M_1 and M_2 are the sample mass for two DSC runs corresponding to the time of preliminary growth, t_{G1} and t_{G2} , respectively.

To derive Eq.9 the exponent in Eq.8 was expanded. Hence Eq.9 is limited to $\alpha \sim 0.2-0.3$. By knowing $A_i, M_i, (i=1, 2)$ and $U(T_G)$, via Eq.9 one can estimate N_{at} together with the number of crystals $N = I t_N$ nucleated at T_N . The number of athermic crystals can be estimated separately by the same equation, with the difference that the preliminary crystallization step does not include the nucleation procedure, i.e. $t_N=0$.

Tests of the above described methods have been performed in refs. [60, 61] using literature data for the nucleation and growth kinetics in stoichiometric lithium disilicate, $\text{Li}_2\text{O} \cdot 2\text{SiO}_2$ (L_1S_2) and sodium calcium silicate, $\text{Na}_2\text{O} \cdot 2\text{CaO} \cdot 3\text{SiO}_2$ ($\text{N}_1\text{C}_2\text{S}_3$) glasses revealing volume nucleation. However, the overall crystallization kinetics is very sensitive to the crystal growth rate, which in turn strongly depends on the glass viscosity, and this can be significantly affected by impurities that are often not controlled, e.g. “water”. Moreover, to correctly employ the value of growth rate one has to know the shape of the crystals.

The aim of this chapter is thus to describe an experimental test of the main assumptions underlying the above DSC/DTA methods by using glass samples produced from the same melts for both the thermo analyses and direct measurements of crystallization kinetics by optical microscopy (sometimes we analyzed by optical microscopy samples before and after a DSC run). We will give special attention to the ratio between surface and volume crystallization, and also to the presence of quenched in nuclei, since the knowledge of their number is relevant for the estimation of the number density of crystals nucleated at given temperature. We do not perform an extensive analysis; our main purpose is merely show that the use of DSC/DTA techniques for the study of crystallization kinetics demands utmost care, since thermo analysis is an integral method and is not self-reliant.

Following refs. [60, 61], two silicate glasses with stoichiometric compositions $\text{Li}_2\text{O}\cdot 2\text{SiO}_2$ (L_1S_2) and $\text{Na}_2\text{O}\cdot 2\text{CaO}\cdot 3\text{SiO}_2$ ($\text{N}_1\text{C}_2\text{S}_3$) were employed as “model” objects. The glasses were synthesized in a platinum crucibles in an electrical furnace at 1450-1500°C for 2 hours. The chemicals were sodium, lithium, and calcium carbonates of analytical grade and ground Brazilian quartz (>99.99% SiO_2). The chemical analysis of the sodium calcium silicate glass is shown in Table 2.

Table 2.

	Na_2O mol %	CaO mol %	SiO_2 mol %
Nominal	16.67	33.33	50
$\text{N}_1\text{C}_2\text{S}_3$ glass	17.2	32.3	50.5

The temperature of the DSC crystallization peak of the parent L_1S_2 glass, which is highly sensitive to small departures of stoichiometry [62], and the experimental values of the nucleation and growth rates give indirect evidence that its composition is close to stoichiometric lithium disilicate. Thermo analyses were performed in a Netzsch 404 Differential Scanning Calorimeter (DSC) using bulk samples of about 35-38 mg. The Tammann method [55] was employed to directly measure the crystal nucleation rates. The crystal sizes, numbers, and respective volume fractions in properly heat treated glass samples were estimated by a Leica DMRX optical microscope coupled with a Leica DFC490 CCD camera.

13.2.1 Number of crystal nuclei and crystallization peak temperature.

To create different numbers of supercritical nuclei, the glass samples were heat treated for different periods of time at temperatures of appreciable nucleation rate. Then each sample was divided into two pieces: one of them was submitted to a DSC run with heating rate of 10°C/min, and the other was heat treated at a higher temperature to develop the nucleated crystals up to visible sizes in an optical microscope and to estimate its number density by stereological methods. Figs.1 and 2 show the number of crystals *versus* nucleation time at $T=473$ at 590°C for L_1S_2 and $\text{N}_1\text{C}_2\text{S}_3$ glasses, respectively. The solid lines resulted from fitting the experimental values $N(t)$ to the Colins and Kashchiev equation [63, 64]

$$N(t) = I_{st} \tau \left[\frac{t}{\tau} - \frac{\pi^2}{6} - 2 \sum_m \frac{(-1)^m}{m^2} \exp\left(-m^2 \frac{t}{\tau}\right) \right], \quad (10)$$

where τ is the time-lag for nucleation, which characterizes the time to achieve a steady-state nucleation rate I_{st} . The dotted lines are the asymptote of Eq.(10)

$$N(t) = I_{st} \left(t - \frac{\pi^2}{6} \tau \right) \quad (11)$$

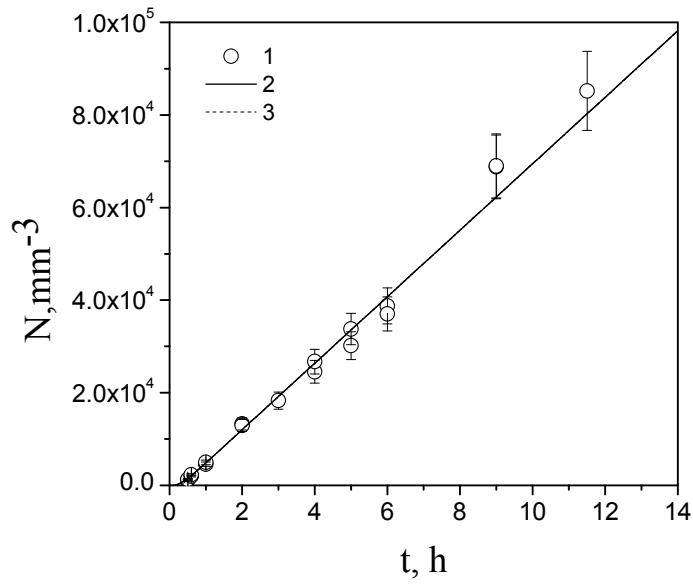


Fig.1 Number density of lithium disilicate crystals versus nucleation time at $T=473^{\circ}\text{C}$ measured by the development method. The lines 2 and 3 were plotted according to Eqs. 10 and 11, respectively.

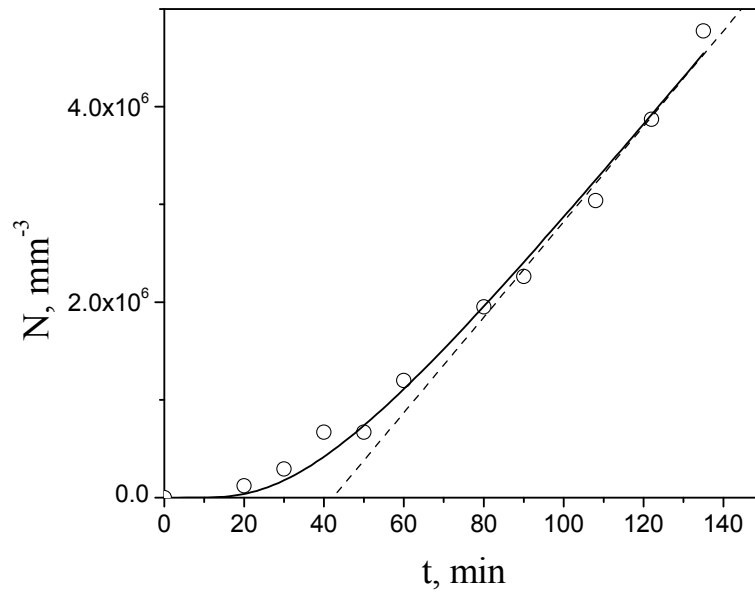


Fig.2. Number density of crystals in $N_1C_2S_3$ glass versus time of nucleation at $T=590^{\circ}\text{C}$ measured by the development method. The solid and dotted lines were plotted by using Eq.10 and Eq.11, respectively.

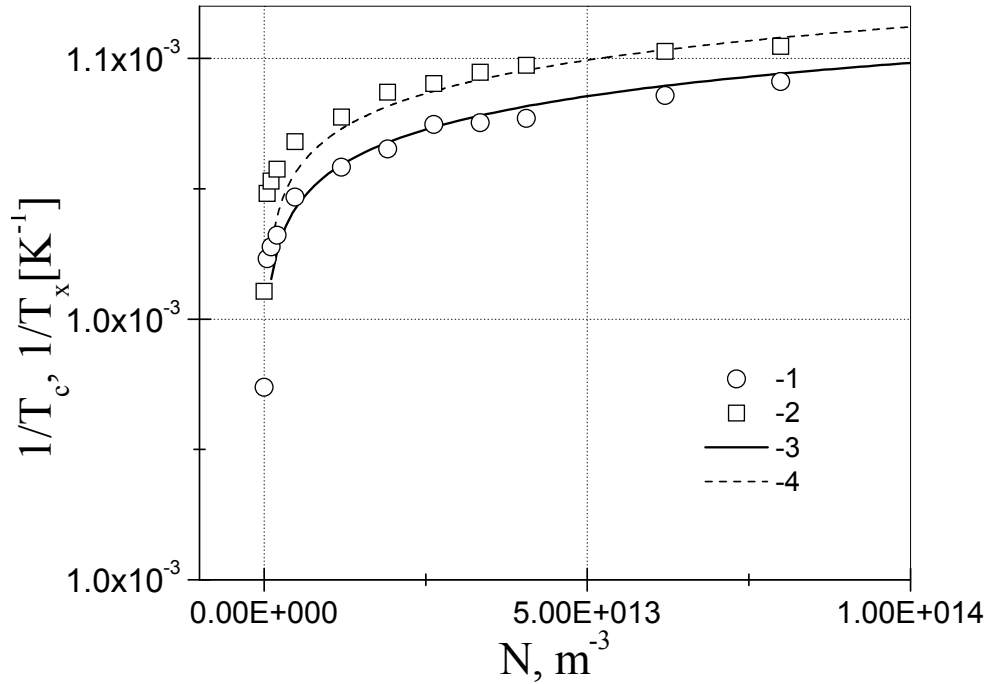


Fig.3. $1/T_c$ (1) and $1/T_x$ (2) versus N for lithium disilicate glass. The lines were fitted to Eq.16, see text.

Fig. 3 shows the dependencies of $1/T_c$ and $1/T_x$ on the number of crystal nuclei preliminary nucleated in glass L_1S_2 at $T=473^\circ\text{C}$. T_x and T_c are, respectively, the temperatures of onset and maximum of the crystallization peaks (the volume fraction of crystals after typical nucleation treatments is vanishingly small and can be neglected). As we expected this dependency is not linear, and close to logarithmic. The non linear dependencies of T_x , peak height and half-width on the nucleation time at $T=453^\circ\text{C}$ were shown in ref. [58] for lithium disilicate glass. However, the induction time for nucleation at this temperature (about 3h) has the same magnitude as the total nucleation time (10h) used in ref. [58]. This fact, however, complicates the analysis of their results.

The following rough model can describe the experimental data shown in Fig.3. We suppose that at the moment when the heat of crystallization is detected by DSC (DTA) the volume fraction crystallized achieved the value α . To estimate the crystallized volume fraction we employ the JMAYK equation (Eqs.8, 12) neglecting crystal growth at temperatures lower than T_x (or T_c). We also neglected the athermic crystals since, as will be shown later, for the present glasses and experimental conditions their number is very low as compared with N .

$$\alpha = 1 - \exp\left(-\frac{4\pi}{3} N U^3 t^3\right) \quad (12)$$

We thus believe that this volume fraction α was crystallized via growth with rate $U(T_x)$ in a narrow temperature interval characterized by some effective temperature close to T_x (T_c) of the crystals preliminary nucleated at T_N [$N = I(T_N)t_N$]. Since, in the temperatures of interest, the morphology of the lithium disilicate crystals is close to an ellipsoid of revolution, with growth rates along the minor and major diameters U_{min} and U_{max} , respectively, the growth rate in Eq.12 must be replaced by:

$$U^3 = U_{min}^2 U_{max} = \frac{U_{max}^3}{K^2}; K = \frac{U_{max}}{U_{min}} \quad (13)$$

Then Eq.12 can be rewritten as

$$\ln(U_{max}) = \frac{1}{3} \ln \left[-\frac{3K^2}{4\pi} \frac{\ln(1-\alpha)}{N t^3} \right] \quad (14)$$

Thus, by knowing the temperature dependence of these crystal growth rates, one can estimate the temperature corresponding to the value of U_{max} given by Eq.14.

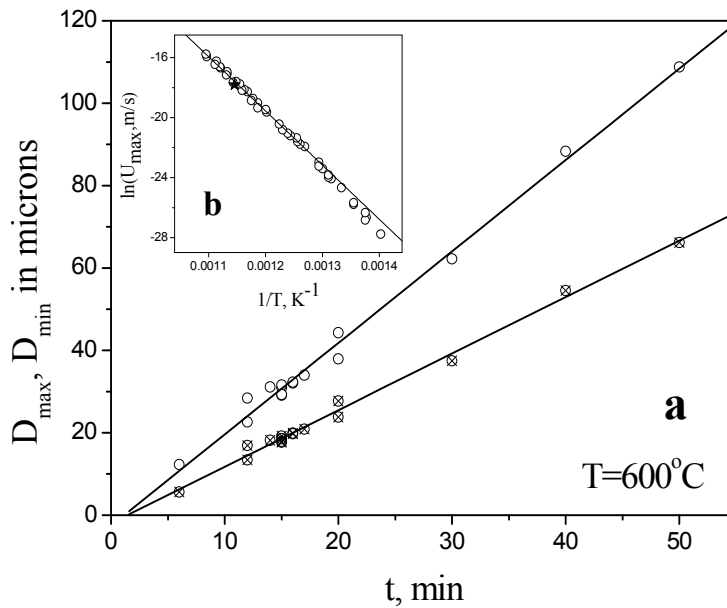


Fig.4. (a) Major and minor crystal axes of lithium disilicate crystals versus time of heat treatment at $T=600^\circ\text{C}$. The lines are linear fits to the experimental points. (b) Arrhenius plot for the crystal growth rate of the major crystal axis [65]. The solid line is a linear fit of the high temperature part of the plot. The black star refers to the data of Fig.4 (a).

Fig.4 shows, as an example, the values of the maximum and minimum diameters of lithium disilicate crystals versus heat treatment time at $T=600^\circ\text{C}$. The inset shows literature data on the temperature dependence of U_{max} for lithium disilicate glass [65] in Arrhenius coordinates. The star corresponding to $T=600^\circ\text{C}$ (our own data for the present

glass) is very close to the other points. At high temperatures $U_{max}(T)$ can be approximated by the following equation (see solid line in Fig.4, inset)

$$\ln(U_{max}, m / s) = 23.79 - 36124.02 \frac{1}{T} ; T \text{ in K.} \quad (15)$$

Combining Eqs.(14) and (15), one obtains

$$\frac{1}{T} = \frac{23.79 - \frac{1}{3} \ln \left[-\frac{3K^2 \ln(1-\alpha)}{4\pi Nt^3} \right]}{36124.02} \quad (16)$$

Thus Eq.16 gives an inverse effective temperature (at which the volume fraction crystallized arrives at the value α during period of time t) as a function of the number of crystals, N . Curves 3 and 4 on Fig.3 were plotted using Eq.16 for $t=90$ s and $\alpha=0.2$ and 0.1, respectively. $C=10$ °C/min with $t=90$ s corresponds to a temperature interval of 15°C. Despite the rough approximations, this model with reasonable parameters gives a semi-quantitative description of the experimental data. It should be noted that the model does not take surface crystallization into account (that is most important for low values of N). May be this would be the reason why at low values of N the experimental points are above the calculated curves (see Fig.3). Fig.5 shows a similar dependence for $N_1C_2S_3$ glass

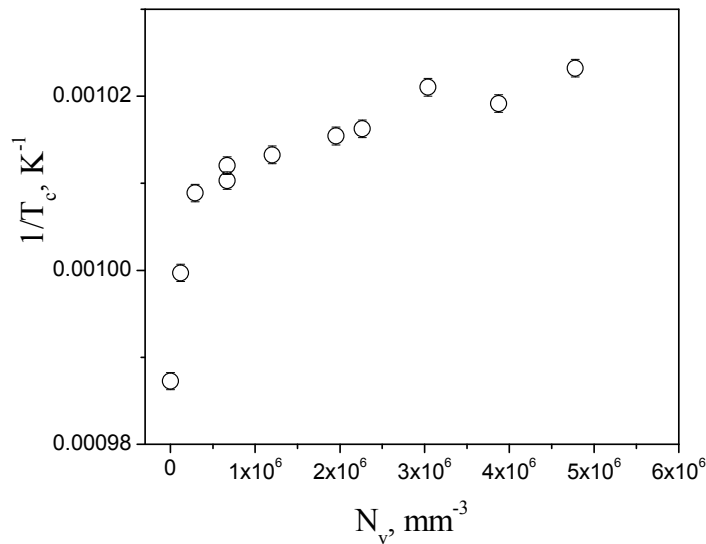


Fig.5 $1/T_c$ versus N for a stoichiometric soda-lime-silica glass, $N_1C_2S_3$.

The following comments on the method employing the shift of the crystallization peak position to estimate nucleation rate curve should be done:

- (i). This method gives an accurate temperature dependence of the nucleation rate only if non-steady nucleation can be neglected, i.e. the equality $N(T_N) = I_{st}(T_N)t_N$ holds, where I_{st} is the steady-state nucleation rate. This is

the case of relative high temperatures or long heat treatment time t_N that significantly exceeds the time-lag for nucleation at all studied temperatures. In all other cases the method will distort the temperature dependence of the nucleation rate at low temperatures (especially close to or below the glass transition temperature). As an illustration, Fig.6 shows the number of lithium disilicate crystals *versus* nucleation temperature for a fixed nucleation time $t=3\text{h}$ (same time used in ref. [58]) together with the number of crystals which should be nucleated during the same period of time if steady-state nucleation had been achieved. Fig.7 shows similar plots for $\text{N}_1\text{C}_2\text{S}_3$ glass. It is clear that due to the time-lag for nucleation the above method has to lead to a significant decrease of the temperature interval of detectable nucleation rate for L_1S_2 glass, and only to a weak one for $\text{N}_1\text{C}_2\text{S}_3$ glass which at given temperatures has a time-lag lower than that in lithium disilicate glass. However, it is difficult to take into account the effect of time-lag if nucleation data is not preliminary available.

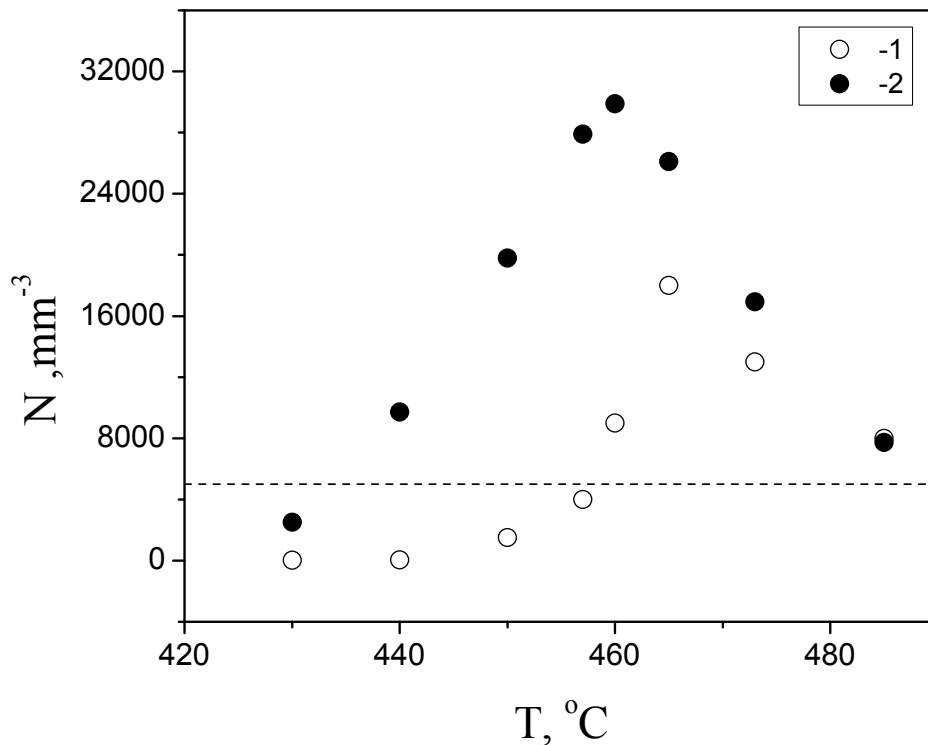


Fig.6. Number of lithium disilicate crystals N nucleated during 3h versus nucleation temperature (1) and nucleated during the same period of time in the case of the steady-state nucleation (2). The dotted line shows the value of N above which the position of the crystallization peak in a DSC curve changes very weakly (see Fig.4). Plots were obtained using experimental data [66].

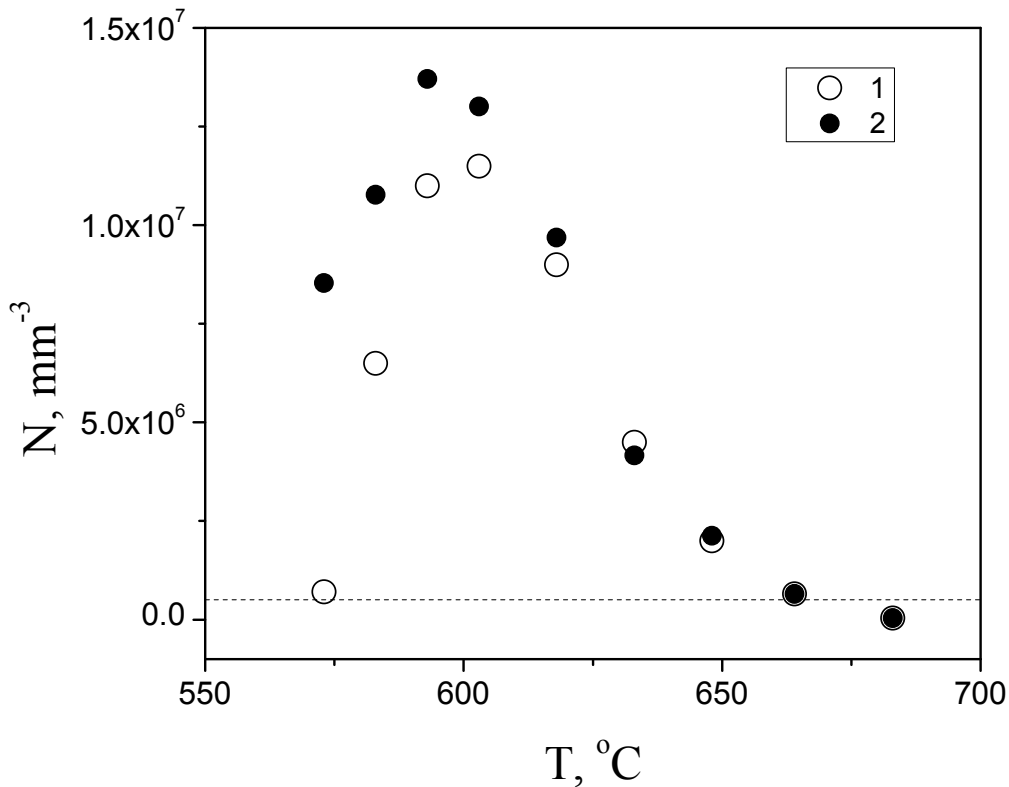


Fig.7. Number of crystals N nucleated in $N_1C_2S_3$ glass during 3h versus temperature of nucleation (1) and nucleated during the same period of time in the case of the steady-state nucleation (2). The dotted line shows the value of N above which the position of the crystallization peak in a DSC curve changes very weakly (see Fig.5). Plots were obtained using experimental data [67].

(ii). As we have shown experimentally and theoretically (see Figs.3 and 5) the dependence of $1/T_c$ on crystal number density is close to logarithmic. This means that the sensitivity of the method depends on N , i.e. the temperature shift of the crystallization peak for low values of N is much stronger than for high values of N . For L_1S_2 glass the change of the sensitivity occurs at N about 5000 mm^{-3} (marked by the dotted line in Fig.6). Since the method implicates a constant nucleation time, t_N , N depends on the temperature of nucleation (see Figs.6 and 7). Hence, if the values of $N(T_N)$ belong to different parts of the $1/T_c$ vs N plot, the shift of the crystallization peak temperature would be stronger for temperatures below and above the maximum nucleation rate than that corresponding to the temperatures of maximum. This is the case of L_1S_2 glass (Fig.6), while for $N_1C_2S_3$ glass all values of $N(T_N)$ belong to the same part of $1/T_c$ vs. N plot (see Fig.7). Thus the logarithmic dependence of $1/T_c$ on N can forge the shape of the temperature dependence of the nucleation rate. Hence, similarly to the case discussed in the previous paragraph, to take into account the non linear dependence of $1/T_c$ on N some nucleation data for the glass understudied are required.

13.2.2. Quench-in and athermic nuclei

As we have shown in the first paragraph, the method to estimate the number of nucleated crystals elaborated by Ray, Fang and Day [60] yields the total number of

nuclei (not only formed at the given nucleation temperature $N(T_N)$, but also the nuclei nucleated at non isothermic (and not always controlled) regime denoted athermal nuclei, N_{at}). To estimate N_{at} independently on the method suggested in ref. [60], we simulated DSC runs with different heating rates in an electrical furnace. Samples of L_1S_2 glass were dropped into a vertical furnace at $T=400^\circ\text{C}$, heated with a rate C up to $T_G=600^\circ\text{C}$, and then treated at this temperature for 40 min to allow crystal growth up to a microscope detectable size.

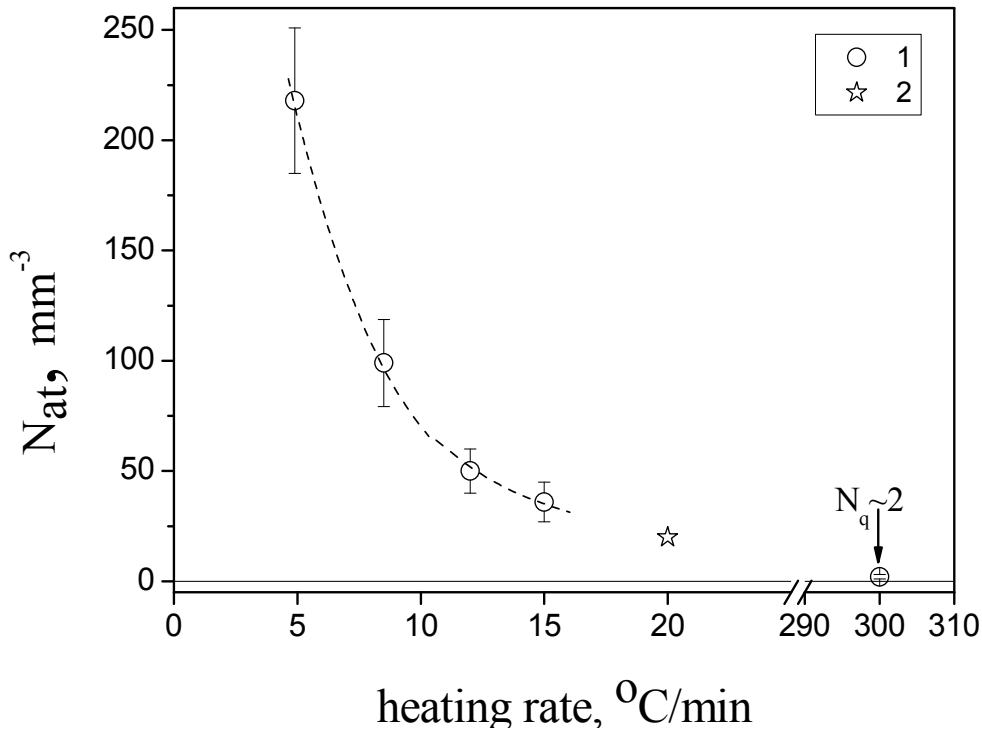


Fig.8. Number density of athermal lithium disilicate crystals versus heating rate . Heat treatments were performed in a vertical electrical furnace (1) and in the DSC furnace (2).

Fig.8 shows N_{at} versus heating rate C . The star refers to heat treatments performed directly in the DSC furnace with the following schedule: $20^\circ\text{C}-5^\circ\text{C}/\text{min}-40^\circ\text{C}$ (5 min) - $20^\circ\text{C}/\text{min}-620^\circ\text{C}$ (20 min) - $20^\circ\text{C}/\text{min}-20^\circ\text{C}$. A higher value of C was realized when the samples dropped into the furnace preliminary stabilized at $T_G=600^\circ\text{C}$. A photo of this sample is shown in Fig.9.

As one can see, the dependence of N_{at} on C is not linear, as could be expected in the case of steady-state nucleation. The effect of non steady-state nucleation is more pronounced at high values of C . In this case the time spent by the sample during the passage through the temperature range corresponding to the non steady-state nucleation is lower than the induction period for nucleation.

One can distinguish two kinds of lithium disilicate crystal morphology. One of them is an ellipsoid of revolution observed in Fig.10, in front and plan views. The other form is spherulitic (Figs.10 and 9). It should be noted that the spherulite diameters are close to the maximal diameters of the ellipsoids (Fig.10). The number density of spherulitic crystals is extremely low (about 2 mm^{-3}) and does not depend on the heating

rate C . This is why we suppose that these spherulitic crystals nucleated on the cooling path during glass preparation and were grown at $T_G=600^\circ\text{C}$. In other words, these are quenched-in crystals. Opposed to the quenched-in crystals, crystals formed via double stage heat treatment at nucleation and growth temperatures, or nucleated during relative low heating or cooling rates (i.e. crystals having some period of time for growth at the nucleation temperature) have a prolate ellipsoidal shape (see e.g. Fig.10). According to the experimental data shown in Fig.8, the number of athermic crystals nucleated during heating with $20^\circ\text{C}/\text{min}$ up to $T_G=600^\circ\text{C}$ is about 20 mm^{-3} . This value is lower than that estimated in ref. [60] by the DTA method (see Eq.9) by a factor of 450. Such overestimation of N_{at} results in the error of estimation $N = It_N$ and the time-lag for nucleation.

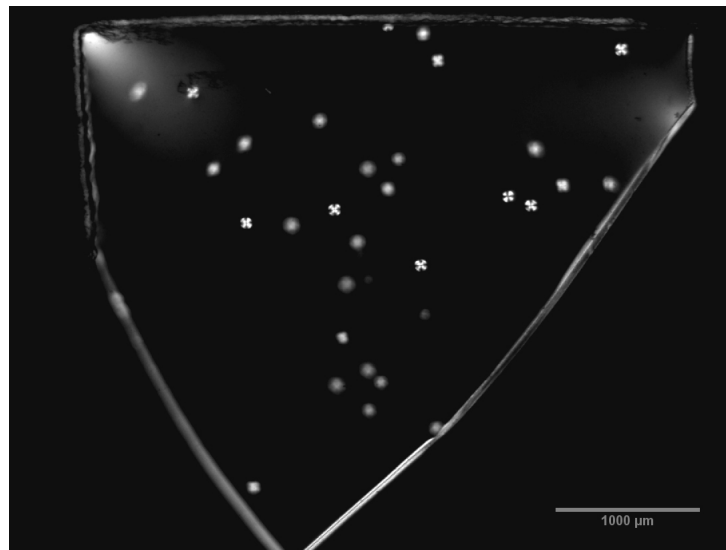


Fig.9. Micrograph (transmitted polarized light) of a L_1S_2 glass sample treated at $T_G=600^\circ\text{C}$ during 40 min (heating rate from 20 to 600°C was about $300^\circ\text{C}/\text{min}$). The sampler is shaped as a plane-parallel plate of thickness 1.4 mm.

One should also recall that the DTA (DSC) method does not take into account surface crystallization *ipso facto* attributing the decrease in the crystallization peak area only to the preliminary volume crystallization. The following part will deal with the discrepancy between calculated and measured numbers of N_{at} , and the ratio between volume and surface crystallization.

13.2.3. Surface and volume crystallization

It is often assumed that if one uses large glass samples it is possible to neglect surface crystallization for analyses of overall crystallization kinetics. For instance, Ray and Day stated [68, 69] that internal crystallization in L_1S_2 glass dominates over surface crystallization when the glass particle size exceeds $\sim 300\mu\text{m}$. However, it is clear that the ratio between the volume and surface crystallized fractions also depends on the intensity of the internal nucleation rates [50].

In the extreme case when the glass does not undergo internal nucleation or when it is very weak, surface crystallization dominates for all particle sizes. Thus the above characteristic size is a relative quantity depending on the time and temperature of crystallization. We carried out heat treatments of a glass powder similar to that used in the DTA run performed in ref. [60] to estimate N_{at} . The L_1S_2 glass powder with size of

400-500 μm was heat treated in the DSC furnace at the following schedule: 20-40 $^{\circ}\text{C}$ (5 $^{\circ}\text{C}/\text{min}$); 40 $^{\circ}\text{C}$ (10 min); 40-600 $^{\circ}\text{C}$ (20 $^{\circ}\text{C}/\text{min}$); $t_G = 20$ min; 600-20 $^{\circ}\text{C}$ (20 $^{\circ}\text{C}/\text{min}$). Fig.11 shows photos of the glass particles subjected to the above heat treatment. It should be noted that the fine structure refers to the morphology of the crystallized surface layer. Only a few isolated crystals are observed in the particle's interior. Due to the non regular form of the particles it is difficult to quantitatively estimate the ratio between the fractions of the surface and volume crystals.

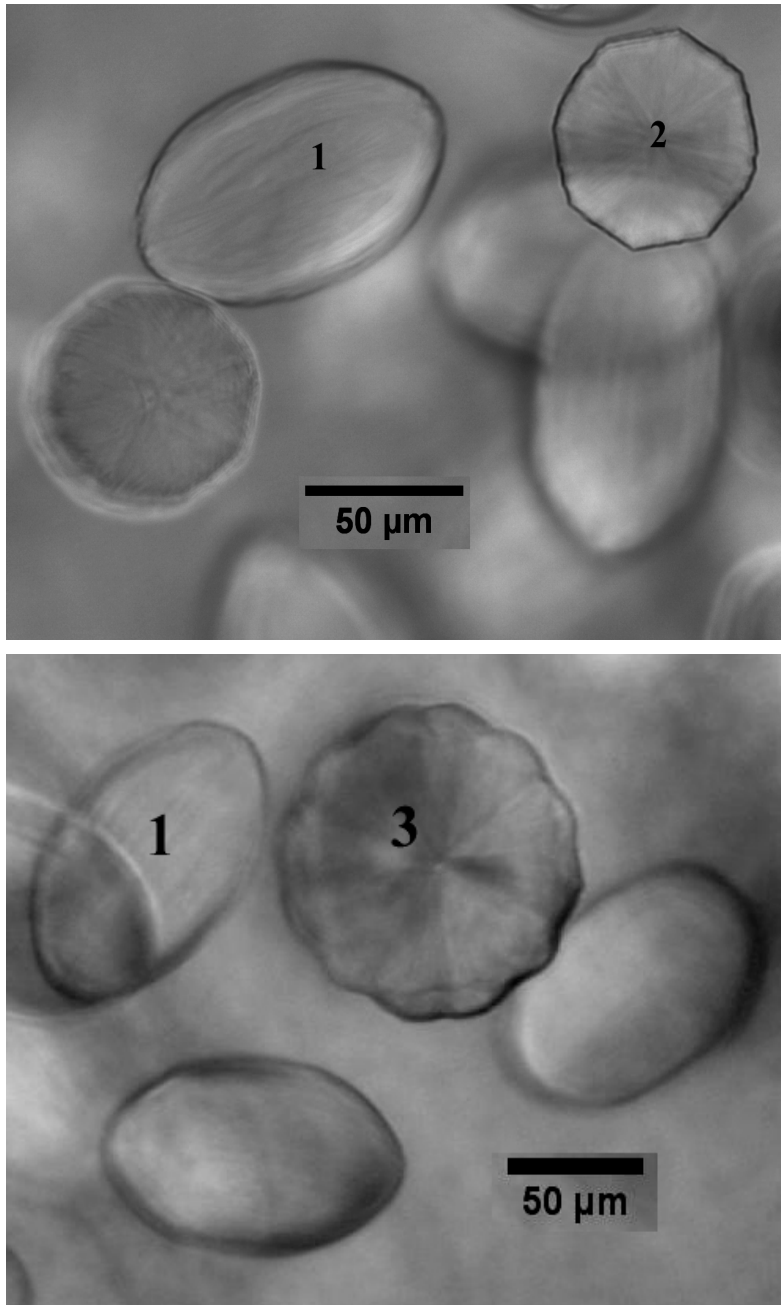


Fig.10. Micrographs (transmitted light) of lithium disilicate crystals in L_1S_2 glass after heating with $C=10^{\circ}\text{C}/\text{min}$ up to $T_G=600^{\circ}\text{C}$ and holding at this temperature during 40 min. Ellipsoids of revolution in plan (1) and front (2) views, and spherulitic (3) lithium disilicate crystals can be observed.

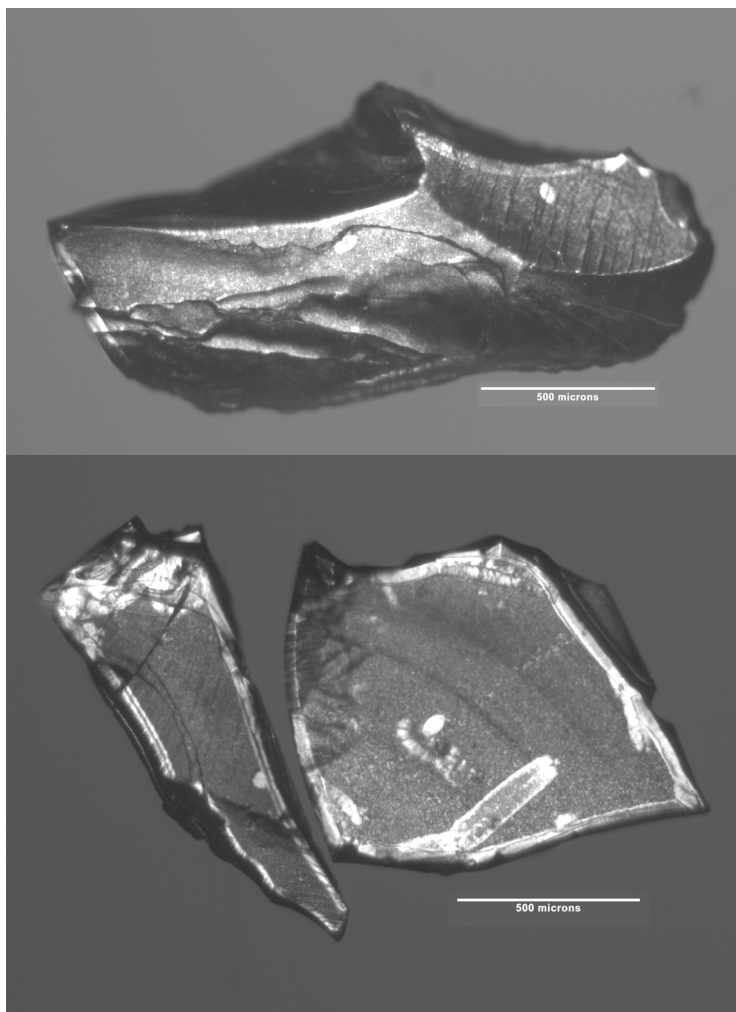


Fig.11. Photos in transmitted light of L_1S_2 glass particles after treatment performed in the DSC furnace (see text).

However, it is obvious that the volume of crystals inside the particles is lower than that of the crystals growing from the surface. For numerical comparison of fractions of surface to volume crystallization we performed DSC run (20°C - $5^\circ\text{C}/\text{min}$ - 40°C (5 min)- $20^\circ\text{C}/\text{min}$ - 620°C ($t_G=20$ min)- $20^\circ\text{C}/\text{min}$ - 20°C) of L_1S_2 glass sampler with regular form $3.3 \times 2.8 \times 1.2 \text{ mm}^3$. Analysis of this sample via optical microscopy show that only 20% of the total crystalline phase corresponds to volume crystallization of athermic crystals. This means that neglecting surface crystallization one attributes its volume to crystals nucleated in the volume of sample and hence overestimates the number density of the latter. This effect is more pronounced when the crystal number density is low, as e.g. in the case of the athermic crystals. Of course, the contribution of volume crystallization increases when the glass sample is subjected to a preliminary nucleation heat treatment. Such the sample of L_1S_2 glass with sizes $3.4 \times 3.5 \times 1.3 \text{ mm}^3$ after DSC run including keeping at nucleation temperature (20 - 40°C ($5^\circ\text{C}/\text{min}$); 40°C (10 min); 40 - 480°C ($20^\circ\text{C}/\text{min}$), $t_N=30$ min; 480 - 620°C ($20^\circ\text{C}/\text{min}$), $t_G = 10$ min; 600 - 20°C ($20^\circ\text{C}/\text{min}$) revealed a ratio between surface and volume fractions of crystalline phase about 1:3.3.

13.2.4. Area of exothermic DTA/DSC crystallization peak

The method of Ray, Fang and Day [60] to estimate the number of nucleated crystals, briefly described previously, is based on the reasonable assumption that the area of a DTA (DSC) crystallization peak is proportional to the mass of crystallized glass. This assumption is correct if the change of sensitivity of the method with temperature is neglected. Thus one can expect that the area of the crystallization peak of the samples with the same mass or reduced per unit mass does not depend on the number density of the preliminary nucleated crystals. The temperature and time of the nucleation heat treatment have to be chosen in such way that the volume of nuclei can be neglected. This condition was fulfilled for the data presented in Fig.12.

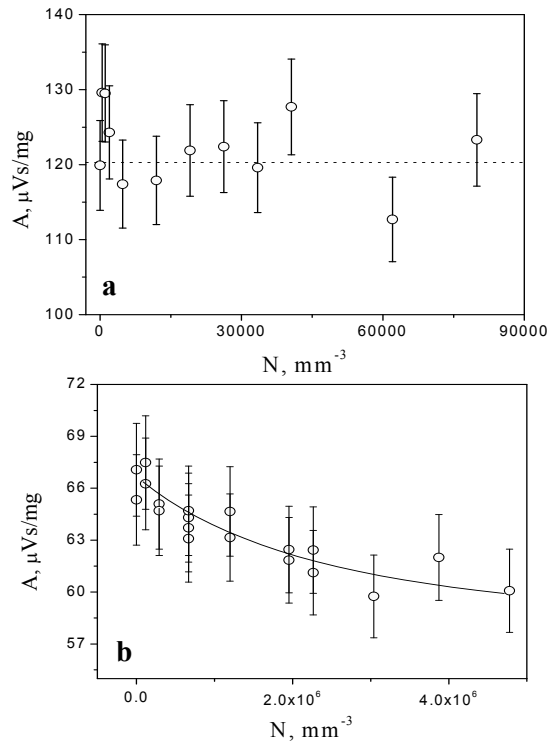


Fig.12. Area of the crystallization peak versus number of crystals for L_1S_2 (a) and $N_1C_2S_3$ (b) silicate glasses.

Indeed the variation of A with the number of crystals for L_1S_2 glass are within the error (Fig.12a), while in the case of $N_1C_2S_3$ glass (Fig.12b) one can see a weak but well defined decrease of A as the number of crystals increases. Note again that the volume of previously formed nuclei did not exceed 0.05%. The observed effect cannot be explained by the change of the sensitivity of method with temperature since an increase of N results in a decrease of T_c (see Fig.5), while the sensitivity increases with decreasing temperature. This means that the fully crystallized $N_1C_2S_3$ glass does not achieve equilibrium and the degree of non equilibrium is higher when the number of crystals is larger, i.e. the system has a more fine structure. Two reasons for the above effect seem now more probable. First of them is the structural and compositional inhomogeneity of the crystallized sample. One should recall that $Na_2O \cdot 2CaO \cdot 3SiO_2$ crystals form via nucleation of a sodium rich solid solution that during the growth process approaches the stoichiometric composition [70]. The second possibility is elastic stresses that can arise in a polycrystal. We show these dependencies of A on N only to illustrate that the obvious assumption about the proportionality of

mass of glass subjected crystallization to the area of an exothermic DSC peak is not always fulfilled.

In conclusion we can say that a robust application of the JMAYK equation, in integral and derivative forms, which is frequently based on the mean values of the crystallization degree (estimated from DTA/DSC measurements) brings some doubtful results, despite the fact that a rather good discrimination of the power exponent can be achieved and can thus be related to distinguishing certain type of nucleation-growth processes, cf. Table 1. This is caused by insensitive management of averaged values determined by DTA/DSC detection of overall heat changes associated with such complex processes. Thus, it is contemplative to concentrate only on a more estranged elementary process, most wishful being the nucleation or growth separately. In this chapter we have focused only on the first the dependence of DSC/DTA crystallization peak position on the number of pre-existing nuclei is not linear. This effect together with the non-steady state nucleation (which is most significant at some temperature range below or just above T_g) modifies the real temperature dependence of the nucleation rate when one employs non-isothermal methods.

The ratio between volume and surface crystallization depends not only on sample size, but also on the internal crystal number density. The role of surface crystallization is more pronounced when the number of crystals in the volume is low, e.g. in the case of athermic crystals. Hence particle size alone is not sufficient to estimate the relative importance of surface crystallization. The area of a DTA/DSC crystallization peak can also be affected by the formation of non equilibrium phases or by elastic stresses. One needs some preliminary data on nucleation and growth rates of the studied glass to take into account all above effects when employing DTA/DSC methods to study crystallization kinetics. On the other hand, when properly employed these non isothermal methods can give useful kinetic information in a rather fast and convenient way.

Acknowledgements: The authors are indebted to Brazilian agencies CNPq # 620249/2006-4 and Fapesp # 2007/08179-9, 2008/00475-0, and # 2008/00475-0 for funding this research. The work was supported by the Grant Agency of ASCR Contract No IAA1010404.

References 13

1. J. Šesták, “*Thermophysical Properties of Solids: theoretical thermal analysis*“ Elsevier, Amsterdam 1984 and “*Тeоретический термический анализ*” Mir, Moscow 1988 (in Russian)
2. J. Šesták (ed), “*Vitrification, Transformation and Crystallization of Glasses*”, special issue of *Thermochim. Acta*, Vol. 280/281, Elsevier, Amsterdam 1996
3. J. Šesták “*Science of Heat and Thermophysical Studies: a generalized approach to thermal analysis*” Elsevier, Amsterdam 2005
4. H.E. Kissinger, *Anal. Chem.* 29 (1957) 1702
5. J. Criado, A. Ortega, *J. Non-cryst. Solids* 87 (1986) 302
6. Y. Nishi, T. Manabe, H. Kameyana, S. Moriya, T. Katagiri, *J Mater. Sci. Letters* 9 (1990) 801
7. J. Llopiz, M.M. Romero, A. Juarez, Y. Laureiro, *Thermochim. Acta* 256 (1995)
8. L. Heireche, M. Belhadji, *Chalcogenide Letters* 4 (2007) 23
9. L.M. Hodge, *J. Non-cryst. Solids* 169 (1994) 211

10. C.T. Moynihan, S.K. Lee, M. Tatsumisago, T. Minami, *Thermochim. Acta* 280/281 (1996) 153
11. J. Šesták, *Thermochim. Acta* 3 (1971) 150
12. E.A. Marseglia, *J. Non-cryst. Solids* 41 (1980) 31
13. H. Yinnon, D.R. Uhlmann, *J. Non-cryst. Solids* 54 (1983) 253
14. S.F. Hulbert, *J. Brit. Ceram. Soc.* 1 (1970) 1
15. J. Šesták, J. Málek, *Solid State Ionics* 63/65 (1993) 245
16. J. Málek, T. Mitsuhashi, J.M. Criado, *J. Mater. Res.* 16 (2001) 1862
17. W.A. Johnson, R.F. Mehl, *Trans. A.I.M.E.* 135 (1939) 416.
18. M. Avrami, *J. Chem. Phys.* 7(1939)1103; 8(1940)212; 9(1941)177
19. B.V. Yerofeyev, *Dokl. Akad. Nauk USSR* 52(1946)511 (in Russian)
20. A.N. Kolmogorov *Izv. Akad. Nauk USSR* (1937)355 (in Russian)
21. E.D. Zanotto, *Thermochim. Acta* 280/281 (1996) 73
22. J. Šesták, *Phys Chem. Glasses* 15 (1974) 137
23. D.W. Henderson, *J Thermal Anal.* 15 (1979) 325
24. T.J.W. DeBroijn, W.A. DeJong, P.J. van den Berg, *Thermochim. Acta* 45(1981)315
25. J. Šesták “*Integration of nucleation-growth equation when considering non-isothermal regime*” in D. Dolimore (ed) *Proc. 2nd ESTAC (Europ. Symp. on Thermal Analysis), “Thermal Analysis”*, Heyden, London 1981, p. 115
26. A. Dobrova, I. Gutzow, *Cryst. Res. Technol.* 26 (1991) 863 and *J Appl. Polym. Sci.* 48 (1991) 473
27. J. Šesták key lecture „*Distinction of crystallization kinetics determined by isothermal and non-isothermal calculation methods*“ at the Chinese symposium on calorimetry and thermodynamic, Handzhow 1984; and T. Kemeny, J. Šesták, *Thermochim. Acta* 110 (1987) 113
28. J. Málek, *Thermochim. Acta.* 267 (1995) 61
29. L.C. Chen, F. Speapen, *J. Appl. Phys.* 69(1991)679 and *Nanostruct. Mater.* 11 (1992) 59
30. E. Illeková, *Thermochim. Acta* 280/281(1996)289 and 387(2002)47
31. H.V. Atkinson, *Acta Metall.* 36(1988)469
32. E. Illeková, *J. Non-cryst. Sol.* 287(2001)167
33. B. Idzikowski, P. Švec, M. Miglierini (eds.), “*Properties and Application of Nano-crystalline Alloys*” Kluwer, Dordrecht 2004
34. J. Šesták, G. Berggren, *Thermochim. Acta.* 3 (1971) 1
35. J.Šesták *J. Thermal Anal.* 36 (1990) 69
36. A.K. Burnham, *J. Thermal Anal. Calor.* 60 (2000) 895
37. J. A. Foreman and R. L. Blaine „*Isothermal crystallization made easy: a simple SB model and modest cooling rates*” and „*Isothermal crystallization using the Q Series*“ in *Thermal Analysis & Rheology Reports*, TA Instrument Inc., New Castle 2000
38. N. Sbirrazzuoli, Y. Girault and L. Elégant, *Thermochimica Acta* 260 (1995) 147 and 293 (1997) 25
39. L. Koudelka, P. Mošner, P. Prokupková, *J. Thermal Anal. Calor.* 54 (1998) 937
40. J. Malek, *Thermochim. Acta* 355 (2000) 239
41. A.A. Joraid, *Thermochim. Acta* 436 (2005) 78

42. N. Koga, J. Šesták, Z. Strnad, *Thermochim. Acta* 203 (1992) 361
43. M.C. Weinberg, *Thermochim. Acta* 194 (1992) 93 and *J. Mining Metal. (Bor, Yugoslavia)* 35 (1999) 197
44. N. Koga, J. Šesták, *J. Amer. Cer. Soc.* 83 (2000) 1753
45. D. Clinto, A. Mercer, R.P. Miller, *J. Mater. Sci.* 5 (1970) 171
46. J. Málek, J. Klikorka, J. Šesták, *Thermochim Acta* 110 (1987) 281
47. J. Šimšová, Z. Šimša, J. Šesták, *J. Non-cryst. Solids* 110 (1979) 375
48. Z. Strnad, J. Šesták "Surface crystallization of $SiO_2-Al_2O_3-ZnO$ glasses" in J. Woods (ed), *Proc. 8th Inter. Conf. Reactivity of Solids, "Reactions of Solids"*, Plenum Press, New York 1977, p. 553
49. J. Šesták, Z. Strnad "Simulation of DTA crystallization peak on basis of nucleation-growth curves determined by optical microscopy" in J. Gotz (ed), *J. Proc. XI Inter. Congress on Glass, DT CVTS, Prague 1977, Vol. II, P. 249*
50. N. Koga, J. Šesták, *Bol. Soc. Esp. Ceram. Vidr.* 1 (1992) 185
51. J. Šesták, *Thermochim. Acta.* 98 (1986) 339
52. G. Tammann, *Z. Phys. Chem.* 25 (1898) 441.
53. M. Ito, T. Sakaino, T. Moriya, *Bull. Tokyo Inst. Technol.* 88 (1968) 124.
54. V.N. Filipovich, A.M. Kalinina, *Izv. Akad. Nauk USSR, Neorgan. Mat.* 4 (1968) 1532 (in Russian).
55. V.M.Fokin, E.D.Zanotto, N.S.Yuritsyn, J.W.P.Schmelzer, *Review, J Non-Cryst. Solids* 352 (2006) 2681.
56. A.Marotta, A.Buri, *Thermochim.Acta*,25 (1981) 341.
57. A.Marotta, A.Buri, F.Branda, S.Saiello "Nucleation and Crystallization of $Li_2O-2SiO_2$ Glass: A DTA Study" in J.H. Simmons, D.R. Uhlman, G.H. Beall (edts) *Advances in Ceramics, Vol.4, Nucleation and Crystallization in Glasses*, American Ceramic Society, Columbus, OH, 1982, pp. 146-152.
58. C.S.Ray, D.E.Day, *J.Am.Ceram.Soc.*,73 (1990) 439.
59. C.S.Ray, D.E.Day, *J.Am.Ceram.Soc.*, 74 (1991) 909.
60. C.S.Ray, X.Fang, D.E.Day, *J.Am.Ceram.Soc.*, 83 (2000) 865.
61. C.S.Ray, D.E.Day, *J. Mater.Science*, 37 (2002) 547.
62. P.C. Soares Jr., E.D. Zanotto, V.M. Fokin, H. Jain, *J Non-Cryst. Sol.* 33 (2003) 217.
63. F.C. Collins, *Z. Electrochem.* 59 (1955) 404
64. D. Kashchiev, *Surf.Sci.* 14 (1969) 209
65. Siglass data –Science Vision Version 5. www.esm-software-com/vci_glass
66. V.M. Fokin, PhD Thesis "The investigation of stationary and non-stationary crystal nucleation rate in model glasses of stoichiometric composition $Li_2O_2SiO_2$ and $2Na_2OCaO_3SiO_2$ " Institute of Silicate Chemistry of Russian Academy Sciences, 1980 (in Russian)
67. O.V. Potapov, V.M. Fokin, V.L. Ugolkov, L.Y. Suslova, V.N. Filipovich, *Glass Physics and Chemistry* 26 (2000) 27.
68. C.S. Ray, D.E. Day, *Thermochim. Acta* 280/281 (1996) 163.
69. C.S. Ray, Q. Yang, W. Huang, D.E. Day, *J.Am.Ceram.Soc.*, 79 (1996) 3155.
70. V.M. Fokin, O.V. Potapov, E.D. Zanotto, F.M. Spiandorello, V.L.Ugolkov, B.Z. Pevzner, *J Non-Cryst. Solids* 331 (2003) 240.



Chapter 14

Metallic glasses

14. CRYSTALLIZATION OF METALLIC MICRO- AND NANO-CRYSTALLINE GLASSES

Emília Illeková, Jaroslav Šesták

14. 1. Introduction to metallic glasses

The precursors of the foregoing kinetic analyses are rapidly quenched alloys by using a rapid cooling rate ($> -10^5$ K min⁻¹ applied by the planar-flow casting technique [1]), which are in the form of ribbon-shape samples (thickness ~ 20 -30 μm , width ~ 6 -10 mm, length of several m) and also slowly cooled samples (cooling rate $< -10^2$ K min⁻¹ providing a bulk-shape metal-metalloid and multi-metallic alloys with the dimension > 1 mm). The products are completely crystalline or partially crystalline heterogeneous composites.

The crystallization of metallic glasses has been studied to a large extent (e.g. in [2-4]) still remaining an active area of research due to various characteristic peculiarities of its crystallization kinetics. A new methodological approach for the kinetic analysis has been practiced; it is based on the complexity of both the isothermal and the continuous heating, differential in its form of integral examinations, where especially the *Suriñach's* curve fitting procedure was introduced and successfully utilized [5,6] for both isothermal and continuous heating. The crystallization kinetic parameters have been determined and followed by the concluding interpretation upon assuming certain mechanisms, which are deduced within the scope of the classical (*nucleation-and-growth abbreviated as JMAYK*) mechanism as well as within an alternative (*normal-grain-growth abbreviated as GG*) kinetic law. Results are a part of a current systematic investigation of the thermodynamic stability and crystallization of the Pd-Si-based, Fe-Co-B, Fe-Si-B-based and Al-based metallic ribbons. Results have been generalized for a variety of rapidly quenched metallic ribbons from a binary metal-metalloid up to the multi-component metallic alloys established according to the kinetics of their crystallization. The glasses have been divided into two types, namely the conventional metallic glasses and the multi-component precursors for the nano-crystalline alloys.

14. 2. General reviewing of crystallization kinetics

The classical theory of crystallization of solids/liquids [7,8] is briefly revised even though the widespread amount of crystallinity can often be detected already before the completion of devitrification into the undercooled liquid state of metallic glasses. Generally saying, crystallization typically occurs by two independent but inter-correlated elementary events, i.e., nucleation and growth, each of them being controlled by either mechanisms: diffusion of atoms (or movable units) to, through, or out of the liquid (or glassy matrix) crystal interface and surface chemical reaction (i.e., incorporation of reacting units into and out of the interface). Nucleation may be homogeneous or heterogeneous, or there may be pre-existing nuclei (homogeneous or heterogeneous, internal or surfacial). Growth may be primary, eutectic or polymorphic [3]. For a partially transformed material, in which the transformed regions, i.e. the crystalline grains, are randomly dispersed, the volume fraction transformed x is related to the extended volume fraction x_{ex} [7-23], When ignoring impingement we obtain a traditional exponential proportionality:

$$x = 1 - \exp(-x_{\text{ex}}) \quad (1)$$

where x_{ex} is easily derivable in the customary isothermal case as shown in comprehensive literature [7-23]. The same treatment, however, can be extended to any exposed thermal

regime (such as a non-isothermal common during DTA/DSC measurements) when assuming temperature-dependent integration [14-16]. Such a distinctive case was analyzed in details by *Kemeny* and *Sestak* [17] yielding the concealed but anticipated fact that that the non-isothermal equivalent of the isothermally derived JMAYK relation is almost correspondent differing just by the integration-dependent multiplying constant, which is reliant to the means of approximation of the temperature integral [18].

Routinely proceeding $x_{ex} = (4\pi/3) N_0 u^3 t^3$ for spherical crystals with radii growing in time t at a constant rate u on a fixed number of nuclei per unit volume N_0 of already existing sites. When nucleation occurs at a constant frequency per unit volume, i.e., with a constant nucleation rate I , then $x_{ex} = (\pi/3) I u^3 t^4$. The extended volumes are additive, so for a material with both the pre-existing and new nuclei sites we can write,

$$x = 1 - \exp [- (\pi/3) u^3 (4N_0 t^3 + I t^4)]. \quad (2)$$

Commonly, isothermal kinetics of crystallization of metals is evaluated using the generalized *Johnson-Mehl-Avrami-Yerofeeyev-Kolmogorov* (JMAYK) relation [9-12] (which is accepted as the rate equation for all types of interface-controlled crystallization as well as the approximate rate equation in the case of the diffusion-controlled crystallization [9,10,20])

$$\alpha_T(t) = 1 - \exp [- (k_T t)^n] \quad (3)$$

where $\alpha(t)$ is the dimensionless extent of a transition in time t or, more commonly, the kinetic degree of conversion (crystallization) $\alpha(t)$ ($0 \leq \alpha(t) \leq 1$), k_T is the overall rate constant (containing both the growth rate and the nucleation rate), and n is a parameter (often called *Avrami* exponent) that depends on the mechanism of crystallization by the way shown given in Table 1 [19,21]. Generally

$$n = n_I + n_u \quad (4)$$

and n_I and n_u are the nucleation and growth Avrami parameters. Endowing with that claim that the temperature range is not too large, the temperature dependence of k_T obeys an Arrhenius type of exponential equation [13,20]

$$k(T) = A \exp (-\Delta E^+/RT), \quad (5)$$

where both the pre-exponential term A and the *Arrhenius* activation energy $\square E^+$ are temperature independent and R is the gas constant. The empirical activation energy $\square E^+$ is a weighted sum of the basic nucleation and growth ones, e.g.

$$\Delta E^+ = (n_I \Delta E_I^+ + n_u \Delta E_u^+) / (n_I + n_u). \quad (6)$$

A detailed discussion directed to the crystallization of metals and alloys can be found in various books (*Burke* [20], *Christian* [21] and *Sestak* [7,13]). At temperatures at which atomic mobility is noticeable, local rearrangements of the various atomic species occur simultaneously as a result of thermal agitation following thus the classical theory of homogeneous nucleation. In the state of non-equilibrium glass or an undercooled liquid (below the melting temperature $T < T_m$), these embryonic regions become of considerable importance because they are a potential source of nuclei ready for a change to a more stable structure. The embryos for crystallization are assumed to be internally uniform and have the

same structure, composition and properties as the final product phase in bulk form, e.g., the crystals. The *Gibbs* free energy of formation of an crystalline embryo of radius r , is

$$\Delta G(r) = 4/3\pi r^3 \Delta G_{cr-l} + 4\pi r^2 \gamma + \Delta G_{elast} + \Delta G_{deform}, \quad (7)$$

Table 1

(a) *Polymorphic changes, eutectoid reactions, discontinuous precipitation, interface controlled growth*

Conditions	n
Increasing nucleation rate, three dimensional growth	>4
Constant nucleation rate, three dimensional growth	4
Decreasing nucleation rate, three dimensional growth	3-4
Zero nucleation rate (saturation of points), three dimensional growth	3
Constant nucleation rate, two dimensional (plate-like) growth	3
Zero nucleation rate (saturation of points), two dimensional (plate-like) growth	2
Constant nucleation rate, one dimensional (needle-like) growth	2
Zero nucleation rate (saturation of points), one dimensional (needle-like) growth	1

(b) *Diffusion controlled growth*

Conditions	n
Increasing nucleation rate, three dimensional growth	>2.5
Constant nucleation rate, three dimensional growth	2.5
Decreasing nucleation rate, three dimensional growth	1.5-2.5
Constant nucleation rate, two dimensional (plate-like) growth	2
Zero nucleation rate (saturation of points), three dimensional growth	1.5
Constant nucleation rate, one dimensional (needle-like) growth	1.5
Zero nucleation rate (saturation of points), two dimensional (plate-like) growth	1
Zero nucleation rate (saturation of points), one dimensional (needle-like) growth	0.5

in which $\Delta G_{cr-l} = < 0$ for $T < T_m$ is the difference between the Gibbs free energy of a crystal and a liquid (or a glass) per unit volume of a crystal being thus the driving force for crystallization, $\gamma > 0$ is the interfacial energy per unit area of the crystal-liquid interface (assumed independent of the interface curvature r). ΔG_{elast} and ΔG_{deform} are respectively the evolved elastic strain energy and lattice deformation energy often administered to be neglected in the instance of crystallization of metallic glasses. $\Delta G(r)$ passes through a maximum, which is denoted by W being the work (or energy) of formation of a stable embryo (traditionally named as nucleus) at a radius r_c , which is the critical nucleus size. Growth of embryos smaller than r_c leads to an increase in $G(r)$ and thus there is a distinctive predisposition for such embryos to disappear rather than grow; only embryos larger than r_c are stable (taking already the shape of crystalline grains) because their growth is accompanied by a decrease in Gibbs energy $G(r)$. Differentiation of eq. (7) with respect to r gives $r_c = -2\gamma / \Delta G_{cr-l}$ so that

$$W = (16\pi\gamma^3)/(3\Delta G_{cr-l}^2). \quad (8)$$

An embryo of radius r_c has an equal chance of shrinking or growing and it becomes a nucleus when gaining one or more atoms. The nucleation rate or the number of nuclei that appear per unit volume of a liquid (or a glass) per unit time (under a steady state condition) is then

$$I_s = N_V N_s p_N v \exp [-(\Delta G_D^+ + W)/(RT)] = I_0 \exp [-\Delta G_N^+/(RT)], \quad (9)$$

where N_V is the number of sites per unit volume at which embryos can form, N_s is the number of atoms in the matrix at the surface of the critical embryo, ν is the frequency of vibration of these atoms, and p_N is the probability that a vibration realizes in the direction of the embryo and ΔG_D^+ is the activation Gibbs free energy of the jump process across the embryo/liquid interface (Generally noting, no distinction is made in the text between activation Gibbs free enthalpy ΔG^+ , activation enthalpy ΔH^+ and activation energy ΔE^+ since this distinction was not done in many older papers in the field. Besides, a particular activation entropy ΔS^+ could formally be integrated into the particular pre-exponential term).

Heterogeneous nucleation taking place on impurity surfaces can be modeled in a similar way to homogeneous nucleation, where the work of formation of critical nuclei W_{het} can be generally reduced in a great extent according to the angle of contact θ as for example shown in ref. [13,20]

$$W_{het} = W (2 + \cos\theta)(1 - \cos\theta)^2/4 . \quad (10)$$

In the classical theory the transient nucleation effect can occur because all clusters of the nucleation phase, i.e., the nuclei are factually assembled ‘molecule-by-molecule’ and thus do not arise by single large fluctuations. Consequently during nucleation, there exists a distribution of cluster sizes. In a steady state the nucleation rate can subsist only if the steady state of size distribution can be established. Attending the steady state, transient effects can arise in nucleation and during the devitrification transient nucleation effects are particularly significant because of low atomic (or molecular) mobility. When a glass is formed at a given quenching rate, which is greatly exceeding the critical quench necessary for glass formation, the population of crystal clusters in the initial glass may be negligible. In such a case there exist single form analytical approximations for nucleation kinetics [20]

$$I(t) = I_s (t - \theta) \quad \text{or} \quad = I_s \exp(-\theta/t) \quad \text{or} \quad = I_s \exp [1 + 2 \sum_{p=1}^{\infty} (-1)^p \exp(-p^2 t / \theta)], \quad (11)$$

where I_s is the steady state nucleation rate, t is the total experimental time, θ is the effective time lag (or better induction time) and p is an integer. However, a wide variety of transient nucleation behavior is observable in the presence of quenched-in clusters. Then nucleation cannot be characterized by a single time lag and a numerical approach is necessary to follow the each particular case.

Growth of a stable nucleus takes place by the thermally activated transfer of atoms from the liquid (or glass) to the crystal lattice causing the interface to advance through the initial phase. The basic atomic process is analogous to diffusion. In the case of the polymorphic transformation type of crystallization the reaction interface involves just the movement of individual atoms across the short distances (characterize by ΔG_D^+). When dealing with an eutectoid formation and precipitation (primary crystallization), when a composition changes are accommodated, the crystallization is accomplished by the long distances transport of various kinds of atoms (characterized by ΔG_D^+). In any case the rate of growth depends upon the relative rates of the interface reaction and diffusion and becomes only constant if the former is vastly slower than the latter. Then, taking into account the concept of activation states and the forward-and-backward interface reactions, the empirical (Turnbull) expression for the linear (or constant) rate of the growth of the crystalline phase u is (being in general use for the crystallization of amorphous metals)

$$u = V_{at} N_s p_u \nu \varepsilon \exp[-\Delta G_D^+ / (RT)] \{1 - \exp[\Delta G_{cr-l} / (RT)]\} \approx u_0 \Delta G_{cr-l} / (RT) \exp[-\Delta G_u^+ / (RT)], \quad (12)$$

where V_{at} is the volume of one atom (or the moving element) and ε is the accommodation coefficient for the crystal, p_v and ΔG_D^{*+} are the probability and the activation Gibbs free energy of the jump process across the crystal/liquid interface. $\{-\Delta G_{cr-l}/(RT)\}$ term simplifies the exponential in curled brackets in eq. (12) for $|\Delta G_{cr-l}| \ll RT$.

The Arrhenius-like expressions (9) and (12) defining I_0 , u_0 , ΔG_N^+ and ΔG_u^+ as the nucleation and crystal growth rate pre-exponential terms and the activation energies are merely apparent because of considerable temperature (and particularly undercooling) dependences of various embraced parameters. In general, it follows from eqs. (8), (9) and (12) that both I and u are zero at T_m (when $\Delta G_{cr-l} = 0$) and also at $T = 0$ K (when $p_N = p_u = 0$), attaining their maxima at some intermediates temperature. Further

$$\gamma(T) = -(\beta / K') \Delta H_{cr-l}(T) (V_{mol} / N_a)^{1/3}, \quad (13)$$

where the constant $\beta \sim 0.43$ (depicted for metals), K' is an interface quality factor, V_{mol} is the molar volume of the substance and N_a is the Avogadro number. At the undercooling, $\Delta T = T - T_m < 0$, and when assuming that both the enthalpy and entropy of crystallization are constant material parameters being equivalent to the melting ones, $\Delta H_{cr-l} = -\Delta H_m$ and $\Delta S_{cr-l} = -\Delta S_m = -\Delta H_m/T_m$, then

$$\Delta G_{cr-l}(T, \Delta T) = \Delta H_{cr-l} - \Delta S_{cr-l} T = \Delta H_m \Delta T / T_m. \quad (14)$$

In general, the JMAYK kinetic law (3) with the time-dependent nucleation and growth rates $I(t)$ and $u(t)$ and under the assumption that the density of nuclei $N(t) = N_0 + \int_0^t I(t') [1 - \alpha(t')] dt'$, (i.e., accounting the impingement effects for nucleation, see e.g. [13,20]) is

$$\alpha(t) = 4\pi/(3V) \cdot \{N_0 [\int_0^t u(t') dt']^{nu} + \int_0^t I(t') [1 - \alpha(t')] \cdot [\int_{t'}^t u(\lambda) d\lambda]^{nu} dt'\}, \quad (15)$$

or assuming that the growing nuclei do not overlap (e.g. [22])

$$\ln [1 - \alpha(t)]^{-1} = 4\pi/(3V) \cdot \{N_0 [\int_0^t u(t') dt']^{nu} + \int_0^t I(t') [\int_{t'}^t u(\lambda) d\lambda]^{nu} dt'\}. \quad (16)$$

Although neither of these versions of the JMAYK expression accounts for a real impingement, the numerically fitted material kinetic parameters more-or-less confirm the validity of this JMAYK model for many cases of metallic glasses, too. For instance it is the simultaneous surface and volume crystallization of glassy ribbon of $Pd_{82}Si_{18}$ [4] or even the crystallization of glassy $Fe_{80}B_{20}$ [2] if the growth rate is allowed to vary with drawing direction. A very limited studies have been done on the quantitative modeling of primary crystallization kinetics in the case of partitioning two-component metallic systems, in which the varying composition of both the clusters and the remaining untransformed glass has to be accounted for [23,24] as well variable mobility, i.e., so called soft-impingement

Alternatively to the JMAYK (nucleation-and-growth crystallization process), the GG normal-grain-growth of extremely fine crystalline grains (coalescence process) were suggested for the condition of nano-crystal formation in certain metallic foils [25]. In the normal-grain-growth process, larger grains in the already crystalline material increase their size at the expense of smaller grains. The driving force for this process provides the decrease in the interfacial enthalpy, i.e,

$$H(t) = H_0 r_0 / r(t), \quad (17)$$

where H_0 and r_0 respectively are the initial interfacial enthalpy and the initial average grain radius (of approximately several angstroms being thus experimentally “invisible”). The increase in the average grain radius $r(t)$ is controlled by the following kinetic equation [27]

$$dr(t)/dt = K(T) / [m r(t) (t)^{m-1}] \quad , \quad (18)$$

where the grain growth rate constant $K(T)$ has the Arrhenius-like temperature dependence

$$K(T) = A_{GG} \exp [-\Delta E_{GG}^+ / (RT)] \quad (19)$$

and where m is the grain growth exponent (depending on the mechanism of the coalescence by the way given in Table 2), A_{GG} and ΔE_{GG}^+ being the pre-exponential factor and activation energy, respectively. Because the evolution of the total interfacial enthalpy is related to the measured DTA/DSC signal $y(t) = dH(t)/dt$ as

$$H(t) = H_0 + \int_0^t y(t') dt' = H_0 [1 - \alpha(t)], \quad (20)$$

the GG integral kinetic equation is [28]

$$[1 - \alpha(t)]^m = \tau_{GG}(T) / [t + \tau_{GG}(T)], \quad (21)$$

where the time constant $\tau_{GG}(T)$ is related to the rate constant $K(T)$ as $\tau_{GG}(T) = r_0^m(T) / K(T)$.

Table 2. Values of m in GG kinetic law $\alpha_T(t) = 1 - [(r_0^m \tau_{GG}) / (t + r_0^m \tau_{GG})]^{1/m}$ [27].

mechanism controlling grain growth		m
pure system		2
impure system	coalescence of second phase by lattice diffusion	3
	coalescence of second phase by grain boundary diffusion	4
	solution of second phase	1
	diffusion through continuous second phase	3
	impurity drag (low solubility)	3
	impurity drag (high solubility)	2

14. 2. Crystallization kinetics of metallic glasses

In classical multi-component metallic glasses, the crystallization is characterized by a sequence of crystallization steps, R1, R2, R3,... and until recently it is an unresolved questions whether all of the steps (especially the first step R1) are always taking place in the whole body of the sample (i.e. questioning the homogeneity in the one-component glassy precursor or the matrix) or only in its separated parts (i.e., the problem of dimensionality of the heterogeneities [28-30] in the two-cluster model [28-32]). Commonly, the higher values of activation energies for crystallization indicate the viscous-flow-dependent mechanism; they eventually decrease with increasing temperature or with increasing degree of conversion [33]. This might suggest occurrence of some changes in the mobile structural units (as for the crystallization of the amorphous matrix [33]) or some modification in either rates controlling the elementary process (as for the FINEMET-type ribbons in the case of JMAYK kinetics [28]) or being in charge of the proportion between the individual processes in the complex transformation [33]. In general, the nucleation-and-growth crystallization (JMAYK kinetics)

with several characteristic peculiarities has been active in the case of conventional metallic glasses [30-33] for long. However, the application of JMAK kinetics completely fails in a specific group of rapidly quenched ribbons, which implicate nano-crystallization, as in the case of nicknamed group of materials like FINEMETs, NANOPERMs, HITPERMs or even some other Al-based alloys [28-32]. In a broader-spectrum, the mathematical formalism of the normal-grain-growth crystallization (GG kinetics [27]) can interpret exclusively the experimental data in the case of stable nano-crystal formation in rapidly quenched ribbons [30,32]. In the case of the primary crystallization of some metallic ribbons some diffusion reactions might take place, too, if the change of the chemical composition in the non-crystalline matrix was indicated (the so called ‘softening effects’) [28-32].

14.2.1. Peculiarities in the JMAK-like crystallization kinetics of conventional metallic glasses

Glassy Fe-Si-B ribbons are of great technological importance because of their functional magnetic properties. In addition, they represent a basic glass-forming material for multi-component alloys formed upon crystallization of a extremely fine crystalline phase, best known as FINEMETs. (The mutual ratio of the elements in the glassy matrix of the FINEMET corresponds approximately to $\text{Fe}_{75}\text{Si}_{15}\text{B}_{10}$ [31].)

A series of both the hypoeutectic and the hypereutectic Fe-Si-B compositions as a source for quenched non-crystalline ribbons (namely $\text{Fe}_{80}\text{Si}_x\text{B}_{20-x}$ with $x = 2, 4, 6, 8$ and 10 and $\text{Fe}_{75}\text{Si}_{15}\text{B}_{10}$), were prepared by planar flow casting method technologically providing their 10 mm width and approximately 25 μm thickness. Their kinetics of crystallization was examined using DSC and high precision electrical resistivity measurements [31,33]. The initial amorphous state and the corresponding phases after the crystallization were observed using transmission electron microscopy (TEM) and x-ray diffraction (XRD) analysis.

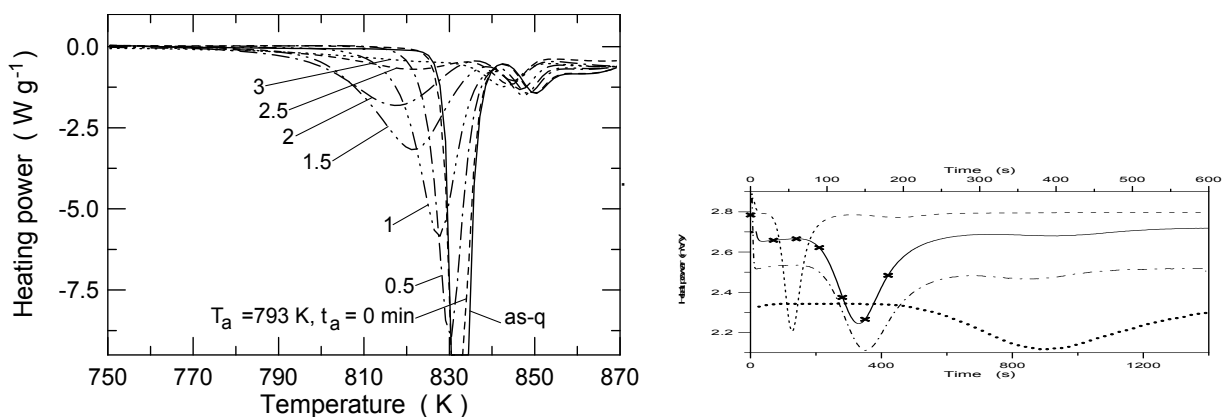
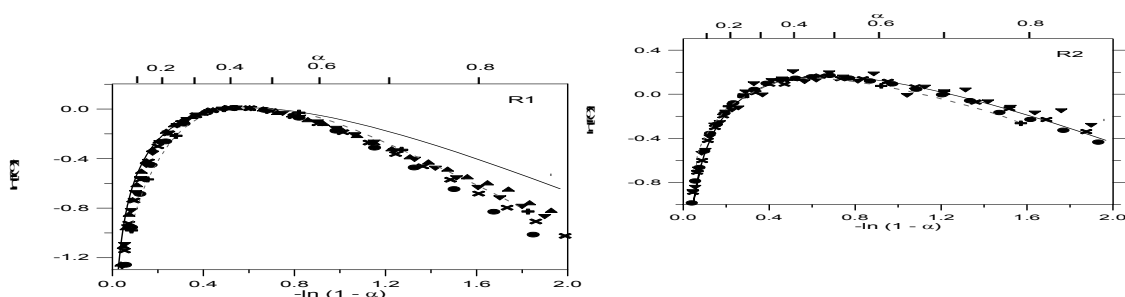


Fig. 1. Effect of pre-annealing on the continuous heating DSC curve of the crystallization of $\text{Fe}_{75}\text{Si}_{15}\text{B}_{10}$ ribbon (the pre-annealing temperature $T_a = 793$ K; the pre-annealing time t_a is the parameter; heating rate $w^+ = 40$ K min^{-1}) [33].

Fig. 2. Isothermal DSC crystallization curves at various temperatures T_a of the as-quenched glassy $\text{Fe}_{75}\text{Si}_{15}\text{B}_{10}$ ribbon. For $T_a = 803$ K (----) and 793 K (—) the upper time scale holds. For $T_a = 783$ K (-.-.-) and 773 K (.....) the lower time scale holds. The symbols (x) mark the partial crystallization effects produced by the pre-annealing heat treatments for the measurements shown in Fig. 1 [33].

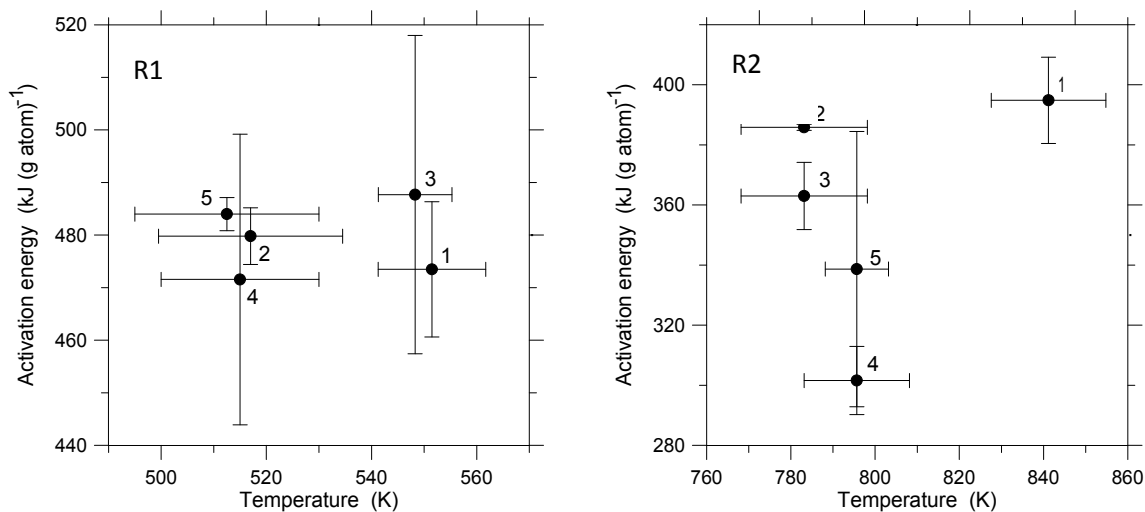
The whole of Fe-Si-B-based glasses with composition in the mentioned region of interest crystallize usually in a two-step crystallization reaction due to their thermal activation taking place in the course of continuous heating or isothermal annealing. The two extensive exothermal reactions are related within the two different phase transformations. Their eventual overlap, the relation between both the enthalpies and also the kinetics of R1 and R2 transformations depends on the actual chemical composition and thermal history of the samples (w^+ , T_a , pre-annealing). As a typical example (shown in Fig. 1.), one large and sharp thermal effect appears closely followed by the smaller secondary one (at the heating of $w^+ = 40 \text{ K min}^{-1}$), which is well visible for $\text{Fe}_{75}\text{Si}_{15}\text{B}_{10}$ ribbon. Both DSC exotherms have slightly slower leading edges than the trailing ones. Any pre-annealing shifts both peaks to lower temperatures significantly decreasing their enthalpies. Also in the isothermal mode, the DSC curves show two exothermal effects as is seen in Fig. 2. Both isothermal transformations are temperature dependent significantly shortening their time by increasing the temperature.



Figs. 3 (a) and (b). The Suriñach plots for R1 and R2, respectively, both for the isothermal and continuous-heating crystallization peaks of the as-quenched glassy $\text{Fe}_{75}\text{Si}_{15}\text{B}_{10}$ ribbon and the theoretical curves obtained for the JMAK kinetic equation with the exponents $n_1 = 2.5$ in the case of R1 and $n_2 = 3$ in the case of R2, respectively. Full lines are the theoretical curves. Symbols are the experimental data for the isotherm at $T_a = 773 \text{ K}$ (\blacktriangle), 783 K (\blacktriangledown), 793 K (\times), 808 K (\bullet); and the continuous heating at 40 K min^{-1} ($+$) (the connecting dashed line is a guide to the eye for $+$ symbols) [33].

The kinetics of the R1- and R2- DSC effects was studied by the complex kinetic analysis [33]. Accordingly, in order to test the relevancy of JMAK nucleation–growth kinetics to study R1 and R2 crystallization steps of the as-quenched $\text{Fe}_{75}\text{Si}_{15}\text{B}_{10}$ ribbon, the Suriñach curve fitting procedure [5] was employed. All measured curves (from Figs. 1 and 2) were used resolving that all measured data for both crystallization steps could be unambiguously characterized by the JMAK kinetics (Figs. 3 (a) and (b)). In the case of R1, Suriñach graphs follow one master curve; however, the value of its JMAK exponent n_1 is not constant. In the early stages, n_1 alternates steeply revealing the transient nucleation effect reaching the value of $n_1 = 2.5$ (see the central part of the transformation). Later n_1 continuously decreases reflecting thus the probable saturation of nucleation and in the dynamic measurements also the influence of the secondary crystallization step. In the case of R2, the transformation can be well characterized by single JMAK exponent ($n_2 = 3$).

The heating rate dependence of the maximum for R1 crystallization peak [34] is specified by the activation energy $\Delta E_{K1}^+ = 473 \pm 13 \text{ kJ mol}^{-1}$ (as-quenched $\text{Fe}_{75}\text{Si}_{15}\text{B}_{10}$ ribbons). However, the temperature dependent Kissinger slope [34] revealed some peculiarities in R2 mechanism with an average activation energy $\Delta E_{K2}^+ = 395 \pm 14 \text{ kJ mol}^{-1}$. The value of $\Delta E_{S1}^+ = 484 \pm 3 \text{ kJ mol}^{-1}$ is independent of T_a , and ΔE_{S2}^+ is decreasing from 384 to 293 kJ mol^{-1} with increasing T_a (found from the vertical shift between the Suriñach plots of DSC isothermal R1 and R2 peaks [6]). The isothermal Arrhenius method (consequential of eq. 5) is providing $\Delta E_{A1,\alpha=0}^+ = 651 \pm 67 \text{ kJ mol}^{-1}$, $\Delta E_{A1,\alpha=0.45}^+ = 480 \pm 5 \text{ kJ mol}^{-1}$ and $\Delta E_{A1,\alpha=1}^+ = 417 \pm 3 \text{ kJ mol}^{-1}$. Both isothermal and continuous heating iso-conversional methods [35] ($\Delta E_{Ih}^+(\alpha)$ in Fig.5 in [33] and $\Delta E_{Ich}^+(\alpha)$) revealed systematic acceleration for R1 transformation with advanced time. $\Delta E_{2}^+(\alpha)$ kept a constant value during the whole R2 transformation,



Figs. 4 (a) and (b) show the dependence of the activation energy on the evaluation method (DSC kinetic analysis applied to the crystallization of respective steps R1 and R2), in the as-quenched $\text{Fe}_{75}\text{Si}_{15}\text{B}_{10}$ glassy ribbon. (1) The Kissinger activation energy ΔE_K^+ , (2) the Arrhenius method activation energy calculated for the isothermal peak maximum $\Delta E_{A,\alpha=0.45}^+$, (3) and (4) the iso-conversional continuous heating and isothermal activation energies ΔE_{Ich}^+ and ΔE_{Ih}^+ , respectively, (5) the isothermal Suriñach method activation energy ΔE_S^+ . Horizontal bars - the width of the temperature interval taken into account; vertical bars – the error of the presented mean value [33].

As is typical for the case of the crystallization of Fe-Si-B ribbons [31] the above-mentioned results demonstrated that the determined activation energies are dependent on the measuring regime and the method of kinetic analysis applied. These quantities are summarized in Figs. 4 (a) and (b). It can be seen, that they agree within the experimental error for both R1 and R2 stages. Nevertheless, on the bases of these absolute values and their error bars (as well as in accordance with the results of the TEM and XRD analyses) the following interpretation has been formulated [33].

Concerning the $\text{Fe}_{75}\text{Si}_{15}\text{B}_{10}$ ribbon, the crystallization of two types of micro-crystals, namely the homogeneous nucleation and growth of <b.c.c.> Fe(Si) (or alternatively Fe_3Si) and also composite crystals consisting <b.c.c.> Fe(Si) nucleating heterogeneously and growing on the surface of the previously formed orthorhombic Fe_3B microcrystalline cores, is proceeding in the R1 crystallization step. The relative proportions of these two types of micro-crystals are dependent on the temperature. The apparent activation energy of this primary crystallization $\Delta E_1^+ = f(\alpha_1)$ and the Avrami exponent $n_1 = f(\alpha_1)$ are independent of temperature and they decrease with increasing α_1 during R1 and with the pre-annealing (namely n_1 decreases from

2.5 to 1.5) promoting thus the formation of the orthorhombic Fe₃B grain-cores. The decay of the nucleation and the three-dimensional diffusion controlled growth of the composite are the prevailing mechanisms in the advanced stages of the R1 transformation (for $\alpha_1 > 0.6$). During the R1 crystallization step the chemical composition of the matrix continuously changes to reach the eutectic one. Finally, following the R2-DSC peak, the primary metastable Fe₃B cores of the composites transform in to the stable Fe₂B micro-crystals. Simultaneously, the remaining amorphous matrix (certainly, if any) crystallizes by the eutectic reaction forming the Fe₃Si and Fe₂B eutectic structure. The apparent activation energy $\Delta E_2^+ = f''(T_1)$ decreases with increasing temperature of the primary R1 reaction and the content of boron in the crystallizing pseudobinary eutectics decreases. The parameters ΔE_2^+ and $n_2 = 3$ are constant during the R2 transformation.

Concerning all Fe-Si-B-based ribbons [31], physical properties such as the Curie points, R1 and R2 crystallization temperatures, partial and total crystallization heats or activation energies, show monotonous tendency along with the increasing silicon content up to 8 at. % Si, culminating for the sample with 10 at. % of Si. However, for the 15 at. % Si the values become significantly different. JMAYK kinetic exponents are almost constant ($n_1 = 2.5$ or 1.5 and $n_2 = 4$ or 3) reflecting alternatively a probable exhaustion of nucleation sites (Tab.1 in Ref. 31).

Generally speaking [31], crystallization kinetics, chemical composition and the morphology of arising phases strongly depend on the mutual ration of components in the amorphous alloy. The investigated region of interest is divided in to the eutectic through the hypoeutectic up to the hypereutectic parts (when respecting to boron content c_B). The R1 crystallization step for hypoutectic compositions corresponds to the formation of α -Fe(Si) crystals; the remaining amorphous matrix transforms during the R2 step to α -Fe(Si) and stable tetragonal Fe₂B. For hypereutectic compositions the R1 step of crystallization is characterized by formation of crystals of metastable Fe₃B. Due to changes in local ordering of atoms the α -Fe phase nucleates and grows on their surface forming the so-called ‘composite crystals’ [31]. The R2 step of crystallization for these compositions besides the transformation of eventually remaining amorphous matrix corresponds to the transformation of metastable borides into stable Fe₂B and α -Fe. The local fluctuations of silicon concentration seem to be very important for the understanding of this process, particularly taking place during the phase transformations of the Fe-Si-B system. The application of the so-called ‘local ordering’ (double-cluster model) based on the role of silicon seems to be justifiable for the explanation of crystallization reactions observed. The determining factor is the co-called critical silicon concentration $c_{Si}^{crit} = \frac{1}{4} (1 - 5 c_B)$; above this value silicon causes changes in local ordering of atoms increasing thus the preference for the nucleation and growth of α -Fe(Si) phase [31].

14.2.2. Kinetics of nanocrystal formation in FINEMETs

Nano-crystalline alloys with the composition close to Fe_{73.5}Cu₁Nb₃Si_{13.5}B₉ (FINEMET[®]) have attracted technological and scientific interest extensively owing to their attractive properties as the soft magnetic materials. It is known that Cu and Nb affect not only the chemical short-range order in the resulting nano-crystalline structure but also the transformation kinetics of this structure. In numerous studies (by XRD, TEM, Mössbauer spectroscopy, as well as microprobe analysis) of the FINEMET the phase analyses revealed (see references in [28,30,32]) the presence of the crystalline iron-based silicon phase as well as the remainder of the amorphous phase with a reduced content of silicon. The nano-crystalline α -Fe(Si) phase with a mean grain size of 10-20 nm has the DO₃ structure of Fe₃Si with a silicon content of 16-22 at.% [28]. On the contrary there still have been contradicting conceptions about the transformation kinetics of the FINEMET-like precursors (as a rapidly quenched ribbon) to the nano-crystalline state. JMAYK kinetics has traditionally been

assumed; however, an unusually low exponent $n \approx 0.5$ and numerous other irregularities were observed [28,31].

Following the continuous heating measurements by DSC, the main transformation (R1 = R_{nano}) in the as-quenched Fe_{73.5}Cu₁Nb₃Si_{13.5}B₉ ribbon (the thick line in Fig. 5) starts at $T_{x,nano} = 816$ K. The exothermal peak is wide, asymmetrical, with a long high temperature tail. Before the beginning of the next pronounced exothermal anomaly (R2 at $T_{x2} = 957$ K) another less energetic exothermal transformation R1' is superimposed, which is associated with changes of some magnetic properties of the material. This effect can be separated from R1 by the isothermal heat treatment [28]. Any heat treatment of the sample at temperature T_a close to $T_{x,nano}$, or even at much lower temperatures in the range of pronounced structural relaxation effects, shifts the main transformation exotherm to higher temperatures diminishing its total enthalpy as is exhibited in Fig. 5. These observations are utterly conflicting the classical JMAK crystallization kinetics (represented by Fe-Si-B glasses in Fig. 1) where the heat-treatment at $T_a \approx T_{x1}$ shifted the R1 peak to lower temperatures diminishing thus the associated Avrami exponent. At $T_a < T_{x1} - 50$ K it was not influencing the peak position neither enthalpy nor the kinetic mechanism of the crystallization.

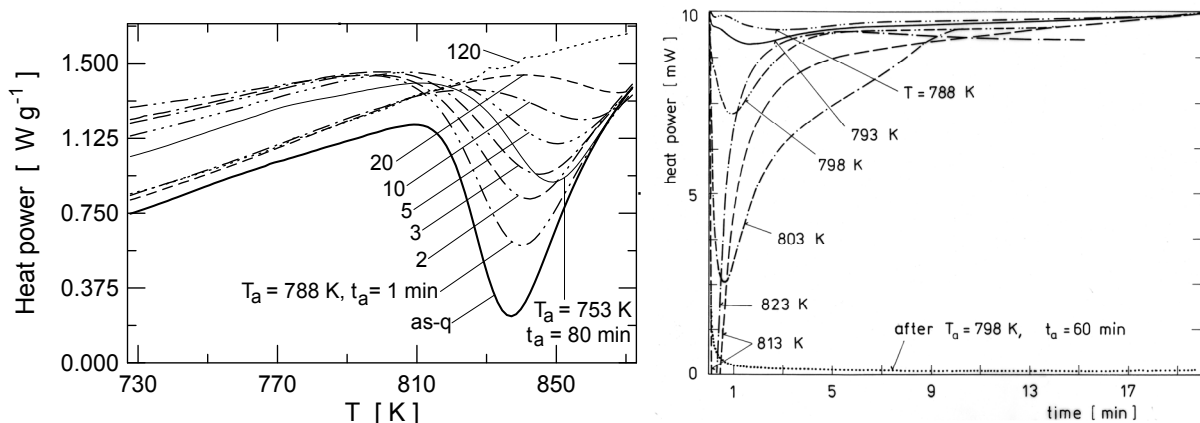


Fig. 5. (Right) Effect of pre-annealing on the continuous heating DSC signal of Fe_{73.5}Cu₁Nb₃Si_{13.5}B₉ ribbon during the main transformation to the nano-crystalline state (the pre-annealing temperature is T_a and the pre-annealing time is t_a being the parameters and the heating rate $w^+ = 40$ K min⁻¹ [28].

Fig. 6. (left) Isothermal DSC traces (first runs) at various temperatures T_a of as-quenched Fe_{73.5}Cu₁Nb₃Si_{13.5}B₉ ribbon representing the transformation to the nano-crystalline state (T_a being the parameter). The dotted line is the baseline obtained as a 2nd run under identical conditions after finishing the main transformation; it was shifted down to be seen in the picture [28].

In the case of the isothermal regime of the main transformation in the Fe_{73.5}Cu₁Nb₃Si_{13.5}B₉ ribbon, the unusual measurements are reported in ref. [28-30] and usually accredit to the work by Illeková. After a steep negative increasing, the isothermal DSC signal is monotonically approaching zero (see Fig. 6). Such decaying signals (or apparent exothermal peaks) were measured at T_a from 783 to 823 K the interval of which exceeds substantially the usual 25 K interval, where the R1 crystallization peak of metallic glasses is conveniently observed by the isothermal DSC technique (compare Fig. 2). Almost no change in the position of this main exothermal effect along with the temperature has ever been monitored. Only the changes of amplitude and slightly of the total enthalpy were detected.

In order to report both the continuous heating and the isothermal experimentation with respect to the interpretation of kinetics of the main transformation R1 in various Fe-Cu-Nb-Si-B ribbons the DSC was carried out and related to such a kinetic treatment revealing the peculiarities of nano-crystalline construction. Therefore various samples were measured with

changeable content of Cu (between 0 and 1 at. %), of Nb (between 0 and 4.5 at.%) and of the Si/B ration (between 0 and 1.5) [32]. In the R1 transformation, the nano-crystalline α -Fe was formed (the case of the FMCu_0Si_0 and FMSi_0 samples - concerning the names follow Table 3) with the mean grain size $d < 10$ nm. In the other samples, which contained more than 1 at. % of Si, the component α -Fe(Si) appeared with increasing tendency to DO_3 ordering with increasing Si content and fine-grained structure (with $d \sim 10$ nm). Therefore, all above mentioned samples are collectively named FINEMETs in all further citations. In the sample FMNb_0 , larger micro-crystals ($d > 100$ nm) grow similarly the case of conventional metallic glasses, discussed in the previous paragraph.

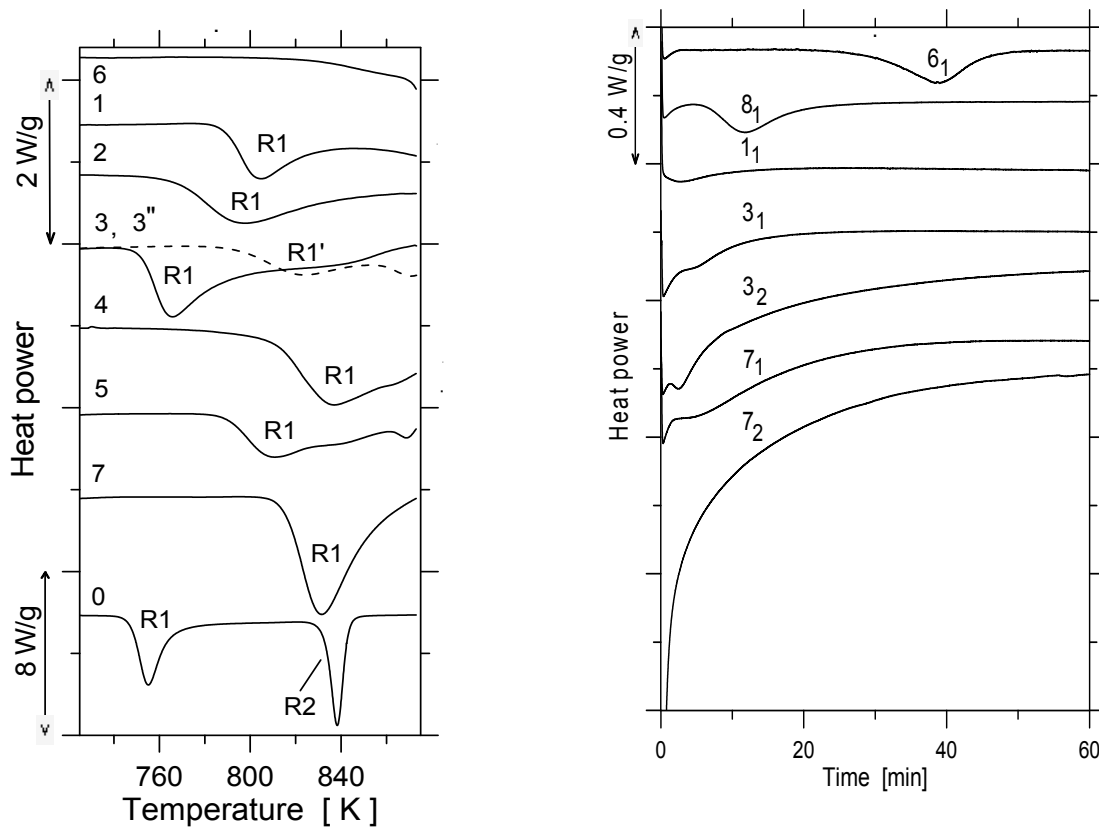


Fig. 7. (Left) Continuous heating DSC signal from the main transformation process of various as-quenched Fe-Cu-Nb-Si-B ribbons. 1- FMCu_0Si_0 , 2- FMSi_0 , 3- $\text{FMSi}_{4.5}$ (dashed line 3'' refers to the isothermally pre-annealed at 713 K for 200 min sample), 4- FMSi_7 , 5- $\text{FMSi}_{7.2}$, 6- $\text{FMCu}_0\text{Si}_{12.7}$, 7- $\text{FMSi}_{13.5}$, 8- FMNb_0 . The chemical compositions of the samples are in Tab. 3. The crystallization stages R_1 , R_1' and R_2 are related to the DSC exothermic peaks for some samples. The heating rate is 40 K min^{-1} . The vertical scale for the sample FMNb_0 (curve 0) is shrunk by the factor of 4. [32].

Fig. 8. (Right) Isothermal DSC traces from the main transformation process of various as-quenched Fe-Cu-Nb-Si-B alloys. 6₁- $\text{FMCu}_0\text{Si}_{12.7}$ (813 K), 8₁- FMNb_0 (698 K), 1₁- FMCu_0Si_0 (763 K), 3₁- $\text{FMSi}_{4.5}$ (713 K), 3₂- $\text{FMSi}_{4.5}$ (723 K), 7₁- $\text{FMSi}_{13.5}$ (778 K), 7₂- $\text{FMSi}_{13.5}$ (823 K). The chemical compositions of the samples are in Tab. 3. [32].

Fig. 7 and Fig. 8 show the continuous heating and isothermal DSC dependencies of all investigated samples. The shape of these curves does not depend on w^+ (excepting its horizontal shift) and it is slightly modified with T_a . In the case of $\text{FM Cu}_0\text{Si}_{12.7}$, the R1 peak occurs above 860 K. In all samples, excepting the FMNb_0 , the DSC continuous heating R1 peak is wide, asymmetrical, with longer high temperature part (Fig. 7); any pre-annealing at a temperature below the main transformation shifts the R1 peak to higher temperatures (the

same as in Fig. 5). The quantitative characteristics of R1 peaks are summarized in Table 3. The onset and minimum temperatures T_{x1} and T_{p1} vary with the actual chemical composition. They are significantly higher in the samples without Cu. All main transformation enthalpies ΔH_1 are less than one-half of the enthalpy of the first crystallization peak of the $\text{Fe}_{75}\text{Si}_{15}\text{B}_{10}$ metallic glass (104 Jg^{-1} in [33]). These quantities are also proportional to the content of the crystalline product. The Kissinger activation energies ΔE_{K1}^+ are less significant because of their dependence on the heat treatment and the used measuring technique [28]. In addition, another minor transformation stage R1' occurs before the termination of R1 peak (as is shown in Fig. 7 for $\text{FMSi}_{4.5}$ or in [28] for $\text{FMSi}_{13.5}$). At higher temperatures, the second complex exothermal peak R2 always stays on due to the additional growth of grains and crystallization of the remaining amorphous matrix. The isothermal main transformation curves have a bimodal character (Fig. 8), i.e. the DSC signal is continuously decaying simultaneously manifesting a superimposed exothermal peak in special cases. The mutual relation between both effects is strongly dependent on temperature due to a typical T_a dependence of the peak mode suggesting the JMAYK kinetics, whereas the decay mode (suggesting the normal-grain-growth (GG) or coalescence kinetics as will be shown in Fig. 10 and Fig. 11) is relatively insensitive to T_a (see curves 3₁ and 3₂ for the sample $\text{FMSi}_{4.5}$). At lower temperatures, $T_a \sim T_{x1} - 50 \text{ K}$ mainly the peak mode was detected (curve 6₁) whereas at higher temperatures, $T_a > T_{x1} - 10 \text{ K}$, only the decay mode could be detected (curve 7₂). Besides, the enthalpic proportion between the GG-like and JMAYK-like modes is strongly related to the chemical composition of samples.

The above-mentioned character of R1 transformation cannot be interpreted by any of the conventional JMAYK crystallization kinetics [6-8, 19-21]. As an example, the isothermal DSC curves from Fig. 8 (excepting curve 8₁ which represents FMNb_0 sample) cannot be linearized using the Avrami linearization method (see Fig. 9) even by subtracting any incubation time τ_{JMA} . The slope of the Avrami plot shows a systematic artificial decrease from 4 to 3 in the case of a TA curve with a large JMAYK-mode participation, finally dropping to 1.5 in the case that the peak-mode provides less significant contribution. Otherwise, the slope of the Avrami plot rapidly decreases after a short time giving an extremely low apparent exponent $n_1 < 1$. The last mentioned case is the most frequent and characteristic mode in the instance of FINEMETs. However, the spherulitic shape of the nano-crystals and the fact that the new grains do still appear also in the advanced stage of the main transformation can hardly be interpreted by any simple step JMAYK nucleation-and-growth kinetics with exponent $n = n_1 + 3n_u \leq 1$.

Besides, the nanocrystal formation reveals the bimodal character in the isothermal regime. In Fig. 10, our hypothesis of the participation of several independent processes in the R1 step in FINEMETs (two modes of the main transformation R1 and the participation of the R1' step) is evidenced and the influence of this fact on the deduced kinetic laws for the decomposed individual processes is demonstrated. The Suriñach curve fitting procedure was used. Thus for the example $\text{FMSi}_{4.5}$, the Suriñach plot [5,6] follows the GG-like kinetics [27] with $m_1 = 1$ for $\alpha_1 < 0.2$, then the kinetics continuously changes (when the peak starts to appear in the DSC signal) fitting well the JMAYK-like one with $n_1 = 3$ and finally with $n_1 = 2$ for $\alpha_1 > 0.5$ for the curve 3₂ from Fig. 8 in Fig. 10. On the other hand, The Suriñach plot representing just the extracted peak from the same curve 3₂ (after the appropriate baseline subtraction [32]) fits only one mode having the JMAYK kinetics with $n_1 = 2$ for all α_1 (see curve 3₂ in Fig. 10. Concerning the other DSC curves containing the peak mode, the JMA exponents vary between 3 and 1.5 depending on the composition of individual samples (they are summarized in Table 3).

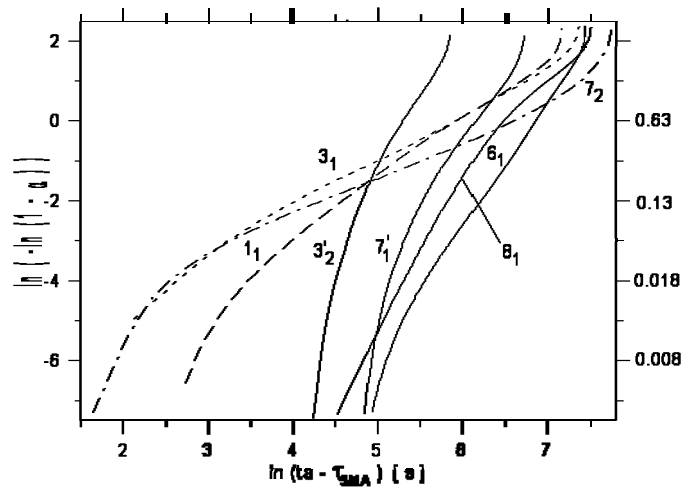


Fig. 9. Linearized Avrami representation of the isothermal DSC traces and presented in Fig. 8. are shown for the main transformation of various as-quenched Fe-Cu-Nb-Si-B ribbons. 7_1 and 3_2 —refer to the separated peaks only. [32].

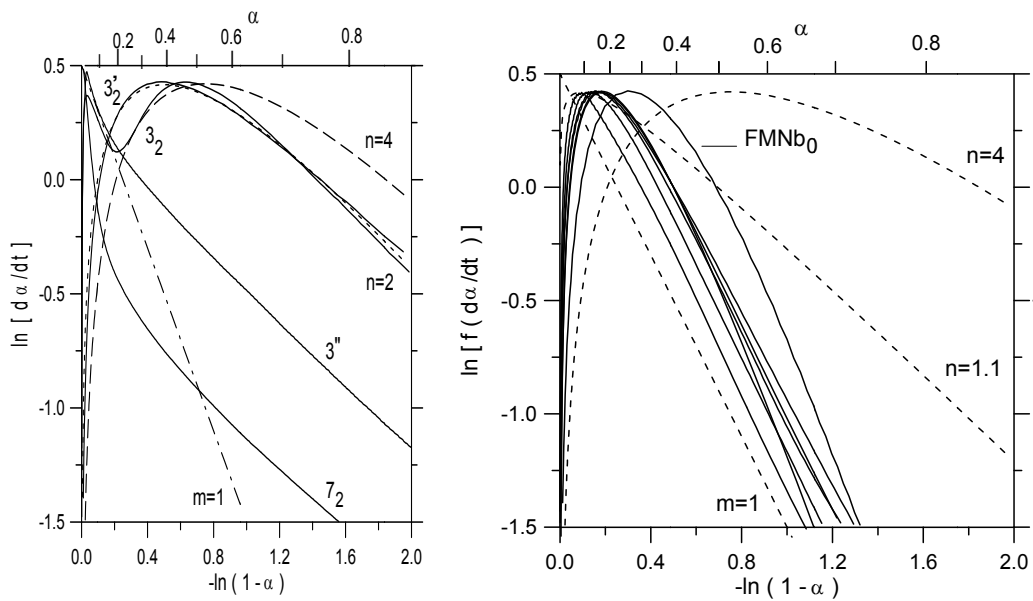


Fig. 10. Suriñach plots, which are showing the difference between the JMAYK-like and GG-like modes in the main transformation of the as-quenched Fe-Cu-Nb-Si-B ribbons. The isothermal data are taken from Fig. 8. 3_2 -FMSi_{4.5} (723 K), $3_2'$ -FMSi_{4.5} separated peak only, 7_2 -FMSi_{13.5} (823 K), $3''$ refers to the continuous heating run of isothermally pre-annealed at 713 K for 200 min FMSi_{4.5} sample (data are from Fig. 7). The curves are shifted to show the maxima at the same level. Dashed lines are the plots for the theoretical JMAYK kinetics with $n = 4$ and 2 and GG kinetics with $m = 1$. [32].

Fig. 11. Suriñach representations of the continuous heating DSC curves (presented in Fig. 7) derived from the main transformation of as-cast Fe-Cu-Nb-Si-B ribbons. The FMNb₀ sample is marked. The curves are shifted to show the maxima at the same level. Dashed lines are the plots for the theoretical JMA kinetics with $n = 4$ and 1.1 and GG kinetics with $m = 1$. [32].

Table 3: Thermodynamic and kinetic characterization of the main transformation of the as-cast FeCuNbSiB ribbons, where T_a and t_a the annealing temperature and time of the isothermal measurements are respectively, T_{x1} , T_{p1} and ΔH_1 are the onset and minimum temperatures and the enthalpy of the continuous-heating DSC peak R1 (heating rate $w = 40 \text{ K min}^{-1}$), respectively. ΔE_{K1}^+ is the activation energy deduced by the Kissinger method [34]. n_1 and m_1 (both ± 0.5) are the JMAK and GG exponents [30] deduced by the Suriñach isothermal and continuous-heating methods [5,6], respectively. The symbols * and # indicate the quantities which were not or could not be given, respectively [32].

Sample /Chart	Chemical composition	T_a, t_a [K,min]	T_{x1} [K]	T_{p1} [K]	ΔH_1 [Jg ⁻¹]	ΔE_{K1}^+ [kJmol ⁻¹]	n_1	m_1
FMCu ₀ Si ₀ (1) (1 ₁)	Fe _{80.5} Nb ₇ B _{12.5}	763, 60	788.7	802.7	-20	532±16	no 1.5	1
FMSi ₀ (2)	Fe _{77.5} Cu ₁ Nb _{4.5} B ₁₇	*	766.9	794.8	-34	*	no	1
FMSi _{4.5} (3) (3 ₁) (3 ₂) (3 ₃)	Fe ₇₈ Cu ₁ Nb ₃ Si _{4.5} B _{13.5}	713, 200 450,6 723, 60 540, 813, 60	751.7	765.8	>-61	298±6	no 2 2 1	1 1 1
FMSi ₇ (4)	Fe _{73.5} Cu ₁ Nb _{3.2} Si ₇ B _{15.3}	*	809.1	837.7	>-27	600±25	*	1
FMSi _{9.2} (5)	Fe _{74.6} Cu ₁ Nb _{3.2} Si _{9.2} B ₁₂	*	789.8	811.7	>-25	357±33	*	1
FMCu ₀ Si _{12.7} (6) (6 ₁)	Fe _{74.7} Nb _{3.1} Si _{12.7} B _{9.5}	813, 180	863.6	>873	#	#	# 4	#
FMSi _{13.5} (7) (7 ₁) (7 ₂)	Fe _{73.5} Cu ₁ Nb ₃ Si _{13.5} B ₉	778, 60 823, 60	815.1	831.4	-45	418±8	no 3 no	1.5 1.5 no
FMNb ₀ (8) (8 ₁)	Fe _{75.6} Cu ₁ Si ₁₄ B _{9.4}	698, 120	744.3	751.8	-66	314±5	* 3- 1.5	no

However, in the case of sufficiently high annealing temperature ($T_a > T_{x1} - 10 \text{ K}$) the GG-mode is only observed (curve 7₂ in Fig. 8) and the Suriñach plot finally showing the concave curvature (see curve 7₂ in Fig. 10) and indicating the long-range diffusion (cf. review in ref. [5]). In the case of DSC continuous heating data, the R1 peaks independently of the used heating rate follow one characteristic master curve for all as-quenched samples except the sample FMNb₀ as it can be seen in Fig. 11 namely, the main transformation begins with the JMAK-like kinetics having the JMAK exponent $1 < n_1 < 1.5$. Next, the JMAK-based kinetics collapses immediately and the master curve is parallel to the GG-like theoretical straight line with the GG exponent $m_1 \geq 1$ for $\alpha_1 \geq 0.2$. Concerning the FMNb₀ sample, its Suriñach plot implies a significantly higher proportion of the JMAK kinetic mode with n_1

decreasing from 2.5 to 1.5 for $\alpha_1 < 0.3$. Then, the curve is gradually degraded due to the presence of R2 crystallization step. The GG-like mode was not detected in that case.

Relying on all the observed facts, the following GG-kinetic bimodal model is rather concisely formulated [30,32]. The nano-structure formation of any type of FINEMET samples is composed of the processes of two types, namely the conventional JMAYK nucleation-and-growth mode [9-12] and the mode, which has been very well described by the GG coalescence kinetic law [27,29]. Let us underline that these two modes are mutually independent. As a rule the JMAYK kinetics is manifested in the early stages of the R1 transformation representing both the nucleation and the three-dimensional crystal growth of the α -Fe-based phase, which is dispersed in the amorphous matrix. The JMAYK exponent n_1 initially being 4 for the samples rich in Si continuously decreases to 1.5 along with increasing time of the thermal treatment. The GG-like mode dominates at higher temperatures and in the advanced stages of the R1 transformation independent of the content of Cu and Si and being controlled by the specific rearrangement of niobium. If the GG-like kinetics takes place in the initial amorphous state of sample consequently a nano-crystalline structure must be formed. Remarkably the $\text{Fe}_{75.6}\text{Cu}_1\text{Si}_{14}\text{B}_{9.4}$ sample (FMNb₀) does not exhibit the GG-like kinetics and it does not form any nano-crystalline (FINEMET-like) structure. After the start of the R1 transformation, the long-range diffusion of Si-controlled reordering occurs during longer times in the FINEMETs containing Si (R1' transformation).

14. 3. Two types of the crystallization kinetics in rapidly quenched ribbons

Our results support an increased significance of DSC investigations applied to the crystallization in glasses. Owing these results, two distinct types of rapidly quenched metallic ribbons have been identified, namely “the conventional metallic glasses” and “the so-called precursors for the stable three-dimensional nanostructure alloys” (being the product of their first devitrification step R1). These ribbons are classified within two different characteristic facets and kinetics of the crystalline product during the R1 crystallization.

Independently of their chemical composition (as Pd-Si-based, some Fe-B-based [31,33], some Al-based, Zr-based multicomponent ribbons, etc.) the conventional metallic glasses principally follow the JMAYK nucleation-and-growth kinetic law. Thus the theoretically calculated shape of the continuous heating DSC peak is asymmetrical [30] with independency of the parameter n being always at a slower rise on the low-temperature side. Any pre-annealing of such samples increases the initial fraction transformed, which shifts the JMAYK peak to lower temperatures and make it broader. If $n > 1$, the JMAYK isothermal signal shows a reportable peak for nonzero degree of conversion, $\alpha_{\min} = 1 - \exp [(1 - n)/n]$, i.e., at a nonzero time ($t_{\min} = \tau [(n-1)/n]^{1/n}$), which (due to $\tau = 1/k$ and the Arrhenius $k(T)$) is dependent on temperature. However, because the extremely non-equilibrium thermodynamic state of metallic glasses (due to rapid quenching) and also owing to their characteristic heterogeneity (characterized by the cluster-type medium-range order and distinct macroscopic anisotropy) reflecting the surface/volume morphology of ribbons, numerous peculiarities within the JMAYK kinetics occur (especially in the case of magnetic alloys). For example, if the $\Delta E_1^+ = f(\alpha_1)$ and $n_1 = f'(\alpha_1)$, which results the transient heterogeneous nucleation of R1 phase and/or if $\Delta E_2^+ = f''(T_1)$, which reflects the subordinated composition of amorphous matrix towards the actual kinetics (of the specific R1 phase in the case of Fe-Si-B ribbons) the JMAYK kinetics come about the application.

Concerning the second type of rapidly quenched alloys, independently of the initial chemical composition (such as FINEMETs [28,32], NANOPERMs [30], HITPERMs or some aluminium based ribbons [30]) the ribbons after the R1 transformation are characterized by extremely high nanocrystal density at relatively low total crystalline content, high enough

thermal stability, extraordinary magnetic, corrosion or mechanical properties. The continuous-heating as well as the isothermal nanocrystal formation, as the main transformation step R1, is characterized by a distinctive kinetics [28-30,32]. Specifically, the isothermal DSC signal possesses a monotonically decreasing feature while the continuous-heating DSC signal retains asymmetry that is reversed to the JMAYK kinetics one. The clearest effect, however, is that the pre-annealing (i.e., increment of the initial grain radius) shifts the onset of the DSC peak to higher temperatures and leads to narrower transformation range. Thus the behavior of such a nano-crystallization is similar to the normal-grain-growth one. Even though the original idea of *Atkinson* [27] of the GG-like mechanism (where the larger grains in the already fine-crystalline sample increase their size at the expense of smaller ones - coalescence) does not correlate well enough with structural observations in our heterogeneous two-phase systems, the GG-like kinetic law may well rationalize all peculiarity of most DSC results without need of any correction [30]. The desired kinetic parameter m and other characteristics of the nanocrystal formation (stage R1) in metallic ribbons under our studies are summarized in Table 4. It can be seen that $m < 2$ may well reflect the presence of a second phase (amorphous matrix) interpretable also in relation to the final grain radius (of the R1 phase).

Table 4: Structural characterization (nano-crystalline phase and final grain diameter) and kinetic parameters (Kissinger activation energy and the normal-grain-growth exponent) of the nanocrystal formation stage in metallic ribbons [30]

Sample	Product	d [nm]	ΔE^+ [kJ mol ⁻¹]	m
Fe ₇₆ Mo ₈ Cu ₁ B ₁₅	α -Fe	<10	511±24	1.7
Fe _{73.5} Cu ₁ Nb ₃ Si _{13.5} B ₉	α -Fe(Si)	12	418±8 ^{**}	1.5
Fe _{87-x} Cu ₁ Nb ₃ Si _x B ₉	α -Fe(Si)	10-12	~300-600 ^{**}	1
Fe _{63.5} Ni ₁₀ Cu ₁ Nb ₃ Si _{13.5} B ₉	α -FeNi(Si)	15-18	429±5 ^{**}	0.5
Al ₉₀ Fe ₇ Nb ₃	α -Al	>10	162±24	0.15

^{**} ΔE^+ is heat-treatment dependent because of the bimodal character of R1 stage

In the case of the Al₉₀Fe₇Nb₃ ribbon [30], both the α -Al nanocrystal formation (R1) and the eutectic-like crystallization of the amorphous matrix into intermetallic one (in a polycrystalline α -Al matrix - R3 step) can take place within the temperature range of standard DSC measurements. Therefore, we can mutually relate the GG-like (in R1 step) and JMAYK-like (in R3 step in this case) kinetics. Namely, in the continuous heating regime, the R1 peak is wider and shifted to higher temperatures while the R3 peak is narrower and shifted to lower temperatures (when treated by appropriate isothermal pre-annealing, cf. Fig. 12. In the isothermal regime, the DSC signal of R1 transformation step is decaying and independent of temperature. However, in the case of the R3 transformation step, the DSC signal forms the peak, which rime-scale significantly prolongs with decreasing T_a , (cf. Fig. 13). The revealing Suriñach plots are straight lines for R1 step (since $\alpha = 0.1$) but become convex curves with a maximum at $\alpha = 0.54$ for R3 step (cf. Fig. 14).

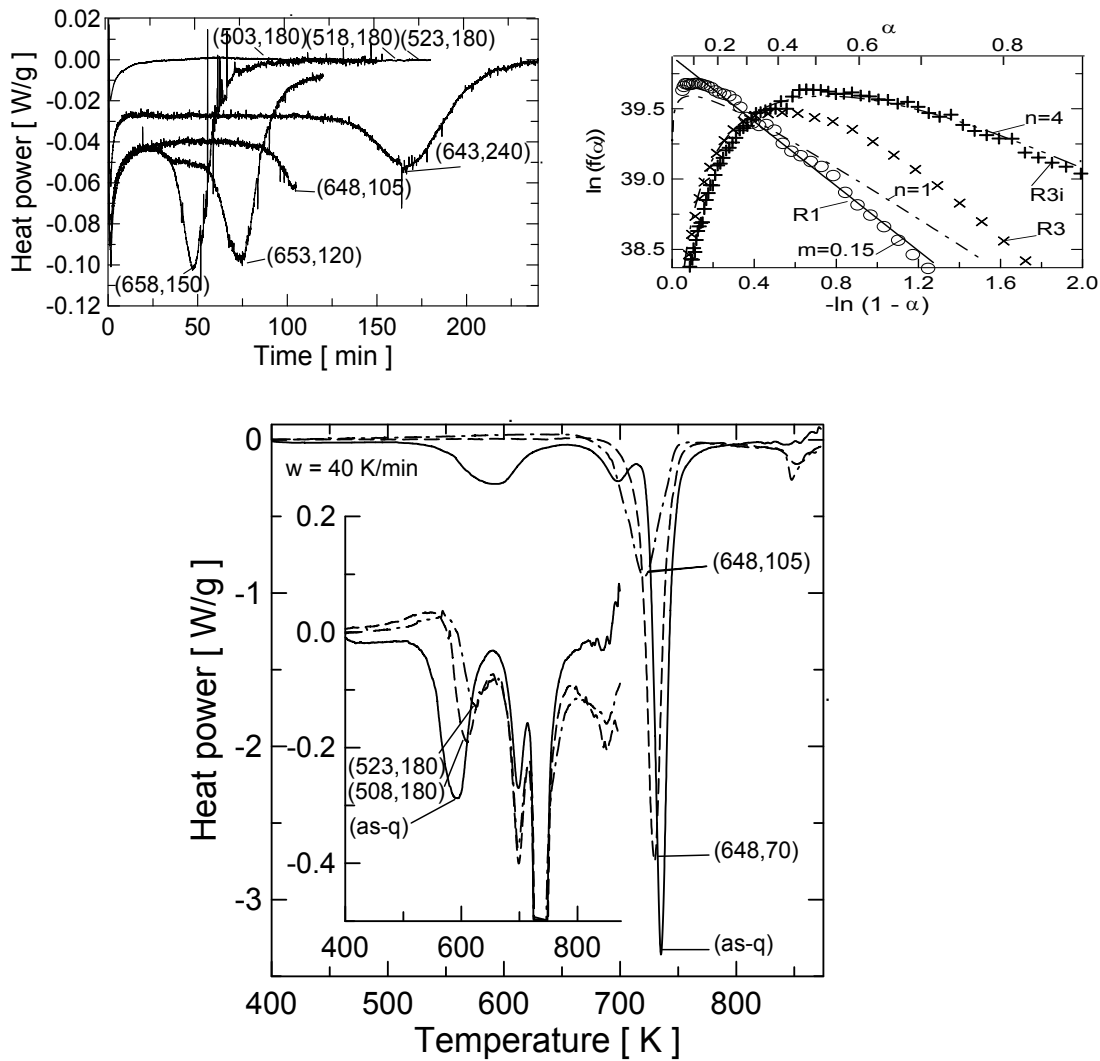


Fig. 12. DSC traces from as-quenched and heat-treated $Al_{90}Fe_7Nb_3$ ribbons. The inset shows an expanded view of the peaks from low-temperature pre-annealed samples. Numbers in parentheses indicate annealing temperature in K and annealing time in min [30].

Fig. 13. Isothermal DSC traces at various temperatures of as-quenched $Al_{90}Fe_7Nb_3$ ribbons. Numbers in parentheses indicate annealing temperature in K and annealing time in min [30].

Fig. 14. Surlinac plots for the continuous heating DSC transformation peaks R1 and R3 from Fig. 12 and for isothermal peaks R3i from Fig. 13 for as-quenched $Al_{90}Fe_7Nb_3$ ribbons. \circ , \times and $+$ correspond to experimental data, respectively, (not all points are shown), — to the theoretical GG kinetics for $m = 0.13$, — · — and — · · — to the theoretical JMAK kinetics for $n = 1$ and 4 , respectively [30].

Acknowledgement: The work was supported by the Grant Agency of ASCR Contract No IAA1010404 and IAA100100639; as well as the Czech foundation NoP204/10/1312

References 14

- [1] P. Duhaj, V. Sládek, P. Mrafko, Czech. J. Physics A23 (1973) 617
- [2] A.L.Greer, Acta Metall. 30 (1982) 171

- [3] U. Köster, in: *Phase Transformations in Crystalline and Amorphous Alloys*, ed. B.L. Mordike, (DGM,Oberursel 1983) p. 113
- [4] K.F. Kelton, F. Spaepen, *Acta Metall.* 33 (1985) 455
- [5] S. Suriñach, M.D. Baró, M.T. Clavaguera-Mora, N. Clavaguera, *J. Non-Cryst. Solids* 58 (1983) 209
- [6] E. Illeková, *Thermochim. Acta* 280/281 (1996) 289
- [7] J. Šesták (ed), “*Vitrification, Transformation and Crystallization of Glasses*”, special issue of *Thermochim. Acta*, Vol. 280/281, Elsevier, Amsterdam 1996
- [8] J. Šesták “*Science of Heat and Thermophysical Studies: a generalized approach to thermal analysis*” Elsevier, Amsterdam 2005
- [9] W.A. Johnson, R.F. Mehl, *Trans. A.I.M.E.* 135 (1939) 416.
- [10] M. Avrami, *J. Chem. Phys.* 7(1939)1103; 8(1940)212; 9(1941)177
- [11] B.V. Yerofeev B.V. Yerofeyev, *Dokl. Akad. Nauk USSR* 52(1946)511...
- [12] A.N. Kolmogorov A.N. Kolmogorov, *Izv. Akad. Nauk USSR* (1937)355
- [13] J. Šesták, “*Thermophysical Properties of Solids: theoretical thermal analysis*“ Elsevier, Amsterdam 1984 and “*Teoretickýj termičeskij analiz*” Mir, Moscow 1988 (in Russian)
- [14] D.W. Henderson, *J Thermal Anal.* 15 (1979) 325
- [15] T.J.W. DeBroijn, W.A. deJong, P.J. van den Berg, *Thermochim. Acta* 45 (1981) 315
- [16] J. Šesták key lecture “*Integration of nucleation-growth equation when considering non-isothermal regime and shared phase separation*” at the. 2nd ESTAC (Europ. Symp. on Thermal Analysis) in “*Thermal Analysis*”(D. Dolimore, ed) Heyden. London 1981, p. 115
- [17] J. Šesták key lecture „*Distinction of crystallization kinetics determined by isothermal and non-isothermal calculation methods*“ at the Chinese symposium on calorimetry and thermodynamic, Handzhow 1984; T. Kemeny, J. Šesták *Thermochim. Acta* 110 (1987) 113
- [18] J. Šesták, *Thermochim. Acta* 3 (1971) 150
- [19] J. Šesták, *Phys Chem. Glasses* 15 (1974) 567
- [20] J. Burke, *The kinetics of phase transformations in metals*, Pergamon Press, New York, 1965.
- [21] J.W. Christian, *The theory of transformations in metals and alloys*, Pergamon Press, Oxford, 1975.
- [22] K.F. Kelton, *Mat. Sci. Eng.* 226-228 (1997) 142-150.
- [23] H. Hermann, N. Mattern, S. Roth, P. Uebele, *Phys. Rev.* B56 (1997) 13888
- [24] K.F. Kelton, T.K. Croat, A.K. Gangopadhyay, L.-Q. Xing, A.L. Greer, M. Weyland, X. Li, K. Rajan, *J. Non-Cryst. Solids* 317 (2003) 71
- [25] L.C. Chen, F. Spaepen, *Nature* 336 (1988) 366
- [26] L.C. Chen, F. Spaepen, *Nanostruct. Mater.* 11 (1992) 59
- [27] H.V. Atkinson, *Acta Metall.* 36 (1988) 469
- [28] E. Illeková, K. Czomorová, F.A. Kuhnast, J.M. Fiorani, *Mat. Sci. Eng.* A205 (1996) 166
- [29] E. Illeková, „*Nanostructured and Non-Crystalline Materials*“, in M. Vázquez, A. Hernando (Eds.) *Proc. 4th International Workshop on Non-Crystalline Solids*, Madrid, Spain, September 1994, World/Scientific, Singapore, 1995, p. 490
- [30] E. Illeková, in: *Properties and Applications of Nanocrystalline Alloys from Amorphous precursors*, NATO Science Series II: Mathematics, Physics and Chemistry, 184. Eds. B. Idzikowski, P. Švec, M. Miglierini, Kluwer Academic Publishers, Dordrecht, 2005, p. 421
- [31] I. Mat’ko, E. Illeková, P. Švec, P. Duhaj, *Mater. Sci. Eng.* A225 (1997) 145
- [32] E. Illeková, *Thermochim. Acta.* 378 (2002) 47
- [33] E. Illeková, I. Mat’ko, P. Duhaj, F.A. Kuhnast, *J. Mater. Sci.* 32 (1997) 4645
- [34] H.E. Kissinger, *Anal. Chem.* 29 (1957) 1702-1706.
- [35] M.J. Starink, *Thermochim. Acta* 404 (2003) 163-



Chapter 15

Phosphate glasses

15. TRANSPORT AND RELAXATION MECHANISMS IN IONIC PHOSPHATE GLASSES

Peter Bury, Peter Hockicko

15. 1. Introduction

Solid state ionic is the field of materials science that deals with the study of technology, theory and application of materials with ionic transport. Solids exhibiting high levels of ionic conductivity are also designated as fast ion conductors or super ion conductors and represent also solid states electrolytes. Solid electrolytes come to the forefront of scientific interest because of application in electrochemical devices, such as solid-state batteries, electrochromic displays and sensors. They can be also a part of capacitors, time switches, electrochemical pumps etc. [1,2].

Solid electrolytes present numerous potential advantages over liquid electrolytes, including absence of liquid containment and leakage problems, ability to operate with more highly reactive electrodes over a wider temperature range, and the possibility for miniaturization using thin-film-processing techniques. The general requirements for practical solid electrolytes are high ionic conductivity, negligible electronic conductivity, stability with respect to adjacent phases and to thermal and electrochemical decomposition, suitable mechanical properties, ease of fabrication, and reasonable cost.

Fast ionic conductivity can be observed in many glasses, especially those with small cations, such as silver, copper, lithium, and sodium. Ternary glasses contain a network former (e.g., SiO_2 , B_2O_3 , P_2O_5 , and GeS_2), a network modifier (e.g., Ag_2O , Li_2O , Cu_2O , and Ag_2S), and a dopant compound, mostly a halide (e.g., AgI , CuI , and LiCl). As the term implies, the glass network structure and, therefore, its physical and chemical properties can be substantially modified by addition of the modifier. Dopant salts apparently do not interact strongly with the network, and cation and anion „dissolve“ into the interstices of the glass structure. Increased ion conductivity can result from two sources: increased carrier density and/or carrier mobility. Composition of glasses can have also remarkable effects on ion conductivity. The mixed alkali effect is often observed in binary glass system where one type of alkali ion is substituted by another and/or the local relaxations of the structure about the mobile ions can create separate path ways appropriate for the ions with different size [3]. Most studies on fast ion conduction glasses have been performed on silver and lithium glasses. However comparable conductivity was observed in corresponding systems with copper ions [4].

Characterization of dynamic processes in glassy materials with ionic conductivity is very important since the ion transport significantly affects their practical performance. Conductivity spectroscopy and dielectric relaxation spectroscopy are powerful techniques that reflect the basic features of the relaxation and transport dynamics of the mobile ions [5,6]. An alternative technique for measuring electrical properties is impedance spectroscopy [7]. In this, ac impedance measurements are made over a wide range of frequencies and the different regions of the material are characterized according to their electrical relaxation times or time constants. Acoustic attenuation spectroscopy similarly as mechanical spectroscopy [8,9] is another technique for the study of sub- T_g relaxations in glasses due to a strong acousto-ionic interaction [10,11]. Relaxation processes occurring on different time scales can be detected in one experiment since the corresponding acoustic loss peaks are spread out on the temperature scale.

15.2 Transport and relaxation properties of ion conductive glasses

Dynamic processes in glassy materials with ionic conductivity concerning both transport and relaxation of mobile ions, are extremely important for their practical application. The formal theories of transport properties and relaxation processes of many ion conducting glasses are similar [12]. However, the interpretation of ionic relaxation processes and ionic conductivity emphasized various aspects, in particular, the role of the glass structure and the role of ionic center potential on the hopping transport [13]. It is namely known that the ionic transport in glasses, at last in the dc regime and in the ac regime at not very high frequencies, is due to hopping of ions between localized states in the glass matrix [14]. However, generally accepted theory of ion transport mechanism does not exist, so that the hopping mechanism is described by several models.

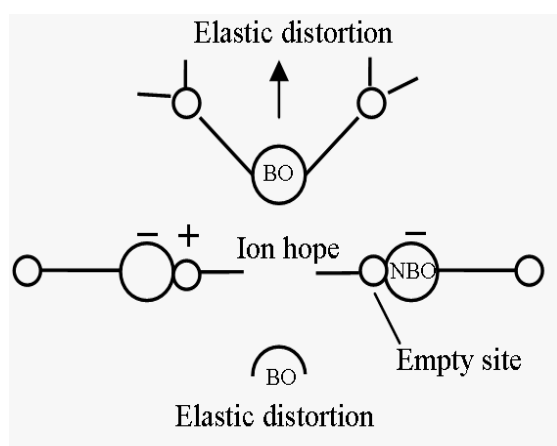


Fig. 1. Illustration of ion hopping in silicate glass [16].

The „classical“ theory of ion transport presented originally for silicate glasses [15] supposed for ions simple hops from one site to another and passes through a door way which opens as it passes through. The cation sites then only require the presence of non-bridging oxygens. The activation energy is then the sum of two terms, one of which represents the electrostatic bridging energy to the original site and another which

represents electrostatic strain energy. Fig. 1 shows a simple visualization of the extended classical model [16]. However, in spite of the fact, that this theory was used as a guide to the successful development of new fast ionic glass composition, the shortage of this model is that can be useful in the case when ions are divided to mobile and standing ions. Another view on transport mechanism carried the *model of random sites* (MRS), that supposed the large continuous distribution of ions in states with different free energy [1]. The change of conductivity is then controlled mostly by changing of ion mobility.

Recently due to the new observed results, several additional models describing non-Debye relaxation in glassy electrolytes were proposed [17]. The key features of the *dynamic structure model* (DSM) [14] accounting the structural relaxation are: (1) the glass structure is not completely “frozen in”, (2) the mobile cations themselves are active in determining and creating the glass structure and (3) the ion transport is a hopping process. The combination of (1) and (2) spines also rise to various relaxation and “memory” effects which are characteristic of ion conductive glasses and strongly influence the hopping processes. The model can explain a simple power law operative in single-cation glasses but also many features of the mixed alkali effect. The basic idea of the dynamic structure model is the following. The mobile A^+ ions create optimally configured A sites for themselves when the glass is formed from the melt, while less favourable C sites also exist. In Fig. 2 a construction of the effective potentials felt by ions hopping from A to A and from A to C sites are presented. The construction is made by superimposing site sensitive and cage effect potentials. Although the A to C barrier height is

assumed to be similar to the A to A one, A to C hops are virtually always unsuccessful because of the enhanced roll-back rate from C to A, which is a consequence of the comparatively small C to A barrier height. The existence of two empty sites leads also to the mixed alkali effect.

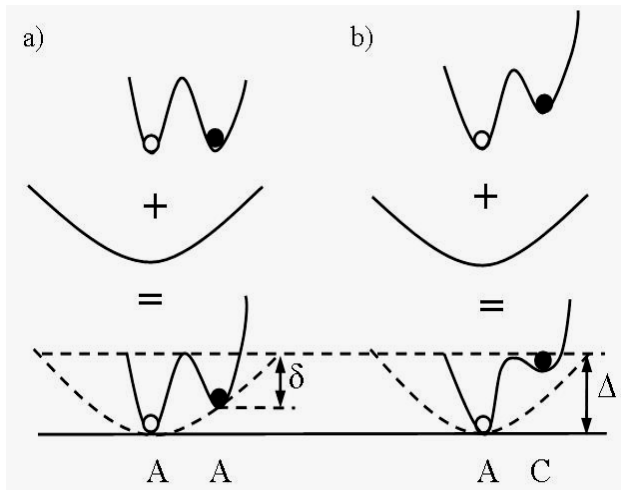


Fig. 2. Schematic illustration of potential for a system described by the DSM involving ions moving to “stepping stores” sites (a) and “less good” sites (b).

The basic idea of the *jump relaxation model* (JRM) is given in Fig. 3. Four assumptions are taking into account: (1) the hopping ions are all of the same kind, (2) there are many more sites than mobile ions, (3) the available sites are all of the same kind and (4) there is repulsive interaction between the mobile ions, resulting in a cage effect. Because of the cage effect, the ions tend to stay at some distance

from each other. If an ion hops into a neighboring site (at time $t = 0$), this causes a mismatch which is described by the cage-effect potential. After the hop, there are two competing ways of relaxing. The ion may hop back to its original site or the neighboring mobile ions rearrange in the course of their own hopping motion. The latter procedure results in a shifting of the cage-effect potential, i.e., in the formation of a new absolute potential minimum for the “central” ion at its new site. It is only in this case that the “initial forward” hop proves successful and contributes to the dc conductivity. In the original version of the jump relaxation model the problem has been treated by solving a set of rate equations [18].

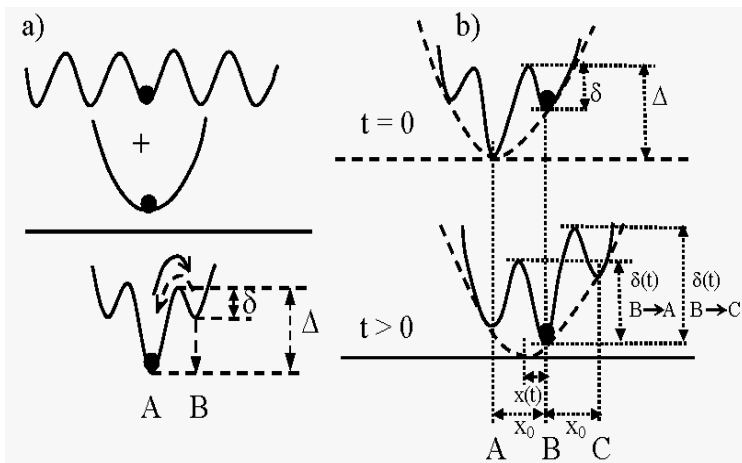


Fig. 3. Basic idea of JRM. (a) The effective single particle potential (solid line) and cage-effect potential (broken line) after a hop from A to B at time $t = 0$. (b) Development of potential after a hop for $t > 0$. δ is the potential barrier for the hop back.

The *unified site relaxation model* (USRM) [19] developed by combining the original JRM and the DSM accounts for the superlinear

frequency dependence of conductivity. This new model is based upon the existence of both Coulombic (at the basis of the JRM) and structural (at the basis of the DSM) relaxations. The existence of two types of site, one adapted to the hopping ion (because it would still have the memory of having been occupied by an ion of the same type) and the second non-adapted (because it would have lost memory of having been occupied) explains the two dispersive

regimes. As a consequence, the ion hopping motion is not a random process, but features a strong preference for so-called correlated forward-backward hopping sequences. If an initial forward jump of an ion is followed by a correlated backward jump, the former can be regarded as unsuccessful. If, however, the ion manages to stay at the new site and neighboring ions rearrange themselves causing site relaxation, then the initial forward hop is called “successful”. The latter relaxation process (Coulomb relaxation) causes a shifting of the Coulomb cage potential “felt” by the central ion and thereby initiates the site relaxation. The “leitmotif” of the unified site relaxation model is demonstrated in the bottom of Fig. 3. The bent line indicates that the ion initially (at $t = 0$) jumps over a barrier of height Δ , from a site A to a vacant neighboring site B. The bent dashed line represents the correlated backward jump and the dotted line shows the site relaxation. Each of these competing ways of relaxing can be characterized by a time constant or by its inverse, the respective rate.

A different approach for modeling the ion dynamics in glass is counter-ion model (CIM) which uses Monte Carlo simulations to determine ac conductivity [19]. Within this model, mobile ions (normally cations) are diffusing in the presence of randomly placed Coulombic traps due to immobile counter-ions (normally anions). The ions are migrating under the influence of both, their mutual Coulomb inter-action and the long-range Coulomb fields caused by the counter-ions. For simplicity, the hopping process is assumed to occur within a three dimensional simple cubic lattice of spacing a and size L with periodic boundary conditions. Mobile ions occupy a given fraction of the lattice sites. These ions can perform jumps of length a to vacant neighboring sites. The model includes no adjustable parameter besides the ionic concentration and a typical Coulomb energy, V , which is normalized by the thermal energy, $k_B T$. Like the unified site relaxation model, the counter-ion model is a microscopic model dealing with individual ionic jumps. On the other hand, it also includes all many body interactions arising from the Coulomb forces. The calculated conductivity is, therefore, determined by single particle movements as well as by cross terms.

The unified site relaxation model and the counter-ion model can be regarded as complementary. As a common feature, they are very simple and give a good picture about ionic transport in glass. Despite their simplicity, the $\sigma(\omega)$ spectra resulting from these models are in good agreement with many experimental findings. Both models basically agree in the interpretation of the different conductivity regimes of glass spectra. The USRM uses simple rate equations and the resulting analytical expressions for the conductivity are easily applied for obtaining fits to the conductivity data. Including two kinds of geometrically different sites, this model gives a more realistic impression about the structural situation found in glass. Aiming at simple analytical solutions, the model, however, neglects all kinds of cross correlations between the movements of different ions. Cross correlations are taken into account in the counter-ion model. They are shown to play an important role in the high-frequency behavior of the conductivity. In the CIM there is no need to superimpose different conductivity contributions, because the underlying processes are inherently included in the model. However, the applicability of a model depends on the individual glass composition and its structure.

15.3. Electrical characterization of ion transport and relaxations

The significance of electrical characterization of ion conductive glasses with respect to their transport mechanisms and relaxation properties is evident. Electrical conductivity

spectroscopy is a powerful technique for study of ion transport mechanisms complete. Complete conductivity spectra of ionic conductors extend from a few Hz up to the far-infrared regime covering more than 12 decades on the frequency scale. They reflect the essential features of the relaxational and translational dynamics of the mobile ions on a time scale whose width is unsurpassed by any other experimental technique. In spite of their potential for unraveling microscopic mechanisms of ionic motion, complete conductivity spectra of ionic conductors are still rare. The reason is the large frequency scale for which the requested radio, microwave and far-infrared equipment should be available. The electrical conductivity, σ , of many solids including glasses, polymers and crystals was shown to consist of a frequency independent and a strongly frequency dependent component [20]. From the experimental data in a limited frequency region it was noted that the overall frequency dependence of σ or the so called “universal dynamic response” (UDR) of ionic conductivity could be approximated by the following simple relation:

$$\sigma(\omega) = \sigma_{\text{dc}} + A\omega^s, \quad (1)$$

where $\omega(=2\pi f)$ is the angular frequency of measurement. For a typical ionic conductor containing moderate to high concentration of mobile ions, $s \approx 0.5-0.6$, and both σ_{dc} and A follow Arrhenius type strong temperature dependencies. Recently, this expression has been updated to include the frequency dependence of σ at low temperatures (< 200 K) and/or high frequencies [17]:

$$\sigma(\omega) = \sigma_{\text{dc}} + A\omega^s + A'\omega^{s'}, \quad (2)$$

where $s' \approx 1.0$ and A' is weakly temperature dependent. If s' is exactly 1.0, the last term amounts to frequency independent dielectric loss and hence its contribution may be called as the nearly constant loss behavior.

The electric modulus representation is another electric method that has been used to provide comparative analysis of the ion transport properties in various ion-conductivity materials [21]. At low frequencies, random diffusion of the ionic charge carriers via activated hopping gives rise to a frequency-independent conductivity. At higher frequencies, however, $\sigma'(\omega)$ exhibits dispersion, increasing roughly in a power-law fashion and eventually becoming almost linear at even higher frequencies. The physical origins are not yet completely understood, but the dispersion clearly reflects a nonrandom or correlated kind of motion of the ions occurring on relatively short time scales.

Dielectric spectroscopy has been traditionally applied to investigate dipolar relaxation in liquids and solids where reorientation of permanent dipoles gives rise to characteristic frequency-dependent features of the complex permittivity, $\varepsilon^*(\omega) = \varepsilon'(\omega) - i\varepsilon''(\omega)$ [6]. In this case, $\varepsilon'(\omega)$ increases with decreasing frequency approaching a limiting value $\varepsilon'(0)$ at low frequencies associated with the polarization resulting from alignment of the dipoles along the direction of the electric field. Concomitantly, the imaginary part $\varepsilon''(\omega)$ passes through a maximum at a frequency which is temperature dependent and whose inverse is commonly associated with the characteristic time required for dipoles to reorient. In the dipolar situation, a dc conductivity is unexpected and when observed usually indicates the presence of impurity ions in the material. This unwanted contribution to the dielectric loss is normally subtracted away in a trivial manner.

However, in practice, the polarization is inseparable from the eventual conduction process. The mobile ion, which creates polarization by reorienting locally, is the same ion that later separates from its immediate neighborhood to produce conduction at lower frequencies. In ion-conducting materials polarization and conduction are, therefore, integrated into a single, continuous process. So that considerably more prominent in the literature is the electric modulus, $M^*(\omega) = 1/(\omega)$ [1]. The modulus shares an important analogy with shear stress relaxation measured by mechanical spectroscopy in solids, and in the case of ion-conducting materials, the frequency dependence of $M^*(\omega)$ can be related to a corresponding time-dependent evolution of the electric field resulting from ion displacements. The loss tangent can be also used for the relaxation spectroscopy that reflects the basic features of the relaxation processes of mobile ions [6].

Both $\sigma^*(\omega)$ and $M^*(\omega)$ or $\text{tg } \delta(\omega)$ are in principle derived from the same experimental data (i.e., real and imaginary components of the sample impedance). However, the shape of the modulus and/or $\text{tg } \delta(\omega)$ are sensitive to $\varepsilon'(\infty)$, the high-frequency limiting permittivity that results from near-instantaneous electronic and atomic polarization which is not directly related to the hopping motion of the mobile ions. Nevertheless, the modulus is still being used and misleading conclusions are still frequently drawn.

15.4. Mechanical and acoustic characterization of ion relaxations

The formal theory of all relaxation processes is similar. However, comparison between the electric and acoustic response functions may give useful insights into the dynamic behavior of ion conducting glasses. In practice, the electrical data are obtained in the frequency domain, while the experimental data of mechanical spectroscopy and acoustic attenuation spectroscopy are usually available in a narrow frequency region and over a wide temperature range. It is well known that the frequency dependent conductivity of ionic glasses is extremely informative and that there have not been systematic comparative studies of mechanical and electrical processes in the same glasses.

Mechanical spectroscopy is a powerful technique for the study of sub- T_g relaxations in glass. Relaxation processes occurring on different time scales can be detected in one experiment since the corresponding mechanical loss peaks are spread out on the temperature scale in an isochronal measurement. The classical studies of the mechanical loss properties of mixed alkali glasses [8] have, e.g., revealed the existence of a relaxation mode that is connected with the transport of the slower alkali ions. By way of contrast, the electrical properties of a glass are usually dominated by the transport of most mobile ions. Therefore, no direct information on slower relaxation processes can be obtained from electrical measurements.

The investigation of acoustic spectra of ionic glasses can also reflect the basic features of the relaxation and transport mechanisms of the mobile ions. Acoustic measurements made over a wide range of frequencies and temperatures can characterize different relaxation processes according to corresponding transport mechanisms due to a strong acousto-ionic interaction [10,11]. In glassy electrolytes, the mobile ions encounter different kinds of sites so that ionic hopping motion and relaxation processes connected with charge mobility can be obviously explained by modified jump relaxation model and suitable response function for transport mechanisms and relaxation processes description, respectively [10,22].

The basic principles of theories describing relaxation processes of many ion conducting glasses, melts and crystals are similar [23]. In the case of systems containing a low concentration of mobile ions the attenuation may be described as a superposition of Debye-like, single relaxation time processes in which the individual ion hops occur independently of each other. In fact all the investigated relaxation peaks are much broader than Debye peak that can be interpreted as arising from the existence of a distribution of relaxation times due to random deviations in the local arrangement of the system. According to this hypothesis when the relaxation losses are not too large one can write for the acoustic attenuation a distribution $f(\tau)$ of relaxation times [10]. As a consequence, the τ distribution can be connected with a distribution of activation energies $f(E)$, representing the heights of the barriers that the ions must surmount to go into the near allowed positions. The acoustic attenuation will exhibit a maximum when the relaxation time τ is comparable to the period ($1/\omega$) of the acoustic perturbation, where

$$\tau = \tau_0 \exp\left(\frac{E_A}{k_B T_{peak}}\right) \quad (3)$$

is the most probable relaxation time [11]. The relaxation processes, described by an Arrhenius equation (X.3), are characterized by activation energy E_A for jumps over the barrier between two potential minima and typical relaxation frequency of ion hopping $1/\tau_0 \approx 10^{13} - 10^{14} \text{ s}^{-1}$.

In fact all the investigated relaxation peaks are much broader than Debye peak. It can be interpreted as arising from the existence of a distribution of relaxation times due to random deviations in the local arrangement of the system. According to this hypothesis that the relaxation losses are not too large, it can be written for the acoustic attenuation, in case of a distribution $f(\tau)$ of relaxation times

$$\alpha = \frac{\Delta}{2\nu} \int \frac{\omega^2 \tau}{1 + \omega^2 \tau^2} f(\tau) d\tau. \quad (4)$$

As a consequence, the τ distribution can be connected with a distribution of activation energies E_a , representing the heights of the barriers that the ions must surmount to go into the near allowed positions. A useful form of equation (X.4) that takes into account only E distribution can be derived by the microscopic theory

$$\alpha = \frac{B^2}{4\pi\rho\nu^3 k_B T} \int P(E) \frac{\omega^2 \tau(E)}{1 + \omega^2 \tau^2(E)} dE, \quad (5)$$

where an average deformation potential B expresses the coupling between the ultrasonic stress and the system and $P(E)$ represents the E distribution function. We can assume for $P(E)$ a Gaussian distribution [24]

$$P(E) = \frac{N}{\sqrt{2\pi E_0^2}} \exp\left[-\frac{(E - E_a)^2}{2E_0^2}\right], \quad (6)$$

in which N is the total number of jumping particles per unit volume, E_a the most probable activation energy and E_0 the width of the distribution.

This approach depends on the assumption that ion migration may be treated in terms of a set of non-interacting Debye-like processes. However, in solid electrolytes the mobile ion concentrations are large and conduction mechanisms are thought to be cooperative. The

relaxation phenomena observed in a wide variety of materials exhibit a power-law type of frequency dependence. The relationship to Debye behaviour is expressed in the form [10]

$$\alpha \approx \frac{1}{T} \left(\frac{(\omega\tau)^m}{1 + (\omega\tau)^{1+m+n}} \right), \quad (7)$$

where m and n are power-law exponents, which take values between 0 and 1. When $m = 1$ and $n = 0$, equation (X.7) reduces to the equation for a single Debye-like process.

Two functions have mainly been used to fit mechanical loss data [11]. The first function is the Kohlrausch-Williams-Watts (KWW) function

$$\Phi(t, T) = \exp \left[- \left(\frac{t}{\tau} \right)^\beta \right] \quad (8)$$

with $0 < \beta \leq 1$. The acoustical attenuation is then given by

$$\alpha(\omega, T) \propto \int_0^\infty \left(- \frac{d\Phi(t)}{dt} \right) \sin(\omega t) dt \quad (9)$$

The second function is the double power law

$$\alpha(\omega, T) \propto \frac{1}{(\omega\tau)^{-n} + (\omega\tau)^m} \quad (10)$$

Recently it has been demonstrated [10] that power law responses can be produced by a simple exponential distribution of relaxation times.

15. 5. Transport and relaxation study of ionic phosphate glasses

Phosphate glasses containing Cu^+ conducting ions have gained attention during last few decades because of their promising potential use in various technological applications. Glassy electrolytes used in these devices should meet some criteria, but the most important is high ionic conductivity at room temperature. The highest ionic conductivities ($\sigma_{298\text{ K}} \approx 10^{-2} \text{ S cm}^{-1}$) are attained in Ag^+ ion-containing glasses [1]. Conductivities comparable to Ag^+ ion-containing glasses were obtained in corresponding systems with Cu^+ conductive ions (Cu^+ ions have similar electronic configuration (d^{10}) to that of Ag^+ ions). These glasses have been mainly prepared in systems based on P_2O_5 [4,25] and/or MoO_3 (see for example [26,27]) as “glass-forming” oxides. The highest conductivities have been recorded in systems containing large mole fractions of cuprous halides, such as CuI , CuBr and CuCl . The maximum halide content is limited by the ability of glass formation of the respective systems. Moreover, in recent literature it has been reported that if two different halide anions are mixed into cation-conducting glasses, a positive deviation of the electrical conductivity from the additivity rule is observed (mixed-anion effect) [28]. Mixing of two anion species in cationic conductors could be one promising way for obtaining high-conductivity glassy electrolytes. The mixed anion effect is in striking contrast to the mixed cation effect which is characterized by negative deviation of the conductivity from additivity.

In recent years, several systems of modified phosphate glasses with different cuprous halides and various compositions of glass forming systems were prepared and investigated using IR, SEM, and X-ray spectroscopy, dc and ac conductivity measurements, electric relaxation measurement and acoustic attenuation spectroscopy [4,26-31]. The presence of several structural units, from discrete monomeric to those with three-dimensional networks and corresponding transport and relaxation behaviors, were observed.

In this part the both acoustic and electrical relaxation processes and transport mechanisms are investigated more completely on identical ionic phosphate glasses of the two systems CuI-CuBr-Cu₂O-P₂O₅ and CuI-CuBr-Cu₂O-P₂O₅-MoO₃ containing Cu⁺ ions. Several distinctive peaks in the acoustic attenuation spectra and at least two conductivity regimes of transport mechanisms were observed. Both the acoustic and electrical measured data are analyzed using suitable model representations.

Two systems of glasses (18.18-x) CuI - x CuBr - 54.55 Cu₂O - 27.27 P₂O₅ (System I) and (25.00-y) CuI - y CuBr - 46.875 Cu₂O - 9.375 P₂O₅ - 18.750 MoO₃ (System II) were completely investigated (their complete sets are in Tab.X.1) and the procedure of their preparation have been already described [4,27,29]. However, for the acoustical attenuation measurements only three samples of System II could be chosen because of their suitable thickness.

The acoustic attenuation measurements using longitudinal acoustic waves of frequency 13, 18 and 27 MHz generated by quartz transducers as well as dc and ac electrical conductivity measurements (50 Hz - 1 MHz) were carried out in the temperature range 140 - 380 K. The quartz buffer rod was used to separate the acoustic signal from quite short sample. The acoustic attenuation was measured using MATEC attenuation comparator and electrical conductivity was measured using FLUKE impedance analyzer. Guard ring gold electrode configuration including blocking electrode were evaporated on glass discs of the thickness ≈ 2 mm and area ≈ 1 cm² for electrical investigation.

The temperature dependencies of dc conductivity for all samples indicate several different transport mechanisms represented with activation energies $E_{a1}^{dc} - E_{a4}^{dc}$ for first system and $E_{a1}^{dc} - E_{a2}^{dc}$ for second system. However energies $E_{a3}^{dc} - E_{a4}^{dc}$ represents probably some dissociation and association processes connected with defect formation [2,31], that is supported also by repeated measurements, the characteristic feature of which was vanishing of these processes with increasing number of temperature cycles. Besides the activation energies E_{a2}^{dc} of the System II are practically constant over a wide range of glass composition of CuI/CuBr halides, the activation energies E_{a1}^{dc} of this system include a strong mixed cation effect [23]. The representative result of measured dc conductivity (sample BIDP5 and IBPM2) as a function of temperature is illustrated in Fig. 4a. The frequency dependences of ac conductivity measured at various temperatures and frequencies (Fig. 4c-d) corresponded to the complete conductivity spectra of glassy samples consisting of low frequency plateau (III) regime and dispersive frequency dependent regime (II) [5,22]. An additional deviation of conductivity from the flat ac plateau was observed at low frequencies and higher temperatures (Fig. 4.d) that is obviously referred to electrode polarization [4]. But our measurements indicate more possible transport mechanisms, so that the shift of ac conductivity can represent different hopping centers. The ac conductivity spectra can be fitted then by the equation

$$\sigma(\omega) = \sigma(0) + A\omega^s, \quad \sigma(0) = \sigma_0 \exp(E_a^{dc}/k_B T), \quad (11)$$

where σ_0 is the pre-exponential factor, E_a^{dc} is the activation energies of the ions transport and hopping processes determined from dc measurements. Because the pre-exponential factor σ_0 is function of temperature, the factor σT was used in Arrhenius plots of dc conductivity. The corresponding activation energies $E_{a1}^{dc} - E_{a4}^{dc}$ are summarized in Table 1.

The imaginary and real part of the complex permittivity $\varepsilon^*(\omega) = \varepsilon'(\omega) - i\varepsilon''(\omega)$ defines the so-called *loss tangent* of the material

$$\tan \delta(\omega) = \varepsilon''(\omega) / \varepsilon'(\omega), \quad (12)$$

that is related to the attenuation constant (or absorption coefficient) of an electromagnetic wave propagating in the material, where $\varepsilon'(\omega)$ and $\varepsilon''(\omega)$ are the real and imaginary parts of the complex permittivity which characterize the *refractive* and *absorptive* properties of the material, respectively. The real and imaginary parts of the complex permittivity were calculated using the sample dimensions and the measured dates of impedance analyzer. The activation energies of the relaxation processes were estimated using the isochronal peaks of $\tan\delta(\omega, T)$ from the plots of

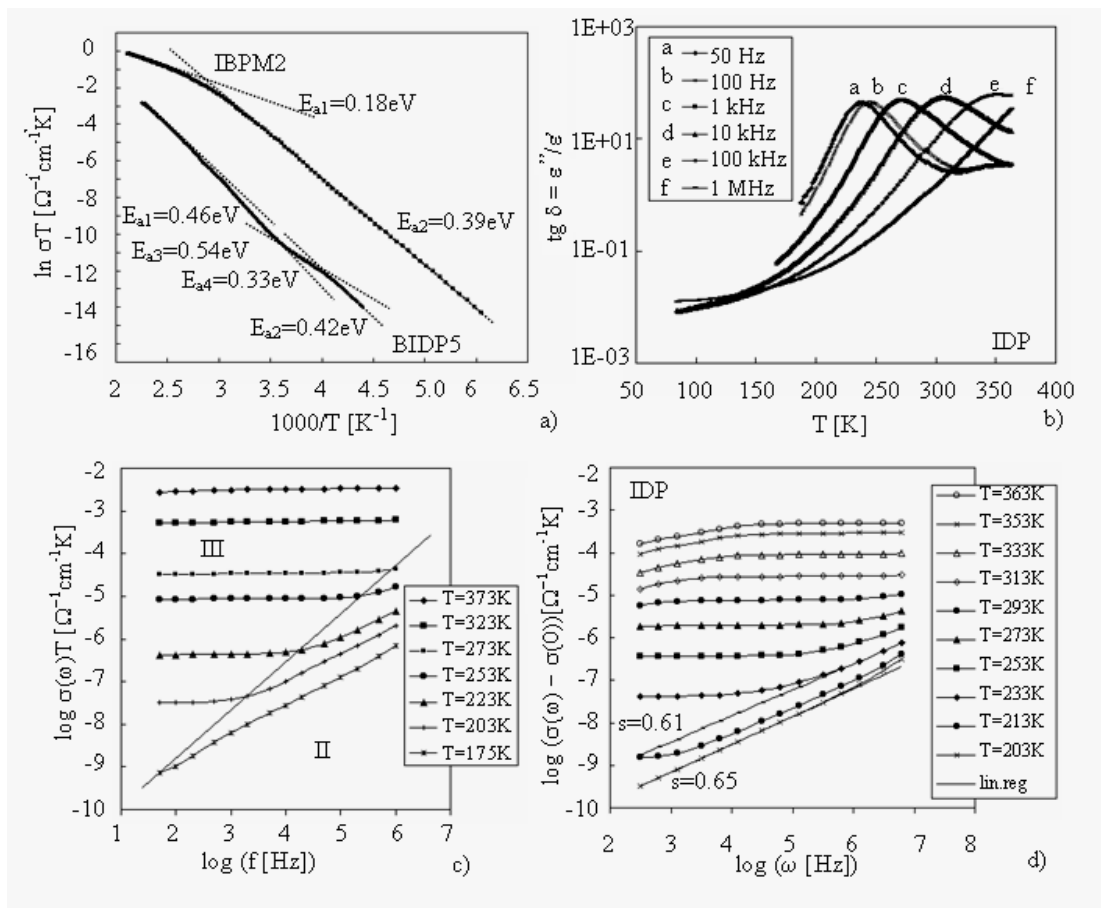


Fig. 4. Representative dc electrical results including Arrhenius plot of dc conductivity (a), temperature dependence of dielectric loss tangent (b) and frequency dependence of ac conductivity (c,d).

$\log f$ vs. $1/T_{max}$. These plots are straight lines in accordance with Arrhenius equation

$$f = f_0 \exp(E_a^{tg\delta} / k_B T_{max}), \quad (13)$$

where f is the frequency of applied electrical field, f_0 is the pre-exponential factor and $E_a^{tg\delta}$ is the value of activation energy of the dielectric losses connected with the ion hopping process. The temperature dependences of the loss tangent illustrated in Fig. 4b shows at given frequency range only one broad peak with maximum position ($\tan \delta(T_{max})$) shifted to higher temperatures with increasing frequency. But at lower frequencies also another peak can be recognized.

The acoustic attenuation spectra of samples of investigated set at all frequencies indicate one broad attenuation peak at higher temperature in which we can distinguish easily two separated peaks (Fig. 5a-c). The acoustic attenuation exhibits a maximum when the relaxation time τ is comparable to the period of the acoustic perturbation ($\omega\tau = 1$), where ω is the angular frequency. The relaxation processes are characterized by activation energy E_a^a for jumps over the barrier between potential minima and typical relaxation frequency of ion hopping $1/\tau_0$. Using the Arrhenius type equation between the peak temperature T_{peak} and the applied frequency ν (3)

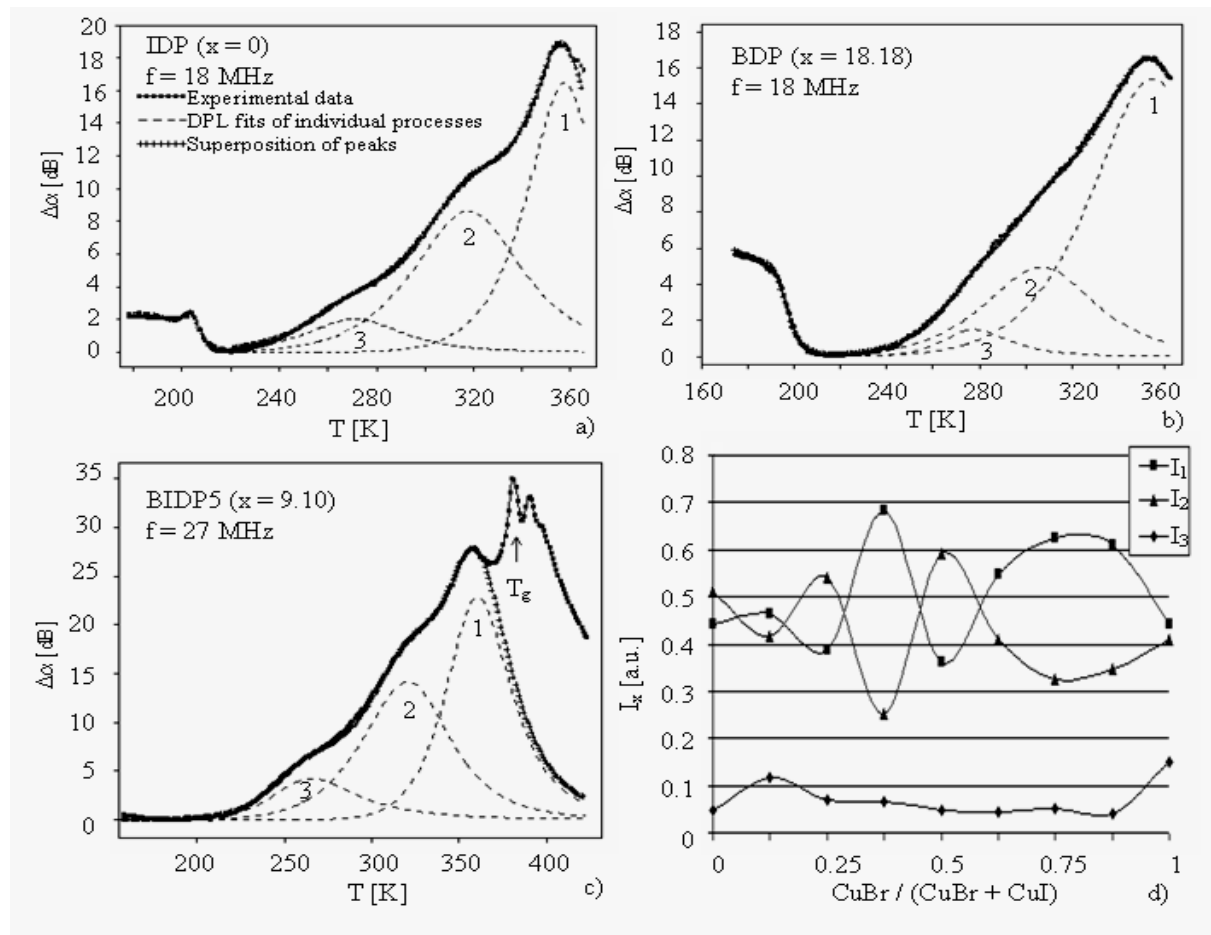


Fig. 5. Representative acoustics attenuation spectra of several glasses of the System I measured at 18 MHz (a,b) and 27 MHz (c) and the dependence of the relative peak intensities on glass

composition (d). Cross-marked lines represent the best fit as superposition of individual peaks (dashed lines). the value of activation energy of the ion hopping process can be determined.

The acoustic attenuation spectra of the investigated cuprous halide glasses were gradually fitted using various theoretical attenuation functions including the Debye, Kohlrausch-Williams-Watts and Double Power Law functions [30] utilizing the mathematical procedure of genetic algorithm with binary representation of the theoretical attenuation function variables [29]. Using the theoretical model with Double Power Law function (10), calculated lines gave an excellent agreement with the measured acoustic spectrum in the whole temperature range.

Table 1. Activation energies calculated from acoustic (E_a^a) and electric dc (E_a^{dc}) and ac ($E_a^{ig\delta}$) measurements using corresponding Arrhenius plots and glass transition temperatures (T_g) determined from acoustic measurements.

		Acoustic measurements				Electrical measurements				
SystemI	x [mol%]	E_{a1}^a [eV]	E_{a2}^a [eV]	E_{a3}^a [eV]	T_g [K]	E_{a1}^{dc} [eV]	E_{a2}^{dc} [eV]	E_{a3}^{dc} [eV]	E_{a4}^{dc} [eV]	$E_a^{ig\delta}$ [eV]
IDP	0	0.48	0.43	0.36	-	0.48	0.44	0.55	0.30	0.48
BIDP1	2.27	0.47	0.41	0.37	395	0.46	0.40	0.52	0.30	0.46
BIDP2	4.55	0.46	0.41	0.36	384	0.46	0.44	0.54	0.35	0.47
BIDP3	6.82	0.46	0.41	0.37	390	0.46	0.42	0.55	0.30	0.48
BIDP5	9.09	0.46	0.42	0.33	380	0.46	0.42	0.54	0.33	0.47
BIDP6	11.36	0.46	0.42	0.35	379	0.45	0.43	0.52	0.35	0.48
BIDP7	13.63	0.45	0.42	0.39	377	0.45	0.43	0.50	0.23	0.47
BIDP8	15.91	0.46	0.43	0.36	372	0.42	0.41	0.52	0.26	0.50
BDP	18.18	0.47	0.43	0.39	379	0.43	0.41	0.51	0.18	0.47
SystemII	y [mol%]									
IPM	0	0.47	0.39	0.34	-	0.39	0.40	-	-	0.39
IBPM2	3.125	-	-	-	-	0.18	0.39	-	-	0.36
IBPM3	6.250	-	-	-	-	0.27	0.40	-	-	0.34
IBPM5	9.375	0.48	0.40	0.35	-	0.33	0.40	-	-	0.34
IBPM1	12.500	-	-	-	-	0.34	0.40	-	-	0.34
IBPM4	18.750	-	-	-	-	0.25	0.38	-	-	0.35
BPM	25.00	0.46	0.43	-	-	0.36	0.38	-	-	0.36

The representative acoustic spectra measured at 18 and 27 MHz of some glasses of the System I are illustrated in Fig. 5 where the change of position and proportion at the broad maxima peaks can be seen. Their theoretical simulation for two different frequencies (18 and 27 MHz) is illustrated for some samples of this set in Fig. 5a-c, respectively. The temperature dependencies of the acoustic attenuation were finally analyzed assuming the existence of three thermally activated relaxation processes of Cu^+ ions in connection with different kinds of sites. The proportion of the intensities of first two peaks (I_1 / I_2) depends on the glass composition, that is on the ratio $\text{CuBr}/(\text{CuI} + \text{CuBr})$ and reaches its maximum at $x = 6.82$ similarly as dc conductivity. The dependences of relative intensities of individual acoustic attenuation peaks on

glass composition are illustrated in Fig. 5d. The third peak, the presence of which only enables to fit the experimental dates thoroughly, represents non-essential transport mechanisms probably dependent only on glass forming system. Using the equation (3) and values of T_{peak} for individual peaks, the activation energies E_a^a were determined (Tab.1).

As it can be seen from the summarization of activation energies in Tab. 1, there are several categories of relaxation processes. High temperature activation energy established by all three methods, E_{a1}^{dc} , E_{a1}^a , $E_{a1}^{tg\delta}$ presents the basic mechanism. The second mechanism observed by both acoustic and conductivity measurements E_{a2}^a , E_{a2}^{dc} can play an important role in ionic transport, too. The existence of the processes characterized by activation energies E_{a3}^{dc} , E_{a4}^{dc} of System I is probably induced by the conditions of glass preparation and can be reduced by thermal treatment. The energy E_{a3}^a represents relaxation mechanism that does not influence the ionic transport significantly.

In addition to relaxation studies, for each glass of System I the glass transition temperature, T_g , was observed from acoustic attenuation measurement. The glass transitions temperature (Tab. 1) determined from acoustic measurements exhibited excellent coincidence with those determined from differential thermal analysis.

Comparing the activation energies obtained from acoustic and electrical measurements, it seems reasonable that essentially the some microscopic processes can be responsible for both acoustic and electrical relaxation processes. However, some differences can be caused by the different relaxation mechanisms connected with ion hopping transport at ac electric field and the hopping of mobile ions due to the interaction of acoustic wave with glass network.

The results from IR spectra of the CuI-CuBr-Cu₂O-P₂O₅ glasses [26-28] indicate that the thermal activated processes of Cu⁺ ions determined for all samples of investigated systems can be associated mainly with three different structural units - monomeric orthophosphate PO₄³⁻, low-condensed dimeric diphosphate oxoanions P₂O₇⁴⁻ and P₃O₁₀⁵⁻ structure phosphate anions. The local electric field around the trivalent orthophosphate anion PO₄³⁻ is stronger than the local electric field around dimeric diphosphate oxoanions P₂O₇⁴⁻ and triphosphate P₃O₁₀⁵⁻ anions because the diphosphate and triphosphate anions has smaller negative electric charge on non-bridging oxygen atoms. Moreover, expanded structure of chain groups creates advantageous conditions for ionic motion [4]. For that the electrostatic interactions between the mobile Cu⁺ ions and orthophosphate anions are stronger than those between Cu⁺ ions and diphosphate and triphosphate anions and we can suppose that the relaxation processes with biggest activation energies can be connected with monomeric orthophosphate anions and the processes with smaller energies can be connected with both dominant diphosphate oxoanions P₂O₇⁴⁻ and low condensed triphosphate anions and maybe other polymeric structural units. However, the existence of two main relaxation and transport mechanisms should support the idea of two equivalent anion structural units.

The infrared study of Cu⁺ ions conducting glasses in the similar systems as System II [26] showed that these glasses contain mainly PO₄³⁻ and MoO₄²⁻ tetrahedral anions groups and cuprous halides as well as their mixtures do not affect significantly the dominant phosphate and molybdate oxide structural units of glasses. For movement of Cu⁺ ions in glass structure also the nature of anion distribution in the network is important. Structure of investigated glasses changes significantly with increasing MoO₃/(P₂O₅+MoO₃) ratio. With increasing content of MoO₃ in glasses the number of non-bridging oxygens (NBO) which is associated probably with increase in polarizability of oxygen atoms increases, too. Mixing of cuprous halides in these systems

causes a negative deviation in the activation energy from the additivity rule, which corresponds with the positive deviation in electrical conductivity.

The fact that some of activation energies determined from dielectric spectroscopy and conductivity measurements on one side and acoustic attenuation spectroscopy on other side have the same or very close values (E_{a1}^a , E_{a1}^{dc} , $E_a^{tg\delta}$; E_{a2}^a , E_{a2}^{dc}) proved that the same mechanisms can influence electrical and acoustical losses in investigated ion conductive glasses.

References 15

- [1] Minami, T.: *Fast ion conducting glasses*. J. Non-Cryst. Solids **73**, 273-284 (1985)
- [2] Knauth, P., Tuller, H.L.: *Solid-State Ionics: Roots, Status and Future Prospects*. J. Am. Ceram. Soc. **85** [7] 1654-1680 (2002)
- [3] Ingram, M. D.: *The mixed alkali glasses / a new look at an old problem*. Glstech. Ber. Glass. Sci. Technol. **67**, 151-155 (1994)
- [4] Znášik, P., Jamnický, M.: *Cu⁺-ion-conducting properties of mixed-halide metaphosphate and orthophosphate glasses*. Solid State Ionics **95**, 207-214 (1989)
- [5] Funke, K.: *Ion transport in fast ion conductors – spectra and models*. Solid State Ionics **97**, 27-32 (1997)
- [6] Richter, R., Wagner, H.: *The dielectric modulus: relaxation versus retardation*. Solid State Ionics **105**, 167-173 (1998)
- [7] Roling, B.: *What do electrical conductivity and electrical modulus spectra tell us about the mechanisms of ion transport processes in melts, glasses and crystals*. J. Non-Crystal. Sol. **244**, 34-43 (1999)
- [8] Roling, B., Ingram, M.D.: *Analysis of mechanical losses due to ion-transport processes in silicate glasses*. Phys. Rev. **B57**, 14192-14199 (1998)
- [9] Roling, B.: *Mechanical loss spectroscopy on inorganic glasses and glass ceramics*, Current Opinion in Solid State and Material Science **5**, 203-210 (2001)
- [10] Almond, D.P., West, A.R.: *Ultrasonic attenuation studies of solid electrolytes*. Solid State Ionics **26**, 265-278 (1988)
- [11] Carini, G., Cutroni, M., Federico, M., Galli, G., and Tripodo, G.: *Acoustic properties and diffusion in superionic glasses*. Phys. Rev. **B30**, 7219 - 7224(1984)
- [12] Cutroni, M., Mandanici, A.: *Mechanical and dielectric behaviour of some ionic glasses*. Sol. State Ionics **105**, 149-157 (1998)
- [13] Baranovskii S. D., and Cordes H.: *On the conduction mechanism in ionic glasses*. J. Chem. Phys. **11**, 7546-7557 (1999)
- [14] Bunde, A., Ingram, M. D., Maass, P.: *The dynamic structure model for ion transport in glasses*. J. Non-Cryst. Solids **172-174**, 1222 - 1236 (1994)
- [15] Ingram, M. D., Robertson, A.H.J.: *Ion transport in glassy electrolytes*. Solid State Ionics **94**, 49-54 (1997)
- [16] Ingram, M.D.: *Superionic glasses: theories and applications*. Current Opinion in Solid State and Materials Science **2**, 399 (1997)

- [17] Pradel, A., Taillades, G., Cramer, C., Ribes, M.: *Ion dynamics in superionic chalcogenide glasses studied in large frequency and temperature ranges*. Solid State Ionics **105**, 139-148 (1998)
- [18] Funke, K.: *Jump relaxation in solid electrolytes*. Prog. Solid State Chem. **22**, 111 - 195 (1993)
- [19] Bunde, A., Funke, K., Ingram, M. D.: *A unified site relaxation model for ion mobility in glassy materials*. Solid State Ionics **86-88**, 1311-1317 (1996)
- [20] Jain, H., Krishnaswami, S.: *Composition dependence of frequency power law of ionic conductivity of glasses*. Solid State Ionics **105**, 129-137 (1988)
- [21] Sidebottom, D.L., Roling, B. and Funke, K.: *Ion conduction in solids: Comparing conductivity and modulus representations with regard to scaling properties*. Phys. Rev. **B63**, 24301 (1-7) (2000)
- [22] Funke, K., Roling, B., Lange, M.: *Dynamics of mobile ions in crystals, glasses and melts*. Solid State Ionics **105**, 195-208 (1998)
- [23] Roling, B., Happe, A., Ingram, M. D., Funke, K.: *Interrelation between Different Mixed Cation Effects in the Electrical Conductivity and Mechanical Loss Spectra of Ion Conducting Glasses*. J. Phys. Chem. **B103**, 4122 - 4127(1999)
- [24] Börjesson, L.: *Secondary relaxations due to fast-ion diffusion in AgI-rich borate glasses observed by Brillouin scattering*. Phys. Rev. **B36** 4600 – 4612 (1987)
- [25] Znášik, P., Jamnický, M.: *Electrical properties of mixed-halide CuI-CuCl-Cu₂O-P₂O₅ glasses*. J. Matter. Sci. lett. **14**, 145-150 (1995)
- [26] Znášik, P., Jamnický, M.: *Preparation, infrared spectra and structure of glasses in the system CuCl-Cu₂O-(P₂O₅+MoO₃)*. J. Non-Cryst. Solids **146**, 74 - 80 (1992)
- [27] Jamnický, M., Znášik, P., Tunega, D., and Ingram, M.D.: *Glass formation and structure in the system Cu₂P₂O₅-MoO₃*. J. Non- Cryst. Solids **185**, 151 – 158 (1995)
- [28] Znášik, P., Jamnický, M.: *Properties of mixed-halide metaphosphate glasses in systems of CuI-CuX-Cu₂O-P₂O₅ (X=Br, Cl)*. Solid State Ionics **92**, 145-150 (1996)
- [29] Bury, P. Jamnický, M., Hockicko, P. Jamnický, I.: *Transport mechanisms study of glassy electrolytes using acoustic attenuation and conductivity spectroscopy*. Glass Science and Technology **77** Suppl. C 354-358 (2004)
- [30] Bury, P., Hockicko, P., Jurečka, S., Jamnický, M.: *Analysis of Acoustic Attenuation Spectra Due to Ion Transport Processes in Glassy Electrolytes*. Physica Status Solidi (c) **11** 2888-2891 (2004)
- [31] Bury, P., Hockicko, P., Jamnický, M., Jamnický, I.: *What do Acoustical Properties about the Mechanisms of Ion Transport Processes in Glassy Electrolytes*. Proceedings of the 18th International Congress on Acoustics, Kyoto 2004, Vol. **II**, 1137-1140 (2004)
- [32] Bury, P. Hockicko, P., and Jamnický, M.: *Transport and relaxation study of ionic phosphate glasses*. Adv. Mater. Research **39**, 111-116 (2008)
- [33] Bury, P., Hockicko, P., Jamnický, M., Jamnický I.: *On the relation between electrical and acoustic properties of ion conducting glasses*. Adv. EEE **2**, 16-23 (2003)



Chapter 16

Thermal properties of oxide glasses

16. STUDYING STRUCTURE AND THERMAL PROPERTIES OF OXIDE GLASSES

Marek Liška

16.1. Introduction

Glass is accompanying people from the early times of mankind. First it was the natural glass generated by the volcanic processes and the glass “produced” by the impact of meteors on the earth. During formation of the earth, highly siliceous melts of rocks froze to natural glasses such as obsidians. After some time the people start the glass melting. Glass was first produced by man about 4000 years ago in ancient Egypt. From this time the need of the knowledge of glass composition, structure and properties is dated. These are the typical questions answered by the glass chemistry [1-6].

Comparing the glass chemistry with other fields of chemistry we can find it relatively young. This is mainly due to the fact that production of well defined and homogeneous glass samples was serious problem due to the need of high temperatures and laboratory equipment that is sufficiently stable at high temperatures and does not contaminate the melted glass (platinum or rhodium crucibles, stirrers etc.). Also the use of platinum stirrers to reach the homogeneity of the glass melt was the crucial step towards the production of homogeneous glass samples. On the other hand the glass “chemistry” covers in fact a boundary area between chemistry, physics, and mineralogy, (and biology and medicine in the field of bioglass). The glassy state is a general phenomenon and we can meet it in the field of inorganic substances, organic substances and metals. Throughout this chapter we will focus mostly on the inorganic (silicate) glasses. The aim of the present contribution is point out the mutual relationships between the understanding of the glass structure and construction of the thermodynamic models of glass. Finally the method of studying glass structure based on combined statistical treatment of Raman spectra with the thermodynamic model will be presented together with the example of its application on the chalcogenide glasses from the pseudobinary system As_2S_3 - As_2Se_3 .

16.2. Thermodynamics of glass formation [7, 8]

The glass is commonly defined (e.g. [9]) as the non-crystalline solid obtained by cooling the melt without crystallization. Despite the fact that glass can be produced also by other ways, like by the sol-gel method or by the amorphization of crystalline solid [6], it is worth noting the uncommon situation when the method of preparation becomes a part of the definition of some kind of substance-material. This indicates the importance of the kinetic factors connected with the glass formation. On the other hand the kinetics – namely the kinetics of nucleation and crystal growth – is determined by the (under-cooled) melt structure. The typical course of the glass formation from the melt can be seen in Fig. 1 where the temperature dependence of the (single component) system volume is plotted against temperature. The melt is in the state of the true thermodynamic equilibrium (corresponding to the global minimum of the Gibbs energy at isothermal-isobaric conditions) at the melting temperature T_m . In case of the multi-component system the melting temperature is replaced by the liquidus temperature, T_{liq} , and during crystallization the temperature gradually decreases tracing the binary, ternary... eutectic lines of the particular equilibrium phase diagram until the multi-component eutectic is reached at the temperature T_{eut} (obviously $T_{\text{eut}} < T_{\text{liq}}$). The true thermodynamic equilibrium of the single-component system under the T_m temperature is then represented by the crystalline state. In case- of multicomponent system the equilibrium

mixture of crystalline phases and the melt corresponds to the true thermodynamic equilibrium in temperature ranging from the liquidus temperature to eutectic temperature and to the crystalline state under the eutectic temperature.

The equilibrium state represented by the equilibrium mixture of crystalline phases is termed the Crystalline Reference State (CRS) by Conradt [Conradt]. It is worth noting that the knowledge of the particular equilibrium phase diagram is sufficient for the knowledge of the composition of the CRS. Thus mole fractions of individual thermodynamically stable crystalline phases in the CRS can be simply calculated from the particular phase diagram, namely from the coordinates of particular eutectics (non-variant points of the phase diagrams).

When the crystallization is avoided (due to sufficiently high cooling rate) the metastable equilibrium state represented by the under-cooled melt is reached below the T_m / T_{liq} temperature. Depending on the cooling rate the system follows the metastable equilibrium until the glass transition region (the curved part of the dashed line) where the increase of the viscosity and thus the structural relaxation time leads to freezing in of the structure. Under the glass transition region characterized by the glass transition temperature T_g the glass is obtained (the dotted line). The kinetic character of the glass transition is expressed by the fact that decreasing the cooling rate (but avoiding the crystallization) shifts the glass transition to lower temperatures. Thus the glass structure depends on the cooling rate, i.e. on its thermal history. It is worth noting that the T_g temperature is in fact not strictly defined. On one side it depends on the cooling rate but also on the method of its determination (thermodilatometry, DSC...). The structure of the glass can be thus characterized by the temperature at which the metastable equilibrium structure was frozen in. This is the fictive or structure temperature T_f introduced by Tool. In the simplified situation of linear volume temperature dependence presented in Fig. 1 the glass transition temperature coincides with the Tool's fictive temperature. In fact the $V(T)$ linearity can be generally assumed with some reasonable accuracy in limited temperature range. This situation may be reached supposing the temperature independent value of the volume thermal expansion coefficient:

$$\beta = \frac{1}{V} \left(\frac{\partial V}{\partial T} \right)_p \quad (1)$$

and replacing the exponential volume temperature dependence resulting from the Eq.(1) by the linear approximation:

$$V_2 = V_1 \exp[\beta(T_2 - T_1)] \cong V_1 [1 + \beta(T_2 - T_1)] \quad (2)$$

Thus the slopes of linear dependences plotted in Fig. 1 are simply related to the particular thermal expansion coefficients. It is worth noting, that the thermal expansion of glass can be well approximated by the thermal expansion of the CRS. In both cases the volume change induced by temperature increase is connected only with the increase of population of higher vibrational states. The real experimentally obtained temperature dependence of volume (length) obtained by the thermodilatometric measurement is plotted in Fig. 2.

Similar picture can be obtained for the temperature dependence of the system enthalpy, H . The slope of lines in the $H(T)$ line is then given by the isobaric heat capacity C_P :

$$C_p = \left(\frac{\partial H}{\partial T} \right)_p \quad (3)$$

Like in the case of the thermal expansion coefficient the temperature independent values of heat capacity can be assumed in the plotted temperature range. Moreover, using the same reasoning as in the case of thermal expansion, the same value of heat capacity of glass and those of the CRS can be assumed. It is also obvious that the value of the heat capacity / thermal expansion coefficient of metastable melt is higher than those of the glass. It is of academic importance only, that assuming the extremely low cooling rate we can reach the hypothetic situation when the volume / enthalpy of the metastable melt will be lower than those of the CRS. Taking into account the logarithmic temperature dependence of the entropy:

$$dS = \frac{dq_{\text{rev}}}{T} = C_p d \ln T \quad (4)$$

the same picture will result when entropy is plotted against $\ln T$. Here the situation when extremely slow cooling would lead to lower entropy of metastable melt than of the CRS is paradoxical. This situation is known as the Kauzmann paradox. The point where the entropy of metastable melt equals to the entropy of the CRS is considered as an ideal glass. The glass close to this state can be obtained by amorphization of some zeolites [6].

To describe the thermodynamics of the glass state we have first to discuss the fact that glass itself is not in the equilibrium state and its structure depends on the kinetics factors, e.g. on the thermal history or the cooling rate when the glass was prepared from the undercooled melt. However, following the reasoning of Conradt [8, 10], we can with some acceptable tolerance accept the glass as a system with definite (mean) values of thermodynamic quantities.

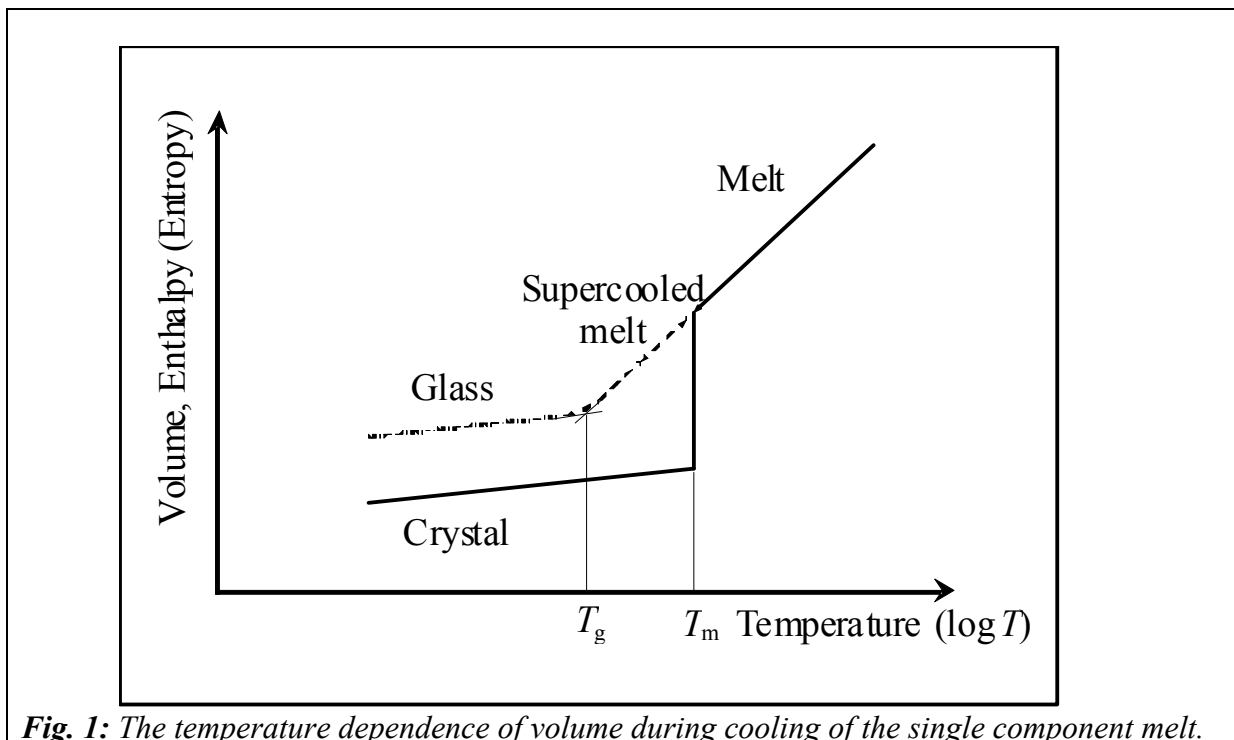


Fig. 1: The temperature dependence of volume during cooling of the single component melt.

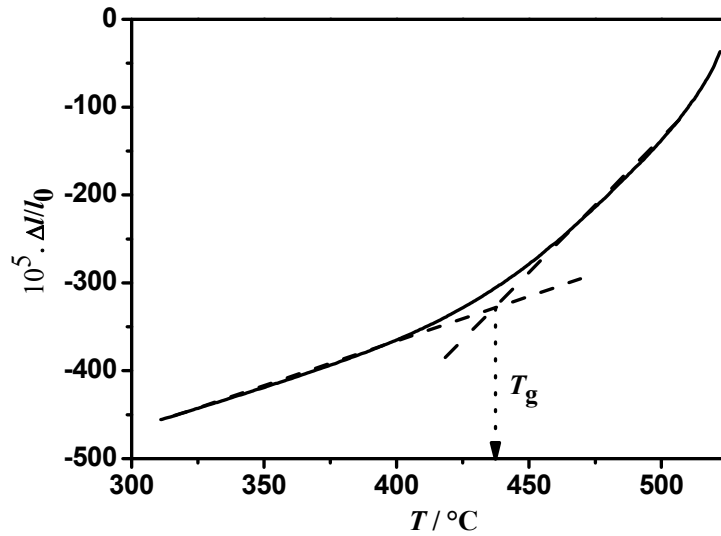


Fig. 2. Thermodilatometric cooling curve (cooling rate 5°C/min.) of the NBS711 viscosity standard glass. Dashed linear parts with the slopes corresponding to the thermal expansion coefficients of glass ($\alpha_g = 10.7 \text{ ppm/}^\circ\text{C}$) and metastable melt ($\alpha_g = 29.2 \text{ ppm/}^\circ\text{C}$) are used for the T_g value estimation ($T_g = 435^\circ\text{C}$).

In analogy with melting where we define the melting difference of any property as the difference between the melt and crystal at the temperature T_m :

$$\Delta_{\text{fus}} = \text{melt at } T - \text{crystal at } T \quad (5)$$

we define the vitrification change of any property as:

$$\Delta_{\text{vit}} = \text{glass at } T - \text{crystal at } T \quad (6)$$

once again in many component incongruent systems, the crystal is replaced by CRS and T_m by T_{liq} (or an effective mean temperature between the T_{liq} and T_{eut}). Due to the assumption $C_{P,\text{glass}} = C_{P,\text{CRS}}$ that results in the parallel course of enthalpy temperature dependence the vitrification enthalpy is constant below T_g , i.e.:

$$\Delta_{\text{vit}} H(T; T \leq T_g) = \Delta_{\text{fus}} H(T_g) \quad (7)$$

The temperature dependence of the enthalpy of melting can be calculated from the known (from calorimetry experiment) enthalpy of melting at T_m assuming the temperature independent heat capacities:

$$\Delta_{\text{fus}} C_P = C_{P,\text{melt}} - C_{P,\text{CRS}} = C_{P,\text{melt}} - C_{P,\text{glass}} = \Delta_{\text{vit}} C_P = \Delta C_P \quad (8)$$

and consequently:

$$\Delta_{\text{fus}} H(T) = \Delta_{\text{fus}} H(T_m) + \Delta C_P \int_{T_m}^T dT' = \Delta_{\text{fus}} H(T_m) + \Delta C_P (T - T_m) \quad (9)$$

The entropy of melting at T_m , $\Delta_{\text{fus}} S(T_m)$, can be obtained from the equilibrium condition:

$$\Delta_{\text{fus}} G(T_m) = \Delta_{\text{fus}} H(T_m) - T_m \Delta_{\text{fus}} S(T_m) = 0 \quad (10)$$

and for the temperature dependence of the melting entropy we obtain:

$$\Delta_{\text{fus}} S(T) = \Delta_{\text{fus}} S(T_m) + \Delta C_P \int_{T_m}^T d \ln T' = \frac{\Delta_{\text{fus}} H(T_m)}{T_m} + \Delta C_P \ln \frac{T}{T_m} \quad (11)$$

Using the same reasoning as in the case of vitrification enthalpy, we obtain:

$$\Delta_{\text{vit}} S(T; T \leq T_g) = \Delta_{\text{fus}} S(T_g) \quad (12)$$

Taking into account Eqs.(7, 12) we can conclude that we have described the thermodynamics of vitrification by the thermodynamic quantities related to crystallization. Obviously, the driving force for isothermal isobaric devitrification (by crystallization) is represented by the positive value of the vitrification Gibbs energy $\Delta_{\text{vit}} G(T)$:

$$\Delta_{\text{vit}} G(T) = \Delta_{\text{vit}} H(T) - T \Delta_{\text{vit}} S(T) \quad (13)$$

or

$$\Delta_{\text{vit}} G(T) = \Delta_{\text{fus}} H(T_m) + \Delta C_P (T_g - T_m) - T \left[\frac{\Delta_{\text{fus}} H(T_m)}{T_m} + \Delta C_P \ln \frac{T_g}{T_m} \right] \quad (14)$$

that can be rewritten as:

$$\Delta_{\text{vit}} G(T) = \Delta_{\text{fus}} H(T_m) \left[1 - \frac{T}{T_m} \right] + \Delta C_P \left[(T_g - T_m) - T \ln \frac{T_g}{T_m} \right] \quad (15)$$

Because of the positive value of the melting enthalpy and the relationship $T_g < T_m$ it can be seen from the above equation that the thermodynamic driving force towards crystallization (i.e. the opposite to vitrification) increases with decreasing temperature.

The following rules of thumb are frequently used in the glass science [8, 10]

$$\Delta_{\text{vit}} S = \frac{1}{3} \Delta_{\text{fus}} S(T_m) = \frac{1}{3} \frac{\Delta_{\text{fus}} H(T_m)}{T_m} \quad (16)$$

$$\Delta C_P = \frac{3}{2} \Delta_{\text{fus}} S(T_m) = \frac{3}{2} \frac{\Delta_{\text{fus}} H(T_m)}{T_m} \quad (17)$$

These rules, although almost never correct in detail, give reasonable estimates of the true values. Inserting the Eq.(16, 17) into the Eq.(11, 12) we obtain the equation:

$$\Delta_{\text{vit}} S = \frac{1}{3} \Delta_{\text{fus}} S(T_m) = \Delta_{\text{fus}} S(T_m) + \frac{3}{2} \Delta_{\text{fus}} S(T_m) \ln \frac{T_g}{T_m} \quad (18)$$

leading to the simple relationship between T_g and T_m :

$$T_g = T_m \exp(-4/9) = 0.641T_m \cong \frac{2}{3}T_m \quad (19)$$

Moreover, inserting the Eq.(19, 17) into the Eq.(7, 9) we obtain simple approximate relationship between $\Delta_{vit}H$ and $\Delta_{fus}H$:

$$\Delta_{vit}H = \Delta_{fus}H(T_g) = \Delta_{fus}H(T_m) + \frac{3}{2} \frac{\Delta_{fus}H(T_m)}{T_m} \left(\frac{2}{3}T_m - T_m \right) \quad (20)$$

or

$$\Delta_{vit}H = \frac{1}{2} \Delta_{fus}H(T_m) \quad (21)$$

Finally, inserting the Eq.(16, 21) into the Eq.(13) we obtain the temperature dependence of the affinity to glass crystallization:

$$\Delta_{vit}G(T_g) = \frac{1}{2} \Delta_{fus}H(T_m) - T_g \frac{1}{3} \frac{\Delta_{fus}H(T_m)}{T_m} = \Delta_{fus}H(T_m) \left(\frac{1}{2} - \frac{2}{9} \right) = \frac{5}{18} \Delta_{fus}H(T_m) \quad (22)$$

and

$$\Delta_{vit}G(0) = \frac{1}{2} \Delta_{fus}H(T_m) \quad (23)$$

The above equations are of especial importance because the enthalpies of melting of crystalline compounds are well experimentally determined and can be obtained from many sources including various thermodynamic databases [11].

16. 3. Glass structure

What is the structure [1-5] of glass and how to describe it? In contrary to the crystalline substances where the 3D translational symmetry takes place the structure of glass cannot be quantified giving a small number of numeric data. Due to the 3D translational symmetry the structure of any crystalline substance is given by specifying the basic cell and giving the fractional coordinates of all atoms located in the basic cell. Positions of all other atoms are then simply given by superposition of translations in the three dimensions. Following this concept the structure of glass would be given by specifying Cartesian coordinates of all atoms - i.e. about $\sim 10^{25}$ data for one mol of glass.

On the other side the relatively uniform coordination polyhedra, like SiO_4 , AlO_4 , BO_4 , BO_3 etc., can be found in the oxide glass. Therefore the glass structure has to be seen in different scales. The uniform coordination polyhedra correspond to the short-range order (SRO) or the nearest neighbor scale. Going to the next nearest neighbor we can distinguish between various types of coordination polyhedra according to their structural position within the glass network. So the SiO_4 tetrahedra can be classified according to the number of bridging oxygen atoms, connecting them with the neighboring polyhedra. For instance Q^i represents the SiO_4 polyhedron with i bridging oxygen atoms, i.e. $\text{Si}(\text{-O-X})_i(\text{-O})_{4-i}$, where X stands for any other networkforming atom (Si, Al, B, P,...). Going to the next nearest neighbor (and next-next nearest neighbor) we can reach more detailed structural description corresponding to the medium range order (MRO). The long range order (LRO) structural

information concerns the large extent of the polymerized 3D network. Different glass properties are structurally influenced in different extent of structural arrangement. So some optical properties are defined by the SRO, mechanical, electrical and thermal properties depend on the MRO and LRO structure.

On the other hand, the usefulness and applicability of any kind of the structure description / quantification is limited by the experimental methods enabling its quantitative determination. So the nearest neighbor and next nearest neighbor description of networkforming coordination polyhedra is possible mainly due to the experimental techniques like EXAFS, XANES, NMR and Raman vibrational spectroscopy.

The most important structural theory of inorganic glasses was developed by Zachariasen and Warren [12, 13]. According to the *Zachariasen-Warren Continuous Random Network* (CRN) theory the following rules are valid for the formation of glass from simple compounds like SiO_2 , B_2O_3 , P_2O_5 , GeO_2 , As_2S_3 , As_2Se_3 , BeF_2 , ZnCl_2 etc.:

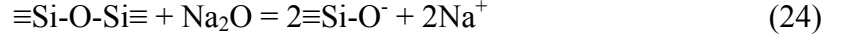
- i) An oxide or compound tends to form a glass if it easily forms polyhedral groups as the smallest building units.
- ii) Polyhedra should not share more than one corner.
- iii) Anions (like O^{2-} , S^{2-} , Se^{2-} , F^- , Cl^- , ...) should not bind more than two central atoms (in simple glasses anions form bridges between two adjacent polyhedra).
- iv) The number of vertices of polyhedron should be less than six.
- v) At least three vertices of a polyhedron must be shared with neighboring polyhedra.

These rules can be well understood when we think about the consequences of their violation. The first rule is in some extent equivalent to the assumption of covalent (or polar covalent) bonding between cations and anions. In another words the covalency implies the sufficient strength of the 3D backbone. The violation of second rule results in more regular (more crystal like) structure and thus the crystallization of the melt can be expected at least when common cooling rates are applied. The same reasoning can be applied in the case of violation of the next rule. The fourth rule can be understood in two different ways. On one side the six (and more) coordinated polyhedra form more regular structures. On the other side the high coordination numbers are typically found in ionic compounds, i.e. in case of electropositive atoms like alkaline and alkaline-earth atoms. The last rule assures the formation of three-dimensional network. In case of sharing only two vertices the chain (or cyclic) structure is formed and the covalent percolation of the melt bulk is not reached.

Zachariasen classified the cations in a glass as follows:

- i) Network-formers (NWF, e.g. Si, B, P, Ge, As, ...) with the coordination number (by oxygen, by fluorine) 3 or 4.
- ii) Network-modifiers (NWM, e.g. Li, Na, K, Ca, Sr, Ba, ...) with coordination numbers generally greater or equal to 6.
- iii) Intermediates that may either reinforce the 3D network by cross-linking (coordination number 3 or 4) or weaken the network by depolymerization (coordination number 6 – 8). Moreover the intermediate cations cannot solely form the single component glass.

In case of silicate glasses the NWM oxides (e.g. Na_2O) depolymerize the network of SiO_4 tetrahedra by disrupting the oxygen bridges (bridging oxygen - BO) and creating the non-bridging oxygen atoms O^- (NBO):



The lack of experimental information about the structure of glass and the difficulties in describing the polymerized structure in the LRO extent can be partially solved by the concept of atom-specific structure elements (ASEs) developed by Sprenger [14, 15, 16].

16. 4. Deducing the structure from stoichiometry

16.4.1. Silicate Glasses

The structure of silica glass is formed by mutually 3D interconnected SiO_4 tetrahedra. Each tetrahedron is sharing four oxygen atoms with neighboring tetrahedra, i.e. the structure is on the SRO level composed from Q^4 structural units. When alkaline or alkaline earth oxide is added to silica glass the 3D silica network is gradually depolymerized due to the reaction (24). According to the ratio between the molar amounts of oxygen and silicon atoms, $R = n(\text{O})/n(\text{Si})$, the structure can be roughly characterized as composed from the mixture of Q^i and Q^{i+1} structural units (Tab. 1). In case of specific glass compositions listed in Tab. 1, the glass can be considered as composed from single type of Q-units.

Table 1: Structural units of silicate glasses and glass compositions of alkali silicate and alkaline earth silicate corresponding to the R value

Structural unit Q^i	R_i	Coordination Formula	Glass composition $R = \text{Li, Na, K, Rb, Cs, Fr}$ $R' = \text{Mg, Ca, Sr, Ba, Ra}$
Q^4	2	$\text{SiO}_{4/2}$	SiO_2
Q^3	2.5	$[\text{SiO}_{3/2}\text{O}_{1/1}]^-$	$\text{R}_2\text{O}\cdot 2\text{SiO}_2, \text{R}'\text{O}\cdot 2\text{SiO}_2$
Q^2	3	$[\text{SiO}_{3/2}\text{O}_{1/1}]^{2-}$	$\text{R}_2\text{O}\cdot \text{SiO}_2, \text{R}'\text{O}\cdot \text{SiO}_2$
Q^1	3.5	$[\text{SiO}_{3/2}\text{O}_{1/1}]^{3-}$	$3\text{R}_2\text{O}\cdot 2\text{SiO}_2, 3\text{R}'\text{O}\cdot 2\text{SiO}_2$
Q^0	4	$[\text{SiO}_{4/1}]^{4-}$	$2\text{R}_2\text{O}\cdot \text{SiO}_2, 2\text{R}'\text{O}\cdot \text{SiO}_2$

It is obvious, that when the assumption of the structure formed by only two successive Q-units (say Q^i and Q^{i+1} , where $0 \leq i \leq 3$) is applied, the relative amount of individual Q-units can be simply calculated from stoichiometry. It is worth noting that this very simple model can provide very important information, e.g. in the field of bioglass [17, 18]. Let us consider the glass of composition given by the formula $x\text{R}_2\text{O}\cdot y\text{R}'\text{O}\cdot (1-x-y)\text{SiO}_2$, where $0 < x, y < 1$, and $x+y < 2/3$. Then the i value is determined from Tab. 1 by the inequality:

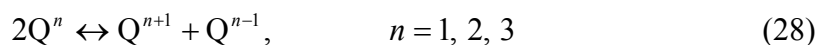
$$R_i \leq \frac{x+y+2(1-x-y)}{1-x-y} = \frac{2-x-y}{1-x-y} \leq R_{i+1} \quad (25)$$

Then the mole fractions, $x(Q^i)$, of particular Q-units are calculated from the mass balance equations:

$$(1-x-y)[x(Q^i)(i/2+4-i) + x(Q^{i+1})(i/2+7/2-i)] = 2-x-y \quad (26)$$

$$x(Q^i) + x(Q^{i+1}) = 1 \quad (27)$$

Unfortunately, the above approach can be used for the rough orientation purposes only. In fact, Q-units disproportionate and the Q-distribution is given by the equilibrium of the disproportionation reactions of the type:



Nevertheless even the very simple approach considering the coexistence of only two successive Q-units, can successfully explain some experimental property – composition relationships. As an example the compositional dependence molar volume of binary Na₂O – SiO₂ glasses at room temperature is presented in Fig. 3. Experimental data of 49 glasses with the SiO₂ content ranging from 51.62 wt.% to 86.12 wt.% taken from [19, 20] were represented by the regression equation:

$$V_m[(1-z)\text{Na}_2\text{O} \cdot z\text{SiO}_2] = x(Q^2)zV_m(Q^2) + x(Q^3)zV_m(Q^3) + x(Q^4)zV_m(Q^4) \quad (29)$$

with the standard deviation of approximation $s_{\text{apr}} = 0.054$ ml/mol. Experimental values of molar volume, V_m^{exp} , were calculated from the tabulated room temperature density, ρ , of glasses melted in platinum crucibles with the composition determined by wet chemical analysis by:

$$V_m^{\text{exp}} = \frac{(1-z)M(\text{Na}_2\text{O}) + zM(\text{SiO}_2)}{\rho} \quad (30)$$

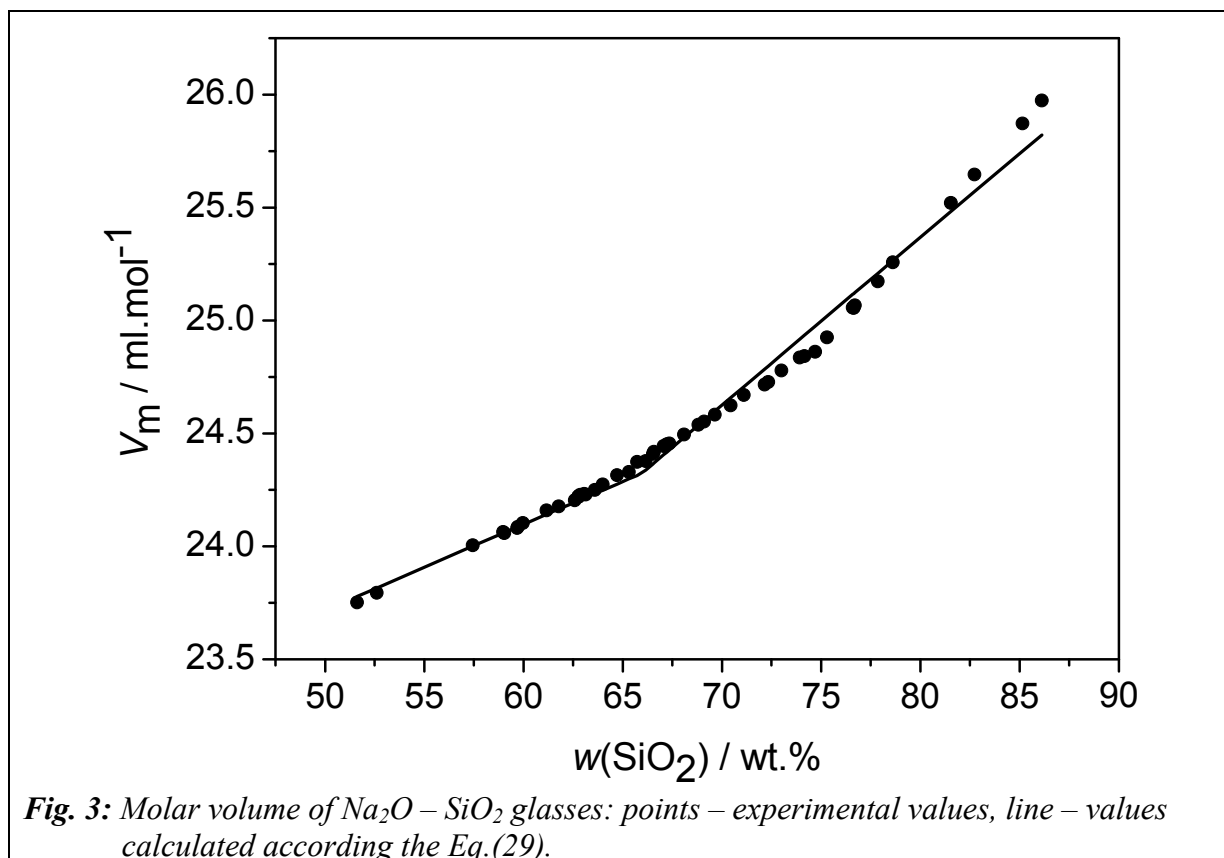
The following regression estimates of molar volumes of individual Q- units were obtained:

$$\begin{aligned} V_m(Q^2) &= (47.37 \pm 0.07) \text{ ml/mol,} \\ V_m(Q^3) &= (36.49 \pm 0.02) \text{ ml/mol, and} \\ V_m(Q^4) &= (26.84 \pm 0.04) \text{ ml/mol.} \end{aligned}$$

It is worth noting, that the Q-units distribution represents the SRO only. Going to the next neighbor the interconnectivity between various Q-units (MRO) is taken into account. These level of structure description is especially important for rationalization of the so-called mixed alkali effect, residing in the non-monotonous dependence of various physical and chemical glasses and melt properties on the degree of equimolar substitution of one alkaline (or alkaline earth) oxide by the other.

16.4.2. Other oxide glasses

When compared with the silicate glasses the structure of borate glasses is more complex namely due to the fact that both trigonal BO₃ and tetrahedral BO₄ polyhedra form the 3D network. The pure B₂O₃ glass is formed from BO₃ triangles (BO_{3/2}) ordered in six-membered boroxol rings. Due to the equilibria between the three- and four-coordinated boron, the compositional dependence of various physical properties of alkali-borate and alkaline earth-borate glasses is not monotonous. This fact is known as the *boron anomaly*. The structure of borosilicate glasses where the SiO₄ Q-units are interconnected with the BO₃ triangles and BO₄ tetrahedra is even more complex.



Similar complexity is found in I structure of aluminosilicate glasses. The crucial point determining the structure is the ratio between the molar amount of alkali and alkaline earth oxides and alumina, i.e. $[n(R_2O)+n(R'O)]/n(Al_2O_3)]$. In the peraluminous region where this ratio is less than 1, the substantial amount of octahedral AlO_6 units is found in the network. In the peralkaline region where sufficient amount of alkalis is present the tetrahedral $[AlO_{4/2}]^-$ units are formed by the reaction:



The borosilicate and aluminosilicate glasses are presented here as an example illustrating the possible complexity of the SRO glass structure. Obviously the distribution of various types of coordination polyhedra cannot be obtained from the stoichiometry even at the crudest simplifying assumptions. Some results may be obtained by the purely statistical method assuming the purely stochastic formation of connection between various structural units. It is in some respect equivalent to maximizing the configurational entropy of the glass. However the decisive role of the enthalpy (roughly speaking the energy of various bonds) is completely neglected by such treatment.

16. 5. Thermodynamic models of glass

The crucial point of each thermodynamic model is the definition of atomic groupings that will be considered as components of the system. This definition implies the structural range described by the particular model. On the SRO level the components of the system are defined as the particular coordination polyhedra (like Q-units). The system entropy can be then described by regular mixing of system components while the enthalpy can be calculated by summing the bond energies. The equilibrium composition of the system is then obtained

by the minimization of the Gibbs energy constrained by the stoichiometry of the system. Such type of models is critically reviewed in the works of Gurman and Conradt [8, 10, 21]. As an example of very simple thermodynamic model of silicate glasses the equations of simultaneous Q-units disproportionation can be presented (Eq.(28)). The model is represented by the values of the equilibrium constants, K_n , of reactions (28) – i.e. by the Gibbs energies of different Q-units.

$$K_n = \exp\left(\frac{\Delta_{r,n}G^\circ}{RT^\circ}\right) = \frac{a(Q^{n-1})a(Q^{n+1})}{[a(Q^n)]^2} \cong \frac{x(Q^{n-1})x(Q^{n+1})}{[x(Q^n)]^2}, \quad n=1,2,3 \quad (32)$$

where $\Delta_{r,n}G^\circ$ is the standard reaction Gibbs energy of Q^n -unit disproportionation, T° – the standard temperature, $a(Q^n)$ – the activity of Q^n unit in the glass (melt) that is (supposing the standard state of pure substance at standard pressure and temperature) commonly approximated by the mole fraction $x(Q^n)$. The values of equilibrium constants are calculated from the Q-speciation that is commonly determined by the ^{29}Si NMR and Raman spectroscopy [4, 5]. However, as far as the energetic and structure of the ionic bonds formed by NWM cations is not included in the model, the K_n values are dependent on the type of NWM cations.

MRO structure is reflected in the thermodynamic models based on the (at least stoichiometric) definition of components as compounds. The computational complexity of the model depends on the number of components. In the model of Conradt [8, 10], the components are defined as having the stoichiometry of crystalline substances forming the CRS. The definition CRS implies that only the coexisting phases are taken into account. Thus the concentrations of all components are straightforwardly defined by the mass balance equations and can be obtained by solving a set of linear equations. As an example we can once again present the molar volume of $\text{Na}_2\text{O} - \text{SiO}_2$ glass at room temperature. According the equilibrium phase diagram the CRS consists – depending on the glass composition – of eutectic mixtures of: $\text{SiO}_2 \leftrightarrow 3\text{Na}_2\text{O} \cdot 8\text{SiO}_2$; $3\text{Na}_2\text{O} \cdot 8\text{SiO}_2 \leftrightarrow \text{Na}_2\text{O} \cdot 2\text{SiO}_2$; $\text{Na}_2\text{O} \cdot 2\text{SiO}_2 \leftrightarrow \text{Na}_2\text{O} \cdot \text{SiO}_2$; $\text{Na}_2\text{O} \cdot \text{SiO}_2 \leftrightarrow 3\text{Na}_2\text{O} \cdot 2\text{SiO}_2$; $3\text{Na}_2\text{O} \cdot 2\text{SiO}_2 \leftrightarrow 2\text{Na}_2\text{O} \cdot \text{SiO}_2$; $2\text{Na}_2\text{O} \cdot \text{SiO}_2 \leftrightarrow \text{Na}_2\text{O}$. Taking one mole of $(1-z)\text{Na}_2\text{O} \cdot z\text{SiO}_2$ glass and supposing it is formed by the mixture of $i\text{Na}_2\text{O} \cdot j\text{SiO}_2 \leftrightarrow k\text{Na}_2\text{O} \cdot l\text{SiO}_2$ we can calculate the molar amount, n , of both compounds from:

$$n(i\text{Na}_2\text{O} \cdot j\text{SiO}_2) = \frac{l}{i.l - j.k} - \frac{k+l}{i.l - j.k} z \quad (33)$$

$$n(k\text{Na}_2\text{O} \cdot l\text{SiO}_2) = -\frac{j}{i.l - j.k} + \frac{i+j}{i.l - j.k} z \quad (34)$$

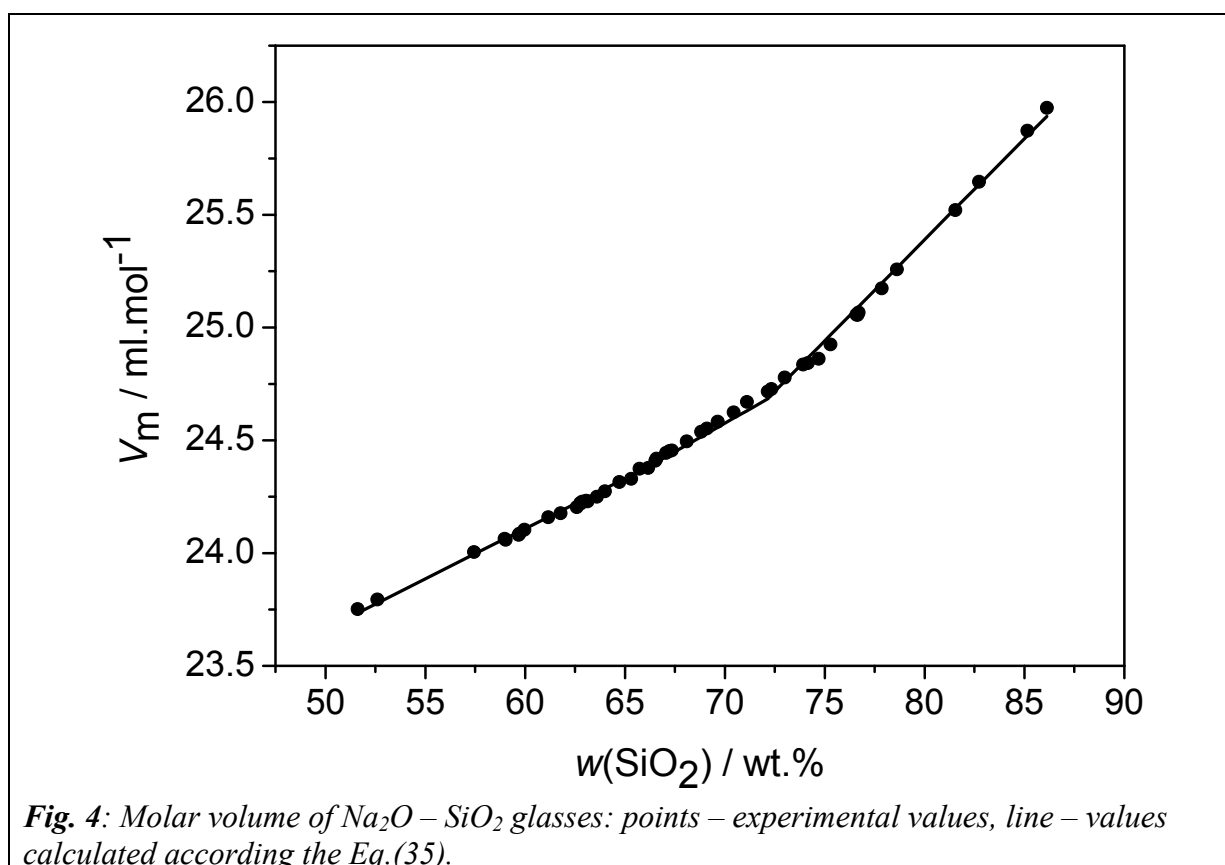
As an example of application of the Conradt's thermodynamic model the compositional dependence molar volume of binary $\text{Na}_2\text{O} - \text{SiO}_2$ glasses at room temperature is presented in Fig. 4. The same experimental data of 49 glasses with the SiO_2 content ranging from 51.62 wt.% to 86.12 wt.% taken from [19, 20] were represented by the regression equation:

$$V_m[(1-z)\text{Na}_2\text{O} \cdot z\text{SiO}_2] = n(\text{SiO}_2)V_m(\text{SiO}_2) + n(3\text{Na}_2\text{O} \cdot 8\text{SiO}_2)V_m(3\text{Na}_2\text{O} \cdot 8\text{SiO}_2) + \\ + n(\text{Na}_2\text{O} \cdot 2\text{SiO}_2)V_m(\text{Na}_2\text{O} \cdot 2\text{SiO}_2) + n(\text{Na}_2\text{O} \cdot \text{SiO}_2)V_m(\text{Na}_2\text{O} \cdot \text{SiO}_2) \quad (35)$$

The regression estimates $V_m(\text{SiO}_2) = (27.17 \pm 0.03)$ ml/mol; $V_m(3\text{Na}_2\text{O} \cdot 8\text{SiO}_2) = (271.50 \pm 0.08)$ ml/mol; $V_m(\text{Na}_2\text{O} \cdot 2\text{SiO}_2) = (73.12 \pm 0.02)$ ml/mol; and $V_m(\text{Na}_2\text{O} \cdot \text{SiO}_2) = (47.25 \pm 0.03)$ ml/mol describe the experimental data with the standard deviation of approximation $s_{\text{appr}} = 0.021$ ml/mol.

It was shown by Conradt [22, 23] that the application of his computationally simple model could explain the dependence of chemical durability of glasses including those used for radioactive waste vitrification. The rate of the glass dissolution in aqueous corrosive media has been found correlated with the hydration change of the Gibbs energy calculated as the sum of the hydration energies of all components of the CRS.

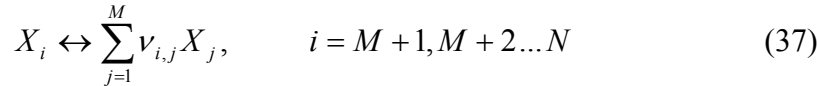
Shakhmatkin and Vedishcheva proposed the associated solutions thermodynamic model of glasses and glassforming melts [24-31] that could be considered as the extension of the Conradt's model. This model considers glasses and melts as a solution formed from salt-like products of interaction between the oxide components and the original (unreacted) oxides. These salt-like products (also called associates, groupings or species) have the same stoichiometry as the crystalline compounds, which exist in the equilibrium phase diagram of the system considered. The model does not use adjustable parameters, only the standard Gibbs energies of formation of crystalline compounds and the analytical composition of the system considered are used as input parameters.



Obviously, contrary to Conradt's model [22, 23] the number of system components is greater than the number ox oxides. Thus the equilibrium composition cannot be obtained on the basis of mass balance equations. That is why the authors present a calculation of the equilibrium system composition based on the values of particular equilibrium constants that are obtained from the Gibbs formation energies by the standard thermodynamic way. More generally, the constrained minimization of the systems Gibbs energy constrained by the overall system composition has to be performed with respect to the molar amount of each system component to reach the equilibrium system composition [32]. The total Gibbs energy is expressed supposing the state of the ideal solution:

$$G(n_1, n_2, \dots, n_N) = \sum_{i=1}^N \Delta_f G_{m,i} + RT \sum_{i=1}^N n_i \ln \frac{n_i}{\sum_{j=1}^N n_j} \quad (36)$$

where N is the number of components, n_i is the molar amount of i -th component, T is the system temperature (i.e. the glass transition temperature, T_g , for particular glass) and $\Delta_f G_{m,i}$ is the molar Gibbs formation energy of pure i -th component at the pressure of the system and temperature T . The system components are ordered such way that X_i ($i = 1, 2, \dots, M < N$) are pure oxides and X_i ($i = M+1, M+2, \dots, N$) are compounds formed from oxides by reversible reactions



Let us suppose the system composition given by the molar amounts of pure unreacted oxides $n_{0,i}$ ($i = 1, 2, \dots, M$). Then the mass balance constraints can be written in the form:

$$n_{0,j} = n_j + \sum_{i=M+1}^N \nu_{i,j} n_i, \quad j = 1, 2, \dots, M \quad (38)$$

The molar Gibbs formation energies of the melts of pure components may be used in more advanced version of this model. However these thermodynamic data are relatively scarce that prevents routine application of the model to the study of multicomponent systems. On the other hand the errors caused by substituting the melt by the crystalline state are partially compensated when the reaction Gibbs energy, $\Delta_r G_{m,i}$ is calculated according:

$$\Delta_r G_{m,i} = \Delta_f G_{m,i} - \sum_{j=1}^M \nu_{i,j} \Delta_f G_{m,j} = -RT \ln K_i, \quad i = M+1, M+2, \dots, N \quad (39)$$

where K_i is the equilibrium constant of the i -th equilibrium reaction described by the Eq.(37).

Recently, the thermodynamic model of Shakhmatkin and Vedishcheva and *ab initio* molecular dynamics were used for the structural study of nonsilicate binary calcium aluminate glass $x\text{CaO} \cdot (1-x)\text{Al}_2\text{O}_3$, where $x = 1/3$ (abbreviated as CA₂) $1/2$ (CA), and $2/3$ (C₂A) [33]. Both methods provided mutually comparable quantitative results in a reasonable agreement with the accessible experimental data and previous results of classical MD simulation. The obtained compositional trends were in agreement with the concept of the increase of Al/O coordination number (accompanied with formation of Al-triclusters) with the decreasing CaO content in the per-aluminous region.

When the crystalline state data are used the model can be simply applied to most multicomponent glasses including the nonoxide once. Especially the application of the model to the multicomponent industrially produced glasses can be very important. Taking into account that the common praxis resides in expressing most of the multicomponent glass properties in the form of (mostly) additive functions of the glass composition expressed in percents (even weight and not molar!) of pure oxides [34, 35, 36] using the thermodynamic model unambiguously represents the significant progress.

The contemporary databases of thermodynamic properties (like the FACT computer database [11]) enable the routine construction of the Shakhmatkin and Vedishcheva model [31] for most of important multicomponent systems. It is worth noting that other methods of

thermodynamic modeling of glasses and glassforming melts (not discussed here, e.g. [5, 37, 38]) do not possess the possibility of routine application to multicomponent systems.

16. 6. Quantitative Raman spectroscopy and Thermodynamic modeling

Raman spectroscopy is commonly used for study of the glass structure allowing the SRO and MRO structural units present to be inferred [4, 5, 39, 40, 41]. As a typical example the Q^n distribution in silicate glasses can be mentioned. The Raman spectra are after the background subtraction and thermal correction [40] deconvoluted typically to Gaussian peaks assigned to various structural groupings. From the corresponding peak areas the relative abundance of particular structural units is obtained using the NMR calibration. Sometimes [Parkinson] the direct proportionality between the ratio of peak areas and molar amounts of various structural groupings is assumed. Relating purely formally the Raman spectroscopy to the absorption optical spectroscopy the non-validity of the Lambert-Beer's law is the main mathematical difference between both methods.

Recently Zakaznova and Malfait [42, 43] proposed a new method of numerical treatment of Raman spectra. The basic assumption of this approach is that the Raman spectra are a sum of partial Raman spectra (generated by individual species) multiplied by the abundance of the species. Thus a set of Raman spectra obtained for series of glasses with different composition spans a linear vector space with the dimensionality given by the number of independent species (i.e. species that independently vary their abundance) with different PRS. Each spectrum is recorded with an arbitrary scaling, i.e. it is known with the exception of an multiplication factors. Principal component analysis (PCA, [44-47]) is then used to find the number of independent components. Following statistical treatment based on proper thermodynamic model results in finding the unknown equilibrium constants. The method of linear programming was used for solving the problem. Zakaznova and Malfait use the proposed method for analysis of the binary K_2O-SiO_2 glassforming melts with the aim to estimate the temperature dependence of the disproportionation constant K_3 (see Eqs.(28, 32)). The resulting values of K_3 and reaction enthalpy were in perfect agreement with independent results obtained by ^{29}Si NMR spectroscopy.

The approach of Zakaznova and Malfait [42,44] can be mathematically formulated as:

$$\mathbf{AP} = \mathbf{EC} \quad (40)$$

where the matrix formalism is used where $\mathbf{A}(N_w/N_s)$ is the matrix of Raman spectra with N_w rows corresponding to N_w wavenumbers and N_s columns corresponding to N_s samples/spectra, $\mathbf{P}(N_s/N_s)$ is the square diagonal matrix with the unknown coefficients each multiplying one particular Raman spectrum, $\mathbf{E}(N_w/N_c)$ is the matrix of PRS stored columnwise (N_c equals to the number of independent components), and $\mathbf{C}(N_c/N_s)$ is the matrix with abundances of N_c individual components in N_s samples. Replacing the product \mathbf{AP} with another matrix \mathbf{A}^{corr} we obtain the equation formally equivalent to the Lambert-Beer's equation of optical absorption spectra – here \mathbf{A}^{corr} is the absorbance matrix, \mathbf{E} – the matrix of molar absorption coefficients and \mathbf{C} the concentration matrix.

Let us suppose that the \mathbf{C} matrix is known from the solution of the thermodynamic model. Then the non-linear least squares problem can be formulated:

$$F(\mathbf{P}, \mathbf{E}) = \sum_j^{N_s} \sum_i^{N_w} \left[A_{i,j} P_{j,j} - \sum_k^{N_c} E_{i,k} C_{k,j} \right]^2 = F_{\min} = \min \quad (41)$$

Without loss of generality we can set $P_{1,1} = 1$. Then the unknown $P_{i,i}$ multiplication factors are obtained together with the unknown \mathbf{E} matrix of PRS by solving the set of $(N_s - 1 + N_w N_c)$ linear equations obtained from:

$$\frac{\partial F}{\partial P_l} = 0, \quad l = 2, 3, \dots, N_s \quad (42)$$

$$\frac{\partial F}{\partial E_{l,m}} = 0, \quad l = 2, 3, \dots, N_w; \quad m = 1, 2, \dots, N_c \quad (43)$$

Minimizing the F_{\min} value with respect to some parameters of the thermodynamic model this method can be used for finding some values of missing thermodynamic data.

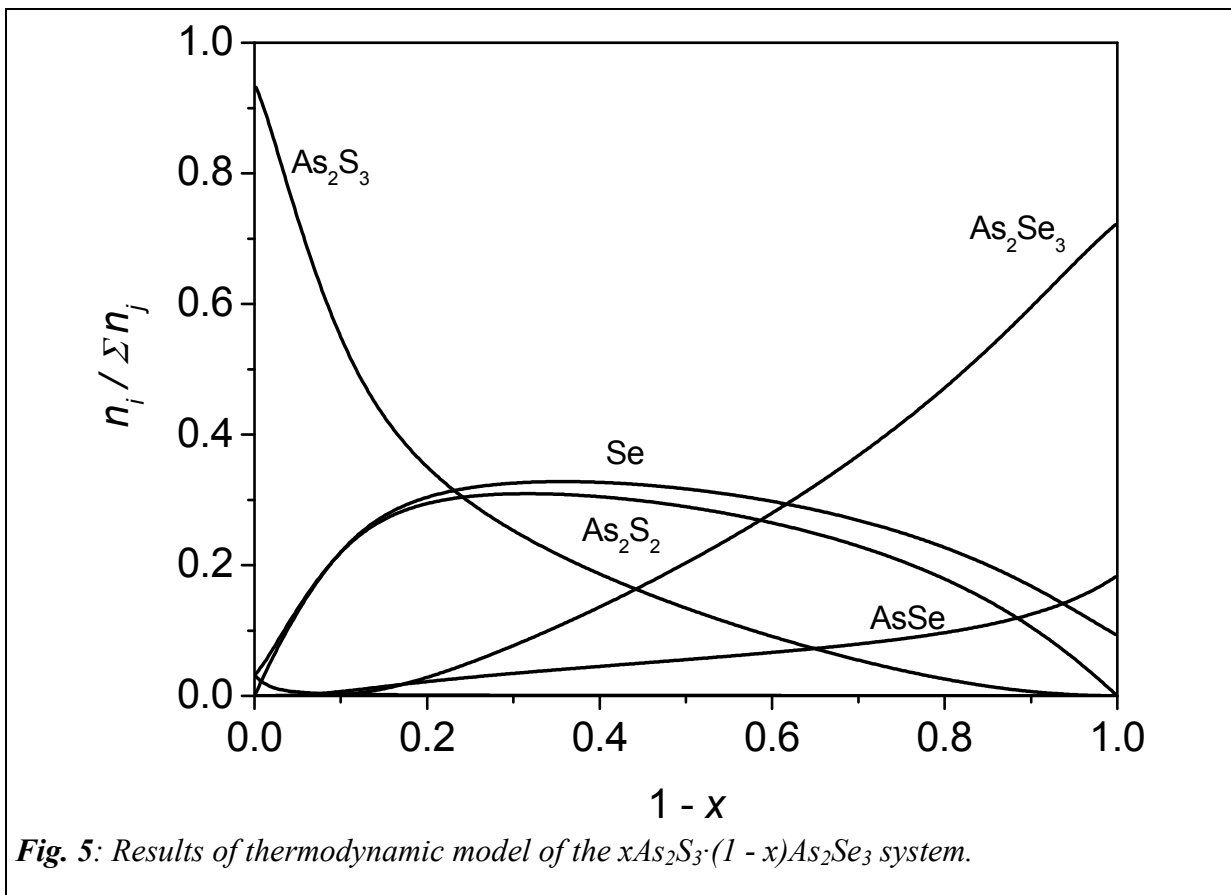


Fig. 5: Results of thermodynamic model of the $x\text{As}_2\text{S}_3 \cdot (1-x)\text{As}_2\text{Se}_3$ system.

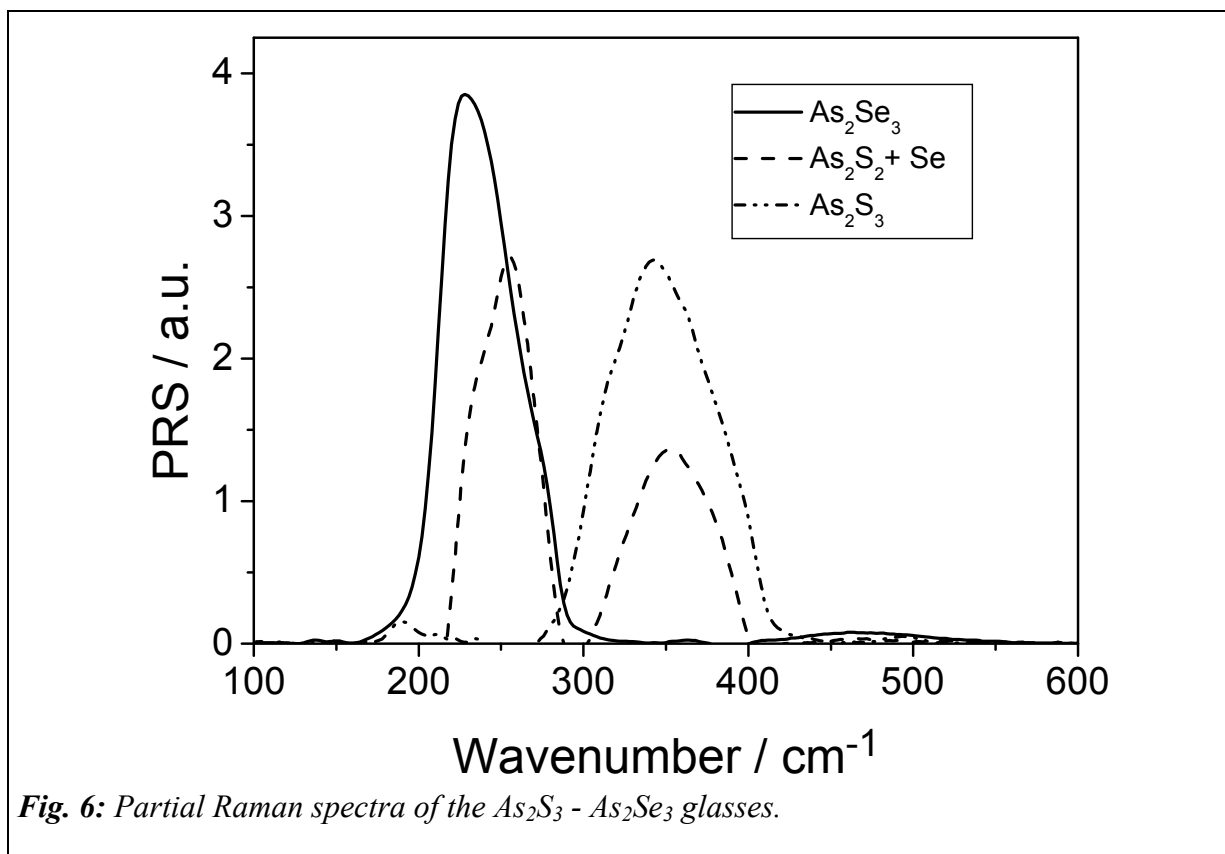


Fig. 6: Partial Raman spectra of the As_2S_3 - As_2Se_3 glasses.

In our recent paper [48] the structure of chalcogenide glasses of the pseudo-binary system As_2S_3 - As_2Se_3 was investigated by comparison of the results of the thermodynamic model of associated solutions with the results obtained by the above analysis of Raman spectra of $xAs_2S_3 \cdot (1-x)As_2Se_3$ ($x = 1; 3/4; 1/2; 2/3; 1/4; 0$) glasses. The results of thermodynamic model are presented in Fig. 5. On the basis of experimental values of T_g published in [49] the following linear approximation of T_g dependence on the glass composition was obtained

$$T_g / K = 478,85 - 23.087 x \quad (44)$$

reproducing the experimental DTA with the standard deviation of approximation $s_{apr} = 1,6$ K. For each glass composition plotted in the Fig. 4 the system temperature was set to the T_g value obtained from the Eq.(44).

The PCA method identified three independent components in the studied spectral series. On the other hand, the thermodynamic modeling resulted in four components with significant abundance in the studied glasses, i.e. Se, As_2S_2 , As_2S_3 and As_2Se_3 . Finally, the correlation analysis proved the strong (correlation coefficient of 0.97) linear dependence between the concentrations of Se and As_2S_2 . Thus the results of Raman spectra analysis were in harmony with the thermodynamic model. Solving the set of Eq.(42, 43) led to the set of PRS plotted in Fig. 6.

References 16

- [1] H. Scholze: *Glass – Nature, Structure, and Properties*. Springer-Verlag, Berlin 1991.
- [2] W. Vogel: *Glass Chemistry*. 2nd Edition. Springer-Verlag, Berlin 1992.
- [3] K. J. Rao: *Structural Chemistry of Glasses*. Elsevier, Amsterdam 2002.

- [4] B.O. Mysen: *Structure and Properties of Silicate Melts*. Elsevier, Amsterdam 1988.
- [5] B.O. Mysen, P. Richet: *Silicate Glasses and Melts – Properties and Structure*. Developments in Geochemistry, Vol. 10. Elsevier, Amsterdam 2005.
- [6] G.N. Greaves, S. Sen: *Inorganic glasses, glass-forming liquids and amorphizing solids*. Advances in Physics, 56, 1–166 (2007).
- [7] I. Gutzow, J. Schmelzer: *The Vitreous State. Thermodynamics, Structure, Rheology, and Crystallization*. Springer-Verlag, Berlin Heidelberg 1995.
- [8] R. Conradt: *Thermochemistry and Structure of Oxide Glasses*. In: *Analysis of the Composition and Structure of Glass and Glass Ceramics*. H. Bach and D. Krause (Editors), pp. 232-254, Springer-Verlag, Berlin Heidelberg 1999.
- [9] ASTM – C162.: *Standard Terminology of Glass and Glass Products*, American Society for Testing and Materials, 1983.
- [10] R. Conradt: *Chemical structure, medium range order, and crystalline reference state of multicomponent oxide liquids and glasses*. J. Non-Cryst. Solids, 345&346, 16-23 (2004).
- [11] C.W. Bale et al.: *FactSage Thermochemical software and databases*. Calphad 26, 189-228 (2002).
- [12] W. H. Zachariasen: *Die Struktur der Gläser*. Glastechn. Ber. 11, 120-123 (1933).
- [13] B.E. Warren: *Summary of Work on Atomic Arrangement in Glass*. J. Amer. Ceram. Soc. 24, 256-261 (1941).
- [14] D. Sprenger: *Spektroskopische Untersuchungen und Berechnung zur Struktur anorganischer Gläser*. PhD Thesis, Mainz 1996.
- [15] D. Sprenger, H. Bach, W. Meisel, P. Gütlich: *Discrete Bond Model (DBM) of Sodium-Silicate Glasses Derived from XPS, Raman and NMR Measurements*. J. Non-Cryst. Solids 159, 187-203 (1993).
- [16] C. Schultz-Münzenberg: *How to Describe the Topological Structure of Glasses*. In: *Analysis of the Composition and Structure of Glass and Glass Ceramics*. H. Bach and D. Krause (Editors), pp. 141-152, Springer-Verlag, Berlin Heidelberg 1999.
- [17] N. Koga, Z. Strnad, J. Šesták, J. Strnad: *Thermodynamics of non-bridging oxygen in silica bio-compatible glass-ceramics*. J. Thermal Anal. Calor. 71, 927-937 (2003).
- [18] J. Šesták, J. Strnad, Z. Strnad, N. Koga, M. Holeček: *Biomedical thermodynamics of bio-compatible glass-ceramics and otherwise modified inorganic material surfaces*. Advanced Materials Research 39&40 329-334 (2008)
- [19] O.V. Mazutin, M.V. Streltsina, T.P. Shvajko-Shavajkovska in: *Handbook of Glass data, part A.*, p. 214, Elsevier, Amsterdam 1983
- [20] J.C. Young, F.W. Glaze, C.A. Faick, A.N. Finn: J. Res. Nat. Bur. Stand. 22, 453-454, (1939)
- [21] S.J. Gurman: *Bond Ordering in Silicate Glasses: A Critique and resolution*. J. Non-Cryst. Solids 125, 151-160 (1990).
- [22] R. Conradt: *Predictive Modeling of Glass Corrosion*. Proc. 5th ESG Conference. B1-2 – B1-10, Czech Glass Society, Prague 1999.
- [23] R. Conradt: *A Proposition for an Improved Theoretical Treatment of the Corrosion of Multi-Component Glass*. J. Non-Cryst. Solids 19-26 (2001).
- [24] B.A. Shakhmatkin, N.M. Vedishcheva, M.M. Shultz, A.C. Wright: *The thermodynamic properties of oxide glasses and glass-forming liquids and their chemical structure*. J. Non-Cryst. Solids 177 249-256, (1994).

- [25] N.M. Vedishcheva, B.A. Shakhmatkin, M.M. Shultz, A.C. Wright *The thermodynamic modelling of glass properties: a practical proposition?* J. Non-Cryst Solids 196, 239-243 (1996)
- [26] B.A. Shakhmatkin, N.M. Vedishcheva, A.C. Wright in: A.C. Wright, S.A. Feller, A.C. Hannon (Editors): *Borate Glasses Crystals and Melts*. Soc. Glass. Technol., Sheffield 1997, p.189.
- [27] B.A. Shakhmatkin, N.M. Vedishcheva, A.C. Wright: *Can Thermodynamics Relate the Properties of Melts and Glasses to their Structure?* J. Non-Cryst Solids 293-295, 220-236 (2001).
- [28] N.M. Vedishcheva, B.A. Shakhmatkin, C.A. Wright: *Thermodynamic modelling of the structure of glasses and melts: single-component, binary and ternary systems*. J. Non-Cryst. Solids, 293-295, 312-317 (2001)
- [29] N.M. Vedishcheva, B.A. Shakhmatkin, C.A. Wright: *Phys. Chem. Glasses* 44, 191 (2003).
- [30] N.M. Vedishcheva, B.A. Shakhmatkin, C.A. Wright: *The structure of sodium borosilicate glasses: thermodynamic modelling vs. experiment*. J. Non-Cryst. Solids 345&346, 39-44 (2004).
- [31] B.A. Shakhmatkin, N.M. Vedishcheva, A.C. Wright: *Thermodynamic modelling of the structure of oxyhalide glasses*. J. Non-Cryst. Solids 345&346, 461-468 (2004).
- [32] P. Vonka, J. Leitner: *Calculation of Chemical Equilibria in Heterogeneous Multicomponent Systems*. Calphad 19, 25-36 (1995).
- [33] M. Liška, J. Macháček, P. Perichta, O. Gedeon, J. Pilát: *Thermochemical Modelling and Ab Initio Molecular Dynamics Simulations of Calcium Aluminate Glasses*. *Ceramics – Silikáty* 52, 61-65 (2008).
- [34] High Temperature Glass Melt Property Database for Process Modeling. T.P. Seward III. and T. Vascott Editors. Amer. Cer. Society, Westerville, Ohio 2005
- [35] Properties of Glass-Forming Melts. L.D. Pye, A. Montenero and I. Josephs Editors. Taylor and Francis, Boca Raton 2005, ISBN 1-57444-662-2.
- [36] <http://www.sciglass.info>
- [37] A.D. Pelton, P. Wu: *Thermodynamic modeling in Glass-Forming Melts*. J. Non-Cryst. Solids 253, 178-197 (1999).
- [38] V.L. Stolyarova: *Thermodynamic properties and structure of ternary silicate glass-forming melts: Experimental studies and modeling*. J. Non-Cryst. Solids 354, 1373-1377 (2008).
- [39] P. McMillan: *Structural Studies of Silicate Glasses and Melts – Applications and Limitations of Raman Spectroscopy*. *Am. Mineral.* 69, 622-644 (1984).
- [40] P.F. McMillan, G.H. Wolf: *Vibrational Spectroscopy of Silicate Liquids*. In: *Structure, Dynamics and Properties of Silicate Melts*. J.F. Stebbins, P.F. McMillan, D.B. Dingwell (Editors), pp. 247-315. Mineralogical Society of America, Washington DC 1995.
- [41] B.G. Parkinson, D. Holland, M.E. Smith, C. Larson, J. Doerr, M. Affatigato, S.A. Feller, A.P. Howes, C.R. Scales: *Quantitative Measurement of Q^3 Species in Silicate and Borosilicate Glasses Using Raman Spectroscopy*. J. Non-Cryst. Solids 354, 1936-1942 (2008).
- [42] V.P. Zakaznova-Herzog, W.J. Malfait, F. Herzog, W.E. Halter: *Quantitative Raman Spectroscopy: Principles and Application to Potassium Silicate Glasses*. J. Non-Cryst. Solids. 353, 4015-4028 (2007).

- [43] W.J. Malfait, V.P. Zakaznova-Herzog, W.E. Halter: *Quantitative Raman Spectroscopy: High-Temperature Speciation of Potassium Silicate Melts*. J. Non-Cryst. Solids. 353, 4029-4042 (2007).
- [44] P. Pelikán, M. Čeppan, M. Liška: *Computational Methods in Molecular Spectroscopy*. CRC Press, Boca Raton 1994.
- [45] E. R. Malinowski: *Factor Analysis in Chemistry*. 3rd Edition, J. Wiley and Sons, New York 2002.
- [46] R. Kramer: *Chemometric Techniques for Quantitative Analysis*. Marcel Dekker, New York 1998.
- [47] Factor analysis Toolbox for MATLAB®. Applied Chemometrics, www.chemometrics.com.
- [48] M. Liška, J. Holubová, M. Chromčíková, E. Černošková: *Raman Spectra, Structure and Thermodynamic Model of As₂S₃ - As₂Se₃ glasses*. pp. 3-36 In: 30th Int. Czech and Slovak Seminar on Calorimetry. University of Pardubice, Pardubice 2008. ISBN 978-80-7395-079-8
- [49] J. Holubová, Z. Černošek, E. Černošková, M. Liška: *Glassy system As-S-Se*. pp.133-136 In: 28th Int. Czech and Slovak Seminar on Calorimetry. University of Pardubice, Pardubice 2006. ISBN 80-7194-859-4.



Chapter 17

Non-bridging oxygen in glasses

17. NON-BRIDGING OXYGEN IN SILICA BIO-COMPATIBLE GLASS-CERAMICS AND MAGNETIC PROPERTIES OF Fe_2O_3 ADDED BORATE GLASSES

Jaroslav Šesták, Nobuyoshi Koga, Zdeněk Strnad

17. 1. Introduction to bridging and non-bridging oxygen

Oxides of alkali and alkaline earth metals or other selected metal oxides (R_2O and/or MO) are the modifiers of the polyanionic glass-forming network of glass-formers such as SiO_2 or B_2O_3 . In the molten state such polyanionic glass-forming network interact with free cations (e.g. Na^+ , Ca^{2+}) and free oxygen anion O^{2-} originated from the modifier added. When adding, for example, an alkali metal oxide to SiO_2 , each oxygen anion breaks one of Si–O–Si bonds resulting in the formation of two non-bridging oxygens, Si–O–, according to the general scheme: $(\text{Si–O–Si}) + \text{O}^{2-} \rightleftharpoons 2(\text{Si–O–})$. According to the primary reports by, *Toop* and *Samis* [1,2], *Masson* [3], and *Fincham* and *Richardson* [4], its equilibrium can be written in shorthand as



where the notation of O° , O^{2-} and 2O^- are bridging oxygen (BO), free oxygen (FO) and non-bridging oxygen (NBO) which complexity, however, might be associated with a range of different cations [5]. Depending on the total composition of the system, the oxygen atoms may play various roles in the silicate melts, acting as FO anions O^{2-} they are bound by two ionic bonds to the present alkali or earth alkali cations. In the role of NBO, they are bound by one covalent bond to the central atom of the SiO_4 tetrahedron and by one ionic bond to the present alkali or earth alkali metal cation. And finally, as BO atoms –O– they are binding two neighboring SiO_4 tetrahedrons by Si–O–Si covalent bonds. From the above it follows that with respect to their bonding nature, oxygen atoms are not equivalent, and their chemical potentials are not equal. This also indicates that even the thermal conductivities [6] of molten silicates are affected by the ionic character of chemical bonds between cations of basic oxides and the state of NBO ions.

The glass network is subsequently formed by mutually interconnected glass-forming units [7-11] such as SiO_4 tetrahedral netting and consequently related to the ratio between the molar amounts of oxygen and silicon atoms, $R = n(\text{O})/n(\text{Si})$. The structure can then be more or less characterized by the amalgamation of so-called Q units derived long ago [9-11] on bases of the above ratio, namely from $Q0$ to $Q4$ following: $Q0 = \text{SiO}_4^{4-}$, $Q1 = \text{Si}_2\text{O}_7^{6-}$, $Q2 = \text{SiO}_3^{2-}$, $Q3 = \text{Si}_2\text{O}_5^{2-}$ and $Q4$ being SiO_2 . A series of equations can be written to describe the equilibria in the bulk melt/glass within the compositional from ortho- to tecto-silicates [9,10] such as



in other words we may note that $Q1 \rightleftharpoons 2Q2 + 2Q4$.

It was suggested that for a given bulk melt polymerization (NBO/Si), the relative abundances of the individual units are systematic functions of the type of the modifying metal cation [7,10]. Characterization of abounding makeup and better understanding of the relations between the structure and properties of various silicate based melts and glasses has been the subject of recent studies [12-16] and is dealt with in separate chapter 16. Recently, the

structural characteristics of many important glasses and melts (including silicates, borates, aluminosilicates, halides and chalcogenide) are drawn in supplementary details (using the results of recent spectroscopy and scattering experiments) by *Greaves and Sen* [16].

In alkali aluminosilicate glasses, the trivalent aluminum cation does not always act as a network former. The structural configuration depends upon the ($r = \text{Al}_2\text{O}_3/\text{R}_2\text{O}$) ratio. Apparently, if the ratio (r) is greater than one the Al^{3+} goes into the network having a tetrahedral coordination. Like (BO_4) group, the excess of unit negative charge on (AlO_4) group is satisfied by alkali ion in the neighborhood. Thus, the further addition of an aluminum ion to a silicate glass removes one NBO. At the ratio equal one there is no NBO in the structure. For the further additions of Al^{3+} , when the ratio r becomes greater than one, the Al^{3+} cations enters the network as a modifier in the tetrahedral coordination and the formation of (AlSiO_6) groups turn out to be unlikely due to the packing difficulties. Presumably three of the oxygen is then non-bridging and three remaining (already) bridging, which favors the formation of triclusters, where an oxygen is shared between three tetrahedrons (one AlO_4 and two SiO_4 or vice versa). The first type of tricluster is electrically neutral while the second requires an associated alkali cation. In principle, the triclusters appear equivalent to an Al^{3+} cation in the form of a modifying ion and is bonded to three NBO.

In other melts of the ternary system, such as $\text{CaO-TiO}_2\text{-SiO}_2$, silica oxide acts always as the network-forming oxide while calcium oxide takes always action as the modifier of the poly-anionic network [17]. The role of TiO_2 can be twofold acting either as a modifier or as a complementary associate undertaking thus the function of the network-forming oxide. Depending on the behavior of TiO_2 in the melt the structure and thus also the activities of the present components of the melt change revealing variously possessed NBO. The structural role of Ti^{4+} in titanium silicate melts is thus a complex function of several variables, namely TiO_2 and SiO_2 concentration, type and content of modifying cations as well as temperature.

17. 2. Some volume considerations about of ionic sites in silicate glasses

Various physico-chemical properties of silicate glasses can be correlated with the concentration of certainly modeled structural units. Properties, such as molar volume, refractive index, molar refraction, thermal expansion and even some magnetic properties can then be practically described by additive relations. In these relations a specific factor can be used for each structural unit. The factor depends on the type of property under consideration. The obtained factors could successfully be used to calculate the magnitude of those physical properties in binary alkali (or alkaline earth) silicate glasses and in other multi-component glasses. Molar volume data of alkali and alkaline earth silicate glasses have been recently used to calculate the free volume associated with the BO and NBO and modifier ions [18]. The volumes of voids in the structure are of special importance for the transport properties. The mobility of movable ions is affected to a great extent by the openness (nature) of the glass matrix. Such an “open matrix”, exhibiting higher concentration of NBO ions, is characterized, e.g., by higher electric conductivity than a closed one. Different spectroscopic studies indicated that up to about 33 mol% of alkali oxide (R_2O) so called $Q3$ units are formed at the expense of $Q4$ unit where $Q3$ units are SiO_4 tetrahedra having one NBO ion per tetrahedron, whereas $Q4$ units are SiO_4 tetrahedra without NBOs. For more than 33 mol% of R_2O about 50 mol% of $Q3$ units converts into $Q2$ units the latter representing SiO_4 tetrahedra with two NBOs for each tetrahedra. Results of Raman spectroscopy revealed that the conversion process continues along with the increasing R_2O content, from $Q2$ to $Q1$ (for > 50 mol% R_2O) and finally from $Q1$ to $Q0$ (for > 60 mol% R_2O) where $Q1$ and $Q0$ refer to SiO_4 tetrahedra having, respectively, with the three and four NBOs per each Si^{4+} cation. In the light of these

findings some relations could be estimated as to describe the concentration of structural units as a function of modifier oxide concentration in binary alkali or alkaline earth silicate glasses.

The relations were modified to calculate the concentration of structural units in mixed alkali silicate glasses on basis of the molar volume (V_m) of a glass, which can be given in the form of an additive relation, such as $V_m = NuVu$, where Nu is the number of the structural unit (u) per mole of glass and Vu is its volume [18]. On the source of the structural unit distribution in alkali silicate glasses, the volumes that the constituting ions occupy in the matrix (V_{Si} , V_ϕ , V_R and V_O) and the volumes of individual structural units can be given as follows:

$$V_4 = V_{Si} + 2V_\phi, V_3 = V_{Si} + 1.5V_\phi + (V_O + V_R), V_2 = V_{Si} + V_\phi + 2(V_O + V_R), \\ V_1 = V_{Si} + 0.5V_\phi + 3(V_O + V_R) \text{ and thus } V_O = V_{Si} + 4(V_O + V_R).$$

Here V_{Si} , V_ϕ , V_O and V_R are, respectively, the volumes occupied by Si^{4+} , BO (ϕ), NBO (O) and alkali ion (R). The volume occupied by an ion is the volume of ion itself and its associated space (its free volume) in the matrix. These relations can be used to calculate V_ϕ and V_O . Thus on the basis of above equations we may write $V_m = N_i V_i$ with N_i being the number of the ion (i) per mole of glass and V_i is the volume occupied by that ion in the given glass. The last above relation can be reformed to $V_m = N_{Si}V_{Si} + N_\phi V_\phi + N_O V_O + N_R V_R$, where N_{Si} , N_ϕ , N_O and N_R are, respectively, the number of Si^{4+} , BO, NBO and alkali ions per mole of glass. The radius of Si^{4+} ion in oxides is $\sim 0.26 \times 10^{-8}$ [cm] whereas that of O^{2-} ion in silicate units is 1.2×10^{-8} [cm]. Thus the volume of Si^{4+} ions in vitreous SiO_2 and then in any modified silicate glass is $\sim 0.5\%$ of the volume of O^{2-} ions. Therefore, for the first approximation, the first term can be neglected with respect to the other terms $V_m \approx N_\phi V_\phi + N_O V_O + N_R V_R$ and further accepting that $N_O = N_R$, we obtain $V_m \approx N_\phi V_\phi + N_O (V_O + V_R)$. A NBO ion is always bound to an alkali ion (or a half alkaline earth ion) and therefore the term between the brackets can be looked as an undividable quantity that can be assigned by V_B , namely $V_B = V_O + V_R$. It follows that $V_m = N_\phi V_\phi + N_O V_B$ which equation can be solved simultaneously for two values of V_m close to each other to get V_ϕ and V_B .

As the modifier oxide content increases the total contribution of BO ions ($N_\phi V_\phi$) decreases, whereas that of the NBO bindings ($N_O V_B$) increases. The decrease in ($N_\phi V_\phi$) is related to the decrease in the SiO_2 content. Up to 33 mol% of the modifier oxide, the values of ($N_\phi V_\phi$) are mostly the same for all types of modifier ions. This behavior reveals that V_ϕ is not affected by the type of modifier ion up to one NBO ion per SiO_4 tetrahedron. Above this concentration ($N_\phi V_\phi$) varies slightly with the type of modifier oxide. On the other hand, ($N_O V_B$) increases when increasing the modifier oxide content. There is a marked difference between the values from one type of modifier to another showing that V_m of a glass decreases with increasing modifier oxide concentration for $|d(N_\phi V_\phi)/dC| > d(N_O V_B)/dC$ and vice versa. The increase in ($N_O V_B$) for a certain modifier concentration, such as Li_2O-SiO_2 up to Cs_2O-SiO_2 reveals that the volume V_B becomes greater with lowering the field strength of the modifier.

The multiparty of the field strength is expressed as q/r^2 , where q is the charge of modifier ion and r is its radius, which provide a linear increase of V_B in all cases and any of these relations can be roughly expressed as $V_B = s(r^2/q) + 13.737 \times 10^{-24}$ [cm³]. It follows that V_O has a constant value and that the increase in V_B with increasing V_R is related to the size of the alkali ion. A greater alkali ion size means lower field strength and weaker bond with the NBO and this leads to a greater V_B value. With reference to the size of the O^{2-} ion in silicate units ($\sim 7.24 \times 10^{-24}$ [cm³]) it can be said that on average each NBO is associated with a space of $\sim 6.50 \times 10^{-24}$ [cm³]. By neglecting the volume of Si^{4+} ion it can be concluded that, in this region, the average associated space is 15.39×10^{-24} [cm³] per each BO ion.

It was concluded [18] that the free volume associated with the BO is almost constant ($15.39 \times 10^{-24} \text{ cm}^3$) for all modifier ions below 33.3 mol% of addend oxide. In the case of alkali or alkaline earth silicate glasses it decreases with the increasing number of NBO ions per a structural unit and/or radius of the modifier ion. In all cases the NBO ion is associated with a constant free volume and the modifier ions are associated with a free volume that increases with increasing number of NBO ions per a structural unit and/or radius of the modifier ion. The above model explores the change in the free volume due to changing the concentration of alkali oxides in mixed alkali silicate glasses where the free volume is always related to a certain type of alkali oxide and intensifies with its increasing content.

It is also in agreement with ref. [19], which showed that the partitioning of NBO in silicate melts is not identical as the segregation of Ca, Mn, Mg, and Fe divalent cations between solid (olivine) and melt revealed an effectual consequence of energetically nonequivalence of NBO regarding its presence in the main structural units of Q_4 , Q_3 , and Q_2 type. For melts with high Q_3/Q_2 -abundance ratio the increasing ratios of Na/(Na+Ca) and/or Na/(Na+Ca+Mn+Mg+Fe) result in a systematic decrease of the partition coefficients because of ordering of the network-modifying Ca, Mn, Mg, and Fe among NBO in Q_3 and Q_2 structural units. This decrease is more pronounced at the smaller value of ionic radius of the cation. With decreasing Q_3/Q_2 abundance ratio (e.g., less-polymerized melts) this effect becomes less pronounced. Activity vs. composition relations among network-modifying cations in silicate melts are, therefore, governed by availability of energetically nonequivalent NBO in individual Q^n -species in the melt. As a result, any composition change that enhances abundance of highly depolymerized Q^n -species will cause partition coefficients to decrease.

This concept of NBO was applied for various cases and treated under different theories [2,20,21] such as the determination of oxygen states in iron-rich borate glasses [22] (see next paragraph). In the forthcoming text we would like to present two examples of analysis regarding the material properties and the role of NBO with respect to the behaviors of matrix glasses.

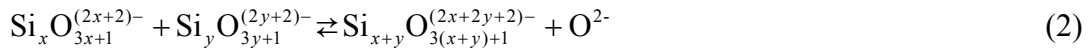
17.3. Simple calculation concept for non-bridging oxygen in silica bio-glasses

As for the soda-lime-silica glass system, the correlation between the structural parameters characterized by the anionic constitution and the bioactivity has been investigated by Strnad *et. al.* [23-26]. As a simple way for describing the glass composition, Steevel's parameters [21], X and Y, which indicate the mean number of NBO and BO ions per polyhedron in the glass lattice, respectively, were employed. The Steevel's parameters can be calculated from the molar composition of glass assuming the following equations, $X = 2R - Z$ and $Y = 2Z - 2R$ where Z and R denote the mean number of all types of oxygen per polyhedron and the ratio of the total number of oxygens to the total number of glass-forming cations in glass, respectively. As for the soda-lime-silica system, the pure silica glass SiO_2 , pseudo-binary $\text{Na}_2\text{O}-2\text{SiO}_2$ glass and pseudo-ternary $\text{CaO}-\text{Na}_2\text{O}-2\text{SiO}_2$ glass are characterized by (X, Y)=(0, 4), (1, 3), and (2, 2), respectively. With $X > 2$ and $Y < 2$, the concentration of FO ions is appreciably large and the glasses in this compositional region are commonly called as "invert glasses" [27].

For $\text{Na}_2\text{O}-\text{CaO}-\text{SiO}_2-\text{P}_2\text{O}_5$ and $\text{CaO}-\text{MgO}-\text{SiO}_2-\text{P}_2\text{O}_5$ bioactive glass-ceramic systems, the parameter Y was correlated to the bioactivity evaluated by in vitro test of mutual bounding after soaking in simulated body fluids (SBF) and also by in vivo test of implantation in dog tibia [23]. It has been concluded that $Y \approx 2$ in the residual glass phase of the glass-ceramics is the preferable condition for the higher bioactivity, whereas $Y > 3$ inhibits the bioactivity. Turing focus on the structural parameter X related to NBO [25,26], the correlation of the X

value to the bioactivity in the Na₂O-CaO-SiO₂-P₂O₅ system was examined by comparing with the bioactivity index, I_B , introduced empirically by Hench [28]. A linear correlation between X and I_B with positive slope was found in $1.5 < X \leq 2$, whereas $I_B = 0$ for $X < 1.5$. Accordingly, with respect to the constitutions of BO and NBO expressed by the Steevel's parameters X and Y , the bioactive compositional region can be suggested as $1.5 < X \leq 2$ and $2 \leq Y < 2.5$.

By assuming that the silicate ions are presented as linear and branched chains of general formula $[\text{Si}_x\text{O}_{3x+1}]^{(2x+2)-}$, the compositional dependences of relative proportion of NBO in binary Na₂O-SiO₂ and CaO-SiO₂ glass forming melts were also calculated [25,26]. According to Masson [3,20,29], it was assumed that silicate ions are in an equilibrium state of poly-condensation reactions expressed generally as following:



where the equilibrium constant k_{xy} of eq.(2) is approximated using that for the lowest k -members k_{11} , i.e., $x=1$ and $y=1$. In view of the constitutions of BO, NBO and FO ions, eq.(2) is apparently expressed by the inverse reaction of eq.(1).

The activity a of the modifier oxide in the CaO-SiO₂ and Na₂O-SiO₂ binary melts can be related to the mole fraction of SiO₂, X , by the equation:

$$\frac{1}{X} = 2 + \frac{1}{1-a} - \frac{3}{1 + a \left(\frac{3}{k_{11}} - 1 \right)} \quad (3)$$

where a is calculated by the *Temkin's* equation [30] as is equivalent to the ion fraction of FO ion, N_{FO} . In addition, the ion fraction N_x of $[\text{Si}_x\text{O}_{3x+1}]^{(2x+2)-}$ with different x is correlated to a as follows.

$$N_x = \frac{(3x)!}{(2x+1)!x!} \left[\frac{1}{1 + \frac{3a}{k_{11}(1-a)}} \right]^{x-1} \left[\frac{1}{1 + \frac{k_{11}(1-a)}{3a}} \right]^{2x+1} (1-a) \quad (4)$$

The fraction of NBO, N_{NBO} , can be evaluated by summing up N_x with different x at the restricted X : $N_{NBO} = \sum N_x$. At the same time, the fraction of BO, N_{BO} , is obtained by: $N_{BO} = 1 - N_{FO} - N_{NBO}$.

Figure 1 below shows the composition-dependant change in the relative proportions of NBO, FO, and BO in the CaO-SiO₂ and Na₂O-SiO₂ binary melts, where the literature values of $k_{11} = 1.6 \times 10^{-3}$ and $= 8 \times 10^{-8}$ [30] were adopted for the respective calculations. By the combination of the compositional dependence of relative proportions of NBO in the two binary melts based on the pseudo-ternary assumption [31], the compositional dependence of the proportion of NBO in the CaO-Na₂O-SiO₂ was simulated. Figure 2 shows the iso-proportional plot for NBO in CaO-Na₂O-SiO₂ ternary melts. The bioactivity of the P₂O₅-free CaO-Na₂O-SiO₂ glasses has been investigated by Kim *et al.* [32] through soaking the glasses with various compositions in SBF. By comparing the reported results with the calculated proportions of NBO, it was found [25] that the bioactive glass compositions are exclusively corresponding to the region of high relative proportion of NBO in the side of SiO₂ rich composition. The calculated compositional dependence of relative proportion of NBO was

also compared with that of Hench's bioactivity Index, I_B , for $\text{CaO-Na}_2\text{O-SiO}_2$ with 6 mass% P_2O_5 glasses [28,33].

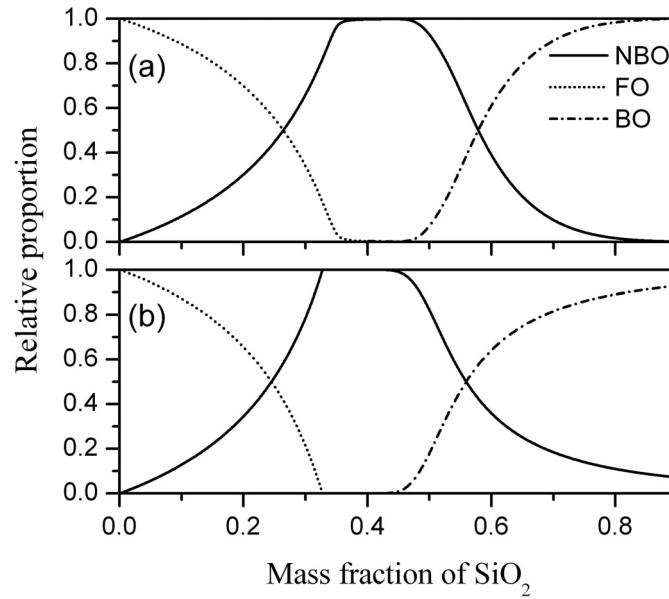


Fig. 1. Calculated constitutions of NBO, FO, and BO in the CaO-SiO_2 (a) and $\text{Na}_2\text{O-SiO}_2$ (b) binary melts.

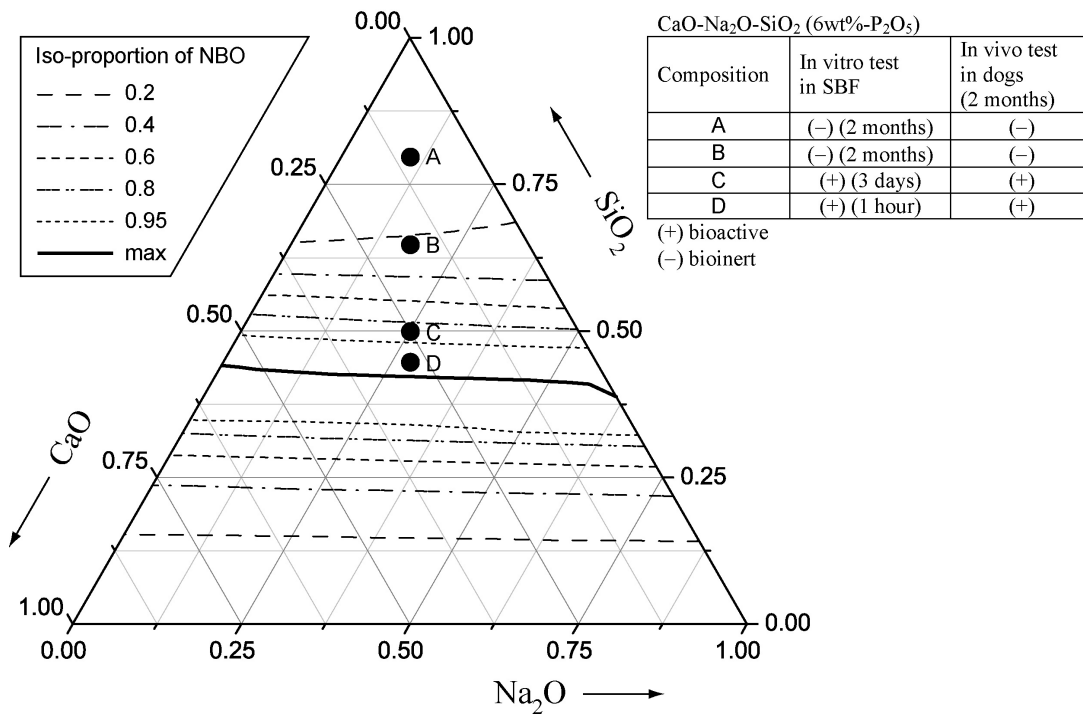


Fig. 2. Calculated iso-proportional plot for NBO in the $\text{CaO-Na}_2\text{O-SiO}_2$ ternary melts, together with the results of bioactive test for the glass with 6 mass% P_2O_5 reported by Strnad and Koga [23] (composition is presented in the mass fraction).

It was pointed out that the remarkable high bioactivity $I_B > 8$ can be found again in the region of the higher relative proportion of NBO ions > 0.8 in the side of SiO_2 -rich composition

[26]. In Fig. 2, the results of in vitro and in vivo tests of the bioactivity for the four selected compositions of CaO-NaO₂-SiO₂ with 6 mass%-P₂O₅ glass-ceramics reported by Strand [23] was indicated. The glasses with compositions C and D which indicate the appreciable high bioactivities position in the region of relative proportion of NBO>0.8 as was expected from the comparison with I_B.

In conclusion, the bioactivity of the glass characterized by the bone-like apatite formation depends largely on the relative proportion of NBO in the CaO-Na₂O-SiO₂ glass and glass-ceramics irrespective of P₂O₅ addition, indicating a close connection between the structural property of the glass characterized by the activity of oxygen ions and the surface chemical processes of bone-like apatite formation.

17. 4. Property and application of bio-active glass-ceramic materials

Merely four decades ago it was considered inconceivable that a man-made material could bond to living tissues in view of the deep-rooted experience that it would result in a foreign body reaction and the formation of non-adherent scar tissue at the interface with inserted material. This understanding was irreversibly altered when a special composition of soda-lime-phosphate-silica glass was synthesized by Hench [33] and successfully implanted in the femurs of rats. About 6 mass% of P₂O₅ was added to simulate the Ca/P constituents of hydroxyapatite, Ca₁₀(PO₄)₆(OH)₂, that is the inorganic mineral phase naturally existing in bones. Therefore the bone-like apatite formation on the surface of implant is of a key importance during the physical and chemical processes leading to the formation of an enough firm connection between the implanted material and the newly formed bone tissue [23,24,35-37]. Its comprehension bears all general aspects of compositional and nucleation-growth phenomena widely discussed for oxide glasses. The bioactivity leads to both the osteoconduction and osteoproduction as a consequence of rapid reaction on the bioactive glass surface. The surface reactions [38] involve ionic dissolution of calcium and sodium ions, phosphates and hydrated silica that give rise to both the intercellular and extra-cellular responses at the interfaces of the glass with its physiological environment. The smartness of such a mimetic process is likely hidden in the activity of oxygen characterized by the action of silanole groups (Si-OH). They likely serve as the nucleation sites for the bio-compatible interface formation capable to coexist between the original tissue and the implants which can be expediently made from glass, glass-ceramics, ceramics, cements and other composites as well as from certainly treated metals (etched titanium) respecting the set-in condition of its suitable surface reactivity.

The uniqueness of such surface-activated materials is their high bioactivity, which opens qualitatively new application fields, especially for anchoring the implant in a host tissue, with practical use in orthopedics, stomatology, neurosurgery, oncology, craniofacial surgery and possibly other fields. We are proud to mention that we have taken part in the research progress of bioactive materials since early eighties [39-43] currently aimed to the surface properties and bio-incorporation of metallic titanium with differently treated surface [35-37] as introduced by early studies of *Branemark et al* [44]. This activity matured in actual appliance in clinical implantology under the trademark IMPLADENT (a system for oral implantology produced by LASAK, Co. Ltd) invented by *Strnad* and BAS-O, BAS-HA, BAS-R – bioactive bone tissue substitutes, see following chapter 25. The bone-bonding ability of BAS-O is based on inorganic, polycrystalline material prepared by controlled crystallization of glass, whose main components are CaO, P₂O₅, SiO₂ and MgO. During the crystallization process, the glassy material is converted to a glass-ceramic material whose main crystalline phases are apatite and wollastonite. BAS-O granules and ground material are used to fill cysts, defects left by injuries, defects left by excochleation of benign tumors, and

can be of help to reconstruct extensive acetabular defects. Compact, wedged-shaped blocks (with various heights and surfaces) became useful for, e.g., condyl elevation. Individually shaped implants can be used in neurosurgery to cover defects left from cranial trepanation and as onlays in plastic surgery. Another case of biomaterial BAS-HA (hydroxyapatite) is synthesized from aqueous solutions under precisely defined pH, temperature and other physical parameters, which ensure reproducible preparation of a highly pure, crystallographically defined product, which does not contain any unwanted calcium phosphates. Its structure and composition are similar to bio-apatite, which is the main inorganic component of living bone tissue. Implants form a strong bond between the bone tissue and the implant material without any intermediate fibrous layer, Fig. 3. Final product is the BAS-R, which is the surface bioactive, resorbable, inorganic, crystalline material based on tricalcium phosphate.

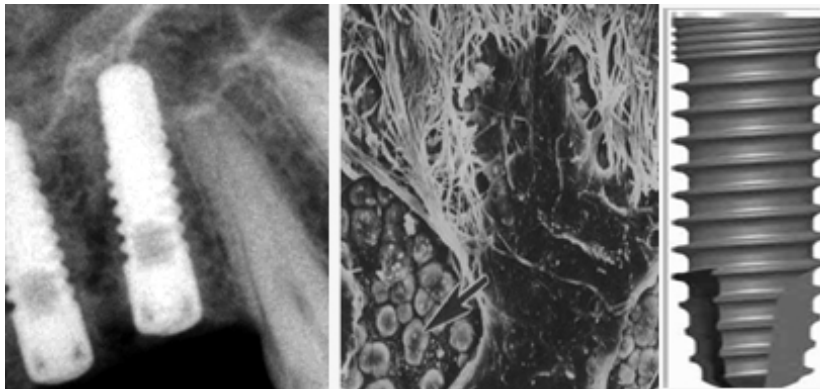


Fig. 3. Left: already implanted titanium surface treated implants with micro photo of the interface between the implant and bond, right: original implant manufactured to fit the given need (length, diameter, crew, etc.).

Bioactivity has since attracted increased attention being aimed to further molecular manipulation (doping surfactants, micro-additives of various organic molecules such as proteins, glyco-proteins and polysaccharides, useful in easier mine-realization) which intelligent response by host organism is evaluated in order to achieve well-tailored implants. Bio-glass-ceramics that activate genes offer the possibilities of repairing, or perhaps even preventing, many disease states, such as osteoporosis, in which a large fraction of women lose a substantial amount of bone mass as they age. They can be also used as a second phase in a composite that mimics the structure and properties of bone. In future the implication of glass activation of genes it may be possible to design therapeutic treatments or food additives that will inhibit the deterioration of connective tissues with age. Further understanding bioactivity may even help in better perception of the creation of life. It shows a great variability in the application of different glasses and amorphous materials in many fields of human activities.

Most recent research shows that the integration of biomaterials implicates a series of cellular and extra cellular matrix events, some of which take place at the tissue-implant interface and which also reflect the host response to the bulk and surface characteristics of the implanted material. As a part of this process, the most frequently implanted material, such as titanium, glass-ceramics, calcium phosphates, and cellular culture substrates, become coated with a layer of electron-dense material, which has been referred to us as ‘lamina limitants’ or ‘cement lines’ customarily consisting of calcium phosphate crystals with incorporated bone-matrix proteins (e.g. bone sialoprotein, osteocalcin, osteopontin) that are naturally circulating in the blood stream (in a very low concentrations only). It was found that there are several potential sources for such proteins, which use to accumulate at the reaction interface. It was also proposed that osteoclasts express and secrete some non-collagenous bone-matrix proteins onto bone surface. The differential deposition of matrix constituents by osteoblasts at the beginning and end of the bone deposition cycle is now believed to be the major source of

interfacial proteins at natural bone and bone-implant interfaces. It is in line of general understanding of life-based building of firm and well-structured inorganic constructions (various shells, etc.) where obviously the morphology and composition play a decisive role.

Earlier studies revealed the concept behind micro porous bioceramic materials, which is the intergrowth of tissue into pores on the surface or throughout the implant. This is often termed '*biological fixation*' which is capable of withstanding more-complex stress states than implants that achieve only mechanical attachment, i.e., '*morphological fixation*'. The limitation associated with porous implants is the pores size, optimally as large as 100-150 μm , which can only assure that the implant remains viable and healthy. The large interfacial area required for such porosity is due to the need to provide a blood supply to the ingrown connective tissue. Vascular tissue does not appear in pores that measure below 100 μm and without sufficient blood supply the tissue expires or inflammation ensues which practically destroys interfacial stability and implant sufficient in-fixation. However the fraction of larger porosity, required for successful bone growth in any materials, degrades the strength of the material applied. Consequently, this approach to solving interfacial stability is best when the material is used as porous coating on surgical metal alloys or as unloaded fillers for bone ingrowths.

Very important is good understanding of reactions that occur at the surface of glassy implants of silica-specialized composition. First, there is a rapid release of soluble ionic species and the formation of a high surface area of hydrated silica and polycrystalline hydroxyl-carbonate apatite bi-layer. It was experimentally observed that the alkali-hydrogen ion exchange and the network dissolution rapidly reduce the amount of the Si-O-Si and Si-O-Ca modes and replace them with Si-OH bonds with NBO [23-26]. Single NBO modes are then gradually replaced by more spherical OH-Si-OH. As early as within several minutes a P-O bending vibration, associated with formation of an amorphous calcium phosphate layer, appears due to the straightforward precipitation from the solution of body liquid. The reaction layers enhances adsorption and desorption of growth factors and influence the length of time macrophages that are required to prepare the implant sites for the tissue repair. It was shown that a Ca- and P- rich layer is also formed on various surfaces that are deficient of these cations. It happens when the surface is exposed to solutions containing these actions (e.g., body or simulated body liquids). The behavior of some additives was also investigated showing, for example, that when F-ions are presented they also get incorporated in hydroxyapatite crystals distorting, however, crystal structure by formation fluorapatite and the addition of multivalent ions delays bonding so that even their small amounts may reduce bioactivity.

The index of bioactivity, I_B , for an active implant depends on both the rate of calcium phosphate film formation and time of crystallization to hydroxyl-carbonate apatite and the selective absorption on the growing hydroxyapatite layer of extra-cellular proteins that control cellular attachment, differentiation and growth. The defect structure of the growing hydroxyapatite crystals is likely to be responsible for the preferential adsorption of the growth factors. Metastable hydrated silica species, such as penta-coordinated silicon ions, $\text{Si}(\text{OH})_5^-$, which is present during the silanol-condensation reaction, may be associated with the enhanced progress of crystallization on surfaces providing, in the same time, specific bonding sites for biological moieties.

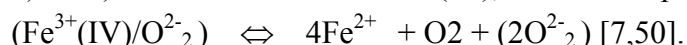
Today's bioceramics are used in a broad field of devices inside the human body. This is mainly due to their good biocompatibility and possibility to adjust their biocompatibility on basis of prefixed glass composition optimized upon the calculation of NBOs in the glass lattice when taking up the assumingly polymeric character of the common matrix silicate glass. Among the ceramic materials used for bone replacement, bioactive glass-ceramics appears, therefore, particularly promising because of their ability to form the reactive but

stable interfaces with living host tissue. However, the major problem of these materials, which inhibits their application on several types of implants, is their poor match of mechanical behavior of the implant with the tissue to be replaced. Principally, the coating, composites, porous structured materials and/or new resorbable materials are promising ways for the next development where thermochemistry and thermodynamics would have their incommutable position. However, no one has currently succeeded to find a material, which would fully corresponds to bone or other living parts of the body. It is the task of a growing number of researchers and institutions working in the field of both the organic and inorganic bioactive composites to achieve a further improvement of material performance. We also should not forget that the nature is still the better engineer than we do.

17. 5. Borate glasses containing Fe₂O₃ and their structural and magnetic properties

Borate glasses are technologically important for microelectronic devices, storage batteries using super ionic conductors, and several other applications including magnetics. During the last several decades numerous compositions of alkali borate glasses were studied showing the glasses structure with composition (B₂O₃)_{12-x}(R₂O)_x where (R= Na, Li, Rb, K), which is known to consist of a B–O network, built up from planar three coordinated and tetrahedral four coordinated boron atoms. Pure B₂O₃ contains only three coordinated boron atoms, but if alkali oxide is added some of these units are transformed into four coordinated tetrahedra. Adjacent BO₃ and BO₄ groups are linked by bridging oxygen atoms, building the glassy network. At higher alkali oxide concentration (greater than 20 mol %), the formation of non-bridging oxygen (NBO) is suggested and the number of NBO is considered to increase with alkali oxide concentration. Several investigations were carried out on ternary borate glasses. These are concerned with the structural aspects of these materials. According to some researchers pure B₂O₃ consists mainly of a B₃O₆ boroxol rings which glass network is almost completely made up of randomly connected boroxol web. With the increase of alkali oxide content, the boroxol rings in the glasses are transformed into rings incorporating one or more four coordinated boron atoms. The existence of boroxol ring structures was indicated by strong and highly polarized peaks in the Raman spectra; however, some doubts have already been expressed against the existence of these boroxol rings in the borate glass network. By the process of molecular dynamics simulations can be suggest showing a glass structure consisting of randomly connected planar BO₃ triangles with no six fold ring structure. In such a continuous random network (CRN) model [10,13], the presence of a strong highly polarized Raman peak is attributed to a localized symmetric breathing mode of the three oxygen atoms with each BO₃ triangle.

The presence of magnetic cations such as Mn³⁺/Mn²⁺ or Fe³⁺/Fe²⁺ in glasses involves their interactions with surrounding oxygen, which has been intensively studied for behavior (redox potential [11-13]) of iron oxides as a particular additive in silicate melts [47-51]. It is widely believed that a similar behavior can be expected in the other glass-forming mixtures. The details of these interactions depend on the type of oxygen polyhedral around ferric and/or ferrous cations. If, for example, Fe³⁺ is considered in tetrahedral (IV) coordination (Fe³⁺(IV)/O²⁻) and Fe²⁺ is in octahedral (VI), we can compose a following relation



However, if the (2O²⁻) anions in the melt are under the affect of the other structural units co-existing in the melt, further associated processes, mostly depolymerization, may occur. An alternative is that both Fe³⁺ and Fe²⁺ are octahedrally coordinated providing thus optional relation



which is adjacent to opposite process of polymerization. Certainly, it is plausible that both Fe^{3+} and Fe^{2+} cations may undergo coordination transformation simultaneously, which would result in structural changes touching all variables as illustrated by the relation

$$(\text{Fe}^{3+}(\text{IV})/\text{O}^{2-}_2) = (\text{Fe}^{3+}(\text{VI})/\text{O}^{2-}_2) + (2\text{O}^{2-}_2).$$

Thus any glass property of iron-bearing mixtures can be related to the ratios of $\text{Fe}^{3+}/\text{Fe}^{2+}$ and/or $\text{Fe}^{3+}/\Sigma\text{Fe}$ [7] the latter being also controlled by other glass-modifying admixtures such as CaO , Na_2O , K_2O with positive and MgO or Al_2O_3 with negative correlations towards the redox data [13] and thus affecting the level of NBO. Simply saying, it implies that the $\text{Fe}^{3+}/\text{Fe}^{2+}$ ratio decreases with increasing NBO in bulk melt.

Actually, the structure of borate glasses is somehow different from other glasses such as germanate, phosphate or silicate and it was suggested that the structure of borate glasses heavily depends on the cooling rate of the melt through the range of glass transition temperature. Therefore most of magnetic properties were found related to the method [45,46] of glass preparation. The behavior changes of borate glasses were intensively studied with respects of considerable addition of iron oxide respecting both its phase equilibrium and oxidation state [47-50] as well as structure [51]. First technological strategy was aimed to initiate a controlled crystallization within glassy state to produce well tailored magnetic particles, such as the precipitation of magnetolumbite from $\text{BaO-Fe}_2\text{O}_3\text{-B}_2\text{O}_3$ glass containing up to 30% of iron oxide [52,53] and ferrite from $\text{CaO-Al}_2\text{O}_3\text{-B}_2\text{O}_3\text{-SiO}_2\text{-Fe}_2\text{O}_3$ glass having up to 12% iron oxide [54] and from $\text{B}_2\text{O}_3\text{-MnFe}_2\text{O}_4$ with up to 20 % iron oxide [55]. One of the first detailed magnetic investigation of $\text{B}_2\text{O}_3\text{-MnFe}_2\text{O}_4$ glasses [56] indicated its superparamagnetic arrangement, which was followed by other borate glasses showing that superparamagnetic behaviors occurs for those compositions, which exhibits more than 10% of Fe_2O_3 (usually prepared by splat quenching [56-58] and often associated with fast laser melting). Probably the first glass to show signs of antiferromagnetic interactions in its magnetic susceptibility measurements were specified within a compositional range of manganese borate glasses [59] specifically followed by a detailed study of $\text{B}_2\text{O}_3\text{-MnFe}_2\text{O}_4$ glasses [23]. Some investigators reported that most of oxide glasses containing a large amount of magnetic ions exhibit magnetic transitions as often observed in spin glasses or superparamagnets. For example, magnetic aging and memory effects were measured in magnetically ordered phase of $32\text{Fe}_2\text{O}_3\text{-48Bi}_2\text{O}_3\text{-20B}_2\text{O}_3$ glass [60], which was prepared by using a conventional melt-quenching method. This glass exhibited a spin-glass transition at about 15K and a super-paramagnetic blocking at about 28K. The rather unique magnetic transition was likable attributed to an inhomogeneous distribution of magnetic moments in the glass providing diluted and concentrated regions of magnetic moments, the former likely responsible for a spin glass-like transition [64] and the latter for a super-paramagnetic clustering. Similar study was carried out in the system $\text{Fe}_2\text{O}_3\text{-Bi}_2\text{O}_3\text{-Li}_2\text{O}$ [61].

The magnetic behavior of $\text{Fe}_2\text{O}_3\text{-Bi}_2\text{O}_3\text{-B}_2\text{O}_3$ was similar to that of the canonical spin glasses. The magnetic structure measured was dependent on the content of Fe_2O_3 and when the content of Fe_2O_3 was above 26 mol%, the glasses became composed of two magnetic components, i.e., the spin glass phase and magnetic clusters manifesting a super-spin glass transition. As the value of Fe_2O_3 increases, the contribution of magnetic clusters to the magnetic properties becomes more remarkable and magnetic clusters executed stronger interactions with each other assisting the occurrence of a super-spin glass transition. The clusters were mainly present as a kind of amorphous state. It was revealed from the measurements of the exchange bias effect that the interplay of the spin glass phase with the magnetic clusters headed to the formation of an exchange anisotropy field after the field cooling. Compared with the magnetic oxide glass systems reported previously, the present

glass system encompassed rather novel magnetic structure in the sense that there exist two magnetic ordered phases interacting with each other.

Laser-impact quenching technique [57,61,62] was applied for the preparation of glassy specimens in BaO-Mn₂O₃-B₂O₃ and/or BaO-Fe₂O₃-B₂O₃ system in air where a small amount (drop) of a pre-sintered starting composition was placed on a water-cooled copper plate, instantaneously melted with a focused beam of CO₂ laser and quenched by striking it with another copper block. Magnetization was measured from 4.2 K to room temperature. Their magnetic properties approved the concept of antiferromagnetic ordering in the short range order [61] exhibiting specificity speromagnetism, which was first noticed in [63]. It was noted, however, that microcrystalline Mn₃O₄ alone could apparently remain present in quenched glass below the resolution of SEM being thus responsible for ferromagnetic behavior. Such nuclei can also act as pre-crystallization sites as the Mn₃O₄ is clearly produced upon thermally induced crystallization. The other explanation likelihood may be thought in the coexistence of different valance states of Mn ions. Thus the double exchange mechanism can lead to the appearance of ferromagnetism in standard Mn-perovskites with coexisting Mn³⁺ and Mn⁴⁺ cations.

Magnetic properties of glasses Bi₂O₃-BaO-based glasses doped either with up to 35% Fe- and/or Mn- oxides [62] showed reciprocally a marked contrast. Fe-glasses were characterized by a typical example of weak sperromagnetism of canted spins in which the antiferromagnetic order of short range was formed while Mn- glasses seemed to be magnetically inhomogeneous, which was well demonstrated in the field dependence of thermo-remanent magnetism. For Fe-glass the magnetic susceptibility obeyed the standard Curie-Weis law giving effective Bohr magneto, $\mu_{\text{eff}} = 5.4\text{-}6.2 \nu_B$ and paramagnetic Curie temperature of about minus 300 K.

In general, magnetic oxide glasses [46] can be regarded as a system in which the magnetic moments localized at cations are randomly distributed in the insulating host glass structure. In addition to the random distribution of magnetic cations, magnetic frustrations can also occur in the configuration of magnetic moments because the short-range antiferromagnetic super-exchange interaction is usually dominant in such a random structure. The antiferromagnetic interaction between two nearest-neighboring ions can thus be altered into ferromagnetic coupling by an additional magnetic ion present near to the two preceding ions. Therefore, the magnetic oxide glass systems can satisfy the prerequisites for a spin glass transition [62-64]. Actually, the freezing of randomly oriented magnetic moments was observed at very low temperatures in magnetic oxide glasses containing a sufficiently large amount of 3d transition metal ions (typically Fe and Mn). Ferromagnetic-like behavior even at room temperature has been reported for some amorphous oxides containing Fe₂O₃ and Bi₂O₃ such as Fe₂O₃-Bi₂O₃-ZnO [65], Fe₂O₃-Bi₂O₃-CaO [66], and Fe₂O₃-Bi₂O₃-CuO [67] systems, in the early 1990s. However, we should mention a conflicting opinion [65,67], which concluded that the ferromagnetic behavior in the Fe₂O₃-Bi₂O₃-based systems [61,66] can be attributable to some remaining ferrimagnetic nano-crystalline phases invisibly embedded in the glassy matrix, because their images are too small to be easy observable by transmission electron micrography (SRD) and X-ray diffraction (XRD). In general we can agree that nucleation processes and particularly possible existence of organized embryos as pre-nucleation sites can play a decisive role in the entire course of glass crystallization [68-70].

17. 6. Magnetic properties of the (Fe,Mn)₂O₃-B₂O₃ splat-quenched system of variously doped melted mixtures

The glasses melted from raw material (mixed from Fe₂O₃, MnO₂, SiO₂, Al₂O₃, B₂O₃ and K₂B₄O₇) and adjusted to the base composition of 31Mn_{1.5}Fe_{1.5}O₄+69B₂O₃ (marked as-

o) and with the addition of 3% K₂O (K), Al₂O₃ (Al) and SiO₂ (Si) and the mixture 2% K₂O and 2%Al₂O₃ (K+Al) was temperature equilibrated and then splat quenched between two copper plates into specimen of about 1.5 mm thick, with the estimated cooling rate of about 10⁻² K/s [22,45,56]. Their glassiness was examined by XRD and SEM and the given cation content was granted by wet chemical analysis. Furthermore, thermal behavior was measured by differential thermal analysis (DTA) [45,72], electric conductivity [73] and magnetic susceptibility by a modified Faraday method using an inhomogeneous field in the temperature range from 4.2 up to 270 K [22,56]. Determination of the hydrostatic sample density, ρ, and the well-defined knowledge of composition can be further used to provide valuation of the average volume per cation, V_c, or the average volume V_{mg} per magnetic cation. The cubic roots of volume give us an estimate of the average distances, i.e., a_c (a_{mg}) = {(M/ρ) u (1/n)}^{1/3}, where n is the number of magnetic cations in the formula units. Similarly we can determine the average volume per an oxygen atom, V_{ox} = {(M/ρ) u (1/n_{ox})} where n_{ox} is the number of oxygen atoms in the formula unit. These data are summarized in Table I.

Basic explorative interest was pointed towards magnetization curves from which typical profile it is apparent that at higher temperatures the reciprocal susceptibility 1/χ is approaching a linear dependence that can be extrapolated to high negative temperatures (of the order of 10² K). Relatively strong interactions among the present magnetic moments can be deduced preferring their antiparallel orientation. However, there is no trace of anomalous behavior at low temperatures bearing witness on an expected ordering of an antiferromagnetic type. On the other hand, the 1/χ temperature dependence displays a downward curvature at low temperature, which can be explained by a simplified model of coexistence of two kinds of magnetic moments. Certain amount of moments, with a relative concentration of t, is not exposed to any appreciable interactions from their neighbors and can be treated as paramagnetic whereas the remaining (1-t) behaves like antiferromagnetic characterized by a paramagnetic Neel temperature, Θ (see next Table).

Table I:

Sample	T _g	stability	Area	energy	density	dist. a _{mg}	vol. v _{ox}
O	528	(1)	(1)	(1)	3,251	4.033	18.42
K	515	0.64	1.0	1.39	3.215	4.096	18.80
Al	525	1.15	1.0	0.42	3.104	4.147	18.15
Si	531	1.0	1.07	0.82	3.338	4.054	17.73
K+Al	520	0.91	0.97	0.89	3.198	4.122	18.74

T_g is glass-transformation temperature [°C], stability, which is given as a relative ratio of (T_c-T_g) with regard to that of the undoped sample (o). Similarly is given the relative values for peak area of crystallization and that for related activation energy. The sample density is measured by an hydrostatic method while the average distance between the magnetic cations a_{mg} [in 10⁻⁸ cm] is calculated. Moreover, the average volume of oxygen anions v_{ox} is also determined [≈18.10⁻²⁴ cm³]. It worth noting that the oxygen volume is about 5% higher than that often exploit from tables [≈17 × 10⁻²⁴ cm³] and even much higher in the case when assuming the volume of bridging oxygen depicted in the paragraph one [≈15.34 × 10⁻²⁴ cm³], which is likely caused by the specificity of borate matrix involved.

Introducing an additional assumption that both these kinds of moments have the same average magnitude an expression for the temperature dependence of reciprocal susceptibility can be easily derive in the form

$$1/\chi = \{T + (1-t) \Theta\}/c - t/\{T/(\Theta + t)\} \{(1-t) \Theta/c\} \quad (5)$$

Here c is the Curie constant, T is the absolute temperature and the meaning t and Θ was shown above. The main features of this dependence reasonably agrees with our experimental data, Fig. 4., so that we could convincingly determine from them the model parameters such as the Curie constant, c , the paramagnetic Néel temperature, Θ , and the concentration, t . In order to do that let us first note, that the asymptotic behavior at high temperatures is only governed by the first term of eq. (5) and the extrapolated Θ' corresponds to $(1-t)\Theta$, the slope being equal to $1/c$. Getting an estimate of t from eq. (5), we calculated temperature T' at which the full dependence of $1/\chi$ is equal to $3/4$ of the first term linear in T . The concentration t of paramagnetic moments is then given by

$$T = \{T'(T' + \Theta')\} / (3\Theta'^2 + T'^2) \quad (6)$$

After t is calculated we can determine Θ from $\Theta'/(1-t)$. All relevant data are summarized in Table II.

Table II:

Sample	Θ'	t	Θ	c_g	$(\mu'/\mu_B)^2$	(μ'/μ_t)
O	140	0.16	167	2.22	22.74	0.83
K	115	0.125	131	2.25	24.3	0.86
Al	77	0.17	93	1.89	20.1	0.78
Si	130	0.105	145	2.56	27.35	0.91
K+Al	121	0.15	121	2.13	22.92	0.83

Magnetic properties consists of extrapolated negative temperature Θ' [in K] and paramagnetic Neel temperature, Θ [K] estimated for a given concentration of antiparallely ordered magnetic moments $(1-t)$. The value c_g is the Curie constant per gram [10^{-2}], μ' is the average magnetic moment per atom of transition metal yielding the revolving squares of average moments $(\mu'/\mu_B)^2$. Using a theoretical value of μ_t equal to $5.76 \mu_B$ we can utilize it for the evaluation and consequent comparison of experimental data in the form of ratio (μ'/μ_t) .

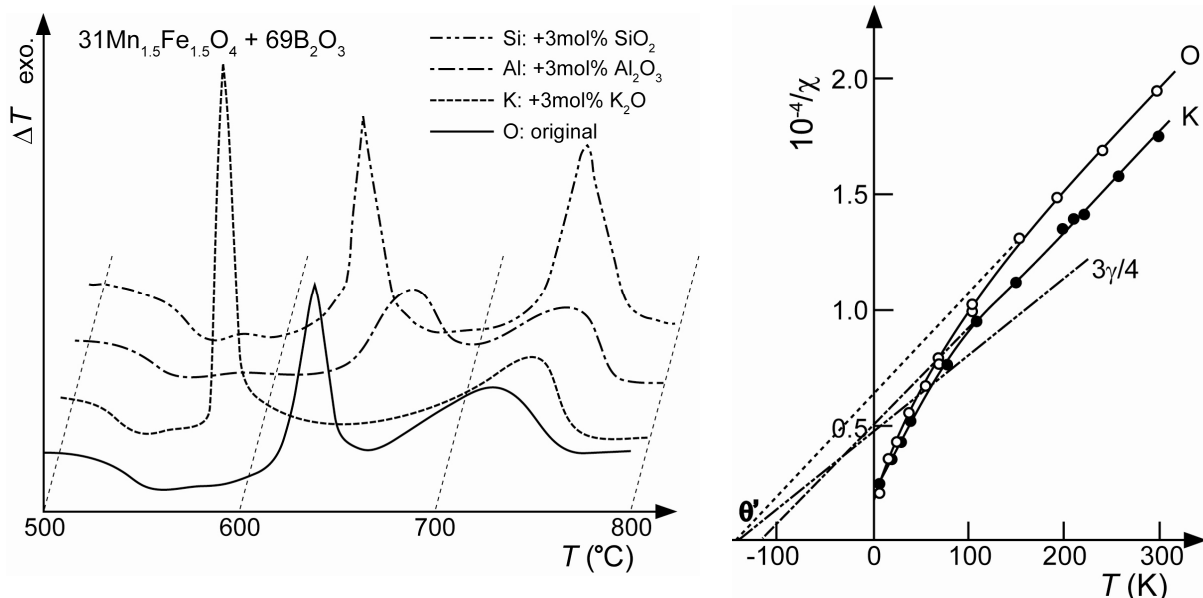


Fig. 4. left: DTA (Netzsch instrument) curves of glasses and resulting data relevant to their stability related to T_g (as the front step-wise change) and T_c (as the onset of the exothermal crystallization peaks), cf. Table I. Right: Temperature dependence of the reciprocal magnetic susceptibility, $1/\chi$, extrapolated to negative temperatures of Neel temperature, Θ' , see text and table II.

The Curie constant c may be further used to calculate the average magnetic moment, μ' per an atom of transition metal using the resolved chemical composition of our sample, i.e.,

$$c_g = N_g \mu'^2 / (3 k T) = N_A a \mu'^2 / (M k T) \quad (7)$$

Here the subscript in c_g stresses the fact that we are using susceptibilities and consequently Curie constants per gram (g), N_g is the number of magnetic moment μ' in one g and N_A is the Avogadro number and $3a$ is equal to the number of magnetic atoms in the formula unit (see Table II).

The squares of these average moments derived from eq. (7) are listed in Table II. In order to calculate the expected average magnetic moment of the present cations we suppose that equilibrium between various valencies of manganese and iron does not deviate in the glass from that stoichiometry found in the standard Mn-Fe spinels with the same Mn^{3+}/Fe^{3+} ratio, i.e., $Fe^{3+}_{1.5}Mn^{3+}_{0.5}O_4$ [71]. Ascribing then to each cation a single spin-only value of

$$\mu'^2_t = g^2 s (s+1) \mu_B^2 \quad (8)$$

with $g=2$ s is the quantum spin number, and μ_B is Bohr magneton. Assuming squares of the moments in accordance with eq. (7) we arrive at a theoretical value of $\mu_t = 5.76 \mu_B$ which is further used for comparison with the experimental values in the last column of Table II.

It is worth noting that DTA was measured on few pieces of glass buried in the powder of fine silver particles placed inside the DTA sample-cell because similar-sized glass pieces were used in all other measurements. Moreover, powdering of glass changed its properties slightly decreasing T_g ($o \rightarrow 524$ C) but doubling crystallization heat ($A/A_o \approx 2.1$) due to the increased surface (a slight increase of the activation energy $E/E_o = 1.2$ was infertile likely enhancing surface crystallization only little).

Glass-forming abilities and associated cation compatibilities with various levels of B_2O_3 [55] shown a decrease from Mn^{3+} through Mn^{2+} , Fe^{3+} to Fe^{2+} and, consequently, we can expect that the transition metal ions will be incorporated into the glass network along this sequence. This idea was corroborated by our findings about crystallization [55], which for boron glasses containing iron and manganese cations crystallization yields the crystal phase enriched in Fe with the remaining glass matrix augmented of Mn (than that corresponding to the average Mn/Fe ratio [56]). The stability of glasses with respect to the different admixtures can be analyzed on the basis of DTA data, see Fig. 3. The ratio of the differences between the temperature of glass crystallization and transformation of the doped glass to the original one (o) may be taken as a measure of the relative glass stability. It is equal to 1 for SiO_2 admixture, which is in accordance with the standard concept that SiO_2 tends to form a separate network within B_2O_3 matrix so that the original matrix remains essentially unaffected. On the other hand Al_2O_3 tends to enter B_2O_3 matrix and to span its network into three dimensions, which results in an apparent gain in the relative glass stability. Potassium cations with a relatively high ionic radius deform in their vicinity the B_2O_3 network, which may thereafter act as potential sites for nucleation and crystallization. In consequence the glass stability decreases. All that is also in accordance with the change in activation energy [68-73] whose high value for K_2O admixture indicates an easier crystallization process started from a large number of ready-to-grow nuclei while its lower value for Al_2O_3 indicates rather slower process controlled by diffusion.

Let us turn now our attention to the magnitude of magnetic moments given in Table II. From the last columns it can be seen that for the basic glass (without admixtures) this value is considerably lower than the moment expected for free ions. Various admixtures bearing the

magnetic moments are able of further changing the moment per atom of transition metal and we believe that both these phenomena are symptoms of the number and type of incorporation into the network. The reasons may be at three-fold:

(i) Increased interaction of incorporated transition metal ions via the intermediating oxygen, which may result in their antiferromagnetic pair (or even small cluster) ordering thus substantially lowering (or even excluding) the contribution of these moments to the Curie constant.

(ii) The spin moment of covalently bound cations, e.g., Fe^{3+} , may be lowered due to the transition to low-spin state [22]. These effects are usually described in terms of strong crystal fields revealed by some compounds supportive of these cations though not so common in oxides.

(iii) To a large extent, the orbital contribution to the magnetic moment is affected by covalent bonding but in our quantitative estimates we only capture into account the spin moment so that this influence cannot be weighted up in a simplified way.

In any cases it seems that the incorporation of either Mn (or less probably Fe) ions into the glass network can only lower its magnetic moment. The number of ions incorporated will be given by the equilibrium of the reactions shown in the introductory paragraphs [1-5,22], $\text{Mn}^{2+} + \text{O}^{2-} = \text{Mn}^{\circ} + \text{O}^{\circ}$ and/or $2\text{Mn}^{3+} + 3\text{O}^{2-} = 2\text{Mn}^{+} + 2\text{O}^{\circ} + \text{O}^{2-} = 2\text{Mn} + 3\text{O}^{\circ}$, where the number of primes denotes the multiplicity of the bond of the given atom in the network.

Concluding on basis of DTA data and magnetic moment determination we suggest the following mechanism for the influence of modifying admixtures. SiO_2 enters the B_2O_3 matrix as $(\text{Si}^{4+} + 2\text{O}^{\circ})$, which likely increases the concentration of BO [2]. The NBO equilibrium is thus shifted to the left hand side, i.e., Mn and/or Fe cations are released from the network. The addition of Al_2O_3 has the opposite effect [7,74], because it prefers the incorporation in the form of AlO^+ groups whose negative charge is compensated by bonding transition metal ions into the network, which means a shift of equilibrium to their right hand side. The expected effect of K_2O admixture as the donor of O^{2-} should be even stronger than that of Al_2O_3 and point in the same direction. Our magnetic measurements show, however, a minor influence though the DTA displays rather significant changes. Similarly as reported in [22,50,75,76] the introduction of K_2O into borate glass would change the B_2O_3 matrix itself so that we can expect both the softening of the glass structure and a smaller effect exerted upon the state of the transition metal ions.

The strength of magnetic interactions can be estimated from the value of Θ as revealed in Fig 3. This quantity Θ actually gives the lower limit for the entire interactions. In a rough approximation, the effect of various admixtures can be explained by the average distance between magnetic ions presented. In quantitative agreement along our expectations, the value of Θ smoothly decreases with the increasing distance. Let us finally comment on the magnitude of this concentration, which was calculated for the accepted model on the basis of eq.(6) and (7), and given in Table II. The moments, described here as paramagnetic, do not have a sufficient number of magnetic cations as their nearest neighbors and, for an assumed random distribution, the number dependence on the average concentration of magnetic atoms turn up to be an increasing function for low values attaining a maximum (and again decreasing). The composition of our glasses clearly belongs to the latter part of this dependence, which explains the seemingly contradictory behavior of the t-value with various admixtures. Namely Si releases transition metal atoms from the network, which factually decreases the concentration t and the effect of Al is laying just on the opposite direction. For describing magnetic susceptibility and approving consistency of our model, we plotted in Fig. 5. the concentration t against the relative magnetic moment μ^2/μ_t (see Tab. II). In agreement with our discussion, introducing admixtures increases the number of transition metal atoms

incorporated into the network, which decreases the average magnetic moment and increases the concentration t and *vice versa*.

Such a magnetically doped glasses provides possibility of a controlled crystallization [55,56,68-70] of two independent magnetic crystallites with narrow but separate distribution curves [77]. If the size of magnetic particles is decreased below a certain limit, which is necessary for the formation of sizable magnetic domains, such a resulting glass-ceramics is applicable as hard magnetic material allowing, moreover, continuous passage from single- to multi-domain particles. Crystallization can further be studied under simultaneous measurements of coercive force helping thus the precipitation of single-domain system [77]. By comparing different glass-forming components the matrix of B_2O_3 provided the highest coercive force in comparison with that based on SiO_2 , Bi_2O_3 or P_2O_5 . Antiparallel ordering [22,56,78] was found in the accordance with the Simpson theoretical model [79] yielding that the temperature of magnetic ordering (T_N) is proportional to the square of mean number of interacting neighbors and the Neel temperature (Θ) lies lower than that for analogous polycrystalline ceramics. Ferromagnetic or sperrimagnetic properties of disordered systems were located in glassy alloys (see the separate chapter on microcrystalline alloys), which numerous compositionally different systems found already practical applications [79].

17.7. Specific case of speromagnetic behavior of rapidly quenched and laser melted $(Fe,Mn)_2O_3$ - $(B,Bi)_2O_3$ glasses

The substitution of Bi_2O_3 for B_2O_3 [76] increases, however, the upper glass forming limit for Fe_2O_3 to about 20mol% (such a composition was still vitrifiable by standard splat quenching method at the cooling rate of $\leq 10^{-2}$ K/s). In the contrast with the simple (Fe, Mn)-B-O system, the substitution of Fe by Mn in the Bi_2O_3 -rich matrix did not improved the glass-formation but only decreased the Curie temperature. Substitution of B for Bi in Fe-B-Bi-O system changed the phase relation substantially enhancing crystallization tendency of crystalline borates on account of previously precipitated crystalline phases of $Fe_4Bi_2O_6$ and $FeBiO_3$ leaving behind glassy matrix with higher magnetic moments.

However, the Fe_2O_3 -rich composition (such as the end compound $FeBiO_3$) required for its vitrification much powerful quenching than is a basic splat cooling used above. In some cases it was necessary to exceed rates above 10^{-3} K/s. Such a rapid freeze-in of melts could only be attained by a specially developed techniques usually aided by fast laser melting and consequent melted drop pressing in a specially modified coolers, such as twin-rollers [45,76] being worth of a more detailed description.

The popular quenching technique has been derived from a familiar doubling machine (calander) enabling intensive rolling between two rapidly rotating wheels (held together under certain pressure and guaranteeing the given gap of separation) often called *twin roll technique* (forming the original basis for continuous production of metallic glass ribbons with even thickness and homogeneous composition assuring also a smooth surface on both sides), Fig. 5. However, a relatively short time of effective cooling along the line between the two wheels (touching each other in a linear link) often causes that the temperature of the departing (cooled) solid (ribbon) still remains high enough to cause the solidified sample re-crystallization (or otherwise undesirable relaxation). Together with another disadvantages (such as difficult synchronization of the outlet velocity of the melt with the circumferential velocity of both wheel revolutions at about 15 – 30 m/s) this method often steered preference towards a practical exploitation of the single wheel quenching, which, however, was found ineffective for the type of oxide melts under investigation.

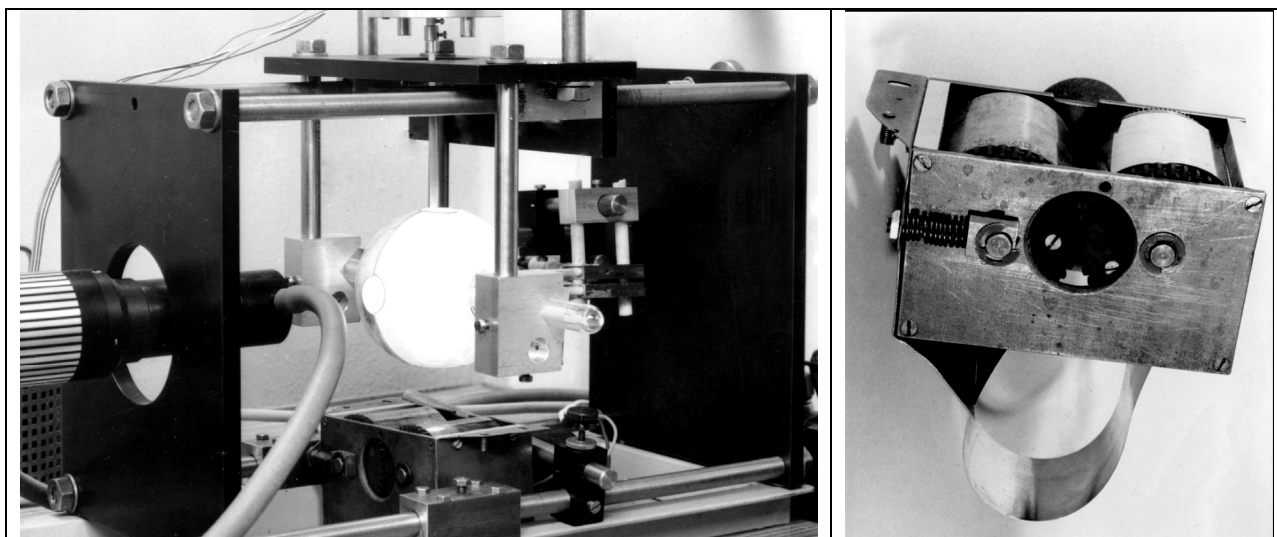


Fig.5. *Left: Photo of a laser-aided heating system, which was actually applied in our laboratory during eighties. The laser furnace consists of globular reflectors, which shield the intense heat created by a small resistance heater made of iridium wire and placed in the center. It provided homogeneous background temperature of about 1800 °C. Inside the heater, a rotating pre-sintered rod-like specimen is mounted, the end of which was additionally heated by focused laser beam entering the furnace by a window. The molten zone thus created discharge a hanging molten drop enabling it consequent quenching either at an underneath trap when the pedant drop is forced to fall down into the quenching device (see right) or by immediate squeeze-in between two miniature copper plates mounted at the ends of tweezers (movable inside the globular shield). Right: Close up of the entire quenching devise (called the belt running roller) where the melt is factually quenched on the surface of inserted (infinitesimally running) metallic (Ag-alloy) ribbon. This adjustment helped to assure prolonged contact of the quenched sample melt onto the cooling substrate (thus avoiding supplementary crystallization of glass after its taking away from the simple wheels' linear contact).*

Nevertheless, the intricate difficulties can be removed by a specially designed set up of the so-called *continuous belt-running method*, which was earlier developed in our laboratory. Fundamental principle ensues that a melted pendant drop (or even free falling melt-stream) is trapped in between the wheels, which roller's link (factually providing the quenching linear contact) was expanded to a plane by an inserted looped filament, which is infinitesimally running metallic ribbon

These quenching options radically extended the range of vitrified compositions, though the glassy samples were very tiny and difficult to become fully reproducible. From magnetic susceptibility measurements, the temperature dependence of (Bi-B)(Fe-Mn)-O glasses revealed certain evidence of stronger interaction of antiferromagnetic types [76]. The composition containing not only Bi but simultaneously B, exhibited a definite Curie-Weiss behavior, Fig. 6. Samples with Bi and Mn probably contained cations' multivalency as a result of their broader distribution, showing their various degree of incorporation into the glass network. Only difficult to prepare glassy FeBiO₃ provided indication of magnetic measurements explainable on the basis of weak ferromagnetism, i.e. , so called speromagnetism, probably caused by canted spins in the antiferromagnetic sub-lattice, which was early suggested to take possibly place in the Fe-Bi-O system [80] and which magnetic ordering was already experimentally noted previously [63].

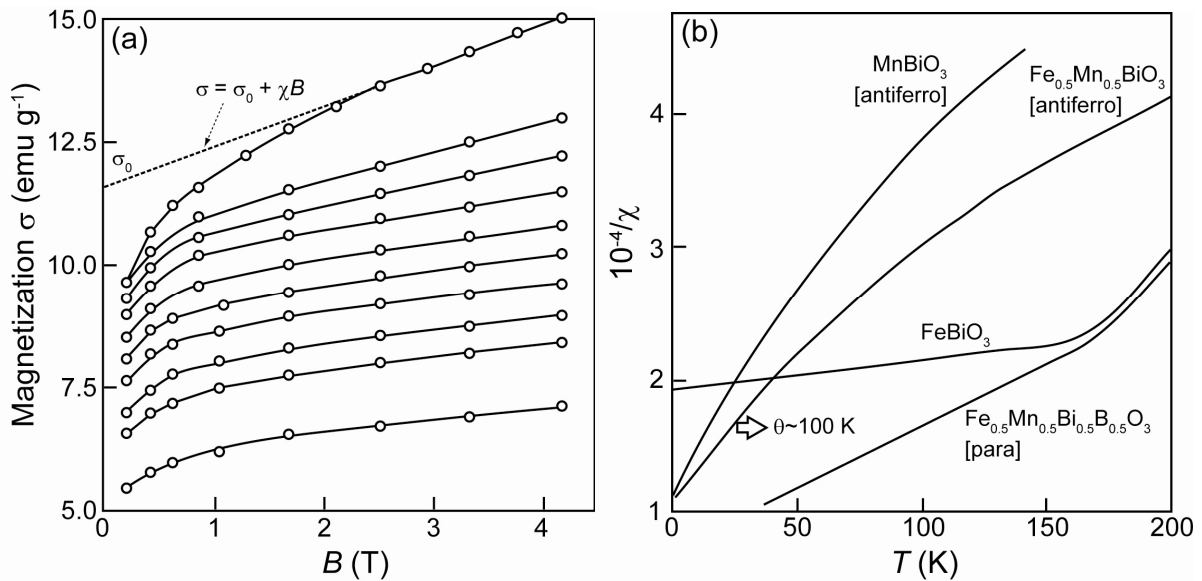


Fig 6a: Magnetization curves of the antiferromagnetic-like as-quenched Fe-Mn-Bi-O glass viewing the experimental curves and their temperatures of measurements from upper curve at 4.2 K proceeding down with the increasing stepwise temperature changes along 24.5, 50.0, 75.0, 100.0, 125.0, 150.0, 175.0, 200.0 up to the final 157.0 K. **Fig 5b:** Temperature dependence of the reciprocal magnetic susceptibility, $1/\chi$, portraying various magnetic behavior, starting from paramagnetic (arbitrary ordering of mag. moments $\uparrow\rightarrow\downarrow\leftarrow$) for $\text{Fe}_{0.5}\text{Mn}_{0.5}\text{Bi}_{0.5}\text{B}_{0.5}\text{O}_3$ to a mixture of paramagnetic and antiferromagnetic ($\leftarrow\downarrow\uparrow\downarrow\uparrow\rightarrow$) phases for $\text{Fe}_{0.5}\text{Mn}_{0.5}\text{BiO}_3$ or MnBiO_3 exhibiting a Neel temperature Θ in the order of ~ 100 K. A very special (almost extraordinary) behavior of so called speromagnetism is displayed by the extremely rapid quenched ($\cong 10^6$ K/s) glassy specimen of FeBiO_3 showing not completely compensated moments (i.e., not fully antiparallel moment ordering, where arrow orientation $\uparrow\downarrow\uparrow\downarrow$ is mutually little angled).

The type of incorporation of cations into the Bi-B-glass network and the formation of NBO predictably affects the resulting magnetic moment. Presumably, the addition of Bi_2O_3 to the B_2O_3 matrix prefers to undertake web incorporations in the form of BiO_3^{3-} groups, their negative charge being compensated by pushing transition metals to bond within the network. Thus the concentration of bridging oxygen is thus decreased, i.e., equilibrium of eq. 1. is shifted to the right. This effect may be similar to that caused by Al_2O_3 but apparently stronger due to the higher deformability of the larger radius of Bi-ions.

Some of above mentioned ideas were found useful even in the subsequent studying of thermal properties of high temperature superconductors based on ceramic and glass-ceramic Bi-Ca-Sr-Y-Cu mixed oxides [81-85]. Concepts extension of the pattern dynamics of the glass structure and the associated glass transition from the undercooled liquid in order to understand the freeze-in phenomena as well as the solid-state amorphization of crystals under the given temperature and pressure regime as to determine the thermodynamic limits of the crystalline and glassy state was recently shown in details by Greaves and Sen [16].

Acknowledgements: The work was partially supported by the Grant Agency of AS CR contract Nos IAA1010404 and IAA100100639 and, furthermore, by the research work at the Institute of Physics under the Institutional Research Plan No AV0Z10100521.

Literature 17

- [1] G.W. Toop and C.S. Samis “Some new ionic concepts of silicate slags” *Canad. Metal. Quater.* 1 (1962) 129
- [2] G.W. Toop and C.S. Samis, “Activities of ions in silica melts” *Trans. Metal. Soc. AIME* 224 (1962) 878
- [3] C.R. Masson “Ionic equilibria in liquid silicates” *Proc. Roy. Soc. A*, 287 (1965) 201
- [4] C. J. B. Fincham and F. D. Richardson, „*The behavior of sulphur in silicate and aluminosilicate melts*“ *Proc. Roy. Soc. A*223 (1954) 40.
- [5] P.C. Hess “Structure and polymerization model for silicate melts“ *Canad. Mineral.* 15 (1980) 162
- [6] M. Hayashi, H. Ishii, M. Susa, H. Fukuyama, K. Nagata “Effect of ionicity of non-bridging oxygen ions on thermal conductivity of molten alkali silicates“ *Phys Chem Glasses* 42 (2001)6
- [7] B.O. Mysen: “*Structure and Properties of Silicate Melts*”. Elsevier, Amsterdam 1988.
- [8] S.A. Brawer, W.B. White “Structure of of silicate glasses“ *J. Chem. Phys.* 63 (1975) 2421 and *J. Non-cryst. Sol.* 23 (1977) 261
- [9] D. Virgo, B.O. Mysen, I. Kushiro “Anionic constitution of silicate melts“ *Science* 208 (1979) 1371
- [10] B.O. Mysen, F. Seifert, D. Virgo “Relation between the ionic structure and viscosity of silicate melts“ *Amer. Mineral.* 65 (1980) 690 and 867
- [11] J.B. Murdugh, J.F. Stebinm, I.S.E. Carmicheal “Effect of network-modifying cations in silicate and alumino-silicate glasses“ *Amer. Mineral.* 70 (1985) 332
- [12] R. Conradt “Chemical structure, medium range order of multicomponent oxide liquids and glasses“ *J. Non-Cryst. Solids*, 345/346 (2004) 16.
- [13] C. Rüssel “Redox state of glasses” *Glasstech. Ber. Glass. Sci. Technol.* 77C (2004) 149
- [14] J. Macháček, O. Gedeon, M. Liška “Group connectivity in binary silicate glasses” *J. Non-Cryst. Sol.* 352 (2006) 2173 and “Q-species in alkali-disilicate glasses” *Silikaty/Ceramics (Prague)* 47 (2003) 45
- [15] M. Liška, J. Macháček, O. Gedeon “Molecular dynamics of the Na₂O-MgO-SiO₂ systém“ *Glasstech. Ber. Glass. Sci. Technol.* 77C (2004) 267; M. Liška, R. Klement, J. Macháček, O. Gedeon ”Inverse thermodynamic modeling of glass from molecular dynamics results” *Phys. Chem. Glasses* 46 (2005) 108
- [16] G. N. Greaves and S. Sen „*Inorganic glasses, glass-forming liquids and amorphizing solids*“ *Advances in Physics*, 56 (2007) 1–166
- [17] V. Daněk, I. Nerad “Phase diagram and structure of melts of the system CaO—TiO₂—SiO₂“ *Chem. Pap. (Bratislava)* 56 (2002) 241
- [18] H. Doweidar “Volume of ionic sites in silicate glasses“ *J. Phys.: Condens. Matter* 19 (2007) 1561
- [19] B.O. Mysen, J. Shang “Evidence from melt partitioning that non-bridging oxygen in silicates are not equivalent” *Geochim. Cosmochim. Acta* 69 (2005) 2861
- [20] C.R. Masson “Anionic constitution of glass-forming melts” in *Proc. Int. Congress on Glass’77*,CVTS Publ. House, Prague, 1977, Vol. 1, p. 1. and *J. No-cryst. Sol.* 1 (1977) 134
- [21] I.M. Steevens, *Philips Tech. Rundschau*, 9/10 (1960) 337.

- [22] K. Závěta, J. Šesták “*Structure and Magnetic Properties of Fe-rich Oxide Glasses*“ in Proc. Int. Con. on Glass’77, ČVTS Publ. House, Vol. 1, p. 399, Prague 1977
- [23] Z. Strnad, “*Role of the glassy phase in bioactive ceramics*” Bioceramics 13 (1992) 317
- [24] Z. Strnad, J. Šesták “*Biocompatible glass-ceramics*” key lecture at the 2nd Inter. Conference on Intelligent Processing and Manufacturing of Materials, Honolulu 1999, proceedings p.123
- [25] Z. Strnad and N. Koga key lecture “*Compositional dependence of non-bridging oxygen ions in bioactive glasses*” key lecture in Forum of New Materials, Florence, Italy 1998, Proceedings p. 11.
- [26] N. Koga, Z. Strnad, J. Strnad, J. Šesták “*Thermodynamics of non-bridging oxygen in silica bio-compatible glass-ceramics for bone tissue substitution*” J. Thermal Anal Calor. 71 (2003) 927
- [27] P. Balta and E. Balta, “*Introduction to Physical Chemistry of the Vitreous State*” Abacus Press, Kent 1976, Chapter 3.
- [28] L.L. Hench “*Handbook of Bioactive Ceramics*” Vol.1, CRT Press, 1990, p. 7.
- [29] C.R. Masson “*Ionic distribution in liquid silicates*” Proc. Roy. Soc. A , 287 (1965) 201 and “*Ionic equilibria in liquid silicates*“ J. Am. Ceram. Soc. 51 (1968) 34.
- [30] M. Temkin „*Mixtures of fused salts as ionic solutions*“ Acta Physicochem. URSS 20 (1945) 4511 and Zh. Fiz. Khim, 20 (1946) 105 (in Russian)
- [31] K. Kawamoto and M. Tomozawa “*Prediction of immiscibility boundaries of ternary silicate glasses*” Phys. Chem. Glasses 22(1981)11.
- [32] H.M. Kim, F. Miyaji, T. Kokubo, C. Ohtsuki and T. Nakamura “*Bioactivity of Na₂O-CaO-SiO₂ glasses*” J. Am. Ceram. Soc., 78 (1995) 2405.
- [33] L. L. Hench, in P. Ducheyne and J. Lemons (Eds) “*Bioceramics*”, Vol. 523, Annals of New York Academy of Sciences, New York 1988, p. 54.
- [34] L.L. Hench, R.J. Splitner, W.C. Allen and T.K. Greenlee, J. Biomed. Mater. Res. 2 (1971) 117 and L.L. Hench and H.A. Paschal, J. Biomed. Mater. Res., 4 (1973) 25 and 5 (1974) 49
- [35] J.E. Davis “*Mechanisms of endosseous integration*”. Int. J. Prosthodont. 11 (1998) 391
- [36] J. Strnad, J. Protivinský, D. Mazur, Z. Strnad, A. Helebrant and J. Šesták, “*Interaction of acid and alkali treated titanium with dynamic simulated body environment*” J. Thermal Anal Calor. 76 (2004) 17
- [37] G.A. Holzapfel, R.W. Ogden (Eds.) “*Mechanics of Biological Tissues*“ Springer, Berlin 2006
- [38] T. Albrektsson, A. Wennerberg “*Oral implant surfaces: review focusing on topographic and clinical properties of different surfaces and in vivo responses*“ Int. J. Prosthodont. 17 (2004) 536
- [39] Z. Strnad, “*Glass-ceramic Materials: liquid separation, nucleation and crystallization*”, Elsevier, Amsterdam 1984
- [40] J. Šesták (ed) monograph “*Vitrification, Transformation and Crystallization of Glasses*” Special issue of Thermochim. Acta, Vol. 280/281 (1996)
- [41] J. Strnad, Z. Strnad, J. Šesták, K. Urban, C. Povýšil “*Bio-activated Titanium Surface Utilizable for Mimetic Bone Implantation in Dentistry: surface characteristics and bone-implant contact formation*”, J. Phys. Chem. Solids 68 (2007) 841
- [42] J. Strnad, Z. Strnad, J. Šesták “*Physico-chemical properties and healing capacity of potentially bioactive titanium surface*”, J. Thermal Anal. Calor. 8 (2007) 775

- [43] J. Šesták, Z. Strnad, J. Strnad, M. Holeček and N. Koga “*Biomedical Thermodynamics and Implantology aspects of Biocompatible Glass-ceramics and otherwise modified inorganic materials and surfaces*“ Advanced Materials Research 39/40 (2008) 329
- [44] P-I. Branemark, B.E. Breine, R. Adell B.O. Hansson, J. Lindstrom, J. A. Olsson. “*Intraosseous anchorage of dental prostheses*”. Scand J. Plast Reconstr Surg. 3 (1969) 81.
- [45] J. Šesták “*Magnetic properties and glass-formation of oxide glasses prepared by methods of fast cooling*“ Sklář a Keramik (Prague) 28 (1978) 321 and 353 (in Czech) and “*Crystallization behavior of rapidly quenched iron oxide containing glasses with regard to thermal and magnetic properties*” Wiss. Ztschr. F-S-Univ. Jena, Math.-Naturwiss. R32 (1983)377
- [46] K. Moorjani, J.M.D. Coey “*Magnetic Glasses*” Elsevier, Amsterdam 1984
- [47] B. Philips, A. Muan “*Phase equilibria in the systém CaO-Fe₂O₃-SiO₂ in air*“ J. Amer. Cer. Soc. 43 (1959) 413
- [48] S. Holmquist “*Ionic formulation of redox equilibria in glass melts*” J. Amer. Cer. Soc. 49 (1966) 228
- [49] B.O. Mysen, F. Seifert, D. Virgo “*Structure and redox equilibria of iron bearing silicate melts*“ Amer. Mineral 65 (1980) 867 and D. Virgo, B.O. Mysen, F.A. Seifert „*Relationship between the oxidation state of iron and structure of silicate melts*“ Washington Year Book 80 (1981) 308
- [50] G.S. Goldman “*Oxidation equilibria of iron in borosilicate glass*“ J. Amer. Cer. Soc. 66 (1983) 205
- [51] M. Pal and D. Chakravortya “*Structural study of iron borate glasses containing NiO and ZnO*“ J. Mater. Res., 13 (1998) 111
- [52] M.M. Layto, A. Herczok Glass Technol. 10 (1960) 50
- [53] B.T. Shirk and W.R. Buessem J Amer Cer Soc 53 (1970) 192
- [54] P.S. Rogers, J. Willimason, Glass Technol. 10 (1969) 128
- [55] J. Šesták “*On ferrimagnetic glass-ceramics based on B₂O₃ and MnFe₂O₄*“ J. Thermal Anal. 5 (1973) 669
- [56] K. Závěta, J. Šesták, V. Roskovec “*Magnetic properties of Mn-Fe-ferrite containing borate glasses*“ key lecture in the 3rd Czechoslovak Conf. On Magnetism in Kosice 1971; J. Amer. Cer. Soc. 55 (1972) 537 and Czech. J. Phys. B23 (1973) 837
- [57] O. Horie, Y. Syono, Y. Nakagawa, A. Ho “*Laser melted and roller quenched magnetic borate glasses*” Sol. State. Com. 25 (1978) 423
- [58] A. Bonnenfant, J.M. Fried, M. Mauer, P. Sanches, J. Physique 43 (1982) 1475 and 1707
- [59] C.J. Shinkel, G.W. Rothenau in book by I. Perins (ed) “*Physics of Non-crystalline Solids*“ Northern Holland, Amsterdam 1965, p.215
- [60] J.L. Shaw, A.C. Wright, R.N. Sinclair, G.K. Marasinghe, D. Holland, M.R. Lees, C.R. Scales, J. Non-Cryst. Solids 345/346 (2004) 245.
- [61] J. Chen, S. Cheney, G. Srinivasan J. Appl. Phys. 75 (1994) 6828
- [62] T. Shishido, K. Okamura, S. Yajima, J. Mater. Sci. 11 (1978) 1006
- [63] J.M.D. Coey, J. Phys. Colloque C6, Suppl.12, 35 (1974) 89
- [62] H. Akamatsu, K. Tanaka, K. Fujita, S. Murai “*Magnetic phase transitions in Fe₂O₃-Bi₂O₃-B₂O₃ glasses*” J. Phys.: Condens. Matter 20 (2008) 111 and 2352
- [63] [64] H. Akamatsu, K. Tanaka, K. Fujita, S. Murai „*Spin dynamics in oxide glass of Fe₂O₃-Bi₂O₃-B₂O₃ systém*“ J. Magn. Magn. Materials 310 (2007) 1506

- [64] [65] N. Ota, M. Okubo, S. Masuda, J. Magn. Mater. 54/57 (1986) 293
- [65] S. Nakamura, N. Ichinose, J. Non-Cryst. Solids 95/96 (1987) 984 and 984
- [66] S. Soeya, S. Nakamura, N. Ichinose, J. Appl. Phys. 68 (1990) 2875
- [67] S. Nakamura, Y. Hirotsu, N. Ichinose, Japan. J. Appl. Phys. 30 (1991) L844
- [68] J. Alton J, T.J. Plaisted, P. Hrma “*Nucleation and Growth of Spinel Crystals in a Borosilicate Glass*” J Non-Cryst Solids 311 (2002) 24
- [69] N. Koga, J. Šesták, Z. Strnad “*Kinetics of Crystallization in the Soda-Lime-Silica System*” Thermochim. Acta 203 (1992) 361.
- [70] N. Koga, J. Šesták “*Crystal nucleation and growth in lithium diborate glass by thermal analysis*” J. Amer. Cer. Soc. 83 (2000) 1753
- [71] Yu.D. Tretyakov “*Thermodynamics of Ferrites*” Khimia, Leningrad 1967 (in Russian)
- [72] J. Šesták “*Some thermodynamics aspects of the glassy state*” Thermochim. Acta 95 (1985) 459 and “*Thermal annealing during processing of metallic glasses*” Thermochim. Acta 110 (1987) 427
- [73] J. Šimšová, Z. Šimša, J. Šesták “*Electrical and structural properties of (Mn,Fe)3O4-B2O3 glasses between 400 and 1000 K*” J. Non-cryst. Sol. 30 (1979) 375
- [74] A. Kilinc, I.S.E Rivers, R.O. Sack “*The ferric/ferrous ratio of natural silicates in air*” Contr. Mineral. Petrol. 83 (1983) 136
- [75] P.G. Bray, A.H. Silver in “*Modern Aspects of Vitreous State*” (J.D. Mackenzie, ed), Butterworths, London 1969, p.92
- [76] J. Šesták, V. Šestáková, K. Závěta „*Glass-formation, phase relation and magnetic properties of the splat quenched system of laser melted (Fe,Mn)2O3-(B,Bi)2O3*“ J. Thermal Anal. 33 (1988) 789
- [77] W.J. Blackburn, B.P. Tilley, J. Mater. Sci. 9 (1974) 1265
- [78] T. Egami, J. Solid State Phys. 5 (1972) 261
- [79] R.W. Cahn, Contemp. Phys. 21 (1980) 43
- [80] K.A. Sablina, Pisma ZTEF (USSR) 24 (1976) 357 (in Russian)
- [81] J. Šesták “*Phase diagram, glass formation and crystallization in the Bi-Ca-Sr-Cu-O superconductive system*“ J. Therm. Anal. 36 (1991) 1639 and Pure Appl. Chem. 64 (1992) 125.
- [82] J. Šesták, chapter “*Oxide melt fast solidification and glass formation as a route for high-T superconductor preparation*“ in the book by A.V. Narlicar (Ed.) „*Studies of HTSC*“, Nova Sci. Publ., New York 1991, Vol. 7, p. 23
- [83] K. Salama, D. F. Lee “*Progress in melt texturing and glass-formation in superconductor oxide materials: a review*“ Supercon. Sci. Tech. 7 (1994) 193
- [84] B. K. Chaudhuri “*Some aspects of glass-ceramic superconductors*“ Bull. Mater. Sci. 18 (1995) 27 and Chinese J. Physics 38 (2000) 211
- [85] J. Šesták “*Modern materials and society*” chapter 19 in the book “*Heat, thermal analysis and society*” Nucleus publ. House, Hradec Kralove 2004, pp. 306



Chapter 18

Structural changes in glasses

18. STRUCTURAL CHANGES IN LIQUIDS, CREATION OF VOIDS, MICRO-MOVEMENT OF VIBRATION CENTERS AND BUILT-IN BLOKS TOWARD THE GLASS TRANSITION TEMPERATURE

Bořivoj Hlaváček, Jaroslav Šesták

18. 1. Model structure of liquids

Considerable fluctuations of liquid density toward the area of critical temperature, T_c , appear as measurable phenomenon, which are even visibly observable to a naked eye [1,6,26]. Under this critical temperature, liquid phase is factually prearranged or better separated into solid-like structures and certain unoccupied vacancies space called voids (in the conspicuous meaning of opening, hollowness or cavity), which are packed with gas-like molecules (so called „wanderers“). This realism has been known for a long time [2]. Some of the modern structural theories (such as the so called ‘mode coupling theory’ – MCT, which is describing the structural phenomena of liquid state at lower temperatures) are also based on a similar idea of local density fluctuation [3]. Such a conjecture of heterogeneities in liquid phase goes back to the assumption of semi-crystalline phase published early by *Kauzman* [4], as well as to the assumptions of coexistence of gas- liquid semi-structures [5,6] as related to numerous works of *Cohen, Grest* and *Turnbull* [7-10].

On one side, liquid structure can be empathized as a certain, mechanically sub-divided structure formed by blocks (in the conspicuous meaning of domains, icebergs or clusters) [6,43] (see Fig. 1. and Fig. 2.) and, on the other side, as an assortment of individual “semi-evaporated” units, which are subjected to non-linear anharmonic motions at high amplitudes [5, 6] (cf. Fig. 4.). It is assumed that highly non-linear oscillators maintain the individual character of their motions and herewith are perceived as the simple individual units about a monomer size [12, 42, 43]. Alternatively, the blocks are assumed to possess interconnected microstructure being composed of identical elastically bonded particles (see Fig. 2.) packed to the high compactness level eventually reaching the density of glassy phase.

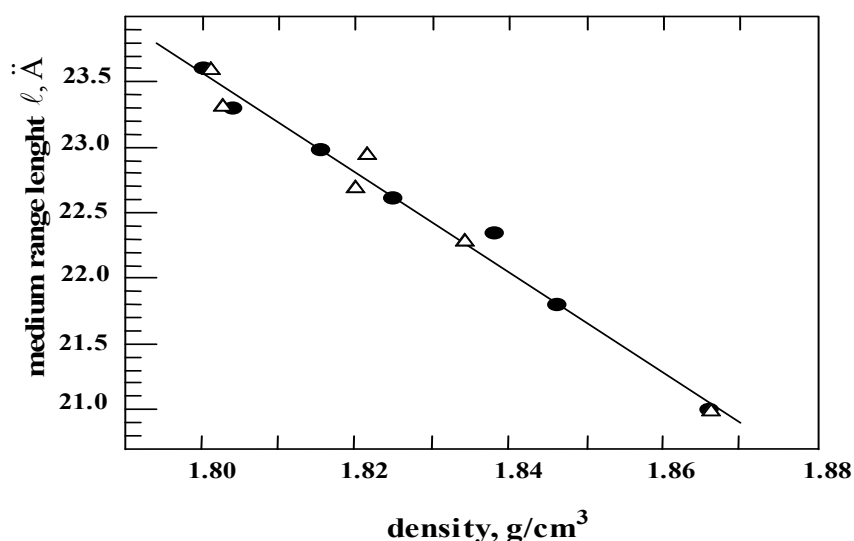


Fig. 1. Mean length of the heterogeneity fluctuation as a function of the glass density (assumed in the terms of MRO - medium range of order) estimated on the basis of sound velocity for two types of glassy materials displayed by the dense and empty triangles (according to *Surovcev* and *Novikov* [11,15,16, 106,107], the dependence compare with the data in Table 1., and § 18.4.1.).

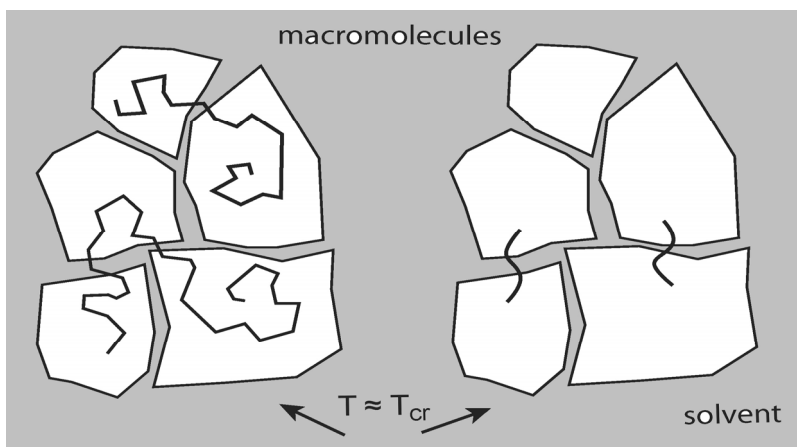


Fig.2. Schematic picture for liquid-like (and also glassy structures) composed of variously bonded blocks illustrating the degree of possible coupling. When the separation of macromolecularly interconnected blocks occurs above the crossover temperature, T_{cr} , it produces rubber elasticity, which is often associated with entanglements. Low molecular compounds [98-100] never

achieve such a rubbery state. The blocks' partition can be found by adequate rheological measurements of a shear viscosity [57-63] at very small gradients.

The blocks are characterized by a compression as well as by a shear module (see Fig. 3.), which can, in due course, reach the level of glassy state keeping the swarm of particles in one block in certain chorus. A dynamical equilibrium takes place between the block-particles and the semi-evaporated particles, which stuck between the blocks as well as between the semi-evaporated particles and the gas phase. These clusters are separated by loosely packed regions. The existence of accidentally distributed, random size molecular clusters in a viscous liquid has been discussed since the beginning of sixties until present days [5-11,13,70,71,79]. Inter-clusters regions, which are containing molecules whose vibrations are strongly anharmonic, are considered herewith to provide a mount towards non-deterministic vibration movements.

The blocks (and their inter-blocks bonding structure) form the focally contributing factor responsible for the significance of specific dynamical parameters, such as the viscosity or bulk elasticity of liquid sample. The blocks are also responsible for complex relaxation effects; because the interconnected linear oscillators are forming their structures interact. On the other hand, the semi-evaporated particles (acting as non-linear oscillators) are responsible for an erratic character of displacements due to the Brownian motion in liquids [14]. The semi-evaporated particles are correspondingly acting against the external pressure and exercise a so called 'push-aside' effect upon the individual blocks effective in their vicinity. Thus created gaps (cf. Fig. 4.) caused by straightforward amplitude jump, can be directed to any direction within amorphous phase. For the non-linear oscillators of semi-evaporated particles, the minimal change in the initial coordinates in phase space brings consequential and substantial changes in the motional trajectories of particles [73-77]. Therefore, particles can perform their oscillations on several different amplitudes [15,16] and these motions bring, in the same time, apparent elements of uncertainty. In most cases it is describable by the non-linear and non-deterministic theories [17-25] of chaos. For non-linear systems, characterized with the different initial coordinates, their subsequent positions and momentums cannot be determined beforehand and the differential changes and variations in initial conditions bring completely different trajectories in the phase space expression. The general rule for the non-deterministic chaos theories [17-25] is consequently reflected into the structure of amorphous soul of glassy state, which durably depends on the experimental course of action deliberated for cooling. It will surface its irregular character, which is subject of discussion connected with the uplift of potential bottom well (and the consecutive particle displacement exposed by the parameter λ as described in the following Fig. 5.).

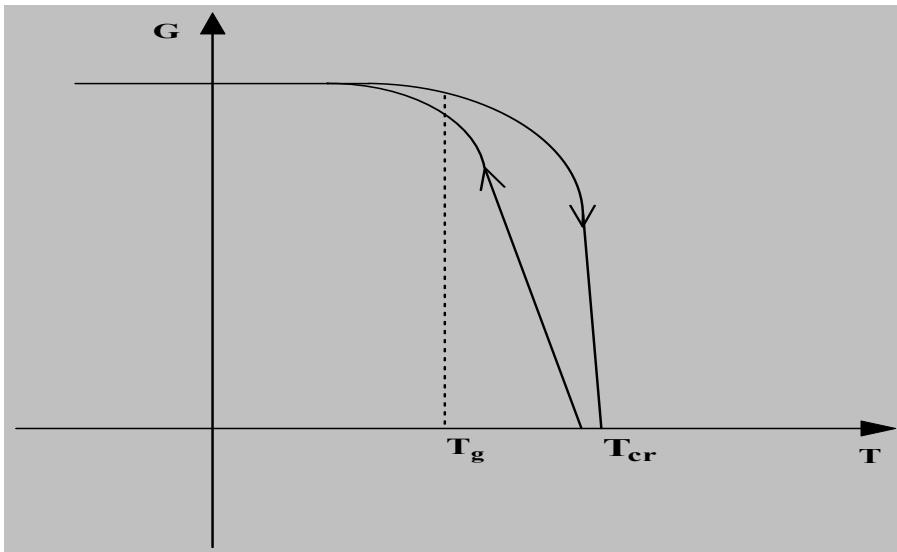


Fig. 3. Course of a shear modulus, G , for a amorphous low-molecular compound around T_g [98-100]. Note that the glass transition region, Temperature T_g , is characterized by the shear modulus $G \cong 10^9 - 10^{10}$ [N/m²], which decreases with increasing temperature and disappears at or closely above the

crossover temperature, T_{cr} , where the proportionality, $T_g \cong 0.8 T_{cr}$, is approximately applicable (compare with Fig.10., which is relevant for high-molecular compounds). Typical allied facts are the time-dependent hysteresis particularly evident during the sample consequent cooling.

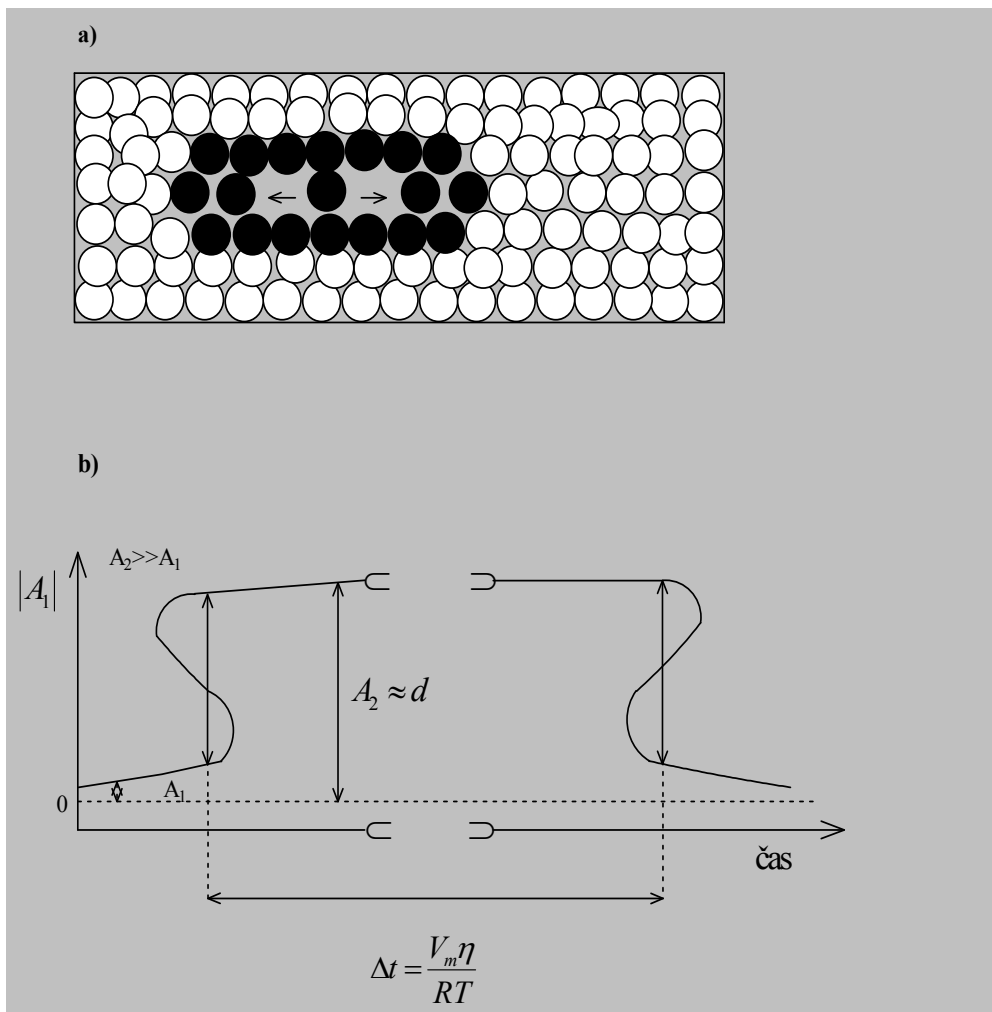


Fig.4. Schematic representation of the amplitude increase (pictured on vertical axis) of a non-linear oscillator causing the serial displacements of neighboring particles on the account of total expansion of the sample volume. (Note that time needed for particle diffusion displacement is depicted on the horizontal axis)

18. 2. Amplitudes of vibration movements below the critical temperature

For the displacement of block as an entirety, the maximum retardation time would reveal the state of interconnections inside of the block structure, characteristic of a given block size and its altering with temperature. It is assumed that the block size, together with maximum block retardation time, τ_{\max} , decreases with the temperature increment. The block progressively disintegrates as the critical temperature is gradually approached [15,16]. On contrary, the blocks bind themselves to form a more rigid structure as the temperature decreases below the crossover temperature, T_{cr} and further on below the glass transition temperature, T_g .

Down from the critical temperature, T_c , we can contemplate four subsequent and the most important temperatures, related to the characteristic points, which are gradually linking liquid and glassy states:

- 1) Boiling/condensation/liquid temperature T_b , characteristic for the first-order transition. At this temperature, vibrating particles are capable to depart their typically nonlinear motion around its vibration focus further loosing it at all to become a part of gaseous phase. Gaseous molecules are moving in translation and rotation modes in the whole volume, which, therefore, is missing vibrational locations characteristic for a condensed state.
- 2) Crossover temperature, T_{cr} , Liquid at this temperature starts to reveal elastic response in shear stress becoming viscously-elastic, which is characterized by a nonzero shear modulus build on energetic basis (An entropic elasticity of a rubbery network is not herewith accounted for [57-61] but is graphically illustrated upon the comparison of Figs. 3. and 10.).
- 3) Glass transition temperature, T_g . The shear modulus at this temperature overcome the value $\sim G \geq 10^8 \text{ N/m}^2$ having a tendency to go ahead its maximum value of $\sim 10^9 - 10^{10} \text{ N/m}^2$
- 4) Vogel's temperature T_v . Below this temperature the Brown move proceeds only in isolated regions mostly along the domain's interfaces. Below the Vogel temperature the spatial adjustment comes about the 'fixation of domains' (by e.g. chemical bounding) making a three-dimensional web within the sample. In the macro-scale the sample undertakes the property of a solid phase incapable of wholesale creep flowing. The time-honored Kauzmann temperature, T_K , may get coincidental with T_v if derived from the entropy plot.

The subsequent succession $T_c \geq T_b \geq T_{cr} \geq T_g \geq T_v$ can be recognized and the following model anticipated, which bears some distinctive characterization of vibration modes at different temperatures (or associated temperature regions) worth of mentioning beforehand of a needful identification. Referring to the simplest expression for P-V-T state equation, such as, for example, is the van der Waals equation, which is suitable to affirm the size of a minimum volume for the associated van der Waals isothermal curve setting thus the limits to the upper boundary of possible amplitudes of oscillators' vibrations. In the moment of the limit overcoming such a volume becomes unstable and can eventually expand toward the volume of gaseous phase. Below T_b , however, such a process of maximum volume expansion can undergo only those particles existing on the liquid surface. The bottom component on the liquid side of saddle part of the van der Waals curve (approximately at $0.385 V_c$, i.e., just a portion of critical volume, V_c) plays an important role for the size evaluation of non-linear vibration amplitude. The onset of the spinodal part of this van der Waals curve seems to pose a sensible restrain on the upper amplitude of vibration motion. If exceeded, this limit leads to a vacancy enlargement in which the particles in vicinity of high-amplitude oscillator have to absorb the vibration energy of particle by their own undertaking the avalanche-like

displacement. Above the liquid point, T_b , this type of an energy withdrawal from high-amplitude vibrating particle can only be performed effectively enough by neighborhood particles without further destruction of the sample netting through creating a gas phase in the sample bulk.

The intercepting level of a van der Waals curve for an isothermal case can be found easily for small volumes by seeking the intercept of spinodal curve [26] with the low volume of van der Waals curve. The intercepting point stays at the volume fraction of ~ 0.385 of a critical volume. At the boiling point T_b , non-linear movement stops for some semi-evaporated particles, as the attachment of particle to the so called “strange” attractor of *Lorenz* type [23,24] enlarges its basin of attraction and is eventually interrupted as the particle leaves the oscillatory movement for a gas phase. Between the crossover temperature and the boiling point, the high amplitudes of vibration are able to mechanically perturb the original bonding of blocks to such a level, that shear module disappears. At such vicinity of a crossover temperatures, a new element for standard behavior of materials is practicality of the substantial rise in the shear module, G , contributing the limitation of vacancy enlargement below the crossover temperature. Accordingly, the sample is able to store internally the elastic energy, W , connected to the shear module [27], namely, $W = 8 \pi G r_o (r_1 - r_o)^2$. The radius r_o represents the radius of a rigid sphere enveloping the particle and r_1 resembles the size of radius of the cavity. For example, the cavity of size $r_1 = 2 r_o$ (formed in a solid with the modulus $G = 10^{10} \text{ Nm}^{-2}$) needs about 125 kJ mol^{-1} [27], while in liquids of the *van der Waals-Eyring's* type, such level of internal void expansion leads to the so called *Trouton's* rule [2,6].

Below the T_{cr} the non-zero shear module has a drastic impact on the void size and on the extent of maximum diffusion jumps, which are depressed or even eliminated when temperature is dropping off. The presence of inter-block bonding will raise the shear module to a non-zero level forming thus an elastic network. The veracity of inter-block bonding in different ways has basic effect on the fragility phenomena, too [28,29]. Above the crossover temperature the diffusion process is driven mainly by small number of particles lying away of the block area, which are undergoing the vibration amplitudes switch. Increase of the free volume is associated with the vibrations slow down and their amplitudes escalation ($A_1 \rightarrow A_2$, see Fig. 4.) as well as by decrement of the local cohesion while mounting its internal energy. Therefore the change of free energy, Φ , is linked to corresponding local volume changes \mathcal{V}_1 , \mathcal{V}_2 and to the customarily used formula, $\{k_B T \ln (\mathcal{V}_1/\mathcal{V}_2)\}$. Below the T_{cr} temperature, less and less particles are eligible for the amplitude switch as the temperature goes down. The relation formed by the product of viscosity, size of diffusing particles and its diffusion coefficient and divided by absolute temperature and the Boltzmann's constant [30,31] is characteristic for the liquid state. It, however, is not retaining its initial form, which is orthodox for liquids because the elastic shear module begins to influence the particles' displacements. A most apparent impact of shear module can thus be demonstrated on the temperature dependence of the so called “alpha” and “beta” relaxation processes, which will be detailed in the following paragraph 18.8. As illustrated by *Buchenau* [32] for the T_g vicinity, the changes in average vibration amplitudes can be determined by experimental measurements of the *Debye-Waller* factor.

18. 3. First experimental justification of the structural heterogeneity of liquids

18. 3. 1. X-ray diffraction

The X-ray diffraction studies belong among the oldest investigational methods that could support the existence of dual structure in the bulk of liquids [33]. For a liquid these studies showed that the coordination number (characterizing the number of particles in the

closest vicinity) falls drastically in the area of temperatures between the boiling point and critical temperature T_c .

However, the distance characteristic of the first peak of radial distribution $g^*(r)$ of particles in their vicinity hardly changes as the temperature approaches the critical temperature region [33]. On the other hand, the experimental proof of compact structure (expressed through unchanged radial distribution $g^*(r)$) implies the existence of unoccupied vacancy space (voids) filled with “semi-evaporated” particles necessary to put together the overall volume of the sample characterized by the average density.

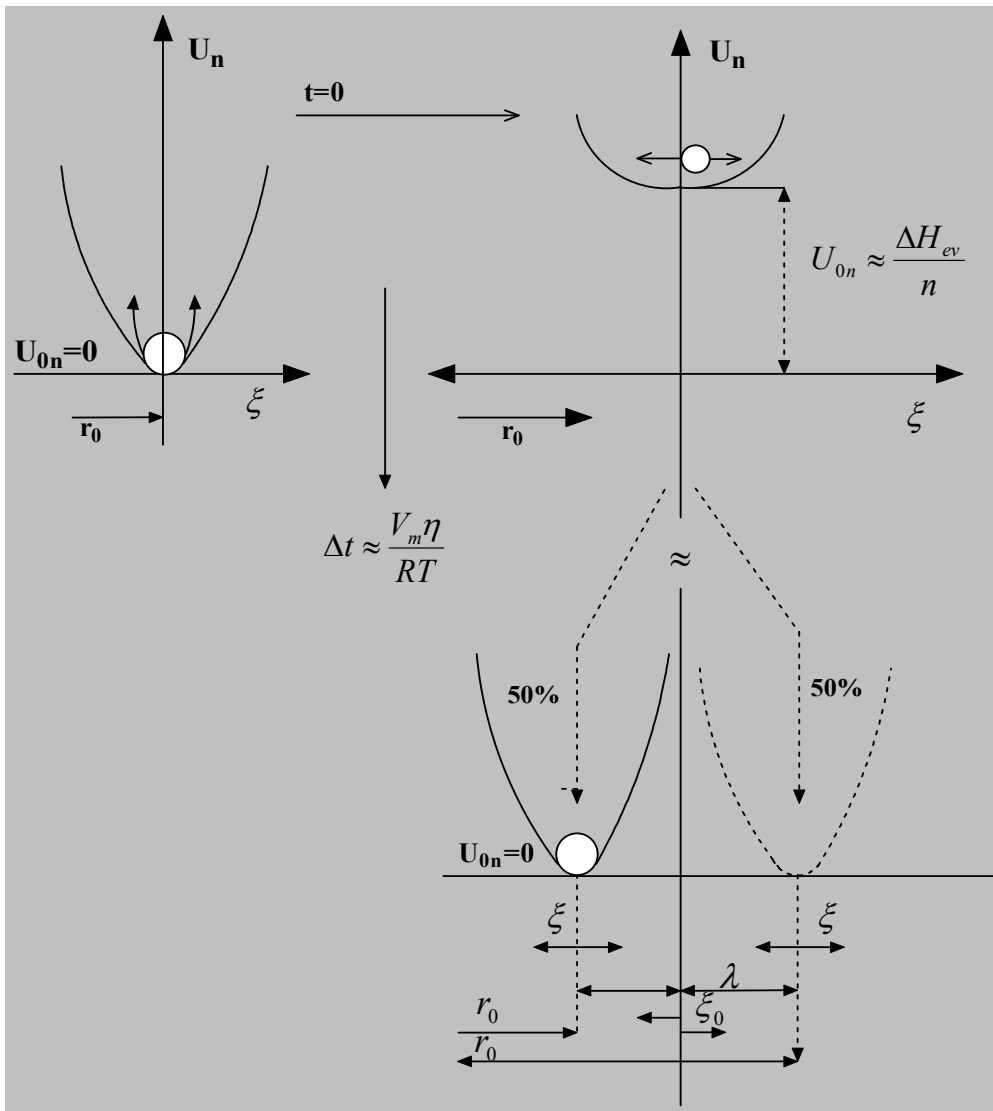


Fig. 5. Model of a void formation upon the changes of basic parameters λ (plotted on horizontal axis) characterizing the potential valley (ξ , r_0 , U_0), (pictured on vertical axis) with a consequent diffusional displacement, where ξ is the vibration independent variable conditioning the particle deviation from the bottom of potential valley. The level of a void increment is given by the energy of potential

valley and the serial shift of particles, shown in the previous figures 4 and 5, results in the reallocation of the bottom of potential valley. After the termination of enlarged space the semi-excited (and partially semi-evaporated) particle leaves its original position and sits in new position moved about the distance $\pm \lambda$. In the same time and at the first approximation, the original state of potential valley is recovered linked with the skew space thus available for the particle. The kinetics of newly sited particle is different lessened by the energy transmitted by migrated particle to its environment. Implication for released motion is that the conformation partition function is enriched due to new degree of freedom. These new variables are characterizing the λ -shift of the bottom of potential valley (cf. Fig. 4.) and are responsible for the avalanche escalation well observable at and above the T_g transition.

18. 3. 2. Distinguishing of local heterogeneity using the positron annihilation spectroscopy

The volumes of voids were exactly determined and reported in numerous papers on positron annihilation spectroscopy - PASCA [34-37]. These PASCA experiments provide the unusually high coefficients of thermal expansion in the vacancies comprising region where the volumes of voids are exceedingly sensitive to the temperature changes above the glassy transition as well as to the external pressure changes in the boiling point area. The coefficient of thermal expansion in vacancies areas is about ten to a hundred times as high as that in the block-containing areas. For an amorphous body (embedded as a whole piece of sample), the coefficient of thermal expansion α below the glass transition temperature, $T \leq T_g$, is roughly $\alpha_1 \approx 10^{-4} \text{ K}^{-1}$ while at $T \geq T_g$ is approximately $\alpha_2 \approx 4.1 \times 10^{-4} \text{ K}^{-1}$ declining very slowly with the change of glass transition temperature [93].

Possible discontinuity in properties for liquid structure turns out to be apparent locally at expanding spots, which bear a responsibility for a high coefficient of their thermal expansion. These locally expanding structures appear particularly above T_g and their number increases with rising temperature and the sample commences to consist of, at least, two kinds of particles. In the presence of such mechanically different units above T_g , the matter turns out to be rather mechanically heterogeneous and in this region around the glass transformation temperature ($T \leq T_g$) it is almost impossible to deduce any serious verdicts (as will be shown later in connection with the subsequent Figs. 7., 8. and 12.). In this light we like to emphasize that the matter structurally transforms in the region of T_{cr} and it seems to be a total historical blunder to conceive any extrapolations associated with changes from one area above T_{cr} to the other below the T_{cr} (such as that in the connection with negative entropies).

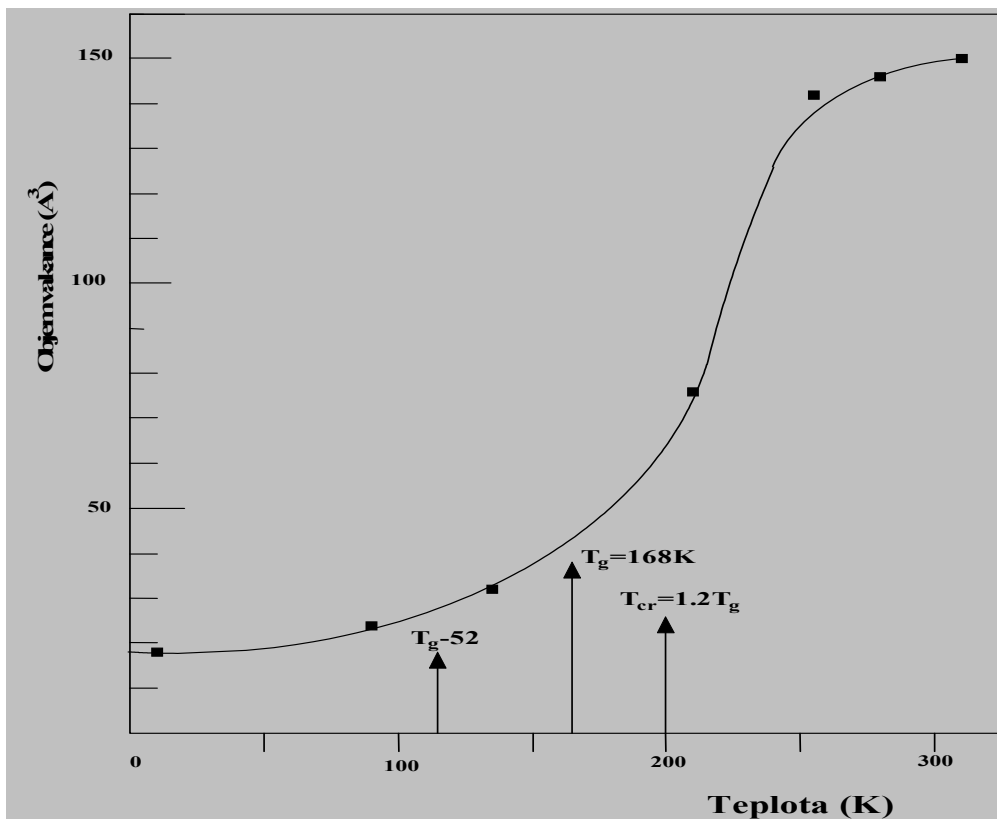


Fig. 6 . Upright is given the size of growing voids (in cubic angstroms) for polybutadiene polymer measured along with increasing temperature (horizontal) from the Vogel's temperature, over T_g , up to the crossover temperature T_{cr} by means of a positron annihilation spectroscopy [5,34-37]. Note that the

vertical notion 'objem' means volume and the horizontal one 'teplota' stands for temperature.

18. 3. 3. Three types of entropy contributions

Keeping up the connection with the semi-evaporated state, see Fig. 4., the entropy contribution, which is created inside the liquid system containing vacancies areas, can be potentially contemplated as shown in ref. [15,16]. For the inherent temperatures regions the entropy main contributions can be portrayed in three gradual ways. Below the Vogel's temperature, T_v the entropy $S \cong k_B \ln W_{th}$, is solely composed by the vibration energy of particles. In the region above the Vogel's temperature, $T \geq T_v$, but below, T_g , the entropy value enlarges by conformation part, i.e., $S \cong k_B [\ln W_{th} + \ln W_{conf}]$, which is associated with the release of particle's migration freeing thus their originally fixed positions in the sample space. Finally at $T \geq T_g$ where $S \cong k_B [\ln W_{th} + \ln W_{conf} + \ln W_{semievap}]$, the overall contribution extends as a result of semi-evaporated non-linear particles at a higher energy vibration level. The number of excited particles increases with rising temperature and acutely above T_{cr} it turns out to form the diffusion process due to high-amplitude changes.

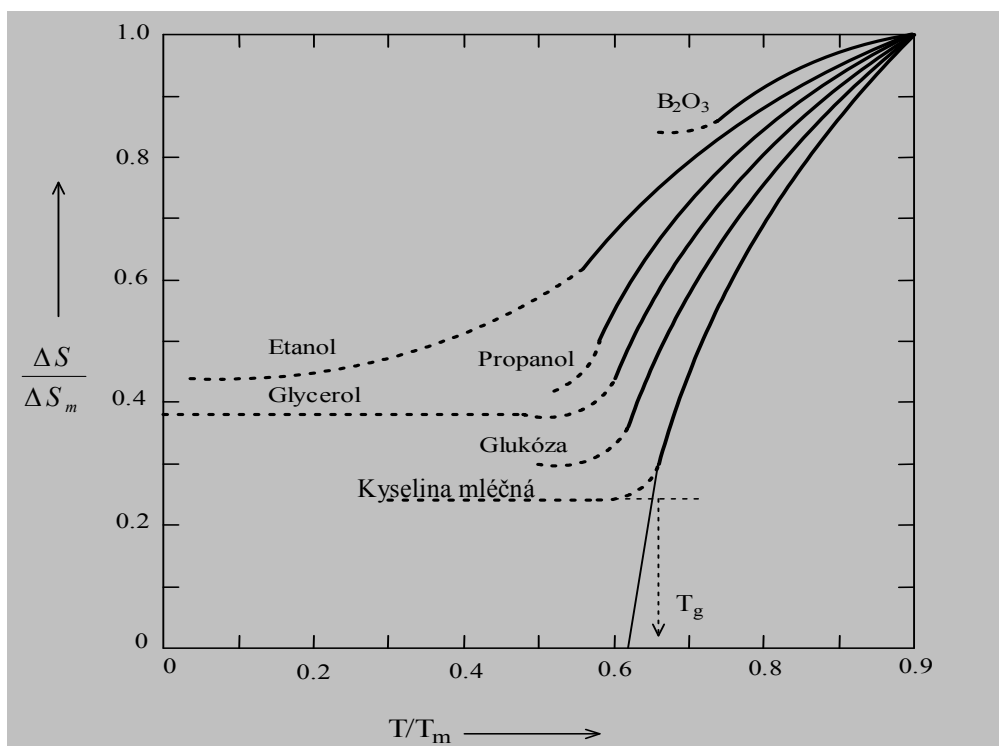


Fig. 7. Extrapolation towards negative entropy is impossible due to Kauzmann paradox [4]. The stepwise change of the entropy derivation occurs as a result of compositional/ structural changes in liquid state when „semi-evaporated“ particles form associates to individual non-linear oscillators.

Above T_g , from mechanical point of view the matter became composed by the other type of oscillators than those existing under the glass formation temperature. The notable increase of entropy above T_g is thus caused by growing number of newly formed non-linear oscillators endowed with the migrating focuses of their oscillations. Note that the Czech notion 'kyselina mléčná' means galactic acid.

These types of entropy changes brought together by three distinct contributions have been experimentally confirmed in recent works of Johari [38]. Thanks to the reports made on the basis of PASCA experiments, the vacancies areas have a rather distinct dimension, which is larger than the van der Waals volume, but smaller than the 0.385-fraction of critical volume V_c of the each particle's involved. Accordingly, the estimate of the enthalpy change can be connected with the semi-evaporated state. As shown by Hirschfelder [2], the total amount of evaporation enthalpy is required to produce an expansion of cavity to the level twice as high as is the particle diameter. As the first estimate for the energy (of void creation producing a cavity of the size of about 0.385 of the fraction of critical volume V_c) a proportionally smaller part of evaporation enthalpy, ΔH_{evap} , can be used. Therefore, the assumption of

$$\Delta H_{\text{semievap}} \cong \Delta H_{\text{evap}}/n$$

where n stays from 2 to 4 (or even higher), is an agreement with the PASCA experiments as well as with the estimate of viscosity figured out by *Eyring* [39,40] and his coworkers.

This reality was well understood by *Goldstein* [41] and furthermore applied in our approach [5,6,15,16,42,43] when presuming that T_g transition is connected with release of vibration motion of monomer (or dimer) units in a preferable rotational sense (such as the rotation of a benzene ring around the vinyl group in polystyrene chain [44]). Above the T_g area, the vacancy thus created can encompass a size larger than 10 \AA^3 typical for inorganic glasses associated with the substructure of SiO_4 . Below the Vogel temperature, the shift of the bottom of a potential well shaping the basis of diffusional motion appears in a much reduced manner taking part on a very limited distance (critically $\leq 1 \text{ \AA}$, preferably along the boundary of freeze-in blocks). Consequently *Buchenau* [32] presumes only 10^{-5} tunneling states per atom and about 10^{-3} states connected to the boson peak at very low temperatures.

Remarkable shifts of the well bottoms occur with the onset the liquid state adjacent to vanishing shear modulus. Disregarding the motion of side chains, then under T_g , the equation for entropy simplifies to comprise merely of a vibrational part so that the *Kauzman* paradox of negative entropy (the so-called “entropy crisis”) can never arise, because just one part of entropy literally disappears under T_g [42,43]. With disappearance of liquid state, only a part of entropy associated with the formulae ($k_B \ln W_{\text{semievap}}$) disappears below T_g where for solid polymers the value of c_p per atom is approximately “ k_B ” or “ $2k_B$ ” and forms a sort of analogy to the *Dulong-Petit* rule for metals [92].

Table 1 : Some characteristic figures of various materials

Brand name of polymer or type of the substance	Approximation of monomer polarizability [\AA^3]	Linear length of a domain for ~ 600 segments in [nm]	Linear length of a domain for ~ 300 segments in [nm]	Linear length of a domain for ~ 100 segments in [nm]	Linear length of a domain for ~ 20 segments in [nm]	Temperature of glass transition, T_g [$^\circ\text{K}$]
Polystyrene	11.6	1.90	1.52	1.04	0.61	353
Polyisobutylene	7.2	1.62	1.29	0.89	0.52	198
Polybutadiene	6.4	1.55	1.24	0.85	0.5	168
Polyvinylacetate	8.0	1.68	1.34	0.92	0.54	298
Polymethylmetakrylate	9.8	1.95	1.56	1.07	0.62	374
SiO_2	6.7	1.59	1.27	0.87	0.51	1473
GeO_2	7.6	1.65	1.32	0.91	0.53	957
B_2O_3	4.4	2.05	1.64	1.13	0.66	523

The molecular polarizability, α , of a monomer can be calculated by simple adding up the tabulated polarizabilities of individual atoms [104, 105,] ultimately using empirical corrections in the line with *Verkoczy* [6,106] such as $\alpha_{\text{molekul}} = \alpha_{C_n} + \alpha_{H_m} + \alpha_{C=C} + \alpha_{C \equiv C}$ where $\alpha_C = 1 \text{ \AA}^3$ for bonded carbon in chained organic molecules and $\alpha_H = 0.4 \text{ \AA}^3$ for hydrogen. Special attention must be paid to double and triple carbon bonds, if isolated, the former increases polarizability by 0.2 \AA^3 while the latter by 0.4 \AA^3 . Polarizability of nitrogen is about 0.9 \AA^3 and of oxygen about 0.8 \AA^3 whilst two coupled free electrons ($\sim \text{NH}_3$) bring an volume enlargement by 0.158 \AA^3 .

18. 4. Linear cooperative phenomena in the built-in blocks

18. 4. 1. Limiting values of block time characteristic

For limits of the time dependence, which is solicitous for a fastest time interval of retardation and/or relaxation, the time interval calculated from the sound velocity, v_{sound} , is most relevant. For solid blocks it is about $10^5 - 10^6$ cm sec⁻¹ having the minimal length of acoustic waves, λ_{min} , which are determined by the mesh size, r_0 . The relation $1/v_{\text{max}} \cong \tau_{\text{min}}$ and $v_{\text{sound}} \cong \lambda_{\text{min}} v_{\text{max}}$, where $\lambda_{\text{min}} \cong 2\Delta r_0$ becomes relevant. Substituting from the value estimate (as outlined above) the maximum frequency, $v_{\text{max}} = 10^{12} - 10^{13}$ sec⁻¹ in the sample body, the fastest time of material response in block, $\tau_{\text{min}} \approx v_{\text{max}}^{-1} = 10^{-12} - 10^{-13}$ sec can be obtained. On behalf of the longest time characteristic of a given material we can take the typical time connected with the permanent displacement in series of elements inside of the block space to be bonded together through the elastic force $\tau_{\text{max}} \cong n^2 \tau_{\text{min}}$ [5]. Ensuing from the subsequent text the most suitable number for $n \cong 600$ we can adapt the next table. (Note that for a particular choice of “n” value see explanative text of paragraph 18.4.2. below)

18. 4. 2. Estimate on the number of n-elements in the built-in blocks and, accordingly, on their size as related to the shear viscosity data

Numerous predictions regarding the size of the blocks are reported in literature by various authors [13,50-56] based upon different experimental techniques. Focusing our attention in a direction not yet fully familiar for the block size estimate we can direct our approximations towards rheology searching for yet unfamiliar parameters. The first one is characterized by the number of linear elements in a block at which blocks start to be interconnected in shear flow and become open for mutual interference when producing a non-zero contribution to the response of elastic shear module. A useful source of data, for the block's interactions, is the measurements of shear viscosity when the data are obtained at zero velocity gradients (already acknowledged for almost forty years regarding different structures of polymer melts with various molecular weight values [57-59]). These data show one common feature: in the dependence of shear viscosity on the number of roughly monomer (acoustical [12]) units in a chain with X sequence. As the first instance, the X- number is small and remains below a certain limit ($X \leq X_c$, where $X_c \approx 500 - 625$) where the polymer melt is characterized by constant and gradient-independent viscosity. In this particular case the module of shear elasticity is zero, as well as the first normal stress difference remains zero, too. The macromolecules are smaller than the critical block size ($X \leq X_c$) and the blocks, if subjected to shear flow, do not exhibit any mutual interference. A different level of viscosity, which rises upon a linear dependence on X, characterizes each polymer at this particular case. However, at the point when the critical value, X_c , is reached along the polymer chains, the changes in the rheological properties occurs. The block interconnections start to interfere through the overgrown size of macromolecules (cf. Fig.2.). For polymers with $X \geq X_c$, the melt viscosity in reliance on shear gradient starts to possess a non-Newtonian character as the gradient grows and the first normal stress difference starts to become an important flow characteristic. This effect is usually explained in connection with the chain entanglements, the concept of which was originally introduced upon sketchy pictures [44,60,61] (such as an evident phenomenon). On the other hand, the nature of couplings [60]) was left undeveloped resuming consequently an alternative in relation to account cooperative motions of molecular areas (also suited for the low molecular structures). The latter case corresponds more closely to a scheme presented herewith (cf. Fig. 2) being

supported by results of *Achibat* [70,71] when reporting a relationship between the domains and the entanglements. This model attributes the property of inter-blocks bonding either to the entanglements (as the individual blocks start to be interwoven by polymer network) or to the inflexible bonds of van der Waals type (or even to the bonds of a chemical nature). The inter-block bonding has a consequence in the development of non-zero shear module. Although different polymers have different levels of viscosity (or else chain flexibility), different molecular weight exhibits different levels of normal stresses. The numerical value of X_c (for the blocks' mechanical interference in shear flow) holds a universal character. Just quoting ref. [59], it subsists for polystyrene the value $X_c = 600$, for poly(vinyl acetate) $X_c = 600$, for polyisobutylene $X_c = 500$, for polydimethylsiloxane $X_c = 625$. If the level of critical interconnection is achieved in a linear sequence for polymers, the blocks become inter-bonded and get exhibiting the shear elasticity represented by shear modulus or by the first normal stress difference. Such elasticity created by flexible macromolecules stays entropy related. This type of interconnection has a "long distance character" relative to the block size and one single macromolecule can "over-bridge" several blocks, as well. In contrast to the blocks coupled by flexible macromolecules, the blocks can also be inter-connected by inflexible chemical bonds. This is the case for the low molecular weight substances under the crossover temperature. The blocks connected by inflexible bonds cannot be stretch to higher deformations and have to break up as the temperature is increased above T_{cr} . The inter-connection of inflexible blocks reflects such a self-character toward the internal energy as related to the contribution of shear module under the T_{cr} .

The other parameter not yet determined herewith is the crossover temperature itself. For the measurement purposes, the dependence of shear relaxation module on temperature in area of main phase transition can provide such a needed capture information [62,63] (cf. Fig. 10). For clarity reasons of having a better explanation within the text, some data of *Schultz* [59] for the main phase transition can provide such a desirable capture of information [62,63] (cf. Fig. 10.). *Alkonis* [63] and *Tobolsky* [62] are exposed for an ideal illustration. The crossover temperature T_{cr} (cf. Fig. 10.) is determined on basis of the shear elasticity of relaxation module related to the internal energy. The value X_c can be determined by sourcing the zero gradient viscosity curves. At this level of internal connection the blocks start to interfere in their flow properties. At the temperature T_{cr} the characteristic domain size become estimable. For lower temperatures, $T \leq T_{cr}$, the part of force responding to the external deformation has a component related to internal energy. Taking the approximate size of one oscillator unit in an interconnecting sequence from the expedient polarizability values [64,65] and using the interconnection number of X_c equal the typical 600, the characteristic size of a domain of about 6 cubic nm is realistically obtained (See Table 1). It is the most typical size of a sub-unit represented, for example, by pentane molecule (cf. § 18.7.1. and Table 2.). For the linear dimension of a domain following number $\sqrt[3]{6} = 1.81$ nm can be located. This seems to be in good agreement with the published values [13,50-56] obtained by different experimental techniques. As the polarizability of molecules is a simple additive property, the domain size can be easily estimated from the polarizability values of individual monomer units and from the X_c values, as hinted in Table 1.

18. 5. Source of diffusional movements on account of non-deterministic elements

As shown in the previous text, the ensemble of low-amplitude vibrating particles can represent reciprocal types of materials in both glassy and crystalline states. It is assumed that the individual vibrating particles are localized in the non-linear potential valleys, U_n , where

they perform oscillations attributable to the energy of thermal motion. The portrayal of a potential valley is shown in Fig. 5. Having the form of a pan in which the individual particles undergo linear mode of a vibration motion possessing the following fashion of potential valley, i.e., $U_n = U_0 + (1/2) f^\otimes \xi^2$, where $\xi^2 = (k_B T) / f^\otimes$ and $f^\otimes (= d^2U/d\xi^2 > 0)$, which is the coefficient of quasi-elastic force connected with a bulk compressibility modulus, $K = f^\otimes / r_0$ [27, 87, 88]. The value of U_0 is the reference level of internal energy, which can be taken equivalent to zero. The variable, $\xi = r - r_0$, endow with the deviation from the bottom of potential valleys (from an equilibrium position) and r_0 is defined as half of the distance separating the bottoms of two potential valleys (from an equilibrium position) and r_0 is defined as half of the distance separating the bottoms of two potential valleys. k_B is the Boltzmann constant. For liquids, the positional value of r_0 can be subjected to diffusion movements.

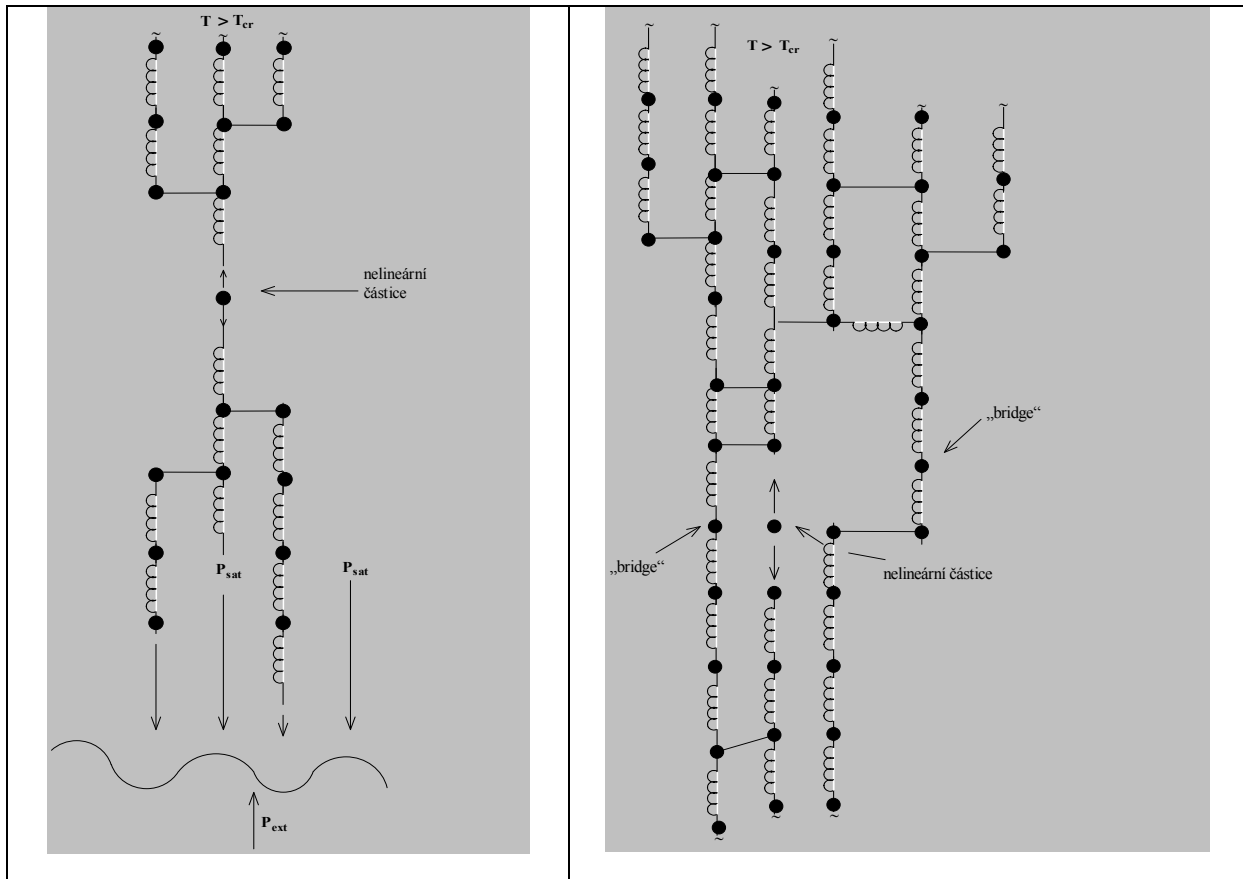


Fig. 8. Left: Illustration of a particle interaction characterized by non-linear oscillative motion within its surroundings (such as a liquid with zero shear modulus but with remaining web of bounding links inside certain areas-domains). Right: Similar example of a particle interaction but for the case of a solid with non-zero shears modulus and large-scale dimensional web of a macroscopic sample. Relaxation time for such a formed elastic structure with " n " as the number of linear elements linked in series is $\tau_{\max} \cong n^2 \tau_{\min}$, where τ_{\min} is the relaxation time of a single element of alone spring attached to a single friction center, for real materials $\tau_{\min} \cong 10^{-13} - 10^{-12}$ sec [101].

For a standard harmonic oscillation, average ξ value would be zero while for anharmonic oscillation average ξ becomes comparatively shifted [27]. For a further non-linear form of potential valley the third order parameter enters the equation as $(f^\otimes g^\otimes \xi^3)/3$ where the parameters f^\otimes , g^\otimes and c^\otimes depend on the distances of closets neighbors and can be determined from the experiments based on the values of the thermal expansion coefficient

and/or of the specific heat [87, 88]. Hence the non-zero coefficient of the thermal expansion, α , and the heat capacity, c_p , reads as

$$\alpha = (1/r_0)(g^{\otimes} k_B / f^{\otimes 2})$$

$$c_p = k_B \{ 1 + (3c^{\otimes} / 2f^{\otimes 2} + 15g^{\otimes 2} / 8f^{\otimes 3}) k_B T \}.$$

The expression for the potential valley has the extended form shown by *Heuer* and *Spiess* [12]. In order to deal with phenomena not customarily treated by solid state science, (such as boiling point, where the individual particles are escaping out of vibration modes) we have to suppose that even the individual parameters, U_{0n} , f_n^{\otimes} , g_n^{\otimes} , will pass through the discontinuity. This case was particularly analyzed for phase transitions in our previous papers [5,6,15,16,25,43,72]. Many classical solutions for particle motion equations subsist, but as the coefficients of these equations start to be time dependent (or even going through a discontinuity) the solution has to be handled through a completely different technique of so-called theories of deterministic chaos [17-22,73-77]. The characteristic situation, which is corresponding to the potential well uplift as well as the agitated particle life termination, are schematically shown on Fig. 4. and 5., where the discontinuity in parameter U_{0n} is schematically depicted, too. The most common feature of these high non-linear oscillators is the S-shaped double-value amplitude with attributable bifurcations points where the vibration amplitude changes its value drastically (cf. Fig. 4). As the consequence, the amplitude jump is followed by the particle “push-aside” effect, which increases the overall volume of sample (see Fig. 8. bottom). The components are subsequently relaxed through the displacements of particles in linear blocks (also Fig. 8.). For a long time, the relaxation fashion in linear blocks is mathematically described in an exactly mode leading to rationally described series of relaxation times [5]. These blocks are the actual source of continuity of particles’ micro-displacements and predictability of mathematical solutions. However, just a contrary behavior accommodates for highly non-linear particles, where the trajectories in phase space depend on starting parameters of the system [17-22,73-77,110-112]. The trajectories for these particles are obtained mostly through numerical solutions. However, two differentially separated points in phase space are leading to completely different trajectories. The most important conclusions, which follow up from the introduction of non-linear elements and which have an explanatory nature are following. There will not survive any identical motions of two non-linear oscillators in the sample. The two almost identical starting positions (defined by r and $m(dr/dt)$ and respective by r_{0n} and $m(dr_0/dt)$) will not lead to the identical trajectory in coordinates of position r and momentum ($m dr/dt$), neither to the equal displacements in r_{0n} . This attribute is the general feature of non-deterministic theories of chaos [73,17,77].

Therefore and furthermore voids created whilst the particle undergoes the amplitude switch, will not have regular shapes, positions or ordinary lifetimes and will not occupied a regular space volume, too. It is possible to observe at Figs. 4., 6. and 8., which is revealing that the average sizing of voids above T_g are substantial, reaching the values exceeding 100\AA^3 . Thus, the non-deterministic character of glassy transition stems from the presence of non-linear oscillators effective in the liquid system at $T \geq T_{cr}$ and throughout the non-deterministic character of oscillation extinction, when the system is cooled down to below T_g . The volume of the whole sample will depend on the thermal history of experimental processes performed. The irregular separation of particles in glassy state is thus a factual necessity. As the solid material softens and the non-linear vibrating particles make steps towards their existence in vacancies, the different mathematical views has to be inaugurated. The non-linear particle will perform the vibrations within a certain limiting cycle [17-22,73-77,114] and will be characterized with a certain limiting or average values of occupied volume. Considering

the non-linear particles, the vacancy volume or the energy associated with vacancy formation can be estimated. To form the vacancy space, the local free volume, which is smaller than critical volume (or even smaller than that indicated by the *Caillet-Mathias* line [1,2,39,40] for liquid phase) must be created. Also the energy comparable with fraction of evaporation enthalpy is needed. The sample is considered to be under an external pressure P_{ext} with a movable responding surface level (see Fig. 8.). For temperatures $T \geq T_{\text{cr}}$ the size of a locally created free volume indicates the validity of approximation, $U = \Delta H_{\text{evap}}/n$, where “n” is the ratio of critical and van der Waals’ volumes ($n \approx 2-4$). On Figs. 4, 5 and 8 there is exposed the ideal formation of vacancy by the action of symmetrical well getting restructured through a sudden annihilation of high amplitude oscillation. For $T \leq T_{\text{cr}}$ the effect of an elastic bridging has to be equally considered. For an elastic body and for a spherical shape of vacancies, *Frenkel* [27] gives the formula for the elastic energy, W , of vacancy erection in the form of $W = 8\pi G r_0 \Delta r_0^2$, where Δr_0 , is the size of a void opening and r_0 is the approximate radius of a particle. Combining simultaneous action of an elastic force with a viscous force we get the expression for energy increase of the well potential bottom uplift in the temperatures range, $T \geq T_{\text{cr}}$, i.e., $U = \Delta H_{\text{evap}}/n + W$. Under a non-regular character of phase trajectories it is assumable that the freeze-in points due to bridging must have a spatially irregular character. Freeze-in bridges need not be the sites with lowest possible energy and thus the glassy state need not be the state with the minimum of internal energy (metastability).

18. 6. Energy associated with the bottom uplift of a potential well participating in viscoelastic structures

The ‘push aside’ process, which is depicted in Fig. 4, has been studied intensively mentioning our previous papers [5,6,15,16,42,43,72]. Mathematical solutions describing the non-linear particle motion were applied to liquid systems. These solutions are available in classical form, for some cases of non-linear systems (cf. *Appleton* [82], *Martinsen* [81]). Referring to *Joos* [91] we can anticipate that the process of amplitude switch in vibration mode must be sudden, thanks to the S-shaped character of the amplitude curve (see Fig. 4.). Creation of a void with a vibrating particle indoors (illustrated in Fig. 4.) is supposed to be connected with changes in the shape of potential valley and thus with the variation of parameters inherent in the differential equations characterizing the motion of non-linear oscillators. It reveals a stepwise change in the parameter U_{0n} of an excited state of the given particle associated with a sudden disappearance of its high amplitude. Referring to Figs. 4. and 5. and 9., the process of a vacancy opening and its sudden closing is connected with the displacement of a well bottom by distance λ . This λ distance is factually a diffusion step connected with diffusional motions of non-linear particles. These particles are able to reach a higher amplitude level. The double values of functions authoritative for vibrational amplitude construct the focal point of perception of non-linear particle movements. The major difference between our approach [5,6,15,16,42,43,72] and that of *Eyring* et al.[39,40] is concealed in time sequence and, in fact, that vacancy in our approach, is actively formed by the feat of vibrating particle vicinity. We assume that the vacancy is formed through switching in the particle amplitude and a subsequent diffusion step can be made by way of the ensuing vacancy closure Linear particles within blocks in Figs 2, and 5 (with the exception of the block’s surface) do not encompass the option of double amplitude. Under T_g temperature, the particles in blocks are undergoing additional displacements of the bottoms of potential wells, however, the changes in U_{0n} , r_{0n} , are considered to be differentially small almost approaching zero.

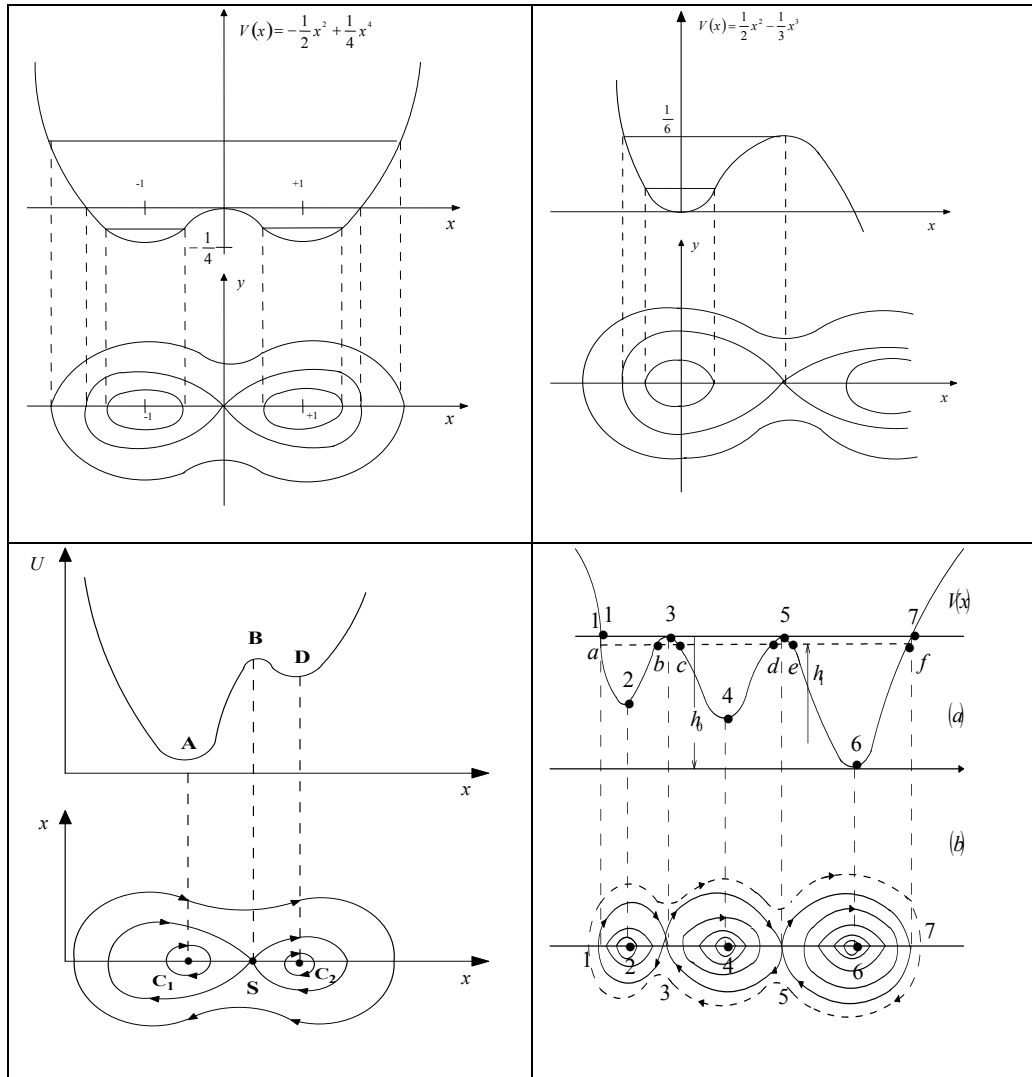


Fig. 9. Nonlinear course of the potential valley, given by the function $V(x)$, which is shaped by the particle swinging within neighborhood. Left above is shown the example of a symmetrical potential valley formed as an operate distortion while below is the asymmetrical representation. Portrayal of the potential, U , with a side variability can be assumed as being time dependent $U = U(t)$ [17,110-112] and can be interpreted in the relation with Brownian motion common liquids, see right bottom. When assuming a diffusion step of the length, λ , the shape changes of potential valley, which enables the particles' jumping [17,110-112], ordinarily proceed in a fluid state above the crossover temperature, T_{cr} . The product of diffusion, D , viscosity, η , and cross-section capture, σ , divided by the liquid temperature and the Boltzmann constant, $k_B T$, is constant and about 5 times lower than the unity [30,31] (approximately $\frac{D \eta \sigma}{k_B T} \cong 0.171$). Replacing cross-section capture, σ , by shift due to the particle interaction, λ , the equation is modified to its more generalized form [30,31], which, moreover, helps to elucidate the associations allied with the crossover temperature region.

These locally and spatially isolated “mini-displacements” come out in spatially limited sites (just inside blocks) linked with the secondary and/or third-order degrees of dissipations of energy maxims (with following text). Except negligible exemptions of block displacements (cf. Figs. 2. and 8.) the deformation of elastic solid blocks is characterized by the modulus of glassy state. This is not applicable for those particles laying in-between blocks and on the

block surfaces, which undergo displacements with the diffusional step, λ , as follows from Figs. 5 and 8. For the summative displacements inside the blocks applies the addition to all differentially small displacements in the form of $\sum_{n=1}^N \Delta r_{0n} = \lambda$ characteristic for the diffusional λ -macro-step. Thus the diffusion in liquids has to bear two components attached in series. Only the particles in blocks carry substantial friction and elastic forces in the present model. Non-linear particles play the role of source of erratic movements in continuum and are acting as “demiurges” of diffusion movements, while the linear particles are providing us the information about the forms of energy dissipation and about the relaxation times series.

Various modifications of potential valleys are shown in the above Fig. 9. They are reliant on a plausible extension of diffusion step λ via reallocating the particle across several indistinctive potential minims revealing that as a certain “slip” effect often inaugurated during diffusion above the temperature T_{cr} . However, below T_{cr} the restriction of diffusion length toward the lower values is anticipated due to the operative interference with shear modules.

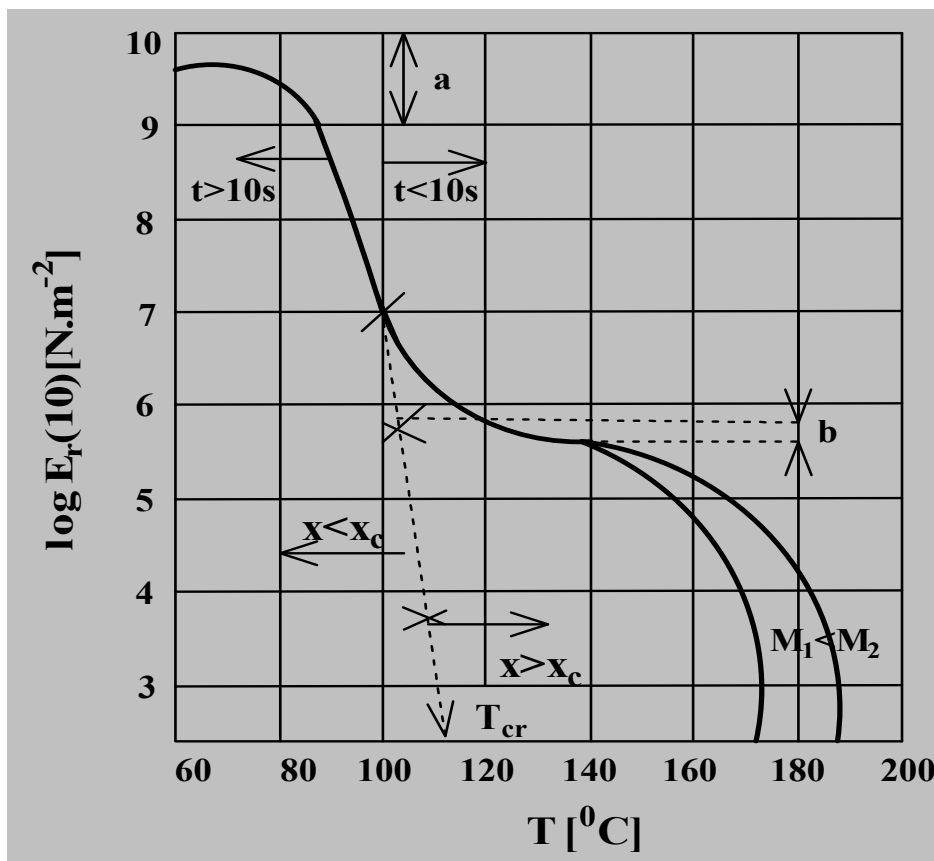


Fig.10. Instructive determination of the crossover temperature, T_{cr} , from the experimental course of relaxation modulus (depicted on the vertical axis) in the main intermediary zone. The graph provides the typical track of relaxation modulus for an ordinary polymer – polystyrene exhibiting two molecular weights, $M_1 < M_2$. Individual characteristic temperatures are determined from the curves at temperature region between

$T_g \approx 80 \text{ }^\circ\text{C}$, $T_{cr} \approx 112 \text{ }^\circ\text{C}$ [62,63] and the crossover temperature is ascertained by extrapolation of the modulus curve, which enlargement is associated with the energy changes due to prolongation. As has been explained in the paragraph 18.4.2., the value of X represents the unit sequence with index c referring to its criticality $X_c \approx 500 - 600$. Symbols “a” refers to glassy zone and “b” refers to a rubber-like plateau while the symbol “t” confers to a time-shift for the different time recording of experiment. Please note also that rubbery zone provides a link with the entropical elasticity and appears only for high-molecular substances while at the case of low-molecular substances is missing [98- 100] (compare Fig. 3.) and herewith is not accounted for.

18. 7. Structure of liquid state at higher temperatures when depicting the growing number of voids

Underlying principle for fluidity of the liquid phase above T_{cr} is located in the absence of shear modulus. Moreover, liquid keeps on their modulus in compression until critical temperature T_c while retaining its certain “structural shape up”. Above this temperature the centers of molecular oscillatory motion disappear and the motion of particles is then defined in the coordinates associated with the boundary of its gas storage space (container boundary) and/or with the room space of an external observer. In Fig. 11., the examples of liquid structure are revealed in connection with standard state equations in order to complete the previous interpretation related to overlap of vibrational amplitude to the region of higher temperatures, $T \geq T_{cr}$, cf. previous Fig. 4. and 8.

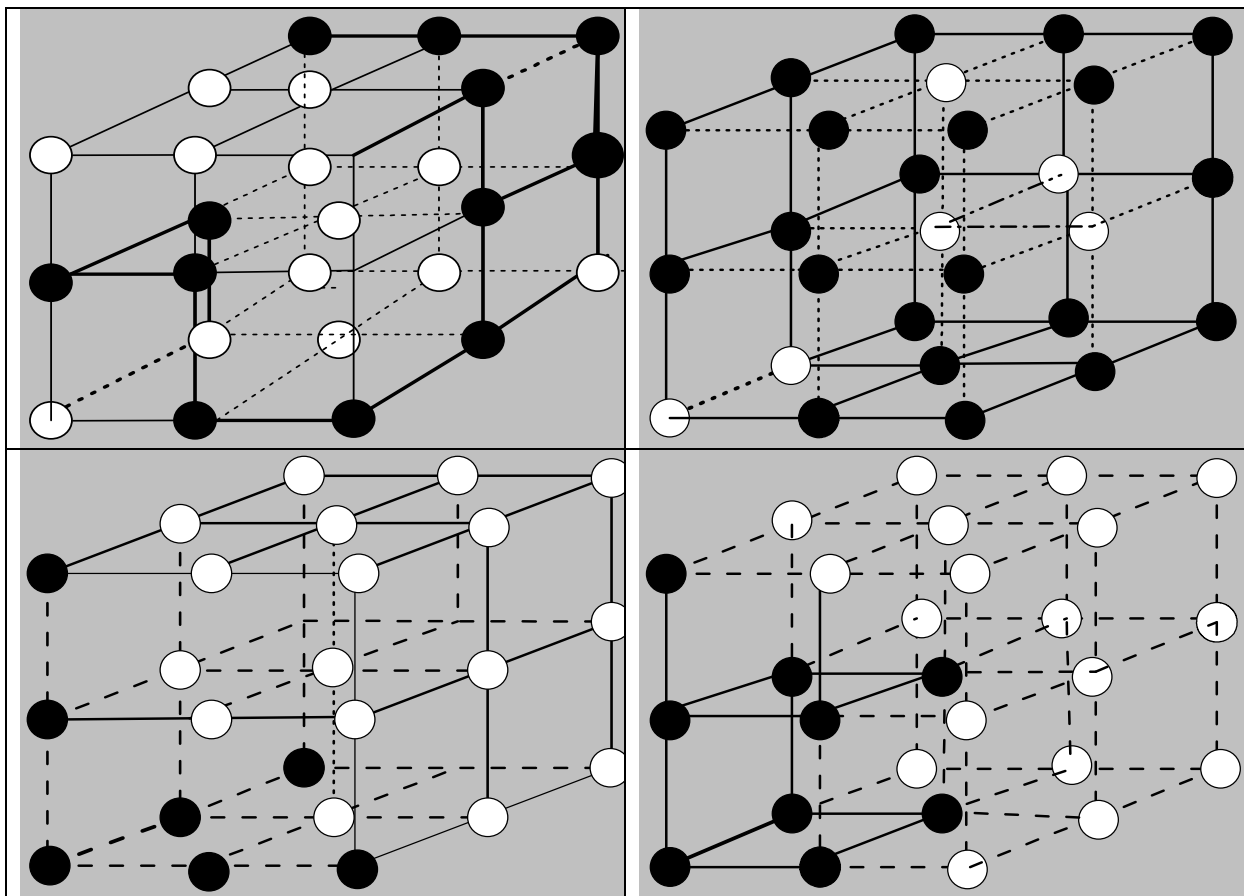


Fig. 11. Illustration of the inter-connected web of structural units revealed at various temperatures situated near critical temperature. Such an example is a pertinent concretization of preceding Fig. 4. specified for various state equations representing the structure of non-linear oscillators at the critical temperature, again. Upper, left: 3D-structure corresponding to the Dieterici equation at T_c [83- 86], which critical volume equals $2b$ and is often used to underline the critical state of helium (with the second constant of allied state equation). Upper, right: Approximate structure at the boiling point where the holes compos about 23 % of the total volume of liquid [15]. Bottom left: Structural model at T_c according to the Peng- Robinson equation [85] suitable for the description of most organic compounds with the critical volume $V_c = 3.9 b$ and the number of holes exceeding that of particles in the ratio higher than 1:2. Bottom right: Structure of Van der Waall's liquid [84] at critical temperature T_c . Increment of voids responsible for the interruption of a given phase in the vicinity of T_c when the number of voids exceeds that of particles in the ratio 1:2 and critical volume is $V_c = 3 b$.

18. 7. 1. Polarizability of molecules determining the critical volume

Polarizability represents the volume response of electron cloud of atom or molecule against the effect of a weak external electric field (where under the notion “weak” is meant the electric field of much smaller intensity in comparison with the electric interaction of the nucleus with orbiting electrons). For some organic molecules it is illustrated in the following table 2., which gives important information that at most compounds the volume allocated to a molecule at a critical temperature is about 50-55 times larger than the volume of its polarizability.

Table 2: Some characteristic accounts for selected compounds.

Substance	Critical volume [cm ³] $V_C \approx 55\alpha_{molekuly} N_{Av}$	Polarizability $\alpha_{molekuly}$ [Å ³] Note [Å ³] = 10 ⁻²⁴ cm ³	Critical volume divided by 55 N_{Av} as related to the polarizability	Notes: Remarkable deviations from the average value
ethan	148	4.47	55.1	
propane	200	6.3	52.8	
butane	255	8.2	52.1	
pentane	311	10.0	51.9	
hexane	368	11.9	51.9	
water	45	1.45	51.5	
ethanol	168	5.41	51.7	
propanol	220	6.74	54.4	
acetone	213	6.4	55.0	
Methyl-propylketon	301	9.93	50.5	
propion acide	230	6.9	55.5	
butter acid	290	8.38	57.6	
methylacetate	230	6.9	55.5	
HCN	139		89.3	Upper anomalies
methanol	117		59.0	„
toluene	316		44.4	Foot anomalies
p-xylen	378		45.8	„
benzene	260		41.6	„
naphthalene	408		38.7	„

It follows that at the critical volume is the average volume related to a single molecule described by the value equal to about fifty times of the relevant volume of electron cloud of each molecule [105]. The table provides beneficial estimate on critical volumes and basis of polarizability, which has correlation not only to critical volume but also dielectric constant, density of cohesion energy and so mutual solubility of liquids and its refraction index [104]. Upper deviation shows possible interconnection of molecules lasting up to the critical temperature (e.g. (H CN)₃). Bottom deviation for aromatic compounds reveals a certain orientation or better a mutual approach of the “face-to-face” arrangement. It is worth noting that polarizability is a decisive parameter adjacent to the notion of liquid state because liquid cannot bears a greater volume than is its critical volume. The least volume of liquid follows from approximations used in the state equation, which consequently provides the adjacent volume of resulting glass.

Polarizability of a molecule can be calculated by a simple adding of the contributions of individual atoms [104,105] whilst it is important to follow deviations both upwards (HCN) or downwards (naphthalene) occurring due to the orientation of aromatic nuclei at the molecule contacts.

18. 8. Alpha process and beta slow processes

For both the explanatory reasons and the basis of simplicity, we have provided our illustrations using only examples of translation forms of diffusion displacements. However, the rotational forms and the orientation forms of diffusion displacements in the angular coordinates, ϕ, ψ , (which signify rotation around the chemical bonds) possess the equivalent importance (see Fig. 12 - left). It was *Bueche* [44] and consequently *Eisenberg* [95] as well as *Boyer* [113,115] who correctly explained the origin of so-called β -slow processes connected with the orientation and side chains movements. (see Fig. 12 .). His explanations were similar to as much later on gives *Rosslar* [101-103], *Vogel*, *Rosslar* and coworkers [89, 67-69], related β slow process on Arrhenius a non-Arrhenius thermal relaxations. According to other authors [44-47,101], the reorientation motions of molecules are associated with a secondary beta- relaxation taking place in super-cooled liquids. We should note that besides the slow β -process some literature unveil fast β -process, which, however, is not accounted for herewith though having some particularities such as time $\tau_{\beta \text{ fast}} \leq \leq \tau_{\beta \text{ slow}}$ is rather shorter in turn of several orders and involves processes $\tau_{\beta \text{ fast}} \approx \tau_{\text{min}}$. Relaxation time $\tau_{\beta \text{ slow}}$ is much longer due to the limited mechanical succession of bonding elements.

Another mechanism, which cannot be excluded, is associated with an explanation given by *Johari* and *Goldstein* [41,49,109] who suggested that the β -slow processes are connected with the “islands-of-mobility” persisting even under T_g . Both approaches seems be acceptable. In our approach, however, the α process is connected with an infinite number of structural network “inter-connections”, which directly contribute to the elastic shear modulus under T_{cr} . As the structural skeletal networks of the macro-sample are formed under cooling, two different polymer motion are freeze-in at T_g . Namely we speak about either the rotational diffusion around chemical bonds at polymer chains and translation motion within certain macro-scale. It follows that one type of diffusion can become structurally deficient or better is bypassed and disappears at lower temperatures or can proceed simultaneously with the α -process. Thus some elements, which participate in β -slow processes, are structurally bypassed and below T_g . are considered as still mobile, Therefore they cannot contribute in a full extent to the shear modulus increment within T_g area and adhere them self fully to the elastic network, which forms the whole sample. This is evident at Fig. 12 , reproduced from the ref. *Eisenberg* and *Bueche* [44,95].

The n -number of elements connected by α -process is rather unspecified or better is only restricted by the sample dimensions. Chaining and interconnecting of the elements, which compose the α process go imaginary toward infinity under forming rigid viscous-elastic web of a solid sample. For the β -slow-process, the limited interconnection of joined elements, “ n ” is restricted inside of blocks (cf. Fig. 2.) by limited number of particles in linear block’s sequentionality. Thus the basic reciprocal temperature dependence of β -slow processes is often expressed by prime line of Arrhenius relation [50, 67-69,101-103,] as the temperature declines under T_g temperature. In this region the ability to have controlled motion of blocks through elastic network is for β -process different than that for α -process. Considering the variable inter-connection, the number “ n ” brings an additional point to the perception of differences of alpha and beta relaxation processes .The relaxation times, τ , of

components with decreasing temperature (for the α -process) increases up to infinity as a result of enormous growth of elements in the relaxation series [$\tau \cong n^2 \tau_{\min}$] [5,6].

The accrual of relaxation time τ due to the increment of number of elements “n” is the main reason for the disposition of shear modulus during cooling below T_{cr} . For the α -process the number of n-elements can increase up to infinity when an elastic web inside the sample is accomplished. Below T_{cr} the cause of relaxation time increase, below T_{cr} , is the strengthening of mechanical interconnection of network connections, cf. Fig. 8. On the other hand, the β -slow process is different because the interconnection characterized by “n” is adjusted at a relatively minor value $n_l = const.$, just composed by several units. Only for some exemptions “n” can reach a higher values and such a fragment have no other choice than to behave Arrhenian. With an increase of the environs density, which is surrounding mechanically interconnected friction centers, the whole aggregate behaves adequately frictionally. For the β_{slow} process the elements growth terminates with the interference of blocks’ boundary below T_{cr} as a consequence of dawdling of n- numeral, which is exhibited by a standard Arrhenius relation upon decreasing temperature. For this reason $\tau_{\beta, slow}$ is not increasing along with the escalating collection but follows mere Arrhenius growing trend at decreasing temperature.

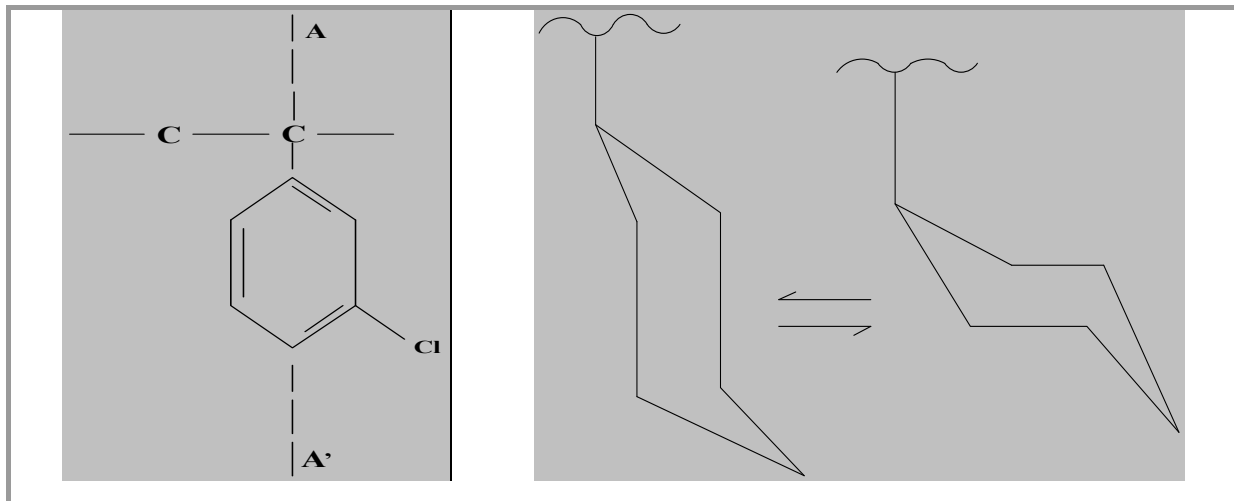


Fig. 12 . Left: Primary illustration of the creation of secondary maxima displayed for poly-m-chlorostyren by Bueche [44] showing its interrelation with the motion of the local groups of molecules as well as with the rotation around various axis given by the sub-units [90] . Right: Interesting maximum of inhibition is noticed by Eisenberg [95] and referred to Heijboer [96], Anet and Bourn [97] who associate secondary maxima with deflecting the pan of side chain ring so called „chair-chair-flip“. According to Eisenberg [95] it occurs, for example, under T_g temperature for the side group of cyclohexyl regardless if the main chain is constituted by methacrylate or other polymer with different characteristics (with T_g in the region of ± 50 C). Freeze-in of cyclohexyl brings a definite secondary maximum below T_g of its own polymer.

18.9. Boson peaks and the „Angel’s fragility“– a correlation between two of vastly separated temperature-judicious areas

In conclusion we can present a brief reflection about the possible nature of maxims of energy dissipation at ultralow temperatures - so called boson peaks. Recently, this area is intensively followed namely in connection with the sensitivity of material viscosity decrement at the main intermediary zone. It is worth noting that the mode of viscosity or the module

decline with increasing temperature in the T_g vicinity is incorporated into the expression of illustrious Angel's fragility, see ref. [108]). According to *Novikov* [106], *Surovtsev* [11,107] and *Angel* [108] it seems be possible to interconnect by a suitable correlations the region of ultralow temperatures (5-10 K) with the regions laying well above T_g and approaching T_{cr} , as to obtained some information about the nature of the processes associated with the motion of particles causing the boson maxims. Because the rate of the viscosity decrement in the main intermediary zone correlates with the lost of elasticity, it is possible to say that to the existence of boson maxims contributes such elements which are surviving on the domain interfaces. These places are the holders of the higher energies of internal energy which can be released to ultralow temperatures for non-linear motion.

Because the activation of vibration activity at low temperatures (5-10 K) is associated with the extent of the boson peak maximum bringing the later influence on the temperature dependence of viscosity above T_g (i.e. for the higher-temperature material flow) we have focus our attention to the particles which give rise to bonds holding the domains together and which factually form the web for shear strength of materials. The authors are accepting this approach though not yet fully comprehended in general because it is logical explanation for amorphous material behavior below T_{cr} when viscosity and onset shear elasticity is reliant on the quality of mutual domain interconnection showing the important role of inter-domain molecules responsible for the significance of linking and exhibiting their higher internal energy.

Using the above presumption on the coexistence of two structures interconnected via a nonlinear oscillatory motion we can arrive to the configuration of non-regularly ordered phase, which in the rigid state we can generally call glass. Overlapping of amplitude for nonlinear vibrations causes a non-regular and erratic Brown motion universal in all liquids. Non-regularity and inestimable trajectories of nonlinear vibrations provides its portrayal in the structure of glassy state, too. Transfer from liquid to solid is accompanied and also characterized by a sharp increase of shear modulus, which may enlighten the nature and help localization of the motion associated with the existence of boson dissipation maxims and consequently illuminating the nature of glass transformation.

The structural characteristics of many important glasses and melts (like silicates, borates, aluminosilicates, halides and chalcogenide) are drawn in more details (using the results of recent spectroscopy and scattering experiments) by *Greaves* and *Sen* [117] as well as other concepts extension of the dynamics of the glass transition from the supercooled liquid in order to understand the solid-state amorphization of crystals under temperature and pressure and to determine the thermodynamic limits of the crystalline and glassy state [116-118].

Literature 18

1/ H. E. Stanley *Introduction to Phase Transitions and Critical Phenomena*, Oxford University Press, New York 1971.

2/ J. O. Hirschfelder, C. F. Curtiss and R. B. Bird *Molecular Theory of Gases and Liquids*, Wiley, New York 1954, pp. 122 & 291.

3/ W. Gotze, L. Sjogren, Rep. Prog. Phys. 55 (1992) 241.

4/ W. Kauzmann, *Nature of the glassy state and the behavior of liquids at lower temperatures* Chem. Rev., 43 (1948) 219.

5/ B. Hlaváček, J. Šesták, L. Koudelka and J.J. Mareš, *Forms of vibrations and structural changes in liquid state* J. Therm. Anal. Cal. 80 (2005) 271

- 6/ B. Hlaváček, J.J. Mareš in J. Šesták (ed.) book: “*Fyzika struktur amorfních a krystalických materiálů*” (Physics of Structures of Amorphous and Crystalline Materials), Publ. House Pardubice University, Pardubice 2008 (in Czech)
- 7/ M. Cohen and D. Turnbull, *Molecular transport in liquids and glasses* J. Chem. Phys. 31 (1959) 1164 and 34 (1961) 120.
- 8/ D. Turnbull in: T. J. Hughel (ed.), *Liquids: Structure, Properties and Solid Interaction*, Proceedings of Symposium, Elsevier, Amsterdam 1965, pp. 6–24.
- 9/ M. H. Cohen and G. S. Grest, Phys. Rev. B20 (1979) 1077 and 21 (1980) 4113..
- 10/ G. S. Grest and M. H. Cohen, in: I. Prigogine and S. T. Rice (eds.) *Advances in Chem. Phys.*, Vol. XLVII, J. Wiley, New York 1981, pp. 455–525
- 11/ N.V. Surovtsev, J. Wiederich, A.E. Batalov, V. N. Novikov, M.A. Ramos, J. Phys. : Condens. Matter 16 (2004) 223.
- 12/ A. Heuer and H. W. Spiess, J. Non-Cryst Solids, 176 (1994) 294.
- 13/ E. Donth, *The Glass Transition, Relaxation Dynamics in Liquids and Disordered Materials*, Springer Verlag, Berlin, Heidelberg 2001.
- 14/ A. Einstein, *Investigation on the theory of the Brownian Movement*, Ed. R. Furth, Dover Publications, Inc., New York, N.Y. 1956.
- 15/ B. Hlaváček, V. Křesálek and J. Souček, “*The Anharmonicity of Motion in the Liquid State and its Consequences*” J. Chem. Phys., 107 (1997) 4658.
- 16/ B. Hlaváček, J. Šesták and J. Mareš, *Mutual interdependence of partitions functions in vicinity T_g of transition* J. Therm. Anal. Cal., 67 (2002) 239.
- 17/ M. I. Rabinowitz, A. B. Ezersky and P. D. Weidman, *The Dynamics of Patterns*, World Sci. Publ., Singapore 2000, pp. 239–279.
- 18/ H. J. Paine, *Physics of Vibrations and Waves*, J. Wiley, New York 1997.
- 19/ U. Ueda, *New Approaches to Non-linear Dynamics*. S.I.A.M., Philadelphia 1980.
- 20/ M. Tabor, *Chaos and Integrability in Non-linear Dynamics*, John Wiley, New York 1989.
- 21/ I. Prigogine and I. Stengers, *Order out of Chaos*, Bantam Books, New York 1984.
- 22/ D. Kondepudi and I. Prigogine, *Modern Thermodynamics*, J. Wiley, New York 1998, pp. 409–452.
- 23/ O. E. Rössler, Phys. Lett., 57A (1976) 397.
- 24/ E. N. Lorenz, J. Atm., Sci. 20 (1963) 130.
- 25/ J. Šesták “*Oscillation modes and modern theories of glassy state*” chapter 14 in the book “*Heat, thermal analysis and society*” Nucleus, Hradec Kralove 2004, p. 242
- 26/ P. G. DeBenedeti, *Metastable Liquids*, Princeton Univ. Press, Princeton, New Jersey 1996.
- 27/ J. Frenkel, *Kinetic Theory of Liquids*, Dover Publ. Inc., New Jersey 1955, p.12.
- 28/ V. Velikov, S. Borick and C. A. Angel, J. Phys. Chem., B106 (2002) 1069.
- 29/ W. Xu, E. I. Cooper and C. A. Angel, J. Phys. Chem., B107 (2003) 6170.
- 30/ H. J. Parkhurst Jr. and J. Jonas, J. Chem. Phys., 63 (1975) 2699.
- 31/ R. Zwanzig, J. Chem. Phys., 79 (1983) 4507.
- 32/ U. Buchenau and M. Zorn, Europhys. Lett., 18 (1993) 523.
- 33/ A. Eisenstein and N. S. Gingrich, Phys. Rev., 62 (1942) 261.
- 34/ J. Bartoš, Colloid Polym. Sci., 274 (1996) 14.

- 35/ J. Bartoš, P. Banduch, O. Šauša, K. Krištiaková, J. Krištiak, T. Kanaya and W. Jenniger, *Macromolecules*, 30 (1997) 6906
- 36/ D. Račko, R. Chelini, G. Cardini, J. Bartoš, S. Califano, *Eur. Phys. J.*, 32, (2005) 289
- 37/ Y. C. Jean, *Microchem. J.*, 42 (1990) 72 and 29 (1996) 5756 and Y. C. Jean, Q. Deng and T. T. Nguyen, *Macromolecules*, 28 (1995) 8840.
- 38/ G. P. Johari, *J. Chem. Phys.*, 112 (2000) 10957 and 116 (2002) 2043.
- 39/ R. E. Powell, W. E. Roseveare and H. Eyring, *Ind. Eng. Chem.*, 33 (1941) 430.
- 40/ S. Glasstone, K. J. Laidler and H. Eyring, *The Theory of Rate Processes*, McGraw-Hill Book, New York–London 1941.
- 41/ M. Goldstein, *J. Chem. Phys.*, 64 (1976) 4767 and 67 (1977) 2246
- 42/ Hlaváček, B., Souček, J., Prokůpek, L. and Večeřa M. “*The Thermal Entropy Concept and T_g Transition*”, *J. of Polym. Eng.*, 17(2), 111 – 137 (1997/1998).
- 43/ B. Hlaváček, J. Šesták “*Vibration perception of T_g transition*“ in Proc. of the First Slovak Glass Conference, by Slovak Glass Society, Trenčín University, Slovakia 2000, pp. 168-172.
- 44/ F. Bueche, *Physical Properties of Polymers*, Interscience, New York/London 1962, p.106.
- 45/ Gibbs, J. H., *J. Chem. Phys.*, 25, 185 (1956) and A1, 1417 (1963)..
- 46/ Gibbs, J. H. and Di Marzio, E. A., *J. Chem. Phys.*, 28, 373 (1958) and 43, 139 (1965)..
- 47/ Di Marzio, E. A. and Gibbs, J. H., *J. Polymer Sci.*, 40, 121 (1959) and Di Marzio, E. A. and Dowell, F., *J. Appl. Phys.*, 50, 10 (1979).
- 48/ E. Rossler, *Phys. Rev.*, 69 (1992) 1595
- 49/ G. P. Johari, *Phil. Mag.*, 81 (2001) 1935.
- 50/ E. Donth, *J. Non-Cryst. Solids*, 53 (1982) 325.
- 51/ T. Dollase, R. Graf, A. Heuer and H. W. Spiess, *Macromolecules*, 34 (2001) 298.
- 52/ J. Bartoš, O. Šauša, J. Krištiak, T. Blochowity and E. Rossler, *J. Phys. Condens. Matter*, 13 (2001) 11473.
- 53/ M. Beiner, H. Huth and K. Schroter, *J. Non-Cryst. Solids*, 279 (2001) 126.
- 54/ E. Hempel, M. Beiner, T. Renner and E. Donth, *Acta Polymer.*, 47 (1996) 525.
- 55/ U. Mohanty, G. Diezeman and I. Oppenheim, *J. Phys. Condens. Matter*, 12 (2000) 6431.
- 56/ S. A. Reinsberg, X. H. Qiu, M. Wilhelm, H. W. Spiess and M. D. Ediger, *J. Chem. Phys.*, 114 (2001) 7299.
- 57/ V. R. Allen and T. G. Fox, *J. Chem. Phys.*, 41 (1964) 337.
- 58/ T. G. Fox and V. R. Allen, *J. Chem. Phys.*, 41 (1964) 344.
- 59/ J. Schulz, *Polymer Material Science*, Prentice-Hall, Englewood Cliffs, New Jersey 1974, p. 337.
- 60/ J. D. Ferry, *Viscoelastic Properties of Polymers*, Wiley, New York–London 1961, p. 225.
- 61/ F. Bueche, *J. Chem. Phys.*, 20 (1956) 599.
- 62/ A. V. Tobolsky, *Properties and Structure of Polymers*, J. Wiley, New York 1960 p. 75.
- 63/ J. J. Aklonis, W. J. MacKnight and M. Shen, *Introduction to Polymer Viscoelasticity*, Wiley-Interscience, New York–London 1972, p. 42.
- 64/ B. Hlaváček, E. Černošková, L. Prokůpek and M. Večeřa “*The Transition Points in Liquid State and their Molecular Modeling*” *Thermochim. Acta*, 280/281, 417, (1996)
- 65/ D. R. Lide, *Handbook of Chemistry and Physics*, and

- 65/ Di Marzio, E. A. and Dowell, F., J. Appl. Phys., 50, 10 (1979). 82nd Ed., 10, CRC Press LLC, Washington D. C. 2002, pp. 160–174.
- 66/ M. Doi and S. F. Edwards, *Theory of Polymer Dynamics*, Clarendon Press, Oxford 1986.
- 67/ M. Vogel and E. Rossler, J. Phys. Chem., B104 (2000) 4285
- 68/ J. Wiederich, N. V. Surovtsev and E. Rossler, J. Chem. Phys., 113 (2000) 1143.
- 69/ M. Vogel and E. Rossler, J. Chem. Phys., 114 (2001) 5802 and 10883
- 70/ T. Achibat, A. Boukenter, E. Duval, G. Lorentz and S. Etienne, J. Chem. Phys., 95 (1991) 2949.
- 71/ E. Duval, A. Boukenter and T. Achibat, J. Phys. Condens. Matter, 2 (1990) 10227.
- 72/ B.Hlaváček, J.Shánělová and J.Málek, “ *Discontinuities in Amplitudes of Particles Micromotions Characterizing Phase Transitions in Liquid State*” *Mechanics of Time-Dependent Materials*, 3: (1999), 351.
- 73/ H.O.Peitegen, H.Jurgens and D.Saupe, *Chaos and Fractals, New Frontiers of Science*, Springer-Verlag, New York, (1992).
- 74/ M.J. Feigenbaum , *Physica* , 7D, 16 , (1978)
- 75/ D. Walgraef, *Spatio-Temporal Pattern Formation*, Springer Verlag, New York, Berlin, (1997),242-301.
- 76/ Z.Chvoj, J.Šesták and J.Tříška, *Kinetic Phase Diagrams; Non-Equilibrium Phase Transitions*, Elsevier, Amsterdam, (1991).
- 77/ H.L. Swiney and J.P.Gollub, *Physics Today* , August, 41 (1978)
- 78/ Y.C.Jean, *Microchem. J.*,42,(1990),72 and *Macromolecules*, 29,(1996), 5756.
- 79/ E.A. Porai – Koshitz , “ *Structure of Glass*” *Proceedings of the 4th All – Union Conference on the Glassy State* , Leningrad 1964.
- 80/ R.W. Gurney ,, *Introduction to Statistical Mechanics*” Dover Inc. , New York (1949).
- 81/ O. Martienssen, *Phys.Z.* XI ,448 (1910).
- 82/ E.V. Appleton, *Pilos.Mag.*,Ser.6, 41, 609 (1924).
- 83/ C.H. Dieterici, *Ann.Phys.*[3], 69,685, (1989)
- 84/ J.D. van der Waals ,” *Over de continuïteit van den gasen Vloeijsfoestand*”, Ph.D. Theses, Leiden , Holland , (1873).
- 85/ D.Y. Peng and D.B. Robinson, *Ind. Eng. Fundamentals*,15, 59, (1976).
- 86/ J.J. Martin, *Ind. Eng.Chem. Fundam.* , Vol. 18,2, 81,(1979)
- 87/ Ch. Kittel “ *Introduction to Solid State Physics*” 3rd , Edition,Wiley, New York, (1966) .
- 88/ Ch. Kittel, W. P. Knight, and M.A. Rudermann, *Berkley Physics Course, Mechanics*, Vol.1, (Mc Graw/Hil, New York, 1965) pp.227-229.
- 89/ A.P. Sokolov, E. Rossler, A.Kisliuk, D. Quitman : *Phys.Rev.Lett.*,71, 2062-2065, (1963)
- 90/ M. Ilavský, J.Hasa and J.Janáček, *Collection Czechoslovak Chem. Comm.*,33, 3197, (1968).
- 91/ G. Joos, “*Lehrbuch der Theoretischen Physik*“ 8 ed. Akademische Verlagsgesellschaft Geest-Portig K.G., Leipzig, (1954),p.84.
- 92/ D.V. van Krevelen , P.J. Hoftyzer ,, *Properties of Polymers* ,, Wiley , New York, London (1979).
- 93/ E. Rossler, *J. Chem .Phys.*, 92, 3725-3735, (1990).
- 94/ A.J. Curtis in J.Birks and Schulman (eds.) “*Progress in Dielectrics*” Vol.2, Wiley , New York , (1960) .

- 95/ A. Eisenberg, “ *The Glassy State and the Glass Transition*”, in J.E. Mark “*Physical Properties of Polymers*”, United Book Press, Baltimore 1993
- 96/ J. Heijboer , Ph.D. Thesis, University of Leiden, Netherlands (1972) .
97. A.L. Anet, A.J. R. Bourn, J. Amer. Chem. Soc., 89, 760, (1967).
- 98/ J. Jackle, Phil. Mag.. 56, 2, 113 – 127 (1986)
- 99/ J. Jackle, Rep.Prog. Phys.49., (p. 177) , 171- 232 (1986)
- 100/ R. Piccireli and Litowitz . J.Acoust. Soc. Am. 29, 1009 (1957)
- 101/ E. Rossler , Phys. Rev. Letters , 65 , 13, 1595 – 1598 (1990).
- 102/ T. Blochowicz , A. Brodin and E.A. Rossler , in T. Coffey and Y.P. Kalmykov “*Fractals, Diffusion, and Relaxation in Disordered Complex Systems*” A Special Volume of Advances in Chemical Physics, Vol. 133 , 127- 256 (2006).
- 103/ A. Brodin and E.A. Rossler, Eur.Phys., J. B., 44, 3-14 (2005)
- 104/ R.J.W. Le Fevre , Adv. Phys. Organ. Chem. 3 , (1965) 1
- 105/ B. Verkoczy , Saskoil Rep. No.113, Saskoil, Regina, Saskatchewan (1986)
- 106/ V. N. Novikov, Y.Ding, and A. P. Sokolov, Phys . Rev. E 71 , 1 (2005)
- 107/ V.K. Malinovsky and N. V. Surovtsev, Glasss Physics Chemistry , Vol. 26, 217 (2000)
- 108/ C. A. Angel , Science 267, 1615 (1995)
- 109/ D. Prevosto, S. Capaccioli, M. Lucchesi, P.A. Rolla and K.L. Ngai, *Does the entropy and volume dependence of the structural α -relaxation originate from the Johari–Goldstein β -relaxation?*, in the compendium "*Glass and Entropy*" (L.Wondraczek, R. Conradt, Edts) J. Non-Crystal. Solids, special issue Vol. 355, pp. 705–711 (2009)
110. N. Minorsky, „ *Non linear Oscilations* „, D. Van Nostrand Company , Inc. Toronto, New York , London (1983), pp.15 & 47.
111. H. Haken: “ *Synergetics* “ Springer, Berlin/Heidelberg , New York 1983
112. C.M. Bender and S.A. Orszag , “ *Advanced Mathematical Methods for Scientists and Engineers* “ , McGraw- Hill, New York 1978
113. R.F. Boyer, Rubber Chem. and Technology ,” *The Relation of Transition Temperatures to Chemical Structure in High Polymers*”, 36, 1303 – 1421 (1963).
114. E. Helflend “*Dynamics of Conformational Transitions in Polymers*” Science 226, 9, 1984
115. R.F. Boyer , “ ΔC_p T_g and Related Quantities for High Polymers:“ , J. Macromol. Sci.- Phys., B7 (3) , 487- 501, (1973)
- 116 C.A. Angell, Y. Yue, L-M. Wang, J.R.D. Copley, S. Borick and S. Mossa „*Potential energy, relaxation, vibrational dynamics and the boson peak, of hyperquenched glasses*“ J. Phys.: Condens. Matter 15 (2003) S1051–S1068
- 117 G. N. Greaves and S. Sen „, *Inorganic glasses, glass-forming liquids and amorphizing solids*“ Advances in Physics, 56 (2007) 1–166
118. L. Leuzzi, Th. M. Nieuwenhuizen, „*Thermodynamics of the Glassy State*“ Taylor and Francis, New York 2008



Chapter 19
Viscosity, diffusion and entropy

19. VISCOSITY, DIFFUSION AND ENTROPY: A NOVEL CORRELATION FOR GLASSES

Isak Avramov

19. 1. Introduction

Unlike the basic thermodynamic equations, the main relations of “kinetic” properties of the systems can be derived in the framework of some models only. This is valid for viscosity, for diffusion coefficients, for characteristic times etc. Therefore, some uncertainty is always present in equations expressing these properties. Here, we demonstrate this comparing diffusion, self diffusion and viscosity. According to the Stokes-Einstein law [1], diffusion coefficient of any particle of radius r is inverse proportional to viscosity

$$D = \frac{k_B T}{Br\eta} \quad (1)$$

where k_B is the constant Boltzmann and B is a dimensionless shape parameter. According to the absolute rate theory [2,3] the numerical coefficient is $B= 2$ while the Stokes formula gives $B= 6\pi$. As soon as Eq.(1) was derived for hydrodynamic motion, it is reasonable to test whether it is applicable at an atomic scale [4]. To do this Eq.(1) is rearranged to the form

$$\lg\left(\frac{D}{T}\right) = \lg\left(\frac{k}{Br}\right) - \lg\eta \quad (2)$$

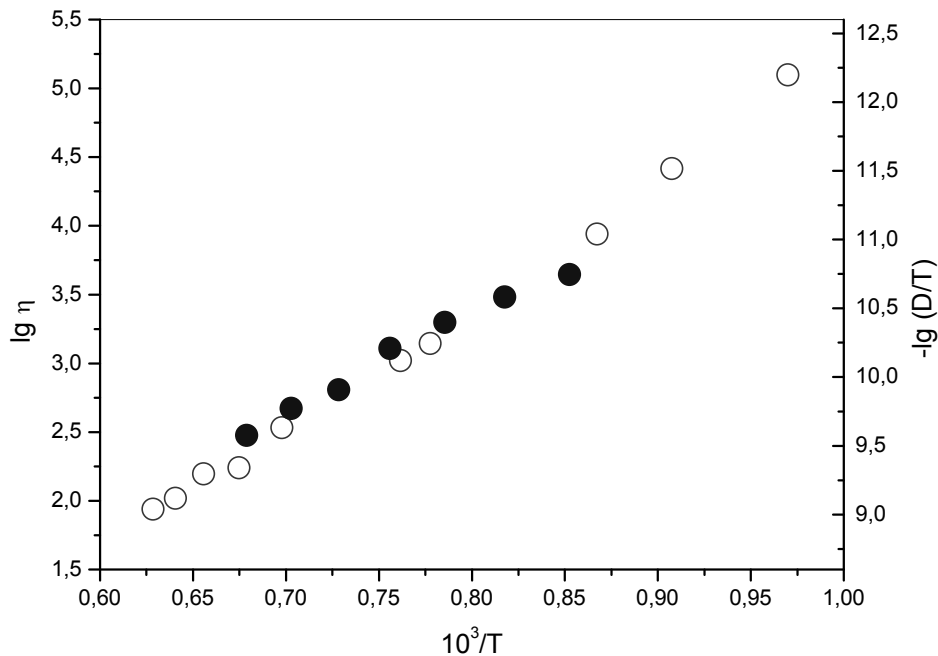


Fig.1 Arrhenius plot of viscosity, in [dPa.s] (open points and left scale) and self-diffusion coefficient, in [$\text{cm}^2/\text{s.K}$] (solid points and right scale) of SiO_2 in $\text{Na}_2\text{O} 2\text{SiO}_2$ glass according to experimental data published in Refs.[5,6].

In Fig.1 we compare viscosity data [5,6] (open points and left scale) of $Na_2O \cdot 2SiO_2$ glass and on self-diffusion data [5,6] of SiO_2 (solid points and left scale). It is seen that they go together reasonably well. The product $\lg\left(\frac{D\eta}{T}\right) = -12.2 \pm 0.1$ is in reasonable agreement with the

expected $\lg\left(\frac{k}{Bd_o}\right) \approx -13$ value. This is an indication that, for self diffusion, Einstein law is

still valid. However, the situation is different when we compare viscosity to diffusion coefficient of smaller and faster moving ions. Fig2 compares viscosity of $Na_2O \cdot 3SiO_2$ (open points) and diffusion coefficient [5] (solid circles and open triangles) of Na^+ ions. Not only is the activation energy of the two properties different. The difference is both quantitative and qualitative. The activation energies are not only different; they depend in different way on temperature. According to viscosity data this glass is quite fragile. However, the activation energy controlling diffusion is constant. The analyses of experimental data unambiguously demonstrate that the lower limit is the self-diffusion coefficient, i.e. the smallest particles for which this equation holds are the main building units of the systems. When particles are even this size they move faster and does not follow Eq.(1). Different models must be created to describe self-diffusion and diffusion as discussed in the following chapters.

19. 2. Mean stay time and mean jump frequency

There is a widespread fallacy that the mean stay time $\langle\tau\rangle$ is determined by the mean activation energy $\langle E\rangle$ according to.

$$\langle\tau\rangle = \tau_o e^{\frac{\langle E\rangle}{RT}} \quad (3)$$

If $f(E)$ is the probability distribution function that activation energy barrier of height E will appear, then, in continuous case, the average activation energy is given by:

$$\langle E\rangle = \int_0^{\infty} E f(E) dE \quad (4)$$

On the other hand, the mean stay time (and the mean jump frequency) could be determined [7,8] in two different ways:

$$\langle\tau\rangle_{diff} = \int_0^{E_{max}} \tau(E) f(E) dE \quad \text{resp.} \quad \langle\nu\rangle_{diff} = \frac{1}{\langle\tau\rangle_{diff}} \quad (5)$$

or

$$\langle\nu\rangle_{visc} = \int_0^{\infty} \nu(E) f(E) dE \quad \text{resp.} \quad \langle\tau\rangle_{visc} = \frac{1}{\langle\nu\rangle_{visc}} \quad (6)$$

It is important to note that $\langle\nu\rangle_{visc} \neq \langle\nu\rangle_{diff}$ as well as $\langle\tau\rangle_{visc} \neq \langle\tau\rangle_{diff}$. Therefore, determining certain "kinetic" properties it is of crucial importance whether we use Eq.(5) or Eq.(6). Meanwhile, the use of Eq.(4) is always wrong.

19. 3. Diffusion of fast moving ions

We already demonstrated that in the glass-forming systems, the diffusion coefficient of small, fast moving ions, is not controlled by the Einstein equation. These ions do not belong to the main network of glasses. Instead, they are known as network modifiers. So, they move along certain “channels” of the main network. For each kind of ions, the barriers in the channels are distributed according to particular probability distribution function $f(E)$. The motion rate is determined by Eq.(5) where E_{max} is the height of the maximal energy barrier that is inevitable to overcome. The successive jumps are strongly correlated and the motion from the origin to a distant area is a typical problem of percolation theory [9-11]. Therefore, in [9-11] it was suggested to define the critical activation energy E_c (the maximal height of barrier that is to be overcome moving along the channels) as the upper limit of the integral of the probability distribution function $f(E)$

$$\int_0^{E_c} f(E)dE = p_c^\infty \quad (7)$$

There are (see for instance [12]) a number of estimations of p_c^∞ . Here we use the formula

$$p_c^\infty = \frac{\Delta}{(\Delta - 1)Z} \quad (8)$$

where Δ is the dimensionality of the space and Z is the average number of ways along which ion could leave a given position. It was found [7,8,13,14] that for most of the inorganic glasses $Z \approx 10$, so that for the three dimensional space $p_c^\infty \approx 0.15$. The upper limit of p_c^∞ is determined by the assumption that the SiO_4 tetrahedra determine the number of channels as $Z = 4$, i.e. $p_c^\infty = 3/8$.

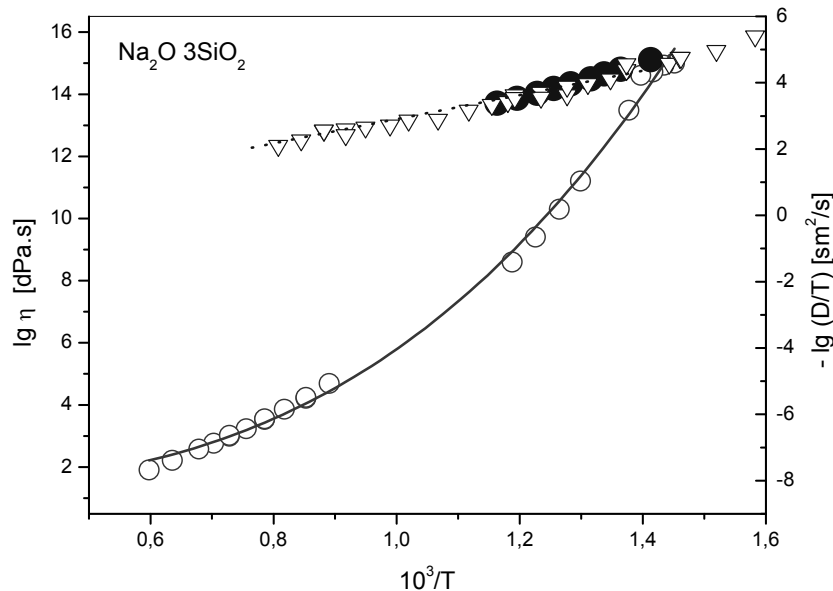


Fig.2 Viscosity of $Na_2O\ 3SiO_2$ (open points and left scale) and diffusion coefficient of Na_2O (solid points, open triangles). The solid line is according to Eq.(18); data are from Ref.[5].

19. 4. Percolation and nucleation

When nucleation kinetics is considered, percolation theory plays an important role in two ways. First, as we already demonstrated, it determines the diffusion coefficient. Second, nuclei are formed preferentially in “floppy” regions of the glass. Although these regions could be considered as density fluctuations, it is important to follow the local number of oxygen bridges BO per network former. Most of the glass forming systems is well described by the continuous-random-network model of Zachariasen [15]. Finney and Bernal [16] describe the glass structure by means of Voronoi polyhedra. Gupta and Cooper [17] used distorted polytypes to describe the structure of glass forming melts. The concept of average coordination number $\langle r \rangle$ is an important logical step in this line. According to Mott [18], the coordination number of covalently bonded atoms is given by the 8-N rule, N being the number of outer shell electrons. It can be connected to the constraint counting concepts of Phillips [19,20] and Thorpe [21-22]. It was shown in ref. [22] that the network is becoming rigid if the mean coordination (in the case of oxide glasses the number $\langle n \rangle$ of bridging oxygen per network former [23,24]) exceeds a critical value $\langle n_c \rangle = 2.4$. As soon as the network consists of SiO_4 tetrahedra, the percolation threshold at which network switches from rigid to floppy is $p_c = \frac{2.4}{4} = 0.6$.

Although for $\langle n \rangle > 2.4$ the glass is rigid, there remain some floppy regions. According to the percolation theory (see for instance [23,24]), the size R of the floppy region determined by the intermolecular distance d_o and the concentration p of the oxygen bridges as follows:

$$R = \frac{d_o}{(p - p_{cr})^\nu} \quad (9)$$

with: $\nu = 0.85$ for three dimensional systems. If the size R of the *floppy* region is smaller than the size r of the critical nucleus, the crystallization cannot start. Fig.3 shows the dependence of the floppy regions (solid line) on the concentration of oxygen bridges p determined according to Eq.(9). This dependence was tested experimentally [23,24]. First we study [23,24] fully reduced fresnoite $(BaO)(Ti_2O_3)_{0.25}(SiO_2)$. This composition is floppy, i.e. $p < p_c$. When cooled at 10 K/min it crystallizes at 35 K below the melting point. A series of fresnoite samples with $p > p_c$ were cooled at the same cooling rate. If the network was floppy, they should crystallize at about the same undercooling.

However, the size of the critical nucleus is larger than the size of the existing floppy regions. The crystallization cannot take place and cooling continues until the size of the critical nucleus is becoming smaller the size of the floppy regions. As the size of the critical nucleus can be determined directly from the undercooling at which crystallization starts, it can be compared to the size of the floppy regions determined by the percolation theory (Eq.(9)). The solid points in Fig.3 are sizes of the critical nuclei determined [23,24] from cooling experiments.

19. 5. Viscosity

The self-diffusion and viscosity concern the motion of the main building units of the system. These particles do not see a network with channels to move along. The network is created by them, so it changes with a rate comparable to the rate of motion of the investigated

particle. Therefore we are at situation when Eq.(6) is to be applied. Note that frequency decays exponentially with the activation energy.

$$\nu(E) = \nu_0 \exp\left(-\frac{E}{kT}\right) \quad (10)$$

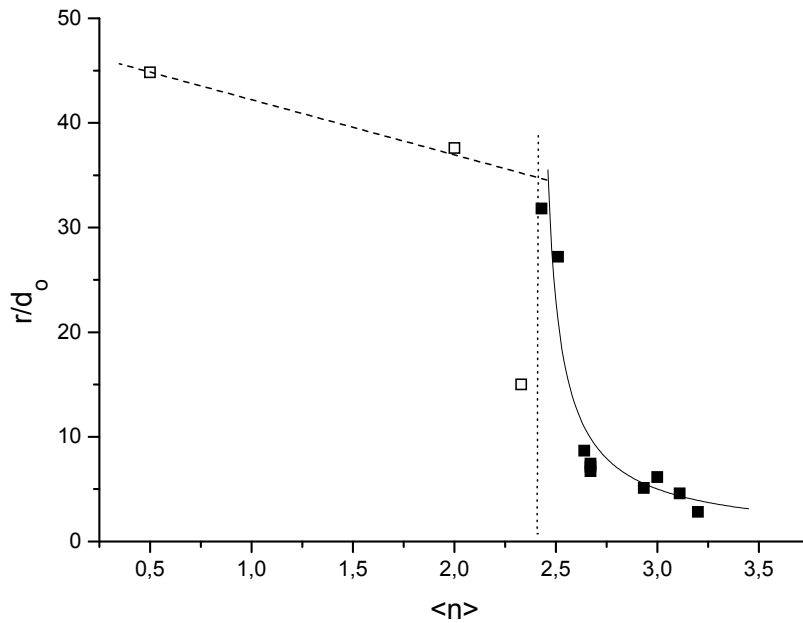


Fig.3 The size of the critical nucleus (the number of molecules in radius r/d_0) against $\langle n \rangle$. The solid line is according to eq.(9). The dashed lines is empirical. Qualitatively it accounts that even in the floppy region there still remains a slight dependence of the diffusion parameter on the number of oxygen bridges.

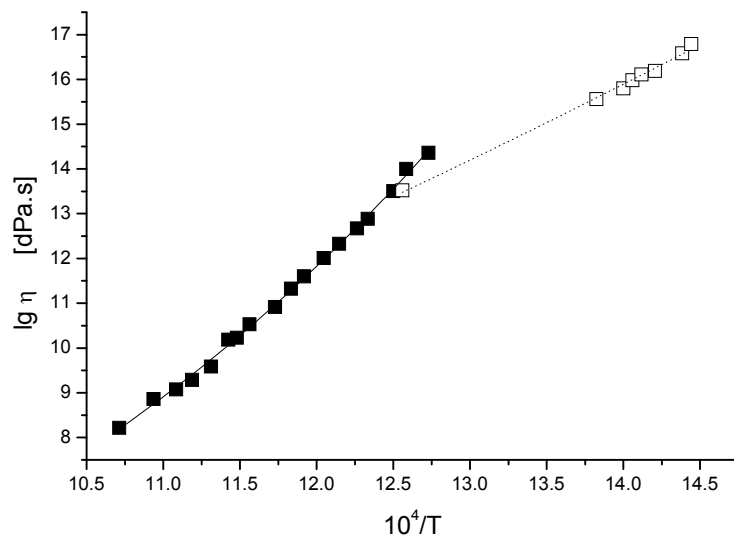


Fig.4 Equilibrium (solid points) and non-equilibrium (open points) of viscosity of of a standard soda-lime silicate glass NBS710. Lines are according to Eqs.(18,28)

At first site it seems that one problem is replaced with another: instead of creating a model for determining the average energy barrier $\langle E \rangle$ the model deals with the determination of $f(E)$. However, there is one very important advantage: Since ν decays exponentially with the activation energy, of significance for the integral is only the low energy part of the probability distribution function. Therefore, a sufficiently accurate result can be obtained easily. This is because most of the probability distribution functions differ near the maximum but are getting together away from the maximum. If the jumps are considered as a sequence of independent events the probability distribution function is represented by Poissonian law

$$f(E) = \frac{\exp\left(\frac{E - E_{\max}}{\sigma}\right)}{\sigma \left(1 - \exp\left(-\frac{E_{\max}}{\sigma}\right)\right)}, \quad E \leq E_{\max} \quad (11)$$

The average jump frequency is obtained introducing Eqs.(10,11) into Eq.(6)

$$\langle \nu \rangle = \frac{\left[1 - e^{-\frac{E_{\max}}{RT} \left(\frac{1}{RT} \frac{1}{\sigma}\right)}\right]}{\left(\frac{\sigma}{RT} - 1\right) \left(1 - e^{-\frac{E_{\max}}{\sigma}}\right)} \nu_o e^{-\frac{E_{\max}}{\sigma}} \quad (12)$$

For $RT < \sigma < E_{\max}$, the term to the left of ν_o , as compared to the exponential term on the right-hand side, is a weak temperature function of the order of unity. Therefore, one can use the approximation:

$$\langle \nu \rangle \approx \nu_o e^{-\frac{E_{\max}}{\sigma}}, \quad \nu_o = \nu_o \frac{RT}{\sigma} \quad (13)$$

Eq.(13) is of little use, unless dispersion σ is expressed through some known and easily measurable variable. There is a strong relationship between the dispersion σ and the entropy S of the system:

$$\sigma = \sigma_g \exp\left[\frac{2(S - S_g)}{ZR}\right] \quad (14)$$

Here σ_g is the dispersion at the reference state with entropy S_g and $Z/2$ is the degeneracy of the system, i.e. Z is the number of escape channels available for the moving particle and each channel can be used in two directions. Taking into account that viscosity is inversely proportional to the mean jump frequency the viscosity can be expressed through Eqs.(13 and 14) as:

$$\lg \eta = \lg \eta_o + \frac{R_{\max}}{\sigma_g} \exp\left[-\frac{2(S - S_g)}{ZR}\right] = \lg \eta_o + \left(\lg \frac{\eta_g}{\eta_o}\right) \exp\left[-\frac{2(S - S_g)}{ZR}\right] \quad (15)$$

where $\lg \eta_g$ is viscosity at the reference state. Note that $\lg \eta_o$ is larger the preexponential constant $\lg \eta_o$ determined in other models. The reason for this is a term $\frac{\sigma}{RT}$ coming from Eq.(13). For this reason it is expected that $\lg \eta_o \approx \lg \eta_o + 1.5$. It is convenient to choose as reference state ambient pressure and temperature T_g at which viscosity of system in

equilibrium is $\lg \eta_g = 13.5 [dPa.s]$. In this way T_g is always within the glass transition interval and could serve as thermodynamic definition of the glass transition temperature. Note that glass transition interval is the region where relaxation time is becoming comparable to observation time. Therefore other definitions of T_g depend on the applied method as well as on the heating (cooling) rate. The proposed here definition is universal and never deviates by more than $\pm 1.5\%$ from the one determined measuring the onset of the changes of a given property with heating (or cooling) at reasonable rates. This is a good example how the proper choice of the reference state helps to reduce the number of adjustable parameters.

Equation (15) is the main viscosity expression. It permits to follow the temperature dependence of viscosity as well as the dependence on pressure and how viscosity change if system is not in equilibrium. To do this it is sufficient to introduce in Eq.(15) the dependence of entropy on the corresponding variables. It is quite natural to try to express S as logarithmic function of temperature and/or pressure. Thus, the temperature T dependence of entropy can be presented as:

$$S(T) = S_r + \int_{T_g}^T C_p d \ln \tilde{T} \quad (16)$$

So, we apply the most frequently used approximation that heat capacity is temperature independent, i.e. C_p is the average value for the interval between T_g and T . Under this assumption, the entropy of a melt in metastable equilibrium is becoming:

$$S(T) = S_g + C_p \ln \left(\frac{T}{T_g} \right) \quad (17)$$

The temperature dependence of viscosity is obtained introducing Eq.(17) into Eq.(15)

$$\lg \eta = \lg \eta_\infty + A \left(\frac{T_g}{T} \right)^F \quad (18)$$

where $A = \lg \frac{\eta_g}{\eta_\infty} \approx 13.5 \pm 10\%$ and the "fragility" parameter F stands for:

$$F = \frac{2C_p}{ZR} \quad (19)$$

When $F=1$ viscosity gives a straight line in Arrhenian coordinates, indicating that glass is strong. The larger is F the more fragile is the glass. Note that there is a simple relation between the Angel's fragility parameter m and the present one because $m=AF$.

The pressure dependence of entropy can be expressed by means of Maxwell relations through the volume expansion coefficient $\kappa = \frac{1}{V} \left(\frac{\partial V}{\partial T} \right)_P$ in the form:

$$S_g - S = V_m \int_{P_1}^P \kappa dp \quad (20)$$

where V_m is the molar volume. An explicit form of the dependence of κ on P is needed to solve Eq.(20). Although there are no data in the literature, it is reasonable to assume that at extremely high pressures κ will reduce in a somewhat inversely proportional to pressure P way, namely:

$$\kappa = \frac{1}{V} \left(\frac{\partial V}{\partial T} \right)_P \approx \kappa_o \frac{\Pi}{\Pi + P} \quad (21)$$

where Π is a constant and κ_o is the volume expansion coefficient at no pressure. In this case the solution of Eq. (20) leads to:

$$S = S_g + C_p \ln \frac{T}{T_f} - \kappa_o V_m \Pi \ln \left(\frac{\Pi + P}{\Pi + P_1} \right) \quad (22)$$

So that, for $P_1 \ll \Pi$, the viscosity equation (22) yields:

$$\eta = \eta_\infty \exp \left\{ A \left(\frac{T_g}{T} \right)^F \left(\frac{\Pi + P}{\Pi + P_1} \right)^\Phi \right\} \approx \eta_\infty \exp \left\{ A \left(\frac{T_g}{T} \right)^F \left(1 + \frac{P}{\Pi} \right)^\Phi \right\} \quad (23)$$

where $\Phi = \frac{\kappa_o V_m}{ZR} \Pi = F \frac{\kappa_o V_m}{C_p}$.

The model becomes more sophisticated if the temperature dependence of compressibility coefficient is taken into account.

In the glass-transition region the experimental time scale becomes comparable with the time scale for structural rearrangements. The relaxation time increases sharply when the temperature is lowered further on. In this way the structure is fixed, so that the state of the system becomes nonequilibrium one. In this case viscosity is derived bearing in mind that fictive temperature T_f is the temperature at which the system with the particular structure will be in equilibrium. Basically, the entropy of undercooled melts splits into two parts: configuration entropy ΔS , and vibration entropy S_{vibr} . Respectively, the entropy of undercooled melts is $C_p = \Delta C_p + C_{gl}$. According to Eq.(15) in Arrhenius coordinates the slope L_e of $\log \eta$ against $1/T$ is

$$L_e = \frac{B}{2.3 \Delta S} \left(1 + \frac{\Delta C_p}{\Delta S} \right) \quad (24)$$

If configurational entropy is fixed, in the same coordinates, the nonequilibrium viscosity will have a slope L_g given by

$$L_g = \frac{B}{2.3 \Delta S} \quad (25)$$

So that the ratio of the two slopes is

$$\frac{L_e}{L_g} = 1 + \frac{\Delta C_p}{\Delta S} \quad (26)$$

The frozen in structure is best described by the fictive temperature T_f . Below the fictive temperature T_f the configurational entropy ΔS is fixed (i.e. ΔC_p vanishes), so that S can be determined as

$$S(T) = S_g + C_p \ln \left(\frac{T_f}{T_g} \right) + C_{gl} \ln \left(\frac{T}{T_f} \right) \quad (27)$$

Taking into account Eq.(27) the nonequilibrium viscosity is given by:

$$\eta = \eta_{\infty} \exp \left[A \left(\frac{T_g}{T_f} \right)^F \left(\frac{T_f}{T} \right)^{\gamma} \right] \quad (28)$$

The dimensionless power γ is proportional to the ratio of the heat capacity C_{gl} of the glass and the heat capacity of the undercooled melt C_p .

$$\gamma = F \frac{C_{gl}}{C_p} \quad (29)$$

In agreement with experimental evidence, the model predicts that in Arrhenius coordinates (see Fig.4), the ratio between the slopes of the lines of nonequilibrium and equilibrium

viscosity, is equal to the ratio $\frac{C_{gl}}{C_p} = \frac{C_p - \Delta C_p}{C_p}$ at the break point T_f .

Equation (18) describes the temperature dependence of viscosity with accuracy superior to all other models [25]. Data on parameters controlling the temperature dependence of viscosity of number of substances are summarized in Table 1. Data on parameters controlling the pressure dependence of viscosity are summarized in Table 2.

Table 2 Parameters for pressure dependence of viscosity

Substance	Π MPa	Φ	F/Φ
glycerol	900	0.7	3.9
di-butyl phthalate	200	0.87	3.8
<i>orto therpenyl</i>	300	2.35	2.7
polymethylphenylsiloxane	499	4.33	1.74

Table 1 Viscosity parameters

Substance	$\lg \eta_{\infty}$	Tg [K]	F
SiO ₂ [^]	-5	1430	1,2
Li ₂ O.2SiO ₂	0,96	719	3,43
2 Li ₂ O.8 SiO ₂	-0,07	734	2,21
3Li ₂ O.7 SiO ₂	0,53	708	3
5Na ₂ O.95SiO ₂	-3,8	911	1,3
13Na ₂ O.87SiO ₂	-2,7	839	2
15Na ₂ O.85SiO ₂	0,45	752	1,7
Na ₂ O. 3SiO ₂ [^]	1,46	726	3,2
Na ₂ O.2SiO ₂	0,8	716	3,2
2 Na ₂ O.8 SiO ₂	0,1	735	2,27
3 Na ₂ O.7 SiO ₂	0,65	711	2,85
4 Na ₂ O.6 SiO ₂	0,57	678	3
4 4Na ₂ O.56SiO ₂	0,28	655	2,9
2 K ₂ O.8SiO ₂	0,42	751	2,5
3K ₂ O.7SiO ₂	1,37	703	3
Li ₂ O 4SiO ₂	--	717	--
Na ₂ O 4SiO ₂	--	741	--
K ₂ O 4 SiO ₂	--	771	--
Rb ₂ O 4SiO ₂	--	781	--
Cs ₂ O 4SiO ₂	--	804	--
BaO.2SiO ₂	-1,5	962	3,25
3 PbO.7SiO ₂	-0,06	743	3
3 .5PbO.6.5SiO ₂	0,53	754	3,25
4 PbO.6SiO ₂	0,66	726	4
4.6 PbO.5.4SiO ₂	0,32	673	3,8
PbO. SiO ₂	-0,03	659	4
5.5PbO.4.5SiO ₂	-0,2	635	4,3
6PbO.4SiO ₂	-0,3	627	4,9
97 8B ₂ O ₃ 2 17SiO ₂	1,38	520	3,25
94B ₂ O ₃ 5 95SiO ₂	1,29	525	3
89 3B ₂ O ₃ 10 7SiO ₂	1,45	527	3
51 6B ₂ O ₃ 48 4SiO ₂	0,6	582	1,5
44 6B ₂ O ₃ 55 4SiO ₂	-0,02	682	1
216Na ₂ O.9CaO.70SiO ₂	0,8	777	3,2
19Na ₂ O.9CaO.72SiO ₂	0,4	784	2,9
21Na ₂ O.7CaO.72SiO ₂	0,5	769	2,9
33Na ₂ O.17CaO.50SiO ₂	-4,54	732	3,2
17Na ₂ O.33CaO.50SiO ₂	-2,57	821	2,77
(CaO)0.423(Al ₂ O ₃ .)0.083(SiO ₂) 0.494	-0,7	1043	4,18
(CaO)0.439(Al ₂ O ₃ .)0.083(SiO ₂) 0.456	-0,7	1057	4,36
(CaO)0.461(Al ₂ O ₃ .)0.105(SiO ₂) 0.413	-0,7	1065	4,4
(CaO)0.479(Al ₂ O ₃ .)0.127(SiO ₂) 0.373	-0,7	1075	4,61
(CaO)0.505(Al ₂ O ₃ .)0.147(SiO ₂) 0.330	-0,7	1084	4,62
(CaO)0.351(Al ₂ O ₃ .)0.164(SiO ₂) 0.498	-0,7	1066	3,83
(CaO)0.385(Al ₂ O ₃ .)0.151(SiO ₂) 0.441	-0,7	1075	4,05

Substance	$\lg \eta_{\infty}$	Tg [K]	F
(CaO)0.405(Al2O3.)0.174(SiO2) 0.395	-0,7	1089	4,25
(CaO)0.427(Al2O3.)0.225(SiO2) 0.348	-0,7	1093	4,4
(CaO)0.459(Al2O3.)0.247(SiO2) 0.294	-0,7	1104	4,56
(CaO)0.428(Al2O3.)0.143(SiO2) 0.428	0,88	1056	4,77
CaO. Al2O3. 2SiO2	-2,06	1105	3,5
3CaO.Al2O3.3SiO2	0,88	1055,6	4,77
Na2O. Al2O3. 6SiO2	-8,58	1012	1
30Na2O.70SiO2	--	735	--
44Na2O.56SiO2	--	669	--
2Na2O.1CaO.3SiO2	--	742,3	--
B2O3	0,94	512	2,73
13 5Na2O.86 5B2O3	-1,68	689	3,25
33 3Na2O 66 7B2O3	-1,1	753	5
6Li2O.94B2O3	0,1	612	4
13.9Li2O.86.1B2O3	-0,7	695	4,25
33.5Li2O.66.5B2O3	-1,5	744	4,5
19.5K2O.80.5B2O3	-0,16	675	4
24.4K2O.75.6B2O3	0	677	4
18BaO.82B2O3	-0,97	790	4
23.9BaO.76B2O3	-0,9	826	4,5
33PbO,67B2O3	-2,9	718	4
PB2:PbO.2 B2O3	0,09	780	9,5
Li2O. P2O5^	0,18	578	5,5
Na2O. P2O5	0,43	544	5,5
5Na2O.95GeO2	0,11	695	2,25
10Na2O.90GeO2	-0,13	743	4,5
29.6Na2O.70.4GeO2	0,43	710	6,5
20PbO.80GeO2	0,33	716	4,25
30PbO.70GeO2	0,66	679	6,25
40PbO.60GeO2	0,25	715	5
50PbO.50GeO2	0,33	626	5,25
5Na2O.10MgO.10Al2O3.75Si	-1,77	1016	1,85
10Na2O.10MgO.10Al2O3.70S	0,21	979	2,5
15Na2O.10MgO.10Al2O3.65S	1,26	961	3,5
20Na2O.10MgO.10Al2O3.60S	1,27	899	3,5
10Na2O.10MgO.5Al2O3.75Si	0,4	933	2,42
10Na2O.10MgO.80Si	-0,43	828,5	2
95Pb1Si,3B2O3	--	613	--
94Pb01SiO2,3B2O3	--	618	--
70Pb10Si,20B2O3	--	539	--
70Pb18Si,12B2O3	--	548	--
65Pb2.9Si,30B2O3	--	563	--
65Pb2.8Si,30.5B2O3	--	580	--
64Pb2.8Si,31.5B2O3	--	586	--
63Pb2.8Si,28.5B2O3	--	596	--
62Pb11Si,26B2O3	--	575	--
60Pb13Si,26B2O3	--	566	--

Substance	$\lg \eta_{\infty}$	Tg [K]	F
60Pb24Si,16B2O3	--	574	--
56Pb15Si,39B2O3	--	607	--
51Pb30Si,19B2O3	--	608	--
40Pb20Si,40B2O3	--	662	--
40Pb36Si,14B2O3	--	634	--
31.8Pb22.7Si,45.5B2O3	--	670	--
31.5Pb41Si,27.5B2O3	--	672	--
23Pb46Si,31B2O3	--	692	--
21Pb26Si,53B2O3	--	702	--
17Pb63Si,20B2O3	--	743	--
15Pb70Si,15B2O3	--	752	--
14Pb52Si,34B2O3	--	712	--
12Pb29.5Si,59B2O3	--	692	--
Polystyrene [^]	-0,2	359	8
glycerol	-1,19	450	4
glucose	-0,99	515	6,25

References 19

1. A. Einstein, *Annalen der Physik: Über die von der molekularkinetischen Theorie der Wärme geforderte Bewegung von in ruhenden Flüssigkeiten suspendierten Teilchen*, 17, 549 (1905)
2. S. Gladstone, H. Laider, H. Eiring, "The theory of Rate Processes" Princeton University, New York, London 1941
3. Y. Frenkel "The Theory of Solid and Liquid Bodies" (in russian) , Leningrad 1934
4. A.Voronel, E. Veliyulin, and V. Sh. Machavariani, A. Kisliuk and D. Quitmann, :*Fractional Stokes-Einstein Law for Ionic Transport in Liquids*, Phys. Rev. Lett. 80 (1998) 2630
5. O. Mazurin, M. Streltsina and T.Shvaiko-Shvaikovskaya, "Handbook of Glass Data" Amsterdam: Elsevier, Amsterdam, 1983 and 1985
6. J. Hlavac, H. Nademlynska, : *Dissolution of spherical silica particles in molten sodium disilicate*, Glass Technol. 10, (1969) 54
7. I. Avramov, J. Non-Cryst. Sol.: *Viscosity in disordered media*, 351 (2005) 3163
8. I. Avramov Journal of Volcanol. and Geotherm. Res. 160, (2007) 165
9. V. Solovev, Physica stat Sol. (a) *Diffusion in amorphous metal films*, 83 (1984) 553
10. M. Kawakami, K. Nagata, K.Goto, J. Electrochem. Soc.: *Electrochemical Determination of Interdiffusivity of Cations in Liquid Li₂O-SiO₂ System at 1100° to 1350°C*, 125 (1978) 395
11. I. Avramov, A. Milchev, J. Non-Cryst. Sol. : *Effect of Disorder on Diffusion and Viscosity in Condensed Systems*, 104 (1988) 253
12. I.Avramov, J. Non-Cryst. Sol.: *Diffusion coefficient of foreign particles on glass-forming melts* 354 (2008) 1537
13. I. Avramov, J. Chem. Phys.: *Influence of disorder on viscosity of undercooled melts*, 95 (1991) 4439

14. I. Avramov, J. Non-Cryst. Sol.: *Pressure dependence of viscosity of glassforming melts*, 262 (2000) 258
15. W. Zachariasen, J. Am. Chem. Soc *The atomic arrangement in glass*, 54, 3841 (1932).
16. G. Finney, J. Bernal, Nature: *Random Close Packing and the Heats of Fusion of Simple Liquids*, 213 (1967) 1079
17. P. Gupta, A. Cooper, „*Topologically Disordered Networks of Rigid Polytopes*“ in Proc. XVI Intern. Congress on Glass, Madrid 1992, Bol. Sociedad Espagniola de Ceram. Vidio 31c (1992) 15
18. N. Mott, Philos. Mag.: *Conduction in non-crystalline materials*, 19 835 (1969)
19. J. Phillips, M. Thorpe, Solid State Comm.: *Constraint theory, vector percolation and glass formation* 53 84 (1986)
20. J. Phillips, J. Non Cryst. Sol. : *Topology of covalent non-crystalline solids I: Short-range order in chalcogenide alloys* , 73 153 (1979)
21. M. Thorpe, J. Non-Cryst. Sol.: *Bulk and surface floppy modes*, 57, 355 (1983).
22. M. Thorpe, Phys. Rev. B : *Floppy Modes in Glasses*, 40, 535 (1989)
23. I. Avramov, R. Keding, C. Russel, J. Non-Cryst. Sol.: *Crystallization kinetics and rigidity percolation in glassforming melts*, 272 (2000) 147
24. I. Avramov, R. Keding, C. Russel, R. Kranold, J. Non-Cryst. Sol.: *Precipitate particle size distribution in rigid and floppy networks*, 278 (2001) 13
25. M. Solvang, Yue, Y., Jensen, S., Dingwell, D., J. of Non-Cryst. Sol.: *Rheological and thermodynamic behaviors of different calcium aluminosilicate melts with the same non-bridging oxygen content*, 336 (2004) 179



Chapter 20

Interdisciplinary diffusion, periodicity

20. TRANSDICIPLINARITY OF DIFFUSION INCLUDING ASPECTS OF QUASIPARTICLES, QUANTUM DIFFUSION AND SELF-ORGANIZED REACTION PERIODICITY

Zdeněk Kalva, Jaroslav Šesták, Jiří J. Mareš, Jiří Stávek

20.1. Historical introduction: Fourier 's heat transfer and the Laws of Fick and Ohm

In the 1850s, *J.C. Maxwell* [1] initiated convincing investigations into the mechanical theory of heat. He argued that the velocities of point particles in a gas were distributed over a range of possibilities that were increased with temperature, which led him to predict, and then verify experimentally, that the viscosity of a gas is independent of its pressure. In the following decade *L.E. Boltzmann* began his investigation into the dynamical theory of gases, which ultimately placed the entire theory on firm mathematical ground. Both men had become convinced that the novel notion of entropy reflected molecular randomness. Maxwell expressed it in such a characteristic way: “*the second law of thermodynamics has the same degree of truth as the statement that, if you throw a tumblerfull of water into the sea, you cannot get the same tumblerfull of water out of it back again.*” These survived as seminal notions that a century later led to the field of non-equilibrium thermodynamics [2].

Although in 1764 *L. Euler* had already formulated a mathematical theory for convection in fluids, for the 19th Century scientists the subject of heat transfer had to begin with the simple notations of Newton's laws of cooling [3] (even if we now consider it rather unimportant in comparison to his other works on mechanics and optics). We may repeat „*the greater the outer conductivity and surface of a cooled solid body the faster is its cooling. On the other hand, the body's thermal inertia, given by the product of its specific heat and mass, slows down its cooling*“. It, however, did not yet distinguish between different modes of heat transfer. Perhaps, that was how ‘*irreversible heat flow*’ acquired its unpleasant moral connotation where the term ‘*dissipation*’ was often taken synonymous to ‘*intemperate or vicious mode of living*’. Nonetheless, the natural behavior of heat entails a distinction between past and future or even illustrates extrapolation to an ultimate heat death of the Universe [4].

In 1818, *P.-L. Dulong* introduced an improved law of cooling, and *A.-T. Petit* suggested that a body absorbs and emits heat at the same time. In 1860 it was *J.C. Maxwell*, who borrowed from *R.J.E. Clausius* the concept of the mean free path traveled by a molecule from one collision to the next, and who introduced the modern view that heat conduction is a special case of a general transport process of which diffusion and viscosity are parallel examples. The T^4 term was later found to fit the corrected *Dulong-Petit* data leading to the gradual establishment of the renowned *Stefan-Boltzmann* law of radiation. The study of temperature distribution was initiated by *J.B. Biot*, showing a method for determining the relative thermal conductivities λ between two well-connected metallic bars of similar shape that are put under a steady heating of their join (λ being *de facto* thermal diffusivity, the term used by *Kelvin* as *a*).

Perhaps the most important contribution came from *J.B.J. Fourier* [5], who in the year 1822 judged thermal properties in more details and summarized them in (the later renowned *Fourier's*) Law of heat conduction in the form of

$$q = - \lambda s \Delta T / \Delta x t. \quad (1)$$

It states that the amount of heat, q , which passes through a surface (as a cross section) s , in time, t , is proportional to the temperature difference, ΔT , per given length, Δx (i.e., to the *unite temperature gradient of 1 degree per 1 meter*). The proportionality constant λ stands for the standard *coefficient of thermal conductivity* while $a = \lambda / (c_p \rho)$ expresses *thermal diffusivity* where c_p is the specific heat capacity and ρ is the specific mass. It complies agreeably with the generalized physical observations of one-dimensional heat flow that results from the temperature non-uniformities, i.e., heat flow and temperature gradients are exactly opposite one another in direction, and the magnitude of the heat flux is directly proportional to this temperature difference.

It is clear that we ought to understand generalized heat flux, q , as a quantity that has a specified direction as well as a specified magnitude. Fourier's Law summarizes this physical experience succinctly as $q = - \lambda_i \nabla T$, where the generalized 3-D temperature gradient, ∇T , is represented by three (i,j,k) - dimensional derivatives. Namely it provides that $\nabla T = i \partial T / \partial x + j \partial T / \partial y + k \partial T / \partial z$ where the standard thermal conductivity can now be instituted to depend on both the position and temperature, i.e., $\lambda_i = \lambda \{(i,j,k)(T)\}$. Fortunately, most materials are nearly homogeneous so that this relation simplifies to mere $\lambda = \lambda(T)$ and for a one-dimensional flow is further simplified to the plain difference $\Delta T / \Delta x$. It is evident that λ may vary from one substance to another, which is accounted for, in part, by varying electron and photon conductance. According to empirical evidence, there is one feature that substances have in common with one another, which is that λ is always a positive constant. Obviously, it makes intuitive implication no less than if the molecular concept of temperature is invoked, the heat (as kinetic energy at the microscopic scale in another sense) tends to flow from the regions of high internal energy to the regions of low internal energy. This is consistent with the above mentioned description that heat flow is opposite to the gradient direction of temperature (being also consistent with the laws of thermodynamics [2]).

Fourier's Law has several enormously important consequences in the related but other category of physical behavior, such as that of mass transfer, called *diffusion*. It was introduced by a young pathologist *A.E. Fick* [6] in his fundamental article "*On Diffusion*" (published in Zurich 1855), who described the mass flux, J , of a (first) dilute component, 1, into a second fluid, 2, which stays proportional to the gradient of its mass concentration, m_1 . Thus we have, $J = - \rho D_{12} \nabla m_1$, where the proportional constant D_{12} is the binary diffusion coefficient and ρ is density. While recognizing the boundary conditions the mathematical solution of basic Fick's equations was pioneered by *J. Stephanm* (1879) sourced on the preliminary but rather unfamiliar work of Scottish chemistry professor *T. Graham* (on diffusion studies of salts in water, 1833) [7]. Thermal dependence of diffusion coefficient was introduced by *S. Arrhenius* (1891). The idea of self-diffusion was already mentioned by Maxwell but seriously analyzed by *G.K. von Hevesy* in the year 1921 [7]. Phenomenon of irregular motion of small particles suspended in a liquid was described by *R. Brown* (1828) later correctly explained by *A. Einstein* (1905).

Despite Fick was amazingly an experimental physiologist (well known for monograph on "*Medical Physics*") his work on diffusion became noticeably theoretical and his approach would be called today as a phenomenological (liner-response) theory applied to mass transport. He started observing "*diffusion in water confined by membranes is not only one of the basic factors of organic life, but is also an extremely interesting physical process and, as such, should attract much more attention than it has so far*". As a matter of fact the carrier particles involved in their current have to flow against the concentration gradient, which is

analogy with the *Fourier's Law* for heat flow and the *Ohm's Law* for electric current. Assumingly, Fick's phenomenological hypothesis missed, however, the probabilistic point of view that is central to statistical mechanisms and it was *A. Einstein*, who fifty years later derived the diffusion equation from the postulates of molecular theory, in which the particles involved move independently under the influence of thermal agitation.

An important corresponding relationship is that of the electrical analogy. Let us consider *Ohm's law* as the description the flux of electric charge, I/A , by means of the electric current density, $J_e = -\sigma \nabla V$, where σ is the electric conductivity, V is the voltage, I are the amperes of electric current and A is an area normal to the current direction (vector). For a one-dimensional current flow we can write Ohm's Law as $J_e = -\sigma \Delta V/\Delta x$. Because ΔV is actually the applied voltage, E , and R_e is the electric resistance of the wire resistor equal to $\Delta x/(\sigma A)$, then, since $I = J_e A$, the equation becomes the standard form of Ohm's Law, $V = R_e I$. The previously written formula, $\Delta x/(\sigma A)$, thus assumes the similar role of thermal resistance, to which we give the analogous symbol, R_t , and which shows how we can represent heat flow through the slab with a diagram that is perfectly identical to a similar electric circuit. By using analogous solution we can find further generalized descriptions for the diffusion of electrons, homogeneous illumination, laminar flow of a liquid along a spherical body (assuming a low-viscosity, non-compressible and turbulent-free fluid) or even the viscous flow applied to the surface tension of a plane membrane [8].

It is important to observe that within phenomenological theories any flux can be generalized as kind of the dissipation function, Φ . Thus it can be written as a sum of all the thermodynamic fluxes, J_i , and their conjugate forces, X_i , i.e., $\Phi = \sum_i J_i X_i$. The fluxes are unknown quantities in contrast to the forces, which are known functions of the state variables and/or their gradients. It has been found experimentally that fluxes and forces are interwoven, i.e., a given flux does not only depend on its own conjugate force but may depend on a whole set of forces acting upon the system as well as on all thermodynamic variables (T, P, \dots). Various fluxes can be thought of the rate of change of an extensive variable, X_i , i.e., $J_i = \partial X_i / \partial t$. Conjugate forces are identical in form to the phenomenological flow equations shown above and can be expressed, close enough to equilibrium, in the linear form of the so called *Onsager relations* [9], or

$$\partial X_i / \partial t = J_i = \sum_k L_{ik} X_k \quad (2)$$

where the constant coefficients, L_{ik} , are called the '*phenomenological coupling coefficients*'. Written in this fashion, thermodynamic forces are thus differences between the instantaneous and equilibrium values of intensive variables (or their gradients). For example the difference $(1/T - 1/T_{eq})$ is actually the thermodynamic force conjugative to the internal energy, which is factually the familiar *Fourier Law*, i.e., $q = -\lambda_i \nabla T$ or *Stokes Law*, i.e., $p^v = -2 \eta \nabla v$ (where η is the viscosity and ∇v is the complex velocity through a continuous fluid. The traditional Fick's Law is then obtained by the condition set up when working at a constant temperature and pressure, while Ohm's Law requests supplementary constraints provided that the magnetic induction and all couplings are ignored. Similarly we can predict a linear relationship between the rate of advancement of a chemical reaction and the affinities, which, however, is correct only within a very narrow domain around equilibrium. Extended knowledge came in the new field of irreversible and rational thermodynamic [2,10-12].

20.2. Non-stationary heat diffusion and the generalized Schrödinger equation

In general, any of these phenomena involves the movement of various entities, such as mass, momentum or energy, through a medium like fluid or solid, by means of virtue of non-

uniform conditions existing within the medium [7,12-14]. Variations of concentration in the medium lead, for example, to the relative motion of the various chemical species present, and this mass transport is generally referred to as diffusion. Variations of velocity within a fluid result in the transport of momentum, which is normally referred to as the viscous flow. Variations in temperature result in the transport of energy, which is a process usually called heat conduction. Besides the noteworthy similarities in the mathematical descriptions of these three phenomena; all three often occur simultaneously in physical manner. In the case of combustion, where a flowing fluid but viscous mixture is undergoing chemical reactions that produce heat, which is conducted away producing various chemical species that inter-diffuse with one another.

Description of a more frequent, non-steady progress [7,14] requires, however, the introduction of second derivatives. These are provided by a three-dimensional control of a finite region of a conducting body with its segmented surface area, denoted as s . The heat conducted out of the infinitesimal surface area ds is $(-\lambda \nabla T)(k ds)$, where \underline{k} is the unit normal vector for the heat flux, $q = -\lambda \nabla T$. The heat thus generated (or absorbed) within the underneath region, v , must thus be added to the total heat flow into the surface, s , in order to get the overall rate of heat addition. Therefore, we need integration and, moreover, the rate for the increase of internal energy, U , for the given region, v , which is granted by the relationship, $dU/dt = \int_v \{\rho c_p (\partial T/\partial t)\} dv$, where the derivative of T is in the partial form (because T is a function of both, v and t). Applying Gauss's theorem, which converts a surface integral into a volume integral, we have to solve the reduced formula of the form, $\int_v \{\nabla \cdot \lambda \nabla T - \rho c_p (\partial T/\partial t)\} dv = 0$

Since the region, v , is arbitrary small, the integrand must vanish identically so that the heat diffusion equation in three dimensions reads, $\nabla \cdot \lambda \nabla T + dq/dt = \rho c_p (\partial T/\partial t)$. If the variation of λ with T is small, λ can be factored out leaving a standard but a more complete version of the heat conduction equation (i.e., the second law of Fourier) $\nabla^2 T = (1/a) (\partial T/\partial t)$, where a is the thermal diffusivity, and the term $\nabla^2 T \equiv \nabla \cdot \nabla T$ is called the *Laplacian* and is arising from a *Cartesian* coordinate system ($i\partial/\partial x + j\partial/\partial y + k\partial/\partial z$) ($i\partial T/\partial x + j\partial T/\partial y + k\partial T/\partial z$) = $i\partial^2 T/\partial x^2 + j\partial^2 T/\partial y^2 + k\partial^2 T/\partial z^2$. This is the standard second order form of the heat equation showing that the change of temperature over time is proportional to how much the temperature gradient deviates from its linearity. In the other words, the bigger the protuberance in the temperature distribution, the faster is its compensation.

However, its mathematical solution is complicated and is not the aim of this text [10-14]. Just as an example, let us consider a massive object of temperature T_0 (at the initial conditions of $T\{x,0\}$) that would affect the temperature of its environment, T_c . The solution in time, t , and space distribution x gives solution in the form, $T(x,t) = T_c + (T_0 - T_c) \Phi [x/2(kt)^{1/2}]$, where Φ stand for the *Bessel* functions, usually available from tables or advanced computer simulations but not so easy to work with at all.

The fact that the second form of Fourier Laws bears a general structure of a *distribution law* is thus worthy of special note [15,16]. The significant reciprocity can be found for the famous Schrödinger equation when taking into account a diffusion process as something fundamental [8,12,15-21] and intimately related to light and matter (close to the physical intuition of *R.P. Feynman* [8]). It is usually written in its simpler form as

$$d\psi/dt = \kappa \Delta\psi \quad (3)$$

where ψ is the wave function, $\kappa = i c'$, where i stays for the standard complex number and c' is an 'imaginary' diffusion constant.

Attempts to think about diffusion in a more general way were repeatedly done [15-21] and the imaginations of new types of diffusion already surfaced previously. For example, the

basic equation of quantum mechanics introduced by *E. Schrödinger* (1887-1961) can be also considered as a diffusion equation for a diffusion of amplitudes of probability to find a particle in the special place and time. Schrödinger discovered his equation to support the idea of universality of the dual, particle-like and wave-like, character of matter. New interpretation of the Schrödinger equation (when suggesting diffusion of probability amplitudes) is mostly known from the lectures of *R. Feynmann* [8] given few years after Schrödinger's discovery. The fundamental ideas of Feynmann's argumentation are possible to localize even few years before Schrödinger's discovery in connection with the search for the "nature's natural numbers" suggested by *R. Steiner* in his lectures (given in Berlin 1920 for scientists and teachers [16]) yielding formally the same equation as done by Schrödinger.

The important difference is that the constant κ has to be a real number for the case of normal diffusion (or thermal conductivity) and κ is an imaginary number in the quantum-mechanical interpretation. In the first case the letter ψ is the normal density (or the heat flow) while in the second case ψ is related to an amplitude of probability that the quantum particle is possible to find in the specific place x within a specific time t . It is worth noting [22,23] that Steiner progressed during searching for the nature of natural numbers even further and considered using as the constant κ the hyper-complex number. He suggested that in such a case the equation (3) could be useful in biodynamic [24].

The different paths along which diffusion with an imaginary diffusion constant occur do not necessarily lead to the toting-up of the observed effects but can, instead, result in a destructive interference. This is asymptotic for a new phase in physics, intimately related to the mathematics of complex functions. It describes diffusion as probability amplitude from one point to the next along the line [25]. If an electron has certain amplitude to be at one point, it will proceed a little later to have the same amplitude at a neighboring point. The imaginary coefficient makes the behavior completely different from the ordinary diffusion equation such as the equation that describes gas spreading out along a thin tube - instead the real exponential solutions the results are revealed in complex waves [26,27].

Physics, however, has already gone one stage beyond the complex numbers in order to describe weak and strong interaction in elementary particle physics (non-abelian gauge theory that uses „hyper-complex“ numbers-multivectors, by working, for example, the SU(2) theory of particle quantum flavor dynamics [28]). Such hyper-complex mathematics of diffusion may be related to the realm of life, however, yet too complex to be solved, nevertheless, recently applied, at least, to the kinematics of a human knee [24]. The complex diffusion problem can also be recollect in the view of the substrate-bound (Maxwellian-like) understanding of light, deeply rooted in the world view of many physicists even today, as well as to *Steiner's* view of electricity as light in a certain 'submaterial' state [29]. Of course, there are now domains of physics, which are unthinkable without hyper-complex mathematics, for example, the physics of elementary particles [25,28].

20.3. Heat as quasiparticles and further concept of diffusion transdisciplinary

Diffusion [7,8,12,14,15,22,23] is an appropriate example to illustrate possibility of transdisciplinary scientific attitude. Diffusion is possible to encounter in many scientific disciplines, but the content of concept could be surprisingly different. Diffusion of gas through a membrane is the usual type of diffusion. On the other hand, the diffusion view to

magnetocaloric effect (MCE) is usually comprehended as a nonlocal and noncoherent transfer of energy between two different types of “*quasiparticles*” (such as magnons and phonons¹).

MCE can be considered as a specific type of heat diffusion but certainly much less usual [22,23,30-33]. It is not the traditional flow of heat through a sample but the transfer of energy accomplished at the same time in the whole volume of magnetic material. Such process cannot be described just by a normal procedure of heat diffusion through a real body/space. For MCE we need to consider some other, more sophisticated, type of diffusion and one of possible suggestions could be diffusion in the space based on the wave vectors.

We think that a contemplative synthesis of above mentioned modification of diffusion can enrich the present knowledge and interpretation. After this general introduction we shall turn our attention in the following paragraphs towards the particular concepts of diffusion: magnetocaloric effect (MCE) and Belousov–Zhabotinsky reactions (BZR).

Description of heat fluctuations by the usage of quasiparticles is mostly known from the theory of solid state. Generalizations to extremely diluted media such as ideal gas are difficult but with certain precaution nevertheless possible.

In the solid state is possible to imagine the creation of standing waves from the originally local perturbation. Local movement perturbation by an external force is in solid state materials transformed into the increase of the heat content. Local movement of atoms made by a perturbation is immediately changed into a collective excitation. The local change of position of atom is transformed into the wavelike moving through the sample. Waves are reflected on the Boundaries of sample and interfere with waves going in opposite directions. Result of such interference procedures is the survival of waves with the wavelengths compatible with the geometry of o the sample in mathematically simple relations (for example $L = \lambda/n$ where L is the dimension of the sample and $n= 1,2,3 \dots$)

To speak about wavelike quasiparticles in the gas alone is, however, difficult because of processes on the boundaries of container. Atoms of gas are absorbed on the walls of container for relatively long time. The time spent by collisions processes inside a gas container is much shorter than time spent by the absorption contact with the boundaries of container and the correlations of directions for incoming and reflected atoms are relatively random.

Nevertheless, we think that the tendency to speak about heat as something like quasiparticles is plausible idea and it is possible to find it by founders of thermodynamic. The sentence “the heat i a movement” does not mean a kinetic energy of atoms but some kind of vibrations.[34]

This subject has encompassed a wide attention in various studies including thermal processes, e.g., [35-37] or comprehension of superconductors, e.g.,[37-41].

1 Scientific definition of so called quasiparticles would stay as a low energy excitation of a system, possessing a set of quantum numbers and/or well-defined expectation values of certain operators (position, charge, momentum, angular momentum, energy) often associated with isolated particles. In such a view phonons are the quanta of classical sound waves and sound waves do not need the notion of atoms while magnons are the quanta of classical spinwaves, which also do not need elementary spins. Photons inside isolator are the quanta of classically dressed electromagnetic waves and do not need the notion of electrons for the definition of the refractive index. Plasmons are the quanta of the plasma oscillations and they only need both the charge and mass density and no electrons or ions. Polarons are the quanta of the oscillating polarization in a lightly doped semiconductor and also do not need elementary charge or mass. Normals modes of vibration are assumed to undertake the progression through a crystal.

20. 4. Magnetocaloric effect

The study of magneto caloric effect (MCE) has now become important particularly from the technological points of view, which, in the last decade, has initiated the boom aimed to its deeper investigation [31-33] The search for materials with a high enough MCE within technologically interesting temperatures intervals is impressive.

As we already said that MCE is the special type of diffusion and can be seen as a transfer of energy between collective excitations of magnetic and elastic structure of materials. The behavior of collective excitations can be effectively represented by *quasiparticles* [22], which are the product of formalism of the second quantization characterized with the quantum of energy necessary for their creation (and with their wave vector). In the case of the weak magneto-elastic interaction MCE is a transfer of energy between the magnons and phonons. In the case of stronger (but not very strong) magneto-elastic interaction the energy flows between such comprehended quasiparticles that, however, are only similar to magnons, and phonons and thus may be called as quasimagnons and quasiphonons. However, the situation in the field of superconductors is different², the details of which lies beyond our passage [41].

Our study of MCE will be here restricted on the adiabatically-isolated systems. The entropy is supposed to be composed from the contribution of both the magnons and the phonons. The requirement of constant entropy provides us with the functional dependence of temperature as a function of varying external magnetic field. It is, however, not the only way how to arrive at MCE. For example, we can consider the degree of correlation in the system describable by Green's functions as a constant parameter. The dependence of Green's function on temperature and magnetic field can be than used for finding of MCE.

The growing interest for MCE has consequence impacts to various sciences. For example, in mathematics there are tested new mathematical tools – even beyond the scope of classical mathematics. We believe that better and more interesting results concerning MCE could be reached with the help of hyper complex mathematics – quaternions or multivectors, which are now reappearing in physical applications.

20.4.1. Some modeling aspects of MCE.

We already published some results of our modeling of MCE [22,31,32]. Some supplementary remarks are included in order to sketch the modeling procedure in order to make the following text about diffusion and phase transitions more comprehensible. Our calculations were done by a standard Heisenberg method of commutation of magnon and phonon operators with the Hamiltonian. It provided us with equations for time derivations of quasiparticle operators (in the Heisenberg representation). We obtained 8 equations with more than 8 unknown operators. Our decoupling (simplification approximations) included the

² Quasiparticles in superconductor [39-41] are trickier to assume than in other materials. Landau's quasiparticles in normal metals are simply dressed electrons having their non-interacting density and usual Coulomb charge. One can say that only their velocity on the Fermi surface is modified by the interaction. In contrast, a charge of a quasiparticle in the superconductor depends on its momentum being electron-like above, hole-like below and smoothly crossing zero at the Fermi level. Its velocity is modified so thoroughly that it changes its sign at the Fermi level. In spite of these two changes, each quasiparticle yields the same electric current as a free electron of equal momentum. This is particularly striking for quasiparticles at the Fermi level which has zero charge and zero velocity. The density of quasiparticles in the superconductor is not fixed but exponentially freezes out. Within the quasiparticle picture, this freezing is responsible for residual currents, i.e., for the superconductivity itself.

neglecting of nonlinear terms. The condition of solubility of our system of homogeneity equations gave us secular equation of 8th order for the energies for 8 quasiparticle modes. We decided to expect two quasiparticles modes of magnon type, with the quadratic dependence of energy on wave vector, and 6 quasiparticle modes of phonon type with the energies depending linearly on wave vectors. The approximate diagonalisation of our Hamiltonian was possible only for some special directions (parallel and perpendicular to the anisotropy axis) and we received for those directions analytical terms for corresponding quasiparticle energies.

The usage of a proper mathematical formalism is very important. For the study of MCE it appears to us as that a most suitable approach is the formalism of quasiparticles. We expect that such an approach is intimately connected with the physics of relevant thermodynamic procedures [22,23,31,32]. The application of the method of second quantization to the mathematical modeling of MCE has, however, some partial problems. Crucial is the proper choice of the Hamiltonian, especially the choice of the term corresponding to the magnon-phonon interaction. We are trying now to find a better mathematical expression for the contribution of magneto elastic energy in the special materials. In connection with it appears to us as promising an exploitation of hyper complex mathematics. We turned our attention, for example, to the indexes of annihilation and creation operators for magnons and phonons. As indexes of creation and annihilation operators for magnons are usually used vectors, but it seems to us that, especially in the case of magnons, it is worth of trying to use some higher multivectors—for example bivectors. The same can be valid for quasiparticle operators describing the collective excitations of vortexes in superconductors of second type. The usage of proper higher multivectors makes formalism more transparent for important physical connotations and also it is possible to avoid some confusion – for example the peculiarity of polar and axial vectors.

Our Hamiltonian (H) was composed from three parts: magnon term, phonon term and the magneto-elastic term H^{m-e} describing the magnon-phonon interaction. For the latter term we have used the simplest mathematical expression combining together the elasticity of a crystalline lattice and magnetic moments. We supposed that the magneto elastic energy is proportional to the numbers of interacting quasiparticles, i.e., $H^{m-e} = gM_i M_k u_{ik}$ (where g is magneto elastic constant, u_{ik} is tensor of deformation for positions i and k).

In our modeling of MCE we considered only the case of thermally isolated material (adiabatic isolation with the constant total entropy of the system) and it had to be done numerically. We used the standard formula for entropy of quasiparticle gas [31,32]

$$S = \sum_{\alpha} \int_{\mathbf{k}, \alpha} \{ (1+n_{\mathbf{k}, \alpha}) \ln(1+n_{\mathbf{k}, \alpha}) - n_{\mathbf{k}, \alpha} \ln(n_{\mathbf{k}, \alpha}) \} k^2 d\mathbf{k}. \quad (4)$$

The change of particular entropy terms made by an application of external magnetic field had to be compensated by the change of temperature. S is the total entropy for the system of quasiparticle modes, $n_{\mathbf{k}, \alpha} = n_{\mathbf{k}, \alpha}(T, H)$ are the numbers of quasiparticles which are the functions of temperature T and the external magnetic field H . Index \mathbf{k} denotes the wave vector and α is the index of quasiparticle mode (quasimagnons or quasiphonons).

The self-consistent numerical calculations provided us with the temperature for which the total entropy of system is unchanged and equal to the total entropy before the application of magnetic field. The dependence of this temperature on external magnetic field $T = T(H)$ than provides the actual MCE.

In the vicinity of some magnetic phase transitions our modeling predicts not only the increase of MCE but also the change of its sign. Our modeling included also the study of crystalline anisotropy of materials illustrated in Fig.1. The energy of our quasi phonons

depends on the transversal or longitudinal speed of sound and we found the local extreme of MCE for the ratio of longitudinal and transversal speed of sound c^l / c^t near the value 1.4. We were happy to see that this number corresponds to the value realistic in specific materials.

Our calculated quasiparticle energies are approximately valid only for the small values of wave vectors, but this constrain is compensated in the process of numerical calculation because the qusiparticles with the bigger wave vector have also relatively higher energy and therefore the probability of their appearance exponentially decreases. In our modeling the quasiparticle energy should be small in comparison with the thermal energy per atom ($\sim k_B T$ where k_B is the Boltzman constant and T is the temperature) and therefore our calculations do not fit for very low temperatures. Actually, we made our calculations for temperatures around 20K.

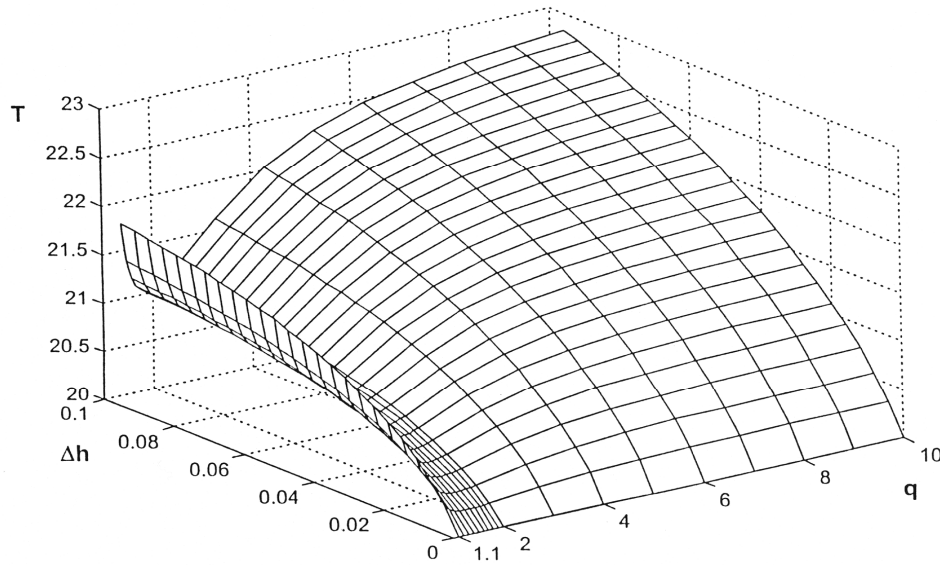


Fig.1. Dependence of the temperature on the external magnetic field (MCE) and on the ratio of longitudinal and transversal speed of sound. It is based on the self-consistent computations similar to computations made in ref. [31]. T is the temperature in K, $\Delta h \approx H - H^{crit} / H^{crit}$ is a relative distance from the phase transition, H is external magnetic field, for H^{crit} is the magnetization of sample turned from the easy direction into the hard direction, $q = c^l / c^t$ is the speed ration where c the speed of sound. Note that there is the change of sign of magnetocaloric effect in the instant of phase transition.

20.4.2. Diffusion of heat and phase transition.

One from the results of our MCE modeling, which is closely connected with both the diffusion of heat and MCE, is following “the energy of one from phonon-like modes (for direction parallel or perpendicular to the anisotropy axis) is going to zero by approaching to the phase transition”. We considered the phase transition of second order, which appears by the rotation of magnetization from the easy anisotropic direction into the hard direction. The driving force for rotations was a growing external magnetic field. Our model predicts the anomalous behavior of MCE by approaching to the above considered phase transition and our theoretical forecast is now going to be partially confirmed by new experiments [33]. MCE was recently measured in nanomagnetic materials in the vicinity of magnetic phase transition of second order. The phase transition in quoted experiment and the one in our model are very

similar. External magnetic field is turning magnetization of sample from the easy direction of magnetic anisotropy into the hard direction. In agreement with our expectations there was observed the significant increase of magneto caloric effect in the vicinity of this phase transition. The existence of an easily excitable mode supposed in our model can explain the magnitude and even the change of MCE sign. The appearance of easily excitable mod by approaching to phase transition could be, however, a more general transdisciplinary phenomenon.

Our considerations could be supported with a possibility of a similar magneto caloric behavior in superconductors in the neighborhood of phase transition from superconductivity to normal conductivity [39-41]. Phase transition in superconductors of second type is made by the increase of external magnetic field to the critical value. We made modeling calculations based on the supposition of a transfer of energy between collective excitations of vortexes and thermal phonons in the super conducting material [31]. Experimental confirmation of this expectation could be even more interesting and important [33]. We also recently learned that such ideas are now going to be practically used in the so-called “thermal machine” where the standard working medium (water) is replaced by superconductor [42]. The phase transition from superconductivity to normal conductivity and vice versa is realized by the change of distance between sample and the space with strong magnetic field. The change of sign of MCE produced by passing through the phase transition is than rhythmically used for engine-like cycling process [42]. Transdisciplinary scientific attitude can be seen here as a driving force leading possibly not only to better knowledge but also to futuristic machines

20.4.3. Some remarks to nanomagnetic materials:

In the center of our special interest are also artificially produced nanomagnetic materials, the research which is now in the focal point for many laboratories. From the point of view of our MCE modeling nanomagnetic materials possess encouraging properties.

Decoherence of longer wavelengths in nanomagnetic structures is smaller than in normal crystalline material (note that coherent behavior is possible if the wavelength is longer than the smallest distance in the medium; in nanomagnetic materials this minimal wavelength is ~10 or even ~10000 times longer than that in normal crystals). The number of allowed wavelengths in nanomagnetic materials is restricted. The resonance condition for transfer energy between magnons and phonons can be better adjusted.

The Debay temperature in nanomagnetic materials is higher comparatively to other materials and therefore the entropy term for thermal lattice vibrations has a magnitude comparable to the entropy term for magnons. On the boundaries of anisotropic nano grains could appear thermal gradients and elastic stresses. Some nanomagnetic materials are even transparent for wavelengths comparable with the size of nanomagnetic clusters and photo elastic method of observation of elastic stresses could be used.

There are indications that dipole-dipole interaction starts to be more important in nano materials than in normal, more homogenous materials. The study of anisotropy of sound velocities can also bring interesting and even practical results.

20.5. Quantum criteria and diffusion

There subsist an everlasting question in what conditions various diffusion modes of particles' dissemination can emerge and when it becomes necessary to use another theory than that customarily classical. A very useful criterion, which enables one to decide whether a particular physical problem belongs to the domain of classical or quantum physics can be formulated as follows [43-45]. For example *A. Sommerfeld* expressed in [44]) “*in every case*

where the quantity of type of action (relevant to a given physical problem) is comparable with Planck's quantum of action $\approx 1,05 \times 10^{34}$ [Js] the linked problem can be solved consistently only within the frame of the quantum theory". Notice, there is no further requirement put on the absolute scale of the system. If any particular system is accordingly to this criterion a quantum system, it can be microscopic or macroscopic as well! At first glance, one can see that this criterion implies immediately the quantum nature of the periodical precipitation of chemical waves experimentally described by below equation [46-50] only if one admits that the magnitude of action can be adjusted as the product of energy (E) and time (t) or better as the outcome of momentum (m v) and distance (λ)³. Employing the latter portrayal we arrive to Sommerfeld's criterion [49,50] in the form of

$$m v \lambda = \hbar \quad (5)$$

where the left-hand side of which represents the "relevant quantity of type action".

In order to have the left side of above equation relevant to the motion of an electron in the typical network of epitaxial structure of semiconductor GaAs/GaAlAs we have to bring in the effective mass of a free electron $\sim 9,1 \times 10^{-31}$ kg reduced by the coefficient 0,07. Upon taking into account that the speed appropriate to the arbitrary thermal motion of an electron in a crystal network is in the order of magnitude of $\sim \sqrt{(k_B T/m)}$, where $k_B = 1,38 \times 10^{-23}$ [J/K] is Boltzmann constant and T is absolute temperature in [K], then we can get an estimate for the characteristic length, λ , at which the non-classical properties of an electron became authoritative, i.e., $\lambda \approx \hbar / \sqrt{(m k_B T)}$. At the helium temperatures ($T \cong 4.2$ K) the above relation yields distinctive $\lambda \approx 5.6 \times 10^{-8}$ m, which is the dimension in tenth of nanometers, which is commonly a characteristic material length technologically adjusted in the sandwiched thin layers structures prepared by epitaxial techniques. Therefore in such nanometric structures we use wave tools of quantum mechanics, eventually its extension towards electromagnetic phenomena, i.e., *quantum electrodynamics* (QED). It, however, brings some considerable predicament because operations with abstract mathematical notions (such as creative and annihilative operators, renormalization of vacuum, etc.), which are difficult to inaugurate to a concrete experimental situation and coordinate with entirely measured data. This circumstances lead to search for alternative solutions more friendly to the users, i.e., more vivid to straightforward mathematics. In this respect an important conjecture is the stochastic interpretation of the above mentioned QED, i.e., *stochastic electrodynamics* (SED), which is based on the classical theory of arbitrary (\sim stochastic) processes best represented by the Brown motion supplemented, however, by hypothesis of real existence of zero electromagnetic fluctuations of vacuum (FPF). The difference in the QEP and SED approaches to a real problem can best be apprehended in the phenomenon called weak localization of electrons [53].

On the way to the description of quantum processes (and so SED) it is possible to use method introduced in the thirties of the past century by the Prague countryman R. Fürth [54]. By identification the source of noise (responsible for stochastic behavior) with the zero electromagnetic fluctuation of vacuum we obtain the depiction almost identical with that known from quantum mechanics. In addition the transfer from stochastic mechanics towards quantum mechanics can be adjusted according to Fürth [54] rather formally by a simple

³ Maupertuis [51] in 1744 envisaged that "when some change takes place in nature, the quantity of action necessary for the change is the smallest possible. The quantity of action is the product obtained by multiplying the mass of the bodies by their velocity and the distance travelled". Similar meaning is the Fermat's principle of least time [52] citing "the Nature acts via the easiest and the most accessible way reached within the shortest time".

replacement of the standard diffusion coefficient, D , in the classical equations given by *A. Einstein* [55] and *M. von Smoluchowski* [56] by an inventive coefficient

$$i D_Q = i \hbar / 2m, \quad (6)$$

where i is imaginary unit and m is the mass of the moving particle. It remains the features discussed in the second paragraph and the sourcing possibilities for the Schrödinger equation. The presence of imaginary unit responsible for generating this transposition (usually recognized as impassable obstacle in understanding of quantum mechanics) as a specific form of stochastic comprehension is, unfortunately, not trivial. It can be shown [49] that the presence of imaginary unit in kinetic equations of a mass particle in the so called *phase space* (i.e., the space of independent pairs of variables of coordinates and momentum) assures that the particle can remember its whole history. Indeed, it must be innate because the past and future chronicle of a particle must be identifiable as follows from the wave function definition. However, for a classical Brownian particle the situation is fundamentally different. After each impact of neighboring molecules the Brownian particle obtains momentum, which value and direction is not relevant with that possessed before this impact as well as with that which the particle will obtain afterwards. The particle motion has not memory as that cannot be described by quantum Schrödinger relation.

The whole situation and pertinent argumentation will drastically change when the same processes are considered not in the previously presupposed phase space but in the novel *configuration space* (i.e., space of geometrical coordinates). Everlasting interaction of a particle with its surroundings have a bearing on the manner in which a kind of measurement of quantum position is determined one by one forcing thus the particle to repeatedly forget its momentum (according to the Heisenberg principle of uncertainty). In the configuration space the motion of a quantum particle becomes principally undistinguishable from stochastic motion of a classical particle. On this is righteous but often omitted fact is possible to base the interpretation of some important and experimentally widely observed phenomena, such as capacitance properties of two-dimensional electron gas [57] at the helium temperatures or more than 70 years old puzzle of quantum-like behavior of diffusion controlled chemical reactions exhibiting periodicity [46,47].

Some of these reactions producing self-organized macroscopically evident structures display extraordinary fact that the characteristic speed of spreading, v , space periodicity, λ , and molecular mass, m , is interrelated by the equation (5), which has an focal function in biology [46-48,58-60]. They are regular and ornamental drawing and painting on shells, annual growth rings of tree or Ranvier grooving on myelin wrap of nerves, etc. The quantity $m v \lambda$ has, of course, the physical dimension of action but the adequacy of its construction as a product of quantities m , v and λ remains uncertain. The physical meaning of λ may be regarded to be more-or-less clear, it is, e.g., the distance between subsequent Liesegang's rings [61] representing the minimal path which has to be passed by particles forming the precipitate. On the other side, it is quite obvious that the actual length of random walk of diffusing Brownian particle (molecule) must be about orders of magnitude longer. Similarly, M , being the mass of a single molecule of end-product and thus possibly not taking a part in the diffusion at all, is evidently also of questionable relevance. Even more problematic is the justification of the use of quantity v sometimes computed, as already mentioned above, as the ratio λ / t . It is not the "speed of diffusion" what is introduced here but it is in fact the time t characterizing the duration of the process of precipitation as a whole and the quantity λ which enters for the second time tacitly the left-hand side term of equation (1). The meaning of quantity v thus remains somehow unclear.

Interestingly, as was pointed out by *E. Mach* [62], the confusions of a very similar type almost invalidated the premise applicability of *P.L.M. Maupertuis* [51], i.e., “*principe de la moindre quantité d’action*” in its original form where the *quantity of action* was for the first time defined. The revision of this concept for a purely mechanical case (due to Euler as transferred from [63]) showed that the properly defined quantity of action should contain the instant velocity of a system in the explicit form as an independent parameter. In fact, the phase space was thus introduced in this way into the classical mechanics.

Even this short excursion shows that the quantities from the left-hand side of equation (5) are not fully apt to represent the physical system under consideration in a convincingly way. To answer the question of “*why the fanciful mix of quantities $M v \lambda$ gives a well defined universal constant \hbar* ” it is necessary to construct the action from other quantities more transparently related to the system under investigation, to make clear the relation of these new quantities to the quantities M , v and λ and then, possibly, to apply the quantum criterion.

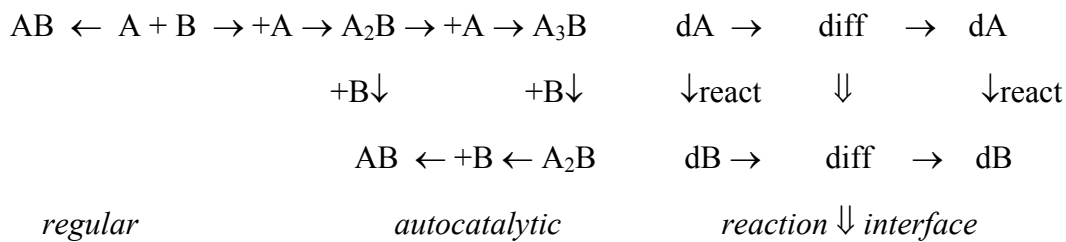
20.6. Oscillatory regimes in some inorganic systems

Assuming that the decisive process controlling the periodic precipitation or oscillating reactions is the diffusion of reactants (i.e., we consider the so-called *Nernst-Brunner* limit [64] of chemical kinetics) we have here again the phenomenon of diffusion. It is a along known puzzle of nature first mentioned in details in the case of dying by *F.F. Runge* [65] citing “*various chemical reactions produce patterns periodic both in space and time when the relative concentrations lie within a certain ranges. These patterns carry order corresponding to the breakdown of both spatial and temporal translational invariance*” and latter often cited and known as *Liesegang rings* [59-61,66].

It is also well known that resistors carrying large electrical current can exhibit negative differential resistance, i.e., currents that even decreases with increasing voltage supporting oscillations, rather than steady currents. Another example may be shown when studying instabilities that occur in thin wafers in certain semiconductors (GaAs). If the electrical potential across the semiconductor exceeds a critical value the steady current that is stable at lower potentials, abruptly gives way to periodical changes in the current, often called Gunn oscillations [67]. Statistics show that the stability of such a non-equilibrium steady state is reflected in the behaviour of the molecular/atomic fluctuations that became larger and larger as the steady state becomes more and more unstable finally becoming cooperative on a long-range order. In many cases this effect is hidden by our insensitive way of observations, particularly for those reactions that we let start far from equilibrium first to exhibit non-equilibrium phenomena but latter either decaying (disappearing) close to its steadiness or abruptly stopped (freeze-in) by quenching (renowned as amorphous or glassy states of non-crystallites, see introduction).

Inorganic solid-state reactions are often proceeding via branching [48,68,69] caused by disproportionate allocation of reactants due to the mixing inadequacies or diffusion irregularities. Let us assume a simple case of synthesis known in the production of cement or geopolymers assuming ideal and real reactions hypothetically supposed to follow processes taking place during silicates formation. According to *V. Jesenak* [69], there are two starting solid reactants A (CaO) and B (SiO₂) undergoing synthesis according the scheme shown below (left) to yield the final product AB (CaSiO₃) either directly or via transient products A₂B (CaSi₂O₄) and A₃B (CaSi₃O₅). The formation of these intermediate products depends, beside the standard thermodynamic and kinetic factors, on their local concentrations. If A is equally distributed and so covered by the corresponding amount of B the production of AB follows standard kinetic portrayal (left headed arrow). For a real mixture, however, the component A may not be statistically distributed everywhere so that the places rich in A may

effect the reaction mechanism to prefer the formation of A_2B (or even A_3B) the latter decomposition of which is due to delayed reacting with deficient B that is becoming responsible for the time prolongation of reaction completion. If the component A tends to agglomerate the condition of intermediate synthesis become more favourable undertaking thus the role of rate controlling process. The entire course of reaction can consequently exhibit an oscillation regime due to the temporary consumption of the final product AB, which is limited to small neighbouring areas. If the intermediates act as the process catalyst the oscillation course is pronounced showing yet more regular nature. Their localised fluctuation micro-character is, however, difficult to be detected by direct physical macro-observations and can be only believed upon secondary characteristics read from the resulting structure (final morphology) [48,68]:



Changes in phase composition and properties of cordierite-based materials showed similar features of periodic reactivity [70] depending on the calcinations temperature and the calcinated ratio in the starting mixture. It results from specific conditions of formation of a dissipative structure in such refractory materials and a specific organization of the phase composition under a spinodal decomposition of solid solutions.

Local effect of counter-diffusion would become another important factor that may not only accelerate above mentioned oscillations but can often outcome most of the interface reaction (see above scheme on right). As a result many of peritectic and eutectic reactions turn out to be in an oscillatory regime providing regularly layered structures. For example, the directional solidification of the $PbCl_2$ - $AgCl$ eutectic [71] is driven by temperature gradient and provides lamellar structure separated repetitively at almost equal lamellae partition. Solidification studied under microgravity [72-74] starts with higher undercooling compared with that observed in terrestrial condition obviously due to the lack of thermal and mass convection not disturbing self-organization and thus exhibiting exceptionally regular lamellae stripping e.g., notice the following Fig. 3.).

Such self-organization may happen during various processing such as the periodical adjustment of jetted fibres during the liquid electrospinning [75] If a competition between several simultaneous processes occurs (as a typical case for many non-equilibrium systems), it may lead to curious repetitive morphologies, such as a plate or needle-shaped crystals precipitated within glass devitrification [76] and benefit useful in modeling micro-heat engines⁴.

⁴ A quasi-harmonic approximation of a piston-type heat engines are subjects of oscillations' theory since they operate in swig regime known as a best example of a parametric self-sustained periodicity. A human on swings is thus a source of energy and is the automaton that implements a swinging algorithm (A.N. Zalkin "Investigation of oscillation regime for a modified Carnot engine, I: Conservation of oscillation regime and II: Generator of self-sustained oscillations" Moscow Univ. Bull. Phys. 63 (2008) I: 339 and II: 344). Correspondingly, the Browning periodic heat engine can be Carnot-modeled as a Brownian particle is hopping in a viscous medium within a saw tooth potential assisted by alternatively placed hot and cold heat baths along the path (M. Asfaw "Modeling an efficient Brownian heat engine" Europ. Phys. J. B 65 (2008) 109).

Oscillatory scheme is very important for all lively processes taking place far from equilibrium. The customary case often repeated are the curious circumstances emerging upon heating a thin layer of liquid from below (known as *Rayleigh-Bénard hydrodynamic instabilities* [68]. First the heat passes through the fluid by conduction but at certain, well-defined critical point of intensified heating, the gradient pattern changes spontaneously but abruptly to a self-organised system of almost hexagonal cells. This high degree of their molecular organisation becomes possible through the transfer of energy from microscopic thermal motion to macroscopic convection currents acting under the force field of gravity. In greater macroscopic scale it is well known as the formation of clouds in warm weather [72].

Similar repetitive pattern can be observed on many other cases from mesoscopic shall ripening to macroscopic geological sediments and variety of biological patterns on animal's skin ornamentation and there arise a question why this separation is so regular and what are its grounds. The domain of oscillatory processes common in chemistry is particularly regarded as the *Belousov-Zhabotinsky* reactions (further abbreviated as BZR).

These processes were successfully simulated by use of computers. Most famous is the scheme known as "Brussellator" [46, 68,77] describing so called cross-catalytic reactions involving two reactants A and B and two products Z and P, see Fig. 2 . The intermediates are X and Y and the catalytic loop is caused by multiplication of the intermediates X, see scheme below. Right graph illustrates the input effect of reactant concentration within the given reaction mechanism (at the threshold concentration of A the steady subcritical region changes from the sterile to the fertile course of action capable of oscillations in supercritical region. Although first assumed hypothetically it enabled to visualise the auto-catalytic nature of many processes and gave to them the necessary practical dimension when applied to various reality situations. Latter this scheme was associated to be close to the life-imperative system of the glycolytic energetic cycles where the oscillatory intermediates are adenosintriphosphate (ATP) and adenosindiphosphate (ADP).

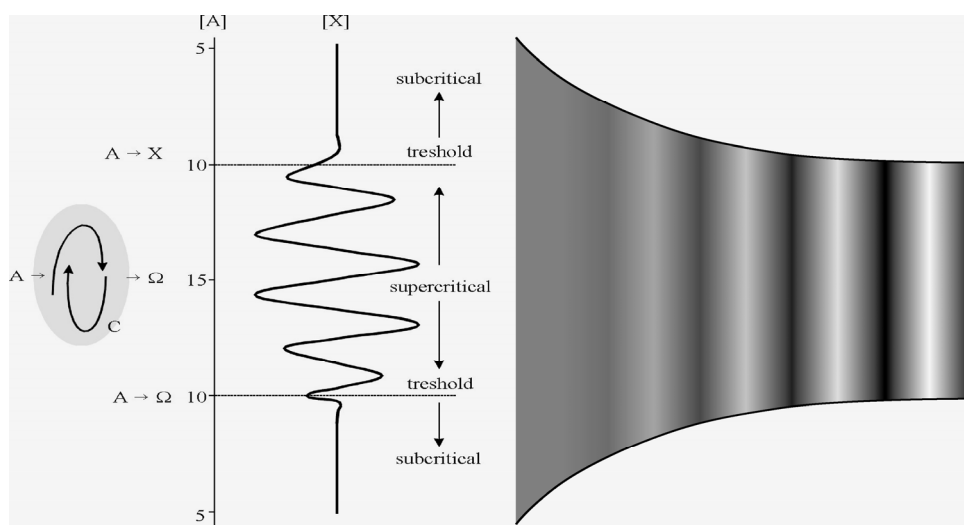
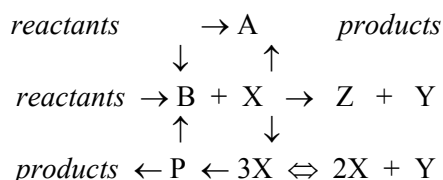


Fig. 2. Schematic diagram showing the subcritical and critical oscillatory regimes of a computer scheme (customary called Brusselator)

In concluding we would like to stress out that herewith we shall try to be consonant with familiar Prigogine's generalized ideas of self-organization dealt with on different levels. The enormous collection of experimental data on the behaviour of BZ waves published throughout the literature represents a very good opportunity for a better tuning of this concept as we attempt to do it in the forthcoming text although we are aware that any break in the traditional world of physics would be extremely difficult as it was not accepted yet despite several attempts during the past decades. We ventured to coin here the term *diffusion action*, which expresses the quantity of action induced by diffusion process of Brownian particles. The experimental values of the diffusion actions of the one dimensional (1D BZ) waves might support the theoretical approach that attempts to interpret the concepts of quantum mechanics based on the behaviour of Brownian particles [78]. The variety of its description about finding mutual links is the goal of this article while the mathematics of non-equilibrium thermodynamics was discussed by us elsewhere [79].

20.7. Belousov–Zhabotinsky periodic reactions

Periodical precipitation of reaction products and oscillatory behavior of certain chemical reactions, known from the literature, such as *Liesegang's effect* [61,65,66], chemical waves, or *Belousov–Zhabotinsky reactions* [58-60,80-84], are now usually considered to be spectacular demonstrations of self-organization in non-equilibrium thermodynamic systems. As these mostly inorganic reactions deny the traditional view on chemical kinetics characterized by the natural tendency of reactions to reach by shortest way the state of equilibrium, they were in the past interpreted even as a precursor of life processes [65]. Moreover, another very peculiar feature of some of these reactions was discovered leading to the above mentioned “effective diffusion action” which is defined, eq. 5, as a product of characteristic macroscopic period of precipitation patterns λ , macroscopically observed “speed of diffusion” v and molecular weight of the precipitated end-product M .

It should be noticed here that in the case where the said “speed of diffusion” cannot be observed directly (e.g. as a speed of chemical wave) it is, as a rule, identified with the ratio λ/t where t means the duration of precipitation. A better quantitative agreement with the experiment (up to 1% accuracy) can be achieved by completing the left-hand side of relation (1) by a geometric factor (e.g. 4π for three dimensional cases) and by a factor characterizing the limiting influence of environment where diffusion takes place, tortuosity, which is of the order of unity [78].

There is no consensus concerning relation (5) in scientific community. It was found by various scholars to be either accidental without any deeper physical meaning or enigmatic, with something very important behind. Such diversity in opinions is partially due to the traditional, rather subjective distinguishing between macroscopic and microscopic phenomena. The quantities v and λ on the left-hand side of equation (1) are, namely, in contrast to M essentially macroscopic, they are, e.g., accessible to the observation by unaided eye, while Planck's quantum of action on the right-hand side is regarded to be characteristic of tiny quantum processes on an atomic scale. There are several attempts to explain this curiosity theoretically. For example, there is a very straightforward interpretation of relation (5) using a concept of the de Broglie wave known from elementary quantum mechanics as a wave controlling the probability amplitude of a particle (*onde pilot* [85]). Accordingly, we have reputedly to do with the de Broglie probability pilot wave of an abstract particle of mass equal to the mass M of the end-product molecule moving with the “speed of diffusion” v . It is further assumed *ad hoc* that the wavelength h/Mv of this de Broglie-like wave coincides with some integer multiple of the period of precipitation, what is just that meets the want. Such a simplistic exploitation of quantum ideas and quite formal approach to the problem, tolerable

in pioneering works, together with the obscure concepts involved is, as we believe, the very reason which has led to the skepticism aimed against the quantum theoretical interpretation of equation (5) and for years effectively damped the activities in this interesting field.

The authors are convinced that the numerous observations confirming the validity of (6) in quite different experimental situations (for review see e. g. [47,48] are not likely to be all accidental and thus they are worthy of further study. We are thus *trying*, using the arguments on a quite elementary level, to turn the attention of researchers to some aspects which may be of importance for understanding of this empirical formula. The problems closely related to the self-organization *per se* are, however, left aside in the present text.

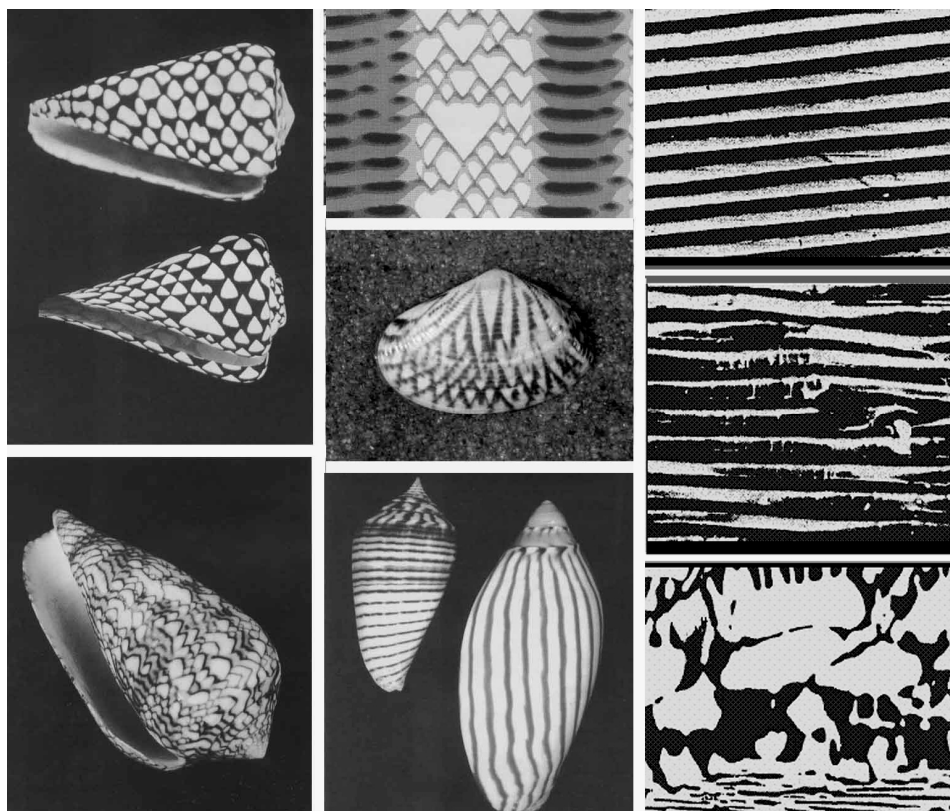


Fig. 4. Photo of various shells and (right column) quenched-in morphology of the directionally solidified eutectics of $PbCl_2-AgCl$ processed at a high melt undercooling ($\Delta T=50$ K) and growth rate ($v = 10$ mm/hr) at both under the microgravity ($G_o \rightarrow 0$, in space, upper) and terrestrial conditions ($G_o=1$, below). It reveals the oscillatory growth of $PbCl_2$ lamellae in the crystallographic direction [100] parallel to the reaction interface (visible at the upper-side [72-74]). The lamellae that solidified directionally at terrestrial conditions (middle) exhibit, however, characteristic growth defects due to the interference of mass flow with gravitational field that is absent for the space experimentation (upper). Time-dependent effect of lamellae coarsening (bottom) provides image of a common pattern of rough morphology regularly achieved for prolonged equilibration/sintering (not in scale).

20.7. Speed of diffusion

Assuming that the decisive process controlling the periodic precipitation or oscillating reactions is the diffusion of reactants (i.e. we consider the so-called *Nernst-Brunner limit of chemical kinetics* [49,64]) we need for the construction of the corresponding “relevant quantity of type action” the definition of something like the instant “*speed of diffusion*”. If we, for the sake of simplicity, confine ourselves only to one dimension, the diffusion can be described by the following differential equation (i.e., the second Fick’s law):

$$\partial n / \partial t = D (\partial^2 n / \partial x^2), \quad (7)$$

where $n(x,t)$ means the concentration and D the diffusion constant. For continuous $n(x,t)$ the “speed of diffusion” is not well defined or it has to be assumed to be infinite. This statement can be elucidated by the following argument [86]. If the concentration n of a substance at time $t = 0$ is finite only in a certain bounded region (e. g. $n = \text{const.}$), being identically zero out of this region, the equation implies that after an arbitrarily small time interval dt the concentration at any point of the whole space is non-zero, so that the transport of matter to any distant point would be instantaneous, i.e. with an infinite speed. On the other side, taking into account the discrete molecular structure of ordinary matter, the concentration at a given point should remain zero till it is reached by the first diffusing particle (molecule), i.e. the velocity should be finite in any case. In spite of this unpleasant discordance between molar and molecular approach to the diffusion, there is a possibility of meaningful definition of its speed even within the continuous approximation of $n(x,t)$. Let us assume that at time $t = 0$ there are N particles concentrated in the plane $x = 0$ (source layer). In this case the solution of equation (2) reads:

$$n(x,t) = N / (2\sqrt{\pi Dt}) \exp(-x^2/4Dt). \quad (8)$$

Since the times of Fourier it has been a well-known property of solution (3) (known as a source–integral) that the time record of concentration taken in a neighborhood of a certain fixed point x has a local maximum. The mathematical condition for this maximum reads $\partial n / \partial t = 0$. This is, however, according to equation (2), equivalent to the condition $\partial^2 n / \partial x^2 = 0$ (for constant $D \neq 0$). The second space derivative of solution (8) gives then the expression:

$$\partial^2 n / \partial x^2 = \{N/4\sqrt{\pi(Dt)^3}\} \exp(-x^2/4Dt) \{(x^2/2Dt) - 1\}. \quad (9)$$

Using now the above-mentioned condition for extreme, we immediately obtain straight and its time derivative formulas bestowing equations:

$$x^2 = 2Dt. \quad (10)$$

$$x u = D, \quad (11)$$

where $u = (\partial x / \partial t)$ has evidently physical meaning of the instant speed of transfer of concentration maximum. As the quantity u , in fact, represents the movement of the most numerous swarm of diffusing molecules, it is quite reasonable just to call u the “instant speed of diffusion”. It is a remarkable circumstance that equations (5) and (6) are practically the same as the equations describing random walk of a single Brownian particle (molecule) [55,56]. The only differences are that here is x no more the position of the concentration maximum but the mean-square-root $\sqrt{\langle x^2 \rangle}$ of the position of a particular Brownian particle at time t and u has a meaning of its mean-square root of stochastic speed $\sqrt{\langle U^2 \rangle}$. If we start, namely, from an alternative form of Fick’s law in a probabilistic notation, i.e. from

$$Uw = -D (\partial w / \partial x), \quad (12)$$

where the probability density is defined as $w = n/N$, U is the stochastic speed and (Uw) has the meaning of the probability flux, we obtain for the mean-square of the stochastic speed the expression (the integrals here are taken over the range from $-\infty$ to $+\infty$)

$$\langle U^2 \rangle = \int (U^2 w) dx = D^2 \int (1/w) (\partial w / \partial x)^2 dx. \quad (13)$$

In consequence of evident inequality $\{(\partial w / \partial x) / w + x / \langle x^2 \rangle\}^2 \geq 0$, one obtains after a simple algebra that $\int (1/w) (\partial w / \partial x)^2 dx \geq 1 / \langle x^2 \rangle$ and therefore eventually

$$\sqrt{\langle x^2 \rangle} \sqrt{\langle U^2 \rangle} \geq D, \quad (14)$$

where equality in this “uncertainty relation” takes place for the probability distribution corresponding just to the source-integral (8). Because equations (11) and (14) describe the same physical process of diffusion, the diffusion constants D must naturally be identical for the microscopic as well as for the macroscopic cases and simultaneously the relations $u = \sqrt{\langle U^2 \rangle}$ and $x = \sqrt{\langle x^2 \rangle}$ must be valid. We can thus conclude that a typical “average” Brownian particle follows the position of the concentration maximum or in other words that the most significant packet of diffusing molecules consists of “average” Brownian particles.

As we believe, this is just the way how Planck’s universal constant can in principle enter essentially macroscopic equation (11). Namely, if the microscopic movement of a Brownian particle of mass M would be controlled by a purely quantum process, where the diffusion constant in three dimensions should have Fürth’s limiting value of $D = D_Q$ [87], i.e.,

$$D_Q = h / 4\pi M.$$

Then equation (11) will formally attain the same form as empirical equation (1), explicitly:

$$4\pi M u x = h, \quad (15)$$

providing that the experimentally observed quantities v and λ are identified with $u = \sqrt{\langle U^2 \rangle}$ (speed of diffusion) and $x = \sqrt{\langle x^2 \rangle}$ (distance spanned by diffusion), respectively.

20.8. Resemblance of quantum and Brownian motion in configuration space

It seems thus plausible that to prove the quantum nature of equation (5) it is enough to make clear conditions under which the numerical value of diffusion constant D attains the Fürth’s value D_Q . Unfortunately, realization of this task is by no means trivial, mainly because the frequently stressed analogy between quantum and Brownian motions [25,88-90] is rather superficial and far from being perfect. On the other side, there is an important common characteristic of these two types of stochastic processes which makes them identical in a certain sense, namely their *Hausdorff’s dimension in the configuration space* [91,92]. To make clearer the relation of this useful mathematical concept to the present problem we must go behind the continuous approximation of diffusion represented e.g. by equation (10). Extrapolating the validity of this formula from the experimentally verified range to arbitrarily small scales, we can use it, however, for the construction of a more realistic model of movement of a Brownian particle in the following way.

Let us make intermittent observations of total duration τ , sampling every (τ/k) seconds the position of a Brownian particle, where k is an arbitrary integer. Every time interval (τ/k)

involves some delay and time necessary to determine the position of the particle. Such a measurement will provide in one dimension a sequence of intervals l_1, l_2, \dots, l_k , which define the apparent length of the path passed through as:

$$L_k = l_1 + l_2 + \dots + l_k. \quad (16)$$

As the movement along every of these intervals is, according to our assumption, controlled by law (10), for a sufficiently large k instead of (11) we can write:

$$L_k = k \sqrt{\langle l^2 \rangle_k}, \quad (17)$$

where index k means the averaging over all k intervals in (16). It is simultaneously clear that the length $\sqrt{\langle l^2 \rangle_k}$ defines for a given k also the length resolution $\Delta l_k = \sqrt{\langle l^2 \rangle_k}$ of the measurement, because the sampling by time intervals (τ/k) evidently ignores the details of the actual path of the Brownian particle finer than Δl_k . Average speed determined from the same experiment as $(k \Delta l_k / \tau)$ must, moreover, fulfill the relation (14) in the form (reduced to equality):

$$\Delta l_k (k \Delta l_k / \tau) = D. \quad (18)$$

It is obvious that the more frequent measurement with a better resolution Δl_k will reveal more details of motion of the Brownian particle. As a result, with increasing k the number of recorded abrupt changes on the Brownian path will increase and also L_k will increase simultaneously. For very large k 's (theoretically for $k \rightarrow +\infty$) the shape of the Brownian path will resemble a continuous, at every point non-differentiable curve. As was shown by *Hausdorff* [92] such a complicated mathematical object may be, without ambiguity, characterized by introducing its fractal (Hausdorff's) measure Λ and generalized dimension d as follows:

$$\Lambda = L_k (\Delta l_k)^{d-1}, \quad (19)$$

where dimension d should (and can) be chosen in such a way that Λ is independent of k . Putting then relations (18) and (19) together, we obtain:

$$\Lambda = (D\tau/\Delta l_k) (\Delta l_k)^{d-1}, \quad (20)$$

from which, due to the said independence of Λ on k , it immediately follows that Hausdorff's dimension of the Brownian motion is arresting $d = 2$ (cf. e.g. [88]).

As was shown by *L.F. Abbott* and *M.B. Wise* [93], just the same Hausdorff's dimension in the configuration space ($d = 2$) has to be ascribed to the jiggling movement ('*Zitterbewegung*') of a quantum particle. This can be proved very easily using, instead of eq. (18), common Heisenberg's uncertainty relation in a (reduced) form

$$\Delta l_k (M k \Delta l_k / \tau) = h/4\pi, \quad (21)$$

preserving the previous meanings of all quantities involved. The corresponding “quantum” expression for Hausdorff’s measure then reads:

$$\Lambda = (h\tau / 4\pi M \Delta l_k) (\Delta l_k)^{d-1}. \quad (22)$$

This formula gives the same value for $d = 2$ as equation (20) and can be obtained from it by a formal substitution of D_Q for D . Because both quantum and Brownian motions have in the configuration space exactly the same Hausdorff’s dimension revealed, e.g., by the intermittent measurement described above, the quantum jiggling can be, from the phenomenological point of view, considered as a continuation of the Brownian motion down the smaller scales. This circumstance enables us to treat the diffusion of a particular molecule together with its quantum jiggling movement as a single stochastic process, formally described by a convenient combination of classical stochastic and quantum diffusion constants, D_S and D_Q , respectively. Using analogy with the composition rule for independent motilities well known from electrochemistry, we can tentatively write:

$$D = D_S D_Q / (D_S + D_Q). \quad (23)$$

Then quantum limit is represented by the inequality $D_S \gg D_Q$, which ensures that $D \approx D_Q$. The quantum effects should prevail in the case, where D_S attains a very high value, or in other words, if the diffusing particle is decoupled from all stochastic sources in environment which are not of quantum nature. We claim that just this inequality, i.e.

$$D_S \gg D_Q, \quad (24)$$

with the accompanying physical meaning mentioned above is the condition we are looking for. If this takes place, namely, equation (15) and consequently equation (5) are valid, satisfying simultaneously the quantum criterion.

To assess the range of validity of inequality (24) it is necessary to evaluate stochastic diffusion constant D_S . Somewhat crude estimate for ball-like particles (molecules) without observable persistency in motion can be provided by a classical Einstein-von Smoluchowski’s formula [55,56] the use of which is justified rather by practical than physical reasons. Then condition (24) reads:

$$k_B T / 3\pi\eta a \gg h / 4\pi M, \quad (25)$$

where η is the dynamic viscosity of environment, T the absolute temperature and a the characteristic dimension of diffusing particle (molecule). To find out among various aqueous solutions at room temperature molecular systems for which the “quantum” behavior is to be expected, we put in (25) $T = 300$ K and $\eta = 10^{-3}$ kg m⁻¹s⁻¹. The resulting condition is:

$$8.4 \times 10^{15} \gg a / M, \quad (26)$$

where a is in meters and $M = (1.67 \times 10^{-27} \times \text{molecular weight})$ in kilograms. Taking for a the ionic diameter [93], we can see that, e. g., sodium, calcium and silver, for which ratios (26) have values 6.0×10^{15} , 3.4×10^{15} and 9.0×10^{14} , respectively, are good candidates for

“quantum” Brownian particles. For H^+ ions (i.e. protons) which are the most mobile ions in aqueous solutions condition (24) is also valid in spite of the fact that estimate (24) (with the ionic diameter $a \approx 10^{-11}$ m) provides rather a high value $\sim 1.2 \times 10^{16}$. It can be accounted for by the fact that the system of protons in water being a Fermionic system requires a consequent quantum-theoretical treatment (involving e.g. Pauli Exclusion Principle), which is essentially non compatible with classical formula (26).

In conclusion we can put across with the aim of comprehensibility that in the configuration space and by intermittent observations, which resemble the actual observations performed on periodic patterns, the classical and quantum stochastic processes are practically indistinguishable. This remarkable fact enabled us to formulate in terms of the classical and quantum diffusion constants the condition where the quantum stochastic process should prevail. It was shown on the basis of this criterion that it is very predictable that ions in aqueous solutions can possess macroscopically observable quantum behavior. Moreover the above survey, which summarizes some quantum aspects of diffusion, is a part of the larger domain covered by “*quantum thermodynamics*” [12,42,89,94-97], which is being extensively dealt with in various conferences [98] and may extent to rather curious corners of science [99-102], see the final illustrative paragraph. Yet it seems be a very challenging subject worth of further cultivation in more widely assumed thermophysical applications [12,89].

20.9. Transmission of information – the photon codes

The analogy between chemical and photon waves can guide us how to re-interpret the experimental data we could find in the scientific literature. It is assumed that the photon with its mass m is able to self-organize its surroundings with the wavelength λ and the propagation speed u . After the rapid and short first stage (*h-tuning stage*) the photons with its surroundings are ready to transmit several kinds of information [99-105]. Table I summarizes events that could be observed during this h-self-organization stage.

Table I. *Transmission of information during the h-self-organization stage*

Process	Type of information	Experimental evidence
Doppler-Voigt.Einstein self-organization	Relative velocity	Stretching of waves in the constant space, redshift, blueshift
Hubble-Nernst self-organization ($v_{rel}=0$)	Distance	Redshift quantization, secondary photon particles, Hubble-Nernst photon decay constant
Schmidt-quasar-redshift self-organization	Not yet decoded	Redshift quantization, secondary photon particles, photon decay constant
Blueshifted self-organization ($v_{rel}=0$)	Pioneer anomaly	Decay inhibition rate of photons in supersaturated ZPE, objects in the same distance have different redshifts

In this concept the photon during the process of the *h-self-organization* has several mechanisms how to transmit the information about the relative velocity, distance and some others. The mechanism of the *c-tuning* enables to transmit to all observers the information about the relative velocity between the source and the observer.

The second important information that should be transmitted is the knowledge about the distance of the observed object. This information could be coded by the decay properties of photons and is expressed by the Hubble-Nernst photon decay constant.

It seems that quasar redshifts bring to us some new kind information (neither relative velocity, nor distance). This kind of information was not decoded yet. Photons emanating from quasars decay with higher specific decaying rate in compare with the natural decay rate described by the Hubble-Nernst photon decay constant.

The analogy between chemical waves and photon waves lead us to postulate a new type of information transmitted by self-organized photon waves – the blueshift self-organization. This effect was already observed as the so-called Pioneer anomaly. The blueshift effect is caused by the inhibition of the decay rate of primary photons or the growth of primary photons with the characteristic fractal dimension $D_R=3.0$. This blueshift self-organization can contribute to the explanation why some objects at the same distance and the same relative velocity to the observer show different redshifts.

The analogy between the evolution of chemical waves and photon waves can be verified in the following observations:

1. *h-tuning stage*: during the first 20 – 30 photon waves h-tuning and c-tuning should be observed,
2. *h-self-organization stage*: four kinds of self-organization mechanisms should be observed. Table I surveys those effects together with the experimental observations,
3. *h-decay stage*: diffusion action departs from the value h, non-linear behaviour of λ , modification of the propagation speed c, critical value h_{crit} could be found experimentally,
4. *zero-point energy*: physical vacuum is filled with photons that cannot form waves.

Literature 20

- [1] J.C. Maxwell “*Theorie der Warme*” Marusche Berendt, Breslau 1877
- [2] C. Truesdell, “*Rational Thermodynamics*”, McGraw-Hill, New York 1969
- [3] J.A. Ruffner „*Interpretation of Genesis of Newton’s Law of Cooling*“ Arch. Hist. Exact. Sci. 2 (1963) 138
- [4] J.D. Barrow “*The Origin of the Universe*” Orion. London 1994,
- [5] J.B. Fourier “*Theorie analytique de la chaleur*“ Paris, 1822
- [6] A.E. Fick “*On liquid diffusion*” London, Edinburgh and Dublin Philos. Mag. & J. Science 10 (1855) 30; “*Über Diffusion*” Annalen der Phys. Chem. von Pogendorff 94 (1855) 59
- [7] H. Mehrer “*Diffusion in Solids*” Springer, Berlin/Heidelberg 2007
- [8] R. P. Feynman, R. B. Leighton, M. Sands : “*The Feynman Lectures on Physics*” (Addison-Wesley publishing Company 1966) and R. Feynman „*Feynman Lectures* » Vol. III, p. 16 and QED The Strange Theory of Light and Matter (third lecture).
- [9] L. Onsager “*Reciprocal Relations in Irreversible Processes*” Physical Review 37 (1931) 405
- [10] D. Jou, J. Casas-Vazques and G. Lebon “*Extended Irreversible Thermodynamics*” Springer, Berlin/Heidelberg 1993
- [11] G. Lebon, D. Jou, J. Casas-Vázquez “*Understanding Non-equilibrium Thermodynamics: foundations, applications and frontiers*“ Springer, Berlin/Heidelberg 2000

- [12] J. Šesták „*Science of Heat and Thermophysical Studies: a generalized approach to thermal analysis*“, Elsevier, Amsterdam 2005
- [13] Č. Strouhal “*Thermika*” (Thermal science), JČMF, Praha 1908 (in Czech)
- [14] R. Černý, P. Rovaničková „*Transport Processes*” SponPress, London 2002
- [15] R.E. Collins “*Quantum Mechanics as a Classical Diffusion Process*” Found. Phys. Lett. 5 (1992) 63
- [16] D. Hardorp, V. Pinkall “*R. Steiner and Schrödinger equation*” Math. Phys. Korrespondenz 201 (2000) 16.
- [17] E. Nelson “*Derivation of the Schrödinger Equation from Newtonian Mechanics*” Phys. Rev. 130 (1966) 150
- [18] M.D. Kostin „*Schrodinger-Furth quantum diffusion theory: Generalized komplex diffusion equation*“ J. Math. Phys. 33 (1992) 111
- [19] K.L. Chung and Z. Zhao „*From Brownian Motion to Schrödinger Equation*“ Springer, Berlin 1995
- [20] B. J. Kim, H. Hong, M.Y. Choi „*Quantum and Classical Diffusion on Small-World Networks*“ Phys. Rev. B 68 (2003) 3
- [21] J. Łuczka, R. Rudnick, P. Hanggi „*The diffusion in the quantum Smoluchowski equation*“ Physica A 351 (2005) 60–68
- [22] Z. Kalva and J. Šesták „*Transdisciplinary aspects of diffusion and magnetocaloric effect*“ J. Thermal Anal. Calor. 76 (2004) 1.
- [23] Z. Kalva , J. Šesták „*Interdisciplinarity of heat diffusion as seen from a more general perspective and its application to the magnetocaloric effect in superconducting and nanomagnetic materials*“, Proc. 9th Conference on Calorimetry and Thermal Analysis in Zakopane 2003, p.202 and also „*Interdisciplinarity of heat diffusion*” in CD Proceedings of the conference THERMANAL, Vysoke Tatry (Slovakia) October 2003
- [24] S. Schreiber „*The displacement workspace of the human knee*” Dissertation, Darmstadt D17, 1997 and A.T.Yang „*Application of Quaternion Algebra and Dual Numbers to the Analysis of Spatial Mechanisms*. Dissertation Columb. Univ. N.Y. Mic. 64-2804
- [25] L. de la Peña and A. M. Cetto: *The Quantum Dice: An Introduction to Stochastic Electrodynamics*. Kluwer, Dordrecht 1996
- [26] M. Jammer „*The Philosophy of Quantum Mechanics*“ Wiley, New York 1974
- [27] P. Stapp “*Mind, Matter and Quantum Mechanics*”, Springer, Berlin/Heidelberg 1993
- [28] R. Penrose, “*The Road to Reality: a complete guide to the laws of the universe*” Vintage, London 2004
- [29] P. Gschwind „*Mass, Zahl und Farbe*“ Mathematisch-Astronomische Blätter, Band 23, Phil.-Anth. Verlag Goetheanum , Dornach, Schweiz 2000.
- [30] Z. Kalva „*The magnetoelastic behavior in nanocrystalline materials*“ Acta Physica Slovaca 46 (1996) 651
- [31] T. Svobodny, Z. Kalva “*Magnetocaloric Effect in Ferromagnetic and Superconducting Materials*” Phys. Stat. Sol.(b) 208 (1998) 187.
- [32] Z. Kalva, P. Manek “*The remark about an analogy between magnetocaloric behavior of type II superconductors and ferromagnetic materials*” Acta Physica Polonica A3 (2000) 407
- [33] X.X.Zhang, H.L.Wei, Z.Q. Zhang, L.Zhang „*Anisotropic magnetocaloric effect in nanostructured magnetic clusters*“ Phys. Rev. Lett. 87 (2001) 157203/1

- [34] R. Clausius, *Die Bewegung der wir Wärme nennen*. Ann. Phys. Chem. (Leipzig) 142 (1871) 433; R. Clausius “*Mechanische Warmetheorie*” Vieweg u. Sohn, Braunschweig 1876
- [35] H. Aubina, K. Behnina, S. Ooi, T. Tamegai „*Quasiparticles and Thermal Conductivity*“ *Science* 280 (1998) 11
- [36] Nguyen Dinh Danga „*Thermal quasiparticle correlations and continuum coupling in nuclei far from stability* „ Nuclear Physica A722 (2003) 383
- [37] M. Ferenc; G. Katalin “*Quasiparticles in a thermal process*” Physical review E 71 (2005) 117
- [38] N. Gedik, J. Orenstein, Ruixing Liang, D. A. Bonn, W. N. Hardy „*Diffusion of Nonequilibrium Quasi-Particles in a Cuprate Superconductor* : Science 300 (2003) 1410
- [39] J. Šesták, P. Lipavský „*On the chronicle of high- T_c oxide superconductors*“ J. Thermal Anal. Calor. 74 (2003) 365
- [40] P. Lipavsky, K. Morawetz, V. Špička “*Kinetic equation for strongly interacting dense Fermi systems*” Annales de Physique, volume 26, No. 1 (2001)
- [41] P. Lipavský, J. Koláček „*Bernoulli potential in superconductors*“ Lecture notes in physics, Vol. 733, Springer, Berlin 2008
- [42] P.D. Keefe “*Coherent magneto-caloric effect heat engine*” Int. Conf. on Quantum limits to the second law” San Diego, 2002, Proc. By AIP Press, Vol. 643 (D.P. Sheehan, ed.), Melville 2002, pp. 213; “*Quantum limits to the second law by magneto-caloric effect: adiabatic phase transition of mesoscopic-size type I superconductor particles*” Physica E29 (2005) 104
- [43]] J.-M. Lévy-Leblond and F. Balibar “*Quantics - Rudiments of Quantum Physics*” North-Holland, Amsterdam 1990, p. 10.
- [44] A. Sommerfeld, Phys. Z. “*Das Plancksche Wirkungsquantum und seine allgemeine Bedeutung für die Molekularphysik*” , 24 (1911) 1062
- [45] W. Weizel, „*Ableitung der Quantentheorie aus einem klassischen, kausal determinierten Modell*“, Z. Physik 134 (1953) 264 - 285.
- [46] R. Lafever: “*Dissipative Structures in Chemical Systems*” J. Chem. Phys. 49(1968) 4977.
- [47] J. Stávek, M. Šípek “*Interpretation of Periodic Precipitation Pattern Formation by the Concept of Quantum mechanics*” Cryst. Res. Tech. 30 (1995)
- [48] J. Stávek, M. Šípek, J. Šesták “*Application of the Principle of Least Action to some Self-organized Chemical Reactions*” Thermochem. Acta 388 (2002) 440
- [49] J.J. Mareš, J. Stávek, and J. Šesták, „*Quantum aspects of self-organized periodic chemical reaction*“ J. Chem. Phys. 121 (2004) 1499.
- [50] J. J. Mareš, J. Šesták, J. Stávek, H. Ševčíková, J. Krištofik, and P. Hubík “*Do periodic chemical reactions reveal Fürth’s quantum diffusion limit?*” Physica E 29 (2005) 145
- [51] P.L.M. Maupertuis „*Oevres de Maupertuis*“ Alyon: Paris, 1768; Vol. IV, p. 36.
- [52] P. Fermant “*Synthesis ad reflexiones*” (a latter to de la Chambre 1662) in “*Oeuvres de P. Fermat*”, Tom 1, Paris 1891, p. 173
- [53] J. J. Mareš, J. Krištofik, P. Hubík, and V. Špička “*Weak localization – an experimental tool to investigate electromagnetic fluctuations*”, Physica E, 29 (2005) 375
- [54] R. Fürth, „*Über einige Beziehungen zwischen klassischer Statistik und quantummechanik*“ Z. Physik 81 (1933) 143
- [55] A Einstein “*Investigations on the Theory of the Brownian Movement*” (edited by R. Fürth) Dover Publications, New York 1956
- [56] M. v. Smoluchowski, "Drei Vorträge über Diffusion, Brownische

- Molekularbewegung und Koagulation von Kolloidteilchen* Physik. Zeitschr., **17** (1916) 557.
- [57] J. J. Mareš, J. Křištofik, P. Hubík, *Weak localization—an experimental tool to investigate electromagnetic vacuum fluctuations* Physica E **12** (2002) 340
- [58] P. Michalev, W. Nikiforov and F.M. Schemyakin, „Über eine neue Gesetzmässigkeit für periodische Reaktionen in Gelen“, Kolloid-Z. **66** (1934) 197 - 200.
- [59] A. Tockstein and L. Treindl “*Chemical Oscillations*” Academia, Prague 1986 (in Czech).
- [60] A.T. Winfree “*The Geometry of Biological Time*” Springer-Verlag: New York; 1980.
- [61] J.A. Christiansen and I. Wolff, „*Untersuchungen über das Liesegang-Phänomen*“, Z. Physik. Chem. **B26** (1934) 187 - 194.
- [62] E. Mach „*Die Mechanik in ihrer Entwicklung*“ Wissenschaftliche Buchgesellschaft, Darmstadt 1988, pp. 395, 435
- [63] L. S. Polak (ed.) “*Variacionnyye principy mechanic*” GIFML, Moscow 1959 (in Russian)
- [64] W. Nernst, “*The New Heat Theorem*” Dover Publications, New York 1969
- [65] F. F. Runge „*Der Bildungstrieb der Stoffe veranschaulicht in selbständig gewachsenen Bildern*“ Selbstverlag, Oranienburg 1855, p. 32; F.F.Runge, R. E. Liesegang, B. P. Belousov and A. M. Zhabotinsky „*Selbsorganisation chemischer Strukturen*“ (L. Kuhnert and U. Niedersen, eds.) Ostwald’s Klassiker, Verlag H. Deutsch, Frankfurt am Main, 1987
- [66] P. Michalev, W. Nikiforov and F.M. Schemyakin, „Über eine neue Gesetzmässigkeit für periodische Reaktionen in Gelen“, Kolloid-Z. **66** (1934) 197 – 200
- [67] S. H. Sze “*Physics of Semiconductor Devices*” Wiley, London 1969]..
- [68] J. Šesták “*Principle of least action and self-organization*” in the book “Heat, thermal analysis and society” Nucleus, Hradec Krákové 2004
- [69] V. Jesenák “*Periodic reactions in cement chemistry*” in TERMANAL '82, (Proc. 8th Czechoslovak Conference on Thermal Analysis), SVST, Bratislava 1982, p.13 (in Slovak)]
- [70] S.M. Logvinkov, G.D. Semchenko, D.A. Kobyzeva, V.S. Tolstoi “*The Effect of Periodic Reactions in the MgO – Al₂O₃ – SiO₂ System on the Phase Composition and Properties of Cordierite-Based Materials*” Refrac. Indust. Ceramics **42** (2001) 236
- [72] Č. Bárta, F. Fendrych, A. Tříška “*Methods of the Characterization of Phases*” in the book “*Kinetic Phase Diagrams: non-equilibrium phase transitions*“ (Z. Chvoj, J. Šesták, A. Tříška, eds) , Elsevier Amsterdam 1991, p. 519
- [73] Z. Chvoj, J. Šesták and F. Fendrych, “*Nonequilibrium phase diagrams in the PbCl₂-AgCl eutectic system*” J. Therm. Anal. **43** (1995) 439
- [74] Č. Bárta, jun., Č. Bárta, sen., J. Šesták „*Thermophysical Research under Microgravity in Space*” key lecture at the 3rd IPMM (Intelligent Processing and Manufacturing of Materials) Vancouver, Canada 2001 (CD proceedings)
- [75] D. Lukas, A. Sarar, OP.Pokorny „*Self-organization of jets in electrospinning from free liquid surface*“ J Appl. Physics **103** (2008) 1]
- [76] I. Avramov, T. Hoche, C. Russel, „*Is there a crystallization pendulum?*” J. Chem. Phys. **110** (1999) 8676
- [77] A. L. Belmonte, Q. Quyang and J.-M. Flessell: “*Experimental Survey of Spiral Dynamics in the Belousov-Zhabotinsky Reaction*” J. Phys. II France **7** (1997) 1425.
- [78] J. Stávek, M. Šípek, J. Šesták and J.J. Mareš “*Diffusion Action of Waves Occurring in the Zhabotinsky-Belousov Kind of Chemical Reactions*”, Proceedings/Acta of the Western Bohemian University in Pilsen **2** (2001) 1
- [79] J. Šesták, Z. Chvoj “*Irreversible thermodynamics and true thermal state dynamics in view of generalized solid-state kinetics*” Thermochim. Acta **388** (2003) 427

- [80] G. Ammon, R. Ammon „*Diffusion in gelatin and rhythmic precipitation of magnesium hydroxide*“ *Kolloid-Z.* 73 (1935) 204 – 219
- [81] B.P. Belousov *Periodical reactions* Collection of Short Papers on Radiation Medicine; Med. Publ.: Moscow. 1959; p. 145; and B.P. Belousov, in *Oscillations and Travelling Waves in Chemical Systems* (R.J. Field and M. Burger, Eds), Wiley, New York, 1985; pp 605
- [82] A.N. Zaikin and A.M. Zhabotinsky “*Concentration wave propagation in 2-D liquid-phase self-oscillating systems*” *Nature* 225 (1970) 535.
- [83] J. Tyson “*The Belousov-Zhabotinsky Reactions*”, Springer, Heidelberg 1976.
- [84] M. Marek, H. Ševčíková (edts.) “*From Chemical to Biological Organization*” Springer, Berlin 1988; p. 103
- [85] L. de Broglie „*Ondes et Mouvements*“ Gauthier- Villars et Cie., Paris 1926, p.1.
- [86] P. Frank "Über die Fortpflanzungsgeschwindigkeit der Diffusion" *Physik. Zeitschr.*, 19 (1918) 516 .
- [88] D. Bohm “*Quantum Theory*” Prentice Hall, New York 1951
- [89] J. J. Mareš, J. Šesták „*An attempt at quantum thermal physics*“ *J Thermal Anal Calor* 80 (2000) 681
- [90] J.-M. Lévy-Leblond and F. Balibar “*Quantics, Rudiments of Quantum Physics*” (North-Holland, Amsterdam 1990
- [91] B. B. Mandelbrot “*The Fractal Geometry of Nature*” W.H.Freeman & Comp., New York 1977, p. 350.
- [92] F. Hausdorff, “*Dimension und Äusseres Mass*“ *Math. Ann.* 79 (1919) 157.
- [93] L.F. Abbott, M.B. Wise, “*Dimension of a quantum-mechanical path*” *Am. J. Phys.* 49 (1981) 37
- [94] V. Čápek, D.P. Sheehan “*Challenges to the second law of thermodynamics*” in *Fundamental Theories of Physics*, Vo. 146, Springer, Dordrecht 2005
- [95] T.L. Hill “*Thermodynamics of Small Systems*” Dower, New York 1994
- [96] J. Gemmer, M. Michel, G. Mahler „*Quantum Thermodynamics: emergence of thermodynamic behavior within composite quantum systems*“ Springer, Berlin 2004
- [97] J. J. Mareš, P. Hubík, J. Šesták, V. Špička, J. Křištofik, J. Stávek “*Relativistic transformation of temperature and Mosengeil-Ott antimony*” *Physica E*, in print 2009
- [98] For example, the conferences: “*Quantum Limits to the Second Law*” San Diego 2002 or “*Frontiers of Quantum and Mesoscopic Thermodynamics*” Prague 2004 and 2007
- [99] H. Arp “*Seeing red: red-shift, cosmology & academic science*” Apeiron, Montreal 1998
- [100] T.J. Broadhurst, R.S. Ellis, D.C. Koo “*Large-scale distribution of galaxies at the galactic poles*” *Nature* 343 (1990) 726
- [101] J. Stávek “*Diffusion action of chemical waves*” *Apeiron* 10 (2003) 183
- [102] J. Stávek “*Diffusion of individual Brownian particles through Young’s double-slits*” *Apeiron* 11 (2004) 175;
- [103] J. Stávek “*Diffusion of self-organized Brownian particles in Michelson-Morley experiment*” *Apeiron* 11 (2004) 373.
- [104] J. Stávek “*Evolution of self-organized photon waves*” *Apeiron* 13 (2005) 102
- [105] J. Šesták “*Advanced trends in understanding our Universe*” chapter 20 in the book “*Heat, thermal analysis and society*” Nucleus publ. house, Hradec Kralove 2004, pp. 326



Chapter 21

Disorder induces effects in 2D

21. LOW-TEMPERATURE MEASUREMENTS OF DISORDER-INDUCED EFFECTS IN LOW-DIMENSIONAL SYSTEMS

Pavel Hubík, Jiří J. Mareš

21.1. Introduction

In this part of the book we introduce and discuss experimental results on low-temperature electron transport obtained in several types of semiconductor structures. Semiconductors, and especially low-dimensional structures prepared by modern sophisticated growth techniques, represent variable systems, which can be modified according to specific demands; they can be designed either for a given application or into the structure that is optimized for research of some fundamental physical problem. However, most of these systems exhibit, besides properties due to periodic lattice, features caused by different amount of disorder. This disorder can originate e.g. from various degree of amorphization of the lattice, from an existence of grains and accompanied grain boundaries or from a high level of doping - just two latter cases will be treated in several examples in this chapter.

Electron transport measured in the above structures can be understood as a probe which test a band of electron energies near the Fermi level. Specifically, it is a sensitive tool which reveals detailed information about fluctuations of the electron potential energy, hence about the disorder. However, a necessary condition for obtaining such experimental data is to reduce an influence of lattice vibrations to a level at which the electron-phonon interaction will be less or comparable with an energy scale of the fluctuations. It implies the lower temperature we will use the more subtle effects and the lower degree of the disorder will be observable. Another reason for the application of low temperatures is the fact that the low-dimensional structures which will be discussed here exhibit quantum properties due to a confinement of the electron motion in one or more dimensions. These properties are, in general, seen in a more pure form if the kT energy (k being the Boltzmann constant and T absolute temperature) is small with respect to the confining potential barriers and with respect to other interactions that can take place in the system (e.g. magnetic-field induced electron motion).

Hence, even if the topic of this chapter can appear, at first glance, a little bit out of the scope of the book we believe that the following pages will show that the low-temperature electron transport is a useful tool for investigation of the low- or medium-disordered systems and will offer a complementary view with respect to high-temperature methods (like thermal analysis) and highly disordered systems (like various glasses).

After this introduction the chapter proceeds with a discussion of some basic concepts relevant to the description of the electron transport in disordered semiconductors, namely, metal-insulator transition, disorder and fluctuations, weak localization and dimensionality (section 21.2). Parts dealing with an experimental research start with section 21.3 where we treat a concept of the weak localization in detail and present experimental effects related to it. Using particular experimental data for particular highly-doped semiconductor systems, it is shown that the weak localization plays a key, or at least non-negligible, role not only in purely two-dimensional (2D) systems (21.3.1) but also in systems where the effective dimensionality is reduced below three (21.3.2) or when the whole system consists of multiple 2D subsystems (21.3.3). Integral quantum Hall effect in 2D systems is well-known phenomenon; however, in section 21.4 it is shown that special experimental methods we have used reveal new features and allow better characterization of the disorder that controls the quantum Hall regime. In part 21.5 we demonstrate, using our experimental results on nanocrystalline diamond, how the grain boundaries can influence the transport properties of the superconducting semiconductor.

21.2. Electron transport in 3D and 2D disordered metals - basic concepts

Even if all systems discussed in this chapter are commonly described as doped semiconductors, we will see that their properties place them, in fact, among disordered metals. Let us start therefore with a definition of the metals and their counterparts - insulators. Since the beginning of the 18th century, when electrical conduction was discovered, solids have been categorized into these two classes. Nevertheless, such a classification, which is very useful for practical purposes, was found to be enormously difficult to reformulate in terms of theory, so that the problem has not been satisfactorily solved yet. In the theoretical literature dealing with this subject, the definitions and the concepts of a metal and an insulator are confined to the absolute zero temperature [1]. As, however, the absolute zero temperature, corresponding to an improper point of hotness manifold [2], does not exist at all, such a definition bears a somewhat metaphysical character. For authors, it is a very strange fact that Planck's warning "all thought experiments which are making use of absolute zero should be avoided" [3] is ignored in the theory quite generally. The consequence of such an approach is, among others, the impossibility to distinguish between metal and insulator experimentally. However, the largest portion of this chapter will deal with systems which are intuitively considered as metallic-like. Therefore it is necessary to have operational criteria enabling us to distinguish between metal and insulator experimentally at finite temperatures.

Relatively simple and effective is the so-called *gap criterion* [1] which is usable for conductors controlled by single-particle excitations. Moreover, it is advantageous for application of this criterion that it can be decided, by means of auxiliary experiments, whether or not the conductivity is due to single-particle excitations. As usually, by gap Γ we mean the energy difference between the Fermi level and the mobility edge where the single-particle excitations become macroscopically extended, i.e. where they correspond to the charge-carrying states. Assuming further that the effective gap, which controls the thermal activation of the carriers, is temperature dependent, the temperature dependence of resistivity may be written in quite a general form

$$R/R_0 = \exp(\Gamma(T)/kT), \quad (1)$$

where the factor $R_0(T)$ is a weak function of temperature T . The parameter $\Gamma(T)$, setting the energy scale of the activation process of charge carriers, can be experimentally determined from the local slope (taken with minus sign) of the temperature dependence of the resistivity plotted in the Arrhenius coordinates (i.e. $\log R$ vs. $1/T$). This fact enables one to recast the gap criterion into the *weak definition of metal and insulator* applicable within a certain finite interval of temperatures J , namely:

If for every $T \in J$, $\Gamma(T) \leq kT$ the conductor is called *metal with respect to J*.

If for every $T \in J$, $\Gamma(T) > kT$ the conductor is called *insulator with respect to J*.

Note that the confinement of the weak definition to an interval J makes, in contrast to the standard strong definition, the metal-insulator classification experimentally provable. In order to comprehend this important fact, the typical $R(T)$ curves are depicted in Fig. 1. There the dashed border line, corresponding to the condition $\Gamma(T) = kT$, unambiguously separates, within the interval J , metallic and insulating regions. Rather frequent misinterpretation of experimental data consists of treating any increase of resistivity with decreasing temperature as a symptom of insulating state. In fact, such a behaviour, which is rather a symptom of localization, may be observed in metal and insulator as well. In case of metal where $0 < \Gamma < kT$, however, the localization cannot bear a character of strong localization characterized by exponential damping of wave-functions [4], but is appropriately called weak localization.

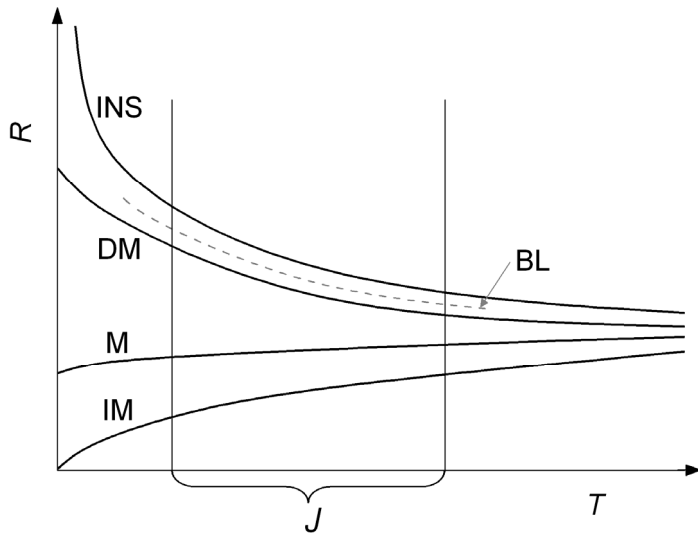


Fig. 1. Various types of $R(T)$ curves are sketched corresponding to insulator (INS), disordered metal (DM), real metal (M) and ideal metal (IM). Dashed curve BL represents the border line between metals (underneath the curve) and insulators (above the curve).

is especially important in the 2D systems where the carriers move in a single plane only. Quantum interference of the split wave function of charge carriers immobilized at the above-mentioned obstacles is a nature of the above-mentioned weak localization effect. Just this phenomenon will be discussed in the following sections in detail and it will be shown to play a key role in interpretation of many low-temperature transport experiments.

In contrast to the weak localization, characteristic for disordered metals, we should mention hopping - another often considered mechanism of electron transport in disordered solids. In this phenomenon (which will not be discussed here in detail-see e.g. Ref. 5) the transport is controlled by the tunnelling between strongly localized sites. In such a case the conductance is governed by the strong localization (i.e. $\Gamma > kT$), and the system is per definition insulator and not metal.

Treatment of a change from the insulating to metallic behaviour in solid-state systems should be completed by the semi-empirical picture of Mott's metal-insulator transition [1]. The doped semiconductor becomes a metal if the concentration of impurities built-in into the host lattice is so high that their localized atomic wave functions start overlap appreciably. If the density of states in such an impurity band is sufficient to pin the Fermi level there, the

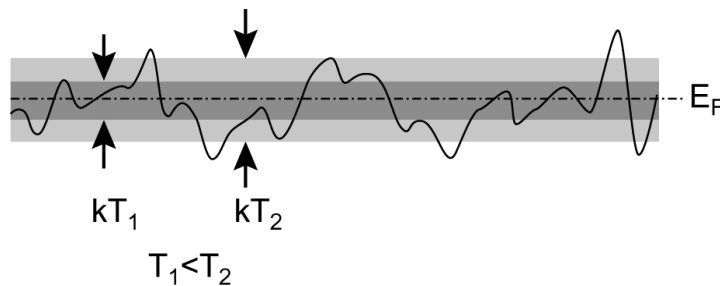


Fig. 2. Illustration of a relation between potential fluctuations and an energy band at the Fermi level in which the electron transport takes place.

In highly doped semiconductors, the impurities are incorporated into the lattice randomly and therefore introduce a disorder into the system. In this case, due to a strong interaction between neighbouring centres, the impurity levels break into an impurity band positioned, as a rule, at the edge of the transport band in the host material. Because of the disorder, the impurity band is inevitably characterized by potential fluctuations. With decreasing temperature more and more potential fluctuations emerge from the kT -band at the Fermi level (see Fig. 2). The corresponding regions become thus classically inaccessible (form obstacles) for the carriers and cause an increased sample resistance. It is

material has to reveal the transport properties of an ordinary metal. The critical threshold concentration of impurities n_M for which the metal-insulator transition takes place is given by Mott's empirical formula [4]

$$a_B n_M^{1/3} = 0.26 \pm 0.01, \quad (2)$$

where a_B is Bohr's impurity radius. Similar relation (with

the right-side constant ~ 0.27) is obtained assuming that the transition occurs when the most probable distance between neighbouring impurities, $(2\pi n_M)^{-1/3}$ [6], equals the characteristic dimension of the impurity wave function represented by Bohr's diameter $2a_B$. It is a remarkable fact, that in many systems (e.g. in diamond doped with boron –see part 21.5.1 below) the metal-insulator transition characterized by the above gap criterion condition $\Gamma \approx kT$ takes place just in close vicinity of Mott's critical concentration n_M .

Finally, let us recall what we mean by a reduced dimensionality or two-dimensional character – concepts often used in the rest of this chapter. In the electron transport, we speak about the reduced-dimensionality if the motion of electron is in one or more directions limited by a potential confinement to a size smaller or comparable with the electron wavelength. Typically, two-dimensional semiconductor system is obtained by a growth a sequence of epitaxial layers with various energy gaps and electron affinities and/or with variable doping profiles. Such a procedure allows us to form a 2D potential well of nanometric width in which the electron motion in direction perpendicular to the well plane is quantized (quantum well) [7]. Because a magnetic field perpendicular to the well plane causes an additional quantization of the electron motion, in the direction parallel to the quantum well, it is evident that magnetotransport measurement is an efficient tool for the experimental research into these systems.

21.3. Weak localization in 2D and 2D-like systems

Since the 1980's, when the notion of the weak localization (WL) [8,9] was worked out, the suppression of electron back-scattering by an external magnetic field in, structures with two-dimensional electron gas (2DEG) and its consequence - the giant negative magnetoresistance (NMR) of these systems [10-12] - have been well established and, generally speaking, well understood effects. However, some peculiar features of these phenomena, e.g. weak dependence of magnetoresistance on or even its independence from the magnetic field in the millitesla range, were studied to a considerably lesser extent and mainly theoretically and were interpreted by various authors in a rather controversial way. This effect, called "low-field magnetoresistance anomaly", bears in fact quite a universal character in 2D systems and it can also be observed in many 2D-like systems. Starting from our measurements of magnetotransport on δ -layers (sheets of doping atoms as thin as one or few atomic layers) embedded into InP we have been able to bring a plausible explanation of the phenomenon which could be later confirmed and extended by investigation of a peculiar system with effective dimension less than three, namely nitrogen-doped ultrananocrystalline diamond. Besides, we have successfully applied the WL concept for a description of multi-delta-systems in parallel (in-plane) magnetic field where the *out-of-plane* weakly localized orbit can control electron transport.

21.3.1. Delta-layers in InP

For our experiment we have chosen as a typical highly disordered 2D system, an InP-based sulphur-doped MOVPE-grown multi- δ -layer structure showing at helium temperatures characteristic features of the presence of 2DEG, such as strongly anisotropic high field magnetotransport with QHE [13]. The 2D subsystem consists of ten δ -layers of an intended donor concentration of $4 \times 10^{15} \text{ m}^{-2}$ per sheet and 100 nm apart embedded into the semiinsulating material. Measurements were performed on usual Hall bar samples ([13], see also section 21.4) provided with AuGe alloyed contacts; for the resistance measurements the four probe d.c. method. Temperature in the range 1.2-4.2 K inside the sample space of the cryostat was controlled by keeping constant He vapour pressure and measured at zero magnetic field by a carbon resistor calibrated with respect to a Ge normal thermometer. Magnetic field generated

by a small superconducting magnet was determined from the current flowing through the series resistance.

Figure 3 presents an example of typical low-field magnetoresistance curves taken at four different temperatures. Close to the beginning the dependences vary only slightly and after passing a certain point they start to decrease with an approximately constant slope. The behaviour of magnetoresistance just described is observed very often in 2D systems provided that the measurements are performed with sufficient accuracy in the millitesla range. As far as we know only the structures with appreciable spin-orbit interaction make an exception (see e.g. Refs. 9,14,15). It can be seen that the slope at higher fields is larger for lower temperatures while the point at which the curves start to deviate is shifted to lower fields at lower temperatures. To describe these facts more precisely we introduce the field B_k at which the tendency to decrease just prevails over the effect constraining the resistance to remain constant. It is defined as an intersection of the straight line parallel to the B-axis corresponding to the initial resistance value with the extrapolation of the straight line fitting the curve at higher fields (see Fig. 3).

The experimental data can be interpreted as follows. In the case where the plane wave representing an electron in the (semi)conductor meets an obstacle, e.g. a cluster of scattering centres, it splits into a system of partial waves. Under favourable conditions these partial waves can add constructively, giving rise to a relatively stable stationary interference pattern. The existence of a stationary pattern means, however, that the electron is effectively localized in the vicinity of the cluster. This type of localization, playing an extraordinary role in the interpretation of low-temperature transport data of disordered metals and semiconductors, is known in the literature as a weak localization [9]. For the realization of an interference process leading to the weak localization, the wavelength and phase coherence of all partial waves involved have to be preserved. In order to ensure these conditions, all the scattering events must be elastic and the electron wave phase coherence length L_ϕ must exceed the characteristic

extension of the scattering cluster. Since the interference is, as a rule, very sensitive to all types of perturbations, it will distinctly depend also on the presence of external electromagnetic fields. The influence of relatively weak electromagnetic fields on the sample resistance, encountered in our experiments, can be fully accounted for by the phase breaking process, treated within the frame of Aharonov-Bohm's theory [16]. Accordingly, the change of the phase $\Delta\varphi$ of a partial electron wave along a path C connecting scattering centres in the cluster is given by an integral

$$\Delta\varphi = \frac{e}{\hbar} \int_C \left(\frac{\partial t}{\partial x} \psi - \mathbf{A} \right) dx, \quad (3)$$

where ψ represents the time dependent electric scalar potential and \mathbf{A} the space dependent magnetic vector potential. It is obvious that if the phase of the partial waves is changed appreciably, (we use for

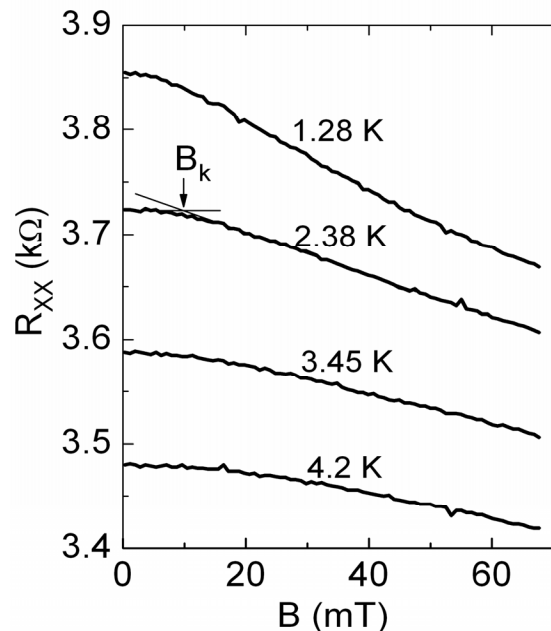


Fig. 3. Dependence of longitudinal resistance on magnetic field in δ -layer system embedded in InP. Labels indicate temperature of measurement. For 2.38 K curve, the method of determination of the characteristic magnetic field B_k is shown.

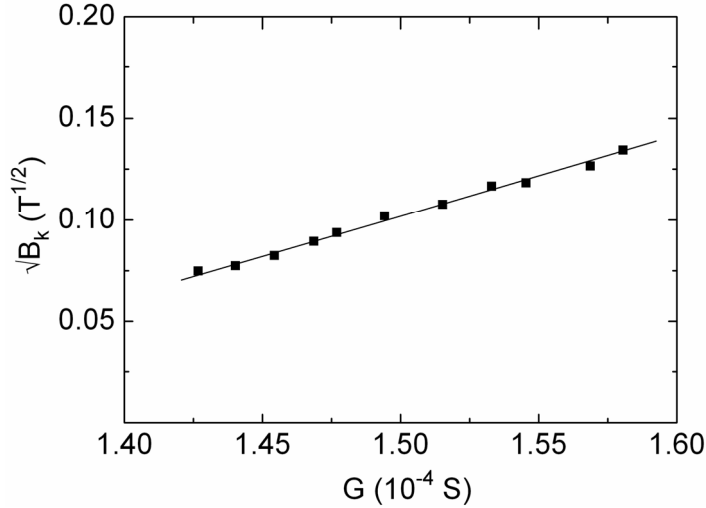


Fig. 4. Dependence of characteristic magnetic field determined from magnetoresistance curves on sheet conductance per one δ -layer embedded in InP. Particular points are obtained from measurements taken at different temperatures (see Fig. 3).

induced process which by limiting the maximal extent of weakly localized orbits to $\sim L\phi(0)$ preserves a part of charge carriers free, and, in this way controls the conductivity of the sample. As the number of free carriers in the system is proportional to the number of virtual orbits the dimensions of which exceed $L\phi(0)$, the corresponding enhancement of conductance $(G-G_0)$, usually called “quantum correction”, can be tentatively expressed by a simple relation

$$\gamma(G - G_0) = 1/L\phi(0), \quad (4)$$

where γ and G_0 are empirical constants. The relative significance of electrically and magnetically induced Aharonov-Bohm’s phase breaking processes on the transport may be assessed as follows. Applying Stokes’s formula to the magnetic term in Eq. (3), one can immediately reformulate a condition for the on-set of magnetically induced phase-breaking sufficient for the destruction of interference pattern $\Delta\phi \approx 1$ in terms of magnetic field $|\mathbf{B}| = B$. Thus, the complete phase-breaking should take place if the dimensions of the WL orbit exceed the so called magnetic length

the sake of definiteness $\Delta\phi \approx 1$), the stable interference pattern can no longer exist, the electron is released from weakly localized orbit and starts to contribute to the conductivity of the sample. It is apparent from formula (3) that the phase breaking Aharonov-Bohm’s process behind may have two independent origins corresponding to electric and magnetic terms, respectively. Since the electromagnetic oscillations (e.g., optical phonons) in the sample at finite temperatures inevitably persist, the electron phase breaking due to the electric term must always be effective there. At zero magnetic fields, it is just this electric-term

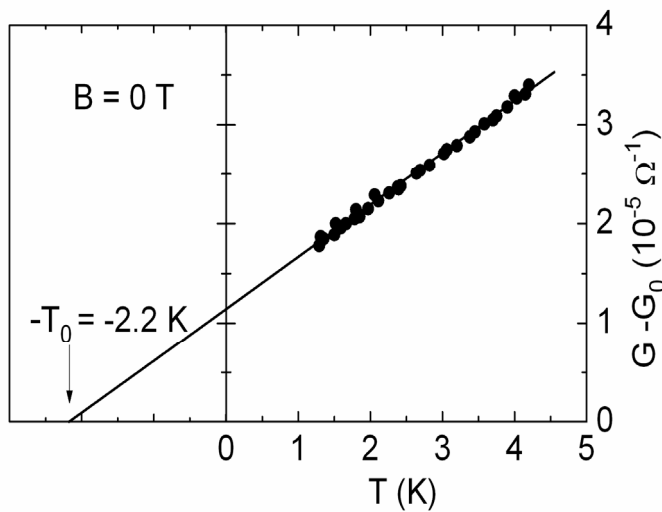


Fig. 5. Temperature dependence of the quantum correction to conductance of the δ -layer system embedded in InP.

induced Aharonov-Bohm’s phase breaking processes on the transport may be assessed as follows. Applying Stokes’s formula to the magnetic term in Eq. (3), one can immediately reformulate a condition for the on-set of magnetically induced phase-breaking sufficient for the destruction of interference pattern $\Delta\phi \approx 1$ in terms of magnetic field $|\mathbf{B}| = B$. Thus, the complete phase-breaking should take place if the dimensions of the WL orbit exceed the so called magnetic length

$$\lambda = (\hbar/eB)^{1/2}. \quad (5)$$

Consequently, the external magnetic fields delocalize, i.e. destroy, the orbits the extent of which, already limited by oscillating electric field to the value $L_\phi(0)$, is larger than magnetic length λ . The magnetic field B_k at which the contributions of the electric and magnetic terms to the phase-breaking process are just the same is then given by

$$L_\phi(0) = (\hbar/e B_k)^{1/2}. \quad (6)$$

Eliminating from equations (4) and (6) the microphysical quantity $L_\phi(0)$, the following correlation accessible to the direct experimental check should be expected:

$$\sqrt{B_k} = \gamma(\hbar/e)^{1/2} (G - G_0). \quad (7)$$

Actually, such a correlation does exist as is shown in Fig. 4 where $\sqrt{B_k}$ versus G is plotted. This plot enables one to determine the constants G_0 and γ and, moreover, approving experimentally relation (7) it confirms indirectly also the validity of Eqs. (4) and (6). The latter equation may then provide a reasonable estimate for the dimensions of the weakly localized orbits involved. For example, in the δ -doped InP based system and for range of used temperatures $L_\phi(0)$ varies from 350 nm at 1.28 K to 200 nm at 4.2 K. Let us briefly comment the temperature dependence of coherence length (more details are discussed in [17] and [18]). As shown in Fig. 5, at low temperatures we have experimentally observed linear dependence of $(G - G_0)$ on temperature. Such a relation together with an assumed (and experimentally supported) validity of Eq. (4) allows us to describe temperature dependence of the zero-field coherence length as

$$L_\phi(0) = \kappa / (T + T_0), \quad (8)$$

where κ and T_0 are constants. We have shown [18], that parameter T_0 can be explained in the framework of the theory based on interpretation of weak localization as result of compensation of the recoil radiation of moving electron by so-called zero-point radiation (ZPR). Namely, quantity T_0 is then due to an absence of the low-frequency part of ZPR spectrum due to the confinement of the electron system in a dielectric cavity (i.e. finite sample).

Briefly, in this subsection we have studied the temperature dependence of low-field magnetoresistance anomaly and conductance in WL regime in highly disordered 2DEG. The anomaly has been accounted for in terms of the competition between phase-breaking processes due to the thermally agitated electrostatic and magnetic Aharonov-Bohm effect. The model proposed provides simple universal formulae containing only minimum of fitting parameters which can be easily compared with experiment.

21.3.2. *N-doped ultrananocrystalline diamond*

While the low-field magnetoresistance anomaly is well-known (even still controversial as for microphysical explanation) for purely two-dimensional systems like the above mentioned δ -layers, its observation in a thick semiconductor layer is, in general, unexpected. Let us remember that in 3D systems the WL effect is possible; however destroying of the weakly localized orbits due to magnetic field is hardly observed [19] because at any orientation of external magnetic field only a small portion of the orbits is perpendicular to the magnetic vector where the effect of magnetic field on phase shift is the largest. Nevertheless, an apparently three-dimensional system can contain a subsystem with an effective dimension near two in which the sensitivity to a magnetic field can be restored. If such a structure controls conductance of the whole system, the effect can be observed experimentally by transport meth-

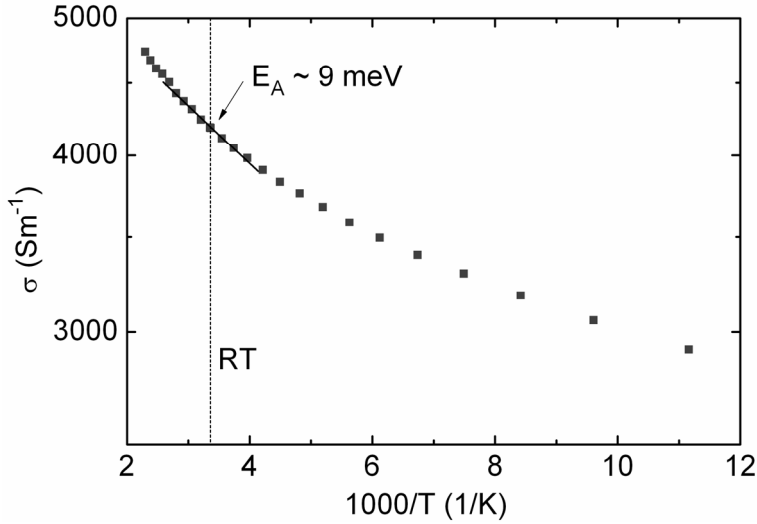


Fig. 6. Temperature dependence of the conductivity measured in nitrogen-doped ultrananocrystalline layer. The data are presented using Arrhenius coordinates and apparent activation energy near room temperature is given.

based contacts for van der Pauw measurement. For the magnetoresistance measurements within the range of 1.2–4.2 K and at fields up to 8 T we used a superconducting magnet and cryostat with temperature controlled by He vapour pressure. Oxford Instruments AVS-47 resistance bridge was employed as a measuring device.

Prior to the low temperature magneto-transport measurements, standard tests at temperatures between 90 and 440 K had been performed. In this temperature range, and at magnetic fields up to 0.4 T, practically no traces of magnetoresistance effects were found and only a very small Hall coefficient, corresponding to an electron mobility of $\sim 2 \times 10^{-4} \text{ m}^2/\text{Vs}$, was observed. On the other side, the samples revealed a remarkably high, weakly temperature dependent electrical conductivity. Such typical temperature dependence of the electrical conductivity plotted in Arrhenius coordinates is depicted in Fig. 6. When approaching lower temperatures, the slope of the curve corresponding to the apparent activation energy E_A for the carriers involved continuously diminishes. The small and varying value of E_A , which is everywhere $< kT$, cannot represent an ordinary activated process but it is more reminiscent of a special kind of disordered metal. Indeed, such a view may be supported by an estimate of Mott's metallic transition threshold σ_M made for this particular case. The relevant formula reads [21]

$$\sigma_M = (8\pi\alpha\epsilon_0 / \hbar) \epsilon E_A. \quad (9)$$

Let us now turn to low temperature magnetotransport data. Figure 7 depicts a set of magnetoresistance curves measured at magnetic fields perpendicular to the sample and at various temperatures ranging from 1.28 to 3.8 K. At the first glance, the curves resemble qualitatively the dependences observed for 2D δ -doped InP system (cf. Fig. 3). At zero magnetic field the resistance increases as the temperature decreases, the fact which may be interpreted as a symptom of electron localization. Crossover between the low-field, practically constant, portion of the curves and decreasing part at higher magnetic fields can be again characterized by a parameter B_k (see Fig. 7) which becomes smaller with decreasing temperature. Total reduction of the resistance in the used range of magnetic fields reaches at $T=1.28$ K more than 20%. Observation of such giant negative magnetoresistance, together with the

ods. We have found just such behaviour in layers on nitrogen-doped ultrananocrystalline diamond (UNCD) as described below.

Nitrogen doped UNCD thin films of grain size ~ 16 nm were grown [20] by microwave PECVD technique from gas phase containing 79% Ar, 1% CH_4 , and 20% N_2 . The films of thickness of $\sim 0.8 \mu\text{m}$ were deposited onto standard highly insulating quartz substrates, enabling reliable transport measurements. The samples were then cut in approximately $5 \text{ mm} \times 5 \text{ mm}$ squares and at the corners provided with vacuum evaporated Ti/Au

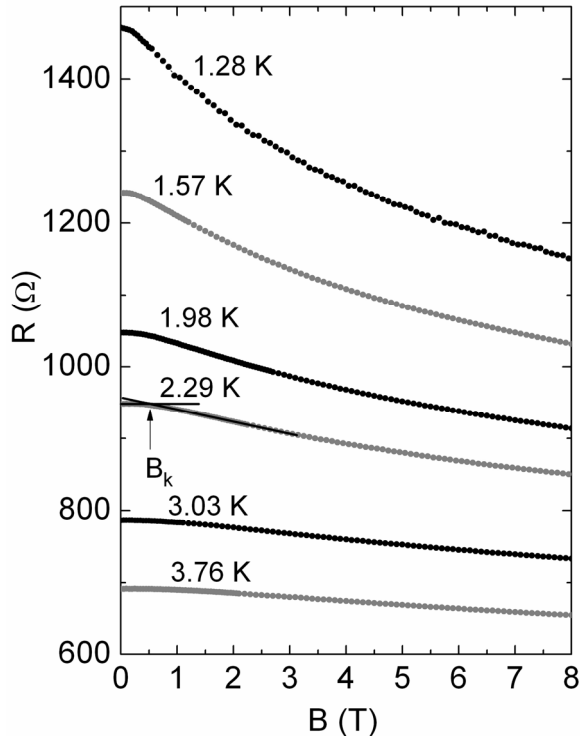


Fig. 7. Dependence of longitudinal resistance on magnetic field in UNCD layer doped with nitrogen. Vector of magnetic field was perpendicular to the layer plane; labels indicate temperature of measurement. For 2.29 K curve, the characteristic magnetic field B_k is shown by an arrow.

according to formula (6) gives an extent of wave function extent of weakly localized electrons in UNCD in the range of 20-70 nm. Comparing it with an average grain size ~ 16 nm we get an indication that electrons are localized in a region involving one or few UNCD grains.

Summarizing this subsection, it is highly probable that the transport in nitrogen-doped ultrananocrystalline diamond is confined to the grain boundaries and that the conductance of this subsystem, which has a character of low-dimensional disordered metal, is controlled by the capture of carriers on weakly localized orbits.

21.3.3. Out-of-plane localization in multi-delta-layer system

In section 21.3.1 we studied a multi- δ -layer system, however each δ -layer was considered independently and their possible interaction was neglected. Main reason why we used the structure with ten layers was to increase current in the 2D system and consequently to improve S/N ratio. In this section we show that by magnetotransport measurements it is possible to observe some, less noticeable, features which arise from the interaction of parallel δ -layers separated by distance comparable with the coherence length.

Samples investigated were basically the same as in section 21.3.1, namely, GaAs or InP based MOVPE grown multi- δ -layer structures. The two-dimensional subsystem consisted of ten parallel δ -layers 100 nm apart. Every δ -layer contained silicon or sulphur induced shallow donors of planar concentrations per layer covering the range of $(2-5) \times 10^{15} \text{ m}^{-2}$.

In perpendicular magnetic fields the low temperature longitudinal magnetoresistance R_{xx} reveals a sharp minimum at a magnetic field B_m accompanied by a plateau (inflection) in the Hall resistance at $R_{xy} \approx h/2e^2$ per layer. This feature is a manifestation of the integral

small apparent activation energies of conductance, witnesses strongly for a transport controlled by a weak localization.

As mentioned above the weak localization manifesting itself by giant negative magnetoresistance is possible only if some low-dimensional subsystem exists which governs conductance in the layer. It is known from optical and electron spectroscopy measurements [22,23] that nitrogen doping leads to a partial conversion of sp^3 (diamond) phase to sp^2 (graphite-like) one at grain boundaries. Further it was found that with increasing doping level the conductance of UNCD strongly increases. Because nitrogen in bulk diamond creates a deep level which has a negligible influence on conductivity at low temperatures and on the other hand, the graphite phase is expected to be highly conductive, it is natural to identify the conductive subsystem with a network of the sp^2 phase rich boundaries. Such a network has inevitably to exhibit a topological dimension less than three; hence, it can reveal large negative magnetoresistance. An estimate of the coherent length

quantum Hall effect and correspond to the Landau level filling factor $\nu = 2$. It proves the fact that multi- δ -layer system behaves at helium temperatures as actually two dimensional and simultaneously provides a more accurate value of the electron concentration $n = \nu e B_m / h$ than that which can be deduced on the basis of technological data (for more details on the quantum Hall effect see section 21.4). Besides the Hall resistance curves exhibit an additional subtle quasiplateau in the range of magnetic field of 1-2 T. A detailed analysis of this aspect showed [24] that it cannot be explain as due to the QHE but that it originates from a mixed 2D and 3D conduction where 3D behaviour is caused by mixing of the excited states of particular δ -layers. Important effect observed in perpendicular as well as parallel fields applied to the multi- δ -layer is due to the so-called shrinkage of the wave functions in the high field limit where their diameter ($\sim 2 \times$ Bohr radius) exceeds the magnetic length $\ell_B = (\hbar/eB)^{1/2}$. According to theory [25] the dependence of $\log R_{xx}$ on the square of magnetic field should be linear in this case which has been in fact observed for $B > 4.5$ T.

The magnetoresistance measurement in low (lower than ~ 3 T) parallel magnetic field has revealed another feature which rises, in our interpretation, from the existence of multi- δ -layer environment. Because of its interesting nature and validity for different multi-layer systems we will pay main attention to it in this section. Fig. 8 shows a set of magnetoresistance curves measured at various temperatures and corresponding to the parallel magnetic field up to 5 T. The common features of these curves may be described as follows. At very low fields (0-0.1 T) the resistance is almost constant (cf. Ref. [17]). Then the curves decrease by about 3%–5% till the magnetic field reaches a certain value B_S (~ 0.5 T in Fig. 8) where this decrease strongly diminishes. After that the symptoms of further oscillations are distinguishable before the high field exponential increase of magnetoresistance prevails. Such behaviour can be described admitting that some universal oscillatory function scaling with characteristic parameter B_S is superimposed on the magnetoresistance curve due to the shrinkage effect.

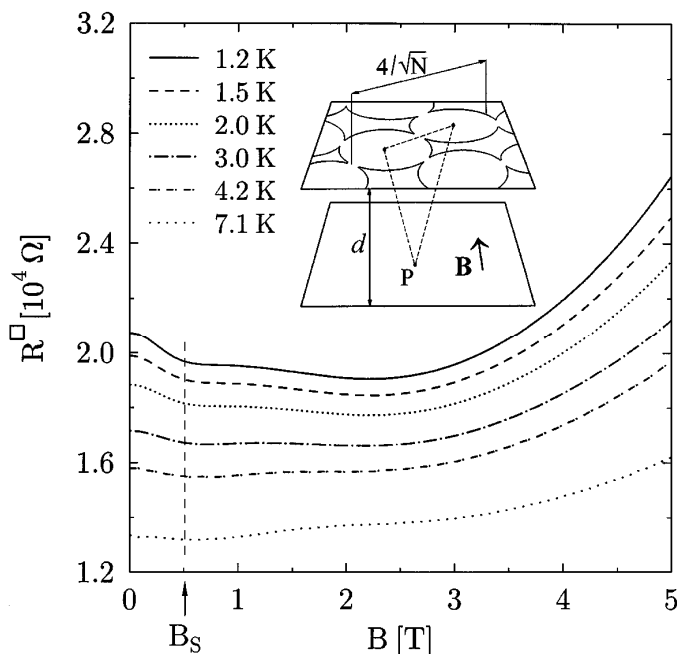


Fig. 8. Magnetoresistance curves measured at various temperatures on InP:Si based multi- δ -layer system. Inset: Schematic illustration to the model of the out-of-plane localization.

Weak localization giving rise to a negative magnetoresistance mentioned in the previous sections vanish in the parallel magnetic field provided that the electrons do not leave the plane of the δ -layer. The above experimental observation of the negative magnetoresistance in the parallel magnetic field may be, however, consistently explained by the assumption that some electrons are also scattered by the centres lying out of the particular δ -layer and especially by those forming adjacent δ -layer. Let us assume that during the transport along the δ -layer the electron shifts over a distance corresponding to mean distance between neighbouring donors, $2/\sqrt{N}$, and simultaneously is scattered by a centre P lying somewhere in a neighbouring parallel δ -layer (see the inset of

Fig. 8). The alternative paths enabling weak localization constitute a triangular loop whose orthogonal projection onto the plane perpendicular to the vector B has an area which is independent of the position of the point P but depends on the angle α between the vector B and the direction of the electron shift in the plane of the δ -layer. By averaging the projected area $\sim(d/\sqrt{N}) \sin(\alpha)$ over the randomly distributed angle α we obtain the average area of the triangular loop orthogonal to the magnetic field as $\sim 2d/\pi\sqrt{N}$. Comparing this area with the square of magnetic length ℓ_B^2 , i.e., with the area which is at a given magnetic field just sufficient to completely destroy the phase coherence of the electron moving on its periphery, we obtain the formula

$$B_S = \pi\hbar\sqrt{N}/2ed, \quad (10)$$

defining the magnetic field B_S at which the constructive interference on the triangular loops of described type is fully suppressed or, in other words, where the negative magnetoresistance reaches its ultimate value. In order to test its validity, formula (10) was compared with experimental data obtained on various multi- δ -layer systems. For this purpose the field B_S was determined graphically as the first point on the magnetoresistance curve at which the decrease of magnetoresistance stops and was plotted versus \sqrt{N}/d (see Fig. 9). While the graphical method of the determination of B_S inevitably brings about a rather large error (15%), the coincidence of experimental data with formula (10) is astonishingly good. This fact strongly supports our opinion that despite the simplifying approach used, the interpretation of the negative magnetoresistance as a consequence of the destruction of out-of-plane weakly localized orbits by a magnetic field parallel to δ -layers is correct.

To generalize the discussion, let us examine the structure of Eq. (10) in more detail. Using dimensional analysis [26], this equation may be obtained very easily in the form of dimensionless monomial,

$$\hbar\sqrt{N}/eBd = \text{const.} \quad (11)$$

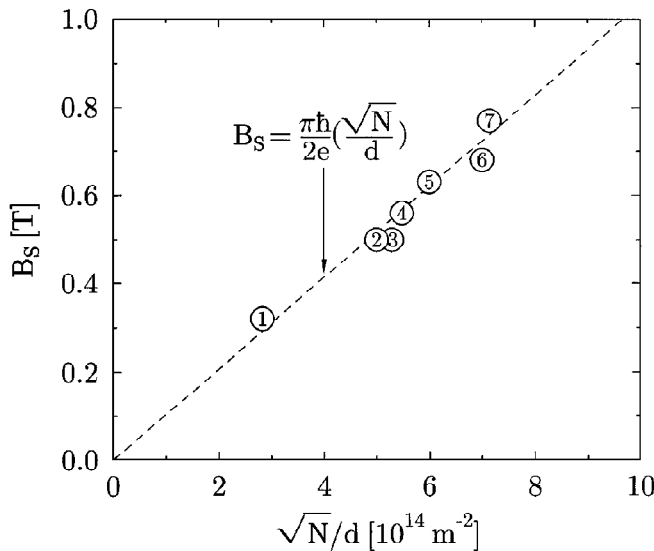


Fig. 9. Dependence of characteristic magnetic field on parameter \sqrt{N}/d for different multi- δ -layer systems. Experimental data for various systems were taken either from literature: 1—GaAs:Si (Ref. 27); 4—InP:S (Ref. 13) or measured by authors: 2—InP:Si, 3—GaAs:Si, 5, 7—InP:S, 6—GaAs:S.

Obviously, the ensemble of universal constants and variables, namely, e , \hbar , N , d , and B , is relevant to a rather wider class of physical situations, and the constant in (11) defining the scaling properties of the solution of any particular problem cannot be, in general, determined without reference to a suitable physical model. To illustrate this circumstance let us apply our approach to a slightly different problem already solved by more sophisticated methods, namely, to the influence of parallel magnetic field on the two-dimensional bilayer electronic system existing in wide quantum wells with remote doping [28]. In this structure the electrons condensing in the vicinity of both sides of quantum well give rise to two parallel 2DEGs, each of which has an effective concentra-

tion of $N/2$. The absence of a strongly fluctuating potential in the remotely doped quantum well has two consequences. First, the characteristic length for planar electronic transport is no longer the size of potential fluctuations but the most probable distance between electrons, i.e., $1/\sqrt{(2\pi N/2)}$, measuring the distance between succeeding scattering events. Second, the moving electrons attain more freedom in comparison with those in δ -layers, because the potential profile does not put further constraints on their motion, which makes the averaging procedure with respect to the angle a superfluous. Then in close analogy with the derivation of (10), we obtain immediately the following expression

$$B_S = 2\hbar v(\pi N)/ed. \quad (12)$$

This formula known from the literature [28] provides the value of the field at which a sharp decrease in the density of states accompanied with the corresponding decrease in conductance is expected and actually observed. Taking into account our derivation of formula (12), we can add that the states disappearing during the application of the magnetic field B_S should be just the states represented by the out-of-plane weakly localized triangular orbits.

In conclusion of this subsection, we have investigated experimentally the influence of a parallel magnetic field on the transport in highly disordered 2DEG subsystems contained in GaAs and InP based multi- δ -layers. The observed negative magnetoresistance was explained using a model of potential fluctuations and the idea of destruction of out-of-plane weakly localized orbits by the magnetic field. Simple formula for the magnetic field B_S characterizing this effect was provided.

21.4. Quantum Hall effect in disordered 2DEG

Quantum Hall effect (QHE) turned out to be one of the most spectacular and, at the same time, the most investigated phenomena in physics of low-dimensional systems of last decades. Not aiming to present here a full review of relevant experimental results and theories, let us only remember that the principal effect characterizing the QHE is an appearance of plateaux in low-temperature magnetic-field dependence of the Hall voltage measured on a suitable shaped structure [29] (usually on the so-called Hall bar – see Fig. 10) containing 2DEG. These plateaux occur at very-well defined values of the Hall resistance R_{xy} (ratio of the Hall voltage V_{xy} and the current I through the structure) determined only by universal physical constants, namely $R_{xy,v} = h/ve^2$ where v is so-called filling factor. Plateaux in R_{xy} curves are accompanied by minima (or even zero values) in the longitudinal resistance R_{xx} ($=V_{xx}/I$) [30].

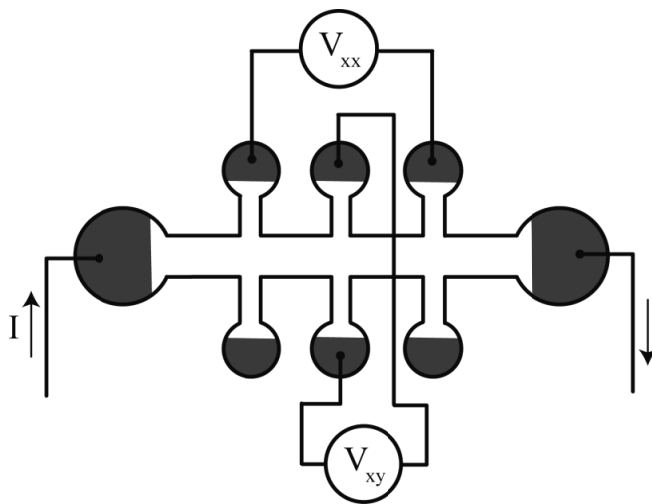


Fig. 10. Shape of the sample (the Hall bar) and wiring commonly used for measurement of the quantum Hall effect. Greyed parts represent metallic contacts. The sample is usually formed by etching of the epitaxial structure grown on a high-resistivity substrate.

Two classes of the QHE are observed, namely the integral QHE where v values are only integers, and the fractional QHE for which v can

also equal fractions of small integers, like $1/2$, $2/3$, etc. [31]. Deciding parameter for an existence of the particular type of the QHE or for its emergence at all is, besides low temperatures, an amount of the disorder in the 2D structure. This characteristic can be assessed experimentally e.g. by measurement of electron mobility. Roughly speaking, for 1 K temperature range the fractional QHE occurs in very clean (low-disordered) samples with the electron mobility above about $200 \text{ m}^2/\text{Vs}$, while traits of the integral QHE can be observed in such extremely disordered structures as δ -layers with the mobility as low as $0.4 \text{ m}^2/\text{Vs}$ [24].

Because we will deal with the structures containing a relatively highly disordered 2DEG (mobility $< 50 \text{ m}^2/\text{Vs}$) we leave aside theories of the fractional QHE, which mostly assume a formation of new kinds of quasiparticles in very little disordered systems (for a recent review see e.g. [32]). We remember here only basic concepts currently used for an explanation of the integral QHE. Starting point is an emergence of the so-called Landau levels if a magnetic field is applied perpendicularly to the 2DEG. These levels arise because of a quantization of the electron motion in the 2D plane (motion in the perpendicular direction is quantized already without magnetic field by spatial confinement). Energy separation of the Landau levels and density of state is proportional to the absolute value of magnetic field B . Shapes of the R_{xy} and R_{xx} curves in the QHE are then explained as due to a relative motion of the Fermi level and the Landau levels caused by a variable occupation of the Landau levels. Namely, at the quantum Hall (QH) plateaux, in the so-called QH regime, the Fermi level lies in-between of the adjacent Landau levels. All Landau levels below the Fermi level are then completely occupied, each with 2D electron concentration equalled to $n_{LL} = eB/h$, while the other upper-lying Landau levels are empty. Filling factor ν is then the ratio of the total electron concentration to n_{LL} . Let us note that at sufficiently high magnetic fields and low temperatures a lifting of spin degeneracy of the Landau levels plays a role, giving rise to the QH plateaux with odd ν 's.

Simultaneously with the above description it is assumed, and experimentally confirmed [33,34], that at edges of the 2DEG (perimeter of the sample) boundary conditions of the electron potential lead to a bending of the Landau levels up in the way that they cross the Fermi level. Such crossings then create near-edge 1D-like channels carrying current in the QH regime.

On the other hand, a necessary condition for an existence of the well-developed QH plateau is a sufficient density of states between the Landau levels able to pin the Fermi level in a finite range of magnetic fields. Such a density of states arises due to disorder present in the sample - it is a reason why integral plateaux are better observed in medium disorder samples than in very clean ones. However, it is generally believed on the

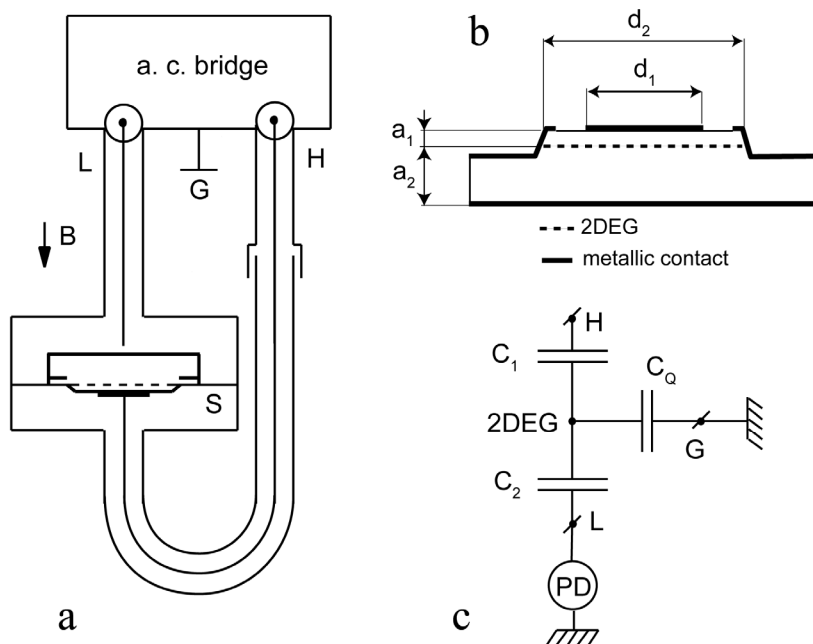


Fig. 11. Measurement setup for electric field penetration method (a), sketch of the sample used (b) and simplified equivalent circuit of the measured structure and its connection to the bridge circuit (c).

basis of experimental as well as theoretical arguments [31] that when the Fermi level is positioned between Landau levels that the only extended states at the Fermi level are located at the edges of the 2DEG while the bulk disorder-induced states are not able to carry current and hence not able to screen the external electric field. In what follows we show how it is possible to investigate the density of states between the Landau levels in the QH regime by means of a sensitive capacitance method and also what new information on the screening ability of these states has been obtained [35].

As a sample we used a GaAs based heterostructure grown on a semi-insulating GaAs substrate. The 2DEG (of mobility $43.0 \text{ m}^2/\text{Vs}$ and concentration $3.3 \times 10^{15} \text{ m}^{-2}$) was located at the interface between an undoped GaAs buffer (spacer) layer with thickness $s=130 \text{ nm}$ and a Si modulation-doped $\text{Al}_x\text{Ga}_{1-x}\text{As}$ layer ($x \approx 0.3$) covered with a thin GaAs (20 nm) cap layer. The sample was shaped by wet etching into a circular mesa of diameter 3 mm. The back contact (substrate) and the periphery of the mesa (2DEG subsystem) were provided with alloyed AuGeNi based Ohmic contacts, and a gold electrode of diameter d_1 was evaporated on top of the structure (cap layer). The details of the geometry are depicted in Fig. 11b ($a_1 = 130 \text{ nm}$, $a_2 = 370 \text{ nm}$, $d_1 = 1 \text{ mm}$, $d_2 = 2 \text{ mm}$). Simultaneously, another part of the same sample was patterned into a Hall bar structure to enable magnetotransport measurements.

For capacitance measurement we used a manually operated ac transformer bridge (GR-1616 [36]) was employed. This unique device working in a three-terminal mode enables one to almost completely eliminate the parasitic impedances down to aF provided that the measuring circuitry is properly designed satisfying certain requirements. Such a circuitry used for our experiments is schematically shown in Fig. 11a. It consists of a metallic (copper) enclosure which is separated by a conducting partition S with a small opening into two parts and is placed inside a superconducting solenoid (0 to 8 T) in a helium cryostat enabling the temperature control within the range 4.2–1.2 K. Both parts of the enclosure are connected to the high (H) and low (L) terminals of the transformer bridge by means of low impedance coaxial cables. To eliminate ground loops the screen of the high terminal cable was interrupted and all of the system of grounds was earthed at one point only (G). This arrangement ensures that the bridge measures only the capacitance corresponding to induction lines passing from one part of the enclosure to another through the opening in the partition.

The outer contact of the circular sample was then cemented by a silver paste to the rim of the opening in the partition, while back contact and the gold top electrode were connected to the low and high terminals of the bridge, respectively. In this configuration when the bridge is balanced properly, the potential difference between the summing point L and the ground is identically zero and the induction lines terminating at high electrode are split in the 2DEG in a certain ratio. Only the penetrating part of them which terminates at the L electrode is indicated by the phase sensitive detector and contributes to the reading C_M of the bridge.

A typical result of capacitance measurement made in magnetic fields perpendicular to the 2DEG subsystem is depicted in Fig. 12. The curve reveals well resolved peaks which become more pronounced and broad with increasing magnetic field. Comparing this curve with the results of routine dc magnetotransport measurements on the Hall-bar structures it is clear at first glance that the maxima in C_M correspond quite exactly to the QH plateaux with integer filling factors ν , which enable us to label the capacitance peaks with the same numbers. At a frequency of $\sim 1 \text{ kHz}$ and at sufficiently low temperatures ($\sim 1.8 \text{ K}$) the even peaks do not exceed the common limit at $C_M \approx 1.1 \text{ pF}$ which is appreciably lower than the capacitance of the sample measured with the 2DEG completely disconnected from the ground (floating stratum). In this case the capacitance of the sample was of purely geometrical origin and had a value of $\sim 2.6 \text{ pF}$. This fact proofs without ambiguity the existence of a residual screening (or, in other words, the existence of radial currents) due to the 2DEG in the integral QH regime with $\nu = 2, 4, 6$, etc. The peaks themselves have no single maximum but have a

characteristic additional structure which is most apparent for the peak at $\nu = 2$. (Although only this case is discussed further, the same arguments are valid also for other even ν 's.) This peak is split into two well distinguished peaks with a flat valley in between. While the position of the bottom of this valley is, within limits specified below, perfectly temperature and frequency independent ($C_{M0} = 0.84 \text{ pF} \pm 0.5 \%$), its width increases with the decreasing temperature and/or increasing frequency, which shifts both the side peaks towards the edges of the QHE plateau. As for the peaks with odd ν 's, they were many times smaller than even peaks and in most cases merged with the baseline. An exception was the peak with $\nu = 3$ the height of which reached about 20% of the saturated height of even peaks.

The observed behaviour is evidently in contradiction with a traditional model of the IQH effect mentioned above – see also [30,31]. Indeed, in our Corbino-like structure the currents supplying the screening charge into the bulk of the 2D system from its grounded periphery have to pass a continuous ring of the 2DEG. In such a case in the integral QH regime the Fermi level should be positioned between two adjacent Landau levels where only strictly localized states exist, which excludes a coherent transport. Accordingly, the screening should be either totally absent or due to another type of incoherent transport which is possible only at finite temperatures. While such a model is admissible for the explanation of the behaviour near the edges of the EFP peak, it can in no way account for the structure of its central part. In order to find out the origin of this discrepancy between our experimental results and commonly accepted meaning, we analyze density of states in the 2DEG and its relation to amplitudes of fluctuating potential induced by disorder.

To evaluate density of states we use so-called quantum capacitance C_Q having a meaning of an effective capacitance of the heterodimensional junction between the 2DEG and the 3D metallic grounded contact [37] that controls the charge supply into the system which is needed for screening of an external applied electric field. Quantitative assessment of the screening ability of the 2DEG is obtained from so-called screening 2D screening length λ [38]

$$\lambda = \epsilon\epsilon_0 / \eta e^2, \quad (13)$$

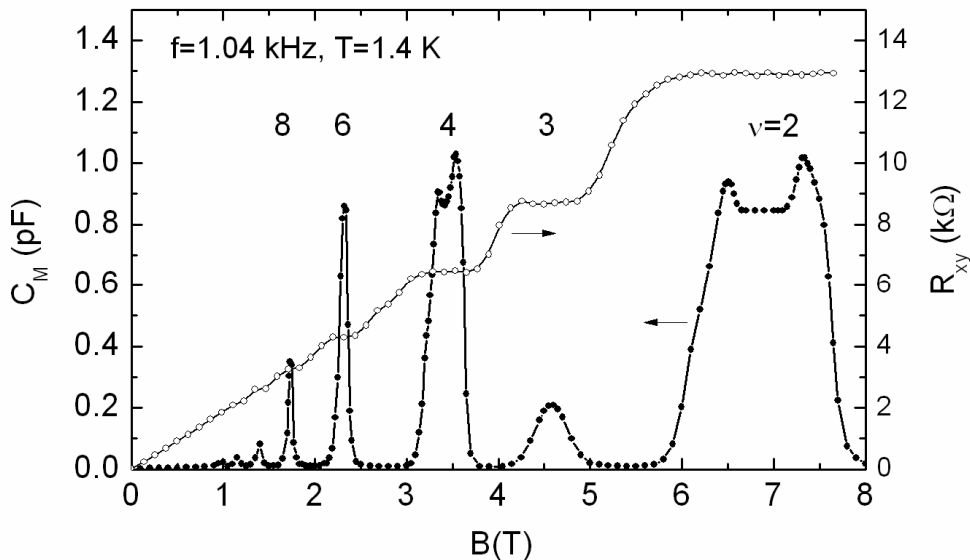


Fig. 12. Dependence of the capacitance measured on the Corbino-like sample containing 2DEG on magnetic field (solid circles) together with magnetic field dependence of the transversal (Hall) resistance obtained on the Hall bar prepared from the same structure (open circles). Numbers indicate filling factors corresponding particular plateaux and peaks.

where ϵ is relative permittivity, ϵ_0 permittivity of vacuum and η is the density of accessible states in 2DEG. Using a relation $C_Q = \epsilon\epsilon_0 A/\lambda$ (A being an area of 2DEG) [35] we can evaluate density of accessible state able to screen from the equation

$$\eta = C_Q / Ae^2. \quad (14)$$

Relation between C_Q and the measured capacitance C_M can simply be obtained from an elementary analysis of circuitry used (see Fig. 11c), and is given by a formula

$$C_Q = C_1 C_2 (1/C_M - 1/C_2), \quad (15)$$

where C_1 and C_2 are capacitance of the layers above and below 2DEG which are calculated from the sample geometry.

The kernel of our model presented is based on the relations between density of accessible states at the Fermi level η and amplitudes of disorder induced fluctuating potential. The role of the disorder in a traditional approach to the integral QH effect is, as a rule, limited only to the conditions necessary for the bare existence of the QH plateau, i.e. breaking of the translation invariance and smoothing of the edge potential [30,31]. It can be shown, however, that the disorder introduced by the random distribution of impurities in the source (doped) layer which is inevitably present in all 2D structures revealing the integral QH effect may be in some cases sufficient to deform the system of the Landau levels in such a way that their amplitude of variation is comparable with their energy distance. Indeed, the amplitude w_0 of long-range potential fluctuations due to the Coulomb interaction over the most probable distance between non-correlated donors of concentration N within the source layer can be estimated using Hertz - von Smoluchowski's [6] formula as

$$w_0 = (e^2/\epsilon\epsilon_0) \sqrt{(N/8\pi)}. \quad (16)$$

Evaluation of formula (16) for $\epsilon=13$ and $N=3.3 \times 10^{15} \text{ m}^{-2}$ gives $w_0 \approx 16 \text{ meV}$ which comparable with Landau level separation (12 meV) at $B=6.7 \text{ T}$, i.e in the middle of plateau with $\nu=2$. The amplitude w of potential fluctuations present in the plane of the 2DEG (i.e. the actual width of the impurity induced energy band) which is a superposition of random harmonics of the source layer potential is essentially given by w_0 multiplied by the aspect ratio $\lambda/2s$ (cf. [39]), where $2s$ is the distance between the source layer and its electrostatic image in the 2DEG. The formula for w then reads

$$w = \sqrt{(N/32\pi)} / \eta s. \quad (17)$$

According to Eq. (17) the width of impurity induced potential profile should change appreciably with the variation of density of accessible states in the vicinity of the Fermi level. It is evident that with decreasing η the concentration of electrons at the Fermi level also diminishes and their number is not sufficient to equalize all irregularities of induced potential profile which thus become more pronounced. This process continues till the density of accessible states reaches a certain critical value η_C at which the complete denudation of the potential profile characterized by the condition $w \approx w_0$ takes place. At this point η_C can be estimated as

$$\eta_C = \epsilon\epsilon_0 / 2se^2 \quad (18)$$

and the corresponding concentration of electrons within the impurity induced band as

$$n_C = \sqrt{(N / 32\pi)} / s. \quad (19)$$

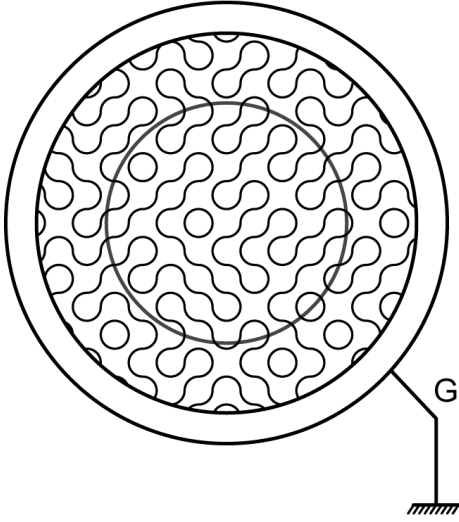


Fig. 13. Model of 1D states penetrating from the edge of Corbino discs to its interior in the quantum Hall regime.

made to create a new phase of dimension < 2 in which the density of states within the limits of experimental error in a certain range of magnetic fields is perfectly constant and independent of temperature and frequency, just as we observed for the flat valley near the centre of the Hall plateau (between 6.6 T and 7.1 T in Fig. 12).

Therefore we have very likely to do with the topological phase transition between the diluted, highly disordered 2DEG and the irregular network of effectively 1D channels. In other words, electron depletion of the 2DEG near the centre of the Hall plateau diminishes the effectiveness of screening there and, consequently, enables in the bulk of the system development of large-scale potential fluctuations with the amplitude comparable to the distance between the consecutive Landau levels. At the intersection of the Fermi level with these Landau levels copying the random potential profile then arise a system of so called Chklovskii-Shklovskii's stripes [40] penetrating along the potential hills and valleys into the bulk of the 2DEL. It is obvious that our picture resembles very closely the Chalker-Coddington model of disordered two-dimensional electron liquid [41] according to which the compressible 1D stripes, reflecting the random structure of potential fluctuations, creep into the bulk of 2D liquid in the form of "dragon paths" having a character of Peano's self-affine curves [42]. A somewhat idealized picture of this model for the Corbino disc is depicted in Fig. 13.

Although we do not discuss here all details of the measured curves, as a final point we should mention why before reaching the flat part, i.e. before the phase transition, the C_M -B dependence falls down. Increase of the amplitude of the potential fluctuations mentioned above results in a development of large scale potential fluctuations. Some of these fluctuations extend to the close vicinity of the contact and therefore create, in regions where the Fermi level cuts the deformed Landau levels, new transport channels which can supply the electrons from the ground into the interior of the 2DEG. The screening ability of the system is improved in spite of further decrease in a number of free electrons involved and the process should be accompanied with decrease of C_M which is actually observed near 6.5 T in Fig. 12.

To recapitulate this section, we have shown as that the high sensitivity capacitance measurement in the special arrangement (improved electric field penetration method) is an extremely useful tool for investigation of density of states in two-dimensional electronic systems. Using this method the finite residual density of the bulk extended states existing in the

We claim that the relations just derived fit very well the behaviour actually observed at the central part of the integral QH plateau. Indeed, the density of states η evaluated by means of formula (14), from the experimental dependence of C_Q on the magnetic field reaches in this region a constant value of $\sim 1.9 \times 10^{34} \text{ J}^{-1} \text{ m}^{-2}$ which is very near to the rough estimate of $\eta_C \approx 1.7 \times 10^{34} \text{ J}^{-1} \text{ m}^{-2}$ made on the basis of equation (18) using $s = 1.3 \times 10^{-7} \text{ m}$. These figures together with the estimate for $n_C \approx 4.4 \times 10^{13} \text{ m}^{-2}$ excellently account for the observed reduction in the screening ability of the 2DEG in the IQH plateau to $\sim 1\%$ with respect to the base-line value ($\eta \approx 1.8 \times 10^{36} \text{ J}^{-1} \text{ m}^{-2}$, $n \approx 3.3 \times 10^{15} \text{ m}^{-2}$).

It should be further stressed out that in the state which is characterized by the condition $\eta_C \approx \eta$ the electrons having concentration as low as n_C are incident only with the oscillating impurity induced band and thus cannot continuously reach all the points in the 2DEG plane. The electrons are thus

integral quantum Hall regime was discovered. It was further shown that these states can be described as 1D quantum channels percolating from an edge of the sample throughout the impurity induced potential profile into the bulk of the system.

21.5. Grain boundaries in superconductive nanodiamond

In nitrogen-doped UNCD samples discussed in section 21.3.2 the grain boundaries form a low-dimensional subsystem which controls the electron transport in UNCD as a whole. Substantially different situation is observed in another diamond-based system, in nanocrystalline diamond (NCD) heavily doped with boron. Here, the boron atoms are incorporated in the diamond lattice mainly substitutionally, forming in this way shallow acceptors. This leads to high p-type conductivity and, at low temperatures, even to superconductivity both in polycrystalline diamond films with different size of grains and in single crystal diamond. However, in heavily boron-doped diamond with grains of size ~ 100 nm we have detected, mainly in superconducting state, some features which are controlled or modified by the grain boundaries. Especially, it turns out that point contacts between the grains, revealing in superconducting state characteristics of the so-called weak links, are decisive for many observed phenomena. Just effects the grain boundaries and involved point contacts, which both can be understood a special kind of disorder, will be discussed in this section. Nevertheless, we start with a short survey of transport properties of highly B-doped diamond in general, which gives us a background for further discussion of the grainy material. Moreover we will see that the weak localization, previously widely discussed for 2D and 2D-like systems, can play a crucial role even in the purely three-dimensional system - bulk single crystal diamond.

21.5.1. Weak localization and superconductivity in boron doped diamond

Boron doped diamond (BDD), prepared either by high pressure high temperature technique (HPHT) [43], by plasma enhanced chemical vapour deposition (PECVD) [44-46] or by hot filament assisted CVD [47], is a unique material which provides the playground for various quantum transport phenomena, such as hopping, weak localization, ballistic transport,

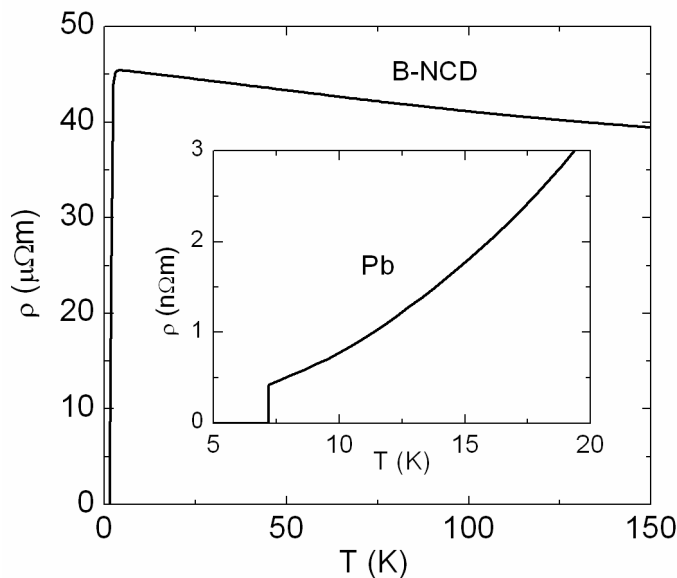


Fig. 14. Temperature dependence of resistivity in highly boron-doped diamond. Behaviour of the resistivity of ordinary metal (Pb) near the superconducting transition is shown in the inset.

unconventional superconductivity and Josephson's effects [48-51]. By different growth technique polycrystalline films with grain size from ~ 100 nm (nanocrystalline diamond) up to ~ 10 μm are obtained. Besides, PECVD technique enables one to prepare single-crystalline epitaxial layers [52,53]. Boron doping concentration, achievable by all growth techniques without appreciable segregation, can reach $\sim 10^{27} \text{ m}^{-3}$.

The most spectacular phenomenon observed in BDD with boron concentration of $\sim 5 \times 10^{26} \text{ m}^{-3}$ or higher is the superconducting (SC) transition observed at temperatures ~ 1 -10 K depending on doping level and growth technique. Figure 14 depicts an example of typical temperature dependence of resistiv-

ity measured in highly boron-doped diamond while a detailed vicinity of the SC transition is displayed in Fig. 15. Let us notice weakly increasing resistivity with decreasing temperature in a wide range of medium and high temperatures above the SC transition. Such behaviour is very characteristic for all highly boron doped diamond samples [43,44,46,54] and it is markedly different from that found in ordinary superconducting metals as lead (see inset of Fig. 14). This difference will be shown essential and will be explained in our model of superconducting BDD presented below.

Let us first recall the conditions which are essential for superconductivity in general [55]. There is a consensus that in a solid state, any attractive interaction near the Fermi level dominating the Coulomb interaction can lead to the charge carrier pairing. Such paired fermions (Cooper's pairs) may occupy, in contrast to the single fermions, the common, "collective" ground state which is separated from the sea of excited single fermions by a finite energy gap $\Delta(T)$. The very property of the Cooper pairs occupying the ground state is that they are indistinguishable by any quantum measurement. Consequently, in case where the ground state is extended from one side of a macroscopic sample to its other side, the transfer of paired carriers via this state is inevitably non-dissipative, i.e. the sample can be regarded superconducting with respect to the transport properties. The aim of any research into the superconductivity may thus be reduced to the identification of pairing mechanism and to the specification of the symmetry of the corresponding ground state.

At present, three types of competitive theories are used for the explanation of the superconductivity in heavily BDD. The main stream is represented by various modifications of classical Bardeen–Cooper–Schrieffer (BCS) theory based on phonon-mediated pairing [56–59]. A review discussing this theory both for BDD and for other semiconductors can be found in [60]. The second approach, correctly describing most of the experimentally observed features, is "correlated impurity band theory" of Baskaran [61]. The third variant of the theory accounting for superconductivity in BDD, which is due to the authors of this article, is based on the spin-flip-driven pairing of holes weakly localized in the vicinity of the Fermi level [50,51]. The simultaneous existence of different, more or less equally justified theories makes

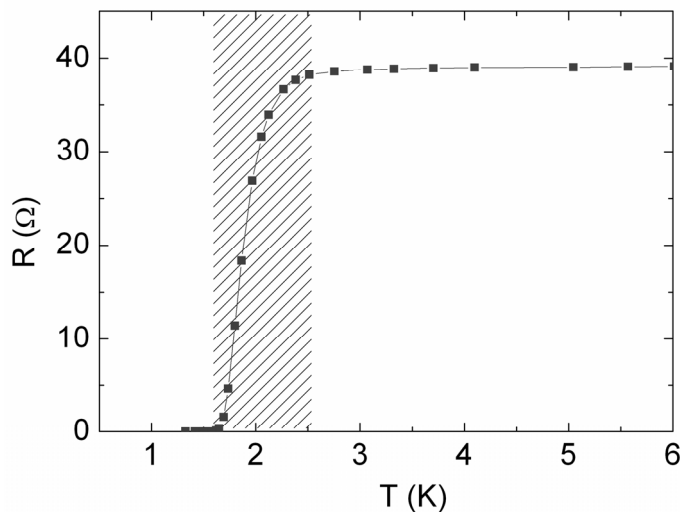


Fig. 15. Resistance of the thin boron-doped nanocrystalline film (thickness ~ 400 nm, grain size ~ 200 nm, boron concentration $\sim 4 \times 10^{27} \text{ m}^{-3}$) as measured by van der Pauw method at low temperatures. Hatched region depicts a width of the superconducting transition.

it obvious that the a-priori choice of a pairing mechanism followed, e.g., by the "derivation of correct value of T_C " cannot serve as a proof of a particular theory. The problem is more complex, requiring the seeking of supplementary experimental indications discriminating some of the pairing mechanisms. An example of a successful identification of pairing mechanism is BCS theory applied to such ordinary metals and alloys as Sn, Pb, Nb_3Ge and others. In that case, isotope effect [62,63] eliminated any pairing not related to the phonons. A very similar idea is also behind recent attempts at proving that the pairing mechanism in heavily boron-doped diamond is phonon mediated [64,65], which, however, cannot be unambiguously interpreted [66]. Hence, the reliable

experimental proof determining the pairing mechanism in superconducting BDD is lacking at present and possible explanation the phenomenon has to be based on combining experimental observations with some arbitrary construction. Our attempt for such reasoning is given in what follows.

As mentioned in section 21.3, a fingerprint of weak localization is the giant negative magnetoresistance. This effect, being dependent on the relative orientation between the plane of weakly localized orbit and the vector of magnetic induction, is in low-dimensional structures of a rather spectacular nature reaching there more than $\sim 10\%$. In 3-dimensional conductors, however, due to the random positions of weakly localized orbits with respect to magnetic vector the effect is not so well pronounced ($\sim 0.1\%$) and, moreover, it is usually overwhelmed by the so called shrinkage effect [5] leading to the positive magnetoresistance. Therefore in 3D we have to look for other traces of WL. We believe that the presence of weak localization in a 3D conductor is manifested by an increase of the sample resistance with decreasing temperature with simultaneous absence of a real energy gap there. Experimentally we could confirm such a feature in BDD by measuring temperature dependence of the conductivity and by evaluation of the apparent activation energy Γ in Arrhenius plot in a wide range of temperatures – see Fig. 16. We found $\Gamma < kT$ everywhere between ~ 2.4 K (onset of the superconductivity transition) and ~ 350 K. As deduced in section 21.2 it implies that the BDD has to be treated, below 350 K, as a disordered metal. The only known microphysical model corresponding of such localization behaviour in disordered metals is a temperature dependent quantum interference of electrons in disorder-induced potential – weak localization.

Further, let us mention an important experimental fact that the superconductivity in highly boron-doped diamond is observed only if the system becomes Mott's metal, i.e. if the actual hole concentration there exceeds the theoretical Mott's threshold value p_M . Formula for this value reads ([4], cf. also formula (2))

$$a_B p_M^{1/3} = 0.26 \pm 0.01, \quad (20)$$

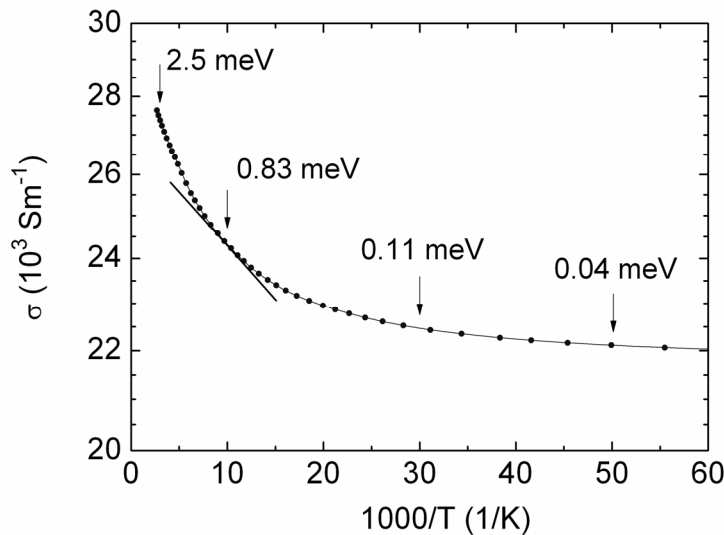


Fig. 16. Temperature dependence of conductance of highly boron-doped diamond film (hole concentration $\sim 3 \times 10^{27} \text{ m}^{-3}$) in Arrhenius coordinates. Apparent activation energies determined from the slope of the dependence are indicated for several different temperatures.

where a_B is Bohr's impurity radius. As the boron behaves in diamond likely as a regular shallow impurity [67] with $a_B \approx 3.1 \times 10^{-10} \text{ m}$, we immediately obtain for the threshold concentration a value $p_M \approx 6 \times 10^{26} \text{ m}^{-3}$. This value describes very well the experimentally observed crossover between weak and strong localization [68] and simultaneously corresponds to a threshold above which is the superconductivity in the BDD is detected [45]. The fact that BDD revealing the superconducting transition is disordered Mott's metal controlled above T_C by weak localization has lead us an assumption that the effects dominating the trans-

port above T_C likely play the dominant role in superconducting transition. (Note that the same conjecture is valid for the superconducting transition in ordinary metals treated within the BCS theory. Indeed, in ordinary metals, the transport above T_C is dominated by electron-phonon interaction, as well as the superconducting transition.) Starting from the above assumption we can build the following deductions [50,69]. In disordered Mott's metal, the Coulomb and exchange interactions at distances larger than the Bohr radius a_B cease to play a substantial role. Simultaneously, the effect of weak localization gives rise to the temporarily stable coherent single-electron (hole) interference patterns having intrinsic extent $\xi = \hbar v_F / 4kT$, where v_F is the Fermi velocity, and characteristic Orstein's coherence time $\tau = \hbar / 2kT$ [70]. Respecting then our conjecture, the attraction between oscillating weakly localized carriers mediated by a periodic polarization of the host lattice (i.e. electron-phonon mediated interaction), should be confined to the energy band of width $\approx \hbar / \tau$. On the other hand, the direct Heitler-London electron-electron interaction is, because of the said screening, reduced to the attractive spin-spin interaction represented by the energy gap [50]

$$\Delta = 2\mu_0\mu_B^2/b^3. \quad (21)$$

Here b is the inter-atomic distance in the host lattice, μ_0 the permeability of vacuum and μ_B the Bohr magneton ($b \approx 1.54 \times 10^{-10}$ m, $\Delta \approx 3.7 \times 10^{-4}$ eV). Obviously, both types of attractive interactions, i.e. the electron-phonon mediated and the direct spin-spin interaction, may operate simultaneously or cooperate in creating Cooper pairs. Taking, however, into account the fact that for temperatures just above the superconducting transition (say for $T \leq 2$ K), it must be $\hbar / \tau = 2kT \approx 3.4 \times 10^{-4}$ eV $< 3.7 \times 10^{-4}$ eV $\approx \Delta$, which means that the spin-spin interaction is the most robust attractive interaction present. Moreover, in contrast to the electron-phonon mediated interaction, the spin-flips are unavoidable for the establishment of proper symmetry of the ground state satisfying the Pauli exclusion principle. Applying the philosophy of Occam's razor, one has to believe in spin-flip model of pairing mechanism in BDD.

For the discussion of the superconductivity in a given system, a consideration of other energy scales involved is also important. The upper cut-off energy for phonons is set by the Debye energy $k\theta_D$. In diamond, the Debye temperature $\theta_D = 2230$ K and $k\theta_D = 0.192$ eV. Analogous cut-off energy for holes is the Fermi energy [71]:

$$E_F = 9.57(\hbar^2/2m)N_B^{2/3}, \quad (22)$$

where N_B is the concentration of electrically active boron acceptors. For Mott's metal of concentration $N_B \approx 2 \times 10^{27}$ m⁻³, the Fermi energy E_F formally amounts to ≈ 0.58 eV. The energy scales in a metallic BDD may thus be in the vicinity of the transition temperature T_C ordered as follows: $\hbar / \tau \approx \Delta \ll k\theta_D < E_F$. This means that the quantities relevant to the superconducting transition are much smaller than other energies characterizing the system as a whole. This circumstance, largely simplifying the theoretical description of the superconducting transition, is the essence of the so called weak coupling approximation originally developed within the BCS theory [55,72]. On the basis of quite general thermodynamics arguments, this approximation leads to the universal scaling relation connecting Δ and T_C , which has the character of the "law of corresponding states", namely:

$$\Delta = 1.76 kT_C. \quad (23)$$

It is worth noting that relation (23) is very often erroneously used as a fingerprint of phonon-driven pairing mechanism, whereas it is merely the direct consequence of weak coupling

approximation, which is also valid for our spin-flip pairing model. Moreover, the experimentally confirmed validity of scaling law (23) excludes any pairing mechanism exploiting high-frequency phonons having energy comparable, e.g., with the Debye energy. These very facts should be considered seriously before accepting a theoretical approach for interpretation of experimental data.

Anyway, the usefulness of relationship (23) is quite obvious. For example, it enables the assessment of change of T_C due to the increase of the gap Δ in consequence of host lattice deformation. Indeed, combining equations (21) and (23) and computing the derivative with respect to parameter b , we obtain a relation

$$dT_C = -(1.14\mu_0\mu_B^2/kb^4)db. \quad (24)$$

Inserting $b = 1.54 \times 10^{-10}$ m, we obtain $dT_C = -4.76 \times 10^{10}$ db. Effective local lattice deformation due to the substitution of C atom by B atom will increase the distance between the nearest neighbouring atoms by an amount of $db \approx 1.1 \times 10^{-11}$ m. (Note that the covalent radii of carbon and boron are 7.7×10^{-11} m and 8.8×10^{-11} m, respectively.) According to formula (24), the T_C has to decrease about ≈ 0.5 K; we thus predict the existence of a maximum in the dependence of T_C on boron concentration followed by a decrease of T_C at appreciably high concentrations [59].

21.5.2. Modulation of superconductivity by grain boundaries

Central concept serving for description of superconductivity in grainy and other inhomogeneous systems is so called weak link. This is a region inserted between two lumps of superconductor where the order parameter is reduced appreciably, however, without ceasing. The weak link has not the properties of a regular superconductor, nevertheless, it is simultaneously assumed to be able to carry supercurrent. The most frequent model of the weak link is a resistively shunted junction. The total current flowing through the weak link is split there into a supercurrent component flowing directly through the junction and a normal current flowing through the shunt resistance. As the amplitude of the supercurrent has its upper limit given by a value of the critical current, i_c , the weak link inserted into the superconducting system brings about the so-called resistive behaviour, i.e. the finite sharpness of superconducting transition and the appearance of ohmic resistance in this region.

Influence of granularity on resistive behaviour may be clearly demonstrated by analysis of experimental data on the SC transition observed in various equally boron-doped diamond systems having different grain size. If we specify the relative width of the SC transition as a ratio $\delta T/T_C$, where δT is the difference between the on-set and the off-set transition temperatures and T_C is the off-set transition temperature (width of hatched region in Fig. 15), we obtain the following figures. For materials having grain size from the ~ 100 nm range, i.e. for really nanocrystalline materials this ratio $\delta T/T_C \approx 0.3-0.4$ [43,44,69] whereas for films composed of crystals larger than ~ 10 μm and for epitaxial single crystal layers this ratio attains an appreciable smaller value, $\delta T/T_C \approx 0.1$ [45,53,54]. Hence presence of numerous grain boundaries in nanodiamond really enhances the resistive behaviour. Let us add that the full account of the finite sharpness of the SC transition would also require considering boron fluctuations and their effect on formation of the superconducting infinite cluster.

Another extremely important consequence of insertion of the weak link into the superconducting circuit is an appearance of Josephson's supercurrents. It is a rather fundamental quantum feature of supercurrent that it is, in a contrast to normal current, driven not by the voltage but by the phase difference. As, on the basis of quite general quantum-mechanical considerations [72], the observed rate of change of the electron (hole) phase difference between two distinct points in the superconductor is directly proportional to the difference of

electrochemical potentials at these points, the following relations between the voltage drop and the supercurrent may be deduced. For zero voltage drop (e.g. in the absence of weak link) the phase difference will be constant giving rise to a constant d.c. supercurrent. Alternatively, at a finite constant voltage drop maintained on the weak link by some external mean the phase difference will continually grow. In such a case, however, because of the 2π periodicity of the phase also an oscillating supercurrent reflecting this periodicity should appear there [55]. The frequency f of this so called Josephson's a.c. supercurrent is given by a fairly simple formula

$$hf = 2eV. \quad (25)$$

Let us now consider the highly boron-doped NCD in superconducting state near the transition temperature T_C . We identify the source of voltage difference between the neighbouring grains with the thermal noise of normal component of electron fluid. The mean square of voltage corresponding to the thermal agitation of this normal component at transition temperature T_C may be evaluated using a simple formula due to de Haas-Lorentz [73]

$$\langle V^2 \rangle = kT_C/C, \quad (26)$$

where brackets mean the time averaging and C is a geometric capacitance of grain junction. Combining then equations (25) and (26), we obtain a relation

$$\langle h^2 f^2 \rangle = 4e^2 kT_C / C, \quad (27)$$

which allows us to express electromagnetic energy hf of the a.c. supercurrent in terms of inter-grain capacitance and transition temperature. Necessary condition for stability of the superconducting state is that this energy is larger than energy $e^2/2C$ for transfer an electron from one grain to another (charging energy). It leads to a criterion for stability of superconductivity in grainy material

$$T_C > e^2/16kC = 1.16 \times 10^{-16}/C. \quad (28)$$

We see that for evaluation of the formula (28) the capacitance between grains has to be estimated. For this purpose we have developed the following simple model. We assume first that in a polycrystalline, otherwise homogeneous material the barriers between neighbouring grains are due only to the orientation mismatch of their lattices so that the expected barrier thickness s should be approximately equal to doubled diamond lattice constant (i.e. $s \approx 2a$). This assumption enables one to make reasonable estimates of upper and lower limits of inter-grain (i.e. interface or junction) capacitance C , an important quantity, which will be employed in further considerations. If the intimate contact area, where the surface of one grain adheres closely to another, were as large as a square of characteristic grain size d , the interface capacitance C would be obviously given by

$$C = \epsilon\epsilon_0 d^2/2a, \quad (29)$$

which gives for $d = 200$ nm value of inter-grain capacitance equal to $\sim 2.8 \times 10^{-15}$ F. On the other hand, if the contact between grains is confined to one point only (see insert of Fig. 17); the following Russell's formula [74] for the capacitance of two spherical conductors when close together is adequate, namely

$$C = \pi \epsilon\epsilon_0 d [\gamma_{EM} + 1/2 \ln(d/2s)]; \quad (30)$$

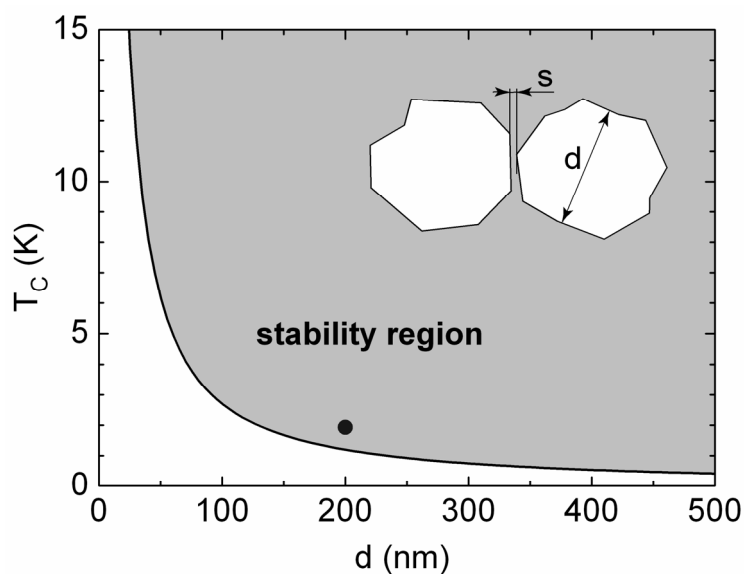


Fig. 17. Stability region (gray area) of superconductivity in a polycrystalline diamond of grain size d . T_C means here the transition temperature intrinsic to the material of the grain. The bold point corresponds to the typical highly boron-doped NCD samples studied. Inset depicts a schematic view of contact between two neighbouring diamond grains separated by a minimum distance s .

ted in Fig. 17. From this plot it is apparent that for grains large enough, i.e. $d \geq 100$ nm, the superconductivity of polycrystalline material should not be appreciably influenced by the absolute size of the grains. Under this limit, however, a rather fast deterioration of superconductivity with decreasing grain size is to be expected. Let us note that the above consideration on the few-point grain junctions agrees very well with what we can deduce from our knowledge on the growth processes [23]. Because of treatment of substrates before growth the positions and orientations of nucleation centres on the substrate are quite random. Therefore, also the matching of the lattices of the neighbouring diamond crystals in ready-made polycrystalline film cannot be perfect in principle. Hence, on purely geometrical grounds, the satisfactory matching of neighbouring grains can be achieved only in a limited number of small spots.

Summarizing this subsection, we have shown that in nanocrystalline heavily boron-doped diamond the superconductivity properties (transition temperature and width of the transition region) are modified by presence of the grain boundaries. These effects are controlled by small (point-like) inter-grain contacts playing a role of superconducting weak links.

21.5.3. Josephson's noise

In this subsection we show that an existence of weak links in superconducting boron-doped diamond can be supported also by noise measurements. The basic idea and the arrangement of the experiment are closely related to that of low-temperature noise thermometry [75], where small voltage differences appearing across an ohmic resistor are converted by a SC loop with a weak link into Josephson's AC (RF) signal. The resistive behaviour of B-NCD observed in the SC transition region (see 21.5.2) ensures, namely, that the current flowing through the sample generates, in the array of weak links, a minute potential gradient and, consequently, oscillating Josephson's supercurrent. Direct observation of such a type of signal may thus serve as a proof of the existence of an array of weak links in the B-NCD sample. For this purpose we set up a simple apparatus which is schematically depicted in Fig. 18a.

$s = 2a$ ($a \approx 3.56 \times 10^{-10}$ m) represents here the nearest distance between the surfaces of two spheres having the same diameter d and $\gamma_{EM} = 0.577\dots$ is Euler–Mascheroni's constant. Lower estimate of the junction capacitance based on this formula then gives for $d \approx 200$ nm a value $C \approx 1.08 \times 10^{-16}$ F. As formula (29) for the inter-grain capacitance put into the criterion (28) would shift the lower limit of T_C down to non-realistic values, we are convinced that the model assuming a few point contacts between the neighbouring grains with, say, a single preferential one is more adequate than the flat contact realized over the whole contact area. The curve based thus on relation (28) and Russell's formula (30) is plotted in Fig. 17.

A floating current source realized by a galvanic cell with potentiometer was connected by a triaxial cable to two neighbouring contacts on a B-NCD sample which was placed in a screened cavity in a helium cryostat. The RF signal was collected from voltage probes of the sample and analyzed by the home-made band-pass filter realized by a normal capacitor with build-in toroidal coil wound on a Teflon core. The band-pass filter being tuneable only in a vicinity of 10MHz (± 0.5 MHz) enabled one to analyze only the low-frequency Josephson signals.

Applying, at a constant temperature of $\sim 1.3\text{K} < T_C$ and zero magnetic field, an exciting current slightly smaller than the critical one, $i = 10$ mA, ($i_C \approx 11.1$ mA), a maximal enhancement of signal at frequency of $\sim 9.7\text{MHz}$ was observed. This effect, which should be according to our expectations due to the generation of RF Josephson oscillations in the sample, may be consistently accounted for as follows. The existence of Josephson's oscillations at this frequency witnesses, namely, to the voltage drop between neighbouring SC grains which has to be a consequence of a certain normal current, i_N , flowing through the resistance R_N shunting the Josephson junction in a corresponding weak link. Taking into account Eq. (25), the normal current necessary for generation of Josephson's oscillations at frequency f can be evaluated using an obvious formula,

$$i_N = \pi h f / e R_N. \quad (31)$$

The corresponding value of normal current shunting the typical weak link is thus in our case $i_N \approx 5.0 \times 10^{-11}$ A. This figure may be immediately compared with the value of the superconducting current component as given by Larkin's formula [76]

$$i_C \approx \Delta(0) / e R_N. \quad (32)$$

For our case where $R_N \approx 400 \Omega$ and superconducting gap (see section 21.5.1) $\Delta(0) \approx 3.7 \times 10^{-4}$ eV, we obtain a value $i_C \approx 9.2 \times 10^{-7}$ A which is much higher than the value of i_N

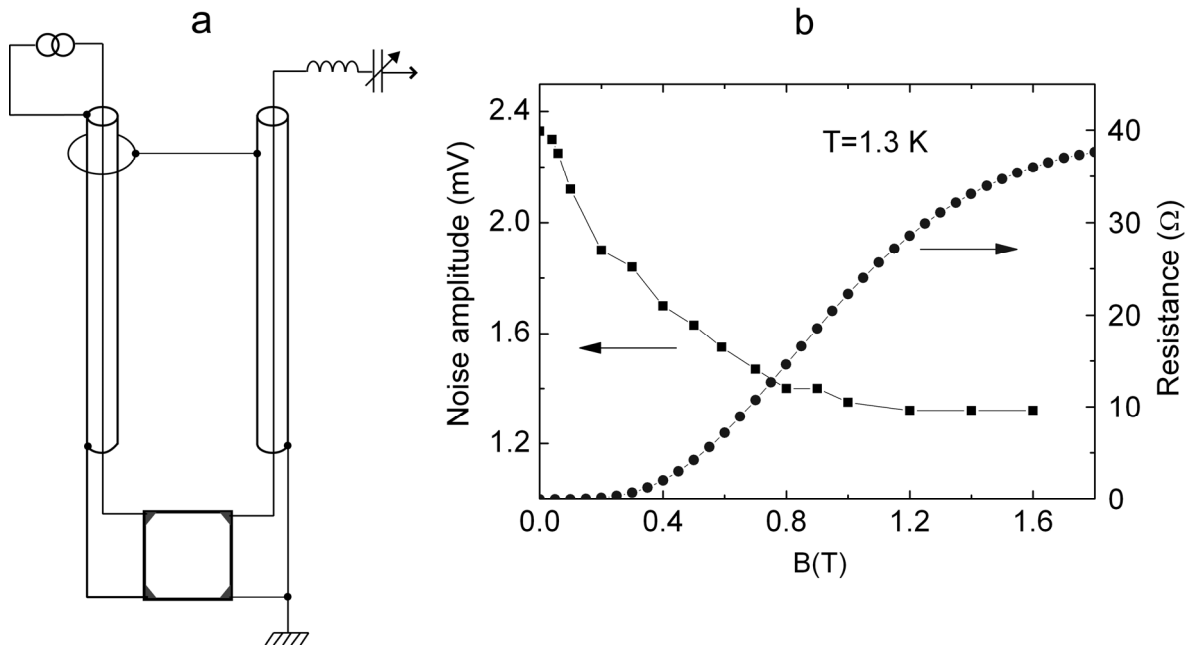


Fig. 18. Schematic view of the experimental apparatus used for the detection of current-induced Josephson's r. f. noise signal (a) and dependence of the noise signal amplitude observed at frequency of ~ 9.7 MHz on magnetic field compared with the magnetoresistance curve measured at the same temperature $T \approx 1.3$ K.

above. We can thus conclude that the branching-off of the normal current component in weak link is almost negligible.

The situation, however, noticeably changes if the magnetic field perpendicular to the NCD layer is applied. It is a well-known fact that, with increasing magnetic field, the critical current diminishes. As, furthermore, the fundamental condition for the supercurrent i_S has to remain valid, $i_S \leq i_C$, then by keeping the total current through the sample constant, the normal current i_N should increase appreciably, giving rise to a voltage drop between neighbouring SC grains and, simultaneously, to the shift of Josephson oscillations to higher frequencies. Just such an effect can be recognized in Fig. 18b where the signal amplitude observed at constant frequency ~ 9.7 MHz decreases with increasing magnetic field. Moreover, the disappearance of a Josephson signal, because of its shift to higher frequencies, is correlated with the magnetoresistance curve measured at the same temperature (depicted also in Fig. 18b). As we believe, this is a natural consequence of the fact that the very mechanism of resistive behaviour is just the branching-off of the normal current from the total current flowing through the weak link.

Hence, the model of boron-doped NCD at low temperatures as a system of superconducting grains connected by weak links is also confirmed by measurement of Josephson's noise and its magnetic field dependence.

Acknowledgment: The research presented in this chapter was supported by the Grant Agency of ASCR Contract Nos IAA100100639, IAA1010404 and by the Czech Science Foundation Contract No 202/06/0040. Furthermore, the work was prepared in the framework of the Institutional Research Plan of Institute of Physics No AV0Z10100521. Miloš Nesládek, Olivier Williams, Dieter M. Gruen, Eduard Hulicius, Jozef Novák and Miroslav Cukr are acknowledged for sample supply. Jozef Krištofik and Dobroslav Kindl have contributed significantly to the experimental work described in this chapter. Valuable discussions with all the above-mentioned persons are appreciated.

References 21

1. Gebhard, F.: *The Mott Metal-Insulator Transition*. Springer, Heidelberg (1997)
2. Serrin, J.: *Conceptual analysis of the classical second laws of thermodynamics*. Archive for Rational Mech. and Analysis **70**, 355 (1979)
3. Planck, M.: *Vorlesungen über die Theorie der Wärmestrahlung*, 5th edition. J. A. Barth, Leipzig (1923)
4. Mott, N.F.: *Conduction in Non-Crystalline Materials*. Oxford University Press, New York (1987)
5. Shklovskii, B.I., Efros, A.L.: *Electronic Properties of Doped Semiconductors*. Springer, Berlin (1984)
6. Hertz P.: *Über den gegenseitigen durchschnittlichen Abstand von Punkten, die mit bekannter mittlerer Dichte im Raume angeordnet sind*. Math. Ann. **67**, 387 (1909)
7. Ferry, D.K., Goodnick, S.M.: *Transport in nanostructures*. Cambridge University Press, Cambridge (1999)
8. Altshuler, B.L., Aronov, A.G.: *Electron-electron interaction in disordered conductors*. In: Efros, A.L., Pollak, M. (eds.), *Electron-Electron Interactions in Disordered Systems*, p. 1, North Holland, Amsterdam (1985)
9. Bergmann, G.: *Physical interpretation of weak localization: A time-of-flight experiment with conduction electrons*. Phys. Rev. **B 28**, 2914 (1983)
10. Zhao, H.L., Spivak, B.Z., Gelfand, M.P., Feng, S.: *Negative magnetoresistance in variable-range-hopping conduction*. Phys. Rev. **B 44**, 10760 (1991)
11. Dorin, V.V.: *Magnetoresistance of layered conductors*. Phys. Lett. **A 183**, 233 (1993)

12. Chang, A.M., Baranger, H.U., Pfeiffer, L.N., West, K.W.: *Weak Localization in Chaotic versus Nonchaotic Cavities: A Striking Difference in the Line Shape*. Phys. Rev. Lett. **73**, 2111 (1994)
13. Feng, X., Mareš, J.J., Raikh, M.E., Koch, F., Grützmacher, D., Kohl A.: *Magnetotransport in planar doping structures*. Surf. Sci. **263**, 147 (1992)
14. Kurdak, Ç., Chang, A.M., Chin, A., Chang, T.Y.: *Quantum interference effects and spin-orbit interaction in quasi-one-dimensional wires and rings*. Phys. Rev. **B 46**, 6846 (1992)
15. Poole, D.A., Pepper, M., Hughes, A.: *Spin-orbit coupling and weak localisation in the 2D inversion layer of indium phosphide*. J. Phys. C: Solid State Phys. **15**, L1137 (1982)
16. Aharonov Y., Bohm, D.: *Significance of Electromagnetic Potentials in the Quantum Theory*. Phys. Rev. **115**, 485 (1959)
17. Mareš, J.J., Krištofik, J., Hubík, P.: *Low-field magnetoresistance anomaly in two-dimensional electron gas*. Solid State Commun. **101**, 243 (1997)
18. Mareš, J.J., Krištofik, J., Hubík, P., Špička V.: *Weak localization - an experimental tool to investigate electromagnetic vacuum fluctuations*. Physica **E 29**, 375 (2005)
19. Fukuyama H.: *Interaction effects in the weakly localized regime of two- and three-dimensional disordered systems*. In: Efros, A.L., Pollak, M. (eds.), *Electron-Electron Interactions in Disordered Systems*, p. 155, North Holland, Amsterdam (1985)
20. Williams, O.A., Curat, S., Gerbi, J.E., Gruen, D.M., Jackman, R.B.: *n-type conductivity in ultrananocrystalline diamond films*. Appl. Phys. Lett. **85**, 1680 (2004)
21. Mareš, J.J., Hubík, P., Krištofik, J., Štěpánek, B., Šestáková, V., Pekárek, L.: *Electrical properties of Mn-doped GaSb*. Mater. Sci. Eng. **B 28**, 134 (1994)
22. Birrel, J., Carlisle, J.A., Auciello, O., Gruen, D.M., Gibson, J.M.: *Morphology and electronic structure in nitrogen-doped ultrananocrystalline diamond*. Appl. Phys. Lett **81**, 2235 (2002)
23. Williams, O.A., Nesládek, M., Mareš, J.J., Hubík, P.: *Growth and properties of nanocrystalline diamond films*. In: Koizumi, S., Nebel, C.E., Nesládek, M. (eds.), *Physics and Applications of CVD Diamond*, p. 13, Wiley-VCH, Berlin, 2008
24. Mareš, J.J., Krištofik, J., Hubík, P., Feng, X., Novák, J., Hasenöhrl, S.: *Highly disordered two-dimensional electron system in a weak magnetic field*. Europhys. Lett. **45**, 374 (1999)
25. Raikh, M.E.: *The incoherent mechanism of negative magnetoresistance for variable-range-hopping transport in two-dimensional electron systems*. Philos. Mag. **B 65**, 715 (1992)
26. Palacios, J.: *Dimensional Analysis*. Macmillan, London (1964)
27. Ye, Q.-Y., Shklovskii, B. I., Zrenner, A., Koch, F., Ploog, K.: *Hopping transport in δ -doping layers in GaAs*. Phys. Rev. **B 41**, 8477 (1990)
28. Jungwirth, T., Lay, T.S., Smrčka, L., Shayegan, M.: *Resistance oscillation in wide single quantum wells subject to in-plane magnetic fields*. Phys. Rev. **B 56**, 1029 (1997)
29. *ASTM Standard F76 – 08: Standard Test Methods for Measuring Resistivity and Hall Coefficient and Determining Hall Mobility in Single-Crystal Semiconductors*, ASTM International, West Conshohocken, PA (2008)
30. Prange, R.E., Girvin S.M. (eds.): *The Quantum Hall Effect*, 2nd edition. Springer, New York (1990)
31. Chakraborty T., Pietilainen, P.: *The Quantum Hall Effects-Fractional and Integer*, Springer Series in Solid-State Sciences **85**. Springer, Berlin (1995)
32. Jain J.: *Composite Fermions*, Cambridge University Press. Cambridge (2007)
33. Arai, K., Hashimoto, S., Oto, K. Murase, K.: *Spatial distribution of edge states in the quantum Hall plateaus investigated by magnetocapacitance*. Phys. Rev. **B 68**, 165347 (2003)

34. McCormick K.L., Woodside, M.T. Huang, M. Wu M., McEuen P.L., Duruoaz C., Harris, J.S., Jr.: *Scanned potential microscopy of edge and bulk currents in the quantum Hall regime*. Phys. Rev. **B 59**, 4654 (1999)
35. Mareš, J.J., Křištofik, J., Hubík, P.: *Bulk Extended States in a Two-Dimensional Electron Gas in the Quantum Hall Regime*. Phys. Rev. Lett. **82**, 4699 (1999)
36. Cole R.H., Gross, P.M., Jr.: *A Wide Range Capacitance-Conductance Bridge*. Rev. Sci. Instrum. **20**, 252 (1949)
37. Luryi, S.: *Quantum capacitance devices*. Appl. Phys. Lett. **52**, 501 (1988)
38. Shik, A.Y.: *Electrodynamics of 2D electron systems*. Semicond. **29**, 697 (1995)
39. Efros, A.L.: *Electrostatics of an inhomogeneous quantum hall liquid*. Phys. Rev. **B 60**, 13343 (1999)
40. Chklovskii, D.B., Shklovskii, B.I., Glazman, L.I.: *Electrostatics of edge channels*. Phys. Rev. **B 46**, 4026 (1992)
41. Chalker, J.T., Coddington, P.D.: *Percolation, quantum tunnelling and the integer Hall effect*. J. Phys. C: Solid State Phys. **21**, 2665 (1988)
42. Mandelbrot, B.B.: *The Fractal Geometry of Nature*. W. H. Freeman and Co., New York (1983)
43. Ekimov, E.A., Sidorov, V.A., Bauer E.D., Mel'nik, N.N., Curro, N.J., Thompson J.D., Stishov, S. M.: *Superconductivity in diamond*. Nature **428**, 542 (2004)
44. Takano, Y., Nagao, M., Sakaguchi, I., Tachiki, M., Hatano, T., Kobayashi, K., Umezawa, H., Kawarada, H.: *Superconductivity in diamond thin films well above liquid helium temperature*. Appl. Phys. Lett. **85**, 2851 (2004)
45. Bustarret, E., Kačmarčík, J., Marcenat, C., Gheeraert, E., Cytermann, C., Marcus, J., Klein, T.: *Dependence of the Superconducting Transition Temperature on the Doping Level in Single-Crystalline Diamond Films*. Phys. Rev. Lett. **93**, 237005 (2004)
46. Nesládek, M., Tromson, D., Mer, C., Bergonzo, P., Hubík, P., Mareš, J.J.: *Superconductive B-doped nanocrystalline diamond thin films: Electrical transport and Raman spectra*. Appl. Phys. Lett. **88**, 232111 (2006)
47. Wu, D., Ma, Y.C., Wang, Z.L., Luo, Q., Gu, C.Z., Wang, N.L., Li, C.Y., Lu, X.Y., Jin Z.S.: *Optical properties of boron-doped diamond*. Phys. Rev. **B 73**, 012501 (2006)
48. Sato, T., Ohashi, K., Sugai, H., Sumi, T., Haruna, K., Maeta, H., Matsumoto, N., Otsuka, H.: *Transport of heavily boron-doped synthetic semiconductor diamond in the hopping regime*. Phys. Rev. **B 61**, 12970 (2000)
49. Mamin, R.F., Inushima, T.: *Conductivity in boron-doped diamond*. Phys. Rev. **B 63**, 033201 (2001)
50. Mareš, J.J., Hubík, P., Nesládek, M., Kindl, D., Křištofik, J.: *Weak localization — Precursor of unconventional superconductivity in nanocrystalline boron-doped diamond*. Diam. Relat. Mater. **15**, 1863 (2006)
51. Mareš, J.J., Hubík, P., Křištofik, J., Kindl, D., Nesládek, M.: *Quantum Transport in Boron Doped Nanocrystalline Diamond*. Chem. Vap. Deposition **14**, 161 (2008)
52. Langrange, J.P., Deneuville, A., Gheeraert, E.: *Activation energy in low compensated homoepitaxial boron-doped diamond films*. Diam. Relat. Mater. **7**, 1390 (1998)
53. Takano, Y., Takenouchi, T., Ishii, S., Ueda, S., Okutsu, T., Sakaguchi, I., Umezawa, H., Kawarada, H., Tachiki, M.: *Superconducting properties of homoepitaxial CVD diamond*. Diam. Relat. Mater. **16**, 911 (2007)
54. Wang, Z.L., Luo, Q., Liu, L.W, Li, C.Y., Yang, H.X., Yang, H.F., Li, J.J., Lu, X.Y., Jin, Z.S., Lu, L., Gu, C.Z.: *The superconductivity in boron-doped polycrystalline diamond thick films*. Diam. Relat. Mater. **15**, 659 (2006)
55. Waldram, J.R.: *Superconductivity of Metals and Cuprates*. IOP Publishing, London (1996)

56. Ortolani, M., Lupi, S., Baldassarre, L., Schade, U., Calvani, P., Takano, Y., Nagao, M., Takenouchi, T., Kawarada, H.: *Low-Energy Electrodynamics of Superconducting Diamond*. Phys. Rev. Lett. **97**, 097002 (2006)
57. Lee, K.-W., Pickett, W.E.: *Boron spectral density and disorder broadening in B-doped diamond*. Phys. Rev. **B 73**, 075105 (2006)
58. Blase, X., Adessi, Ch., Connétable, D.: *Role of the Dopant in the Superconductivity of Diamond*. 2004 Phys. Rev. Lett. **93**, 237004 (2004)
59. Moussa, J. E., Cohen, M.L.: *Constraints on T_c for superconductivity in heavily boron-doped diamond*. Phys. Rev. **B 77**, 064518 (2008)
60. Cardona, M.: *Superconductivity in diamond, electron–phonon interaction and the zero-point renormalization of semiconducting gaps*. Sci. Technol. Adv. Mat. **7**, S60 (2006)
61. Baskaran, G.: *Resonating Valence Bond Mechanism of Impurity Band Superconductivity in Diamond*. J. Supercond. Nov. Magn. **21**, 45 (2008)
62. Maxwell, E.: *Isotope Effect in the Superconductivity of Mercury*. Phys. Rev. **78**, 477 (1950)
63. Reynolds, C.A., Serin, B., Wright, W.H., Nesbitt, L.B.: *Superconductivity of Isotopes of Mercury*. Phys. Rev. **78**, 487 (1950)
64. Dubrovinskaia, N., Dubrovinsky, L., Papageorgiou, T., Bosak, A., Krisch, M., Braun, H. F., Wosnitza, J.: *Large carbon-isotope shift of T_C in boron-doped diamond*. Appl. Phys. Lett. **92**, 132506 (2008)
65. Ekimov, E.A., Sidorov, V.A., Zoteev, A., Lebed', Yu.B., Thompson, J.D., Stishov, S.M.: *Structure and superconductivity of isotope-enriched boron-doped diamond*. Sci. Techn. Adv. Mater. **9**, 044210 (2008)
66. Mareš, J.J., Hubík, P., Krištofik, J., Nesládek, M.: *Selected topics related to the transport and superconductivity in boron-doped diamond*. Sci. Techn. Adv. Mater. **9**, 044101 (2008)
67. Thonke, K.: *The boron acceptor in diamond*. Semicond. Sci. Technol. **18**, S20 (2003)
68. Werner, M., Job, R., Zaitzev, A., Fahrner W.R., Seifert, W., Johnston, C., Chalker, P.R.: *The Relationship between Resistivity and Boron Doping Concentration of Single and Polycrystalline Diamond*. phys. status solidi **a 154**, 385 (1996)
69. Mareš, J.J., Nesládek, M., Hubík, P., Kindl, D., Krištofik, J.: *On unconventional superconductivity in boron-doped diamond*. Diam. Relat. Mater. **16**, 1 (2007)
70. Ornstein, L.S.: *On the Brownian Motion*. Versl. Acad. Amst. **26**, 1005 (1917) (=Proc. Acad. Amst. **21**, 96 (1919))
71. Blakemore, J.S.: *Semiconductor Statistics*. Pergamon Press, Oxford (1962)
72. Tilley, D.R., Tilley, J.: *Superfluidity and Superconductivity*. Van Nostrand Reinhold Co., New York (1974)
73. de Haas-Lorentz, G.L.: *Die Brownsche Bewegung und einige verwandte Erscheinungen*. F. Vieweg u. Sohn, Braunschweig (1913)
74. Russell, A.: *The Coefficients of Capacity and the Mutual Attractions or Repulsions of Two Electrified Spherical Conductors When Close Together*. Proc. R. Soc. Lond., **A 82**, 524 (1909)
75. Kamper, R.A., Zimmerman, J. E.: *Noise Thermometry with the Josephson Effect*. J. Appl. Phys. **42**, 132 (1971)
76. Likharev, K.K.: *Superconducting weak links*. Rev. Mod. Phys. **51**, 101 (1979).



Chapter 22

Diffusion structural diagnostics

22. DIFFUSION STRUCTURAL DIAGNOSTICS OF SELF-IRRADIATED AMORPHOUS MINERALS

Vladimir Balek, Igor von Beckman

22. 1. Diffusion structural diagnostics of solids

Diffusion structural diagnostics of solids consists in the characterization of diffusion properties of solid samples by using inert gases as traces. Changes in surface morphology and microstructure of the solid samples during thermal treatments and changes due to chemical, mechanical or radiation interactions can be studied by the diffusion structural diagnostics methods.

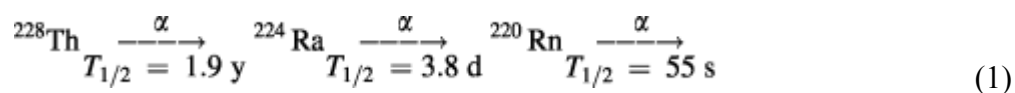
Emanation thermal analysis (ETA) [1-3], based on the measurement of the radon release from samples, is one of the methods used in the diffusion structure diagnostics of solids.

As most of the solids to be investigated do not naturally contain atoms of radon it is necessary to introduce the radon atoms in the samples prior to the ETA measurements.

To introduce the radioactive trace into the solids, the samples are labeled by parent radio-nuclides ^{228}Th and ^{224}Ra , serving as a quasi-permanent source of radon atoms ^{220}Rn . The used specific activity of the parent radionuclide ^{228}Th is in the order 10^5 Bq per gram of the sample.

22.1.1. Use of recoil energy of α -decay for radon atoms implantation into solids

Atoms of ^{220}Rn radon radionuclide are formed by a spontaneous α -decay of ^{228}Th and ^{224}Ra radio-nuclides according to scheme Eq.1



and the ^{220}Rn atoms can be introduced into the solid owing to the recoil energy of the spontaneous α -decay (85 keV per atom). The samples can be labelled by using an adsorption of traces of ^{228}Th as nitrate from a solution.

Due to the energy of the spontaneous α -decay of ^{228}Th and ^{224}Ra radio-nuclides the atoms of ^{220}Rn can penetrate into the sample several tens of nanometers from the surface depending on the composition of the materials. The values of the maximum penetration depths of ^{220}Rn were determined by the Monte Carlo method using TRIM code [4], e.g. for SiO_2 :65.4 nm, for zircon (Zr SiO_4) : 60 nm and brannerite mineral ($\text{U}_{1-x}\text{Ti}_{2+x}\text{O}_6$): 60 nm.

22.1.2. Trapping and release of radon atoms from solids

Radon atoms can be trapped in solids at structure defects such as vacancy clusters, grain boundaries and pores. The structure defects in the solids can serve both as traps and as diffusion paths for radon atoms.

The radon formed by spontaneous α -decay of ^{224}Ra may escape from the solid either by recoil energy ejection or by diffusion. The term emanation rate, E , has been

used to express the release of radon from solids. It is defined as the ratio of the radon release rate to the rate of radon formation by the spontaneous α -decay of ^{228}Th and ^{224}Ra in the investigated solids.

It has been determined experimentally (in relative units) as $E = A_\alpha/A_{\text{total}}$, where A_α is the α -radioactivity of radon released in unit time from the labeled sample and A_{total} is the total γ -radioactivity of the labeled sample. The A_{total} value is proportional to the rate of radon formation in the sample.

In the evaluation of the radon release from solids several mechanisms have been supposed, namely the radon release by recoil mechanism, the diffusion in open pores, and the volume diffusion mechanism.

The experimentally obtained values of the emanation rate, E , can be considered as:

$$E = E(\text{recoil}) + E(\text{pores}) + E(\text{solid}). \quad (2)$$

The emanation rate due to recoil, $E(\text{recoil})$, can be expressed as

$$E(\text{recoil}) = K_1 S_1 \quad (3)$$

where K_1 is a temperature independent constant, proportional to the penetration depth of recoiled radon atoms in solids investigated and S_1 is external surface area of sample particles. The path of recoiled atoms of radon is dependent on the “nuclear stopping power” of the sample material.

The emanation rate due to diffusion in pores, $E(\text{pores})$, is expressed as

$$E(\text{pores}) = K_2 S_2 \quad (4)$$

where K_2 is a constant that depends on temperature and S_2 is internal surface area of the sample depending on the surface of open pores, cracks and intergranular space. The emanation rate due to volume diffusion mechanism, $E(\text{solid})$, is expressed as

$$E(\text{solid}) = K_3 \exp(-Q/2RT) S_3 \quad (5)$$

where K_3 is a constant related to the atomic properties of the lattice, Q is the activation energy of Rn diffusion in the solid, S_3 is surface area, R is molar gas constant, and T is temperature.

The growth of the emanation rate values, $E(T)$, may characterize an increase of the surface area of interfaces, whereas a decrease in the $E(T)$ may reflect processes like closing up structure irregularities that serve as paths for the radon migration, closing pores and/or a decrease in the surface area of the interfaces [3, 5].

22.1.3. Measurement of radon release from solids

During the ETA measurements, a constant flow of the carrier gas (air, nitrogen, or another gas) has been used to take the radionuclide of radon of ^{220}Rn released by the sample into the detector of α -activity of radon (semiconductor detectors) [6]. Figure 1 depicts a scheme of the apparatus for radon measurement used in the emanation thermal analysis.

In the study of the self- irradiated amorphous materials the ETA measurements were carried out by using modified NETZSCH DTA-ETA equipment, Type 404. Details of the measurements and the data treatments are described elsewhere [2,3,6]. During the ETA measurements the samples were heated at the rate of $6 \text{ K}\cdot\text{min}^{-1}$ in air

(zircon sample) and argon (brannerite sample). The specific activity of the labelled samples was 10^5 Bq.g^{-1} . The used amounts of the samples were 0.02 and 0.1 g respectively.

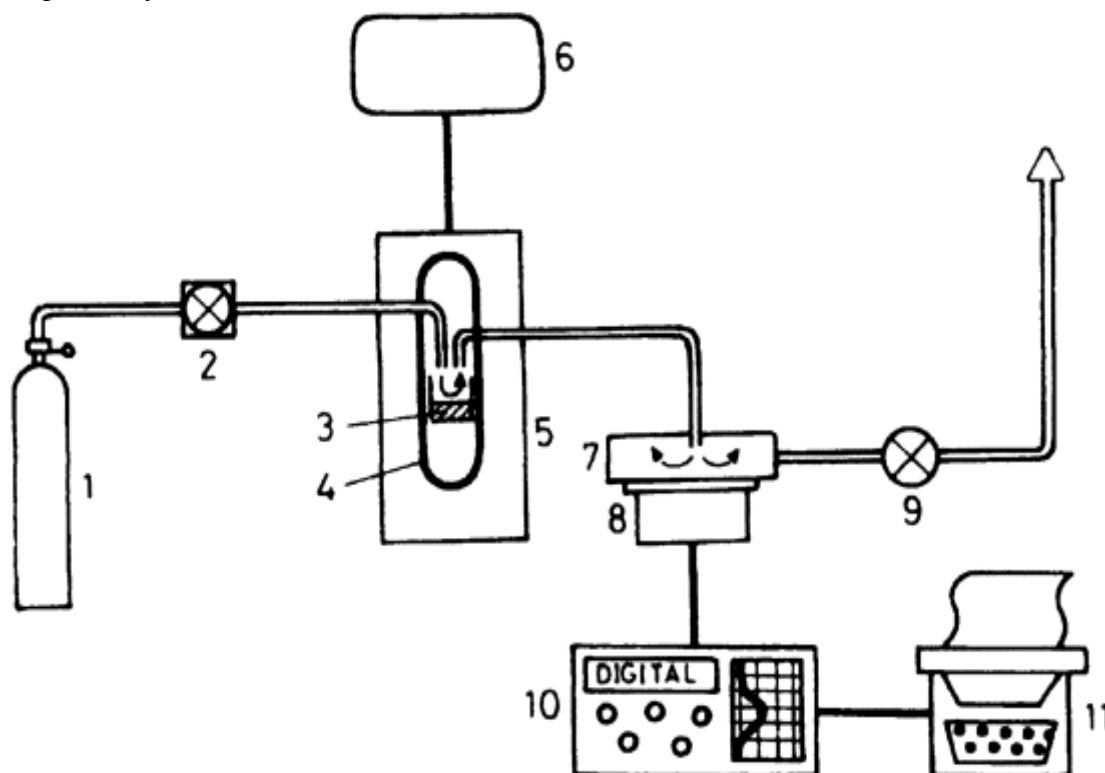
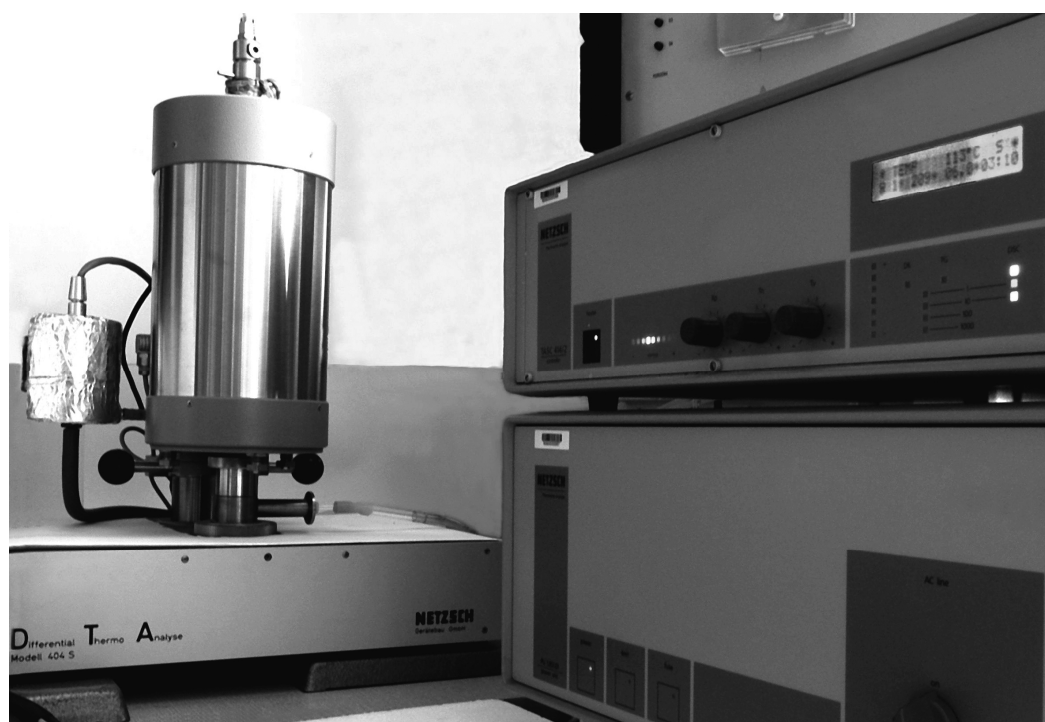


Fig. 1 Scheme of the apparatus for emanation thermal analysis: 1—gas supply; 2—gas flow stabilizer; 3—labeled sample; 4—sample holder; 5—furnace; 6—temperature controller; 7—measuring chamber; 8—radioactivity detector; 9—flow-rate meter; 10—counts-meters; 11—data processor and printer (plotter). Below the photo of the updated Netzsch DTA-ETA 404 (digitalized equipment commercially produced by Netzsch Gerätebau GmbH, Selb, Germany).



22.2. The ETA application in the diffusion structural diagnostics of materials

Equipment for the emanation thermal analysis (ETA) was developed in the 1960s at the *Nuclear Research Institute, Řež*. (Czech Republic) [1,2]. Since that time the ETA method was used in various investigations, e.g. the re-crystallization of solids, annealing of structure defects and changes in the defect state of both crystalline and amorphous solids, sintering, phase changes, the characterization of surface and morphology changes accompanying chemical reactions in solids and on their surfaces, including the thermal degradation, solid–gas, solid–liquid, and solid–solid interactions [7-11]. The ETA made it possible to reveal even fine changes in poorly crystalline or amorphous solids. Differences in the morphology and behavior of samples prepared by the sol–gel technique under different conditions were revealed by the ETA.

Changes in defects annealing and pore sintering of the samples were characterized by using the ETA results under in situ conditions of their heat treatments. The determination of optimized conditions for the preparation and thermal treatments of advanced ceramic materials was achieved [10,11]. By this way the ETA results contributed to the solution of practical tasks in the materials technology.

Recently, this method made it possible to characterize the thermal stability of ceramic materials designed for the immobilization/encapsulation of high level radioactive waste [12]. Moreover, the thermal stability of self- irradiated amorphous minerals that serve as natural analogues of the ceramic matrices was evaluated by using the emanation thermal analysis.

22.2.1. Thermal behavior of amorphous zircon mineral

Natural zircon mineral (general formula $ZrSiO_4$), containing an average concentration up to 0.4 % of uranium and 0.2 % of thorium, has attracted much interest from both fundamental and technological view points. The α -particles and heavy recoil nuclei released during the decay of radioactive impurities (typically ^{238}U , ^{235}U and ^{232}Th) interact with the surrounding crystalline matrix displacing atoms from their equilibrium positions [13]. Over geological periods of time this process disrupts the crystalline order to such a point that specimens covering all the stages from fully crystalline to amorphous can be found, depending on the uranium/thorium content.

Understanding the radiation effects in crystalline zircon and the determination of the structure of the aperiodic state are essential to ensure the reliability of zircon based ceramics for nuclear waste disposition [13,14]. During nuclear disintegration, the emission of the α -particle is accompanied by a recoil nucleus. Amorphization taking place in natural zircon is called metamictization. The α -particles have an energy of 4-6 MeV, and almost all the energy is dissipated by the ionization processes. It is believed that various isolated defects, such as Frenkel pairs, are formed along their paths. A number of studies have been devoted to structural changes of zircon under irradiation, in particular to understanding the amorphization and/or metamictization process [15]. This process can lead to an increased solubility and fracturing [16].

Ceramic forms used in the encapsulation of nuclear waste are subjected to a similar transformation, with the corresponding variation of their physical and chemical properties. An understanding of radiation effects in crystalline zircon and a determination of the structure of the aperiodic state are essential to ensure the reliability of zircon and related ceramics for nuclear waste disposition [13, 14].

Zircon ceramics can incorporate significant amount of UO_2 , PuO_2 or ThO_2 in a

solid solution with ZrO_2 . The zircon undergoes an amorphization promoted by α -decay events of radiogenic elements. During the nuclear disintegration, the emission of an α -particle is accompanied by a recoil nucleus and ballistic collisions of the recoil nucleus cause displacement cascades. A number of studies have been devoted to the evolution of amorphous zircon under irradiation, in particular to understanding of the metamictization process [15].

Natural zircon mineral sample characterized by ETA was from the locality in New Mexico, USA. The sample was X-ray amorphous [16].

Figure 2 below shows ETA results of the zircon mineral sample measured on heating (curve 1a) in air flow in the temperature range 20 – 1100 °C and subsequent cooling (curve 1b). The increase of the emanation rate, E , observed in the temperature range of 170 – 250 °C characterized the diffusion mobility of radon atoms along surface cracks and other subsurface defects, the subsequent decrease of the E values in the range 250 – 420 °C can be ascribed to healing the surface and subsurface defects.

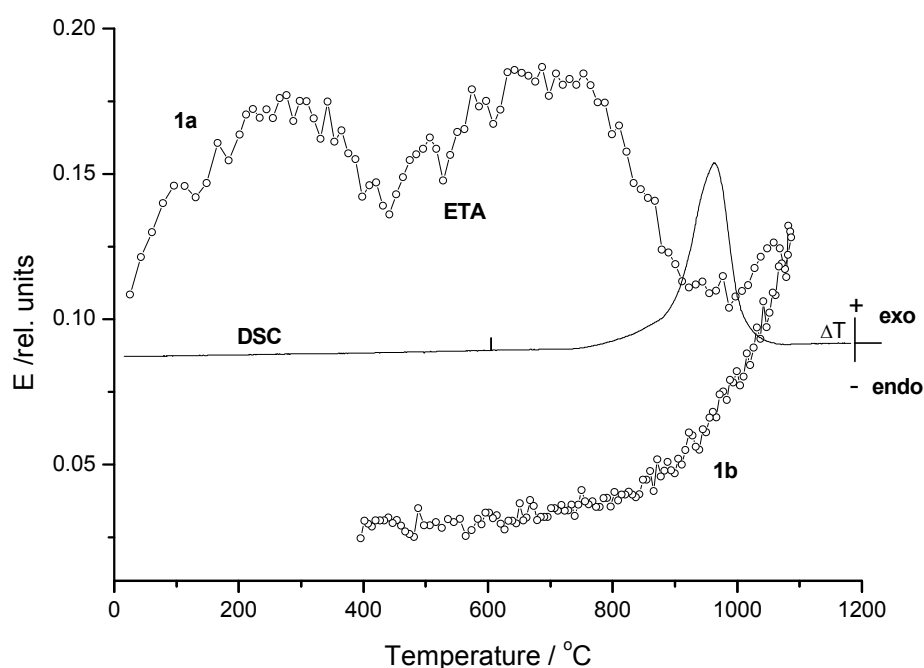


Fig. 2 ETA results (points) of natural self irradiated zircon mineral sample measured on heating (curve 1a) and subsequent cooling (curve 1b) in air in the range 20-1100 °C. DSC results measured on the sample heating are depicted as the full line curve

We supposed that the increase of the emanation rate, E , in the range 420 – 750 °C is due to the radon diffusion along structure irregularities in the amorphous zircon. The phase transformation of initially amorphous zircon was characterized by the decrease of the emanation rate values E in the range 750 – 950 C. From ETA results of the amorphous zircon mineral sample measured on heating to 1200 °C and subsequent cooling to room temperature it followed that the microstructure changes taking place in the sample on heating were irreversible.

The results of DSC measured on a parallel sample of amorphous/metamict zircon are demonstrated in Figure 2 as the full line curve. The transformation of amorphous zircon to the crystalline zircon was characterized by a DSC exothermal effect with the maximum at 918 °C.

22.2.2. Thermal behavior of amorphous brannerite mineral

Brannerite mineral (general formula $U_{1-x}Ti_{2+x}O_6$) has been found in nature as amorphous due to α -decay damage caused by high content of U, Th. The formula of natural brannerite can also be written $(U, Th)_{1-x}Ti_{2+x}O_6$. The natural brannerite generally contains impurity elements like Pb, Ca, Th, Y and rare earth elements (REE) on the U-site and Si, Al and Fe on the Ti-site. The brannerite is a minor phase in titanate-based ceramics designed for the geological immobilization of surplus Pu [17,18]. Therefore, it was of interest to investigate the thermal behaviour of brannerite mineral as a natural analogue of the brannerite ceramics to be used for immobilization of hazardous radioactive elements.

The diffusion structural diagnostics based on the results of emanation thermal analysis (ETA) made it possible to characterize the annealing of the structure irregularities in the brannerite mineral sample on heating to various temperatures up to 1200°C. Natural brannerite mineral was from the locality El Cabril mine near Cordoba, Spain. The sample was X-ray amorphous and contained Ca, Pb and other impurity elements [17].

Figure 3 shows the ETA results of the mineral brannerite sample measured during heating in argon in the range 20 – 1200 °C and subsequent cooling. The increase of emanation rate, E , observed on the sample heating in the range of 40 – 300 °C characterized the diffusion mobility of radon atoms along surface cracks and other subsurface defects to depth of 60 nm.

The slight decrease of $E(T)$ observed in the temperature range of 400 – 500 °C (curve 1a, Figure 3) was ascribed to healing surface cracks and voids. The decrease of the emanation rate $E(T)$ observed on the ETA curve in the range 800 – 880 °C, corresponding to the healing microstructure irregularities, was considered as a first step of the formation of crystalline brannerite. The increase of $E(T)$ observed in range 900 – 965 °C followed by the sharp decrease of $E(T)$ in the range 970 – 1020 °C indicated the formation of the crystalline brannerite phase, as confirmed by XRD spectroscopy [16]. From ETA results of the brannerite mineral sample measured on heating up to 1200 °C and subsequent cooling it followed that the microstructure changes on sample heating are irreversible.

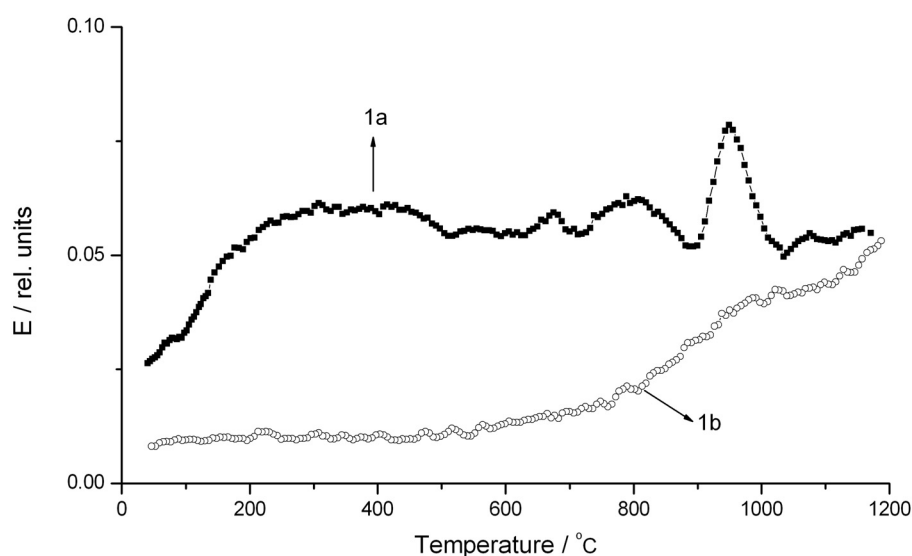


Fig. 3. ETA results of self-irradiated amorphous brannerite mineral sample measured on heating (curve 1a) and subsequent cooling (1b) in argon in the range 2–1200 °C.

The release of CO₂ was detected by mass spectrometry of evolved gases in the temperature range 700-800°C [16] due to the thermal degradation of minor carbonate containing components of the sample. The release of CO₂ gave rise to the sample porosity [16].

Microstructure differences of the self-irradiated brannerite mineral samples before and after heating to 1200°C are characterized by the SEM micrographs (Figure 4). The crystallization of initially amorphous brannerite was characterized by the ETA as changes of radon the diffusion rate in the range 900-1020 °C (Figure 3), in agreement with X-ray diffraction results [17-19].

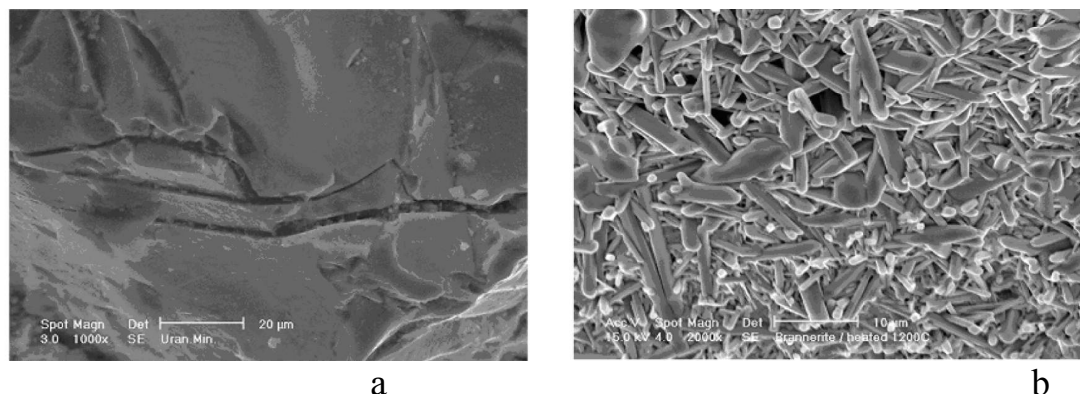


Fig. 4 SEM micrographs of amorphous brannerite mineral sample: (a) as received (b) heated to 1200 °C

It was of interest to investigate the self-irradiated brannerite mineral during “step by step” heating and subsequent cooling of the sample to the temperatures of 300, 550, 750, 880, 1020 and 1150 °C, respectively. Results of ETA measured by the “step by step” heating runs (Figure 5) made it possible to compare the annealing of microstructure irregularities of the sample in the selected temperature intervals .

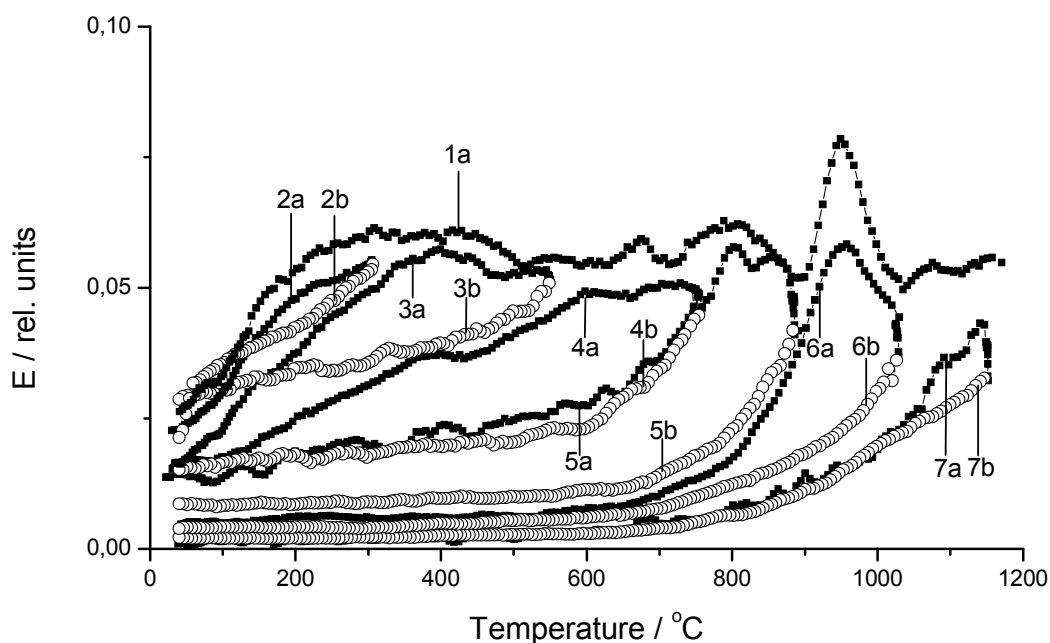


Fig. 5 ETA results of the self-irradiated amorphous brannerite mineral sample measured on heating and subsequent cooling in argon in the range 20-1150 °C: curve 1a corresponds to the “as received” sample measured during heating from 20 to 1150 °C, curves 2a/2b, 3a/3b, 4a/4b, 5a/5b, 6a/6b and 7a/7b were measured with a parallel samples pre-heated to the temperatures of 300, 550, 750, 880 and 1020 °C, respectively.

As it follows from the ETA results in Figure 5, the “step by step” heating of the sample to these temperatures caused a decrease of the amount of structure irregularities serving as radon diffusion paths.

A good reproducibility of the ETA results measured on heating from 20 to 300 °C is obvious from the comparison of the results in Figure 5, curve 2a and curve 1a. The ETA curves 3a/3b, 4a/4b and 5a/5b characterized the thermal behaviour of brannerite sample pre-heated to 300 and 750 °C, respectively. The increase of the emanation rate, E , in the temperature range of 20 – 360 °C, due to the diffusion of radon along micropores in the sample, was followed by the decrease of E , characterizing the partial healing of voids and structure irregularities that served as diffusion pathways for radon.

The ETA curves 6a/6b in Figure 5 characterized the thermal behaviour of the sample pre-heated to 880 °C. As already observed by curve 1a the amount of structure irregularities serving as radon diffusion paths further diminished in the sample pre-heated to 880 °C. The decrease of the emanation rate on sample observed on heating in the range of 970 – 1020 °C indicated the next step of the formation of crystalline brannerite. A good reproducibility of the ETA measurements can be seen from the temperature coincidence of the effects on the curve 1a and curve 6a in Figure 5.

From curves 7a/7b characterizing the thermal behaviour of the sample pre-heated to 1020 °C, it is obvious that after the pre-heating the sample to this temperature an irreversible crystallization of amorphous self-irradiated brannerite mineral took place.

From Figure 5 it is obvious the amount of structure irregularities serving as radon diffusion paths further diminished and the radon permeability in the pre-heated brannerite samples decreased with the temperature used for pre-heating of the samples.

Values of the emanation rate, E_{RT} , measured at room temperature before and after each heating run were used for the assessment of the relative changes of the surface area affected by the heat treatments used. The E_{RT} values summarized in Table 1 are in agreement with our considerations of the annealing of surface area and subsurface irregularities.

Table 1 Microstructure defects characteristics of self-irradiated amorphous brannerite mineral sample pre-heated to various temperatures

ETA curves measured on heating/cooling	Temperature of sample pre-heating	Defect amount characteristics ξ^*	E_{RT} [rel. units]	$\Delta\xi^{**}$ [%]
Curves 1a/1b, Fig.2	as received	38.1	0.026	100
Curves 2a/2b, Fig.4	as received	0.41	0.023	1.08
Curves 3a/3b, Fig.4	300 °C	3.82	0.017	10.02
Curves 4a/4b, Fig.4	550 °C	10.26	0.015	26.93
Curves 5a/5b, Fig.4	750 °C	13.62	0.014	35.75
Curves 6a/6b, Fig.4	880 °C	6.30	0.005	16.54
Curves 7a/7b, Fig.4	1020 °C	0.98	0.001	2.57

$$* \xi(T_{\max}) = \int_{T_{\min}}^{T_{\max}} E(T)_{\text{heating}} dT - \int_{T_{\min}}^{T_{\max}} E(T)_{\text{cooling}} dT \quad ** \Delta\xi = \frac{\xi_2}{\xi_1} \times 100 \quad [\%]$$

From the temperature dependences of the emanation rate, $E(T)$, measured during heating to selected temperatures and subsequent cooling, the decrease in the amount of radon diffusion paths was assessed. To this aim we used the parameter ξ defined in Eq. 6 as:

$$\xi(T_{\max}) = \int_{T_{\min}}^{T_{\max}} E(T)_{\text{heating}} dT - \int_{T_{\min}}^{T_{\max}} E(T)_{\text{cooling}} dT \quad (6)$$

Moreover, values of $\Delta\xi$ (see Eq. 7) were calculated with the aim to compare the amounts of the annealed microstructure defects during the “step by step” heating of the sample. The difference of integrals used for the assessment of the amount of the microstructure defects can be expressed as $\Delta\xi$ defined as

$$\Delta\xi = \frac{\xi_n}{\xi_1} \times 100[\%] \quad (7)$$

As it followed from values of ξ and $\Delta\xi$ summarized in Table 1, the most significant decrease of the structure irregularities serving as diffusion paths for radon diffusion was annealed prior to the crystallization of the sample in the range of 970 – 1020 °C.

Fig. 6 depicts a comparison of the relative amount of structure irregularities, expressed by parameter ξ , that were annealed during heat treatments to the selected temperatures.

It was shown that the emanation thermal analysis revealed differences in the amount of structure irregularities that served as radon diffusion paths in the amorphous brannerite samples. Additional information about thermal behaviour of self-irradiated amorphous minerals was obtained by using the diffusion structural diagnostics.

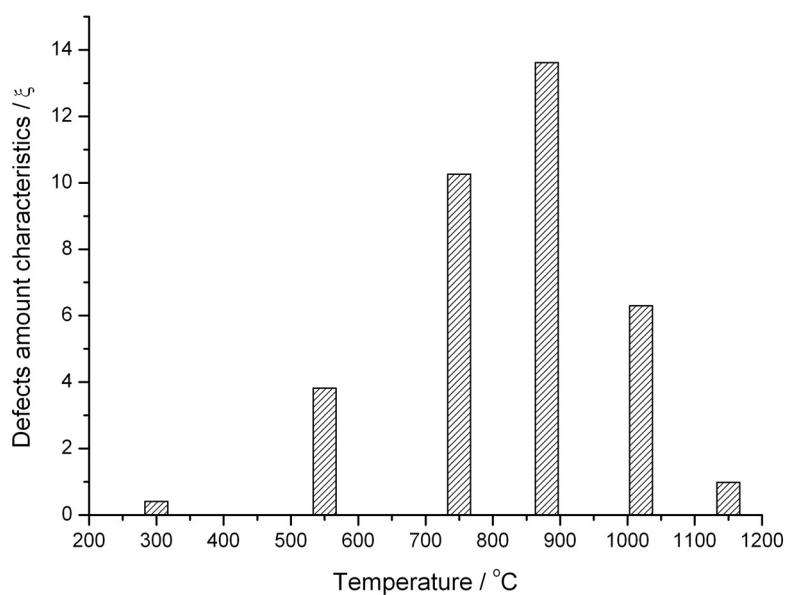


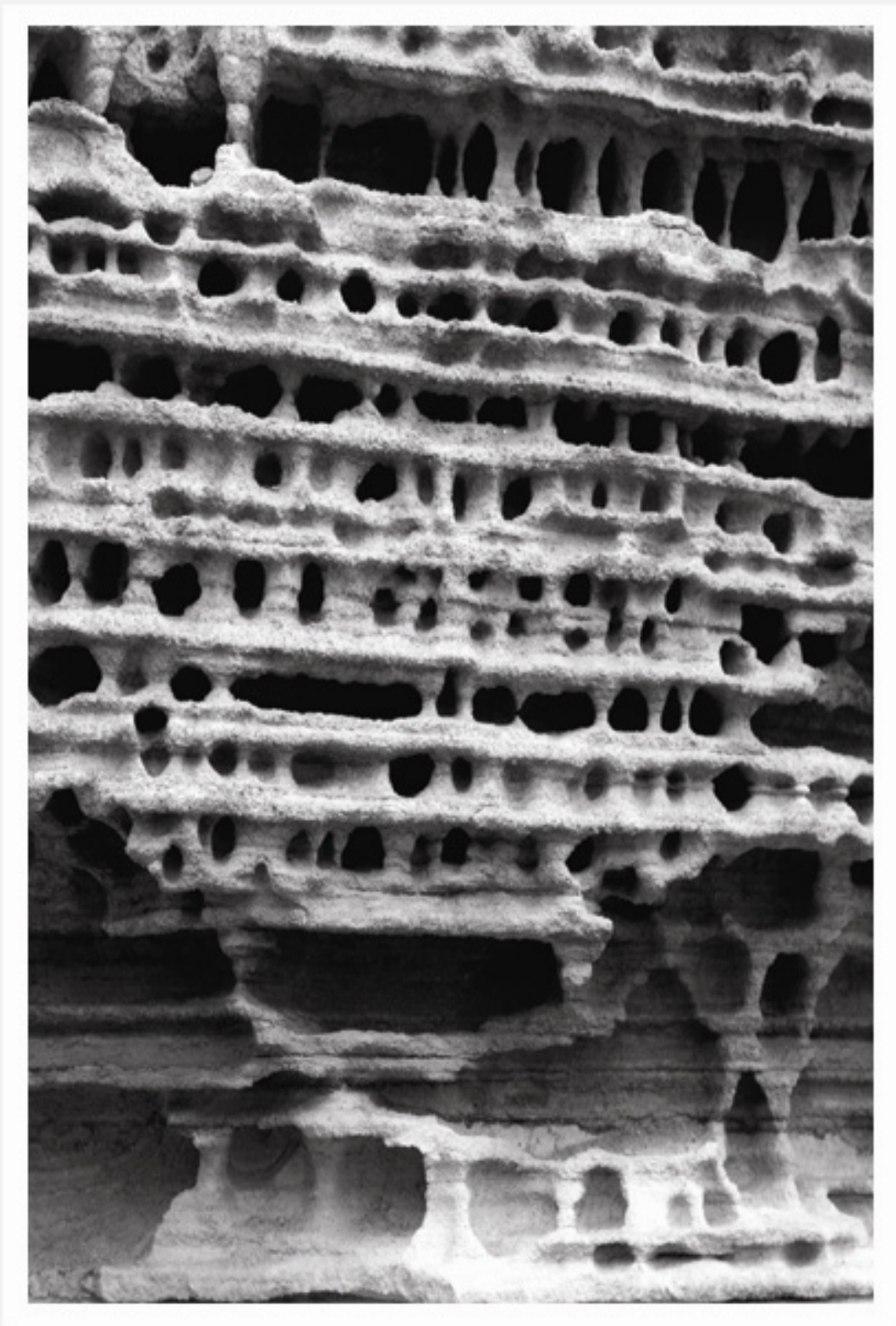
Fig. 6. Relative amounts of structure irregularities in the self-irradiated amorphous brannerite sample heated in the heating runs to temperatures 20 - 300, 20 - 550, 20 - 750, 20 - 880, 20 - 1020 and 20 - 1150 °C. Parameter ξ was used to characterize the amount of structure irregularities of the following samples: preheated to 300, 550, 750, 880 and 1020 °C respectively.

Acknowledgement: The preparation of this part was supported by the Ministry of Education, Youth and Sports of the Czech Republic (Projects No. MSM 2672244501 and No. KONTAKT ME-879)

References 22

1. V. Balek, *Emanation thermal analysis*. Thermochim. Acta , 22 (1978) 156.
2. V. Balek, *Emanation thermal analysis and its application potential*. Thermochim Acta, 192 (1991) 1.
3. V. Balek, J. Šubrt, T. Mitsuhashi, I.N. Beckman and K. Györyová, *Emanation thermal analysis: ready to fulfill the future needs of materials characterization*. J. Therm. Anal. Cal. 67 (2002) 15
4. J.F. Ziegler, J.P Biersack, and U. Littmark, *The Stopping and Range of Ions in Solids*, Pergamon Press, New York, 1985.
5. I.N. Beckman and V.Balek, *Theory of emanation thermal analysis XI. Radon diffusion as the probe of microstructure changes in solids*. J. Therm. Anal. Cal. 67 (2002) 49.
6. W.D. Emmerich, V.Balek , *Simultaneous application of DTA, TG, DTG, and emanation thermal analysis*. High.Temp.-High Press.5 (1973) 67
7. V. Balek, J. Tölgyessy: *Emanation thermal analysis and other radiometric emanation methods*, in Wilson and Wilson's Comprehensive Analytical Chemistry, Part XIIC, G. Svehla Ed.; Elsevier Science Publishers, Amsterdam, 1984, 304pp.
8. V. Balek, M.E. Brown, *Less common techniques*, in: Handbook on Thermal analysis and calorimetry, Vol.1 Chapter 9, Edited by M.E. Brown, ELSEVIER SCIENCE B.V., 1998 p.445.
9. V. Balek , *Characterization of high-tech materials by means of emanation thermal analysis*. J. Therm. Anal. 35(1989) 405
10. V. Balek , J. Šesták , *Use of emanation thermal analysis in characterization of superconducting $YBa_2Cu_3O_x$* . Thermochim. Acta ,133(1988) 23
11. V. Balek, J.L. Pérez-Rodríguez, L.A. Pérez-Maqueda, J. Šubrt, J. Poyato, *Thermal behaviour of ground vermiculite*. J.Therm. Anal. Cal., 88 (2007) 819.
12. V. Balek , Y. Zhang V. Zeleňák, J. Šubrt, I.N. Beckman, *Emanation thermal analysis study of brannerite ceramics for immobilization of hazardous waste*. J. Therm. Anal. Cal., 92 (2008) 155
13. S. Ríos, T. Boffa-Ballaran, *Microstructure of radiation-damage zircon under pressure*. J. Appl. Cryst., 36 (2003) 1006
14. R. Devanathan, L. R. Corrales, W.J. Weber, *Molecular dynamics simulation of disordered zircon*. The American Physical Society, Phys. Rev. B, 69 (2004) 064115-1
15. P. Carrez, Ch. Forterre, D. Braga, H. Leroux, *Phase separation in metamict zircon under electron irradiation*. Nucl. Inst. Meth. in Phys.Res., B 211 (2003) 549
16. L.M. Wang, R.C. Ewing, *Detailed in situ study of ion beam-induced amorphization of zircon*. Nucl. Inst. Methods in Phys. Res., B 65 (1992) 324

17. V. Balek, E.R.Vance, V. Zelenák, Z. Málek, J. Šubrt, *Use of emanation thermal analysis to characterize thermal reactivity of brannerite mineral*. J. Therm. Anal. Cal. ,88 (2007) 93
18. J. Lian, L.M. Wang, G. R. Lumpkin, R.C. Ewing, *Heavy ion irradiation effects of brannerite-type ceramics*. Nucl. Inst. Methods in Phys. Res. B 191(2002)565
19. Y. Zhang, G.R. Lumpkin, H. Li, M.G. Blackford, M. Colella, M.L. Carter, E.R. Vance, *Recrystallisation of amorphous natural brannerite through annealing: The effect of radiation damage on the chemical durability of brannerite*. J. Nucl. Mat., 350, (2006) 293.



Chapter 23

Basaltic glassy filaments

23. BASALT FILAMENTS – PROPERTIES AND APPLICATIONS

Jiří Militký, Vladimír Kovačič, Dana Křemenáková

23. 1. Introduction

Basalt materials are attractive for creation of composites with polymeric and inorganic matrices. The main advantages are low price of raw materials, cheap production of filaments and possibilities of creation of textile structures (weaves, knitted forms etc.).

Basalt products can be used from very low temperatures (about -200°C) up to the comparative high temperatures $700 - 800^{\circ}\text{C}$. At higher temperatures the structural changes occur. It is possible to use some dopes for increasing or enhancing of Basalt properties as well.

The main problems of basalt fibers preparation are due to gradual crystallization of some structural parts (plagioclase, magnetite, pyroxene) and due to non-homogeneity of melt. Utilization of the technology of continuous spinning overcomes the problems with unevenness and resulted filament yarns are applicable in the textile branch.

It is possible to use these yarns for production of planar or 3D textile structures for composites, special knitted fabrics and also as the sewing threads. Especially an application of basalt yarns as the sewing threads is very attractive. It is possible to use these threads for joining of filtering bags for hot media, filtering bags for very aggressive chemical environment, etc.

In this contribution selected properties of basalt filaments are presented. As starting material the laboratory prepared filaments are used. Mechanical properties are investigated at room temperature and after tempering to the 50, 100, 200, 300, 400, 500°C , in some experiments up to 800°C . The analysis of fibrous fragment evolved during abrasion of basalt weave is presented.

The degradation kinetics of Basalt filaments in hydrochloride acid HCl and sodium NaOH or calcium $\text{Ca}(\text{OH})_2$ hydroxides is investigated. The process of degradation is characterized qualitatively by scanning electron microscopy.

23. 2. Basalt fibres

Basalt is generic name for solidified lava which poured out the volcanoes [1, 2, 5]. This name is often applied to the solid rock, lava and magma, which, on the eruption become lava. Basaltic rocks are melted approximately in the range $1400 - 1600^{\circ}\text{C}$. Glass like nearly amorphous solid is result of quickly quenched melt. Slow cooling leads to more or less complete crystallization, to an assembly of minerals.

Two essential minerals plagiocene and pyroxene make up perhaps 80% of many types of basalt. Classification of basaltoid rocks based on the contents of main basic minerals is described in the book [5].

From the point of view of chemical composition the silicon oxide dominates, Al_2O_3 is next in abundance and CaO, MgO and FeO are closely similar. Other oxides are almost always below 5% level. The chemical composition of typical glasses and Basalt fiber forming rocks is presented in the Table I.

The color of basalt is from brown to the dully green in dependence on the ferrous oxides content. Basalts are more stable in strong alkalis than glass. Stability in strong acids is lower [2]. Basalt products can be used from very low temperatures (about -200°C) up to the comparative high temperatures $700 - 800^{\circ}\text{C}$ [3]. At higher temperatures the structural changes occur. According to the content of SiO_2 is basalt classified into three groups:

1. Alkaline basalt with the contents of SiO₂ below 42%;
2. slightly acidic basalt with the contents of SiO₂ from 43 to 46%;
3. acid basalt with the content of SiO₂ over 46%.

Table I. Chemical composition of glasses and Basalt fiber forming rocks [16]

	E-glass	S-glass	C-glass	Basalt Vestany	Basalt standard
SiO ₂	53 – 56	65	64 – 68	51,56	13,5 – 47
Al ₂ O ₃	12 – 16	25	3 – 5	18,24	11 – 18
CaO	16 – 25	0	11 – 15	5,15	10 – 15
MgO	0 – 5	10	2 – 4	1,3	8 – 11
B ₂ O ₃	5 – 10	0	4 – 6	0	0
Na ₂ O	0,8	0,3	7 – 10	6,36	2 – 3,5
K ₂ O	0,8	0,3	7 – 10	4,5	1 – 2
TiO ₂				1,23	2 – 3,5
Fe ₂ O ₃				1,02	4 – 7
FeO				2,14	5 – 8
MnO				0,28	0,2 – 0,3
H ₂ O				0,46	0
P ₂ O ₅				0,26	0

In order to produce fibers the acid basalt are used. Basalt rocks suitable for the preparation of fibers must meet the following requirements:

- (i) SiO₂ content around 46% and constant chemical composition;
- (ii) (ii) the ability to melt without solid residues;
- (iii) (iii) the optimal viscosity of the melted basalt;
- (iv) (iv) the ability of the cooling without significant crystallization.

The basic criterion for the selection of technology suitable for the manufacture of basalt fiber is the acidity coefficient M_k defined by $M_k = (SiO_2 + Al_2O_3) / (CaO + MgO)$, where M_k value must be within the range from 1.1 to 3.0. The ideal technological conditions for production of fibers are at $M_k = 1.65$ [8]. Complex criteria that take into account the impact of various oxides on the melt viscosity were published in the work [8]. Basaltic rocks suitability for the manufacture of fiber is connected not only with chemical and mineralogical composition, but also with the texture of rocks [9].

Raw material for the manufacture of basalt fiber is natural basalt, which crushes on the grit of 8 - 10 cm for traditional furnace and 0.6 - 0.8 cm for the microwave oven. Quality of basalt fiber affects the level of technological equipment and technology of whole production process. Basalt fibers can be made in the traditional oven in the form of short fibers (centrifugal method or blowing). Basalt multifilaments are produced either in the oven with electrical resistance heating, followed by small diameter die drawing or heating using microwave technology. The microwave oven plays an important role in keeping the heat from the center to the surface and the quality of lining furnaces. There is no way to escape the heat and speed up the process of melting. In the microwave oven, the rock melts continuously and is thus more homogeneous. After 5 minutes in the classic oven it is visible that grit obeys slow changes only, while in microwave oven after 5 minutes the grit is nearly molten (see Fig. 1).

The main advantages of a microwave oven are short time preheating and cheap material needed for the manufacture of the oven. Basalt fibers are produced by melt spinning in the range 1500-1700 °C. Fibers can be drawn at temperatures around 1300°C. The diameter

of standard fibers is° around 9-12 μm . From the cross-section of broken fibers (see Fig. 4b) it is evident brittle fracture caused by heterogeneity in structure.

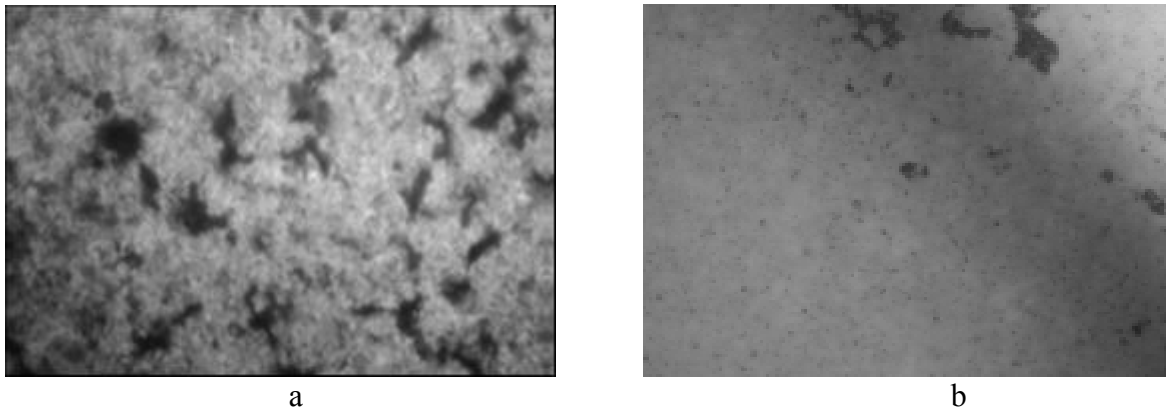


Fig. 1 Basalt melts after 5 min at 1300°C in a) classical oven, b) microwave oven [17]

The typical basic physical and chemical properties of basalt and glass fibers are presented in Table II. According to our previous finding it was proved that the stability of basalt in alkalis is generally very good. The stability in acids is comparatively small. Prolonged acids action leads to the full disintegration of fibers.

Table II. Chemical and physical properties of glass and Basalt fibers [18]

PROPERTIES	BASALT	GLASS
DENSITY (AT 20°C) [kg/m ³]	2800	2600
MOISTURE REGAIN [%]	0,5	1
MELTING TEMPERATURE [°C]	1450	1550
SOFTENNING TEMPERATURE [°C]	960	840
WORKING TEMPERATURE [°C]	-200 till +800	-60 till +460
THERMAL CONDUCTIVITY [W.m ⁻¹ .K ⁻¹]	0,027 till 0,035	0,034 till 0,04
ELECTRICAL SURFACE RESISTANCE [Ω .m]	2.3 10 ¹⁰	~10 ¹¹
SURFACE ENERGY γ_c [mN/m]	34,94 – 48,40	-
SOUND ABSORPTION COEFFICIENT [-]	0,9 – 0,99	0,8 – 0,92
INITIAL MODULUS - TENSILE [GPa]	89	77
TENSILE STRENGTH [MPa]	1 850 - 4250	1 850 - 3450
COMPRESSIVE STRENGTH [MPa]	300	250
BREAK ELONGATION [%]	3,15	4,70
CHANGE OF TENSILE STRENGTH [%]		
IN COLD WATER AFTER 3 hours	99,8	99,3
IN COLD WATER AFTER 64 days	91	72
IN 2N HCL AFTER 3 hours	81,8	53,9

23. 3. Materials

Basalt rocks from KAMENNIY VEK – Russia and from Czech source (Vrestany) were used as a raw materials in this work. The marbles and filament roving were prepared under laboratory conditions. From marbles the thick rods were prepared by grinding. The

roving contained 952 single filaments are used. Mean fineness of roving was 320 tex. The basic physical properties of basalt fibers are presented in Tab. III.

Table III. Basic physical properties of glass and basalt fibers

Property	E-glass	basalt
Diameter [μm]	9 - 13	12.96
Density [kgm^{-3}]	2540	2733
Softening temperature [$^{\circ}\text{C}$]	840	960

23. 4. Statistical Analysis of Fibres Strength

The fracture of fibers can be generally described by the micro mechanical models or on the base of pure probabilistic ideas [8]. The probabilistic approach is based on these assumptions:

- (i) fiber breaks at specific place with critical defect (catastrophic flaw),
- (ii) defects are distributed randomly along the length of fiber (model of Poisson marked process),
- (iii) fracture probabilities at individual places are mutually independent.

The cumulative probability of **fracture** $F(V, \sigma)$ depends on the tensile stress level σ and fiber volume V . The simple derivation of the stress at break distribution described for example by Kittl and Diaz [9] leads to the general form

$$F(V, \sigma) = 1 - \exp(-R(\sigma)) \quad (1)$$

The $R(\sigma)$ is known as the specific risk function. For Weibull distribution has function $R(\sigma)$ the form [14]

$$R(\sigma) = [(\sigma - A) / B]^C \quad (2)$$

Here A is lower strength limit, B is scale parameter and C is shape parameter. For brittle materials is often assumed $A=0$.

Weibull models are physically no correct due to unsatisfactory upper limit of strength.

Kies proposed more realistic risk function in the form

$$R(\sigma) = \left(\frac{\sigma - A}{A1 - \sigma} \right)^C \quad (3)$$

Here $A1$ is upper strength limit. For brittle materials can be also assumed $A=0$. Further generalization of $R(\sigma)$ have been published by Phani

$$R(\sigma) = \frac{\left(\frac{\sigma - A}{B1} \right)^D}{\left(\frac{A1 - \sigma}{B} \right)^C} \quad (4).$$

It can be proved that the B and $B1$ cannot be independently estimated. Therefore the constraint $B1=1$ is used in sequel. Simplified version of eqn. (4) has $A=0$. For well known Gumbell distribution is $R(\sigma)$ described as

$$R(\sigma) = e^{-\frac{\sigma-A}{B}} \quad (5)$$

Main aim of the statistical analysis is specification of $R(\sigma)$ and parameter estimation based on the experimental strengths $\sigma_i, i=1,2,\dots,N$. Based on the preliminary computation it has been determined that for basalt fibers strength the Weibull distribution is suitable.

The individual basalt fibers removed from roving were tested. The fibers were mounted into paper frame before testing (see. Fig. 2).

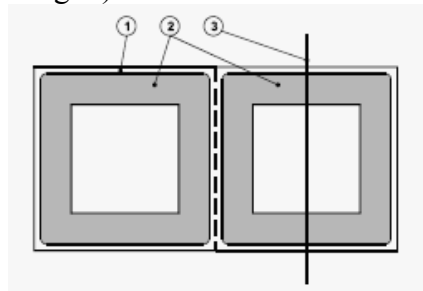


Fig. 2 Mounting frame for individual fiber testing

The loads at break were measured under standard conditions at sample length 10 mm. Load data were transformed to the stresses at break σ_i [GPa]. The sample of 65 stresses at break values was used for evaluation of the $R(\sigma)$ functions and estimate of their parameters.

Rearrangement of eqn. (3) leads to the form

$$y(\sigma) = \ln[R(\sigma)] \quad (6)$$

where $y(\sigma) = \ln[-\ln(1 - F(\sigma))]$. $F(\sigma)$ is distribution function.

For further simplification the so called strength rank statistics $\sigma_{(i)}$ can be used. Denote that $\sigma_{(i)} \leq \sigma_{(i+1)}, i=1,2,\dots,N-1$ [10]. Values $\sigma_{(i)}$ are rough estimates of strength quantile function for probabilities

$$p_i = F(\sigma_{(i)}) = \frac{i - 0.5}{N + 0.25} \quad (7)$$

The parameter estimates of $R(\sigma)$ models can be then obtained by nonlinear least squares i.e. by minimizing of criterion

$$S = \sum_{i=1}^N \left[y(\sigma_{(i)}) - \ln R(\sigma_{(i)}) \right]^2 \quad (8)$$

Due to the roughness of $\sigma_{(i)}$ and their no constant variances the special weights can be defined [7]. Transformation of parameter estimation problems in $R(\sigma)$ models to the regression problem enables to use the statistical criteria for selection of the optimal model form. Suitable is Akaike information criterion AIC defined as [11]

$$AIC = N \cdot \ln \left(\frac{S^*}{N} \right) + 2M \quad (9)$$

Here M is number of estimated parameters and S^* is minimal value of S (see eqn. (8)). Another possibility is estimation of strength probability density function $f(\sigma)=F'(\sigma)$ parameters by the maximum likelihood method.

Simple graphical method for checking of Weibull distribution suitability is based on the so called Q-Q plot as comparison of experimental strength quantiles $\sigma_{(i)}$ and Weibull model quantiles. After rearrangements the linear dependence, $y = a x + b$, in Q-Q plot occurs.

For two parameter Weibull distribution it is:+

$$y = \ln[-\ln(1-p_i)] , \quad x = \ln(\sigma_{(i)}) , \quad a = C \text{ and } b = -\ln(B)*C .$$

This Q-Q graph is shown in the Fig 3a. From parameters of regression line is shape parameter $B = 3.796$ and scale parameter $C = 3.6$.

For three parameter Weibull distribution it is:

$$y = \ln[-\ln(1-p_i)] , \quad x = \ln(\sigma_{p(i)} - A) , \quad a = C \text{ and } b = -\ln(B)*C .$$

In this case it is necessary to know estimator of lower strength limit A . One simple possibility is to use the moment estimator $A=0.3391$ obtained from eqn. (11). This Q-Q graph is shown in the Fig 3b. From parameters of regression line is shape parameter $B=3.435$ and scale parameter $C=3.12$.

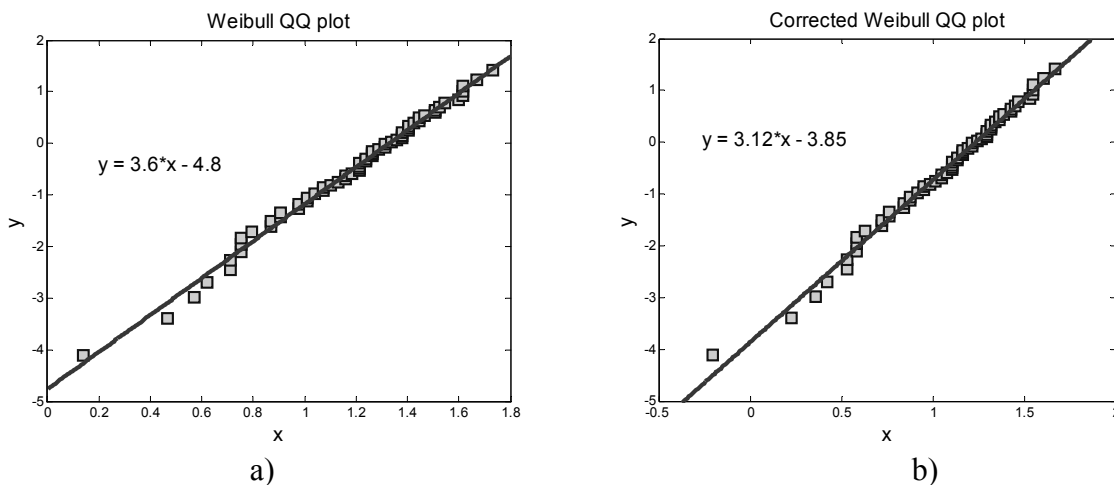


Fig. 3 : Weibull Q-Q plot for: a) two parameter case, b) three parameter case.

For quick and rough parameter estimates of three parameter Weibull models the moment based method can be used. The main idea of this method is very simple. Based on the m sample moments and corresponding theoretical moments for selected strength distribution the m nonlinear equations can be created. Their complexity is based on the suitable selection of moments [10].

Cran [15] used this technique for estimation of the parameters in three parameter Weibull distribution. Shape parameter C can be estimated from relation

$$C = \frac{\ln(2)}{\ln(m_1 - m_2) - \ln(m_2 - m_4)} \quad (10).$$

For estimation of the lower limiting strength A is valid

$$A = \frac{m_1 m_4 - m_2^2}{m_1 + m_4 - 2m_2} \quad (11)$$

and estimate of scale parameter B is in the form

$$B = \frac{m_1 - A}{\Gamma\left(1 + \frac{1}{C}\right)} \quad (12)$$

where $\Gamma(x)$ is Gamma function. In these relations m_r are special, so-called Weibull sample moments defined as

$$m_r = \sum_{i=0}^{N-1} \left(1 - \frac{i}{N}\right)^r [x_{(i+1)} - x_{(i)}] \quad (13)$$

For $i=0$ is formally $x_{(0)}=0$. This very simple technique can be used for the rough estimation of strength distribution parameters. It is suitable for prediction of importance of parameter A in Weibull models [15]. For two parameter Weibull model is $A=0$ and C is estimated from relation

$$C = \frac{\ln(2)}{\ln(m_1) - \ln(m_2)} \quad (14)$$

The assumption $A=0$ is valid if the B and C estimates for two and three parameter Weibull model are reasonable close.

For the experimental data are moment estimators $A=0.3391$, $B=3.4121$ and $C=3.3297$. The closeness between parameters obtained from Q-Q plot and by using of moments is acceptable. Advantage of Q-Q plot is inspection of all points and possibility to identify outliers. The differences between three and two parameters Weibull distribution are for these data negligible.

The SEM of longitudinal portion of broken fiber (magnification 10 000) demonstrate that surface is very smooth without flaws or crazes (see Fig.4a). Based on these findings we can postulate that fracture occurs due to non homogeneities in fiber volume (probably near the small crystallites of minerals, see Fig.4b).

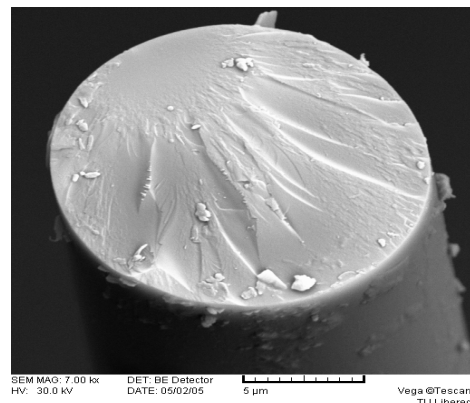
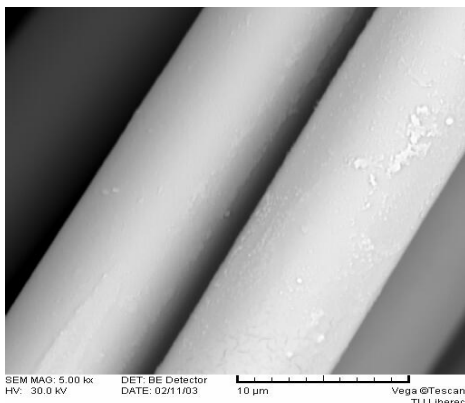


Fig. 4 a.: The longitudinal view of tested basalt fiber. **Fig. 4 b.:** the view of broken basalt fiber – the typical cross-section of brittle failure

23. 5. Basalt fibres properties after the thermal exposition

Behavior of basalt fibers after long - term thermal exposition was simulated by tempering of fibers at the selected temperatures to the chosen time of exposition. Four sets of experiments were applied

In the first set of experiments, the thermal exposition influence on the ultimate mechanical properties and dynamic acoustical modulus of basalt filament roving for the tempering temperature 50, 100, 200, 300, 400, 500°C was evaluated. The time of exposition was 60 min. After the tempering the following properties were measured:

- Tensile strength [N.tex^{-1}].
- Deformation to break [%].
- Dynamic acoustic modulus [Pa] (dynamic acoustic modulus was determined from sound wave spread velocity in the material).

The changes of properties of basalt fibers after tempering were investigated by the analysis of variance. It was determined, that tempering on 300°C and higher led to statistically significant drop of strength and dynamic acoustical modulus. Probably, the changes of these properties are based on the changes of crystalline structure of fibers.

In the second set of experiments the strength distribution of basalt filament roving was measured on the samples tempered in oven at temperatures $T_T = 20, 50, 100, 200, 300, 400$ and 500°C in time intervals $t_T = 15$ and 60 min. For roving strength measurements the TIRATEST 2300 machine was used. The 50 samples of strengths P_i were collected. These values were recalculated to stress at break values σ_i [GPa].

The strength distribution of tempered multifilament roving was nearly Gaussian with parameters: mean σ_p and variance s^2 . These parameters are estimated by the sample arithmetic mean and sample variance.

The dependence of the roving strength on the temperature exhibits two nearly linear regions. One at low temperature to the 180°C with nearly constant strength and one up to the 340°C with very fast strength drop.

For description of this dependence the linear spline model was used [11]. The strengths σ_1 for temperature $T_1=180^\circ\text{C}$ and σ_2 for temperature $T_2=340^\circ\text{C}$ were computed by the linear least squares. These values and the rate of strength drop $Ds = (\sigma_1 - \sigma_2)/160$ [GPa deg⁻¹] are given in the Table IV.

Table IV. Parameters of roving strength dependence on temperature

t_T [min]	σ_1 [GPa]	σ_2 [GPa]	Ds [GPa deg ⁻¹]
15	1.1070	0.343	0.0048
60	1.1750	0.158	0.0064

It is clear that increasing of the time of tempering leads to the acceleration of structural changes and drops of strength fastening (increasing Ds).

In the third set of experiments the influence of thermal exposition on the shear modulus was investigated. The individual basalt filaments removed from roving were tested. The apparatus based on the torsion pendulum principle was used. In this apparatus a fiber of length l_o hanged with pendulum (moment of inertia M) is subjected to a small shear strain imposed by a small initial twist. The period P and amplitude A of successive oscillations were measured. The shear modulus of circular fiber having radius r is

$$G = \frac{2.I_0.M.\omega^2}{\pi.r^4} \quad (15)$$

where frequency of oscillations is in the form

$$\omega = \frac{2.\pi}{P} \quad (16)$$

As a pendulum the cylindrical disc of radius R and mass m was used. Corresponding moment of inertia is

$$M = \frac{1}{2}m.R^2 \quad (17)$$

The computed shear modulus for tempering temperatures T_T and time of expositions t_T are shown in the Table V.

Table V. Shear modulus of basalt fibers.

T_T [°C]	t_T [min]	G [GPa]
-	-	21.76
100	15	19.43
100	60	11.34
250	15	18.04
250	60	12.76

The shear modulus is comparatively high. The prolongation of tempering leads to high drop of G .

In the fourth set of experiments, the thermal exposition influence on the fiber fragility was investigated. Fragility F_r was defined as ratio of critical loop diameter D_c and fiber diameter d

$$F_r = \frac{D_c}{d}$$

Critical loop diameter was estimated by deformation of basalt loop under microscope to failure (see. Fig. 5a). Samples were tempered in oven at temperatures $T_T = 50, 150, 250$ and 350 °C in time interval $t_T = 60$ min.

Results are shown in the Fig. 5b. In accordance with assumption of flexibility loss due to chemical changes (partial oxidation of FeO) are fragilities increasing function of tempering temperature [19].

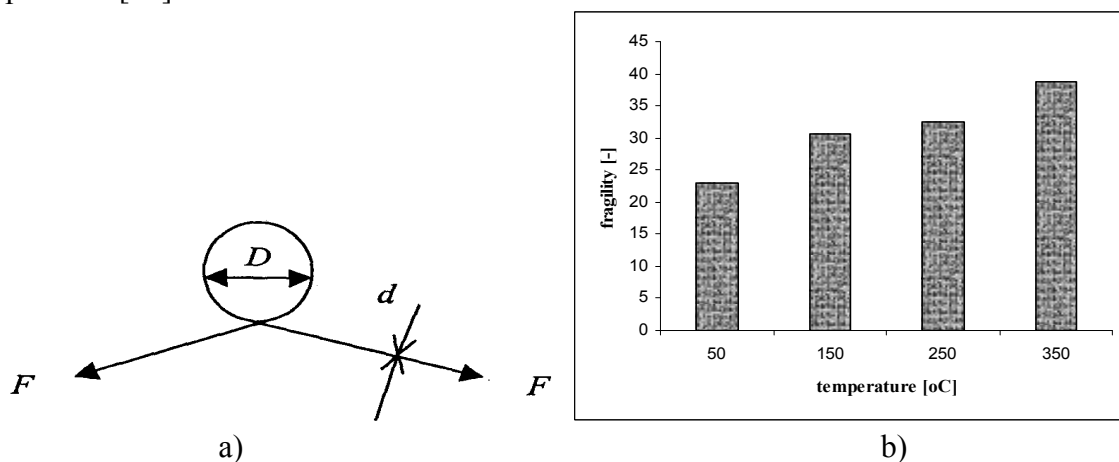


Fig. 5 a) Evaluation of critical loop diameter, b) Fragility of tempered Basalt fibers

23. 6. Thermomechanical analysis

In thermo-mechanical analysis (TMA) the dimensional changes (expansion or contraction) are measured under defined load and chosen time. The TMA requires a high-resolution measurement of the linear displacement and excellent stability of measured conditions. Most TMA instruments on the market are not able to be sensitive to very small displacement. This was the main reason for construction of special device TMA CX 03RA/T at University of Pardubice. This device was developed to provide highly sensitive tool for reproducible measurement of subtle dimensional changes even at extremely long thermal expositions. The sample is placed on the movable sample holder connected with displacement sensor which measures dimensional changes of the sample. Detail description of this TMA instrument is in [3].

The instrument is fully computer controlled with programmable time - temperature profiles and loading in static or dynamic mode. The special adapters for application of this instrument for bending and tension deformations are now under preparation. Described apparatus were used for all kinds of measurements. The basalt rods (abbreviation R) and linear composite from roving glued by epoxy resin CHS 1200 (abbreviation C) were used.

23.6.1. Thermal expansion

The dilatation curves, i.e., dependence of height of basalt rod on the temperature were measured at rate of heating 10 deg min^{-1} and compressive load 10 mN. These curves consist of two nearly linear portions connected at glass transition temperature T_g [3].

The coefficients of linear thermal expansions a for region below and above T_g were computed from models

$$L = L_g + a_1 \cdot (T - T_g) \quad \text{for } T < T_g \quad (18)$$

$$L = L_g + a_2 \cdot (T - T_g) \quad \text{for } T > T_g \quad (19)$$

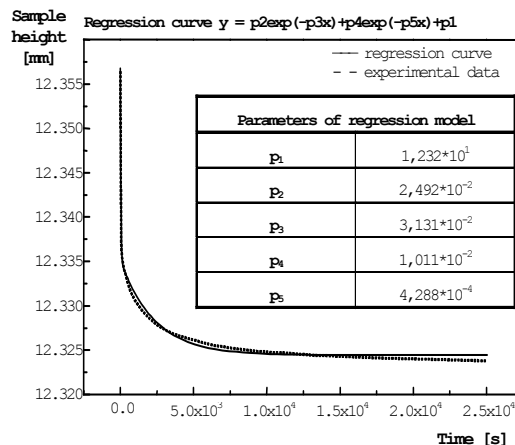
By the nonlinear least squares the: $T_g = 596.3 \text{ }^\circ\text{C}$, $a_1 = 4.9 \cdot 10^{-6} \text{ deg}^{-1}$, $a_2 = 19.1 \cdot 10^{-6} \text{ deg}^{-1}$ were computed.

23.6.2. Isothermal compressive creep

The responses of basalt on the compressive loads under isothermal conditions were investigated from creep type experiments. The load was 200 mN. For the basalt rods and linear composites the dependence of sample height L on the time t were measured. The experimental data have been described by the simple exponential type model [12]

$$L = L_p + L_1 e^{-k_1 \cdot t} + L_2 e^{-k_2 \cdot t} \quad (20)$$

Parameters L_p , L_1 , L_2 , k_1 and k_2 were estimated by nonlinear least squares. Typical result is shown in the following **Fig. 6** Regression curve and experimental data for creep at $250 \text{ }^\circ\text{C}$



The maximum dilatation

$$D = L_1 + L_2 \quad (21)$$

and half time of dilatation $t_{1/2}$ were computed. Denote that $t_{1/2}$ is time for which is the dilatation equal to $L_p + (L_1 + L_2)/2$. These parameters are given in the Table IV.

Table VI. Parameters of compressive creep

Linear composite (C)			Basalt rod (R)	
T_T [°C]	D [mm]	$t_{1/2}$ [s]	D [mm]	$t_{1/2}$ [s]
30	0.0030	145.1	0.0145	16015
50	0.0289	36.90	-	-
100	0.0532	29.80	0.0083	21.30
250	0.0350	41.10	-	-
300	-	-	0.0426	51.7

23.6.3. Longitudinal compressive modulus

From compressive creep data the longitudinal compressive modulus was predicted by the following way. Let one has the linear composite (index C) consisted from the phase of basalt fibres (index K) and epoxy resin matrix (index E) as is show in the Fig. 7. Let the both phases are deformed elastically that their Poisson ratio is the same and that the stresses cause no debonding of the interfaces. The volumetric ratio of basalt fibres (composite has the same length as individual phases) is Φ_K .

Fig. 7 a) Linear composite, b) Two phase model



From the simple rule of mixture (derivation is in [4]) it follows

$$E_C = \Phi_K E_K + (1 - \Phi_K) E_E \quad (22)$$

Here E_c is longitudinal creep modulus of linear composite E_E is longitudinal creep modulus of epoxy resin and E_K is longitudinal creep modulus of basalt fibers. For known Φ_K and E_C , E_E the longitudinal compressive modulus of basalt fibers is equal to

$$E_K = \frac{E_C - (1 - \Phi_K) E_E}{\Phi_K} \quad (23)$$

For our case the Φ_K was estimated by the image analysis and value $\Phi_K = 0.9$ was obtained. The modulus E_C at individual temperatures was computed as the ratio

$$E_C = \frac{F}{A_C \varepsilon_{C(30)}} \quad (24)$$

where $F=200$ mN is applied load, $A_C= 20.725$ mm² is cross sectional area of tested composite sample and $\varepsilon_{C(30)}$ is deformation under compressive creep in time $t = 30$ s. Values $\varepsilon_{C(30)}$ were computed from dimensional changes after 30 sec. of compressive creep for linear composite at individual temperatures. By the same way the modulus E_E was estimated from the compressive creep curve of pure epoxy resin. In this case $F=200$ mN, $A_E=20.725$ mm² and $\varepsilon_{E(30)}$ were computed from dimensional changes after 30sec. of compressive creep for epoxy resin at individual temperatures.

Computed values of E_E , E_C and E_K are summarized in the Table VII.

Table VII. Longitudinal compressive modulus of linear composite, epoxy resin and basalt fibers

T [°C]	E_K (Basalt) [GPa]	E_C (Composite) [GPa]	E_E (Resin) [GPa]
25	112.27	105.41	40.5129
50	95.256	87.49	17.5076
100	114.084	108.575	58.9869
200	99.76	90.95	11.6239

It is evident that in the investigated temperature range is modulus of Basalt fibers no systematically dependent on temperature.

23.6.4. Non-isothermal compressive creep

The responses of basalt on the compressive loads under no isothermal conditions were investigated from creep type experiments similar as for isothermal conditions. The load was 200 mN. For the basalt rod the dependence of sample height L on the temperature T increased linearly with time t were measured. Starting temperature was $T_0 = 30$ °C and rate of heating was 10 °C/min. For avoiding the initial sample height L_0 the dilatation $d_i = L_0 - L$ has been recorded. The experimental points and Reinsch smoothing spline curve (parameter $s = 1$) are shown in the Fig. 8a.

From isothermal experiments is deduced that the rate of creep only is markedly temperature dependent. The rate of height changes can be therefore expressed by differential equation

$$\frac{dL}{dt} = f(K, L, L_\infty, t) \quad (25)$$

where K is the rate constant and L_∞ is sample height in equilibrium. Function $f(.)$ is creep rate model. By analogy with classical reaction kinetics the creep rate can be expressed in the form

$$\frac{dL}{dt} = -K (L - L_\infty)^n \quad (26)$$

where n is constant (order of reaction). For $n = 1$ the simple exponential model of creep (rate process of first order) results. For description the temperature dependence of the creep rate constant K the Arrhenius type model

$$K = K_0 \exp\left(-\frac{E}{RT}\right) \quad (27)$$

is usually applied. In eqn. (27) is K_0 pre-exponential term (corresponding to the activation entropy of creep), E [kJ mol⁻¹] is the activation energy of creep and R is the gas constant. In non-isothermal conditions it is assumed that temperature dependent is rate constant only

$$\frac{dL_t}{dt} = K(T)f(L_t, L_\infty) \quad (28)$$

By the formal integration of the eqn. (28) for exponential type model ($n = 1$ in eqn. (26) the following relation results

$$L = L_\infty + (L_o - L_\infty) * \exp(-F(t)) \quad (29)$$

Here L_∞ is initial sample height. For the case of linear heating during creep is valid

$$F(t) = G(t) - G(T_o) \quad (30)$$

Symbol T_o denotes initial temperature and $G(x)$ is the integral

$$G(x) = \frac{K_o}{\Theta} \int_0^x \exp(-E/(Rx)) dx \quad (31)$$

where Θ is rate of heating. The integration of eqn. (31) cannot be realized analytically and therefore the various approximate equations can be used. Simple and precise approximation of temperature term has the form [20]

$$\int \exp\left(-\frac{E}{RT}\right) dT \approx \frac{RT^2}{E} \left[\frac{1 - 2\left(\frac{RT}{E}\right)}{1 - 5\left(\frac{RT}{E}\right)} \right] \exp\left(-\frac{E}{RT}\right) \quad (32)$$

The relative error of eqn (32) is for $E/RT > 7$ under 1%. The model expressed in the form (29) can be now used in analytical form. Three parameters K_o , E and L_∞ should be estimated from experimental data. The nonlinear regression has to be used [11].

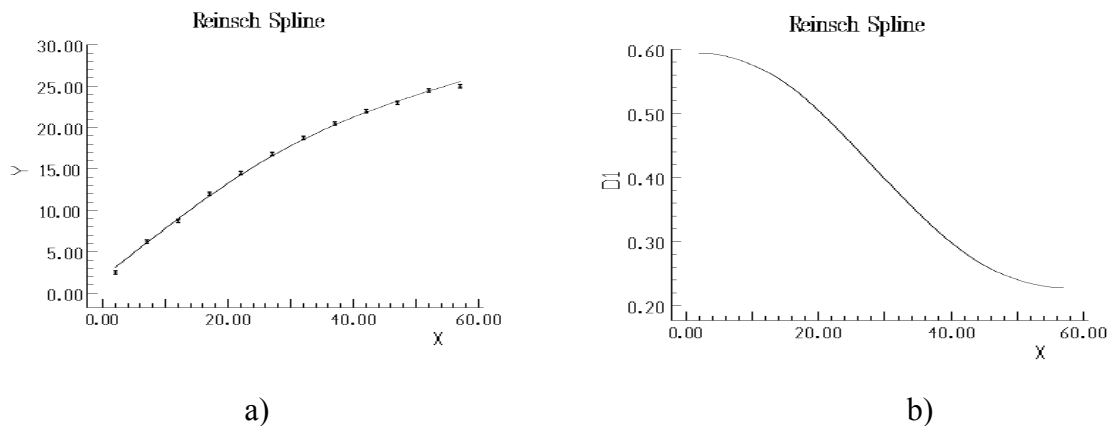


Fig. 8 a) No isothermal creep curve (expressed as dilatation y [ppm] time x [min] dependence), b) Creep rate curve as derivative

Simpler alternative is to use rate equation for first order model combined with Arrhenius dependence in the linearized form

$$\ln\left(\frac{dL}{dt}\right) - \ln(L_\infty - L) = \ln(K_o) - \frac{E}{R(T_o + \Theta * t)} \quad (33)$$

Application of eqn. (33) requires knowledge of L_∞ and computation of creep rate $\frac{dL}{dt}$ from experimental data. For this purpose the cubic spline smoothing procedure can simply applied [21]. The resulted rate of creep curve for Reinsch smoothing procedure ($s=1$) is shown on the Fig 8b. The L_∞ can be approximately selected from the last few points by linear least squares assuming exponential behavior of dilatation curve at steady state .For this case $L_\infty = 25.5$ [ppm] in term of dilatation has been evaluated.

The dependence of $\ln\left(\frac{dL}{dt}\right) - \ln(L_\infty - L)$ on $1/T$ (in absolute temperature scale) is shown in the Fig. 9.

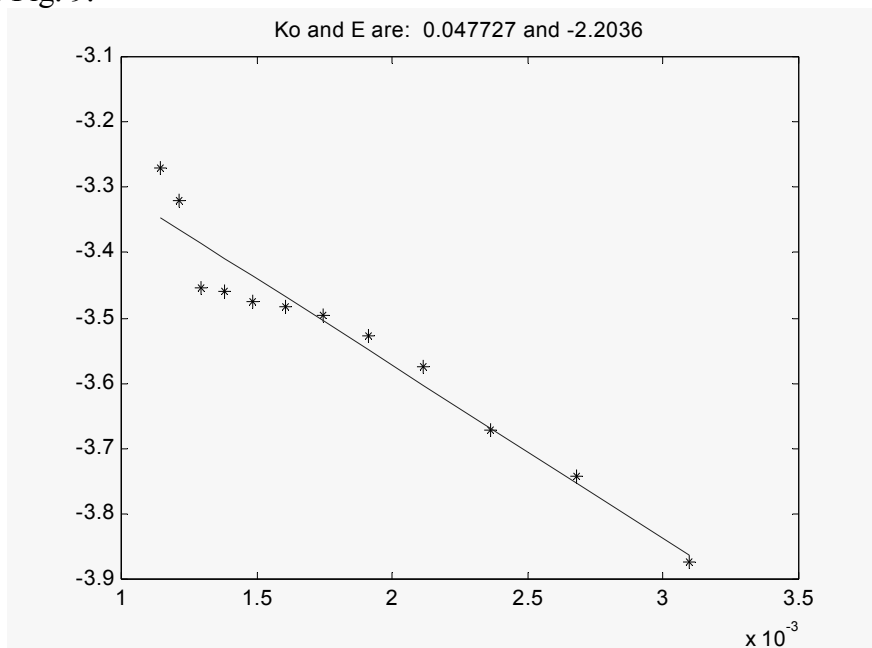


Fig. 9 Estimation of compressive creep activation parameters

The solid line represents linear least squares fit. From parameters of this fit the pre exponential factor $K_o = 0.04772$ and activation energy of creep $E = 2.203$ kJ/mol were computed. The fit in Fig. 12 is sufficient for parameter estimation. More precisely it will be necessary to use general order of rate process and investigate n as well (see eqn. (26)). Thermally stimulated creep is successfully used in the area of polymers. [22]., The compressive creep of non-polymeric solids is due to rearrangements of molecular clusters and structural reordering The rate models is then quite sufficient.

23. 7. Degradation in liquids

The degradation were realized at room temperature in 10 % solution of HCl, NaOH and $\text{Ca}(\text{OH})_2$. Samples were firstly treated one day in acetone for removing of sizing agent. After selected times were samples removed rinsed three times in hot water, dried and weighted. The rest weight after degradation was computed from relation

$$R_Z = \frac{M_K}{M_P} \cdot 100 \text{ [%]} \quad (34)$$

where M_K [g] is weight after degradation and M_P [g] is sample weight after acetone cleaning. For comparison of degradation in various times is better to use relative rate of degradation defined by relation

$$K_P = \frac{M_P - M_K}{t_p \cdot M_P} = \frac{100 - R_Z}{t_p} \text{ [%}\cdot\text{hour}^{-1}] \quad (35)$$

where t_p is degradation time [hours]. Higher relative degradation rate corresponds to more severe action of degradation agents. The values R_Z and K_P for HCl are in the table VIII and for alkalis in the table IX.

Table VIII. Rest weights and relative degradation rates for acid

t [hour]	R_Z [%] 10% HCl	K_P [%·hour⁻¹] 10% HCl
0	100,000	0,000
2	94,713	2,640
5	90,436	1,913
10	80,936	1,906
15	67,080	2,195
24	66,982	1,376

Table IX. Rest weights and relative degradation rates for alkalis

t [hour]	R_Z [%] 10% NaOH	K_P [%·hour⁻¹] 10% NaOH	R_Z [%] 10% Ca(OH)₂	K_P [%·hour⁻¹] 10% Ca(OH)₂
0	100,000	0,000	100,000	0,000
2	96,889	1,556	100,000	0,000
5	95,845	0,831	99,888	0,022
24	94,968	0,2097	99,278	0,030

23.7.1. Degradation kinetics

During the degradation process the chemical solution attacks the surface and subsurface layers. Direct investigation of fibers diameter after long-term degradation has shown that the predominant mechanism is opening of crazes and degradation in the volume of fibers. Step by step removal of surface layers was negligible. Therefore the reason of degradation is the reaction of chemical solution with some cations (in the case of acids) or anions (in the case of alkalis) from Basalt fiber body. The kinetic model is therefore based on the assumption of first order reaction. The instantaneous rate of degradation is dependent on the difference between actual weight and weight in equilibrium

$$\frac{dM_t}{dt} = -K \cdot (M_t - M_\infty) \quad (36)$$

Solving of this differential equation in the intervals $[M_0, M_t]$ and $[0, t]$ the following equation results

$$M_t = M_\infty + (M_0 - M_\infty) \cdot \exp(-K \cdot t) \quad (37)$$

After introducing the rest weight the final relation is obtained

$$R_z = R_\infty + (100 - R_\infty) \cdot \exp(-K \cdot t) \quad (38)$$

where R_∞ [%] is equilibrium rest weight and K [hour^{-1}] is degradation rate constant.

23.7.2. Degradation in HCl

The parameters characterizing weight loss for degradation in 10% HCl are given in the table VIII. The parameters of degradation model $R_\infty = 54,883$ [%] and $K = 0,063$ [hour^{-1}] were obtained by using of nonlinear least squares criterion. Experimental points and model curve are shown in the Fig. 10a.

The surface of degraded fibers is shown in the Fig. 11 and Fig. 12. It is very interesting that degradation is due to opening and creation of long crazes in the fiber axis mainly. After long-term exposure the crazes in direction perpendicular to fiber axis are appeared.

Result is great loss of durability and disintegration of fibers in long degradation times. The degradation is accompanied by the great loss of mechanical properties especially tensile strength [6]. The density computed from diameter and weight of treated Basalt is for 2 hours of acid action 2511 kgm^{-3} . This value is slightly lower than density 2572 kgm^{-3} for untreated Basalt fiber.

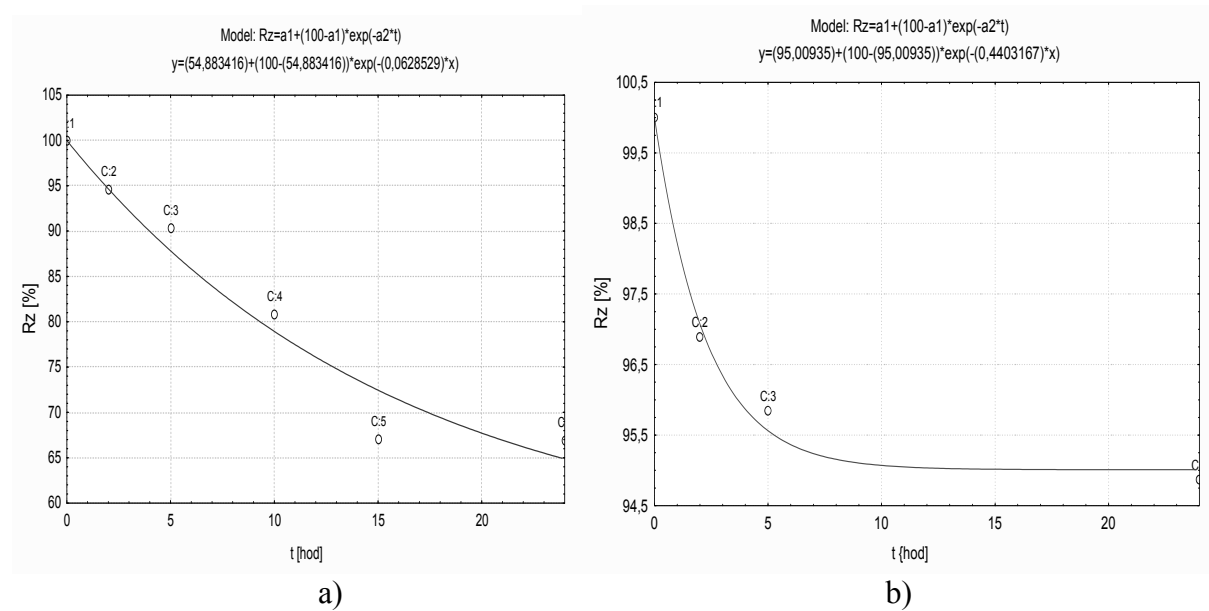


Fig. 10 Kinetics of weight loss a) in 10% HCl, b) in 10% NaOH

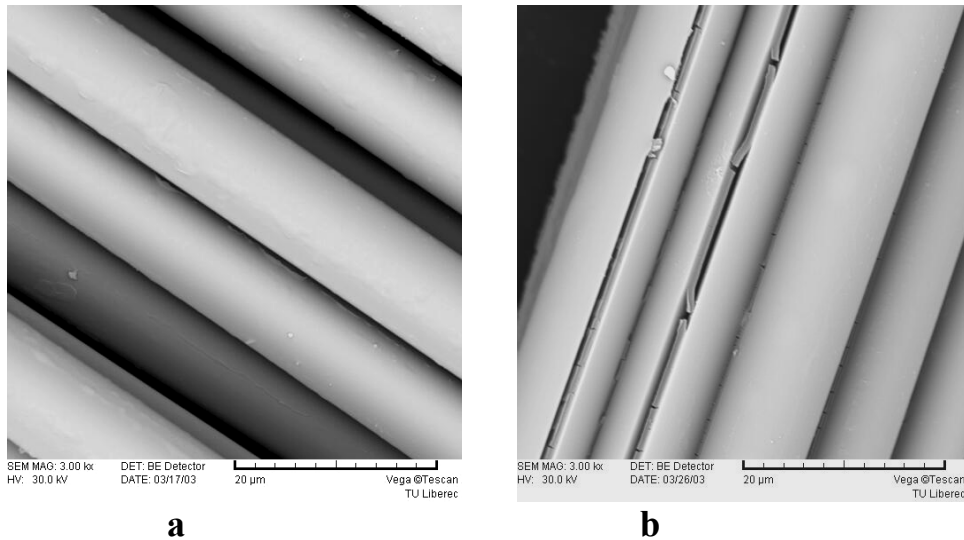


Fig. 11 Basalt fiber after degradation in 10% HCl for 2 hours (a) and 5 hours (b)

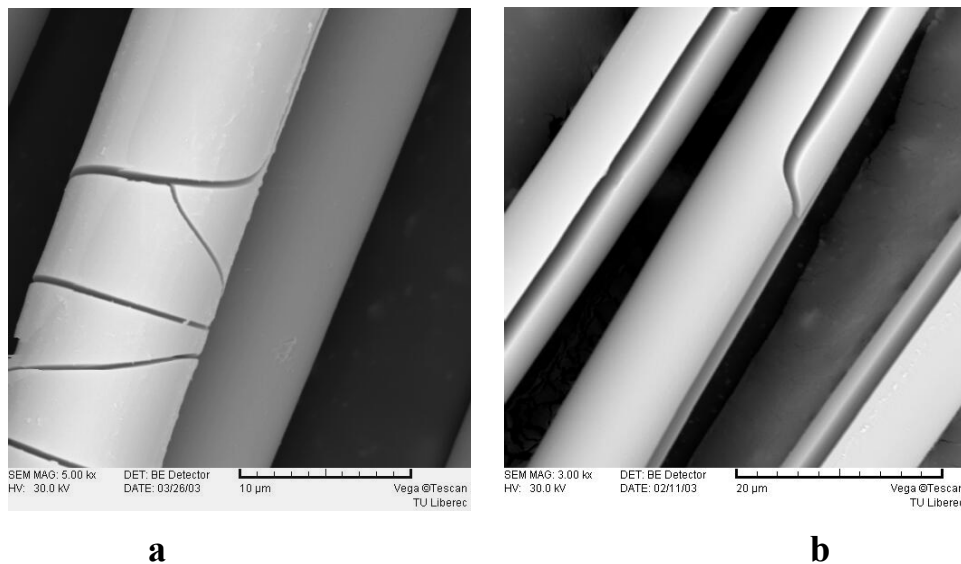


Fig. 12 Basalt fiber after degradation in 10% HCl for 15 hours (a) and 24 hours (b)

The increasing of pH acid solution after degradation is in accordance with assumption of reaction of HCl with cations and destroying the glass like network. The chloride salts replace the intermediate oxides as MnO_2 , Fe_2O_3 and Al_2O_3 . These salts are typically well soluble in water and these phenomena supported the Basalt degradation due to action of acid.

23.7.3. Degradation in alkalis

It is known that alkali attacks the silica network directly. The hydroxyl ion of the alkali breaks the Si-O-Si linkage. The presence of intermediate oxides like MnO_2 , Fe_2O_3 and Al_2O_3 should always improve the alkaline durability [6].

Degradation in 10% alkaline solutions is relatively small. The durability in 10% $Ca(OH)_2$ is excellent. Action of 10% NaOH is more severe but in comparison with acid the weight loss is very low.

The parameters characterizing weight loss for degradation in 10% alkalis are given in the table IX. The degradation kinetic was modeled for the case of 10% NaOH only. The

parameters of degradation model $R_{\infty} = 95,009$ [%] and $K = 0,440$ [hour⁻¹] were obtained by using of nonlinear least squares criterion. Experimental points and model curve are shown on the fig. 10b.

The very high rest weight equilibrium and high rate constant in comparison with the same values for acid degradation indicate that the degradation processes are mainly on surface of fibers. The glass like network breaking increases number of free hydroxyl group.

The surface of degraded fibers is shown on the fig. 13. It is very interesting that the surface is now without crazes and the precipitation of insoluble materials on the fiber surface is visible. The very small weight loss indicates good stability of Basalt in strong alkalis.

The small loss of mechanical properties especially tensile strength was found [23]. The volumetric density computed from diameter and weight of treated Basalt is for 2 hours of NaOH action equal to 2308 kgm⁻³. This relatively low value supports assumption about surface ablation in alkaline conditions.

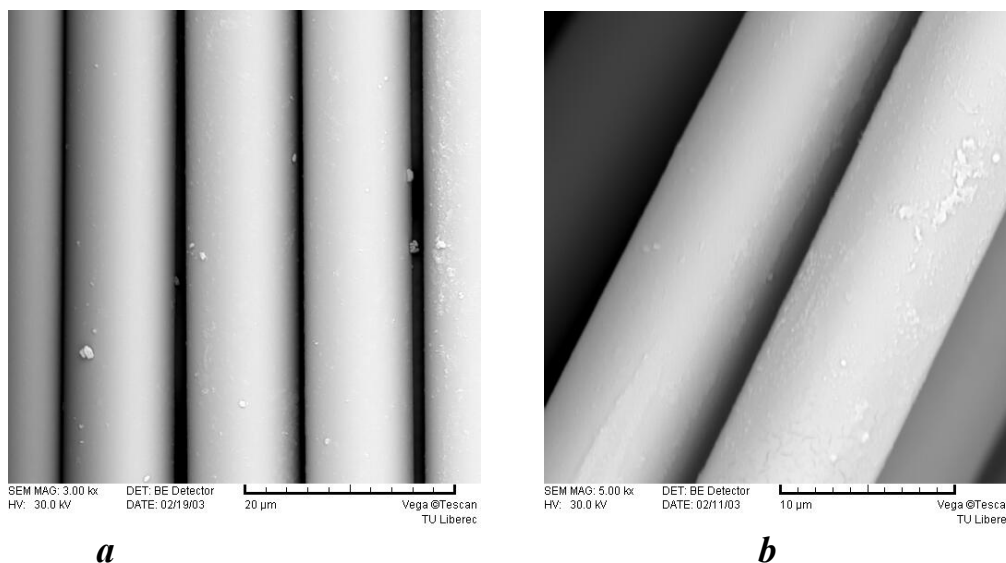


Fig. 13 Basalt fiber after degradation in 10% $Ca(OH)_2$ for 24 hours (a) and in 10% NaOH for 24 hours (b)

23 . 8. Analysis of emitted particles during basalt handling

Some characteristics of the basalt fibers are similar to the asbestos. Since the mechanisms for asbestos carcinogenicity are not fully known it cannot be excluded that basalt fibers may also be hazardous to health. Thus there is a need for analysis of fibrous fragment characteristics in production and handling in order to control their emission.

Based on the results of workshop held by April 1988 at Oak Ridge National Laboratory the fibrous fragments with diameter of 1.5 µm or less and length of 8 µm or greater should be handled and disposed of using the widely accepted procedures for asbestos. Fibers falling within the following three criteria are of concern [13].

- a) *The fibers are respirable.* Diameters of less than 1.5 µm (some say less 3.5 µm) allow fibers to remain airborne and respirable.
- b) *The fibers have a length/diameter ratio R greater than 3.* Short stubby fibers (particles) do not seem to cause the serious problems associated with asbestos.
- c) *The fibers are durable in the lungs.* If fibers are decomposed in the lungs, they do not cause a problem.

Most of nonpolymeric fibers have diameter significantly larger than 3.5 μm but break into long thin pieces. Emission of particles, including fibers, occurs during handling. For simulation of these phenomena the abrasion of basalt weaves were made.

The weave from basalt filaments was used. The fragmentation was realized by the abrasion on the propeller type abrader. Time of abrasion was 60 second. It was proved by microscopic analysis that basalt fibers are not split and the fragments have the cylindrical shape. Fiber fragments were analyzed by the image analysis, system LUCIA M. The fragments shorter than 1000 μm were only analyzed. Results were lengths L_i of fiber fragments. For comparison the diameters D_i of fiber fragments were measured as well. It is assumed that fibrous fragments lengths L_i are in nature independent stochastic variables fully characterized by distribution function $F(L)$ or probability density function $f(L)$. The failure of nonpolymeric fibers as basalt one is frequently caused by volume nonhomogenities and therefore the unimodal distribution is expected. Generally, the number of modal values is an indicator of presence of specific kinds of defects (obviously surface defects and volume ones).

For experimental fragment lengths analysis it is then necessary to use special techniques for [10]:

- a) estimation of number of modal values by nonparametric method,
- b) comparison of experimental fragment lengths distribution with theoretical ones,
- c) estimation of parameter for selected fragment lengths distribution.

In sequel, the sample containing N experimentally measured independent fragment lengths $(L_i) i = 1, \dots, N$ is assumed.

23.8. 1. Nonparametric density estimation

Number of modes (local maxima) on the fragment length probability density function is important from point of view of evaluation of kinds of fragmentation mechanisms (or kinds of defects causing the fiber failure).

Classical nonparametric estimators as the histogram lead often to the artifacts. It is well known that histogram quality is critically dependent on the number and lengths of bins (class intervals). For approximately symmetric distribution a suitable number of bins L is given by [10]

$$L = \text{int} [2 / \sqrt{N}] \quad (39)$$

where $\text{int}[x]$ is integer part of number x .

For nonsymmetrical distributions the bins of variable length have to be used. Especially for complicated shapes of sample distribution the smooth kernel density estimator

$$f(L) = \frac{1}{N * H} \sum_{i=1}^N K \left[\frac{L - L_i}{H} \right] \quad (40)$$

is suitable. In this equation H is bandwidth, which controls the smoothness of $f(L)$ and $K(x)$ is kernel function, which is symmetric around zero, and also has the properties of probability density function. The choice of kernel function form is not critical. The biquadratic kernel is usually sufficient [10]

$$\begin{aligned} K(x) &= 0.9375 (1 - x^2)^2 && \text{for } -1 \leq x \leq 1 \\ K(x) &= 0 && \text{elsewhere} \end{aligned} \quad (41)$$

The quality of kernel estimator $f(L)$ is controlled mainly by the selection of parameter H . If H is too small, the estimator is too rough; if it is too large, the shape of $f(L)$ is flattened too

much. For nearly normal distributions the optimal bandwidth can be calculated from expression

$$f(L) = \frac{1}{N} \sum_{i=1}^N K \left[\frac{L - L_i}{H_i} \right] \quad (42)$$

For complicated density shapes the Lejenne, Dodge and Koelin procedure can be adopted [24]:

(1) From eqn.(40) an initial guess of probability density function $f^0(L)$ is calculated. The constant bandwidth H is computed as

$$H^0 = \frac{2.34 s}{\sqrt{N}} \quad (43)$$

where s is sample standard deviation.

(2) The final estimator of probability density function with no constant bandwidth H_i is constructed. The local bandwidth H_i is calculated from relation

$$H_i = H_i = H^0 \left[\frac{f^0(L_i)}{\max f^0(L_i)} \right]^{-A} \quad (44)$$

Parameter A is defined in the interval $[0,1]$ and controls the smoothness of $f(L)$. The parameter A is usually chosen to be equal to $1/3$. For complex sample distribution (polymodal) it is useful to construct $f(L)$ for various values A and select the one corresponding to pleasant visual smoothness.

Kernel nonparametric density estimator of the distribution of fibrous fragments lengths is shown on Fig 14a (dotted line). The solid line represents normal distribution with mean value and variance computed from data. It is clear that the number of modes $Mo = 1$ and normal distribution is quite different from data based nonparametric one.

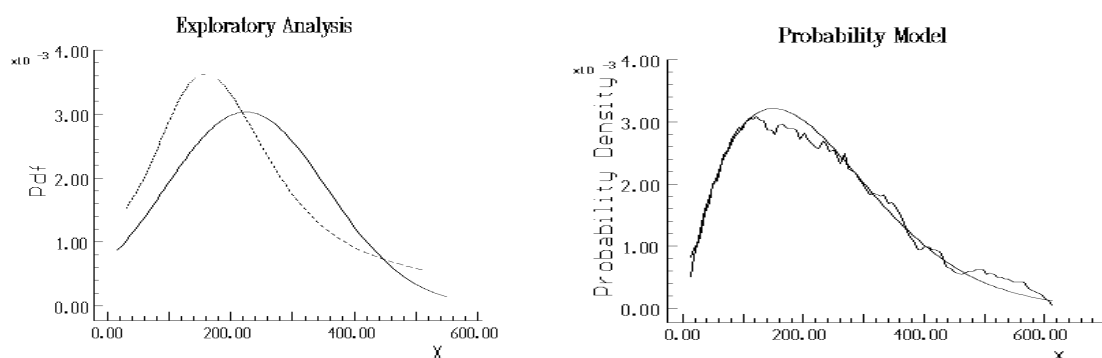


Fig. 14 a) Kernel nonparametric density estimator of the distribution of fibrous fragments lengths (dotted line) and normal approximation (solid line) ,

23.8.2. Comparison of optimal PDF (smooth curve) with „Rosemblatt moving histogram“ (rough curve)

The probability density function (PDF) with optimal parameters (smooth curve) is compared with raw nonparametric estimate „Rosemblatt moving histogram“ (rough curve) on the Fig. 14b. The agreement of both shapes is very good.

The basalt fragment lengths distribution is then unimodal and positively skewed to the right. This type of distribution can be well approximated by Weibull one [3]

$$F(L) = 1 - \exp\left(-\frac{L-L_0}{A}\right)^C \quad (45)$$

The quality of fibrous fragment lengths distribution approximation by the Weibull one is checked by using of Q-Q plot (see. [10]). The Q-Q plot generally allows the comparison of the sample distribution being described by the empirical $Q_E(p_i)$ quantile function with the given theoretical one characterized by theoretical quantile function $Q_T(p_i)$.

The empirical $Q_E(p_i)$ function can be simply approximated by sample order statistics of fibrous fragments length $L_{(i)}$ which are ordered sample values. These order statistics are $100p_i$ %-th quantiles of sample distribution for [10]

$$p_i = \frac{i}{(N+1)} \quad (46)$$

For given theoretical fragment lengths distribution the quantile function $Q_T(p_i)$ is inverse to the cumulative density function. For Weibull distribution defined by eqn.(45) the quantile function $Q_T(p_i)$ has the form

$$Q_T(p_i) = L_0 + A[-\ln(1-p_i)]^{\frac{1}{C}} \quad (47)$$

When the theoretical and sample distribution are the same then

$$Q_T(p_i) = L_{(i)} \quad (48)$$

The eqn. (48) shows that for *Weibull distribution* the dependence of $L_{(i)}$ on $[-\ln(1-p_i)]^{1/C}$ will be straight line. For given shape parameter C it is then simple to compare sample distribution with the Weibull ones.

The parameters L_0 , A , C of Weibull distribution can be then estimated by minimizing of criterion

$$S = \sum_{i=1}^N \left\{ L_i - L_0 - A[-\ln(1-p_i)]^{\frac{1}{C}} \right\}^2 \quad (49)$$

This is typical problem of nonlinear least squares and minimization can be performed by nonlinear regression software [10]. The parameter estimates re shown in the Table X.

Table X. Parameters of fiber fragment length distribution

Distribution	L_0 [μm]	A [μm]	C [-]
Weibull	8,687	246,82	1,618

It is evident that the Weibull distribution is suitable for description of fibrous fragments length distribution. Basic statistical characteristics fiber fragments lengths are:

mean value $L_M = 230.51 \mu\text{m}$

standard deviation $\sigma_L = 142.46 \mu\text{m}$

skewness $g_1 = 0.969$

kurtosis $g_2 = 3.97$

These parameters show that the distribution of fiber fragments is unimodal and positively skewed. By the direct investigation using microscope it has been found that no splitting occurs and fragments have the same diameter as the fibers. The distribution of fiber diameters is positively skewed as well. Basic statistical characteristics of fiber fragments diameters are:

mean value $D_M = 11.08 \mu\text{m}$

standard deviation $\sigma_L = 2.12 \mu\text{m}$

skewness $g_1 = 0.641$

kurtosis $g_2 = 2.92$

Because the mean value of fiber fragment diameter is the same as diameter of fibers no splitting of fibers during fracture occurs. It is known, that from point of view of cancer hazard the length/diameter ratio R is very important. For basalt fiber fragments is ratio

$$R = 230.51/11.08 = 20.8.$$

Despite of fact that basalt particle are too thick to be respirable the handling of basalt fibers must be carried out with care.

23. 9. Creation of textile structures

The basalt filament yarns were prepared in the form of yarn with fineness 40x2x3. The yarn was used for preparation of woven and knitted fabric and as a sewing thread. Utilization of basalt for preparation of fabric was without problems (see. Fig. 21).

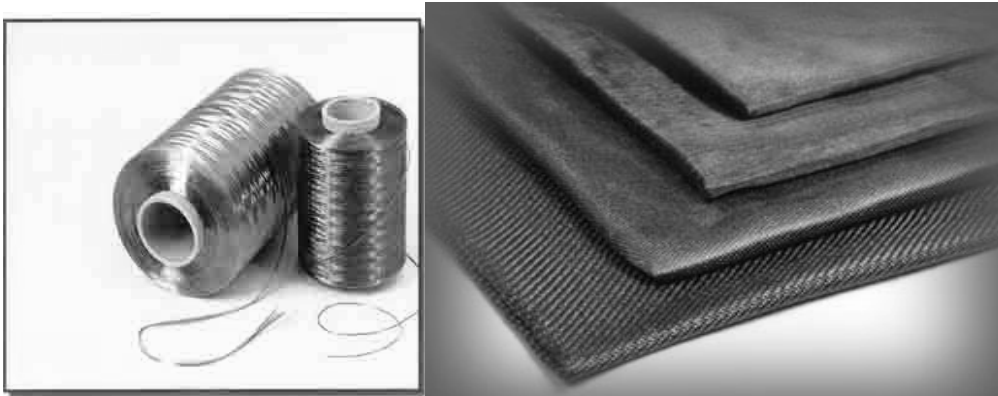


Fig. 15 Typical products from basalt filaments

Table XI. Properties of Basalt and Glass Sewing Thread

Property	Glass sewing thread	Basalt/PET
fineness [tex]	284 ± 2	283.3 ± 1.6
yarn twist 1 [m^{-1}]	397 ± 8.1	208 ± 7.4
yarn twist 2 [m^{-1}]	338 ± 6.1	400 ± 9.8
yarn twist 3 [m^{-1}]	111 ± 5.4	180 ± 5.6
diameter. of thread [mm]	0.56 ± 0.02	0.72 ± 0.05
strength to break [N.tex^{-1}]	0.32	0.34
strength to break in loop [%]	49.81	33.35
deformation to break [%]	1.87 ± 0.16	2.3 ± 0.2
abrasion resistance[cycles]	1214 ± 178	180 ± 49.8
number of break at sewing test	8	0

On the other hand during sewing tests the basalt yarns were frequently broken due to its brittleness. Therefore the composite basalt thread coated by PET was prepared. This composite thread was tested by sewing of filtering bags from glass fabrics. The properties of linear basalt composite were compared with glass sewing thread. Results are given in above Table XI.

It is evident that sewing properties of Basalt/PET thread are very good in comparison with *glass one*. The conclusion is valid for industrially produced basalt fibers as well [12]. The shear and compressive modulus of basalt filaments is comparatively high. The health problems with this class of fibers are not known. Very thick fragments of basalt cannot be easily inhaled. According to the previous finding it was proved that the stability of Basalt in alkalis is generally very good. The stability in acids is comparatively small. Prolonged acids action leads to the full disintegration of fibers.

Acknowledgements: This work was supported by the research project GACR 106/531/2005 and projects IM4674788501 and IM06 047.

References 23

- [1] Douglas, R.W. - Ellis, B.: *Amorphous Material*. Wiley, London, 1972
- [2] Kopecký, L. Voldán, J.: *Crystallization of melted rocks*. CSAV, Prague, 1959
- [3] Rubnerová, J.: *Thermomechanical properties of inorganic fibres*. (Diploma work), TU Liberec, 1996
- [4] Militký J. , Kovačič V. : Proc. Int. Conf. Special Fibres, Lodz 1997
- [5] Morse S. A.: *Basalts and Phase Diagrams*, Springer Verlag, New York 1980
- [6] Krutsky N: Geol. Pruzkum 22, 33. 1980
- [7] Slivka M., Vavro M. : *Ceramics* 40, 149. 1996
- [8] Wagner H. D.: *J. Polym. Sci. Phys. B27*, 115. 1989
- [9] Kittl P., Díaz G.: *Res. Mechanica* 24, 99. 1988
- [10] Meloun M., Militký J., Forina M.: *Chemometrics for Analytic Chemistry vol. I, Statistical Data Analysis*, Ellis Horwood, Chichester 1992
- [11] Meloun M., Militký J., Forina M.: *Chemometrics for Analytic Chemistry vol II, Regression and related Methods*, Ellis Horwood, Hempstead 1994
- [12] Militký J: Proc. 25th. Textile Research Symposium at Mt. Fuji, August 1996
- [13] Weddell J.K.: *Continuous Ceramic Fibres*. J. Text. Inst. No.4, 333, 1990
- [14] Weibull W.: *J. Appl. Mech.* 8,293, 1951
- [15] Cran G. W.: *IEEE Trans. Reliability* 37, 360 (1988)
- [16] Jakeš, P.: Report for Leroy Eclat AG, „*Tažená bazaltová vlákna*“, Prague, 2002
- [17] Jamborová J.: Strength of Basalt Fibers, Diploma work, FT TUL, Liberec, June 2003
- [18] Holland B.V.: *Basalt – The material for the 21st century*, available from <http://basalt-alf.narod.ru/>
- [19] Ostrowski, J.; Rzechula, J.: *J. Non-Crystalline Solids* , 64, 433-41 , (1984)
- [20] Agrawal R.K.: *J. Thermal. Anal.* 32, 149 (1987)
- [21] Militký J. et. all : Proc. Int. Conf. Special Fibers, Lodz 1997
- [22] Monpagens J.C. et all: *J. Polym. Sci. Phys.* 15, 767-772, (1977)
- [23] Paul A.: *J. Mater. Sci.*, No.12, 2246, (1977)
- [24] Lejenne M., Dodge Y., Koelin E.: Proc Conf. COMPSTAT 82, Toulouse, vol. III, p.173 (1982)
- [25] Weibull W.: *J. Appl. Mech.* 8,293 (1951)



Chapter 24

Nuclear waste glasses

24. NUCLEAR WASTE GLASSES: BEAUTIFUL SIMPLICITY OF COMPLEX SYSTEMS

Pavel R. Hrma

24. 1. Introduction

High-level waste (HLW) glasses contain 40 to 60 components, of which around 15 are present at sufficiently high concentrations to significantly influence the glasses' properties, such as viscosity, density, chemical durability, or crystallization behavior. Properties of binary or ternary glasses are typically nonlinear functions of composition. Scientists who study these simple glasses find themselves challenged by their behavior to the point that they are often unwilling to study glasses with more than three to four major components. However, the advantage of systems with a high number of components is that their properties are simple smooth functions of composition.

The majority of nuclear wastes in the world originate from nuclear fuel cycles and nuclear weapons reprocessing. At least 108 sites containing radioactive waste exist in the United States. Perhaps the most prominent among these is the Hanford Site in the State of Washington [1], where 177 underground radioactive waste tanks contain roughly 200,000 m³ of radioactive liquid and sludge from plutonium production from 1944–1987.

Hanford tank HLW will be retrieved and separated into HLW and low-activity waste (LAW) fractions. Both HLW and LAW will be vitrified in the Hanford Tank Waste Treatment and Immobilization Plant (WTP). According to current plans, the WTP can process roughly half of the LAW [2]. The current reference process for the other half of the LAW is bulk vitrification—a process in which the glass is melted in a large metallic box lined with refractory and remains in this box for disposal [3]. To make nuclear-waste glass, the waste streams from a pretreatment facility, in the form of HLW slurries or LAW solutions, will be mixed with glass-forming and modifying additives in the HLW or LAW vitrification facilities, respectively. In both facilities, the resulting melter feeds will be charged into electrically heated continuous melters from which the molten glass will be poured into stainless-steel canisters. The HLW canisters will be stored onsite and then disposed of in the Yucca Mountain repository in Nevada. The LAW containers will be disposed of onsite in the Hanford Integrated Disposal Facility (IDF).

It is projected that about 6000 batches of HLW will be processed at WTP during its life-cycle, each with a distinct composition [4]. To maintain consistent glass properties, a glass of an appropriate composition must be formulated separately for each of these wastes.

Regarding its properties, HLW glass is subjected to various restrictions [5]. It would be inefficient if not impossible to develop a specific glass for each waste composition individually in the laboratory by trial-and-error experiments, especially considering that the projected HLW compositions are subjected to change as new analyses and pretreatment techniques become available. In fact, the planning of the design and operation of the vitrification facility requires that thousands of glasses need to be formulated, optimized, and qualified for disposal within a short time of 1 to 2 hours [5,6]. This goal of formulating glasses within a short time for thousands of HLW compositions can be achieved based on composition-property functions experimentally determined for the HLW composition region [7].

Table 1 shows the composition region of glasses formulated for roughly 6000 Hanford HLW compositions considered for vitrification. Interestingly, in these glasses, SiO₂ is expected to vary within 20 mass%, B₂O₃ and Fe₂O₃ within 15 mass%, Al₂O₃ within 14 mass%,

Na₂O within 10 mass%, and all the rest within 2 to 7 mass% (the component “Others” is the sum of all minor components). These ranges are relatively narrow. They are narrow enough to allow us to approximate the effects of glass composition on its properties by linear functions.

Table 1. Projected composition region of Hanford high-level waste glasses in mass fractions [5]

Com- ponent	Mini- mum	Maxi- mum	Range
Al ₂ O ₃	0.060	0.200	0.140
B ₂ O ₃	0.050	0.200	0.150
Bi ₂ O ₃	0.000	0.050	0.050
CaO	0.000	0.070	0.070
Cr ₂ O ₃	0.001	0.020	0.019
F	0.001	0.020	0.019
Fe ₂ O ₃	0.050	0.200	0.150
K ₂ O	0.000	0.060	0.060
Li ₂ O	0.015	0.040	0.025
MnO	0.001	0.040	0.039
Na ₂ O	0.100	0.200	0.100
NiO	0.001	0.020	0.019
P ₂ O ₅	0.000	0.025	0.025
SiO ₂	0.300	0.500	0.200
ZrO ₂	0.001	0.050	0.049
Others	0.014	0.019	0.006

Linearization has far-reaching consequences for the glass-formulation effort. As the following section describes, with the linear property-composition relationships, glasses can be formulated quickly and easily.

However, the behavior of glass, especially high-temperature molten glass, cannot be completely described by means of properties. Phenomena such as settling of solids, segregation of molten salts, or generation of foam in the melter require special attention because they can severely impair melter performance. Crystallization of the glass during cooling can affect the quantity of the glass product and its acceptability for the repository. Also, it remains unclear whether glass durability as defined by means of standard tests is predictive to the glass performance over the hundred thousand years needed for the decay of radionuclides. The major processing problems are also addressed in this article. Questions associated with the long-term durability are only briefly mentioned.

24. 2. HLW Glass Formulation

Waste glasses are formulated to meet three types of requirements [8]. First, the glass must possess properties required for smooth processing that occurs in a continuous melter located

in a hot cell and operated via remote control. The operation is expected to run without major problems for five or more years. To protect the Inconel electrodes, the temperature of the melt is maintained within a narrow range of around 1150°C at which the glass viscosity must be within 2 to 8 Pa·s and the electric conductivity within 1 and 70 S/m. It is not desirable for solids to settle and molten salts to segregate during the melting operation or melter idling because this may shorten melter life. Excessive foaming should be avoided because it will reduce the production-rate requirement of between 6 and 7.5 MT of glass per day (~1050 kg/m²/d).

Second, the glass product must satisfy quality requirements defined in terms of chemical durability measured by selected standard methods, such as the Product Consistency Test (PCT) [9] and regulatory requirements determined by response to the Toxicity Characteristic Leaching Procedure (TCLP) [10]. Finally the economy requires that the fraction of waste material (the waste loading) in the glass should be as high as possible to minimize the volume of waste glass, and the rate of melting should be as high as possible to minimize the processing time.

The processing and quality-defining properties are expressed by means of the following linear functions:

$$b_j = b_{ji}x_i \quad i=1,2, \dots, N \quad (1)$$

where b_j is the transformed j -th property, b_{ji} is the i -th component coefficient for j -th transformed property, x_i is the i -th component mass fraction, and N is the number of the j -th property affecting coefficients (i.e., $N-1$ major components plus “Others”). Here the summation convention is being used, $b_{ji}x_i = \sum_{i=1}^N b_{ji}x_i$.

The properties are transformed in such a way that the linear functions allow an acceptable fit. For example, in case of melt viscosity (η) that is an Arrhenius function of temperature (T), i.e., $\eta = \exp(A + B/T)$, where A is an composition-independent constant, the transformed property is the activation energy, $B = (\ln \eta - A)T$; hence, $B = B_i x_i$ [11].

The component coefficients are obtained experimentally. The composition region, such as that shown in Table 1, is covered by data points representing compositions of glasses that are fabricated and whose properties are measured. The property-composition relationships are then fitted to data by the linear-regression method to obtain the component coefficients.

Waste glasses are made by adding to the waste selected glass-forming and glass-modifying components, such as SiO₂, B₂O₃, Na₂O, and Li₂O in proportions that provide the glass the desired properties while maximizing the waste loading.

The i -th component mass balance can be written as

$$x_i = Ww_i + (1 - W)a_i \quad i=1,2, \dots, N \quad (2)$$

where W is the waste loading (the mass fraction of waste material in the glass) and w_i and a_i are the i -th component mass fractions in the waste and additive portions of the glass, respectively.

Substituting for x_i from Equation (2) to Equation (1), we obtain j equations, one for each transformed property. The task is to determine the a_i value for each additive constituent such that the glass properties are within the prescribed limits, and W is maximized (considering

various uncertainties determined by the statistical analysis). As mentioned above, the linearity of the property-composition relationships, Equation (1), allows this task to be done quickly and easily for a large number of HLWs that possess a large number of components.

Regarding the component coefficients, we can expect that these coefficients are related to fundamental characteristics of the glass structure. This has been empirically demonstrated for the liquidus temperatures of the spinel mineral that forms in HLW glasses— $[\text{Fe,Ni,Zn,Mn}][\text{Fe,Cr}]_2\text{O}_4$ [12].

24.3. Settling of Solids in HLW Glass Melter

In the waste-glass melter, spinel can settle and disrupt melter operation and shorten its lifetime. Spinel typically forms octahedron crystals (Figure 3.1). However, in more viscous, low-temperature melts, it can precipitate in more complicated shapes (Figure 3.1).

By the Stokes equation, the settling velocity of a sphere is proportional to the square of its radius. Thus, the main factor that determines the rate of settling of spinel crystals is the crystal size. A simple calculation indicates that micron-sized spinel crystals virtually do not settle and leave the melter with glass. However, large crystals, those of tens or hundreds of micrometers, are likely to settle and accumulate in the melter. Several centimeters of spinel sludge has been found accumulated after a relatively short time of testing various experimental melters [14].

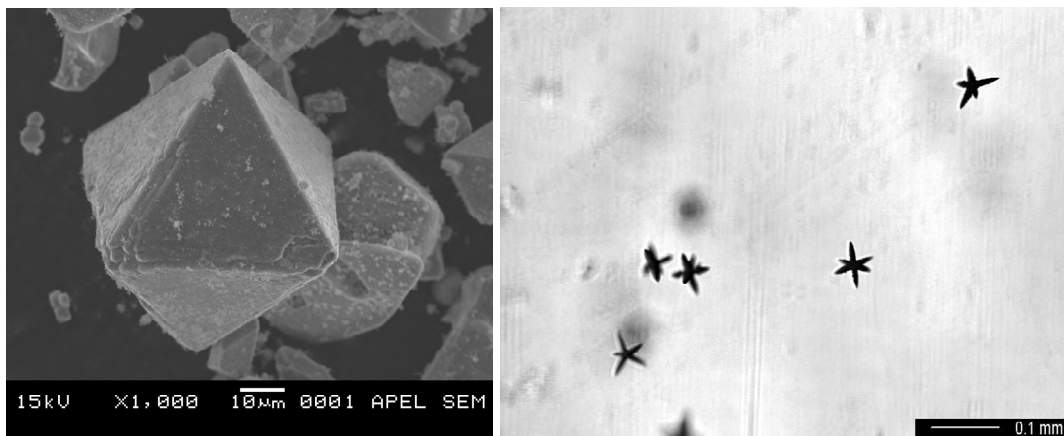


Fig. 3.1. Crystals of spinel in HLW glass; the left SEM image shows a typical octahedron form; the right optical image shows spinel that precipitates during rapid cooling at lower temperatures [13]

What determines the crystal size? While the nucleation and growth of spinel crystals from the glass melt is well understood [15], the mechanism of their formation during the early melting reactions is not clear. However, crucible experiments have shown that spinel crystals can grow to the size over 100 μm in the absence of noble metals. Figure 3.2 shows an optical image of a thin section of a spinel sludge found at the bottom of a pilot-scale melter in which the simulated waste was processed without adding noble metals (to save the expenses, these test are often run without expensive components).

Noble metals (Ru, Rh, Pd) are common components of radioactive waste glasses. Their particles provide sites for heterogeneous nucleation of spinel. Crucible tests have shown that

when the noble metals are present in the melter feed, spinel crystals precipitate with such a high number density that their size drops to approximately $1 \mu\text{m}$ [16,17].



Fig. 3.2. Optical image of a thin section from sludge found at the bottom of an experimental melter [14]

The formation of hematite, which precipitates in the form of pink hexagonal platelets, may precede spinel crystallization (Figure 3.3). As Figure 3.3 shows, hematite later reacts with other spinel-forming oxides (NiO , MnO , FeO , Cr_2O_3) to form spinel [18].

Another solid phase that can settle in the melter and disrupt its operation is RuO_2 . Though RuO_2 crystals are too tiny to settle as individual particles, their settling rate is increased by orders of magnitude because of their tendency to form large agglomerates [19]. Electric conductivity data exist for RuO_2 sludge [20], but not on spinel sludge or sludge that combines RuO_2 and spinel. Little is known about the mechanism of RuO_2 agglomeration and the conditions that influence it. An interesting case of the interaction between spinel octahedrons and RuO_2 needles is shown in Figure 3.4 [21], see also [22].

The key step in the sequence of events that determine the rate of settling of spinel and RuO_2 is the nucleation and growth of their crystals and crystal-agglomerates during the early melting reactions. This mechanism cannot be understood without understanding the complex process of the conversion of melter feed to molten glass. Moreover, RuO_2 agglomerates can further join and form super-agglomerates by the shear-flocculation mechanism that operates when the velocity gradients in molten glass subjected to natural or forced convection bring the aggregates to close proximity.

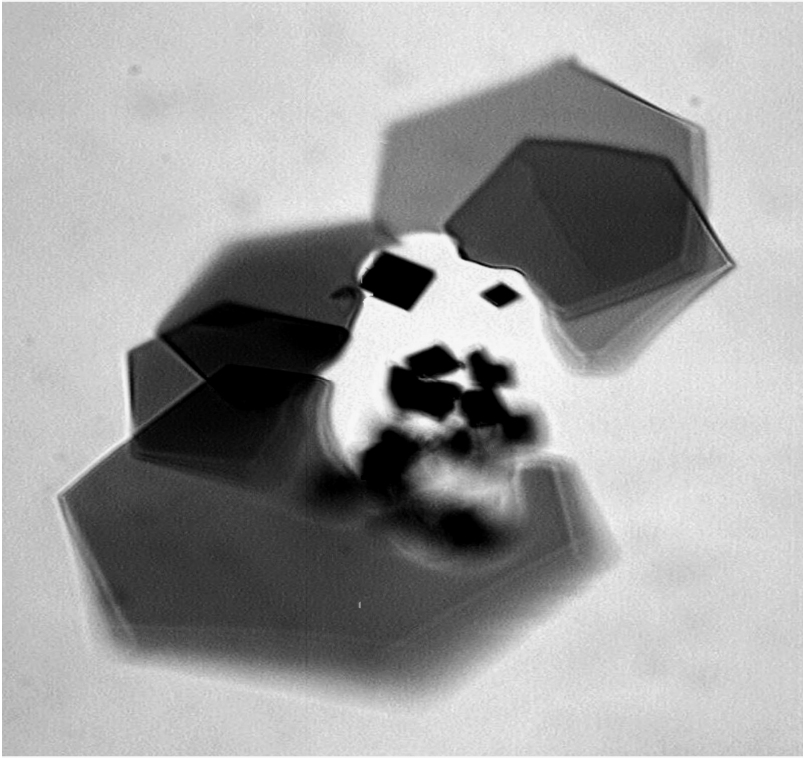


Fig. 3.3. Hematite crystals in the process of conversion to spinel

With the exception of zirconium-containing crystals (Figures 3.5 and 3.6), most of the crystalline phases that can precipitate from the waste glass form at temperatures at which the glass has been poured out of the melter [23,24]. Figure 3.7 depicts the formation of intermediate solid phases [25] (e.g., spinel, zircon, and sodalite).

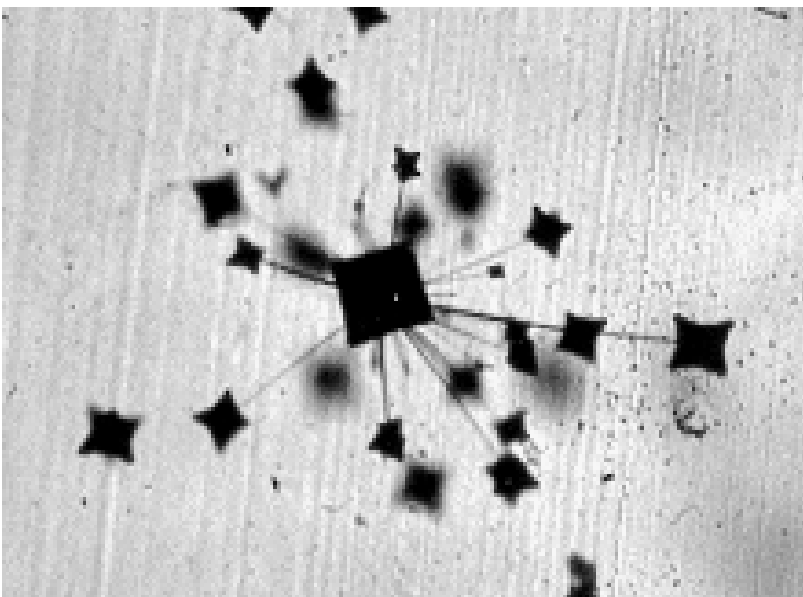


Fig. 3.4. Needles of RuO_2 growing on a central crystal of spinel; secondary spinel crystals have been nucleated on the RuO_2 needles [21]

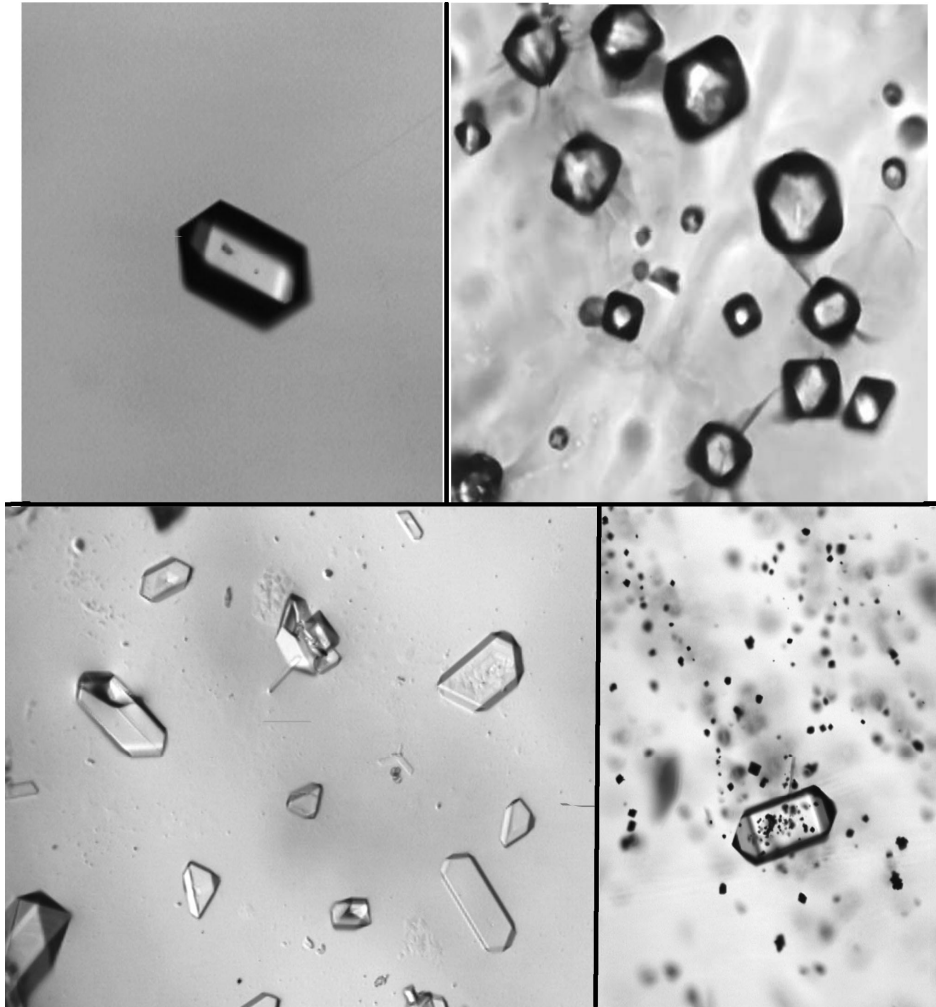


Fig. 3.5. From top left clockwise: zircon, baddeleyite, rare earth zirconate, sodium zirconium silicate (parakeldyshite)

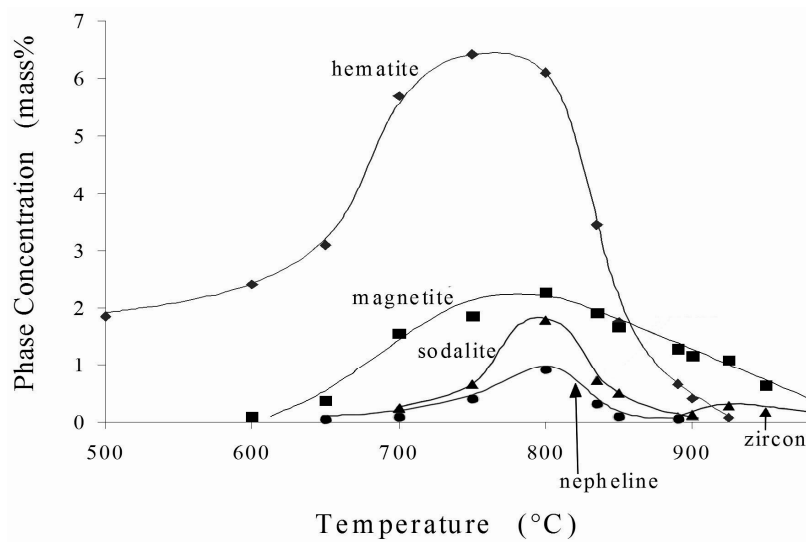


Fig. 3.7. Content of various intermediate crystalline phases in the melter feed as a function of temperature during heating at 5°C/min (as determined by XRD in quenched samples) [25]

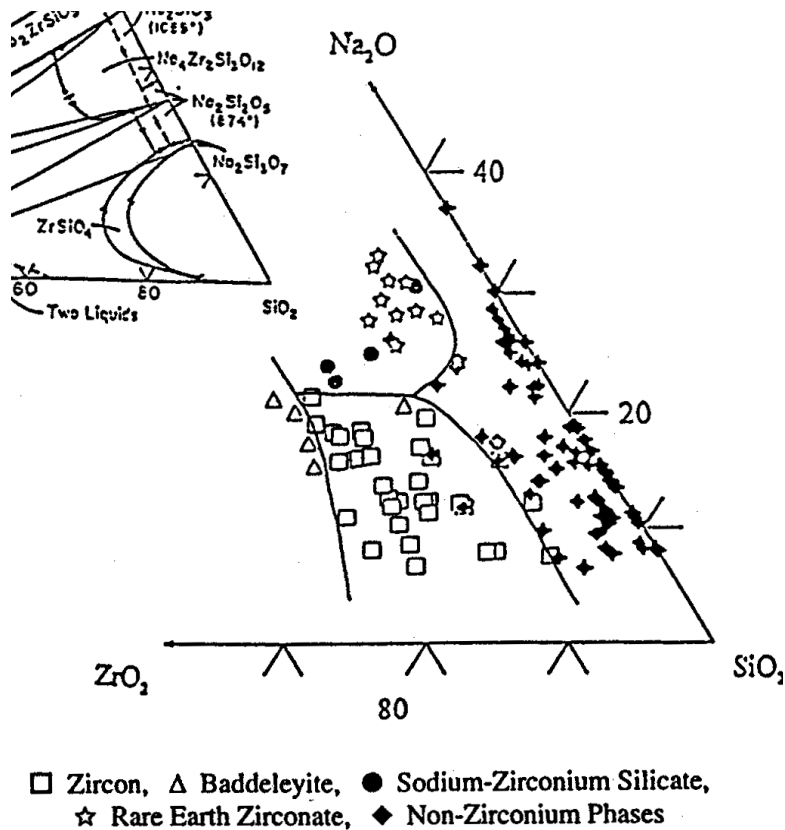


Fig. 3.6. Occurrence of various zirconium-containing crystals in terms of ZrO_2 - SiO_2 - Na_2O submixture [24]

24. 4. Foaming

Two types of foam occur during glass melting. Figure 4.1 shows the development of the primary foam caused by the residual gas from the feed reactions trapped in the glass-forming melt after it became connected. The left graph shows the specific volume of an HLW feed heated at $5^\circ\text{C}/\text{min}$. The feed rapidly expands when the temperature reaches 750°C . At about 900°C , the foam volume became eight times larger than the melt volume in this particular melter feed. The foam collapsed before the temperature reached 1000°C . The right graph shows a similar experiment conducted with E-glass [26]; in this case, the foam collapsing was visible through the crucible walls. The graph also shows the shrinkage of the glass batch before the beginning of foaming. Feeds or batches associated with the primary foam expand to various extents, from 0 to 10 times, depending on the feed makeup. It affects heat conductivity of the feed and assists the dissolution of solid particles in the melt.

The secondary foam is caused by gas-producing reactions in molten glass. Gas (oxygen) is produced in HLW glasses mainly by such reactions as a multi-valent metal, such as Fe_2O_3 , being reduced to FeO . Foam insulates the reacting layer on the top of molten glass (called the cold cap in waste glass melters and batch blanket in commercial glass-melting furnaces) from the heat transfer from the melt. Bubbling may remove secondary foam and certainly brings the hot melt to the cold cap, thus greatly enhancing the heat transfer and increasing the rate of melting.

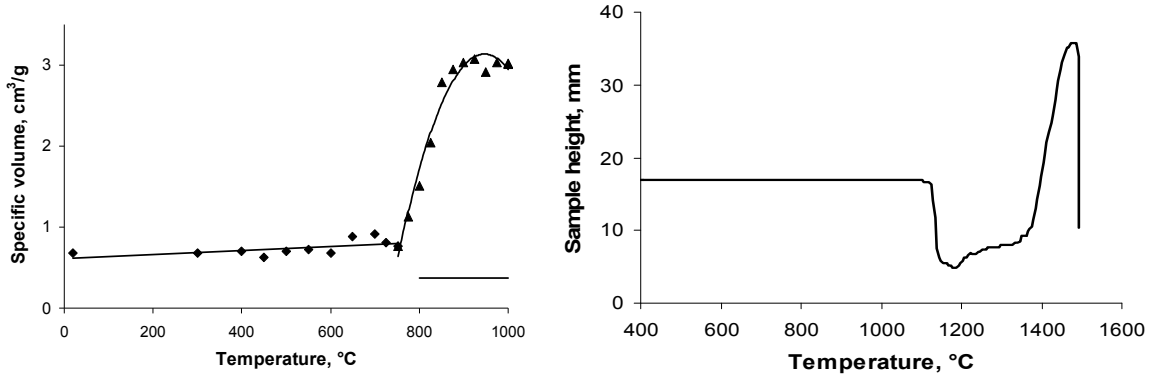


Fig. 4.1. Expansion of HLW melter feed (left) and E-glass batch (right) during heating at 5°C/min

25. 5. Salt Segregation

Molten salt, predominantly sulfate, tends to segregate from molten glass in the melter and accumulate on the melt surface. The sulfate phase contains also metallic chromates and phosphates. Sulfate segregates at an SO_3 concentration well below the solubility limit. How can a well-dispersed, easily soluble component segregate at such low levels of concentration? Sulfate is a minor component in nitrate-carbonate molten salt, which exists in the feed at temperatures below about 750°C. When nitrate and carbonates decompose and the glass-forming phase becomes connected, molten sulfate becomes trapped in bubbles and is carried to the melt surface.

Figure 5.1 shows fracture surfaces of partly melted LAW feeds. The fracture passes either through a bubble or leaves a shell of sulfate intact, thus evidencing the mechanism of segregation [27,28].

The following equation was derived for the final concentration of the dissolved sulfate [28]:

$$c_{\text{dis}} = \frac{4\pi}{k_s k_L} n h \Delta c \left(\frac{D \eta}{\Delta \rho g} \right)^{\frac{2}{3}} \quad (3)$$

where k_s is the Stokes constant, k_L the Levich constant, n the bubble-number density, h the bubble-path length, D the diffusion coefficient, η the melt viscosity, $\Delta \mu$ the difference between the melt density and the average bubble density, g the acceleration due to gravity, and $\Delta c = c_{\text{sat}} - c_{\text{dis}}$; here c_{sat} is the SO_3 solubility.

The term in parentheses in the right-hand side of Equation 3 changes little with melt composition and temperature. Although the viscosity and diffusion coefficient change exponentially with composition and temperature, their product, by the Stokes-Einstein equation, is nearly constant. Therefore, neither viscosity nor the diffusion coefficient significantly affects sulfate retention.

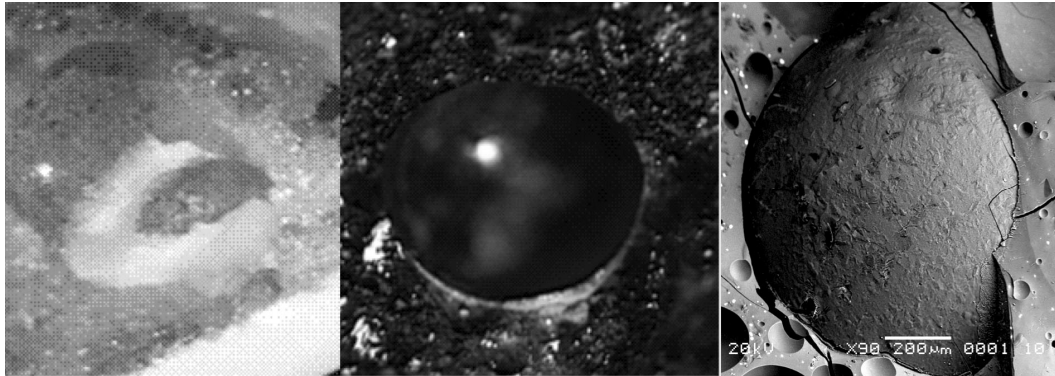


Fig. 5.1. Sulfate in a bubble at 900°C (left); scanning electron microscopy (SEM) micrographs of a crescent of sulfate in a bubble at 950°C (middle) and of a spherical layer of sulfate in a bubble at 875°C (right) [27,28]

24. 6. Molten Salt Migration

Molten salts in the HLW or LAW feeds migrate when there are high fractions of molten salts in the feed and a low specific surface area of the feed solids. It rarely occurs in WTP HLW feeds that have relatively small fractions of molten salts, and the solid components are high-surface-area oxides from amorphous gels present in the waste (a different situation probably exists in feeds made from waste and premelted frit). However, LAW contains up to 90% salts that make up nearly half of the volume of the condensed phase in the feed at temperatures above 300°C. If the feed solids are silica sand and crushed minerals of low surface area, only a small fraction of liquid salts is immobilized by wetting the solids while the rest can freely move and get segregated. This free molten salt migrated into the castable refractory used as the lining of the metallic boxes employed for bulk vitrification of LAWs. Combining two measures solved the problem: using very fine silica as a glass former and adding cellulose to the feed [29]. Fine silica immobilized most of the nitrates in the reactive grain surfaces. The rest of the mobile sulfate was destroyed by the cellulose that reacted with nitrates before they could migrate.

24. 7. Feed-to-Glass Conversion

So far, little effort has been made to understand the relationship between the feed-make-up parameters and the rate of melting. Such an understanding can cast light on the role of molten salts in the reactions between solid constituents of melter feeds, the mechanism of glass-melt formation, the dissolution of residual solids in the glass melt, and melt homogenization. Such an understanding can also help avoid nuisance phenomena that slow down the rate of melting and necessitate melter idling, such as melt foaming, salt segregation, and cold-cap freezing.

The cold cap is the melter feed in the process of being converted to molten glass and floating on the pool of molten glass; it is the most important and most neglected area of the waste-glass melter. Even though some valuable experience in feed/batch-to-glass conversion studies has accumulated over the years, the relationship between the feed reactions and the rate of melting has not been well established.

The melting rate is jointly controlled by the heat-transfer rate and the rate of feed-to-glass conversion, consisting of various chemical reactions and phase transitions [30]. This can be roughly expressed with the formula

$$N = \frac{N_C^2}{2N_H} \left[\left(1 + \frac{4N_H^2}{N_C^2} \right)^{1/2} - 1 \right] \quad (4)$$

where N is the rate of melting (mass per time and area), N_C is the conversion-controlled rate of melting, and N_H is the heat-transfer-controlled rate of melting. These rates are defined as

$$N_C = \left[\frac{k\rho\lambda_c(T_M - T_C)}{Q} \right]^{1/2} \quad (5)$$

and

$$N_H = \frac{\lambda_H(T_M - T_C)}{\delta Q} \quad (6)$$

where λ_c and λ_H are effective heat conductivities of the cold cap and molten glass, T_C and T_M are the temperatures of the cold cap and the bulk melt, respectively, δ is the thermal boundary layer thickness, k is the conversion-rate coefficient, ρ is the feed density, and Q is the conversion heat (the energy needed to turn slurry feed under ambient conditions to 1 kg of molten glass). The thickness of the thermal boundary layer is defined as $\delta = (T_M - T_I)/(\delta T/\delta y)_{y=0}$, where y is the vertical distance from the cold-cap–melt interface, and T_I is the temperature of the cold-cap–melt interface.

Both the heat transfer and the conversion process are upset if fluxes (that are present in the form of low-viscosity molten ionic salts, also called the primary melt, existing at temperatures at which the glass-forming melt has not yet developed) migrate out of the cold cap. This leads to cold-cap freezing and inability to reach a steady state in the melter.

An important factor affecting the heat-transfer rate is the melt viscosity that influences the velocity of natural convection in the melter and the extent of bubble/foam accumulation under the cold cap [31,32]. Because viscosity depends on glass composition, glass formulation is of a crucial importance for melter operation. For fast melting, the viscosity near the cold-cap bottom surface should be as low as possible.

24. 8. Crystallization [33]

The HLW glass is poured into stainless steel canisters of 60-cm inner diameter and about 3 m long. The glass in the canister centerline takes about 20 hours to cool below the glass transition temperature (Figure 8.1). During this slow cooling, the glass may precipitate crystals that remove components from the amorphous matrix, thus changing its corrosion resistance. Figure 8.2 shows a dendrite of baddeleyite (this form would occur as a result of fast cooling near the canister wall) and crystals of nepheline. Most of the crystalline phases found in Hanford HLW glasses do not form in a sufficient quantity to influence glass durability. However, a massive precipitation of nepheline can significantly decrease glass durability and must be avoided.

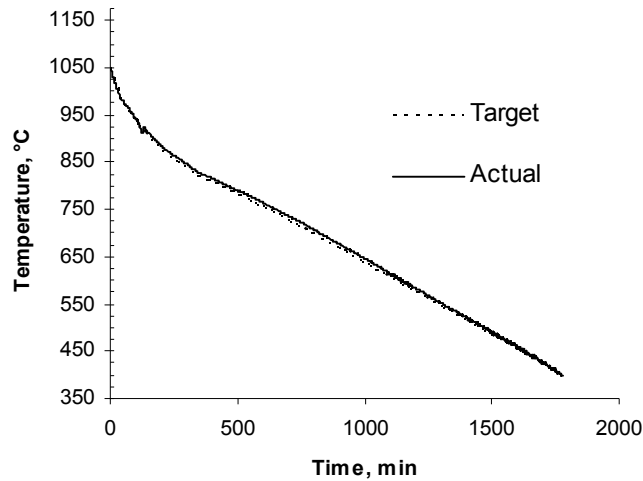


Fig. 8.1. Hanford canister centerline glass cooling curve

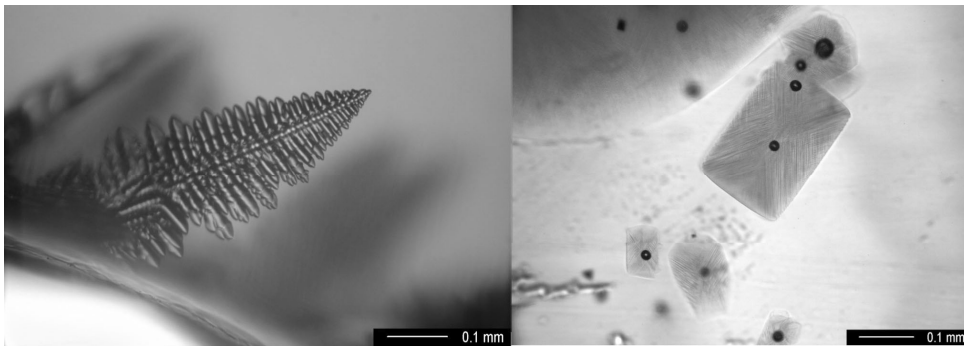


Fig. 8.2. Dendrite of baddeleyite (left) and crystals of nepheline (right) i HLW glass

24. 9. Chemical Durability

Chemical durability is a term for expressing the resistance of glass to corrosion by aqueous media. Some glasses dissolve incongruently, i.e., some of their components are preferentially leached out of the glass structure. Durable glasses usually dissolve congruently. Under static conditions, the glass remains in contact with a given volume of the aqueous medium for a prescribed length of time. The solution is then analyzed, and the amount of glass dissolved is estimated based on the concentration of elements that do not precipitate from the solution and do not remain on the glass surface in the form of a gel. The process of dissolution goes through several phases [34]. In the initial phase, the solution is unsaturated. In the advanced phase, the solution becomes oversaturated with respect to various clays and zeolites, such as analcime. At the end of this phase, these minerals are suddenly nucleated and rapidly precipitate. The precipitation lowers the solution concentration of orthosilicic acid, thus increasing the driving force for dissolution. As a result, glass dissolution is greatly accelerated until, in the final stage, the process becomes controlled by the rate of precipitation of minerals from the solution. Figure 9.1 shows zeolites and clays that form on the glass surface during an accelerated test [35].

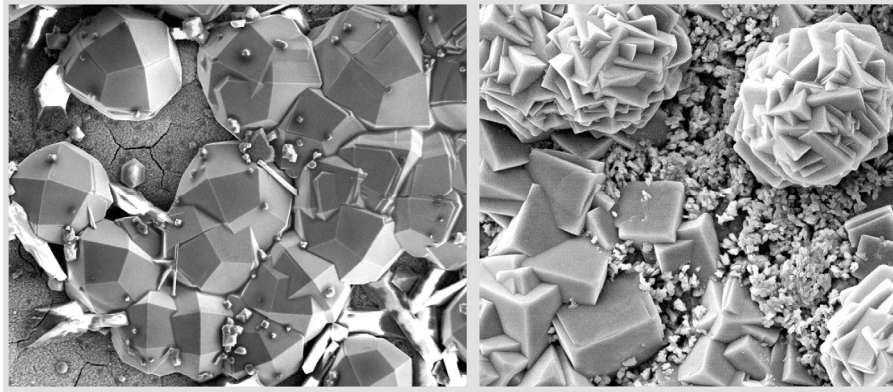


Fig. 9.1. SEM images of crystals on the glass surface

Accelerated tests, such as the vapor hydration test, expose a glass coupon to saturated steam at 200 to 300°C for 2 to 3 weeks. A nondurable glass can be totally converted to gel (Figure 9.2).

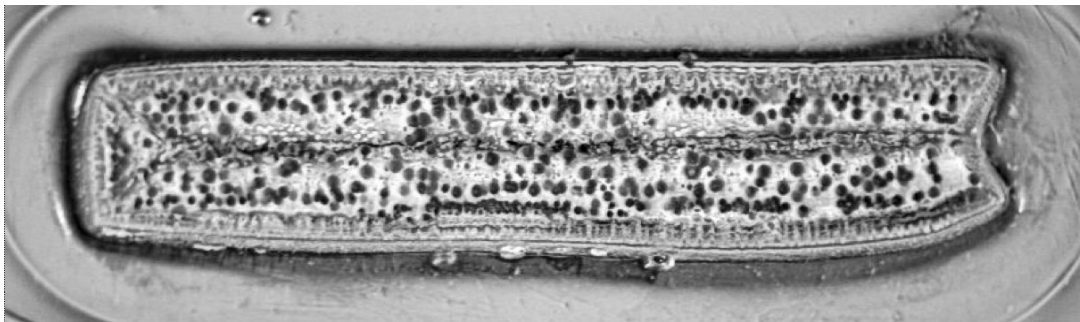


Fig. 9.2. An example of a cross-section of a coupon of a non-durable LAW glass subjected to vapor-hydration test

Acknowledgments: I am grateful to John Vienna for careful review and useful suggestions and Wayne Cosby for editorial support.

References 24

1. Department of Energy Environmental Management Home Page. <http://www.em.doe.gov/pages/emhome.aspx>. Accessed 28 October 2008
2. Certa PJ, Allen GK, Crawford TW, Hohl TM, Jordan KN, Kirkbride RA, Lytle RL (2008) *River Protection Project System Plan – Revision 3A, ORP-11242, Rev. 3a*, U.S. Department of Energy Office of River Protection, Richland, Washington
3. Thompson LE, McClure L, Hamilton D (2005) *Status and Direction of the Bulk Vitrification Program for the Supplemental Treatment of Low Activity Tank Waste at Hanford*. In: Proceedings of WM'05 Symposia. WM-5138, AMEC Earth and Environmental, Inc., Richland, Washington

4. Lee E (2007) Dynamic (G2) *Flowsheet Assessment of the Effect of M-12 Modifications on Pretreatment Capacity*, 24590-WTP-RPT-PO-07-002, Rev. 0, River Protection Project, Waste Treatment Plant, Richland, Washington
5. Vienna JD, Kim DS (2008) *Preliminary IHLW Formulation Algorithm Description*, 24590-HLW-RPT-RT-05-001, Rev. 0, River Protection Project, Hanford Tank Waste Treatment and Immobilization Plant, Richland, Washington
6. a) Vienna JD (2005) *ILAW Formulation Algorithm Description*, 24590-LAW-RPT-RT-04-0003, Rev. 0, River Protection Project, Waste Treatment Plant, Richland, Washington
b) Vienna JD (2005) *Nuclear Waste Glasses*. In: *Properties of Glass Forming Melts*, eds. Pye LD, Montenegro A, and Joseph I, CRC Press, Boca Raton
7. a) Piepel GF, Cooley SK, Heredia-Langner A, Landmesser SM, Kot WK, Gan H, Pegg IL (2008) *IHLW PCT, Spinel T1%, Electrical Conductivity, and Viscosity Model Development*, VSL-07R1240-4, Rev. 0, Vitreous State Laboratory, The Catholic University of America, Washington, D.C.
b) Piepel GF, Cooley SK, Muller IS, Gan H, Joseph I, Pegg IL (2007) *ILAW PCT, VHT, Viscosity and Electrical Conductivity Model Development*, VSL-07R1230-1, Rev. 0, Vitreous State Laboratory, Washington, D.C.
8. a) Hrma P, Crum JV, Bates DJ, Bredt PR, Greenwood LR, Smith HD (2005) *Vitrification and testing of a Hanford high-level waste sample. Part 1: Glass fabrication, and chemical and radiochemical analysis*. *J Nucl Mater* 345:19–30
b) Hrma P, Crum JV, Bredt PR, Greenwood LR, Arey BW, Smith HD (2005) *Vitrification and testing of a Hanford high-level waste sample. Part 2: Phase identification and waste form leachability*. *J Nucl Mater* 345:31–40
9. American Society for Testing and Materials, *Standard Test Methods for Determining Chemical Durability of Nuclear, Hazardous, and Mixed Waste Glasses: The Product Consistency Test (PCT) C 1285-97* (1998) In: *1998 Annual Book of ASTM Standards*, Vol. 12.01, West Conshohocken, Pennsylvania
10. U.S. Environmental Protection Agency (1997) *Test Methods for Evaluation of Solid Waste Physical/Chemical Methods*, SW-846, 3rd Ed. Washington, D.C.
11. Hrma P (2008) *Arrhenius Model for High-Temperature Glass Viscosity with a Constant Pre-Exponential Factor*. *J Non-Cryst Solids* 354:1962–1968
12. Vienna JD, Hrma P, Crum JV, Mika M (2001) *Liquidus Temperature-Composition Model for Multicomponent Glasses in the Fe, Cr, Ni, and Mn Spinel Primary Phase Field*. *J Non-Cryst Solids* 292:1–24
13. Hrma P, Kruger AA (2008) *Nuclear waste glasses: continuous melting and bulk vitrification*. *Adv Mater Res* 39–40:633–640
14. Jiricka M, Hrma P (2002) *Chemical and Mechanical Properties of Spinel Sludge in High-Level Waste Glass*. *Ceramics-Silikaty* 46(1):1–7
15. Alton J, Plaisted TJ, Hrma P (2002) *Nucleation and Growth of Spinel Crystals in a Borosilicate Glass*. *J Non-Cryst Solids* 311:24–35
16. Plaisted TJ, Alton J, Wilson BK, Hrma P (2001) *Effect of Minor Component Addition on Spinel Crystallization in Simulated High-Level Waste Glass*. *Ceram Trans* 119:291–299
17. Hrma P, and Alton J (2001) *Dissolution and Growth of Spinel Crystals in a High-Level Waste Glass*. In: *The 8th Int. Conf. Proc. (ICEM'01)*, CD-ROM, Bruges, Belgium
18. Hrma P (2002) *Crystallization in High-Level Waste Glasses*. *Ceram Trans* 132:243–256

19. Cooper MF, Elliott ML, Eyer LL, Freeman CJ, Higginson JJ, Mahoney LA, Powell MR (1994) Research-scale melter test report, PNL-9428, Pacific Northwest Laboratory, Richland, Washington
20. Fort JA, Lessor DL, Michener TE, Recknagle KP, Elliott ML (2002) *Model predictions of the West Valley demonstration Project with Noble Metals and Alternative Electrode Configurations*, WVSP 02-09, Pacific Northwest National Laboratory, Richland, Washington
21. Casler DG, Hrma P (1999) *Nonisothermal Kinetics of Spinel Crystallization in a HLW Glass*. *Mat Res Soc Proc* 556:255–262
22. Mika M, Hrma P, Schweiger MJ (2000) Rheology of Spinel Sludge in Molten Glass. *Ceramics-Silikaty* 44:86–90
23. Plaisted TJ, Hrma P, Vienna JD, Jiricka A (2000) *Liquidus Temperature and Primary Crystallization Phases in High-Zirconia High-Level Waste Borosilicate Glasses*. *Mat Res Soc Proc* 608:709–714
24. Crum JV, Schweiger MJ, Hrma P, Vienna JD (1997) *Liquidus Temperature Model for Hanford High-Level Waste Glasses with High Concentrations of Zirconia*. In: *Scientific Basis for Nuclear Waste Management* (Editors Gray WJ, Triay IR), 465:79–85, Material Research Society, Pittsburgh, Pennsylvania
25. Hrma P, Matyáš J, Kim D-S (2002) *The Chemistry and Physics of Melter Cold Cap*. In: *9th Biennial Int. Conf. On Nucl. And Hazardous Waste Management*, Spectrum '02, American Nuclear Society, CD-ROM
26. Kim D-S, Dutton BC, Hrma P, Pilon L (2006) *Effect of Furnace Atmosphere on E-glass Foaming*. *J Non-Cryst Solids* 352:5287–5295
27. Hrma P, Vienna JD, Ricklefs JS (2003) *Mechanism of Sulfate Segregation during Glass Melting*. *Mat Res Soc Proc* 757:147–152
28. Hrma P, Vienna JD, Buchmiller WC, Ricklefs JS (2004) *Sulfate Retention during Waste Glass Melting*. *Ceram Trans* 155:93–100
29. Hrma P, Bagaasen LM, Schweiger MJ, Evans MB, Smith BT, Arrigoni BM, Rodriguez CP, Yokuda ST, Matyas J, Buchmiller WC, Gallegos AB, Fluegel A, Kim D-S (2007) *Bulk Vitrification Performance Enhancement: Refractory Lining Protection Against Molten Salt Penetration*, PNNL-16773, Pacific Northwest National Laboratory, Richland, Washington, USA
30. Hrma P (1990) *Melting of Foaming Batches: Nuclear Waste Glass*. *Glastech Ber* 63K:360–369
31. Kim D-S, Hrma P (1990) *Volume Changes During Batch to Glass Conversion*. *Ceram Bull* 69[6]:1039–1043
32. Kim D-S, Hrma P (1991) *Foaming in Glass Melts Produced by Sodium Sulfate Decomposition under Isothermal Conditions*. *J Am Ceram Soc* 74[3]:551–555
33. a) Riley BJ, Hrma P, Rosario JA, Vienna JD (2002) *Effect of Crystallization on High-Level Waste Glass Corrosion*. *Ceram Trans* 132:257–265
b) Hrma P, Riley BJ, Vienna JD (2003) *Corrosivity of Partially Crystallized Glasses*. *Ceram Trans* 143:291–298
34. Hrma P, Vienna JD, Yeager JD (2003) *Waste Glass Corrosion: Some Open Questions*. *Ceram Trans* 143:245–251
35. Jiricka A, Vienna JD, Hrma P, Strachan DM (2001) *The effect of experimental conditions and evaluation techniques on the alteration of low activity glasses by vapor hydration*. *J Non-Cryst Solids* 292:25–43



Chapter 25

Modified surfaces for implants

25. PHYSICO-CHEMICAL SURFACE PROPERTIES, THEIR MODIFICATIONS AND HEALING CAPACITY OF INORGANIC ENDOSTEAL BIOMATERIALS USED FOR MIMETIC BONE SUBSTITUTION IN IMPLANTOLOGY

Jakub Strnad, Zdeněk Strnad

25.1. Healing and new bone formation

Healing of a bone defect represents a complex process comprising multiple simultaneous and consecutive phenomena, some of which might be affected by the presence of an implanted material. Healing of an injury caused by implanting a material into the bone has common features with healing a fracture. Discontinuity of bone tissue occurs in both cases with the presence of blood, which is also the first medium interacting with the surface of the implant. Releasing of blood into the point of the defect causes activation of platelets which, together with additional blood plasma coagulation factors, participate in the formation of a blood clot, consisting of fibrin mesh [1], persisting at the point of the defect for several days to 2 weeks. Activated platelets release growth factors (e.g. PDGF, TGF- β 1,2), which support stem cells osteoblastic differentiation, and thus might cause rapid increase of the number of osteogenic cells, capable of forming an underdeveloped woven bone tissue [3,4]. The main type of cells that are present at the point of healing are the white blood cells – neutrophils, which are later replaced (after 24 - 48 hours) with monocytes - macrophages. These are also the main type of cells, interacting with the material surface in the first healing phases. Blood clot and necrotic (dead tissue) is degraded by macrophages. Anaerobic metabolism occurs due to a lack of oxygen in the centre of the blood clot which is not sufficiently vascularised, the main product of which – lactate – locally reduces the pH value [1]. The initial blood clot is replaced with fibrous vascularised tissue.

Like in the case of bone fracture, in the case of a foreign implant material the new bone tissue regenerates through the processes of osteoconduction, the new formation of the bone and its remodelling. The osteoconduction process is carried out by migrating osteogenic cells that differentiate into osteoblasts and, after settlement, begin formation of a new bone. This can be effected both in the 3D space of the biological environment and also on the surface of a solid substrate – a remodelled bone or e.g. an implant. Settling new osteogenic cells along the substrate surface, their differentiation and subsequent new bone formation thus cause an observed and apparent “growth” of bones along the surface of the implant. The new-formation proceeds in four steps: adsorption of non-collagen proteins to the surface, their mineralisation by crystal growth, creation of collagen matrix-osteoid and its mineralisation [1]. Formation of bones by osteoconduction and new bone formation differs from the mechanism of appositional growth where the new bone matrix is already formed by differentiated osteoblasts of which the already formed bone consists. The growth of the bone as described is 50 to 80 times slower than the growth by osteoconduction.

Bone represents a dynamic tissue where continuous formation and resorption take place. In general, formation proceeds by composition of collagen matrix-osteoid which subsequently mineralises through bone apatite crystals formation. However, under certain circumstances, formation of bones is non-continuous which results in formation of resting and reversal lines. In the case of a resting line, the differentiated osteoblast osteogenic activity (of appositional growth) drops temporarily, which comes out in formation of bone lamellas. When the osteogenic activity renews, osteoid is formed, and osteoblastic protrusions remain

in contact with the osteocytes in the formerly formed bone. Resting line represents a temporary drop of osteogenic activity. When renewed, osteoid comes into existence. The reversal line represents discontinuity on which a new bone is formed by the population of newly differentiating osteocytes. The first structure that is formed is the cement line (mineralization line), the main constituent of which is crystalline bone apatite.

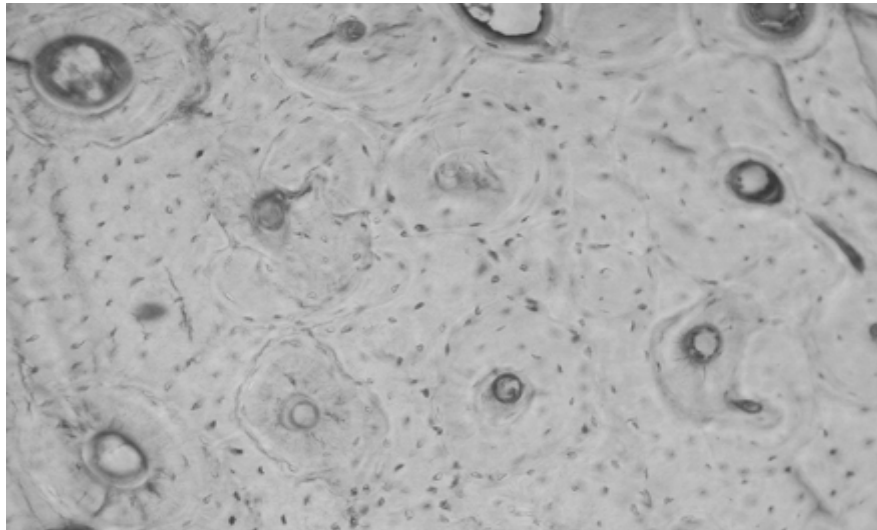


Fig. 1. Bone lamellas bounded with cement lines.

Reversal or cement lines (mineralization line) are formed when a bone is formed in areas where the bone was removed by e.g. osteoblastic activity or in surgery during preparation of the implant bed. In the above described case, the cement line is formed as the first step of the new-formation process (through a new population of differentiating osteogenic cells that already have no contact with the osteocytes of the bone on which the new formation takes place. The osteoblastic cell protrusions proceed to the new source of nutrition – from the original bone. An example of a cement line can be demarcation of bone lamellas from the neighbouring bone, the first description of which dates back to 1875 (*von Ebner*) (Fig. 1). As was found out by the analysis of cement lines in the bone, they contain mainly calcium and phosphorus but in a lower amount than in the neighbouring bone tissue. On the contrary, higher content of sulphur than in the neighbouring area was detected, which is probably caused by the presence of sulphated non-collagen bone proteins [5, 6]. The cement line thus represents a structure, formation of which on the surface of discontinuity precedes the formation of a new bone, and which is a reaction of osteoblastic cells to a foreign but biocompatible body. Davies et al. observed in the bone marrow cell culture formation of a similar extracellular matrix, consisting of globular non-collagen accretions, rich in phosphorus and calcium, and containing sulphur. These accretions were formed on all the tested materials that formed the surface of culture dishes (polystyrene, PTFE- Teflon, pure titanium and Ti6Al4V alloy) [2].

25.2. Main types of bone-implant interface

25.2.1 Biocompatibility

Implantation of material into the body environment causes mutual interaction. Body fluids represent a reactive environment which causes material degradation – e.g. depolymerisation of polymers, metal corrosion, dissolving of glassy materials. Products of this interaction act on their neighbourhood, thus inducing a response (e.g. an inflammation).

Biocompatibility is defined as an ability of material to induce such reaction that allows its functionality in specific application [7]. Thus the material can be biocompatible under certain conditions, however not under any conditions. For instance, the same material used in a different form (powder and monolithic) can induce a totally different reaction of tissue. Biocompatibility is not a purely material feature but has to be evaluated in relation to the situation in which the material was used. Toxicity-showing materials can be identified as insufficiently compatible. Toxicity is connected with increased material reactivity in the body environment, causing formation of toxic reaction (corrosive) products. The organism tries to isolate such material by means of non-adherent bushing of connective tissue when the thickness of soft tissue grows with the material toxicity. This reaction (*fibrointegration*) can be observed with certain metal materials. The fibrous case, enclosing the implanted material, disables the direct link with the bone and, at the same time, disallows transfer of mechanical load to the neighbouring tissue. Thus the implant cannot fulfil its function and, in most cases, just fails. Interaction of bone tissue with biomaterials, leading to the formation of the bone-implant function interface, can proceed in several basic manners. There are a number of factors that decide about the way of interaction and the type of the resulting interface. These factors are listed in Table 1 below:

Tab. 1. Factors affecting the bone-implant interface [8]

<i>Tissue side</i>	<i>Implant side</i>
<i>Type of tissue</i>	<i>Chemical and phase composition</i>
<i>Health condition of tissue</i>	<i>Surface morphology</i>
<i>Age of tissue</i>	<i>Surface porosity</i>
<i>Blood circulation – vascularity</i>	<i>Chemical reactivity, stability</i>
<i>Implantation method – congruence with tissue</i>	<i>Implantation method – congruence with tissue</i>
<i>Mechanical load – mobility</i>	<i>Mechanical load – mobility</i>

25.2.2. Bioinert materials

Non-reactive, almost inert materials are characteristic with high corrosion resistance (low reactivity) in the body environment. It is shown in e.g. oxide ceramic materials based on ZrO_2 , Al_2O_3 , polymer materials, such as PE (polyethylene), PTFE (teflon) and also metal materials, such as surface-untreated titanium or tantalum. A fibrous case is formed even in these materials. Its thickness depends on the factors specified in Table 1, and usually is significantly smaller than in the case of toxicity-showing, more reactive materials. For instance, if the bone bed congruency and the implant surface are excellent and there is no motion on the interface, direct contact with bone tissue can be achieved (e.g. in the case of the so-called press fit implantation).

25.2.3. Bioactive materials

A common characteristic of bioactive materials is the type of their chemical reactivity. Bioactive materials are either directly calcium phosphates, or the creation of calcium phosphates on their surface is the result of their reaction with blood plasma. Thus they successfully imitate the chemical and phase composition of the primary inorganic component of bone tissue – apatite, which serves as a substrate for the formation of a new bone even in the case of natural bone tissue formation.

In the case of bioactive glasses or glass-ceramic materials [8], SiO_2 gel structure is

formed, rich in Si-OH groups, supporting adsorption of calcium and later phosphate ions from the solution. Calcium phosphates, the composition and structure of which is similar to that of bone apatite, serve subsequently to osteogenic cells as a substrate for the formation of a mineralization line – the first structure of the newly forming bone tissue. This bioactive reactive material characteristic can thus speed up the formation of mechanically stable interaction with the newly formed bone. The induction ability of hydroxyl groups observed with bioglasses of hydroxyapatite (HA)-based bioactive materials is replaced with structural and chemical similarity to the substrate (synthetic hydroxyapatite) and the originating bone apatite (epitaxial growth). The calcium and phosphorus ions, dissolved from the hydroxyapatite surface, also increase supersaturation of the neighbouring solution towards the apatite, thus enhancing the driving power of its formation. The main representatives of bioactive materials are e.g. bioactive glasses (Bioglass®), glass-ceramic materials, some calcium phosphates (e.g. hydroxyapatite) or some chemically modified titanium surfaces. Unlike inert materials, bioactive materials create a direct, mechanically resistant bond with the bone tissue, which allows uniform transfer of load to the bone tissue, thus providing a prerequisite of long-term functionality of bioactive material. Also the interface of bioactive material with bone depends on such factors as micro movement on interface, quality of bone tissue, congruency of bone bed and implant (Tab.1). However, this dependency is not that significant as in the case of inert materials. In general, bioactive materials are more tolerant to unfavourable conditions of healing, such as movement of implant, or gap on the bone-implant interface. As was demonstrated, a bioactive surface (e.g. hydroxyapatite) is capable of creating a direct bond to the bone even at a high level of incongruence of the bone-implant interface, up to 1mm [51-57]. In the case of machined titanium, the soft tissue intercalates under the same conditions. In addition, bioactive material tolerates better micro movements on the interface, caused by low primary stability of the implant, caused by gross incongruence of bone bed with the implant (cf. Fig.2).

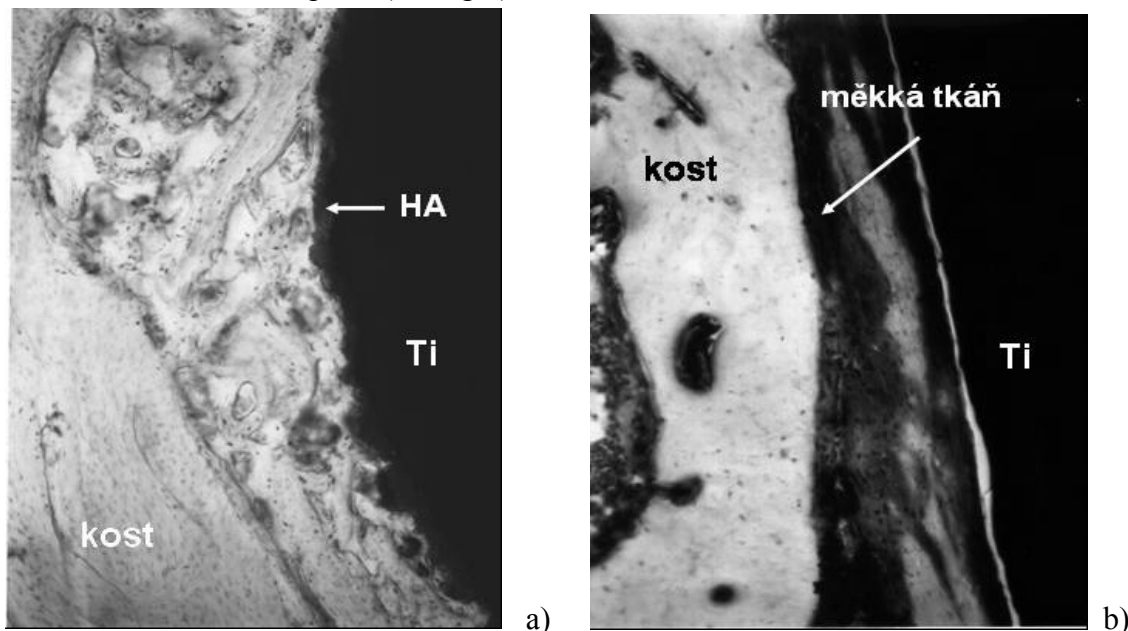


Fig. 2. Interface image of a) hydroxyapatite-coated titanium and b) mere machine-finished titanium with the intergrown bone after implantation with a low primary stability caused by gross discongruency of bone bed with the implant (stained with toluidine blue, but presented in gray portrayal) [9]. English reading on the inserted notions: kost = bone, měkká tkáň = soft tissue, HA = hydroxyapatite interface, Ti = titanium

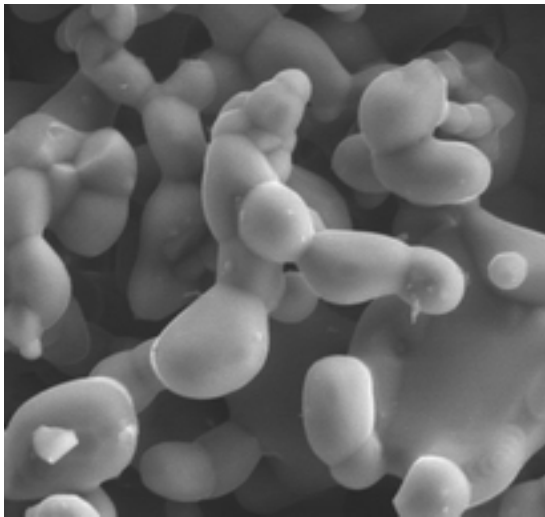
Similarly, morphology does not play such a big role in the creation of a bond with

bone as it does in inert materials (e.g. titanium). As was demonstrated, bioactive glasses create a bond regardless of the surface roughness [10]. In this context, an important characteristic of bioactive materials is their *osteoconductivity*, i.e. the ability to serve as a substrate for the process of *osteoconduction*, described in Chapter 1.1. Significantly faster formation of bone by osteoconduction on the surface of bioactive material, compared to appositional growth of the original bone in the case of inert materials, leads to a difference observed in the speed of healing and creation of direct contact with the bone of both these material groups.

It has to be taken into account that the material classification in bio-inert and bioactive can serve for indication only. The type of the interface formed between the implant and the bone is decided by the factors specified in Table 1 and, often even in case of a single material, formation of various interfaces with the bone can be observed [9]. A typical example can be titanium which, thanks to its perfect passivation with oxide layer, shows high chemical resistance which results in excellent biocompatibility. Therefore it is often classified as inert material. Yet at the end of 60s, coincidentally at the time when *L.L. Hench* discovered bioactive glasses, *P.I. Branemark* documented the ability of titanium to create direct (when observed in optical microscope) and mechanically resistant contact with bone tissue under certain circumstances [11]. This phenomenon was named *osseointegration* and represented the beginning of mass application of titanium as a material for the construction of mechanically loaded implants, especially dental and orthopaedic implants. The ability of osseointegration is explained by the character of the surface oxide layer which, upon sufficient hydration, supports absorption of calcium and phosphate ions from blood plasma, thus imitating the reaction of bioactive materials. However, considering the overall low reactivity of titanium and its alloys, the creation of bioactive interface is slower and therefore more dependent on the parameters listed in Table 1. Congruency with bone bed, and stability of the implant or its surface texture therefore have an enormous impact on the ability of osseointegration of titanium implants [12].

25.2.4. Resorbable materials

Resorbable materials represent a prospective group of biomaterials for bone tissue replacements. These materials are chemically or mechanically degraded, the process of which takes place simultaneously with the formation of new bone tissue. The resorption can only result in origin of non-toxic products that are led away by body fluids, and easy degradation of macrophage material particles must be ensured [8]. The speed of resorption should correspond with the speed of the bone tissue formation. Most important representatives of this material group are some polymer materials (e.g. based on lactic acid derivatives), some calcium phosphates (β -tri calcium phosphate) or calcium sulphate (plaster). The main function of resorbable materials is to provide scaffolding allowing migration and differentiation of osteogenic cells, their attachment and formation of an extracellular matrix with subsequent resorption of implanted material [13]. Ceramic resorbable materials on the basis of calcium-phosphoric salts show significant osteoconductive and even osteoinductive properties, affected mainly with micro and macro structure. *Z. Xingdong* [14] demonstrated that the 3D microstructure decides about the osteoconductive qualities of material, and also about the osteoconductive mechanisms. Adhesion of signal molecules depends mainly on the chemical composition and topography of material surface. Porous calcium-phosphoric ceramics are, under certain conditions, capable of capturing and concentrating morphogenic proteins to the level which allows initiating the differentiation of mesenchymal cells to osteoblastic-type cells. Thanks to its parameters, material porosity is then capable of selective prioritising of migration, attachment and proliferation of osteoblasts. This initiation of new



bone tissue formation by means of differentiating mesenchymal cells in an environment free of differentiated osteocytes is called *osteinduction*.

Fig.3. β tri-calcium phosphate. Resorbable material with optimised microporosity (scanning electron microscope – magnification 4000x, PORESORB-TCP, LASAK Ltd.).

25.3 Surface characteristics of titanium implants and their effect on osseointegration

25.3.1. Physico-chemical characteristics

Titanium used in dental implantology or orthopaedics is mostly in the form of pure titanium or Ti6Al4V alloy (Ti-6-4 hm. % by weight V). Pure titanium is formed by single phase α Ti (cryst. structure hcp) and, according to the minority element contents, purity levels are distinguished (grade 1-4). The 1-4 grades differ in the content of minority elements (ferrum, silica, oxygen, carbon, nitrogen, etc.) but mainly in the oxygen content which enhances rigidity significantly. The tensile strength of titanium thus moves from 240 (grade 1) to 740MPa (grade 4). The Ti6Al4V alloy is a double-phase material, containing α and β phases. Unlike pure titanium it shows higher tensile strength (900-1200MPa), the yield point corresponds with the corrosion-resistant steel used, and is almost double that of the Co-Cr-Mo alloy.

An important mechanical characteristic of titanium and its alloys is relatively low modulus of elasticity (100-105 GPa) which, compared to corrosion-resistant steel (210 GPa) or other metal biomaterials, is closer to the values of cortical bone (10-30GPa). If the difference between the elasticity modulus of the implanted material and that of the bone is too significant, the stress cannot be distributed perfectly to the neighbouring tissue. Areas showing non-physiological stresses (too high or too low) are created which leads to damage or resorption of the bone tissue in the area of the implant. Within the range of 1500-2500 microstrain (deformation by ppm of the original length) the bone is stationary and deformation within this range correspond with physiological load. Titanium and its alloys are among the most compatible materials used for bone replacements.

The biocompatibility of titanium is determined by its excellent corrosion resistance, caused by the presence of a protective (passivating) oxide layer on the surface which originates directly after the contact of metal titanium with traces of oxygen or water. Unless the formed passivating layer is chemically or mechanically disturbed, it prevents active dissolving of titanium and minimises the interaction of the metal with the environment. The chemical properties of titanium implants are thus, in fact, determined by the qualities of the oxide layers on their surface. The typical layer thickness is less than 10nm and, in the majority of aqueous environments, consists of titanium oxides (TiO_2 , Ti_2O_3 or TiO). The nature, composition and thickness of the layer depend on the conditions of its formation. High-temperature oxidation supports formation of crystalline TiO_2 – rutile, whilst lower temperatures usually give rise to anatase, a mixture of anatase-rutile or amorphous form of TiO_2 . The passivating layer is highly chemically resistant. Among the attacking substances are e.g. hot and concentrated mineral acids (HCl , H_2SO_4 , H_3PO_4 , HF) and alkali (NaOH).

Hydrofluoric acid and water solutions of fluorides dissolve the protective passivating layer even in low concentrations at room temperature. The oxide layer subjects to ageing and in body environment increases its thickness, becomes hydrated, and the calcium and phosphoric ions incorporate simultaneously into the surface [15]. With this particular ability to support adsorption of calcium phosphates the surface passivating layer of titanium oxides differ from the passivating layers of other, commonly used metal materials, such as corrosion-resistant steels or chromium-cobalt alloys. The main constituent of the passivating layer of these metals are chromium oxides (chrome oxide) which do not adsorb the calcium ions as they do with the titanium oxides during the initial interaction with the body environment. *Magaz* [16] explained this difference by different isoelectric point of both oxides and therefore different surface charge. In the body environment (pH ca 7.4) the steel surface has a positive charge, and therefore cannot (unlike the negatively charged titanium surface) induce adsorption of calcium ions. The difference in this fastest and initial interaction phase of the implant surface with the body environment (blood) might affect further and slower interactions with the blood plasma proteins. These results demonstrate better osseointegration ability of titanium and its alloys, compared to corrosion-resistant steels.

It can therefore be anticipated that, thanks to the convenient features of the oxide passivating layer, titanium nears to bioactive materials. However, titanium does not show the same bioactivity level as e.g. hydroxyapatite or bioactive glasses [17,18]. The difference between titanium and bioactive materials lies mainly in the kinetics of surface reactions which lead to formation of calcium-phosphoric layers. Bioactive glasses form an apatite layer of micrometer units thickness in single or tens of hours [19]. The precipitation acceleration is explained also by increased supersaturation of the simulated plasma solution towards the apatite, which is caused by pH, growing as a result of elution of alkali from the bioactive glasses surface.

Ducheyne [20] detected by means of RTG diffraction apatite on the surface of worked titanium only after 30 days of exposure in SBF. Films of calcium phosphates detected on the surface of titanium by Hanawa using XPS reached 7.9 nm thickness after 30 days of exposure in simulation solution [21]. *Hanawa* states that these thin calcium phosphate films are under electrostatic influence of metal titanium and the passivation titanium oxide layer, and therefore cannot demonstrate the calcium phosphate character in the body environment. Hanawa claims 1 μm the limit thickness of the layer when calcium phosphates begin to show their bioactive properties.

25.3.2. Surface roughness and morphology

The first enosteal dental implants (the Branemark system) were used with machined surface, without any additional surface treatment. Machined titanium can be taken as bioinert material showing strong dependency of osseointegration on the conditions of implantation (Table 1), such as implant stability, quality of bone tissue, micro movements on the interface or congruency of the bone bed with the implant. In order to achieve successful osseointegration they were extremely particular about the accurate preparation of bones, high primary stability of the implant in the bone and sufficiently long healing period (6 months in the upper and 3 months in the lower jaw) during which the implant was protected against mechanical load and micromovements. The effect of bioinert character of machined titanium can be observed in clinical studies comparing the successfulness in the upper and lower jaw, since in the upper jaw certain unfavourable conditions combine, such as low quality of bone or low primary stability of the implant after implanting. *Adell* evaluated a group of 734 implants in the upper jaw with 88% successfulness and 721 implants in the lower jaw with 94% successfulness, 1 year after the implantation. 15 years after implantation Branemark also

documented a significantly lower successfulness in the upper jaw (81%), compared to the lower (91%). The pretence at improving successfulness of osseointegration led to development of methods, modifying the implant surface.

The most frequently used surface treatments of titanium implants modify the surface morphology (roughness). To characterize the surface, longitudinal, height and shape parameters of roughness are applied which describe the extent of surface deviation from the central line, longitudinal division and shape of inequalities formed. The most frequently used parameters include: mean arithmetic profile deviation (average roughness) Sa and Mean profile spacing Sm. The Sa (or Ra in 2D) parameter is often used to characterize the surface roughness. However, this parameter does not define sufficiently the surface character as shown in Fig.4. Two surfaces with similar Ra value can thus show totally different functional properties.



Fig.4. Two surfaces with identical Ra values

The effect of surface roughness to the formation of the titanium implant bond with bone was often demonstrated in literature. The originally used machined surface used to be replaced with roughened surface through various technological procedures which resulted in better healing-in of titanium implants.

Among the least complex titanium implant surface modifications is sand blasting which is currently mostly used either as the final treatment or just as the basic surface modification of the implant. As blasting media, mostly alumina (Al_2O_3), rutile (TiO_2), glassy or calcium-phosphate powder of various grain sizes are used. Positive effect of sand blasting to the rigidity of the bone – implant bond was demonstrated in a number of studies [22, 23, 24]. *Wennerberg* et al. [25] determined on histological sections a larger contact area of implants with bone, roughed by sand blasting (if Al_2O_3 and TiO_2 are used as the sand-blasting media), than if the surface is only machined, even if Al_2O_3 and TiO_2 are used as the blasting media. In *Gottfredsena* et al.'s [25] study, dependency of the implant surface roughness was found, characterised with average deviation of surface profile from the central line (Ra) and the values of the explantation torque, necessary for interrupting the bone-implant bond. With growing size of the blasting medium (within the range of 10-125 μm), the Ra roughness value also grows, as well as the explantation torque value.

For the same roughing purposes, plasma spraying of titanium powder on the surface of titanium implants is often utilised. This modification is used to achieve roughing that is more significant or comparable to the sand blasting [26,29]. Also, the positive effect of plasma spraying of titanium to the formation of the implant/bone bond was often demonstrated [25,26]. Both plasma spraying and sand blasting about ten times increase the area of the surface with regard to the original machined surface. The positive effect of sand blasting to the formation of the implant/bone bond is mostly explained by extending the surface, interacting with environment, and thus also the space in which new bone tissue forms.

However, some works state [27,28] that the titanium surface roughness also has impact on the acting of osteoblastic-type cells which are responsible for the formation of new bone tissue in the space between the old bone and the implant surface. As was found out by *Kieswetter* et al., rough surfaces, obtained by sand blasting, titanium plasma spraying and even by etching with HCl and H_2SO_4 , affect cellular production of growth factors that influence cells differentiation. In cellular cultures in contact with rougher surfaces higher levels of alkaline phosphatase were detected, compared to a smooth machined surface, which

signal differentiation of osteoblastic cells, the LTGF- β growth factor and the bone matrix protein – osteocalcine.

Roughening of the titanium surface in micro-scale is achieved by etching in mineral acids, mainly in hydrochloric and sulphuric acid (HCl and H₂SO₄) at raised temperature. The result of active titanium dissolving is a highly rugged surface, composed of concave unevenness with spacing of protrusion in micrometer scale (see Fig. 5). Etching in acids is therefore a subtractive method and does not form any further layer on the surface of etched titanium. A micro rough surface, finished in the above described manner, is used either directly on the machined surface (the Osseotite surface, BIOMET 3i), or as a further stage of surface finishing of titanium roughened in macro-scale, i.e. by sand blasting (SLA surface, Fig 5).

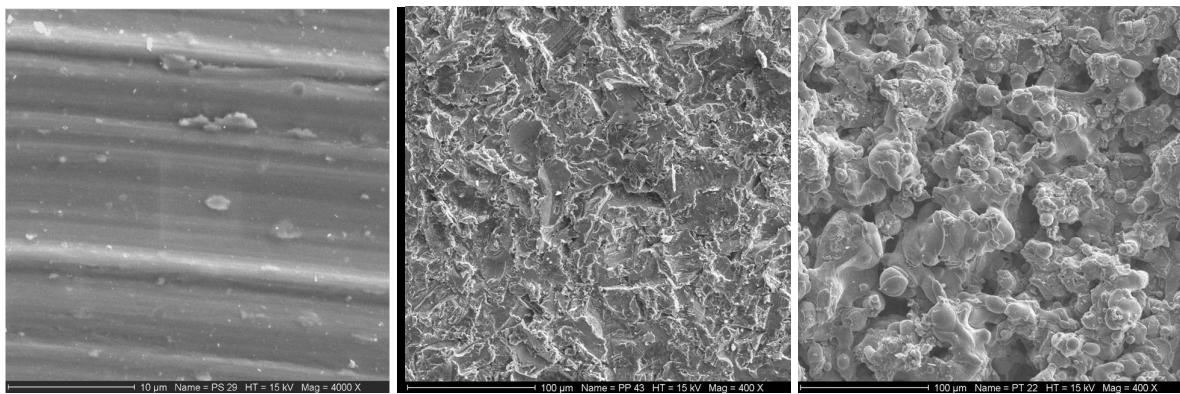


Fig. 4. Surface finishes of titanium implants that are currently in use, modifying roughness from the left: machining, sand blasting, titanium plasma spraying - TPS).

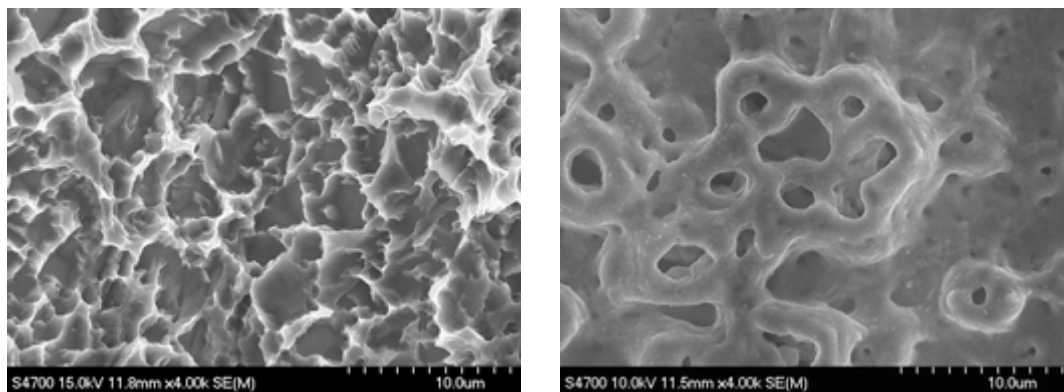


Fig.5. Currently used roughness-modifying surface finishes of titanium implants in micrometer units scale: on the left the surface is sand-blasted and etched in acid (SLA surface), on the right anodically oxidized surface (Tiunite surface)

The positive effect of acid etching to the speed of in-healing of titanium dental implants was demonstrated in a number of studies [30,31,32,33,34]. Gemmell [35] developed a hypothesis of a mechanism through which a microtextured surface contributes to accelerated healing of an implant, especially in the first phase after the implantation, when blood clot is formed. Blood clot consists of fibrin mesh, representing an environment through which osteogenic cells migrate to the surface of the implant. At the same time, blood platelets, producing growth, morphogenic factors affecting differentiation and proliferation of osteogenic cells, activate. Capturing this fibrin mesh by the micro rough implant surface causes the healing process to maintain on the implant surface, thus forming a new bone

(contact osteogenesis, see above). Lazzara [34] studied growth of bone into the hollow chamber of machined titanium and sand-blasted titanium, subsequently etched with acid. Although bone ingrowth occurred in both cases, a significantly larger surface of finished titanium was covered with a new bone, than in the case of a machined surface. After two weeks of healing in a rabbit's femur, Klokkevold [37] measured 4 times higher values of explantation torque in implants etched with acid, than in machined implants. Higher values of explantation torques were mostly measured in surfaces combining macro rough surface, achieved by sand blasting with micro roughness created by acid etching, than in surfaces that were just acid-etched [36]. Mechanical modification of roughness by sand blasting and also modification of microroughness by etching in acids improve the clinical characteristics of implants, thus enabling formation of more solid interface of bone-implant, compared to unfinished (machined) surface. However, none of these modifications change the chemical reactivity of titanium towards bioactive materials or allow easier incorporation of calcium and phosphate ions into the surface structure. Acid-etched, microrough surfaces of dental implants are currently offered by majority of dental implants manufacturers.

Another modification of titanium implants is represented by anodic oxidation in aqueous solutions of acids and salts. This modification lies in anodic oxidation in solution of mineral acid or its salt. The consequence of electric current passage is that the surface oxide layer grows to the thickness of units to tens micrometers at simultaneous formation of micropores (Fig. 5).

25.4. Bioactivation of titanium

25.4.1. Surface coating

The effort to increase bioactivity of titanium implants was solved in the eighties by coating titanium with bioactive material, mostly hydroxyapatite. This solution promised combination of bioactive properties of the coating with the good mechanical qualities of the titanium base. Synthetic hydroxyapatite $\text{Ca}_{10}(\text{PO}_4)_6(\text{OH})_2$, used mostly for coating, differs from biological apatites contained in hard tissues mainly in its crystalline structure and also in its chemical composition. Bone apatites contain as minority constituents magnesium and sodium ions and also carbonate or chloride ions.

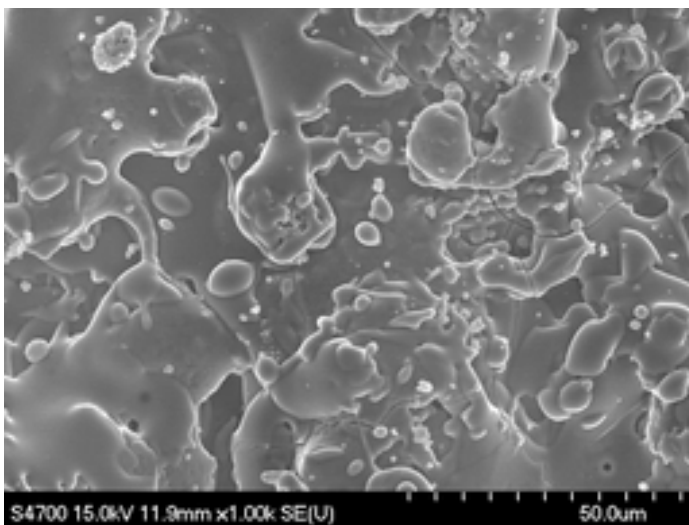


Fig. 6: Plasma-sprayed hydroxyapatite coating.

The most frequently used method of coating titanium and its alloys became plasma spraying. As a mixture of gases (Ar, He, N_2 , H_2) passes through electric arc, a plasma stream originates into which the sprayed material is brought by the carrying gas. The plasma-sprayed material melts and falls on cooler substrate [42] (Fig.6).

Main disadvantages of plasma spraying are structure changes, HA composition in consequence of thermal decomposition, imperfect adhesion of the coating to the surface,

difficult control of the crystallinity grade and the phase composition of the product.

The HA adhesion to the surface must be enhanced by surface roughening, e.g. by sand blasting. Crystallinity affects significantly resorption of the layer in the body. Highly crystalline coatings are more stable but more incline to fragmentation (release larger particles). The most frequent thicknesses achieved by plasma-sprayed layers are several tens micrometers. Thus they modify the shape of the titanium base and its fine shapes (e.g. fine threads or edges of self-cutting implants).

During hydroxyapatite plasma spraying, dehydroxylation and formation of additional phases might occur, e.g. oxyapatite CaO, α -TCP (tricalcium phosphate), β -TCP, tetracalcium phosphate (TTCP) and amorphous calcium phosphates. [43]

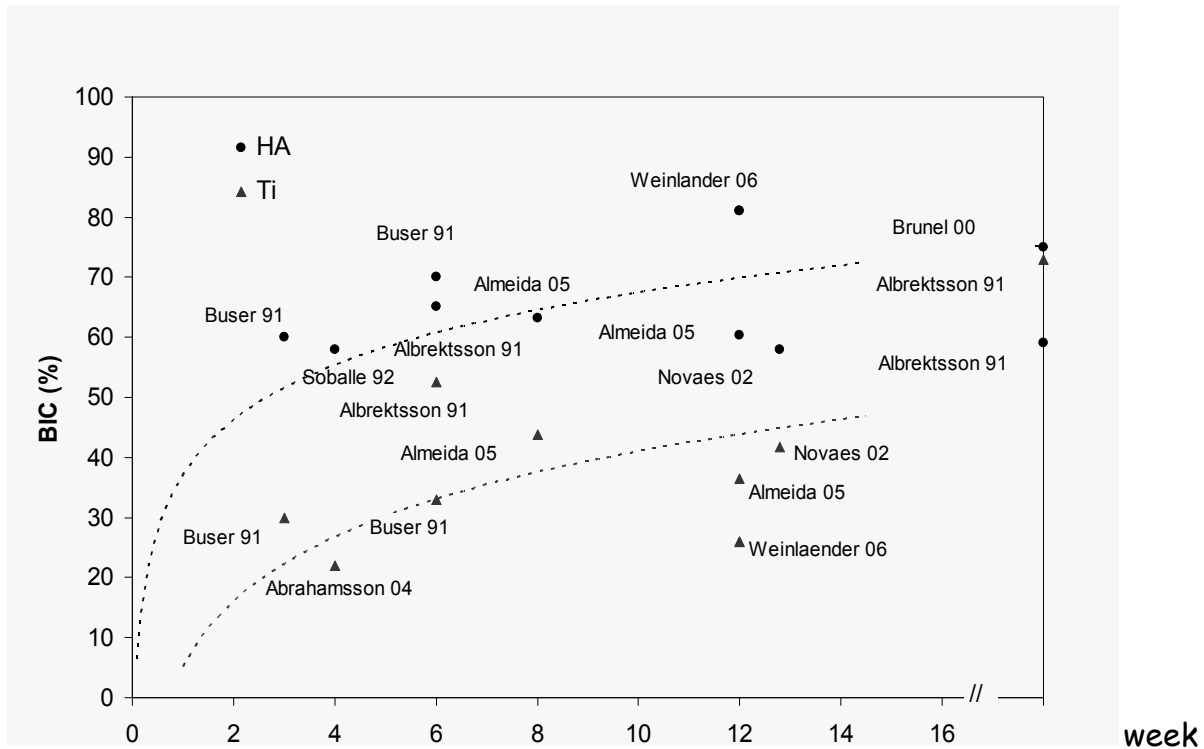


Fig. 7. Published percentage values of bone-implant contact (BIC) for plasma-sprayed hydroxyapatite surface (HA) and uncoated titanium (Ti).

β - tricalcium calcium phosphate, (β -Ca₃(PO₄)₂, β -TCP) is, together with hydroxyapatite, the most frequently used material in bone tissue regeneration. It differs from hydroxyapatite mainly in the type of crystalline structure, chemical composition (molar ratio Ca/P=1.5) and in some chemical any physical properties. TCP forms high-temperature (α -TCP) and low-temperature β - TCP phases that differ in their crystalline structure which causes higher α -TCP reactivity and thus resorbability in aqueous environment [44]. Solubility of most frequent calcium phosphates drops as follows: TTCP >> α -TCP >> β -TCP >>HA, and, at the same time, increases significantly with decreasing pH. Calcium phosphate-based coatings and augmentation materials are therefore very sensitive to the presence of acidic medium, caused e.g. by inflammation. The literature documents observations of partial or full degradation of hydroxyapatite coatings [12,49] after implantation but there are also works in which degradation was not documented at all. Degradation of coatings is often associated with new formation of bone which replaces the dissolved coating whilst maintaining tight contact with the bone tissue [47]. Despite the aforementioned disadvantages, implants coated with hydroxyapatite are capable of significantly faster bond with bone tissue, compared to implants of pure machined or only roughened titanium. A faster and stronger bond to the bone

is mostly demonstrated by higher values of percentage contact of the implant with the bone (BIC, bone-implant contact) (12,46,48) or by higher values of the force or torque that is necessary to disturb the bone-implant interface [47,45] (Fig.7).

Thanks to bioactive characteristic, hydroxyapatite coatings show higher ability of bonding to bone, mainly in unfavourable conditions of implantation, such as micro movement on interface, low bone stability or quality [9,47]. As was recorded, bioactivity of HA coatings contributes more significantly to the formation of stable interface with bone than the macro rough relief of plasma surface. Plasma-sprayed titanium showed lower BIC in the same time, compared to HA coating [51,52]. In the 1990s, first efforts were made for modification of surface of implants not only considering the ideal morphology but, by means of chemical modification; bring the behaviour of titanium implants near bioactive materials, without coating titanium with a layer of bioactive material. This objective was achieved in several ways.

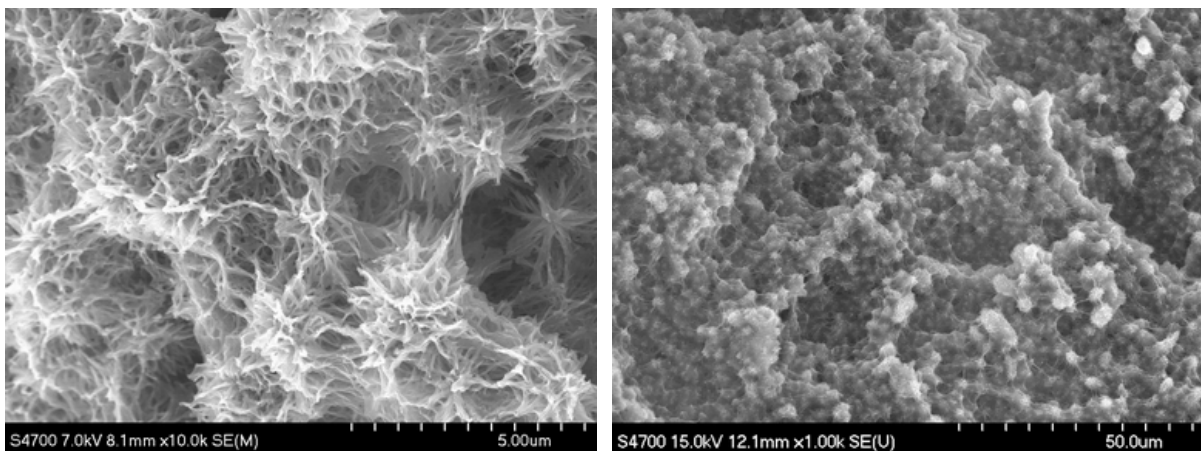


Fig 8. Biosurface (chemically modified bioactive surface of titanium of Lasak Ltd. ®), on the left: sub microstructure of Biosurface; on the right: Surface macro- and microstructure

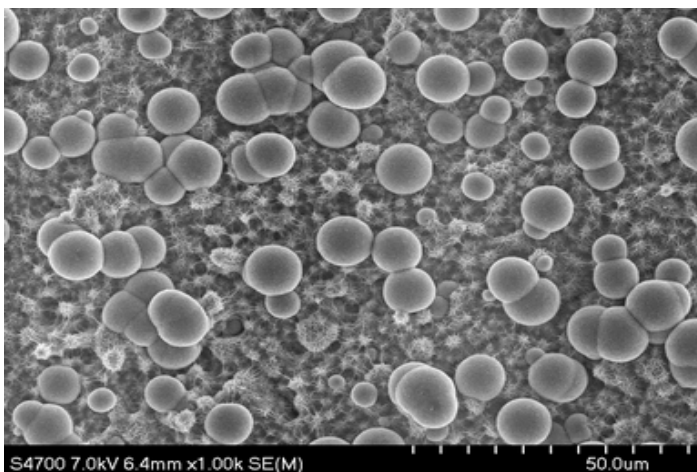


Fig. 9. Bone apatite spherulites, precipitating on surface of chemically modified bioactive titanium (Biosurface ®, scanning electron microscope)

25.4.2. Surface chemical bioactivation

The first procedure through which the bioactive reaction characteristic was achieved was surface treatment in alkaline environment [38]. During the said process, the passivation oxide layer dissolves and, by subsequent active dissolving of metal, ended with interaction with aqueous environment, hydrated, porous titanium oxide originates. (fig.8).

The same as bioactive materials (bioglasses, hydroxyapatite), this surface shows the ability to induce adsorption of calcium phosphates from blood plasma solution and, in solution simulated by inorganic part of blood plasma, induces formation of apatite mineral, the main inorganic constituent of bones (cf. Fig. 9).

The alkaline surface treatment was applied on a surface that was pre-roughed by sand blasting using rough blasting medium and subsequent etching in acid. By this combination of surface treatments, surface morphology at three levels was achieved: macrorough surface as the result of sand blasting, microroughness as the result of acid etching and alkaline treatment, modifying reactivity and creating micro- to nano- porosity (BIO surface ®, LASAK Ltd.). Using this method, a bioactive reaction characteristic of final surface was achieved. Thanks to relative complexity of the surface, high relative surface area increase was achieved in relation to machined titanium (about 140 times) [52]. The presence of hydroxyl groups on titanium surface provides excellent wetting properties of the modified surface. Wetting angle achieves relatively low values (approx. 20°) mainly in relation to strongly hydrophobic, acid-etched surfaces (119°). This feature allows instant interaction of blood with the entire complex implant surface whilst in hydrophobic surfaces instant ion and other interactions with blood might be significantly complicated (Fig.10).

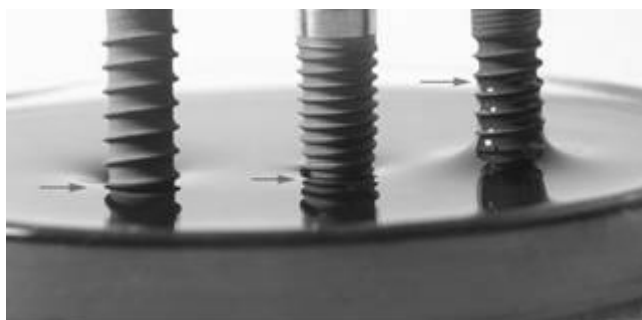


Fig. 10. Contact of three selected surfaces with blood (left: anodically oxidised titanium, in the middle: sand-blasted and acid-etched surface, right: bioactive sand-blasted, acid-etched and in alkaline-environment modified titanium (biosurface), the arrows point the highest point of the implant-blood contact).

Results of in-vitro study [39], comparing cellular reaction of osteoblastic cells on three tested surfaces (machine titanium, sand-blasted titanium and acid-etched titanium, Biosurface) demonstrated the effect of Biosurface on cellular adhesion and osteoblastic differentiation. Biosurface showed significantly higher percentage of adhering cells (cf. Fig.11) when

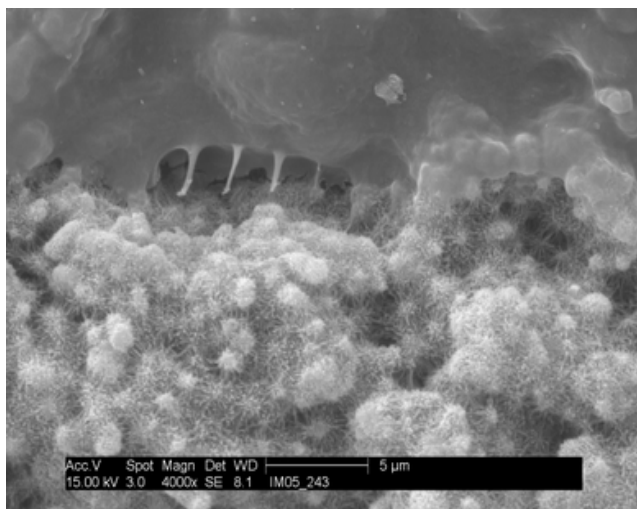


Fig 11. Osteoblastic-type cell adhering to the surface of chemically modified titanium (Biosurface ®, Lasak Ltd.)

compared to sand-blasted acid-etched and machined surfaces. The attractiveness of Biosurface for osteoblastic cells was confirmed by increased adsorption of fibronectin (binding cellular protein), compared to other surfaces. The cells cultivated on Biosurface showed, compared to other tested surfaces, higher production of osteopontin, the main component of the first mineralised bone

matrix, formed by osteogenic cells on the implant surface. The ability of alkaline-modified titanium to induce formation of bone tissue was tested in vivo even in soft tissues of dorsal dogs' muscles, i.e. in localities without osteogenic cells and other osteogenic factors, where

ossification does not normally occur. Samples of modified and unmodified titanium in form of porous blocks and fibrillar nets were implanted for 3 to 12 months. After 12 months bone was only identified in the samples of alkaline-modified titanium. This study represents the first evidence of osteoinductive properties of metal biomaterial [41].

Another way of chemical bioactivation was studied by *Elingsen* [40]. Modification of titanium by aqueous fluoride solution was achieved by enriching the surface with fluorine which, similarly as bioactive materials hydroxyl groups, initiates adsorption of bone mineral to the implant surface. The advantage of this modification is the fact that fluoride ions modify bone apatite to fluorapatite which shows higher crystallinity than hydroxyapatite. Bioactive behaviour in vivo conformed to the results observed during the exposition of fluoride-modified titanium in simulated blood plasma solution where apatite spherulites of similar morphology were formed as in case of Biosurface (cf. Fig. 9). [40]. The fluoride surface treatment, ensuring titanium bioactivity, is utilised in preparation of implant surfaces by *Astratech* company (surface Osseospeed). These unique procedures point at potential trend of dental implants modification development, ranging from macro- and microroughness optimisation to optimisation of nanostructure and related chemical reactivity in body environment.

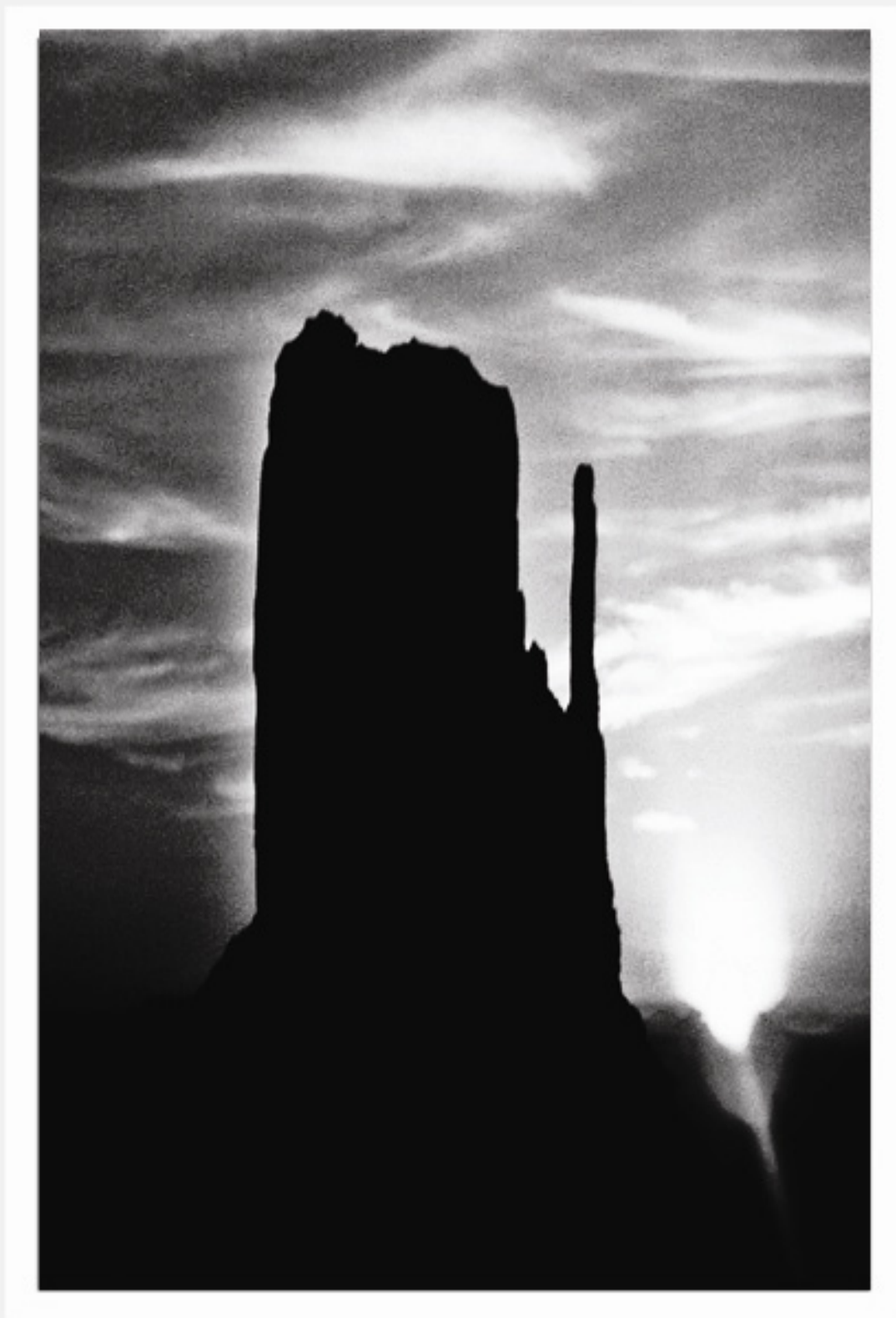
References 26:

1. J.E.Davies J.E. Hosseini M.M.: *Histodynamics of Endosseous Wound Healing in Bone engineering*, ed. J.E.Davies, EM squared Inc. 2000, p.9.
2. J.E.Davies, N. Nagai, N. Takeshita, D.C. Smith. *Deposition of cement-like matrix on implant materials*, In: the bone-biomaterial interface, ed. J.E. Davies, University of Toronto Press, 1990, p. 284-294.
3. R.E.Marx: *Platelet Concentrate: A strategy for accelerating and improving bone regeneration in Bone engineering*, ed. J.E.Davies, EM squared Inc. 2000, p.9.
4. R.E.Marx, E.R. Carlson, Eichenstaedt RM, Schimmele SR, Strauss JE, Georges KR *PRP: growth factor enhancement for bone graft*. Oral Surg Oral Med Oral Pathol Oral Radiol Endod. 1998; 85(6): 638-646
5. M.B.Schaffler, D.B.Burr, R.G.Frederickson, *Morphology of the osteonal cement line in human bone* Acta Anat 217, 1987, 223-228
6. J.E. Davies, P.Ottensmeyer, X.Shen, M. Hashimoto, S.A.F. Peel *Early Extracellular matrix synthesis by bone cells*, In: The bone-biomaterial Interface, ed. J.E. Davies, University of Toronto Press, 1990., p.214
7. Langeland K. *Biocompatibility An Overview*, Concise encyclopedia of Medical and dental mat.,pergamon press (1990)
8. Hench L.L., Anderson O. *Bioactive glasses*. In: *An introduction to Bioceramics*, eds. Hench L.L.Wilson J, World Scientific Publishing 1993, 41-63
9. Z.Strnad, J.Strnad, C.Povýšil, K.Urban: *Effect of plasma-sprayed hydroxyapatite coating on osteoconductivity of commercially pure titanium implants*, Int. J. Oral Maxillofac. Implants, Vol.15, No.2 2000,483
10. J. Eulenberger, Kelm F, Schroeder A., Steinemann S.G., *Haftung zwischen knochen und titan: 4. DVM Vortrags-reihe Implantate*, Ed. DVM, (1983) 108
11. P.I. Brånemark, *Intraosseous anchorage of dental prostheses*, Scand. J. Plast. Reconstr. Surg, 1969;3:81-93.

12. D. Buser, R.K. Schenk, S. Steinemann, J.P.Fiorellini, C.H. Fox, H.Stich, *Influence of surface characteristics on bone integration of titanium implants. A histomorphometric study in miniature pigs.* J. of Biomed. Mater. Res, 25, 889-902, 1991
13. J.S.Temenoff, L.Lu, A.G.Mikos, *Bone-tissue engineering usány syntheticbiodegradable polymer scaffolds* In: Bone Engineering,, ed. J.E.Davies, EM squared Inc. 2000, p.454
14. Z. Xingdong, Y.Huipin, K. de Groot: *Calcium Phosphate Biomaterials with Intrinsic Osteoinductivity*, In: Proceedings of Sixth World biomaterials Congress, Kamuela, Hawaii, USA, May, 2000
15. P. Li, I Kangasniemi, K. de Groot, Kokubo, *Bonelike HA induction by a gel-derived titania on a titanium substrate*, J. Am. Ceram. Soc., 77(5), 1307 (1994)
16. Magaz G. E. Rodenas L.G. Morando P.J. Blesa M.A. *Electrokinetic behavior and interaction with ozalid acid of different hydrous chromium III oxides.* Croatica Chemica Acta 71, (4), 1998, 917-927
17. Sun L, Berndt CC, Gross KA, Kucuk A. *Material fundamentals and clinical performance of plasma-sprayed hydroxyapatite coatings: a review.* J Biomed Mater Res, 58(5), 2001, 570-592
18. Vercaigne S, Wolke JG, Naert I, Jansen JA. Clin Related Articles, *Bone healing capacity of titanium plasma-sprayed and hydroxylapatite-coated oral implants.* Oral Implants Res 9(4), 1998, 261-271
19. Ogino M., Ohuchi F. Hench L.L. *Compositional dependence of the formation of calcium phosphatite films on Bioglass*, J. Biomed Mater. Res. 14, 1980, 55-64
20. Li P, Ducheyne P. *Quasi-biological apatite film induced by titanium in a simulated body fluid.* J Biomed Mater Res ; 1998;5, 41(3); 341-348
21. Hanawa T. *Titanium and its oxide film: A substrate for formation of apatite.* In: *The Bone-biomaterial interface.* Ed: J.E. Davies, University of Toronto Press, 1990, 33-48
22. Wennerberg A, Albrektsson T, Lausmaa J *Torque and histomorphometric evaluation of c.p. titanium screws blasted with 25-and 75-microns-sized particles of Al₂O₃.* J Biomed Mater Res. 1996 Feb; 30(2):251-60
23. Wennerberg A, Albrektsson T, Andersson B, Krol J.J.. *A histomorphometric and removal torque study of screw-shaped titanium implants with three different surface topographies.* Clin Oral Implants Res. 1995 Mar; 6(1):24-30
24. Wennerberg A, Ektessabi A, Albrektsson T, Johansson C, Andersson B.. *A 1-year follow-up of implants of differing surface roughness placed in rabbitbone,* Int J Oral Maxillofac Implants 1997 Jul-Aug; 12(4):486-94
25. Wennerberg A, Albrektsson T, Johansson C, Andersson B. *Experimental study of turned and grit-blasted screw-shaped implants with specialempphasis on effects of blasting material and surface topography.* Biomaterials 1996 Jan; 17(1):15-22
26. Gotfredsen K, Berglundh T, Lindhe J. *Anchorage of titanium implants with different surface characteristics: an experimental study in rabbits.* Clin Implant Dent Relat Res 2000; 2(3):120-8
27. Kieswetter K, Schwartz Z, Hummert TW, Cochran DL, Simpson J, Dean DD, Boyan BD. *Surface roughness modulates the local production of growth factors and cytokines by osteoblast-like MG-63 cells.* J Biomed Mater Res. 1996 Sep; 32(1):55-63.
28. Boyan BD, Batzer R, Kieswetter K, Liu Y, Cochran DL, Szmuckler-Moncler S, Dean *Titanium surface roughness alters responsiveness of MG63 osteoblast-like cells to I alpha,25-(OH)2D3* J Biomed Mater Res. 1998 Jan; 39(1):77-85..

29. M.H.Prado da Silva, G.A.Soaes, C.N. Elias,J.H.C.Lima, H. Schechtman,I.R.Gibson, S.M.Best, *Surface Analysis of Titanium Dental Implants with Different Topographies*, Materials Research, Vol. 3, No. 3, 61-67, 2000.
30. Rocuzzo M, Bunino M, Prioglio F, Bianchi SD. *Early loading of sandblasted and acid-etched (SLA) implants: a prospective split-mouth comparative study*. Clin Oral Implants Res 2001 Dec; 12(6):572-8
31. Cochran DL, Buser D, ten Bruggenkate CM, Weingart D, Taylor TM, Bernard JP, Peters F, Simpson JP. *The use of reduced healing times on ITI implants with a sandblasted and acid-etched (SLA) surface: early results from clinical trials on ITI SLA implants*. Clin Oral Implants Res 2002 Apr; 13(2):144-53
32. Klokkevold PR, Johnson P, Dadgostari S, Caputo A, Davies JE, Nishimura RD. *Early endosseous integration enhanced by dual acid etching of titanium: a torque removal study in the rabbit*. Clin Oral Implants Res 2001; 12(4): 350-357.
33. Khang W, Feldman S, Hawley CE, Gunsolley J. *A multi-center study comparing dual acid-etched and machined-surfaced implants in various bone qualities*. J Periodontol 2001; 72(10):1384-1390
34. Lazzara RJ, *Bone response to Dual Acid-Etched and Machined Titanium Implant Surfaces*. In: Davies JE. Bone engineering. Toronto: Em squared Inc, 2000, p.381-388.
35. Gemmell C.H. Park J.Y. *Initial blood interactions with endosseous implant materials* In: Bone Engineering, ed. J.E. Davies, EM squared Inc. 2000, p 108
36. Li D, Ferguson SJ, Beutler T, Cochran DL, Sittig C, Hirt HP, Buser D. *Biomechanical comparison of the sandblasted and acid-etched and the machined and acid-etched titanium surface for dental implants*, J Biomed Mater Res. 2002 May;60(2):325-32.
37. Klokkevold PR, Nishimura RD, Adachi M, Caputo A. *Osseointegration enhanced by chemical etching of the titanium surface. A torque removal study in the rabbit*. Clin Oral Implants Res. 1997 Dec; 8(6):442-7.
38. Kokubo T, Myaji F, Kim HM, Nakamura T, *Spontaneous formation of bonelike apatite layer on chemically treated titanium metals*, J. Am. Ceram. Soc, 79, 4,1127-1129, 1996
39. Protivinsky J., Appleford M., Strnad J., Helebrant A. Ong J.L. *The influence of titanium surface morphology on protein adsorption and osteoblast response*, In: Proceedings of the Biomedical Engineering Society Meeting, USA, 2005.
40. Elingsen J.E. *On the properties of surface-modified titanium*. In: Davies JE. Bone engineering. Toronto: Em squared Inc, 2000, p.183-189
41. S. Fujibayashi, M. Neo, H.M. Kim, T. Kokubo, T. Nakamura: *Osteoinduction of porous bioactive titanium metal*. Biomaterials, 25(3), Feb 2004, p.443-450.
42. Lugscheider E. et al., *Plasma sprayed coatings of calcium titanium phosphate*, Bioceramics 8, 317 (1995)
43. Whitehead R.Y et.al, *Structure and integrity of a plasma sprayed HA coating on titanium*, J. of Biomed. Mat. Res, 27,1501 (1993)
44. Elliot J. C (ed.). *Structure and Chemistry of the Apatites and Other Calcium Orthophosphates*, The London Hospital Medical College, Elsevier: Amsterdam. 1994.
45. C.P. Klein, P. Patka, J.G. Wolke, J.M. de Blicck-Hogervorst, K. de Groot: *Long-term in vivo study of plasma-sprayed coatings on titanium alloys of tetracalcium phosphate, hydroxyapatite and alpha-tricalcium phosphate*, Biomaterials, 15(2), Jan 1994, p.146-150.

46. Gottlander M, Johansson CB, Albrektsson T. *Short- and long-term animal studies with a plasma-sprayed calcium phosphate-coated implant.* Clin Oral Implants Res. 1997 Oct;8(5):345-51.
47. Soballe K. Acta Orthop Scand (Suppl 255) 1993; 64
48. Conner KA, Sabatini R, Mealey BL, Takacs VJ, Mills MP, Cochran DL. *Guided bone regeneration,* J Periodontol. 2003 May;74(5):658-68.
49. Pilliar RM, Deporter DA, Watson PA, Pharoah M, Chipman M, Valiquette N, Carter, S, De Groot K. *The effect of partial coating with hydroxyapatite on bone remodeling in relation to porous-coated titanium-alloy dental implants in the dog.* J Dent Res. 1991 Oct;70(10):1338-45.
50. Strnad J., Protivínský J., Strnad J., Veselý P “*Chemically treated titanium: early surface activity detected in vitro:*” Clin. Oral impl. Res., Vol.13, 4, 2002
51. Strnad J, Urban K, Strnad Z *The effect of bioactive surface on implant stability during healing,* Clin. Oral. Impl. Res. Vol. 16, 4, 2005
52. Štěpánek A, Strnad J, Strnad Z *Effect of primary stability on early loaded implants,* Clin. Oral. Impl. Res. Vol 16, 4, 2005
53. Clemens JAM, Klein CPAT, Dhert WJA., Rozing PM “*Bone apposition on apatite coatings inhibited by large gaps*” Bioceramics, Vol. 7
54. Strnad J, Protivinsky J, Mazur D, Veltruská K, Helebrant A, Šesták J, Strnad Z, *Interaction of acid and alcali treated titanium with dynamic simulated body environment* J. Thermal Anal. Calor. 76, 17, 2004
55. Strnad J, Strnad Z, Šesták J, Urbana M, Povýšil C „*Bio-activated Titanium Surface Utilizable for Mimetic Bone Implantation in Dentistry; Part III: surface characteristics and bone-implant contact formation*” J. Phys. Chem. Solids 68, 841, 2007
56. Strnad J, Strnad Z, Šesták J „*Physico-chemical properties and healing capacity of potentially bioactive titanium surface*“ J. Thermal Anal. Calor. 8, 775, 2007
57. Šesták J, Strnad Z, Strnad J, Holeček M, Koga N “*Biomedical thermodynamics and implantology aspects of biocompatible glass-ceramics and otherwise modified inorganic materials and surfaces*” Advanced Materials Research 39/40, 329, 2008
58. J. Šesták “*Modern materials and society*” chapter 19 in the book “*Heat, thermal analysis and society*” Nucleus publ. house, Hradec Kralove 2004, pp. 306



Chapter 26

Amorphous geopolymers

26. GEOPOLYMERS – AMORPHOUS CERAMICS VIA SOLUTION

František Šoukal, Tomáš Opravil, Petr Ptáček, Bronislav Foller,
Jiří Brandštetr, Pavel Roubíček

Geopolymers are materials prepared by alkaline activation process in which a powder material of an aluminosilicate nature, such as metakaolin or fly ash, is mixed with an alkaline activator to produce a paste that is able to set and harden in a short time. These materials, frequently termed alkaline inorganic polymers, geopolymers, hydroceramics, etc., constitute a new family of products which, among other interesting properties, are able to combine qualities peculiar to cements with those of traditional ceramics and zeolites. This is a reason that some author (according of the main application) suggested a new generic name to these materials: "Zeoceramic" or "Zeocements" [1].

26.1. Geopolymers – introduction and history

Geopolymers may be defined in a number of ways, in terms of their principal constituents (alumina and silica), their structure (tetrahedral Al-O and Si-O units in random 3D framework charge-balanced by alkali ions), their synthesis (room temperature condensation of alumina and silica resources at high pH) or their properties (moderately strong and hard, stable at least 1000 °C) [2]. As a result of the recent upsurge of interest on environmentally friendly and energy-efficient materials and processes, geopolymers, which behave as ceramics but are formed at ambient temperature, have attracted increasing attention. One result is that the generic term is tending to be used more loosely and indiscriminately for any material bonded with alkali metal silicate, irrespective of its structure and properties [3]. The alkali containing composites of similar composition were produced as early as in ancient times and the still well-preserved buildings document very good long-term durability of this material [2,4].

The study of composition and structure of natural sodium and potassium aluminosilicates (zeolites, mica) initiated research teams to synthesize analogous material possessing excellent mechanical and chemical properties. First experiments of the action of alkalis on blast-furnace slag were published in 1940 by Purdon [5]. Important research was performed in Kiew by Gluchovskij such as alkali-activated aluminosilicates called gruntosilicates [6] and afterwards in Krakow [7] and later in Finland [8], Czech Republic [9], Canada [10] and other countries. Some important steps in the development of alkali-activated and alkaline cements are chronologically summarized in Table 1.

The term „geopolymer“ was coined by Joseph Davidovits and Michel Davidovits in the 1980s to describe aluminosilicate materials consisting of tetrahedral aluminate and silicate units condensed at ambient temperatures into a framework structure charge-balanced by the presence of monovalent alkali metal ions [11]. A strict formalism was developed which investigated the structural units in the terms of fragments such as [-Si-O-Al-O-] (called sialate units by Davidovits, or polysialate when condensed together). Other postulated units contained different Si:Al ratios, thus, [-Si-O-Al-O-Si-O-] (sialate siloxo in the Davidovits terminology) and [-Si-O-Al-O-Si-O-Si-O-] (sialate disiloxo). There the Si:Al atomic ratio is 1, 2 and 3, respectively. Units with Si:Al > 3 are designated as sialate links. Terminology of poly(sialate) geopolymers are presented on Figure 1 (according to J. Davidovits) [2,12].

Table 1: The bibliographic history of some important events during alkali-activated systems investigation [13]. Added dates were provide by a reference.

Author(s)	Year	Significance
Kuhl	1930	Investigated setting behavior of slag in the presence of caustic potash [58]
Chassvent	1937	Measured reactivity of slag using caustic potash [58]
Feret	1939	Slags used for cement
Purdon	1940	Alkali-slag combinations
Glukhovskiy	1959	Theoretical basis and development of alkaline cements
Glukhovskiy	1965	Fist called "alkaline cements" because natural substances used as components
Davidovits	1979	"Geopolymer" term-emphasizes grater polymerization
Malinowski	1979	Ancient aqueducts characterized
Fors	1983	F-cement (slag-alkali-superplasticizer)
Krivenko	1984	Slag-alkaline cements and concrete [14]
Langton and Roy	1984	Ancient building materials characterized (Roman, Greek, Cyprus)
Davidovits and Sawyer	1985	Patent leading to "Pyrament"
Krivenko	1986	D.Sc. Thesis, $R_2O-RO-R_2O_3-SiO_2-H_2O$
Malolepsy and Petri	1986	Activation of synthetic melilite slags
Malek at al.	1986	Slag cement-low level radioactive waste forms
Davidovits	1987	Ancient and modern concretes compared
Deja and Malolepsy	1989	Resistance to chlorides shown
Kaushal at al.	1989	Adiabatic cured nuclear waste forms from alkaline mixtures including zeolite formation
Roy and Langton	1989	Ancient concretes analogs
Majumdar at al.	1989	$C_{12}A_7$ – slag activation
Talling and Brandstedtr	1989	Alkali – activated slag
Wu at al.	1990	Activation of slag cement
Roy at al.	1991	Rapid setting alkali-activated cements
Roy and Silsbee	1992	Alkali-activated cements: overview
Palomo and Glasser	1992	CBC with metakaolin
Roy and Malek	1993	Slag cement
Glukhovskiy	1994	Ancient, modern and future concretes
Krivenko	1994	International conferences on alkali-activated cements
Wang and Scrivener	1995	Slag and alkali-activated slag microstructure
Krivenko	1999	International conference on alkali-activated cements
Davidovits	1999	International conference on geopolymer
Van Deventer	2002	International conference on geopolymer
Davidovits	2005	International conference on geopolymer
Davidovits	2008	Workshop Geopolymer Special Event at ICC2

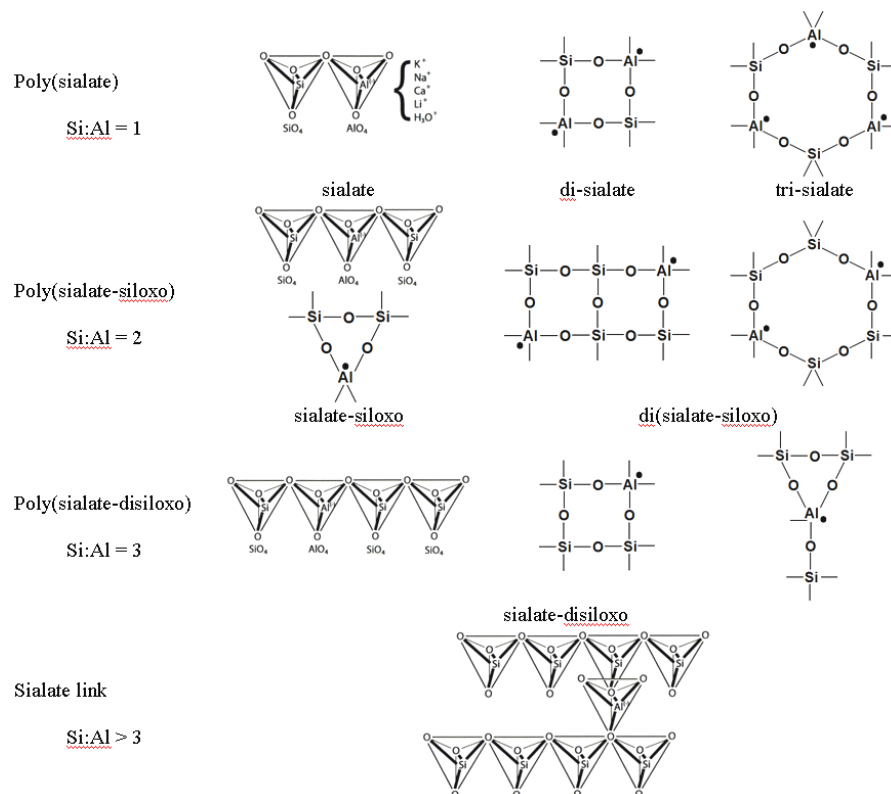


Fig. 1: Terminology of poly(sialate) geopolymers [2]. The Al atom is highlighted with a dot.

For the chemical designation of geopolymers based on silicon-aluminates, poly(sialate) was suggested. Sialate is an abbreviation for silicon-oxo-aluminate. The sialate network consists of SiO_4 and AlO_4 tetrahedrons linked alternately by sharing all the oxygens. Positive ions (Na^+ , K^+ , Li^+ , Ca^{2+} , Ba^{2+} , NH_4^+ , H_3O^+) must be present in the framework cavities to balance the negative charge of Al^{3+} in IV-fold coordination [7]. Poly(sialates) are chain and ring polymers with Si^{4+} and Al^{3+} in IV-fold coordination with oxygen and range from amorphous to semi-crystalline [15].

Common silicate minerals according to the terminology used above are strictly spoken polycondensed sialates. In that sense the majority of the Earth's crust is composed of siloxo-sialates and sialates¹. It can easily be checked that according to this terminology the common feldspar series albite-anorthite ($\text{NaAlSi}_3\text{O}_8 - \text{CaAl}_2\text{Si}_2\text{O}_8$) can be described as poly(sialate-disiloxo) for albite to poly(disialate) for anorthite [12]. According to Löwenstein's law two aluminate tetrahedrons cannot be connected via oxygen creating Al-O-Al bridge, however dialuminate ions do not exist whereas silicate polyanions are common. The idealized geopolymeric structure is illustrated on Figure 2.

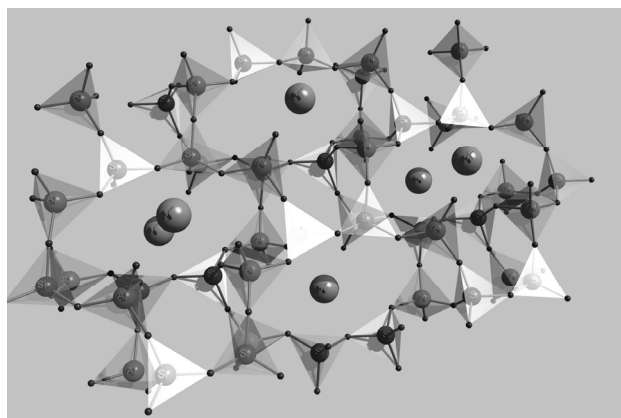


Fig. 2: Proposed amorphous geopolymeric structure (negative charge on AlO_4 tetrahedrons is compensated by K^+) (edited by author).

Geopolymers can be classified into two major groups: pure organic geopolymers and organic containing geopolymers, synthetic analogue of naturally accruing macromolecules. Further possible criteria for defining a geopolymer [2]:

- **Definitions in terms of chemical composition:** Attempts to define geopolymer system in terms of their composition may be unnecessarily prescriptive, for the following reasons:
 - a) The too precise composition limits of even the best-known aluminosilicate geopolymer require further exploration. Possible existence of other true geopolymer system based on phosphate (Phosphate and Silico-phosphate geopolymers) or borate tetrahedral units and organic-mineral geopolymers (Silicone and Humic-acid based geopolymers), with their own compositional requirements, would further complicate such a classification.
 - b) The possibility of in situ geopolymerization of mineral grains blurs the compositional distinction between the geopolymer matrix and the mineral filler, militating against classification of the former on the basis of chemical composition.
- **Definition on the basis of structure:** Since the conventional geopolymers are X-ray amorphous materials consisting of randomly cross-linked tetrahedral units with built-in charge compensating mechanisms as necessary, these structural criteria and their retention

¹ This terminology is proposed by Davidovits, but authors strongly recommend using of common mineralogical term, i.e. aluminosilicates, as a main component of the Earth's crust.

to high temperatures seem to be useful concept, particularly since they can readily be monitored by solid state NMR. However, it must be borne in mind that only a part of the material may be geopolymeric, so the presence of crystalline components may not necessarily rule out geopolymerization.

Geopolymers can be included to alkali activated cements that refer to any system that uses an alkali activator to initiate a reaction or a series of reactions (Figure 10) that will produce a material that possesses cementitious property (Figure 3). Alkali activated cement (AAC), alkali activated slag (AAS) and fly ash (AAFA), and geopolymers are all considered to be alkali activated cementitious systems, however, it is expected that the structures of these materials are vastly different as results from different chemical mechanistic paths. It is commonly acknowledged that calcium silicate hydrates (CSH) is the major binding phase in Portland cement (PC) [16,17] and alkali activated slags [18]. However, the binding property of geopolymers is generally assumed to be the result of the formation of a three-dimensional amorphous aluminosilicate network [15,19-22].

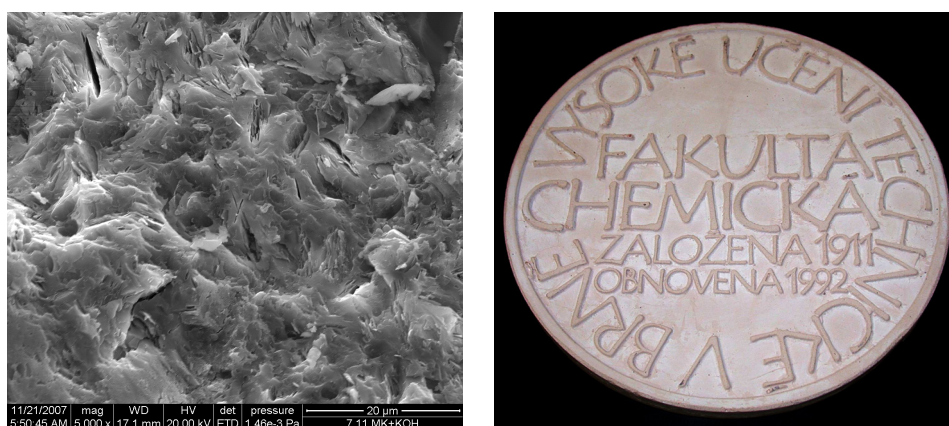


Fig. 3: SEM image of fracture surface and anniversary medal prepared from pure geopolymer based on metakaolin [23].

In terms of chemical composition, the major difference between geopolymers and Portland cement is in presence of calcium. It is important to note that calcium is not essential in any part of a basic geopolymeric structure. Given that CSH will be formed when soluble calcium and silicate species are present in a neutral to mild alkaline pH environment, it is thought that provided sufficient calcium is added to a geopolymeric system, a CSH based cementitious material may form instead [24]. Thus the amorphous microstructure of alkali activated aluminosilicates containing calcium is a combination of geopolymeric and CSH based structure elements [25].

The most important practical property of these materials is that they are formed by condensing alumina and silica components under appropriate conditions (high pH and controlled water content [26]) at ambient temperatures, and thus constitute a group of inorganic materials with the high-temperature properties of ceramics but which, unlike ceramics, do not require high temperatures to attain their properties of durability and hardness [27]. The resulting energy-efficiency of these materials has attracted increasing interest in the world which is becoming more ecologically aware and unfavorably disposed towards energy-intensive and polluting industrial operations.

Ideas of alkali treatment on silicates brings possibilities to rearrangement of structure during dissolution of raw material, improving transport properties of formed structure groups and formation of new structure by relatively slow hardening, which is supported by polymerization of silica acid (Figure 9) from solution and controlled by processes

on interphases of rising particles. Formation of material may be characterized by condensation reaction, where water is gradually excluded from new structure, a new 3D ordering is achieved. Transport of liquid water or vapor from core of particle or solid product through pores evokes retardation of process of hardening and in next step this fact positively contribute to formation of perfect structure with required properties [12].

As has been mentioned, amphoteric behavior of silica and therefore sensitivity to pH are main conditions for reconstruction of structure with variety of stable localized tetrahedron of SiO_4 . It is evident that covalent bonds in fundamental unit (tetrahedron) play very important role in construction (stability) of structure and reconstruction processes of structure (kinetics). Both parameters are advantageous for production of stable structure. The big tetrahedral unit with low transport properties causes low mobility of particles, because viscosity of heterogeneous system allows systematical formation of required shape by slow rearrangement and rates of partial polymerization reactions are in agreement with rate of structure ordering process. These conditions are important for formation of structure with high mechanical parameters. Fortunately many natural raw materials (minerals, rocks) had been formed by similar processes. Task of principal rearrangement of micro and macrostructure from natural resources to stable process is possible by the formation of product from melt or by chemical processing.

First of them predominantly possible in special working places and main problem is in preservation of dimensions of product and gradients of properties generated by cooling of system. Second one, chemical way supposed preparation of acceptable starting compounds or precursors and formation operation is managed at room temperature or conditions where volume changes do not play significant role.

There are also two major drawbacks of ordinary Portland cement (OPC) binders that increase importance of development of materials such as geopolymers. (1) About 1.5 tones of natural mineral raw material is needed in the production of every ton of PC, at the same time, about one ton of carbon dioxide (CO_2) is released into the environment during the production. Therefore, the production of PC is extremely resource and energy consuming process. (2) Concrete made of PC deteriorates when exposed to the severe environments, either under the normal or severe conditions. Cracking and chemical corrosion have significant influence on its service behavior, long term durability and safety [28].

In the manufacture of cement, the CO_2 is emitted from the calcination process of limestone, from combustion of fuels in the kiln, as well as from the power generation. Carbon dioxide emissions, largely a byproduct of energy generation and use, are the largest source of greenhouse gases associated with global warming. Cement production is the third largest cause of man-made carbon dioxide emissions [29]. The important demand is to increase the long-term durability of materials. Nature does not like high calcareous silicates or aluminates hydrates. The possibility of their carbonation, delayed ettringite formation and weak resistance to different kinds of chemical corrosion turns our attention on other materials.

Table 2: *The composition of the earth crust, Portland cement and some secondary raw materials.*

Material	SiO_2	Al_2O_3	Fe_2O_3	CaO	Na_2O	MgO	K_2O	SO_3
Earth crust	64	17	7	6	2	2	2	< 1
Portland cement	16-26	4-8	2-5	59-67	1-4	0.5-1.5	0.5-1.5	< 0.5
Blast furnace slag	28-38	8-24	1-3	30-50	1-20	0.2-1	0.5-3	1-3
Siliceous fly ash	55	26	7	8	1	0.5	0.6	0.6

The composition of the earth crust, Portland cement and some secondary raw materials (see Table 2 above) show the principal differences and forces us to the considerations about

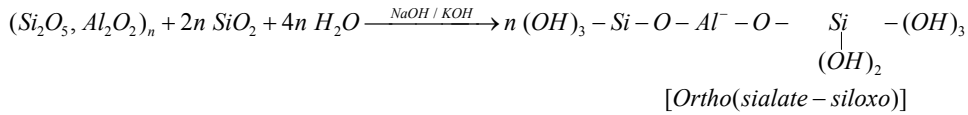
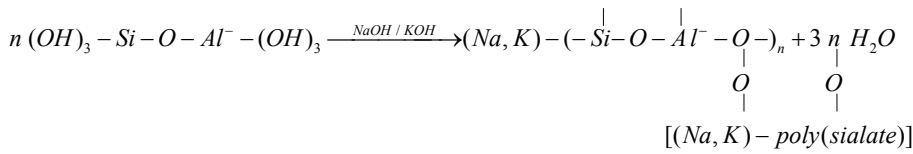
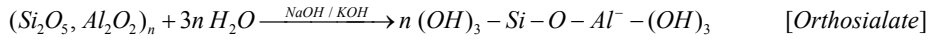


Fig. 5: Scheme of geopolymerization reactions according to Davidovits [34].

The exact reaction mechanism which explains the setting and hardening of alkali-activated binders is not yet quite understood, although it is thought to be dependent on the prime material as well as on the alkaline activator and curing conditions. It is assumed that the mechanism of alkali-activation is composed of conjoined reactions of destruction-condensation. Process includes destruction of the prime material into low stable structural units, their interaction with coagulation structures and creation of condensation structures [35]. A schematic diagram of the chemical reaction sequence which takes place during formation of geopolymers is presented on Figure 6(a). This sequence is an extension of Faimon model [36].

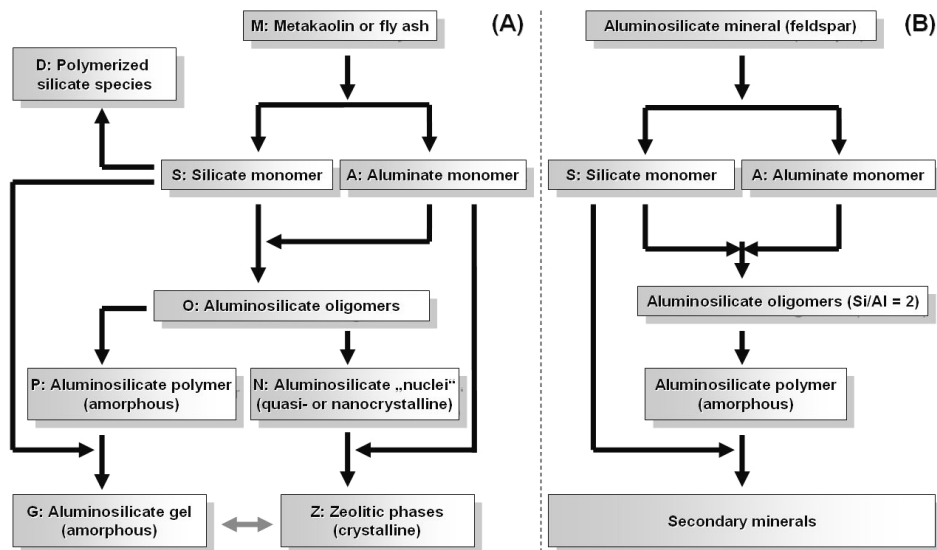


Fig. 6: The reaction sequence of geopolymerization (a) and aluminate weathering model according to Faimon (b) [36].

The Faimon model, as shown in Figure 6(b) allows for dissolution of a primary mineral into aluminate and silicate monomer association of these monomers via both addition and autocatalytic polymerization routes and formation of an undefined “secondary mineral” phase. Its extension to geopolymerization is relatively straightforward, requiring only:

- 1) Incorporation of the effect of silicate oligomerisation (species D) into the concentrated activator solutions;
- 2) Deviation of oligomer (species O) stoichiometry from 2:1 to the Si/Al ratios with which geopolymers may be synthesized;

- 3) Identification of the secondary mineral product G as the amorphous aluminosilicate gel component of the geopolymeric binder;
- 4) Inclusion of a second reaction direction by which the zeolitic phases (N and Z) observed in geopolymers are formed. The Z-type species have slightly higher content of Al than its amorphous counterparts, following the observation that the crystalline products of hydrothermal zeolite synthesis tend to be enriched in Al compared to their amorphous (gel or fly ash) precursor, and to the system as a whole.

Including these effects into the Faimon model then yields to Figure 6. An additional reaction, drawn as a gray arrow, shows the conversion of gel to zeolite over extend curing period [36].

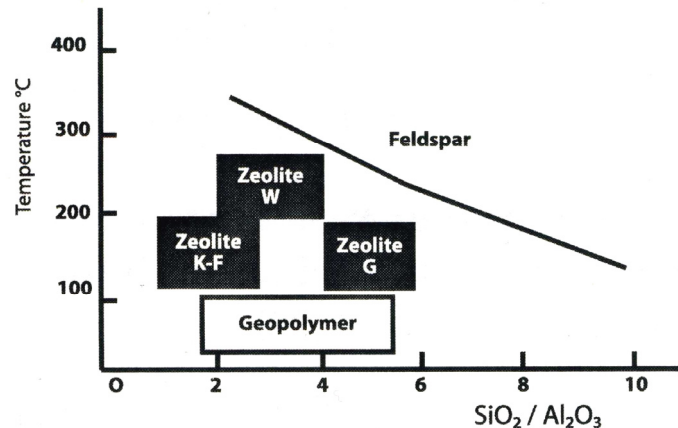


Fig. 7: Crystallization temperature ranges for $K_2O-Al_2O_3-SiO_2$ system [2].

Formation of zeolite nuclei requires the depolymerization of the geopolymer micelle in the hydrous aluminosilicate gel. The gel phase contains relatively large units of aluminosilicate macromolecules, the geopolymer micelle, with molecular weights from 100 000 to 500 000 and ranging size from 10 to 20 nm. The time needed for crystallization varies from a few hours to several days. Ageing time at room temperature is 24 hours; crystallization time at 100 °C from 50 to 100 hours. For the $K_2O-Al_2O_3-SiO_2$ system, crystallization temperatures range from 150 to 230 °C [2].

26.2.1. Alkali dissolution of silica

In Iller's "The Chemistry of Silica" [37] is deeply analyzed the behavior of pure silica. Results of the rate of silica dissolution are important when the process of geopolymer manufacture is based on material containing SiO_2 particles. Mechanism of dissolution is controlled by many factors, because dissolution is a depolymerization through hydrolysis and driving force defined by difference of solubility and actual concentration in solution. Solubility is concentration of $Si(OH)_4$ reached in steady state in depolymerization – polymerization equilibrium. In agreement with Iller, the "catalyst" is a material that can be chemisorbed and coordination number of a silicon atom on the surface has increasing to more the four, thus weakening the oxygen bonds to the underlying silicon atoms. The hydroxyl ion is the unique catalyst in alkaline solutions and hydrofluoric acid in acid solutions.

The structure of amorphous silica is of even more open arrangement than that of cristobalite, to which it is closely related. On the surface there are spaces between oxygen ions sufficiently large to accommodate hydroxyl ions. Such a surface then bears an ionic charge and silica is constantly being exchanged in equilibrium between solution and surface, as indicated. The first step is the adsorption of OH^- ion, after which a silicon atom goes into solution as a silicate ion. If the pH is much below to 11 the silicate ion hydrolyzes to soluble silica acid ($Si(OH)_4$, monomer) and OH^- ions and the process is repeated.

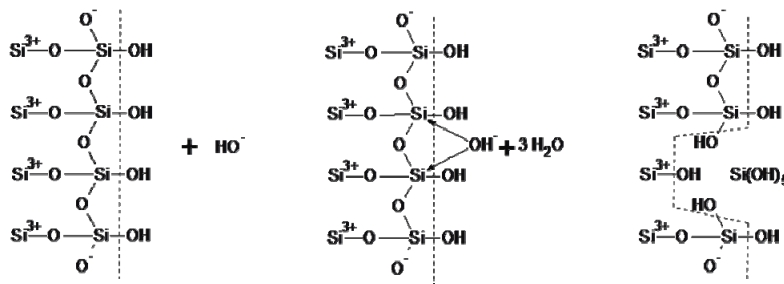


Fig. 8: Proposed mechanism of dissolution of silica in water in the presence of hydroxyl ions [37].

The relative rates of dissolution of different forms of silica at pH = 8.5 have been reported by Stöber (10 m² in 500 ml volume) [37]:

Table 3: Dissolution of different forms of silica.

Type of silica	Rate of dissolution [10 ⁻⁴ g·ml ⁻¹ ·day ⁻¹]	Type of silica	Rate of dissolution [10 ⁻⁴ g·ml ⁻¹ ·day ⁻¹]
Fused glass (vitreous)	39.0	Tridymite	4.5
Quartz	2.8	Coesite	0.7
Cristobalite	6.0	Stishovite	11.0

In patent issued to Balthis [37] a method is described whereby a sample of deionized silica sol is put into an excess of 0.01 N NaOH solution at 30 °C and after 90 min samples are removed from the solution and amount of monomeric silica is determined by molybdate method. The rate related to A , the specific surface area of silica (in square meters per gram) determined by the following equation:

$$(1) \quad AK_D = 100 \frac{dy}{dt} (1-y)^{-\frac{2}{3}},$$

where K_D is a constant defined as the specific depolymerization rate for the particular type of silica, dy/dt is a rate of monomer formation per 100 min and y is the fraction of original silica converted to monomer at time t , in minutes.

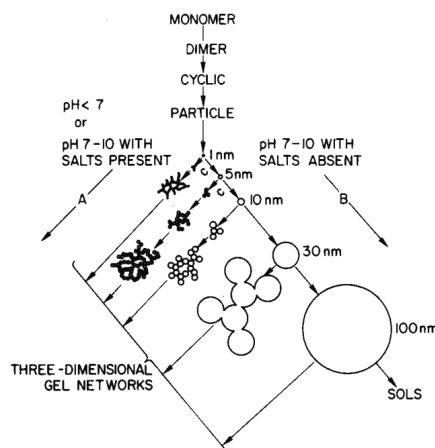


Fig. 9: Polymerization behavior of silica. In basic solution (B) particles in sol grow in size with decrease in numbers; in acid solution or in presence of flocculating salts (A), particles aggregate into three-dimensional networks and form gels [37].

The structure of silicate and polysilicate ions is still not well understood. In past solutions of alkali metal silicates obtained by dissolving sodium or potassium silicate glasses in water seemed to be clearly different from sols of colloidal silica stabilized with a minor amount

of alkali. Silica solutions were made by dissolving glasses with SiO₂ : Na₂O ratios (silicate modulus) less than 4:1. Since these glasses with more silica and less alkali can't be dissolved, silica solutions of higher ratios were not available.

The condensation polymerization involves an ionic mechanism. Above pH 2 the rate is proportional to the concentration of OH⁻ ion and below 2 to the H⁺ ion. Succeeding steps in polymerization from monomer (monosilic acid) to large particles and gels have been represented schematically by Iller as in Figure 9.

Rapid gelation of silicate solution upon adding acid appeared to support the idea that the gelling mechanism involved cross-linking of preexisting linear polymers is analogous to organic polymer systems. Thus developments in the theory of organic polymers, improperly applied to soluble silicates, may have delayed a correct interpretation of this inorganic system. Polymeric silicate species certainly occur in solution, but they are not highly linear, because of polymerization mechanism is entirely different from that of any organic system [37].

26.2.2. Alkali dissolution of aluminosilicates

Alkali activation of aluminosilicate materials represents a complex process that has not been described fully thus far. The reaction of aluminosilicate materials in a strong alkaline environment results, first of all, in a breakdown of Si-O-Si bonds; later, new phases arise and the mechanism of their formation seems to be a process that includes a solution as a first step ("synthesis via solution" or polycondensation). The penetration of Al atoms into the original Si-O-Si structure represents a substantial feature of this reaction. Aluminosilicate gels (zeolite precursors) are mostly formed. Their composition can be characterized by the general formula M_n[-(Si-O)_z-Al-O]_n·wH₂O. The C-S-H and C-A-H phases may also be originated in dependence on the composition of the starting materials and the conditions of the reaction. During these (poly-condensation) reactions, secondary water is formed.

Table 4: The extent of dissolution of sixteen minerals in terms of the concentration of Al or Si in 20 ml of solution after 5 hours of contact with 0.50 gram of mineral [40].

Mineral	2N NaOH		2N KOH		5N NaOH		5N KOH		10N NaOH		10N KOH	
	ppm											
	Si	Al	Si	Al	Si	Al	Si	Al	Si	Al	Si	Al
Almandine	59,2	39,6	62,3	39,8	51	34,2	59	36	69,5	44,8	65	41,8
Grossular	60,6	1,5	50,1	1,82	66	2,02	29	1,4	231	3,05	189,5	3,1
Sillimanite	21,1	27,4	17	23,4	23,4	28,4	23,4	26,4	33,8	33,8	39,9	34,7
Andalusite	31,5	33,3	30,2	32,6	31,2	33,2	34	33,6	42,5	43,8	37,1	39,3
Kyanite	22,6	20,9	21,1	20,3	26,4	24,4	24,8	21,6	32,5	30,2	29,9	28,2
Pumpellyite	30,6	14,9	31,1	14,5	19,8	11	29,4	13,7	41,3	20,9	38	18,8
Spodumene	34,2	20,2	29,6	17,5	39,4	23,2	36,4	19,8	54	32	45,5	25,8
Augite	59,3	19,8	53,1	20,9	164,8	74,4	83,4	38	215,5	133	236,5	135,5
Lepidolite	36,8	25,1	32,5	22,5	34,4	24,4	37	24,2	42,2	29,4	37,3	27
Illite	42,2	19,8	42	15,8	52	23,4	47	16,6	76	30,6	72,5	29
Celsian	78	62,7	65,8	56,6	78,8	68,2	81,4	63,8	157,5	121	119	97
Sodalite	68,5	13,6	82,1	38	101	37,2	141,2	41,2	78	88,5	30,1	246
Hydroxyapophyllite	58,4	1,28	49,7	1,42	135	2,3	40,8	1	140	1,5	107,5	3
Stilbite	116	45,9	98,7	32,9	122,8	44,4	124	44	615	201,5	491	165
Heulandite	127	45,8	94,8	35	141,4	51,6	75	28,4	293	105	216	82,5
Anorthite	86,2	36,2	69,5	29	79,6	36,6	71,2	30	156	73	131	61,5

Amorphous (gel-like) or partially amorphous or crystalline substances may be originated in dependence on the character of starting raw materials and on the conditions of the reaction. The concentration of the solid matter and specific surface of the particles plays a substantial role in the process of alkali activation. Mostly crystalline zeolite-type products (analcime, hydro-sodalite and other) are formed in extremely diluted suspensions (w > 1...10). Therefore, the above process is used for the synthesis of man-made zeolites as this was

presented by numerous publications. Predominantly amorphous products are originated at higher concentrations of the solid phase in the suspension ($w < 1$) [38].

Interesting data concerning the production of zeolites under different condition (pressure, temperature, concentrations) were presented by Koloušek [39]. Table 4 above [40] gives the extent of dissolution of sixteen minerals in terms of the concentration of Al or Si in 20 ml of solution after 5 hours of contact with 0.50 gram of finely dispersed mineral. The alkaline solutions contained NaOH or KOH at concentrations of 2 N, 5 N and 10 N. The following general trends can be observed from above mentioned Table 4:

- Minerals dissolve easier with increasing concentrations of alkaline solution.
- Minerals show a higher extent of dissolution in the NaOH than in the KOH solution of the same concentration, except for sodalite.
- The concentrations of Si are higher than the corresponding Al, which could be caused partly by the higher content of Si than Al in the minerals, but also by the higher intrinsic extent of dissolution of Si than Al.
- Si and Al appear to have synchro-dissolution behaviour in alkaline solution, which means that Si and Al could dissolve from the mineral surface in some linked form.
- Minerals with framework structure possess a higher extent of dissolution than di-, ortho, ring, chain and sheet structures in both NaOH and KOH solutions.

26.2.3. Geopolymer polycondensation

As stated before, the process of geopolymerization starts with the dissolution of Al and Si from Al-Si materials in alkaline solution as hydrated reaction products with NaOH or KOH, hence forming the $[M_x(AlO_2)_y(SiO_2)_z \cdot nMOH \cdot mH_2O]$ gel. Subsequently, after a short time setting proceeds, next the gel is hardening into geopolymers. Consequently, an understanding of the extent of dissolution of natural Al-Si minerals is important for study and description of geopolymerization reactions.

A matter requiring further consideration is the degree of constraint imposed upon a geopolymerizing system by its chemical composition. The original aluminosilicate composition were clearly defined and prescribed in terms of Al:Si ratios ranging from 1:1 in poly(sialate), through 1:2 in poly(sialate-siloxo) to 1:3 in poly(sialate-disiloxo). Non-integer ratios intermediate between 1:1 and 1:3 may therefore be envisaged as varying combinations of these basic units, provided the content of charge-balancing cations is correct, and as was found, the water content is controlled [41].

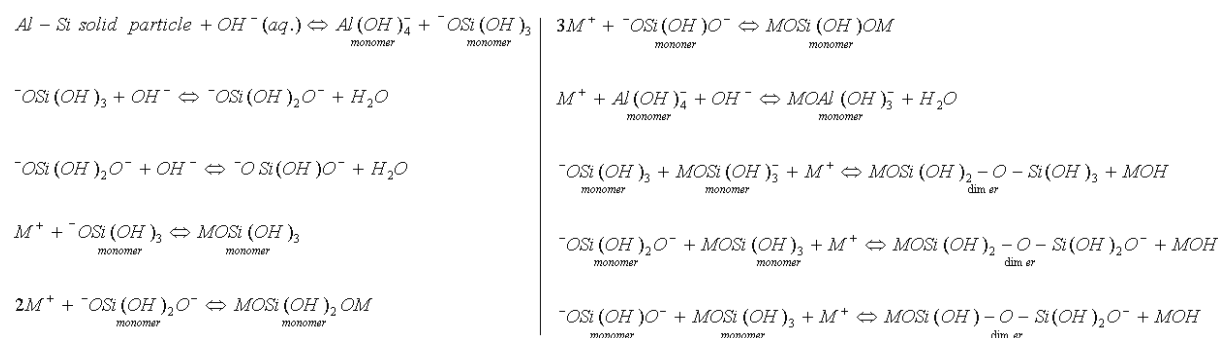


Fig. 10: Proposed mechanism of dissolution and further condensation of aluminosilicate materials [40,42].

However, a rigorous exploration appears to be lacking as how far these compositions may range towards the pure alumina and/or silica end members. Further, if it is accepted that the structure contains only tetrahedral units, the question arises as to whether other well-known

tetrahedral glass-formers such as phosphate and borate may also be accepted into geopolymer family, with or without silicate. Normally, the possible chemical process for the dissolution of Al-Si minerals and silicates under strongly alkaline conditions can be expressed by reaction schemes are shown on the Figure 10 [42].

26.3. Raw materials

Raw (source) material used for geopolymers preparation may be defined as compound or mixture of more components which are able to enter in reaction process with water and especially with activator. The condition concerned the negative Gibbs energy of activation process is in principle fulfilled in most events because a reaction with relatively active/aggressive electrolyte is expected. For practical purposes deciding role play kinetics of process and therefore more important is the rate of activation process.

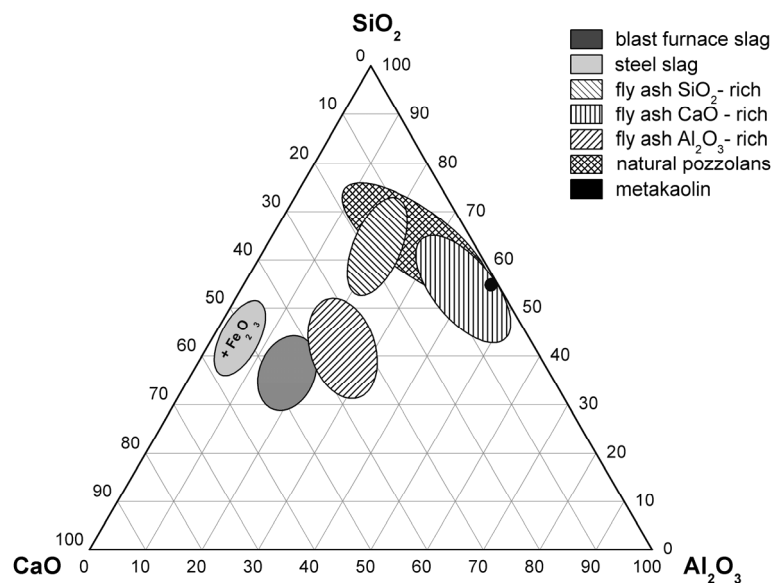


Fig. 11: Typical composition of usual raw materials used for alkali activation (edited by author).

Generally any material that contains mostly amorphous aluminosilicates is a possible source material for the manufacture of geopolymer. Several minerals and industrial by-product materials have been investigated in the past.

Table 5: Raw material for geopolymers.

Raw materials		
Type	Origin	Approximate availability
Granulated blast-furnace slag	Iron metallurgy	Very high
Steel making slag	Iron metallurgy	High
Foundry slag	Foundry	Medium
Fluid-bed fly ash	Energetics	Very high
High-temperature fly ash	Energetics	Very high
Metakaolin	Calcined kaolin	Medium
Red mud	Aluminum industry	Low
Mine wastes	Natural minerals, soils	High

Note: Approximate availability:

- low (up to 50 000 t / year / Europe)
- medium (50 000 – 1 000 000 t / year / Europe)
- high (1 000 000 – 50 000 000 t / year / Europe)
- very high (over 50 000 000 t / year / Europe)

Preparation of starting compounds must be focused on increasing of reaction by magnification of specific surface or partially defective or thermodynamically metastable volume structure. Second one may be represented e.g. by glass phase, where process of structure ordering had been stopped by high rate of cooling. Specific surface and volume energy of starting material are often main conditions for acceleration of activation process.

As the starting natural material may be used phases based on thermal processes performed during volcanic activity (e.g. volcanic glass), industrial mineral phases from high temperature processes, where latent energy is conserved (difference between energy of actual state and equilibrium state e.g. energy of glass and crystal), energy of reaction anhydrous form and hydrate, carbonate etc (Table 5) as far as the reaction with water or carbon dioxide and activator does not converge to original raw material.

26.4. Alkaline activators

Usually, caustic alkalis or alkaline salts are used as alkaline activators of alkali-activated cements and geopolymers (Table 6). Glukhovskiy et al. [43] classified them into six groups according to their chemical compositions:

1. caustic alkalis: MOH;
2. non-silicate weak acid salts: M_2CO_3 , M_2SO_3 , M_3PO_4 , MF, etc.;
3. silicates: $M_2O.nSiO_2$;
4. aluminates: $M_2O.nAl_2O_3$;
5. aluminosilicates: $M_2O.Al_2O_3.(2-6)SiO_2$;
6. non-silicate strong acid salts: M_2SO_4 .

Of all these activators, NaOH, $Na_2O.nSiO_2$, Na_2CO_3 , Na_2SO_4 are the most widely available and economical chemicals. Some potassium compounds have been used in laboratory studies and in last years also in pilot production. However, their potential application is very limited due to their availability and costs. On the other hand, the properties of sodium and potassium compounds are very similar. The certain advantage of potassium activators is the lower tendency to form efflorescence. Intensification of the process of alkali activation is able through the high-shear mixing, bringing about chemical-mechanical activation in mixing the solid constituents with small amount of water.

Table 6: Alkali-activators solutions [43].

Type	Solution concentration	Dosage	Usual combination with
MOH	50 %	1 – 7 % M_2O /solid	all
M_2CO_3	Solid	3 – 10 % of solid	MOH
M_2SO_3	Solid	3 – 10 % of solid	MOH
$M_2O.nSiO_2$	35 %	5 – 15 % M_2O /solid	MOH
$M_2O.nAl_2O_3$	35 %	5 – 15 % M_2O /solid	MOH
$M_2O.Al_2O_3.(2-6)SiO_2$	35 %	5 – 15 % M_2O /solid	MOH

The kinetics of blast furnace slag activation can be studied by calorimetric measurement (Figure 12(a)). Induction period isn't influenced by increasing content of Na_2O in the solution of alkaline activator, but setting time decreases significantly as well as amount of heat released during activation reaction. Because of the formation of geopolymeric structure proceeds via solution, the first step is to dissolve the basic aluminosilicates in the 15 – 20 M solutions of NaOH or KOH at ambient temperature. Then, water glass of the silicate modulus around 1.2 is added, keeping the content of Na_2O within 3 - 8 % to the slag amount.

The polycondensation bringing about setting and hardening can be accelerated by increased temperature (Figure 12(b)).

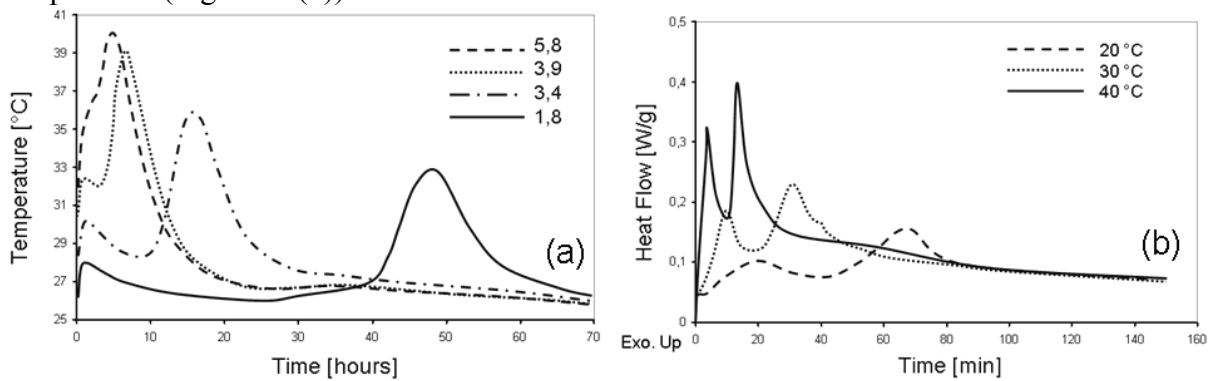


Fig. 12: Calorimetric measurement (a) - the effect of Na₂O content (wt. %) in the solution of alkaline activator on the kinetic of granulated BFS activation and DSC analysis (b) of AAC (measured by authors in NTC, Pilsen).

The study by Fernandes-Jimenez [32] shows that alkaline activation of metakaolin and fly ash and metakaolin mixture (1:1) leads to formation of similar, but not identical alkaline aluminosilicates gels as the main products, and different types of zeolites (sodalite, zeolite A and faujasite) as by-products, in both cases. When the fly ash powder is mixed with a small volume of alkaline solution, a paste is formed which quickly transforms into harden solid. In such a situation, there is not sufficient time and space for the gel (product of reaction) to grow into a well-crystallized structure such as in the case of zeolites formation. The hypothetical evolution of this gel (zeolitic precursor) to form an orderly zeolitic crystal would entail depolymerization of gel structure.

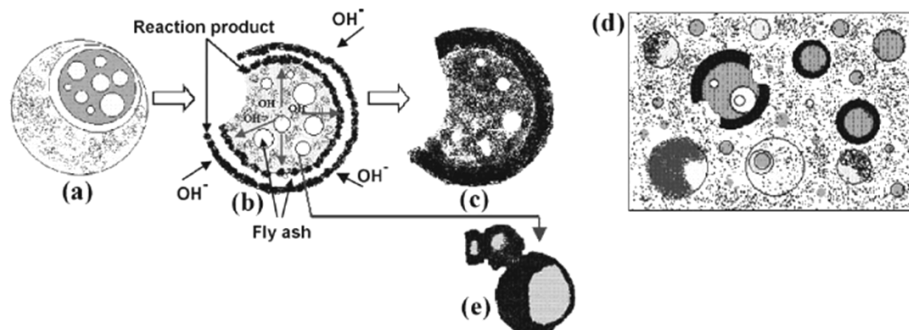


Fig. 13: Descriptive model for the alkali activation of fly ash [44].

Figure 13 presents a descriptive model of the alkali activation of fly ash. The initial chemical attack at the point on the surface of a particle, which then expands into larger pore (b), exposing smaller particles, whether hollow or partially filled with other yet smaller microparticles, to bi-directional alkaline attack: i.e., from the outside in and from the inside out. Consequently, reaction product is generated both inside and outside the shell of the sphere, until the ash particle is completely or almost completely consumed (c). The mechanism involved at this stage of the reaction is dissolution. At the same time, as the alkaline solution penetrates and contact the smaller particles inside the larger spheres, the interior space of the latter starts to fill up with reaction product, forming a dense matrix.

One of the consequences of the massive precipitation of reaction products is that a layer of these products covers certain portion of the smaller particles. This crust prevents their further contact with the alkaline medium (e). Ongoing reactions within the bulk of the matrix consolidate such crusts, with the concomitant effect on the pH gradient across the fly ash

reaction product. As alkaline activation continues, the unreacted fly ash under reaction product may not be affected by the very high pH of the activator solution, thereby reducing the reaction rate. In this case, activation is governed by a diffusion mechanism [44].

The influence of Cs and Sr hydroxides, carbonates (weak acid salt) and nitrates (strong acid salts) onto geopolymerization kinetic was studied by J. L. Provis et al. [45]. Each of the six compounds has a different effect on the early stages of geopolymerization. CsOH is particularly enhancing dissolution of metakaolin and accelerating gel formation. Sr(NO₃)₂ causes a very marked disruption to the development of the geopolymer gel network, while Sr(OH)₂ due to removing of water from the already water-poor geopolymerization process. Soluble or sparingly soluble strontium salts tend to be converted to SrCO₃ by atmospheric carbonation as geopolymerization proceeds. No crystalline reaction products, other than NaNO₃ in the nitrate containing system, are observed during formation of Cs-containing geopolymer that indicates that Cs⁺ cations are chemically incorporated within the geopolymer binder.

There was observed that the optimum mixing order for alkali-activated binders is as follows: first, the solid constituents are mixed, and then the activator solution is added and thoroughly mixed with the solids. This procedure was confirmed on alkali-activation of metakaolin and blast furnace slag [26,46,47].

Several models have been proposed to describe the hydration kinetic of Portland cement. All of them assume that cement particles are spherical although they are actually very irregular. Jander proposed an equation for solid-state sintering diffusion controlled by diffusion:

$$(2) \quad \left(1 - [1 - y]^{1/3}\right)^n = Kt ,$$

where y is degree of conversion, K is reaction constant, t is reaction time and n is reaction grade. The reaction grade takes the value $n \leq 1$, $1 < n \leq 2$ and $n \geq 2$ for process limited by surface reaction, diffusion through layer of porous and dense reaction product, respectively. Ginstling and Brounstein proposed an equation when the thickness of the d diffusion layer on cement particles is considered [58]:

$$(3) \quad \left(1 - [1 - y]^{1/3}\right) - \frac{2}{3} \left(1 - [1 - y]^{1/3}\right)^3 = Kt .$$

Kinetic of hydration of alkali-activated slag (AAS) have been for different temperatures studied by Fernández-Jiménez and Puertas [48]. Water glass (4 % wt.) with silica module 1.5 was used as alkaline activator for the blast furnace slag (BFS). The value of y was determined from heat of hydration after the induction period: $y = Q_t/Q_{max}$, where Q_t and Q_{max} is total heat at general time t and maximum released heat when hydration is completed. It was found that reaction mechanism can be satisfactory described by Jander equation, i.e. D3 morphologic model. It means that hydration kinetic is limited by steady-state diffusion through layer of porous hydration products. Activation energy was determined by logarithmic form of Arrhenius equation to the 57.6 kJ·mol⁻¹. Similar value (53.6 kJ·mol⁻¹) was found by Huanhai et al. [49].

26.5. Physical and mechanical properties of geopolymers

26.5.1. Strength and its development

In addition to the factors which affect the strength development of Portland cement, the nature and the dosage of activators play a crucial role in determining the strength of alkali-activated geopolymer. Many results confirm that alkaline activators demonstrate selectivity;

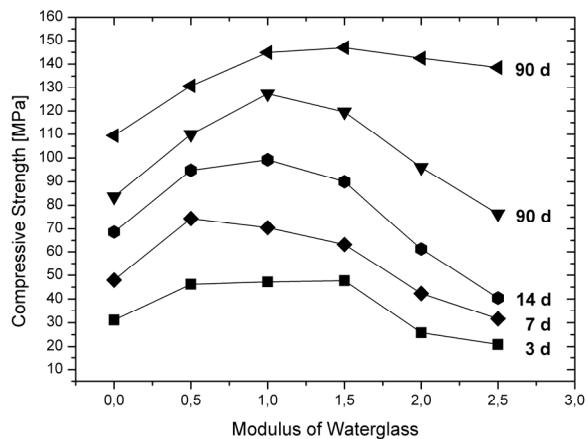


Fig. 14: The effect of the silicate modulus of water

glass on strength development of alkali-activated phosphorus slag cement pastes [53]

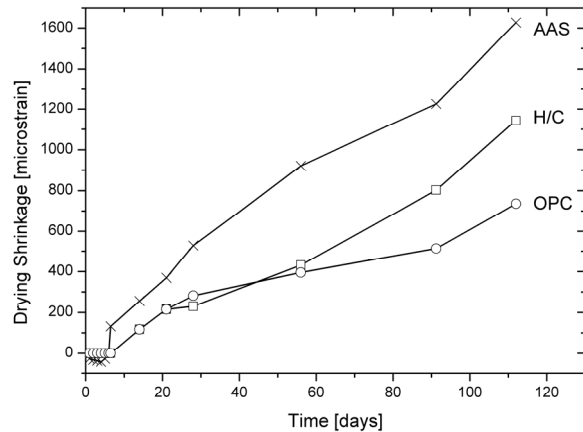


Fig. 15: Drying shrinkage of portland cement concrete, sodium silicate-activated slag cement concrete and sodium hydroxide-sodium carbonate-activated slag cement concrete [59].

i.e., the effect that an activator has on strength development may be different for slags of different origins. It is reported that Na_2CO_3 is especially suitable for slags rich in C_2MS , and NaOH is a effective activator for slags rich in C_2AS .

Krivenko [50] examined the activation of CaO-SiO_2 , $\text{CaO-Al}_2\text{O}_3$, $\text{CaO-Al}_2\text{O}_3\text{-SiO}_2$, CaO-MgO-SiO_2 and $\text{CaO-Al}_2\text{O}_3\text{-MgO-SiO}_2$ systems with NaOH , Na_2CO_3 and NaO.SiO_2 . It was found that NaO.SiO_2 is the most effective for CaO-SiO_2 , $\text{CaO-Al}_2\text{O}_3$, $\text{CaO-Al}_2\text{O}_3\text{-SiO}_2$ and CaO-MgO-SiO_2 systems, and Na_2CO_3 is effective for $\text{CaO-Al}_2\text{O}_3$ system. Many researchers have confirmed that water glass is a very effective activator. Variation of chemical composition among different blast furnace slags results in different hydration products for a given activator, which is the main reason for the selectivity [51,52].

Many studies have confirmed that the silicate modulus of the water glass has a significant effect on the properties of alkali-activated slag cements. Following Figure 14 shows the effect of the modulus of water glass on compressive strength development of alkali-activated phosphorus slag cement pastes [53]. From 3 to 90 days, NaOH -activated phosphorus slag always shows a lower strength than that of $\text{Na}_2\text{O}\cdot 0.5\text{SiO}_2$ -activated slag. The silicate modulus does not show an obvious effect on strength as it increases from 0.5 to 1.5. However, the strength decreases almost linearly with the increase of modulus from 1.5 to 2.5 between 3 and 28 days. Based on the strength results, it can be concluded that the optimum modulus for the slag is around 1.0 to 1.5.

Wang et al. [54] investigated the activation of acidic, neutral and basic blast furnace slags with water glass having different silicate module. Based on the strength at 28 days, the optimum modulus for the acidic slag was around 1.0 for the neutral slag, and around 1.25 for the basic slag, respectively. Those slight differences are not surprising since slag has certain selectivity for activators as discussed above. Malolepszy and Nocun-Wczelik [55] found that both compressive and flexural strengths of sodium silicate activated slag cement mortars decreased with the modulus as it increased from 1 to 2.5. The strength differences for mortars cured at room temperature were more obvious than those cured at elevated temperature.

Bakharev et al. [56] found that the modulus of water glass did not show a distinct effect on strength at early ages at room temperature, but the highest strength was achieved when the modulus of the water glass was around 1.25, regardless of the activator dosage. Shi and Li [53] attributed the optimum modulus phenomena to the formation of "primary C-S-H" and/or polymerization of silicate anions in the water glass, which promotes the hydration of slag and the formation of less porous structure.

26.5.2. Modulus of elasticity and its development

When a load is applied to a concrete material, it always deforms. The deformation is called strain. Stress-strain relationship is very important in structural design. Concrete, like many other construction materials show elastic behavior only to certain degree. Strictly speaking, the Young's modulus of elasticity is only applied to the straight part of stress-strain curve. The tangent to the curve at the origin is called initial tangent modulus. The deformation occurring during loading is elastic and the sequent increase in strain is regarded as creep. The secant modulus is a static modulus.

The stress-strain relationship of Portland cement and AAC-concrete show no obvious difference (Figure 15(a)) [58].

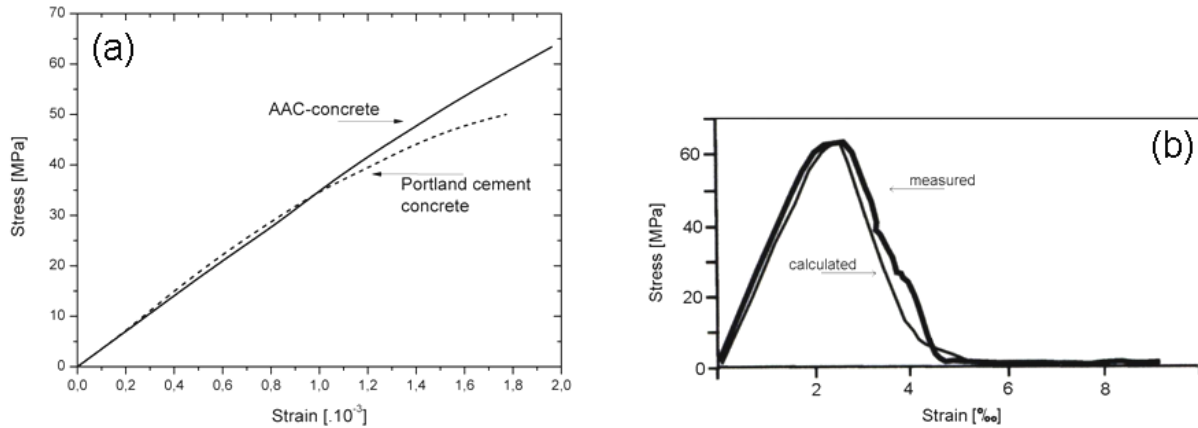


Fig. 16: Stress-strain curves of AAC-concrete and Portland cement concrete [58] (a) and predicted and test stress-strain behavior of geopolymer concrete (b) [2].

Thus, secant modulus of elasticity (ε_c) of AAC-concrete can be estimated from the compressive strength of the conventional Portland cement concrete. The American Concrete Institute (ACI) Committee 318 and 363 has recommended the following expressions to calculate the modulus of elasticity from compressive strength (f_{cm}) [58,2]:

$$(4) \quad \varepsilon_c = 4,73 \cdot \sqrt{f_{cm}} \quad [GPa] ;$$

$$(5) \quad \varepsilon_c = 3320 \cdot \sqrt{f_{cm}} + 6900 \quad [MPa] .$$

The Australian Standard AS3600 recommends equation able to calculate the value of the modulus of elasticity within an error of $\pm 20\%$ [2]:

$$(6) \quad \varepsilon_c = \rho^{\frac{3}{2}} x (0,024 \sqrt{f_{cm}} + 0,12) \quad [MPa] ;$$

where ρ is the unit-weight of concrete in $kg \cdot m^{-3}$.

As mentioned above, the elastic properties of hardened geopolymers and the behavior and strength of structural members are similar to those of Portland cement concrete. Therefore, the design provisions in the current standards and codes may be used to design fly ash-based geopolymer concrete members [10]. The stress-strain relation of Portland cement concrete has form (according to Collins) [2]:

$$(7) \quad \sigma_c = f_{cm} \frac{\varepsilon_c}{\varepsilon_{cm}} \frac{n}{n-1 + \left(\frac{\varepsilon_c}{\varepsilon_{cm}} \right)^{nk}} ;$$

where: f_{cm} is peak stress; ε_{cm} is strain at peak stress; $n = 0.8 + (f_{cm}/17)$; $k = 0.67 + (f_{cm}/62)$ when $\varepsilon_c/\varepsilon_{cm} > 1$ and $k = 1.0$ when $\varepsilon_c/\varepsilon_{cm} \leq 1$.

The equation can be applied to both normal and high strength Portland cement concrete. Figure 15(b) shows a typical stress-strain curve of geopolymer concrete. Aitcin and Mehta [57] reported Young's modulus values of 31.7 GPa and 33.8 GPa when $f_{cm} = 84.8$ MPa and 88.6 MPa, respectively. These values are similar to those measured for geopolymer concrete reported in [58].

26.5.3. Volume changes

The nature and amount of activator is one of the most important factors determining the properties of alkali-activated slag cements and concrete. Of course, it will have a significant effect on the drying volume changes of alkali-activated slag cement and concrete. Following figure shows the drying shrinkage of Portland cement concrete, sodium silicate-activated slag cement concrete and sodium hydroxide-sodium carbonate-activated slag cement concrete. Those specimens were cured in water during the first seven days and showed some expansion. Once they were exposed to drying, sodium silicate-activated slag cement concrete displayed considerably higher dry shrinkage than the OPC concrete.

The drying shrinkage of sodium hydroxide-sodium carbonate-activated slag cement concrete was similar to that of Portland cement concrete up to 56 days, but became significantly higher than that of Portland cement concrete between 56 and 112 days. Thus, it is important to measure the long-term drying shrinkage of the concrete. It was found that lignosulphonate-based admixture caused a slight reduction in shrinkage, while naphthalene-based superplasticiser significantly increased the shrinkage and reduced the strength of alkali-activated slag cement concrete. Air entraining and shrinkage reducing admixtures, as well as gypsum (6 %) were effective in reducing shrinkage of alkali-activated slag cement concrete.

The drying shrinkage of alkali-activated slag cement concrete with different amounts of sodium silicate with a ratio of 1.47 was investigated [58]. Test showed that, after seven days of water curing, there were no obvious differences for the drying shrinkage of those alkali-activated slag cement concretes containing different amounts of sodium silicate. However, those drying shrinkages were obviously higher than Portland cement concrete or Portland slag cement concrete with equivalent water-to-cementing materials ratio and workability [59,58]. Drying shrinkage is caused by the loss of evaporable water. It is generally agreed that there are at least four phenomena involved in the drying shrinkage of the cement paste: capillary stress, disjoining pressure, changes in surface free energy and movement on interlayer water.

Collins and Sanjayan [60] examined the relationship between pore size distribution and drying shrinkage. They noticed that although AASC showed a less porous structure and lost less mass than Portland cement concrete during drying, the former had greater shrinkage than the latter. The drying shrinkage behavior of concrete materials can be described by the pore size distribution and thermodynamic behavior of water in the pores. Pore size distribution can be characterized by r_s , which is defined as the radius of the pores where the meniscus forms; i.e., the pores whose radii are smaller than r_s , are assumed to be filled with liquid water while pores larger than this are dry. As the drying progresses, the parameter r_s would decrease. The smaller the pore size is, the larger the capillary tensile forces set up at the meniscus, hence higher the resulting shrinkage.

26.5.4. Influence of curing condition

Although low-calcium fly ash-based geopolymer concrete can be cured in ambient conditions, heat-curing is generally recommended. Important factors that influence

the properties of hardened fly ash-based geopolymer concrete are the curing temperature and the curing time. Both curing time and curing temperature influence the compressive and flexural strength of geopolymer concrete (Figure 17) [2,58,61]. Higher curing temperature leads to the higher compressive strength. In fly ash-based geopolymer concrete, it's believed that the curing temperature and the curing time play significant roles not only as accelerators of chemical reaction, but also determine the extent of the reaction in question [10]. As the curing temperature in the range of 30 °C to 90 °C increasing, the compressive strength of fly ash-based geopolymer concrete has increasing too [58].

Curing temperature increase seems to affect the development of the strength more at early ages. Higher curing temperature accelerates the slag alkali-activation process, but as reaction time increases at later ages, the curing temperature increment has a negative effect and leads to decrease of final strength values. The explanation for this phenomenon is based in the formation of a large amount of reaction product and a more heterogeneous distribution of the product at early ages in these mixes cured at higher temperature, with subsequent paste densification a microstructure modification. So, as reaction time increases, diffusion processes are more difficult to develop and the following reaction occur slowly [61].

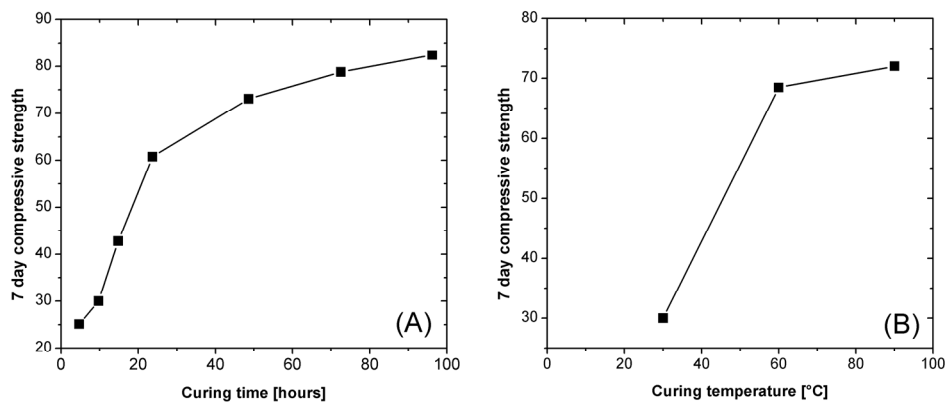


Fig. 17: Effect of curing time (A) and temperature (B) on compressive strength of geopolymer concrete [2].

26.6. Geopolymers durability

26.6.1. Temperature durability

The geopolymeric AAFA material exposed to the effect of high temperatures loses a substantial part of its strength which dropped to 40 percent of its original value. The loss of compressive strength becomes already obvious at a temperature around 250 °C, the heating at higher temperatures does not practically affect this parameter. The minimal values of the residual compressive strength were observed in the temperature range of 600 to 700 °C; they were caused by the occurrence of the melt that began to form. The values of compressive strength (measured on cold samples after their firing) of AAFA materials subjected to the effect of higher temperatures showed a growing tendency; however, this behavior is due to the solidifying melt. Nevertheless, the residual strength of AAFA bodies after their heat treatment is relatively higher than that of the materials on the basis of Portland cement [3].

Concrete strength tests showed that geopolymeric coatings based on metakaolin are effective thermal barriers that can be used to protect concrete from high temperature environments. They exhibit better thermal stability than PC concrete up to 1000 °C, which make them perfect candidates for this application. Although the difference in compressive strength between samples coated with geopolymers of Si/Al ratios between 2 and 6 seems

to be minimal, it is important to point out that the samples with higher Si/Al ratio presented minimal deterioration and absence of cracks besides providing a stronger bond to the concrete substrate which will allow it to retain its insulation properties at higher temperatures or longer periods of time. We believe that this difference will be greater at higher temperatures for longer times.

The original aluminosilicate geopolymers, for example those formed by reaction of dehydroxylated kaolin with sodium silicate at high pH, are initially X-ray amorphous and remain so throughout the curing and drying process [41]. The long-term durability of this amorphous structure depends first on the temperature and time of curing. Alkali-activated slag concrete, is different from geopolymers based of metakaolin by the content of calcium, loses up to 90 % of its initial strength when heated at 1000 °C. The strength decrease is connected with its structure partially consisting of CSH gel phase that undergoes dehydration during the thermal treatment. Further heating on 1200 °C leads to consequent strength increase caused by melting of dehydrated CSH phase that creates new compact binder [63,64].

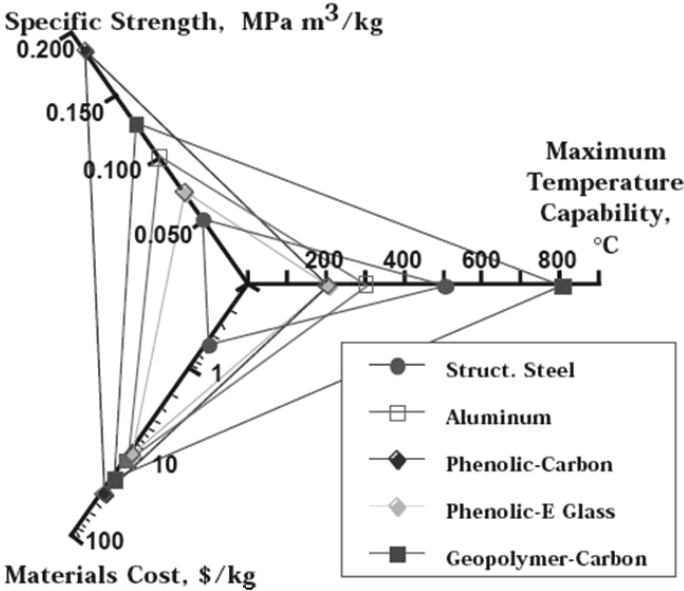


Fig. 18: Specific flexural strength versus materials cost and maximum temperature capability [62].

26.6.2. Carbonation

Carbonation refers to the reaction of hydrated cement with carbon dioxide in the environment. All the cement hydration products can react with carbon dioxide to form calcium carbonate and other products. Moisture is an important factor in carbonation. Carbonation does not proceed in dry cement paste or cement paste at 100 % relative humidity. The optimum condition of carbonation appears to be around 50 % relative humidity [58]. Carbonation of concrete reduces the pH of the material from original > 13 down to about 8, which destroys the passivation and induces the corrosion of steel reinforcement in the concrete. Also, carbonation is usually accompanied with a shrinkage, which may produce cracking or surface deterioration of concrete.

The carbonation of alkali-activated slag cement concrete in 0.352 M sodium bicarbonate (NaHCO₃) solution and in an atmosphere containing 20 % CO₂ at 70 % relative humidity was studied [65]. NaHCO₃ solution was used to simulate carbonated ground water. A conventional PC concrete with the same water-to-binder ratio and similar strength at 28 days was used for comparison purpose. Both strength and carbonated depth were measured and plotted in following Figure 19. It was found that the strength of both alkali-activated slag cement

concrete and Portland cement concrete increased with time, but lower than that of those immersed in water. The difference between the two alkali-activated slag cement concrete was about 10 %, but was only about 4 % for the Portland cement concrete.

After 12 months of immersion in the sodium bicarbonate solution, the alkali-activated slag concrete showed a carbonated depth of 20 mm, and Portland cement concrete a depth of 12 mm. A soft surface could be observed on those carbonated specimens in the solution. The differences between the two concrete can be attributed to the difference in products in the two kinds of concrete before and after carbonation Figure 19.

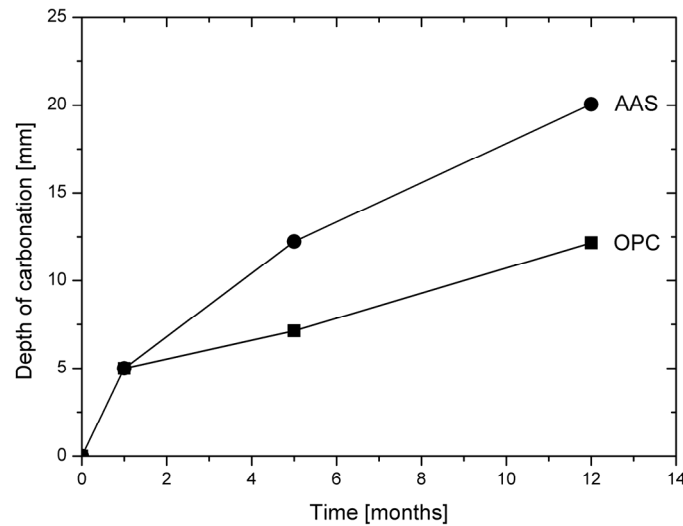
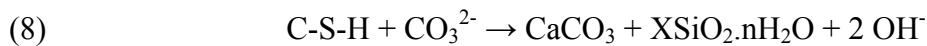


Fig. 19: Carbonation depth of Portland cement concrete and alkali activated slag concrete immersed in sodium bicarbonate solution [65].

It is well known that the main hydration product of alkali-activated slag is C-S-H with a low Ca/Si ratio and geopolymeric structure of polycondensed Al and Si tetrahedrons. The carbonation of C-S-H can be expressed as follows:



Fully hydrated Portland cement pastes, consist roughly of 70 % C-S-H with a high Ca/Si ratio, 20 % Ca(OH)₂, 7 % AFt and 3 % AFm. The carbonation of Ca(OH)₂ is a solid volume increase process:



Carbonation did not show a distinct effect on the strength of Portland cement concrete, but carbonated alkali-activated slag cement concrete showed a lower strength as compared with the reference concrete. The fast carbonation of alkali-activated slag cement concrete may be attributed to the formation of cracks due to both drying and carbonation during the carbonation test [56].

As discussed above, hydrated alkali-activated slag pastes consist mainly of C-S-H with a low Ca/Si ratio and contain almost no crystallized compounds. Under such drying condition, it can be expected that the drying shrinkage of alkali-activated slag pastes is very large as reported previously. Actually, cracking is often observed under scanning electronic microscope in hardened alkali-activated cement and concrete due to drying, which results in fast carbonation, especially at lower relative humidity. Hardened non-crystalline geopolymers are considered to be precursors of zeolites, which can be prepared from the same

starting material, especially at high temperatures and/or pressures [39]. To test the real very long term durability of geopolymeric material prepared by activation of mineral components – pozzolans is not easy to imitate, but their transformation into crystalline phases during several centuries can be expected. At present, different accelerated test are developed [38,25].

26.6.3. Resistance to chloride penetration

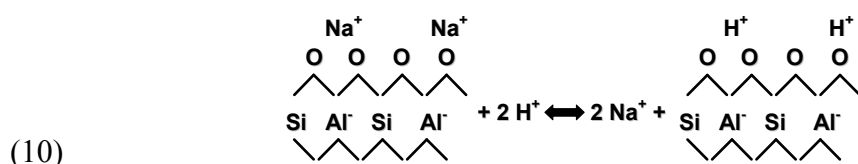
The alkali activated fly ash materials kept in NaCl solution for long periods of time is resistant to the corrosion and does not exhibit any sign of deterioration. The values of compressive strength of AAFA geopolymer materials exposed to the NaCl solution increased over the whole period of measurement (720 days) and achieved as much as 70 MPa. The mass of samples kept in the NaCl solution increased during the 1st year by about 3 rel. % and remained stable afterwards. The penetration of chloride ions into the AAFA body (measured perpendicularly in the direction from the surface in contact with the chloride solution) showed a decreasing tendency and the chloride concentration in the body was low.

The penetration of chloride ions was greater than that of sulfates, which is probably due to the smaller size of chloride ions. Practically no corrosion products were observed on the surface of AAFA geopolymer materials kept in the NaCl solution. No new crystalline phases formed when the AAFA materials were kept in Na₂SO₄ and NaCl solutions. The resistance of AAFA materials to salt solutions is very good as compared with that of the Portland cement-based concrete in which crystalline ettringite or the Friedel salt is formed thus giving rise to the body disintegration due to the crystallization force [3].

26.6.4. Resistance to chemical attack

The deterioration of geopolymer materials in acidic media brings about consequent depolymerization of aluminosilicate polymers and liberation of silicic acid, replacement of Na⁺ and K⁺ cations by hydrogen or oxonium ion and delamination of the aluminosilicate structure. It is also connected to condensation of siliceous polymers and zeolites, which in some cases lead to a significant loss of strength. In acidic environment, high-performance geopolymer materials deteriorate with the formation of microcracks in amorphous polymer matrix, while low performance geopolymers deteriorate due to crystallization of zeolites and formation of fragile grainy structures.

To understand the process that takes place in the geopolymer materials immersed in the acidic solution, let us start with the reactions that occur in the materials before immersion. The possible chemical processes of dissolution of the starting materials and condensation of silicate and aluminate monomers can be represented by the following reaction scheme [6]:



Interaction of geopolymers with the acid solutions can also cause replacement of the exchangeable cations (Na⁺, K⁺) in polymers by hydrogen or oxonium ions [66]. However, treatment of a geopolymer with a strong acid may result in a direct attack on the aluminosilicate framework and dealumination. This attack will cause breakage of the Si–O–Al bonds, increased number of Si–OH and Al–OH groups and increased amount of silicic acid ions and [Si₂O₅]²⁻ in solution. Therefore, this process leads to a mass loss of the geopolymer materials. Polymer structures with a Si/Al ratio of 1 are more subject to the attack by the acid

than more siliceous polymers. Acid consumption for the complete matrix destruction of Portland cement and alkali-activated slag cement is listed in Table 7.

Table 7: Amount of acid required for complete matrix destruction of cementing material [58].

Corrosion media	pH	Consumed acid (mmol of acid/ g of dry hardened paste)	
		Portland cement	Alkali-activated slag cement
HNO ₃	3	19	25
CH ₃ COOH		160	360
CH ₃ COOH	5	21	12

Stability of geopolymeric materials in aggressive environment depends on the intrinsic ordering present within aluminosilicate gel. More crystalline geopolymer material prepared with sodium hydroxide was more stable in the aggressive environment of sulfuric and acetic acid solutions than amorphous geopolymers prepared with the sodium silicate activator. The chemical instability would also depend on the presence of the active sites on the aluminosilicate gel surface, which appeared to increase in the presence of K⁺ ions. Instability of strength in some geopolymers must be taken into account in their use as a construction material, and careful consideration should be given to this aspect [67].

26.6.5. Frost – thaw resistance

The frost resistance of concrete is of considerable importance in areas where freezing happens. The moisture in concrete will freeze when concrete is cooled to certain temperatures. Due to the capillary effect, water in capillary pores is freezing at a lower temperature than bulk water [58]:

$$(11) \quad \left(1 - \frac{T}{T_0}\right) = \frac{2v_f \sigma_f}{f q};$$

where: T_0 is normal freezing temperature (273.15 K) of water; T is freezing temperature in a capillary pores with a radius r ; v_f is molar volume ($18.018 \cdot 10^{-6} \text{ m}^3 \cdot \text{mol}^{-1}$); σ_f is surface tension of water ($75.62 \cdot 10^{-3} \text{ N} \cdot \text{m}^{-1}$); q is latent heat of fusion of water ($6017 \text{ J} \cdot \text{mol}^{-1}$).

The mass of the samples did not change (no body disintegration occurred) during the freezing and thawing cycles in aqueous environment. The values of the compressive strength of samples were smaller after thawing cycles as compared with the values obtained for the samples after 28 days without any frost resistance testing. No damage or deformation could be detected after 150 cycles. The strength of the samples after 150 freezing cycles dropped to about 70 percent of that determined in standard samples after the same period of time [3]. It is obvious from the results obtained that the geopolymers materials on the basis of the fly ash possess an excellent frost resistance [68].

The deformation of alkali-activated slag cement pastes during freezing is different from that of Portland cement, which may be attributed to different electrolyte in their pore solution. The solution in capillary pores of Portland cement pastes freezes spasmodically and the meniscus disappears, whereas the solution in capillary pores of alkali-activated slag cement paste freezes gradually and the meniscus remains during freezing. Furthermore is freezing point of the pore solution affected by the nature of alkaline activator. For example potassium carbonate eutectic mixture show freezing point $-36 \text{ }^\circ\text{C}$, while sodium carbonate only $-2.1 \text{ }^\circ\text{C}$.

The other reason for the lower freezing point of alkali activated slag cement pastes, compared with Portland cement pastes, could be attributed to the difference in their pore structure. Alkali-activated cement pastes contain more gel pores while Portland cement pastes contain more capillary pores for given water-to-cement or water-to-slag ratio. Like Portland

cement concrete, the frost resistance of alkali-activated slag cement concretes, to a great extend, depends upon the pore solution chemistry, freezing rate a curing condition [58].

26.7. Some examples of utilization of geopolymers

Alkali activated cements have found a variety of applications, particularly since the 1970s, such as agricultural, industrial, residential, transportation (e.q. railway), mining, breakwater, various high volume applications, oil well cements and water stop or sealing applications. There appears to be much evidence for including alkali-activated cements among those used to generate high performance. Some applications are summarized in Table 8 [13], but many other possible applications of geopolymer, such as fiber composites, foam and ceramic..., was described in literature [2,58,69].

Table 8: *Applications of alkali-activated cements* [13].

	Roads	Agriculture	Industrial	Residential	Mining	Hydraulic
Construction	Heavy-duty pavements cast in situ and pre-cast; reinforced	Cast in situ and pre-cast concrete; storage	Acid-resistant buildings; garages floor slabs; self computing floors; foundations; waste water tubes; fire resistant materials; isolations;	Pre-cast and in situ concrete buildings; slabs; foundations; tiles; fire resistant applications; isolations;	Oil well grouts; sealing; prevent water penetrations	Irrigation systems; break waters
Nonconstruction	Waste immobilization		Bodies of machine tools	Dies; molds		Linings

Utilization of geopolymers such as alternative to Portland cement concrete having increasing importance and extension is based on thirty years of R&D and on experiences with first buildings and elements produced as soon as in seventieth. First multi-storey house was built in Lipeck (Russia), later irrigation ditches, concrete blocks, wall panels, slabs, pavements, railway sleepers, tiles etc. have been produced in Ukraine, China, Finland, Poland, Romania and in Czechoslovakia. Very promising is the use of geopolymers in architecture and sculpture. Advanced production is developed also in France, Australia and in Spain. Increasing utilization of geopolymers possessing ion-exchanging properties is in immobilizing of potentially toxic elements. One of the main advantages is the possibility to use industrial secondary raw mineral products (slag, fly ashes...) – aluminosilicates possessing pozzolanic properties, which save mineral resources and contribute to the reduction of carbon dioxide emissions.

Geopolymers are relatively new types of inorganic binder for the production of building materials, which can partly substitute of Portland cement used nowadays for these purposes. Application of geopolymeric binder is also favorable from ecological point of view, because of considerably lower amount of carbon dioxide formed during production of geopolymeric binder in comparison with Portland cement, which contributes substantially to the amount of greenhouse gases in atmosphere. One of main restrictive factor for spreading geopolymers is the cost of raw materials (metakaolin, hydroxides and silicates of alkali metals). As a possible way how to reduce the price of geopolymeric binder is a utilization of secondary raw materials, e.g. fly ash, slag or low-quality natural aluminosilicates. In case of these raw materials, the chemical and mineralogical composition of geopolymer can be very different.

Geopolymers have been frequently suggested as a material suitable for stabilization/solidification (S/S) hazardous wastes containing heavy metals. In immobilization of potentially toxic elements, a geopolymer system works similarly to cement binders in terms of encapsulation, exhibit improved chemical and physical properties, such as structural integrity, low permeability, high compressive strength and long term durability.

Low permeability is the property that favors the use of these materials as immobilization systems for hazardous metals. The mechanisms of encapsulation are believed to be either physical or chemical nature, where metals are taken into the geopolymer network and possibly bound into the structure for charge balancing roles or remain physically trapped by surrounding network. There was found that fly ash-based geopolymer systems show improved immobilization of heavy metals in S/S solids. The results of many studies tested on wastes containing many different heavy metals, such as Cr^{6+} , Cr^{3+} , Cd^{2+} , Cu^{2+} , Pb^{2+} , Zn^{2+} and other, show that these elements can be effectively immobilized in the geopolymeric matrices. However, many of the exact details of the processes by which heavy metals cations are incorporated into the geopolymer structure are not yet fully explained [70-72].

The resistance of heavy metals containing geopolymers to leaching in different environments depends very strongly on both nature of the heavy metal and the aggressive components of the leaching solution [71]. The leachate pH is one of the most important variables for the immobilization of many metals [70]. Geopolymers have ability to reduce the leaching rate of heavy metals, particularly at high pH. Leaching behavior of Cd, Cu, Pb and Cr indicates that the concentration of alkali activators influence distinctly immobilization efficiency. Alkali activators concentration has greater influence on Cu and Cd than Pb and Cr. Encapsulation efficiency of Cd and Cu is enhanced in early curing time at high pH than that of at low pH. Moreover, immobilization of Cu within fly ash-based geopolymers was not as effective due to increased lability of Cu precipitates. The Cr and Pb show better immobilization efficiency which isn't obviously influenced by pH [34,72].

It was found, that mechanism of immobilization of Pb and Cu not only involves a physical encapsulation mechanism, but the formation of a new phases through the reaction of the insoluble Pb or Cu compounds with Al- and Si- species dissolved from the aluminosilicate source. Moreover, the immobilization mechanism of Pb is directly affected by the extractable cations from the Al source, while the physical characteristics (suspension viscosity and final compressive strength) of the Al source largely control the immobilization of Cu [34].

26.8. Conclusion

To increase the productivity of material, it is necessary to prevent wasting. The utilization of mineral "wastes" is demanded, solving economical and ecological problems at the same time. In fact, many thus far neglected and dumped industrial by-products are very good material possessing different important properties useful for further production activities. The necessity to decrease considerably the CO_2 emissions in the 21st century will lead to the broader production of binders and concrete – geopolymers of different composition and properties, enlarging the assortment of binders and concrete, based thus far primarily on Portland cement. The production of geopolymers from different aluminosilicates at ambient temperature, their dense amorphous micro(nano)structure and resistance to chemical corrosion predestinates geopolymer as very important, ecologically favorable material for the 21st century in many branches of the building industry.

Acknowledgement: This study was supported by the Czech Science Foundation No. SP 20422416 and the Czech industrial grant FR-TI 1/335.

Shortcuts and symbols index:

A	– Specific surface area	NMR	– Nuclear Magnetic Resonance
AAC	– Alkali-Activated Cement	OPC	– Ordinary Portland Cement
AAFA	– Alkali-Activated Fly Ash	PC	– Portland cement
AAS	– Alkali-Activated Slag	Q	– Heat released during hydration

AASC	– Alkali-Activated Slag Cement	q	– Latent heat of fusion of water
ACI	– American Concrete Institute	r_s	– Pore radius
AF _m	– Monosulphate	S/S	– Stabilization or Solidification
AF _t	– Ettringite, Trisulphate	SEM	– Scanning Electron Microscopy
BFS	– Blast Furnace Slag	T	– Temperature
CH	– Portlandite	t	– Time
CS	– Calcium Sulfate	v_f	– Molar volume of water
CSH	– Calcium Silicate Hydrate	y	– Degree of reaction
f_{cm}	– Compressive strength	ε_c	– Modulus of elasticity
K	– Reaction constant	ε_{cm}	– Strain at f_{cm}
K_D	– Depolymerization rate constant	ρ	– Unit weight
N	– Reaction grade	σ_f	– Surface tension of water

References 26

- [1] Fernández-Jiménez, A., Monzó, M., Vincent, M., Barba, A., Palomo, A.: *Alkaline activation of metakaolin–fly ash mixtures: Obtain of Zeoceramics and Zeocements*, Microporous and Mesoporous Materials 108 (2008) 41 – 49.
- [2] Davidovits, J.: *Geopolymer, Chemistry & Application*. Geopolymer Institute, Saint-Quentin, France, 2008, p.595. ISBN: 2-9514820-1-9.
- [3] Mackenzie, K.J.D.: *What Are These Things Called Geopolymers? A Physicochemical Perspective*. In: *Advances in ceramic matrix composites IX: Proceedings of the symposium held at the 105th Annual Meeting of The American Ceramic Society, April 27, in Nashville, Tennessee, Ceramic Transactions, Vol. 153, 1st edition*. Editors: Bansal, N.P., Singh, J.P., Kriven, W.M., Schnaider, H.: Wiley-American Ceramic Society, 2003, p.175 – 186. ISBN 1574982079.
- [4] Davidovits, J.: *Why the pharaohs built the Pyramids with fake stones, 2009*, p.288. ISBN: 9782951482043.
- [5] Purdon, A.O.: *The action of alkalis on blast-furnace slag*. Journal of the Society of Chemical Industry 59 (1940) 191 – 202.
- [6] Gluchovski, V.D.: *Gruntosilikaty*. Grosstrojizdat, Kiev 1959.
- [7] Derdacká, A., Malolepszy, J.: *The Use of Granulated Blast Furnace Slag for Manufacturing Clinkerless Hydraulic Binding Materials*. Cement - Vapno - Gips 29 (1975) 291 – 295.
- [8] Talling, B., Brandstetr, J.: *Present State and Future of Alkali Activated Slag Concrete*. In: *Proceedings of the 3rd Conference on Fly Ash, Silica Fume, Slag and Natural Pozzolans in Concrete (Malhotra V.M. Ed.)*, Trondheim. Spec Publ. 114 – 74, p.1519 – 1545. ACI/CANMET, Ottawa 1989.
- [9] Brandstetr, J.: *Slag-alkaline Concretes* (in Czech). Stavivo 64 (1984) 10 – 114.
- [10] Douglas E., Biloodeau, A, Brandstetr, J., Malhotra, M.: *Activated Ground Granulated Blast-Furnace Slag: Preliminary Investigation*. Cement and Concrete Research 21 (1991) 101 – 108.
- [11] Davidovits, J.: *Ancient and Modern Concretes: What is the Real Difference?* Concrete International 9 (1987) 23 – 35.
- [12] Davidovits, J.: *Geopolymer chemistry and sustainable development. The Poly(sialate) terminology : a very useful and simple model for the promotion and understanding of green-chemistry*. In : *Proceedings of the World Congress "Geopolymer 2005"*. Geopolymer Institute, Saint-Quentin, France, 2005.
- [13] Roy, D.M.: *Alkali-activated cement Opportunities and challenges*. Cements and Concrete Research 29 (1999) 249 – 254.

- [14] Krivenko, P.V.: *Slag-alkaline cements and concrete*. Proceedings of the conference in Kiev, 1984.
- [15] Van Jaarsveld, J.G.S., Van Deventer, J.S.J.: *The Potential Use of Geopolymeric Materials to Immobilize Toxic Metals: Part 1: Theory and Applications*. Minerals Engineering 7 (1996) 659 – 669.
- [16] Taylor, H.F.W.: *The Chemistry of Cements*, vol. 1, 1st ed., Academic Press, London, 1964.
- [17] Phair, J.W., Van Deventer, J.S.J.: *Characterization of fly-ash based geopolymeric binders activated with sodium aluminate*. Industrial and Engineering Chemistry Research 41 (2002) 4242 – 4251.
- [18] Richardson, G., Cabrera, J.G.: *The nature of C–S–H in model slag cements*. Cement and Concrete Composites 22 (2000) 259–266.
- [19] Davidovits, J.: *Geopolymers: Inorganic Polymeric New Materials*. Journal of Thermal Analysis 37 (1991) 1533 – 1656.
- [20] Xu, H., Van Deventer, J.S.J.: *The geopolymerisation of alumino-silicate minerals*. International Journal of Mineral Processing 59 (2000) 247 – 266.
- [21] Phair, J.W., Van Deventer, J.S.J.: *Characterization of fly-ash based geopolymeric binders activated with sodium aluminate*. Industrial and Engineering Chemistry Research 41 (2002) 4242 – 4251.
- [22] Lee, W.K.W., Van Deventer, J.S.J.: *Structural reorganization of class F fly ash in alkaline silicate solutions*. Colloids and Surfaces A: Physicochemical and Engineering Aspects 211 (2002) 49– 66.
- [23] Opravil, T., Brandstetr, J., Ptáček, P., Šoukal, F.: *Preparation and properties of pure geopolymer systems and some application for preparation of synthetic sandstone*. In Proceedings: "Ecology and new building materials and products", Telč 2008, p. 163-166. Výzk. ústav stavebních hmot Brno. ISBN: 978-80-254-2029-4.
- [24] Van Jaarsveld, J.G.S., Van Deventer, J.S.J.: *Effect of the alkali metal activator on the properties of fly ash-based geopolymers*, Industrial and Engineering Chemistry Research 38 (1999) 3932 – 3941.
- [25] Škvára, F.: *Alkali activated materials or geopolymers?* Ceramics-Silikáty 51 (2007) 173 – 178.
- [26] Brandstetr, J., Havlica, J., Opravil, T.: *Geopolymeric Materials: Ancient and Contemporaneous*. In 9th CANMET/ACI International Conference on Fly Ash, Silica Fume, Slag and Natural Pozzolans in Concrete. Supplementary papers, p. 1 - 8. Warsaw, 2007.
- [27] Roy, D.M.: *New Strong Cement Materials: Chemically Bonded Ceramics*. Ceramics Science 235 (1987) 651 – 658.
- [28] Li, Z., Ding, Z., Yunsheng, Z.: *Development of Sustainable Cementitious Materials*. In: International Workshop on Sustainable Development and Concrete Technology. 1st edition, 2004, p. 55-76.
- [29] Kavalerova, E.: *Alkaline cements and concretes: economical, ecological and legislative aspects*. In. Proceedings - see [22], p. 293 – 302.
- [30] Brandstetr, J., Havlica, J., Opravil, T., Šoukal, F.: *Some non-traditional binders and composites tested at the student laboratories of the Institute of Materials Chemistry, Brno University of Technology*. Chemické listy 102 (2008) 822 – 826.
- [31] Duxson, P., Provis, J.L., Lukey, G.C., Van Deventer, J.S.J.: *The role of inorganic polymer technology in the development of 'green concrete'*. Cement and Concrete Research 37 (2007) 1590 – 1597.
- [32] Fernández-Jiménez, A., Monzó, M., Vincent, M., Barba, A., Palomo, A.: *Alkaline activation of metakaolin–fly ash mixtures: Obtain of Zeoceramics and Zeocements*. Microporous and Mesoporous Materials 108 (2008) 41 – 49.

- [33] Fernández-Jiménez, A., Palomo, A., Criado, M.: *Microstructure development of alkali-activated fly ash cement: a describe model*. Cement and Concrete Research 35 (2005) 1204 – 1209.
- [34] Phair, J.W., Van Deventer, J.S.J., Smith, J. D.: *Effect of Al source and alkali activation on Pb and Cu immobilization in fly-ash based “geopolymers”*. Applied Geochemistry 19 (2004) 423 – 434.
- [35] Pacheco-Torgal, F., Castro-Gomes, J., Jalali, S.: *Alkali-activated binders: A review Part 1. Historical background, terminology, reaction mechanisms and hydration products*. Construction at Building Materials 22 (2008) 1305 – 1314.
- [36] Provis, J.L., Van Deventer, J.S.J.: *Geopolymerization kinetic. 2. Reaction kinetic modeling*. Chemical Engineering Science 62 (2007) 2318 – 2329.
- [37] Iller, R.K.: *The Chemistry of Silica*. Wiley, New York, 1979, p.866. ISBN: 0-471-02404-X.
- [38] Škvara, F.: *Alkali Activated Material - Geopolymer*. In the proceedings "Alkali Activated Materials - Research, Production, Utilisation.", (Zethamlová M., Ed.) Agentura Action M, Praha 2007, p. 661-676. ISBN: 978-80-86742.
- [39] Koloušek, D., Štyriáková, I., Kovanda, F., Tannenberk, R., Dorničák, V.: *Environmental aspects of zeolite synthesis from fly ashes*, In: Opportunities and Limitations, Morrella, Spain, 2000, p. 4 – 7.
- [40] Xu, H., Van Deventer, J.S.J.: *The geopolymerisation of natural aluminosilicates*. In: Proceedings of the conference "Geopolymer 1999". Geopolymer Institute, Saint-Quentin, France, 1999.
- [41] Barbosa, V.F.F., Mackenzie, K.J.D., Thamarurgo, C.: *Synthesis and Characterisation of Materials Based on Inorganic Polymers of Alumina and Silica*. International Journal of Inorganic Materials 2 (2000) 309 – 317.
- [42] Xu, H., Van Deventer, J.S.J.: *The geopolymerisation of alumino-silicate minerals*, International Journal of Mineral Processing 59 (2000) 247 – 266.
- [43] Glukhovskiy, V.D., Rostovskaya, G.S., Roumyna, G.V.: *High strength slag-alkali cement*. In: Proceedings "7th International Congress on Chemistry of Cements". Paris, France, 1980.
- [44] Fernández-Jiménez, Palomo, A., Criado, M.: *Microstructure development of alkali-activated fly ash cement: a describe model*. Cement and Concrete Research 35 (2005) 1204 – 1209.
- [45] Provis, J.L., Walls, A.W., Van Deventer, J.S.J.: *Geopolymerization kinetics. 3. Effects of Cs and Sr salts*. Chemical Engineering Science 63 (2008) 4480 – 4489.
- [46] Pacheco-Torgal, F., Castro-Gomes, J., Jalali, S.: *Alkali-activated binders: A review Part 2. About materials and binders manufacture*. Construction and Building Materials 22 (2008) 1315 – 1322.
- [47] Cheng, T.W., Chiu, J.P.: *Fire-resistant geopolymer produced by granulated blast furnace slag*. Minerals Engineering 16 (2003) 205 – 210.
- [48] Fernández-Jiménez, A., Puertas, F.: *Alkali-activated slag cements: Kinetic studies*. Cement and Concrete Research 27 (1997) 359 – 368.
- [49] Huanhai, Z., Xuequan, W., Zhongzi, X., Mingshu, T.: *Kinetic study on hydration of alkali-activated slag*. Cement and Concrete Research 23 (1993) 1253 – 1258.
- [50] Krivenko, P.V.: *Alkaline cements*. 1st International Conference on Alkaline Cements and Concretes. Kiev, Ukraine 1 (1994) 11 – 130.
- [51] Shi, C., Day, R.L.: *Factors affecting early hydration characteristics of alkali-slag cements*. Cement and Concrete Research 26 (1996) 439 – 438.
- [52] Shi, C., Day, R.L.: *Selectivity of alkaline activators for the activation of slags cement*. Concrete and Aggregate 18 (1996) 8 – 14.

- [53] Shi, C., Li, Y.: *Investigation on some factors affecting the characteristics of alkali-phosphorous slag cement*. Cement and Concrete Research 19 (1989) 527 – 533.
- [54] Wang, S., Scrivener, K.L., Pratt, P.L.: *Factors affecting the strength of alkali-activated slag*. Cement and Concrete Research 24 (1994) 1033 – 1043.
- [55] Malolepszy, J., Nocun-Wczelik, W.: *Microcalorimetric studies of slag alkaline binders*. Journal of Thermal Analysis 33 (1988) 431 – 434.
- [56] Bakharev, T., Sanyayan, J.G., Cheng, Y.B.: *Alkaline activation of Australian slag cements*. Cement and Concrete Research 29 (1999) 113 – 120.
- [57] Aitcin, P.C., Mehta, P.K.: *Effect of Coarse-Aggregate Characteristics on Mechanical Properties of High-Strength Concrete*. ACI Materials Journal 87 (1990) 103 – 107.
- [58] Shi, C., Krivenko P.V., Roy D.M.: *Alkali-Activated Cements and Concretes*. Taylor & Francis, 2006. ISBN10: 0-415-70004-3.
- [59] Douglas, E., Bilodeau, A., Malhotra, V. M.: *Properties and durability of alkali-activated slag concrete*. ACI Materials Journal 89 (1992) 509 – 516.
- [60] Collins, F.G., Sanyayan, J.G.: *Effect of ultra fine materials on workability and strength of concrete containing alkali-activated slag as the binder*. Cement and Concrete Research 29 (1999) 459 – 462.
- [61] Fernández-Jiménez, Palomo, A., Pueratas, F.: *Alkali-activated slag mortars: Mechanical strength behaviour*. Cement and Concrete Research 29 (1999) 1313 – 1321.
- [62] Lyon, R.E., Foden, A.J., Balaguru, P., Davidovits, J., Davidovcs, M.: *Properties of geopolymer matrix-carbon fiber composites*. in Geopolymer 1999. Geopolymer Institute, Saint-Quentin, France, 1999.
- [63] Rovnaník, P., Bayer, P., Rovnaníková, P.: *The influence of the kind of aggregate during heating of silicate composites to high temperatures*. In Czech: Vliv druhu kameniva na vlastnosti silikátových kompozitů při zahřívání na vysoké teploty. In: Proceedings X. conference - Ekologie a nové stavební hmoty a výrobky, p.145-149. Telč, Výzkumný ústav stavebních hmot Brno, 2006. ISBN 80-239-7146-8.
- [64] Rovnaníková, P., Bayer, P., Rovnaník, P., Novák, J.: *Properties of alkali-activated aluminosilicate materials with fire-resistant aggregate after high temperature loading*. In: Cement Combinations for Durable Concrete, p.277–286. Dundee 2005. ISBN 0-7277-3401-6.
- [65] Bakharev, T., Sanyayan, J.G.: Cheng, Y.-B., *Resistance of alkali-activated slag concrete to carbonation*. Cement and Concrete Research 31 (2001) 1277 – 1283.
- [66] Cambell, D.H., Folk, R.L.: *The ancient Egyptian pyramids - concrete or rock?* Concrete International, August 1991, p.29 – 44.
- [67] Langton, C.A., Roy, D.A.: *Longevity of borehole and shaft sealing materials: Characterisation of ancient cement-based building materials*. Symposium Proceedings No.26, Materials Research Society, Pittsburgh, 1984, p. 543 – 549.
- [68] Wu, Y.D., Meure, S., Solomon, D.: *Review of recent research on alkali-activated concrete in China*. Magazine of Concrete Research 43 (1991) 29 – 35.
- [69] Wagh, A.S.: *Chemically bonded phosphate ceramics: 21st Century Materials with Diverse Application*. Elsevier, 2004. ISBN: 0-08-044505-5.
- [70] Pereira, F.C., Luna, Y., Querol, X., Antenucci, D., Vale, J.: *Waste stabilization/solidification of an electric arc furnace dust using fly ash-based geopolymers*. Fuel 88 (2009) 1185 – 1193.
- [71] Zhang, J., Provis, J.L., Feng, D., Van Jannie, J.S.J.: *Geopolymers for immobilization of Cr⁶⁺, Cd²⁺ and Pb²⁺*. Journal of Hazardous Materials 157 (2008) 587 – 598.
- [72] Xu, J.Z., Zhou, Y.L., Chang, Q., Qu, H.Q.: *Study on the factors of affecting the immobilization of heavy metals in fly ash-based geopolymers*. Materials Letters 60 (2006) 820 – 822.



Chapter 27

Scanning transitiometry

27. APPLICATION OF SCANNING TRANSITIOMETRY IN PETROLEUM INDUSTRY AND IN POLYMER AND FOOD SCIENCES

Jean-Pierre E. Grolier

27. 1. Introduction

Investigation of solid phase equilibria in asymmetric binary mixtures is not only of general interest to explore phase equilibria in three-phase (gas, liquid, solid) systems but it has a major role in understanding and monitoring the pT -behaviour of petroleum fluids. Such fluids present a vast variety of compositions in terms of their respective constituents from light gases and liquids of various molecular sizes to macromolecular solids. Nowadays, the lack of thermodynamic data on asphaltenic fluids prevents the large scale exploitation of heavy oils in deep deposits. The main concern is the uncontrolled precipitation/flocculation of heavy fractions (asphaltenes, waxes) which causes obstruction and plugging of underground as well as surface installations and pipes. Research in polymer science continues to develop actively while the concepts of thermodynamics and kinetics together with polymer chain structure enhance the domain of polymer development and transformation. In many industrial applications, during extrusion processing or as all purpose materials, polymers are usually submitted to extreme conditions of temperature and pressure. Furthermore they are also very often in contact with gases and fluids, either as on-duty materials (containers, pipes) or as process intermediates (foaming, molding). Since such materials are often used in special environments or under extreme conditions of temperature and pressure, their careful characterization must be done not only at the early stage of their development but also all along their life cycle. Furthermore, their properties as functions of temperature and pressure must be well established for the optimal control of their processability. This also stands for phase transitions; ignorance of a phase diagram, particularly at extreme conditions of pressure, temperature, and of chemical reactivity, is a limiting factor to the development of an industrial process, *e.g.*, sol-gel transitions, polymerization under solvent near supercritical conditions, micro-and nano-foaming processes. Natural and bio-polymers constitute an important class of components largely used in food science. Among the numerous such polymers, starch serves to illustrate the complexity of state equilibria of systems containing other species like fibers, fat, proteins, in addition of extended ranges of water percentages.

In food science, industrial processing of such systems, for example during cooking extrusion, requires in depth thermodynamic as well as thermophysical characterization of the systems to process. All above fields to cite a few, in oil industry and in polymer and food applications, necessitate the acquisition of key data. Undoubtedly, thermal and calorimetric techniques are essential in this respect. In relating thermal as well as mechanical behavior to materials' structures these techniques are perfectly adapted to provide accurate data in wide ranges of temperature and pressure.

Typically, thermophysical properties feature the most important information expected when dealing with materials submitted to thermal variations and/or mechanical constraints. The properties of interest are of two types, bulk properties and phase transition properties. The bulk properties are either caloric properties, like heat capacities C_p , and mechanical properties, like isobaric thermal expansivities α_p , isothermal compressibilities κ_T , and isochoric thermal pressure coefficients β_V . The two main thermal properties concern the first order transitions, fusion and crystallization, and the glass transition. All these properties are now accessible thanks to recent progress in various technologies which allow measurements in the three physical states over extended ranges of p and T , including in the vicinity of the critical point. In this respect, knowledge, *i.e.* measurements, of the thermophysical properties of polymers over extended ranges of temperature and pressures and in different gaseous environments is absolutely necessary to improve the use and lifetime of end products made of such polymers. The purpose of this chapter is to demonstrate the contribution of the new technique, *scanning transitiometry*, in providing accurate information to meet the demand for the different data pointed out. Examples have been selected in three main domains, oil exploitation and transport, polymer foaming and modification, and starch-water systems. As a matter of fact, these examples are directly connected to industrial activities: the petroleum industry, the insulating material industry, and the food industry. In many cases, gases and polymers of different types and from different origins (synthetic, natural) are intimately interacting under external conditions of temperature (T) and pressure (p). In the subsequent examples the gas/polymer systems are either selected for a targeted industrial purpose *i.e.* foaming materials and materials processing, or are polymeric materials in contact with gas/liquid systems, *i.e.* pipes or tanks in gas and petroleum industry. The foaming materials industry is a rapidly growing area where constant innovation and added value products are key factors for economic success where international competition is high. The mastering of polymer degradation (typically blistering) by high pressure dissolved gases is another key issue. In what follows, in a first section the newly developed technique will be described. In a second section selected examples will illustrate how such technique is providing valuable data for significant progresses in different fields.

27. 2. Scanning transitiometry

Calorimetry is certainly a major technique to measure thermodynamic properties of substances and to follow phase change phenomena. In most applications, calorimetry is carried out at constant pressure while the tracked phenomenon is observed on increasing or decreasing the temperature. The possibility of controlling the three most important thermodynamic variables (p , V and T) in calorimetric measurements makes it possible to perform simultaneous measurements of both thermal and mechanical contributions to the thermodynamic potential changes caused by the perturbation. Calorimetric techniques provide valuable additional information on transitions in complex systems. Their contributions to the total change of thermodynamic potential not only leads to the complete thermodynamic description of the system under study, but also permits investigation of systems with limited stability or systems with irreversible transitions. By a proper external change of the controlling variable the course of a transition under investigation can be

accelerated, impeded or even stopped at any degree of its advancement and then taken back to the beginning, all with simultaneous recording of the heat and mechanical variable variations. In what follows the main characteristics of scanning transitiometry are reviewed.

The seminal presentation by Randzio [1] of thermodynamic fundamentals for the use of state variables (p, V, T) in scanning calorimetric measurements has opened the path [2-4] from p, V, T -calorimetry to the now well established scanning transitiometry technique [5]. With this technique the simultaneous determination of thermal and mechanical responses of the investigated system, perturbed by a variation of an independent thermodynamic variable while the other independent variable is kept automatically constant, allows the determination of thermodynamic derivatives over extended ranges of pressure and temperature, impossible to obtain by other known techniques. Four thermodynamic situations are thus possible to realize in the instruments based on such technique, namely, pVT-controlled scanning calorimeters or simply *scanning transitiometers*, since they are particularly adapted to investigate transitions by scanning one of the three thermodynamic variables. The four possible thermodynamic situations (see Figure 1) are obtained by simultaneous recording of both heat flow (thermal output) and the change of the dependable variable (mechanical output).

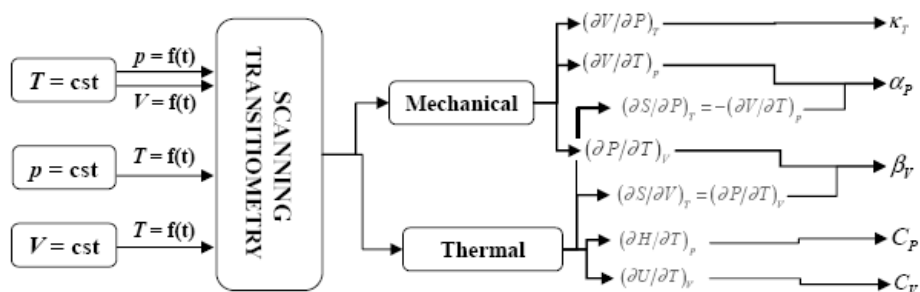


Fig. 1. Thermodynamic scheme of scanning transitiometry showing the four possible modes of scanning. Each of these modes delivers two output derivatives (mechanical and thermal) which in turn lead to four pairs of the different thermomechanical coefficients, namely: α_P , κ_T , β_V , C_P , and C_V .

Then, making use of the respective related Maxwell relations one readily obtains the main thermophysical properties as follows: *a)* scanning pressure under isothermal conditions yields the isobaric thermal expansivity α_P and the isothermal compressibility κ_T as functions of pressure at a given temperature; *b)* scanning volume under isothermal conditions yields the isochoric thermal pressure coefficient β_V and the isothermal compressibility κ_T as functions of volume at a given temperature; *c)* scanning temperature under isobaric conditions yields the isobaric heat capacity C_P and the isobaric thermal expansivity α_P ; *d)* scanning temperature under isochoric conditions yields the isochoric heat capacity C_V and the isochoric thermal pressure coefficient β_V .

Then, making use of the respective related Maxwell relations one readily obtains the main thermophysical properties as follows: *a)* scanning pressure under isothermal conditions yields the isobaric thermal expansivity α_P and the isothermal compressibility κ_T as functions of pressure at a given temperature; *b)* scanning volume under isothermal

The whole assembly is placed in a thermal insulation enclosed in a stainless steel body and placed on a stand, which permits to move the calorimeter up and down over the calorimetric vessels. The actual operating ranges of scanning transitiometry are respectively $173\text{ K} < T < 673\text{ K}$ and $0.1\text{ MPa} < p < 200\text{ MPa}$ (or 400 MPa).

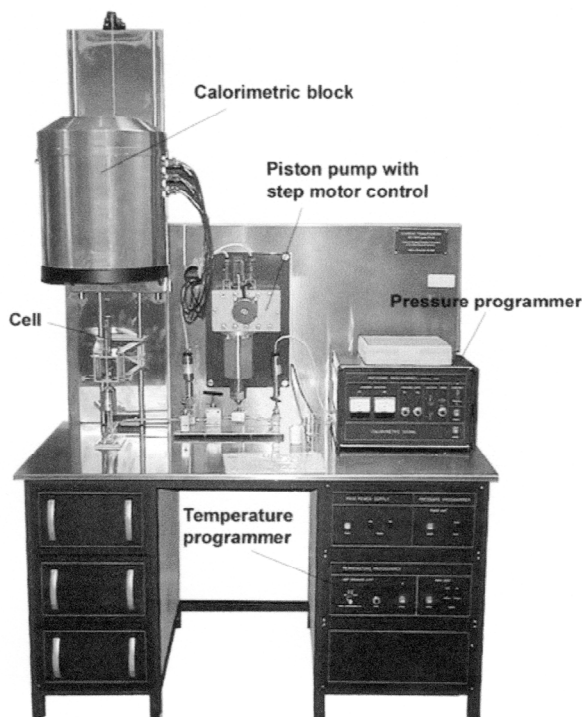


Fig. 3. Photography of a standard scanning transitiometer (from BGR TECH, Warsaw). The calorimetric detector which can be moved up and down over the measuring and reference cells (in twin differential arrangement) is shown in the upper position. In this position the cells which are firmly fixed on the stand table are then accessible for loading.

Actually, transitiometry is at the centre of different modes of utilization since with such technique, bulk properties, transitions as well as reactions (for example polymerization) can be advantageously studied. In the case of a non-reacting system which remains in a homogeneous state, both the mechanical and thermal outputs as explained before give straightforward access to pairs of the thermomechanical coefficients. When the system or the material sample goes through a chemical reaction or a phase change, the recorded information yields the corresponding heat and pVT characteristics. In the case of polymer synthesis, a scanning transitiometer is used as an isothermal reaction calorimeter, the advancement of a polymerization reaction being accurately monitored through the rigorous control of the thermodynamic parameters [7]. Two reaction cells - measuring and reference - are made as equal as possible to each other and they operate in common surroundings in a so-called *twin differential* arrangement.

The thermocouples composing the fluxmeters serve as a heat conduction path between cell walls and the block. To gather additional information on a reaction, the reaction can be coupled with other analytical devices (e.g., on-line FTIR, particle sizing

probes, turbidity probes, pH or other ion selective probes, etc). A photographic presentation of a transitiometer is given in Figure 3.

27. 3. Selected results

Performances and advantages of scanning transitiometry are well demonstrated by typical applications in several important fields: *i*) asymmetric fluid mixtures and petroleum fluids; *ii*) transitions of polymer systems under various constraints (temperature, pressure, gas sorption) including first-order phase transitions [8, 9] and biopolymer gelatinization [10-13]; *iii*) polymer thermophysical properties and influence of gas sorption [9, 14]. In what follows three illustrative examples have been selected namely: in the petroleum industry, in polymer science and in food science.

27.3.1. Petroleum Industry

The oil industry, where petroleum products and associated fluids of different nature with multicomponent and complex compositions present a large variety of phases and phase equilibria, is certainly the domain by excellence for scanning transitiometry applications. The ongoing determinations of the thermophysical properties (C_P , α_P , κ_T) over extended p and T ranges of newly developed fuels (including biofuels) will not be reported here. Instead, two other completed studies are worth to report: *i*) appearance of the solid phase in asymmetric binary systems and *ii*) precipitation of heavy cuts in asphaltenic fluids under p and T conditions of deep underground reservoirs.

The investigation of asymmetric systems *i.e.* binary mixtures of two components having large difference in the molecular size is of interest in relation with the solid precipitation or flocculation of heavy components in high pressure reservoir fluids containing large concentrations of light components like methane. Typically these systems exhibit a three-phase equilibrium curve (solid-liquid-vapor) with a high temperature segment. Scanning transitiometry allows to precisely detecting up to high pressures the transition through the three-phase line in both directions by varying any of the state variables (p , V , T). The method was tested [6] with the system {tetracosane + methane} by comparing with the reference data measured using the conventional visual method [15]. The Figure 4 shows the very good agreement of data obtained with scanning transitiometry and the indirect method based on the visual observation of phase boundaries.

Precipitation or flocculation of asphaltenes is a major concern for different activities in the petroleum industry such as extraction, production and transport. Due to their complex molecular structures, asphaltenes constitute large aggregates which contribute to a large extent to the stability of crude oils. Asphaltenes are identified by their insolubility in *n*-alkanes and their solubility in aromatic solvents like toluene. Their particular molecular and thermodynamic properties are such that under slight changes of p and T asphaltenes can flocculate in the crude oil causing the formation of heavy deposits. Therefore it is essential to document the thermodynamic comportment of asphaltenes undergoing temperature and pressure differences between in-well and surface conditions. To this end scanning transitiometry was used to investigate the thermodynamic behavior of asphaltenic fluids under in-well p and T conditions.

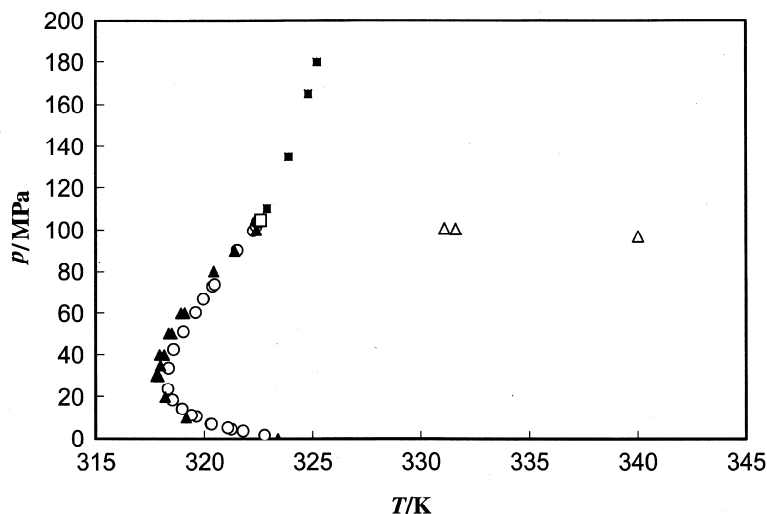


Fig. 4. Phase equilibria in the system {tetracosane + methane}. ▲, Our work on the three-phase equilibrium [6]. ○, Three-phase equilibria data of Flöter et al. [15]. □, Second critical endpoint. ■, Our work for the high pressure equilibrium (solid + fluid + liquid) [6]. Note that the three (open triangles) points correspond to a near critical liquid-vapor isopleth at 0.04 mole fraction of tetracosane

The study of real (live) fluids was a challenge [16] as regards the introduction of an asphaltenic fluid (provided in a high pressure cylinder by TOTAL France) into the transtiometric cell under isobaric conditions from the high pressure cylinder. Effectively, the fluid has been collected and kept in the cylinder under the in-well conditions, thus the isobaric transfer must be carefully made to prevent any drop in pressure which would inevitably cause precipitation/flocculation of asphaltenes. A special setup was designed to insure the isobaric transfer of the fluid into the active calorimetric detector [16]; this was facilitated by the use of mercury as hydraulic fluid to pressurize the whole (transfer setup and calorimetric cell) system and push the fluid into the calorimetric cell during the operation of transfer. It was then possible to bring the fluid sample in the calorimetric cell to the nominal p , T in-well conditions. Cycles of compression/decompression could be performed over extended time periods in order to allow the system to relax and return to equilibrium and observe possible precipitation/flocculation of asphaltenes. The isothermal (at 430 K) thermograms obtained with a given asphaltenic fluid (61 MPa and 430 K respectively) are presented in Figure 5. The shallow exothermal maximum shown for the first expansion would correspond to the precipitation/flocculation of asphaltenes; for the second decompression (after recompression) only a small effect is visible and for the fourth decompression under the same conditions no more such effect appears. It can be concluded that after few decompression/re-compression the original asphaltenic fluid behaves as a “normal” fluid [4] since the asphaltenes have precipitated and were not redissolved by successive recompressions during the time frame of the experiment. These preliminary investigations have shown the advantage of scanning transtiometry to characterize real (live) oils and systematic studies are underway on heavy oils from different geological origins.

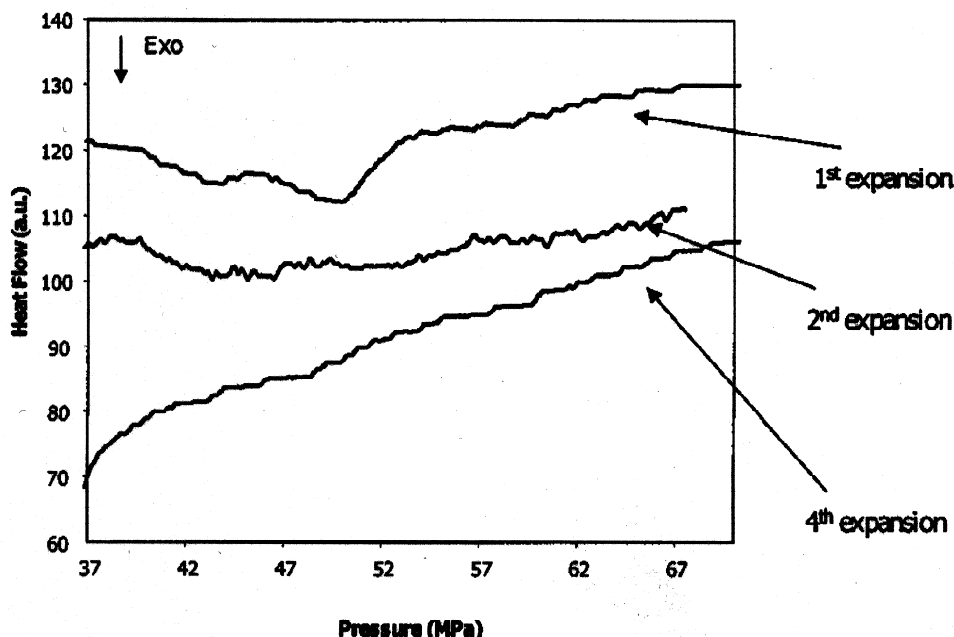


Fig. 5. Thermograms obtained after cycling successive decompressions and recompressions. During the first expansion the exothermic effect which would correspond to the precipitation / flocculation of asphaltenes clearly appears; it is slightly visible for the second expansion and completely disappears after the third one. The shape of the fourth expansion thermogram is similar to what is observed for a simple fluid [4].

27. 3.2. Polymer science

When dealing with polymer materials, the glass transition must be unambiguously established in particular with respect to its dependence with temperature, pressure and plasticizers, especially high pressure gases. Although the following examples might appear as simply relevant of “applied” science, they imply fundamental approaches in terms of developing specific instruments and associated methodologies to investigate the glass transition temperature T_g which is the pivotal transition to understand and control for the proper processing of polymeric materials. Herein, an account of the influence on T_g of p , T and gas solubility, is reported.

The thermodynamic principle of scanning transitiometry is based on the Maxwell equality

$$\left(\frac{\partial V}{\partial T}\right)_p = -\left(\frac{\partial S}{\partial p}\right)_T \cong -\frac{1}{T}\left(\frac{dQ}{dp}\right)_T \quad (1)$$

Thus, if a sample of a polymer of a mass m_s is placed in the calorimetric vessel and is submitted to a pressure variation dp , then the heat exchanged in such a process, dQ_{pl} , is defined by the following equation

$$dQ_{pl} = m_s T \left(\frac{\partial V_s}{\partial T} \right)_p dp \quad (2)$$

On the other hand, if the substance contained in the calorimetric vessel is in the fluid state and the pressure is exerted through the fluid itself then the real mass of the fluid sample contained in the calorimetric vessel is changing along with the pressure variation and is equal to V_E/V_s , where V_E is the active internal volume of the calorimetric vessel accessible for the fluid and V_s is the specific (or molar) volume of that fluid. Thus, in this case the thermal effect, dQ_{fl} , associated with the pressure variation is defined by the following equation

$$dQ_{fl} = -\frac{V_E}{V_s} T \left(\frac{\partial V_s}{\partial T} \right)_p dp = V_E T \alpha_p dp \quad (3)$$

where $\alpha_p = 1/V_s (\partial V_s / \partial T)_p$ is the isobaric thermal expansivity of the fluid. Then, if a polymer sample is placed in the calorimetric vessel and is compressed or decompressed by intermediary of a fluid like a gas or mercury, the total thermal effect will be composed of the main three following terms: compression of the solid (equation 2), compression of the fluid phase (equation 3) and “pure” interaction of the fluid with the polymer. Of course it is assumed that there are no state or phase transitions in both the fluid and the polymer within the experimental p, T range.

The thermal calibration (energy and temperature) was done with the use of benzoic acid. The thermomechanical calibration, especially the determination of the internal active volume V_E (equation 3) was done with the use of nitrogen, for which the thermal expansion is known from its equation of state.

A) Glass transition temperatures of elastomers under high pressure

The glass transition temperature is affected by pressure since an increase of pressure causes a decrease in the total volume and an increase in T_g is expected due to the decrease of free volume. This result is important in engineering operations such as molding or extrusion, when operations too close to T_g can result in a stiffening of the material. Investigation of the glass-transitions of polymers under pressure is not a simple problem, especially in the case of elastomers of which T_g 's are usually well-below the ambient temperature. In the case of scanning transitiometry the traditional pressure-transmitting fluid, mercury, must be replaced since its crystallization temperature is relatively high, i.e. 235.45 K. Then the choice of the replacement fluid is again a challenge [17] because it should be chemically inert with respect to the investigated sample. Also, values of its thermomechanical coefficients, compressibility, κ_T , and thermal expansivity, α_p , should be smaller than those of the investigated sample. An additional difficulty in the investigation of second order type transitions is the relatively weak effect measured. It is well-known that the amplitude of the heat flow at the glass transition T_g increases with the temperature scanning rate while the time-constant of heat flow type calorimeters, like scanning transitiometers, imposes temperature scan rates which are slow compared to typical DSC scan rates.

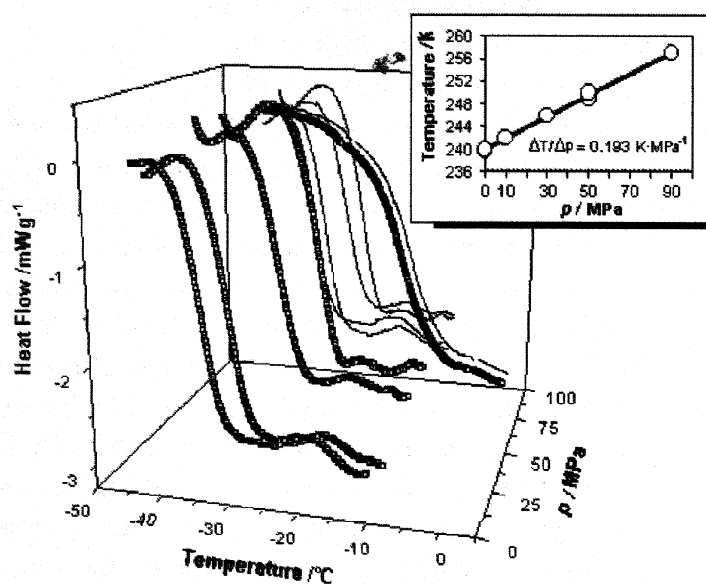


Fig. 6. Illustration of the scanning transitiometry technique for the investigation of polymers glass transition temperature at low-temperature and high pressure. The typical thermograms (heat flow vs T) for the transition domain of a vulcanized rubber are shown for different pressures. The pressure coefficient of the glass transition temperature is given in the inset.

For the present measurements silicon oil was used instead of mercury as the hydraulic pressurizing fluid, and the polymer sample was placed in a lead (soft metal) ampoule. Test measurements were made on polyvinyl acetate for which the $\Delta T_g/\Delta p$ coefficient was found to be $0.212 \pm 0.002 \text{ K MPa}^{-1}$ in good agreement with the literature value 0.22 K MPa^{-1} [18]. The calorimetric traces obtained with the same method for a poly(butadiene-*co*-styrene) vulcanized rubber [19] during isobaric scans of temperatures ranging from 218.15 K to 278.15 K at 0.4 K min^{-1} are shown in Figure 6. The Figure 6 shows also the evolution of T_g at different pressures, at 0.25, 10, 30, 50, and 90 MPa, respectively: T_g increases linearly with pressure with a $\Delta T_g/\Delta p$ coefficient of $0.193 \pm 0.002 \text{ K MPa}^{-1}$. It should be noted that T_g is expressed as the temperature corresponding to the peak of the first derivative of the heat flux (i.e. the inflexion point of the heat flow).

b) Glass transition temperature of polystyrene modified by high pressur methane

There is not much information available in the literature on calorimetric study of plasticization of polymers at high pressures, above say 50 MPa, induced by gases. Plasticization is well characterized by the shift of the temperature of the glass transition, T_g . Actually, when pressure is induced by a gas, both plasticization and hydrostatic effects contribute to the shift of T_g . If plasticization tends to lower T_g because of the gain of mobility of the polymeric chains, the hydrostatic effect raises it in diminishing the free volume. Methane (CH_4) is assumed to be a non-plasticizing gas but, our results show that, at higher pressures, plasticization overtakes again the hydrostatic effect, due to a probably higher solubility of the gas in polystyrene (PS) at higher pressures; this kind of behavior has been suggested for high enough pressures [20]. The plasticization of PS using CH_4

seems to be possible but it is necessary for this to apply high pressure, *i.e.* 200 MPa, in order to obtain approximately the same shift of the T_g as with ethylene (C₂H₄) under 9,0 MPa! In this respect CH₄ cannot really be considered as a good plasticizing gas.

c) Shift of the glass transition temperature by high pressure gases

An important aspect of polymer foaming is certainly the “easiness” of the blowing agent to enter, to dissolve and to diffuse into the polymer matrix. Two parameters, T and p , are essential to control these phenomena. The nature and properties of the polymer and of the fluid play evidently a major role. In this context, the physical state of the polymer must be appropriately modified to undergo plasticization; this optimal condition for having the “blowing” effect taking place depends upon the glass transition temperature T_g . Plasticization depends on all the thermodynamics variables and parameters listed above. In particular, it is necessary to know to what extent T_g is advantageously decreased in order to optimise the foaming process. From a practical point of view the ΔT_g shift should be accurately determined or predicted. Moreover, many properties can be correlated with the glass transition temperature depression ΔT_g due to plasticization. In order to predict the ΔT_g the model of Chow [21] was selected. The calculations using the model of Chow were made using experimental data of solubilities directly measured with a new technique combining a vibrating wire (VW) weight sensor and a pVT setup [22].

Chow has proposed a relation based on Gibbs and Di Marzio principle (the entropy of the glassy state is zero) to account for the change in T_g due to the sorbed component as follows:

$$\ln\left(\frac{T_g}{T_{go}}\right) = \beta[(1-\theta)\ln(1-\theta) + \theta\ln\theta] \quad (4)$$

where :

$$\beta = \frac{zR}{M_p \Delta C_p} \quad \theta = \frac{M_p}{zM_d} \frac{\omega}{1-\omega}$$

T_g and T_{go} are the glass transition temperatures for the polymer-gas system and the pure polymer respectively, M_p is the molar mass of the polymer repeat unit, M_d is the molar mass of the (diluent) gas, R is the gas constant, ω the mass fraction of the gas in the polymer, ΔC_p is the heat capacity change associated with the glass transition of the pure polymer and z is the lattice coordination number. All parameters of the model have physical meanings, except the number z . The value of this parameter may change according to the state of the diluent : $z = 2$ when the diluent is in the liquid state and $z = 1$ for a gas.

In order to compare the model calculations with experimental calorimetric data, polystyrene (PS) samples were modified in a transitiometer used in the present case as a small reactor to modify under equilibrium conditions the polystyrene in presence of a chosen fluid. Modifications of polystyrene have been done in presence of N₂ and CO₂, along isotherms at a given pressure. For these two fluids, a final temperature of 398.15 K and a final pressure of 80 MPa have been attained. The glass transition temperatures T_g 's of modified and non modified PS samples were determined by Temperature Modulated DSC (TMDSC). The solubilities of the different gases were measured using the VW- pVT

sorption technique [22, 29] along different isotherms and the mass fraction of the gas in the polymer was then determined following the equation:

$$\omega = \frac{s}{s+1} \quad (5)$$

s being the solubility of the fluid in the polymer, in mg of fluid/mg of polymer.

Using the values of ω determined for each system PS/gas, the Chow equation (4) has allowed to estimate the variation with pressure, ΔT_g , of the temperature of the glass transition this, along the different isotherms of the sorption measurements. The use of the Chow model is then rather delicate since the choice of the value of z that is to say in fact, the state of the diluent, influences significantly the results. The T_g -shift under CO_2 pressures is spectacular showing the high plasticizing effect of CO_2 . The good agreement of the literature data for PS/ CO_2 with the calculated values [23] as seen in Figure 7 can certainly be explained by the state of the diluent which is most likely in the critical state in the ranges of T and p considered.

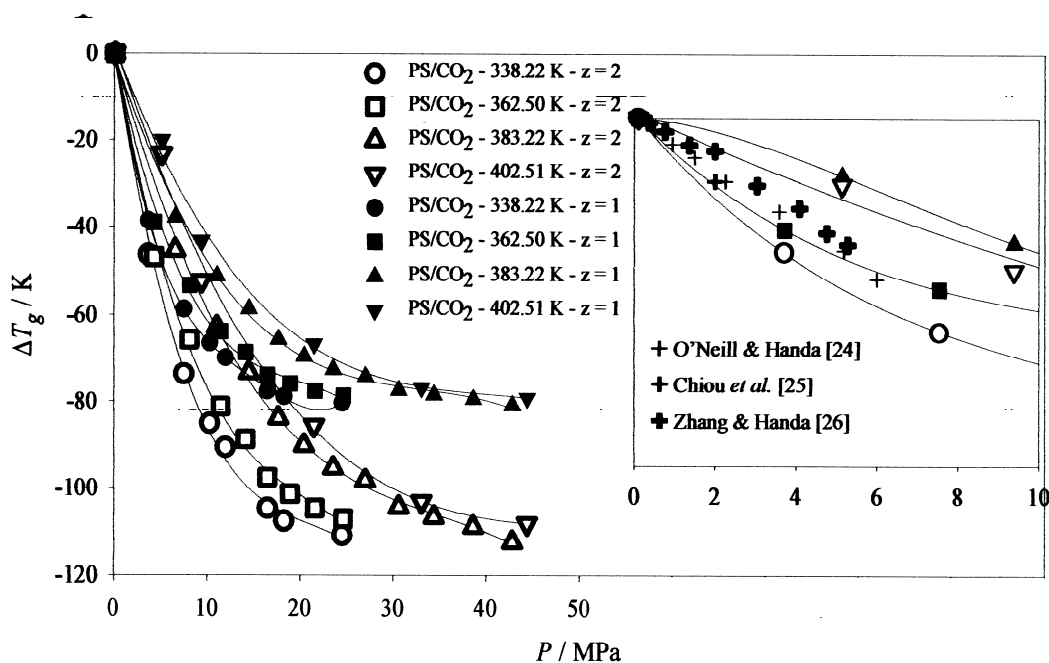


Fig. 7. Variation of the glass transition temperature with pressure for the system polystyrene- CO_2 . Calculations have been made for the four temperatures 338.22, 362.50, 383.22 and 402.51 K. of experimental measurements. Full symbols represent results for $z = 1$ and empty symbols for $z = 2$. Literature values are represented by crosses in the zoom of the graph (the same scale of temperature being kept). Lines are hand drawn through the points.

Effectively, the critical temperature T_c and critical pressure p_c of CO_2 support the hypothesis of the gas being in the near critical region. As a matter of fact, depending on the experimental conditions in the vicinity of the critical point, the fluid can exist in one or the other state (gas or liquid) or even in both. In the present case, literature data for the PS/ CO_2 system have been obtained under a pressure $p \leq p_c$ and at a temperature $T \geq T_c$ for CO_2 ; then two phases of the diluent can coexist in different proportions. Despite the difficulty to

determine exactly the variation of T_g , particularly under supercritical conditions of a diluent fluid, the model of Chow is actually a useful guide in order to predict the variation of the glass transition of a polymer modified by a high pressure fluid. However, the exact determination of the glass transition depression, ΔT_g , becomes more difficult when the pressure increases, specially near and above the critical point of the diluent fluid. This means that when plotting ΔT_g as a function of pressure, the temperature of measurement plays a major role. If we do not take into account this temperature, it is preferable to represent ΔT_g as a function of the mass fraction of the fluid in the polymer.

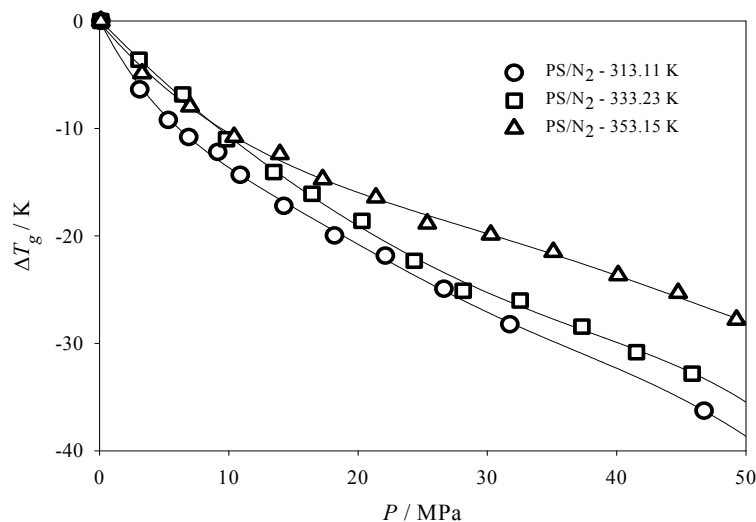


Fig. 8. Variation of the glass transition temperature as a function of pressure for the system polystyrene- N_2 . Calculations have been made for the three temperatures 313.11, 333.23 and 353.15 K of experimental measurements, using $z = 1$. Lines are hand drawn through the points.

Compared to polar CO_2 and because of its non polarizability, N_2 should be a weaker plasticizing agent although as shown in Figure 8 it induces significant shifts of T_g under N_2 pressures [23]. However, N_2 which should be also a good foaming agent is not used in the foaming industry because of the need of too high a pressure to attain the desired depression in T_g .

27.3.3. Food Science

Recent and fast developments in food science result from the large scale use of extruders to process different types of products from biscuits, crackers, breakfast cereals, flours to more elaborate food components and pet food. Actually, food materials are extruded as other materials like polymers for example. Extrusion processes shape the final products in terms of structural organization (fibre like crystallisation, foam, soft or hard species..) in combining elevated temperatures and pressures.

Optimization of extrusion processes requires a detailed knowledge of the properties of the starting ingredients. In this respect, the properties of starch which is a major component of food systems are essential to document, particularly over extended pressure and temperature ranges as well as concerns the water content. In this context, the

contribution of scanning transitiometry to investigate starch-water systems has been recently demonstrated [13, 27]. Figure 9 presents an example of a transitiometric study of a 56% water suspension of wheat starch. Temperature scans have been performed at various pressures while recording simultaneously two output signals, heat flow and the thermal expansion. Interestingly, the endothermic main transition (positive enthalpy) corresponding to gelatinization is associated with a negative volume change, in complete agreement with the Clapeyron equation characterizing the transition

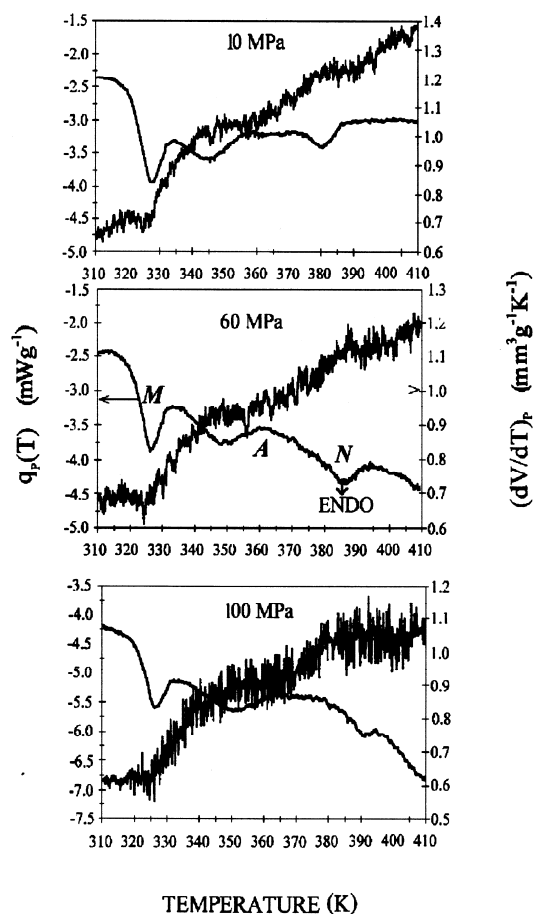


Fig. 9. Transitiometric traces (thermal and mechanical outputs per gram of dry starch) obtained simultaneously *in situ* by scanning temperature at the rate 2.5 mK s^{-1} at three different pressures for a starch-water suspension (56 mass % total water content). The middle graph allows distinguishing between the heat flow q_p (thermal) thermogram and the volume change $(dV/dT)_p$ (mechanical) trace.

27. 4. Concluding Remarks

New developments in calorimetric techniques like Temperature Modulated DSC, (TMDSC), which permits to determine unambiguously glass transition temperatures [28], and in associated techniques like the VW- pVT technique [29] which allows measuring simultaneously the amount of gas entering a polymer sample and the subsequent volume

change of the polymer, have contributed to notably broaden the area of experimental thermodynamics, with incursions in several major domains. In addition, the field of calorimetric techniques has witnessed an impressive impetus with the concept of scanning transitiometry. The main characteristic of scanning transitiometry is its great versatility in the sense that all physical states, homogeneous as well heterogeneous systems can be thoroughly investigated. A special feature is the possibility it gives to take full advantage of the four possible modes of scanning. Remarkably, it is possible after loading the measuring cell to activate either one of the four scanning modes and to shift from one to another without removing or reloading the cell. The possibility to use different hydraulic fluids to pressurize the investigated sample or system is undoubtedly another great advantage. The hydrostatic effect of a neutral fluid like mercury can serve as a reference against which to compare the hydrostatic/plasticization effects of other fluids (liquids or gases). Furthermore, a scanning transitiometer can be used as an instrumented reactor to perfectly control the modifications induced by T , p and the pressurizing fluid as for example for polymer foaming [30] or for self assembling of nanoscale molecular structures [31-33]. The possibility to use supercritical fluids to transmit pressure adds a new feature to the technique which becomes ideally suited to investigate state transitions in various thermodynamic situations. A scanning transitiometer can also be used as a reaction calorimeter in which additional devices (for example reagents feeding capillaries, stirrer, pH and spectroscopic probes) allow to collect complete information on a reacting medium [34-37]. Among other possible fields of applications, biology and biochemistry are important fields where scanning transitiometry should certainly contribute to provide original results.

This technique plays an important role in defining the most probable thermodynamic path to follow in order to in depth investigate a special region of interest in a system undergoing imposed changes or self developing modifications kinetically dependent. In making accessible new data, often impossible to obtain with other known techniques, scanning transitiometry contributes to reinforce the place of rigorous thermodynamics in providing key information to develop theoretical models; a typical illustration being for example the use of recently obtained thermophysical (isobaric thermal expansion) data on fluids to design new equations of state [38,39].

References 27

- [1] *Scanning calorimeters controlled by an independent thermodynamic variable: definitions and some metrological problems.* S.L. Randzio. *Thermochim. Acta*, **89**, 215 (1985).
- [2] *An automated calorimeter for the measurement of isobaric expansivities and isothermal compressibilities of liquids by scanning pressure from 0.1 to 400 MPa at temperatures between 303 and 503 K.* S.L. Randzio, D.J. Eatough, E.A. Lewis, L.D. Hansen. *J. Chem. Thermodyn.*, **20**, 937 (1988).
- [3] *Scanning calorimetry with various inducing variables and multi-output signals.* S.L. Randzio. *Pure and Applied Chem.*, **63**, 1409 (1991).
- [4] *An isothermal scanning calorimeter controlled by linear pressure variations from 0.1MPa to 400 MPa. Calibration and comparison with the piezothermal technique.* S.L. Randzio, J-P. E. Grolier, J.R. Quint. *Rev. Sci. Instrum.*, **65**, 960 (1994).

- [5] (a) *Procédé et dispositif pour l'étude des transitions physicochimiques et leur application*. S.L. Randzio, J-P. E. Grolier, J. Zaslona, J.R. Quint. French Patent 91-09227, Polish Patent P-295285. (b) *Procédé et dispositif pour l'étude de l'effet d'un fluide supercritique sur la transition d'un matériau de l'une à l'autre des deux phases condensées et leur application au cas d'un matériau polymère*. S.L. Randzio, J-P. E. Grolier. French Patent 97-15521. See also the web site www.transitiometry.com.
- [6] *Transitiometric determination of the three-phase curve in asymmetric binary systems*. S.L. Randzio, Ch. Stachowiak, J-P. E. Grolier. *J. Chem. Thermodyn.*, **35**, 639 (2003).
- [7] *Isothermal fluxmetry and isoperibolic calorimetry in anionic lactames polymerization in organic media*. F. Dan, J-P.E. Grolier. *Setaram News*, **7**, 13 (2002).
- [8] *Transitiometric analysis of pressure effects on various phase transitions*. S.L. Randzio. *J. Therm. Anal. Cal.*, **57**, 165 (1999).
- [9] *The use of scanning transitiometry to investigate thermodynamic properties of polymeric systems over extended T and p ranges*. J-P.E. Grolier, F. Dan, S.A.E. Boyer, M. Orłowska, S.L. Randzio. *Int. J. Thermophys.*, **25**, 297 (2004).
- [10] *Re-examination of phase transformations in the starch-water systems*. S.L. Randzio, I. Flis-Kabulska, J-P.E. Grolier. *Macromolecules*, **35**, 8852 (2002).
- [11] *Influence of fiber on the phase transformations in the starch-water system*. S.L. Randzio, I. Flis-Kabulska, J-P.E. Grolier. *Biomacromolecules*, **4**, 937 (2003).
- [13] *Transitiometric in situ measurements of pressure effects on the phase transitions during starch gelatinization*. M. Orłowska, S. L. Randzio, J-P.E. Grolier. In *Advances in High Pressure Bioscience and Biotechnology* (R. Winter ed.), Springer Berlin, 393 (2003).
- [14] *Supercritical transitiometry of polymers*. S.L. Randzio, J-P. E. Grolier. *Anal. Chem.*, **70**, 2327 (1998).
- [15] *High pressure solid-fluid and vapour-liquid equilibria in the system (methane + tetracosane)*. E. Flöter, Th. W. De Loos, J. de Swan Arons. *Fluid Phase Equilib.*, **127**, 129 (1997).
- [16] *Transitiometric investigation of asphaltenic fluids under in-well temperature and pressure conditions*. Ch. Stachowiak, J-P. E. Grolier, S.L. Randzio. *Energy & Fuels*, **15**, 1033 (2001).
- [17] *High pressure-low temperature calorimetry. I. Application to the phase change of mercury under pressure*. F. Dan, J-P. E. Grolier. *Thermochim. Acta.* **446**, 73 (2006).
- [18] *The effect of pressure on glass temperature and dielectric relaxation time of polyvinyl acetate*. J. M. O'Reilly. *J. Polym. Sci.* **57**, 429 (1962).
- [19] *Calorimetric measurements of thermophysical properties for industry*. J-P.E. Grolier, F. Dan. In *Chemical Thermodynamics for Industry* (T. Letcher, ed.), The Royal Society of Chemistry Oxford, 144 (2004).
- [20] *Modification of polystyrene glass transition by high pressure methane*. M. Ribeiro, L. Pison, J-P. E. Grolier. *Polymer*, **42**, 1653 (2001).
- [21] *Molecular interpretation of the glass transition temperature of polymer-diluent systems*. T.S. Chow, *Macromolecules*, **13**, 362 (1980).
- [22] *Modification of the glass transitions of polymers by high pressure gas solubility*. S.A.E. Boyer, J-P. E. Grolier. *Pure and Applied Chem.*, **77**, 593 (2005).
- [23] J-P. E Grolier. Unpublished results.

- [24] *Plasticization of polystyrene by high pressure gases: A calorimetric study.* M.L.O'Neill, Y.P. Handa. In *Assignment of the Glass Transition* (R.J. Seyler, ed.) ASTM, Philadelphia, 165 (1994).
- [25] *Plasticization of glassy polymers by CO₂.* J.S. Chiou, J.W. Barkow, D.R. Paul. *J. Appl. Polym. Sci.*, **30**, 2633 (1985).
- [26] *An in situ study of plasticization of polymers by high pressure gases.* Z. Zhang, Y.P. Handa. *J. Polym. Sci., Part B : Polym. Phys.* **36**, 977 (1998).
- [27] *Simultaneous and in situ analysis of thermal and volumetric properties of starch gelatinization over wide pressure and temperature ranges.* S.L. Randzio, M. Orłowska. *Biomacromolecules*, **6**, 3045 (2005).
- [28] *Temperature modulated DSC for the investigation of polymer materials: a brief account of recent studies.* M. Ribeiro, J-P.E. Grolier. *J. Therm. Anal. Cal.*, **57**, 253-263 (1999).
- [29] *Simultaneous measurement of the concentration of a supercritical gas absorbed in a polymer and of the concomitant change in volume of the polymer. The coupled VW-pVT technique revisited.* S.A.E. Boyer, J-P.E. Grolier. *Polymer*, **46**, 3737 (2005).
- [30] *Supercritical {gas-polymer} interactions with applications in the petroleum industry. Determination of thermophysical properties.* S.A.E. Boyer, M-H. Klopffer, J. Martin, J-P. E. Grolier. *J. Appl. Pol. Sc.*, **103**, 1706 (2006).
- [31] *Isotropic transition behavior of an amphiphilic di-block copolymer under pressure using carbon dioxide and mercury as pressure medium.* S.A.E. Boyer, J-P.E. Grolier, L. Pison, C. Iwamoto, H. Yoshida, T. Iyoda. *J. Therm. Anal. Cal.*, **85**, 699 (2006).
- [32] *Effect of interface on thermodynamic behavior of liquid crystalline type amphiphilic di-block copolymers.* S.A.E. Boyer, J-P. E. Grolier, H. Yoshida, T. Iyoda. *J. Pol. Sci. B: Pol. Phys.*, **45**, 1354 (2007).
- [33] *Effect of CO₂ pressure on isotropic transition of amphiphilic side-chain type liquid crystalline di-block copolymers.* T. Yamada, S.A.E. Boyer, T. Iyoda, H. Yoshida, J-P. E. Grolier. *J. Therm. Anal. Cal.*, **89**, 717 (2007).
- [34] *Spectrocalorimetric screening for complex process optimization.* F. Dan, J-P.E. Grolier. In *Chemical Thermodynamics for Industry* (T. Letcher, ed.), The Royal Society of Chemistry Oxford, 88 (2004).
- [35] *New developments and applications in titration calorimetry and reaction calorimetry.* F. Dan, M.H. Hamed, J-P. E. Grolier. *J. Therm. Anal. Cal.*, **85**, 531 (2006).
- [36] *The use of advanced calorimetric techniques in polymer synthesis and characterization.* J-P. E. Grolier, F. Dan. *Thermochimica Acta*, **450**, 47 (2006).
- [37] *Advanced calorimetric techniques in polymer engineering.* J-P.E. Grolier, F. Dan. In *Polymer Reaction Engineering* (H-U. Moritz, W. Pauer, Eds.), Macromolecular Symposia 259, 371 (2007).
- [38] *Thermodynamic testing of equations of state of dense simple liquids.* S.L. Randzio, U.K. Deiters. *Ber. Bunsenges. Phys. Chem.*, **99**, 1179 (1995).
- [39] *A combined determination of phase diagrams of asymmetric binary mixtures by equations of state and transitiometry.* U.K. Deiters, S.L. Randzio. *Fluid Phase Equilib.*, **260**, 87 (2007).



Historical building of the
Institute of Physics and
modern construction of the
Technological Centre



NEW TECHNOLOGIES
RESEARCH CENTRE
UNIVERSITY
OF WEST BOHEMIA



Advertisement

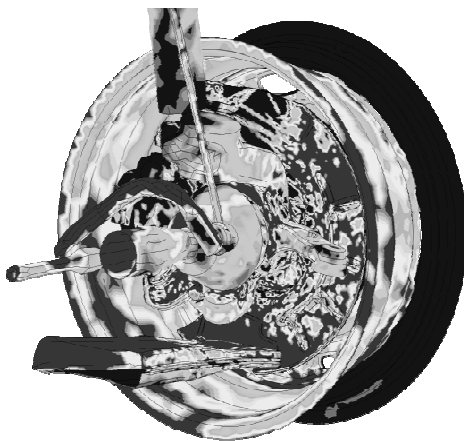
New Technologies - Research Centre in the Westbohemian Region

The New Technologies Research Centre is the institution of the West Bohemia University for the applied research and the transfer of technologies. Moreover, its employees have also the educational work on the university faculties and are the supervisors of diploma and doctoral thesis at the departments of mechanics, physics and materials.



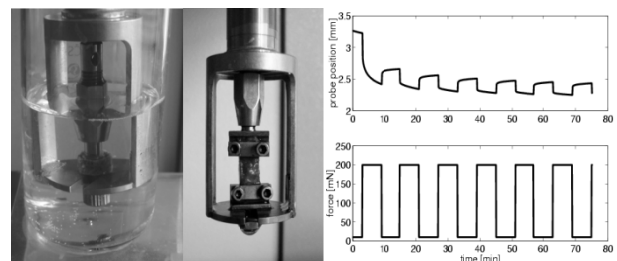
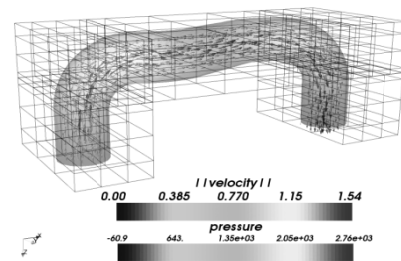
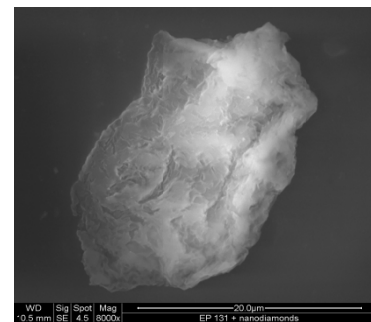
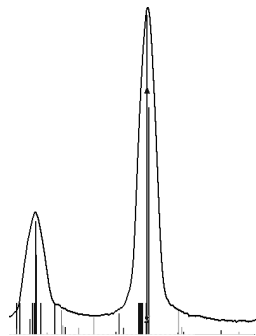
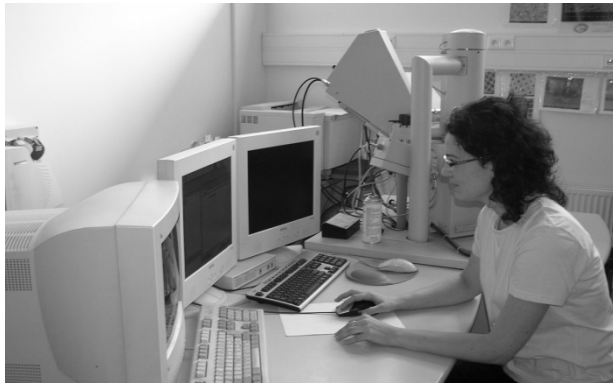
Laboratory of thermomechanical and thermal analysis is an all-inclusive focal point recently equipped by TA Instruments to turn into a top thermal laboratory in the European frame (from left Dr. Bronislav Foller, head of polymer department, Dr. Peter Martinec, manager, Prof. Jaroslav Šesták, program auspice and Doc. Miroslav Holeček, director).

The Research Centre manages modern instrumentation used mainly for investigating various material properties with ensuing material production. It develops successfully material research in the field of new perspective resources (such as materials for barrier-layer photocells, polymer and biomaterials), advanced laser techniques used for modification of classical materials, etc. It intensively pursues the development in the new modern built laboratories (laboratory of thermophysical measurements, for the research of structural properties of thin-film materials, etc.). All research fields are supported by highly sophisticated computational simulations.



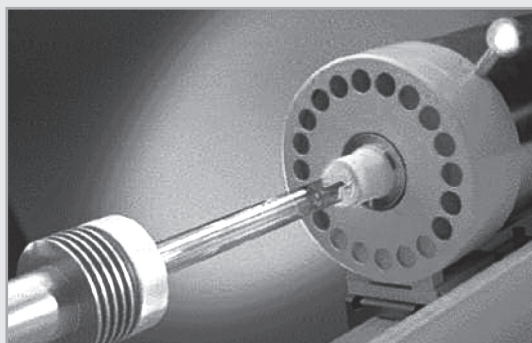
One-third of the Research Center costs is covered by industry orders and the two-thirds from the projects foundation through the grants by both the Czech Republic and the European Union. The Research Centre has specific, mostly permanent contacts and collaboration with more than 50 industrial subjects maintaining also interactions with various institutes of the Academy of Science and of Universities.

Welcome to our sophisticated laboratories



New Technologies Research Centre:
Your partner in research, development and
innovations in industrial applications

Leading Thermal Analysis



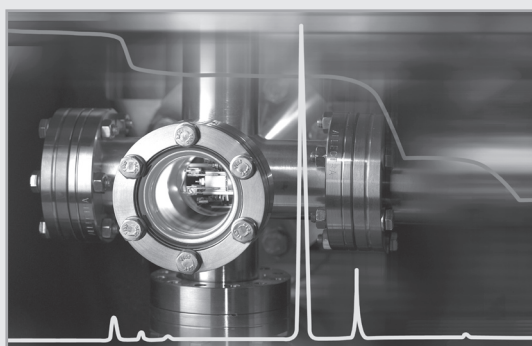
Dilatometry (DIL)

- Excellent CTE Repeatability
- Unmatched Reproducibility
- Outstanding Accuracy
- Adjustable Contact Pressure
- Thermostatic Control
- Broadest Temperature Range



Simultaneous Thermal Analysis (TG-DSC)

- The World's First Nano-Thermobalance
- Vacuum Tight - Optimal Atmosphere Control
- Automatic Sample Changer for up to 20 Samples
- Excellent Long-Term Stability
- Maximum Flexibility
- Wide Range of Accessories



Evolved Gas Analysis (EGA)

- Single and Double Step Pressure Reduction
- Perfect Gas Flow Conditions
- Top Line Capillary Coupling
- Fully Integrated TA-MS Software
- Fast Parameter Input for Routine Experiments
- Versatile Programming for Research Work

NETZSCH

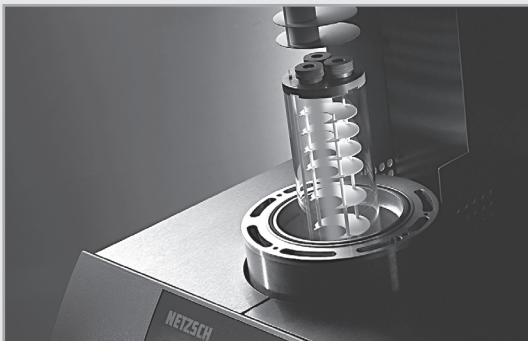
NETZSCH-Gerätebau GmbH
Wittelsbacherstraße 42 · 95100 Selb/Germany
Phone: +49 9287 881-0 · Fax: +49 9287 881-505
E-mail: at@netsch.com

www.netzsch.com



Heat Flow Meter (HFM) - Thermal Conductivity

- Insulations, fibre, foam boards
- Large sample sizes
- Fast and easy to use
- QC estimates in under 15 minutes
- Patented plate temperature control system
- Stand alone or PC controlled evaluations



Laser Flash Analysis (LFA)

- Thermal diffusivity, specific heat, thermal conductivity
- Safe (laser class 1)
- Small sample sizes, easy sample preparation
- Simple insertion of the sample
- Static, dynamic oxidizing, inert gas atmosphere or vacuum measurements possible
- Comprehensive software including all known calculation models



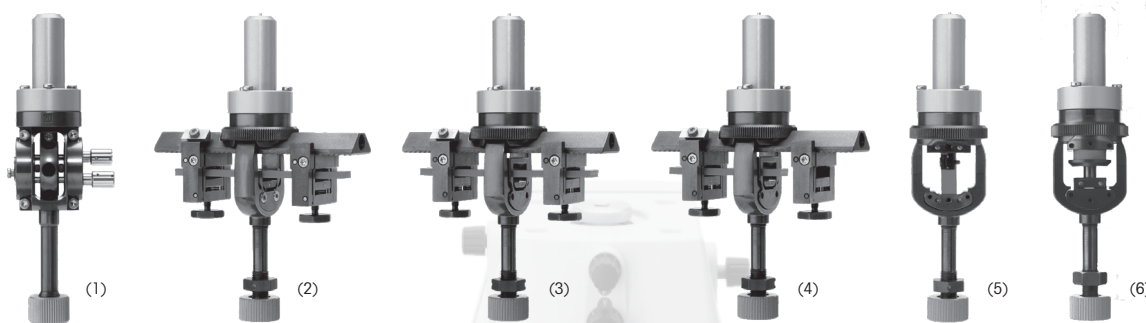
Guarded Hot Plate (GHP) - Thermal Conductivity

- Motorized hoist for the vacuum housing and hot/cold plates
- High resolution temperature measurement using separately calibrated temperature sensors
- Guaranteed mechanical stability of the plates even at minimum or maximum service temperature
- Newly-developed computerized temperature control system for increased test speed
- Flexible sample sizes

METTLER TOLEDO

Dynamic Mechanical Analysis

Dynamic mechanical analysis (DMA) is used to measure the mechanical and viscoelastic properties of materials as a function of temperature, time and frequency when they are subjected to a periodic stress.



Important application areas include:

- thermoplastics
- elastomers
- paints and lacquers
- composites
- pharmaceutical
- ceramic materials
- metals
- thermosets
- adhesives
- films and fibers
- foodstuffs
- fats and oils
- constructional materials

Summary of the following effects and properties that can be investigated with DMA:

- viscoelastic behavior
- glass transition
- damping behavior
- viscous flow
- phase separations
- changes in morphology
- filler activity
- curing reactions
- vulcanization systems
- relaxation behavior
- mechanical modulus
- softening
- crystallization and melting
- gelation
- composition of blends
- material faults
- cross-linking reactions

Six different deformation modes

The DMA/SDTA861e has six different deformation modes:

- Shear (1)
- 3-point bending (2)
- Dual cantilever (3)
- Single cantilever (4)
- Tension (5)
- Compression (6)

Temperature

Range	-150 ... 500 °C
-------	-----------------

Force

Range	0.001 ... 40 N, (12, 18 or 40 N)
-------	----------------------------------

Frequency

Range	0.001 ... 1000 Hz
-------	-------------------

Measurement modes

Bending 3-point, Dual cantilever, Shear, Tension, Compression



Quality certificate Development, production and testing according to ISO 9001. Environment management system according to ISO 14001.

Service worldwide Our large service network is among the best in the world and ensures maximum availability and service life of your product.

Mettler-Toledo, s.r.o.

Trébohostická 2283/2, 100 00 Prague 10, Czech Republic
Tel.: +420 272 123 150, Fax: +420 272 123 170
E-mail: sales.mtcz@mt.com



METTLER TOLEDO

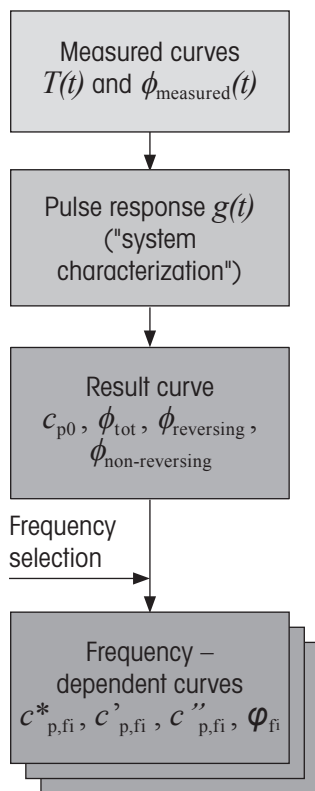
www.mt.com/ta

For more information

METTLER TOLEDO

TOPEM[®] – multi-frequency TMDSC technique

TMDSC (Temperature Modulated DSC Technique) methods allow both temperature-dependent and time-dependent processes to be separated. The basic idea of TOPEM[®] is to overlay the isothermal or ramped temperature with a time series of stochastic (random) temperature pulses of different durations. The new advanced multi-frequency temperature modulation technique, uses a large number of different frequencies (broadband).



Flow diagram of the TOPEM[®] evaluation

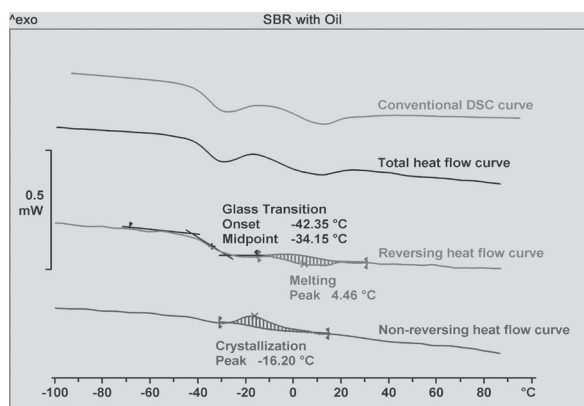
Features and benefits

- **One measurement** – simultaneous measurement of sample properties as a function of time and temperature over a large frequency range
- **c_p determination from the pulse response** – very accurate determination of the quasi-static heat capacity
- **Simultaneous high sensitivity and high resolution** – allows the measurement of low energy transitions and/or close-lying temperature-dependent effects
- **Separation of reversing and non-reversing processes** – heat capacities can be determined with unrivaled quality even if the effects overlap
- **Simplifies interpretation** – frequency-dependent effects (e.g. glass transitions) can be very easily distinguished from frequency-independent effects (e.g. loss of moisture)
- **Extended PEM technique** – eliminates instrumental influences and extends the measurable frequency range
- **Automatic c_p adjustment** – provides accurate frequency-dependent heat capacity values based on one single measurement

SBR elastomer containing a low molecular weight oil

The conventional DSC curve of SBR containing a low molecular weight oil shows overlapping thermal effects that are difficult to identify and properly assign. In contrast, a TOPEM[®] measurement performed at 2 K/min allowed the transitions to be quickly and unambiguously identified.

In the reversing heat flow curve, the glass transition of the elastomer is observed as a characteristic step at -34 °C. In addition, the reversing heat flow curve exhibits an endothermic effect at 4 °C. This can be assigned to the melting of the oil. The non-reversing heat flow shows an exothermic effect at about -16 °C. This is due to the cold crystallization of the low molecular weight constituents.



www.mt.com/ta

For more information

NEW MICROCALORIMETRY PRODUCTS

FROM

TA INSTRUMENTS

...THE WORLD LEADER IN THERMAL ANALYSIS



NANO DSC

- High Sensitivity Scanning Calorimeter
- Protein Denaturation, Stability

NANO ITC

- High Sensitivity Titration Calorimeter
- Protein Binding, Interactions, Kinetics

TAM III

- High Sensitivity Isothermal Calorimeter
- Stability, Compatibility, Morphology

AMEDIS

www.amedis.cz
www.tainstruments.com

AMEDIS, spol. s r. o., Bobkova 786, 198 00 Praha 9,
tel.: +420 28191 8191, fax: +420 28191 7500,
email: sales@amedis.cz



TA INSTRUMENTS



NEW Q SERIES™ THERMAL ANALYSIS



NEW Q2000

- SUPERIOR BASELINE PERFORMANCE
- UNPARALLELED SENSITIVITY & RESOLUTION

NEW Q5000 IR

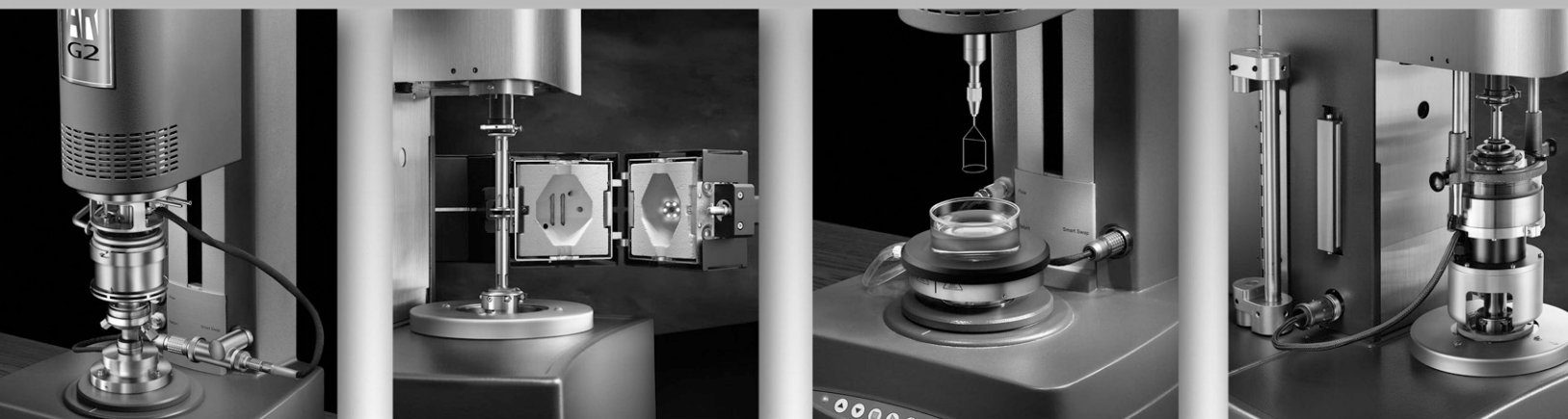
- HIGH SENSITIVITY THERMOBALANCE
- INNOVATIVE IR HEATING FURNACE
- INTEGRATED ELECTROMAGNET

NEW Q5000 SA

- PRECISE HUMIDITY & TEMPERATURE CONTROL
- MULTI-POSITION AUTOSAMPLER

WWW.TAINSTRUMENTS.COM

NEW ARES AND AR RHEOMETERS



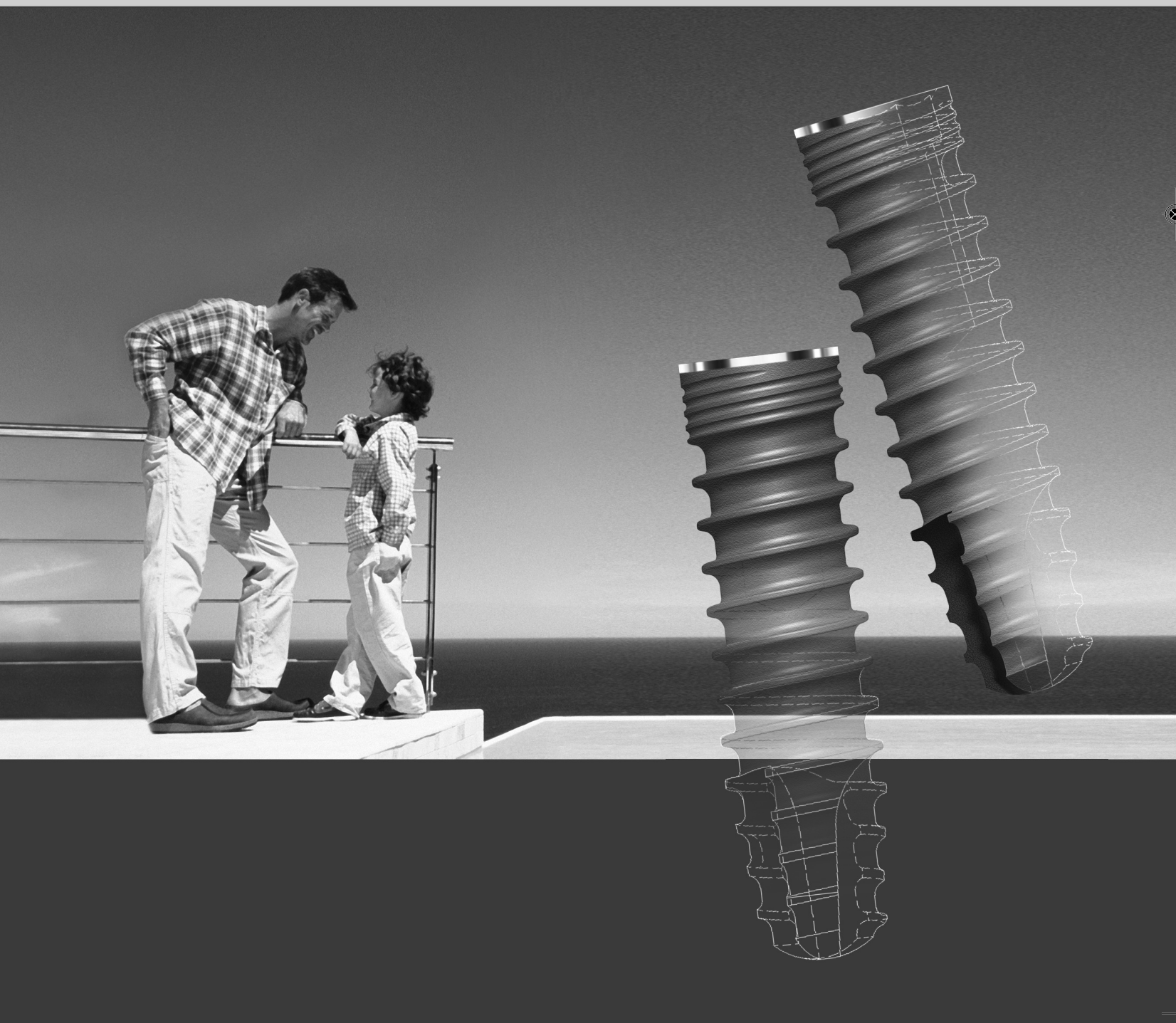
AMEDIS

www.amedis.cz
www.tainstruments.com

AMEDIS, spol. s r. o., Bobkova 786, 198 00 Praha 9,
tel.: +420 28191 8191, fax: +420 28191 7500,
email: sales@amedis.cz



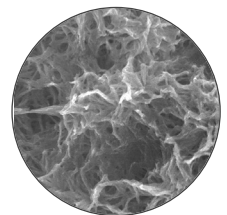
IMPLADENT®
PORESORB®-TCP
IMPLASPIN



Original Concept of Bioactive Surface Predictable Bone Regeneration Bioactive Titanium in Neurosurgery

BIOACTIVE TITANIUM

Nanostructured
Hydrophilic
Osteoconductive



The unique alkali-treated bioactive surface of the STI-Bio-C implant accelerates the process of bone-implant contact formation, providing the implant with increasing secondary stability at the earliest stages of healing. This phenomenon helps to reduce the healing time and enables early and immediate loading to become a predictable and safe treatment protocol.

PORESORB[®]-TCP

Bone regeneration material,
resorbable, synthetic, osteoconductive



LASAK, Ltd.

Papírenská 25, Prague 6, 160 00, Czech Republic
tel: +420 233 324 280, fax: +420 224 319 716
email: lasak@lasak.cz, www.lasak.cz



STUDY PROGRAMMES

accredited in English

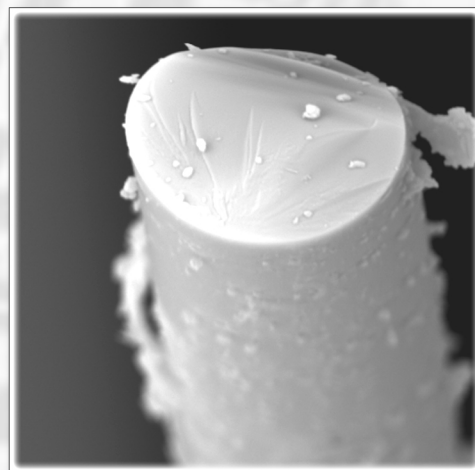
Study for a Bachelor's degree "B.Sc." (3 years)

Textile and Clothes Design
 Textile marketing
 Clothing Production Technology and Management
 Chemical Processing Improvement Technology
 Mechanical Textile Technology



Study for a Master's degree "M.Sc." (2 years)

Textile Technology
 Clothing Production Technology
 Textile Material Engineering
 Chemical Textile Technology
 Non-woven Fabrics



Study for a Doctorate "Ph.D." (3 years)

Textile Technology
 Textile Material Engineering

SCIENTIFIC CENTERS

- national Research Center "Textile"
- center of Excellence "Intelligent textile structures, applications, production, testing"

RESEARCH TOPICS

- new materials (piezo-, nano-, basalt, carbon, chemosensors)
- fibre and textile measuring (termomechanical analysis, electron microscope)
- theoretical modeling of textile structures, processes and systems (USTER TESTER 4)
- development of experimental methods, handle, roughness, comfort measuring (Kawabata system)
- designing products for use of 3D non-woven fabrics
- fabrics finishing, dyeing, final fabrics finishing, colorimetrics, appearance measuring
- production systems simulation, CAD systems
- expert's judgements in textile area
- textile and clothes design, design of clothes and interior accessories
- research in surface characterization by fractal dimension

OLYMPUS

Your Vision, Our Future

CONFOCAL LASER SCANNING
MICROSCOPE

LEXT™

OLS3100

LEXT OLS3100

Confocal Laser Scanning Microscope

**Welcome to the new world
of observation!**

LEXT is a new confocal laser scanning microscope that enables sub-micron 3D imaging of surfaces up to the accuracy of 0.12 μm . With the magnification range from 120x to 14400x, it works between the limits of optical microscopes and scanning electron microscopes (SEM). However, unlike SEM, samples can be observed immediately, without the necessity of using the vacuum chamber. The combination of laser-beam 3D imaging and the color image of light microscopy enables to obtain a realistic image of the examined surface. LEXT can be used, among other things, as a 3D metrological device in industrial production of parts with very narrow tolerances, in the investigation of nanofibers, as well as for the observation of detailed structures of mineral, vegetal and animal surfaces in natural science.





Albert Einstein was professor of theoretical physics in Prague in 1911-1912 and read his lectures in the Clementinum and at the Physical Institute. In the same time a new view of space appeared in the Prague cubistic architecture which is unique in the world.

Ernst Mach lived in Prague and contributed to the development of several parts of physics. Christian Doppler discovered and formulated in Prague the physical effect now known as the Doppler principle.



In the first half of the 19th century, Bernhard Bolzano, mathematician and philosopher, advanced significantly fields of logic, variables, limits, continuity and concept of infinity.



Joseph Stepling, a member of the Jesuit Order at St Clement College, represented a new trend in science based on Newton's work. In 1751 he founded the Clementinum observatory which keeps the longest series of meteorological records in the world.



Johannes Marcus Marci of Kronland (1595-1667), professor and rector of the Charles University, investigated e.g. different properties of light (spectral colors, wave nature, diffraction), being a predecessor of Huygens and Newton.

Frontiers of Quantum and Mesoscopic Thermodynamics

26-29 July 2004, Prague, Czech Republic

Satellite of the 20th General Conference of the EPS Condensed Matter Division organized by Institute of Physics ASCR and Faculty of Mathematics and Physics of the Charles University, Prague

www.fzu.cz/activities/conferences/fqmt04



The high level of science in Prague at that time is confirmed by the sophisticated Prague Astronomical Clock at the Old Town Hall. Its mathematical model was developed by professor Jan Sindel. The clock was made by Mikulas of Kadan in 1410.



The beginning of science in the Czech territory is related to the founding of the Charles University in 1348, the first university in the Central European region. Prague became the capital of the Holy Roman Empire.

Civilization, science, physics - Prague milestones



The Prague Castle was founded around 880, Prague became a centre of Czech Lands.



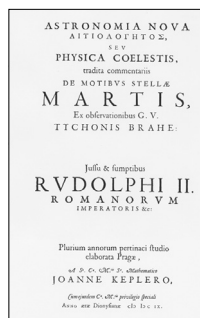
Rudolph II (1576-1612) invited to Prague many significant scientists, painters, architects and musicians. During his reign Prague became the European centre of science and arts.

Tycho Brahe came to Prague in 1599 and began to form a circle of younger co-workers. In 1600 Johannes Kepler arrived.



The paper in which Brahe explained his planetary system was published in Prague.

Tycho Brahe is buried in the Church of Our Lady before Tyn at the Old Town Square.



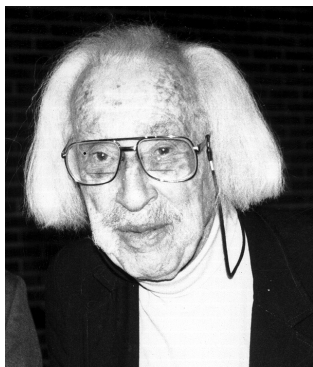
Brahe's high precision astrometric observations of the planets combined luckily with Kepler's theoretical knowledge and resulted in the discovery of law of planetary motion, the most significant and famous scientific result of that time.

Topics:

- Quantum, mesoscopic and (partly) classical thermodynamics
- Quantum measurement and decoherence
- Mesoscopic and nanomechanical systems
- Classical and quantum molecular motors and ratchets
- Quantum Brownian motion
- Quantum computing
- Relevant experiments

Confirmed speakers:

- A. Aharony (Tel Aviv)
- B. L. Altshuler (Princeton)
- R. Balian (CEA-Saclay)
- J. Berger (Karmiel)
- T. Brandes (Manchester)
- M. Buttiker (Genova)
- A. O. Caldeira (Campinas)
- P. Hanggi (Augsburg)
- H. Grabert (Freiburg)
- M. Grifoni (Regensburg)
- D. E. Gross (Berlin)
- F. Haake (Dusseldorf)
- H. Linke (Oregon)
- A. J. Leggett (Urbana)
- A. MacKinnon (London)
- J. E. Mooij (Delft) - tentatively
- R. C. O'Connell (Baton Rouge)
- M. O. Scully (Princeton)
- K. Schwab (Maryland)
- T. Seideman (Northwestern Univ.)
- U. Weiss (Stuttgart)
- A. Zeilinger (Vienna) - tentatively
- W. H. Zurek (Los Alamos) - tentatively



Norbert J. Kreidl
July 3, 1904, + July 11, 1994

The Slovak Glass Society and Czech Glass Society in cooperation with RONA Lednické Rovne, under the auspices of the International Commission on Glass, organize the Norbert Kreidl Memorial Conference. The conference will be dedicated to the 100th birthday anniversary of Prof. Norbert Kreidl. The venue of the conference was selected with respect to the close personal links of Prof. Norbert Kreidl with Lednické Rovne where he spent part of his fruitful life, as well as the family links with Jozef Schreiber, the founder and original owner of the Rona Company. The conference is dedicated to "Building the Bridges between Glass Science and Glass Technology", the message of Norbert Kreidl to next generations of glass scientists and technologists. The program commemorating the work and life of Prof. Norbert Kreidl will be the inseparable part of the conference.

After receiving doctor's degree in physics from Vienna University 1928, Norbert J. Kreidl became interested in a career in the glass industry, i.e., at J. Schreibers Neffen, at the Moravian-Slovakian border. His life changed dramatically in 1938 when he left with his family Czechoslovakia and joined his former teacher, Prof. W. Weyl in the USA starting to work lifelong for Bausch & Lomb Co. Later after retirement he became professor at the Universities of Rutgers, Missouri (Rolla), New Mexico (Santa Fe), and Arizona (Tucson). Kreidl's international prominence and activities were longstanding and exceptional. He already participated at the 1st Glass Congress of the International Commission on Glass (ICG) in Venice in 1933. He was the president of ICG 1969 to 1972. He always fascinated his students and colleagues by the breadth of his knowledge, his way of thinking in larger contexts and his captivating rhetoric. Previous symposium "Present state and future prospects of glass science and technology" was held in Triesenberg (Liechtenstein 1994) honoring the 90th birthday of Professor Norbert J. Kreidl and was chaired by Wolfram Höland, Volker Rheinberger, Osama El-Bayoumi and Donald Uhlmann. The proceedings were published as a separate issue of *Glastech. Ber. Glass Sci. Technol.* 70C, Frankfurt /M 1997 under the editorial of W. Höland and V. Rheinberger.



Norbert Kreidl Memorial Conference



Building the Bridges between Glass Science and Glass Technology



June 23-26, 2004

Trenčín and Lednické Rovne
Slovak Republic

Organized by Slovak Glass Society and Czech Glass Society in cooperation with RONA Lednické Rovne, Alexander Dubček University of Trenčín, Institute of Inorganic Chemistry, Slovak Academy of Sciences, Academy of Sciences of the Czech Republic and Slovak Chamber of Business and Commerce Trenčín, and under the auspices of International Commission of Glass

International advisory board

Ruud Beerkens
Edward N. Boulous
Delbert E. Day
Larry L. Hench
Wolfram Höland
John D. Mackenzie
Robert E. Moore+
Fabiano Nicoletti
David L. Pye
Helmut A. Schaeffer
Peter C. Schultz
Donald R. Uhlmann
Michael C. Weinberg+

Organizing committee

Peter Vačko
Josef Matoušek
Marek Liška
Jaroslav Šesták
Lubomír Němec
Dušan Galusek
Miroslava Arkosiová
Stanislav Foltín
Peter Vrábel
Pavol Šajgalík
Peter Šimurka
Robert Klement

Invited speakers

Salah Arafa
Hervé Arribart
Edward N. Boulous
Richard K. Brow
Alexis G. Clare
Reinhard Conradt
Aleš Helebrant
Larry L. Hench
Jong Heo
Wolfram Höland
Charles R. Kurkjian
Leonid and Ksenia Landa
Huang Liping
Marek Liška
Luboš Němec
Christian Rüssel
Bianca M. Scalet
Helmut A. Schaeffer
Peter C. Schultz
Zdeněk and Jakub Strnad
Jaroslav Šesták
Peter van Nijnatten
Frederic T. Wallenberger
Adrian C. Wright

Past-Chairman



Wolfram Höland

Chairman

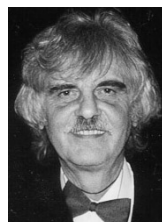


Peter Vačko

Chairmen of the Scientific Committee



Marek Liška



Jaroslav Šesták



Lubomír Němec

Secretary



Dušan Galusek



RONA, a.s.

Schreiberova 365

020 61 Lednické Rovne

Slovenská republika

tel.: 00421/42/463 37 21

fax: 00421/42/469 36 28

e-mail: sales@rona.sk

web: www.rona.sk

RONA

International Journal of Applied Glass Science

A quarterly, peer-reviewed journal devoted to cutting edge of glass research

Published on behalf of The American Ceramic Society and in partnership with Wiley-Blackwell



Edited by DR. L. DAVID PYE

Chief Executive Officer, Dean and Professor of Glass Science, Emeritus, the New York State College of Ceramics at Alfred University; and past President of The American Ceramic Society and the International Commission on Glass.

AIM AND SCOPE

The *International Journal of Applied Glass Science (IJAGS)* is an indispensable source of information dealing with the application of glass science and engineering across the entire materials spectrum. Through the solicitation, editing, and publishing of cutting-edge peer-reviewed papers, *IJAGS* will develop into a highly respected and enduring chronicle of major advances in applied glass science throughout this century. It is of critical value to the work of scientists, engineers, educators, students, and organizations involved in the research, manufacture and utilization of the material *glass*. Guided by an International Advisory Board, *IJAGS* focuses on topical issue themes that broadly encompass the advanced description, application, modeling, manufacture, application, and experimental investigation of glass.

Contributed papers are welcome in the following areas:

- Definition, nomenclature, and description of the vitreous state/non-crystalline solids.
- Properties, experimental and computational methods, and glass forming systems.
- Manufacturing including the properties of glass forming melts, transition range behavior, forming methods, modeling; and quality control.
- Secondary processing including controlled crystallization, tempering, ion-exchange, coatings, and decoration.
- Application and/or utilization of glass in areas such as communications; transportation; medicine; energy; architecture; process control and sensors; optical, electrical, nuclear, mechanical, and chemical systems; archaeology; planetology; and art.
- Characterization by techniques such as optical and electron microscopy; thermal analysis and property measurements; and x-ray and electron diffraction/absorption/scattering.
- Review papers on advanced glass research methods

LEARN MORE ABOUT THIS GROUND-BREAKING NEW JOURNAL

Inquiries can be made directly to members of the Advisory Board or
Dr. L. David Pye, Editor at pye@alfred.edu

Journal CERAMICS-SILIKÁTY

The journal *Ceramics-Silikáty* publishes papers relating to the composition, structure and microstructure, processing, properties and applications of wide range of inorganic non-metallic materials including:

- Glasses
- Ceramics
- Biomaterials
- Cements
- Inorganic Binding Materials
- Other Inorganic Material Groups

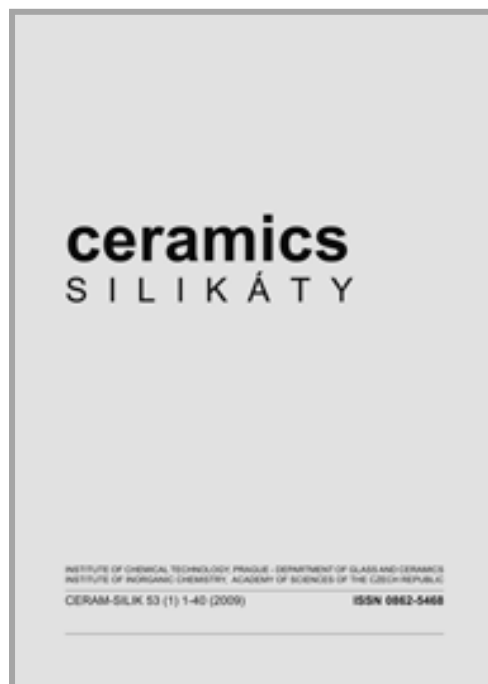
Published by:

- Department of Glass and Ceramics,
(*Institute of Chemical Technology, Prague*)
- Institute of Inorganic Chemistry, v.v.i.,
(*Academy of Sciences of the Czech Republic*)

Subscription: <postmaster@kubon-sagner.de>
<periodika@volny.cz>

Editors: Miloslav Bartuška, Jaroslav Kloužek

Department of Glass and Ceramics
Institute of Chemical Technology, Prague
Technická 5, 166 28 Prague, Czech Republic
E-mail: <klouzekj@vscht.cz>, Tel.: +420 220 444 002, <http://www.ceramics-silikaty.cz>



Czech Glass Society Slovak Glass Society

Some representatives of the Czech Glass Society, *from left*: Dr. Pavel Hrna (USA guest), Doc. Jaroslav Kloužek (Editor of *Ceramics-Silikáty*), Prof. Aleš Helebrant (secretary), Prof. Josef Matoušek (former president), Prof. Jaroslav Šesták



Some representatives of the Slovak Glass Society, *from left*: Prof. Pavol Šajgalík, Prof. Marek Liška (vice-president), Dr. Peter Vačko (former president), Doc. Peter Vrábek, Doc. Peter Šimurka (president).

SCIENCE OF HEAT AND THERMOPHYSICAL STUDIES: a generalized approach to thermal analysis

by

Jaroslav Šesták, Institute of Physics of the Academy of Sciences, Praha, Czech Republic

Book provides a non-traditional bridging of historical, philosophical, societal and scientific aspects of heat with a comprehensive approach to the field of generalized thermodynamics. It involves Greek philosophical views and their impact on the development of contemporary ideas in across-the-board thermal physics.

Covered topics include:



- concept of heat (caloric and entropy), temperature, gradients and generalization of flows (Fick, Fourier, Ohm, Schrödinger's laws).
- thermometry and calorimetry, methods, classification, theory and practice of DTA and DSC, functional applications
- from Greek philosophy, via alchemy to modern physical thoughts
- power laws, logarithmic functions, fractal geometry, applicability
- from classical thermodynamics (thermostatistics) to non-equilibrium conditions and to critical mesoscopic and quantum thermodynamics
- equilibrium and kinetic phase diagrams, T-T-T, T-C, T-H and ΔT -T drawings, aspects of variant and invariant processes, nucleation and glass-formation, T_g , kinetic laws, experimental studies
- route of thoughts: from heat to entropy, exploring order/disorder and related information, societal aspects, thermal efficiency
- chemical kinetics, modeling of reaction mechanism, specificity of non-isothermal studies, activation energy and its determination
- thermal science applied to economy ('econophysics'), efficiency, economic production and generalized Carnot cycle, laws versus feelings, exergy in ecosystems, strategy for survival and evolution

- diffusion interdisciplinarity and quantum diffusion, periodic self-organized reactions, zero-point radiation
- importance of energy science and its influence to societal life, energy resources and sustainability, environmental queries, thermal analysis of atmosphere, green house effect, weather and climate
- modern assessment of thermal analysis instrumentation, calibration, reliable measurements and set up

Audience: This title is recommended to specialists in thermal science as well as the general scientist. It can serve as a reference text for those interested in the many concepts behind thermal physics and specifically thermal analysis and its applications in other areas, providing the reader with a wide scientific and sequential background and framework of thermal sciences, with 712 references.

Contents/Chapters:

1. Some Philosophical Aspects of Scientific Research.
 2. Miscellaneous Features of Thermal Science.
 3. Fire as a Philosophical and Alchemical Archetype.
 4. Concept of Heat in the Renaissance and New Age.
 5. Understanding Heat, Temperature and Gradients.
 6. Heat, Entropy and Information.
 7. Thermodynamics and Thermostatistics.
 8. Thermodynamics, Econophysics, Ecosystems and Societal Behavior.
 9. Thermal Physics of Processes Dynamics.
 10. Modeling Reaction Mechanism: The use of Euclidian and Fractal Geometry.
 11. Non-Isothermal Kinetics by Thermal Analysis.
 12. Thermometry and Calorimetry.
 13. Thermophysical Examinations and Temperature Control
- App.: 500 brief characteristics of some important scholars and scientists



Book christening by Prof. Jiří Fiala, speaker; globetrotter Miroslav Štětina, Senator; the author; Prof. Josef Průša, Rector, Plzeň; Prof. Jiří Málek, Rector, Pardubice; Prof. Václav Pačes, President of Academy.

Bibliographic & ordering Information Hardbound, 486 pages, publication date: NOV-2005,

ISBN-13: 978-0-444-51954-2 ; ISBN-10: 0-444-51954-8,

Price: GBP 120, USD 190, EUR 175

INDEX

- Activators, **568**
Alpha process, **19,406**
Basalt fibers, **498**
Bioactive, **370,539**
Biological glass, **177,186**
Borate glass, **373,522**
Bridging oxygen, **349,364**
Calorimetry, **135,147,163,213,220**
Carnot, **69,80,90**
Chalcogenide, **4,17,220,266**
Cooperative phenomena, **397**
Cryogenic/low temp., **182,193,456**
Crystallization, **2,238,532**
Diagnostics, **486**
Diffusion, **398,416,430,444,486**
Durability, **574**
Electron transport, **335,457**
Equilibrium, **62,85,172,346,373**
Fictive temperature, **11,349**
Foaming, **529**
Food science, **598**
Geopolymers, , **556**
Glass transition,
50,132,221,229,346,390
Healing, **371**
Heat capacity, **125,167**
Heat transfer, **428**
Heterogeneity, **16,394**
History, **32,62,82,98**
Hruby parm., **20,43,190**
Hydration, **561**
Iron oxide, **375,380,526**
Isoconversional method, **250,257**
Kauzmann temp., **13,236,391**
Kinetics, **241,286,308,388**
Magnetic, **375,434**
Metallic glass, **315**
Models, **32,234,249,357**
Moldavites, **209**
Nano-phase, **4,152,309,473**
Natural glass, **158,200**
Nucleation,
179,255,267,290,310,417
Opal, **48,202**
Optical, **48,271**
Oxide glass, **47,344,352,365,522**
Periodic, **440,443**
Phase transition/spinodal, **143**
Phosphate glasses, **328**
Polarizability, **405**
Polymers, **140,150**
Quantum, **437,446,467**
Quasimolar, **105**
Quasiparticle, **432**
Quenching, **10,315,381**
Relaxation, **15,308**
Scanning, **220,286,586**
Stoichiometry, **98,351**
Super/under-cooled, **11**
Temperature, **72,91**
Thermodynamics,
9,39,80,100,344,353
Transformation, **43,118,129**
Transport, **328**
Thermal prop./anal., **40,121,507**
VFTM eq., **14,192,224**
Vibrations, **128,391,415**
Viscosity, **401,414**
Vitrification, **2,26**
Water, **177,188,190**